Climate of the Past

An interactive open-access journal of the European Geosciences Union

20 YEARS

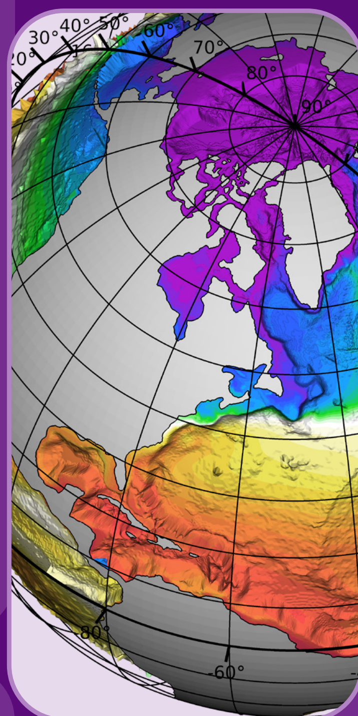

EGU European Geosciences Union

Copernicus Publications
The Innovative Open Access Publisher

About Climate of the Past

An interactive open-access journal of the European Geosciences Union

Climate of the Past (CP) is a not-for-profit international scientific journal dedicated to the publication and discussion of research articles, short communications, and review papers on the climate history of the Earth. CP covers all temporal scales of climate change and variability, from geological time through to multidecadal studies of the last century. Studies focusing mainly on present and future climate are not within scope.

Published by Copernicus GmbH (Copernicus Publications) on behalf of the European Geosciences Union (EGU).

www.climate-of-the-past.net

Copernicus Publications
The Innovative Open Access Publisher

European Geosciences Union

publications@copernicus.org
http://publications.copernicus.org

Image credits:

Ice core: Hans Oerter, AWI Bremerhaven, Germany (submitted by Gerrit Lohmann)
Model: Gerrit Lohmann, AWI Bremerhaven, Germany | Pollen: Dartmouth Electron Microscope Facility, Dartmouth College, public domain, via Wikimedia Commons (submitted by Marie-France Loutre) | Coral uplift after earthquake: Michael Gagan, ANU, Canberra, Australia (submitted by Nerilie Abram) | Close up of a section of ice core from Berkner Island, Antarctica, depth 120 m. Bubbles of trapped air (an archive of the past atmosphere) are visible in the ice: © C. Gilbert (British Antarctic Survey)

Table of contents

Climate of the Past publications by EGU Medallists

Table of contents

2005–2025:
Celebrating 20 years of an incredible journey

From 2005 to 2025 – 2 decades of incredible progress and achievement. What began as a simple idea has grown into a position of leadership, thanks to the contributions of many dedicated individuals. This milestone is a tribute to their teamwork and commitment, and it deserves our sincere congratulations.

To commemorate this 20th anniversary, we are proud to showcase a special collection of articles published by EGU Medallists in *Climate of the Past*. As the only journal with a dedicated special issue celebrating the contributions of our honoured colleagues, this initiative highlights their invaluable support for the journal. Beyond their published works, many of these distinguished individuals contribute as reviewers and editors, further strengthening the quality and impact of the journal.

Finally, this celebration is also an opportunity to extend our deepest thanks to Copernicus and the European Geosciences Union for their extraordinary collaboration. We look forward to marking future anniversaries with the same success and enthusiasm.

Climate of the Past co-editors-in-chief, April 2025

Clim. Past, 2, 131–136, 2006
www.clim-past.net/2/131/2006/

Climate of the Past

Equatorial insolation: from precession harmonics to eccentricity frequencies*

A. Berger[1], M. F. Loutre[1], and J. L. Mélice[2]

[1]Université catholique de Louvain, Institut d'Astronomie et de Géophysique G. Lemaître, 2 Chemin du Cyclotron, 1348 Louvain-la-Neuve, Belgium
[2]Institut de Recherche pour le Développement, Department of Oceanography, University of Cape Town, Rondebosch 7701, South Africa

*Invited contribution by A. Berger, EGS Milutin Milankovic Medal winner 1994

Received: 22 June 2006 – Published in Clim. Past Discuss.: 24 July 2006
Revised: 5 October 2006 – Accepted: 5 October 2006 – Published: 12 October 2006

Abstract. Since the paper by Hays et al. (1976), spectral analyses of climate proxy records provide substantial evidence that a fraction of the climatic variance is driven by insolation changes in the frequency ranges of obliquity and precession variations. However, it is the variance components centered near 100 kyr which dominate most Upper Pleistocene climatic records, although the amount of insolation perturbation at the eccentricity driven periods close to 100-kyr (mainly the 95 kyr- and 123 kyr-periods) is much too small to cause directly a climate change of ice-age amplitude. Many attempts to find an explanation to this 100-kyr cycle in climatic records have been made over the last decades. Here we show that the double maximum which characterizes the daily irradiation received in tropical latitudes over the course of the year is at the origin in equatorial insolation of not only strong 95 kyr and 123 kyr periods related to eccentricity, but also of a 11-kyr and a 5.5-kyr periods related to precession.

1 Introduction

The tropics have been long neglected by paleoclimatologists who mostly followed the hypothesis by Murphy (1876), later independently popularized by Milankovitch (1941), that the driver of the long-term climatic variations is summer in the high northern polar latitudes. For these authors, the progressive build-up of ice sheets requires indeed primarily cool summers in high latitudes, in order to prevent winter snow to melt. But under these conditions, northern latitudes winters are receiving more energy. For example, let us see what has happened at Marine isotopic Stage 5d (MIS-5d) and at MIS-5e in high polar latitudes as compared to low latitudes at the summer solstice. 114 kyr ago, 70° N in June received 97 $\mathrm{Wm^{-2}}$ less than 126 kyr ago and the equator in December 63 $\mathrm{Wm^{-2}}$ more (insolation values from Berger, 1978). This is representing respectively a relative decrease of 18% at 70° N and a relative increase of about the same amount at the equator. This leads to more evaporation in the equatorial regions, a larger latitudinal gradient in the northern hemisphere (remember that if we consider the winter hemisphere, the maximum of the energy received from the Sun is at the equator), a more active transport to the north and possibly more precipitation in polar latitudes. When extended to winter precipitation, the Milankovitch hypothesis is therefore also involving the equatorial and intertropical regions. Much new paleoclimate information indicates that these regions are indeed more important than previously thought. They seem to play an important role in the glacial-interglacial cycles and even in the warming of the last 50 years (see Kerr, 2001, 2003, for a few references).

In this paper, we show an additional reason to emphasize that the equatorial and intertropical regions can play an important role in the response of the climate system to the astronomical forcing. This reason is the presence of significant 123-kyr, 95-kyr, 11-kyr and 5.5-kyr cycles in the amplitude of the seasonal cycle of the energy that the equatorial (and to a lesser extend the intertropical) regions receive from the Sun, cycles directly related to eccentricity and harmonics of precession.

2 Insolation at the Equator

In contrast with the extra-tropical latitudes, which exhibits a simple maximum of insolation each year, the Sun comes overhead twice a year at each latitude in the intertropical belt. In particular at the equator, the Sun culminates at the

Correspondence to: A. Berger
(berger@astr.ucl.ac.be)

Published by Copernicus GmbH on behalf of the European Geosciences Union.

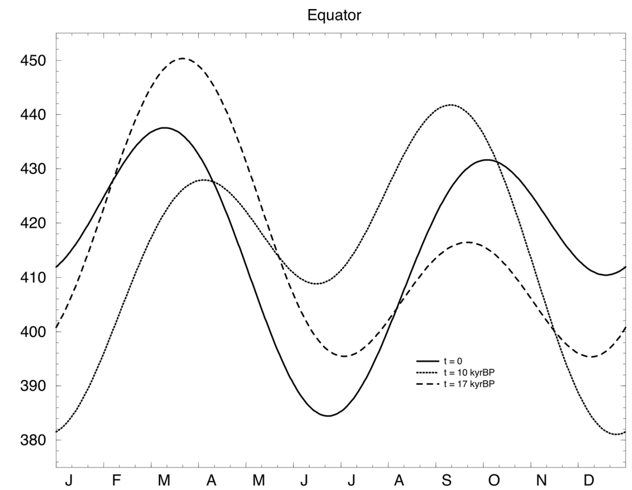

Fig. 1. Seasonal cycle of insolation at the equator at present (full line), at 10 kyr BP (dotted line) and at 17 kyr BP (dashed line). Units are Wm^{-2}.

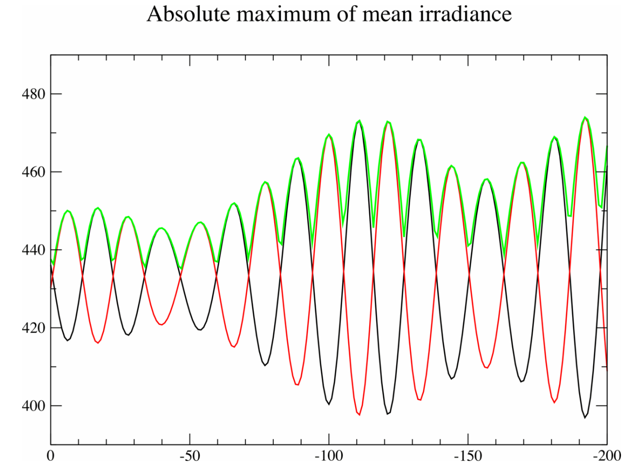

Fig. 2. Time evolution over the last 200 kyr of the 24-h mean irradiance at the equator at spring equinox (black curve) and at autumn equinox (red curve). The time evolution of the maximum of these two series is drawn in green. Units are Wm^{-2}.

zenith at both equinoxes. From classical insolation formula (e.g. Berger et al., 1993) the 24-h mean irradiance at the equator for a given day is given by:

$$\bar{W}_{eq} = \frac{S_a}{\pi}\left(\frac{1+e\cos(\lambda-\omega)}{1-e^2}\right)^2 \cos\delta \qquad (1)$$

S_a is the amount of solar energy received by unit of time on a surface of unit area perpendicular to the Sun rays and situated at the distance a from the Sun. a is the semi-major axis of the Earth's elliptical orbit around the Sun. It is an invariant in celestial mechanics contrary to the so-called solar constant S_0, which is defined at the mean distance r_m from the Earth to the Sun. On an energy point of view, r_m is given by $r_m^2 = a^2\sqrt{1-e^2}$ where e is the eccentricity of the Earth's orbit. r_m and therefore S_0 are varying with e as:

$$S_0 = \frac{S_a}{\sqrt{1-e^2}} \qquad (2)$$

In our calculations of the astronomically driven insolation, the energy output from the Sun is assumed to remain constant over the last millions of years and therefore S_a is a constant taken to be 1368 Wm^{-2}. In Bard and Frank (2006), this solar constant is shown to vary from 1363 to 1368 Wm^{-2}. A constant value of 1365 Wm^{-2} is suggested by the Paleoclimate Modelling Intercomparison Project (PMIP, phase 2) and is used in various modeling studies. The observed value during the last decades was slightly higher, but latest publications concluded that solar activity during the last decades was exceptionally high compared to the previous centuries (Fröhlich and Lean, 2004) and even millennia (Solanki et al., 2004).

– The declination δ is related to the true longitude of the Sun by

$$\sin\delta = \sin\lambda\ \sin\varepsilon \qquad (3)$$

ε being the obliquity and λ identifying the calendar days.

– ω is the longitude of the perihelion. Its numerical value is obtained by adding 180° to the values calculated from Berger (1978) (see Berger et al., 1993, for more explanations).

– The distance from the Earth to the Sun, r, δ and λ are assumed to be constant over one day.

From Eq. (1), the energy received at the equinoxes (δ=0; λ=0 for the spring equinox, SE, or $\lambda=\pi$, for the fall equinox, FE) and solstices ($\delta=\varepsilon$ or $\lambda=\frac{\pi}{2}$ for summer solstice, SS and $\delta=-\varepsilon$ or $\lambda=\frac{3\pi}{2}$ for winter solstice, WS) can be calculated.

For the present-day with e=0.0167, ω=282° and ε=23°27′, SE=439 Wm^{-2}, SS=387 Wm^{-2}, FE=433 Wm^{-2} and WS=413 Wm^{-2} leading to a seasonal contrast of 52 Wm^{-2} (SE–SS). Because of precession, the insolation at SE will alternatively be higher and lower than at FE (see Fig. 1). The same holds for the insolation at SS and WS. However, strictly speaking, the insolation values at SE and FE on one hand, and at SS and WS on the other hand, do not provide the absolute maxima and minima over the year. Indeed, these extrema do not occur exactly at the equinoxes and solstices because the Earth-Sun distance modulates the effect of δ in the course of the year.

Fortunately however, the error made by assuming that the maximum is occurring at one of the equinoxes (Fig. 2) and the minimum (Fig. 3) at one of the solstices remains small. For example, assuming that the summer solstice occurs at the perihelion maximizes the energy received at that particular time. At 198 kyr BP, $\omega\simeq$90° and the absolute maximum arises in August (with 451 Wm^{-2}), but is only 13 Wm^{-2}

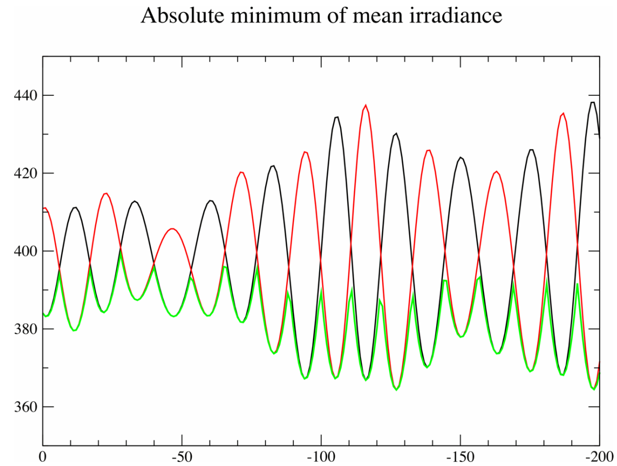

Fig. 3. Time evolution over the last 200 kyr of the 24-h mean irradiance at the equator at summer solstice (black curve) and at winter solstice (red curve). The time evolution of the minimum of these two series is drawn in green. Units are Wm^{-2}.

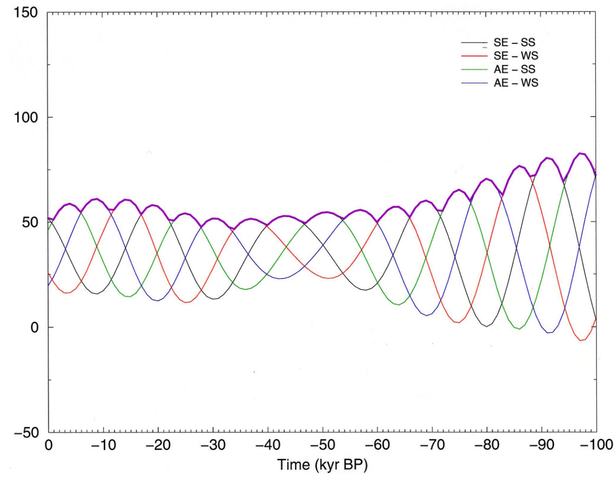

Fig. 4. Time evolution over the last 100 kyr of the amplitude of the 24-h mean irradiance at the equator between spring equinox and summer solstice (black), spring equinox and winter solstice (red), autumn equinox and summer solstice (green) and autumn equinox and winter solstice (blue), and the largest amplitude in the seasonal cycle (purple). Units are Wm^{-2}.

larger than the insolation at the fall equinox (438 Wm^{-2}). This means that the error assuming that the maximum occurs at FE is less than 3%. As the minimum is actually at WS (364 Wm^{-2}), the real seasonal difference amounts to 87 Wm^{-2}, instead of 74 Wm^{-2} if FE-WS is used. Although the error on the seasonal difference reaches 15%, it does not affect the spectral characteristics of the long-term variations of this seasonal difference calculated between the maximum and the minimum values. So for an analytical calculation we will assume that the maximum is occurring at the equinoxes (SE, spring, or FE, fall) and the minimum at the solstices (SS, summer, or WS, winter).

If we assume e and ε constant over a precessional period, it is easy to see that:

$$\begin{array}{lll} \text{SE is maximum} & \text{for} & -90° \leq \omega \leq 90° \\ \text{FE is maximum} & \text{for} & 90° \leq \omega \leq 270° \\ \text{SS is minimum} & \text{for} & 180° \leq \omega \leq 360° \\ \text{WS is minimum} & \text{for} & 0° \leq \omega \leq 180° \end{array} \tag{4}$$

In these conditions, the seasonal contrast measured by Δ=Max (SE,FE)−min (SS,WS) (Fig. 4) is equal to:

$$\begin{array}{lll} \text{SE–WS} & \text{for} & 0° \leq \omega \leq 90° \\ \text{FE–WS} & \text{for} & 90° \leq \omega \leq 180° \\ \text{FE–SS} & \text{for} & 180° \leq \omega \leq 270° \\ \text{SE–SS} & \text{for} & 270° \leq \omega \leq 360° \end{array} \tag{5}$$

(Let us recall that the perihelion coincides with the spring equinox for ω=0°, with the summer solstice for ω=90°, with the fall equinox for ω=180° and with the winter solstice for ω=270°).

This is again an approximation because the insolation at the equinoxes and solstices are also functions of e and ε. This approximation is actually used to allow an easy analytical range of ω values to be calculated (in reality, the boundaries of these ranges are not constant in time, varying slightly around 0, 90, 180 and 270°). However, calculations over the last and next million years show that Δ is practically equivalent to the real seasonal amplitude of insolation at the equator.

The most striking feature of Fig. 5 (top panel), reproducing the long term variations of Δ over the last 1 Myr is the significant eccentricity cycles (both the 100 and the 400-kyr) dominating its long-term variations. In addition, a clear and significant 5-kyr period is present with large amplitudes (∼10 Wm^{-2}) for large values of e and small ones for low values of e. The explanation of the high frequency variability finds an origin similar to the half-precession cycle discussed in Berger and Loutre (1997). It was indeed stressed that, although the insolation at the equinoxes follows the climatic precession pattern, the existence of a double maximum at the equator offers the possibility of generating a half-precession cycle (∼11 kyr) if the climate system is supposed to respond to the largest value of the two. This is clearly seen in Figs. 2 and 3. If now, the largest seasonal amplitude, Δ, is supposed to drive the climate system behaviour, the two maxima and the two minima are involved. Δ(=Max(SE,FE)−min(SS,WS)) is therefore equal to the largest value of the four following parameters: SE–WS, FE–WS, FE–SS, SE–SS (Fig. 4). This means that, according to Eqs (4 and 5), a one-fourth-precession cycle is generated. This high frequency signal has an amplitude of the order of a few Wm^{-2}, but it is carried by a signal of much larger amplitude (a few tens of Wm^{-2}). Moreover, it must

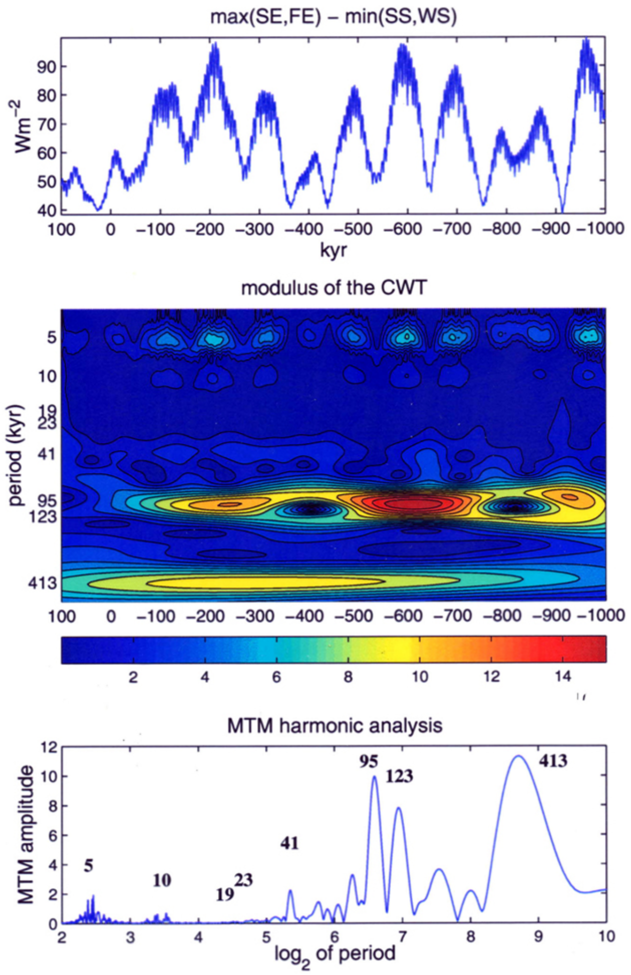

Fig. 5. From top to bottom: (top) time evolution between 1000 kyr BP and 100 kyr AP of the maximum of the amplitude of the seasonal cycle of the 24-h mean irradiance at the equator, (centre) the modulus of the wavelet transform of the signal on top, (bottom) amplitude in the multi taper analysis of the signal on top.

also be noted that local minima of this index (e.g. 86 Wm^{-2} at 198 kyr BP) might be much larger than local maxima (e.g. 66 Wm^{-2} at 154 kyr BP). This is related to the 400-kyr cycle of eccentricity which modulates the amplitude of this seasonal index. The signal of obliquity, which comes from SS and WS is actually weak compared to the harmonics of precession because ε is not a purely periodic function, but instead is equal to a constant plus a series of periodic terms, the most important having a period of 41 kyr. Therefore cos ε can be considered as a constant to the first order of approximation.

As all values at the equinoxes and solstices are principally a function of precession, their amplitude is modulated by eccentricity (which is therefore the envelope of insolation). Therefore, through the procedure of the maximum and minimum selection, this envelope becomes naturally the carrier of the "seasonal" contrast of insolation at the equator leading to the existence of eccentricity in the spectra.

As a consequence, the spectrum of Δ shows the 400, 123, 95, 41, ~10 and ~5-kyr quasi-periods, all being significant, especially those of ~100 and ~5-kyr (Fig. 5 middle and lower panels). The characteristics of their behaviour are the same as those of eccentricity and precession discussed in Berger et al. (1998).

As this double culmination of the Sun at the zenith is true for the whole intertropical belt, it is interesting to see if this equatorial feature holds for all the other intertropical latitudes. Actually, the spectra for these latitudes continue to show all the frequencies but the amplitude of the 123, 95, 11 and 5.5 kyr-cycles decreases rapidly when getting away from the equator. For example, at 5° N, the largest spectral amplitude is related to precession, followed by eccentricity, then the obliquity and the 11 kyr. The harmonic 5.5 kyr is still present but its amplitude is 10 times less than the amplitude of the 11-kyr harmonic.

3 Conclusions

One of the questions which might be raised is how this result can help paleoclimatologists in their research. It is true that climate changes at the geological time scale cannot be understood by looking at orbital forcing only. Instead, as already stated by Milankovitch, insolation forcing is only one step in an astronomical theory of paleoclimate. How forcing is transferred to climate (i.e. climate modelling, including climate feedbacks, land-sea distribution and many other processes); how past climates evolved (i.e. data compiling) and how modelled and reconstructed past climates compare each others, are other fundamental steps of paleoclimate studies. However, in this paper, we wanted to focus only on one of these points, i.e. the insolation forcing. More precisely, we want to insist, once again, that in addition to the well-known daily insolation, many other types of insolation parameters might be candidates for explaining climatic records. It is hoped that our mathematical demonstration of the existence at the equator and, to a lesser extend, in the whole intertropical region of the eccentricity, precession and some harmonic periods will tempt the modelers to test this hypothesis.

Clearly, the tropics which cover half of the world play a major role in the climate system. The energy gradient between low and high latitudes which fuels the general circulation in the atmosphere and ocean implies that the dynamics of glacial-interglacial cycles cannot be understood without the tropics. But whether the tropics or the high latitudes are the key for triggering the glacials and the intergklacials cannot be understood by looking at orbital forcing only. Instead, models of the natural Earth system are needed to understand the climate processes and feedbacks. In particular, by using an Earth system model of intermediate complexity, Claussen et al. (2006) showed that an atmosphere-ocean-vegetation model in which inland ice masses and greenhouse gas concentrations are kept constant, yields a clear response to climatic precession. If only atmosphere and ocean are coupled, then the amplitude of global mean temperature at climatic precession is reduced, and the eccentricity dominates the temperature variability. The reason for that behaviour is – in their model – a response of the meridional overturning circulation which mediates the impact of the climatic precession at high latitudes in the global mean.

On the other hand, field paleoclimatologists might attempt to look for these short periods in their intertropical geological records. Some of them are already questioning whether the origin of the glacial-interglacial cycles lies only in the high latitudes. They show some evidence that the low latitudes are maybe as or more important than the high latitudes. McIntyre and Molfino (1996) suggested from spectra of high resolution records from the equatorial Atlantic spanning the last 50 kyr, that climatic changes in high polar latitudes may be caused by events that occur in low latitudes. Tropical climate systems such as the low-latitude monsoons are known to be sensitive to the seasonal variability of insolation and coupled transequatorial pressure differences (Rossignol-Strick et al., 1998; Clemens, 1998; Leuchner and Sirocko, 2003). Peeters et al. (2004) suggested a teleconnection between the monsoon system and the ocean circulation, stressing that the Mozambique and Agulhas currents in the western Indian Ocean could be an efficient carrier of the tropical climate signal to the global scale. Thibault de Garidel-Toron et al. (2005) inferred from high resolution records of sea-surface temperature from the Pacific warm pool that the temperature contrast across the equatorial Pacific Ocean might have had a significant influence on the mid-Pleistocene climate transition.

Others suggest that the tropics, particularly for moisture availability, is controlled by precession. Palaeoclimate evidence comes from both South America and Africa (de Menocal, 1995, 2004; Maslin et al., 2000; Bush et al., 2002; Trauth et al., 2003; Clement et al., 2004; Cruz et al., 2005) as well as strong evidence from the Mediterranean and Indian Ocean for precessional control over monsoon (e.g., Clemens et al., 1991).

But why are the precession cycles found in the tropics and not the 11 kyr and the 5.5 kyr. Is it because we are only focussing on the cycles close to 21 kyr and not looking for the harmonics? Or is it that the moisture at the tropics is controlled by shifting in the monsoon which is ultimately controlled by the sub-tropics which are dominated by the full precessional mode (Ruddiman, 2006). There are however some relevant papers where these harmonics of precession were claimed to be found. For example, Hagelberg et al. (1994) found climate variability at periods from 10 to 12 kyr in three locations for the late Pleistocene. They concluded that this variability may derive from high sensitivity of the tropics to summer time insolation in both hemispheres. An amplified response of tropical precipitation and temperature may then be transmitted to high latitudes in the Atlantic via advective transport, a mechanism appearing consistent with their observations. However, the cycles between 10–12 kyr could be very miss-leading as they could be recording the time-transgressive Heinrich events.

Transient simulations with a coupled atmosphere/ocean/vegetation model of intermediate complexity (CLIMBER-2) (Tuenter et al., 2006) found variations at sub-Milankovitch periods of about 10 kyr (Asia and Africa) and about 5 kyr (Asia) in the monsoonal runoff caused by the dynamic response of the vegetation.These sub-Milankovitch periods were identified neither in temperature nor in precipitation.

Turney et al. (2004) found semi-precessional periods and suggested that climate variations in the tropical Pacific Ocean exerted an influence on North Atlantic climate through atmospheric and oceanic teleconnections. The Lake Naivasha record of Trauth et al. (2003) demonstrates that periods of increased humidity in East Africa mainly followed maximum equatorial solar radiation in March or September Another very significant proof of the existence of half-precessional cycles comes from the Chinese loess. According to Sun and Huang (2006), the well-defined half-precessional cycle found in magnetic susceptibility and particle size records from the north western Loess Plateau in China is a direct response of the low-latitude insolation forcing through its modulation on the East Asian Summer monsoon. It might be expected that, if resolution permits, the 5.5-kyr cycle should be found and used as a relevant test of the real role played by the tropics.

These are a few examples only and more must be made to show that indeed the tropics can play a leading role in generating long-term climatic variations. In this paper we have demonstrated that the spectrum of the insolation forcing at the equator is as informative as in the high polar latitudes where only the precession and obliquity signals are present. The double insolation maximum and minimum arising in the tropical regions in the course of one year, which is at the origin of the 100 and 5.5 kyr cycles might explain some of the important features of the climate system and environment over the Pleistocene and the Holocene, like it is suggested also by Lorenz et al. (2006) and Reuning et al. (2006) for example.

Edited by: G. M. Ganssen

References

Bard, E. and Frank, M.: Climate change and solar variability, What is new under the Sun, Earth Planet. Sci. Lett., 248, 280–298, 2006.

Berger, A.: Long-term variations of daily insolation and Quaternary climatic changes, J. Atmos. Sci., 35(12), 2362–2367, 1978.

Berger, A., Loutre, M. F., and Tricot, Ch.: Insolation and Earth's orbital periods, J. Geophys. Res., 98(D6), 10 341–10 362, 1993.

Berger, A. and Loutre, M. F.: Intertropical latitudes and precessional and half-precessional cycles, Science, 278(5342), 1476–1478, 1997.

Berger, A., Loutre, M. F., and Mélice, J. L.: Instability of the astronomical periods from 1.5 Myr BP to 0.5 Myr AP, Palaeoclimates, Data and Modelling, 2(4), 239–280, 1998.

Bush, M. B., Moreno, E., de Oliveira, P. E., and Colinvaux, P. A.: Orbital-forcing signal in sediments of two Amazonian lakes, J. Paleolim., 27, 341–352, 2002.

Claussen, M., Fohlmeister, J., Ganopolsky, A., and Brovkin, V.: Vegetation dynamics amplifies precessional forcing, Geophysical Research Letters, 33(9), L09709; doi:10.1029/2006GL0266111, 2006.

Clemens, S., Prell, W., Murray, D., Shimmield, G., and Weedon, G.: Forcing mechanisms of the Indian Ocean monsoon, Nature, 353, 720–725, 1991.

Clemens, S.: Dust response to seasonal atmospheric forcing: Proxy evaluation and calibration, Paleoceanography, 13, 471–490, 1998.

Clement, A. C., Hall, A., and Broccoli, A. J.: The importance of precessional signals in the tropical climate, Clim. Dyn., 22, 327–341, 2004.

Cruz Jr., F. W., Burns, S. J., Karmann, I., Sharp, W. D., Vuille, M., Cardoso, A. O., Ferrari, J. A., Silva Dias, P. L., and Viana, O.: Insolation-driven changes in atmospheric circulation over the past 116,000 years in subtropical Brazil, Nature, 434, 63–66, 2005.

de Garidel-Thoron, Th., Rosenthal, Y., Bassinot, F., and Beaufort, L.: Stable sea surface temperatures in the Western Pacific warm pool over the past 1.75 million years, Nature, 433(7023), 294–298, 2005.

deMenocal, P.: Plio-Pleistocene African Climate, Science, 270, 53–59, 1995.

deMenocal, P.: African climate change and faunal evolution during the Pliocene-Pleistocene, Earth Planet. Sci. Lett., 220, 3–24, 2004.

Fröhlich, C. and Lean, J.: Solar radiative output and its variability: evidence and mechanisms, Astron. Astrophys. Rev., 12, 273–320, 2004.

Hagelberg, T. K., Bond, G., and de Menocal, P.: Milankovitch band forcing of sub-Milankovitch climate variability during the Pleistocene, Paleoceanography, 9(4), 545–558, 1994.

Hays, J. D., Imbrie, J., and Shackleton, N. J.: Variations in the Earth's orbit: pacemaker of the Ice Ages, Science, 194, 1121–1132, 1976.

Kerr, R. A.: The Tropics return to the climate system, Sciences, 292(5517), 660–661, 2001.

Kerr, R. A.: Tropical Pacific a key to deglaciation, Science, 299(5604), 183–184, 2003.

Leuschner, D. C. and Sirocko, F.: Orbital insolation forcing of the Indian Monsoon – a motor for global climate changes?, Palaeogeography, Palaeoclimatology, Palaeoecology, 197(1–2), 83–95, 2003.

Lorenz, S. J., Kim, J. H., Rimbu, N., Schneider, R. R., and Lohmann, G.: Orbitally driven insolation forcing on Holocene climate trends: evidence from alkenone data and climate modelling, Paleoceanography, 21, PA1002, doi:10.1029/2005PA001152, 2006.

Maslin, M. A. and Burns, S. J.: Reconstruction of the Amazon Basin effective moisture availability over the last 14,000 years, Science, 290, 2285–2287, 2000.

McIntyre, A. and Molfino, B.: Forcing of Atlantic equatorial and subpolar millennial cycles by precession, Science, 274(5294), 1867–1870, 1996.

Milankovitch, M.: Kanon der Erdbestrahlung und seine Anwendung auf das Eiszeitenproblem, Royal Serbian Sciences, Spec. pub. 132, section of Mathematical and Natural Sciences, vol. 33, pp. 633, Belgrade, 1941; ("Canon of Insolation and the Ice Age problem", English Translation by Israël Program for Scientific Translation and published for the U.S. Department of Commerce and the National Science Foundation, Washington D.C., 1969, and by Zavod za Udžbenike i Nastavna Sredstva in cooperation with Muzej nauke i tehnike Srpske akademije nauka i umetnosti, Beograd, 1998).

Murphy, J. J.: The glacial climate and the polar ice-cap, Quarterly Journal Geological Society, 32, 400–406, 1876.

PMIP2: http://www-lsce.cea.fr/pmip2/.

Peeters, F. J. C., Acheson, R., Brummer, G. J. A., de Ruijter, W. P. M., Schneider, R. R., Ganssen, G. M., Ufkes, E., and Kroon, D.: Vigorous exchange between the Indian and Atlantic ocean at the end of the past five glacial periods, Nature, 430(7000), 661–665, 2004.

Reuning, L., Reijmer, J. J. G., Betzler, Ch., Timmermann, A., and Steph, S.: Sub-Milankovitch cycles in periplatform carbonates from the early Pliocene Great Bahama Bank, Paleoceanography, 21, PA1017, doi:10.1029/2004PA001075, 2006.

Rossignol-Strick, M., Paterne, M., Bassinot, F. C., Emeis, K.-C., and de Lange, G. J.: An unusual mid-Pleistocene monsoon period over Africa and Asia, Nature, 392, 269–272, 1998.

Ruddiman, W. F.: What ist he timing of orbital-scale monsoon changes?, Quaternary Science Review, 25(7–8), 657–658, 2006.

Solanki, S. K., Usoskin, I. G., Kromer, B., Schüssler, M., and Beer, J.: Unusual activity of the Sun during recent decades compared to the previous 11,000 year, Nature, 431, 1084–1087, doi:10.1038/nature02995, 2004.

Sun, J. and Huang, X.: Half-precession cycles recorded in Chinese loess: response to low-latitude insolation forcing during the Last Interglaciation, Quaternary Science Reviews, 25(9–10), 1065–1972, 2006.

Trauth, M. H., Deino, A., Bergner, A. G. N., and Strecker, M. R.: East African climate change and orbital forcing during the last 175 kyr BP, Earth Planet. Sci. Lett., 206, 297–313, 2003.

Tuenter, E., Weber, S. L., Hilgen, F. J., and Lourens, L. J.: Simulating sub-Milankovitch climate variations associated with vegetation dynamics, Clim. Past Discuss., 2, 745–769, 2006, http://www.clim-past-discuss.net/2/745/2006/.

Turney, C. S. M., Kershaw, A. P., Clemens, S. C., Branch, N., Moss, P. T., and Fifield, L. K.: Millennial and orbital variations of El Niño/Southern oscillation and high-latitude climate in the last glacial period, Nature, 428(6980), 306–310, 2004.

Clim. Past, 5, 203–216, 2009
www.clim-past.net/5/203/2009/

Climate of the Past

Late Quaternary vegetation-climate feedbacks

M. Claussen*

Max Planck Institute for Meteorology, Bundesstr. 53, 20146 Hamburg, Germany

Meteorological Institute, University Hamburg, Bundesstr. 55, 20146 Hamburg, Germany

**Invited contribution by M. Claussen, recipient of the EGU Milutin Milankovic Medal 2005.*

Received: 29 December 2008 – Published in Clim. Past Discuss.: 24 February 2009
Revised: 13 May 2009 – Accepted: 14 May 2009 – Published: 3 June 2009

Abstract. Feedbacks between vegetation and other components of the climate system are discussed with respect to their influence on climate dynamics during the late Quaternary, i.e., the last glacial-interglacial cycles. When weighting current understanding based on interpretation of palaeobotanic and palaeoclimatic evidence by numerical climate system models, a number of arguments speak in favour of vegetation dynamics being an amplifier of orbital forcing. (a) The vegetation-snow albedo feedback in synergy with the sea-ice albedo feedback tends to amplify Northern Hemisphere and global mean temperature changes. (b) Variations in the extent of the largest desert on Earth, the Sahara, appear to be amplified by biogeophysical feedback. (c) Biogeochemical feedbacks in the climate system in relation to vegetation migration are supposed to be negative on time scales of glacial cycles. However, with respect to changes in global mean temperature, they are presumably weaker than the positive biogeophysical feedbacks.

1 Introduction

Daisyworld paradigms

With their conceptual Daisyworld model, Watson and Lovelock (1983) demonstrated that, in theory, feedbacks between biosphere and atmosphere may stabilize the climate[1] without any teleological foresight of flora and fauna. The stabilizing feedback in the Daisyworld is designed to be a vegetation-albedo feedback in which dark daisies absorb more sunlight than the grey, bare planet and much more than white daisies. Thereby, dark daisies provide favourable conditions for life on the Daisyworld planet in cold climate when insolation is weak. White daisies, on the other hand, reflect sunlight more strongly and tend to cool the planet which is the key for survival in hot climate with relatively strong insolation. When dark and white daisies co-exist, Daisyworld's mean temperature is nearly constant over a wide range of changes in solar energy flux (see Fig. 1).

Watson and Lovelock formulated the Daisyworld model as a proof of concept rather than any realistic description of the dynamics of the Earth's climate system. Therefore, it is instructive to explore the concept further by varying one of the decisive ecological parameters. In the original Daisyworld model, the same set of ecological parameters is used for white and dark daisies. In particular, their growth rates peaks at the same optimum temperature. Alternatively, one could assume that for some reason, white daisies like it cooler than dark daisies. The boreal biosphere of tundra and taiga might serve as a real-world example. With this assumption, everything else being unchanged, the Daisyworld paradigm changes completely. With a difference of 15 K in optimum temperatures, the Daisyworld sees stable temperatures if daisies – either white or dark daisies, respectively – exist. At a certain insolation threshold, however, a change

[1]Here, climate is defined in terms of state and statistics of the climate system which encompasses the atmosphere, the biosphere, the cryosphere, the hydrosphere, and the pedosphere.

Correspondence to: M. Claussen
(martin.claussen@zmaw.de)

Published by Copernicus Publications on behalf of the European Geosciences Union.

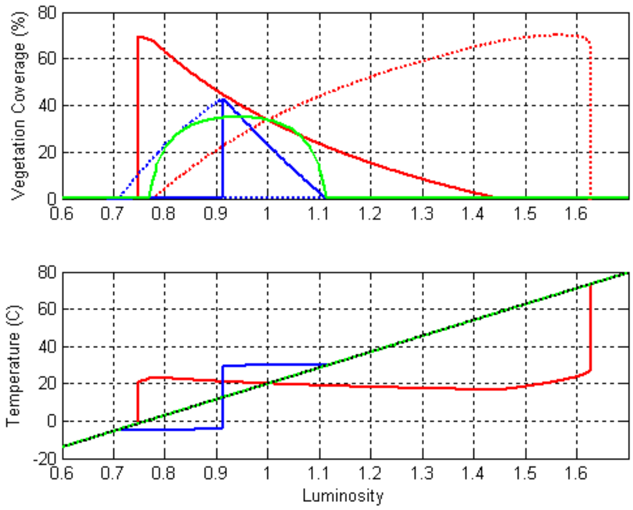

Fig. 1. Variants of Watson and Lovelock's (1983) Daisyworld model. The red lines depict results of the original model where the full red line and the dotted red line in the upper figure indicate the fractional coverage of the Daisyworld planet by dark and white daisies, respectively, as function of luminosity, i.e. the relative solar energy flux density. The lower figure shows the mean temperature of the Daisyworld planet. The dotted black line represents the temperature of the bare planet. (The dotted black line and the green line in the lower figure are identical.) For details of the equations of Daisyworld's vegetation and temperature dynamics, see Weber (2001). The parameter such as albedo values of 0.25, 0.5, 0.75 for dark daisies, bare planet, and white daisies, respectively, are the same as in the original model of Watson and Lovelock. In the original model, dark and white daisies have the same temperature for optimum growth (i.e., 20°C). This assumption is modified here: the blue curves refer to results, if white daisies grow at an optimum temperature which is 15°C lower than that of dark daisies. If the optimum temperature of white daisies is chosen to be 10°C lower, then the green curves result. In the latter case dark and white daisies occupy the same fraction of the planet, and the mean temperature of the Daisyworld planet does not differ from that of the bare planet. Hence the dotted black line and the green line in the lower figure are identical.

in the biosphere is triggered, and the vegetation-albedo feedback causes an abrupt increase in global mean temperature and an abrupt change in vegetation cover from white to dark daisies (Fig. 1, blue curves). A particularly interesting, special solution emerges for a difference of 10 K in optimum temperatures. In this case, white and dark daisies grow in harmony covering precisely the same fraction of their planet. Although the vegetation-albedo feedback causes local climate changes, an observer from space would not detect any difference in global mean temperatures between the living Daisyworld and a bare planet (Fig. 1, green curves; in the lower figure, the green curve and the dotted black curve are identical).

The question of which paradigm most appropriately characterizes the Earth's climate system – (a) the original conjecture of homoeostatic system (Lovelock and Margulis, 1974), (b) the system with locally important, but on global scale non-detectable, effects of biospheric feedbacks on global climate, or (c) the "mixed" case of a piecewise homoeostatic system in which long phases of a negative, stabilizing feedback exist as well as the possibility of abrupt climate changes – is hard, if not impossible, to answer. Indeed, it has been questioned whether falsifiable hypotheses could be posed in this context at all (Kirchner, 1989). However restriction to specific geological epochs and to subcomponents of the biosphere might lead to formulation of tractable questions.

Here, discussion is focused on the late Quaternary terrestrial vegetation-climate feedbacks, more precisely: feedbacks between terrestrial vegetation and other components of the climate system. The late Quaternary (by and large the last several glacial-interglacial cycles) is more accessible to falsification of models than the "deep past", because of its wealth of palaeoclimatic and palaeobotanic reconstruction. Moreover, the late Quaternary is the current geological epoch which is now being strongly affected by human activities. It is seems conceivable that humans might trigger destabilizing biospheric feedbacks – if they exist.

Discussion focuses on palaeoclimate questions, however, not on anthropogenic land-cover change. It centres on biogeophysical and, to a lesser extent, on biogeochemical feedbacks. Biogeophysical feedbacks directly affect near-surface energy, moisture, and momentum fluxes via changes in surface structure and plant physiology. These feedbacks include the biogeographical aspect, if vegetation pattern change. Biogeochemical feedbacks affect the chemical composition of the atmosphere. In nature, biogeophysical and biogeochemical feedbacks do not operate in isolation. Nonetheless, it is useful for many purposes to differentiate between them (e.g., Claussen, 2004).

This paper points in a similar direction as Bonan's (2008) recent review of biosphere-atmosphere interactions of tropical, boreal, and temperate forests. Also Bonan (2008) highlights the role of biogeophysical and biogeochemical feedbacks, and he focuses on the uncertainty of modelling these feedbacks. Here the topic is tackled from the palaeoclimatic and palaeobotanic perspective in the belief that interpretation of palaeoclimatic and palaeobotanic records by using climate system models could offer an inroad to testing hypotheses on the role of vegetation-climate feedbacks in climate system dynamics.

2 Biogeophysical aspects

2.1 Boreal feedbacks

2.1.1 Mid-Holocene warming

During the mid-Holocene some 6000 years ago, boreal forests extended north of the modern tree line (Frenzel et al., 1992; TEMPO et al. 1996; Cheddadi et al., 1997; Tarasov et al., 1998; Prentice and Webb III, 1998; MacDonald et al., 2000). These differences between mid-Holocene and present boreal biome patterns were presumably caused by steady changes in the Earth's orbit which led to stronger insolation (incoming solar energy flux density) than today and stronger near-surface warming during Northern Hemisphere summer.

Mid-Holocene boreal winter insolation was weaker than today (Berger, 1978). Hence by assuming that near-surface climate responds to changes in insolation linearly, one would expect mid-Holocene boreal winters to be colder than today. However at least in North-East Europe, mid-Holocene winters were reconstructed to be warmer than present (Cheddadi et al., 1997). This seeming paradox has been called the "biome paradox" by Berger (2001) who supposes that mid-Holocene winter time warming might have been caused by strong vegetation-snow albedo feedback. According to Otterman et al. (1984), more extended boreal forest, as reconstructed for mid-Holocene climate, could lead to a decrease in the surface albedo during the snowy season as snow-covered tall vegetation appears to be darker than snow-covered flat vegetation or bare ground. This, in turn, favours further warming due to reduced reflection of sunlight and further expansion of boreal forests (see also Foley et al., 1994; deNoblet et al., 1996; Texier et al., 1997; Foley, 2005).

Coupled atmosphere-ocean-vegetation models yield an ambiguous answer. Crucifix et al. (2002) report on strong vegetation-snow albedo feedback in their model. In other model studies (e.g. Ganopolski et al., 1998; Wohlfahrt et al., 2004), the vegetation-snow albedo feedback is too small to yield mid-Holocene winters which are warmer than present (pre-industrial) winters. Only in synergy with the sea-ice climate feedback, warmer winters can be found at northern, extra-tropical latitudes (see Fig. 2). (The sea-ice climate feedback encompasses two loops: the sea-ice albedo feedback and the sea-ice heat flux feedback. Both are positive as a change in sea-ice extent is amplified by near-surface warming/cooling due to changes in albedo or in heat flux from open water into the atmosphere; see Fig. A.22 in Claussen, 2004.) More recent studies by Gallimore et al. (2005) and Otto et al. (2009, Fig. 2) suggest a smaller effect of vegetation dynamics on mid-Holocene warming at high northern latitudes. They attribute the mid-Holocene warm winters mainly to ocean and sea-ice dynamics.

In the numerical models cited above, the effect of the vegetation-snow albedo on near-surface temperatures is strongest in spring by enhancing snow melt in a warmer climate. For example in the model of Gallimore et al. (2005), more wide-spread boreal forests in mid-Holocene high latitudes cause the strongest warming due to reduced snow cover in May. At mid latitudes more extended grass and shrub area produces a cooling between mid-Holocene and present climate mainly by enhanced snow cover which appears to be strongest in April. The situation in summer is more complex as other processes than changes in snow cover become important. For example, enhanced forest cover during mid-Holocene could increase evaporation thereby leading to a cooling. Increased evaporation, on the other hand, increases atmospheric water content and thereby, the wet greenhouse effect. In summary, however, biogeophysical feedback and associated synergies yield some amplification of mid-Holocene warming at high northern latitudes in most models.

Reconstructions of transient changes in boreal biomes suggest a rather steady southward shift of tree line and steady changes in pollen records during the Holocene (Brovkin et al., 2002) with perhaps some faster retreat between 4000 and 2000 years (uncalibrated ^{14}C ages) ago (MacDonald et al., 2000). This has been recaptured by numerical simulations

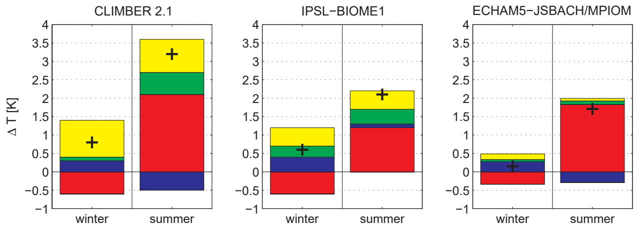

Fig. 2. Factors contributing to differences in winter and summer temperatures between mid-Holocene (some 6000 years ago) and pre-industrial climate for the Northern Hemisphere. The factor separation proposed by Stein and Alpert (1993) has been applied to CLIMBER 2.1, a model of intermediate complexity (data taken from Ganopolski et al., 1998, left figure), to the comprehensive atmosphere-ocean model IPSL asynchronously coupled to a (static) biome model (Wohlfahrt et al., 2004, middle figure), and to the comprehensive coupled atmosphere-vegetation-ocean model ECHAM5-JSBACH/MPI-OM (Otto et al., 2009, right figure). Temperature changes between mid-Holocene and present-day climate are considered over ice-free land areas north of 0° N for CLIMBER 2.1 and north of 40° N, for the comprehensive models. Red colours indicate the results in cases in which only the atmospheric dynamics are switched on in the climate models, i.e. the direct response of atmospheric dynamics to changes in orbitally induced solar energy flux is computed. Blue colours reveal the contribution due to ocean and sea-ice dynamics, i.e., additional warming or cooling due to ocean-atmosphere interaction. Green colours indicate the contribution to changes in vegetation patterns, i.e., the difference between the results of the atmosphere-vegetation models and the atmosphere-only models. Yellow colours show the contribution of a synergy between atmosphere-ocean and atmosphere-vegetation feedback.

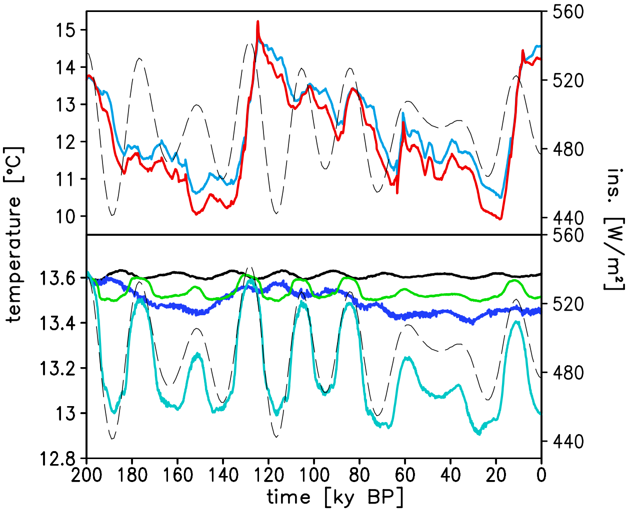

Fig. 3. Simulated global annual mean near-surface air temperatures for the last 200 ky BP (thousand years before present). The red line in the upper figure indicates results of a model run in which changes in inland ice and atmospheric CO_2 concentration are prescribed to force an atmosphere-ocean-vegetation model. The blue line in the upper figure indicates results of an atmosphere-ocean model in which vegetation cover is kept constant at initial values. The lower figure depicts results of the atmosphere-only model in which inland ice, atmospheric CO_2 concentration, vegetation cover, sea-surface temperature, and sea-ice cover are prescribed at values reconstructed or simulated (in the case of vegetation cover and ocean state) at 200 ky BP (black line). The green line indicates results of the atmosphere-vegetation model, the dark blue line, results of the atmosphere-ocean model, and the light blue line, results of the atmosphere-ocean-vegetation model. The dashed line shows the monthly mean insolation in June at 60° N. (This figure is taken from Claussen et al., 2006.)

(e.g. Brovkin et al., 2002; Crucifix et al., 2002). Theoretical studies in which the stability of boreal forest dynamics has been analysed (Levis et al., 1999; Brovkin et al., 2003) do not reveal any bifurcation of the atmosphere-biosphere system. Hence shifts in boreal vegetation patterns seem to follow orbital forcing rather steadily without any indication of abrupt changes in vegetation and climate.

2.1.2 Amplification of glacial-interglacial temperature change

Suppose that biogeophysical feedback, directly of by synergy with other feedbacks, tend to enhance global temperature change. What would be the consequence for late Quaternary climate dynamics? Firstly, it is to be expected that during the last interglacial, the Eemian some 126 000 years ago, the amplifying effect on global mean temperature should have been stronger than during the mid-Holocene due to stronger changes in orbital forcing. This surmise is consistently recaptured by models (e.g. Crucifix and Loutre, 2002; Kubatzki et al., 2000; Schurgers et al., 2006). Secondly, the disappearance of the last remnants of the Laurentian ice sheet between 8000 to 6000 years ago presumably induced a warming associated with the vegetation-snow-albedo feedback which overcomes the Holocene cooling trend due to orbital forcing (Wang et al., 2005b)

For glacial climate, the opposite effect of vegetation migration on global mean temperature is expected. In an increasingly colder climate, the retreat of boreal forests to the south tends to cool the climate more strongly than without any vegetation shift (Kubatzki and Claussen, 1998). The same effect is found by Berger (2001) for the last glacial inception. Ganopolski (2003) and Jahn et al. (2005) quantify the overall effect of biogeophysical feedbacks (and synergies with other feedbacks) to account for some 0.6–0.7 K of the global mean cooling of approximately 5 K. Although biogeophysical feedbacks at northern high latitudes tend to be stronger in colder climate than in warmer climate due to a longer snow season (Brovkin et al., 2003), Jahn et al. (2005) show that during glacial climate (i.e., Marine Isotope Stages 3 and 2), the biogeophysical effect of vegetation on global mean temperature is still smaller than other processes such as changes in ice sheets and atmospheric CO_2 concentration.

First studies with interactive ice sheets highlight the importance of vegetation dynamics on glacial inception. Meissner et al. (2003) conclude that land related feedbacks double the atmospheric cooling, and the introduction of vegetation related feedbacks increases the surface area with perennial snow significantly. In turn, keeping vegetation at interglacial level might mitigate glacial inception (Wang et al., 2005; Kageyama et al., 2007) or even inhibit glacial inception (Kubatzki et al., 2006, 2007).

So far, no complete factor separation of feedbacks has been performed over the course of several glacial-interglacial cycles, i.e., many precessional cycles. A first modelling study with prescribed varying ice sheets and atmospheric CO_2 concentrations (Claussen et al., 2006) indicates that the biogeophysical feedback of boreal biomes and its synergy with the sea-ice albedo feedback could be an important amplifier of the precessional signal such that this signal appears in global mean temperature variations (Fig. 3). (The climatic precession itself induces only a seasonal cycle in solar energy flux, but no change in the annual mean flux.) More interestingly, the signal of precessional forcing emerges in simulated global mean temperature if only atmospheric and vegetation dynamics are included, and this signal is amplified by including ocean and sea-ice dynamics. This example illustrates that not only ice sheet dynamics could amplify the precessional signal (e.g. Köppen and Wegener, 1924), but also, albeit with a presumably much smaller amplitude, biogeophysical feedbacks and synergies.

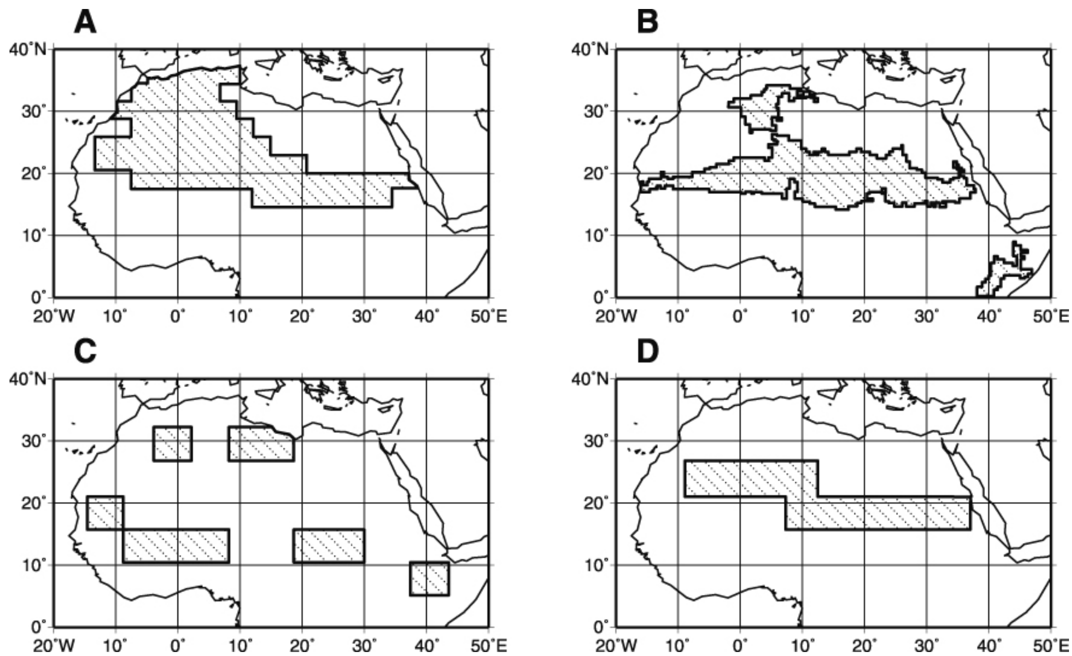

Fig. 4. Differences between present-day and mid-Holocene Sahara as simulated by various coupled vegetation (or biome)-climate models. The hatched area indicates the vegetated fraction irrespective of the density of vegetation coverage. Results are shown from **(A)** Claussen and Gayler (1997), **(B)** Doherty et al. (2000), **(C)** Schurgers et al. (2006), and **(D)** Liu et al., (2007).

2.2 Subtropical desert feedbacks

2.2.1 North African wet phase

The largest subtropical desert, the Sahara, was much greener and moister than today during the early and mid-Holocene according to palaeobotanic reconstructions (Jolly et al., 1998; Hoelzmann et al., 1998; Prentice et al., 2000), and lake level and water balance reconstructions (e.g. Yu and Harrison, 1996; Coe and Harrison, 2002). Like the difference in boreal biomes, the difference between the smaller ("greener") mid-Holocene Sahara and more extended modern Sahara has been attributed to changes in orbital forcing and associated changes in ocean-continent temperature contrast (e.g., Spitaler, 1921; Kutzbach and Guetter, 1986). The stronger mid-Holocene summer monsoon triggered by changes in the Earth's orbital around the sun and in the tilt of the Earth's axis, however, did not seem to be large enough to explain a large areal difference between mid-Holocene and modern Sahara (Joussaume et al., 1999).

Claussen and Gayler (1997) find a strong positive feedback between vegetation and precipitation – mainly in the western part of the Sahara – which could amplify the summer monsoon to foster a stronger coverage of the Sahara with Sahelian vegetation in the mid-Holocene. Claussen and Gayler explain the positive feedback by an interaction between high albedo of Saharan sand deserts and tropical atmospheric circulation. This desert-albedo feedback was originally proposed by Otterman (1974) and described in a model by Charney (1975) to explain the opposite process of desertification in the Sahel region. Charney (1975) hypothesizes that the high albedo over subtropical deserts causes a radiative cooling above deserts because the sum of incoming solar radiation, reflected solar radiation and outgoing long-wave radiation is negative at the top of the atmosphere: more radiation leaves than enters the atmosphere above a subtropical desert. The local radiative cooling induces a subsidence of air masses which compensates the cooling by adiabatic heating. The sinking motion suppresses convective precipitation. The reduction of precipitation is supposed to cause further vegetation degradation, thus enhancing the growth of desert-like conditions. Xue and Shukla (1993) and Eltahir and Gong (1996) argue that the albedo changes in the Sahel are too weak to explain any strong feedback in relation to albedo. But for the region of the Sahara, the desert-albedo feedback seems to work both to amplify a decrease in precipitation with an increase in desert area and to amplify an increase in precipitation with a decrease in desert area (Claussen and Gayler, 1997).

The extent of Saharan vegetation coverage during the mid-Holocene wet phase is still not fully known. Areal reconstructions (e.g. Petit-Maire and Guo, 1996; Hoelzmann et al., 1998; Anhuf et al., 1999), differ, so do model simulations (Claussen and Gayler, 1997; Texier et al., 1997; Broström et al., 1998; Doherty et al., 2000; Schurgers et al., 2006; Liu et al., 2007) (Fig. 4). Summarizing the results of the Paleoclimate Modeling Intercomparison

Project 2, Braconnot et al. (2007) conclude that the biogeophysical feedback might be weaker than previously thought. However this statement is based on results obtained from an ensemble of models which strongly differ in present-day values of North African albedo as well as calculated albedo differences between present-day and mid-Holocene Sahara. Moreover, most model simulations were not set up such that a consistent feedback and factor separation could have been derived.

There is at least one model which indicates a negative biogeophysical feedback (Wang et al., 2008; Notaro et al., 2008) which sustains vegetation in a mid-Holocene vegetated Sahara. In this model, evaporation from bare ground appears to be stronger than transpiration from grassland in wet conditions. Thereby, the drying of soil is stronger in the absence of plants. Hence it is conceivable that on short time scales during the early and mid Holocene, negative feedbacks could dominate when changes in albedo were small. On longer time scales however, changes in soils from dark to bright soils should be considered. An illustrative example is the desiccation of the Lake Mega-Chad where today, very high values of albedo can be found (Knorr and Schnitzler, 2006). Therefore, on time scales of climatic precession, most models show a stronger response of climate change when vegetation dynamics are included (Braconnot et al., 2007). Alternative explanations include feedbacks between atmosphere and ocean via changes in cool updraft regions along the North African Coast (e.g. Kutzbach and Liu, 1997; Hewitt and Mitchell, 1998; Liu et al., 2004). However, the strength of these feedbacks is too weak to explain the climate change in North Africa alone. Also the synergy between vegetation-atmosphere and ocean-atmosphere feedbacks seems to be smaller than the vegetation-atmosphere feedback (Ganopolski et al., 1998; Braconnot et al., 1999).

2.2.2 Saharan dynamics

The transient dynamics of the Sahara appear to be more complex than boreal vegetation dynamics. Earlier model studies with asynchronous coupling of atmospheric and biome models demonstrate the possibility of multiple equilibrium solutions. For present-day climate Claussen (1994, 1997) found two solutions: a desert like today, if the model is initialized with present-day vegetation pattern, and a Sahara which is much greener than today in its western part, if the model is initialized with forest or grass or even dark deserts all over the world. Similar is valid for glacial conditions (Kubatzki and Claussen, 1998). For mid-Holocene conditions, however, only one solution of the model, the “green (West-)Sahara” is obtained irrespective of initial vegetation patterns (Claussen and Gayler, 1997).

The appearance of multiple equilibrium states of a dynamical system as function of varying forcing suggests the potential of abrupt transitions between states, if external forcing varies with time. This can happen either in the form of a single, abrupt transition or in the form of multiple switches, so-called flickering, until the system stays in one of the stable equilibria (for conceptual visualization see Scheffer et al., 2001).

Brovkin et al. (1998) have set up a mathematical conceptual model of subtropical vegetation-precipitation interaction. By applying this model to the results of the comprehensive asynchronously coupled atmosphere-biome model they found that the jump from the green to the desert state should have happened between 6000 and 3600 y BP. This conclusion has been corroborated by the Claussen et al. (1999) (Fig. 5a) who used a dynamically coupled global atmosphere-ocean-vegetation model of intermediate complexity, CLIMBER-2.1. They predicted a fast expansion of the Sahara around 5500 y BP.

More recent model simulations reveal a more mixed picture. In their model, ECBilt-CLIO-VECODE, Renssen et al. (2003) find a steady decline of Saharan vegetation on millennial average. However, variability in Saharan vegetation changes with particularly strong variations in vegetation cover between 7000 and 5000 y BP (Fig. 5b). Renssen et al. (2003), show that the change in variability in their model could be attributed to a bistability of the system during the period of strong variations. Using a zonally symmetric model of vegetation dynamics and air-flow over West Africa, Irizarry-Oritz et al. (2003) obtain bistability of the atmosphere - vegetation system for the mid-Holocene period thereby corroborating the results by Renssen et al. (2003). Liu et al. (2006b) have analysed the stability of the biogeophysical system in the presence of rainfall variability which is implicit in randomly varying atmospheric dynamics. They conclude that rainfall variability could induce abrupt vegetation change – as found in their model, the comprehensive atmosphere-ocean-vegetation model FOAM-LPJ (Fig. 5c). They conclude that their model reveals a strong non-linear response of vegetation to precipitation, but only a weakly non-linear feedback.

Shortly after Claussen et al. (1999) published their model predictions, deMenocal et al. (2000) reported on an abrupt increase in terrestrial dust flux around 5500 y BP in marine sediments of the coast of North Africa near Cape Blanc, Mauretania (Fig. 5d). They interpret the abrupt change in dust flux as abrupt aridification of West Africa. The dust record of deMenocal et al. (2000) has long been considered as corroboration of abrupt climate and vegetation change in the western part of the Sahara. However, this record should be interpreted with care since the abrupt change in the dust deposition might reflect not only a decrease in vegetation cover but also an increase in the source area of the dust caused by lake desiccations.

For the eastern part of the Sahara (east of approximately 10° E), Pachur (1999) found that aridification increased more gradually with a period of larger variability in between 7000 to 4500 y BP (Fig. 5e). Rapid swings between the arid and the wet state were detected in reconstructions from several hundred ^{14}C dates around the Tropic of Cancer by Petit-Maire and Guo (1996) and from tree rings in the Central Sahara by Cremaschi et al. (2006). Recently, Kröpelin et al. (2008) presented fascinating details of desiccation from Lake Yoa located northeast of the ancient Lake Mega Chad. This record spans some 6000 years, and for the oldest 1000 years multiple swings with decreasing amplitude in tropical and grass pollen were detected. Kröpelin et al. (2008) (Fig. 5f) interpret their reconstruction as a rather smooth, non-abrupt transition in climate and vegetation cover. This could be a valid statement. However, the Lake Yoa record is just too short for a detailed statistical analysis to exclude the possibility that the multiple swings in vegetation are a manifestation of flickering of the system.

2.2.3 Long-term Saharan change

Looking further back into the past, it appears that there is a strong link between Dansgaard-Oeschger cycles, Heinrich events and climate changes in North Africa (Claussen et al., 2003a; Chang et al., 2008; Tjallingii et al., 2008). No or only very small changes are detectable in the Sahara which during the cold MIS 4, 3 and 2 remains an extended desert. In the Sahel region, however, stadials lead to a reduction in precipitation and vegetation cover where the effect of Heinrich events is stronger than the effect of Dansgaard-Oeschger cycles. Superimposed on these effects is the imprint of precessional forcing.

As mentioned above, the Sahara was much greener than today during the Eemian and MIS 5e according to model simulations and archaeological evidence (e.g. Osborne et al., 2008). Interestingly not only MIS 5e, but also MIS 5c and MIS 5a had seen a greener Sahara than today according to palaeoclimate reconstructions and model results (Tjallingii et al., 2008) (Fig. 6). From these studies one can conclude that in sufficiently warm climate states, such as interglacials, the Sahara expands and retreats following precessional forcing. Precessional forcing, however, is only the trigger, as the change in vegetation and climate appears to be much faster than the subtle change in forcing. In cold and dry climate states like glacials (e.g. MIS 4, 3, and 2), no great changes are expected in the Sahara.

3 Biogeophysical vs. biogeochemical aspects

3.1 Carbon cycle-climate feedbacks

In the previous sections, biogeophysical processes have been considered, and it has been concluded that from the biogeophysical point of view, vegetation dynamics tend to be an amplifier of late Quaternary climate change. However changes in vegetation cover not only affect the energy fluxes, but also biogeochemical fluxes which modify the chemical composition and subsequently, the energy cycle of the atmosphere. When focussing on the carbon cycle, mainly three feedbacks stand out: the so-called climate-greenhouse, or climate-carbon, feedback, the CO_2 fertilization-CO_2 uptake feedback and a biogeochemistry-climate feedback caused by shifts in vegetation patterns.

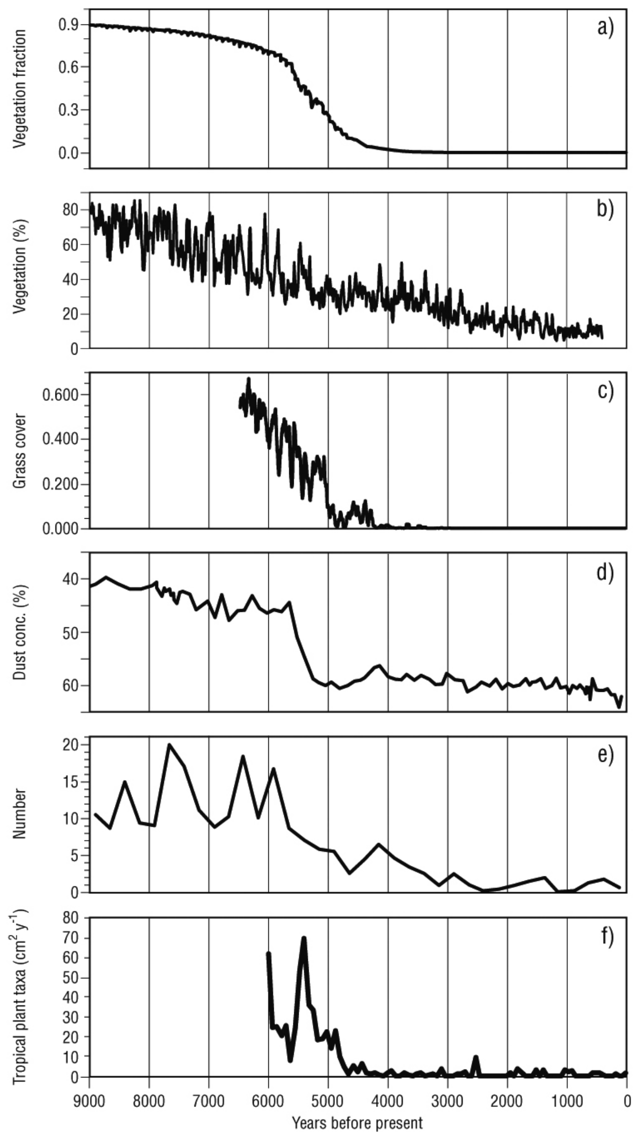

Fig. 5. Transient development of vegetation fraction and climate in the Sahara. **(a)** Simulated changes in vegetation fraction on average over the entire Sahara by Claussen and Gayler (1997). **(b)** Simulated changes in vegetation fraction in the Western Sahara/Sahel region (14° W to 3° E, 17° N to 28° N) by Renssen et al. (2003). **(c)** Simulated changes in grass cover in the Eastern Sahara (11° E to 34° E, 18° N to 23° N) by Liu et al. (2007). **(d)** Reconstructed dust concentration in North Atlantic marine sediment (at approximately 20.8° N, 18.5° W) by deMenocal et al. (2000). **(e)** Number of ^{14}C dates in the Sahara east of 11° E by Pachur (1999). **(f)** Reconstructed change in tropical plant taxa from Lake Yoa (at approximately 19° N, 20.3° E) by Kröplin et al. (2008).

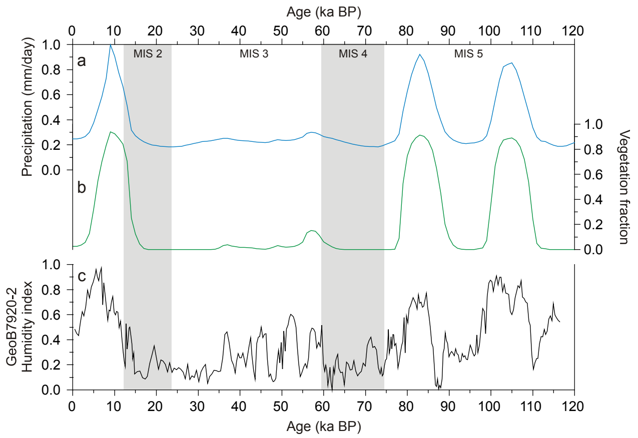

Fig. 6. Simulated annual mean daily precipitation (mm/day) (upper, blue line) and relative vegetation coverage (middle, green line) over the Saharan region between 20° N and 30° N over the last 120 ka (ka BP = thousand years before present). The black line depicts temporal variations of the proportion of non-aeolian terrigeneous sediment reconstructed from marine core GeoB7920-2 (at approximately 20.5° N, 18.5° W). (This figure is taken with modifications from Tjallingii et al., 2008.)

The climate-carbon feedback implies that warming increases soil emissions of CO_2 and reduces carbon storage in terrestrial and ocean ecosystems. The net result is an increase in atmospheric CO_2 concentration which, in turn, leads to further warming. The CO_2 fertilization-CO_2 uptake feedback is considered a negative feedback. It increases uptake of CO_2 with increasing atmospheric CO_2 concentrations, thereby reducing atmospheric CO_2 concentrations (House et al., 2006).

Both feedbacks are considered to exist with high certainty (House et al., 2006). The net effect seems to be positive, as Scheffer et al. (2006) found from analysing past trends in atmospheric CO_2 concentration. This is supported by numerical simulations with prescribed, increasing CO_2 emissions from fossil fuel burning. They yield an amplification of the increase in atmospheric CO_2 concentration owing to a reduced uptake of CO_2 by the terrestrial biosphere and the ocean (e.g. Cox et al., 2000; Friedlingstein et al., 2006; Raddatz et al., 2007). However the strength of these feedbacks is much less certain (Denman et al., 2007). Bonan (2008) summarizes that in a comparison of eleven models, feedbacks related to the terrestrial carbon cycle could increase atmospheric CO_2 concentrations by 4 to 44% at the end of the 21st century. Much of the model uncertainty arises from the CO_2 fertilization-CO_2 uptake feedback.

The climate-carbon feedback and the CO_2 fertilization-CO_2 uptake feedback have been explored in simulations of the recent past, the last centuries, and the near future. So far no estimates of their effect on long time scales of glacial cycles seem to exist. On these longer time scales, shifts in vegetation patterns have presumably provided a negative feedback in the climate system. During glacial inception forest were reduced in their extent which led to an increase in atmospheric CO_2 concentration, while during deglaciation, atmospheric CO_2 concentration should have decreased due to the built up of forest. In the following, only the last, long-term feedback will be considered, and a quantitative estimate is given below.

Possibilities of a positive feedback on long time scales of glacial cycles due to burial of terrestrial carbon during glacials have been discussed (Zeng, 2003), but have not yet been corroborated. A burial of vegetation and soils by ice sheets during a glacial inception would inhibit the exchange of CO_2 between the terrestrial biosphere and the atmosphere thereby lowering the atmospheric CO_2 concentration and, hence, the atmospheric greenhouse effect. When ice sheets retreat, the buried carbon is released to the atmosphere thereby increasing the warming during deglaciation by strengthening the greenhouse effect.

3.2 A thought experiment

Is it possible to evaluate the strength of biogeophysical versus biogeochemical effects of large-scale land cover change? Claussen et al. (2001) tried to quantify the relative magnitude of these processes and their synergism by using the CLIMBER-2 model. Their sensitivity studies show that when the climate system has reached an equilibrium, changes in forest fraction and changes in atmospheric CO_2 are negatively correlated, i.e., deforestation yields an increase in atmospheric CO_2 concentration and afforestation, a decrease (Fig. 7). With respect to global mean temperature, however, correlation changes sign. Tropical deforestation tends to warm the climate, because the increase in atmospheric CO_2 and hence, the greenhouse effect, outweighs the biogeophysical effects. In mid and high northern latitudes, however, biogeophysical processes – mainly the vegetation-snow albedo feedback in synergy with the sea-ice albedo feedback – win over biogeochemical processes, thereby eventually leading to a global cooling in the case of deforestation and to a global warming, in the case of afforestation. Since CLIMBER-2 does not explicitly simulate synoptic variability, the question of significance of the biogeophysical and biogeochemical signals in the presence of ubiquitous climate variability has not been answered. Furthermore, the question of time scales has not been addressed. It is conceivable that time scales of biogeophysical and biogeochemical processes differ. Hence the study by Claussen et al. (2001) should be considered a thought experiment. The result of this experiment is, however, consistent with model simulations by Betts (2000) and Bala et al. (2007). Betts (2000) compared estimates of a positive radiative forcing and associated warming due to decreasing albedo caused by afforestation of current agricultural land with the estimates of a negative radiative forcing caused by a lowering of atmospheric CO_2 due to enhanced carbon uptake by new forests. Bala et al. (2007) used a coupled atmosphere-ocean-vegetation model to assess temperature changes in potential future climate change with deforestation of global, tropical, temperate, and boreal forests, respectively.

3.3 Glacial implications

How does the thought experiment apply to the question on the role of vegetation-climate feedback on late Quaternary climate? Tropical forests were presumably reduced in their extent during glacial climate, (Crowley, 1995) with tropical rainforest being replaced by tropical seasonal forest in tropical lowlands and by xerophytic woods in tropical highlands (Elenga et al., 2000). Model simulations yield a slight areal increase (Prentice et al., 1993), little change (Jahn, 2004), and a slight decrease (Kubatzki and Claussen, 1998; Kutzbach et al., 1998) in tropical forests. Boreal forests, however, regressed equatorwards with a compression and fragmentation of the forest zones (Prentice et al., 2000) covering a much smaller fraction, roughly 1/3, of its present-day area according to the model studies cited above. Hence one might conclude that because of its strong areal changes, boreal biogeophysical feedbacks could have been the dominant factor in modifying global mean temperature during glacial-interglacial cycles

These considerations are corroborated by an estimate of the strength of the effect of changes in terrestrial carbon on atmospheric CO_2 concentration and on glacial cooling The amount of carbon stored in the glacial biosphere is estimated to be at least by 500 GtC less than during the pre-industrial period (Crowley, 1995; Francois et al., 1999; Joos et al., 2004). Most of the resulting increase in CO_2 flux into the atmosphere was likely to be buffered by the oceanic biogeochemical processes including carbonate compensation, so that atmospheric CO_2 concentration should have increased by no more than 20–25 ppmv due to the shrinkage of the terrestrial biosphere (Archer et al., 2002; Brovkin et al., 2007). A change in atmospheric CO_2 concentration by 20–25 ppmv would lead to a change in global mean temperature by some 0.2–0.3 K, if a best guess of present-day climate sensitivity is considered (i.e., an increase in global mean temperature by 3 K caused by a doubling in atmospheric CO_2 concentration). An alternative estimate of climate sensitivity to changes in atmospheric CO_2 concentration in glacial climate is given by Jahn et al. (2005). From their model they found a decrease in global mean temperature of some 1.5 K due to a drop in atmospheric CO_2 concentration by 90 ppmv. This value implies a temperature change of some 0.3–0.4 K for a change in atmospheric CO_2 concentration by 20–25 ppmv. Hence the biogeochemical feedback caused by changes in vegetation patterns between glacial and interglacial climate may have resulted in a temperature change by some 0.2–0.4 K which is – in absolute values – smaller than the global mean temperature of some 0.6–0.7 K due to biogeophysical feedback according to Ganopolski (2003) and Jahn et al. (2005).

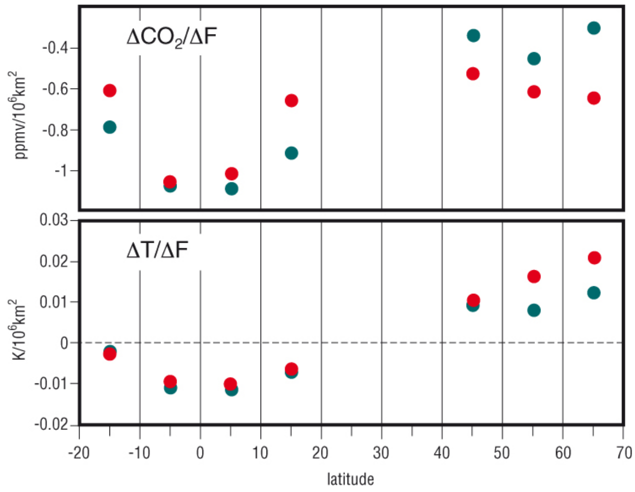

Fig. 7. Simulated ratio of changes in global atmospheric CO_2 concentration (upper figure) and global mean near-surface temperature (lower figure) to changes in forest area due to deforestation (red dots) and afforestation (green dots) in latitudinal belts of 10 degrees width. (This figure is taken with modifications from Claussen et al., 2001.)

4 Conclusion and perspective

The interaction between vegetation and climate must be considered an important component in climate system dynamics. This sentence, today, sounds almost trivial owing to advances in empirical and theoretical research. But some ten years ago, it was not. In fact in a review article in 2000 (Grassl, 2000), the distribution of global vegetation pattern was considered a boundary conditions to climate system models. Only short-term plant physiology and, to some extent, fractional vegetation and leaf area were allowed to change with meteorological conditions. Over the last decade, some climate system models have been developed in which not only atmospheric and oceanic, but also vegetation dynamics are simulated explicitly including biogeochemical cycles. Hence only now, comprehensive feedback analyses of the interaction between these climate system components can be tackled.

Despite great advances in modelling feedbacks between most components of the climate system, the question on the overall role of biogeophysical and biogeochemical feedbacks in the climate system is not yet solved. This is partly due to the lack of rigorously accounting for these feedbacks in numerical studies. Both feedbacks can be positive or negative, thereby partly compensating each other. When weighting current understanding based on the interpretation of palaeobotanic and palaeoclimatic evidence by using numerical climate system models, a number of arguments speak in favour of vegetation dynamics being an amplifier of orbital forcing in the late Quaternary.

Firstly, the vegetation-snow albedo feedback in synergy with the sea-ice-climate feedback tends to amplify global mean temperature changes between glacial-interglacial states. In one model of intermediate complexity, the climatic precession (which itself induces only a seasonal cycle in solar energy flux, but no change in the annual mean flux) can be detected in annual mean temperature variations even if ice sheet cover and atmospheric CO_2 concentrations are held constant over many precessional periods. Other simulations, which include interactive atmosphere-ocean-vegetation-ice sheet dynamics, suggest that glacial inception could be strongly weakened or even suppressed, if vegetation pattern is kept constant at interglacial values.

An amplifying effect caused by migrating boreal vegetation is seen in most models. However regarding the magnitude of the biogeophysical feedback and any synergy associated with it, models differ. It is hard to judge on which model is "correct". In most cases, a formally complete factor separation analysis (following Stein and Alpert, 1993) has not been done. Further insight could be gained by undertaking model intercomparison in the form sensitivity studies with identically prescribed land-cover change. Moreover, comparison of present-day climate simulations with satellite-derived information could be helpful (Wang et al., 2005a). Based on the statistical analysis of remote sensing observations, for example, Liu et al. (2006a) suggest strong positive boreal vegetation-temperature feedback.

Secondly, variations in the extent of the largest desert on Earth, the Sahara, appear to be amplified by biogeophysical feedback when considering orbital time scales. This is seen in most models. Furthermore, it seems to be safe to state that expansion and retreat of the Sahara occurs at a faster pace than the driving orbital forcing. The dynamics of the Sahara is, however, still being explored. Theoretically it seems possible that the biosphere-atmosphere system in this region exhibits multiple steady states which would imply the potential of abrupt changes.

This aspect is interesting also for projections of potential future climate and precipitation change in the Sahel region and the Southern Sahara. If Saharan precipitation would increase in a greenhouse gas induced warmer climate and if a strong positive vegetation-climate feedback would exist, then an abrupt Saharan greening is likely to occur (Claussen et al., 2003b). So far, model simulations of potential future precipitation change disagree even with respect to the sign of change in this region (Meehl et al., 2007). For a step towards solving this problem, sufficiently long, multi-millennia records of climate archives are needed. These should provide independent palaeoclimatic and palaeobotanic information to reconstruct the dynamics of individual climate system components separately. Only then model-based interpretation of such records will allow an assessment of the strength of feedbacks between relevant climate system components.

Thirdly, biogeochemical feedbacks (the climate-carbon feedback, the CO_2 fertilization-CO_2 uptake feedback and a biogeochemistry-climate feedback caused by shifts in vegetation patterns) can be positive or negative, but on time scales of glacial cycles, they are supposedly negative: the land surface and terrestrial vegetation looses carbon during the transition from interglacial to glacial climate and gains carbon during the transition from glacial to interglacial climate thereby opposing the general trend of atmospheric CO_2 concentration.

Unfortunately no estimates on the relative strength of different biogeochemical feedbacks seem to exist. First estimates suggest that biogeochemical vegetation feedbacks in the climate system are, at the end, weaker than biogeophysical feedbacks. However, this assertion is based on reasoning and on analysing results of simplified models. Important processes with respect to terrestrial carbon cycle such as the storage and loss of carbon in peat and wetlands have not yet been explicitly included in this analysis.

In terms of the Daisyworld paradigms introduced in the beginning of this discussion, one might tentatively conclude that for the late Quaternary, the picture of a biosphere-atmosphere system that could trigger abrupt vegetation and climate changes is more appropriate than the picture of a purely homoeostatic biosphere-atmosphere interaction. Implicit in this conclusion is the assumption that the biosphere does not adjust itself to climate via evolution on orbital time scales – an assumption which awaits falsification.

Acknowledgements. The author would like to thank the reviewers, N. deNoblet-Ducoudré, LSCE, Gif-sur-Yvette, France, and H. Renssen, Vrije Universiteit Amsterdam, The Netherlands, for constructive comments on the original manuscript. Thanks are also due to V. Brovkin, Max Planck Institute for Meteorology, Hamburg, Germany, and Z. Liu, Center for Climatic Research, Madison, Wisconsin, USA, for constructive discussion and B. Zinecker, K. Niedl and N. Noreiks, Max Planck Institute for Meteorology, for editorial and technical assistance. Furthermore the author thanks C. Reick and T. Raddatz, Max Planck Institute for Meteorology, and A. Ganopolski and V. Petoukov, Potsdam Institute for Climate Impact Research, for stimulating discussion over the last years.

Edited by: J. Guiot

References

Anhuf, D., Frankenberg, P., and Lauer, W.: Die postglaziale Warmphase vor 8000 Jahren, Geol. Rundsch. 51, 454–461, 1999.

Archer, D., Winguth, A., Lea, D., and Mahowald, N.: What caused the glacial/interglacial atmospheric pCO$_2$ cycles? Rev. Geophys., 38, 159–189, 2000.

Bala, G., Caldeira, K., Wickett, M., Phillips, T. J., Lobell, D. B., Delire, C., and Mirin, A.: Combined climate and carbon-cycle effects of large-scale deforestation, 17 April, PNAS, 104, 6550–6555, 2007.

Berger, A.: Long-term variations of daily insolation and quaternary climatic change, Journal of Atmospheric and Oceanic Science, 35, 2362–2367, 1978.

Berger, A.: The role of CO_2, sea-level and vegetation during the Milankovitch-forced glacial-interglacial cycles, in: Geosphere-Biosphere Interactions and Climate, edited by: Bengtsson, L. O.

and Hammer, C. U., Vatican City, Cambridge University Press, New York, 119–146, 2001.

Betts, R. A.: Offset of the potential carbon sink from boreal forestation by decreases in surface albedo, Nature, 408, 187–190, 2000.

Bonan, G. B.: Forests and Climate Change: Forcings, Feedbacks, and the Climate Benefits of Forests, Science, 320, 1444–1449, 2008.

Braconnot, P., Joussaume, S., Marti, O., and deNoblet-Ducoudre, N.: Synergistic feedbacks from ocean and vegetation on the African monsoon response to mid-Holocene insolation, Geophys. Res. Lett., 26(16), 2481–2484, 1999.

Braconnot, P., Otto-Bliesner, B., Harrison, S., Joussaume, S., Peterchmitt, J.-Y., Abe-Ouchi, A., Crucifix, M., Driesschaert, E., Fichefet, Th., Hewitt, C. D., Kageyama, M., Kitoh, A., Lan, A., Loutre, M.-F., Marti, O., Merkel, U., Ramstein, G., Valdes, P., Weber, S. L., Yu, Y., and Zhao, Y.: Results of PMIP2 coupled simulations of the Mid-Holocene and Last Glacial Maximum – Part 1: experiments and large-scale features, Clim. Past, 3, 261–277, 2007, http://www.clim-past.net/3/261/2007/.

Brovkin, V., Claussen, M., Petoukhov, V., and Ganopolski, A.: On the stability of the atmosphere-vegetation system in the Sahara/Sahel region, J. Geophys. Res., 103(D24), 31613–31624, 1998.

Brovkin, V., Bendtsen, J., Claussen, M., Ganopolski, A., Kubatzki, C., Petoukhov, V., and Andreev, A.: Carbon cycle, vegetation and climate dynamics in the Holocene: Experiments with the CLIMBER-2 model, Global Biogeochem. Cy., 16(4), 1139, doi:10.1029/2001GB001662, 2002.

Brovkin, V., Levis, S., Loutre, M. F., Crucifix, M., Claussen, M., Ganopolski, A., Kubatzki, C., and Petoukhov, V.: Stability analysis of the climate-vegetation system in the northern high latitudes, Climatic Change, 57(1), 119–138, 2003.

Brovkin, V., Ganopolski, A., Archer, D., and Rahmstorf, S.: Lowering of glacial pCO_2 in response to changes in oceanic circulation and marine biogeochemistry, Paleoceanography, 22, PA4202, doi:10.1029/2006PA001380, 2007.

Broström, A., Coe, M., Harrison, S. P., Gallimore, R., Kutzbach, J. E., Foley, J. A., Prentice, I. C., and Behling, P.: Land surface feedbacks and palaeomonsoons in northern Africa, Geophys. Res. Lett., 25(19), 3615–3618, 1998.

Chang, P., Zhang, R., Hazeleger, W., Wen, C., Wan, X., Ji, L., Haarsma, R. J., Breugem, W.-P., and Seidel, H.: Oceanic link between abrupt changes in the North Atlantic Ocean and the African monsoon, Nature Geoscience, 1(7), 444–448, 2008.

Charney, J. G.: Dynamics of deserts and droughts in the Sahel, Q. J. Roy. Meteorol. Soc., 101, 193–202, 1975.

Cheddadi, R., Yu, G., Guiot, J., Harrison, S. P., and Prentice, I. C.: The climate of Europe 6000 years ago, Clim. Dyn., 13, 1–9, 1997.

Claussen, M.: On coupling global biome models with climate models, Climate Res., 4, 203–221, 1994.

Claussen, M.: Modelling biogeophysical feedback in the African and Indian Monsoon region, Clim. Dynam., 13, 247–257, 1997.

Claussen, M. and Gayler, V.: The greening of Sahara during the mid-Holocene: Results of an interactive atmosphere-biome model, Global Ecol. Biogeogr., 6, 369–377, 1997.

Claussen, M., Kubatzki, C., Brovkin, V., Ganopolski, A., Hoelzmann, P., and Pachur, H. J.: Simulation of an abrupt change in Saharan vegetation at the end of the mid-Holocene, Geophys. Res. Lett., 24, 2037–2040, 1999.

Claussen, M., Brovkin, V., Petoukhov, V., and Ganopolski, A.: Biogeophysical versus biogeochemical feedbacks of large-scale land-cover change, Geophys. Res. Letters, 26(6), 1011–1014, 2001.

Claussen, M., Ganopolski, A., Brovkin, V., Gerstengarbe, F.-W., and Werner, P.: Simulated Global-Scale Response of the Climate System to Dansgaard-Oeschger and Heinrich events, Clim. Dynam., 21, 361–370, 2003a.

Claussen, M., Brovkin, V., Ganopolski, A., Kubatzki, C., and Petoukhov, V.: Climate Change in Northern Africa: The past is not the future, Climatic Change, 57(1), 99–118, 2003b.

Claussen, M. (Ed.): Does land surface matter in climate and weather?, in: Vegetation, Water, Humans and the Climate, Part A., edited by: Kabat, P., Claussen, M., Dirmeyer, P., Gash, J., de Guenni, L. B., Meybeck, M., Pielke Sr., R. A., Vörösmarty, C., Hutjes, R., and Lütkemeier, S., Springer-Verlag, Heidelberg, 5–153, 2004.

Claussen, M., Cox, P. M., Zeng, X., Viterbo, P., Beljaars, A. C. M., Betts, R., Bolle, H.-J., Chase, T., and Koster, R.: The Global Climate – Chapter A.4., in: Vegetation, Water, humans and the climate: A new perspective on an interactive system, edited by: Kabat, P., Claussen, M., Dirmeyer, P. A., Gash, J. H. C., de Guenni, L. B., Meybeck, M. Pielke Sr., R. A., Vörösmarty, C. J., and Lütkemeier, S., Springer-Verlag, Heidelberg, 33–57, 2004.

Claussen, M., Fohlmeister, J., Ganopolski, A., and Brovkin, V.: Vegetation dynamics amplifies precessional forcing, Geophys. Res. Lett., 33, L09709, doi:10.1029/2006GL026111, 2006.

Coe, M. T. and Harrison, S. P.: The water balance of northern Africa during the mid-Holocene: An evaluation of the 6 ka BP PMIP simulations, Clim. Dynam., 19, 155–166, 2002.

Cox, P. M., Betts, R. A., Jones, C. D., Spall, S. A., and Totterdell, I. J.: Acceleration of global warming due to carbon-cycle feedbacks in a coupled climate model, Nature, 404, 184–187, 2000.

Cremaschi, M., Pelfini, M., and Santilli, M.: Cupressus dupreziana: a dendroclimatic record for the middle-late Holocene in the central Sahara, The Holocene, 16(2), 293–303, 2006.

Crowley, T. J.: Ice age terrestrial carbon changes revisited, Global Biogeochem. Cy., 9(3), 377–389, 1995.

Crucifix, M. and Loutre, M. F.: Transient simulations over the last interglacial period (126–115 kyr BP): feedback and forcing analysis, Clim. Dynam, 19(5–6), 417–433, 2002.

Crucifix, M., Loutre, M. F., Tulkens, P., Fichefet, T., and Berger, A.: Climate evolution during the Holocene: a study with an Earth system model of intermediate complexity, Clim. Dynam, 19(1), 43–60, 2002.

deMenocal, P. B., Ortiz, J., Guilderson, T., Adkins, J., Sarnthein, M., Baker, L., and Yarusinski, M.: Abrupt onset and termination of the African Humid Period: Rapid climate response to gradual insolation forcing, Quarternary Sci. Rev., 19, 347–361, 2000.

Denman, K. L., Brasseur, G., Chidthaisong, A., Ciais, P., Cox, P. M., Dickinson, R. E., Hauglustaine, D., Heinze, C., Holland, E., Jacob, D., Lohmann, U., Ramachandran, S., da Silva Dias, P. L., Wofsy, S. C. and Zang, X.: Couplings between changes in the climate system and Biogeochemistry, in: Climate Change 2007: The Physical Science Basis, Contribution of Working Group I to the Fourth Assessment Report of the Intergovernmental Panel on Climate Change, edited by: Solomon, S., Qin, D., Manning, M., Chen, Z., Marquis, M., Averyt, K. B., Tignor, M., and Miller, H.

L., Cambridge University Press, Cambridge, UK and New York, NY, USA, 499–587, 2007.
de Noblet, N., Prentice, I. C., Joussaume, S., Texier, D., Botta, A., and Haxeltine, A.: Possible role of atmosphere-biosphere interactions in triggering the last glaciation, Geophys. Res. Lett., 23(22), 3191–3194, 1996.
Doherty, R., Kutzbach, J., Foley, J., and Pollard, D.: Fully coupled climate/dynamical vegetation model simulations over Northern Africa during the mid-Holocene, Clim. Dynam., 16, 561–573, 2000.
Elenga, H., Peyron, O., Bonnefille, R., Jolly, D., Cheddadi, R., Guiot, J., Andrieu, V., Bottema, S., Buchet, G., De Beaulieu, J.-L., Hamilton, A. C., Maley, J., Marchant, R., Perez-Obiol, R., Reille, M., Riollet, G., Scott, L., Straka, H., Taylor, D., Van Campo, E., Vincens, A., Laarif, F., and Jonson, H.: Pollen-based biome reconstruction for southern Europe and Africa 18 000 yr bp, J. Biogeogr., 27, 621–634, 2000.
Eltahir, E. A. B. and Gong, C.: Dynamics of wet and dry years in West Africa, J. Climate, 9(5), 1030–1042, 1996.
Foley, J. A., Kutzbach, J. E., Coe, M. T., and Levis, S.: Feedbacks between climate and boreal forests during the Holocene epoch, Nature, 371, 52–54, 1994.
Foley, J. A.: Tipping points in the Tundra, Science, 310, 627–628, 2005.
Francois, L. M., Godderis, Y., Warnant, P., Ramstein, G., de Noblet, N., and Lorenz, S.: Carbon stocks and isotopic budgets of the terrestrial biosphere at mid-Holocene and last glacial maximum times, Chem. Geol., 159, 163–189, 1999.
Friedlingstein, P., Bopp, L., Ciais, P., Dufresne, J.-L., Fairhead, L., LeTreut, H., Monfray, P., and Orr, J.: Positive feedback between future climate change and the carbon cycle, Geophys. Res. Lett., 28(8), 1543–1546, 2001.
Friedlingstein, P., Cox, P., Betts, R., Bopp, L., von Bloh, W., Brovkin, V., Cadule, P., Doney, S., Eby, M., Fung, I., Bala, G., John, J., Jones, C., Joos, F., Kato, T., Kawamiya, M., Knorr, W., Lindsay, K., Matthews, H. D., Raddatz, T., Rayner, P., Reick, C., Roeckner, E., Schnitzler, K.-G., Schnur, R., Strassmann, K., Weaver, A. J., Yoshikawa, C., and Zeng, N.: Climate-carbon cycle feedback analysis, results from the C4MIP model intercomparison, J. Climate, 19, 3337–3353, 2006.
Frenzel, B., Pesci, M., and Velichko, A. A. (Eds.): Atlas of paleoclimates and paleoenvironments of the Northern Hemisphere: Late Pleistocene – Holocene, Budapest: Geographical Research Institute, 153 pp., 1992.
Gallimore, R. G., Jacob J., and Kutzbach, J. E.: Coupled atmosphere-ocean-vegetation simulations for modern and mid-Holocene climates: role of extratropical vegetation cover feedbacks, Clim. Dynam., 25, 755–776, 2006.
Ganopolski, A., Kubatzki, C., Claussen, M., Brovkin, V., and Petoukhov, V.: The influence of vegetation-atmosphere-ocean interaction on climate during the mid-Holocene, Science, 280, 1916–1919, 1998.
Ganopolski, A.: Glacial Integrative modelling, Philos. T. R. Soc. A, London, 361, 1871–1884, 2003.
Grassl, H.: Status and improvements of coupled general circulation models, Science, 288, 1991–1997, 2000.
Hewitt, C. D. and Mitchell, J. F. B.: A fully coupled GCM simulation of the climate of the mid-Holocene, Geophys. Res. Lett., 25(3), 361–364, 1998.
Hoelzmann, P., Jolly, D., Harrison, S. P., Laarif, F., Bonnefille, R., and Pachur, H.-J.: Mid-Holocene land-surface conditions in northern Africa and the Arabian Peninsula: A data set for the analysis of biogeophysical feedbacks in the climate system, Global Biogeochem. Cy., 12, 35–51, 1998.
House, J. I., Brovkin, V., Betts, R., Constanza, R., Silva Dias, M. A., Holland, E., le Quere, C., Kim Phat, N., Riebesell, U., and Scholes, M.: Climate and air quality, in Ecosystems and Human Well-Being: Current State and Trends, Findings of the Condition and Trends Working Group of the Millennium Ecosystem Assessment, Island Press, Washington, Covelo, London, 1, 357–390, 2006.
Irizarry-Ortiz, M., Wang, G., and Elthair, E. A. B.: Role of the biosphere in the mid-Holocene climate of West Africa, J. Geophys. Res., 108(D2), 4042, doi:10.1029/2001JD000989, 2003.
Jahn, A.: Atmosphere-vegetation feedback in the climate system of the last glacial, Diploma thesis, Fachbereich Geowissenschaften, Freie Universität Berlin, Germany, 2004.
Jahn, A., Claussen, M., Ganopolski, A., and Brovkin, V.: Quantifying the effect of vegetation dynamics on the climate of the Last Glacial Maximum, Clim. Past, 1, 1–7, 2005, http://www.clim-past.net/1/1/2005/.
Jolly, D., Prentice, I. C., Bonnefille, R., et al.: Biome reconstruction from pollen and plant macrofossil data for Africa and Arabian Peninsula at 0 and 6 k, J. Biogeogr., 25, 1007–1027, 1998.
Joos, F., Gerber, S., Prentice, I. C., Otto-Bliesner, B. L., and Valdes, P. J.: Transient simulations of Holocene atmospheric carbon dioxide and terrestrial carbon since the Last Glacial Maximum, Global Biogeochem. Cy., 18, GB2002, doi:10.1029/2003GB002156, 2004.
Joussaume, S., Taylor, K. E., Braconnot, P., Mitchell, J. F. B., Kutzbach, J. E., Harrison, S. P., Prentice, I. C., Broccoli, A. J., Abe-Ouchi, A., Bartlein, P. J., Bonfiels, C., Dong., B., Guiot, J., Herterich, K., Hewit, C. D., Jolly, D., Kim, J. W., Kislov, A., Kitoh, A., Loutre, M. F., Masson, V., McAvaney, B., McFarlane, N., deNoblet, N., Peltier, W. R., Peterschmitt, J. Y., Pollard, D., Rind, D., Royer, J. F., Schlesinger, M. E., Syktus, J., Thompson, S., Valdes, P., Vettoretti, G., Webb, R. S., and Wyputta, U.: Monsoon changes for 6000 years ago: Results of 18 simulations from the Paleoclimate Modeling Intercomparison Project (PMIP), Geophys. Res. Lett., 26(7), 859–862, 1999.
Kageyama, M., Charbit, S., Ritz, C., Khodri, M., and Ramstein, G.: Mechanisms leading to the last glacial inception over North America.: Results from the CLIMBER-GREMLINS atmosphere-ocean-vegetation northern hemisphere ice-sheet, model, in: The climate of past interglacials, edited by: Sirocko, F., Claussen, M., Sanchez Goni, M. F., and Litt, T., Elsevier, Amsterdam, 573–582, 2007.
Kirchner, J. W.: The GAIA Hypothesis: can it be tested? Rev. Geophys., 27(2), 223–235, 1989.
Knorr, W. and Schnitzler, K.-G.: Enhanced albedo feedback in North Africa from possible combined vegetation and soil formation processes, Clim. Dynam., 26, 55–63, 2006.
Köppen, W. and Wegener, A.: Die Klimate der geologischen Vorzeit, Borntraeger, Berlin, 255 pp., 1924.
Kröpelin, S., Verschuren, D., Lézine, A.-M., Eggermont, H., Cocquyt, C., Francus, P., Cazet, J.-P., Fagot, M., Russell, J. M., Darius, F., Conley, D. J., Schuster, M., von Suchodoletz, H., and Engstrom, D. R.: Climate-driven ecosystem succession in the

Sahara: The past 6000 years, Science, 30, 765–768, 2008.
Kubatzki, C. and Claussen, M.: Simulation of the global biogeophysical interactions during the last glacial maximum, Clim. Dynam., 14, 461–471, 1998.
Kubatzki, C., Montoya, M., Rahmstorf, S., Ganopolski, A., and Claussen, M.: Comparison of a coupled global model of intermediate complexity and an AOGCM for the last interglacial, Clim. Dynam., 16, 799–814, 2000.
Kubatzki, C., Claussen, M., Calov, R., and Ganopolski, A.: Sensitivity of the last glacial inception to initial and surface conditions, Clim. Dynam., 27, 333–344, 2006.
Kubatzki, C., Claussen, M., Calov, R., and Ganopolski, A.: Modelling the end of an interglacial (MIS 1,5,7,9,11), in: The climate of past interglacials, edited by: Sirocko, F., Claussen, M., Litt, T., and Sanchez-Goni, M., Elsevier, Amsterdam, 583–593, 2007.
Kutzbach, J. E. and Guetter, P. J.: The influence of changing orbital parameters and surface boundary conditions on climate simulations for the past 18 000 years, J. Atmos. Sci., 43, 1726–1759, 1986.
Kutzbach, J. E., Gallimore, R., Harrison, S., Behling, P., Selin, R., and Laarif, F.: Climate and biome simulations for the past 21 000 years, Quarternary Sci. Rev., Elsevier Science Ltd., 17, 473–506, 1998.
Kutzbach, J. E. and Liu, Z.: Oceanic feedback on the western African monsoon at 6000 BP, Science, 278, 440–443, 1997.
Levis, S., Foley, J. A., Brovkin, V., and Pollard, D.: On the stability of the high-latitude climate-vegetation system in a coupled atmosphere-biosphere model, Global Ecol. Biogeogr., 8, 489–500, 1999.
Lovelock, J. E. and Margulis, L.: Atmospheric hoeostasis by and for the biosphere: the gaia hypothesis, Tellus, 26, 1–9, 1974.
Liu, Z., Harrison, S. P., Kutzbach, J. E., and Otto-Bliesner, B.: Global monsoons in the mid-Holocene and oceanic feedback, Clim. Dynam., 22, 157–182, 2004.
Liu, Z., Notaro, M., Kutzbach J., and Liu, N.: Assessing global vegetation-climate feedbacks from the observation, J. Climate, 19(5), 787–814, 2006a.
Liu, Z., Wang, Y., Gallimore, R., Notaro, M., and Prentice, I. C.: On the cause of abrupt vegetation collapse in North Africa during the Holocene: Climate variability vs. vegetation feedback, Geophys. Res. Lett., 33, L22709, doi:10.1029/2006GL028062, 2006b.
Liu, Z., Wang, Y., Gallimore, R., Gasse, F., Johnson, T., deMenocal, P., Adkins, J., Notaro, M., Prentice, I. C., Kutzbach, J. E., Jacob, R., Behling, P., Wang, L., and Ong, E.: Simulating the transient evolution and abrupt change of Northern Africa Atmosphere-Ocean-Terrestrial Ecosystem in the Holocene, Quarternary Sci. Rev., 26, 1818–1837, 2007.
MacDonald, G. M., Velichko, A. A., Kremenetski, C. V., Borisova, O. K., Goleva, A. A., Andreev, A. A., Cwynar, L. C., Riding, R. T., Forman, S. L., Edwards, T. W. D., Aravena, R., Hammarlund, D., Szeicz, J. M., and Gattaulin, V. N.: Holocene treeline history and climate change across Northern Eurasia, Quaternary Res., 53, 302–311, 2000.
Meehl, G. A., Stocker, T. F., Collins, W. D., Friedlingstein, P., Gaye, A. T., Gregory, J. M., Kitoh, A., Knutti, R., Murphy, J. M., Noda, A., Raper, S. C. B., Watterson, I. G., Weaver, A. J., and Zhao, Z.-C.: Global Climate Projections, in: Climate Change 2007: The Physical Science Basis Contribution of Working Group I to the Fourth Assessment Report of the Intergovernmental Panel on Climate Change, edited by: Solomon, S., Qin, D., Manning, M., Chen, Z., Marquis, M., Averyt, K. B., Tignor, M., and Miller H. L., Cambridge University Press, Cambridge, UK and New York, NY, USA, 747–845, 2007.
Meissner, K. J., Weaver, A. J., Matthews, H. D., and Cox, P. J.: The role of land-surface dynamics in glacial inception: a study with the UVic Earth System Model, Clim. Dynam., 21, 515–537, 2003.
Notaro, M., Wang, Y., Liu, L., Gallimore, R., and Levis, S.: Combined statistical and dynamical assessment of the simulated negative vegetation feedback on North African annual precipitation during the mid-Holocene, Global Change Biol., 14, 347–368, 2008.
Osborne, A. H., Vance, D., Rohling, E. J., Barton, N., Rogerson, M., and Fello, N.: A humid corridor across the Sahara for the migration of early modern humans out of Africa 120 000 years ago, PNAS, 105, 16444–16447, 2008.
Otterman, J.: Baring high-albedo soils by overgrazing: A hypothesized desertification mechanism, Science, 186, 531–533, 1974.
Otterman, J., Chou, M.-D., and Arking, A.: Effects of nontropical forest cover on climate, J. Clim. Appl. Meteorol., 23, 762–767, 1984.
Otto, J., Raddatz, T., Claussen, M., Brovkin, V., and Gayler, V.: Separation of atmosphere-ocean-vegetation feedbacks and synergies for mid-Holocene climate, Geophys. Res. Lett., 36, L09701, doi:10.1029/209GL037482, 2009.
Petit-Maire, N. and Guo, Z.: Mise en évidence de variations climatiques holocènes rapides, en phase dans les déserts actuels de Chine et du Nord de l'Afrique, Sciences de la Terre et des Planètes, 322, 847–851, 1996.
Pachur, H.-J.: Paläo-Environment und Drainagesysteme der Ostsahara im Spätpleistozän und Holozän, in: Nordost-Afrika: Strukturen und Ressourcen; Ergebnisse aus dem Sonderforschungsbereich "Geowissenschaftliche Probleme in Ariden und Semiariden Gebieten", edited by: Klitzsch, E. and Thorweihe, U. , Wiley – VCH, Weinheim, 366–455, 1999.
Prentice, I. C., Sykes, M. T., Lautenschlager, M., Harrison, S. P., Denissenko, O., and Bartlein, P.: Modelling global vegetation patterns and terrestrial carbon storage at the last glacial maximum, Global Ecol. Biogeogr., 3, 67–76, 1993.
Prentice, I. C. and Webb III, T.: BIOME 6000: reconstructing global mid-Holocene vegetation patterns from palaeoecological records, J. Biogeogr., 25, 997–1005, 1998.
Prentice, I. C., Jolly, D., and BIOME 6000 members: Mid-Holocene and glacial-maximum vegetation geography of the northern continents and Africa, J. Biogeogr., 27, 507–519, 2000.
Raddatz, T. J., Reick, C. H., Knorr, W., Kattge, J., Roeckner, E., Schnur, R., Schnitzler, K.-G., Wetzel, P., and Jungclaus, J.: Will the tropical land biosphere dominate the climate-carbon cycle feedback during the twenty-first century? Clim. Dynam., 29, 565–574, 2007.
Renssen, H., Brovkin, V., Fichefet, T., and Goosse, H.: Holocene climate instability during the termination of the African Humid Period, Geophys. Res. Lett., 30(4), 1184, doi:10.1029/2002/GL016636, 2003.
Scheffer, M., Carpenter, S., Foley, J. A., Folke, C., and Walker, B.: Catastrophic shifts in ecosystems, Nature, 413, 591–596, 2001.
Scheffer, M., Brovkin, V., and Cox, P. M.: Positive feedback between global warming and atmospheric CO_2 concentration

inferred from past climate change, Geophys. Res. Lett., 33, L10702, doi:10.1029/2005GL025044, 2006.

Schurgers, G., Mikolajewicz, U., Gröger, M., Maier-Reimer, E., Vizcaíno, M., and Winguth, A.: Dynamics of the terrestrial biosphere, climate and atmospheric CO_2 concentration during interglacials: a comparison between Eemian and Holocene, Clim. Past, 2, 205–220, 2006, http://www.clim-past.net/2/205/2006/.

Spitaler, R.: Das Klima des Eiszeitalters, Selbstverlag, Prag, 138 pp., 1921.

Stein, U. and Alpert, P.: Factor separation in numerical simulations, J. Atmos. Sci., 50, 2107–2115, 1993.

Tarasov, P. E., Webb III, T., Andreev, A. A., Afanaseva, N. B., Berezina, N. A., Bezusko, L. G., Blyakharchuk, T. A., Bolikhovskaya, N. S., Cheddadi, R., Chernavskaya, M. M., Chernova, G. M., Dorofeyuk, N. I., Dirksen, V. G., Elina, G. A., Filimonova, L. V., Glebov, F. Z., Guiot, J., Gunova, V. S., Harrison, S. P., Jolly, D., Khomutova, V. I., Kvavadze, E. V., Osipova, I. M., Panova, N. K., Prentice, I. C., Saarse, L., Sevastyanov, D. V., Volkova, V. S., and Zernitskaya, V. P.: Present-day and mid-Holocene biomes reconstructed from pollen and plant macrofossil data from the former Soviet Union and Mongolia, J. Biogeogr., 25, 1029–1053, 1998.

TEMPO: Potential role of vegetation feedback in the climate sensitivity of high-latitude regions: A case study at 6000 years B.P., Global Biogeochem. Cy., 10(4), 727–736, 1996.

Texier, D., de Noblet, N., Harrison, S. P., Haxeltine, A., Jolly, D., Joussaume, S., Laarif, F., Prentice, I. C., and Tarasov, P.: Quantifying the role of biosphere-atmosphere feed-backs in climate change: coupled model simulations for 6000 years BP and comparison with palaeodata for northern Eurasia and northern Africa, Clim. Dynam., 13, 865–882, 1997.

Tjallingii, R., Claussen, M., Stuut, J.-B. W., Fohlmeister, J., Jahn, A., Bickert, T., Lamy, F., and Röhl, U.: Coherent high- and low latitude control of the Northwest African hydrological balance and continental vegetation cover, Nature Geoscience, 1, 670–675, 2008.

Wang, Y., Notaro, M., Liu, Z., Gallimore, R., Levis, S., and Kutzbach, J. E.: Detecting vegetation-precipitation feedbacks in mid-Holocene North Africa from two climate models, Clim. Past, 4, 59–67, 2008, http://www.clim-past.net/4/59/2008/.

Wang, Y., Mysak, L .A., Wang, Z., and Brovkin, V.: The greening of the McGill Paleoclimate Model. Part I: Improved land surface scheme with vegetation dynamics, Clim. Dynam., 24, 469–480, 2005a.

Wang, Y., Mysak, L. A., Wang, Z., and Brovkin, V.: The greening of the McGill Paleoclimate Model. Part II: Simulation of Holocene millennial-scale natural climate changes, Clim. Dynam., 24, 481–496, 2005b.

Wang, Z. M., Cochelin, A. S. B., Mysak, L. A., and Wang, Y.: Simulation of the last glacial inception with the green McGill Paleoclimate Model, Geophys. Res. Lett., 32(12), L12705, doi:10.1029/2005GL023047, 2005.

Watson, A. J. and Lovelock, J. E.: Biological Homeostasis of the Global Environment: The Parable of Daisyworld, Tellus, 35B, 284–289, 1983.

Weber, S. L.: On homeostasis in Daisyworld, Climatic Change, 48, 465–485, 2001.

Wohlfahrt, J., Harrison, S. P., and Braconnot, P.: Synergetic feedbacks between ocean and vegetation on mid- and high-latitude climates during the mid-Holocene, Clim Dynam., 22, 223–238, 2004.

Xue, Y. and Shukla, J.: The influence of land surface properties on Sahel climate. Part I: Desertification, J. Climate, 6, 2232–2245, 1993.

Yu, G. and Harrison, S. P.: An evaluation of the simulated water balance of Eurasia and northern Africa at 6000 y BP using lake status data, Clim. Dynam., 12, 723–735, 1996.

Zeng, N.: Glacial-interglacial atmospheric CO_2 change – The glacial burial hypothesis, Adv. Atmos. Sci., 20(5), 677–693, 2003.

Clim. Past, 5, 269–283, 2009
www.clim-past.net/5/269/2009/

Climate of the Past

Mid-Pliocene shifts in ocean overturning circulation and the onset of Quaternary-style climates

M. Sarnthein[1,2,*], **G. Bartoli**[1,3], **M. Prange**[4], **A. Schmittner**[5], **B. Schneider**[1], **M. Weinelt**[1], **N. Andersen**[6], **and D. Garbe-Schönberg**[1]

[1]Institute for Geosciences, University of Kiel, 24098 Kiel, Germany
[2]Institute for Geology and Paleontology, University of Innsbruck, 6020, Innsbruck, Austria
[3]Geologisches Institut, ETH Zuerich, 8092 Zurich, Switzerland
[4]MARUM Center for Marine Environmental Sciences and Faculty of Geosciences, University of Bremen, 28334 Bremen, Germany
[5]College of Ocean and Atmospheric Sciences, Oregon State University, Corvallis OR 97331-5503, USA
[6]Leibniz Laboratory, University of Kiel, 24098 Kiel, Germany

[*]*Invited contribution by M. Sarnthein, recipient of the EGU Milutin Milankovic Medal 2006.*

Received: 11 December 2008 – Published in Clim. Past Discuss.: 26 January 2009
Revised: 27 May 2009 – Accepted: 27 May 2009 – Published: 30 June 2009

Abstract. A major tipping point of Earth's history occurred during the mid-Pliocene: the onset of major Northern-Hemisphere Glaciation (NHG) and of pronounced, Quaternary-style cycles of glacial-to-interglacial climates, that contrast with more uniform climates over most of the preceding Cenozoic and continue until today (Zachos et al., 2001). The severe deterioration of climate occurred in three steps between 3.2 Ma (warm MIS K3) and 2.7 Ma (glacial MIS G6/4) (Lisiecki and Raymo, 2005). Various models (sensu Driscoll and Haug, 1998) and paleoceanographic records (intercalibrated using orbital age control) suggest clear linkages between the onset of NHG and the three steps in the final closure of the Central American Seaways (CAS), deduced from rising salinity differences between Caribbean and the East Pacific. Each closing event led to an enhanced North Atlantic meridional overturning circulation and this strengthened the poleward transport of salt and heat (warmings of +2–3°C) (Bartoli et al., 2005). Also, the closing resulted in a slight rise in the poleward atmospheric moisture transport to northwestern Eurasia (Lunt et al., 2007), which probably led to an enhanced precipitation and fluvial runoff, lower sea surface salinity (SSS), and an increased sea-ice cover in the Arctic Ocean, hence promoting albedo and the build-up of continental ice sheets. Most important, new evidence shows that the closing of the CAS led to greater steric height of the North Pacific and thus doubled the low-saline Arctic Throughflow from the Bering Strait to the East Greenland Current (EGC). Accordingly, Labrador Sea IODP Site 1307 displays an abrupt but irreversible EGC cooling of 6°C and freshening by ∼2 psu from 3.25/3.16–3.00 Ma, right after the first but still reversible attempt of closing the CAS.

1 Introduction – links to present concerns about future climate?

At first glance, the mid-Pliocene onset of major Northern Hemisphere Glaciation and Quaternary-style climates, in particular the build-up of a continent-wide ice sheet on Greenland, seems to be a fairly academic question. However, this event may be linked to burning, unresolved questions on the Earth's uncertain future climate change.

A broad spectrum of model intercomparison data (Huybrechts et al., 2004) show that the present trend of global warming will induce both a modest increase in precipitation and an annual temperature rise by up to 8°C in Greenland over the 21st century, two processes that counteract in their role for ice formation on Greenland. To test these opposing forces, Huybrechts et al. (op. cit.) ran a duplicate model experiment, using the ECHAM-4 and HadAM3 models (Fig. 1). Results from both experiments agree that the present greenhouse warming will lead to ice growth over most parts of Central Greenland (up to 2 cm/yr ice gain), whereas large ice melt will occur along the West Greenland margin and in the far northeastern corner (up to 100 cm/yr and more). In the models, the melting volume outweighs

Correspondence to: M. Sarnthein
(ms@gpi.uni-kiel.de)

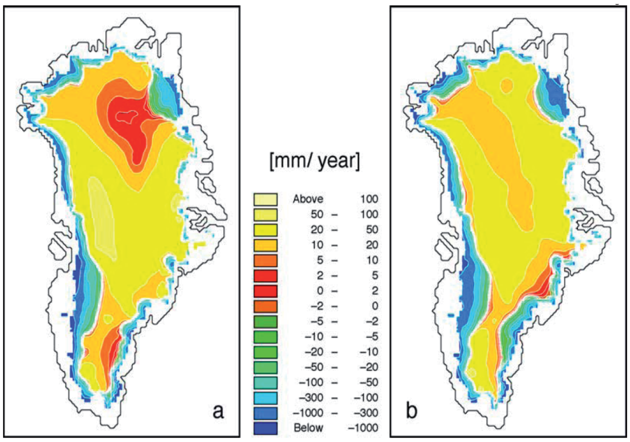

Fig. 1. Huybrechts' (2004) model of potential future variations in ice thickness on Greenland, modelled using the ECHAM4 **(a)** and HadAM3H **(b)** models.

growth and, therefore, a volume loss of Greenland ice is predicted for the 21st century. However, the magnitude of this melting is highly uncertain, ranging from an equivalent of 2 to 7 cm (in contrast to an overall gain of ice mass, predicted for Antarctica; Huybrechts et al., op. cit.). Likewise, modern elevation changes of the Greenland Ice Sheet derived from either satellite or aircraft altimetry are still controversial for altitudes of more than 2200 m (Hvidegaard and Sandberg, 2009; presented as EGU poster, 2009). In summary, these tests resulted in the burning question; how sensitive is the Greenland ice sheet to a warming climate? Alley et al. (2005) tried to answer the question and argued for the possibility of rapid and major ice loss and significant global sea level rise. Much of the answer may depend on the orders of magnitude of the competing poleward heat and the moisture transports reaching the northern North Atlantic and Eurasia.

It is the objective of this study to test a potential analogue case in the Late Neogene, the onset of Quaternary-style climates with the formation of Major Northern Hemisphere glaciation (NHG) approximately 3.0–2.7 Ma. This event is clearly revealed as a major tipping point in the long-term benthic oxygen isotope (δ^{18}O) record of the Cenozoic (Zachos et al., 2001) and as a somewhat more gradual transition on top of some distinct steps of abrupt change in the millennial-scale resolution stacked benthic δ^{18}O record LR04 of Lisiecki and Raymo (2005) (Fig. 2).

At the beginning of this paper, we shortly discuss the pros and cons of various hypotheses that try to explain the potential forcings controlling the onset of *Major* NHG in the mid-Pliocene. In this context, we stress the term "major", because minor, regional ice sheets in the Northern Hemisphere, particularly on Greenland, have already been registered since the Late Eocene (Eldrett et al., 2007) and in particular, since the Late Miocene as recently summarized in Paleoceanography (vol. 23/3) and by DeConto et al. (2008). However, a major rise in the discharge of ice rafted debris (IRD) to ambient seas suggests that full glaciation was only reached near 3.0–2.7 Ma, as first outlined by Shackleton et al. (1984) and displayed in further detail below. The main target of this paper is to summarize some recent lines of evidence (Bartoli et al., 2005, 2006; prelim. results of Groeneveld, 2005; Groeneveld et al., 2006; Schneider and Schmittner, 2006; Steph et al., 2006) that suggest direct links between the final closure of the Central American Seaways (CAS), more precisely that of Panama, and various follow-up processes in the North Atlantic, the atmosphere, and elsewhere, that may have triggered changes in poleward heat and moisture transports and finally, have been responsible for the onset of full glaciation on Greenland and for the numerous and gradually intensifying Quaternary-style glaciations in Eurasia and Laurentia.

2 Conceptual models that try to explain the onset of major NHG

Cane and Molnar (2001) first proposed the gradual closure of the Indonesian Seaways near 4 Ma as forcing important to set the stage for the onset of Quaternary-style climates. More precisely, they suggested that the (poorly dated) northward plate-tectonic shift and the volcanic build-up of the (previously little known) small, elongated island of Halmahera northwest of New Guinea finally barred the West Pacific Warm Pool from warming the Indonesian Throughflow subsequently fed by cooler subsurface waters from the subtropical Northern Pacific (Fig. 3). On the other hand, the near-surface heat export from the West Pacific Warm Pool was then diverted to the northwestern Pacific. However, the Halmahera event occurred approximately one million years prior to the actual onset of the major NHG (∼3.2–2.7 Ma) and thus cannot adequately explain this turning point in climate history.

Changes in orbital forcing of climate form a further potential mechanism to initiate the onset of major NHG, first proposed by Maslin et al. (1995, 1996) and recently by several authors such as Ravelo et al. (2006). Indeed, the amplitudes of orbital obliquity cycles increased significantly ∼3.0–2.5 Ma. This trend closely paralleled the major increase in global ice volume as recorded by the benthic δ^{18}O signal (Fig. 2). However, the increase in amplitudes of obliquity cycles were reversible (at 2.25–1.8 Ma; Laskar et al., 2004) whereas the onset of major NHG was not or only to a minor degree and, thus, cannot be properly explained.

Huybers and Molnar (2007) established a more sophisticated approach to test the potential influence of orbital forcing on the onset of major NHG. They calculated the number of positive-degree days (PDD) for North America >50° N, obtained by applying temperature perturbations at high latitudes, expected to result from tropical anomalies and orbital variations (Fig. 4b). After ∼4.2 Ma the PDD number decreased gradually down to a lowstand that persisted after

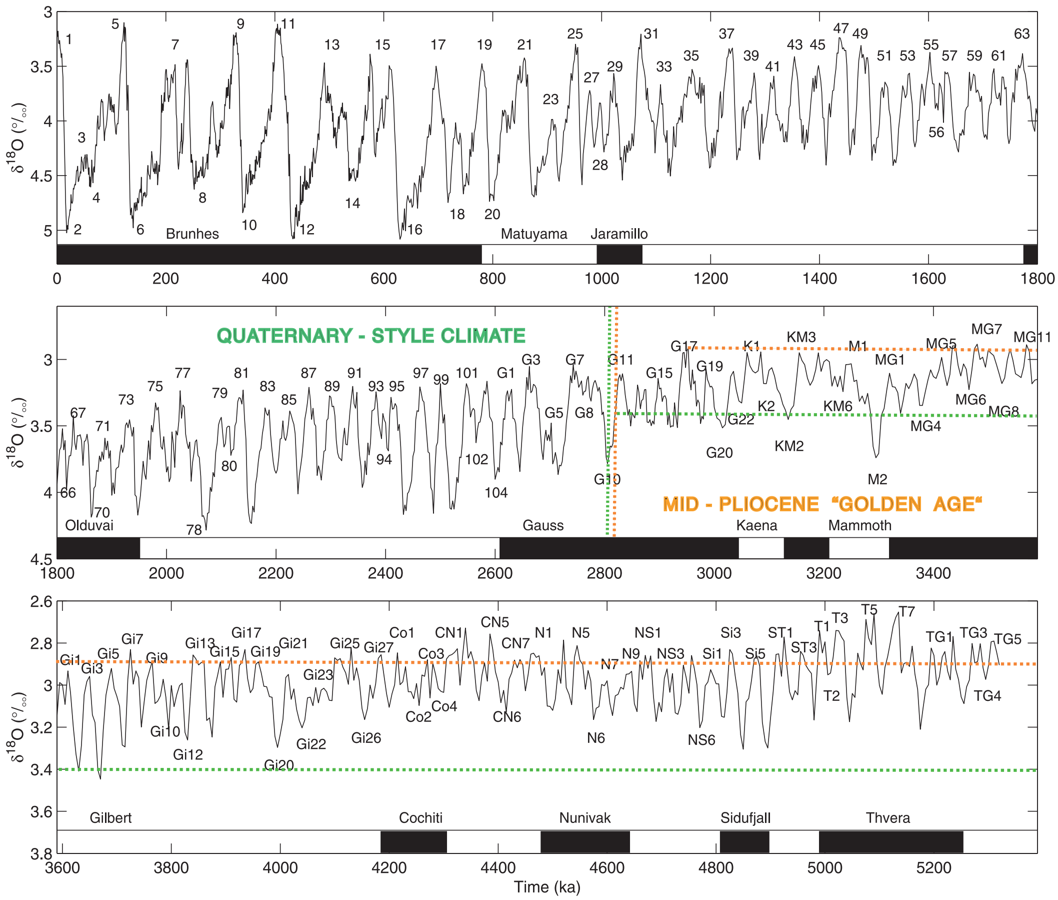

Fig. 2. "LR04" benthic δ^{18}O record of global ice volume changes over the last 5 m.y. (Lisiecki and Raymo, 2005; modified): Transition from the mid-Pliocene "Golden Age" (2.9–3.4‰) to Quaternary-style climates near 3.0–2.8 Ma. Note the expanded vertical scale at >3.6 Ma. The "Golden Age" represents a state of small-scale and fairly uniform climate oscillations that continued since 4.0 Ma, subsequent to a further 0.2–0.3‰ increase of cold δ^{18}O excursions only near 4.2–4.0 Ma in the middle Early Pliocene. Numbers are marine isotope stages (MIS).

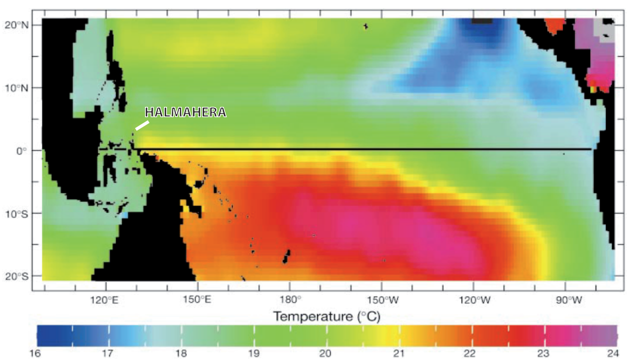

Fig. 3. Location of the island of Halmahera, today preventing the WPWP from flowing into the Indonesian Throughflow (Cane and Molnar, 2001; modified).

~1.8 Ma. This trend preceded the start of the long-term cooling of sea surface temperatures (SST) in the eastern equatorial Pacific (Lawrence et al., 2006) by ~0.5 My (Fig. 4a). Likewise, it led the build-up of major NHG by more than 1 My (Fig. 4c). This time span requires an extremely long-lasting internal memory effect in the climate system, difficult to conceive, thus leading the authors to the honest conclusion: "Understanding the puzzle of what caused the eastern equatorial Pacific to cool off on a timescale too long to invoke the atmosphere-ocean-cryosphere system by itself now appears all the more pressing."

Recently, Lunt et al. (2008) made a strong argument that a decline in Pliocene atmospheric CO_2 levels from 400 to 280 ppmv may have controlled the onset of major NHG (Fig. 5). This decline won't affect precipitation patterns over Greenland and the ambient sea regions but will trigger a significant decrease of surface temperatures by 2–3°C all over Greenland, thus, triggering major ice growth – as to be expected from predicting a negative greenhouse effect.

The main problem of this model study is the sedimentary records published so far, which hardly show any evidence for an atmospheric CO_2 drop as postulated for the mid-Pliocene. The two reconstructions cited (Kürschner et

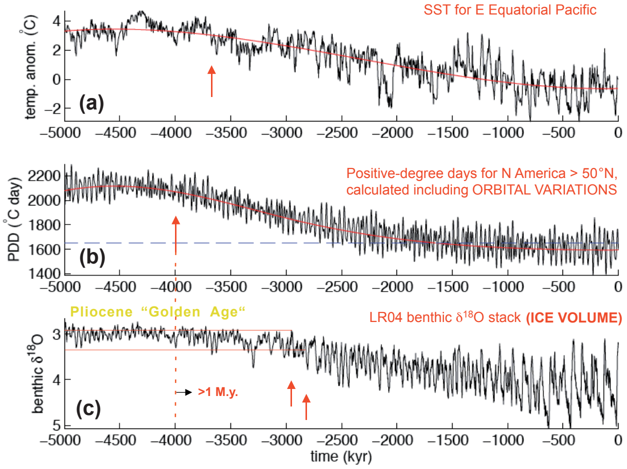

Fig. 4. Model of Huybers and Molnar (2007; suppl.) on **(b)** North America's "Positive Degree Days" (PDD), compared with East Pacific cooling/temperature anomalies (Lawrence et al., 2006) **(a)**, and the δ^{18}O record of growth of global ice volume (Lisiecki and Raymo, 2005) over the last 5 M.y **(c)**. Vertical arrows mark major tipping points in climate records. The time span between the onset of reduced positive-degree days and the end of the Pliocene "Golden Age" amounts to >1 M.y.

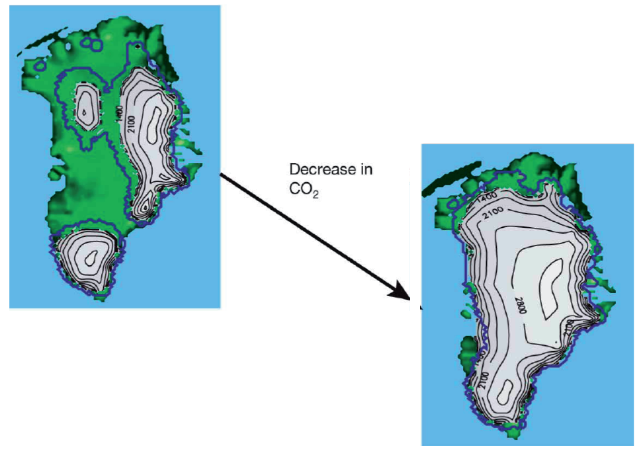

Fig. 5. Growth of Greenland ice sheet, induced by the decline in atmospheric CO_2 from 400 to 280 ppmv (model of Lunt et al., 2008; modified).

al., 1996; Raymo et al., 1996) do not display the postulated long-term shift in CO_2 coeval with the onset of major NHG, moreover, they show a range of uncertainty of ∼120 ppmv, that is as large as the shift investigated, and finally, short-term trends that contradict each other. On the other hand, both alkenone- and boron-isotopes-based Cenozoic CO_2 records established by Pagani et al. (2005) and Zachos et al. (2008) just revealed the contrary, no general CO_2 decrease around 3 Ma ago but a fairly constant "pre-industrial" CO_2 level near 280–320 ppmv persisting over the last 25 My. Also, the cited records do not display a potential 400-ky cycle in atmospheric CO_2, which may be expected as implication of various planktic δ^{13}C records of low-latitude ocean surface waters (Wang et al., 2004 and 2009) and may also play an important role in climate change, little recognized yet.

Finally and most important, in case we indeed identify sound evidence for the postulated unique and abrupt CO_2 drop, the open question on the ultimate forcing for the onset of major NHG was just postponed one step further back. That is, we needed to solve the problem, which change in global carbon reservoirs, in particular which changes in ocean Meridional Overturning Circulation (MOC) may have triggered a fairly abrupt and long-lasting drop in atmospheric CO_2 during the mid-Pliocene, then serving as a mere amplifier mechanism for climate change, similar to orbital-scale CO_2 oscillations found over the last 400 ky (Kawamura et al., 2007).

Possibly, the final closure of the CAS, which triggered major changes in the Atlantic MOC (see below), may have formed *the* mechanism suitable to induce the postulated but not yet identified major CO_2 drop. For example, foraminiferal δ^{11}B and alkenone-based records (Foster et al., 2008; prelim. data presented as AGU poster) suggest various short-term and marked positive and negative shifts in mid-Pliocene pCO_2. Apparently, they were coeval with the short-term re-openings and closings of CAS shown further below, but finally, around 2.75 Ma ago, may have summed up to a long-term decline of 100–120 ppmv.

3 Models and concepts on the final closure of the Panamanian Isthmus and implications for global climate change

The final closure of Central American Seaways (CAS) presents the most recent plate-tectonic change of ocean configuration in geological history, an uplift process resulting from the subduction of the Galapagos aseismic ridge (Meschede and Barckhausen, 2002). Weyl (1968) and thereafter Keigwin (1982) first proposed this event as the potential forcing for the onset of major NHG and Quaternary-style climates. On the basis of diverging nannofossil communities, Kameo and Sato (2000) first succeeded to pin down the final closure of CAS to an age close to 2.76 Ma (marine isotope stage (MIS) G6; equal to 2.73 Ma on the revised timescale LR04; Lisiecki and Raymo, 2005), a timing that indeed comes close to the onset of major NHG as first derived by Shackleton et al. (1984).

Maier-Reimer et al. (1990) first employed an ocean general circulation model (O-GCM) to simulate the potential impact of the closure of CAS on ocean circulation. Accordingly, the closure stopped the incursion of Pacific lower-salinity surface waters diluting West Atlantic surface water salinity (SSS), thus inducing a profound rise in poleward heat

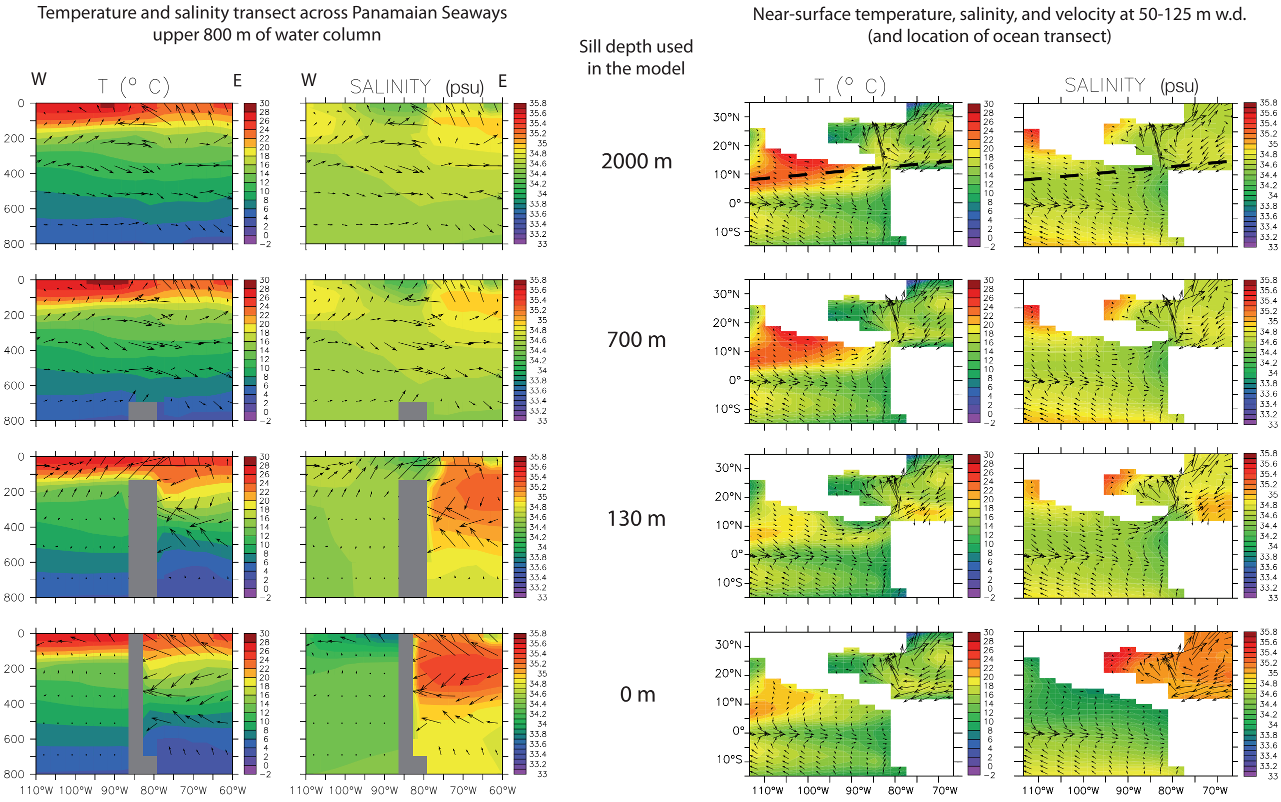

Fig. 6. Impact of shoaling of Panamanian Seaways on Caribbean and equatorial east Pacific upper ocean water mass signatures in a high-diffusion (HD) experiment with the UVic-ESCM model (Schneider and Schmittner; 2006).

and salt transport and in turn, in Atlantic MOC. Later-on, a number of more sophisticated GCM tests basically confirmed these results (e.g., Murdock et al., 1997; Mikolajewicz et al., 1997; Prange and Schulz, 2004; Klocker et al., 2005; Schneider and Schmittner, 2006; Lunt et al., 2007, 2008). Schneider and Schmittner (Fig. 6) focussed on testing the role of four subsequent Panamanian sill depths from −2000 up to zero m on adjacent sub-SSS and sea surface temperature (SST) distributions. Different from previous concepts (Haug et al., 2001), they found Pacific-to-Atlantic sub-SSS contrasts at 50–125 m water depth, which did not respond with any noteworthy rise to the closure of intermediate waters from 2000 to 700–500 m water depth. At sill depths of 300 to 250 m only one third, at 130 m sill depth, however, already two thirds of the final sub-SSS contrasts (i.e., 1.2 psu) were established (Figs. 6 and 7). Accordingly, it was only the closing of the last 250–130 m depth of the Panamanian gateways, that was finally crucial in triggering major changes in Atlantic MOC.

Driscoll and Haug (1998) first conceived the implications of an enhanced North Atlantic MOC for the onset of major NHG (Fig. 8). Their “Panama Hypothesis” tries to reconcile the effects of two actually counteracting forcings, increased poleward heat and moisture transports for the build-up of a continent-wide ice sheet on Greenland. Driscoll and Haug postulated that stronger heating of the northern North Atlantic will result (1) in enhanced evaporation and moisture transport via the westerlies to northwestern Eurasia, as also displayed by the model of Lunt et al. (2007), (2) in much increased river discharge from Siberia to the Arctic Ocean, in turn leading to (3) more sea ice formation and (4) more Arctic albedo, and therefore, to (5) more favorable conditions for the growth of Northern Hemisphere ice sheets.

On the basis of their fully coupled, fully dynamic ocean-atmosphere models, Klocker et al. (2005) and later Lunt et al. (2007) indeed confirmed that the closure of Panamanian Seaways provided the warming expected for the North Atlantic (Fig. 9), more intense Atlantic thermohaline circulation, and enhanced precipitation over Greenland and the Northern Hemisphere continents. However, they found that these forcings may be too small by an order of magnitude to produce the observed major ice sheet growth which marked the onset of major NHG and Quaternary-style climates. Though we wonder, to which degree the HadCM3 global climate model is able to capture the full possible range of regional sea-ice variations in the Arctic and the corresponding changes in surface albedo. The model used in the study of Lunt et al. (2007, 2008) does not include a realistic

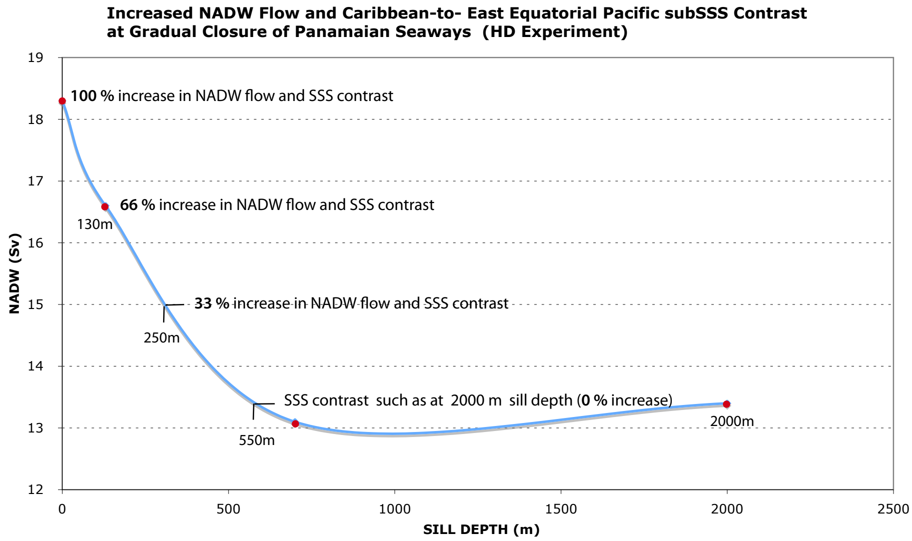

Fig. 7. Increase in NADW flow and underlying East-Pacific-to-Caribbean sub-sea surface salinity (subSSS) contrasts over the final closure of the Panamanian Seaways. Changes in NADW flow were calculated from HD model results of Schneider and Schmittner, 2006; changes in SSS anomaly at 50–125 m w.d. in waters ambient to Sites 999 and 1241 were estimated from Fig. 6 values and considered as forming a largely linear relationship with changes in NADW flow.

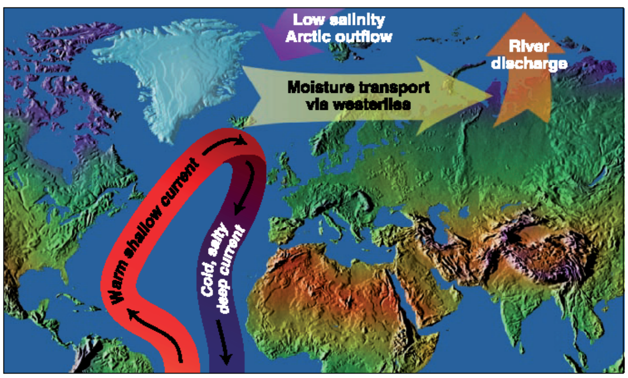

Fig. 8. Driscoll and Haug (1998) model on "Panama Hypothesis". As a result of closing CAS the poleward transport of heat with the North Atlantic Current is intensified, inducing enhanced evaporation in the North Atlantic and in turn, a rise of poleward atmospheric moisture transport and finally, a freshening of the Arctic Ocean, sea ice formation, and enhanced albedo.

sea-ice rheology (Bryan, 1969) and uses simplistic parameterizations for sea-ice albedo (Gordon et al., 2000). Therefore, climate feedbacks that involve changes in sea-ice cover and the associated surface albedo are subject to large uncertainties in these model simulations. Moreover, we note that ice albedo is commonly used as a tuning parameter in coupled climate models, which makes the models less reliable with respect to predictions of future or past Arctic sea-ice changes (Eisenman et al., 2007).

Recently, Molnar (2008) published harsh critiques on the proposed linkages between closing CAS and the onset of Quaternary-style Ice Age climates, arguments that need to be compared with the records presented below.

4 Sediment records on the final closure of CAS

In contrast to the view of Molnar (2008), most of the model-predicted rise in SSS differences between the Caribbean and the eastern Equatorial Pacific forms a clear record of the closure of the Panama Seaways over the last 250–300 m water depth (Figs. 6, 7). A range of rising SSS differences closely similar to the modelled anomalies was obtained from calculating the anomaly record between millennial-scale mid-Pliocene SSS records from Ocean Drilling Program (ODP) sites 999 and 1241 drilled to the northeast and southwest of the Panama Isthmus (Fig. 10; based on Groeneveld, 2005; Groeneveld et al., 2006; Steph et al., 2006; Tiedemann et al., 2007), two sites that were well selected for this study. As first discussed by Bartoli et al. (2005), these SSS differences remained close to zero until ~4 Ma. First but still reversible events of rising SSS differences occurred near 3.75 Ma and 3.5–3.3 Ma, then reaching up to 0.5 psu and more; at 3.16 Ma they first reached 0.8–1.0 psu. These short precursor events of a major shallowing and/or closure of the Panama seaways may in part record short-term volcano-tectonic events, in part orbital ice and sea level cycles. In contrast, largely irreversible SSS contrasts of 0.4–0.9 and 1.0–1.3 psu were found after 2.95 Ma and at 2.5 Ma, respectively, values that came close to the model-predicted maximum anomalies in SSS. The latter two events reflect the two-step final closure of the shelf seaway induced by the uplift of the Panama Isthmus, a forcing this time stronger than any ongoing overlapping orbital sea-level fluctuations also seen in the record of Fig. 10. Land-based evidence from Panama likewise documents the first full closure of the seaway near 2.85 Ma (Coates et al., 2004, and oral communication).

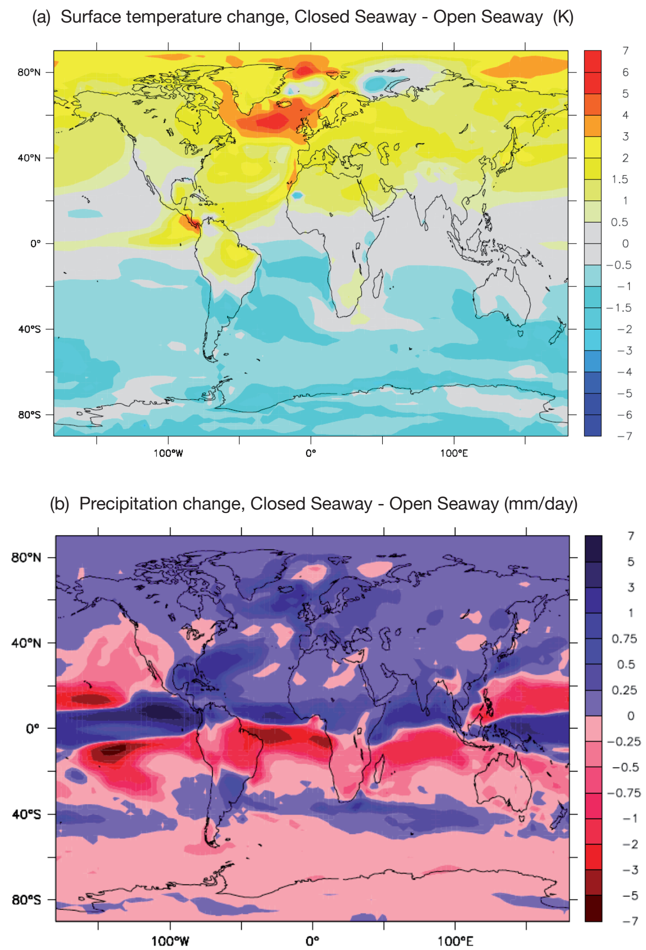

Fig. 9. Changes in surface temperatures **(a)** and precipitation **(b)**, comparing Closed Panamanian Seaways with Open Seaways (model experiments of Lunt et al., 2007).

In terms of both millennial-scale age control and environmental evidence for the final closure of CAS, we regard the SSS anomaly record of Fig. 10 as clearly superior to the various early published low-resolution and, in part, poorly dated and discontinuous marine records and bioevolution-based evidence listed for constraining the closure of CAS by Molnar (2008). Last but not least, we see a great advantage of the Caribbean-to-East Pacific SSS anomaly record in its close resemblance to SSS trends suggested by the model results of Figs. 6 and 7. In contrast to Molnar's objections, we conclude that initially still reversible, however, after 2.95 Ma irreversible steps in closing the CAS are well defined in terms of age by means of rising SSS differences between the S.W. Caribbean and eastern Equatorial Pacific (Fig. 10) and consistent with land-based evidence.

Model-based evidence suggests that the final closure of the CAS necessarily led to two counteracting climatic forcings with an opposed effect on high-latitude glaciation, similar to the opposed forcings on modern Greenland ice (Fig. 1). (a) An increased poleward heat transport (Fig. 9a) implied enhanced glacial melt, whereas (b) an increased poleward transport of atmospheric moisture to northern Eurasia (Fig. 9b) induced a freshening of the Arctic ocean and enhanced snow and ice accumulation, in particular at perennial temperatures below zero centigrade. In the following, we display sediment records from the northern North Atlantic that provide independent evidence for the two opposed processes and their potential links to a coeval and/or slightly delayed onset of NHG.

5 North Atlantic sediment records of the onset of major NHG

The onset of major NHG is best documented at ODP Site 907 to the east of Greenland and the East Greenland and East Iceland Currents (Figs. 11–13), a position ideal in monitoring the discharge of ice rafted debris (IRD) of icebergs coming from northeast Greenland and the Arctic ocean. A second IRD record measured at Site 1307 (Fig. 11; Expedition 303 Scientists, 2006) also includes IRD originating from mountain glaciers calving nearby in southeast Greenland up to the extended Scoresby Sound. Accordingly, IRD changes at Site 907 (Jansen et al., 2000; Bartoli et al., 2005) may best display the long-term and major trends in the evolution of NHG, whereas IRD of Site 1307 near the southern tip of Greenland may add interesting aspects with regard to the East Greenland Current (EGC) and short-term orbital-scale climate oscillations.

IRD abundances at Site 907 (Fig. 12) already suggest some kind of causal link between the build-up of major NHG on northern Greenland and the final changes in CAS aperture, in harmony with the model of Driscoll and Haug (1998). The suite of changes in IRD 3.4–2.6 Ma follow with great detail and a persisting lag of ~40 ky a closely similar suite of distinct steps in the evolution of CAS (Fig. 12). For example, SSS contrasts between East Pacific and Caribbean document a first full closure at 3.24–3.16 Ma, a subsequent suite of three short re-openings and minor closings 3.13–2.97, and a final closure 2.96–2.87 Ma. Except for the final episode of CAS closure around 2.67 Ma (when a major Greenland ice sheet was already established; see below), each of these events was followed directly by a distinct rise or drop in IRD abundance (on an exponential scale), and a final IRD extreme at MIS G10, 2.82 Ma. However, this match of two records does not yet provide the actual evidence necessary to infer the origin of major NHG (in harmony with doubts of Molnar, 2008). Certainly, the persistent lag of changes in IRD abundance demonstrates (1) significant memory effects in the climate system, and (2) that the oscillations in the build-up and melt of continental ice volume and resulting eustatic sea level variations cannot have controlled primarily the closing events of the CAS, but viceversa, that the CAS events have somehow controlled variations in IRD.

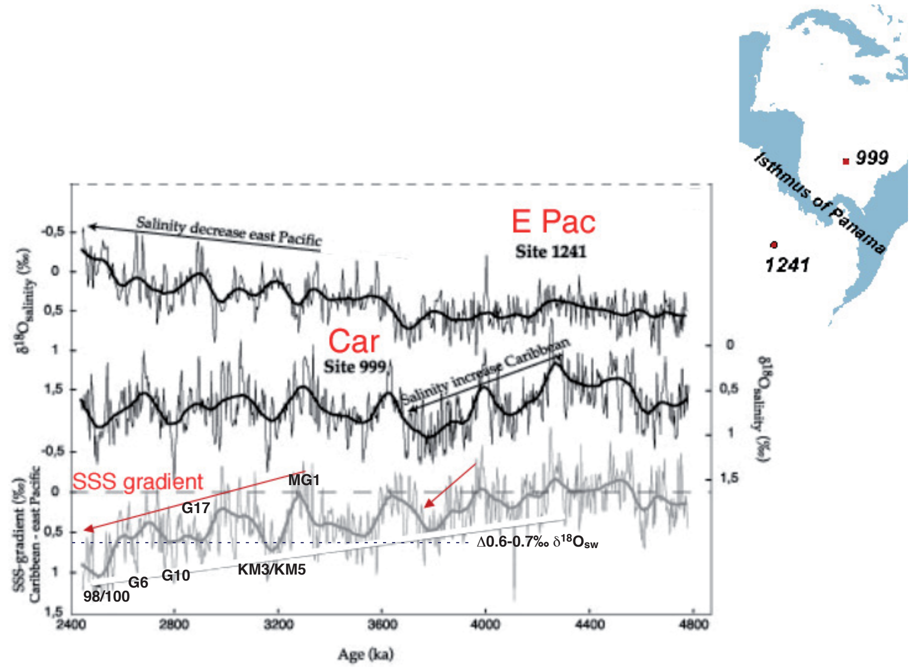

Fig. 10. Mid-Pliocene increase in SSS gradient between Caribbean (CAR) and eastern equatorial Pacific (E Pac), deduced from δ^{18}O and Mg/Ca-based SST values of *Globigerinoides sacculifer*, a species growing at ~50–100 m water depth (Groeneveld, 2005; Groeneveld et al., 2006; Steph et al., 2006). A $\delta^{18}O_W$ gradient of 0.6–0.7‰ (hatched line; uncertainty of ~0.07‰ for the 10-point running average of $\delta^{18}O_W$) equates to a SSS gradient of 1.2–1.8 psu (Simstich et al., 2002) which correspond to a full closure of CAS according to the gradients shown in Fig. 6. Age scales tuned to Tiedemann et al. (1994), slightly modified by Tiedemann et al. (2007), come close to LR04 (Lisiecki and Raymo, 2005). Small letters and numbers at SSS gradient record (98/100, G6, G10, etc.) label marine isotope stages.

The IRD record from IODP Site 1307 (Fig. 12a) appears less straightforward for correlations with the closings of CAS because of multiple potential IRD sources – and two competing age models (Fig. 13). Using age model 1, a first increase in IRD paralleled the first full closure of CAS around 3.2 Ma (MIS KM3–KM2), without any time lag. However, this increase continued later on from 3.17–3.02 Ma, in contrast to the coeval step-wise re-opening of CAS. Using age model 2, which appears slightly superior to model 1 (Fig. 13), IRD showed a medium-high IRD peak during the eminent glacial precursor stage M2, 3.33–3.24 Ma, but the main IRD increase only occurred from 3.11–3.02 Ma, that was 50 kyr after the first closure and coeval with the re-opening of CAS. After a subsequent minor abundance drop, IRD formed a plateau at high level, starting with the major re-opening of CAS near 3.0 Ma and ending with a further major increase 2.7–2.66 Ma.

In summary, we need to consider significant memory effects linked to the build-up of continental ice volume, behavior of mountain glaciers, ice break-outs, and IRD formation at cold stages, effects controlled by overlapping consequences of ice isostasy, size of pre-existing ice sheets and fjords, supposed thermal isolation of Greenland, changing amplitudes of orbital cycles, etc. These effects are inbuilt into the complex climate system and imply significant lags for the IRD signal, that may amount to >40 kyr, likewise during the long period of MIS MG7–MG11 (3.67–3.33 Ma), when CAS have been very shallow, and at MIS KM2 (3.13 Ma), right after the first full closure of CAS (Fig. 12a).

6 Sediment records showing increased poleward heat transport and enhanced MOC in the North Atlantic

After each major closing event of CAS we found evidence – with hardly any phase lag – for an increased poleward North Atlantic heat transport recorded at two different sediment profiles obtained from the eastern and central North Atlantic (Figs. 11 and 14; Bartoli et al., 2005). At both sites, lines enveloping short-term interglacial (Mg/Ca-based) SST maxima also display a distinct temperature rise by 2°–3°C coeval with or slightly lagging the major closing events of CAS near 3.33, 3.16, 2.92–2.8, and 2.66 Ma (except for the poorly recovered MIS G4–G1 at Site 609). Vice versa, most subsequent drops in maximum temperature are linked to renewed openings of the seaways. Accordingly, mid-Pliocene changes of poleward ocean heat transport linked to both the North Atlantic and Irminger Currents indeed appear closely related to the final closing and re-opening of CAS, as

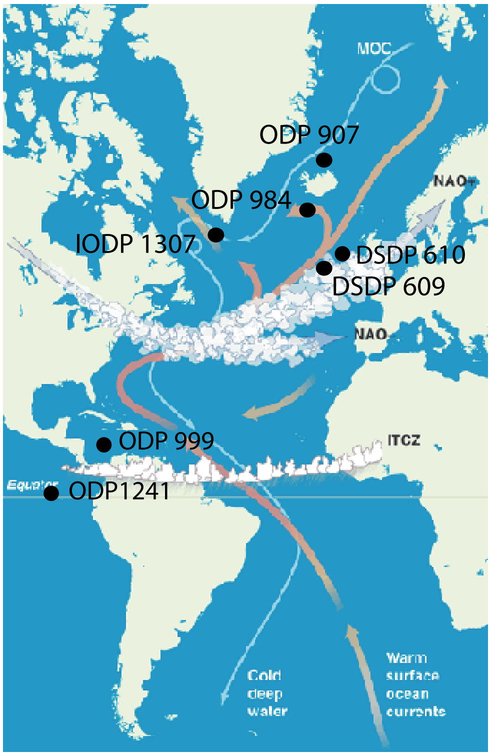

Fig. 11. DSDP, ODP, and IODP site locations and surface and deepwater currents in the Atlantic.

predicted by model simulations and in contrast to the doubts of Molnar (2008).

Each warming of the North Atlantic Current matched an increase in sea surface salinity by 0.2–0.4 psu (as inferred from paired planktic δ^{18}O and Mg/Ca-based SST values; Bartoli et al., 2005). Accordingly, each closing of CAS and, in particular, the major event 2.95–2.82 Ma resulted in significantly intensified convection of deepwater in the Nordic Seas. The result of stronger Atlantic overturning circulation is suggested by a long-term temperature drop ($-1.5°$ and $-2°$C), a slight salinity rise, and an increase in density (benthic δ^{18}O values) of North Atlantic Deep Water at Sites 609 and 610 (Fig. 14). These trends paralleled clearly the major twofold (exponential) rise in IRD at Site 907, that depicts the onset of major Northern Hemisphere Glaciation and Quaternary-style climates, in particular, around 2.93–2.82 Ma, when high IRD contents started to persist. The coeval changes suggest a causal linkage between enhanced MOC and the build-up of continental ice sheets.

7 Sediment records of increased poleward freshwater transport

Model simulations (Lunt et al., 2007; Prange and Schulz, 2004; Schneider and Schmittner, 2006) suggest that the closure of Panamanian Seaways led to increased precipitation, in particular, over East Greenland, the northeastern North Atlantic, and western and central Europe (Fig. 9b), and fairly minor, all over the Northern Hemisphere. Today, the East Greenland Current (EGC) and its low sea surface salinity (SSS) of 32–33 psu and temperatures near 0°C provide a summary record of the outflow of low-saline surface waters from the Arctic Ocean into the northwestern North Atlantic. Thus IODP Site 1307 drilled near to the southern tip of Greenland (Fig. 11; Expedition 303 Scientists, 2006) occupies an ideal location for monitoring past changes in the EGC and its source region, the Arctic Ocean, including potential events of mid-Pliocene freshening and cooling to test the "Panama Hypothesis".

As soon as a full closure of Panamanian Seaways had been completed for the first time around 3.2–3.16 Ma (although then still reversible), the sediment record of Site 1307 indeed showed a significant change in the composition of EGC waters from 3.15/3.08–3.02 Ma with Age Model 2 and from 3.3/3.22–3.02 Ma with Age model 1 (Fig. 12b and c; SST/SSS records over Kaena subchron are irregular because of insufficient foraminiferal tests; Fig. 13). Both SST maxima and minima started to decrease by 6°C in parallel with SSS oscillations that dropped by ~1‰ $\delta^{18}O_{\text{surface water}}$ equal to ~2 psu. This immense change in the density of subsurface waters (probable habitat of *N. atlantica* per analogy to *N. pachyderma s*; Simstich et al., 2002) exceeds by far any model predictions of enhanced poleward atmospheric moisture transport (Klocker et al., 2005; Lunt et al., 2007). The freshening of the EGC led necessarily to enhanced stratification of the northwestern North Atlantic and reduced stability of Atlantic MOC and introduced a new, "Quaternary"-style regime of the EGC, which was traced at Site 1307 at least until 2.7 Ma.

The great freshening of the EGC, in turn, is an immediate record of Arctic sea surface conditions, hence providing indirect but important evidence for a coeval substantial expansion of perennial sea ice and enhanced albedo in the Arctic Ocean, the condition crucial for promoting the onset of major NHG as result of the full closure of CAS. Our evidence appears in harmony with early diatom records (Herman, 1974; Stein, 2008) and opposed to various low-resolution records (Darby et al., 2008; Frank et al., 2008) that suggest a much earlier date for the onset of perennial sea ice in the Arctic Ocean.

Obviously the mid-Pliocene increase of poleward freshwater transport has overcompensated by far the coeval effect of enhanced poleward heat transport. However, the question, as to where the freshwater flow of the EGC has actually originated, remains unsolved. Although GCM models show that

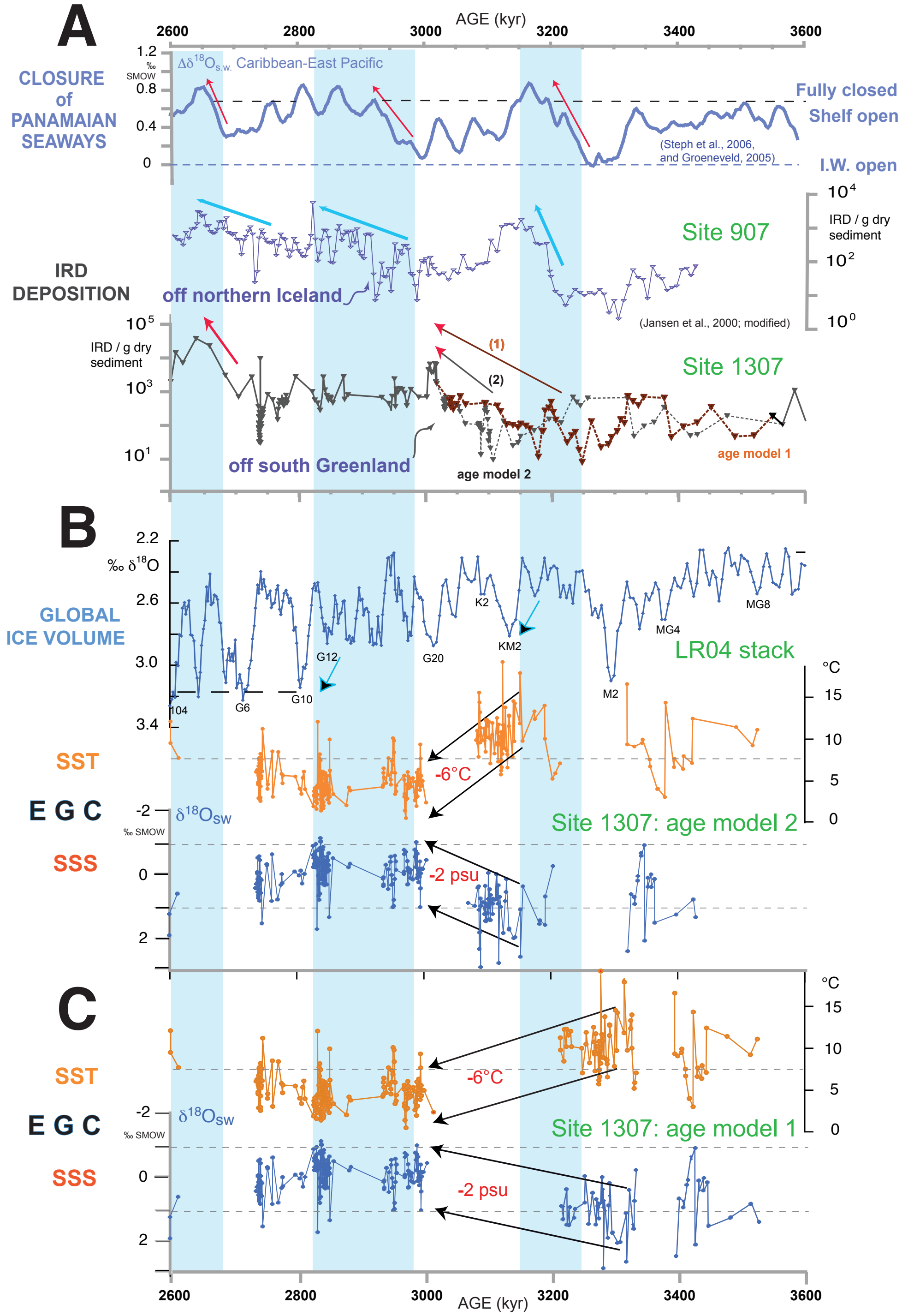

Fig. 12. **(A)** Closure of CAS (record inverted from Fig. 10) and IRD abundance at ODP Site 907 (Jansen et al., 2000; age model modified by Lacasse et al., 2002) and IODP Site 1307 (age models 2 and 1 are displayed in Fig. 13), where the great IRD increase 3.12/3.22–3.02 Ma matches a major cooling and freshening of the East Greenland Current (EGC), shown below. **(B)** and **(C)** Stacked benthic δ^{18}O record LR04 (Lisiecki and Raymo, 2005; small letters and numbers label marine isotope stages 104 – MG8) versus major sub-sea surface temperature (SST) and salinity (SSS) drops of the EGC at IODP Site 1307, 3.5–2.7 Ma, displayed for age models 2 and 1. Sub-SST estimates are based on the Mg/Ca ratio of planktic subsurface species *Neogloboquadrina atlantica*. Two-psu shift in SSS is derived from a shift in $\delta^{18}O_{\text{surface water}}$ ($\delta^{18}O_{sw}$, i.e., the $\delta^{18}O_{\text{carbonate}}$ record of *N. atlantica* as depicted in Fig. 13, after correction for SST) using a conversion factor of 1:2 as for modern EGC water (Simstich et al., 2002).

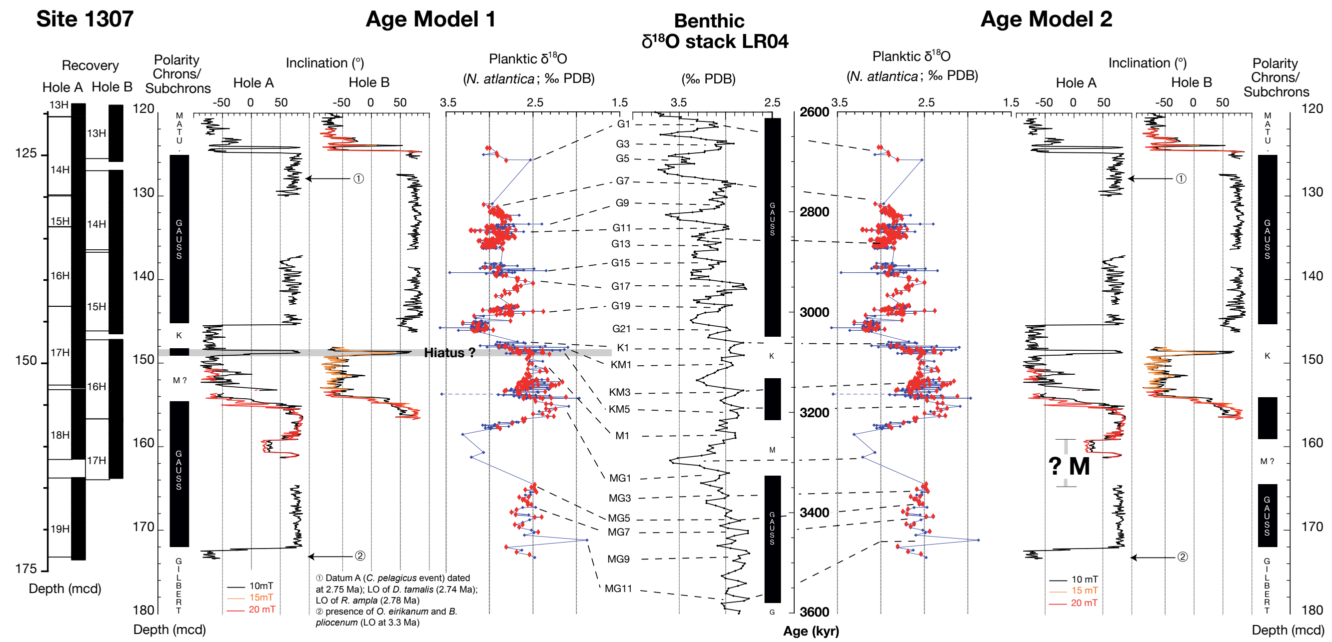

Fig. 13. Alternative mid-Pliocene age models 1 and 2 for IODP Site 1307. Far left: Site 1307 core recovery vs. depth. Left and far right margins: Magnetic polarity chrons and subchrons (Expedition 303 Scientists, 2006). Magnetic inclination obtained at 10, 15, and 20 milli Tesla. Note two different choices in assigning the Kaena (K) and Mammoth (M) subchrons. MATU. = Matuyama chron. Figure center: Two different modes for tuning (thin hatched lines) the planktic δ^{18}O record of Site 1307 to benthic δ^{18}O stack LR04 (Lisiecki and Raymo, 2005); interglacial marine isotope stages are labeled. Red planktic δ^{18}O values are measured on >10, blue values on <10 specimens. Potential hiatus in Age Model 1 is marked as grey bar. Biostratigraphic datums are numbered by (1) and (2).

the closure of CAS indeed implied a modest rise in poleward atmospheric moisture transport over vast parts of the northern Hemisphere (Fig. 9b) with a runoff into the Arctic Sea, this increase appears too modest for generating the major freshening found for the EGC and climatic changes such as the onset of major glacification on Greenland (Lunt et al., 2007, 2008).

Thus, we need a substantial further forcing to explain the striking SST/SSS decrease near MIS KM3 to G21. A recent model study (Steph et al., 2006) now suggests a suitable mechanism not yet considered (Fig. 15). Using the NCAR Community Climate System Model, version CCSM2/T31x3a (Prange, 2008), it shows that the full closing of CAS led to an increased steric height in the North Pacific (+15 cm as compared to the open CAS scenario), a decreased steric height in the North Atlantic (−20 cm) and, as a consequence, a doubling of the low-saline Arctic Throughflow (∼1 Sv today) from the North Pacific through the Bering Strait up to a strongly intensified EGC, when assuming a Holocene sea level stand.

Unfortunately, no SST and SSS records have been established yet in the subarctic North Pacific for the interval 3.2–3.0 Ma. However, the global δ^{18}O reference record LR04 (Fig. 2) indicates mid-Pliocene interglacial and in part, also cold-stage sea level stands (i.e., MIS M1-G17, except for MIS KM2 and G20) that were up to 30–40 m higher than today. Accordingly, the aperture of the Bering Strait near ∼3.15 Ma may have been much wider and in turn, the increase in Bering Strait throughflow even larger. On the other hand, one may assume that the Bering Strait valley, today roughly 50 m deep, was gradually deepened by erosion with each emergence due to repetitive eustatic sea level lowerings which marked the 60 glacial stages of the last 3 m.y. In this case the model-based conclusion on a doubling of the throughflow appears more realistic. Possibly, the enhanced throughflow may be also reflected by increased advection of Pacific, in particular siliceous plankton.

Once low temperatures and low salinity of the EGC had been established, this current led to robust thermal isolation of East Greenland from the poleward heat transport further east through the North Atlantic and Norwegian Currents. Since this time the EGC formed a barrier important to promote the growth of continental ice. However, this feature is difficult to assess by any low-resolution climate models. Nevertheless, while almost the entire Northern Hemisphere becomes warmer in response to CAS closure, the simulations with CCSM2/T31x3a exhibit a year-round regional cooling over Central and South Greenland (up to 2°C) along with enhanced annual snowfall (up to 50 kg/m^2 in South Greenland). Further details of these model results will be presented elsewhere (Prange and Schulz, 2009, in preparation). The Greenland continental ice sheet, once established, strengthened the

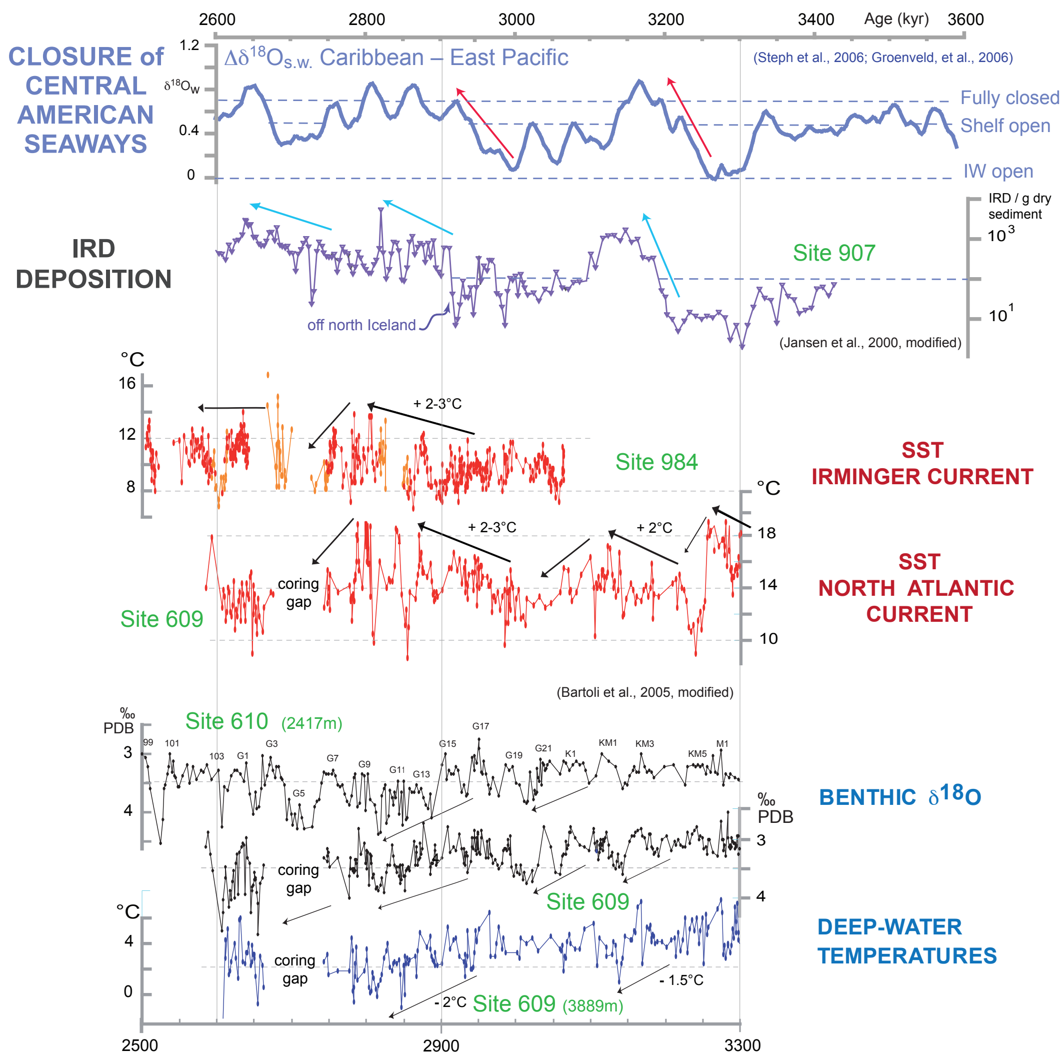

Fig. 14. Closing of CAS (record inverted from Fig. 10), IRD abundance at Site 907, warming of northern North Atlantic (Mg/Ca-based SST records from ODP Sites 609 and 984), and increased Atlantic MOC deduced from a drop in Mg/Ca-based bottom water temperatures (BWT) at ODP Site 609 and increased benthic δ^{18}O values at ODP Sites 609 and 610 (Bartoli et al., 2005, modified; Kleiven et al., 2002). Age scales tuned to Tiedemann et al. (1994). Small letters and numbers (101 – M1) label marine isotope stages (MIS).

Greenland High and, in particular, northerly winds along its eastern margin (cf. Toniazzo et al., 2004). In turn, the enhanced winds again strengthened the EGC flow. This positive feedback, a kind of long-term memory effect, may have been crucial in keeping the low-salinity and cold regime of the EGC going over interglacial stages K1, G21, and G19, when the CAS was shortly re-opened until the renewed and final closure after 2.95 Ma (Fig. 12), when both effects (closed CAS and pronounced northerly winds along the East Greenland coast) were strong enough to drive a vigorous, similar to present-day, EGC that pushes the polar front across Site 1307.

In summary, we may conclude that the final linkage between the full closure of CAS and the onset of major NHG was accomplished through a significantly strengthened low-saline Bering Strait and Arctic Throughflow hitherto overseen (Molnar, 2008). The effects of this flow were far more substantial than the atmospheric poleward moisture transport and have clearly overcompensated the effects of enhanced poleward heat transport in the North Atlantic also resulting from the final closing of CAS. Once a major Greenland ice sheet had been established near 3.18–3.12 Ma and, in particular, after 2.9 Ma, it formed together with the outlined secondary feedback mechanisms, an ongoing nucleus for Quaternary-style climates recorded by Quaternary-style glaciations persisting in the Northern Hemisphere over the last 2.8–3.0 Ma.

Finally, it turns out that the outlined mid-Pliocene buildup of major NHG definitively does not form any analogue for a better understanding of the present and future evolution of

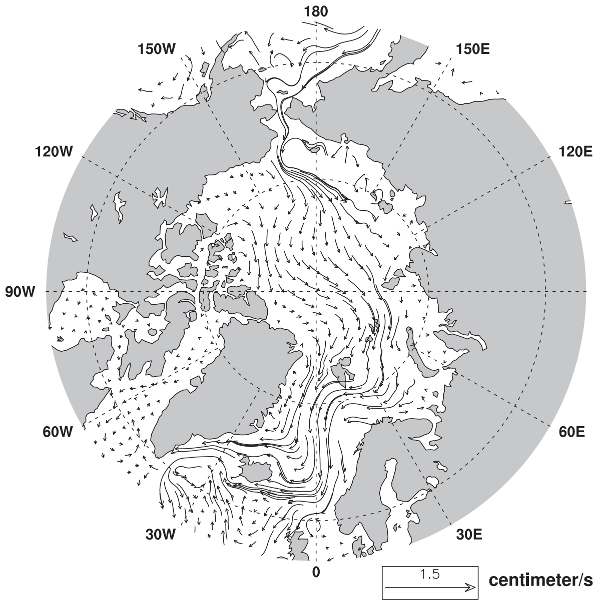

Fig. 15. Increased (doubled) flow rate of low-saline surface water through the Bering and Fram straits ("Arctic Throughflow") as a result of closing the CAS as simulated by the NCAR Community Climate System Model, version CCSM2/T31x3a (Prange, 2008). Shown here, is the difference between the two equilibrium runs (one with closed CAS, the other with open CAS arbitrarily applying a sill depth of 800 m and a width of ~200 km) in which the model is forced with present-day boundary conditions (i.e., a sensitivity study rather than a "true" simulation of Pliocene climates). The ocean component has a mean resolution of $3.6° \times 1.6°$ with 25 levels, while the atmosphere has a resolution of $3.75° \times 3.75°$ with 26 levels (detailed description of experimental set-up in Steph et al., 2006).

the Greenland ice sheet as a result of "Global Warming" in the northern North Atlantic. Whereas the modern warming is induced by increased atmospheric CO_2, that is particularly effective at high latitudes, the mid-Pliocene warming of the North Atlantic was linked to enhanced Atlantic MOC and the closing of equatorial seaways, forcings that were overcompensated by a significantly intensified cold Arctic Throughflow, in addition to the enhanced atmospheric poleward moisture transport. We have no reason to expect any analogue case of these ocean-driven changes in mid-Pliocene climate for the near future.

8 Conclusions

- Sediment records from the northern North Atlantic suggest that the final closing of Panamanian Seaways has led to the model-predicted increase in poleward heat transport and Atlantic MOC first near 3.25–3.15, later-on at 3.00–2.85 Ma.

- As result of the full closure of Panamanian Seaways the poleward flux of atmospheric moisture increased noteworthy and more important, a model study indicates that the flow of low-saline and cold surface waters from the North Pacific through the Bering Strait and Arctic Ocean was doubled. Together these two freshwater fluxes obviously have overcompensated the increased heat transport, thereby inducing a dramatic cooling and freshening of the EGC, a substantial expansion of perennial Arctic sea ice and albedo ~3.2–3.0 Ma, and in turn, the onset of major northern Hemisphere glaciation, first culminating near 2.82 Ma (MIS G10).

- Cooling and freshening of the EGC probably involved a positive feedback, the thermal isolation of Greenland from increased poleward heat transport, thus further promoting a persistent glaciation of Greenland and NHG.

- The onset of NHG and the Quaternary is most likely *no analogue* for today: Increased atmospheric pCO_2 is warming high latitudes in particular, thus leading to an enhanced melt of the ice on Greenland, whereas our results suggest that the mid-Pliocene formation of the full Greenland ice sheet was mainly induced by enhanced poleward freshwater transport and Arctic Throughflow, then compensating for a warming that mainly affected the temperate (Sites 609 and 610) and subpolar North Atlantic (Site 984).

Acknowledgements. We thank J. Groeneveld, P. Molnar, M. Schulz, S. Steph, R. Stein, and R. Tiedemann for fruitful discussions. Dan Lunt and a second anonymous reviewer for very helpful comments on a first version of the manuscript. Our studies are based on ample ODP and IODP sample materials analyzed with generous support by DFG Research Unit "Ocean Gateways" and project WE2679/2-1. The CCSM model experiments were performed on the IBM pSeries 690 Supercomputer of the Norddeutscher Verbund für Hoch- und Höchstleistungsrechnen (HLRN).

Edited by: G. M. Ganssen

References

Alley, R. B., Clark, P. U., Huybrechts, P., and Joughin, I.: Ice-sheet and sea-level changes, Science, 310, 456–460, 2005.

Bartoli, G., Sarnthein, M., and Weinelt, M.: Late Pliocene millennial-scale climate variability in the northern North Atlantic prior to and after the onset of Northern Hemisphere glaciation, Paleoceanogr., 21, PA4205, 1–15, 2006.

Bartoli, G., Sarnthein, M., Weinelt, M., Erlenkeuser, H., Garbe-Schönberg, D., and Lea, D.: Final closure of Panama and the onset of northern hemisphere glaciation, Earth Planet. Sci. Lett., 237, 33–44, doi:10.1016/j.epsl.2005.06.020, 2005.

Bryan, K.: A numerical method for the study of the circulation of the world ocean, J. Comp. Physics, 4, 347–376, 1969.

Cane, M. A. and Molnar, P.: Closing of the Indonesian seaway as precursor to east African aridification around 3–4 million years ago, Nature, 411, 157–162, 2001.

Coates, A. G., Collins, L. S., Aubry, M.-P., and Berggren, W. A.: The geology of the Darien, Panama, and the late Miocene-Pliocene collision of the Panama arc with northwestern South America, Geol. Soc. Amer. Bull., 116, 1327–1344, doi:10.1130/B25275.1, 2004.

Darby, D. A.: Arctic perennial ice cover over the last 14 million years, Paleoceanogr., 23, PA1S07, doi:10.1029/2007PA001479, 2008.

DeConto, R. M., Pollard, D., Wilson, P. A., Pälike, H., Lear, C. H., and Pagani, M.: Thresholds for Cenozoic bipolar glaciation, Nature, 455, 652–656, 2008.

Driscoll, N. W. and Haug, G. H.: A short circuit in thermohaline circulation: A cause for Northern Hemisphere Glaciation?, Science, 282, 436–438, 1998.

Eisenman, I., Untersteiner, N., and Wettlaufer, J. S.: On the reliability of simulated Arctic sea ice in global climate models, Geophys. Res. Lett., 34, L10501, doi:10.1029/2007GL029914, 2007.

Eldrett, J., Harding, I. C., Wilson, P. A., Butler, E., and Roberts, A. P.: Continental ice in Greenland during the Eocene and Oligocene, Nature, 446, 176–179, doi:10.1038/nature05591, 2007.

Expedition 303 Scientists, Site U1307, in: Proc. IODP, edited by: Channell, J. E. T., Kanamatsu, T., Sato, T., Stein, R., Alvarez Zarikian, C. A., Malone, M. J., and the Expedition 303/306 Scientists, 303/306, College Station TX (Integrated Ocean Drilling Program Management International, Inc.), doi:10.2204/iodp.proc.303306.107, 2006.

Foster, G. L., Seki, O., Schmidt, D. N., Kawamura, K., and Pancost, R.: Plio-Pleistocene pCO_2 – a multiproxy approach using alkenone and boron based carbonate system proxies, Eos Trans. AGU, 89(53), Fall Meet. Suppl. Abstract PP41D-1484, 2008.

Frank, M., Backman, J., Jacobsson, M., Moran, K., et al.: Beryllium isotopes in central Arctic Ocean sediments over the past 12.3 million years: Stratigraphic and paleoclimatic implications, Paleoceanogr., 23, PA1S02, doi:10.1029/2007/PA00147, 2008.

Gordon, C., Cooper, C., Senior, C. A., Banks, H., Gregory, J. M., Johns, T. C., Mitchell, J. F. B., and Wood, R. A.: The simulation of SST, sea ice extents and ocean heat transports in a version of the Hadley Centre coupled model without flux adjustments, Clim. Dynam., 16, 147–168, 2000.

Groeneveld, J.: Effect of the Pliocene closure of the Panamaian gateway on Caribbean and east Pacific sea surface temperatures and salinities by applying combined Mg/Ca and $\delta^{18}O$ measurements (5.6–2.2 Ma). PhD Thesis, University of Kiel, 2005.

Groeneveld, J., Steph, S., Tiedemann, R., Garbe-Schönberg, D., Nürnberg, D., and Sturm, A.: Pliocene mixed-layer oceanography for Site 1241 using combined Mg/Ca and $\delta^{18}O$ analyses of *Globigerina sacculifer*, in: Proc. ODP, Sci. Results, 202, edited by: Tiedemann, R., Mix, A. C., Richter, C., and Ruddiman, W. F., College Station, TX (Ocean Drilling Program), 1–27, doi:10.2973/odp.proc.sr.202.209. 2006.

Groeneveld, J., Nürnberg, D., Tiedemann, R., Reichart, G.-J., Steph, S., Reuning, L., D. Crudeli, D., and Mason, P.: Foraminiferal Mg/Ca increase in the Caribbean during the Pliocene: Western Atlantic Warm Pool formation, salinity influence, or diagenetic overprint?, Geochem. Geophys. Geosyst., 9(1), Q01P23, doi:10.1029/2006GC001564, 2008.

Haug, G. H., Tiedemann, R., Zahn, R., and Ravelo, A. C.: Role of Panama uplift on oceanic freshwater balance, Geology, 29, 207–210, 2001.

Huybers, P. and Molnar, P.: Tropical cooling and the onset of North American glaciation, Clim. Past, 3, 549–557, 2007, http://www.clim-past.net/3/549/2007/.

Hvidegaard, S. M. and Sandberg, L.: Study of elevation changes along a profile crossing the Greenland Ice Sheet, Poster EGU Vienna, EGU2009-8790, 2009.

Huybrechts, P., Gregory, J., Janssens, I., and Wild, M.: Modelling Antarctic and Greenland volume changes during the 20th and 21st centuries forced by GCM time slice integrations, Global Planet. Change, 42, 83–105, 2004.

Jansen, E., Fronval, T., Ranck, F., and Channell, J. E. T.: Pliocene-Pleistocene ice rafting history and cyclicity in the Nordic Seas during the last 3.5 Myr, Paleoceanogr., 15, 709–721, 2000.

Kameo, K. and Sato, T.: Biogeography of Neogene calcareous nannofossils in the Caribbean and the eastern equatorial Pacific – floral response to the emergence of the Isthmus of Panama, Mar. Micropal., 39, 201–218, 2000.

Kawamura, K., Parrenin, F., Lisiecki, L., Uemura, R., Vimeux, F., Severinghaus, J. P., Hutterli, M. A., et al.: Northern Hemisphere forcing of climatic cycles in Antarctica over the past 360,000 years, Nature, 448, 912–927, 2007.

Keigwin, L. D.: Isotopic paleoceanography of the Caribbean and East Pacific: Role of Panama uplift in Late Neogene time, Science, 217, 350–353, 1982.

Kleiven, H. F., Jansen, E., Fronval, T., and Smith, T. M.: Intensification of Northern Hemisphere glaciations in the circum Atlantic region (3.5–2.4 Ma), Paleogeogr. Paleoclimatol. Paleoecol., 184, 213–223, 2002.

Klocker, A., Prange, M., and Schulz, M.: Testing the influence of the Central American Seaway on orbitally forced northern hemisphere glaciation: Geophys. Res. Lett., 32, L03703, doi:10.1029/2004GL021564, 2005.

Kürschner, W. M., Van der Burgh, J., Visscher, H., and Dilcher, D. L.: Oak leaves as biosensors of late Neogene and early Pleistocene paleoatmospheric CO_2 concentrations, Mar. Micropal., 27, 299–312, 1996.

Lacasse, C. and van den Bogaard, P.: Enhanced airborne dispersal of silicic tephras during the onset of Northern Hemisphere glaciations, from 6 to 0 Ma records of explosive volcanism and climate change in the subpolar North Atlantic, Geology, 30, 623–626, 2002.

Laskar, J., Robutel, P., Joutel, F., Gastineau, M., Correia, A. C. M., and Levrard, B.: A long-term numerical solution for the insolation quantities of the Earth, Astronomy and Astrophysics manuscript no. La'2004, 1–26, 2004.

Lawrence, K., Liu, Z., and Herbert, T.: Evolution of the eastern tropical Pacific through Plio-Pleistocene glaciations, Science, 312, 79–83, 2006.

Lisiecki, L. E., and Raymo, M. E.: A Pliocene-Pleistocene stack of 57 globally distributed benthic $\delta^{18}O$ records, Paleoceanogr., 20, PA1003, doi:10.1029/2004PA001071, 2005.

Lunt, D. J., Foster, G. L., Haywood, A. M., and Stone, E. J.: Late Pliocene Greenland glaciation controlled by a decline in atmospheric CO_2 levels, Nature, 454, 1102–1105, 2008.

Lunt, D. J., Valdes, P. J., Haywood, A. M., and Rutt, I. C.: Closure of the Panama Seaway during the Pliocene: implications for climate and Northern Hemisphere glaciation, Clim. Dynam., 30, 1–18, doi:10.1007/s00382-0070265-6, 2007.

Maier-Reimer, E., Mikolajewicz, U., and Crowley, T.: Ocean general circulation model sensitivity experiment with an open Central American Isthmus, Paleoceanogr., 5, 349–366, 1990.

Maslin, M. A., Haug, G., Sarnthein, M., Tiedemann, R., Erlenkeuser, H., and Stax, R.: Northwest Pacific Site 882: The initiation of Northern Hemisphere Glaciation, Sci. Res. ODP Leg, 145, 315–332, 1995.

Maslin, M., Haug, G., Sarnthein, M., and Tiedemann, R.: The progressive intensification of Northern Hemisphere glaciation as seen from the North Pacific, ICES-Geol. Rdsch. 85, 452–465, 1996.

Meschede, M. and Barckhausen, U.: Twin hotspot tracks and ridge jumps: the evolution of the Cocos Nazca Spreading Center, in: ODP's Greatest Hits, edited by: White, K. and Urquhart, E., Vol. 2, 1 pp., available from: http://www.oceandrilling.org/greatest_hits2/PDFs/meschedehotspot.pdf, 2002.

Molnar, P.: Closing of the Central American Seaway and the Ice Age: A critical review, Paleoceanogr., 23, PA2201, doi:10.1029/2007PA001574, 2008.

Murdock, T. Q., Weaver, A. J., and Fanning, A. F.: Paleoclimatic response of the closing of the Isthmus of Panama in a coupled ocean-atmosphere model, Geophys. Res. Lett., 24, 253–256, 1997.

Pagani, M., Zachos, J. C., Freeman, K. H., Tipple, B., and Bohaty, B.: Marked decline in atmospheric carbon dioxide concentrations during the Paleogene, Science, 309, 600–603, 2005.

Prange, M.: The low-resolution CCSM2 revisited: new adjustments and a present-day control run, Ocean Sci., 4, 151–181, 2008, http://www.ocean-sci.net/4/151/2008/.

Ravelo, A. C., Dekens, P. S., and McCarthy, M.: Evidence for El Nino-like conditions during the Pliocene, GSA Today, 16(3), 4–11, 2006.

Raymo, M. E., Grant, B., Horowitz, M., and Rau, G. H.: Mid-Pliocene warmth: stronger greenhouse and stronger conveyor, Mar. Micropaleont., 27, 313–326, 1996.

Schneider, B. and Schmittner, A.: Simulating the impact of the Panamanian seaway closure on ocean circulation, marine productivity and nutrient cycling, Earth Planet. Sci. Lett., 246, 367–380, doi:10.1016/j.epsl.2006.04.028, 2006.

Shackleton, N. J., Backman, J., Zimmerman, H., et al.: Oxygen isotope calibration of the onset of ice-rafting and history of glaciation in the North Atlantic region, Nature, 307, 620–623, 1984.

Simstich, J., Sarnthein, M., and Erlenkeuser, H.: Paired δ^{18}O signals of *N. pachyderma* (s) and *T. quinqueloba* show thermal stratification structure in the Nordic Seas, Mar. Micropal., 48, 107–125, 2002.

Steph, S., Tiedemann, R., Prange, M., Groeneveld, J., Nürnberg, D., Reuning, L., Schulz, M., and Haug, G.: Changes in Caribbean surface hydrography during the Pliocene shoaling of the Central American Seaway, Paleoceanogr., 21, PA4221, doi:10.1029/2004PA001092, 2006.

Stein, R.: Arctic Ocean Sediments – Processes, Proxies, and Paleoenvironment, in: Developments in Marine Geology, vol. 2, Elsevier, 1–592, 2008.

Tiedemann, R., Sarnthein, M., and Shackleton, N. J.: Astronomic timescale for the Pliocene Atlantic δ^{18}O and dust flux records of ODP Site 659, Paleoceanogr., 9, 619–638, 1994.

Tiedemann, R., Sturm, A., Steph, S., Lund, S. P., and Stoner, J. S.: Astronomicaslly calibrated timescales from 6 to 2.5 Ma and benthic isotope stratigraphies, Sites 1236, 1237, 1239, and 1241, in: Proc. ODP, Sci. Results, 202, edited by: Tiedemann, R., Mix, A. C., Richter, C., and Ruddiman, W. F., College Station, TX (Ocean Drilling Program), 1–69, doi:10.2973/odp.proc.sr.202.210.2007, 2007.

Toniazzo, T., Gregory, J. M., and Huybrechts, P.: Climatic impact of a Greenland deglaciation and Its possible irreversibility, J. Climate, 17, 21–33, 2005.

Wang, P. X., Tian, J., Cheng, X. R., et al.: Major Pleistocene stages in a carbon perspective: The South China Sea record and its comparison, Paleoceanogr., 19, PA4005, doi:10.1029/2003PA000991, 2004.

Wang, P. X.: Global monsoon in a geological perspective, Chinese Science Bulletin, 54(7), 1113–1136, 2009.

Weyl, P. K.: The role of the oceans in climate change; a theory of the ice ages, Meteorol. Monogr., 8, 37–62, 1968.

Zachos, J., Pagani, M., Sloan,L., and Thomas, E.: Trends, rhythms, and aberrations in global climate 65 Ma to present, Science, 292, 686–693, 2001.

Zachos, J., Dickens, G. R., and Zeebe, R. E.: An early Cenozoic perspective on greenhouse warming and carbon-cycle dynamics, Nature, 451, 279–283, 2008.

Clim. Past, 5, 297–307, 2009
www.clim-past.net/5/297/2009/

Climate of the Past

Ecosystem effects of CO_2 concentration: evidence from past climates

I. C. Prentice[1] and S. P. Harrison[2]

[1]QUEST, Department of Earth Sciences, University of Bristol, Wills Memorial Building, Bristol BS8 1RJ, UK
[2]School of Geographical Sciences, University of Bristol, University Road, Bristol BS8 1SS, UK

Received: 17 February 2009 – Published in Clim. Past Discuss.: 12 March 2009
Revised: 16 June 2009 – Accepted: 18 June 2009 – Published: 3 July 2009

Abstract. Atmospheric CO_2 concentration has varied from minima of 170–200 ppm in glacials to maxima of 280–300 ppm in the recent interglacials. Photosynthesis by C_3 plants is highly sensitive to CO_2 concentration variations in this range. Physiological consequences of the CO_2 changes should therefore be discernible in palaeodata. Several lines of evidence support this expectation. Reduced terrestrial carbon storage during glacials, indicated by the shift in stable isotope composition of dissolved inorganic carbon in the ocean, cannot be explained by climate or sea-level changes. It is however consistent with predictions of current process-based models that propagate known physiological CO_2 effects into net primary production at the ecosystem scale. Restricted forest cover during glacial periods, indicated by pollen assemblages dominated by non-arboreal taxa, cannot be reproduced accurately by palaeoclimate models unless CO_2 effects on C_3-C_4 plant competition are also modelled. It follows that methods to reconstruct climate from palaeodata should account for CO_2 concentration changes. When they do so, they yield results more consistent with palaeoclimate models. In conclusion, the palaeorecord of the Late Quaternary, interpreted with the help of climate and ecosystem models, provides evidence that CO_2 effects at the ecosystem scale are neither trivial nor transient.

1 Introduction

Atmospheric CO_2 concentration has varied in a quasi-cyclical manner from minima of 170–200 ppm in glacials to maxima of 280–300 ppm in the recent "warm" interglacials, varying predictably with Antarctic temperature variations through the past 0.8 million years (Siegenthaler et al., 2005; Lüthi et al., 2008). Atmospheric CO_2 concentration (c_a) is a limiting factor for the photosynthesis of C_3 plants even at today's elevated values (>380 ppm), and was much more strongly limiting at glacial values (Polley et al., 1993, 1995; Beerling and Woodward, 1993; Cowling and Sage, 1998; Guiot et al., 2001). Free Air Carbon dioxide Enrichment (FACE) experiments have shown that an increase of c_a by 200 ppm increases net primary production (NPP) in temperate forests by 23±2% (Norby et al., 2005). The response of photosynthesis to CO_2 in C_3 plants is a consequence of both substrate (CO_2) limitation and competition from O_2 at the reaction site on Rubisco, the enzyme reponsible for CO_2 fixation. Plants using the C_4 photosynthetic pathway are less strongly influenced by c_a because they are anatomically and physiologically adapted to low c_a, using mechanisms that concentrate CO_2 near the chloroplasts. Because CO_2 concentration affects C_3 photosynthesis, and must indirectly influence the competition between C_3 and C_4 plants (e.g. between C_3 trees and C_4 grasses in tropical savannas), it makes sense to look for CO_2 effects that might be superimposed on climate change effects in palaeoecological records. Moreover, if these variations in c_a have caused changes that are detectable in compositional data, such as pollen assemblages, then conventional approaches to reconstructing past climate using statistical or analogue methods – if applied to periods with c_a different from that of the late Holocene – are certain to yield incorrect results. Although this potential problem in palaeoclimate reconstruction has been known in principle for more than two decades (Solomon, 1984; Idso, 1989; Farquhar, 1997; Street-Perrott, 1994; Street-Perrott et al., 1997; Cowling and Sykes, 1999, 2000; Bennett and Willis, 2000; Williams et al., 2000; Loehle, 2007), until recently few systematic attempts have been made to rectify it.

The relative neglect of CO_2 effects in Quaternary palaeoecology may have been encouraged by an influential school of thought in contemporary biogeochemistry, which questions the relevance of plant-physiological effects of CO_2 over the

Correspondence to: I. C. Prentice
(colin.prentice@bristol.ac.uk)

Published by Copernicus Publications on behalf of the European Geosciences Union.

long term and at the ecosystem scale (e.g. Körner, 2000). A much-debated hypothesis suggests, in particular, that limitations in the supply of nitrogen needed to support increased plant growth should over time reduce or eliminate any effect of c_a on NPP (Luo et al., 2004). However, clear evidence in support of this "progressive nitrogen limitation" (PNL) hypothesis has not emerged to date (see e.g. Moore et al., 2006). Equivocal results from a single FACE experiment in a mature forest have been interpreted as indicating a limited or non-existent CO_2 fertilization effect in mature forests generally (Körner et al., 2005; see Norby et al., 2005 for a critique). Interpretations of experimental data have tended to emphasize the influence of N limitation on the CO_2 effect (e.g. Nowak et al., 2004). Nevertheless, it is well established that elevated CO_2 can increase NPP, even in ecosystems where N supply is demonstrably limiting to plant growth (e.g. Lloyd and Farquhar 1996, 2000; Nowak et al., 2004). There is some evidence that plants can increase their N supply to support CO_2-enhanced growth, perhaps by increased root penetration or increased labile carbon subsidy to the rhizosphere (Finzi et al., 2007). The extent to which ecosystems can respond to CO_2 enhancement over timescales longer than a decade has not been unambigously demonstrated by experiments, and is subject to our still incomplete quantitative understanding of the mechanisms of N acquisition by plants.

Controversy thrives in this field in part because the evidence base from contemporary studies is, inevitably, limited. FACE has provided a great deal of extremely valuable information, and remains the key experimental technology needed to unravel CO_2 effects in intact ecosystems. However, FACE experiments are expensive and technically challenging, especially in forests. No feasible experiment can test the multi-decadal responses of ecosystems and biomes on a large spatial scale. In this paper, we show that long-term, ecosystem- and biome-level effects of CO_2 effects on plant physiology can be inferred from the palaeorecord. We argue that CO_2 effects are fundamental in establishing consistency between palaeovegetation data and palaeoclimate models.

2 Background

The concentration of CO_2 in the substomatal cavity, or "internal" CO_2 concentration (c_i), is a key quantity for photosynthesis in C_3 plants. The internal concentration in illuminated leaves is less than the ambient concentration, because photosynthesis draws down CO_2 while the stomata present a resistance to the inward diffusion of CO_2. The relationship between photosynthesis and the CO_2 concentration gradient across the leaf epidermis is represented by the diffusion equation,

$$A = g(c_a - c_i) \tag{1}$$

where A is the net rate of carbon assimilation and g is the stomatal conductance (the reciprocal of resistance) to CO_2. Stomatal conductance is regulated in a way that maintains the c_i/c_a ratio typically around 0.7–0.8 in C_3 plants and 0.3–0.4 in C_4 plants under conditions of moderate vapour pressure deficit (vpd) and adequate soil moisture (Wong et al., 1979). Diffusion through the stomata also controls plant water loss:

$$E = 1.6gD \tag{2}$$

where E is the rate of transpiration per unit leaf area, and D is the vpd at the leaf surface. As D increases, g declines; in consequence, under conditions of increasing D, c_i/c_a is reduced while E increases towards a maximum (Monteith, 1995).

Equation (1) describes the control of c_i by A. At the same time, A is controlled by c_i, according to the following equation which summarizes the biochemical controls of photosynthesis (Farquhar et al., 1980: simplified here for expository purposes):

$$A = \min(A_c, A_j) - R_d \tag{3}$$

where:

$$A_c = V_{c\,\max}(c_i - \Gamma)/(c_i + K),$$

$$A_j = \phi_o I(c_i - \Gamma)/(c_i + 2\Gamma),$$

$$R_d = bV_{c\,\max}.$$

Here A_c is the Rubisco-limited photosynthetic rate, $V_{c\,\max}$ is a maximum rate (dependent on the activity of Rubisco), Γ is the CO_2 compensation point (the concentration at which photosynthesis is zero), and K is an effective Michaelis-Menten coefficient (dependent on O_2 concentration, but this has not varied significantly over the time scales considered here). A_j is the light-limited photosynthetic rate, ϕ_o is the intrinsic quantum efficiency of photosynthesis, and I is the absorbed flux of photosynthetically active radiation (PAR). R_d is the respiration rate required to maintain the activity of Rubisco and other photosynthetic enzymes; b is a small constant, representing a respiratory loss of 1–2% of $V_{c\,\max}$.

Leaves typically operate with values of $V_{c\,\max}$ such that typical daytime values of A_c and A_j are similar, i.e. there is approximate co-limitation by Rubisco and PAR (Farquhar et al., 1980). Co-limitation yields the optimum assimilation rate, because a lower $V_{c\,\max}$ would result in reduced utilization of available PAR while a higher $V_{c\,\max}$ would increase the loss of carbon in maintenance respiration for no gain in photosynthesis (e.g. Haxeltine and Prentice, 1996a). In practice, with light and other environmental conditions varying over the diurnal cycle, photosynthesis can be limited by Rubisco at some times and by PAR at others. However, both rates are characterized by a response to c_i that increases most steeply just above $c_i = \Gamma$, and approaches an asymptote at high c_i. Thus, the response of A to c_a is steepest at low

c_a and approaches saturation at high c_a. If $V_{c\,max}$ is optimal, increased c_a should lead to reduced $V_{c\,max}$ (this "down-regulation" of $V_{c\,max}$ has been observed widely in raised-CO_2 experiments: see e.g. Ainsworth and Long, 2005). Low c_a, similarly, should lead to increased $V_{c\,max}$. Down-regulation of $V_{c\,max}$ at high c_a would tend to reduce the plant demand for N, while increasing A would tend to increase it. Allocation of carbon to fine roots is increased at high c_i, suggesting an adaptive response to an overall increased N demand (e.g. Palmroth et al., 2006). Provided that N demands are met, increased c_a should lead to increased NPP, and reduced c_a should lead to reduced NPP, although changing allocation patterns might limit the magnitude of this response.

The asymptotic nature of the relation between A and c_i, combined with the conservatism of c_i/c_a, implies that g should decline with increasing c_a. This stomatal response to CO_2 has been observed in many species. It could allow water conservation, further increasing photosynthesis in seasons and climates where soil moisture is limiting. Similarly, g should increase with declining c_a. Leaf area index (LAI) under changing CO_2 concentrations is therefore subject to several competing effects. With increasing c_a, increasing A should promote increased LAI, and increasing g might be compensated by increased LAI; but increasing below-ground allocation would reduce LAI. A survey of experimental results by Cowling and Field (2003) indicated that LAI generally declines as CO_2 decreases below present values, while at higher CO_2 levels there is no consistent response of LAI to CO_2.

C_4 plants, with their characteristic CO_2-concentrating leaf anatomy, are believed to have evolved and spread in response to low CO_2 levels (relative to earlier geological epochs) that developed during the Cenozoic (Cerling et al., 1993; Cowling, 2001; Sage, 2004). The rate of C_4 plant photosynthesis can be roughly approximated by disregarding CO_2 effects on A in Eq. (2) and using a reduced value for the quantum efficiency, representing the "cost" of the CO_2-concentrating mechanism. Using the known temperature dependencies of the various photosynthetic parameters, it can be shown that there is a crossover temperature above which C_4 plants can fix carbon at a faster rate than C_3 plants (Ehleringer et al., 1997). Below this temperature, C_4 plants fix carbon at a slower rate than C_3 plants. The crossover temperature increases with increasing CO_2 concentration. Thus, other things being equal, we would expect C_4 plants to be more competitive relative to C_3 plants at low CO_2 (Cole and Monger, 1994; Ehleringer et al., 1997; Collatz et al., 1998). In today's world, by contrast, C_3 plants should be gaining ground. A widespread trend towards an increase of (C_3) tree cover at the expense of (C_4) grasses has indeed been observed in tropical savannas, and may be an effect of increasing CO_2 concentration (Bond and Midgley, 2000; Eamus and Palmer, 2007). However, other factors including climate change and grazing intensity have been advanced as alternatives (e.g. Archer et al., 1995). This debate continues, while contemporary observations seem unable to resolve it.

Past environments offer a variety of scenarios involving large and long-lasting CO_2 changes. Although CO_2 changes are inevitably accompanied by climate changes due to the greenhouse effect of CO_2, the involvement of other climate drivers (orbital variations and ice-sheet growth and decay) implies a degree of decoupling between CO_2 and climate which is potentially useful for attempts to attribute causes. Here however we concentrate exclusively on the major shifts in CO_2, climate and vegetation between the last glacial maximum (LGM) and the Holocene, and we use climate and ecosystem modelling results to separate effects of CO_2 from effects of climate on vegetation. In doing so, we briefly survey the history of attempts to depict and model glacial-interglacial variations in the terrestrial biosphere. This endeavour has included some false starts but has now led to a broad consensus, with wide-ranging implications for palaeoclimatology and for carbon cycle science.

3 Glacial-interglacial variations in carbon storage

Shackleton (1977) noted that the calcium carbonate shells of subfossil benthic forminifera from the last glacial period are light in ^{13}C, presumably indicating a change in the stable isotope composition of dissolved inorganic carbon (DIC) in the ocean. His estimate of the $\delta^{13}C$ offset was -0.7 per mille for the LGM, relative to the Holocene. His hypothesis to explain this offset relies on a transfer of carbon between the land and ocean reservoirs. Terrestrial organic carbon is depleted in ^{13}C, so a simple mass balance can be used to infer that terrestrial organic carbon storage was substantially reduced in glacial times.

A glacial-interglacial shift in the $\delta^{13}C$ of DIC has been confirmed, although its global mean value appears to be smaller, in the range of -0.3 to -0.4 per mille (Curry et al., 1988; Duplessy et al., 1988; Sarnthein et al., 1988; Ku and Luo 1992). Using a canonical value of -0.32 per mille, Bird et al. (1994, 1996) estimated a terrestrial carbon storage reduction of 310–550 PgC at the LGM relative to pre-industrial time. This calculation took account of changes in atmospheric CO_2 content and its $\delta^{13}C$, as measured in ice cores, and a possible shift in land carbon towards values up to 2 per mille heavier in glacial time (Crowley, 1991). Allowing for further uncertainty in the isotopic shift, Bird et al. (1996) obtained a range of 300–700 PgC. Later estimates have continued to lie within this interval, for example 430–665 PgC (Street-Perrott et al., 1998) and 550–680 PgC (Beerling, 1999), respectively constrained by observations and modelling of the ^{13}C content of land carbon at the LGM. Ikeda and Tajika (2003) estimated 630 PgC, by assimilating atmospheric CO_2 concentration and surface- and deep-water ^{13}C records into a box model of the ocean carbon cycle. Köhler and Fischer (2004) estimated 600 PgC, using ice-core measurements of the concentration and $\delta^{13}C$ of atmospheric CO_2 to constrain a box model of the land carbon cycle.

Various sources of bias in this ocean carbon isotope constraint on terrestrial carbon storage have been suggested, including a dependence of isotopic fractionation during shell formation on carbonate ion concentration (Spero et al., 1997; Pedersen et al., 2003) and degassing of CH_4 clathrates with strongly negative isotopic signatures followed by conversion of the degassed CH_4 to CO_2 (Maslin and Thomas, 2003). We do not attempt a critical analysis of these mechanisms; however, none of them is likely to have a large enough effect to overturn Shackleton's hypothesis, or to require substantial revision of the broad range of estimates of LGM terrestrial carbon storage indicated by Bird et al. (1996). In particular, we note that hypotheses seeking to explain glacial-interglacial CO_2 changes by *increased* carbon storage during glacial times, e.g. buried under ice (Zeng, 2003) or in permafrost soils (Zimov et al., 2006), are manifestly incompatible with the ocean carbon isotope constraint.

Reduced carbon storage on land cannot be accounted for simply by the presence of continental ice sheets, because the area of exposed continental shelf – mainly in the tropics – roughly balanced the land area occupied by ice (Prentice et al., 1993; Montenegro et al., 2006). The explanation requires a change in the distribution of terrestrial biomes, and/or their carbon content. During the early 1990s, many independent estimates of terrestrial carbon storage change between glacial and interglacial regimes were made using "book-keeping" methods that assign *fixed* vegetation and soil carbon storage per unit area to each biome. Such estimates were based either on cartographic reconstructions of past vegetation (e.g. Adams et al., 1990; van Campo et al., 1993; Crowley, 1995; Maslin et al., 1995; Adams and Faure, 1998; and numerous regional studies not cited here), or on palaeoclimate and biogeography modelling using the simple models available at that time (Prentice and Fung, 1990; Friedlingstein, 1992; Prentice, 1993; Prentice et al., 1993; Prentice and Sykes, 1995). All of these estimates should now be rejected, because (a) they overlook variations in carbon storage within biomes, which are large today, and might well vary systematically between climate states; (b) they exclude a priori any effect of CO_2 concentration on carbon storage; and (c) the data-based estimates, in particular, offer no consistent way to deal with pollen assemblages that lack modern analogues.

The first modelling studies on this topic produced no reduction in carbon storage at the last glacial maximum (LGM) (Prentice and Fung, 2000), or too small a reduction (e.g. Friedlingstein, 1992; Prentice et al., 1993). This last study invoked peatland development as an additional cause of net postglacial carbon accumulation, but this now seems implausible: there is abundant evidence for glacial-age peats in tropical lowlands, including the exposed continental shelf, which may have stored on the order of 200 PgC that has largely been removed subsequently (Faure et al., 1996). Esser and Lautenschlager (1994), Peng et al. (1995, 1998) and Friedlingstein et al. (1995) applied early process-based land carbon cycle models to simulate changes in carbon storage since the LGM. These studies noted the potential of physiological CO_2 effects to further reduce carbon storage, and used empirical formulations to demonstrate that the impact could be substantial. Friedlingstein et al. (1995), for example, obtained a total reduction in carbon storage of 470 PgC when the CO_2 effect was included. They also showed that the near-zero carbon change previously simulated by Prentice and Fung (1990) was an artefact, caused by an uncorrected bias in the model used to simulate the LGM climate. Thus, although much was made in older literature of a supposed discrepancy between a small or zero shift in carbon storage (based on models) and a very large shift (based on observations), neither the model-based or the observationally-based estimates can now be considered well-founded.

More recent studies have exploited the advances in palaeoclimate and biosphere modelling made since the 1990s. The current standard approach starts with a palaeoclimate simulation made with a general circulation model (GCM), and applies anomalies (differences in mean monthly climate variables between the simulation and the GCM's control run) to correct a baseline climatology; the altered climate then drives a terrestrial biosphere model (e.g. François et al., 1998). Current models calculate the CO_2 effect based on the Farquhar equations to give changes in photosynthesis, which are propagated through carbon allocation and plant competition algorithms to generate effects at the ecosystem level. Snapshot analyses (e.g. comparisons between the LGM and pre-industrial time slices) can be made using equilibrium models such as CARAIB (Warnant et al., 1994); transient analyses apply dynamic global vegetation models such as LPJ (Sitch et al., 2003). A consensus finding has emerged from these analyses, namely that a carbon shift of approximately the right magnitude *can* be reproduced – but *only* if physiologically mediated effect of CO_2 are included (François et al., 1998, 1999; Otto et al., 2002; Kaplan et al., 2002). These recent analyses have shown consistently that the carbon storage reduction (LGM minus pre-industrial Holocene) with the CO_2 effect "turned off" either is too small, or in some cases even has the wrong sign, i.e. the terrestrial biosphere is modelled to have slightly ($<$100 PgC) greater carbon storage at the LGM than during the Holocene. The result of François et al. (1998) is typical: producing a carbon storage reduction of 610 PgC when the physiological effect of CO_2 is included, but only 160 PgC when it is not.

There is a simple reason why climate change alone is not sufficient to account for the glacial-interglacial change in terrestrial carbon storage. Other things being equal, the (dominant) soil component of terrestrial carbon storage increases as global temperatures decline, due to slow decomposition of soil organic matter. This explains, for example, why the highest soil carbon storage today occurs in the boreal zone and not in the tropics. This response is steeper than the positive response of NPP to warming, over a wide range of temperatures. It is a key component of the feedback mechanism believed to be responsible for the small reduction in atmospheric CO_2 content during the Little Ice Age (Joos et al., 2004a; Cox and Jones, 2008). Gerber et al.'s (2003) equilibrium sensitivity analysis with the LPJ model suggested that global cooling to LGM levels would have had a minor impact on total terrestrial carbon storage, whereas the CO_2 change would have reduced terrestrial carbon storage substantially. Kaplan et al. (2002) used LPJ to perform transient simulations of land carbon storage changes since the LGM. They obtained an increase of 820 PgC after the LGM, mainly due to the CO_2 effect. Without the CO_2 effect, the simulated increase was only 210 PgC (Joos et al., 2004b). The increase implies a net extraction of carbon from the ocean to build biospheric carbon on land. This in turn triggered the carbonate compensation mechanism in the ocean, and if the larger figure for post-LGM carbon storage increase is accepted, this mechanism accounts for the greater part of the observed rise in atmospheric CO_2 concentration during the pre-industrial Holocene (Joos et al., 2004b).

The carbon isotope palaeorecord of deep ocean water as preserved in benthic foraminiferal shells, combined with process-based modelling studies to separate the climate and CO_2 effects, thus contains two important messages for contemporary biogeochemistry. (1) The 100 ppm increase in CO_2 concentration from the last glacial period to the Holocene had a major, long-lasting effect on NPP and carbon storage. (2) The approximate magnitude of this effect can be predicted (within the uncertainties of the models and the ocean carbon isotope constraint), but only by models that propagate the physiological effect of CO_2 on photosynthesis into NPP. The earlier proposal by Prentice and Sarnthein (1993) – that climate-induced biome shifts alone might be sufficient to explain glacial-interglacial changes in carbon storage – can no longer be supported. The available evidence on glacial-interglacial changes in terrestrial carbon cycling indicates an important role for physiological effects of CO_2.

4 Biome shifts

The reconstruction of glacial-interglacial changes in terrestrial carbon storage is indirect and therefore subject to rather large uncertainties, as discussed above. The reconstruction of biome shifts is more directly linked to the extremely rich set of observations in the form of pollen and plant macrofossil records from terrestrial sediments. Here, too, current evidence supports a major role for changes in CO_2. Although climate change can certainly influence biome distribution, physiological CO_2 effects modify the growth and competition of different plant functional types (PFTs) and thereby are expected to influence vegetation composition, LAI, structure and biome boundaries (Cowling, 1999, 2004; Bond et al., 2003; Cowling and Shin, 2006).

Jolly et al. (1997) used BIOME3, a process-based coupled biogeochemistry-biogeography model (Haxeltine and Prentice 1996b), to show that CO_2 changes could profoundly affect montane vegetation zonation in the African tropics. BIOME3 is a forerunner of LPJ that lacks only the transient vegetation dynamics which LPJ simulates; it mimics the response of LAI and NPP of different PFTs to climate and CO_2, and competition among PFTs. Jolly et al. (1997) were the first to use a process-based model to analyse the effects of changing CO_2 concentration on ecosystem composition and structure in a palaeoecological context. Their analysis indicated that the large elevational extension of the heath belt on East African mountains was a predictable consequence of the low CO_2 concentration in glacial time. Indirect support for this finding came from ^{13}C measurements on leaf waxes preserved in the sediments of a high-elevation lake in the region, which indicated a marked shift towards C_4 plant dominance during the last glacial period (Street-Perrott et al., 1997; Huang et al., 1999). Boom et al. (2002) produced similar results for South America, and used BIOME3 to derive a function relating C_4 plant abundance (as indicated by leaf-wax ^{13}C measurements) to temperature and CO_2 concentration which they then inverted to yield a proxy CO_2 record that is broadly consistent with ice-core measurements – a further, indirect confirmation of the role of CO_2 in controlling C_3/C_4 plant competition over glacial-interglacial cycles.

Some early discussions had assumed that effects of glacial CO_2 concentration would be greater at higher elevations, because of low atmospheric pressure (implying a low partial pressure of CO_2 for the same concentration). However the elevation effect also lowers the partial pressure of O_2, which competes with CO_2 at the Rubisco reaction sites; this effect counters the hypothesized effect of a low partial pressure of CO_2 at high elevations (Terashima et al., 1995). In fact, the effects are expected a priori to be greater in warmer climates because the O_2 competition effect is stronger at high temperatures, as reflected in the temperature dependence of the photosynthetic parameters (Cowling, 1999a). Indeed there is abundant evidence in pollen and carbon isotope records from tropical lowland regions for shifts away from forest, toward C_4 dominated vegetation, during glacial times. This evidence comes principally from records of the $\delta^{13}C$ changes in lake sediments (e.g. Talbot and Johanessen, 1992; Giresse et al. 1994), which can be related to changes in the relative abundance of C_3 and C_4 plants. Modelling with BIOME3 has also indicated consequences for the structure of tropical forests ecosystems which would be largely "silent" in terms of the palaeorecord, yet could be profoundly significant for biogeography (Cowling et al., 2001).

Harrison and Prentice (2004) quantified CO_2 effects at a global scale, based on the BIOME 6000 synthesis, which compiled mid-Holocene and LGM pollen records worldwide and assigned a biome to each record using a standardized method (Prentice et al., 2000). The effect of LGM climate was accounted for by using *all* of the available GCM experiments from the Palaeoclimate Modelling Intercomparison Project (PMIP) to drive BIOME3. The results were unambiguous. Whichever GCM was used to simulate the LGM climate, the extent of simulated global forest reduction fell short of that observed when CO_2 effects were neglected; but became closer to observations when these effects were included. The influence of CO_2 was largest and most consistent in the tropics, but not confined there: the same effect was seen in the northern and southern extratropics as well. Thus finding is consistent with that of Cowling (1999b), who had also used BIOME3 to show that the pattern of LGM vegetation in eastern North America can be explained satisfactorily only through consideration of reduced water use efficiency (A/g) by C_3 plants in low CO_2, favouring more drought-tolerant plant types, as well as climate change; a point also taken up by Loehle (2007).

The conclusion from these studies is that physiological CO_2 effects, as simulated by models based on the fundamentals of photosynthesis and propagated into the simulation of LAI and NPP of different PFTs, are essential in order to fully account for global shifts in forest cover, and probably also to explain a wider range of changes in the relative abundances of PFTs, between glacial and interglacial regimes.

5 Climate reconstruction

Until recently, methods to reconstruct past climates from palaeovegetation data were all statistical, based on the assumption that the climate controls on plant distribution are invariant. These methods broadly fall into two families: those based on some form of regression, and those based on modern analogues – either using a direct search among a set of analogues, or using response surfaces to fit the empirical relationship between the abundances of pollen taxa and climate variables (see e.g. Brewer et al., 2008). It has occasionally been noted that physiologically mediated CO_2 effects could compromise climate reconstructions made by such methods (e.g. Idso, 1989; Cowling and Sykes 1999), but this observation had no impact on research practice until Guiot et al. (2000) developed a novel approach to palaeoclimate reconstruction, based on the numerical inversion of BIOME3.

In inversion-based palaeoclimate reconstruction, a climate change (between the past time under consideration and recent times) is selected using a search algorithm that seeks to maximize goodness of fit between the palaeodata and simulated ecosystem composition (in terms of simulated abundances or productivity of PFTs). A major advantage of using inversion is that it allows the CO_2 level to be accounted for, as it can be prescribed to the model independently of the palaeovegetation data. Guiot et al. (2000) found that prescribing the correct (low) CO_2 made a substantial difference to LGM climate reconstructions. A key finding was that when low CO_2 was prescribed for the LGM, reconstructed winter conditions in the Mediterranean region became (a) *warmer* than in earlier, analogue-based reconstructions, and (b) systematically closer to the predictions made by climate models for the LGM (Ramstein et al., 2007). This result is all the more remarkable because BIOME3 does not model any direct effect of CO_2 on plants' low-temperature tolerance. However, low atmospheric CO_2 implies both reduced NPP (so that the distribution of trees towards climates offering low potential production becomes more restricted) and increased water use per unit of NPP, reinforcing this restriction. As a consequence, steppe vegetation can expand under low CO_2 at the expense of forest. The earlier, analogue-based methods has selected modern analogues for the glacial steppe in central Asia in climates with very cold winters and short growing seasons. Low CO_2, however, permitted the occurrence of steppe vegetation under milder conditions. An expanded set of analogues produced milder reconstructed winters than the original set, but could not produce consistency with palaeoclimate model results. This case study illustrates a relatively little-discussed problem with analogue methods. Although the "no-analogue" problem (fossil pollen assemblages for which similar modern pollen assemblages cannot be found) is well known, there is also potentially a "wrong-analogue" problem whereby the method of modern analogues selects similar pollen assemblages that actually originated in very different physical environments. The Mediterranean case study shows how this problem can be alleviated through the inversion of process-based models. The inversion method has been applied in three continents (Wu et al., 2007a, b; Guiot et al., 2008).

The use of inverse modelling to reconstruct past climates has further advantages that are beginning to explored, using BIOME3 and most recently its successor, BIOME4 (Kapan et al., 2003). Inverse modelling provides a natural way to incorporate additional observational constraints, such as palaeo ^{13}C information (e.g. Hatté and Guiot, 2005; Rousseau et al., 2006; Hatté et al., 2009; Guiot et al., 2009). It makes it straightforward to incorporate additional external forcing of vegetation changes, such as insolation changes caused by orbital variations, and by the differences in latitude between locations at which particular vegetation types occured during glacial versus interglacial climates; these differences may have implications for plant productivity and water use (Kaplan et al., 2003). The involvement of a process-based model should also allow the use of a data-assimilation approach to the reconstruction of ecosystem properties that palaeodata do not directly record, such as NPP and carbon storage (Wu et al., 2009). Finally, a recent development of the inversion approach builds on a version of the LPJ model to allow time-dependent climate reconstruction taking account temporal lags in the response of vegetation to climate (Guiot et al., 2009). What began as a solution to a specific problem in palaeoclimate reconstruction may turn out to be a tool with a wide field of application in palaeoclimatic analysis.

6 Conclusions

Despite persistent controversies about the contemporary and future effects of rising CO_2, surprisingly few attempts have been made to use palaeorecords to help resolve them. We have summarized evidence based on a model-assisted interpretation of the palaeorecord, which supports the idea that physiological effects do scale up to ecosystem effects, through changes in primary production and through competition between plants with different photosynthetic pathways.

This palaeoperspective has practical implications for modelling of the contemporary carbon cycle. Atmospheric O_2 and $^{13}CO_2$ concentration measurements show that the land biosphere has been taking up a part of the CO_2 emitted by human activities during recent decades (Prentice et al., 2001; Denman et al., 2007). The land biosphere, in other words, is a net sink for CO_2 due to some process which outweighs the CO_2 release due to land-use change. Process-based models consistently identify this process as a consequence of rising CO_2 concentration, acting through the physiological effect of CO_2 on photosynthesis (McGuire et al., 2001). Without this, models would predict a higher rate of atmospheric CO_2 increase than is observed. Models also predict that this uptake will increase while CO_2 continues to rise, as expected during this century, although it will eventually decline again due to the asymptotic nature of equation (3) and competing effects of warming on the terrestrial carbon balance (Cramer et al., 2001). The palaeorecord suggests that the assumptions underlying existing models regarding CO_2 effects are broadly correct. We do not find support for the opinion (e.g. Körner, 2000) that other constraints effectively eliminate the ecosystem-level effects of changing CO_2 concentration on carbon storage over long time scales. The palaeorecord also supports the attribution of increases in the woody component of tropical savannas to physiological effects of rising CO_2, although this does not rule out a contribution of other factors such as land-use change.

Our findings further imply that for palaeoclimate reconstruction involving periods with substantially different CO_2 levels, inversion of process-based models is likely to yield more realistic results than statistical modelling that excludes physiological effects of CO_2. Recent advances in inverse vegetation modelling offer a promising way forward for the integration of biophysical process understanding into palaeoclimate analysis.

7 Epilogue

Dominique Jolly made pioneering contributions to Quaternary palaeoecology, especially of Africa. He was closely involved in the development of the data analysis technique called "biomization" which made the global BIOME 6000 project possible, and he developed a vision of how modelling and data analysis could work together to achieve new insights about the past. He also produced the first global-scale simulations of the LGM world that took low CO_2 into account, using an early version of BIOME3. These results were showcased in Berrien Moore III's plenary presentation at the first International Geosphere-Biosphere Programme Congress in 1996, and presented as an example of how different disciplines of global change science could productively collaborate, and of the power of the new process-based approaches to terrestrial biosphere modelling. We have dealt here with a few of the themes to which Dominique contributed important results and insights. We dedicate this article to the memory of an inspiring colleague and friend.

Edited by: J. Guiot
Reviewed by: N. Viovy and E. Gritti

Publication of this paper was granted by
EDD (Environnement, Développement Durable)
and INSU (Institut des Sciences de l'Univers) at CNRS.

References

Adams, J. M. and Faure, H.: A new estimate of changing carbon storage on land since the last glacial maximum, based on global land ecosystem reconstruction, Global Planet. Change, 16–17, 3–24, 1998.

Adams, J. M., Faure, H., Faure-Denard, L., McGlade, J. M., and Woodward, F. I.: Increases in terrestrial carbon storage from the Last Glacial Maximum to the present, Nature, 348, 711–714, 1990.

Ainsworth, E. A. and Long, S. P.: What have we learned from fifteen years of Free Air Carbon Dioxide Enrichment (FACE)? A meta-analytic review of the responses of photosynthesis, canopy properties and plant production to rising CO_2, New Phytologist, 165, 351–372, 2005.

Archer, S., Schimel, D. S., and Holland, E. A. Mechanisms of shrubland expansion: land use, climate or CO_2?, Clim. Change, 29, 91–99, 1995.

Beerling, D. J.: New estimates of carbon transfer to terrestrial ecosystems between the last glacial maximum and the Holocene, Terra Nova, 11, 162–167, 1999.

Beerling, D. J. and Woodward, F. I.: Ecophysiological responses of plants to global environmental change since the last glacial maximum, New Phytologist, 125, 641–648, 1993.

Bennett, K. D. and Willis, K. J.: Effect of global atmospheric carbon dioxide on glacial-interglacial vegetation change, Global Ecol. Biogeogr., 9, 355–361, 2000.

Bird, M. I., Lloyd, J., and Farquhar, G. D.: Terrestrial carbon storage at the LGM, Nature, 371, p. 566, 1994.

Bird, M. I., Lloyd, J., and Farquhar, G. D.: Terrestrial carbon storage from the last glacial maximum to the present, Chemosphere, 33, 1675–1685, 1996.

Bond, W. J. and Midgley, G.: A proposed CO_2-controlled mechanism of woody plant invasion in grasslands and savannas, Global Change Biol., 6, 865–869, 2000.

Bond, W. J., Midgely, G. F., and Woodward, F. I.: The importance of low CO_2 and fire in promoting the spread of grasslands and savannas, Global Change Biol., 9, 973–982, 2003.

Boom, A., Marchant, R., Hooghiemstra, H., and Sinninghe Damsté, J. S.: Palaeogeography, Palaeoclimatology, Palaeoecology, 177, 151–168, 2002.

Brewer, S., Guiot, J., Sánchez-Goñi, M. F., and Klotz, S.: The climate in Europe during the Eemian: a multi-method approach using pollen data, Quaternary Sci. Rev., 25–26, 2303–2315, 2008.

Cerling, T. E., Wang, Y., and Quade, J.: Expansion of C4 ecosystems as an indicator of global ecological change in the late Miocene, Nature, 361, 344–345, 1993.

Cole, D. R. and Monger, H. C.: Influence of atmospheric CO_2 on the decline of C_4 plants during the last deglaciation, Nature, 368, 533–536, 1998.

Collatz, G. J., Berry, J. A., and Clark, J. S.: Effects of climate and atmospheric CO_2 partial pressure on the global distribution of C_4 grasses: present, past, and future, Oecologia, 114, 441–454, 1998.

Cowling, S. A.: Plants and temperature-CO_2 uncoupling, Science, 285, 1500–1501, 1999a.

Cowling, S. A.: Simulated effects of low atmospheric CO_2 on structure and composition of North American vegetation at the Last Glacial Maximum, Global Ecol. Biogeogr., 8, 81–93, 1999b.

Cowling, S. A.: Plant carbon balance, evolutionary innovation and extinction in land plants, Global Change Biol., 7, 231–239, 2001.

Cowling, S. A.: Tropical forest stucture: a missing dimension to Pleistocene landscapes, J. Quaternary Sci., 19, 733–743, 2004.

Cowling, S. A. and Field, C. B.: Environmental controls of leaf area production: implications for vegetation and land surface modelling, Global Biogeochem. Cy., 17, 1007, doi:10.1029/2002GB001915, 2003.

Cowling, S. A. and Sykes, M. T.: Physiological significance of low atmospheric CO_2 for plant-climate interactions, Quaternary Res., 52, 237–242, 1999.

Cowling, S. A. and Sykes, M. T.: Reply: Do low CO_2 concentrations affect pollen-based reconstruction of LGM climate?, Quaternary Res., 53, 405–406, 2000.

Cowling, S. A. and Sage, R. F.: Interactive effecsts of low atmospheric CO_2 and elevated temperature on growth, photosynthesis, and respiration in *Phaseolus vulgaris*, Plant, Cell and Environ., 21, 427–435, 1998.

Cowling, S. A. and Shin, Y.: Simulated ecosystem threshold responses to co-varying temperature, precipitation and atmospheric CO_2 within a region of Amazonia, Global Ecol. Biogeogr., 15, 553–566, 2006.

Cowling, S. A., Maslin, M. A., and Sykes, M. T.: Paleovegetation simulations of lowland Amazonia and implications for theories of neotropical allopatry and speciation, Quaternary Res., 55, 140–149, 2001.

Cramer, W., Bondeau, A., Woodward, F. I., Prentice, I. C., Betts, R. A., Brovkin, V., Cox, P. M., Fisher, V., Foley, J. Friend, A. D., Kucharik, C. Lomas, M. R., Ramankutty, N., Sitch, S., Smith, B., White, A., and Young-Molling C.: Global responses of terrestrial ecosystems to changes in CO_2 and climate, Global Change Biol., 7, 357–373, 2001.

Crowley, T. J.: Ice age carbon, Nature, 352, 575–576, 1991.

Crowley, T. J.: Ice age terrestrial carbon changes revisited, Global Biogeochem. Cy., 9, 377–389, 1995.

Curry, W. B., Duplessy, J. C., Labeyrie, L. D., and Shackleton, N. J.: Changes in the distribution of $\delta^{13}C$ of deepwater ΣCO_2 between the last glaciation and the Holocene, Paleoceanography, 3, 327–337, 1988.

Denman, K. L., Brasseur, G., Chidthaisong, A., Ciais, P., Cox, P. M., Dickinson, R. E., Hauglustaine, D., Heinze, C., Holland, E., Jacob, D., Lohmann, U., Ramachandran, S. da Silva Dias, P. L., Wofsy, S. C., and Zhang, X.: Couplings Between Changes in the Climate System and Biogeochemistry, in Climate Change 2007: The Physical Science Basis. Contribution of Working Group I to the Fourth Assessment Report of the Intergovernmental Panel on Climate Change, edited by: Solomon, S., Qin, D., Manning, M., Chen, Z., Marquis, M., Averyt, K. B., Tignor M., and Miller, H. L., Cambridge University Press, Cambridge, United Kingdom and New York, NY, USA, 2007

Duplessy, J.-C., Shackleton, N. J., Fairbanks, R. G., Labeyrie, L., Oppo, D., and Kallel, N.: Deepwater source variations during the last climatic cycle and their impact on the global deepwater circulation. Paleoceanography, 3, 343–360, 1988.

Eamus, D. and Palmer, A. R.: Is climate change a possible explanation for woody thickening in arid and semi-arid regions?, Res. Lett. Ecol, 2007, 37364, doi:10.1155/2007/37364, 2007.

Ehleringer, J. R., Cerling, T. E., and Helliker, B. R.: C_4 photosynthesis, atmospheric CO_2 and climate, Oecologia, 112, 285–299, 1997.

Esser, G. and Lautenschlager, M.: Estimating the change of carbon in the terrestrial biosphere from 18 000 BP to present using a carbon cycle model, Environ. Pollut., 83, 45–53, 1994.

Farquhar, G. D.: Climate change: carbon dioxide and vegetation, Science, 278, 1411, doi:0.1126/science.278.5342.1411, 1997.

Farquhar, G. D., von Caemmerer, S., and Berry, J. A.: A biochemical model of photosynthetic CO_2 assimilation in leaves of C_3 species, Planta, 149, 78–90, 1980.

Faure, H., Adams, J. M., Debenay, J. P., Faure-Denard, L., Grant, D. R., Pirazzoli, P. A., Thomasin, B., Velichko, A. A., and Zazo, C.: Carbon storage and continental land surface change since the last glacial maximum, Quaternary Sci. Rev., 15, 843–849, 1996.

Finzi, A. C., Norby, R. J., Calfapietra, C., Gallet-Budynek, A., Gielen, B., Holmes, W. E., Hoosbeek, M. R., Iversen, C. M., Jackson, R. B., Kubiske, M. E., Ledford, J., Liberloo, M., Oren, R., Polle, A., Pritchard, S., Zak, D. R., Schlesinger, W. H., and Ceulemans, R.: Increases in nitrogen uptake rather than nitrogen-use efficiency support higher rates of temperate forest productivity under elevated CO_2, Proceedings of the National Academy of Sciences, 104, 14014–14019, 2007.

François, L. M., Delire, C., Warnant, P., and Munhoven, G.: Modelling the glacial-interglacial changes in the continental biosphere, Global Planet. Change, 16–17, 37–52, 1998.

François, L. M., Goddéris, Y., Warnant, P., Ramstein, G., de Noblet, N., and Lorenz, S.: Carbon stocks and isotopic budgets of the terrestrial biosphere at mid-Holocene and last glacial maximum

times, Chem. Geol., 159, 163–189, 1999.
Friedlingstein, P., Delire, C., Müller, J. F., and Gérard, J. C.: The climate-induced variation of the continental biosphere: a model simulation of the Last Glacial Maximum, Geophys. Res. Lett., 19, 897–900, 1992.
Friedlingstein, P., Prentice, K. C., Fung, I. Y., John, J. G., and Brasseur, G. P.: Carbon-biosphere-climate interactions in the last glacial maximum, J. Geophys. Res., 100, 7203–7221, 1995.
Gerber, S., Joos, F., and Prentice, I. C.: Sensitivity of a dynamic global vegetation model to climate and atmospheric CO_2, Global Change Biol., 10, 1223–1239, 2004.
Giresse, P., Maley, J., and Brenac, P.: Late Quaternary palaeoenvironments in the Lake Barombi Mbo (West Cameroon) deduced from pollen and carbon isotopes of organic matter, Palaeogeography, Palaeoclimatology, Palaeoecology, 107, 65–78, 1994.
Guiot, J., Torre, F., Jolly, D., Peyron, O., Boreux, J. J., and Cheddadi, R.: Inverse vegetation modeling by Monte Carlo sampling to reconstruct palaeoclimates under changed precipitation seasonality and CO_2 conditions: application to glacial climate in Mediterranean region, Ecol. Modell., 127, 119–140, 2000.
Guiot, J., Prentice, I. C., Peng, C., Jolly, D., Laarif, F., and Smith, B.: Reconstructing and modelling past changes in terrestrial primary production, in: Terrestrial Global Productivity, edited by: Roy, J., Mooney, H. A., and Saugier, B., Academic Press, 479–498, 2001.
Guiot, J., Wu, H. B., Garreta, V., Hatté, C., and Magny, M.: A few prospective ideas on climate reconstruction: from a statistical single proxy approach towards a multi-proxy and dynamical approach, Clim. Past Discuss., 5, 99–125, 2009, http://www.clim-past-discuss.net/5/99/2009/.
Guiot, J., Hai Bin Wu, Wen Ying Jiang, and Yun Li Luo: East Asian Monsoon and paleoclimatic data analysis: a vegetation point of view, Clim. Past, 4, 137–145, 2008, http://www.clim-past.net/4/137/2008/.
Harrison, S. P. and Prentice, I. C.: Climate and CO_2 controls on global vegetation distribution at the last glacial maximum: analysis based on palaeovegetation data, biome modeling and palaeoclimate simulations., Global Change Biol., 9, 983–1004, 2003.
Hatté, C. and Guiot, J.: Paleoprecipitation reconstruction by inverse modelling using the isotopic signal of loess organic matter: application to the Nußloch loess sequence (Rhine Valley, Germany), Clim.Dynam., 25, 315-327, doi:10.1007/s00382-005-0034-3, 2005.
Hatté, C., Rousseau, D.-D., and Guiot, J.: Climate reconstruction from pollen and $\delta^{13}C$ records using inverse vegetation modeling - Implication for past and future climates, Clim. Past, 5, 147–156, 2009, http://www.clim-past.net/5/147/2009/.
Haxeltine, A. and Prentice, I. C.: A general model for the light use efficiency of primary production, Functional Ecology, 10, 551–561, 1996a.
Haxeltine, A. and Prentice, I. C.: BIOME3: an equilibrium terrestrial biosphere model based on ecophysiological constraints, resource availability and competition among plant functional types, Global Biogeochem. Cy., 10, 693–709, 1996b.
Huang, Y., Street-Perrott, F. A., Perrott, R. A., Metzger, P., and Eglinton, G.: Glacial-interglacial environmental changes inferred from molecular and compound-specific $\delta^{13}C$ analyses of sediments from Sacred Lake, Mt. Kenya, Geochimica et Cosmochimica Acta, 9, 1383–1404, 1999.
Idso, S. B.: A problem for paleoclimatology?, Quaternary Res., 31, 433–434, 1989.
Ikeda, T. and Tajika, E.: Carbon cycling and climate change during the last glacial cycle inferred from the isotope records using an ocean biogeochemical carbon cycle model, Global Planet. Change, 35, 131–141, 2003.
Joos, F. and Prentice, I. C. A palaeoperspective on changes in atmospheric CO_2 and climate, in: The Global Carbon Cycle, edited by: Field, C. B. and Raupach, M. R., SCOPE 62, Island Press, Washington, 165–186, 2004.
Joos, F., Gerber, S., Prentice, I. C., Otto-Bliesner, B. L., and Valdes, P. J.: Transient simulations of Holocene atmospheric carbon dioxide and terrestrial carbon since the Last Glacial Maximum, Global Biogeochem. Cy., 18, GB2002, doi:2010.1029/2003GB002156, 2004.
Kaplan, J. O., Prentice, I. C., Knorr, W., and Valdes, P. J.: Modeling the dynamics of terrestrial carbon storage since the Last Glacial Maximum, Geophys. Res. Lett., 29, 2074, doi:10.1029/2002GL015230, 2002.
Kaplan, J. O., Bigelow, N. H., Prentice, I. C., Harrison, S. P., Bartlein, P. J., Christensen, T. R., Cramer, W., Matveyeva, N. V., McGuire, A. D., Murray, D. F., Razzhivin, V. Y., Smith, B., Walker, D. A., Anderson, P. M., Andreev, A. A., Brubaker, L. B., Edwards, M. E., and Lozhkin, A. V.: Climate change and Arctic ecosystems II: Modeling, palaeodata-model comparisons, and future projections, J. Geophys. Res., 108(D19), 8171, doi:10.1029/2002JD002559, 2003.
Köhler, P. and Fischer, H.: Simulating changes in the terrestrial biosphere during the last glacial/interglacial transition, Global Planet. Change, 43, 33–55, 2004.
Körner, C.: Biosphere responses to CO_2 enrichment, Ecological Applications, 10, 1590–1619, 2000.
Körner, C., Asshoff, R., Bignucolo, O., Hättenschwiler, S., Keel, S. J., Peláez-Riedl, S., Pepin, S., Siegwolf, R. T. W., and Zotz, G.: Carbon flux and growth in mature deciduous forest trees exposed to elevated CO_2, Science, 309, 1360–1362, 2005.
Ku, T. L. and Luo, S.: Carbon isotopic variations on glacial-to-interglacial time scales in the ocean: modeling and implications, Paleoceanography, 7, 543–562, 1992.
Loehle, C.: Predicting Pleistocene climate from vegetation in North America, Clim. Past, 3, 109–118, 2007, http://www.clim-past.net/3/109/2007/.
Lloyd, J. and Farquhar, G. D.: The CO_2 dependence of photosynthesis, plant growth responses to elevated CO_2 concentrations and their interactions with soil nutrient status. I. General principles and forest ecosystems, Funct. Ecol., 10, 4–32, 1996.
Lloyd, J. and Farquhar, G. D.: Do slow-growing species and nutrient-stressed plants consistently respond less to elevated CO_2? A clarification of some issues raised by Poorter (1998), Global Change Biol., 6, 871–876, 2000.
Luo, Y., Su, B., Currie, W. S., Dukes, J. S., Finzi, A., Hartwig, U., Hungate, B., McMurtrie, R. E., Oren, M., Parton, W. J., Pataki, D. E., Shaw, R., Zak, D. R., and Field, C. B.: Progressive nitrogen limitation of ecosystem responses to rising atmospheric carbon dioxide, BioScience, 54, 731–739, 2004.
Lüthi, D., Le Floch, M., Bereiter, B., Blunier, T., Barnola, J.-M., Siegenthaler, U., Raynaud, D., Jouzel, J., Fischer, H., Kawamura, K., and Stocker, T. F.: High-resolution carbon dioxide concentra-

tion record 650 000–800 000 years before present, Nature, 453, 379–382, 2008.

Maslin, M., Adams, J. M., Thomas, E., Faure, H., and Haines-Young, R.: Estimating the carbon transfer between oceans, atmosphere and terrestrial biosphere since the Last Glacial Maximum: a review of two contrasting methods of estimation, Terra Nova, 7, 358–366, 1995.

McGuire, A. D., Sitch, S., Clein, J. S., Dargaville, R., Esser, G., Foley, J., Heimann, M., Joos, F., Kaplan, J., Kicklighter, D. W., Meier, R. A., Melillo, J. M., Moore III, B., Prentice, I. C., Ramankutty, N., Reichenau, T., Schloss, A., Tian, H. Williams, L. J., and Wittenberg, U.: Carbon balance of the terrestrial biosphere in the twentieth century: Analyses of CO_2, climate and land-use effects with four process-based ecosystem models, Global Biogeochem. Cy., 15, 183–206, 2001.

Montenegro, A., Eby, M., Kaplan, J. O., Meissner, K. J., and Weaver, A. J.: Carbon storage on exposed continental shelves during the glacial-interglacial transition, Geophys. Res. Lett., 33, L08703, doi:10.1029/2005GL025480, 2006.

Monteith, J. L.: A reinterpretation of stomatal responses to humidity, Plant, Cell Environ., 18, 357–364, 1995.

Moore, D. J. P., Aref, S., Ho, R. M., Pippen, J. S., Hamilton, J., and DeLucia, E. H.: Inter-annual variation in the response of *Pinus taeda* tree growth to long term Free Air Carbon dioxide Enrichment (FACE), Global Change Biol., 12, 1367–1377, 2006.

Norby, R. J., DeLucia, E. H., Gielen, B., Calfapietra, C., Giardina, C. P., King, J. S., Ledford, J., McCarthy, H. R., Moore, D. J. P., Ceulemans, R., De Angelis, P., Finzi, A. C., Karnosky, D. F., Kubiske, M. E., Lukac, M., Pregitzer, K. S., Scarascia-Mugnozza, G. E., Schlesinger, W. H., and Oren, R.: Forest response to elevated CO_2 is conserved across a broad range of productivity, Proceedings of the National Academy of Sciences, 102, 18052–18056, 2005.

Nowak, R. S., Ellsworth, D. S., and Smith, S. D. Functional responses of plants to elevated atmospheric CO_2 – Do photosynthetic and productivity data from FACE experiments support early predictions? New Phytologist, 162, 253–280, 2004.

Otto, D., Rasse, D., Kaplan, J., Warnant, P., and François, L.: Biospheric carbon stocks reconstructed at the Last Glacial Maximum: comparison between general circulation models using prescribed and computed sea surface temperatures, Global Planet. Change, 33, 117–138, 2002.

Palmroth, S., Oren, R., McCarthy, H. R., Johnsen, K. H., Finzi, A. C., Butnor, J. R. and Ryan, M. G.: Aboveground sink strength in forests controls the allocation of carbon below ground and its [CO_2]-induced enhancement, Proceedings of the National Academy of Sciences, 103, 19362–19367, 2006.

Pedersen, T. F., François, R., François, L., Alverson, K., and McManus, J.: The Late Quaternary history of biogeochemical cycling of carbon, in: Paleoclimate, global change and the future, edited by: Alverson, K. D., Bradley, R. S., and Pedersen, T. F., Springer, Berlin, 63–79, 2003.

Peng, C. H., Guiot, J., and van Campo, E.: Reconstruction of past terrestrial carbon storage in the northern hemisphere from the Osnabrück biosphere model and palaeodata, Clim. Res., 5, 107–118, 1995.

Peng, C. H., Guiot, J., and van Campo, E.: Estimating changes in terrestrial vegetation and carbon storage: using palaeoecological data and models, Quaternary Science Reviews, 17, 719–735, 1998.

Polley, H. W., Johnson, H. B., Marino, B. D., and Mayeux, H. S.: Increases in C_3 plant water-use efficiency and biomass over glacial to present CO_2 concentrations, Nature, 361, 61–64, 1993.

Polley, H. W., Johnson, H. B., and Mayeux, H. S.: Nitrogen and water requirements of C_3 plants grown at glacial to present carbon dioxide concentrations, Funct. Ecol., 9, 86–96, 1995.

Prentice, I. C.: Biome modelling and the carbon cycle, in: The Global Carbon Cycle, edited by: Heimann, M., Springer, Berlin, 219–238, 1993.

Prentice, I. C., Farquhar, G. D., Fasham, M. J. R., Goulden, M. L., Heimann, M., Jaramillo, V. J., Kheshgi, H. S., Le Quéré, C., Scholes, R. J., and Wallace, D. W. R.: The carbon cycle and atmospheric carbon dioxide, in: Climate Change 2001: The Scientific Basis, edited by: Houghton, J. T., Ding, Y., Griggs, D. J., Noguer, M., van der Linden, P. J., Dai, X., Maskell, K., and Johnson, C. A., Cambridge University Press, Cambridge, 183–237, 2001.

Prentice, I. C. and Sarnthein, M.: Self-regulatory processes in the biosphere in the face of climate change, in: Global Changes in the Perspective of the Past, edited by: Eddy, J. and Oeschger, H., Wiley, Chichester, 29–38, 1993.

Prentice, I. C. and Sykes, M. T.: Vegetation geography and global carbon storage changes, in: Biotic Feedbacks in the Global Climatic System, edited by: Woodwell, G. M. and Mackenzie, F. T., Oxford University Press, New York, 304–312, 1995.

Prentice, I. C., Jolly, D., and BIOME 6000 participants: Mid-Holocene and glacial-maximum vegetation geography of the northern continents and Africa, J. Biogeogr., 27, 507–519, 2000.

Prentice, I. C., Sykes, M. T., Lautenschlager, M., Harrison, S. P., Denissenko, O., and Bartlein, P. J.: Modelling global vegetation patterns and terrestrial carbon storage at the last glacial maximum, Global Ecol. Biogeogr., 3, 67–76, 1993.

Prentice, K. C. and Fung, I. Y.: The sensitivity of terrestrial carbon storage to climate change, Nature, 346, 48–50, 1990.

Ramstein, G., Kageyama, M., Guiot, J., Wu, H., Hély, C., Krinner, G., and Brewer, S.: How cold was Europe at the Last Glacial Maximum? A synthesis of the progress achieved since the first PMIP model-data comparison, Clim. Past, 3, 331–339, 2007, http://www.clim-past.net/3/331/2007/.

Rousseau, D. D., Hatté, C., Guiot, J., Duzera, D., Schevina, P., and Kukla, G.: Reconstruction of the Grande Pile Eemian using inverse modeling of biomes and $\delta^{13}C$, Quaternary Sci. Rev., 25, 2806–2819, 2006.

Sage, R. F.: The evolution of C_4 photosynthesis, New Phytologist, 161, 341–370, 2004.

Sarnthein, M., Winn, K., Duplessy, J.-C., and Fontugne, M. R.: Global variations of surface ocean productivity in low and mid latitudes: influence on CO_2 reservoirs of the deep ocean and atmosphere during the last 21 000 years, Paleoceanography, 3, 361–399, 1988.

Shackleton, N. J.: Carbon-13 in Uvigerina: tropical rainforest history and the equatorial Pacific carbonate dissolution cycles, in: The Fate of Fossil Fuel CO_2 in the Oceans, edited by: Andersen, N. R. and Malahoff, A., Plenum, New York, 401–427, 1977.

Siegenthaler, U., Stocker, T. F., Monnin, E., Lüthi, D., Schwander, J., Stauffer, B., Raynaud, D., Barnola, J.-M., Fischer, H., Masson-Delmotte, V., and Jouzel, J.: Stable carbon cycle-climate relationship during the Late Pleistocene, Science, 310, 1313–1317, 2005.

Sitch, S., Smith, B., Prentice, I. C., Arneth, A., Bondeau, A., Cramer, W., Kaplan, J. O., Levis, S., Lucht, W., Sykes, M. T., Thonicke, K., and Venevsky, S.: Evaluation of ecosystem dynamics, plant geography and terrestrial carbon cycling in the LPJ dynamic global vegetation model, Global Change Biol., 9, 161–185, 2003.

Solomon, A. M.: Forest responses to complex interacting full-glacial environmental conditions, AMQUA Abstracts, 8, 120, 1984.

Spero, H. J., Bijma, J., Lea, D. W., and Bemis, B. E.: Effect of seawater carbonate concentration on formainiferal carbon and oxygen isotopes, Nature, 390, 497–500, 1997.

Street-Perrott, F. A.: Palaeoperspectives: changes in terrestrial ecosystems, Ambio, 23, 37–43, 1994.

Street-Perrott, F. A., Huang, Y., Perrott, R. A., and Eglinton, G.: Carbon isotopes in lake sediments and peats of last glacial age: implications for the global carbon cycle, in: Stable Isotopes, edited by: Griffiths, H., BIOS, Oxford, 381–396, 1998.

Street-Perrott, F. A., Huang, Y., Perrott, R. A., Eglinton, G., Barker, P., Ben Khelifa, L., Harkness, D. D., and Olago, D. O.: Impact of lower atmospheric carbon dioxide on tropical mountain ecosystems, Science, 278, 1422–1426, 1997.

Talbot, M. R. and Johanessen, T.: A high resolution palaeoclimate reconstruction for the last 27,500 years in tropical West Africa from the carbon and nitrogen isotope composition of lacustrine organic matter, Earth Planet. Sc. Lett., 110, 23–37, 1992.

Terashima, I., Masuzawa, T., Ohba, H., and Yokoi, Y.: Is photosynthesis suppressed at higher elevations due to low CO_2 pressure?, Ecology, 76, 2663–2668, 1995.

van Campo, E., Guiot, J., and Peng, C.: A data-based re-appraisal of the terrestrial carbon budget at the last glacial maximum, Global Planet. Change, 8, 189–201, 1993.

Warnant, P., François, L. M., Strivay, D., and Gérard, J.-C.: CARAIB: a global model of terrestrial biological productivity, Global Biogeochem. Cy., 8, 255–270, 1994.

Williams, J. W., Webb III, T., Shuman, B. N., and Bartlein, P. J.: Do low CO_2 concentrations affect pollen-based reconstructions of LGM climates? A response to 'Physiological significance of low atmospheric CO_2 for plant-climate interactions' by Cowling and Sykes, Quaternary Res., 53, 402–404, 2000.

Wong, S. C., Cowan, I. R., and Farquhar, G. D.: Stomatal conductance correlates with photosynthetic capacity, Nature, 282, 424–426, 1979.

Wu, H., Guiot, J., Brewer, S., and Guo, Z.: Climatic changes in Eurasia and Africa at the Last Glacial Maximum and mid-Holocene: reconstruction from pollen data using inverse vegetation modelling, Clim. Dynam., 29, 211–229, 2007a.

Wu, H., Guiot, J., Brewer, S., Guo, Z., and Peng, C.: Dominant factors controlling glacial and interglacial variations in the treeline elevation in tropical Africa, Proceedings of the National Academy of Sciences, 104, 9720–9724, 2007b.

Wu, H., Guiot, J., Peng, C., and Guo, Z.: New coupled model used inversely for reconstructing past terrestrial carbon storage from pollen data: validation of model using modern data, Global Change Biol., 15, 82–96, 2009.

Zeng, N.: Glacial-interglacial atmospheric CO_2 change – the glacial burial hypothesis, Adv. Atmos. Sci., 20, 677–693, 2003.

Zimov, S. A., Schuur, E. A. G., and Chapin III, F. S.: Permafrost and the global carbon budget, Science, 312, 1612–1613, 2006.

Clim. Past, 9, 2003–2011, 2013
www.clim-past.net/9/2003/2013/
doi:10.5194/cp-9-2003-2013

Climate of the Past
Open Access

On the Milankovitch sensitivity of the Quaternary deep-sea record

W. H. Berger[1,*]

[1]Geosciences Research Division, Scripps Institution of Oceanography, University of California, San Diego, USA

[*]*Invited contribution by W. H. Berger, recipient of the Milutin Milankovic Medal 2012.*

Correspondence to: W. H. Berger (wberger@ucsd.edu)

Received: 11 January 2013 – Published in Clim. Past Discuss.: 4 March 2013
Revised: 19 June 2013 – Accepted: 15 July 2013 – Published: 21 August 2013

Abstract. The response of the climate system to external forcing (that is, global warming) has become an item of prime interest, especially with respect to the rate of melting of land-based ice masses. The deep-sea record of ice-age climate change has been useful in assessing the sensitivity of the climate system to a different type of forcing; that is, to orbital forcing, which is well known for the last several million years. The expectation is that the response to one type of forcing will yield information about the likely response to other types of forcing. When comparing response and orbital forcing, one finds that sensitivity to this type of forcing varies greatly through time, evidently in dependence on the state of the system and the associated readiness of the system for change. The changing stability of ice masses is here presumed to be the chief underlying cause for the changing state of the system. A buildup of vulnerable ice masses within the latest Tertiary, when going into the ice ages, is thus here conjectured to cause a stepwise increase of climate variability since the early Pliocene.

1 Introduction

The ice-age record of deep-sea sediments demonstrates changing sensitivity of the climate of the last 2 Myr to "Milankovitch forcing" (MF in what follows). This is hardly in doubt any more. The pioneer studies of Hays et al. (1976) and the milestone articles in A. Berger et al. (1984) established that MF is present in the record, and can be used for tuning (i.e., for detailed age assignment). Also, by the mid-1980s it was shown that MF history can drive geophysical models able to generate an ice-mass history that closely mimics the real world (Pollard, 1984). These findings also opened the possibility of assessing the stability of the planetary orbits in the solar system, which are ultimately responsible for MF history through geologic time (A. Berger et al., 1992). In short, Milankovitch theory has become central to all discussion of the long-term climate history of the ice ages and beyond, and not only for the deep-sea record (e.g., Fischer et al., 1985; A. Berger et al., 1989; Einsele et al., 1991; Schwarzacher, 1993; EPICA Community Members, 2004).

It is true that the problems arising when linking orbital forcing to the observed climate response are complex. The ice-age climate system does not produce a random walk but is constrained to fluctuations between rather well defined boundaries while tending to avoid a central position, facts that imply the presence of both positive and negative feedbacks, with sign and strength of feedback dependent on the state of the system. Many or most of these problems have been aired and discussed following the pioneer studies mentioned. They are a matter of much discussion still (Ruddiman et al., 1989; Liu and Chao, 1998; W. Berger, 1999, 2008; Ridgwell et al., 1999; Elkibbi and Rial, 2001; Leuschner and Sirocko, 2003; Raymo and Nisancioglu, 2003; Paillard and Parrenin, 2004; A. Berger et al., 2005; Huybers and Wunsch, 2005; Maslin and Ridgwell, 2005; Claussen et al., 2006; Raymo et al., 2006; Meyers et al., 2008; Lisiecki, 2010; Huybers, 2007, 2009, 2011; Holden et al., 2011; Nie, 2011). Here I do not propose to address the various issues arising in this discussion. Instead, my intent is to highlight certain implications of traditional Milankovitch theory, which may not have received the attention that they deserve.

Of special interest in the ongoing discussions are obvious changes in the ice-age climate's sensitivity to forcing through time, which express themselves as changes in the response to various portions of the spectrum in the orbital forcing. These changes illustrate that there are a host of different feedbacks within the climate system, some apparently linked to certain portions of the spectrum. The central idea in Milankovitch theory, albedo feedback in high latitudes, no longer holds the monopolistic position it was once accorded by many adherents of the theory. Processes in the tropics and feedbacks associated with monsoon activity have to be considered as well. Nevertheless, faced with the ensuing complexity, it makes sense to return to the simple approach implicit in the original theory. The main reason for doing so is that the original theory produces usable results, and is indeed widely employed by geologists.

In the present essay, the emphasis is on a simple comparison of high-latitude summer forcing (as calculated by A. Berger and Loutre, 1991) and the oxygen isotope record on the deep-sea floor (as compiled by Zachos et al., 2001, and by Lisiecki and Raymo, 2005). What emerges from this comparison is that there is no single valid definition of "Milankovitch sensitivity" as the response of the climate system depends entirely on the contemporary state of the system and its readiness to move in one direction or another.

For good reasons, then, what may be called the Milankovitch sensitivity of the climate system (MS in what follows, defined as the ratio of the standardized amplitudes of "response" to those of the "forcing," that is, of the derivative of the oxygen isotope record to the Milankovitch-type insolation as given by A. Berger and Loutre, 1991) remains elusive, even in the Quaternary, with its strong Milankovitch affiliations. Superficially, within the late Quaternary, the main reason for the difficulty of relating MF to the climate response is the problem of the 100 kyr cycle. The "100 kyr problem", much discussed by the pioneers (Imbrie and Imbrie, 1980; Imbrie et al., 1984, 1992, 1993) and since, reflects the fact that the dominant climate cycle of the time span studied by Milankovitch (the last 650 kyr; that is, the "Milankovitch chron" of W. Berger and Wefer, 1992) has a period near 100 kyr. There is, however, no readily identifiable MF that could drive climate variation on this cycle. Many solutions to this conundrum have been proposed. Perhaps the most radical proposition rejects Milankovitch theory altogether and invokes the cyclic variation of the inclination of the average orbital plane of the planets in our solar system (Muller and McDonald, 2000). Other possible solutions, staying within Milankovitch theory, postulate long-term internal oscillation that is captured by eccentricity-related MF, notably varying precession, presumably with the help of stochastic forcing, or else elements of orbital forcing combined with a chaotic response.

Even if the 100 kyr problem were solved, however, the difficulty of defining MS would remain. It certainly would continue to exist for the time before the Milankovitch chron, a time when there were no 100 kyr cycles. The MS changes considerably both within the 100 kyr cycles (as exemplified by the presence of terminations; that is, threshold events) and it changes noticeably on longer timescales as well, presumably largely owing to a strong link to the size of the ice mass present in the Northern Hemisphere and its stability (Dolan et al., 2011). In addition, the MS is strongly influenced, presumably, by tectonic processes and associated erosion rates (Roe and Baker, 2007; Tomkin and Roe, 2007; A. Berger et al., 2008; Brocklehurst, 2008; Champagnac et al., 2012).

Thus, the attempt to obtain a quantitative measure of Milankovitch sensitivity must fail. However, it is worth exploring whether there are ways to track this elusive parameter semi-quantitatively, mainly for the purpose of obtaining a record of stability. MS did change greatly through geologic time, presumably initially because of the buildup of northern ice (identified by Milankovitch as the crucial element in the ice-age climate system; Milankovitch, 1930), and at a later stage in consequence of the increasing vulnerability of ice masses to a rise in sea level. This particular element of instability presumably was caused by the erosion of fjords and basins that allowed deep penetration of seawater to below existing ice masses, as well as the expansion of ice, which moved ice margins into waters offshore.

The implication of a changing MS for using the ice ages as a source of lessons for recent and present climate change is to greatly increase uncertainty. The chief lesson of the present exercise indeed is that forcing is just one element of the problem; the response depends largely on the state of the system. Presumably, the best analog periods for today's situation would be those for which the MS pattern is similar to the present one. If the MS cannot be measured, however (as seems to be the case), its patterns cannot be compared in detail from one period to another. Substituting MF for MS (for example, by taking Stage 11 as a good analog for the Holocene; A. Berger and Loutre, 2003) may work, but moves the argument into the realm of geologic time, with other problems arising, notably long-term secular changes in feedback mechanisms from erosion and from the buildup of major coral reef structures within the Pleistocene.

2 System response to Milankovitch forcing

The evidence that orbital forcing (Milankovitch forcing) is involved in guiding ice-age fluctuations is largely based on spectral analysis of the type pioneered by Hays et al. (1976). This type of analysis compares the spectra of the orbital variation with those obtained from climate records and finds that there are similarities. Similarities, in fact, can be greatly increased if one compares the spectrum of orbitally controlled insolation at a given location (here, the latitude of 65° N in July; A. Berger and Loutre, 1991) with the first derivative of the oxygen isotope record for benthic foraminifers (Zachos et al., 2001, and Lisiecki and Raymo, 2005, combined and re-dated; W. Berger, 2011). The derivative of the record emphasizes short-term fluctuations in the 10 kyr scale in preference to long-term changes in the 100 kyr scale, an effect that is favorable for the comparison (Fig. 1). Also, using the

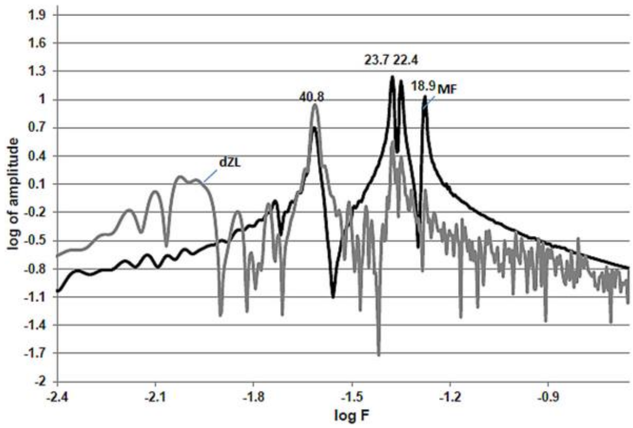

Fig. 1. Comparison of the spectra of orbital variations (as reflected in the insolation at 65° N, in July; A. Berger and Loutre, 1991) and in the oxygen isotope record of benthic foraminifers, for the last million years (Table A1 in W. Berger, 2011).

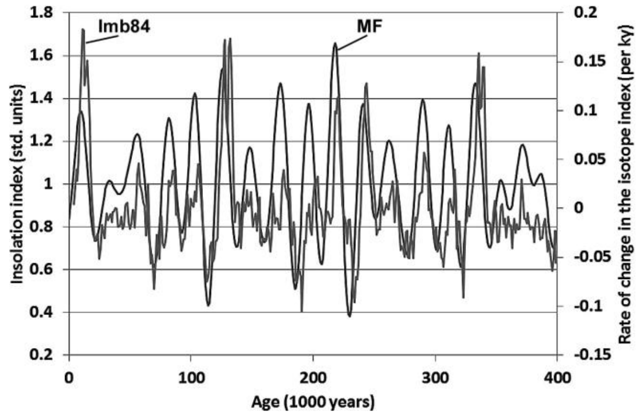

Fig. 2. Comparison of the derivative of the SPECMAP template (Imbrie et al., 1984) with MF as given in A. Berger and Loutre (1991). All values are standardized (by linear transform). The rate of change in the oxygen isotope record (secondary y axis) can be read as meters of sea-level change per decade, approximately.

derivative of the proxy seems to adjust the phase of forcing and response in a favorable manner.

The comparison of the two spectra (forcing and proxy derivative) documents that obliquity and precession effects are well represented in the record, but that there is additional information in the climate record, near 100 kyr (log $F \sim 2$), that has no equivalency in the forcing. This is the well known but poorly understood 100 kyr problem that was already mentioned. Finding matching lines within the spectra of orbital forcing and the climate record supports the Milankovitch theory (as pointed out by Hays et al., 1976, and many since). However, it does not uniquely identify the translation mechanism that converts the forcing to climate change. In fact, the 100 kyr problem raises the possibility that no such mechanism exists for portions of the spectrum. Clearly, it is the response of the climate system to forcing that we are interested in when discussing sensitivity within the framework of ice-age history. With the translation mechanism unidentified, such sensitivity remains a somewhat fuzzy concept. The fundamental insight of Milankovitch (1930) was the realization that the response of the system most likely originates in high latitudes of the Northern Hemisphere, and that the ice masses there are particularly vulnerable to melting within warm northern summers (Fig. 1). This insight led him to postulate forcing in terms of summer insolation in high northern latitudes.

Although aware of positive feedback from albedo (hence the choice of a crucial latitude in the far north, where snow can persist through the summer), Milankovitch assumed that the response to forcing would be predictable and well behaved. This assumption allowed him to use MF as a template for the reconstruction of conditions in the ice ages (most prominently in his graph published by Kőppen and Wegener, in 1924). The proposition that ice growth and ice decay display the type of behavior postulated by Milankovitch can be tested. It fails the test. The test here applied consists in finding the linear windowed correlation of two series, MF and the derivative of the oxygen isotope record in deep-sea sediments, after precise matching of MF with that proxy derivative.

As suggested by the comparison of spectra (Fig. 1), the matching (or "Milankovitch tuning") is best done between MF and the derivative of the proxy record; that is, the oxygen isotope stratigraphy of benthic or planktonic foraminifers. After all, Milankovitch theory refers to *change* in response to orbitally controlled insolation. A match of the high-latitude summer insolation series to environmental *conditions* (such as ice mass) is actually not a correct representation of the theory (even if it was done by Milankovitch himself).

The most widely used proxy record tuned to Milankovitch forcing and available for decades is the stacked record published by Imbrie et al. (1984) and commonly referred to as the "SPECMAP" template (here: "Imb84"). Its numerical derivative is readily made in a spreadsheet. Comparison with MF shows the good fit expected from tuning (MF here is taken as the series calculated by A. Berger and Loutre (1991); that is, the insolation for July at 65° N.). The precise phase between MF and response is unknown, as is the variability of that phase. The good fit between MF and proxy derivative seen represents an assumption of zero phase shift and zero variability of phase between the two series considered, a conjecture that simplifies the issue but has no inherent heuristic value.

It is immediately obvious from inspecting Fig. 2 that the fit is in the timing, but that the magnitude of the response is not closely linked to the magnitude of the MF (the mean is set to unity, and one standard deviation to 0.25). Evidently the sensitivity of the system to forcing changes through time,

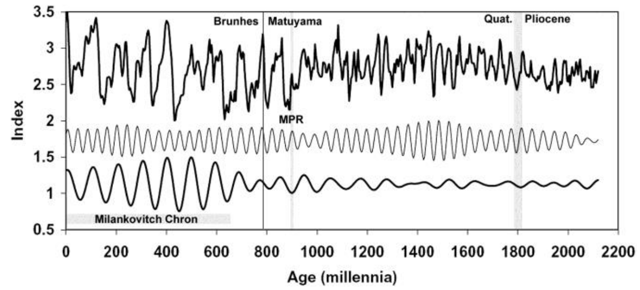

Fig. 3. Oxygen isotope record of ODP (Ocean Drilling Program) Site 806: extraction of ca. 40 kyr and ca. 100 kyr cycles by Fourier analysis. Adapted from W. Berger and Wefer (1992).

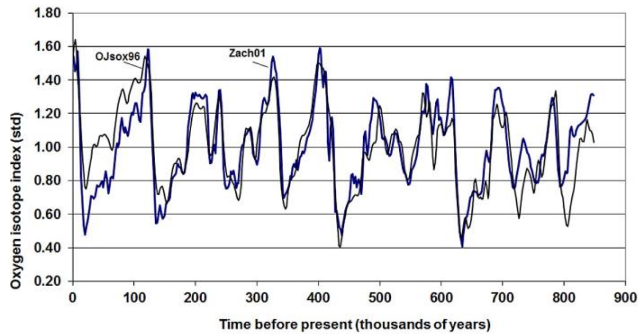

Fig. 4. Comparison of standardized oxygen isotope series from deep-sea sediments, one based on planktonic foraminifers (*G. sacculifer*), ODP Site 806, Ontong Java Plateau (W. Berger et al., 1993); the other based on 1 kyr interpolation of a compilation of benthic values by Zachos et al. (2001), on a global scale.

reflecting the changing state of the system. That this is the case has been well known for several decades. A major change in sensitivity during the Pleistocene manifests itself, for example, in the Mid-Pleistocene climate shift, when the system started to strongly respond to precession (and hence indirectly to eccentricity) in addition to the changing tilt of Earth's axis (Pisias and Moore, 1981; Ruddiman et al., 1989). The appearance of a strong 100 kyr cycle some 650 kyr ago (W. Berger and Wefer, 1992; Mudelsee and Stattegger, 1997; Mudelsee and Schulz, 1997) is another major change in climate response (Fig. 3). In fact, the apparent striking sensitivity of the climate system to forcing associated with the ca. 100 kyr cycle has provided a rich field for investigation and conjecture since the 1990s (Imbrie et al., 1993; W. Berger, 1999; A. Berger et al., 2005; Maslin and Ridgwell, 2005; Ganopolski and Calov, 2011; Nie, 2011). In the case of this long-term cycle internal oscillation and threshold response to both nonlinear orbital forcing and stochastic forcing have to be considered, in addition to orbital effects (Tziperman et al., 2006). It is interesting that the somewhat shorter obliquity cycles persisted throughout the Quaternary, despite the remarkable changes in the mixture of climate cycles seen in the appearance of the 100 kyr cycle (Fig. 3).

3 "Deaf zones"

Traditionally, the assessment of MS relies on globally relevant proxy records thought to be Milankovitch driven, commonly the oxygen isotope record of either benthic or planktonic foraminifers. Remarkably, the difference between the two types of proxy records is not important in the context (Fig. 4). This suggests that both records reflect the dominant parameter of climate change (ice mass) or else that other parameters that matter (such as local temperature) are highly correlated to the primary one (that is, to ice mass). Given the observed similarities, I shall analyze the compilations of benthic proxy records in what follows, confident that they represent global signals rather than local ones. Therefore, the implication is that any effects of changing bottom-water properties on the proxy record can be neglected, since they run parallel to the main response factor and do not impact the global signal.

The compilations are based on tuned records. Thus, a good fit to Milankovitch forcing can be taken to be built in. Nevertheless, I have combined the compilations of Zachos et al. (2001) and of Lisiecki and Raymo (2005) and re-tuned the resulting series to Milankovitch forcing (high-latitude summer insolation; A. Berger and Loutre, 1991) by matching the derivative of the stacked record (Table A1 in W. Berger, 2011) to MF, as indicated in Fig. 2. Both series employed ("forcing" and "response") comprise the last million years in 1 kyr intervals. The procedure should yield maximum values for MS. To get a general assessment of the behavior of MS over large time intervals I have used windowed linear correlation, as mentioned. The procedure answers the question of how well proxy series and MF are correlated along a sliding window after making the described match. To establish the effects of window size on the outcome, I chose 12 kyr, 25 kyr, 50 kyr (Fig. 5) and 100 kyr (not shown). The larger windows, in essence, represent summations of the shorter ones.

Whatever the window size chosen, there are some striking stretches of very low correlation, suggesting very little influence of MF on the climate record in spite of the presence of ice-age cycles. I have referred to such time spans as "deaf zones" elsewhere (W. Berger, 2011, 2013). However, the term "deaf," while describing the situation correctly as far as a lack of agreement between forcing and climate record, may be misleading. Some of the "deafness" may result from a lack of power in the forcing; that is, from insufficient power of MF to move the system, and not from an inherent lack of sensitivity of the system to outside influence (Fig. 5, bottom panel). If true, a difficult question arises: to what degree does "sufficiency" in the MF depend on the state of the system, and, therefore, does "sufficiency" change through time? Changes in sufficiency of the forcing presumably may affect the practice of Milankovitch tuning through geologic time, generating periods of high resolution

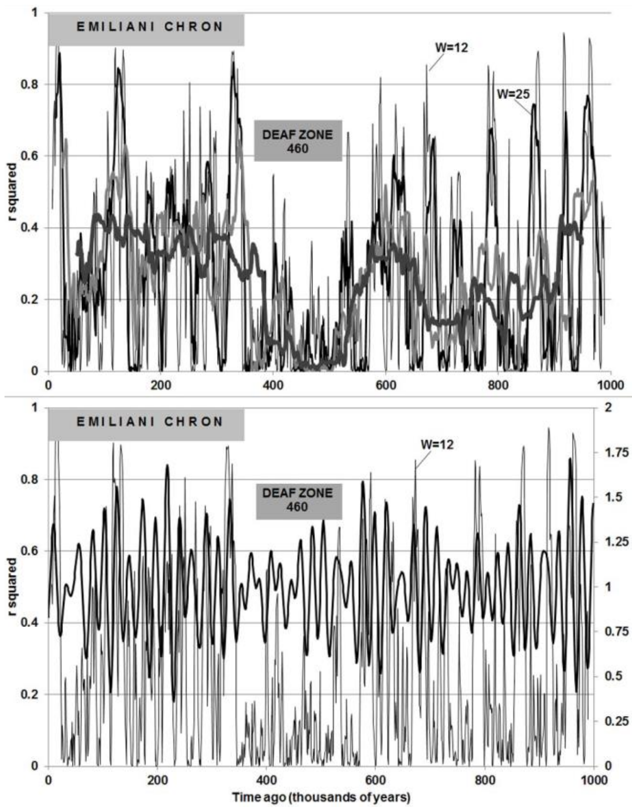

Fig. 5. Evidence for a lack of MS in climate change ("deaf zone") centered on 460 kyr, in windowed correlation of MF and a proxy series based on compilations of Zachos et al. (2001) and Lisiecki and Raymo (2005), combined, interpolated, and re-tuned to Milankovitch forcing (W. Berger, 2011; Table A1). The "deaf zone" includes Stage 12. Its end defines the beginning of the "Emiliani chron," the time span studied by Emiliani (1955) and recognized as rich in climate cycles. $W = 12$, window width is 12 kyr. Heavy gray line (top graph), window width is 50 kyr. Black line (bottom graph): MF (from A. Berger and Loutre, 1991).

but also periods with greater uncertainty in age assignments. Such tuning is now widely applied, following the success of Shackleton et al. (1990) in correctly dating sediments of Pleistocene age and of various authors in finding verifiable ages for sediments considerably older than that (e.g., Hilgen et al., 1995; Shackleton et al., 1995; Liebrand et al., 2011). In any case, the term "deaf" refers strictly to Milankovitch forcing, so it might usefully be changed to "M-deaf."

4 "Terminations"

The response of the climate system to Milankovitch forcing is observed to be at maximum strength during deglaciation events; that is, the relatively brief periods when large ice masses in the Northern Hemisphere disappear entirely, and sea level rises accordingly. The periodic switch within the system from buildup of ice to its rapid demise gives rise to asymmetric cycles, as noted first by Broecker and van Donk (1970), who also coined the label "termination" for the large-scale melting of glacial ice masses. That the rapid decay of ice indicates instability within the system was emphasized by Hughes (1987), among others.

Questions surrounding the stability of ice masses both in Greenland and in Antarctica have become of urgent importance in recent years, given that global warming is inexorably proceeding (e.g., Jansen et al., 2007; Holden et al., 2011). It seems obvious, from comparing MF with the timing of the onset of terminations (Fig. 6) that MF acts as a trigger in these circumstances rather than as a driver; that is, we are dealing with threshold phenomena when looking at fast melting. Threshold events may not be amenable to sensitivity analysis. Presumably, patterns observed arise in response to the contemporary conditions of the system. I suspect that conditions are uniquely defined by the amount of ice mass present and its age (W. Berger, 1997; Paul and Berger, 1997).

The implication for the urgent question arising in present circumstances (stability of ice masses in the face of global warming) is that the stability of large polar ice masses varies through time and is a product of preceding history. The masses either are stable or unstable, presumably largely dependent on their internal temperature and on the presence of backstops such as shelf ice. The sensitivity of the system to external forcing is not a given quantity but freely adjusts to the environment, which is itself defined by contingencies. There is one very clear message from the record, however. It is that there is plenty of inertia in the system. History suggests that once large ice masses start deteriorating they will continue to do so for more than a thousand years, presumably largely reflecting internal system feedback rather than only external forcing. If so, this would imply that a disintegration of large ice masses, once started, is irreversible on a timescale of centuries. To what degree such disintegration reflects the participation of the ocean in climate system processes (e.g., Broecker and Denton, 1989) is an interesting question that remains to be investigated. Simple physical principles suggest that disintegrating ice heats up from fast motion and breaks up, thus admitting lubricating water to the base of the ice. Essentially, we are facing the complexities posed by landslides of a very special nature. In addition, ice masses that terminate within the sea are vulnerable to a rise in sea level, as well as to tsunamis. These vulnerabilities introduce stochastic forcing from earthquakes and high frequency astronomical forcing from the tides. Evidently, both types of forcing are of interest in the context of threshold events. Stochastic forcing presumably is most effective whenever a system is ready to move on its own anyway.

5 Agitation through time

A highly variable climate system may be said to have a high level of "agitation"; that is, its various elements change

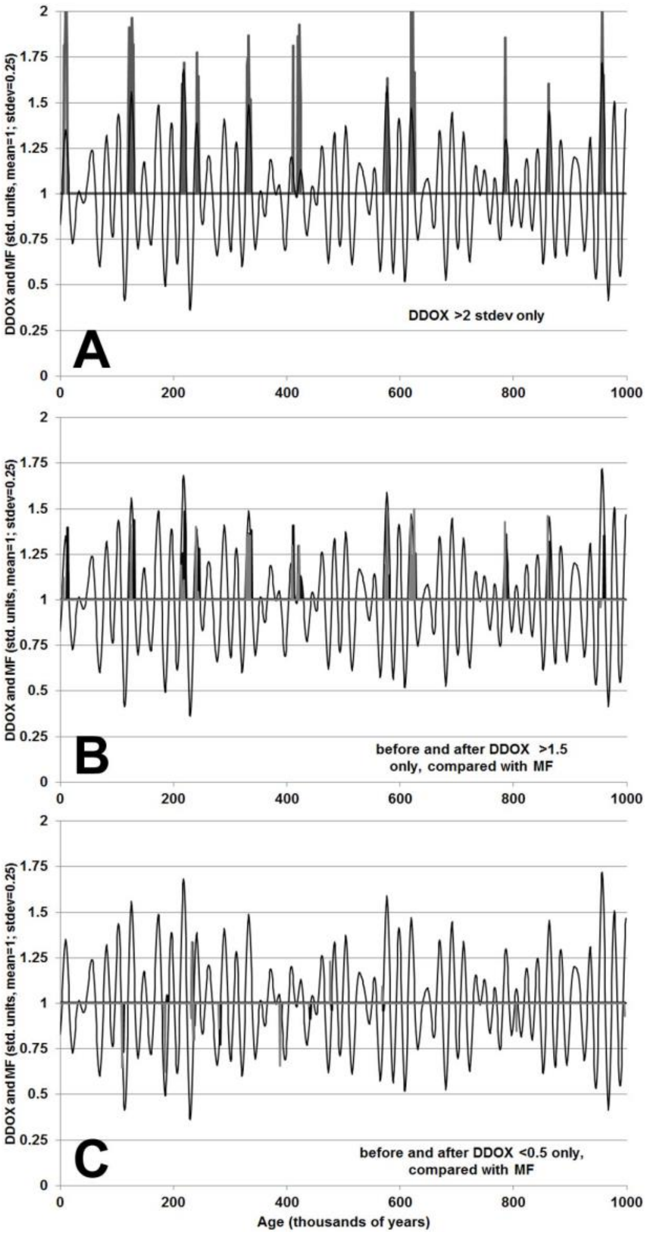

Fig. 6. Unusually large rates of change compared with MF. **A**, derivative of δ^{18}O record (Table A1 in W. Berger, 2011) larger than 2 standard deviations above the mean, placed along the MF series (calculated by A.Berger and Loutre, 1991). These are the "terminations." **B**, rates of change before and after events for which positive δ^{18}O' values exceed 2 standard deviations (search for persistence of fast positive rates). **C**, rates of change before and after events for which negative δ^{18}O' values exceed 2 standard deviations (search for persistence) (mean of the series set to one, standard deviation to 0.25).

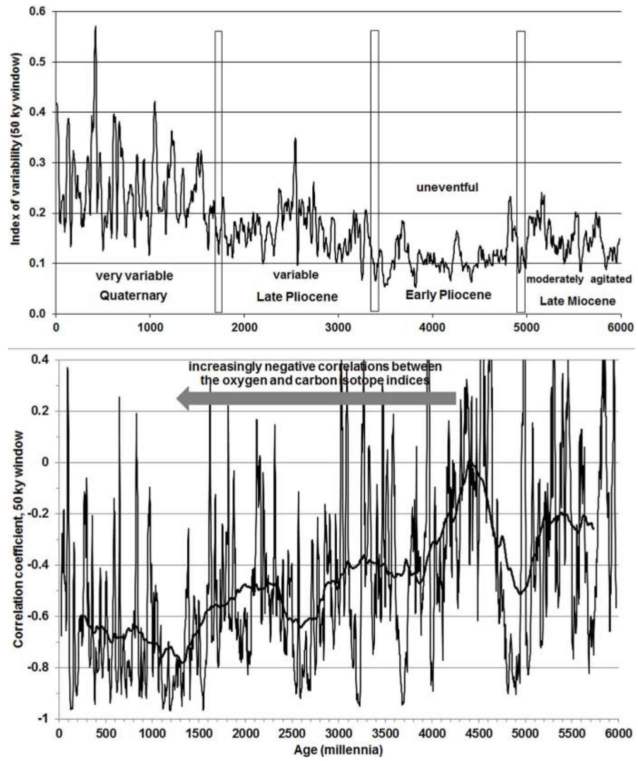

Fig. 7. The late Tertiary-to-Quaternary trend of increased variability (as seen in the oxygen isotopes) and the increased constraints on the carbon system (as seen in the evolution of correlation coefficients between oxygen and carbon isotopes). Data are from the compilation of Zachos et al. (2001), interpolated for 2 kyr intervals. The correlation in the lower graph is based on a moving 50 kyr window, with the solid line showing average conditions for 500 kyr.

rather rapidly. A system can enter a state of high agitation in response to unchanged forcing because of a high content of instability, which implies increased sensitivity to outside disturbance. In such a situation, forcing that "triggers" a response may be more important than forcing that gradually "drives" a system toward a new state. Any effects of a "trigger", of course, are inherently less predictable than those of a "driver". In this sense, it seems, the Quaternary, and especially the late Quaternary, is a less predictable environment than, say, the early Pliocene (Fig. 7). The change from predictable to unpredictable is of considerable interest in the context of evolution in the last 5 Myr, which presumably includes the invasion of the increasingly variable northern realm by migrating birds and various types of arctic mammals.

The overall trend toward increased agitation in the global climate system is not subtle at all, but is very evident. The trend is a result of a stepwise increase in variability, measured in terms of the changing standard deviation of the proxy parameter in a window (here: 50 kyr). The general increase in variability observed is presumably linked to the buildup of large ice masses in northern land areas. A step near 3 Ma (million years ago) supports the concept (based on the discovery of glacial debris by drilling in the North Atlantic) that northern glacial ice masses (vulnerable to fast melting) date from roughly that time (Berggren, 1972; and many authors since). The moderately high agitation level at the end of the Miocene may owe to an earlier northern ice buildup (Jansen and Sjøholm, 1991; Larsen et al., 1994). If so, a decrease in agitation would be expected from northern warming, on a timescale of tens of thousands of years (as observed for the early Pliocene).

I suspect that increased heat transport by the Gulf Stream system was an important factor in northern warming, in consequence of closing the connection between the Caribbean and Pacific within the late Pliocene. Presumably, the northern ice buildup was not entirely prevented by the newly available heat, but was delayed for some time (W. Berger and Wefer, 1996). Eventually, northern ice appeared anyway, as the planet continued to cool. The increased supply of Gulf Stream heat, in the geologic time that followed, then helped make the northern ice masses unstable and vulnerable to sporadic removal. In this sense, the Quaternary may indeed owe some of its main features to the emergence of the Panama Isthmus, although not in the way envisaged by those who call on the additional heat to make vapor and snow.

It seems clear from inspection of Fig. 7 that the currently accepted boundaries between Miocene and Pliocene ($\sim$ 5 Ma), and between Pliocene and Pleistocene ($\sim$ 1.8 Ma), are readily reconciled with the evidence for changes in climate variability. In addition, it is of interest that the general increase in climate variability parallels increasing participation of the carbon cycle in the climate narrative. The latter expresses itself as an increase in negative correlation (linear, windowed) between oxygen and carbon isotopes in the benthic deep-sea foraminifers, with a maximum (in negative correlation) near 1.3 Ma. The cause for the correlation is not known; it may reflect climate control on the buildup and destruction of forests, soil, or peat deposits on land, or high-latitude control on carbon content in the deep sea, or a combination of these processes, or factors involving the ocean.

Notably, there is no evidence, in these records, of a quiet time in the middle of the Pliocene. This relatively warm period (3 Myr to 3.3 Myr) has been studied for sensitivity to Milankovitch forcing (by climate modeling), and was found to likely have had substantial sea-level fluctuations around a mean that was substantially higher than today (Dolan et al., 2011).

6 Conclusions

The use of Milankovitch theory for the purpose of dating deep-sea sediments is an important and widespread practical application of the theory to deep-sea stratigraphy. Apparently, for the procedure to work, it is not necessary to understand how Milankovitch forcing is translated into changes in the climate system. However, a lack of understanding does negatively affect any use of ice-age history in drawing lessons for the climate problems of the present. The fact that understanding is very limited emerges from an inability to capture quantitatively the response of the global climate system to MF and any other forcing. An important problem is that the system responds as much to triggers as to drivers. Whenever MF provides the trigger it is not clear why the trigger was effective exactly at the time observed. Presumably the system is in a crucial state at that time; a state that is difficult or perhaps impossible to define using available proxies. As concerns the response of the climate system to drivers, it appears that this response is subject to unknown factors causing either enthusiastic or reluctant response.

Trends of increasing variability in climate response, when moving into the Quaternary, at the end of the late Tertiary, suggest that the buildup of large polar ice masses was responsible for the increased sensitivity of the system to disturbance, in agreement with the theory formulated by Milankovitch (1930). As the amplitudes of change became larger, the carbon cycle became increasingly involved as one element in the climatic variations.

Acknowledgements. I thank Didier Rousseau for asking me to write the essay, and I am indebted to two anonymous reviewers for cogent remarks with regard to the original draft of the manuscript.

Edited by: D. Fleitmann

References

Berger, A.: Pleistocene climate variability at astronomical frequencies, Quaternary Int., 2, 1–14, 1989.

Berger, A. and Loutre, M. F.: Insolation values for the climate of the last 10 million years, Quaternary Sci. Rev., 10, 297–317, 1991.

Berger, A. and Loutre, M. F.: Climate 400,000 years ago, a key to the future?, in: Earth's Climate and orbital Eccentricity, edited by: Droxler, A. W., Poore, R. Z., and Burckle, L. H., American Geophysical Union, Washington DC, 17–26, 2003.

Berger, A., Imbrie, J., Hays, J., Kukla, G., and Saltzman, B. (Eds.): Milankovitch and Climate: Understanding the Response to Astronomical Forcing: Dordrecht (D. Reidel), Vol. 2, 895 pp., 1984.

Berger, A., Schneider, S., and Duplessy, J. C. (Eds.): Climate and Geo-Sciences, A Challenge for Science and Society in the 21st Century, Kluwer Academic, Dordrecht, 724 pp., 1989.

Berger, A., Loutre, M. F., and Laskar, J.: Stability of the astronomical frequencies over the Earth's history for paleoclimate studies, Science, 255, 560–566, 1992.

Berger, A., Mélice, J. L., and Loutre, M. F.: On the origin of the 100-kyr cycles in the astronomical forcing, Paleoceanography, 20, PA4019, doi:10.1029/2005PA001173, 2005.

Berger, A. L., Gulick, S. P. S., Spotila, J. A., Upton, P., Jaeger, J. M., Chapman, J. B., Worthington, L. A., Pavlis, T. L., Ridgway, K. D., Willems, B. A., and and McAleer, R. J.: Quaternary tectonic response to intensified glacial erosion in an orogenic wedge, Nat. Geosci., 1, 793–799, doi:10.1038/ngeo334, 2008.

Berger, W. H.: Experimenting with ice-age cycles in a spreadsheet, J. Geoscience Education, 45, 428–439, 1997.

Berger, W. H.: The 100-kyr ice-age cycle: internal oscillation or inclinational forcing?, Int. J. Earth Sci., 88, 305–316, 1999.

Berger, W. H.: Sea level in the Late Quaternary: Patterns of variation and implications, Int. J. Earth Sci., 97, 1143–1150, 2008.

Berger, W. H.: Geologist at sea: Aspects of ocean history, Ann. Reviews Marine Science, 3, 1–34, 2011.

Berger, W. H.: Milankovitch tuning of deep-sea records: Implications for maximum rates of change of sea level. Global Planet. Change, 101, 131–143, 2013.

Berger, W. H. and Wefer, G.: Klimageschichte aus Tiefseesedimenten – Neues vom Ontong-Java- Plateau (Westpazifik), Naturwissenschaften, 79, 541–550, 1992.

Berger, W. H. and Wefer, G.: Expeditions into the past: Paleoceanographic studies in the South Atlantic, in: The South Atlantic: Present and Past Circulation, edited by: Wefer, G., Berger, W. H., Siedler, G., and Webb, D. J., Springer-Verlag Berlin Heidelberg, 363–410, 1996.

Berger, W. H., Bickert, T., Schmidt, H., and Wefer, G.: Quaternary oxygen isotope record of pelagic foraminifers: Site 806, Ontong Java Plateau, Proceedings of the Ocean Drilling Program, Scientific Results, 130, 381–395, 1993.

Berggren, W. A.: Late Pliocene-Pleistocene glaciation, in: Init. Rept. DSDP, edited by: Laughton, A. and Berggren, W. A., Vol. 12, Washington DC, (US Govt. Printing Office), 953–963, 1972.

Brocklehurst, S. H.: A glacial driver of tectonics, Nat. Geosci., 1, 732–733, 2008.

Broecker, W. S. and Denton, G. H.: The role of ocean–atmosphere reorganizations in glacial cycles, Geochim. Cosmochim. Ac., 53, 2465–2501, 1989.

Broecker, W. S. and van Donk, J.: Insolation changes, ice volumes, and the O-18 record in deep-sea cores, Rev. Geophys. Space GE, 8, 169–198, 1970.

Champagnac, J.-D., Molnar, P., Sue, C., and Herman, F.: Tectonics, climate, and mountain topography, J. Geophys. Res., 117, B02403, doi:10.1029/2011JB008348, 2012.

Claussen, M., Fohlmeister, J., Ganopolski, A., and Brovkin, V.: Vegetation dynamics amplifies precessional forcing, Geophys. Res. Lett., 33, L09709, doi:10.1029/2006GL026111, 2006.

Dolan, A. M., Haywood, A. M., Hill, D. J., Dowsett, H. J., Hunter, S. J., Lunt, D. J., and Pickering, S. J.: Sensitivity of Pliocene ice sheets to orbital forcing, Palaeogeogr. Palaeocl., 309, 98–110, 2011.

Einsele, G., Ricken, W., and Seilacher, A. (Eds.): Cycles and Events in Stratigraphy, Springer Verlag, Berlin Heidelberg etc., 955 pp., 1991.

Elkibbi, M. and Rial, J. A.: An outsider's review of the astronomical theory of the climate: Is the eccentricity-driven insolation the main driver of the ice ages?, Earth. Sci. Rev., 56, 161–177, 2001.

Emiliani, C.: Pleistocene temperatures, J. Geol., 63, 538–578, 1955.

EPICA Community Members: Eight glacial cycles from an Antarctic ice core, Nature, 429, 623–628, 2004.

Fischer, A. G., Herbert, T. D., and Premoli-Silva, I.: Carbonate bedding cycles in Cretaceous pelagic and hemipelagic sediments, in: Fine-grained deposits and biofacies of the Cretaceous Western Interior Seaway: evidence of cyclic sedimentary processes, edited by: Pratt, L. M., Kauffman, E. G., and Zelt, F. B., Soc. Econ. Paleontol. Mineral, 2nd Annual Mid-year Meeting, Golden, Colorado, Field Trip Guide Book 4, 1–10, 1985.

Ganopolski, A. and Calov, R.: The role of orbital forcing, carbon dioxide and regolith in 100 kyr glacial cycles, Clim. Past, 7, 1415–1425, doi:10.5194/cp-7-1415-2011, 2011.

Hays, J. D., Imbrie, J., and Shackleton, N. J.: Variations in the Earth's orbit: Pacemaker of the ice ages?, Science, 194, 1121–1132, 1976.

Hilgen, F. J., Krijgsman, W., Langereis, C. G., Lourens, L. J., Santarelli, A., and Zachariasse, W. J.: Extending the astronomical (polarity) timescale into the Miocene, Earth Planet. Sc. Lett., 136, 495–510, 1995.

Holden, P. B., Edwards, N. R., Wolf, E. W., Valdes, P. J., and Singarayer, J. S.: The Mid-Brunhes Event and West Antarctic ice sheet stability, J. Quaternary Sci., 26, 474–477, 2011.

Hughes, T.: Ice dynamics and deglaciation models when ice sheets collapsed, in: North America and Adjacent Oceans During the Last Deglaciation, edited by: Ruddiman, W. F. and Wright, H. E., The Geology of North America, v. K-3. Geol. Soc. America, Boulder, Colorado, 183–220, 1987.

Huybers, P.: Glacial variability over the last two million years: an extended depth-derived age model, continuous obliquity pacing, and the Pleistocene progression, Quaternary Sci. Rev., 26, 37–55, 2007.

Huybers, P.: Pleistocene glacial variability as a chaotic response to obliquity forcing, Clim. Past, 5, 481–488, doi:10.5194/cp-5-481-2009, 2009.

Huybers, P.: Combined obliquity and precession pacing of late Pleistocene deglaciations, Nature, 480, 229–232, 2011.

Huybers, P. and Wunsch, C.: Obliquity pacing of the late Pleistocene glacial terminations, Nature, 434, 491–494, 2005.

Imbrie, J. and Imbrie, J. Z.: Modelling the climatic response to orbital variations, Science, 207, 943–953, 1980.

Imbrie, J., Hays, J. D., Martinson, D. G., McIntyre, A., Mix, A. C., Morley, J. J., Pisias, N. G., Prell, W. L., and Shackleton, N. J.: The orbital theory of Pleistocene climate: Support from a revised chronology of the marine δ^{18}O record, in: Milankovitch and Climate (Part 1), edited by: Berger, A. L., Imbrie, J., Hays, J. D., Kukla, G., and Saltzman, B., 269–305, Hingham, Mass. (Reidel), 1984.

Imbrie, J., Boyle, E. A., Clemens, S. C., Duffy, A., Howard, W. R., Kukla, G., Kutzbach, J., Martinson, D. G., McIntyre, A., Mix, A. C., Molfino, B., Morley, J. J., Peterson, L. C., Pisias, N. G., Prell, W. L., Raymo, M. E., Shackleton, N. J., and Toggweiler, J. R.: On the structure and origin of major glaciation cycles 1. Linear responses to Milankovitch forcing, Paleoceanography, 7, 701–738, 1992.

Imbrie, J., Berger, A., Boyle, E. A., Clemens, S. C., Duffy, A., Howard, W. R., Kukla, G., Kutzbach, J., Martinson, D. G., McIntyre, A., Mix, A. C., Molfino, B., Morley, J. J., Peterson, L. C., Pisias, N. G., Prell, W. L., Raymo, M. E., Shackleton, N. J., and Toggweiler, J. R.: On the structure and origin of major glaciation cycles 2. The 100,000-year cycle, Paleoceanography, 8, 699–735, 1993.

Jansen, E. and Sjøholm, J.: Reconstruction of glaciation over the past 6 million years from ice-borne deposits in the Norwegian Sea, Nature, 349, 600–604, 1991.

Jansen, E., Overpeck, J., Briffa, K. R., Duplessy, J.-C., Joos, F., Masson-Delmotte, V., Olago, D., Otto-Bliesner, B., Peltier, W.

R., Rahmstorf, S., Ramesh, R., Raynaud, D., Rind, D., Solomina, O., Villalba, R., and Zhang, D.: Palaeoclimate, in: Climate Change 2007: the Physical Science Basis; Contribution of Working Group I to the Fourth Assessment Report of the Intergovernmental Panel on Climate Change, edited by: Solomon, S., Qin, D., Manning, M., Chen, Z., Marquis, M., Averyt, K. B., Tignor, M., and Miller, H. L., Cambridge University Press, 433–497, 2007.

Kőppen, W. and Wegener, A.: Die Klimate der geologischen Vorzeit, Bornträger, Berlin, 256 pp., 1924.

Larsen, H. C., Saunders, A. D., Clift, P. D., Beget, J., Wei, W., Spezzaferri, S., and ODP 152 Scientific Party: Seven million years of glaciation in Greenland, Science, 264, 952–955, 1994.

Leuschner, D. C. and Sirocko, F.: Orbital insolation forcing of the Indian monsoon – a motor for climate changes?, Palaeogeogr. Palaeocli., 197, 83–95, 2003.

Liebrand, D., Lourens, L. J., Hodell, D. A., de Boer, B., van de Wal, R., Pälicke, H., and Gibbs, S. J.: Dynamics of ∼100-kyr glacial cycles during the early Miocene, Geophys. Res. Abstr., EGU2011-230-2.2011, EGU General Assembly 2011, Vienna, Austria, 2011.

Lisiecki, L. L.: Links between eccentrity forcing and the 100,000-year glacial cycle, Nat. Geosci., 2, 349–352, doi:10.1038/ngeo828, 2010.

Lisiecki, L. E. and Raymo, M. E.: A Pliocene-Pleistocene stack of 57 globally distributed benthic δ^{18}O records, Paleoceanography, 20, PA1003, doi:10.1029/2004PA001071, 2005.

Liu, H. L. and Chao, B. F.: Wavelet spectral analysis of the Earth's orbital variations and paleoclimatic cycles, J. Atmos. Sci., 55, 227–236, 1998.

Maslin, M. A. and Ridgwell, A.: Mid-Pleistocene Revolution and the eccentricity myth, Special Publication of the Geological Society of London 247, 19–34, 2005.

Meyers, S. R., Sageman, B. B., and Pagani, M.: Resolving Milankovitch: Consideration of signal and noise, Am. J. Sci., 308, 770–786, 2008.

Milankovitch, M.: Mathematische Klimalehre und astronomische Theorie der Klimaschwankungen, in: Handbuch der Klimatologie, edited by: Köppen, W. and Geiger, R., Vol. 1, Gebrüder Bornträger, Berlin, 1–176, 1930.

Mudelsee, M. and Schulz, M.: The mid-Pleistocene climate transition: onset of 100 ka cycle lags ice volume build-up by 280 ka, Earth Planet. Sci. Lett., 151, 117–123, 1997.

Mudelsee, M. and Stattegger, K.: Exploring the structure of the mid-Pleistocene revolution with advanced methods of time-series analysis, Geologische Rundschau, 86, 499–511, 1997.

Muller, R. A. and MacDonald, G. J.: Ice Ages and Astronomical Causes: Data, Spectral Analysis, and Mechanisms, Springer-Praxis, London, 318 pp., 2000.

Nie, J.: Coupled 100-kyr cycles between 3 and 1 Ma in terrestrial and marine paleoclimatic records, Geochem. Geophy. Geosy., 12, Q10Z32, doi:10.1029/2011GC003772, 2011.

Paillard, D. and Parrenin, F.: The Antarctic ice sheet and the triggering of deglaciation, Earth Planet. Sci. Lett., 227, 203–271, 2004.

Paul, A. and Berger, W. H.: Modellierung der Eiszeiten: Klimazyklen und Klimasprünge, Geowissenschaften, 15, 20–27, 1997.

Pisias, N. G. and Moore, T. C.: The evolution of Pleistocene climate: a time series approach, Earth Planet Sc. Lett., 52, 450–456, 1981.

Pollard, D.: Some ice-age aspects of calving ice-sheet model, in: Milankovitch and Climate, Part 2, edited by: Berger, A. L., Imbrie, J., Hays, J. D., Kukla, G., and Saltzman, B., 541–564, D. Reidel, Dordrecht, 1984.

Raymo, M. E. and Nisancioglu, K. H.: The 41 kyr world: Milankovitch's other unsolved mystery, Paleoceanography, 18, 11-1–11-6, 2003.

Raymo, M. E., Lisiecki, L. E., and Nisancioglu, K. H. Plio-Pleistocene ice volume, Antarctic climate, and the global δ18O record, Science, 313, 492–495, 2006.

Ridgwell, A., Watson, A., and Raymo, M.: Is the spectral signature of the 100-kyr glacial cycle consistent with a Milankovitch origin?, Paleoceanography, 14, 437–440, 1999.

Roe, G. H. and Baker, M. B.: Why is climate sensitivity so unpredictable?, Science, 318, 629–632, 2007.

Ruddiman, W. F., Raymo, M. E., Martinson, D. G., Clement, B. M., and Backman, J.: Mid-Pleistocene evolution of Northern Hemisphere climate, Paleoceanography, 4, 353–412, 1989.

Schwarzacher, W.: Cyclostratigraphy and the Milankovitch Theory, Elsevier Amsterdam London etc., 225 pp., 1993.

Shackleton, N. J., Berger, A., and Peltier, W. R.: An alternative astronomical calibration of the lower Pleistocene timescale based on ODP Site 677, T. RSE Earth, 81, 251–261, 1990.

Shackleton, N. J., Crowhurst, S., Hagelberg, T., Pisias, N. G., and Schneider, D. A.: A new late Neogene time scale: Application to Leg 138 sites, Proc. Ocean Drill. Program Sci. Results, 138, 73–101, 1995.

Tomkin, J. H. and Roe, G. H.: Climate and tectonic controls on glaciated critical taper-orogens, Earth Planet. Sc. Lett., 262, 385–397, 2007.

Tziperman, E., Raymo, M. E., Huybers, P., and Wunsch, C.: Consequences of pacing the Pleistocene 100 kyr ice ages by nonlinear phase locking to Milankovitch forcing, Paleoceanography, 21, PA4206, doi:10.1029/2005PA001241, 2006.

Zachos, J., Pagani, M., Sloan, L., Thomas, E., and Billups, K.: Trends, rhythms, and aberrations in global climate 65 Ma to present, Science, 292, 686–693, 2001.

Clim. Past, 9, 2525–2547, 2013
www.clim-past.net/9/2525/2013/
doi:10.5194/cp-9-2525-2013

Climate of the Past
Open Access

A brief history of ice core science over the last 50 yr

J. Jouzel[1]

[1]Laboratoire des Sciences de Climat et de l'Environnement/Institut Pierre Simon Laplace, CEA-CNRS-UVSQ – UMR8212, CEA Saclay, L'Orme des Merisiers, Bt. 701, 91191 Gif/Yvette, Cedex, France
Invited contribution by J. Jouzel, recipient of the EGS Milutin Milankovic Medal 1997.

Correspondence to: J. Jouzel (jean.jouzel@lsce.ipsl.fr)

Received: 30 April 2013 – Published in Clim. Past Discuss.: 3 July 2013
Revised: 24 September 2013 – Accepted: 30 September 2013 – Published: 6 November 2013

Abstract. For about 50 yr, ice cores have provided a wealth of information about past climatic and environmental changes. Ice cores from Greenland, Antarctica and other glacier-covered regions now encompass a variety of time scales. However, the longer time scales (e.g. at least back to the Last Glacial period) are covered by deep ice cores, the number of which is still very limited: seven from Greenland, with only one providing an undisturbed record of a part of the last interglacial period, and a dozen from Antarctica, with the longest record covering the last 800 000 yr. This article aims to summarize this successful adventure initiated by a few pioneers and their teams and to review key scientific results by focusing on climate (in particular water isotopes) and climate-related (e.g. greenhouse gases) reconstructions. Future research is well taken into account by the four projects defined by IPICS. However, it remains a challenge to get an intact record of the Last Interglacial in Greenland and to extend the Antarctic record through the mid-Pleistocene transition, if possible back to 1.5 Ma.

1 Introduction

It was a great honour to be invited to give a lecture on the "History of ice core science" at the 2012 open Science Conference of IPICS, the International Partnerships in Ice Core Science. I did it as a scientist and not as an historian, using material from books such as "Frozen Annals" by Dansgaard (2004), the "Two-Mile Time Machine" by Alley (2000) and "White Planet" co-authored by Claude Lorius, Dominique Raynaud and myself, recently published by Princeton University Press (2013). My presentation was also based on a review article by Langway (2008) about "The history of early polar ice cores" and on many other scientific articles, reports and websites. I was also interested in looking at how ice core research, which for about fifty years has produced such a wealth of information about past changes in our climate and our environment, is perceived outside our scientific community; one well-documented example is given by Spencer Weart, an historian of science, who has written a book called "The discovery of global warming" (Weart, 2008, updated in 2013) with a chapter on Greenland ice drilling.

This review is written in the same spirit, and as a scientist I am probably unable to give an unbiased account of the history of ice core science, as a large part is also based on my own perception. I started environmental research forty-five years ago and, thanks to Claude Lorius, had the opportunity to be involved in the first French deep drilling project, which in 1978 allowed us to recover a 905 m-deep ice core at the Dome C site on the Antarctic Plateau (Lorius et al., 1979). Except for Dye 3 (southern Greenland) and more recent projects such as WAISCORE (West Antarctica), I have been lucky to be part of or associated with major projects conducted since the eighties in Antarctica (Vostok, EPICA Dome C and EDML, Dome F, Law Dome, Talos Dome) and Greenland (GRIP, GISP2, North GRIP and NEEM); see Fig. 1 for the location of these Greenland and Antarctic sites. My participation in field work is more limited, with field seasons at GRIP, North GRIP and NEEM, but only a short visit in Antarctica.

This article deals both with the history of ice core drilling, including a brief account of ice cores recovered outside polar regions, and with ice core science. However, this would be too broad to cover all scientific aspects. Rather, I will focus on topics I am most familiar with, namely climate (in

Published by Copernicus Publications on behalf of the European Geosciences Union.

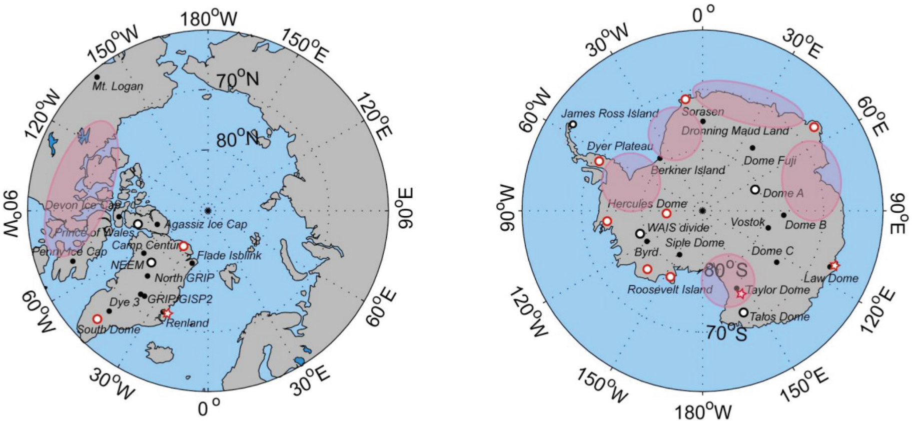

Fig. 1. Greenland and Antarctic deep drilling sites synthesised for the International Partnership for Ice Core Science (from http://www.pages-igbp.org/ipics/).

particular water isotopes) or climate-related (e.g. greenhouse gases) reconstructions as well as dating issues. Aspects dealing with the chemical composition of snow and ice, with the information that can be derived on past changes in atmospheric chemistry and biogeochemical cycles, with the fallout of cosmogenic isotopes, with the physics of ice, and with the modelling of ice flow and ice sheets, will not be covered.

2 Ice core drillling: from Camp Century to the WAIS divide ice core

As reviewed by Langway (2008), the first attempt to probe the interior of an ice sheet was conducted by Sorge (1935) from the study of a 15 m-deep pit recovered at Station Eismitte (Greenland). The first ice cores were obtained about twenty years later by three separate international research teams (Langway, 2008): the Norwegian–British–Swedish Antarctic Expedition on the Queen Maud Land – now Dronning Maud Land – coast (Swithinbank, 1957; Schytt, 1958), the Juneau Ice Field Research Project in Alaska (Miller, 1954) and the Expeditions Polaires Françaises in central Greenland (Heuberger, 1954). These ice cores drilled in the early fifties were about 100 m deep, with generally low quality of ice recovery preventing detailed analytical studies (Langway Jr., 1958), and one can mark the 1957–1958 International Geophysical Year (IGY) as the starting point of ice core research. One of the IGY's priorities was deep core drilling into polar ice sheets for scientific purposes. Five nations were particularly active in the early period of deep drilling projects in polar regions – the sixties and seventies – the USA, the Soviet Union, Denmark, Switzerland and France.

Under the leadership of Henri Bader and then of Chet Langway, US teams were very active thanks to two US Army Corps of Engineers research laboratories: the Snow, Ice and Permafrost Research Establishment (SIPRE) merged in 1961 with another US Army research laboratory to form the (current) Cold Regions Research and Engineering Laboratory (CRREL). In Greenland, two cores were drilled at Site 2 in 1956 (305 m) and 1957 (411 m), closely followed by two cores in Antarctica, at Byrd Station in 1957/1958 (309 m), and at Little America V, on the Ross Ice Shelf, in 1958/1959 (264 m). The drilling operation moved in Camp Century in northwestern Greenland in the fall of 1960 and it then took a strenuous six-year field effort to recover the first ever continuous ice core to the bedrock depth, 1388 m long (Hansen and Langway, 1966; Langway, 2008). The drillers of CRREL went on to Antarctica at Byrd Station, a site in West Antarctica chosen (as Camp Century) because of its accessibility. The drilling was a success, reaching 2164 m in 1968, but unfortunately the drill remained at the bottom of the hole and US drillers had to wait until 1993 to again celebrate the success of a deep drilling.

Over this period, international partnership was established between CRREL and other US teams with teams from the University of Copenhagen and Bern led respectively by Willi Dansgaard and Hans Oeschger. Dansgaard was a pioneer in the establishment of the close link between the isotopic composition of polar snow (δ^{18}O and δD) and the temperature at the precipitation site (Dansgaard, 1953, 1964). With his Copenhagen team, he was the first to recover continuous isotopic profiles along deep ice cores (Dansgaard et al., 1969; Johnsen et al., 1972); such an isotopic approach was also developed in the US, largely on the initiative of Sam Epstein (Epstein et al., 1970). The initial interest of Oeschger, a specialist in low-level carbon 14 dating, was about radiocarbon dating of ice (Oeschger et al., 1966, 1967). Following the success of the Camp Century and Byrd drillings, this collaboration between the USA, Denmark and Switzerland developed the concept of a Greenland Ice Sheet Project (GISP) in the early seventies. After the loss of the drill at Byrd, the Copenhagen team took over and, under the direction of Niels Gunderstrup and Sigfus Johnsen, developed their own drill, known as Istuk. For logistical reasons the Dye 3 site in southern Greenland was chosen for this new drilling project; after three seasons (1979–1981) the bedrock was reached at a depth of 2038 m (Dansgaard et al., 1982).

Soviet and Russian activities started in 1955 with drilling in the Arctic and non-polar regions, and in 1956 in Antarctica with a 377 m deep core drilled near Mirny in 1957. The first attempt at deep-hole drilling at Vostok was started in April 1970, with a depth of 506.9 m reached by September 1970 (Ueda and Talalay, 2007 and references therein). At this site, the drilling activity, under the leadership of Ye. S. Korotkevich, culminated in the recovery of the deepest core ever obtained, reaching a depth of 3623 m (Petit et al., 1999) in a project joined in the eighties by French teams led by Claude Lorius and later by US teams with the strong involvement of Michael Bender (now at Princeton University). This Vostok drilling was recently extended down to the interface with Lake Vostok at a depth of 3769 m in February 2012 (V. Lipenkov, personal communication, 2012). As fully discussed below, in the eighties the Vostok ice core was the first ice core to cover a full glacial–interglacial cycle.

French drilling activities started in Antarctica with drilling undertaken in the sixties and seventies in the coastal regions at proximity of French base Dumont d'Urville (Adelie Land, East Antarctica). The French team then carried out a 905 m deep drilling at the inland site of Dome C (Lorius et al., 1979), at a location – which, unlike Camp Century, Byrd and Vostok – was deliberately chosen on a dome where the interpretation of ice core data is in principle easier because ice at depth is formed from snow which has fallen on the site itself. Involving teams from Grenoble, Saclay and Orsay, this core was the basis for new investigations such as measurements of beryllium 10, a cosmogenic isotope (Raisbeck et al., 1981), of carbon dioxide (Delmas et al., 1980), of δD and δ^{18}O (Jouzel et al., 1982), and of the oxygen 18 of O_2 (Bender et al., 1985).

Two other nations, Australia and Canada, started drilling in polar regions in the sixties and seventies. The Australian National Antarctic Research Expeditions (ANARE) focused on Law Dome, a small ice sheet located at the edge of the Indian Ocean sector of East Antarctica, where a 382 m ice core was drilled in 1969 and to 477 m in 1977 (Hamley et al., 1986); in the nineties, a new drilling was performed at a different site (Dome Summit South), with a depth of 553 m reached in 1991–1992 and completion down to the bedrock in February 1993 (Morgan et al., 1997). Stan Paterson and Roy Koerner played a key role in the development of Canadian activities in the Arctic, where the first ice cores were recovered down to the bedrock on Devon Ice Cap in the seventies (Paterson et al., 1977; Koerner, 1977) and later on Agassiz Ice Field, Penny Ice Cap and and Prince of Wales Ice Sheet (Fisher et al., 2011).

Focusing on deep drilling that we define as extending beyond the Last Glacial Maximum, 20 000 yr ago (hereafter LGM), we now briefly describe the projects which have been undertaken in Greenland and Antarctica over the last thirty years. We also mention shorter cores drilled outside these regions.

2.1 Deep drilling in Greenland

Both the Camp Century and the Dye 3 drilling sites (Fig. 1) were chosen for their accessibility from Thule (Pituffik) to the northwest and Sondrestrom Air Base (Søndre Strømfjord/Kangerlussuaq) to the southwest, and for existing infrastructures. Camp Century was drilled as part of the Camp Century cold war "city under the ice" experiment and Dye-3 was an American cold war Distant Early Warning radar base on the ice sheet. Both cores reach the Last Glacial period, with the discovery of a succession of abrupt climate changes, but they do not provide reliable information about the Last Interglacial. Indeed, Dansgaard and his GISP colleagues were persuaded of the interest of drilling in the centre of Greenland to cover this key period – an objective reached in Antarctica in the mid-eighties thanks to the Vostok operation (Lorius et al., 1985). However, it was not simple to convince the US National Science Foundation (NSF) of the merit of such a project.

Dansgaard found an effective ally in Wally Broecker, a geochemist and oceanographer at Columbia University (New York), who like Hans Oeschger was fascinated by the connection between the rapid variations discovered at Dye 3 and the potential changes in the ocean current in the North Atlantic (Oeschger, 1985; Oeschger et al., 1984; Broecker et al., 1985). In January 1987, Broecker, who was in favour of an international project between US and European teams, organised a meeting involving scientists from both sides. At this Boston meeting, Dansgaard pledged for the drilling of two cores, one European, the other American. This proposition was collectively adopted, as the expected results were of such importance that it appeared indispensable to confirm them in parallel on a second drilling site. The Europeans chose the highest point for their GRIP (GReenland Ice core Project) project, the Americans a site 28 km farther west (GISP 2).

At the European site, the Eurocore project started by the Eurocore programme involving Denmark, France and Switzerland, launched in 1989 with the strong support of the European Communities, was dedicated to the study of the last 1000 yr from a 300 m core. Under the auspices of the European Science Foundation (ESF), five other countries – Germany, the UK, Belgium, Iceland and Italy – joined to launch GRIP in June 1990. One of the novelties was the building of an expanded "science trench" (a concept already used at Camp Century, Byrd and Dye 3) with, in addition to the preparation of the samples, measurements of some ice properties; this strategy has been adopted for other Greenland sites (Fig. 3) and for EPICA Dome C. The drilling was carried out over three summers, reaching 3028.8 m on 12 July 1992 (Dansgaard et al., 1993) using Istuk. The

Fig. 2. Some pioneers of ice core research: left panel: Willi Dansgaard, Chet Langway and Hans Oeschger (from left to right); upper right panel: Claude Lorius; lower right panel: Lonnie Thompson.

Fig. 3. The science trench at NEEM.

American team had less luck: the drill was entirely satisfactory but the cable proved problematic. After three years of drilling, a new cable had to be used, postponing the success of the drilling by one season (bottom reached in July 1993 at 3054 m).

Due to disturbances related to the proximity of the bedrock, neither of these two cores provided reliable climatic information beyond 100 000 yr or so (Grootes et al., 1993; Taylor et al., 1993); this was disappointing for all the teams involved in either logistic, drilling or scientific activities. As this could be linked to the hilly subglacial relief in this area of central Greenland, there was hope that a site with a flatter relief would allow one to overcome this problem. A zone located 200 km north of GRIP appeared a priori favorable; in 1995, the Copenhagen team, under the leadership of first Claus Hammer and later Dorthe Dahl-Jensen, launched the North GRIP international project joined by colleagues from Belgium, France, Germany, Iceland, Japan, Sweden, Switzerland and the USA. The drilling began successfully in 1996, but the drill (an expanded version of the Hans Tausen drill developed by the Copenhagen team and tested in 1995 at Hans Tausen Glacier with French participation) was blocked the following season at a depth of ∼ 1400 m. In 1999, the international team decided to start again from the surface, and a depth of 2931 m was reached in two seasons, but the drilling was subsequently greatly slowed down because of "warm" ice due to high geothermal flux in this area. The drilling ended in 2003 at a depth of 3085 m in a subglacial river, the presence of liquid water in fact reducing the risk of ice flow perturbation as observed at GRIP and GISP2. As a result, North GRIP provides undisturbed climatic time series over the last 123 000 yr, covering a significant part of the last interglacial period (North GRIP community, 2004).

Further extending the Greenland record was the objective of a drilling undertaken farther north, between North GRIP and Camp Century, at the NEEM (North Greenland Eemian ice drilling) site. New teams (Canadian, Chinese and Korean) joined the project which reached the bedrock at a depth of 2537 m in July 2010. As for GRIP and GISP2, the bottom part is perturbed by ice flow below ∼ 2.2 km. However, available data shows that a correct time sequence can be reconstructed back to 128 500 yr ago, thus providing records over a large part of the Eemian (NEEM Community Members, 2013).

2.2 Deep drillings in Antarctica

In the seventies, the high ground in paleoclimate studies was indisputably held by paleoceanographers, who were able to produce climatic time series covering several climatic cycles. These long records allowed Hays et al. (1976) to establish the validity of the Milankovitch theory of ice ages. To make a significant contribution, glaciologists, with no ice core extending beyond the last glacial period, must necessarily go back in time. The drilling team of the Leningrad Mining Institute, which alternated the use of thermal and electromechanical drills (Ueda and Talalay, 2007), was the first to recover ice from the previous glacial period, 150 000 yr ago (Lorius et al., 1985), thanks to very low accumulation.

At this site, where drilling was carried out throughout the year despite winter temperatures below −70 °C, the second core was completed at 950 m depth in 1972, starting from a deviation from the first hole. In case of difficulty, this technique, developed by the Soviet drillers and often used during the Vostok project (Fig. 4), allows one to continue drilling without starting from the surface again. Overall, it took 12 yr between the first ice core (1970) and the recovery of previous interglacial ice on core 3G, the third core, which reached a depth of 2083 m on 11 April 1982 (Ueda and Talalay, 2007). The next day the electric generator used for the camp caught fire and the operations were suspended because the generator for the drillers was indispensable for ensuring the survival of the camp.

This fire did not alter the enthusiasm of the Soviet drillers. In 1984, they undertook the drilling of core 4G from the surface. In parallel, they attempted a deviation at the bottom of 3G which provided an extension down to 2200 m, a

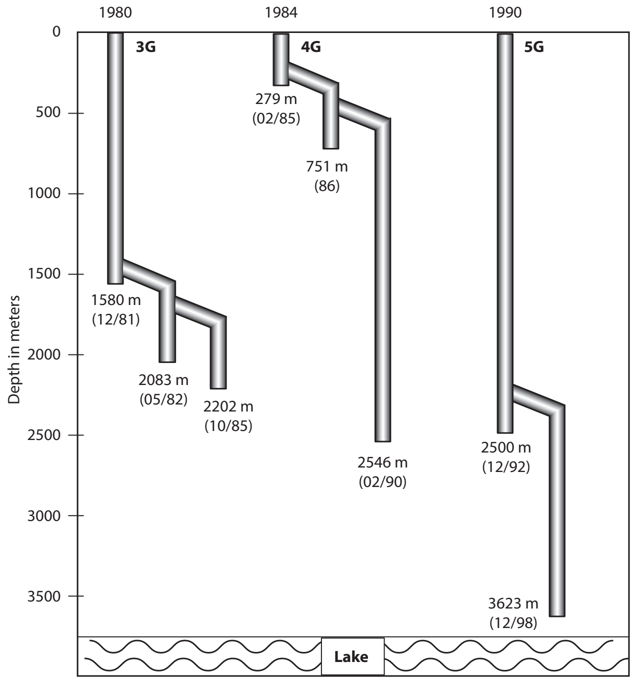

Fig. 4. Deep drilling at the Vostok site.

depth at which the drill was blocked and drilling in this hole definitely abandoned in November 1985. Drilling of 4G continued relatively slowly but without problems until February 1990. Again, the drill was blocked, at a deeper depth (2546 m) but still in the previous glacial period, ∼ 220 000 yr ago (Jouzel et al., 1993). During the eighties, Soviet drillers recovered two other cores (Ueda and Talalay, 2007): a 850 m ice core extending into the last transition at Komsomolskaïa in 1983 (Nikolaiev et al., 1988; Ciais et al., 1992) and, in 1988, a 780 m core covering the last 30 000 yr at Dome B (Jouzel et al., 1995).

The project might well have been abandoned, but thanks to the Russian drillers, to the support of the French and US teams, and to the heavy involvement of two scientists, Volodya Lipenkov and Jean-Robert Petit, the project went on even if it was necessary to start again from the surface at the end of 1990. A depth of 2755 m was reached in January 1994 and the core then covered two full climatic cycles (Waelbroeck et al., 1995; Jouzel et al., 1996). Then a depth of 3350 m was reached in January 1996, with an estimated age of 420 000 yr at 3310 m (Petit et al., 1999), a depth below which mixing of ice makes the climatic interpretation of the records more difficult (Raynaud et al., 2005). Close to thirty years after the operation began, core drilling was stopped in December 1998 at around 120 m above the interface with Lake Vostok. As mentioned, drilling operations have resumed and this interface was reached in February 2012.

The success of GRIP has created a spirit of collaboration between all European partners involved, and it is natural that they built a European Project for Ice Coring in Antarctica just after this success. The GRIP collaboration was extended to teams from the Netherlands, Norway and Sweden, and to the Russian team of V. Lipenkov. The idea was for two complementary sites in East Antarctica, one at Dome C in a low accumulation area with a previous drilling operation, and one to be located in the Atlantic sector, which was then completely unexplored, so as to enable an optimal comparison with the records in Greenland. An EPICA electromechanical drill was developed based on the Danish North GRIP – Hans Tausen design, and the project was launched in 1995 under my responsibility, with Bernhard Stauffer as chair of the science group; these responsibilities were taken over by Heinz Miller and Eric Wolff in 2002. The Dome C drilling, which benefited from the logistical support of France and Italy, began in November 1997, but the drill was stuck at a depth of 780 m after two seasons. The operations very successfully resumed at the end of 2000, and a depth of 2871 m was reached in two seasons; at this depth the retrieved climate record was already older than at Vostok (more than 500 000 yr old). The drilling conditions then became increasingly difficult; the bedrock (3260 m) was reached in January 2005, with the longest exploitable records covering slightly more than 800 000 yr (EPICA Community Members, 2004; Jouzel et al., 2007a). The second EPICA drilling logistically supported by Germany (Kohnen Station in the Dronning Maud Land sector) began in 2001 and, using the North GRIP drill, reached the bedrock (2760 m) during the 2005–2006 field season without noticeable difficulties. It extends, at least, in the previous glacial period (EPICA Community Members, 2006).

Another drilling project was carried out in the nineties by the Japanese team of NIPR (National Institute of Polar Research) then under the responsibility of Okitsugu Watanabe. As at Vostok, the drilling team was operating throughout the year with a drill designed for this drilling. At the chosen site of Dome F, a depth of 2503 m (ice ∼ 330 000 yr old) was reached in two years, 1995 and 1996 (Watanabe et al., 2003). Due to the drill loss, a new drilling had to be started from the surface. The bedrock (3035 m) was reached at the beginning of 2006; this successful operation provides ice records spanning the last 720 000 yr (Kawamura et al., 2012). The interest of China in ice core drilling is more recent: in 2004/2005, a 110 m-long ice core was recovered at Dome Argus, the summit of the East Antarctic plateau, by the Chinese National Antarctic Research Expedition (Xiao et al., 2008).

During this period, US logistical support was primarily devoted to the reconstruction of the permanent base on the South Pole and to the Icecube experiment dedicated to the detection of neutrinos. US scientists concentrated on sites easily accessible from McMurdo with two drillings completed respectively in 1994 and 1999, a 554 m drilled at Taylor Dome using the PICO drill (Grootes et al., 1994; Steig et al., 1998) and a 1004 m core retrieved at Siple Dome using the GISP-2 drill (Gow and Engelhardt, 2000; Taylor et al., 2004). Both cores gave access to ice from the last glacial period. A more ambitious drilling project, WAIS for West Antarctic Ice Sheet, has recently been carried out (between 2008 and 2011) using a new DISC (Deep Ice Sheet Coring) drill, 160 km from the location of the Byrd ice core. The bedrock has been reached at a depth of 3405 m; due to the high accumulation, the core does not extend beyond the last 62 000 yr, but has the advantage of providing very high resolution records (WAIS, 2013).

Other teams have chosen one of the small and more easily accessible domes in the coastal regions. We have already cited the Australian drilling intiated in the late sixties at Law Dome (Hamley et al., 1986; Morgan et al., 1997). More recently, successful drilling operations have been conducted at Berkner Island (Mulvaney et al., 2007) and Talos Dome (Stenni et al., 2011) as collaborative projects under the respective leadership of UK and Italy. Talos Dome covers a full glacial–interglacial cycle, while the Law Dome and Berkner Island cores extend into the last glacial period. This is also the case for a 364 m core drilled by a UK–French team on James Ross Island (Mulvaney et al., 2012), where two shorter cores were drilled in the eighties in collaboration between Argentinian and French teams (Aristarain et al., 1986, 1990). Ice from glacial periods is also accessible from near-coastal sites (Yao et al., 1990) or from "horizontal" ice cores allowing one to retrieve old ice in the ice margins (Reeh et al., 2002; Dunbar et al., 2008).

2.3 Drilling in the Andes and the Himalaya

Lonnie Thompson (Ohio State University) was the first scientist to launch extensive ice core drilling and to believe in the scientific value of cores extracted from tropical glaciers, some of them being at risk of disappearing under the effect of global warming. With his team, he was able to circumvent the difficulties of drilling above 6000 m by developing light drills that run on solar energy, and means to bring the ice back down as quickly as possible to avoid melting. Several tropical ice cores have been obtained that reached back the Last Glacial period, either in the Himalayas, Dunde (Thompson et al., 1989) and Guliya (Thompson et al., 1997), or in the Andes, Huascaran (Thompson et al., 1995) and Sajama (Thompson et al., 1998). Other teams have followed on this pioneering work both in the Andes (Ramirez et al., 2003) and the Himalayas, now referred to as the Third Pole (Yao et al., 2012). Although some of these cores extend back to the Last Glacial period, their main interest is that they are excellent archives of past El Niños (Andean glaciers) and of past monsoons (Himalayan glaciers). A presentation of associated scientific results is beyond the scope of this article, as well as a comprehensive review of ice cores drilled in glaciers from non-polar regions (Alps, Kilimanjaro, Mongolia, Russia, Canada etc.) and in the Arctic.

3 Deep ice cores: what do we learn about past climate changes?

In the line of the seminal paper "Stable isotopes in precipitation" published by Dansgaard (1964), climate reconstruction from ice cores has long been based on interpreting δ^{18}O (oxygen 18) or δD (deuterium) profiles measured along ice cores. This approach is still extensively used, but alternative methods such as paleothermometry and the use of the isotopic composition of permanent gases (δ^{15}N and δ^{40}Ar) have been developed since the nineties. Before examining the information obtained by these complementary approaches, we briefly mention the various methods used to date ice cores as summarized in Jouzel and Masson-Delmotte (2010a). Based on a recent review (Jouzel et al., 2013), we then briefly discuss how isotopic models are useful for interpreting isotopic profiles measured along ice cores, and mention the interest in combining measurements of δD, δ^{18}O and, as recently developed, of δ^{17}O.

3.1 Establishing ice core chronologies

Complementary methods are used to establish ice core chronologies. They fall into four categories: (1) layer counting, (2) glaciological modelling, (3) use of time markers and correlation with other dated time series, and (4) comparison with insolation changes (i.e. orbital tuning). Layer counting based on a multi-parametric approach is extensively used for Greenland cores (Hammer et al., 1986; Johnsen et al., 1992; Meese et al., 1997; Alley et al., 1997; Rasmussen et al., 2006; Svensson et al., 2008) and for high-accumulation Antarctic sites. It is not feasible in low-accumulation areas such as central Antarctica, where other approaches must be employed. For example, the Vostok core has been initially dated combining an ice flow and an accumulation model assuming a link between accumulation and temperature (Petit et al., 1999). Orbital information contained in various time series such as methane (Ruddiman and Raymo, 2003), δ^{18}O of atmospheric oxygen (Jouzel et al., 1996, 2002; Petit et al., 1999; Shackleton, 2000; Dreyfus et al., 2007; Bazin et al., 2013), N_2–O_2 ratio in air bubbles (Bender, 2002; Kawamura et al., 2007; Suwa and Bender, 2008; Landais et al., 2012) and total air content (Raynaud et al., 2007; Lipenkov et al., 2011) are also used. Additional dating information, either relative or absolute, is also obtained from comparison with other paleorecords (Raisbeck et al., 2006, 2007; Waelbroeck et al., 2008). The idea of an optimal use of the different sources of chronological information and of the various glaciological constraints has been exploited through an inverse modelling approach (Parrenin et al., 2001, 2004 and references therein). Inverse modelling is now of current use to provide a consistent dating of Greenland Antarctic ice cores (Lemieux-Dudon et al., 2010; Bazin et al., 2013).

At a given depth, the age of the gas is younger than the age of the ice, due to the fact that air bubbles are trapped

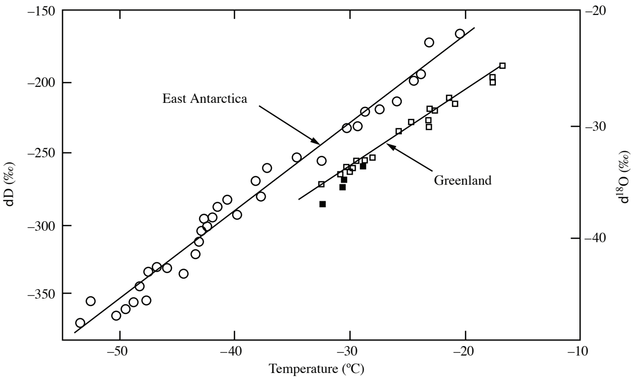

Fig. 5. Isotope content of snow versus local temperature (annual average). Antarctic data (δD, left scale) are from Lorius and Merlivat (1977) and Greenland data (δ^{18}O, right scale) are from Johnsen et al. (1989).

when firn closes off at depth. The ice age – gas age difference can be estimated as a function of temperature and accumulation through firnification models (Barnola et al., 1991; Arnaud et al., 2000). The application of such models is however subject to discussion (Landais et al., 2006), and clearly contradicted by independent estimates based on alternative methods (Parrenin et al., 2013).

3.2 Water isotopes as indicators of past temperatures

The isotopic change measured between the LGM and the more recent period is relatively similar for ice cores from the central regions of Antarctica and Greenland, with a range of δ^{18}O variations around 5 ‰. This range, also observed for some near-coastal sites, is larger for sites affected by significant altitude changes for LGM ice as, for example, observed at Camp Century (Dansgaard et al., 1969; Raynaud and Lorius, 1973; Vinther et al., 2009).

The interpretation of these isotopic data is largely based on their present-day distribution characterized by a linear relationship between their annual values and the mean annual precipitation site temperature, particularly well obeyed over Greenland and Antarctica (Fig. 5). While Dansgaard and his team opted for a qualitative interpretation of δ^{18}O profiles, Lorius and colleagues proposed quantitative estimates of associated temperature changes based on the use of this observed present-day spatial slope. This approach was first used for the old Dome C core (Lorius et al., 1979). Corrections for changes in the isotopic composition of oceanic waters, in the altitude of the ice sheet and, if necessary, for the upstream origin of the ice (EPICA Community Members, 2006), are applied. With this interpretation, the four long East Antarctic isotopic records (Vostok, Dome F, EPICA Dome C and EDML) show a consistent range of ∼ 8 to 10 °C between the LGM and present-day surface temperatures (Fig. 6).

Over a longer timescale, the minimum isotopic values reached during the coldest parts of the glacial periods are

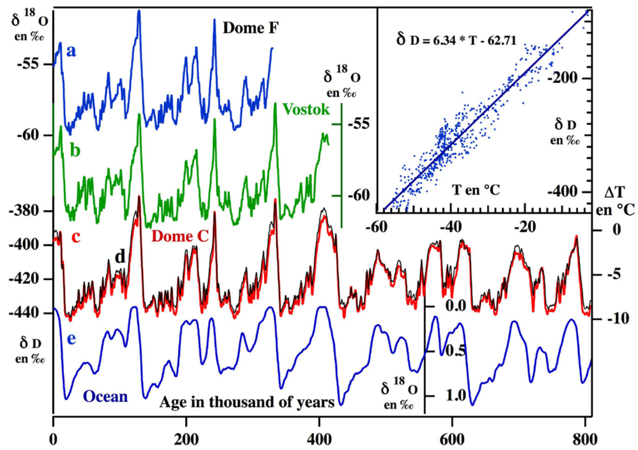

Fig. 6. Stable isotope records from deep Antarctic ice cores: Dome F (Watanabe et al., 2003), Vostok (Petit et al., 1999) and Dome C (Jouzel et al., 2007a), in addition to the Dome C temperature (red curve, temperature scale on the right) estimated using the conventional approach (based on the use of the spatial slope, see insert adapted from Masson-Delmotte et al., 2008) as a surrogate of the temporal slope. The oceanic record adapted from Lisiecki and Raymo (2005) is used as a proxy of sea-level change.

remarkably similar. Instead, high values can be more variable from one interglacial to the next; for example, during the Last Interglacial, δ^{18}O was higher than during the recent Holocene (Masson-Delmotte et al., 2011), which is also true for the three previous interglacials (Petit et al., 1999; Watanabe et al., 2003; EPICA community Members, 2004; Jouzel et al., 2007a). The EPICA Dome C record illustrates a change in pacing at the time of the Mid-Brunhes event about 430 kyr BP, with lower glacial–interglacial isotopic changes before this event (which is followed by an exceptional ∼ 28 ka-long interglacial; EPICA Community Members, 2004).

The most important characteristic of the Greenland records deals with the existence of rapid climatic changes during the last glacial period and the last transition (Fig. 7). These "Dansgaard–Oeschger" events (named by Wally Broecker) were discovered in the Camp Century and Dye 3 Greenland cores (Dansgaard et al., 1982, 1984). Rapid isotopic changes, often more than half of those corresponding to the glacial–interglacial difference and taking place in a few decades or even less (Steffensen et al., 2008), are followed by a slower cooling and a generally rapid return to glacial conditions. These isotopic events are accompanied by rapid changes in snow accumulation (Alley et al., 1993) and in dust fallout (Taylor et al., 1993). The existence and characteristics of these events were fully confirmed at GRIP (Dansgaard et al., 1993) and GISP2 (Grootes et al., 1993), and more recently at North GRIP (North GRIP Community Members, 2004) and NEEM (Neem Community, 2013). For Camp Century (Dansgaard et al., 1969) and Dye 3 (Dansgaard et al.,

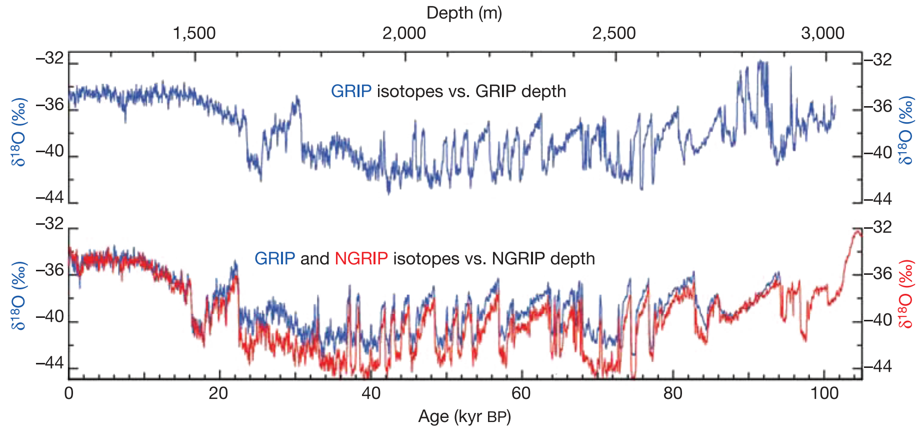

Fig. 7. The GRIP (**a**, blue) and NGRIP (**b**, red) oxygen isotopic profiles with respect to depth. For comparison, the GRIP record (blue) has been plotted on the NGRIP depth scale using the rapid transitions as tie points (adapted from North GReenland Ice core Project members, 2004).

1982), the δ^{18}O profile was used as a proxy of temperature change, but only on a qualitative basis (Johnsen et al., 1972). Instead, the conventional approach was applied for GRIP (Johnsen et al., 1992) and GISP 2 (Grootes et al., 1993), leading to estimates of the LGM cooling of ~ 10 to 13 °C.

3.3 Alternative estimates of temperature changes in Greenland and Antarctica

It appeared that this conventional approach significantly underestimates Greenland past temperature changes. This was somewhat a surprise in our community, when the interpretation of the borehole temperature profile clearly showed that the temperature increase from glacial maximum to Holocene was higher than 20 °C, and up to 25 °C at Summit (Cuffey et al., 1995; Johnsen et al., 1995; Dahl-Jensen et al., 1998), about two times higher than the conventional approach factor. Indeed, such factors as the evaporative origin and the seasonality of precipitation can also affect δD and δ^{18}O. If these factors change markedly under different climates, the spatial slope can no longer be taken as a reliable surrogate of the temporal slope for interpreting the isotopic signal. This is the case for Greenland, where the seasonality of the precipitation is substantially increased during the LGM (Werner et al., 2000), unlike for Antarctica (Krinner et al., 1997).

A new method was then developed by Severinghaus and colleagues based on the fact that air composition is very slightly modified by physical processes, among them the gravitational and thermal fractionation. In the case of a rapid temperature change, these processes cause a detectable anomaly in the isotopic composition of nitrogen and argon, which allows us to infer its size. This method was applied to the rapid changes associated with the end of the Younger-Dryas (Severinghaus et al., 1996, 1998) and with the abrupt warming that led to the Bølling (Severinghaus and Brook, 1999), providing higher warming estimates (~ up to a factor of 2) than derived from ice δ^{18}O. The abrupt warming that marked the start of the numerous DO events during the Last Glacial period are also larger than initially thought (Lang et al., 1999; Schwander et al., 1997; Landais et al., 2004a,b; Huber et al., 2006; Landais, 2011; Capron et al., 2010). To sum up, all the results derived either from borehole paleothermometry or from isotopic anomalies significantly underestimate temperature changes in central Greenland, thus seriously challenging the conventional isotopic approach. Fractionation processes occurring during firnification are now studied for other noble gases: neon, kryton and xenon (Severinghaus and Battle, 2006); due to the dependence of gas solubility on temperature, the krypton–nitrogen ratio has been used to reconstruct past mean ocean temperature (Headly and Severinghaus, 2007).

In Antarctica, both paleothermometry and the use of nitrogen and argon isotopes pose some problems due to the low accumulation and to the fact that Antarctica did not experience abrupt temperature changes. Thus, there is no perfect alternative to calibrating the isotopic paleothermometer there. Still, there are useful arguments coming from the isotopic composition of the air bubbles (Caillon et al., 2001), from constraints with respect to ice core chronologies (Parrenin et al., 2001, 2007; Blunier et al., 2004) and from paleothermometry (Salamatin et al., 1998). As reviewed by Jouzel et al. (2003), they converge towards the idea that the observed present-day spatial slope can be used to interpret Antarctic isotopic profiles with however a slight underestimation, of the order of ~ 10 %, of temperature changes.

A noticeable feature of the distribution of water isotopes, which at the surface are affected by wind scouring (Fisher et al., 1983), is the smoothing due to the diffusion in firn and ice (Johnsen, 1977) which affects the seasonal cycle and can also erase sub-millennial variations in old ice (Pol et al., 2010). The difference in firn diffusion of water isotopes (Johnsen et al., 2000) offers the possibility to estimate past

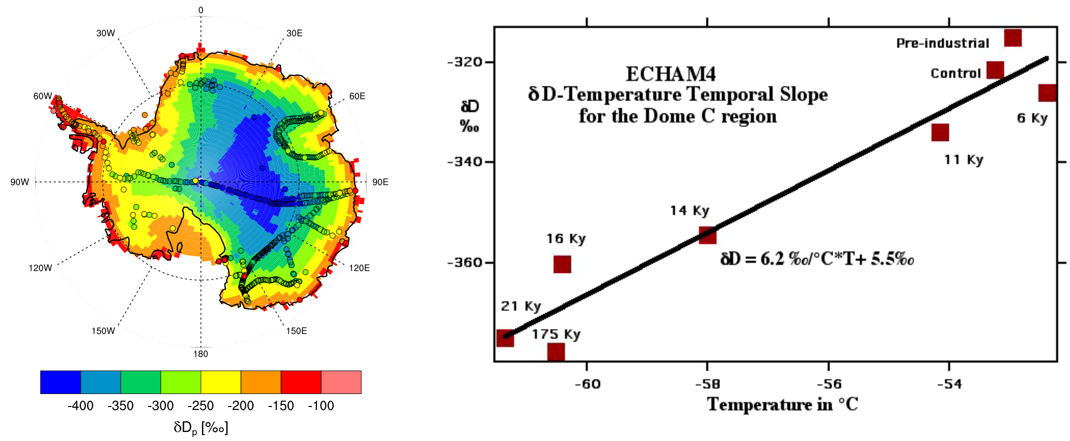

Fig. 8. Left panel: observed (coloured circles from a compilation by Masson-Delmotte et al., 2008) and simulated (ECHAM5-wiso with fine spatial T159L31) annual mean HDO values in precipitation (δDp) for Antarctica (after Werner et al., 2011). Right panel: the temporal slope as derived from ECHAM 5 IGCM for the Dome C region (Jouzel et al., 2007b).

temperature changes from very detailed δD and δ^{18}O profiles in ice cores (Simonsen et al., 2011). Co-isotopic measurements (δD and δ^{18}O) have also been applied to study basal ice as a result of the fractionation processes taking place during melting/refreezing processes (Jouzel and Souchez, 1982; Souchez and Jouzel, 1984; Jouzel et al., 1999).

At last, climate information can be retrieved from the melt-feature percentage. This simple method has been used in climate reconstructions for many of the ice core sites across the Canadian Arctic. When summer temperatures are high enough, surface melt occurs that refreezes at depths of a few tens of centimetres and is easy to recognize, because refrozen melt has few bubbles compared to ice that forms by compression of unmelted firn (Koerner, 1977; Koerner and Fisher, 1990). Using this method, Fisher et al. (2011) have shown that recent melt rates of Canadian Arctic ice caps are the highest in four millennia and resemble those of the early Holocene optimum.

3.4 The contribution of isotopic models

The δD and δ^{18}O of snow have long been the unique tool for reconstructing past temperatures in polar regions; these parameters are still the basis for climate reconstruction from ice cores, as they provide continuous, and potentially high resolution, records. In turn, the ice core community has a long tradition in the modelling of these isotopes, which have been incorporated into a hierarchy of models. While the dynamically simple Rayleigh model applied by Dansgaard (1964) has been extended to account for kinetic fractionation processes taking place from the oceanic surface to polar regions (Merlivat and Jouzel, 1979; Jouzel and Merlivat, 1984; Ciais and Jouzel, 1994), water isotopes have been implemented in atmospheric general circulation models (IGCMs), which allow one to account for the dynamical complexity of the Earth atmosphere.

After the pioneering work of Joussaume et al. (1984) using the LMD GCM, δD and δ^{18}O were implemented in the GISS (Jouzel et al., 1987a) and ECHAM (Hoffmann and Heimann, 1993) models. Since these early IGCMs there has been an increasing interest in this approach, with currently a dozen modelling groups involved (Jouzel, 2013). Their increased spatial resolution clearly improves the data-model intercomparison on a regional scale (Fig. 8). Such models allow a direct comparison between spatial and temporal slopes by simulating different climatic periods. Using the ECHAM model, Werner et al. (2000) convincingly explained the observed discrepancy between borehole and isotope temperatures in Greenland. Instead, this same model (Hoffmann et al., 1998; Jouzel et al., 2007b) indicates that in central Antarctica the temporal slope is close to its modern spatial analogue (Fig. 8), justifying the use of present-day observations to interpret paleodata. As fully discussed in Jouzel (2013), more recent simulations (Lee et al., 2008; Sime et al., 2008, 2009; Risi et al., 2010) do not fully support this conclusion. In particular, Sime et al. (2008, 2009) have pointed out that using present-day observations underestimates (again with a factor of up to ~ 2) temperature changes for warmer than present-day climates in Antarctica, while Sime et al. (2013) have shown the influence of sea-ice limits on isotopic changes in Greenland.

3.5 Combining information from δD, δ^{18}O and δ^{17}O

On a global scale, precipitation δD and δ^{18}O are linearly related to each other throughout the world, with a slope of about 8 (Craig, 1961) and a deuterium excess, hereafter the d excess, defined as $d = \delta\mathrm{D} - 8 \cdot \delta^{18}\mathrm{O}$, of about 10 ‰ (Dansgaard, 1964). Early ice core isotopic studies were based on the analysis of either δ^{18}O (Dansgaard et al., 1969, 1982; Epstein et al., 1970; Johnsen et al., 1972) or δD (Lorius et al., 1979), which independently provide access to past temperature changes. Due to their close linear relationship, it was thought that measuring both isotopes would not bring additional climatic information, until the work of Merlivat and Jouzel (1979) showed that the *d* excess of a precipitation is influenced by the conditions prevailing in the oceanic moisture source region (temperature, relative humidity and, to a lesser degree, wind speed). This link has further been confirmed for polar snow (Johnsen et al., 1989; Petit et al., 1991; Ciais and Jouzel, 1994); its use for extracting information about moisture sources was developed in the eighties (Jouzel et al., 1982; White et al., 1988; Dansgaard et al., 1989; Johnsen et al., 1989). Since then, δD and δ^{18}O are quite systematically measured in order to provide such additional information from ice cores drilled in both Antarctica (Jouzel et al., 1982; Vimeux et al., 1999, 2002; Cuffey and Vimeux, 2001; Stenni et al., 2001, 2003, 2010; Uemura et al., 2004, 2012) and Greenland (Masson-Delmotte et al., 2005; Jouzel et al., 2007b), where deuterium excess is also used as a marker of rapid climatic changes (Steffensen et al., 2008).

In contrast, it is only recently that measurements of the triple isotopic composition of water has found applications in paleoclimatology (Landais et al., 2008; Winkler et al., 2012). Combining deuterium, oxygen 18 and oxygen 17 measurements in ice cores is promising for getting access to variations in both average temperature and relative humidity in the oceanic source region, which is not possible from *d* excess alone. However, this approach appears more reliable for relatively coastal than for inland sites (Winkler et al., 2012).

4 Greenhouse gases and other properties recorded in the entrapped air

There was already an interest in entrapped air bubbles in ice cores in the sixties (Langway, 2008). Measuring their chemical composition and applying ^{14}C dating to its CO_2 component – which appeared less promising than initially thought – were the main motivations of Hans Oeschger and his team for studying ice cores. In France, Dominique Raynaud developed the measurement of the total gas content, a parameter interpreted as an indicator of the change in the altitude of the ice sheet (Lorius et al., 1968; Raynaud and Lorius, 1973). However, due to the lack of a proper extraction method, it then took 10 yr or so to reliably measure the CO_2 concentration of ancient air, one common goal of the Swiss and French teams. This difficulty was overcome by Robert Delmas, Dominique Raynaud and colleagues in Grenoble, and Bernhard Stauffer and his team in Bern. The Swiss team at Byrd and the French team at Dome C then contributed to a major discovery and confirmed the prediction of S. Arrhenius at the end of the 19th century: at the LGM, CO_2 concentration was indeed 30 % less than that of the preindustrial period before human activity began to change it.

Thanks to the Vostok ice core, French researchers had access a few years later to ice covering a full glacial–interglacial cycle: throughout the last 150 000 yr, CO_2 concentration in entrapped air appears closely correlated with the temperature derived from the isotopic composition of the ice (Barnola et al., 1987; Jouzel et al., 1987b; Genthon et al., 1987; Raynaud et al., 1993). Colder periods are associated with lower CO_2 and vice-versa, a property which holds true all along the 4 climatic cycles covered by the Vostok ice core (Petit et al., 1999). High-resolution measurements have also shown that CO_2 changes are associated with millennial scale climate variations (Stauffer et al., 1998; Ahn and Brook, 2008). The Swiss and French teams have both contributed to the extension of the CO_2 record over the last 800 000 yr (Siegenthaler et al., 2005; Lüthi et al., 2008). The change in pacing characterized by less warm interglacials for the earlier period (Jouzel et al., 2007a) is accompanied by a parallel change in CO_2 which makes the relationship between this greenhouse and climate truly impressive (Fig. 9).

The same type of correlation – lower concentration during glacial periods than during interglacials – is observed for CH_4 and N_2O (Fig. 9), two greenhouse gases which also show significant increases due to human activity. Analysis of CH_4 has been developed by the Bern team (Stauffer et al., 1985) and by the Grenoble team (Raynaud et al., 1988). Between the LGM and the preindustrial period, a doubling or so of CH_4 has been documented (Stauffer et al., 1988). N_2O also increases between these two periods (Zardini et al., 1989; Leuenberger and Siegenthaler, 1992; Sowers, 2001) and shows variations during abrupt climate changes (Flückiger et al., 1999). Obtained by Chappellaz et al. (1990), the CH_4 record covering the last glacial–interglacial cycle reveals a close correlation with temperature changes and also appears influenced by monsoonal activity. It has been extended to the entire Vostok core (Petit et al., 1999) and more recently to the last 800 000 yr, showing, as for CO_2, lower interglacial values for the earlier period (Delmotte et al., 2004; Spahni et al., 2005; Loulergue et al., 2008). Greenland ice cores revealed another very interesting feature of the CH_4 record, namely its close link with the rapid temperature warming associated with DO events (Chappellaz et al., 1993; Brook et al., 1996) and with rapid changes occuring during the last deglaciation (Severinghaus and Brook, 1999); we note here that reliable CO_2 measurements are not accessible on Greenland ice due to their high level of impurities. The N_2O Antarctic record shows also glacial–interglacial changes, but is disturbed by artefacts linked with elevated dust concentration (Sowers et al., 2003; Spahni et al., 2005; Schilt et al., 2009). Ice core data on more recent periods prove extremely useful to document the increases in CO_2, CH_4 and N_2O over the last two centuries (MacFarling Meure et al., 2006).

For CO_2, natural variations imply the circulation of the oceans and their productivity and, to a certain degree, interactions with the continental biosphere. On the contrary, variations in CH_4 essentially come from the impact of the

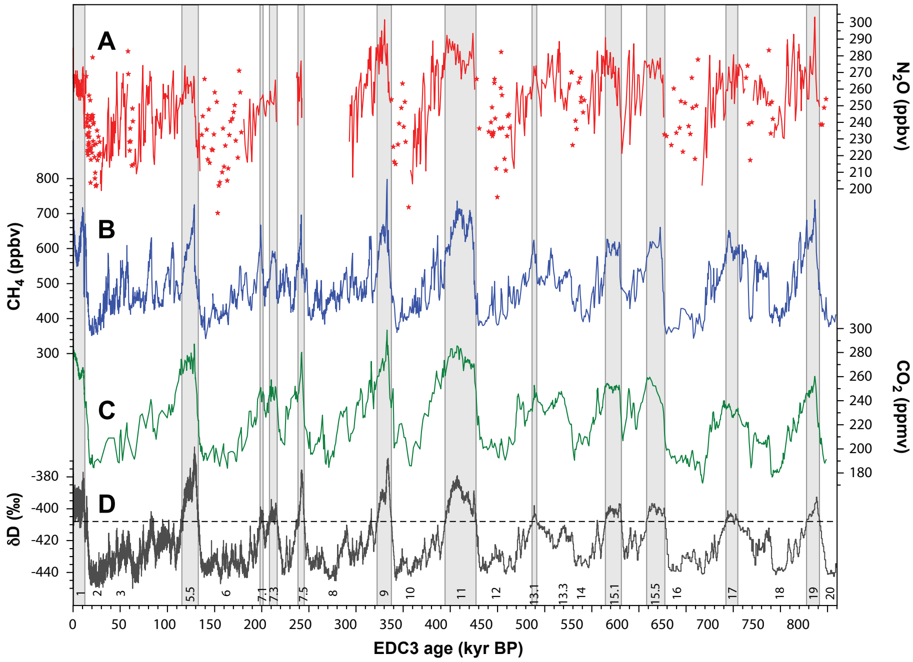

Fig. 9. Variations, over the last 800 000 yr, of deuterium (δD; black), a proxy for local temperature, and the atmospheric concentrations of the greenhouse gases CO_2 (green), CH_4 (blue), and nitrous oxide (N_2O; red) derived from air trapped within ice cores from Antarctica (Schilt et al., 2009).

climate on its earthly sources, including swamp zones and perhaps the frozen ground of high northern latitudes. Isotopic measurements, which need to be extremely precise, have allowed us to shed light on the mechanisms involved. This includes ^{13}C in CO_2 (Leuenberger et al., 1992; Indermühle et al., 1999; Elsig et al., 2009; Lourantou et al., 2010; Schmitt et al., 2012), and ^{13}C (Ferretti et al., 2005; Schaefer et al., 2006; Fischer et al., 2008) and δD (Bock et al., 2010) in methane. These results have been completed by biogeochemical modelling aiming to account for both the changes in concentrations and isotopic composition (Köhler et al., 2010; Bouttes et al., 2011). In relation with the CO_2 cycle, the oxygen 17 composition of entrapped air bubbles has been measured over the last 60 000 yr, allowing us to estimate the biologic oxygen productivity (Blunier et al., 2002). The isotopic composition of N_2O (^{15}N and ^{18}O) also proves interesting for a better understanding of processes at the origin of atmospheric variations and of the artifacts recorded in ice cores (Sowers, 2001). Many other gaseous species such as CO (Haan et al., 1996; Haan and Raynaud, 1998; Haan et al., 1996; Haan and Raynaud, 1998), COS (Sturges et al., 2001a), various chlorine, bromine and iodide, and other species of interest for atmospheric chemistry (Sturges et al., 2001b; Reeves et al., 2005) have also been measured in firn and ice.

The Vostok data published in the eighties and nineties led to the idea that the variations in greenhouse gases have played an important climatic role in the past as amplifiers vis-à-vis changes in insolation (Genthon et al., 1987; Lorius et al., 1990; Jouzel et al., 1993; Petit et al., 1999). Further confirmed by the extension of the CO_2 and CH_4 records to the last 800 000 yr, this interpretation – which was already taken as a clear illustration of the climatic role of CO_2 at the time of the launching of the Intergovernmental Panel on Climate Change (1988) – is fully supported by climate models. At the glacial–interglacial timescale, the natural variations in concentrations of CO_2 and CH_4 are equivalent to those linked to human activity during the last two hundred years. The correlation between the greenhouse effect associated with these two gases led Lorius et al. (1990) to propose an estimate of the climate sensitivity (e.g. for CO_2 doubling) based on paleodata. They inferred a range of ∼3 to 4 °C, in broad agreement with currently cited values (2 to 4.5 °C as in IPCC, 2007).

The approach followed by Lorius et al. (1990) did not require that the complexity of the mechanisms of glacial–interglacial climatic changes be completely deciphered or that a definitive response to the “chicken or egg” question be given: which is the cause, which is the effect? Indeed, there is a difficulty in determining precisely the timing between greenhouse and climate changes because of the uncertainty associated with the difference between the age of the gas, estimated from a firnification model (Barnola et al., 1991), and the age of the ice; at low accumulation sites such as Vostok, this uncertainty can be higher than 1000 yr (Petit et al., 1999). Based on this approach, two studies pointed to a lead of Antarctic warming with respect to the CO_2 increase during the last 3 terminations (Fischer et al., 1999; Monnin et al., 2001). Caillon et al. (2003) confirmed this result for termination III from a completely different method based on the surprising similarity between the δD (or δ^{18}O) of ice and the isotopic composition of argon – then taken as a proxy of climate change in the gas phase. However, the existence of such a lead is now challenged by a third method: using the air δ^{15}N to determine the depth at which air in the ice is permanently trapped, Parrenin et al. (2013) concluded that Antarctic temperature did not began to rise before CO_2 during termination I.

Other properties are recorded in the entrapped air bubbles. In collaboration with French colleagues, Michael Bender pioneered the measurement oxygen 18 of O_2, focusing on the last deglaciation (Bender et al., 1985). This parameter is influenced by the productivity of the continental and oceanic biosphere and by the δ^{18}O of continental and oceanic waters, and thus sea-level change (Bender et al., 1994a; Sowers et al., 1991; Malaizé et al., 1999; Jouzel et al., 1996; Severinghaus et al., 2009; Landais et al., 2010). The extension of this record (Jouzel et al., 1996; Petit et al., 1999; Kawamura et al., 2007; Dreyfus et al., 2007; Landais et al., 2010) pointed to the influence of insolation changes with the presence of a strong precessional cycle which has been used to place chronological constraints on the chronologies of the Vostok, Dome F and EPICA Dome C cores. Bender was also at the origin of the discovery of a link between small measured variations of the N_2/O_2 ratio and insolation changes (Bender, 2002). Although not fully understood, these variations which are linked to the firnification process are now extensively used for dating purposes (Kawamura et al., 2007, 2012; Suwa and Bender, 2008; Landais et al., 2012). The same applies for the record of total gas content; beyond being influenced by the air pressure and thus the altitude of the ice sheet (Raynaud and Lorius, 1973), the obliquity cycle is clearly imprinted in the glacial–interglacial record (Raynaud et al., 2007; Lipenkov et al., 2011). Vinther et al. (2009) pointed out that this gas content information confirms the Holocene thinning of the Greenland ice sheet derived by combining isotopic data from deep ice cores (Camp Century, Dye 3, GRIP and North GRIP) and from ice cores from small marginal ice caps (Renland and Agassiz); this approach gives a convincing example of how one can separate the Greenland temperature and surface elevation histories.

Understanding the link between isotopic records from both polar regions became a topic of interest in the nineties (Jouzel et al., 1994; Bender et al., 1994b). Establishing this link has considerably benefitted from measurements of properties such as δ^{18}O of O_2 and methane concentration, which should show similar variations in air entrapped either in Greenland or in Antarctic ice, except for the existence of a small interpolar CH_4 gradient (Dällenbach et al., 2000). This approach was first applied using slow changes of δ^{18}O of O_2 (Bender et al., 1994b, 1999) and then developed using well-defined methane variations (Blunier et al., 1998; Blunier and Brook, 2001; Morgan et al., 2002). This allowed one to correlate Greenland and Antarctic records, showing that abrupt Greenland events have smooth counterparts in Antarctica with, in general, the onset of isotopic changes preceding the onset in Greenland by 1500 to 3000 yr, whereas their maxima are apparently coincident. This one-to-one coupling (EPICA Community Members, 2006), which supports the bipolar seesaw hypothesis (Broecker, 1998; Stocker and Johnsen, 2003), has been fully confirmed from the comparison of the δ^{18}O records obtained along the North GRIP and EDML cores (Fig. 10). Note that recent studies have also demonstrated the possibility of directly and closely correlating ice records from Greenland and Antarctica, at least for some specific time periods. This is done using either the well-defined beryllium 10 peak around 41 000 yr ago (Raisbeck et al., 2007) or easily identifiable volcanic events (Svensson et al., 2013), and allows one to test the reliability of gas age–ice age estimates.

Beyond their use for correlating Greenland and Antarctic ice cores, measurements of δ^{18}O of O_2 and of CH_4 have been applied to identify stratigraphic disturbances in the deepest parts of Greenland ice cores. Due to the proximity of the bedrock, such disturbances can be identified by a mismatch between the gas records derived for a given period from this Greenland ice and from the Antarctic undisturbed record (Bender et al., 1994b; Fuchs and Leuenberger, 1996; Chappellaz et al., 1997), and/or by the lack of a depth difference between a climatic event, such as a rapid change, recorded both in the ice and in the entrapped air (Landais et al., 2004c). Combined with isotopic measurements in ice, these gas data can also be used to recontruct, at least partly, the correct ice sequence (Landais et al., 2003; Suwa et al., 2006). The same strategy has been used to extend the Greenland Eemian sequence from the NEEM folded ice core, partly covered in the North GRIP core (North GRIP community, 2004), back to 128.5 kyr BP (NEEM community).

5 Future challenges

Thanks to pioneers who initiated ice core drilling in Greenland, Antarctica and in non-polar glaciers, to their scientific and technical teams, to the continuous development of drills and to their successful deployment, to the logistical and financial support of numerous organisations, to international collaborations and to their capacity to continuously attract young scientists, the ice core community can be proud of what has been achieved and produced since the first deep drilling which allowed it to recover ice from the last glacial period (1966 at Camp Century). This applies to the topics on which I have focused (mainly climate and atmospheric composition) and holds equally true for the aspects I have not covered (atmospheric chemistry, biogeochemical cycles, cosmogenic isotopes, physics of ice, modelling of ice sheets). Beyond shedding light on past changes, ice cores provide

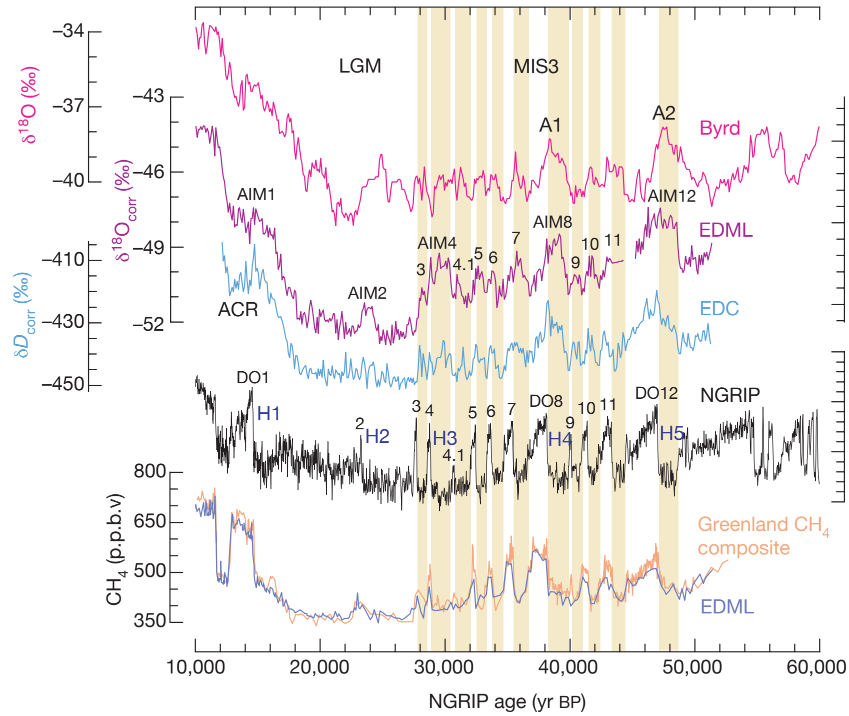

Fig. 10. Methane synchronization of the EDML and the NGRIP records reveals a one-to-one assignment of each Antarctic warming with a corresponding stadial in Greenland (adapted from EPICA Community Members, 2006)

a lot of information relevant to future climate change, with the discovery, in Antarctica, of a strong link between greenhouse gases and climate over the last 800 000 yr and of rapid and abrupt climate changes in Greenland. They allow us to document past climate variability at various time scales, contribute to establishing the links between climate changes in the Northern and Southern hemispheres. They are unique in that they provide access to past climate forcings. This includes greenhouse gases but also solar (from cosmegenic isotopes), volcanic and other aerosols forcings (from the chemical composition of the ice) allowing them to test the sensitivity of climate models and their ability to identify the contribution of human activities to recent climate change.

Future challenges in ice core research are well taken into account by the four projects defined by IPICS (Brook et al., 2006): (1) to get a 1.5 million year record of climate and greenhouse gases from Antarctica, (2) to cover the Last Interglacial and beyond in Greenland, (3) to build a network of bipolar ice core records spanning the past 40 000 yr and (4) to get ultra-high-resolution records of climate variability and climate forcings spanning the past 2000 yr. Projects dealing with the latter objectives (2000 and 40 000 yr) have developed since the launching of the IPICS initiative, but after the drilling of NEEM, it appears more challenging than initially thought to get an undisturbed ice core reaching back the previous glacial period in Greenland.

The case for extending the ice core record to 1.5 Ma, very well established by the IPICS initiative (IPICS, 2008), is indeed reinforced by results recently published by the deep-sea core community. For the oldest half of this period, we are mainly reliant on marine sediment records which allow us to depict the transition from a 40 ka world to a world dominated by a 100 ka cyclicity, and point to a shift corresponding to the start of the Mid-Pleistocene Transition (MPT) 1.25 Ma ago. Despite rapid progresses in the reconstruction of past atmospheric CO_2 concentration from various proxies in terrestrial and marine archives, there is still a need for a direct and detailed determination from air bubbles trapped in ice cores (Jouzel and Masson-Delmotte, 2010b). In this scientifically very exciting context, the major challenge of the ice core community concerns the selection of the best possible drilling site to obtain undisturbed records covering the last 1.5 Ma in Antarctica and the last 150 ka in Greenland. High-resolution cartographies, radar mapping as well as high resolution modelling will be needed. In a recent article, Fischer et al. (2013) strongly argue for significantly reduced ice thickness (maximum of ∼2500 m) to avoid basal melting which leads to loss of ice and diminishes the age of the ice at the bottom. Because of the huge logistical costs to set up a new base in remote places in central Antarctica, new rapid reconnaissance technologies can be envisaged to qualify the chosen drilling site at low cost (Severinghaus et al., 2010). For example, an innovative instrument combining a drill and a probe is currently being developed (Chappellaz et al., 2012); it would allow one, within one field season, to drill down through 3 km of ice and at the same time to measure key parameters such as water isotopic composition and greenhouse gas composition. Similar projects which were developed and tested (unfortunately without success) in the seventies and eighties both in Greenland and Antarctica, are being or have been explored by other groups in Switzerland and in the USA. Such technology would also provide preliminary climate information prior to the heavy deep drilling operations. Given its high expected outcome, the opportunity for new technological breakthroughs and the ongoing international collaborative effort of the ice core community under IPICS, one should be optimistic about the recovery in the coming years of one, or better several, very old Antarctic ice cores spanning the MPT transition.

Acknowledgements. I would like to thank the ice core community as a whole – drillers, logisticians, scientists and technicians and others – and all the organisations which have supported ice core research, for their invaluable contribution to our knowledge and understanding of climate and environmental changes. It is an honour, and a great pleasure, to be part of this community. I would like also to acknowledge J. P. Steffensen and an anonymous reviewer for their very thorough reviews, and David Fisher for his comments.

Edited by: E. Wolff

References

Ahn, J. and Brook, E. J.: Atmospheric CO_2 and climate on millennial time scales during the last glacial period, Science, 322, 83–85, doi:10.1126/science.1160832, 2008.

Alley, R. B.: The Two-Mile Time Machine: Ice Core, Abrupt Climate Change and Our Future, Princeton University Press, Princeton, 2000.

Alley, R. B., Meese, D. A., Shuman, C. A., Gow, A. J., Taylor, K. C., Grootes, P. M., White, J. W. C., Ram, M., Waddington, E. D., Mayewski, P. A., and Zielinski, G. A.: Abrupt increase in Greenland snow accumulation at the end of the Younger Dryas event, Nature, 362, 527–529, 1993.

Alley, R. B., Shuman, C. A., Meese, D. A., Gow, A. J., Taylor, K. C., Cuffey, K. M., Fitzpatrick, J. J., Grootes, P. M., Zielinski, G. A., Ram, M., Spinelli, G., and Elder, B.: Visualstratigraphic dating of the GISP2 ice core: basic, reproducibility, and application, J. Geophys. Res., 102, 26367–26381, 1997.

Aristarain, A., Jouzel, J., and Pourchet, M.: Past Antarctic Peninsula Climate (1850–1980) deduced from an ice core isotope record, Climatic Change, 8, 69–90, 1986.

Aristarain, A., Jouzel, J., and Lorius, C.: A 400 years isotope record of the Antarctic Peninsula climate, Geophys. Res. Lett., 17, 2369–2372, 1990.

Arnaud, L., Barnola, J.-M., and Duval, P.: Physical modeling of the densification of snow/firn and ice in the upper part of polar ice sheets, in: Physics of Ice Core Records, edited by: Hondoh, T., Hokkaido University Press, Sapporo, 285–305, 2000.

Barnola, J.-M., Raynaud, D., Korotkevich, Y. N., and Lorius, C.: Vostok ice-core provides 160,000 yr record of atmospheric CO_2, Nature, 329, 408–414, 1987.

Barnola, J. M., Pimienta, P., Raynaud, D., and Korotkevich, Y. S.: CO_2 climate relationship as deduced from the Vostok ice core: a re-examination based on new measurements and on a reevaluation of the air dating, Tellus B, 43, 83–91, 1991.

Bazin, L., Landais, A., Lemieux-Dudon, B., Toyé Mahamadou Kele, H., Veres, D., Parrenin, F., Martinerie, P., Ritz, C., Capron, E., Lipenkov, V., Loutre, M.-F., Raynaud, D., Vinther, B., Svensson, A., Rasmussen, S. O., Severi, M., Blunier, T., Leuenberger, M., Fischer, H., Masson-Delmotte, V., Chappellaz, J., and Wolff, E.: An optimized multi-proxy, multi-site Antarctic ice and gas orbital chronology (AICC2012): 120–800 ka, Clim. Past, 9, 1715–1731, doi:10.5194/cp-9-1715-2013, 2013.

Bender, M. L.: Orbital tuning chronology for the Vostok climate record supported by trapped gas composition, Earth Planet. Sc. Lett., 204, 275–289, 2002.

Bender, M. L., Labeyrie, L., Raynaud, D., and Lorius, C.: Isotopic composition of atmospheric O_2 in ice linked with deglaciation and global primary productivity, Nature, 318, 349–352, 1985.

Bender, M. L., Sowers, T., and Labeyrie, L.: The Dole effect and its variations during the last 130 000 years as measured in the Vostok ice core, Global Biogeochem. Cy., 8, 363–376, 1994a.

Bender, M. L., Sowers, T., Dickson, M. L., Orchado, J., Grootes, P., Mayewski, P. A., and Meese, D. A.: Climate connection between Greenland and Antarctica during the last 100 000 years, Nature, 372, 663–666, 1994b.

Bender, M. L., Malaizé, B., Orchado, J., Sowers, T., and Jouzel, J.: High precision correlations of Greenland and Antarctic ice core records over the last 100 kyr, in: Mechanisms of Global Climate Change at Millenial Timescales, Geophysical Monograph, 112, edited by: Clark, P. U., Webb, R. S., and Keigwin, L. D., AGU, Washington, D.C., 149–164, doi:10.1029/GM112p0149, 1999.

Blunier, T. and Brook, E. J.: Timing of millenial-scale climate change in Antarctica and Greenland during the Last Glacial Period, Science, 291, 109–112, 2001.

Blunier, T., Chappellaz, J., Schwander, J., Dällenbach, A., Stauffer, B., Stocker, T., Raynaud, D., Jouzel, J., Clausen, H. B., Hammer, C. U., and Johnsen, S. J.: Asynchrony of Antarctic andGreenland climate change during the last glacial period, Nature, 394, 739–743, 1998.

Blunier, T., Barnett, B., Bender, M. L., and Hendricks, M. B.: Biological oxygen productivity during the last 60 000 years from triple oxygen isotope measurements, Global Biogeochem. Cy., 16, 1029, doi:10.1029/2001GB001460, 2002.

Blunier, T., Schwander, J., Chappellaz, J., and Parrenin, F.: What was the surface temperature in central Antarctica during the last glacial maximum ?, Earth Planet. Sc. Lett., 218, 379–388, 2004.

Bock, M., Schmitt, J., Moeller, L., Spahni, R., Blunier, T., and Fischer, H.: Hydrogen isotopes preclude marine hydrate CH_4 emissions at the onset of Dansgaard–Oeschger events, Science, 328, 1686–1689, doi:10.1126/science.1187651, 2010.

Bouttes, N., Paillard, D., Roche, D. M., Brovkin, D. M., and Bopp, L.: Last Glacial Maximum CO_2 and $\delta^{13}C$ successfully reconciled, Geophys. Res. Lett., 38, L02705, doi:10.1029/2010GL044499, 2011.

Broecker, W. S.: Paleocean circulation during the last deglaciation: a bipolar seesaw?, Paleoceanography, 13, 119–121, 1998.

Broecker, W. S., Peteet, D. M., and Rind, D.: Does the ocean–atmosphere system have more than one stable mode of operation?, Nature, 315, 21–26, doi:10.1038/315021a0, 1985.

Brook, E. J., Sowers, T., and Orchardo, J.: Rapid variations in atmospheric methane concentration during the past 110 000 years, Science, 273, 1087–1091, 1996.

Brook, E. J., Wolff, E., Dahl-Jensen, D., Fischer, H., and Steig, E.: The future of ice coring, International Partnership in Ice Core Sciences (IPICS), PAGES News, 14, 6–10, 2006.

Caillon, N., Severinghaus, J. P., Barnola, J. M., Chappellaz, J. C., Jouzel, J., and Parrenin, F.: Estimation of temperature change and of gas age–ice age difference, 108 kyr BP, at Vostok, Antarctica, J. Geophys. Res., 106, 31893–31901, 2001.

Caillon, N., Severinghaus, J. P., Jouzel, J. P., Barnola, J. M., Kang, J., and Lipenkov, V. Y.: Timing of atmospheric CO_2 and Antarctic temperature changes across termination III, Science, 299, 1728–1731, 2003.

Capron, E., Landais, A., Chappellaz, J., Schilt, A., Buiron, D., Dahl-Jensen, D., Johnsen, S. J., Jouzel, J., Lemieux-Dudon, B., Loulergue, L., Leuenberger, M., Masson-Delmotte, V., Meyer, H., Oerter, H., and Stenni, B.: Millennial and sub-millennial scale climatic variations recorded in polar ice cores over the last glacial period, Clim. Past, 6, 345–365, doi:10.5194/cp-6-345-2010, 2010.

Chappellaz, J., Barnola, J. M., Raynaud, D., Korotkevich, Y. S., and Lorius, C.: Ice-core record of atmospheric methane over the past 160 000 years, Nature, 345, 127–131, 1990.

Chappellaz, J., Blunier, T., Barnola, J. M., Raynaud, D., Schwander, J., and Stauffer, B.: Synchronous changes in atmospheric CH_4 and Greenland climate between 40 and 8 kyr BP, Nature, 366, 443–445, 1993.

Chappellaz, J., Brook, E., Blunier, T. and Malaizé B.: CH_4 and $\delta^{18}O$ of O_2 records from Antarctic and Greenland ice: A clue for stratigraphic disturbance in the bottom part of the Greenland Ice Core Project and the Greenland Ice Sheet Project 2 ice cores, J. Geophys. Res., 102, 26547–26557, 1997.

Chappellaz, J., Alemany, O., Romanini, D., and Kerstel, E.: The IPICS "oldest ice" challenge: a new technology to qualify potential sites, Ice Snow, 4, 57–64, 2012.

Ciais, P. and Jouzel, J.: Deuterium and oxygen 18 in precipitation: an isotopic model including mixed cloud processes, J. Geophys. Res., 99, 16793–16803, 1994.

Ciais, P., Petit, J. R., Jouzel, J., Lorius, C., Barkov, N. I., Lipenkov, V., and Nicolaïev, V.: Evidence for an early Holocene climatic optimum in the Antarctic deep ice core record, Clim. Dynam., 6, 169–177, 1992.

Craig, H.: Isotopic variations in meteoric waters, Science, 133, 1702–1703, 1961.

Cuffey, K. M. and Vimeux, F.: Covariation of carbon dioxyde and temperature from the Vostok ice core after deuterium-excess correction, Nature, 421, 523–527, 2001.

Cuffey, K. M., Clow, G. D., Alley, R. B., Stuiver, M., Waddington, E. D., and Saltus, R. W.: Large Arctic temperature change at the Winconsin-Holocene glacial transition, Science, 270, 455–458, 1995.

Dahl-Jensen, D., Mosegaard, K., Gundestrup, N., Clow, G. D., Johnsen, S. J., Hansen, A. W., and Balling, N.: Past temperatures directly from the Greenland ice sheet, Science, 282, 268–271, 1998.

Dällenbach, A., Blunier, T., Flückiger, J., Stauffer, B., Chappellaz, J., and Raynaud, D.: Changes in the atmospheric CH_4 gradient between Greenland and Antarctica during the Last Glacial and the transition to the Holocene, Geophys. Res. Lett., 27, 1005–1008, 2000.

Dansgaard, W.: The abundance of ^{18}O in atmospheric water and water vapour, Tellus, 5, 461–469, 1953.

Dansgaard, W.: Stable isotopes in precipitation, Tellus, 16, 436–468, 1964.

Dansgaard, W.: Frozen Annals, Niels Bohr Institute, Copenhagen, Denmark, 2004.

Dansgaard, W., Johnsen, S. J., Moller, J., and Langway, C. C. J.: One thousand centuries of climatic record from Camp Century on the Greenland ice sheet, Science, 166, 377–381, 1969.

Dansgaard, W., Clausen, H. B., Gundestrup, N., Hammer, C. U., Johnsen, S. J., Krinstindottir, P., and Reeh, N.: A new Greenland deep ice core, Science, 218, 1273–1277, 1982.

Dansgaard, W., Johnsen, S., Clausen, H. B., Dahl-Jensen, D., Gundestrup, N., Hammer, C. U., and Oeschger, H.: North Atlantic climatic oscillations revealed by deep Greenland ice cores, in: Climate Processes and Climate Sensitivity, edited by: Hansen, J. E. and Takahashi, T., Am. Geophys. Union, Washington, D.C., 288–298, doi:10.1029/GM029p0288, 1984.

Dansgaard, W., White, J. W. C., and Johnsen, S. J.: The abrupt termination of the Younger Dryas, Nature, 339, 532–534, 1989.

Dansgaard, W., Johnsen, S. J., Clausen, H. B., Dahl-Jensen, D., Gunderstrup, N. S., Hammer, C. U., Steffensen, J. P., Sveinbjörnsdottir, A., Jouzel, J., and Bond, G.: Evidence for general instability of past climate from a 250-kyr ice-core record, Nature, 364, 218–220, 1993.

Delmas, R. J., Ascensio, J. M., and Legrand, M.: Polar ice evidence that atmospheric CO_2 20 000 yr BP was 50 % of present, Nature, 284, 155–157, 1980.

Delmotte, M., Chappellaz, J., Brook, E., Yiou, P., Barnola, J. M., Goujon, C., Raynaud, D., and Lipenkov, V. I.: Atmospheric methane during the last four glacial–interglacial cycles: rapid changes and their link with Antarctic temperature, J. Geophys. Res., 109, D12104, doi:10.1029/2003JD004417, 2004.

Dreyfus, G. B., Parrenin, F., Lemieux-Dudon, B., Durand, G., Masson-Delmotte, V., Jouzel, J., Barnola, J.-M., Panno, L., Spahni, R., Tisserand, A., Siegenthaler, U., and Leuenberger, M.: Anomalous flow below 2700 m in the EPICA Dome C ice core detected using $\delta^{18}O$ of atmospheric oxygen measurements, Clim. Past, 3, 341–353, doi:10.5194/cp-3-341-2007, 2007.

Dunbar, N. W., McIntosh, W. C., and Esser, R. P.: Physical setting and tephrochronology of the summit caldera ice record at Mount Moulton, West Antarctica, GSA Bull., 120, 796–812, 2008.

Elsig, J., Schmitt, J., Leuenberger, D., Schneider, R., Eyer, M., Leuenberger, M., Joos, F., Fischer, H., and Stocker, T. F.: Stable isotope constraints on Holocene carbon cycle changes from an Antarctic ice core, Nature, 461, 507–510, doi:10.1038/nature08393, 2009.

EPICA Community Members: Eight glacial cycles from an Antarctic ice core, Nature, 429, 623–628, 2004.

EPICA Community Members: Interhemispheric coupling of millenial scale variability during the last glacial, Nature, 444, 195–198, 2006.

Epstein, S., Sharp, R. P., and Gow, A. J.: Antarctic ice sheet: stable isotope analyses of Byrd station cores and interhemispheric climatic implications, Science, 16, 1570–1572, 1970.

Ferretti, D. F., Miller, J. B., White, J. W. C., Etheridge, D. M., Lassey, K. R., Lowe, D. C., MacFarling Meure, C. M., Dreier, M. F., Trudinger, C. M., van Ommen, T. D., and Langenfelds, R. L.: Unexpected changes to the global methane budget over the past 2000 years, Science, 309, 1714–1717, 2005.

Fischer, H., Wahlen, M., Smith, J., Mastroianni, D., and Deck, B.: Ice core records of atmospheric CO_2 around the last three glacial terminations, Science, 283, 1712–1714, 1999.

Fischer, H., Behrens, M., Bock, M., Richter, U., Schmitt, J., Loulergue, L., Chappellaz, J., Spahni, R., Blunier, T., Leuenberger, M., and Stocker, T. F.: Changing boreal methane sources and constant biomass burning during the last termination, Nature, 452, 864–867, doi:10.1038/nature06825, 2008.

Fischer, H., Severinghaus, J., Brook, E., Wolff, E., Albert, M., Alemany, O., Arthern, R., Bentley, C., Blankenship, D., Chappellaz, J., Creyts, T., Dahl-Jensen, D., Dinn, M., Frezzotti, M., Fujita, S., Gallee, H., Hindmarsh, R., Hudspeth, D., Jugie, G., Kawamura, K., Lipenkov, V., Miller, H., Mulvaney, R., Pattyn, F., Ritz, C., Schwander, J., Steinhage, D., van Ommen, T., and Wilhelms, F.: Where to find 1.5 million yr old ice for the IPICS "Oldest Ice" ice core, Clim. Past Discuss., 9, 2771–2815, doi:10.5194/cpd-9-2771-2013, 2013.

Fisher, D. A., Koerner, R. M., Paterson, W. S. B., Dansgaard, W., Gundestrup, N., and Reeh, N.: Effect of wind scouring on climatic records from ice-core oxygen-isotope profiles, Nature, 301, 205–209, 1983.

Fisher, D. A., Koerner, R. M., Bourgeois, J. C., Zielinski, G., Wake, C., Hammer, C. U., Clausen, H. B., Gundestrup, N., Johnsen, S., Goto-Azuma, K., Hondoh, T., Blake, E., Gerasimoff, M.: Penny Ice Cap, Baffin Island, Canada and the Wisconsinan Foxe Dome connection: two states of Hudson Bay ice cover, Science, 279, 692–695, 1998.

Fisher, D., Zheng, J., Burgess, D., Zdanowicz, C., Kinnard, C., Sharp, M., and Bourgeois, J.: Recent melt rates of Canadian arctic ice caps are the highest in four millennia, Global Planet. Change, doi:10.1016/j.gloplacha.2011.06.005, in press, 2011.

Flückiger, J., Dällenbach, A., Blunier, T., Stauffer, B., Stocker, T. F., Raynaud, D., and Barnola, J. M.: Variations in atmospheric N_2O concentration during abrupt climatic changes, Science, 285, 227–230, 1999.

Fuchs, A., and Leuenberger, M. C.: $\delta^{18}O$ of atmospheric oxygen measured on the GRIP ice core document stratigraphic disturbances in the lowest 10 % of the core, Geophys. Res. Lett., 23, 1049–1052, 1996.

Genthon, C., Barnola, J. M., Raynaud, D., Lorius, C., Jouzel, J., Barkov, N. I., Korotkevitch, Y. S., and Kotlyakov, V. M.: Vostok ice core: the climate response to and orbital forcing changes over the last climatic cycle (160 000 years), Nature, 329, 414–418, 1987.

Gow, A. J. and Engelhart, H.: Preliminary analysis of ice core from Siple Dome, West Antarctica, in: Physics of Ice Core Records, edited by: Hondoh, T., Hokkaido University Press, Sapporo, 64–82, 2000.

Grootes, P. M., Stuiver, M., White, J. W. C., Johnsen, S. J., and Jouzel, J.: Comparison of the oxygen isotope records from the GISP2 and GRIP Greenland ice cores, Nature, 366, 552–554, 1993.

Grootes, P. M., Steig, E. J., Stuiver, M., Waddington, E. D., and Morse, D. L.: A new ice core record from Taylor Dome, Antarctica, EOS Transactions, 75, 225, 1994.

Haan, D. and Raynaud, D.: Ice core record of CO variations during the last two millennia: atmospheric implications and chemical interactions within the Greenland ice, Tellus B, 50, 253–262, 1998.

Haan, D., Martinerie, P., and Raynaud, D.: Ice core data of atmospheric carbon monoxide over Antarctica and Greenland during the last 200 years, Geophys. Res. Lett., 23, 2235–2238, 1996.

Hamley, T. C., Morgan, V. I., Thwaites, R. J., and Gao, X. Q.: An ice-core drilling site at Law Dome summit, Wilkes Land, Antarctica, ANARE Research Notes 37, AAS Projects 15, Information Services Section, Antarctic Division, Dept. of Science and Technology, Kingston, Tasmania, Australia, 34 pp., 1986.

Hammer, C. U., Clausen, H. B., and Tauber, H.: Ice-core dating of the Pleistocene/Holocene boundary applied to a calibration of the ^{14}C time scale, Radiocarbon, 28, 284–291, 1986.

Hansen, L. B. and Langway Jr., C. C.: Deep core drilling in ice and core analysis at Camp Century, Greenland, 1961–1966, Antarct. J. US, 207–208, 1966.

Hays, J. D., Imbrie, J., and Shackleton, N. J.: Variations in the Earth's orbit: pacemaker of the ice ages, Science, 194, 1121–1132, 1976.

Headly, M. A. and Severinghaus, J.: A method to measure Kr/N2 ratios in air bubbles trapped in ice cores and its application in reconstructing past mean ocean temperature, J. Geophys. Res., 112, D19105, doi:10.1029/2006JD008317, 2007.

Heuberger, J. C.: Groenland, glaciology, Forages sur I'inlandis, Hermann and Cie, Paris, 1, 63–84, 1954.

Hoffmann, G. and Heimann, M.: Water tracers in the ECHAM general circulation model, in: Isotope Techniques in the Study of Past and Current Environmental Changes in the Hydrosphere and the Atmosphere, International Atomic Energy Agency, Vienna, 3–14, 1993.

Hoffmann, G., Werner, M., and Heimann, M.:Water isotope module of the ECHAM Atmospheric General Circulation Model: a study on time scales from days to several years, J. Geophys. Res., 103, 16871–16896, 1998.

Huber, C., Leuenberger, M., Spahni, R., Flückiger, J., Schwander, J., Stocker, T. F., Johnsen, S., Landais, A., and Jouzel, J.: Isotope calibrated Greenland temperature record over marine isotope stage 3 and its relation to CH_4, Earth Planet. Sc. Lett., 243, 504–519, 2006.

Indermühle, A., Stocker, T. F., Joos, F., Fischer, H., Smith, H. J., Wahlen, M., Deck, B., Mastroianni, D., Tschumi, J., Blunier, T., Meyer, R., and Stauffer, B.: Holocene carbon cycle dynamics based on CO_2 trapped in ice at Taylor Dome, Antarctica, Nature, 398, 121–126, doi:10.1038/18158, 1999.

IPCC: Summary for Policymakers, in: Climate Change 2007: The Physical Science Basis, Contribution of Working Group I to the Fourth Assessment Report of the Intergovernmental Panel on Climate Change, edited by: Solomon, S., Qin, D., Manning, M., Chen, Z., Marquis, M., Averyt, K. B., Tignor, M., and Miller, H. L., Cambridge University Press, Cambridge, UK and New York, NY, USA.

IPICS white paper: The oldest ice core: A 1.5 million year record of climate and greenhouse gases from Antarctica, Science and outline implementation plan, http://www.pages-igbp.org/ipics/ (last access: November 2013), 2008.

Johnsen, S. J.: Stable isotope homogenization of polar firn and ice, Proc. Symp. on Isotopes and Impurities in Snow and Ice, I.U.G.G. XVI, General Assembly, Grenoble August September 1975, Washington, 210–219, 1977.

Johnsen, S. J., Dansgaard, W., Clausen, H. B., and Langway, C. C.: Oxygen isotope profiles through the Antarctic and Greenland ice sheets, Nature, 235, 429–434, 1972.

Johnsen, S. J., Dansgaard, W., and White, J. W. C.: The origin of Arctic precipitation under present and glacial conditions, Tellus, 41, 452–469, 1989.

Johnsen, S. J., Clausen, H. B., Dansgaard, W., Fuhrer, K., Gunderstrup, N. S., Hammer, C. U., Iverssen, P., Jouzel, J., Stauffer, B., and Steffensen, J. P.: Irregular glacial interstadials recorded in a new Greenland ice core, Nature, 359, 311–313, 1992.

Johnsen, S. J., Dahl-Jensen, D., Dansgaard, W., and Gundestrup, N.: Greenland paleotemperatures derived from GRIP bore hole temperature and ice core isotope profiles, Tellus B, 47, 624–629, 1995.

Johnsen, S. J., Clausen, H. B., Cuffey, K. M., Hoffmann, G., Schwander, J., and Creyts, T.: Diffusion of stable isotopes in polar firn and ice: the isotope effect in firn diffusion, in: Physics of Ice Core Records, 159, edited by: Hondoh, T., Hokkaido University Press, Sapporo, 121–140, 2000.

Joussaume, S., Jouzel, J., and Sadourny, R.: A general circulation model of water isotope cycles in the atmosphere, Nature, 311, 24–29, 1984.

Jouzel, J.: Water stable isotopes: atmospheric composition and applications in polar ice core studies, in: Handbook of Geochemistry, Elsevier Ltd, 2013.

Jouzel, J. and Masson-Delmotte, V.: Paleoclimates: what do we learn from ice cores?, Climatic Change, 1, 654–669, 2010a.

Jouzel, J. and Masson-Delmotte, V.: Deep ice cores: the need for going back in time, Quaternary Sci. Rev., 29, 3683–3689, 2010b.

Jouzel, J. and Merlivat, L.: Deuterium and oxygen 18 in precipitation: modeling of the isotopic effects during snow formation, J. Geophys. Res., 89, 11749–11757, 1984.

Jouzel, J. and Souchez, R. A.: Melting refreezing at the glacier and the isotopic composition of the ice, J. Glaciol., 28, 34–42, 1982.

Jouzel, J., Merlivat, L., and Lorius, C.: Deuterium excess in an East Antarctic ice core suggests higher relative humidity at the oceanic surface during the last glacial maximum, Nature, 299, 688–691, 1982.

Jouzel, J., Russell, G. L., Suozzo, R. J., Koster, R. D., White, J. W. C., and Broecker, W. S.: Simulationsof the HDO and $H_2^{18}O$ atmospheric cycles using the NASA/GISS general circulation model: the seasonal cycle for present-day conditions, J. Geophys. Res., 92, 14739–14760, 1987a.

Jouzel, J., Lorius, C., Petit, J. R., Genthon, C., Barkov, N. I., Kotlyakov, V. M., and Petrov, V. M.: Vostok ice core: a continuous isotope temperature record over the last climatic cycle (160 000 years), Nature, 329, 402–408, 1987b.

Jouzel, J., Barkov, N. I., Barnola, J. M., Bender, M., Chappelaz, J., Genthon, C., Kotlyakov, V. M., Lipenkov, V., Lorius, C., Petit, J. R., Raynaud, D., Raisbeck, G., Ritz, C., Sowers, T., Stievenard, M., Yiou, F., and Yiou, P.: Extending the Vostok ice-core record of paleoclimate to the penultimate glacial period, Nature, 364, 407–412, 1993.

Jouzel, J., Lorius, C., Johnsen, S. J., and Grootes, P.: Climate instabilities: Greenland and Antarctic records, C. R. Acad. Sci. Paris, 319, 65–77, 1994.

Jouzel, J., Vaikmae, R., Petit, J. R., Martin, M., Duclos, Y., Stievenard, M., Lorius, C., Toots, M., Mélières, M. A., Burckle, L. H., Barkov, N. I., and Kotlyakov, V. M.: The two-step shape and timing of the last deglaciation in Antarctica, Clim. Dynam., 11, 151–161, 1995.

Jouzel, J., Waelbroeck, C., Malaizé, B., Bender, M., Petit, J. R., Barkov, N. I., Barnola, J. M., King, T., Kotlyakov, V. M., Lipenkov, V., Lorius, C., Raynaud, D., Ritz, C., and Sowers, T.: Climatic interpretation of the recently extended Vostok ice records, Clim. Dynam., 12, 513–521, 1996.

Jouzel, J., Petit, J. R., Souchez, R., Barkov, N. I., Lipenkov, V. Y., Raynaud, D., Stievenard, M., Vassiliev, N. I., Verbeke, V., and Vimeux, F.: Evidence of more than 200 m thick of lake ice above the subglacial lake Vostok, Central East Antarctica, Science, 286, 2138–2141, 1999.

Jouzel, J., Hoffmann, G., Parrenin, F., and Waelbroeck, C.: Atmospheric oxygen 18 and sealevel changes, Quaternary Sci. Rev., 21, 1–3, 2002.

Jouzel, J., Vimeux, F., Caillon, N., Delaygue, G., Hoffmann, G., Masson, V., and Parrenin, F.: Magnitude of the isotope/temperature scaling for interpretation of central Antarctic ice cores, J. Geophys. Res., 108, 4361, doi:10.1029/2002JD002677, 2003.

Jouzel, J., Masson-Delmotte, V., Cattani, O., Dreyfus, G., Falourd, S., Hoffmann, G., Nouet, J., Johnsen, S. J., Leuenberger, M., Oerter, H., Parrenin, F., Raisbeck, G., Schwander, J., Souchez, R., Selmo, E., Stenni, B., Stocker, T., and Werner, M.: Orbital and millenial antarctic climate variability over the last 800 000 years, Science, 317, 793–796, doi:10.1126/science.1141038, 2007a.

Jouzel, J., Stiévenard, M., Johnsen, S. J., Fuhrer, K., Landais, A., Masson-Delmotte, V., Sveinbjörnsdottir, A. E., Vimeux, F., and White, J. W. C.: The GRIP deuterium-excess record, Quaternary Sci. Rev., 26, 1–17, 2007b.

Jouzel, J., Lorius, C., and Raynaud, D.: The White Planet, Princeton University Press, 306 pp., 2013.

Kawamura, K., Parrenin, F., Lisiecki, L., Uemura, R., Vimeux, F., Severinghaus, J. P., Hutterli, M. A., Nakazawa, T., Aoki, S., Jouzel, J., Raymo, M. E., Matsumoto, K., Nakata, H., Motoyama, H., Fujita, S., Goto-Azuma, K., Fujii, Y., and Watanabe, O.: Northern Hemisphere forcing of climatic cycles in Antarctica over the past 360 000 years, Nature, 912–916, doi:10.1038/nature06015, 2007.

Kawamura, K., Aoki, S., Nakazawa, T., Suzuki, K., and Parrenin, F.: Accurate age scale of the Dome Fuji ice core, Antarctica from O_2/N_2 ratio of trapped air, EGU General Assembly Conference Abstracts, Vienna, 14, 8309, 2012.

Koerner, R. M.: Devon Island Ice Cap: core stratigraphy and paleoclimate, Science, 196, 15–18, 1977.

Koerner, R. M. and Fisher, D. A.: A record of Holocene summer climate from a Canadian High Arctic ice core, Nature, 343, 630–631, 1990.

Köhler, P., Fischer, H., and Schmitt, J.: Atmospheric $\delta^{13}CO_2$ and its relation to pCO_2 and deep ocean $\delta^{13}C$ during the late Pleistocene, Paleoceanography, 25, PA1213, doi:10.1029/2008PA001703, 2010.

Krinner, G., Genthon, C., and Jouzel, J.: GCM analysis of local influences on ice core d signals, Geophys. Res. Lett., 24, 2825–2828, 1997.

Landais, A.: Utility of stable isotopes of N and Ar as tracers to retrieve past air temperature from air trapped in ice cores, in: Handbook of Environmental Isotope Geochemistry, Springer, 865–886, 2011.

Landais, A., Chappellaz, J., Delmotte, M., Jouzel, J., Blunier T., Bourg, C., Caillon, N., Cherrier, S., Malaizé, B., Masson-Delmotte, V., Raynaud, D., and Schwander J.: A tentative reconstruction of the last interglacial and glacial inception in Greenland based on new gas measurements in the Greenland Ice Core Project (GRIP) ice core, J. Geophys. Res., 108, 4563, doi:10.1029/2002JD003147, 2003.

Landais, A., Caillon, N., Goujon, C., Grachev, A., Barnola, J. M., Chappellaz, J., Jouzel, J., Masson-Delmotte, V., and Leuenberger, M.: Quantification of rapid temperature change during DO event 12 and phasing with methane inferred from air isotopic measurements, Earth Planet. Sc. Lett., 225, 221–232, 2004a.

Landais, A., Barnola, J.-M., Masson-Delmotte, V., Jouzel, J., Chappellaz, J., Caillon, N., Huber, C., Leuenberger, M., and Johnsen, S. J.: A continuous record of temperature evolution over a whole sequence of Dansgaard–Oeschger during Marine Isotopic Stage 4 (76 to 62 kyr BP), Geophys. Res. Lett., 31, L22211, doi:10.1029/2004GL021193, 2004b.

Landais, A., Steffensen, J. P., Caillon, N., Jouzel, J., Masson-Delmotte, V., and Schwander, J.: Evidence for stratigraphic distortion in Greenland Ice Core Project (GRIP) ice core during Event 5e1 (120 kyr BP) from gas isotopes, J. Geophys. Res., 109, D06103, doi:10.1029/2003JD004193, 2004c.

Landais, A., Barnola, J. M., Kawamura, K., Caillon, N., Delmotte, M., Dreyfus, G., Jouzel, J., Masson-Delmotte, V., Minster, B., Freitag, J., Leuenberger, M., Huber, C., Schwander, J., Etheridge, D., Morgan, V., and Van Ommen, T.: Air $\delta^{15}N$ in modern firns and glacial-interglacial ice: a model-data mismatch during glacial periods in Antarctica?, Quaternary Sci. Rev., 25, 49–62, 2006.

Landais, A., Barkan, E., and Luz, B.: The record of ^{18}O and ^{17}O-excess in ice from Vostok Antarctica during the last 150 000 years, Geophys. Res. Lett., 35, L02709, doi:10.1029/2007GL032096, 2008.

Landais, A., Dreyfus, G., Capron, E., Masson-Delmotte, V., Sanchez-Goñi, M. F., Desprat, S., Hoffmann, G., Jouzel, J., Leuenberger, M., and Johnsen, S.: What drives the millennial and orbital variations of $\delta^{18}O_{atm}$?, Quaternary Sci. Rev., 29, 235–246, 2010.

Landais, A., Dreyfus, G., Capron, E., Pol, K., Loutre, M. F., Raynaud, D., Lipenkov, V. Y., Arnaud, L., Masson-Delmotte, V., Paillard, D., Jouzel, J., and Leuenberger, M.: Towards orbital dating of the EPICA Dome C ice core using $\delta O_2/N_2$, Clim. Past, 8, 191–203, doi:10.5194/cp-8-191-2012, 2012.

Lang, C., Leuenberger, M., Schwander, J., and Johnsen, S. J.: 16 °C rapid temperature variation in central Greenland 70 000 years ago, Science, 286, 934–937, 1999.

Langway, C. C.: The history of early polar ice cores, Cold Reg. Sci. Technol., 52, 101–117, 2008.

Langway Jr., C. C.: A 400 meter deep ice core in Greenland, preliminary Report, J. Glaciol., 3, 216–217, 1958.

Lee, J.-E., Fung, I., DePaolo, D. J., and Otto-Bliesner, B.: Water isotopes during the Last Glacial Maximum: new general circulation model calculations, J. Geophys. Res., 113, D19109, doi:10.1029/2008JD009859, 2008.

Lemieux-Dudon, B., Blayo, E., Petit, J.-R., Waelbroeck, C., Svensson, A., Ritz, C., Barnola, J.-M., Narcisi, B. M., and Parrenin, F.: Consistent dating for Antarctic and Greenland ice cores, Quaternary Sci. Rev., 29, 8–20, doi:10.1016/j.quascirev.2009.11.010, 2010.

Leuenberger, M. and Siegenthaler, U.: Ice-age atmospheric concentration of nitrous oxide from an antarctic ice core, Nature, 360, 449–451, 1992.

Leuenberger, M., Siegenthaler, U., and Langway, C.: Carbon isotope composition of atmospheric CO_2 during the last ice age from an Antarctic ice core, Nature, 357, 488–490, 1992.

Lipenkov, V. Y., Raynaud, D., Loutre, M. F., and Duval, P.: On the potential of coupling air content and O_2/N_2 from trapped air for establishing an ice core chronology tuned on local insolation, Quaternary Sci. Rev., 30, 3280–3289, 2011.

Lisiecki, L. and Raymo, M.: A Pliocene–Pleistocene stack of 57 globally distributed benthic $\delta^{18}O$ records, Paleoceanography, 20, PA1003, doi:10.1029/2004PA001071, 2005.

Lorius, C. and Merlivat, L.: Distribution of mean surface stable isotope values in East Antarctica, Observed changes with depth in a coastal area, in: Isotopes and Impurities in Snow and Ice, Proceedings of the Grenoble Symposium, August/September 1975, IAHS, Grenoble, 118, 125–137, 1977.

Lorius, C., Raynaud, D., and Dolle, L.: Ice density and studies of gas taken from a deep levels of an Antarctic Glacier, Tellus, 20, 449–455, 1968.

Lorius, C., Merlivat, L., Jouzel, J., and Pourchet, M.: A 30 000 yr isotope climatic record from Antarctic ice, Nature, 280, 644–648, 1979.

Lorius, C., Jouzel, J., Ritz, C., Merlivat, L., Barkov, N. I, Korotkevitch, Y. S. and Kotlyakov, Y. M.: A 150 000 year climatic record from Antarctic ice, Nature, 591–596, 1985.

Lorius, C., Jouzel, J., Raynaud, D., Hansen, J., and Le Treut, H.: The ice-core record: climate sensitivity and future greenhouse warming, Nature, 347, 139–145, 1990.

Loulergue, L., Schilt, A., Spahni, R., Masson-Delmotte, V., Blunier, T., Lemieux, B., Barnola, J. M., Raynaud, D., Stocker, T., and Chappelaz, J.: Orbital and millenial-scale features of atmospheric CH_4 over the last 800 000 years, Nature, 453, 383–386, 2008.

Lourantou, A., Chappellaz, J., Barnola, J. M., Masson-Delmotte, V., and Raynaud, D.: Changes in atmospheric CO_2 and its carbon isotopic ratio during the penultimate deglaciation, Quaternary Sci. Rev., 29, 1983–1992, 2010.

Lüthi, D., Floch, M. L., Bereiter, B., Blunier, T., Barnola, J. M., Siegenthaler, U., Raynaud, D., Jouzel, J., Fischer, H., Kawamura, K., and Stocker, T. F.: High resolution carbon dioxide concentration record 650 000–800 000 years before present, Nature, 453, 379–382, 2008.

MacFarling Meure, C., Etheridge, D., Trudinger, C., Steele, P., Langenfelds, R., van Ommen, T., Smith, A., and Elkins, J.: Law Dome CO_2, CH_4 and N_2O ice core records extended to 2000 years BP, Geophys. Res. Lett., 33, L14810, doi:10.1029/2006GL026152, 2006.

Malaizé, B., Paillard, D., Jouzel, J., and Raynaud, D.: The Dole effect over the last two glacial–interglacial cycles, J. Geophys. Res., 104, 14199–14208, 1999.

Masson-Delmotte, V., Jouzel, J., Landais, A., Stiévenard, M., Johnsen, S. J., White, J. W. C., Werner, M., Sveinbjörnsdottir, A., and Fuhrer, K.: GRIP deuterium excess reveals rapid and orbital changes of Greenland moisture origin, Science, 309, 118–121, 2005.

Masson-Delmotte, V., Hou, S., Ekaykin, A., Jouzel, J., Aristarain, A., Bernardo, R. T., Bromwich, D., Cattani, O., Delmotte, M., Falourd, S., Frezzotti, M., Gallée, H., Genoni, L., Isaksson, E., Landais, A., Helsen, M. M., Hoffmann, G., Lopez, J., Morgan, V., Motoyama, H., Noone, D., Oerter, H., Petit, J. R., Royer, A., Uemura, R., Schmidt, G. A., Schlosser, E., Simoes, J. C., Steig, E. J., Stenni, B., Stievenard, M., van den Broeke, M. R., van de Wal, R. S. W., van de Berg, W. J., Vimeux, F., and White, J. W. C.: A review of Antarctic surface snow isotopic composition: observations, atmospheric circulation, and isotopic modeling, J. Climate, 21, 3359–3387, doi:10.1175/2007JCLI2139.1, 2008.

Masson-Delmotte, V., Buiron, D., Ekaykin, A., Frezzotti, M., Gallée, H., Jouzel, J., Krinner, G., Landais, A., Motoyama, H., Oerter, H., Pol, K., Pollard, D., Ritz, C., Schlosser, E., Sime, L. C., Sodemann, H., Stenni, B., Uemura, R., and Vimeux, F.: A comparison of the present and last interglacial periods in six Antarctic ice cores, Clim. Past, 7, 397–423, doi:10.5194/cp-7-397-2011, 2011.

Meese, D. A., Gow, A. J., Alley, R. B., Zielinski, G. A., Grootes, P. M., Ram, M., Taylor, K. C., Mayewski, P. A., and Bolzan, J. F.: The Greenland Ice Sheet Project 2 depth-age scale: methods and results, J. Geophys. Res., 102, 26411–26423, 1997.

Merlivat, L. and Jouzel, J.: Global climatic interpretation of the deuterium–oxygen 18 relationship for precipitation, J. Geophys. Res., 84, 5029–5033, 1979.

Miller, M. M.: Juneau Icefield Research Project, Alaska, 1950, American Geographical Society, JIRP Report 7, Amer. Geographical Soc., NY, 97 pp., 1954.

Monnin, E., Indermühle, A., Dällenbach, A., Flückiger, J., Stauffer, B., Stocker, T. F., Raynaud, D., and Barnola, J.-M.: Atmospheric CO_2 concentrations over the last glacial termination, Science, 291, 112–114, 2001.

Morgan, V. I., Wookey, C. W., Li, J., van Ommen, T. D., Skinner, W., and Fitzpatrick, M. F.: Site information and initial results from deep ice drilling on Law Dome, Antarctica, J. Glaciol., 43, 3–10, 1997.

Morgan, V., Delmotte, M., van Ommen, T., Jouzel, J., Chappellaz, J., Woon, S., Masson-Delmotte, V., and Raynaud, D.: The timing of events in the last deglaciation from a coastal east Antarctic core, Science, 297, 1862–1864, 2002.

Mulvaney, R., Alemany, O., and Possenti, P.: The Berkner Island (Antarctica) ice-core drilling project, Ann. Glaciol., 47, 115–124, 2007.

Mulvaney, R., Abram, N. J., Hindmarsh, R. C. A., Arrowsmith, C., Fleet, L., Triest, J., Sime, L. C., Alemany, O., and Foord, S.: Recent Antarctic peninsula warming relative to Holocene climate and ice shelf history, Nature, 489, 141–144, 2012.

NEEM Community Members: Eemian interglacial reconstructed from a Greenland folded ice core, Nature, 493, 489–494, 2013.

Nikolaiev, V. I., Kotlyakov, V. M., and Smirnov, K. E.: Isotope studies of the ice from the Komsolmoskaia station, Antarctica, data of glaciological studies, USSR Acad. Sci., 63, 97–102, 1988.

NorthGRIP community members: High resolution climate record of the Northern Hemisphere back to the last interglacial period, Nature, 431, 147–151, 2004.

Oeschger, H.: The contribution of ice core studies to the understanding of environmental processes, in: Greenland Ice Cores: Geophysics, Geochemistry, and the Environment, Geophysical Monograph 33, AGU, Washington, D.C., 9–17, 1985.

Oeschger, H., Alder, B., and Langway Jr., C. C.: Radiocarbon dating of ice, Earth Planet. Sc. Lett., 1, 49–54, 1966.

Oeschger, H., Alder, B., and Langway Jr., C. C.: An in situ gas extraction system to radiocarbon date glacier ice, USA CRREL Research Report 236, October 1967, J. Glaciol., 6, 939–942, 1967.

Oeschger, H., Beer, J., Siegenthaler, U., Stauffer, B., Dansgaard, W., and Langway, C. C.: Late climate history from ice cores, in: Climate Processes and Climate Sensitivity, edited by: Hansen, J. E. and Takahashi, T., Geophysical Monograph 29, Maurice Ewing vol. 5, AGU, Washington, D.C., 299–306, 1984.

Parrenin, F., Jouzel, J., Waelbroeck, C., Ritz, C., and Barnola, J. M.: Dating the Vostok ice core by an inverse method, J. Geophys. Res., 106, 31837–31851, 2001.

Parrenin, F., Rémy, F., Ritz, C., Siegert, M. J., and Jouzel, J.: New modeling of the Vostok ice flow line and implication for the glaciological chronology of the Vostok ice core, J. Geophys. Res., 109, D20102, doi:10.1029/2004JD004561, 2004.

Parrenin, F., Barnola, J.-M., Beer, J., Blunier, T., Castellano, E., Chappellaz, J., Dreyfus, G., Fischer, H., Fujita, S., Jouzel, J., Kawamura, K., Lemieux-Dudon, B., Loulergue, L., Masson-Delmotte, V., Narcisi, B., Petit, J.-R., Raisbeck, G., Raynaud, D., Ruth, U., Schwander, J., Severi, M., Spahni, R., Steffensen, J. P., Svensson, A., Udisti, R., Waelbroeck, C., and Wolff, E.: The EDC3 chronology for the EPICA Dome C ice core, Clim. Past, 3, 485–497, doi:10.5194/cp-3-485-2007, 2007.

Parrenin, F., Masson-Delmotte, V., Kohler, P., Raynaud, D., Paillard, D., Schwander, J., Barbante, C., Landais, A., Wegner, A., and Jouzel, J.: Synchronous change of atmospheric CO_2 and Antarctic temperature during the last deglacial warming, Science, 339, 1060–1063, doi:10.1126/science.1226368, 2013.

Paterson, W. S. B., Koerner, R. M., Fisher, D., Johnsen, S. J., Clausen, H. B., Dansgaard, W., Bucher, P., and Oeschger, H.:. An oxygen-isotope climatic record from the Devon Island ice cap, Arctic Canada, Nature, 266, 508–511, 1977.

Petit, J. R., White, J. W. C., Young, N. W., Jouzel, J., and Korotkevich, Y. S.: Deuterium excess in recent Antarctic snow, J. Geophys. Res., 96, 5113–5122, 1991.

Petit, J. R., Jouzel, J., Raynaud, D., Barkov, N. I., Barnola, J. M., Basile, I., Bender, M., Chappellaz, J., Davis, J., Delaygue, G., Delmotte, M., Kotyakov, V. M., Legrand, M., Lipenkov, V. Y., Lorius, C., Pépin, L., Ritz, C., Saltzman, E., and Stievenard, M.: Climate and atmospheric history of the past 420 000 years from the Vostok ice core, Antarctica, Nature, 399, 429–436, 1999.

Pol, K., Masson-Delmotte, V., Johnsen, S. J., Jouzel, J., Cattani, O., Durand, G., Falourd, S., Minster, B., Parrenin, F., Ritz, C., Steen-Larsen, H. C., and Stenni, B.: New MIS 19 EPICA Dome C high resolution deuterium data: hints for a problematic preservation of climate variability in the "oldest ice", Earth Planet. Sc. Lett., 298, 95–103, 2010.

Raisbeck, G. M., Yiou, F., Fruneau, M., Loiseaux, J. M., Lieuvin, M., Ravel, J. C., and Lorius, C.: Cosmogenic Be-10 concentrations in Antarctic ice during the past 30 000 years, Nature, 292, 825–826, 1981.

Raisbeck, G. M., Yiou, F., Cattani, O., and Jouzel, J.: Be-10 evidence for the Matuyama–Brunhes geomagnetic reversal in the EPICA Dome C ice core, Nature, 444, 82–84, 2006.

Raisbeck, G. M., Yiou, F., Jouzel, J., and Stocker, T. F.: Direct north–south synchronization of abrupt climate change record in ice cores using Beryllium 10, Clim. Past, 3, 541–547, doi:10.5194/cp-3-541-2007, 2007.

Ramirez, E., Hoffmann, G., Taupin, J. L., Francou, B., Ribstein, P., Caillon, N., Landais, A., Petit, J. R., Pouyaud, B., Schotterer, U., and Stiévenard, M.: A new Andean deep ice core from the Illimani (6350 m), Bolivia, Earth Planet. Sc. Lett., 212, 337–350, 2003.

Rasmussen, S. O., Andersen, K. K., Svensson, A. M., Steffensen, J. P., Vinther, B. M., Clausen, H. B., Siggaard-Andersen, M.-L., Johnsen, S. J., Larsen, L. B., Dahl-Jensen, D., Bigler, M., Rothlisberger, R., Fischer, H., Goto-Azuma, K., Hansson, M. E., and Ruth, U.: A new Greenland ice core chronology for the last glacial termination, J. Geophys. Res., 111, D06102, doi:10.1029/2005JD006079, 2006.

Raynaud, D. and Lorius, C.: Climatic implications of total gas content in ice at Camp Century, Nature, 243, 283–284, 1973.

Raynaud, D., Chappellaz, J., Barnola, J. M., Korotkevich, Y. S., and Lorius, C.: Climatic and CH4-cycle implications of glacial–interglacial CH_4 change in the Vostok ice core, Nature, 333, 655–657, 1988.

Raynaud, D., Jouzel, J., Chappellaz, J., Delmas, R. J., and Lorius, C.: The ice record of greenhouse gases, Science, 259, 926–934, 1993.

Raynaud, D., Barnola, J. M., Souchez, R., Lorrain, R., Petit, J. R., Duval, P., and Lipenkov, V. Y.: Palaeoclimatology – the record for marine isotopic stage 11, Nature, 436, 39–40, 2005.

Raynaud, D., Lipenkov, V., Lemieux-Dudon, B., Duval, P., Loutre, M. F., and Lhomme, N.: The local insolation signature of air content in Antarctic ice, a new step toward an absolute dating of ice records, Earth Planet. Sc. Lett., 261, 337–349, 2007.

Reeh, N., Oerter, H., and Thomsen, H. H.: Comparison between Greenland ice-margin and ice-core oxygen-18 records, Ann. Glaciol., 35, 136–144, 2002.

Reeves, C. E., Sturges, W. T., Sturrock, G. A., Preston, K., Oram, D. E., Schwander, J., Mulvaney, R., Barnola, J.-M., and Chappellaz, J.: Trends of halon gases in polar firn air: implications for their emission distributions, Atmos. Chem. Phys., 5, 2055–2064, doi:10.5194/acp-5-2055-2005, 2005.

Risi, C., Bony, S., Vimeux, F., and Jouzel, J.: Water stable isotopes in the LMDZ4 General Circulation Model: model evaluation for present day and past climates and applications to climatic interpretation of tropical isotopic records, J. Geophys. Res., 115, D12118, doi:10.1029/2009JD013255, 2010.

Ruddiman, W. F. and Raymo, M. E.: A methane-based time scale for Vostok ice, Quaternary Sci. Rev., 22, 141–155, 2003.

Salamatin, A. N., Lipenkov, V. Y., Barkov, N. I., Jouzel, J., Petit, J. R., and Raynaud, D.: Ice core age dating and paleothermometer calibration on the basis of isotopes and temperature profiles from deep boreholes at Vostok station (East Antarctica), J. Geophys. Res., 103,8963–8977, 1998.

Schaefer, H., Whiticar, M. J., Brook, E. J., Petrenko, V. V., Ferretti, D. F., and Severinghaus, J. P.: Ice record of $\delta^{13}C$ for atmospheric CH_4 across the Younger-Dryas-Preboreal transition, Science, 313, 1109–1112, 2006.

Schilt, A., Baumgartner, M., Blunier, T., Schwander, J., Spahni, R., Fischer, H., and Stocker, T. F.: Glacial–interglacial and millennial-scale variations in the atmospheric nitrous oxide concentration during the last 800 000 years, Quaternary Sci. Rev., 29, 182–192, 2009.

Schmitt, J., Schneider, R., Elsig, J., Leuenberger, D., Lourantou, A., Chappellaz, J., Këhler, P., Joos, F., Stocker, T. F., Leuenberger, M., and Fischer, H.: Carbon isotope constraints on the deglacial CO_2 rise from ice cores, Science, 336, 711–714, 2012.

Schwander, J., Sowers, T., Barnola, J. M., Blunier, T., Malaizé, B., and Fuchs, A.: Age scale of the air in the summit ice: implication for glacial–interglacial temperature change, J. Geophys. Res., 102, 19483–19494, 1997.

Schytt, V.: Norwegian-British-Swedish Antarctic Expedition 1949–1952, Scientific Results 4, Glaciology II, Norsk Polarinstitut, Oslo, Norway, 1958.

Severinghaus, J. P. and Battle, M.: Fractionation of gases in polar ice during bubble close-off: new constraints from firn air Ne, Kr, and Xe observations, Earth Planet. Sc. Lett., 244, 474–500, 2006.

Severinghaus, J. P. and Brook, E.: Simultaneous tropical-Arctic abrupt climate change at the end of the last glacial period inferred from trapped air in polar ice, Science, 286, 930–934, 1999.

Severinghaus, J. P., Brook, E. J., Sowers, T., and Alley, R. B.: Gaseous thermal diffusion as a gas-phase stratigraphic marker of abrupt warmings in ice core climate records, 157, EOS Supplement AGU Spring meeting, San Francisco, 1996.

Severinghaus, J. P., Sowers, T., Brook, E., Alley, R. B., and Bender, M. L.: Timing of abrupt climate change at the end of the Younger Dryas interval from thermally fractionated gases in polar ice, Nature, 391, 141–146, 1998.

Severinghaus, J. P., Beaudette, R., Headly, M. A., Taylor, K., and Brook, E. J.: Oxygen-18 of O_2 records the impact of abrupt climate change on terrestrial biosphere, Science, 324, 1431–1434, 2009.

Severinghaus, J. P., Wolff, E., and Brook, E. J.: Searching for the oldest ice, EOS T. Am. Geophys. Un., 91, 357–368, 2010.

Shackleton, N. J.: The 100 000-year ice-age cycle identified and found to lag temperature, carbon dioxide, and orbital eccentricity, Science, 289, 1897–1902, 2000.

Siegenthaler, U., Stocker, T. F., Monnin, E., Luthi, D., Schwander, J., Stauffer, B., Raynaud, D., Barnola, J.-M., Fischer, H., Masson-Delmotte, V., and Jouzel, J.: Stable carbon cycle–climate relationship during the Late Pleistocene, Science, 310, 1313–1317, 2005.

Sime, L. C., Tindall, J. C., Wolff, E. W., Connolley, W. M., and Valdes, P. J.: Antarctic isotopic thermometer during a CO_2 forced warming event, J. Geophys. Res., 113, D24119, doi:10.1029/2008JD010395, 2008.

Sime, L. C., Wolff, E. W., Oliver, K. I. C., and Tindall, J. C.: Evidence for warmer interglacials in East Antarctic ice cores, Nature, 462, 342–346, doi:10.1038/nature08564, 2009.

Sime, L. C., Risi, C., Tindall, J. C., Sjolte, J., Wolff, E. W., Masson-Delmotte, V., and Capron, E.: Warm climate isotopic simulations: what do we learn aboutinterglacial signals in Greenland ice cores?, Quaternary Sci. Rev., 67, 59–80, 2013.

Simonsen, S. B., Johnsen, S. J., Popp, T. J., Vinther, B. M., Gkinis, V., and Steen-Larsen, H. C.: Past surface temperatures at the NorthGRIP drill site from the difference in firn diffusion of water isotopes, Clim. Past, 7, 1327–1335, doi:10.5194/cp-7-1327-2011, 2011.

Sorge, E.: Glaziologische Untersuchungen in Eismitte (Glaciological research at Eismitte), in: Wissenschaftliche Ergebnisse der Deutschen Groenland Expedition Alfred Wegener 1929 und 1930–31, F. A. Brokaus, Leipzig, Germany, 3, 270 pp., 1935.

Souchez, R. and Jouzel, J.: On the isotopic composition of δD and δ^{18}O of water and ice during freezing, J. Glaciol., 30, 369–372, 1984.

Sowers, T.: N_2O record spanning the penultimate deglaciation from Vostok ice core, J. Geophys. Res., 106, 31903–31914, 2001.

Sowers, T., Bender, M., Raynaud, D., Korotkevich, Y. S., and Orchardo, J.: The delta ^{18}O of atmospheric O_2 from air inclusions in the vostok ice core: timing of CO2 and ice volume changes during the penultimate deglaciation, Paleoceanography, 6, 679–696, 1991.

Sowers, T., Alley, R. B., and Jubenville, J.: Ice core records of atmospheric N_2O covering the last 106 000 years, Science, 301, 945–948, 2003.

Spahni, R., Chappellaz, J., Stocker, T. F., Loulergue, L., Hausammann, G., Kawamura, K., Flückiger, J., Schwander, J., Raynaud, D., Masson-Delmotte, V., and Jouzel, J.: Atmospheric methane and nitrous oxide of the late Pleistocene from Antarctic ice cores, Science, 310, 1317–1321, 2005.

Stauffer, B., Fischer, G., Neftel, A., and Oeschger, H.: Increase of atmospheric methane recorded in Antarctic ice core, Science, 229, 1386–1388, 1985.

Stauffer, B., Lochbronner, E., Oeschger, H., and Schwander, J.: Methane concentration in the glacial atmosphere was only half that of the preindustrial holocene, Nature, 332, 812–814, 1988.

Stauffer, B., Blunier, T., Dällenbach, A., Indermühle, A., Scwander, J., Stocker, T. F., Tschumi, J., Chappellaz, J., Raynaud, D., Hammer, C. U., and Clausen, H. B.: Atmospheric CO_2 concentration and millennial scale climate change during the last glacial period, Nature, 392, 59–62, doi:10.1038/32133, 1998.

Steffensen, J. P., Andersen, K. K., Bigler, M., Clausen, H. B., Dahl-Jensen, D., Fischer, H., Goto-Azuma, K., Hansson, M., Johnsen, S. J., Jouzel, J., Masson-Delmotte, V., Popp, T., Rasmussen, S. O., Rothlisberger, R., Ruth, U., Stauffer, B., Siggaard-Andersen, M.-L., Sveinbjörnsdóttir, A. E., Svensson, A., and White, J. W. C.: High resolution ice core data show abrupt climate change happens in few years, Science, 321, 680–689, 2008.

Steig, E., Brook, E. J., White, J. W. C., Sucher, C. M., Bender, M. L., Lehman, S. J., Morse, D. L., Waddigton, E. D., and Clow, G. D.: Synchronous climate changes in Antarctica and the North Atlantic, Science, 282, 92–95, 1998.

Stenni, B., Masson, V., Johnsen, S. J., Jouzel, J., Longinelli, A., Monnin, E., Roethlisberger, R., and Selmo, E.: An oceanic cold reversal during the last deglaciation, Science, 293, 2074–2077, 2001.

Stenni, B., Jouzel, J., Masson-Delmotte, V., Röthlisberger, R., Castellano, E., Cattani, O., Falourd, S., Johnsen, S. J., Longinelli, A., Sachs, J. P., Selmo, E., Souchez, R., Steffensen, J. P., and Udisti, R.: A late-glacial high resolution site and source temperature record derived from the EPICA Dome C isotope records (East Antarctica), Earth Planet. Sc. Lett., 217, 183–195, 2003.

Stenni, B., Masson-Delmotte, V., Selmo, E., Oerter, H., Meyer, H., Rothlisberger, R., Jouzel, J., Cattani, O., Falourd, S., Fischer, H., Hoffmann, G., Iacumin, P., Johnsen, S., and Minster, B.: The deuterium excess records of EPICA Dome C and Dronning Maud Land ice cores (East Antarctica), Quaternary Sci. Rev., 29, 146–159, 2010.

Stenni, B., Buiron, D., Frezzotti, M., Albani, S., Barbante, C., Bard, E., Barnola, J. M., Baroni, M., Baumgartner, M., Bonazza, M., Capron, E., Castellano, E., Chappellaz, J., Delmonte, B., Falourd, S., Genoni, L., Iacumin, P., Jouzel, J., Kipfstuhl, S., Landais, A., Lemieux-Dudon, B., Maggi, V., Masson-Delmotte, V., Mazzola, C., Minster, B., Montagnat, M., Mulvaney, R., Narcisi, B., Oerter, H., Parrenin, F., Petit, J. R., Ritz, C., Scarchilli, C., Schilt, A., Schüpbach, S., Schwander, J., Selmo, E., Severi, M., Stocker, T. F., and Udisti, R.: Unified Antarctic and Greenland climate seesaw during the last deglaciation, Nat. Geosci., 4, 46–49, 2011.

Stocker, T. F. and Johnsen, S. J.: A minimum thermodynamic model for the bipolar seesaw, Paleoceanography, 18, 1087, doi:10.1029/2003PA000920, 2003.

Sturges, W. T., Penkett, S. A., Barnola, J. M., Chappellaz, J., Atlas, E., and Stroud, V.: A longterm record of carbonyl sulfide (COS) in two hemispheres from firn air measurements, Geophys. Res. Lett., 28, 4095–4098, 2001a.

Sturges, W. T., McIntyre, H. P., Penkett, S. A., Chappellaz, J., Barnola, J. M., Mulvaney, R., Atlas, E., and Stroud, V.: Methyl bromide, other brominated methanes and methyl iodide in polar firn air, J. Geophys. Res., 106, 1595–1606, 2001b.

Suwa, M. and Bender, M. L.: Chronology of the Vostok ice core constrained by O_2/N_2 ratios of occluded air, and its implication for the Vostok climate records, Quaternary Sci. Rev., 27, 1093–1106, 2008.

Suwa, M., von Fischer, J. C., Bender, M. L., Landais, A., and Brook, E. J.: Chronology reconstruction for the disturbed bottom section of the GISP2 and the GRIP ice cores: Implications for Termination II in Greenland, J. Geophys. Res., 111, D02101, doi:10.1029/2005JD006032, 2006.

Svensson, A., Andersen, K. K., Bigler, M., Clausen, H. B., Dahl-Jensen, D., Davies, S. M., Johnsen, S. J., Muscheler, R., Parrenin, F., Rasmussen, S. O., Röthlisberger, R., Seierstad, I., Steffensen, J. P., and Vinther, B. M.: A 60 000 year Greenland stratigraphic ice core chronology, Clim. Past, 4, 47–57, doi:10.5194/cp-4-47-2008, 2008.

Svensson, A., Bigler, M., Blunier, T., Clausen, H. B., Dahl-Jensen, D., Fischer, H., Fujita, S., Goto-Azuma, K., Johnsen, S. J., Kawamura, K., Kipfstuhl, S., Kohno, M., Parrenin, F., Popp, T., Rasmussen, S. O., Schwander, J., Seierstad, I., Severi, M., Steffensen, J. P., Udisti, R., Uemura, R., Vallelonga, P., Vinther, B. M., Wegner, A., Wilhelms, F., and Winstrup, M.: Direct linking of Greenland and Antarctic ice cores at the Toba eruption (74 ka BP), Clim. Past, 9, 749–766, doi:10.5194/cp-9-749-2013, 2013.

Swithinbank, C.: Norwegian-British-Swedish Antarctic Expedition 1949–1952, Scientific Results 3, Glaciology I, Norsk Polarinstitut, Oslo, Norway, 1957.

Taylor, K. C., Hammer, C. U., Alley, R. B., Clausen, H. B., Dahl-Jensen, D., Gow, A. J., Gundestrup, N. S., Kipfstuhl, J., Moore, J. C., and Waddington, E. D.: Electrical conductivity measurements from the GISP2 and GRIP Greenland ice cores, Nature, 366, 549–552, 1993.

Taylor, K. C., White, J. W. C., Severinghaus, J. P., Brook, E. J., Mayewski, P. A., Alley, R. B., Steig, E. J., Spencer, M. K., Meyerson, E., Meese, D. A., Lamorey, G. W., Grachev, A., Gow, A. J., and Barnett, B. A.: Abrupt climate change around 22 ka on the Siple coast of Antarctica, Quaternary Sci. Rev., 23, 7–15, 2004.

Thompson, L. G., Mosley-Thompson, E., Davis, M. E., Bolzan, J. F., Dai, J., Klein, L., Yao, T., Wu, X., Xie, Z., and Gundestrup, N.: Holocene–Late Pleistocene climatic ice core records from Qinghai-Tibetan Plateau, Science, 246, 474–477, 1989.

Thompson, L. G., Mosley-Thompson, E., Davis, M. E., Lin, P.-N., Henderson, K. A., Cole-Dai, J., Bolzan, J. F., and Liu, K.-B.: Late Glacial Stage and Holocene tropical ice core records from Huascaran, Peru, Science, 269, 46–50, 1995.

Thompson, L. G., Yao, T., Davis, M. E., Henderson, K. A., Mosley-Thompson, E., Lin, P.-N., Beer, J., Synal, H.-A., Cole-Dai, J., and Bolzan, J. F.: Tropical climate instability: the Last Glacial Cycle from a Qinghai-Tibetan ice core, Science, 276, 1821–1825, doi:10.1126/science.276.5320.1821, 1997.

Thompson, L. G., Davis, M. E., Mosley-Thompson, E., Sowers, T. A., Henderson, K. A., Zagorodnov, V. S., Lin, P.-N., Mikhalenko, V. N., Campen, R. K., Bolzan, J. F., Cole-Dai, J., and Francou, B.: A 25 000-year tropical climate history from bolivian ice cores, Science, 282, 1858–1864, 1998.

Ueda, H. T. and Talalay, P. G.: Fifty Years of Soviet and Russian Drilling Activity in Polar and Non-Polar Ice, Report ERDC/CRREL TR-07–20, US Army Engineer Research and Development Center Cold Regions Research and Engineering Laboratory, Hanover, USA, 130 pp., 2007.

Uemura, R., Yoshida, N., Kurita, N., Nakawo, M., and Watanabe, O.: An observation-based method for reconstructing ocean surface changes using a 340 000-year deuterium excess record from the Dome Fuji ice core, Antarctica, Geophys. Res. Lett., 31, L13216, doi:10.1029/2004GL019954, 2004.

Uemura, R., Masson-Delmotte, V., Jouzel, J., Landais, A., Motoyama, H., and Stenni, B.: Ranges of moisture-source temperature estimated from Antarctic ice cores stable isotope records over glacial–interglacial cycles, Clim. Past, 8, 1109–1125, doi:10.5194/cp-8-1109-2012, 2012.

Vimeux, F., Masson, V., Jouzel, J., Stiévenard, M., and Petit, J. R.: Evidence of a link between deuterium excess in polar snow and ocean conditions over a full glacial–interglacial cycle, Nature, 398, 410–413, 1999.

Vimeux, F., Cuffey, K., and Jouzel, J.: New insights into Southern Hemisphere temperature changes from Vostok ice cores using deuterium excess correction, Earth Planet. Sc. Lett., 203, 829–843, 2002.

Vinther, B. M., Buchardt, S. L., Clausen, H. B., Dahl-Jensen, D., Johnsen, S. J., Andersen, K. K., Blunier, T., Rasmussen, S. O., Steffensen, J. P., Svensson, A., Fisher, D. A., Koerner, R. M., Raynaud, D., and Lipenkov, V.: Holocene thinning of the Greenland ice sheet, Nature, 461, 385–388, 2009.

Waelbroeck, C., Jouzel, J., Labeyrie, L., Lorius, C., Labracherie, M., Stiévenard, M., and Barkov, N. I.: Comparing the Vostok ice deuterium record and series from Southern Ocean core MD 88–770 over the last two glacial–interglacial cycles, Clim. Dynam., 12, 113–123, 1995.

Waelbroeck, C., Jouzel, J., Parrenin, F., Masson-Delmotte, V., and Genty, D.: Tranferring radiometric dating of the last interglacial sea level high stand to marine and ice core records, Earth Planet. Sc. Lett., 265, 183–194, 2008.

WAIS Divide Project Members: Onset of deglacial warming in West Antarctica driven by local orbital forcing, Nature, 500, 440–444, doi:10.1038/nature12376, 2013.

Watanabe, O., Jouzel, J., Johnsen, S., Parrenin, F., Shoji, H., and Yoshida, N.: Homogeneous climate variability accross East Antarctica over the last three glacial cycles, Nature, 422, 509–512, 2003.

Weart, S.: The discovery of global warming, Web hypertext (250 000 words with extensive bibliography and illustrations and more than 2000 hyperlinks), revised annually 2003 http://www.aip.org/history/climate, 2008.

Werner, M., Mikolajewicz, U., Heimann, M., and Hoffmann, G.: Borehole versus isotope temperatures on Greenland: seasonality does matter, Geophys. Res. Lett., 27, 723–726, 2000.

Werner, M., Langebroek, P. M., Carlsen, T., Herold, M., and Lohmann, G.: Stable water isotopes in the ECHAM5 general circulation model: toward high-resolution isotope modeling on a global scale, J. Geophys. Res., 116, D15109, doi:10.1029/2011JD015681, 2011.

White, J. W. C., Johnsen, S. J., and Dansgaard, W.: The origin of Arctic precipitation as deduced from its deuterium excess, Ann. Glaciol., 10, 219–220, 1988.

Winkler, R., Landais, A., Sodemann, H., Dümbgen, L., Prié, F., Masson-Delmotte, V., Stenni, B., and Jouzel, J.: Deglaciation records of ^{17}O-excess in East Antarctica: reliable reconstruction of oceanic normalized relative humidity from coastal sites, Clim. Past, 8, 1–16, doi:10.5194/cp-8-1-2012, 2012.

Xiao, C., Li, Y., Allison, I., Hou, S., Dreyfus, G., Barnola, J. M., Ren, J., Bian, L., and Kameda, T.: Surface characteristics at Dome A, Antarctica: first measurements and a guide to future ice coring sites, Ann. Glaciol., 48, 82–87, 2008.

Yao, T., Petit, J. R., Jouzel, J., Lorius, C., and Duval, P.: Climatic record from an ice margin area in East Antarctica, Ann. Glaciogeol., 14, 323–327, 1990.

Yao, T., Thompson, L. G., Mosbrugger, V., Zhang, F., Ma, Y., Luo, T., Xu, B., Yang, X., Joswiak, D. R., Wang, W., Joswiak, M. E., Devkota, L. P., Tayal, S., Jilani, R., and Fayziev, R.: Third Pole Environment (TPE), Environ. Develop., 3, 52–64, 2012.

Zardini, D., Raynaud, D., Scharffe, D., and Seiler, W.: N_2O measurements of air extracted from Antarctic ice cores: implication on atmospheric N_2O back to the last glacial-interglacial transition, J. Atmos. Chem., 8, 189–201, 1989.

Clim. Past, 13, 1259–1267, 2017
https://doi.org/10.5194/cp-13-1259-2017

Climate of the Past
Open Access

The Plio-Pleistocene climatic evolution as a consequence of orbital forcing on the carbon cycle

Didier Paillard[1,*]

[1]Laboratoire des Sciences du Climat et de l'Environnement (LSCE, UMR 8212), IPSL-CEA-CNRS-UVSQ, Centre d'Etudes de Saclay, 91191, Gif-sur-Yvette, France
[*] *Invited contribution by Didier Paillard, recipient of the EGU Milutin Milankovic Medal 2013.*

Correspondence to: Didier Paillard (didier.paillard@lsce.ipsl.fr)

Received: 9 January 2017 – Discussion started: 11 January 2017
Revised: 10 August 2017 – Accepted: 21 August 2017 – Published: 25 September 2017

Abstract. Since the discovery of ice ages in the 19th century, a central question of climate science has been to understand the respective role of the astronomical forcing and of greenhouse gases, in particular changes in the atmospheric concentration of carbon dioxide. Glacial–interglacial cycles have been shown to be paced by the astronomy with a dominant periodicity of 100 ka over the last million years, and a periodicity of 41 ka between roughly 1 and 3 million years before present (Myr BP). But the role and dynamics of the carbon cycle over the last 4 million years remain poorly understood. In particular, the transition into the Pleistocene about 2.8 Myr BP or the transition towards larger glaciations about 0.8 Myr BP (sometimes referred to as the mid-Pleistocene transition, or MPT) are not easily explained as direct consequences of the astronomical forcing. Some recent atmospheric CO_2 reconstructions suggest slightly higher pCO_2 levels before 1 Myr BP and a slow decrease over the last few million years (Bartoli et al., 2011; Seki et al., 2010). But the dynamics and the climatic role of the carbon cycle during the Plio-Pleistocene period remain unclear. Interestingly, the $\delta^{13}C$ marine records provide some critical information on the evolution of sources and sinks of carbon. In particular, a clear 400 kyr oscillation has been found at many different time periods and appears to be a robust feature of the carbon cycle throughout at least the last 100 Myr (e.g. Paillard and Donnadieu, 2014). This oscillation is also visible over the last 4 Myr but its relationship with the eccentricity appears less obvious, with the occurrence of longer cycles at the end of the record, and a periodicity which therefore appears shifted towards 500 kyr (see Wang et al., 2004). In the following we present a simple dynamical model that provides an explanation for these carbon cycle variations, and how they relate to the climatic evolution over the last 4 Myr. It also gives an explanation for the lowest pCO_2 values observed in the Antarctic ice core around 600–700 kyr BP. More generally, the model predicts a two-step decrease in pCO_2 levels associated with the 2.4 Myr modulation of the eccentricity forcing. These two steps occur respectively at the Plio-Pleistocene transition and at the MPT, which strongly suggests that these transitions are astronomically forced through the dynamics of the carbon cycle.

1 Introduction

The idea that the orbital parameters of the Earth may influence climate has a long history, linked mostly to the development of theories of ice ages (e.g. Paillard, 2015). But it is clear from geological records that astronomical climatic variations have occurred throughout the Earth's history, with or without ice being present on Earth. It is therefore certain that the astronomical parameters are influencing climate through other mechanisms than the growth and decay of ice sheets. This is well known concerning records of monsoons or records of low-latitude precipitations, which are strongly influenced by precession. A very illustrative example is given by the Mediterranean sapropels (Lourens et al., 1996; Hilgen et al., 1999) which are used to calibrate the $^{40}Ar\,/\,^{39}Ar$ radiochronometers (Kuiper et al., 2008). Similarly, a 400 kyr oscillation is observed in the $\delta^{13}C$ of the foraminifera recovered from marine records, throughout most of the Cenozoic (Pälike et al., 2006; Cramer et al., 2003; Sexton et al., 2011; Billups et al., 2004; Wang et al., 2010). This oscillation is present in the benthic records, but also in many planktic ones, suggesting that these δ^{13}C variations are linked to global ocean δ^{13}C changes. This persistent oscillation was recently used to reconstruct the evolution of the Earth's carbon over the last 100 Myr (Paillard and Donnadieu, 2014). A key difficulty is to understand the dynamics of this cycle. In particular, during the last million years these oscillations appear to stretch and the relationship with eccentricity becomes less clear (e.g. Wang et al., 2004, 2010), as illustrated in Fig. 1.

Before 1 Myr BP when ice sheets remained medium sized, the cyclicity appears locked to eccentricity, with high eccentricity values associated with decreasing or low values in δ^{13}C. This phase relationship appears consistent with earlier time periods, with the chronology of Cenozoic marine cores being sometimes based on the association of high eccentricity and low δ^{13}C values (e.g. Pälike et al., 2006; Cramer et al., 2003). A simple deduction is that, most probably, the dynamics behind this oscillation are essentially stable and linked to the astronomical forcing before 1 Myr BP, but it is strongly disturbed by the large Quaternary glaciations afterwards. This observation has major implications on the possible mechanisms, as we will see further on.

There is no consensus on the cause of these δ^{13}C oscillations, but monsoons or the associated low-latitude precipitations are known to respond to precessional forcing, and therefore to be modulated by the 400 kyr eccentricity cycles. Still many factors may contribute to the evolution of the carbon cycle on these timescales, like erosion, vegetation dynamics, ocean biogeochemical or dynamical changes. It was therefore suggested that the δ^{13}C cycles could be caused by the modulation of weathering in monsoonal regions (Pälike et al., 2006) or by ecological shifts in marine organisms, possibly linked to nutrient availability (Wang et al., 2004; Rickaby et al., 2007). It is worth emphasizing that during the last million years, if the link with eccentricity is less obvious, there are clear indications that these δ^{13}C shifts are associated with major changes in the Earth carbon cycle. For instance, carbonate deposition exhibits major changes, well correlated with these global δ^{13}C changes (Bassinot et al., 1994; Wang et al., 2004), and the record of atmospheric $p\mathrm{CO_2}$ from Antarctic ice cores also shows a 10 to 20 ppm long-term modulation with a minimum level around 0.6–0.7 Myr BP and a maximum around 0.3–0.4 Myr BP (Lüthi et al., 2008) in phase with the long-term carbonate preservation cycle. A mechanistic modelling of these 400 to 500 kyr cycles is therefore a critical missing element in our understanding of climate–carbon evolution over the Plio-Pleistocene period.

With a simple ocean box model (Russon et al., 2010), it was shown that silicate weathering alone could not account for the simultaneously observed rather large δ^{13}C changes (> 0.4 ‰) and rather small $p\mathrm{CO_2}$ variations (< 20 ppm) in this frequency band during the last million years. Furthermore, with silicate weathering only, the model-predicted phase relationships were also inconsistent with observations of δ^{13}C, carbonate deposition and $p\mathrm{CO_2}$. Changes in organic matter fluxes are therefore a necessary ingredient in order to account for the observed rather large δ^{13}C changes. A possible mechanism could therefore be linked to ocean organic matter burial, associated with changes in nutrient supply or ecological shifts (Rickaby et al., 2007). But it is then very difficult to explain why this mechanism would change drastically with the occurrence of major glaciations, as suggested by Fig. 1. We will therefore build our model on a different perspective, involving a more direct link between monsoons and organic matter burial, that should be strongly affected by sea level changes.

Organic matter burial takes place mostly on the continental shelves. Recent reassessments of riverine carbon fluxes to the ocean have emphasized the role of the erosion of continental organic carbon in the overall balance (e.g. Galy et al., 2007; Hilton et al., 2015). When investigating the influence of monsoons on the carbon cycle, it is natural to have a closer look at river discharges in monsoonal areas. Carbon budgets on major present-day erosional systems have provided some contrasted results, with riverine organic matter being either a net carbon source for the ocean (Burdige, 2005) or a net sink through organic carbon burial in sedimentary fans (Galy et al., 2007). The first study was mostly based on the Amazon basin, while the second estimation is from the Himalayan system. The differences are likely linked to different river basin configurations and different sedimentary deposition dynamics. This dramatically highlights the impact of geomorphology on terrestrial organic carbon burial, and suggests that the long-term global balance might be different in a context of large glacial–interglacial sea level variations like the last million years, when compared to earlier periods with much smaller sea level changes. Our conceptual model is therefore built on the impact of monsoon-driven terrestrial organic matter burial on the global carbon cycle.

2 Conceptual model

We are interested in the evolution of the global Earth carbon, that is, the carbon content of the atmosphere, the ocean and the biosphere, which amounts today approximately to $C = 40\,000$ PgC (petagrams of carbon, i.e. 10^{15} gC). This evolution results from possible imbalances between the volcanic inputs V, the oceanic carbonate deposition flux D associated with silicate weathering and its alkalinity flux to the ocean W, and the organic carbon burial B. Our model equations are

$$\mathrm{d}C/\mathrm{d}t = V - B - D, \tag{1a}$$

$$\mathrm{d}A/\mathrm{d}t = W - 2D, \tag{1b}$$

where the second equation represents the alkalinity balance, assuming that alkalinity is dominated by carbonate alkalinity. Silicate weathering W takes one $\mathrm{CO_2}$ molecule from the atmosphere, or more precisely one $\mathrm{H_2CO_3}$ from precipitation

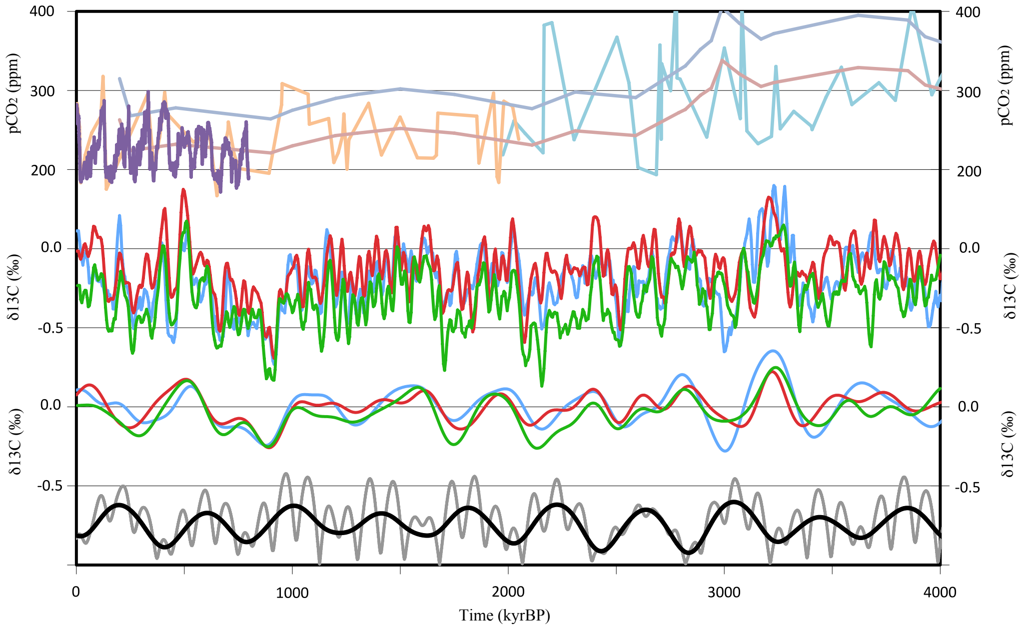

Figure 1. From top to bottom: pCO_2 records from Antarctic ice cores (purple: Lüthi et al., 2008); from boron isotopes in marine cores (orange: Hönisch et al., 2009; light blue: Bartoli et al., 2011) and alkenone isotopes (pink and blue lines for the min and max envelope, from Seki et al., 2010). δ^{13}C in cores 1143 (red: Wang et al., 2004); 849 (blue: Mix et al., 1995); 846 (green: Shackleton et al., 1995). The same δ^{13}C records filtered at 400 kyr (bandpass = 2.5 Myr^{-1}), eccentricity (grey, from Laskar et al., 2004) and filtered eccentricity (black).

and runoff, and transforms it into a HCO_3^- that finally reaches the ocean. When considering the "global" Earth surface budget C which includes the ocean and atmosphere, W has therefore no direct effect on C and does not appear in Eq. (1a) for $\mathrm{d}C/\mathrm{d}t$, but only as a source of alkalinity in Eq. (1b). On timescales larger than several millennia, if we assume that the oceanic calcium concentration does not change significantly over the last few millions of years, carbonate compensation will restore the oceanic carbonate content. Therefore, to first order, we can write

$$\mathrm{d}[CO_3^{2-}]/\mathrm{d}t = \mathrm{d}(A - C)/\mathrm{d}t = 0 = W - D - V + B.$$

Solving for D, this leads to the long-term evolution equation for carbon:

$$\mathrm{d}C/\mathrm{d}t = 2(V - B) - W. \quad (2a)$$

For simplicity, we will assume that the main stabilizer of the carbon system is the silicate weathering, with a fixed relaxation time τ_C, i.e. $W = C/\tau_C$. Solving the present-day equilibrium with $\delta^{13}_{Eq} = 0\,‰$ as a typical value for carbonates, we easily deduce typical equilibrium values for the fluxes: $B_0 = V/5$; $C_{Eq} = (8/5)\tau_C V = 40\,000$ PgC. If we assume a relaxation time τ_C of 200 kyr (Archer et al., 1997), we obtain $V = (5/8)C_{Eq}/\tau_C = 125$ TgC yr^{-1} and $B_0 = 25$ TgC yr^{-1}. For a larger value $\tau_C = 400$ kyr (Archer, 2005), we would get $V = 62$ TgC yr^{-1}. There is no consensus on the actual total carbon emissions from volcanism (including all aerial and submarine sources), but these values for V (or τ_C) span more or less the range of current estimates from about 40 to 175 TgC yr^{-1} (Burton et al., 2013).

It must be stressed that B stands for all organic carbon fluxes, whether they correspond to organic carbon burial (positive contributions to B) or to organic matter oxidation (negative contributions to B). While the long-term average equilibrium value B_0 needs to be positive to account for the isotopic balance as shown above, this is not necessarily always the case for the instantaneous values of B, as we will illustrate in what follows with the astronomical forcing. Indeed, B represents a sum of positive and negative terms whose individual absolute magnitudes are much larger than the long-term net value B_0. For instance, the oxidation of petrogenic organic carbon alone will contribute negatively to B, with a magnitude that may be as large as 40 TgC yr^{-1} (Blair et al., 2003).

The isotopic ^{13}C budget can be written as

$$\mathrm{d}/\mathrm{d}t(C\delta^{13}\mathrm{C}) = V\delta^{13}V - B\delta^{13}B - D\delta^{13}D,$$

where δ^{13}C is the isotopic composition of ocean carbon, $\delta^{13}V$ the isotopic composition of the volcanic carbon input, $\delta^{13}B$ the isotopic composition of organic matter and $\delta^{13}D$ the isotopic composition of marine carbonates. This can be rewritten as

$$C(\mathrm{d}\delta^{13}\mathrm{C}/\mathrm{d}t) + (\mathrm{d}C/\mathrm{d}t)\delta^{13}\mathrm{C} = V\delta^{13}V - B\delta^{13}B - D\delta^{13}D$$

or

$$\begin{aligned}C(\mathrm{d}\delta^{13}\mathrm{C}/\mathrm{d}t) &= V\delta^{13}V - B\delta^{13}B - D\delta^{13}D\\ &\quad -(V-B-D)\delta^{13}\mathrm{C}\\ &= V(\delta^{13}V-\delta^{13}\mathrm{C}) - B(\delta^{13}B-\delta^{13}\mathrm{C})\\ &\quad - D(\delta^{13}D-\delta^{13}\mathrm{C}).\end{aligned}$$

If we neglect isotopic fractionation during carbonate precipitation (in other words, $\delta^{13}D = \delta^{13}\mathrm{C}$) and more generally during carbonate compensation, we finally obtain

$$\mathrm{d}\delta^{13}\mathrm{C}/\mathrm{d}t = (V(\delta^{13}V-\delta^{13}\mathrm{C}) - B(\delta^{13}B-\delta^{13}\mathrm{C}))/C. \quad (2b)$$

In the following we will assume a constant $-5\,‰$ volcanic source $\delta^{13}V$, as well as a constant $-25\,‰$ organic matter value $\delta^{13}B$ (e.g. Porcelli and Turekian, 2010).

In order to translate the total carbon content C into an equivalent $p\mathrm{CO}_2$ level, we will use a simple scaling. Indeed, if we assume, to first order, that C may represent the carbon content of a well-mixed ocean, then from chemical equilibrium $p\mathrm{CO}_2$ should be proportional to $\left[\mathrm{HCO}_3^-\right]^2/\left[\mathrm{CO}_3^{2-}\right]$. After carbonate compensation (i.e. assuming that $\left[\mathrm{CO}_3^{2-}\right]$ remains constant) and considering that C is dominated by bicarbonates $\left[\mathrm{HCO}_3^-\right]$ under standard pH conditions, we end up with the approximate scaling that $p\mathrm{CO}_2$ varies roughly as C^2, or $p\mathrm{CO}_2 = 280\,(C/40\,000)^2$ (in ppm). To reproduce a multi-million year trend, we need to add one explicitly in the weathering relaxation: $W = C/\tau_\mathrm{C} = (\Delta C + C_\mathrm{Eq} - \gamma t)/\tau_\mathrm{C}$, with the coefficient γ set to $1.2\,\mathrm{TgC\,yr^{-1}}$ to obtain the desired $p\mathrm{CO}_2$ levels at the start of the simulation, i.e. about 350 ppm at 4 Myr BP, according to current estimates (Bartoli et al., 2011; Seki et al., 2010). The model is integrated from an arbitrary initial condition at 5 Myr BP and the first 1 Myr is discarded.

In the following, we describe how carbon burial B should vary with monsoons, and what consequences these variations have on the total carbon content C as well as on carbonate isotopes $\delta^{13}\mathrm{C}$. In order to represent the monsoon's response to astronomical forcing, we introduce a simple truncation of the precessional forcing:

$$F_0(t) = \max(0, -e\sin\omega),$$

where e is the eccentricity and ω the climatic precession.

Indeed, soil erosion or sediment transport are dominated by intense events, not by the average climate. Such a nonlinear response can be mimicked in a simple way by the above expression that accounts only for positive monsoonal forcing, not for a negative one. Consequently, the model will be influenced by the amplitude modulation of the precessional forcing, i.e. the eccentricity. To avoid useless parameters, we furthermore introduce the normalization

$$F = F_0/\mathrm{Max}(F_0) - \langle F_0/\mathrm{Max}(F_0)\rangle,$$

which results in a precessional forcing $F(t)$ with amplitude 1 and 0 mean.

We implicitly account for a slow terrestrial organic carbon reservoir (soil) as "buried organic carbon". It is reasonable to assume that monsoon or enhanced precipitation will favour primary production and soil formation. But this recent soil together with older soils and with petrogenic organic carbon (Galy et al., 2008) will be eroded and transported to the ocean through enhanced river discharges. If the corresponding carbon is remineralized in the ocean without too much burial in the alluvial fan, the net perturbation of the burial flux is likely to be negative (i.e. net "old" soil erosion and remineralization). We will refer to this case as the "Amazon-like" situation, with the perturbation $F(t)$ being subtracted to the baseline burial B_0 by writing $B = B_0 - aF(t)$. In contrast, if most of the organic carbon is buried and preserved in the sediment, then the perturbation is likely to be positive, since it induces a net "recent" soil formation and burial. We call this the "Himalayan-like" situation, with now $B = B_0 + aF(t)$. Before 1 Myr BP and the associated major sea level changes, the river fans and continental shelves should evolve mostly in a progradational way (see scheme in Fig. 3), a situation which a priori favours organic carbon remineralization, while aggradational situations are likely to be more frequent in the late Pleistocene, with therefore a possible temporary reversal of the organic carbon burial.

3 Results

Our first simulations, with $B = B_0 - aF(t)$, correspond to a perpetual "Amazon-like" situation. They correspond to experiment a (black lines) with no trend in the total carbon, and experiment b (blue lines), with an explicit linear trend in carbon. The value of the parameter a is chosen in order to obtain approximately the correct amplitude for these simulated 400 kyr oscillations ($a = 50\,\mathrm{TgC\,yr^{-1}}$). Still, as can be seen in Fig. 2, we obtain a surprisingly good match between the simulated and observed $\delta^{13}\mathrm{C}$, with overall very similar cycles. More specifically, the $\delta^{13}\mathrm{C}$ black and blue simulated curves are superimposed and almost undistinguishable, since the linear trend added to the carbon cycle has almost no impact on the $\delta^{13}\mathrm{C}$. They are both most of the time within the range of observed values (grey curves). The two main exceptions occur at about 0.3 and 2.3 Myr BP, with the simulated $\delta^{13}\mathrm{C}$ being significantly too high. In experiment a (black lines), $p\mathrm{CO}_2$ is oscillating around its equilibrium value, with two significant negative excursions occurring near 2.5 Myr BP and near 0.5 Myr BP. These lower values are directly linked to the ~ 2.4 Myr modulation of eccentricity. Obviously, with fixed or periodic parameters, this model cannot simulate a long-term decreasing trend in carbon. When explicitly adding such a linear decreasing trend (experiment b, blue lines), the two minima described above become two decreasing steps. The first one, occurring around

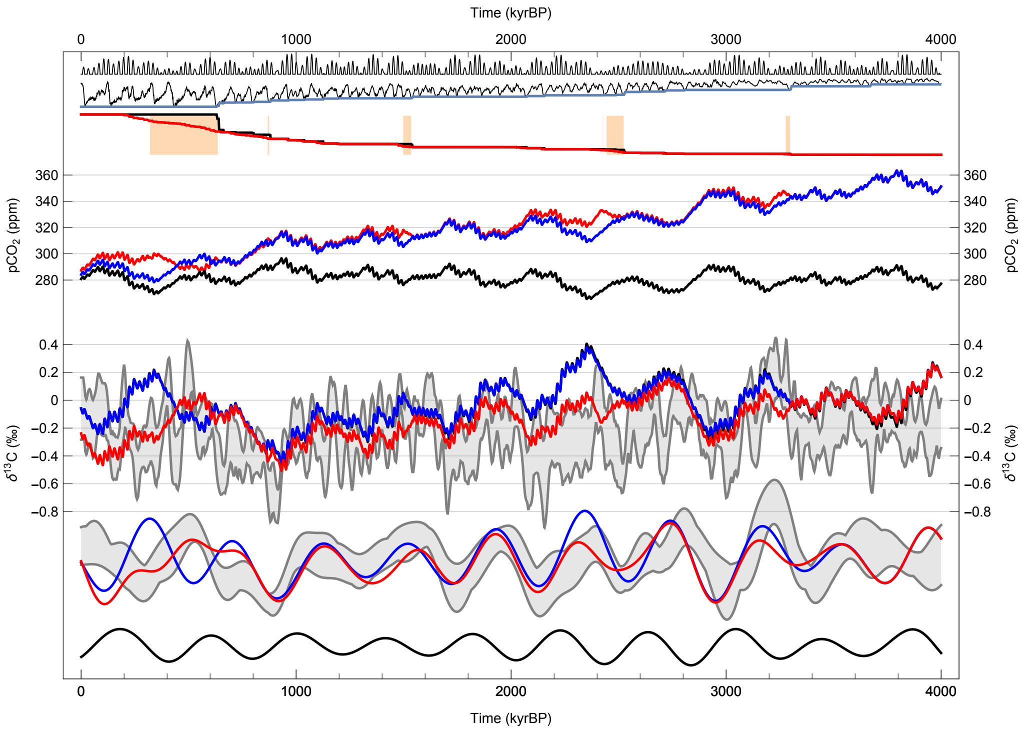

Figure 2. From top to bottom: precessional forcing $F_0(t) = \mathrm{Max}(0, -e\sin\omega)$ (black line) from Laskar et al. (2004). Sea level curve LR04 (black line) from Lisiecki and Raymo (2005) used to compute the river incision z_{MIN} defined as the previous sea level minima (blue line). The geomorphological variable s used from experiment c (red lines) relaxed to its prescribed maximum value $s_{\mathrm{MAX}} \sim z^3_{\mathrm{MIN}}$ (black line). The orange shaded areas correspond to the aggradation regimes (i.e. $s < 0.85 s_{\mathrm{MAX}}$). Total carbon C rescaled as $p\mathrm{CO}_2$ for experiments a (black, precessional forcing only), b (blue, similar experiment but with a linear trend in carbon), and c (red, using the geomorphological dynamics from Eq. 3). Carbon isotopic composition $\delta^{13}\mathrm{C}$ for experiments a (black), b (blue), and c (red). In grey, the min and max values of the $^{13}\mathrm{C}$ records from Fig. 1. The 400 kyr filtered values of $\delta^{13}\mathrm{C}$ results (blue and red) together with the range of filtered records (grey). The 400 kyr filtered eccentricity as in Fig. 1. In order to obtain these results, we chose $\tau_{\mathrm{C}} = 200$ kyr (Archer et al., 1997) or equivalently $V = 125\,\mathrm{TgC\,yr^{-1}}$. The trend (experiments b and c) is set to $\gamma = 1.2\,\mathrm{TgC\,yr^{-1}}$ to induce a drift from about 350 to about 280 ppm. The amplitude of the organic matter burial perturbation (experiments a, b and c) is set to $a = 50\,\mathrm{TgC\,yr^{-1}}$. The filling rate of the sedimentary reservoir (experiment c) is set to $b = (160\,\mathrm{kyr})^{-1}$. The model is integrated from an arbitrary initial condition at 5 Myr BP and the first 1 Myr is discarded.

2.8 Myr BP, is coincident with the Plio-Pleistocene transition and the development of Northern Hemisphere glaciations. The second one near 0.8 Myr BP is coincident with the mid-Pleistocene transition (MPT) and the significant amplification of glaciations. Note that the timing of these two steps is directly linked to the astronomical forcing: it does not depend at all on the specifics of the trend that we used here. Two similar $p\mathrm{CO}_2$ decreasing episodes are also seen in the data (Fig. 1), though it is difficult to associate them with a precise timing, due to the difficulties in accurately reconstructing $p\mathrm{CO}_2$ from indirect proxies.

In order to account for the observed departure of the $\delta^{13}\mathrm{C}$ oscillations from a simple eccentricity forcing, we need to introduce a retroaction of Quaternary sea level changes onto the sedimentary dynamics of alluvial fans and continental shelves, and consequently onto organic carbon burial. As explained above, we will reverse the sign of our burial flux perturbation, and change it into $B = B_0 + aF(t)$ when some conditions are met on the geomorphology of river outputs. In particular, it is necessary to account for a changing reservoir size that can be filled with sediments in an aggradational way. Indeed, at the first major sea level drop, rivers are incising though the river and fan bedrock, thus providing room for the accumulation of sediments loaded with organic carbon. This volume should be filled progressively with sedimentary organic carbon up to a point when further river incision, and consequent aggradation of sediment, no longer affect the global organic carbon but only move sedimentary carbon from one place to another. In other words, we will assume that the global "Himalayan-like" situation (i.e. net organic carbon burial) is only a transient situation, linked to the first occurrence of a sea level minimum. In order to illustrate this mechanism, we add a new equation for the slow geomorphological reservoir S for organic carbon in river beds or river fans. We define its maximal size S_{MAX} from the observed sea level changes using the reference stack LR04 (Lisiecki

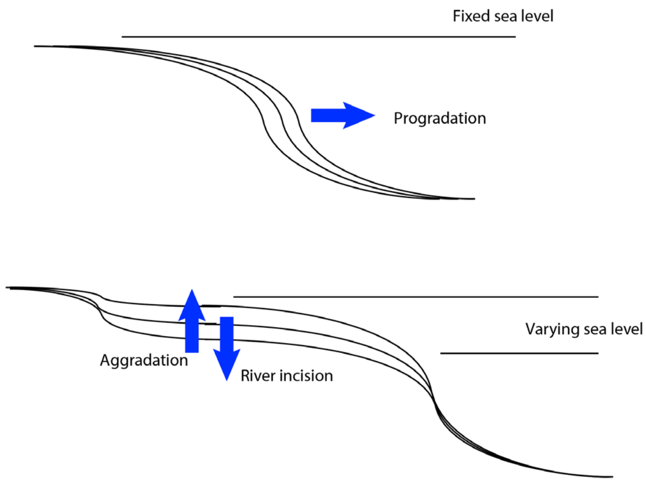

Figure 3. Simple scheme of the two different geomorphological dynamics considered here. (top) With small sea level changes, we assume that the dominant sedimentary regime is progradation, with rather small organic carbon burial in coastal areas. The net effect of precessional forcing is (old) soil erosion, therefore a net transfer of carbon to the ocean–atmosphere. (bottom) With large sea level changes during the late Quaternary, the dominant sedimentary regime can switch temporarily to aggradation just after major sea level drops and river incisions. During these transitory phases, the net effect of precessional forcing is reversed, with net organic carbon burial in river beds and river fans.

and Raymo, 2005) by finding the previous sea level minimum z_{MIN} (i.e. the lower envelope) with the scaling $S_{\mathrm{MAX}} \sim z_{\mathrm{MIN}}^3$ since it represents a volume of sediment (see Fig. 2):

$$\begin{aligned} &\text{if } S < S_{\mathrm{MAX}}: \ \mathrm{d}S/\mathrm{d}t = bF_0(t) \\ &\text{otherwise}: \ S = S_{\mathrm{MAX}}. \end{aligned} \tag{3a}$$

In other words, the sedimentary organic carbon reservoir S grows at the pace of the above-mentioned astronomical perturbation $F_0(t)$ up to its maximal size S_{MAX}. After a short transient period, this reservoir remains therefore equal to this maximum value S_{MAX} in the absence of major sea level drops, as during the pre-Quaternary period. In contrast, for each significant sea level drop, S_{MAX} increases abruptly and we start a new transient phase whose duration is linked to parameter b. When S is small compared to the maximal reservoir size S_{MAX}, then the aggradational scheme is favoured, with river beds and deltaic net organic carbon burial. But when S is close to its maximum value, we switch back to a mostly progradational sedimentation scheme, meaning that potential sea level changes will no longer affect net global organic carbon burial:

$$\begin{aligned} &\text{if } S < 0.85 S_{\mathrm{MAX}}: \ B = B_0 + aF(t) \\ &\text{otherwise}: \ B = B_0 - aF(t). \end{aligned} \tag{3b}$$

Using this simple crude criterion, we obtain the results shown in Fig. 2 (experiment c, red lines). As expected, this simple model does switch from the background "Amazon-like" or progradational burial mode to a "Himalayan-like" or aggradational mode, after each significant sea level drop, and most notably at two time periods, the first one between 2.4 and 2.5 Myr BP (as a consequence of the Plio-Pleistocene transition) and the second and largest one between 350 and 650 kyr BP (as a consequence of the MPT). The start of these transient periods is directly linked to sea level drops, according to the LR04 forcing, while the duration of these transients is linked both to the 0.85 S_{MAX} threshold and the b parameter, whose values are chosen to qualitatively better match the δ^{13}C data. For the results shown in Fig. 2, $b = (160\,\mathrm{kyr})^{-1}$. Indeed, this sedimentary switch mechanism allows for a much better agreement with measured δ^{13}C around 0.3 and 2.3 Myr BP, while the first simulations were systematically too high at this time, as illustrated by the difference between the blue and red curves in Fig. 2. We also simulate correctly the δ^{13}C maximum around 500 kyr BP and the occurrence of two broad "500 kyr" cycles over the last million years. With this burial mode switching mechanism, we are also able to predict an absolute minimum in carbon content, or long-term $p\mathrm{CO_2}$, around 600 kyr BP, in rather good agreement with the long-term trend of $p\mathrm{CO_2}$ measured in Antarctic ice cores. Indeed, $p\mathrm{CO_2}$ from the Dome C record is about 5 to 10 ppm lower before the MPT (between 400 and 800 kyr BP), which is also what we obtain in our experiment c.

4 Discussion

When variations in B, as determined by parameter a, are smaller than the baseline value B_0, the model cannot reproduce the oceanic amplitude of δ^{13}C observed in marine benthic records. The observed 400 kyr signal in δ^{13}C records therefore requires major changes in the organic carbon burial, with almost no global net burial, but net oxidation episodes, during maxima of precessional forcing. This strong forcing therefore implies significant oscillations in the Earth carbon cycle for this time frequency, up to 4 or 5 % in total carbon content. This is translated here into 10 to 20 ppm variations of $p\mathrm{CO_2}$ using our simple scaling, but it is very likely that these changes would be much larger, when accounting for interactions between $p\mathrm{CO_2}$ and climate. Indeed, colder climates are more favourable to oceanic carbon storage, as observed during the last glacial cycles. According to this mechanism, in the ordinary sedimentary regime (progradation), we obtain changes in the carbon cycle with $p\mathrm{CO_2}$ maxima and δ^{13}C minima associated directly with eccentricity maxima. This is indeed consistent with long Cenozoic records (e.g. Pälike et al., 2006).

When we allow for changes in the sedimentary regime triggered by sea level changes, the model can also reproduce more peculiar features. Indeed, up to now it has been difficult to explain the last two long-term cycles observed in the marine δ^{13}C, each being approximately 500 kyr long, with a maximum now (δ^{13}Cmax-I), a well-marked maximum at about 500 kyr BP (δ^{13}Cmax-II) and a previous one around 1000 or 1100 kyr BP (δ^{13}Cmax-III). In the model described here, these two long oscillations are generated from the eccentricity forcing, but with an abrupt switch to aggradation mode at about 620 kyr BP caused by the sea level drop at MIS 16. This switch reverses the phase of the 400 kyr carbon oscillation during a few hundred thousands of years. Interestingly, this also induces a slight minimum in the carbon (or $p\mathrm{CO_2}$) results, consistent with the observed low $p\mathrm{CO_2}$ values observed in the Antarctic ice core around 600–700 kyr BP. This mechanism also allows for simulated marine δ^{13}C in better agreement with data at about 2.4 Myr BP.

It has already been noted (Wang et al., 2004) that the climatic evolution over the last million years, in particular the MPT (about 0.8 Myr BP) and the Mid-Brunhes Event (MBE, about 0.4 Myr BP) is associated with the carbon isotopic maxima δ^{13}Cmax-II and δ^{13}Cmax-III. This is a strong indication of a possible causal link between the long-term well-recognized eccentricity forcing on the carbon cycle and the Plio-Pleistocene climatic evolution. There is therefore a strong incentive to build a mechanistic astronomical theory of the carbon cycle. But a prerequisite towards understanding this long-term precessionally forced carbon cycle and its climatic consequences is to explain the observed changes during the Quaternary, in terms of δ^{13}C, and simultaneously in the atmospheric $\mathrm{CO_2}$ levels (Lüthi et al., 2008). The model results outlined above are a first step in this direction.

As detailed above, the fact that the 400 kyr carbon isotope cycle is perturbed during the Pleistocene strongly points towards a major role for organic matter burial over continental shelf areas being affected by sea level changes. Obviously, this model is far too simple to represent faithfully the complexities of sedimentary dynamics in coastal areas, its consequences on organic matter preservation, on carbon cycle and ultimately on climate. Furthermore, we provide here no explanation for the prescribed multi-million-year decreasing trend in $p\mathrm{CO_2}$. There is unfortunately no clear consensus on the actual mechanisms involved, though this trend has been often attributed to long-term changes in continental weathering linked either to mountain uplift (Raymo and Ruddiman, 1992), to continental drift or mantle degassing rate (Lefebvre et al., 2013). Furthermore, we considered only sea level changes as a potential feedback on organic matter burial in coastal areas. Obviously, many other important climatic feedbacks would also play a role. For instance, increased temperature would probably reduce net primary production as a consequence of increased stratification, and therefore reduce organic carbon deposition in coastal sediments, but it would also decrease oxygen concentrations and consequently would favour organic matter preservation. Similarly, stronger monsoon events would enhance the delivery of nutrients to the continental shelves, and therefore biological productivity. This would in addition deliver more fine-grained clay minerals that are necessary to seal and preserve organic matter from oxidation. This would work opposite to our continental soil–carbon mechanism for which enhanced monsoons lead to more organic carbon oxidation in agreement with the isotopic records. But, as a proof of concept, our model is chosen as minimalistic as possible. It does not attempt to include all potentially important mechanisms.

5 Conclusion

Our basic assumptions are primarily based on recent reassessments of riverine organic carbon inputs to the ocean. With the above conceptual model, we demonstrate that simple mechanistic assumptions can account for the major patterns of the observed global evolution of carbon and carbon isotopes over this time period. First, enhanced precessional forcing linked to high eccentricity leads to more continental organic carbon being washed out and remineralized, and therefore a net decrease in overall organic carbon burial. Second, this mechanism is temporarily reversed following major sea level drops associated with glaciations. This model was built on the premises that changes in organic matter or petrogenic organic carbon fluxes are responsible for the 400 kyr oscillations observed in Cenozoic ^{13}C records, and that the large sea level variations occurring during the Quaternary strongly affect this process. Continental margins and sedimentary fans are a very likely key component, as illustrated by our simple conceptual model. But obviously, many complex processes are involved in the interactions between organic matter burial or oxidation, monsoons and sea level changes. The geomorphological mechanism described here is one possibility which allows us, for the first time, to account both for the persistent 400 kyr oscillation observed in ^{13}C records during the Cenozoic and its change during the last million years. It also suggests the occurrence of possibly significant $\mathrm{CO_2}$ drops at about 0.8 Myr BP (mid-Pleistocene transition) and at about 2.8 Myr BP (Plio-Pleistocene transition), which would ultimately link the timing of these transitions to the astronomical forcing. Our model also provides a possible explanation for the puzzling shifted level in the $\mathrm{CO_2}$ records associated with the MBE.

Data availability. No data sets were used in this article.

Competing interests. The author declares that he has no conflict of interest.

Acknowledgements. The author thanks Nathaëlle Bouttes, Peter Köhler and the two anonymous reviewers for their useful comments and suggestions.

Edited by: Arne Winguth
Reviewed by: two anonymous referees

References

Archer, D.: Fate of fossil fuel CO_2 in geologic time, J. Geophys. Res., 110, C09S05, https://doi.org/10.1029/2004JC002625, 2005.

Archer, D., Kheshgi, H., and Maier-Raimer, E.: Multiple timescales for neutralization of fossil fuel CO_2, Geophys. Res. Lett., 24, 405–408, 1997.

Bartoli, G., Hönisch, B., and Zeebe, R. E.: Atmospheric CO_2 decline during the Pliocene intensification of Northern Hemisphere glaciations, Paleoceanography, 26, PA4213, https://doi.org/10.1029/2010PA002055, 2011.

Bassinot, F., Beaufort, L., Vincent, E., Labeyrie, L., Rostek, F., Müller, P., Quidelleur, X., and Lancelot, Y.: Coarse fraction fluctuations in pelagic carbonate sediments from the tropical Indian Ocean: A 1500-kyr record of carbonate dissolution, Paleoceanography, 9, 579–600, 1994.

Billups, K., Pälike, H., Channell, J., Zachos, J., and Shackleton, N.: Astronomic calibration of the late Oligocene through early Miocene geomagnetic polarity time scale, Earth Planet. Sc. Lett., 224, 33–44, 2004.

Blair, N. E., Leithold, E. L., Ford, S. T., Peeler, K. A., Holmes, J. C., and Perkey, D. W.: The persistence of memory: the fate of ancient sedimentary organic carbon in a modern sedimentary system, Geochim. Cosmochim. Ac., 67, 63–73, 2003.

Burdige, D. J.: Burial of terrestrial organic matter in marine sediments: A re-assessment, Global Biogeochem. Cy., 19, GB4011, https://doi.org/10.1029/2004GB002368, 2005.

Burton, M. R., Sawyer, G. M., and Granieri, D.: Deep carbon emissions from volcanoes, Rev. Mineral. Geochem., 75, 323–354, 2013.

Cramer, B., Wright, J. D., Kent, D. V., and Aubry, M.-A.: Orbital climate forcing of $\delta^{13}C$ excursions in the late Paleocene–early Eocene (chrons C24n–C25n), Paleoceanography, 18, 1097, https://doi.org/10.1029/2003PA000909, 2003.

Galy, V., France-Lanord, C., Beyssac, O., Faure, P., Kudrass, H., and Palhol, F.: Efficient organic carbon burial in the Bengal fan sustained by the Himalayan erosional system, Nature, 450, 407–410, 2007.

Galy, V., Beyssac, O., France-Lanord, C., and Eglinton, T.: Recycling of Graphite During Himalayan Erosion: A Geological Stabilization of Carbon in the Crust, Science, 322, 943–945, 2008.

Hilgen, F. J., Abdul Aziz, H., Krijgsman, W., Langereis, C. G., Lourens, L. J., Meulenkamp, J. E., Raffi, I., Steenbrink, J., Turco, E., Van Vugt, N., Wijbrans, J. R., and Zachariasse, W. J.: Present status of the astronomical (polarity) time-scale for the Mediterranean Late Neogene, Philos. T. R. Soc. A, 357, 1931–1947, 1999.

Hilton, R. G., Galy, V., Gaillardet, J., Dellinger, M., Bryant, C., O'Regan, M., Gröke, D. R., Coxall, H., Bouchez, J., and Calmels, D.: Erosion of organic carbon in the Arctic as a geological carbon dioxide sink, Nature, 524, 84–87, 2015.

Hönisch, B., Hemming, N. G., Archer, D., Siddall, M., and McManus, J.: Atmospheric Carbon Dioxide Concentration Across the Mid-Pleistocene Transition, Science, 324, 1551–1554, 2009.

Kuiper, K. F., Deino, A., Hilgen, F. J., Krijgsman, W., Renne, P. R., and Wijbrans, J. R.: Synchronizing Rock Clocks of Earth History, Science, 320, 500–504, 2008.

Laskar, J., Robutel, P., Joutel, F., Gastineau, M., and Correia, A. C. M.: A long-term numerical solution for the insolation quantities of the Earth, Astron. Astrophys., 428, 261–285, https://doi.org/10.1051/0004-6361:20041335, 2004.

Lefebvre, V., Donnadieu, Y., Goddéris, Y., Fluteau, F., and Hubert-Théou, L.: Was the Antarctic glaciation delayed by a high degassing rate during the early Cenozoic?, Earth Planet. Sc. Lett., 371–372, 203–211, 2013.

Lisiecki, L. and Raymo, M.: A Pliocene-Pleistocene stack of 57 globally distributed benthic $\delta^{18}O$ records, Paleoceanography, 20, PA1003, https://doi.org/10.1029/2004PA001071, 2005.

Lourens, L. J., Antonarakou, A., Hilgen, F. J., VanHoof, A. A. M., Vergnaud-Grazzini, C., and Zachariasse, W. J.: Evaluation of the Plio-Pleistocene astronomical timescale, Paleoceanography, 11, 391–413, 1996.

Lüthi, D., Le Floch, M., Bereiter, B., Blunier, T., Barnola, J.-M., Siegenthaler, U., Raynaud, D., Jouzel, J., Fisher, H., Kawamura, K., and Stocker, T.: High-resolution carbon dioxide concentration record 650,000–800,000 years before present, Nature, 453, 379–382, 2008.

Mix, A. C., Pisias, N. G., Rugh, W., Wilson, J., Morey, A., and Hagelberg, T. K.: Benthic foraminifer stable isotope record from Site 849 (0–5 Ma): Local and global climate changes, Proc. Ocean Drill. Program Sci. Results, 138, 371–412, 1995.

Paillard, D.: Quaternary glaciations: from observations to theories, Quaternary Sci. Rev., 107, 11–24, 2015.

Paillard, D. and Donnadieu, Y.: A 100 Myr history of the carbon cycle based on the 400 kyr cycle in marine $\delta^{13}C$ benthic records, Paleoceanography, 29, https://doi.org/10.1002/2014PA002693, 2014.

Pälike, H., Norris, R. D., Herrle, J. O., Wilson, P. A., Coxall, H. K., Lear, C. H., Shackleton, N. J., Tripati, A. K., and Wade, B. S.: The heartbeat of the Oligocene climate system, Science, 314, 1894–1898, 2006.

Porcelli, D. and Turekian, K. K.: The History of Planetary Degassing as Recorded by Noble Gases, §6.6.1 in Readings from the Treatise on Geochemistry, edited by: Holland, H. D. and Turekian, K. K., 2010.

Raymo, M. and Ruddiman, W. F.: Tectonic forcing of late cenozoic climate, Nature, 359, 117–122, 1992.

Rickaby, R., Bard, E., Sonzogni, E., Rostek, F., Beaufort, L., Barker, S., Rees, G., and Schrag, D.: Coccolith chemistry reveals secular variations in the global ocean carbon cycle?, Earth Planet. Sc. Lett., 253, 83–95, 2007.

Russon, T., Paillard, D., and Elliot, M.: Potential origins of 400–500 kyr periodicities in the ocean carbon cycle: A box model approach, Global Biogeochem. Cy., 24, GB2013, https://doi.org/10.1029/2009GB003586, 2010.

Seki, O., Foster, G. L., Schmidt, D. N., Mackensen, A., Kawamura, K., and Pancost, R. D.: Alkenone and boron-based Pliocene pCO_2 records, Earth Planet. Sc. Lett., 292, 201–211, 2010.

Sexton, P., Norris, R. D., Wilson, P. A., Pälike, H., Westerhold, T., Röhl, U., Bolton, C. T., and Gibbs, S.: Eocene global warming events driven by ventilation of oceanic dissolved organic carbon, Nature, 471, 349–352, 2011.

Shackleton, N. J., Hall, M. A., and Pate, D.: Pliocene stable isotope stratigraphy of Site 846, Proc. Ocean Drill. Program Sci. Results, 138, 337–355, 1995.

Wang, P., Tian, J., Cheng, X., Liu, C., and Xu, J.: Major Pleistocene stages in a carbon perspective: The South China Sea record and its global comparison, Paleoceanography, 19, PA4005, https://doi.org/10.1029/2003PA000991, 2004.

Wang, P., Tian, J., and Lourens, L.: Obscuring of long eccentricity cyclicity in Pleistocene oceanic carbon isotope records, Earth Planet. Sc. Lett., 290, 319–330, 2010.

Clim. Past, 17, 1483–1506, 2021
https://doi.org/10.5194/cp-17-1483-2021

Climate of the Past
Open Access

Deep ocean temperatures through time

Paul J. Valdes[1,★], **Christopher R. Scotese**[2], **and Daniel J. Lunt**[1]

[1]School of Geographical Sciences, University of Bristol, Bristol BS8 1SS, UK
[2]Northwestern University, Dept Earth & Planetary Sci, Evanston, IL, USA
[★]*Invited contribution by Paul J. Valdes, recipient of the EGU Milutin Milankovic Medal 2015.*

Correspondence: Paul J. Valdes (p.j.valdes@bristol.ac.uk)

Received: 15 June 2020 – Discussion started: 6 July 2020
Revised: 8 May 2021 – Accepted: 10 May 2021 – Published: 19 July 2021

Abstract. Benthic oxygen isotope records are commonly used as a proxy for global mean surface temperatures during the Late Cretaceous and Cenozoic, and the resulting estimates have been extensively used in characterizing major trends and transitions in the climate system and for analysing past climate sensitivity. However, some fundamental assumptions governing this proxy have rarely been tested. Two key assumptions are (a) benthic foraminiferal temperatures are geographically well mixed and are linked to surface high-latitude temperatures, and (b) surface high-latitude temperatures are well correlated with global mean temperatures. To investigate the robustness of these assumptions through geological time, we performed a series of 109 climate model simulations using a unique set of paleogeographical reconstructions covering the entire Phanerozoic at the stage level. The simulations have been run for at least 5000 model years to ensure that the deep ocean is in dynamic equilibrium. We find that the correlation between deep ocean temperatures and global mean surface temperatures is good for the Cenozoic, and thus the proxy data are reliable indicators for this time period, albeit with a standard error of 2 K. This uncertainty has not normally been assessed and needs to be combined with other sources of uncertainty when, for instance, estimating climate sensitivity based on using $\delta^{18}O$ measurements from benthic foraminifera. The correlation between deep and global mean surface temperature becomes weaker for pre-Cenozoic time periods (when the paleogeography is significantly different from the present day). The reasons for the weaker correlation include variability in the source region of the deep water (varying hemispheres but also varying latitudes of sinking), the depth of ocean overturning (some extreme warm climates have relatively shallow and sluggish circulations weakening the link between the surface and deep ocean), and the extent of polar amplification (e.g. ice albedo feedbacks). Deep ocean sediments prior to the Cretaceous are rare, so extending the benthic foraminifera proxy further into deeper time is problematic, but the model results presented here would suggest that the deep ocean temperatures from such time periods would probably be an unreliable indicator of global mean surface conditions.

1 Introduction

One of the most widely used proxies for estimating global mean surface temperature through the last 100 million years is benthic $\delta^{18}O$ measurements from deep-sea foraminifera (Zachos et al., 2001, 2008, Cramer et al., 2009, Friedrich et al., 2012, Westerhold et al., 2020). Two key underlying assumptions are that $\delta^{18}O$ from benthic foraminifera represents deep ocean temperature (with a correction for ice volume and any vital effects) and that the deep ocean water masses originate from surface water in polar regions. By further assuming that polar surface temperatures are well correlated with global mean surface temperatures, then deep ocean isotopes can be assumed to track global mean surface temperatures. More specifically, Hansen et al. (2008) and Hansen and Sato (2012) argue that changes in high-latitude sea surface temperatures (SSTs) are approximately proportional to global mean surface temperatures because changes are generally amplified at high latitudes but that this is offset because temperature change is amplified over land areas. They therefore directly equate changes in benthic ocean temperatures with global mean surface temperature.

The resulting estimates of global mean surface air temperature have been used to understand past climates (e.g. Zachos et al., 2008; Westerhold et al., 2020). Combined with estimates of atmospheric CO_2, they have also been used to estimate climate sensitivity (e.g. Hansen et al., 2013) and hence contribute to the important ongoing debate about the likely magnitude of future climate change.

However, some of the underlying assumptions behind the method remain largely untested, even though we know that there are major changes to paleogeography and consequent changes in ocean circulation and location of deep-water formation in the deep past (e.g. Lunt et al., 2010; Nunes and Norris, 2006); Donnadieu et al., 2016; Farnsworth et al., 2019a; Ladant et al., 2020). Moreover, the magnitude of polar amplification is likely to vary depending on the extent of polar ice caps and changes in cloud cover (Sagoo et al., 2013; Zhu et al., 2019). These issues are likely to modify the correlation between deep ocean temperatures and global mean surface temperature or, at the very least, increase the uncertainty in reconstructing past global mean surface temperatures.

The aim of this paper is two-fold: (1) we wish to document the setup and initial results from a unique set of 109 climate model simulations of the whole Phanerozoic era (last 540 million years) at the stage level (approximately every 5 million years), and (2) we will use these simulations to investigate the accuracy of the deep ocean temperature proxy in representing global mean surface temperature.

The focus of the work is to examine the link between benthic ocean temperatures and surface conditions. However, we evaluate the fidelity of the model by comparing the model-predicted ocean temperatures to estimates of the isotopic temperature of the deep ocean during the past 110 million years (Zachos et al., 2008; Cramer et al., 2009; Friedrich et al., 2012) and model-predicted surface temperatures to the sea surface temperature estimates of O'Brien et al. (2017) and Cramwinckel et al. (2018). This gives us confidence that the model is behaving plausibly but we emphasize that the fidelity of the simulations is strongly influenced by the accuracy of CO_2 estimates through time. We then use the complete suite of climate simulations to examine changes in ocean circulation, ice formation, and the impact on ocean and surface temperature. Our paper will not consider any issues associated with assumptions regarding the relationship between deep-sea foraminifera $\delta^{18}O$ and various temperature calibrations because our model does not simulate the $\delta^{18}O$ of sea water (or vital effects).

2 Simulation methodology

2.1 Model description

We use a variant of the Hadley Centre model, HadCM3 (Pope et al., 2000; Gordon et al., 2000), which is a coupled atmosphere–ocean–vegetation model. The specific version, HadCM3BL-M2.1aD, is described in detail in Valdes et al. (2017). The model has a horizontal resolution of 3.75° × 2.5° in longitude–latitude (roughly corresponding to an average grid box size of ∼ 300 km) in both the atmosphere and the ocean. The atmosphere has 19 unequally spaced vertical levels, and the ocean has 20 unequally spaced vertical levels. To avoid singularity at the poles, the ocean model always has to have land at the poles (90° N and 90° S), but the atmosphere model can represent the poles correctly (i.e. in the pre-industrial geography, the atmosphere considers there is sea ice covered ocean at the N. Pole but the ocean model has land and hence there is no ocean flow across the pole). Though HadCM3 is a relatively low-resolution and low complexity model compared to the current CMIP5/CMIP6 state-of-the-art model, its performance in simulating modern climate is comparable to many CMIP5 models (Valdes et al., 2017). The performance of the dynamic vegetation model compared to modern observations is also described in Valdes et al. (2017), but the modern deep ocean temperatures are not described in that paper. We therefore include a comparison to present-day observed deep ocean temperatures in Sect. 3.1.

To perform paleosimulations, several important modifications to the standard model described in Valdes et al. (2017) must be incorporated:

a. The standard pre-industrial model uses a prescribed climatological pre-industrial ozone concentration (i.e. prior to the development of the "ozone" hole) which is a function of latitude, atmospheric height, and month of the year. However, we do not know what the distribution of ozone should be in these past climates. Beerling et al. (2011) modelled small changes in tropospheric ozone for the early Eocene and Cretaceous, but no comprehensive stratospheric estimates are available. Hence, most paleoclimate model simulations assume unchanging concentrations. However, there is a problem with using a prescribed ozone distribution for paleosimulations because it does not incorporate ozone feedbacks associated with changes in tropospheric height. During warm climates, the model predicts that the tropopause would rise. In the real world, ozone would track the tropopause rise. However, this rising ozone feedback is not included in our standard model. This leads to substantial extra warming and artificially increases the apparent climate sensitivity. Simulations of future climate change have shown that ozone feedbacks can lead to an overestimate of climate sensitivity by up to 20 % (Dietmuller et al., 2014; Nowack et al., 2015; Hardiman et al., 2019). Therefore, to incorporate some aspects of this feedback, we have changed the ozone scheme in the model. Ozone is coupled to the model-predicted tropopause height every model time step in the following simple way:

   - 2.0×10^{-8} kg kg^{-1} in the troposphere,
   - 2.0×10^{-7} kg kg^{-1} at the tropopause,
   - 5.5×10^{-6} kg kg^{-1} above the tropopause, and
   - 5.5×10^{-6} kg kg^{-1} at the top model level.

These values are approximate averages of present-day values and were chosen so that the tropospheric climate of the resulting pre-industrial simulation was little altered compared with the standard pre-industrial simulations; the resulting global mean surface air temperatures differed by only 0.05 °C. These modifications are similar to those used in the FAMOUS model (Smith et al., 2008) except that the values in the stratosphere are greater in our simulation, largely because our model vertical resolution is higher than that in FAMOUS.Note that these changes improve upon the scheme used by Lunt et al. (2016) and Farnsworth et al. (2019a). They used much lower values of stratospheric ozone and had no specified value at the top of the model. This resulted in their model having ~ 1 °C cold bias for pre-industrial temperatures and may have also affected their estimates of climate sensitivity.

b. The standard version of HadCM3 conserves the total volume of water throughout the atmosphere and ocean (including in the numerical scheme) but several processes in the model "lose or gain" water:

   1. Snow accumulates over ice sheets but there is no interactive loss through iceberg calving resulting in an excess loss of fresh water from the ocean.
   2. The model caps salinity at a maximum of 45 PSU (and a minimum of 0 PSU) by artificially adding/subtracting fresh water to the ocean. This mostly affects small, enclosed seas (such as the Red Sea or enclosed Arctic) where the model does not represent the exchange with other ocean basins.
   3. Modelled river runoff includes some river basins which drain internally. These often correspond to relatively dry regions, but any internal drainage simply disappears from the model.
   4. The land surface scheme includes evaporation from subgrid-scale lakes (which are prescribed as a lake fraction in each grid box, at the start of the run). The model does not represent the hydrological balance of these lakes; consequently, the volume of the lakes does not change. This effectively means that there is a net source–sink of water in the model in these regions.

In the standard model, these water sources–sinks are approximately balanced by a flux of water into the surface ocean. This is prescribed at the start of the run and does not vary during the simulations. It is normally set to a pre-calculated estimate based on an old HadCM3-M1 simulation. The flux is strongest around Greenland and Antarctica and is chosen such that it approximately balances the water loss described in (1), i.e. the net snow accumulation over these ice sheets. There is an additional flux covering the rest of the surface ocean which approximately balances the water loss from the remaining three terms (2–4). The addition of this water flux keeps the global mean ocean salinity approximately constant on century timescales. However, depending on the simulation, the drift in average oceanic salinity can be as much as 1 PSU per 1000 years and thus can have a major impact on ultra-long runs of > 5000 years (Farnsworth et al., 2019a).

For the paleosimulations in this paper, we therefore take a slightly different approach. When ice sheets are present in the Cenozoic, we include the water flux (for the relevant hemisphere) described in (1) above, based on modern values of iceberg calving fluxes for each hemisphere. However, to ensure that salinity is conserved, we also interactively calculate an additional globally uniform surface water flux based on relaxing the volume mean ocean salinity to a prescribed value on a 20-year timescale. This ensures that there is no long-term trend in ocean salinity. Tests of this update on the pre-industrial simulations revealed no appreciable impact on the skill of the model relative to the observations. We have not directly compared our simulations to the previous runs of the Farnsworth et al. (2019a) because they use different CO_2 and different paleogeographies. However, in practice, the increase of salinity in their simulations is well mixed and seems to have relatively little impact on the overall climate and ocean circulation.

We have little knowledge of whether ocean salinity has changed through time, and so we keep the prescribed mean ocean salinity constant across all simulations.

2.2 Model boundary conditions

There are several boundary conditions that require modification through time. In this sequence of simulations, we only modify three key time-dependent boundary conditions: (1) the solar constant, (2) atmospheric CO_2 concentrations, and (3) paleogeographic reconstructions. We set the surface soil conditions to a uniform medium loam everywhere. All other boundary conditions (such as orbital parameters, volcanic aerosol concentrations, etc.) are held constant at pre-industrial values.

The solar constant is based on Gough (1981) and increases linearly at an approximate rate of 11.1 W m^{-2} per 100 Myr (0.8 % per 100 Myr), to 1365 W m^{-2} currently. If we assume a planetary albedo of 0.3, and a climate sensitivity of 0.8 °C W^{-1} m^{2} (approximately equivalent to 3 °C per doubling of CO_2), then this is equivalent to a temperature increase of ~ 0.015 °C per 1 million years (~ 8 °C over the whole of the Phanerozoic).

Estimates of atmospheric CO_2 concentrations have considerable uncertainty. We, therefore, use two alternative estimates (Fig. 1a). The first uses the best-fit local regression (LOESS) curve from Foster et al. (2017), which is also very similar to the newer data from Witkowski et al. (2018). The CO_2 levels have considerable short- and long-term variability throughout the time period. Our second estimate removes much of the shorter-term variability in the Foster et al. (2017) curve. It was developed for two reasons. Firstly, a lot of the finer temporal structure in the LOESS curve is a product of differing data density of the raw data and does not necessarily correspond to real features. Secondly, the smoother curve was heavily influenced by a previous (commercially confidential) sparser sequence of simulations using non-public paleogeographic reconstructions. The resulting simulations were generally in good agreement with terrestrial proxy datasets (Harris et al., 2017). Specifically, using commercial-in-confidence paleogeographies, we have performed multiple simulations at different CO_2 values for several stages across the last 440 million years and tested the resulting climate against commercial-in-confidence proxy data (Harris et al., 2017). We then selected the CO_2 values that best matched the data. For the current simulations, we linearly interpolated these CO_2 values to every stage. The resulting CO_2 curve looks like a heavily smoothed version of the Foster curve and is within the (large) envelope of CO_2 reconstructions. The first-order shapes of the two curves are similar, though they are very different for some time periods (e.g. Triassic and Jurassic). In practice, both curves should be considered an approximation to the actual evolution of CO_2 through time which remains uncertain.

We refer to the simulation using the second set of CO_2 reconstructions as the "smooth" CO_2 simulations, though it should be recognized that the Foster CO_2 curve has also been smoothed. The Foster CO_2 curve extends back to only 420 Ma, so we have proposed two alternative extensions back to 540 Ma. Both curves increase sharply so that the combined forcing of CO_2 and solar constant is approximately constant over this time period (Foster et al., 2017). The higher CO_2 in the Foster curve relative to the "smooth" curve is because the initial set of simulations showed that the Cambrian simulations were relatively cool compared to data estimates for the period (Henkes et al., 2018).

2.3 Paleogeographic reconstructions

The 109 paleogeographic maps used in the HadleyCM3 simulations are digital representations of the maps in the PALEOMAP paleogeographic atlas (Scotese, 2016; Scotese and Wright, 2018). Table 1 lists all the time intervals that comprise the PALEOMAP paleogeographic atlas. The paleogeographic atlas contains one map for nearly every stage in the Phanerozoic. A paleogeographic map is defined as a map that shows the ancient configuration of the ocean basins and continents, as well as important topographic and bathymetric features such as mountains, lowlands, shallow sea, continental shelves, and deep oceans. Paleogeographic reconstructions older than the oldest ocean floor ($\sim$ Late Jurassic) have uniform deep ocean floor depth.

Once the paleogeography for each time interval has been mapped, this information is then converted into a digital representation of the paleotopography and paleobathymetry. Each digital paleogeographic model is composed of over 6 million grid cells that capture digital elevation information at a 10 km $\times$ 10 km horizontal resolution and 40 m vertical resolution. This quantitative paleodigital elevation model, or "paleoDEM", allows us to visualize and analyse the changing surface of the Earth through time using GIS software and other computer modelling techniques. For use with the HadCM3L climate model, the original high-resolution elevation grid was reduced to a ~ 111 km$\times \sim 111$ km ($1^\circ \times 1^\circ$) grid.

For a detailed description of how the paleogeographic maps and paleoDEMs were produced, the reader is referred to Scotese (2016), Scotese and Schettino (2017), and Scotese and Wright (2018). The work of Scotese and Schettino (2017) includes an annotated bibliography of the more-than-100 key sources of paleogeographic information. Similar paleogeographic paleoDEMs have been produced by Baatsen et al. (2016) and Verard et al. (2015).

The raw paleogeographic data reconstruct paleoelevations and paleobathymetry at a resolution of $1^\circ \times 1^\circ$. These data were re-gridded to $3.75^\circ \times 2.5^\circ$ resolution that matched the climate model using a simple area (for land–sea mask) or volume (for orography and bathymetry) conserving algorithm. The bathymetry was lightly smoothed (using a binomial filter) to ensure that the ocean properties in the resulting model simulations were numerically stable. This filter was applied multiple times in the high latitudes. The gridding sometimes produced single-grid-point enclosed ocean basins, particularly along complicated coastlines, and these were manually removed. Similarly, important ocean gateways were reviewed to ensure that the re-gridded coastlines preserved these structures. The resulting global fraction of land is summarized in Fig. 1b and examples are shown in Fig. 2. The original reconstructions can be found at https://www.earthbyte.org/paleodem-resource-scotese-and-wright-2018/ (last access: 30 June 2021). Maps of each HadCM3L paleogeography are included in the Supplement as figures.

The paleogeographic reconstructions also include an estimate of land ice area (Scotese and Wright, 2018; Fig. 1c). These were converted to GCM boundary conditions assuming a simple parabolic shape to estimate the ice sheet height. These ice reconstructions suggest small amounts of land ice were present during the early Cretaceous, unlike Lunt et al. (2016), who used ice-free Cretaceous paleogeographies.

2.4 Spin-up methodology

The oceans are the slowest evolving part of the modelled climate system and can take multiple millennia to reach equilibrium, depending on the initial condition and climate state. To speed up the convergence of the model, we initialized the ocean temperatures and salinity with the values from previous model simulations from similar time periods using the commercial-in-confidence paleogeographies. Specifically, we had a set of 17 simulations covering the last

Table 1. List of paleogeographic maps and paleoDEMs.

Map number	Stratigraphic age description	Plate model age
1	Present day (Holocene, 0 Ma)	0
2	*Last Glacial Maximum (Pleistocene, 21 ka)*	0
3	*Late Pleistocene (122 ka)*	0
4	*Middle Pleistocene (454 ka)*	0
5	*Early Pleistocene (Calabrian, 1.29 Ma)*	0
6	*Early Pleistocene (Gelasian, 2.19 Ma)*	0
7	Late Pliocene (Piacenzian, 3.09 Ma)	5
8	*Early Pliocene (Zanclean, 4.47 Ma)*	5
9	*Latest Miocene (Messinian, 6.3 Ma)*	5
10	Middle/Late Miocene (Serravallian and Tortonian, 10.5 Ma)	10
11	Middle Miocene (Langhian, 14.9 Ma)	15
12	Early Miocene (Aquitanian and Burdigalian, 19.5 Ma)	20
13	Late Oligocene (Chattian, 25.6 Ma)	25
14	Early Oligocene (Rupelian, 31 Ma)	30
15	Late Eocene (Priabonian, 35.9 Ma)	35
16	Late Middle Eocene (Bartonian, 39.5 Ma)	40
17	Early Middle Eocene (Lutetian, 44.5 Ma)	45
18	Early Eocene (Ypresian, 51.9 Ma)	50
19	Paleocene–Eocene boundary (PETM, 56 Ma)	55
20	Paleocene (Danian and Thanetian, 61 Ma)	60
21	Cretaceous–Tertiary boundary (latest Maastrichtian, 66 Ma)	65
22	Late Cretaceous (Maastrichtian, 69 Ma)	70
23	Late Cretaceous (late Campanian, 75 Ma)	75
24	Late Cretaceous (early Campanian, 80.8 Ma)	80
25	Late Cretaceous (Santonian and Coniacian, 86.7 Ma)	85
26	Mid-Cretaceous (Turonian, 91.9 Ma)	90
27	Mid-Cretaceous (Cenomanian, 97.2 Ma)	95
28	Early Cretaceous (late Albian, 102.6 Ma)	100
29	Early Cretaceous (middle Albian, 107 Ma)	105
30	Early Cretaceous (early Albian, 111 Ma)	110
31	Early Cretaceous (late Aptian, 115.8 Ma)	115
32	Early Cretaceous (early Aptian, 121.8 Ma)	120
33	Early Cretaceous (Barremian, 127.2 Ma)	125
34	Early Cretaceous (Hauterivian, 131.2 Ma)	130
35	Early Cretaceous (Valanginian, 136.4 Ma)	135
36	Early Cretaceous (Berriasian, 142.4 Ma)	140
37	Jurassic–Cretaceous boundary (145 Ma)	145
38	Late Jurassic (Tithonian, 148.6 Ma)	150
39	Late Jurassic (Kimmeridgian, 154.7 Ma)	155
40	Late Jurassic (Oxfordian, 160.4 Ma)	160
41	Middle Jurassic (Callovian, 164.8 Ma)	165
42	Middle Jurassic (Bajocian and Bathonian, 168.2 Ma)	170
43	Middle Jurassic (Aalenian, 172.2 Ma)	175
44	Early Jurassic (Toarcian, 178.4 Ma)	180
45	Early Jurassic (Pliensbachian, 186.8 Ma)	185
46	Early Jurassic (Sinemurian/Pliensbachian, 190.8 Ma)	190
47	Early Jurassic (Hettangian and Sinemurian, 196 Ma)	195
48	Late Triassic (Rhaetian/Hettangian, 201.3 Ma)	200
49	Late Triassic (Rhaetian, 204.9 Ma)	205
50	Late Triassic (late Norian, 213.2 Ma)	210
51	Late Triassic (mid-Norian, 217.8 Ma)	215
52	Late Triassic (early Norian, 222.4 Ma)	220
53	Late Triassic (Carnian/Norian 227 Ma)	225
54	Late Triassic (Carnian, 232 Ma)	230
55	Late Triassic (early Carnian, 233.6 Ma)	235
56	Middle Triassic (Ladinian, 239.5 Ma)	240
57	Middle Triassic (Anisian, 244.6 Ma)	245
58	Permo-Triassic boundary (252 Ma)	250

Table 1. Continued.

Map number	Stratigraphic age description	Plate model age
59	Late Permian (Lopingian, 256 Ma)	255
60	Late Middle Permian (Capitanian, 262.5 Ma)	260
61	Middle Permian (Wordian–Capitanian boundary 265.1 Ma)	265
62	Middle Permian (Roadian and Wordian, 268.7 Ma)	270
63	Early Permian (late Kungurian, 275 Ma)	275
64	Early Permian (early Kungurian, 280 Ma)	280
65	Early Permian (Artinskian, 286.8 Ma)	285
66	Early Permian (Sakmarian, 292.6 Ma)	290
67	Early Permian (Asselian, 297 Ma)	295
68	Late Pennsylvanian (Gzhelian, 301.3 Ma)	300
69	Late Pennsylvanian (Kasimovian, 305.4 Ma)	305
70	Middle Pennsylvanian (Moscovian, 311.1 Ma)	310
71	Early–Middle Carboniferous (Bashkirian–Moscovian boundary, 314.6 Ma)	315
72	Early Pennsylvanian (Bashkirian, 319.2 Ma)	320
73	Late Mississippian (Serpukhovian, 327 Ma)	325
74	Late Mississippian (Visean–Serpukhovian boundary, 330.9 Ma)	330
75	Middle Mississippian (late Visean, 333 Ma)	335
76	Middle Mississippian (middle Visean, 338.8 Ma)	340
77	Middle Mississippian (early Visean, 344 Ma)	345
78	Early Mississippian (late Tournaisian, 349 Ma)	350
79	Early Mississippian (early Tournaisian, 354 Ma)	355
80	Devonian–Carboniferous boundary (358.9 Ma)	360
81	Late Devonian (middle Famennian, 365.6 Ma)	365
82	Late Devonian (early Famennian, 370 Ma)	370
83	Late Devonian (late Frasnian, 375 Ma)	375
84	Late Devonian (early Frasnian, 380 Ma)	380
85	Middle Devonian (Givetian, 385.2 Ma)	385
86	Middle Devonian (Eifelian, 390.5 Ma)	390
87	Early Devonian (late Emsian, 395 Ma)	395
88	Early Devonian (middle Emsian, 400 Ma)	400
89	Early Devonian (early Emsian, 405 Ma)	405
90	Early Devonian (Pragian, 409.2 Ma)	410
91	Early Devonian (Lochkovian, 415 Ma)	415
92	Late Silurian (Pridoli, 421.1 Ma)	420
93	Late Silurian (Ludlow, 425.2 Ma)	425
94	Middle Silurian (Wenlock, 430.4 Ma)	430
95	Early Silurian (late Llandovery, 436 Ma)	435
96	Early Silurian (early Llandovery, 441.2 Ma)	440
97	Late Ordovician (Hirnantian, 444.5 Ma)	445
98	Late Ordovician (Katian, 449.1 Ma)	450
99	Late Ordovician (Sandbian, 455.7 Ma)	455
100	Middle Ordovician (late Darwillian, 460 Ma)	460
101	Middle Ordovician (early Darwillian, 465 Ma)	465
102	Early Ordovician (Floian–Dapingian boundary, 470 Ma)	470
103	Early Ordovician (late Early Floian, 475 Ma)	475
104	Early Ordovician (Tremadoc, 481.6 Ma)	480
105	Cambro-Ordovician boundary (485.4 Ma)	485
106	Late Cambrian (Jiangshanian, 491.8 Ma)	490
107	Late Cambrian (Paibian, 495.5 Ma)	495
108	Late Middle Cambrian (Guzhangian, 498.8 Ma)	500
109	Late Middle Cambrian (early Epoch 3, 505 Ma)	505
110	Early Middle Cambrian (late Epoch 2, 510 Ma)	510
111	Early Middle Cambrian (middle Epoch 2, 515 Ma)	515
112	Early–Middle Cambrian boundary (520 Ma)	520
113	Early Cambrian (late Terreneuvian, 525 Ma)	525
114	Early Cambrian (middle Terreneuvian, 530 Ma)	530
115	Early Cambrian (early Terreneuvian, 535 Ma)	535
116	Cambrian–Precambrian boundary (541 Ma)	540

Simulations were not run for the time intervals highlighted in italics.

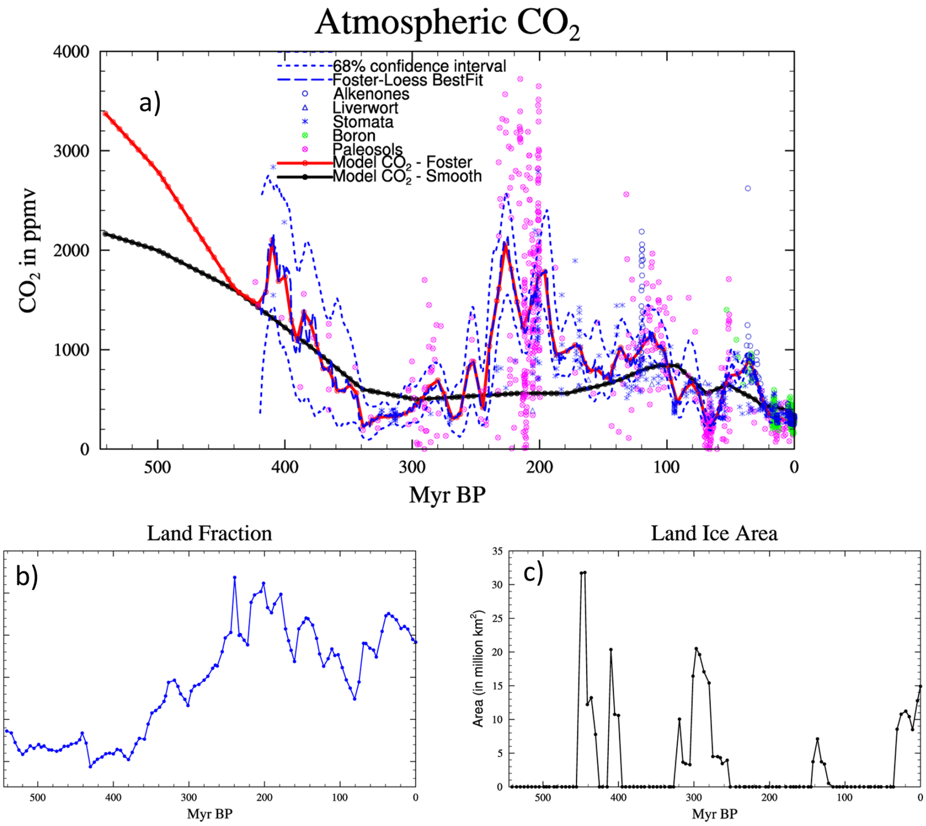

Figure 1. Summary of boundary condition changes to model of the Phanerozoic, **(a)** CO_2 reconstructions (from Foster et al., 2017) and the two scenarios used in the models, **(b)** land–sea fraction from the paleogeographic reconstructions, and **(c)** land ice area input into model. The paleogeographic reconstructions can be accessed at https://www.earthbyte.org/paleodem-resource-scotese-and-wright-2018/ (last access: 30 June 2021). An animation of the high-resolution ($1^\circ \times 1^\circ$) and model resolution (3.75° longitude $\times$ 2.5° latitude) maps can be found here: https://www.paleo.bristol.ac.uk/~ggpjv/scotese/scotese_raw_moll.normal_scotese_moll.normal.html (last access: 30 June 2021).

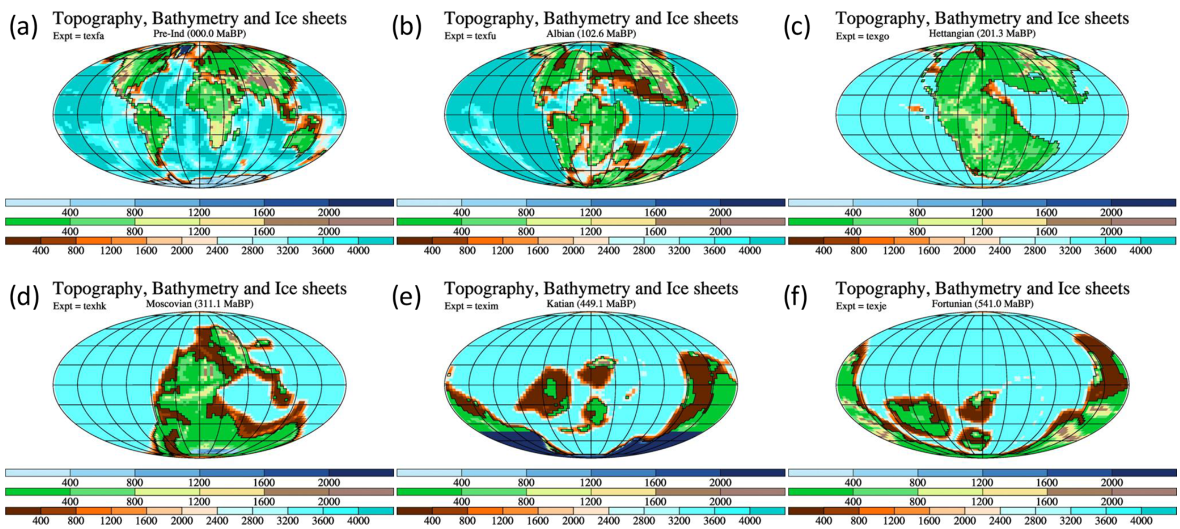

Figure 2. A few example paleogeographies, once they have been re-gridded onto the HadCM3L grid. The examples are for **(a)** present day, **(b)** Albian, 102.6 Ma (Lower Cretaceous), **(c)** Hettangian, 201.3 Ma (lower Jurassic), **(d)** Moscovian, 311.1 Ma (Pennsylvanian, Carboniferous), **(e)** Katian, 449.1 Ma (Upper Ordovician), and **(f)** Fortunian, 541.0 Ma (Cambrian). The top colour legend refers to the height of the ice sheets (if they exist), the middle colour legend refers to heights on land (except ice), and the lower colour legend refers to the ocean bathymetry. All units are metres.

440 Myr. We selected the nearest simulation to the time period. For instance, the 10.5, 14.9, and the 19.5 Ma simulations were initialized from the 13 Ma simulation performed using the alternative paleogeographies. Table 2 summarizes the simulations performed in this study and shows the initialization of the model. The Foster CO_2 simulations were initialized from the end point of the smooth CO_2 simulations. In the first set of simulations (smooth CO_2), we also attempted to accelerate the spin-up by using the ocean temperature trends at year 500 to linearly extrapolate the bottom 10 level temperatures for a further 1000 years. This had limited success and was not repeated. The atmosphere variables were also initialized from the previous model simulations but the spin-up of the atmosphere is much more rapid and did not require further intervention.

Simulations were run in parallel and thus were not initialized from the previous stage results using these paleogeographies. In total, we performed almost 1 million years of model simulation, and if we ran simulations in sequence, it would have taken 30 years to complete the simulations. By running these in parallel, initialized from previous modelling studies, we reduced the total runtime to 3 months, albeit using a substantial amount of our high-performance computer resources.

Although it is always possible that a different initialization procedure may produce different final states, it is impossible to explore the possibility of hysteresis/bistability without performing many simulations for each period, which is currently beyond our computing resources. Previous studies using HadCM3L (not published) with alternative ocean initial states (isothermals at 0, 8, and 16 °C) have not revealed multiple equilibria, but this might have been because we did not locate the appropriate part of parameter space that exhibits hysteresis. However, other studies have shown such behaviour (e.g. Baatsen et al., 2018). This remains a caveat of our current work and one which we wish to investigate when we have sufficient computing resources.

The simulations were then run until they reached equilibrium, as defined by the following:

1. The globally and volume-integrated annual mean ocean temperature trend is less than 1 °C per 1000 years, in most cases considerably smaller than this. We consider the volume-integrated temperature because it includes all aspects of the ocean. However, it is dominated by the deep ocean trends and is nearly identical to the trends at a depth of 2731 m (the lowest level that we have archived for the whole simulation).

2. The trends in surface air temperature are less than 0.3 °C per 1000 years.

3. The net energy balance at the top of the atmosphere, averaged over a 100-year period at the end of the simulation, is less than 0.25 W m^{-2} (in more than 80 % of the simulations, the imbalance is less than 0.1 W m^{-2}). The Gregory plot (Gregory et al., 2004) implies surface temperatures are within 0.3 °C of the equilibrium state.

These target trends were chosen somewhat arbitrarily but are all less than typical orbital timescale variability (e.g. temperature changes since the last deglaciation were approximately 5 °C over 10 000 years). Most simulations were well within these criteria. In total, 70 % of simulations had residual net energy balances at the top of the atmosphere of less than 0.1 W m^{-2}, but a few simulations were slower to reach full equilibrium. The strength of using multiple constraints is that a simulation may, by chance, pass one or two of these criteria but was unlikely to pass all three tests. For example, all the models that we extended failed at least two of the criteria. The resulting time series of volume-integrated global annual mean ocean temperatures are shown in Fig. 3. The figures in the Supplement also include this for each simulation, as well as the trends at 2731 m.

The "smooth" CO_2 simulations were all run for 5050 model years and satisfied the criteria. The Foster CO_2 simulations were initially run for a minimum of 2000 years (starting from the end of the 5000-year runs), at which point we reviewed the simulations relative to the convergence criteria. If the simulations had not converged, we extended the runs for an additional 3000 years. If they had not converged at the end of 5000 years, we extended them again for an additional 3000 years. After 8000 years, all simulations had converged based on the convergence criteria. In general, the slowest converging simulations corresponded to some of the warmest climates (final temperatures in Fig. 3b and c were generally warmer than those in Fig. 3a). It cannot be guaranteed that further changes will not occur; however, we note that the criteria and length of the simulations greatly exceed Paleoclimate Modelling Intercomparison Project – Last Glacial Maximum (PMIP-LGM) (Kageyama et al., 2017) and Deep-Time Model Intercomparison Project (PMIP-DeepMIP) (Lunt et al., 2017) protocols.

3 Results

3.1 Comparison of deep ocean temperatures to benthic ocean data

Before using the model to investigate the linkage of deep ocean temperatures to global mean surface temperatures, it is interesting to evaluate whether the modelled deep ocean temperatures agree with the deep ocean temperatures obtained from the isotopic studies of benthic foraminifera (Zachos et al., 2008; Friedrich et al., 2012). It is important to note that the temperatures are strongly influenced by the choice of CO_2, so we are not expecting complete agreement, but we simply wish to evaluate whether the model is within plausible ranges. If the modelled temperatures were in complete disagreement with data, then it might suggest that the model was too far away from reality to allow us to adequately discuss

Table 2. Summary of model simulations. The table summarizes the simulations performed in this study. The sixth and seventh columns refer to how the model was initialized. The smooth CO_2 simulations were initialized from existing simulations using paleogeographies which were provided commercial in confidence. The time periods that these paleogeographies correspond to are listed in column 6, and the CO_2 value used in the runs is in column 7. The Foster CO_2 simulations were initialized from the end point of the smooth CO_2 simulations.

Time period (in Ma)	CO_2 for the smooth CO_2 (in ppmv)	CO_2 for the Foster CO_2 (in ppmv)	Length of run (smooth CO_2) (in years)	Length of run (Foster CO_2) (in years)	Time period from existing simulations used for the initial condition for smooth CO_2 simulation (in Ma)	CO_2 used for the initial conditions (in ppmv)
0.0	280	276	5000	5000	0	280
3.1	384	298	5000	2000	3	401
10.5	410	299	5000	2000	13	280
14.9	423	10	5000	2000	13	280
19.5	430	338	5000	2000	13	280
25.6	439	502	5000	2000	26	560
31.0	500	764	5000	5000	26	560
35.9	533	901	5000	5000	26	560
39.5	557	796	5000	5000	26	560
44.5	594	751	5000	8000	26	560
51.9	649	736	5000	8000	52	560
56.0	630	570	5000	5000	52	560
61.0	604	335	5000	5000	52	560
66.0	576	229	5000	5000	69	560
69.0	560	262	5000	5000	69	560
75.0	633	559	5000	2000	69	560
80.8	704	667	5000	2000	69	560
86.7	775	590	5000	8000	69	560
91.9	839	466	5000	8000	92	560
97.2	840	707	5000	8000	92	560
102.6	840	1008	5000	5000	92	560
107.0	840	1028	5000	5000	92	560
111.0	827	1148	5000	8000	92	560
115.8	811	1103	5000	8000	92	560
121.8	784	986	5000	5000	92	560
127.2	752	898	5000	5000	92	560
131.2	728	896	5000	5000	92	560
136.4	699	1020	5000	8000	136	840
142.4	677	832	5000	8000	136	840
145.0	667	713	5000	8000	136	840
148.6	654	721	5000	8000	136	840
154.7	631	802	5000	5000	155	560
160.4	617	785	5000	5000	155	560
164.8	606	868	5000	8000	155	560
168.2	596	1019	5000	5000	167	840
172.2	581	1046	5000	5000	167	840
178.4	560	986	5000	5000	178	1120
186.8	560	949	5000	5000	178	1120
190.8	560	1181	5000	5000	178	1120
196.0	560	1784	5000	5000	178	1120
201.3	560	1729	5000	5000	178	1120
204.9	560	1503	5000	5000	218	560
213.2	560	1223	5000	5000	218	560
217.8	560	1481	5000	5000	218	560
222.4	557	1810	5000	5000	218	560
227.0	553	2059	5000	5000	218	560
232.0	549	1614	5000	5000	218	560

Table 2. Continued.

Time period (in Ma)	CO_2 for the smooth CO_2 (in ppmv)	CO_2 for the Foster CO_2 (in ppmv)	Length of run (smooth CO_2) (in years)	Length of run (Foster CO_2) (in years)	Time period from existing simulations used for the initial condition for smooth CO_2 simulation (in Ma)	CO_2 used for the initial conditions (in ppmv)
233.6	548	1492	5000	5000	218	560
239.5	543	1034	5000	8000	218	560
244.6	540	419	5000	2000	218	560
252.0	534	879	5000	2000	257	1120
256.0	531	811	5000	2000	257	1120
262.5	526	352	5000	2000	257	1120
265.1	524	321	5000	2000	257	1120
268.7	521	311	5000	2000	257	1120
275.0	517	556	5000	2000	257	1120
280.0	513	690	5000	2000	257	1120
286.8	508	626	5000	2000	257	1120
292.6	503	495	5000	2000	297	280
297.0	500	445	5000	2000	297	280
301.3	510	393	5000	2000	297	280
305.4	520	358	5000	2000	297	280
311.1	534	338	5000	2000	297	280
314.6	542	327	5000	2000	297	280
319.2	553	328	5000	2000	297	280
327.0	571	317	5000	2000	297	280
330.9	581	296	5000	2000	339	420
333.0	586	263	5000	2000	339	420
338.8	600	233	5000	2000	339	420
344.0	653	565	5000	2000	339	420
349.0	705	645	5000	2000	339	420
354.0	758	589	5000	2000	339	420
358.9	809	587	5000	2000	339	420
365.6	880	806	5000	2000	339	420
370.0	926	811	5000	2000	339	420
375.0	979	1052	5000	2000	339	420
380.0	1029	1269	5000	2000	339	420
385.2	1079	1377	5000	2000	377	1680
390.5	1131	1093	5000	2000	377	1680
395.0	1174	1297	5000	2000	377	1680
400.0	1223	1731	5000	2000	377	1680
405.0	1271	1689	5000	2000	377	1680
409.2	1319	2102	5000	2000	377	1680
415.0	1368	1579	5000	2000	377	1680
421.1	1427	1457	5000	2000	377	1680
425.2	1466	1490	5000	2000	377	1680
430.4	1517	1531	5000	2000	377	1680
436.0	1571	1576	5000	2000	377	1680
441.2	1614	1643	5000	2000	439	1877
444.5	1636	1708	5000	2000	439	1877
449.1	1666	1799	5000	2000	439	1877
455.7	1710	1929	5000	2000	439	1877
460.0	1738	2013	5000	2000	439	1877
465.0	1770	2111	5000	2000	439	1877
470.0	1803	2210	5000	2000	439	1877
475.0	1836	2308	5000	2000	439	1877

Table 2. Continued.

Time period (in Ma)	CO_2 for the smooth CO_2 (in ppmv)	CO_2 for the Foster CO_2 (in ppmv)	Length of run (smooth CO_2) (in years)	Length of run (Foster CO_2) (in years)	Time period from existing simulations used for the initial condition for smooth CO_2 simulation (in Ma)	CO_2 used for the initial conditions (in ppmv)
481.6	1879	2438	5000	2000	439	1877
485.4	1904	2513	5000	2000	439	1877
491.8	1946	2639	5000	2000	439	1877
495.5	1970	2711	5000	2000	439	1877
498.8	1992	2776	5000	2000	439	1877
505.0	2020	2870	5000	2000	439	1877
510.0	2040	2940	5000	2000	439	1877
515.0	2060	3010	5000	2000	439	1877
520.0	2080	3080	5000	2000	439	1877
525.0	2100	3150	5000	2000	439	1877
530.0	2120	3220	5000	2000	439	1877
535.0	2140	3290	5000	2000	439	1877
541.0	2164	3374	5000	2000	439	1877

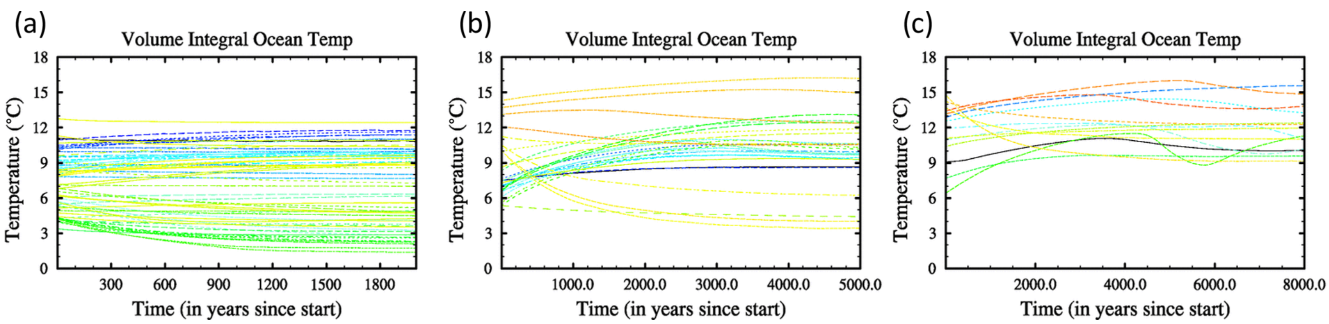

Figure 3. Time series of the annual volume mean ocean temperature for all 109 simulations. Panel **(a)** shows those simulations for which 2000 years was sufficient to satisfy the convergence criteria described in the text (these were for all simulations listed in Table 1 except those listed in panels **b** and **c**), **(b)** those simulations which required 5000 years (these were for all the simulations for 31.0, 35.9, 39.5, 55.8, 60.6, 66.0, 69.0, 102.6, 107.0, 121.8, 127.2, 154.7, 160.4, 168.2, 172.2, 178.4, 186.8, 190.8, 196.0, 201.3, 204.9, 213.2, 217.8, 222.4, 227.0, 232.0, and 233.6 Ma), and **(c)** those simulation which required 8000 years (these were simulations for 44.5, 52.2, 86.7, 91.9, 97.2, 111.0, 115.8, 131.2, 136.4, 142.4, 145.0, 148.6, 164.8, and 239.5 Ma). The different coloured lines show the different runs. The plots simply show the extent to which all runs have reached steady state. For more details about specific simulations, please see the figures in the Supplement.

deep ocean–surface ocean linkages. If the modelled temperatures are plausible, then it shows that we are operating within the correct climate space. A detailed comparison of modelled surface and benthic temperatures to data throughout the Phanerozoic, using multiple CO_2 scenarios, is the subject of a separate ongoing project.

Figure 4a compares the modelled deep ocean temperature to the foraminifera data from the Cenozoic and Cretaceous (115 Ma). The observed isotope data are converted to deep ocean temperature using the procedures described by Hansen et al. (2013). The modelled deep temperature shown in Fig. 4a (solid line) is the average temperature at the bottom level of the model, excluding depths less than 1000 m (to avoid continental shelf locations which are typically not included in benthic data compilations). The observed benthic data are collected from a range of depths and are rarely at the very deepest levels (e.g. the new cores in Friedrich et al. 2011 are from current water depths ranging from 1899 to 3192 m). Furthermore, large data compilations rarely include how the depth of a particular site changed with time, and thus effectively assume that any differences between basins and through time are entirely due to climate change and not to changes in depth. Hence, throughout the rest of the paper, we frequently use the modelled 2731 m temperatures as a surrogate for the true benthic temperature. This is a pragmatic definition because the area of deep ocean reduces rapidly (e.g. there is typically only 50 % of the globe deeper than 3300 m). To evaluate whether this procedure gave a reasonable result, we also calculated the global average temperature at the model bottom and at the model level at a depth of 2731 m. The latter is shown by the dashed line in Fig. 4a. In general, the agreement between model bottom water temperatures and 2731 m temperatures is very good. The standard deviation between model bottom water and constant depth of 2731 m is 0.7 °C, and the maximum difference is 1.4 °C. Compared to the overall variability, this is a relatively small difference and shows that it is reasonable to assume that the deep ocean has weak vertical gradients.

The total change in benthic temperatures over the Late Cretaceous and Cenozoic is well reproduced by the model, with the temperatures associated with the "smooth" CO_2 record being particularly good. We do not expect the model to represent substage changes (hundreds of thousands of years) such as the Paleocene-Eocene Thermal Maximum excursion or ocean anoxic events, but we do expect that the broader temperature patterns should be simulated.

Comparison of the two simulations illustrates how strongly CO_2 controls global mean temperature. The Foster-CO_2-driven simulation substantially differs from the estimates of deep-sea temperature obtained from benthic foraminifera and is generally a poorer fit to data. The greatest mismatch between the Foster curve and the benthic temperature curve is during the Late Cretaceous and early Paleogene. Both dips in the Foster CO_2 simulations correspond to relatively low estimates of CO_2 concentrations. For these periods, the dominant source of CO_2 values is from paleosols (Fig. 1), and thus we are reliant on one proxy methodology. Unfortunately, the alternative CO_2 reconstructions of Witkowski et al. (2018) have a data gap during these periods.

A second big difference between the Foster curve and the benthic temperature curve occurs during the Cenomanian–Turonian. This difference is similarly driven by a low estimate of CO_2 in the Foster CO_2 curve. These low CO_2 values are primarily based on stomatal density indices. As can be seen in Fig. 1, stomatal indices frequently suggest CO_2 levels lower than estimates obtained by other methods. The CO_2 estimates by Witkowski et al. (2018) generally supports the higher levels of CO_2 (near 1000 ppmv) that are suggested by the "smooth" CO_2 curve.

Both sets of simulations underestimate the warming during the middle Miocene. This issue has been seen before in other models, e.g. You et al. (2009), Knorr et al. (2011), Krapp and Jungclaus (2011), Goldner et al. (2014), and Steinthorsdottir et al. (2021). In order to simulate the surface warmth of the middle Miocene (15 Ma), CO_2 concentrations in the range 460–580 ppmv were required, whereas the CO_2 reconstructions for this period (Foster et al., 2017) are generally quite low (250–400 ppmv). This problem may be either due to the climate models having too low a climate sensitivity or that the estimates of CO_2 are too low (Stoll et al., 2019).

The original compilation of Zachos et al. (2008) represented a relatively small portion of the global ocean, and the implicit assumption was made that these results represented the entire ocean basin. Cramer et al. (2009) examined the data from an ocean basin perspective and suggested that these inter-basin differences were generally small during the Late Cretaceous and early Paleogene (90–35 Ma), and the differences between ocean basins were larger during the late Paleogene and early Neogene. Our model largely also reproduces this pattern. Figure 5 shows the ocean temperature at 2731 m during the Late Cretaceous (69 Ma), the late Eocene (39 Ma), and the Oligocene (31 Ma) for the "smooth"

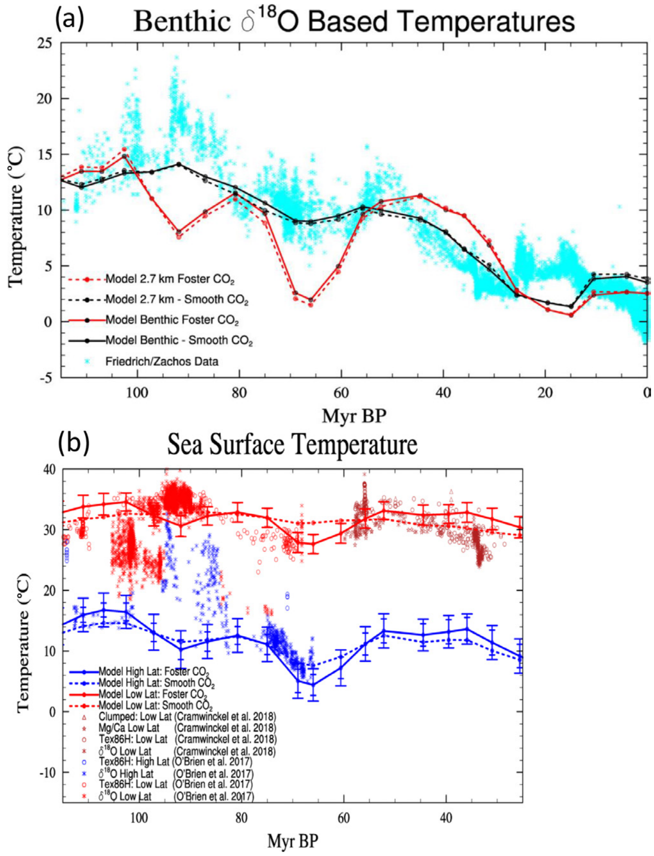

Figure 4. **(a)** Comparison of modelled deep ocean temperatures versus those from Zachos et al. (2008) and Friedrich et al. (2012) converted to temperature using the formulation in Hansen et al. (2013). The model temperatures are global averages over the bottom layer of the model but exclude shallow marine settings (less than 1000 m). The dashed lines show the modelled global average ocean temperatures at the model layer centred at 2731 m and **(b)** comparison of modelled sea surface temperatures with the compilations of O'Brien et al. (2017) and Cramwinckel et al. (2018). The data are a combination of Tex_{86}, $\delta^{18}O$, Mg/Ca, and clumped isotope data. The model data show low-latitude temperatures (averaged from 10° S to 10° N) and high-latitude temperatures (averaged over 47.5 to 65° N and 47.5 to 65° S). The Foster CO_2 simulations also show a measure of the spatial variability. The large bars show the spatial standard deviation across the whole region, and the smaller bars show the average spatial standard deviation along longitudes within the region. Note that the ranges of both the x and y axes differ between panels **(a)** and **(b)**.

CO_2 simulations. In the Late Cretaceous, the model temperatures are almost identical in the North Atlantic and Pacific (8–10 °C). There is warmer deep water forming in the Indian Ocean (deep mixed layer depths; not shown) and off the west coast of Australia (10–12 °C), but otherwise the pattern is very homogeneous. This is in agreement with some paleoreconstructions for the Cretaceous (e.g. Murphy and Thomas, 2012).

By the time we reach the late Eocene (39 Ma), the North Atlantic and Pacific remain very similar but cooler deep water (6–8 °C) is now originating in the South Atlantic. The South Atlantic cool bottom water source remains in the Oligocene, but we see a strong transition in the North Atlantic to an essentially modern circulation with the major source of deep, cold water occurring in the high southerly latitudes (3–5 °C) and strong gradient between the North Atlantic and Pacific.

Figure 5 also shows the modelled deep ocean temperatures for the present day (Fig. 5d) compared to the World Ocean Atlas data (Fig. 5e). It can be seen that the broad patterns are well reproduced in the model, with good predictions of the mean temperature of the Pacific. The model is somewhat too warm in the Atlantic itself and has a stronger plume from the Mediterranean than is shown in the observations.

3.2 Comparison of model sea surface temperature to proxy data

The previous section focused on benthic temperatures, but it is also important to evaluate whether the modelled sea surface temperatures are plausible (within the uncertainties of the CO_2 reconstructions). Figure 4b shows a comparison between the model simulations of sea surface temperature and two published syntheses of proxy SST data. O'Brien et al. (2017) compiled TEX_{86} and $\delta^{18}O$ for the Cretaceous, separated into tropical and high-latitude (polewards of 48°) regions. Cramwinckel et al. (2018) compiled early Cenozoic tropical SST data, using Tex_{86}, $\delta^{18}O$, Mg/Ca, and clumped isotopes. We compare these to modelled SST for the region 15° S to 15° N and for the average of the Northern Hemisphere and Southern Hemisphere between 47.5 and 60°N/S. The proxy data include sites from all ocean basins and so we also examined the spatial variability within the model. This spatial variability consists of changes along longitude (effectively different ocean basins) and changes with latitude (related to the gradient between the Equator and the poles). We therefore calculated the average standard deviation of SST relative to the zonal mean at each latitude (this is shown by the smaller tick marks) and the total standard deviation of SST relative to the regional average. In practice, the equatorial values are dominated by inter-basin variations, and hence the two measures of spatial variability are almost identical. The high-latitude variability has a bigger difference between the longitudinal variations and the total variability, because the Equator-to-pole temperature gradient (i.e. the temperatures at the latitude limits of the region) is a few degrees warmer or colder than the average. The spatial variability was very similar for the smooth CO_2 and Foster CO_2 simulations, so for clarity, in Fig. 4b, we only show the results as error bars on the model Foster CO_2 simulations.

Overall, the comparison between model and data is generally reasonable. The modelled equatorial temperatures largely follow the data, albeit with considerable scatter in the data. Both simulations tend to be towards the warmest equatorial data in the early Cretaceous (Albian). These temperatures largely come from Tex_{86} data. There are many $\delta^{18}O$-based SSTs which are significantly colder during this period. These data almost exclusively come from cores 1050/1052, which are in the Gulf of Mexico. It is possible that these data are offset due to a bias in the $\delta^{18}O$ of sea water because of the relatively enclosed region. The Foster CO_2 simulations are noticeably colder than the data at the Cenomanian peak warmth, which is presumably related to the relatively low CO_2, as discussed for the benthic temperatures. The benthic record also showed a cool (low CO_2) bias in the Late Cretaceous. This is not such an obvious feature of the surface temperatures. The Foster simulations are colder than the smooth CO_2 simulations during the Late Cretaceous but there is not a strong mismatch between model and data. Both simulations are close to the observations, though the smooth CO_2 simulations better match the high-latitude data (but show slightly poorer match with the tropical data).

The biggest area of disagreement between model and data is at high latitudes in the mid-Cretaceous warm period. In common with previous work with this model in the context of the Eocene (Lunt et al., 2021), the model is considerably cooler than the data, with a 10–15 °C mismatch between models and data. The polar sea surface temperature estimates may have a seasonal bias because productivity is likely to be higher during the warmer summer months, and, if we select the summer season temperatures from the model, then the mismatch is slightly reduced by about 4 °C. The problem of cool high latitudes in models is seen in many model studies, and there is increasing evidence that this is related to the way that the models simulate clouds (Kiehl and Shields, 2013; Sagoo et al., 2013; Zhu et al., 2019; Upchurch et al., 2015). Of course, in practice, deep water is formed during winter so the benthic temperatures do not suffer from a summer bias.

3.3 Correlation of deep ocean temperatures to polar sea surface temperatures

The previous sections showed that the climate model was producing a plausible reconstruction of past ocean temperature changes, at least within the uncertainties of the CO_2 estimates. We now use the HadCM3L model to investigate the links between deep ocean temperature and global mean surface temperature.

In theory, the deep ocean temperature should be correlated with the sea surface temperature at the location of deep-water

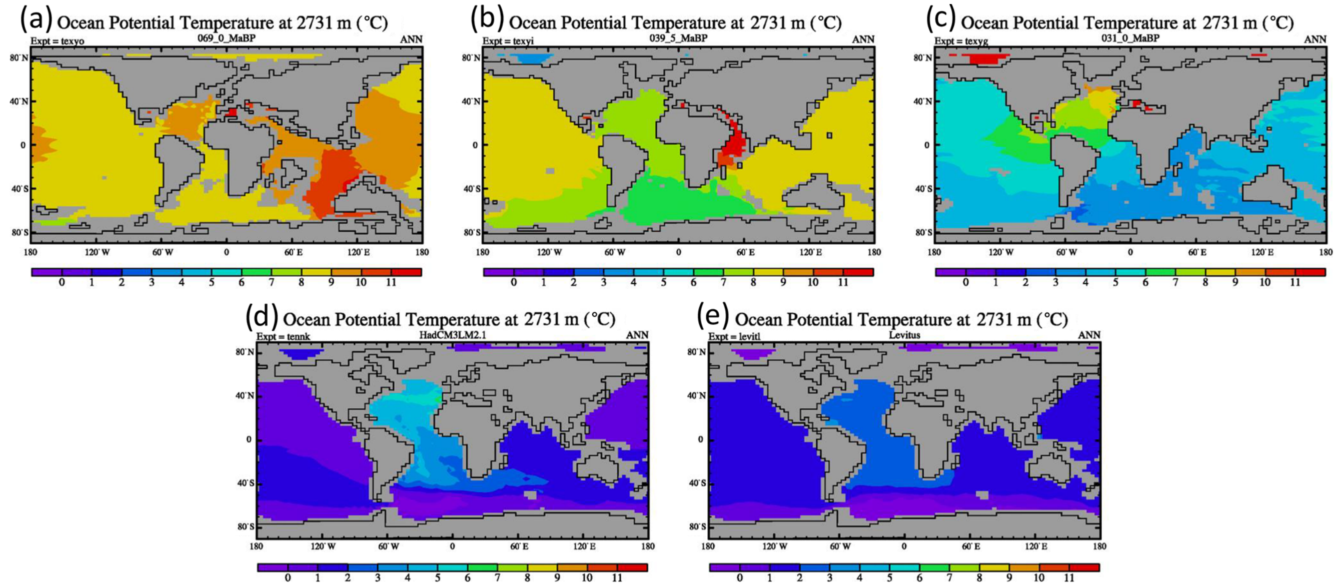

Figure 5. Modelled annual mean ocean temperatures at 2731 m depth for three examples of past time periods. Panel **(a)** is for the Late Cretaceous, panel **(b)** is for the late Eocene (39.5 Ma), and panel **(c)** is for the Oligocene (31 Ma). These are results from the smooth CO_2 set of simulations which agree better with the observed benthic temperature data. Also included are **(d)** the pre-industrial simulations and **(e)** the World Ocean Atlas 1994 observational data, provided by the NOAA-ESRL Physical Sciences Laboratory, Boulder, Colorado, from their website at https://psl.noaa.gov/ (last access: 30 June 2021). The thin black lines show the coastlines, and the grey areas are showing where the ocean is shallower than 2731 m.

formation which is normally assumed to be high-latitude surface waters in winter. We therefore compare deep ocean temperatures (defined as the average temperature at the bottom of the model ocean, where the bottom must be deeper than 1000 m) with the average winter sea surface temperature polewards of 60° (Fig. 6). Winter is defined as December, January, and February (DJF) in the Northern Hemisphere and June, July, and August (JJA) in the Southern Hemisphere. Also shown in Fig. 6 is the best-fit line, which has a slope of 0.40 (±0.05 at the 97.5 % level), an r^2 of 0.59, and a standard error of 1.2 °C. We obtained very similar results when we compared the polar sea surface temperatures with the average temperature at 2731 m instead of the true benthic temperatures. We also compared the deep ocean temperatures to the mean polar sea surface temperatures when the mixed layer depth exceeded 250 m (poleward of 50° N/S). The results were similar, although the scatter was somewhat larger ($r^2 = 0.48$).

Overall, the relationship between deep ocean temperatures and polar sea surface temperatures is clear (Fig. 6) but there is considerable scatter around the best-fit line, especially at the high end, and the slope is less steep than perhaps would be expected (Hansen and Sato, 2012). The scatter is less for the Cenozoic and Late Cretaceous (up to 100 Ma: green and orange dots and triangles). If we used only Cenozoic and Late Cretaceous simulations, then the slope is similar (0.43) but with $r^2 = 0.92$ and a standard error of 0.47 °C. This provides strong confirmation that benthic data are a robust approximation to polar surface temperatures when the continental configuration is similar to the present.

However, the scatter is greater for older time periods, with the largest divergence observed for the warm periods of the Triassic and early Jurassic, particularly for the Foster CO_2 simulations (purple and blue dots). Examination of climate models for these time periods reveals relatively sluggish and shallow ocean circulation, with weak horizontal temperature gradients at depth (though salinity gradients can still be important; Zhou et al., 2008). For instance, in the Ladinian, mid-Triassic stage (∼ 240 Ma), the overturning circulation is extremely weak (Fig. 7). The maximum strength of the Northern Hemisphere overturning cell is less than 10 Sv and the southern cell is less than 5 Sv. Under these conditions, deep ocean water does not always form at polar latitudes. Examination of the mixed layer depth (not shown) shows that during these time periods, the deepest mixed layer depths are in the subtropics. In subtropics, there is very high evaporation relative to precipitation (due to the low precipitation and high temperatures). This produces highly saline waters that sink and spread out into the global ocean.

The idea that deep water may form in the tropics is in disagreement with early hypotheses (e.g. Emiliani, 1954), but they were only considering the Tertiary, and our model does not simulate any low-latitude deep-water formation during this period. We only see significant tropical deep-water formation for earlier periods, and this has previously been suggested as a mechanism for warm Cretaceous deep-

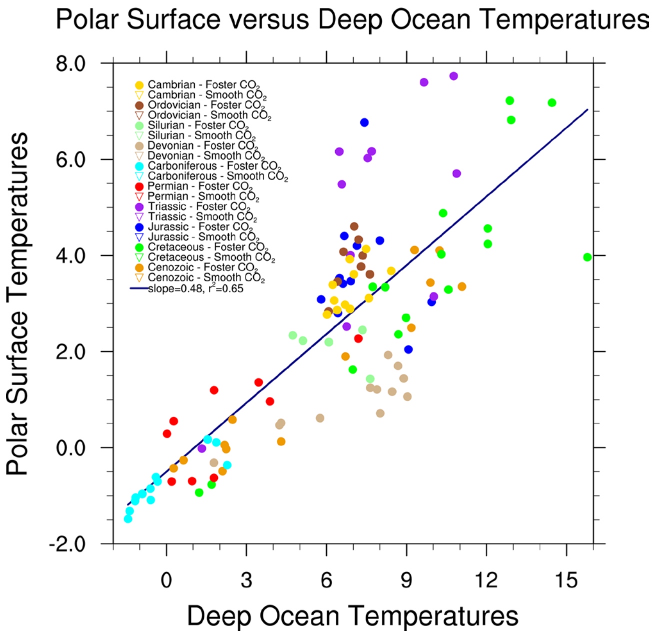

Figure 6. Correlations between deep ocean temperatures and surface polar sea surface temperatures. The deep ocean temperatures are defined as the average temperature at the bottom of the model ocean, where the bottom must be deeper than 1000 m. The polar sea surface temperatures are the average winter (i.e. northern polar in DJF and southern polar in JJA) sea surface temperature polewards of 60°. The inverted triangles show the results from the smooth CO_2 simulations and the dots refer to the Foster CO_2 simulations. The colours refer to different geological eras.

water formation (Brass et al., 1982; Kennett and Stott, 1991). Deep water typically forms in convective plumes. Brass et al. (1982) showed that the depth and spreading of these plumes are related to the buoyancy flux, with the greatest flux leading to bottom water and plumes of lesser flux leading to intermediate water. Brass et al. (1982) suggested that this could occur in warm conditions in the tropics, particularly if there were significant epicontinental seaways, and hypothesized that it "has been a dominant mechanism of deep-water formation in historical times". It is caused by a strong buoyancy flux linked to strong evaporation at high temperatures.

Our computer model simulations are partly consistent with this hypothesis. The key aspect for the model is a relatively enclosed seaway in the tropics and warm conditions. The paleogeographic reconstructions (see figures in the Supplement) suggest an enclosed Tethyan-like seaway starting in the Carboniferous and extending through to the Jurassic and early Cretaceous. However, the colder condition of the Carboniferous prevents strong tropical buoyancy fluxes. When we get into the Triassic and Jurassic, the warmer conditions lead to strong evaporation at low latitudes and bottom water formation in the tropics. This also explains why we see more tropical deep water (and hence poorer correlations between deep and polar surface temperatures in Fig. 6) when using the Foster CO_2 since this is generally higher (and hence warmer) than the smoothed CO_2 record.

An example of the formation of tropical deep water is shown in Fig. 8. This shows a vertical cross section of temperature and salinity near the Equator for the Ladinian stage, mid-Triassic (240 Ma). The salinity and temperature cross section clearly shows high-salinity warm waters sinking to the bottom of the ocean and spreading out. This is further confirmed by the water age tracer in Fig. 9. This shows the water age (measured as time since it experienced surface conditions; see England, 1995) at 2731 m in the model for the Permian, Triassic, Cretaceous, and the present day. The present-day simulation shows that the youngest water is in the North Atlantic and off the coast of Antarctica, indicating that this is where the deep water is forming. By contrast, the Triassic period shows that the youngest water is in the tropical Tethyan region and that it spreads out from there to fill the rest of the ocean basin. There is no young water at high latitudes, confirming that the source of bottom water is tropical only. For the Permian, although there continues to be a Tethyan-like tropical seaway, the colder conditions mean that deep water is again forming at high latitudes only. The Cretaceous is more complicated. It shows younger water in the high latitudes, but also shows some young water in the Tethys which merges with the high-latitude waters. An additional indicator of the transitional nature of the Cretaceous is the mixed layer depth (see figures in the Supplement). This is a measure of where water is mixing to deeper levels. For this time period, there are regions of deep mixed layer in both the tropics and high latitudes, whereas it is only deep in the tropics for the Triassic and at high latitudes for the present day.

This mechanism for warm deep-water formation has also been seen in other climate models (e.g. Barron and Peterson, 1990). However, Poulsen et al. (2001) conclude that in their model of the Cretaceous, high-latitude sources of deep water diminish with elevated CO_2 concentrations but did not see the dominance of tropical sources. Other models (e.g. Ladant et al., 2020) do not show any significant tropical deep-water formation, suggesting that this feature is potentially a model-dependent result.

The correlation between deep ocean temperatures and the temperature of polar surface waters differs between the "smooth" CO_2 simulations and the Foster CO_2 simulations. The slope is only 0.30 ($r^2 = 0.57$) for the "smooth" CO_2 simulations, whereas the slope is 0.48 ($r^2 = 0.65$) for the Foster simulations. This is because CO_2 is a strong forcing agent that influences both the surface and deep ocean temperatures. By contrast, if the CO_2 does not vary as much, then the temperature does not vary as much, and the influence of paleogeography becomes more important. These paleogeographic changes generally cause subtle and complicated changes in ocean circulation that affect the location and latitude of deep-water formation.

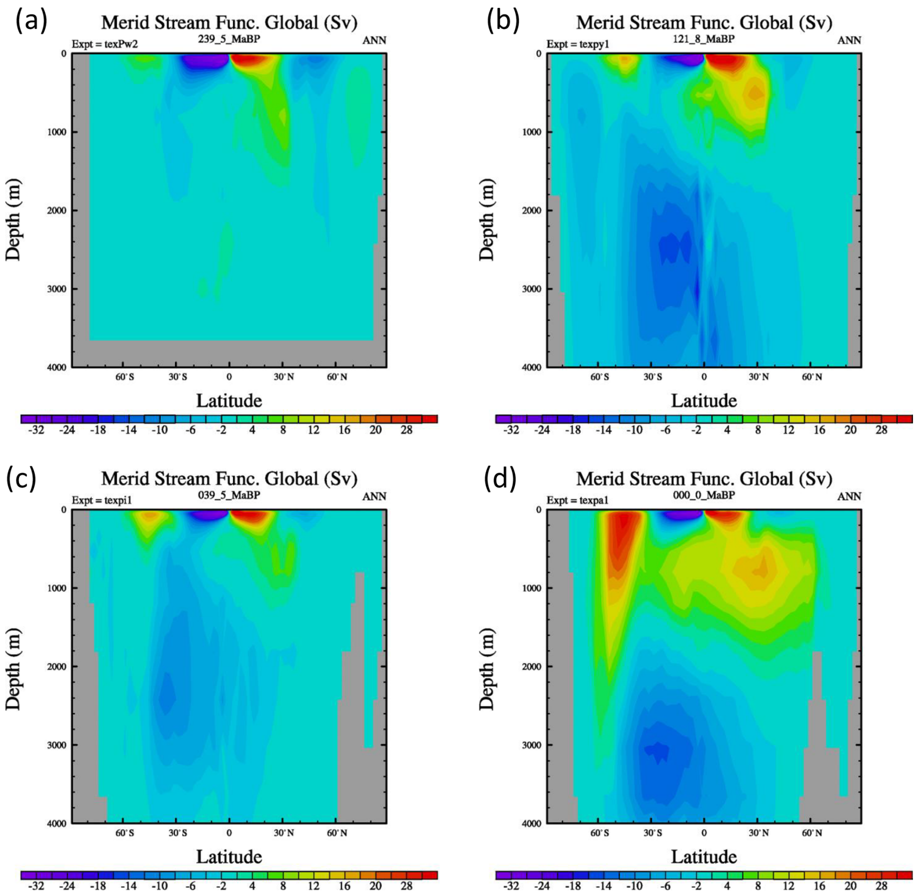

Figure 7. Global ocean overturning circulation (in Sverdrups) for four different time periods for the Foster CO_2 simulations. Positive (yellow/red) values correspond to a clockwise circulation; negative (dark blue/purple) values represent an anti-clockwise circulation. **(a)** Middle Triassic, Ladinian, 239.5 Ma, **(b)** Lower Cretaceous, Aptian, 121.8 Ma, **(c)** Late Eocene, Bartonian, 39.5 Ma, and **(d)** present day. Paleogeographic reconstructions older than the oldest ocean floor (∼ Late Jurassic) have uniform deep ocean floor depth.

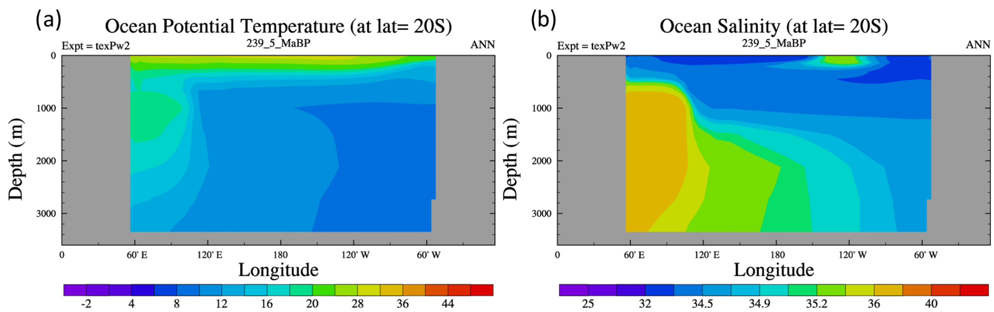

Figure 8. Longitudinal cross section at 20°S of **(a)** ocean potential temperature and **(b)** salinity for the Ladinian (240 Ma). Temperature is in Celsius and salinity is in PSU.

In contrast, the mid-Cretaceous is also very warm but the continental configuration (specifically, land at high southern latitudes) favours the formation of cool, high-latitude deep water. Throughout the Cretaceous, there is a significant southern high-latitude source of deep water, and hence deep-water temperatures are well correlated with surface high-latitude temperatures. The strength of this connection, however, may be overexaggerated in the model. Like many climate models, HadCM3 underestimates the reduction in the pole-to-Equator sea surface temperature (Lunt et al., 2012, 2021). This means that during the Cretaceous the high latitudes are probably too cold. Consequently, some seasonal sea ice does form, which encourages the formation of cold deep water, via brine rejection.

In the late Eocene (∼ 40 Ma), the ocean circulation is similar to the Cretaceous, but the strong southern overturning cell is closer to the South Pole, indicating that the main source of deep water has moved further polewards. The poleward movement of the region of downwelling waters explains some of the variability between deep ocean temperatures and temperature of polar surface waters.

For reference, we also include the present-day meridional circulation. The modern Southern Hemisphere circulation is essentially a strengthening of late Eocene meridional circulation. The Northern Hemisphere is dominated by the Atlantic meridional overturning circulation. The Atlantic circulation pattern does not resemble the modern pattern of circulation until the Miocene.

3.4 Surface polar amplification

The conceptual model used to connect benthic ocean temperatures to global mean surface temperatures assumes that there is a constant relationship between high-latitude sea surface temperatures and global mean annual mean surface air temperature. Hansen and Sato (2012) argue that this amplification is partly related to ice–albedo feedback but also includes a factor related to the contrasting amplification of temperatures on land compared to the ocean. To investigate the stability of this relationship, Fig. 10 shows the correlation between polar winter sea surface temperatures (between 60 and 90° in both hemispheres) and global mean surface air temperature. The polar temperatures are the average of the two winter hemispheres (i.e. average of DJF polar SSTs in the Northern Hemisphere and JJA polar SSTs in the Southern Hemisphere). Also shown is a simple linear regression, with an average slope of 1.3 and with $r^2 = 0.79$. If we only use northern polar winter temperatures, the slope is 1.1; if we only use southern polar winter temperatures, then the slope is 0.7. Taken separately, the scatter about the mean is considerably larger (r^2 of 0.5 and 0.6, respectively) than the scatter if both datasets are combined ($r^2 = 0.79$). The difference between the Southern Hemisphere and Northern Hemisphere response complicates the interpretation of the proxies and leads to potentially substantial uncertainties.

As expected, there appears to be a strong non-linear component to the correlation. There are two separate regimes: (1) one with a steeper slope during colder periods (average polar winter temperature less than about 1 °C) and (2) a shallower slope for warmer conditions. This is strongly linked to the extent of sea-ice cover. Cooler periods promote the growth of sea ice which strengthens the ice–albedo feedback mechanism, resulting in a steeper overall temperature gradient (strong polar amplification). Of course, the ocean sea surface temperatures are constrained to be −2 °C but an expansion of sea ice moves this further equatorward. Conversely, the warmer conditions result in less sea ice and hence a weaker sea ice–albedo feedback, resulting in a weaker temperature gradient (reduced polar amplification). This suggests that using a simple linear relationship (as in Hansen et al., 2008) could be improved upon.

Examining the Foster CO_2 and "smooth" CO_2 simulations reveals an additional factor. If we examine the smooth CO_2 simulations only, then the best-fit linear slope is slightly less than the average slope (1.1 versus 1.3). This can be explained by the fact that we have fewer very cold climates (particularly in the Carboniferous) due to the relatively elevated levels of CO_2. However, the scatter in the "smooth" CO_2 correlation is much larger, with an r^2 of only 0.66. By comparison, correlation between global mean surface temperature and polar sea surface temperature using the Foster CO_2 has a similar overall slope to the combined set and a smaller amount of scatter. This suggests that CO_2 forcing and the polar amplification response have an important impact on the relationship between global and polar temperatures. The variations of carbon dioxide in the Foster set of simulations are large and they drive large changes in global mean temperature. Conversely, significant sea-ice–albedo feedbacks characterize times when the polar amplification is important. There are several well-studied processes that lead to such changes, including albedo effects from changing ice but also from poleward heat transport changes, cloud cover, and latent heat effects (Sutton et al., 2007; Alexeev et al., 2005; Holland and Bitz, 2003). By contrast, the smooth CO_2 simulations have considerably less forcing due to CO_2 variability, which leads to a larger paleogeographic effect. For instance, when there is more land at the poles, there will be more evaporation over the land areas, and hence simple surface energy balance arguments would suggest different temperatures (Sutton et al., 2007).

In Fig. 10, there are a few data points which are complete outliers. These correspond to simulations in the Ordovician; the outliers happen irrespective of the CO_2 model that is used. Inspection of these simulations shows that the cause for this discrepancy is related to two factors: (1) a continental configuration with almost no land in the Northern Hemisphere and (2) a reconstruction which includes significant Southern Hemisphere ice cover (see Figs. 1 and 2). Combined, these factors produced a temperature structure which is highly non-symmetric, with the southern high latitudes being more than 20 °C colder than the northern high latitudes. This anomaly biases the average polar temperatures shown in Fig. 10.

3.5 Deep ocean temperature versus global mean temperature

The relationships described above help to understand the overall relationship between deep ocean temperatures and global mean temperature. Figure 11 shows the correlation between modelled deep ocean temperatures (> 1000 m) and global mean surface air temperature, and Fig. 12 shows a comparison of changes in modelled deep ocean temperature

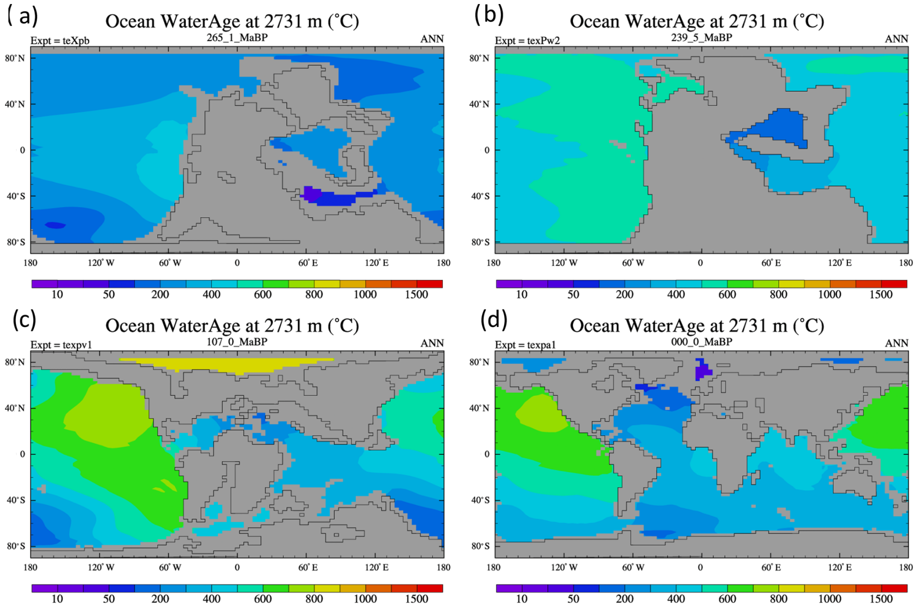

Figure 9. Modelled age of water tracer at 2731 m for four different time periods: **(a)** 265 Ma, **(b)** 240 Ma, **(c)** 107 Ma, and **(d)** 0 Ma. Units are years.

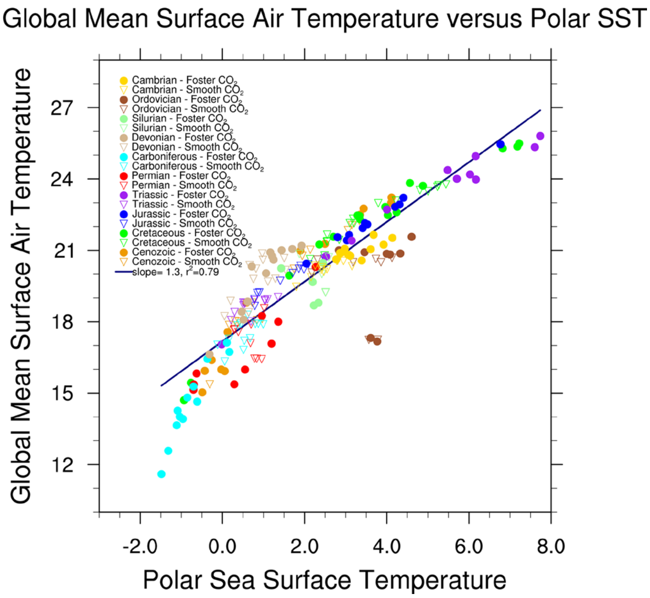

Figure 10. Correlation between high-latitude ocean temperatures (polewards of 60°) and the annual mean, global mean surface air temperature. The polar temperatures are the average of the two winter hemispheres (i.e. northern DJF and southern JJA). Other details are as in Fig. 6.

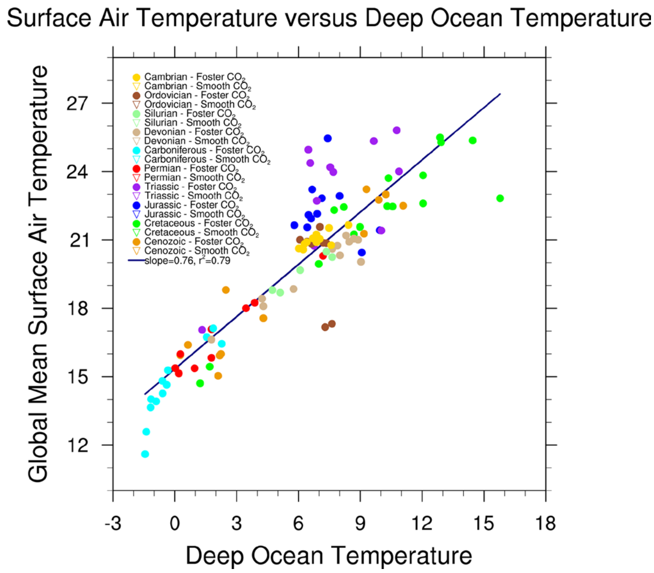

Figure 11. Correlation between the global mean, annual mean surface air temperature and the deep ocean temperature. The deep ocean temperatures are defined as the average temperature at the bottom of the model ocean, where the bottom must be deeper than 1000 m. Other details are as in Fig. 6.

compared to model global mean temperature throughout the Phanerozoic.

The overall slope is 0.64 (0.59 to 0.69) with $r^2 = 0.74$. If we consider the last 115 Myr (for which there exist compiled benthic temperatures), then the slope is slightly steeper (0.67 with an $r^2 = 0.90$). Similarly, the smooth CO_2 and the Foster CO_2 simulation results have very different slopes. The smooth CO_2 simulations have a slope of 0.47, whereas the Foster CO_2 simulations have a slope of 0.76. The root mean square departure from the regression line in Fig. 11 is 1.3 °C. Although we could have used a non-linear fit as we might expect such a relationship if the pole-to-Equator temperature gradient changes, all use of benthic temperatures as a global mean surface temperature proxy is based on a linear relationship.

The relatively good correlations in Fig. 11 are confirmed when examining Fig. 12a and b. On average, the deep ocean temperatures tend to underestimate the global mean change (Fig. 12b), which is consistent with the regression slope being less than 1. However, the errors are substantial, with the largest errors occurring during the pre-Cretaceous, and can be 4–6 °C. This is an appreciable error that would have a substantial impact on estimates of climate sensitivity. Even within the Late Cretaceous and Cenozoic, the errors can exceed 2 °C, which can exceed 40 % of the total change.

The characteristics of the plots can best be understood in terms of Figs. 6 and 10. For instance, most of the Carboniferous simulations plot below the regression line because the polar SSTs are not well correlated with the global mean temperature (Fig. 10). By contrast, the Triassic and Jurassic Foster CO_2 simulations plot above the regression line because the deep ocean temperature is not well correlated with the polar temperatures (Fig. 6).

4 Discussion and conclusion

The paper has presented the results from two unique sets of paleoclimate simulations covering the Phanerozoic. The focus of the paper has been to use the HadCM3L climate model to evaluate how well we can predict global mean surface temperatures from benthic foraminifera data. This is an important consideration because benthic microfossil data are one of the few datasets used to directly estimate past global mean temperatures. Other methods, such as using planktonic foraminiferal estimates, are more challenging because the sample sites are geographically sparse, so it is difficult to accurately estimate the global mean temperature from highly variable and widely dispersed data. This is particularly an issue for older time periods when fewer isotopic measurements from planktonic microfossils are available and can result in a bias because most of the isotopic temperature sample localities are from tropical latitudes (30° S–30° N) (Song et al., 2019).

By contrast, deep ocean temperatures are more spatially uniform. Hence, benthic foraminifera data have frequently been used to estimate past global mean temperatures and climate sensitivity (Hansen et al., 2013). Estimates of uncertainty for deep ocean temperatures incorporate uncertainties from CO_2 and from the conversion of $\delta^{18}O$ measurements to temperature but have not been able to assess assumptions about the source regions for deep ocean waters and the importance polar amplification. Of course, in practice, lack of an ocean sea floor means that benthic compilations exist only for the last 110 Ma.

Changes in heat transport also play a potentially important role in polar amplification. In the figures in the Supplement, we show the change in atmosphere and ocean poleward heat fluxes for each time period. Examination of the modelled poleward heat transport by the atmosphere and ocean shows a very complicated pattern, with all time periods showing the presence of some Bjerknes compensation (Bjerknes, 1964) (see Outten et al., 2018, for example, in CMIP5 models). Bjerknes compensation is where the change in ocean transport is largely balanced by an equal but opposite change in atmospheric transport. For instance, compared to the present day, the mid-Cretaceous and Early Eocene warm simulations show a large increase in northward atmospheric heat transport, linked with enhanced latent heat transport associated with the warmer, moister atmosphere. However, this is partly cancelled by an equal but opposite change in the ocean transport. For example, compared to present day, the early Eocene Northern Hemisphere atmospheric heat transport increases by up to 0.5 PW (petawatts), but the ocean transport is reduced by an equal amount. The net transport from Equator to the North Pole changes by less than 0.1 PW (i.e. less than 2 % of total). Further back in time, the compensation is still apparent, but the changes are more complicated, especially when the continents are largely in the Southern Hemisphere. Understanding the causes of these transport changes will be the subject of another paper.

We have shown that although the expected correlation between benthic temperatures and high-latitude surface temperatures exists, the correlation has considerable scatter. This is caused by several factors. Changing paleogeographies results in changing locations for deep-water formation. Some paleogeographies result in significant deep-water formation in the Northern Hemisphere (e.g. our present-day configuration), although for most of the Phanerozoic, the dominant source of deep-water formation has been the Southern Hemisphere. Similarly, even when deep water is formed in just one hemisphere, there can be substantial regional and latitudinal variations in its location and the corresponding temperatures. Finally, during times of very warm climates (e.g. mid-Cretaceous), the overturning circulation can be very weak, and there is a marked decoupling between the surface waters and deep ocean. In the HadCM3 model during hothouse time periods, high temperatures and high rates of evaporation produce hot and saline surface waters which sink to become intermediate and deep waters at low latitudes.

Similar arguments can be made regarding the link between global mean temperature and the temperature at high latitudes. Particularly important is the area of land at the poles and the extent of sea ice and/or land ice. Colder climates and paleogeographic configurations with more land at the pole will result in a steeper latitudinal temperature gradient and hence exhibit a changing relationship between polar and global temperatures. But the fraction of land versus ocean is also important.

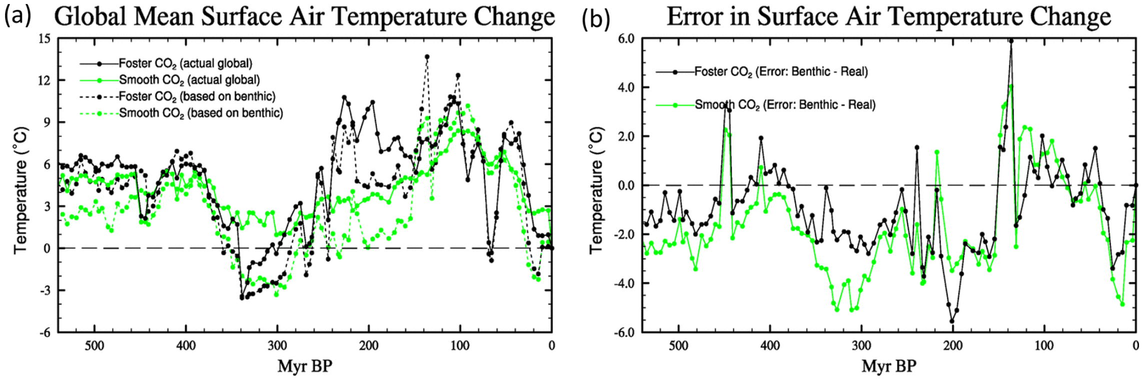

Figure 12. Phanerozoic time series of modelled temperature change (relative to pre-industrial) for the smooth (green lines) and Foster CO_2 (black) simulations **(a)** showing the actual modelled global mean surface air temperature (solid lines), whereas the dashed line shows the estimate based on deep ocean temperatures, and **(b)** error in the estimate of global mean temperature change if based on deep ocean temperatures (i.e. deep ocean – global mean surface temperatures).

Finally, the overall relationship between deep ocean temperatures and global mean temperature is shown to be relatively linear, but the slope is quite variable. In the model simulations using the "smooth" CO_2 curve, the slope is substantially shallower (0.48) than slope obtained using the Foster CO_2 curve (0.76). This is related to the different controls that CO_2 and paleogeography exert (as discussed above). In the simulation that uses the smooth CO_2 dataset, the levels of CO_2 do not vary much, so the paleogeographic controls are more pronounced.

This raises the interesting conundrum that when trying to use reconstructed deep ocean temperatures and CO_2 to estimate climate sensitivity, the interpreted global mean temperature also depends, in part, on the CO_2 concentrations. However, if we simply use the combined slope, then the root mean square error is approximately 1.4 °C, and the maximum error is over 4 °C. The root mean square error is a relatively small compared to the overall changes, and hence the resulting uncertainty in climate sensitivity associated with this error is relatively small ($\sim 15\,\%$) and the CO_2 uncertainty dominates. However, the maximum error is potentially more significant.

Our work has not addressed other sources of uncertainty. In particular, it would be valuable to use a water isotope-enabled climate model to better address the uncertainties associated with the conversion of the observed benthic $\delta^{18}O$ to temperature. This requires assumptions about the $\delta^{18}O$ of sea water. We hope to perform such simulations in future work, though this is a particularly challenging computational problem because the isotope-enabled model is significantly slower and the completion of the multi-millennial simulations required for deep ocean estimates would take more than 18 months to complete.

Our simulations extend and develop those published by Lunt et al. (2016) and Farnsworth et al. (2019b, a). The simulations reported in this paper used the same climate model (HadCM3L) but used an improved ozone concentration and corrected a salinity drift that can lead to substantial changes over the duration of the simulation. Our simulations also use an alternative set of geographic reconstructions that cover a larger time period (540 Ma – present day). They also include realistic land ice cover estimates, which were not included in the original simulations (except for the late Cenozoic) but generally have a small impact in the Mesozoic.

Similarly, the new simulations use two alternative models for past atmospheric CO_2 use more realistic variations in CO_2 through time, compared with idealized constant values in Farnsworth et al. (2019a) and Lunt et al. (2016), while at the same time recognizing the levels of uncertainty. Although the Foster CO_2 curve is more directly constrained by CO_2 data, it should be noted that these data come from multiple proxies and there are large gaps in the dataset. There is evidence that the different proxies have different biases, and it is not obvious that the correct approach is to simply fit a LOESS-type curve to the CO_2 data. This is exemplified by the Maastrichtian. The Foster LOESS curve shows a minimum in CO_2 during the Maastrichtian, which results in the modelled deep ocean temperatures being much too cold. However, detailed examination of the CO_2 data shows most of the Maastrichtian data are based on stomatal index reconstructions which often are lower than other proxies. Thus, the Maastrichtian low CO_2, relative to other periods, is potentially driven by changing the proxy rather than by real temporal changes.

Though the alternative "smooth" CO_2 curve is not the optimum fit to the data, it does pass through the cloud of individual CO_2 reconstructions and hence represents one possible "reality". For the Late Cretaceous and Cenozoic, the smooth CO_2 simulation set does a significantly better job simulating the deep ocean temperatures of the Friedrich–Cramer–Zachos curve.

Although the focus of the paper has been the evaluation of the modelled relationship between benthic and surface temperatures, the simulations are a potentially valuable resource for future studies. This includes using the simulations for paleoclimate–climate dynamic studies and for climate impact studies, such as ecological niche modelling. We have therefore made the results from our simulations available on our website: https://www.paleo.bristol.ac.uk/ummodel/scripts/papers/Valdes_et_al_2021.html (last access: 30 June 2021).

Data availability. All simulation data are available from https://www.paleo.bristol.ac.uk/ummodel/scripts/papers/Valdes_et_al_2021.html (last access: 30 June 2021, Valdes et al., 2021).

Supplement. The supplement related to this article is available online at: https://doi.org/10.5194/cp-17-1483-2021-supplement.

Author contributions. The study was developed by all authors. All model simulations were performed by PJV, who also prepared the manuscript with contributions from all co-authors.

Competing interests. The authors declare that they have no conflict of interest.

Acknowledgements. Daniel J. Lunt and Paul J. Valdes acknowledge funding from NERC through grant no. NE/P013805/1. The production of paleogeographic digital elevation models was funded by the sponsors of the PALEOMAP project. This work is part of the PhanTASTIC project led by Scott Wing and Brian Huber from the Smithsonian Institution's National Museum of Natural History and was initiated at a workshop supported by Roland and Debra Sauermann. This work was carried out using the computational facilities of the Advanced Computing Research Centre, University of Bristol (http://www.bris.ac.uk/acrc/, last access: 30 June 2021).

Financial support. This research has been supported by the UK Natural Environment Research Council (NERC) (grant no. NE/P013805/1).

Review statement. This paper was edited by Yannick Donnadieu and reviewed by two anonymous referees.

References

Alexeev, V. A., Langen, P. L., and Bates, J. R.: Polar amplification of surface warming on an aquaplanet in "ghost forcing" experiments without sea ice feedbacks, Clim. Dynam., 24, 655–666, https://doi.org/10.1007/s00382-005-0018-3, 2005.

Baatsen, M., van Hinsbergen, D. J. J., von der Heydt, A. S., Dijkstra, H. A., Sluijs, A., Abels, H. A., and Bijl, P. K.: Reconstructing geographical boundary conditions for palaeoclimate modelling during the Cenozoic, Clim. Past, 12, 1635–1644, https://doi.org/10.5194/cp-12-1635-2016, 2016.

Baatsen, M. L. J., von der Heydt, A. S., Kliphuis, M., Viebahn, J., and Dijkstra, H. A.: Multiple states in the late Eocene ocean circulation, Global Planet. Change, 163, 18–28, https://doi.org/10.1016/j.gloplacha.2018.02.009, 2018.

Barron, E. J. and Peterson, W. H.: mid-cretaceous ocean circulation: results from model sensitivity studies, Paleoceanography, 5, 319–337, https://doi.org/10.1029/PA005i003p00319, 1990.

Beerling, D. J., Fox, A., Stevenson, D. S., and Valdes, P. J.: Enhanced chemistry-climate feedbacks in past greenhouse worlds, P. Natl. Acad. Sci. USA, 108, 9770–9775, https://doi.org/10.1073/pnas.1102409108, 2011.

Bjerknes, J.: Atlantic Air-Sea Interaction, Adv. Geophys., 10, 1–82, https://doi.org/10.1016/S0065-2687(08)60005-9, 1964.

Brass, G. W., Southam, J. R., and Peterson, W. H.: Warm Saline Bottom Water in the Ancient Ocean, Nature, 296, 620–623,https://doi.org/10.1038/296620a0, 1982.

Cramer, B. S., Toggweiler, J. R., Wright, J. D., Katz, M. E., and Miller, K. G.: Ocean overturning since the Late Cretaceous: Inferences from a new benthic foraminiferal isotope compilation, Paleoceanography, 24, PA4216, https://doi.org/10.1029/2008PA001683, 2009.

Cramwinckel, M. J., Huber, M., Kocken, I. J., Agnini, C., Bijl, P. K., Bohaty, S. M., Frieling, J., Goldner, A., Hilgen, F. J., Kip, E. L., Peterse, F., van der Ploeg, R., Rohl, U., Schouten, S., and Sluijs, A.: Synchronous tropical and polar temperature evolution in the Eocene, Nature, 559, 382–386, https://doi.org/10.1038/s41586-018-0272-2, 2018.

Dietmuller, S., Ponater, M., and Sausen, R.: Interactive ozone induces a negative feedback in CO_2-driven climate change simulations, J. Geophys. Res.-Atmos., 119, 1796–1805, https://doi.org/10.1002/2013jd020575, 2014.

Donnadieu, Y., Puceat, E., Moiroud, M., Guillocheau, F., and Deconinck, J. F.: A better-ventilated ocean triggered by Late Cretaceous changes in continental configuration, Nat. Commun., 7, 10316, https://doi.org/10.1038/ncomms10316, 2016.

Emiliani, C.: Temperatures of Pacific Bottom Waters and Polar Superficial Waters during the Tertiary, Science, 119, 853–855, 1954.

England, M. H.: The Age Of Water And Ventilation Timescales In A Global Ocean Model, J. Phys. Oceanogr., 25, 2756–2777, https://doi.org/10.1175/1520-0485(1995)025<2756:TAOWAV>2.0.CO;2, 1995.

Farnsworth, A., Lunt, D. J., O'Brien, C. L., Foster, G. L., Inglis, G. N., Markwick, P., Pancost, R. D., and Robinson, S. A.: Climate Sensitivity on Geological Timescales Controlled by Nonlinear Feedbacks and Ocean Circulation, Geophys. Res. Lett., 46, 9880–9889, https://doi.org/10.1029/2019gl083574, 2019a.

Farnsworth, A., Lunt, D. J., Robinson, S. A., Valdes, P. J., Roberts, W. H. G., Clift, P. D., Markwick, P., Su, T., Wrobel, N., Bragg, F., Kelland, S. J., and Pancost, R. D.: Past East Asian monsoon evolution controlled by paleogeography, not CO_2, Sci Adv, 5, eaax1697, https://doi.org/10.1126/sciadv.aax1697, 2019b.

Foster, G. L., Royer, D. L., and Lunt, D. J.: Future climate forcing potentially without precedent in the last 420 million years, Nat. Commun., 8, 14845, https://doi.org/10.1038/ncomms14845, 2017.

Friedrich, O., Norris, R. D., and Erbacher, J.: Evolution of Cretaceous oceans: A 55 million year record of Earth's temperature and carbon cycle, Grzyb. Found. Spec. Pub., 17, 85–85, 2011.

Friedrich, O., Norris, R. D., and Erbacher, J.: Evolution of middle to Late Cretaceous oceans–A 55 m.y. record of Earth's temperature and carbon cycle, Geology, 40, 107–110, https://doi.org/10.1130/G32701.1, 2012.

Goldner, A., Herold, N., and Huber, M.: The challenge of simulating the warmth of the mid-Miocene climatic optimum in CESM1, Clim. Past, 10, 523–536, https://doi.org/10.5194/cp-10-523-2014, 2014.

Gordon, C., Cooper, C., Senior, C. A., Banks, H., Gregory, J. M., Johns, T. C., Mitchell, J. F. B., and Wood, R. A.: The simulation of SST, sea ice extents and ocean heat transports in a version of the Hadley Centre coupled model without flux adjustments, Clim. Dynam., 16, 147–168, 2000.

Gough, D. O.: Solar Interior Structure and Luminosity Variations, Sol. Phys., 74, 21–34, https://doi.org/10.1007/Bf00151270, 1981.

Gregory, J. M., Ingram, W. J., Palmer, M. A., Jones, G. S., Stott, P. A., Thorpe, R. B., Lowe, J. A., Johns, T. C., and Williams, K. D.: A new method for diagnosing radiative forcing and climate sensitivity, Geophys. Res. Lett., 31, L03205, https://doi.org/10.1029/2003gl018747, 2004.

Hansen, J., Sato, M., Russell, G., and Kharecha, P.: Climate sensitivity, sea level and atmospheric carbon dioxide, Philos. T. Roy. Soc. A, 371, 20120294, https://doi.org/10.1098/rsta.2012.0294, 2013.

Hansen, J., Sato, M., Kharecha, P., Beerling, D., Berner, R., Masson-Delmotte, V., Pagani, M., Raymo, M., Royer, D. L., and Zachos, J. C.: Target atmospheric CO2: Where should humanity aim?, Open Atmos. Sci. J., 2, 217–231, https://doi.org/10.2174/1874282300802010217, 2008.

Hansen, J. E. and Sato, M.: Paleoclimate Implications for Human-Made Climate Change, in: Climate Change, edited by: Berger, A., Mesinger, F., and Sijacki, D., Springer, Vienna, https://doi.org/10.1007/978-3-7091-0973-1_2, 21–47, 2012.

Hardiman, S. C., Andrews, M. B., Andrews, T., Bushell, A. C., Dunstone, N. J., Dyson, H., Jones, G. S., Knight, J. R., Neininger, E., O'Connor, F. M., Ridley, J. K., Ringer, M. A., Scaife, A. A., Senior, C. A., and Wood, R. A.: The Impact of Prescribed Ozone in Climate Projections Run With HadGEM3-GC3.1, J. Adv. Model. Earth Sy., 11, 3443–3453, https://doi.org/10.1029/2019MS001714, 2019.

Harris, J., Ashley, A., Otto, S., Valdes, P., Crossley, R., Preston, R., Watson, J., Goodrich, M., and Team., M. P.: Paleogeography and Paleo-Earth Systems in the Modeling of Marine Paleoproductivity: A Prerequisite for the Prediction of Petroleum Source Rocks, in: Petroleum Systems Analysis – Case Studies, edited by: AbuAli, M. A., Moretti, I., and Nordgård Bolås, H. M., AAPG Memoir, 27–60, https://doi.org/10.1190/ice2015-2210991, 2017.

Henkes, G. A., Passey, B. H., Grossman, E. L., Shenton, B. J., Yancey, T. E., and Perez-Huerta, A.: Temperature evolution and the oxygen isotope composition of Phanerozoic oceans from carbonate clumped isotope thermometry, Earth Planet. Sc. Lett., 490, 40–50, https://doi.org/10.1016/j.epsl.2018.02.001, 2018.

Holland, M. M. and Bitz, C. M.: Polar amplification of climate change in coupled models, Clim. Dynam., 21, 221–232, https://doi.org/10.1007/s00382-003-0332-6, 2003.

Kageyama, M., Albani, S., Braconnot, P., Harrison, S. P., Hopcroft, P. O., Ivanovic, R. F., Lambert, F., Marti, O., Peltier, W. R., Peterschmitt, J.-Y., Roche, D. M., Tarasov, L., Zhang, X., Brady, E. C., Haywood, A. M., LeGrande, A. N., Lunt, D. J., Mahowald, N. M., Mikolajewicz, U., Nisancioglu, K. H., Otto-Bliesner, B. L., Renssen, H., Tomas, R. A., Zhang, Q., Abe-Ouchi, A., Bartlein, P. J., Cao, J., Li, Q., Lohmann, G., Ohgaito, R., Shi, X., Volodin, E., Yoshida, K., Zhang, X., and Zheng, W.: The PMIP4 contribution to CMIP6 – Part 4: Scientific objectives and experimental design of the PMIP4-CMIP6 Last Glacial Maximum experiments and PMIP4 sensitivity experiments, Geosci. Model Dev., 10, 4035–4055, https://doi.org/10.5194/gmd-10-4035-2017, 2017.

Kennett, J. P. and Stott, L. D.: Abrupt Deep-Sea Warming, Palaeoceanographic Changes and Benthic Extinctions at the End of the Paleocene, Nature, 353, 225–229, https://doi.org/10.1038/353225a0, 1991.

Kiehl, J. T. and Shields, C. A.: Sensitivity of the Palaeocene-Eocene Thermal Maximum climate to cloud properties, Philos. T. Roy. Soc. A, 371, 20130093, https://doi.org/10.1098/rsta.2013.0093, 2013.

Knorr, G., Butzin, M., Micheels, A., and Lohmann, G.: A warm Miocene climate at low atmospheric CO_2 levels, Geophys. Res. Lett., 38, L20701, https://doi.org/10.1029/2011gl048873, 2011.

Krapp, M. and Jungclaus, J. H.: The Middle Miocene climate as modelled in an atmosphere-ocean-biosphere model, Clim. Past, 7, 1169–1188, https://doi.org/10.5194/cp-7-1169-2011, 2011.

Ladant, J.-B., Poulsen, C. J., Fluteau, F., Tabor, C. R., MacLeod, K. G., Martin, E. E., Haynes, S. J., and Rostami, M. A.: Paleogeographic controls on the evolution of Late Cretaceous ocean circulation, Clim. Past, 16, 973–1006, https://doi.org/10.5194/cp-16-973-2020, 2020.

Lunt, D. J., Valdes, P. J., Dunkley Jones, T., Ridgwell, A., Haywood, A. M., Schmidt, D. N., Marsh, R., and Maslin, M.: CO_2-driven ocean circulation changes as an amplifier of Paleocene-Eocene thermal maximum hydrate destabilization, Geology, 38, 875–878, https://doi.org/10.1130/G31184.1, 2010.

Lunt, D. J., Dunkley Jones, T., Heinemann, M., Huber, M., LeGrande, A., Winguth, A., Loptson, C., Marotzke, J., Roberts, C. D., Tindall, J., Valdes, P., and Winguth, C.: A model–data comparison for a multi-model ensemble of early Eocene atmosphere–ocean simulations: EoMIP, Clim. Past, 8, 1717–1736, https://doi.org/10.5194/cp-8-1717-2012, 2012.

Lunt, D. J., Farnsworth, A., Loptson, C., Foster, G. L., Markwick, P., O'Brien, C. L., Pancost, R. D., Robinson, S. A., and Wrobel, N.: Palaeogeographic controls on climate and proxy interpretation, Clim. Past, 12, 1181–1198, https://doi.org/10.5194/cp-12-1181-2016, 2016.

Lunt, D. J., Huber, M., Anagnostou, E., Baatsen, M. L. J., Caballero, R., DeConto, R., Dijkstra, H. A., Donnadieu, Y., Evans, D., Feng, R., Foster, G. L., Gasson, E., von der Heydt, A. S., Hollis, C. J., Inglis, G. N., Jones, S. M., Kiehl, J., Kirtland Turner, S., Korty, R. L., Kozdon, R., Krishnan, S., Ladant, J.-B., Langebroek, P., Lear, C. H., LeGrande, A. N., Littler, K., Markwick, P., Otto-Bliesner, B., Pearson, P., Poulsen, C. J., Salzmann, U., Shields, C., Snell, K., Stärz, M., Super, J., Tabor, C., Tierney, J. E., Tourte, G. J. L., Tripati, A., Upchurch, G. R., Wade, B. S., Wing, S. L., Winguth,

A. M. E., Wright, N. M., Zachos, J. C., and Zeebe, R. E.: The DeepMIP contribution to PMIP4: experimental design for model simulations of the EECO, PETM, and pre-PETM (version 1.0), Geosci. Model Dev., 10, 889–901, https://doi.org/10.5194/gmd-10-889-2017, 2017.

Lunt, D. J., Bragg, F., Chan, W.-L., Hutchinson, D. K., Ladant, J.-B., Morozova, P., Niezgodzki, I., Steinig, S., Zhang, Z., Zhu, J., Abe-Ouchi, A., Anagnostou, E., de Boer, A. M., Coxall, H. K., Donnadieu, Y., Foster, G., Inglis, G. N., Knorr, G., Langebroek, P. M., Lear, C. H., Lohmann, G., Poulsen, C. J., Sepulchre, P., Tierney, J. E., Valdes, P. J., Volodin, E. M., Dunkley Jones, T., Hollis, C. J., Huber, M., and Otto-Bliesner, B. L.: DeepMIP: model intercomparison of early Eocene climatic optimum (EECO) large-scale climate features and comparison with proxy data, Clim. Past, 17, 203–227, https://doi.org/10.5194/cp-17-203-2021, 2021.

Murphy, D. P. and Thomas, D. J.: Cretaceous deep-water formation in the Indian sector of the Southern Ocean, Paleoceanography, 27, PA1211, https://doi.org/10.1029/2011pa002198, 2012.

Nowack, P. J., Abraham, N. L., Maycock, A. C., Braesicke, P., Gregory, J. M., Joshi, M. M., Osprey, A., and Pyle, J. A.: A large ozone-circulation feedback and its implications for global warming assessments, Nat. Clim. Change, 5, 41–45, https://doi.org/10.1038/nclimate2451, 2015.

Nunes, F. and Norris, R. D.: Abrupt reversal in ocean overturning during the Palaeocene/Eocene warm period, Nature, 439, 60–63, https://doi.org/10.1038/nature04386, 2006.

O'Brien, C. L., Robinson, S. A., Pancost, R. D., Damste, J. S. S., Schouten, S., Lunt, D. J., Alsenz, H., Bomemann, A., Bottini, C., Brassell, S. C., Farnsworth, A., Forster, A., Huber, B. T., Inglis, G. N., Jenkyns, H. C., Linnert, C., Littler, K., Markwick, P., McAnena, A., Mutterlose, J., Naafs, B. D. A., Puttmann, W., Sluijs, A., van Helmond, N. A. G. M., Vellekoop, J., Wagner, T., and Wrobel, N. E.: Cretaceous sea-surface temperature evolution: Constraints from TEX_{86} and planktonic foraminiferal oxygen isotopes, Earth-Sci. Rev., 172, 224–247, https://doi.org/10.1016/j.earscirev.2017.07.012, 2017.

Outten, S., Esau, I., and Ottera, O. H.: Bjerknes Compensation in the CMIP5 Climate Models, J. Climate, 31, 8745–8760, https://doi.org/10.1175/jcli-d-18-0058.1, 2018.

Pope, V. D., Gallani, M. L., Rowntree, P. R., and Stratton, R. A.: The impact of new physical parametrizations in the Hadley Centre climate model: HadAM3, Clim. Dynam., 16, 123–146, 2000.

Poulsen, C. J., Barron, E. J., Arthur, M. A., and Peterson, W. H.: Response of the mid-Cretaceous global oceanic circulation to tectonic and CO_2 forcings, Paleoceanography, 16, 576–592, https://doi.org/10.1029/2000pa000579, 2001.

Sagoo, N., Valdes, P., Flecker, R., and Gregoire, L. J.: The Early Eocene equable climate problem: can perturbations of climate model parameters identify possible solutions?, Philos. T. Roy. Soc. A, 371, 20130123 https://doi.org/10.1098/rsta.2013.0123, 2013.

Scotese, C. R.: PALEOMAP PaleoAtlas for GPlates and the PaleoData Plotter Program, PALEOMAP Project, EarthByte, available at: https://www.earthbyte.org/paleomap-paleoatlas-for-gplates/ (last access: 30 June 2021), 2016.

Scotese, C. R. and Schettino, A.: Late Permian – Early Jurassic Paleogeography of Western Tethys and the World, in: Permo-Triassic Salt Provinces of Europe, North Africa and the Atlantic Margins, edited by: Soto, J. I., Flinch, J., and Tari, G., Elsevier, 57–95, 2017.

Scotese, C. R. and Wright, N.: PALEOMAP Paleodigital Elevation MOdels (PaleoDEMS) for the Phanerozoic PALEOMAP Project, EarthByte, available at: https://www.earthbyte.org/paleodem-resource-scotese-and-wright-2018 (last access: 30 June 2021), 2018.

Smith, R. S., Gregory, J. M., and Osprey, A.: A description of the FAMOUS (version XDBUA) climate model and control run, Geosci. Model Dev., 1, 53–68, https://doi.org/10.5194/gmd-1-53-2008, 2008.

Song, H. J., Wignall, P. B., Song, H. Y., Dai, X., and Chu, D. L.: Seawater Temperature and Dissolved Oxygen over the Past 500 Million Years, J. Earth Sci., 30, 236–243, https://doi.org/10.1007/s12583-018-1002-2, 2019.

Steinthorsdottir, M., Coxall, H. K., de Boer, A. M., Huber, M., Barbolini, N., Bradshaw, C. D., Burls, N. J., Feakins, S. J., Gasson, E., Henderiks, J., Holbourn, A., Kiel, S., Kohn, M. J., Knorr, G., Kurschner, W. M., Lear, C. H., Liebrand, D., Lunt, D. J., Mors, T., Pearson, P. N., Pound, M. J., Stoll, H., and Stromberg, C. A. E.: The Miocene: the Future of the Past, Paleoceanography and Paleoclimatology, 36, e2020PA004037. https://doi.org/10.1029/2020PA004037, 2021.

Stoll, H. M., Guitian, J., Hernandez-Almeida, I., Mejia, L. M., Phelps, S., Polissar, P., Rosenthal, Y., Zhang, H. R., and Ziveri, P.: Upregulation of phytoplankton carbon concentrating mechanisms during low CO_2 glacial periods and implications for the phytoplankton pCO_2 proxy, Quat. Sci. Rev., 208, 1–20, https://doi.org/10.1016/j.quascirev.2019.01.012, 2019.

Sutton, R. T., Dong, B. W., and Gregory, J. M.: Land/sea warming ratio in response to climate change: IPCC AR4 model results and comparison with observations, Geophys. Res. Lett., 34, L02701, https://doi.org/10.1029/2006gl028164, 2007.

Upchurch, G. R., Kiehl, J., Shields, C., Scherer, J., and Scotese, C.: Latitudinal temperature gradients and high-latitude temperatures during the latest Cretaceous: Congruence of geologic data and climate models, Geology, 43, 683–686, https://doi.org/10.1130/G36802.1, 2015.

Valdes, P. J., Armstrong, E., Badger, M. P. S., Bradshaw, C. D., Bragg, F., Crucifix, M., Davies-Barnard, T., Day, J. J., Farnsworth, A., Gordon, C., Hopcroft, P. O., Kennedy, A. T., Lord, N. S., Lunt, D. J., Marzocchi, A., Parry, L. M., Pope, V., Roberts, W. H. G., Stone, E. J., Tourte, G. J. L., and Williams, J. H. T.: The BRIDGE HadCM3 family of climate models: HadCM3@Bristol v1.0, Geosci. Model Dev., 10, 3715–3743, https://doi.org/10.5194/gmd-10-3715-2017, 2017.

Valdes, P. J., Scotese, C. R., and Lunt, D. J.: Deep Ocean Temperatures through Time, Bristol Research Initiative for the Dynamic Global Environment (BRIDGE) [data set], available at: https://www.paleo.bristol.ac.uk/ummodel/scripts/papers/Valdes_et_al_2021.html, last access: 30 June 2021.

Verard, C., Hochard, C., Baumgartner, P. O., and Stampfli, G. M.: 3D palaeogeographic reconstructions of the Phanerozoic versus sea-level and Sr-ratio variations, Journal of Palaeogeography, 4, 64–84, https://doi.org/10.3724/Sp.J.1261.2015.00068, 2015.

Westerhold, T., Marwan, N., Drury, A. J., Liebrand, D., Agnini, C., Anagnostou, E., Barnet, J. S. K., Bohaty, S. M., De Vleeschouwer, D., Florindo, F., Frederichs, T., Hodell, D. A., Holbourn, A. E., Kroon, D., Lauretano, V., Littler, K., Lourens, L. J., Lyle, M., Pälike, H., Röhl, U., Tian, J., Wilkens, R. H., Wilson, P. A., and Zachos, J. C.: An astronomically dated record of Earth's climate and its predictability over the last 66 million years, Science, 369, 1383–1387, https://doi.org/10.1126/science.aba6853, 2020.

Witkowski, C. R., Weijers, J. W. H., Blais, B., Schouten, S., and Damste, J. S. S.: Molecular fossils from phytoplankton reveal secular P_{CO_2} trend over the Phanerozoic, Sci. Adv., 4, eaat4556, https://doi.org/10.1126/sciadv.aat4556, 2018.

You, Y., Huber, M., Muller, R. D., Poulsen, C. J., and Ribbe, J.: Simulation of the Middle Miocene Climate Optimum, Geophys. Res. Lett., 36, L04702, https://doi.org/10.1029/2008gl036571, 2009.

Zachos, J., Pagani, M., Sloan, L., Thomas, E., and Billups, K.: Trends, rhythms, and aberrations in global climate 65 Ma to present, Science, 292, 686–693, 2001.

Zachos, J. C., Dickens, G. R., and Zeebe, R. E.: An early Cenozoic perspective on greenhouse warming and carbon-cycle dynamics, Nature, 451, 279–283, https://doi.org/10.1038/Nature06588, 2008.

Zhou, J., Poulsen, C. J., Pollard, D., and White, T. S.: Simulation of modern and middle Cretaceous marine $\delta^{18}O$ with an ocean-atmosphere general circulation model, Paleoceanography, 23, PA3223, https://doi.org/10.1029/2008pa001596, 2008.

Zhu, J., Poulsen, C. J., and Tierney, J. E.: Simulation of Eocene extreme warmth and high climate sensitivity through cloud feedbacks, Sci. Adv., 5, eaax1874, https://doi.org/10.1126/sciadv.aax1874, 2019.

Clim. Past, 19, 1951–1974, 2023
https://doi.org/10.5194/cp-19-1951-2023

Climate of the Past
Open Access

A transient coupled general circulation model (CGCM) simulation of the past 3 million years

Kyung-Sook Yun[1,2], **Axel Timmermann**[1,2,★], **Sun-Seon Lee**[1,2], **Matteo Willeit**[3], **Andrey Ganopolski**[3], and **Jyoti Jadhav**[1,2]

[1]Center for Climate Physics, Institute for Basic Science (IBS), Busan, Republic of Korea
[2]Pusan National University, Busan, Republic of Korea
[3]Potsdam Institute for Climate Impact Research, Potsdam, Germany
★*Invited contribution by Axel Timmermann, recipient of the EGU Milutin Milankovic Medal 2017.*

Correspondence: Kyung-Sook Yun (kssh@pusan.ac.kr) and Axel Timmermann (axel@ibsclimate.org)

Received: 16 May 2023 – Discussion started: 22 May 2023
Revised: 4 September 2023 – Accepted: 14 September 2023 – Published: 13 October 2023

Abstract. Driven primarily by variations in the earth's axis wobble, tilt, and orbit eccentricity, our planet experienced massive glacial/interglacial reorganizations of climate and atmospheric CO_2 concentrations during the Pleistocene (2.58 million years ago (Ma)–11.7 thousand years ago (ka)). Even after decades of research, the underlying climate response mechanisms to these astronomical forcings have not been fully understood. To further quantify the sensitivity of the earth system to orbital-scale forcings, we conducted an unprecedented quasi-continuous coupled general climate model simulation with the Community Earth System Model version 1.2 (CESM1.2, $\sim 3.75°$ horizontal resolution), which covers the climatic history of the past 3 million years (3 Myr). In addition to the astronomical insolation changes, CESM1.2 is forced by estimates of CO_2 and ice-sheet topography which were obtained from a simulation previously conducted with the CLIMBER-2 earth system model of intermediate complexity. Our 3 Ma simulation consists of 42 transient interglacial/glacial simulation chunks, which were partly run in parallel to save computing time. The chunks were subsequently merged, accounting for spin-up and overlap effects to yield a quasi-continuous trajectory. The computer model data were compared against a plethora of paleo-proxy data and large-scale climate reconstructions. For the period from the Mid-Pleistocene Transition (MPT, ~ 1 Ma) to the late Pleistocene we find good agreement between simulated and reconstructed temperatures in terms of phase and amplitude (-5.7 °C temperature difference between Last Glacial Maximum and Holocene). For the earlier part (3–1 Ma), differences in orbital-scale variability occur between model simulation and the reconstructions, indicating potential biases in the applied CO_2 forcing. Our model-proxy data comparison also extends to the westerlies, which show unexpectedly large variance on precessional timescales, and hydroclimate variables in major monsoon regions. Eccentricity-modulated precessional variability is also responsible for the simulated changes in the amplitude and flavors of the El Niño–Southern Oscillation. We further identify two major modes of planetary energy transport, which played a crucial role in Pleistocene climate variability: the first obliquity and CO_2-driven mode is linked to changes in the Equator-to-pole temperature gradient; the second mode regulates the interhemispheric heat imbalance in unison with the eccentricity-modulated precession cycle. During the MPT, a pronounced qualitative shift occurs in the second mode of planetary energy transport: the post-MPT eccentricity-paced variability synchronizes with the CO_2 forced signal. This synchronized feature is coherent with changes in global atmospheric and ocean circulations, which might contribute to an intensification of glacial cycle feedbacks and amplitudes. Comparison of this paleo-simulation with greenhouse warming simulations reveals that for an RCP8.5 greenhouse gas emission scenario, the projected global mean surface temperature changes over the next 7 decades would be comparable to the late Pleistocene glacial-interglacial range; but the anthropogenic warming rate will exceed any previous ones by a factor of ~ 100.

1 Introduction

Glacial cycles during the Pleistocene (2.58 million years ago (Ma) to 11.7 thousand years ago (ka)) were characterized by global mean surface temperature (GMST) swings that attained values of up to $\sim 6\,^{\circ}\mathrm{C}$ (Schneider Von Deimling et al., 2006; McClymont et al., 2013; Tierney et al., 2020). These variations in temperature and the associated waxing and waning of continental ice sheets were accompanied by relatively small changes ($<\sim 0.5\,\mathrm{W\,m^{-2}}$) in the earth's global mean radiation balance (Baggenstos et al., 2019), but considerable variations in the seasonal and latitudinal distribution of insolation (Masson-Delmotte et al., 2013). Transient coupled atmosphere/ocean simulations either with earth system models of intermediate complexity (EMICs) (Menviel et al., 2011; Timm and Timmermann, 2007; Timm et al., 2008; Timmermann et al., 2009, 2014b; Timmermann and Friedrich, 2016) or based on coupled general circulation models (CGCMs) (Timmermann et al., 2007, 2022; Liu et al., 2009; Singarayer and Valdes, 2010; Zhang et al., 2021) have helped elucidate how orbital-scale forcings translate into global and regional climate responses. Transient orbital-scale ice-sheet sensitivities and feedbacks with the atmosphere and ocean have so far only been explored with intermediate-complexity models (Ganopolski et al., 2010; Willeit and Ganopolski, 2018; Willeit et al., 2019; Heinemann et al., 2014) or forced offline ice-sheet models with various representations of climatic feedbacks (Tigchelaar et al., 2018, 2019; Abe-Ouchi et al., 2013).

To gain a better understanding of how glacial/interglacial variability emerged during the Pleistocene, it has been beneficial to study the lateral flow of energy in our climate system. Orbital-scale shifts in atmospheric and oceanic heat transports influence key atmospheric circulation features such as the Hadley circulation, the Intertropical Convergence Zones (ITCZs), and mid-latitude storm tracks (Liu et al., 2015, 2017; Chiang and Bitz, 2005; Kaspar et al., 2007). Previous modeling studies (Timmermann et al., 2014b; Liu et al., 2017; Kamae et al., 2016; Donohoe et al., 2020; Kim, 2004) have elucidated the relationship between external forcings, climate feedbacks, and lateral energy redistributions by focusing on specific Pleistocene periods, such as the Last Glacial Maximum (LGM) or extreme orbital conditions. However, little is known on how the interplay between orbital and greenhouse gas forcing (GHG) has shaped the meridional transport of heat in the atmosphere and ocean over the past 3 million years (Myr) and whether these two components reinforced or compensated each other (Bjerknes, 1964; Stone, 1978). To understand how Milanković forcing generates glacial variability, it is necessary to determine how changes in atmospheric and oceanic heat transports feed back to the climate mean state. This is particularly interesting in the context of the Mid-Pleistocene Transition (MPT; $\sim$ 1.25–0.7 Ma) when the dominant periodicity of ice volume and global mean temperature changed from 41 to 80–120 thousand year (kyr) cycles (Clark et al., 2006; Bintanja and van de Wal, 2008; McClymont et al., 2013).

To address these fundamental questions, we conducted an unprecedented transient CGCM simulation that covers the climate history of the past 3 Myr. This quasi-continuous model simulation, represents a 1 Myr extension of the 2 Ma Community Earth System Model (CESM) simulation, which has originally been conducted to study how climate shaped early human habitats (Timmermann et al., 2022). The 2 and 3 Ma simulations are based on the CESM version 1.2 in 3.75° atmospheric and nominal 3° oceanic horizontal resolutions (T31_gx3v5). Our CESM1.2 3 Ma simulation represents the first full Pleistocene transient model simulation conducted with a 3 dimensional CGCM to date and it has been used previously (Zeller et al., 2023; Ruan et al., 2023; Margari et al., 2023) to determine and quantify the effects of past climate shifts on different human evolutionary processes.

This paper describes the overall performance of the 3 Ma climate simulation and highlights important processes related to changes in Pleistocene global heat transport, feedbacks, and variability. The paper is organized as follows. Section 2 introduces the model set-up and experimental design and discusses several disadvantages of the modeling approach. In Sect. 3, we compare the simulation with proxy data for mean temperature, hydroclimate, and large-scale westerly winds. Section 4 illustrates how the large-scale external forcings can influence modes of natural climate variability, exemplified here by the El Niño–Southern Oscillation (ENSO) phenomenon. We then investigate the global energy transport changes in Sect. 5 and the related large-scale atmosphere and ocean changes in Sect. 6. Section 7 discusses the main results and provides a future outlook.

2 Model set-up and experimental design

Our transient Pleistocene paleoclimate model simulation uses the coupled CESM version 1.2 (Hurrell et al., 2013), with CAM4 atmospheric physics (T31, $\sim 3.75°$ resolution, 26 levels), the POP2 ocean model (gx3v5, 100×116 horizonal grids and 25 vertical levels), CLM4.0 land physics (prescribed vegetation), and CICE4 (Los Alamos Sea Ice Model) sea ice components. Unlike previous transient EMIC simulations (Willeit et al., 2019; Timmermann et al., 2014b; Ganopolski et al., 2010; Goosse et al., 2010), the CESM1.2 simulation includes more realism and complexity, e.g., interactive clouds, a realistic representation of tropical processes, a 3-dimensional ocean circulation, and a fully dynamic atmosphere. We split the simulation into 42 chunks (minimum chunk length 32 kyr and maximum length 125 kyr) which overlapped by about 5000 years (see Fig. 1a) and ran them in parallel on the ICCP/IBS supercomputer *Aleph*. Each chunk was initialized with peak interglacial conditions (maximum boreal summer insolation, e.g., 125, 243 ka, and so on) using the same initial and restart data from a preindustrial

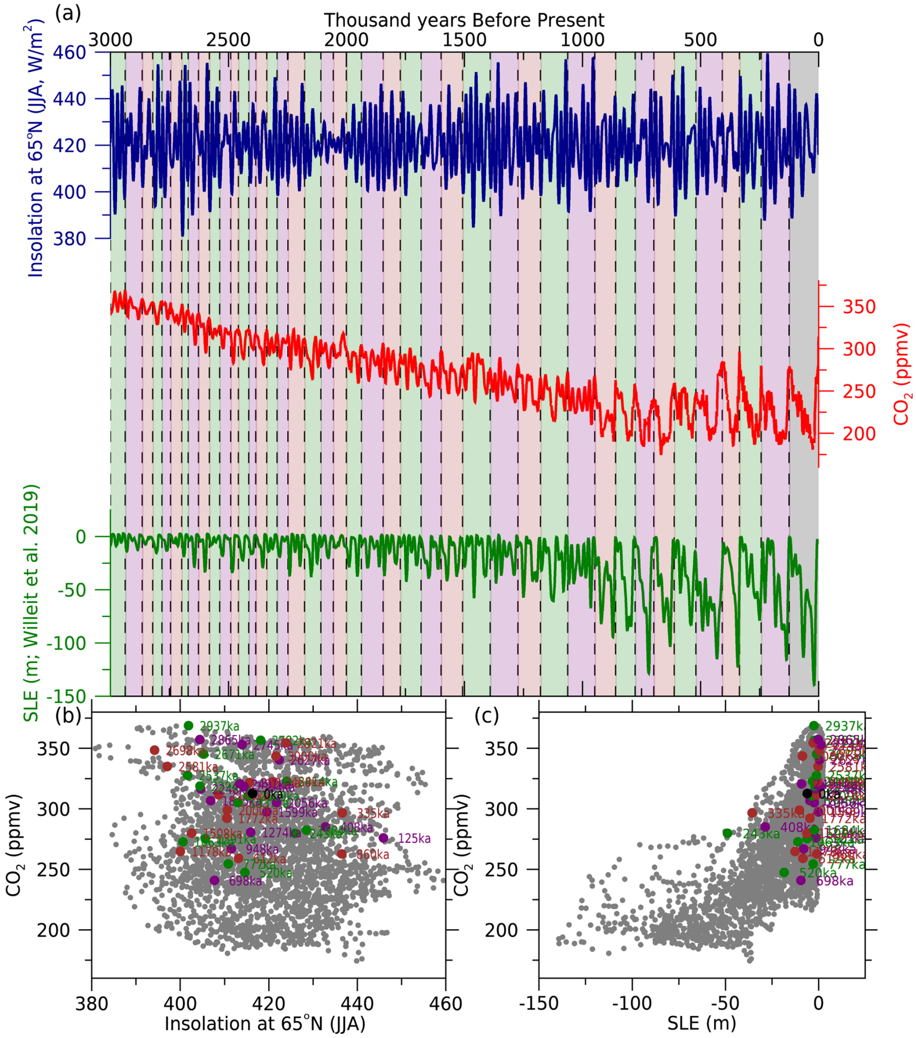

Figure 1. "3 Ma" ensemble simulation strategy. **(a)** Transient climate variability of summer insolation at 65° N, CO_2, and ice volume in sea level equivalent (SLE, m) from Willeit et al. (2019). Each color shading indicates the respective period of 42 individual ensemble simulations. **(b, c)** Scatter plot of **(b)** summer insolation versus CO_2, and **(c)** SLE versus CO_2. Each ensemble run was initiated at interglacial peaks (e.g., 125 and 243 ka) of having higher CO_2 and lower ice volume, as displayed by colored dots.

2300-year-long spin-up control simulation and then orbital forcings (Berger, 1978), and estimates of greenhouse gases and ice-sheet albedo and topography (Willeit et al., 2019) were applied. In our simulation, we did not account for the freshwater forcing originating from the ice sheets, which will likely lead to an underestimation of the simulated Atlantic Meridional Overturning Circulation (AMOC) variability, both on orbital (Timmermann et al., 2010) and millennial (Menviel et al., 2014) timescales. We finally obtained the "3 Ma" full history of climate by concatenating the data from each chunk a posteriori and by applying a time-sliding linear interpolation for the overlap periods following the methodology of an earlier study (Timmermann et al., 2014b).

We also applied the acceleration technique (Lorenz and Lohmann, 2004; Lunt et al., 2006) to the external forcings (i.e., orbital, GHG, and ice-sheets forcings) of the 3 Ma transient simulation. Using this method with an acceleration factor of 5 reduces the 3 000 000 orbital year forcing to 600 000 model years in CESM. Previous studies have demonstrated that accelerated simulations with acceleration factors of less than 10 reproduce well the unaccelerated climate response to external forcings, except for deep ocean variables and some surface ocean variables in high-latitude regions where the climate is closely connected to the deep ocean (Timm and Timmermann, 2007; Varma et al., 2016; Lunt et al., 2006). Our choice of a relatively small acceleration factor of 5 (Timmermann et al., 2014b) presents a reasonable compromise between increasing computational performance and minimizing disequilibrium processes. Moreover, with an acceleration factor of 5 the fastest "accelerated" forcing timescale (Timm and Timmermann, 2007) – i.e., the precessional cycle – is applied as a ∼ 4000 year model forcing, which allows the deep ocean to adjust at least on advective timescales (Friedrich and Timmermann, 2012). However, for deep-ocean diffusive processes, we would still expect disequilibrium effects for the precessional cycle, but less distortion for obliquity and eccentricity scales.

The CESM uses the constant LGM ocean bathymetry and land-sea mask (i.e., 21 ka) based on ICE-6G_C data (Argus et al., 2014). This choice can in principle generate large-scale climate biases due to glacial/interglacial changes in land-sea distributions, in areas such as the Sunda and Sahul shelves (Di Nezio et al., 2016), the Bering Strait (Hu et al., 2012), and the Falkland Islands (Malvinas) continental shelf. However, the alternative of running a volume-conserving Boussinesq ocean model (POP2) with time-evolving sea level and ocean volume may also cause ambiguities and biases that have not been fully explored yet.

Figure 1a illustrates the temporal evolution of CESM1.2 forcings: orbital forcing (represented here by summer insolation at 65° N), greenhouse gas forcing (represented by the time-varying CO_2 in CESM1.2), and topographic and albedo forcing due to ice-sheet changes (represented here by the global ice volume in sea level equivalent) (Willeit et al., 2019). Overall, the interglacial peaks (initial time at each ensemble simulation, colored dots in Fig. 1b and c) are characterized by high CO_2 concentrations and low ice volume, with the orbital phase being less constrained (Fig. 1b and c). In our 3 Ma experiment, we updated the forcings of GHG concentrations (Lüthi et al., 2008; Willeit et al., 2019; Lisiecki and Raymo, 2005), Northern Hemisphere (NH) ice-sheet extent and topography (Willeit et al., 2019), and astronomical insolation variations (Berger, 1978) every 100 orbital years (i.e., 20 model years). For GHGs, we combined different datasets: after 800 ka, measured air-bubble CO_2 concentrations from the European Project for Ice Coring in Antarctica (EPICA) Dome C ice core (Jouzel et al., 2007) were used; prior to 800 ka, we used the simulated CO_2 from the CLIMBER-2 transient simulation (Willeit et al., 2019), which includes an interactive carbon cycle. We also included estimates of the CH_4 and N_2O concentrations as a CESM forcing using a regression of the EPICA CH_4 and N_2O concentrations with the global benthic $\delta^{18}O$ stack (Lisiecki and Raymo, 2005) (post 800 ka) and extended this linear statistical model to 3 Ma using the benthic $\delta^{18}O$ stack data (see Fig. S1). The ice mask and ice-sheet topography changes were also obtained from the simulated CLIMBER-2 orography data. It is worth mentioning that before the past 1 Myr, our applied orbital forcing (Berger, 1978) is somewhat different from that of later numerical estimates (Laskar et al., 2004). This discrepancy in pre-MPT orbital forcing and the resulting changes in the climate system need to be evaluated in future work. CESM1.2 in our resolution has a relatively weak equilibrium climate sensitivity of 2.4 °C warming for a doubling relative to preindustrial CO_2 levels. This is about 1.5-fold smaller than the Coupled Model Intercomparison Project Phase 6 (CMIP6) multi-model ensemble-based estimation (3.7 ± 1.1 °C within 37 multi-models) (Meehl et al., 2020). To compensate for this relatively weak climate sensitivity of CESM1.2 and to indirectly account for the effect of unresolved and highly uncertain dust forcing (Friedrich et al., 2016; Kohler et al., 2010), which is also correlated with the reconstructed CO_2 or the benthic $\delta^{18}O$ stack, we re-scaled the GHGs forcing anomalies relative to preindustrial conditions by a factor of 1.5.

3 Model-proxy comparison

3.1 Climate sensitivity and polar amplification

An important question to address is whether the 3 Ma simulation reproduces the magnitude and timing of glacial/interglacial variability during the Pleistocene. We first compare results of our 3 Ma simulations with a variety of long-term paleo-proxy data and the CLIMBER-2 simulation. Figure 2a illustrates the model's capability in capturing the magnitude and timing of GMST variations, shown by previous model- and proxy-based estimates (Willeit et al., 2019; Friedrich et al., 2016). Our simulation exhibits a −5.7 °C glacial cooling for LGM (∼ 21 ka) relative to preindustrial conditions (∼ 0 ka). This magnitude of cooling agrees well with a combined proxy-model estimate of −6.3 to −5.6 (95 % confidence interval) (e.g., Tierney et al., 2020). Simulated sea surface temperatures (SSTs) also reveal a high degree of coherence for the post-MPT period with tropical proxy-based SST reconstructions (Herbert et al., 2010) (Fig. 2b) and elsewhere (Petrick et al., 2019; Cartagena-Sierra et al., 2021; Lawrence et al., 2009; de Garidel-Thoron et al., 2005; Russon et al., 2010) (Fig. 2c–g), indicating a reliable simulation of spatial SST patterns in addition to the temporal evolution. However, prior to the MPT, the model simulation diverges considerably from some of the SST proxies in terms of representing the exact orbital phase, as well as the long-term extratropical gradual Pleistocene trends. For instance, the tropical SST stack (Herbert et al., 2010) exhibits higher pre-MPT variability on obliquity timescales of 41 kyr (Fig. 3a), as compared to the 3 Ma simulation, which features a more pronounced precessional cycle (∼ 21 kyr) (Fig. 3b). This mismatch might be in part due to an unrealistic orbital-scale variability (e.g., presence of precession) of the estimated pre-MPT CO_2 forcing (Fig. 3c) or potential seasonal biases of some of the SST alkenone proxies in the tropics (Timmermann et al., 2014a).

Various temperature reconstructions and simulations reveal amplified Arctic/Antarctic surface air temperature changes on glacial/interglacial timescales relative to the global average (Stap et al., 2018). This polar amplification is very pronounced in temperature reconstructions based on the EPICA Dome C ice core (Jouzel et al., 2007) and North Greenland Ice Core Project (NGRIP) (Barker et al., 2011), with Greenland's amplification being about twice as strong as Antarctica's, as documented by the LGM cooling of −18.2 °C for Greenland and −9.5 °C for Antarctica (Fig. 4a and b). Stronger polar amplification in Green-

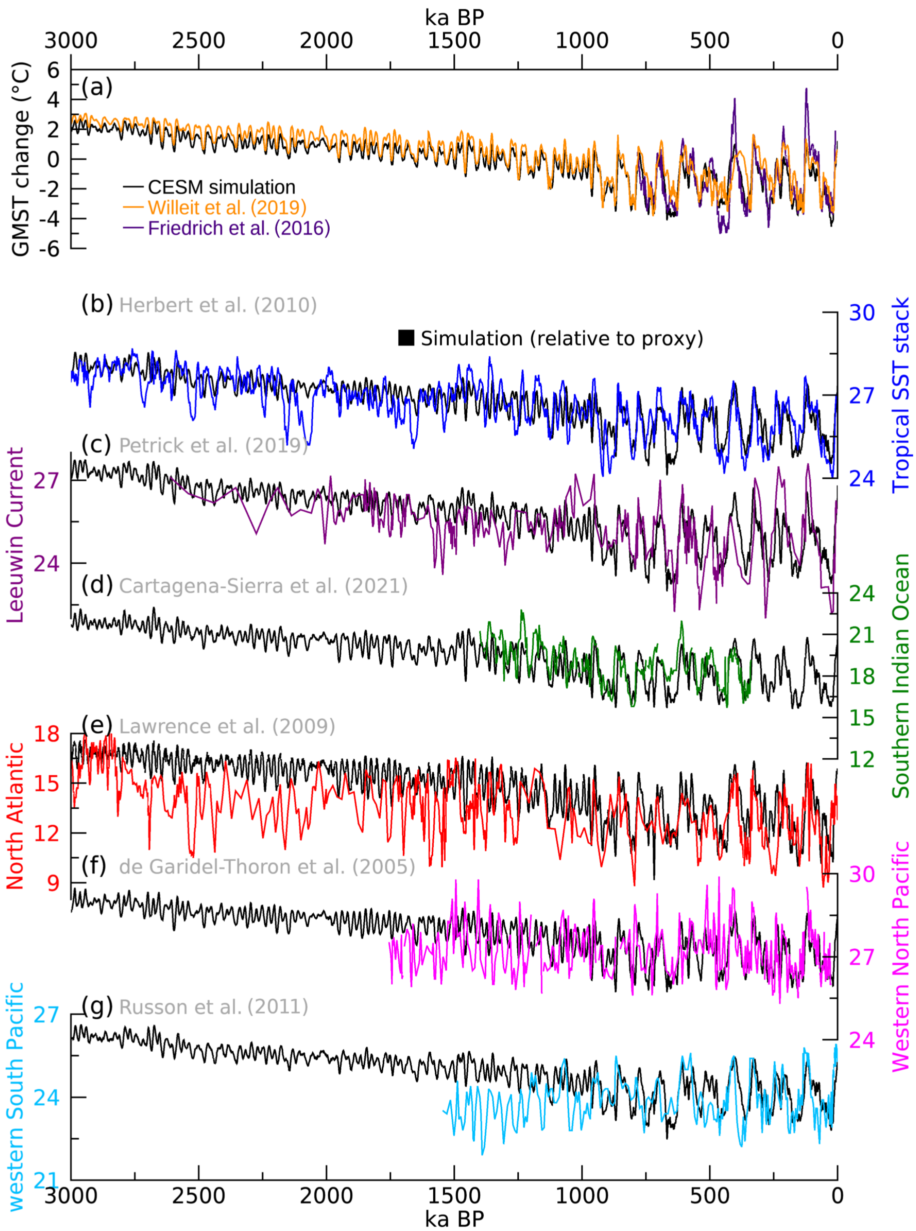

Figure 2. CESM 3 Ma simulation and climate sensitivity. **(a)** The simulated global averaged annual mean surface air temperature anomalies relative to the mean over the entire 3 Ma (black). Previous global mean temperature estimates are displayed in different colors: orange (Willeit et al., 2019) and violet (Friedrich et al., 2016). **(b–g)** Annual mean SST comparison between paleo-proxy data and CESM simulation (black): **(b)** tropical SST stack (Herbert et al., 2010) and tropical SST simulation (averaged over 5° S–5° N, unit: °C), **(c)** Leeuwin Current from Integrated Ocean Drilling Program (IODP) site U1460 (Petrick et al., 2019). **(d)** Southern Indian Ocean from sediment core MD96-2048 (Cartagena-Sierra et al., 2021). **(e)** North Atlantic from Ocean Drilling Program (ODP) 982 (Lawrence et al., 2009), **(f)** Western North Pacific from International Marine Global Change Study (IMAGES) core MD97-2140 (de Garidel-Thoron et al., 2005), and **(g)** western South Pacific from MD06-3018 (Russon et al., 2010). The proxy locations are also displayed in Fig. S2.

land can be partly explained by a larger lapse rate feedback (Hahn et al., 2020) and local impacts from the extensive NH ice sheets (Smith and Gregory, 2012). The 3 Ma simulation also captures the difference in polar amplification between Greenland and Antarctica: the amplitude of LGM cooling attains values of ~ -15.7 °C for Greenland (75° N, 42° W) and -8.6 °C for Antarctica (75° S, 123° E). The simulation also captures well the higher post-MPT variability on eccentricity timescales of 100 kyr (Fig. 4c and d) and the rapid trends of deglacial warming in both the NH and Southern hemisphere (SH), which can be explained by a similar evolution of the GHG (Fig. 1a). Overall, temperature reconstructions

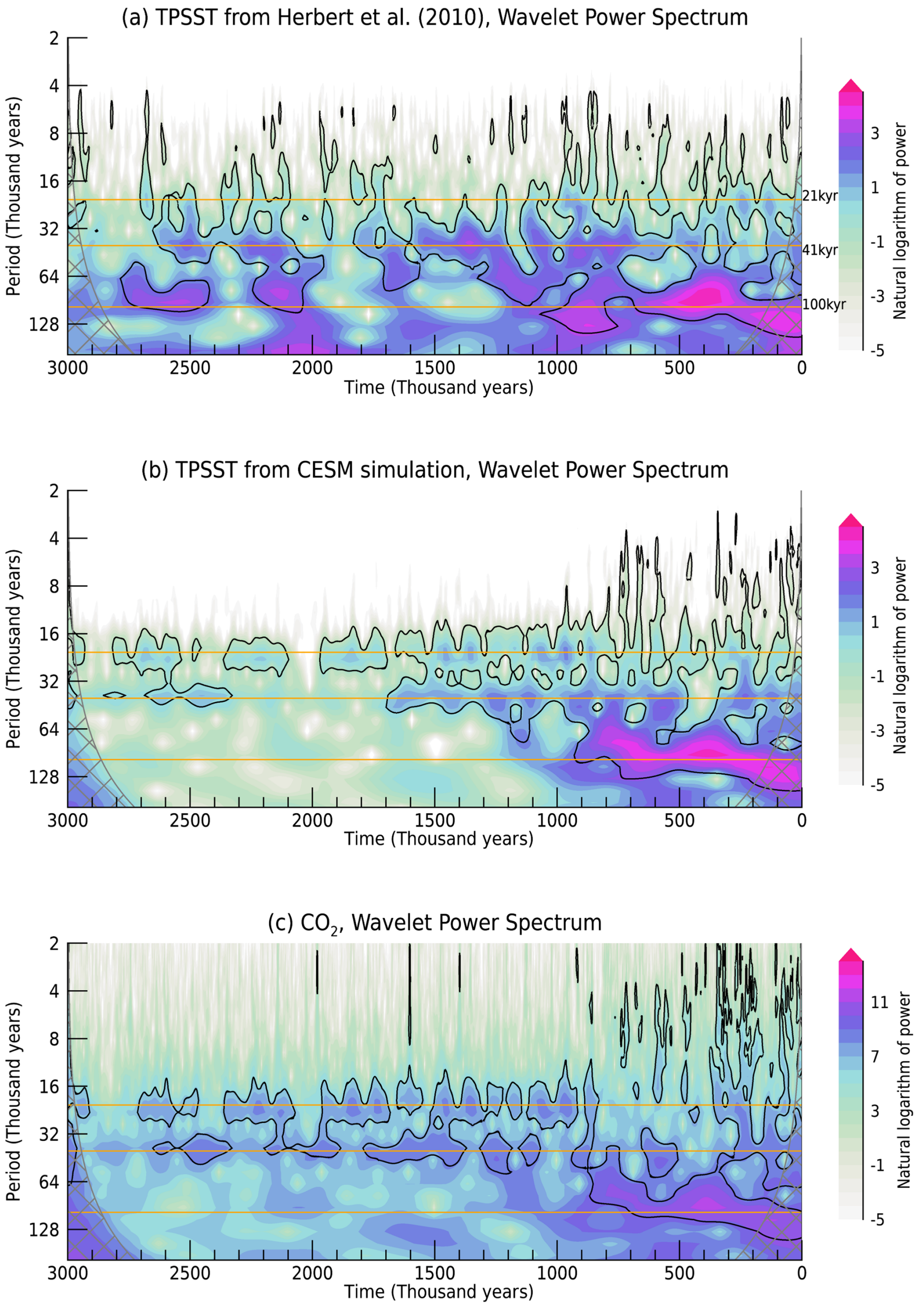

Figure 3. Wavelet power spectrum of tropical SSTs and CO_2. The wavelet power spectrum of **(a, b)** tropical SST obtained from **(a)** alkenone data and **(b)** CESM simulation and of **(c)** CO_2 concentration. The black contour indicates the value significant at the 95 % confidence level. The horizonal orange lines show 21 kyr (precession), 41 kyr (obliquity), and 100 kyr (eccentricity) periods.

from Greenland and Antarctica (Jouzel et al., 2007; Barker et al., 2011; Kindler et al., 2014) correlate well on orbital timescales with the 3 Ma simulation. These results reflect the high fidelity of the climate sensitivity of the simulation on global and regional scales and its response to the variety of acting forcings. Our simulation also provides a model-based glimpse into what temperature variability to expect in ongoing ice-core projects (Lilien et al., 2021) that plan to retrieve Antarctic ice, which is significantly older than the oldest EPICA ice.

3.2 Hydroclimate and large-scale westerly variability

Apart from the mean temperatures, orbital-scale changes in large-scale temperature gradients also play a crucial role in driving anomalies in hydroclimate (Schneider et al., 2014) and the extratropical atmospheric circulation (Timmermann

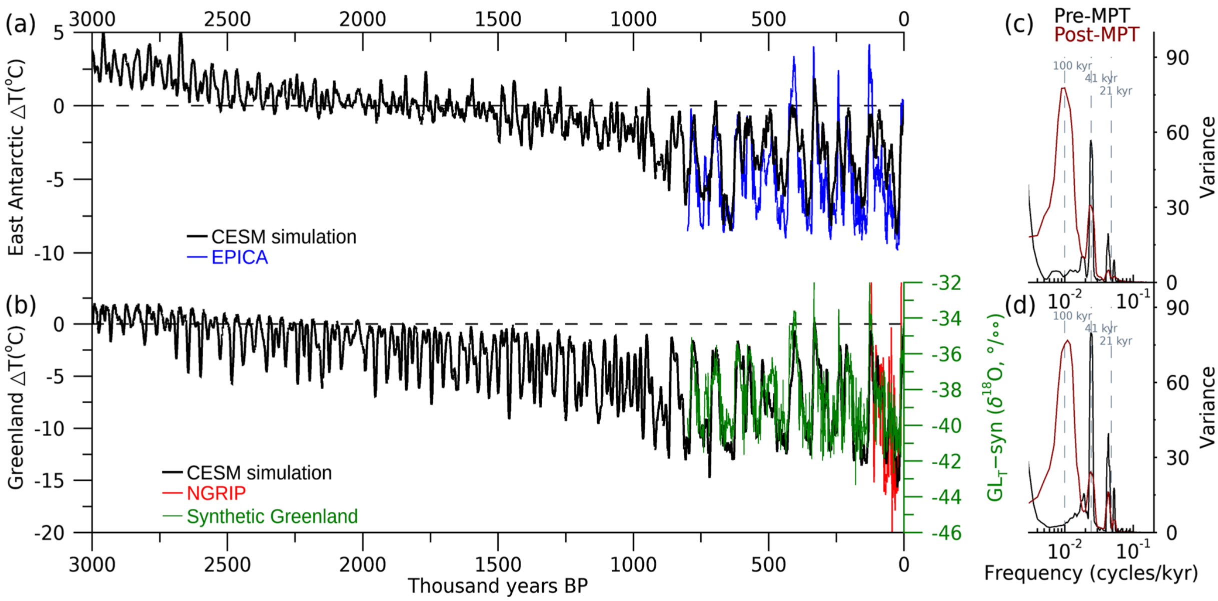

Figure 4. Polar climate changes. **(a, b)** The simulated annual mean surface air temperature anomalies relative to 0 ka in east Antarctica (**a**; 75° S, 123° E) and in Greenland (**b**; 75° N, 42° W) (black lines). Proxy-based estimations, i.e., Antarctic temperature from European Project for Ice Coring in Antarctica (EPICA) Dome C ice core (Jouzel et al., 2007; blue in upper part), North Greenland Ice Core Project (NGRIP) Greenland temperature (Kindler et al., 2014; red in bottom part; left axis), Synthetic reconstruction of Greenland δ^{18}O (Barker et al., 2011; green in bottom; right axis), scaled to match the δ^{18}O/temperature range in Kindler et al. (2014), are also displayed. **(c, d)** Spectral variance of simulated pre-MPT (3Ma-2Ma; black) and post-MPT (1–0 Ma; brown) temperatures in east Antarctica **(c)** and Greenland **(d)**. The vertical dashed lines show 21 kyr (precession), 41 kyr (obliquity), and 100 kyr (eccentricity) periods.

et al., 2014b). Here we compare simulated changes in precipitation and atmospheric westerlies with proxy-data that show strong sensitivity to these factors.

As the rising branch of the Hadley circulation, the ITCZ is characterized by a belt of deep convective precipitation near the Equator. Paleoclimate studies suggest that the latitudinal migration of the ITCZ was mainly driven by the precessional cycle (Schneider et al., 2014; Clement et al., 2004; Davis and Brewer, 2009; Liu et al., 2015). For low precession values (i.e., NH summer perihelion), NH summers receive more insolation, which leads to summer warming and a northward migration of the ITCZ and Hadley circulation (e.g., Kang et al., 2018; Tigchelaar and Timmermann, 2016). Our simulation reaffirms the precession-driven ITCZ movement (Fig. 5f and g), which is further amplitude-modulated by the 100 and 405 kyr eccentricity cycles, in agreement with some proxy records from tropical South America and Africa (Fig. 5c). Our simulation emphasizes the importance of the 405 kyr eccentricity cycle in tropical hydroclimate, which has received less attention in previous studies. Since precipitation is a positive definite non-Gaussian climate variable, the 100 and 405 kyr amplitude modulations of the precessional cycle (Fig. 5b) also rectify into a long-term mean signal (as illustrated here for Cariaco Basin precipitation; orange line in Fig. 5c) with the same frequencies, thereby introducing eccentricity as a mean forcing into the climate system (Fig. 5g).

The seasonal migration of the Hadley cell is also linked to shifts in the global monsoon precipitation (An et al., 2015; Schneider et al., 2014). With the precessional cycle modulating the amplitude of the seasonal solar forcing, monsoon systems, such as the Indian, East Asian, African, and Australia monsoons, thus show dominant variability on precessional timescales (Fig. 6) as well as contributions on obliquity and eccentricity timescales (Fig. 6e–h). Previous studies demonstrated that the past global monsoon precipitation variabilities were controlled by the orbitally driven land–sea thermal contrast, meridional pressure gradients, atmospheric CO_2 concentrations, and the growth of the NH ice sheet (Clemens and Prell, 2003; Clark et al., 2006; Kutzbach and Guetter, 1986). Although the global monsoons share similar dynamics and behaviors, there are distinct features of regional monsoon systems that need to be considered. For example, the proxy-inferred western Australia monsoon precipitation was weakened, and the amplitude of variability was strengthened during the late Pleistocene (Fig. 6a). The amplitude of observed Indian summer monsoon variability increased after 1.5 Ma to mid-Pleistocene and then decreased during the late Pleistocene (Fig. 6b). Whereas the reconstructed East Asian summer monsoon proxy shows a gradual increase in variability from 1.5 Ma to mid-late Pleistocene (An et al., 2015) (Fig. 6c), this trend in variability is absent in the reconstructed African monsoon (Fig. 6d) proxy (see Fig. S3). The situation is relatively well produced for the

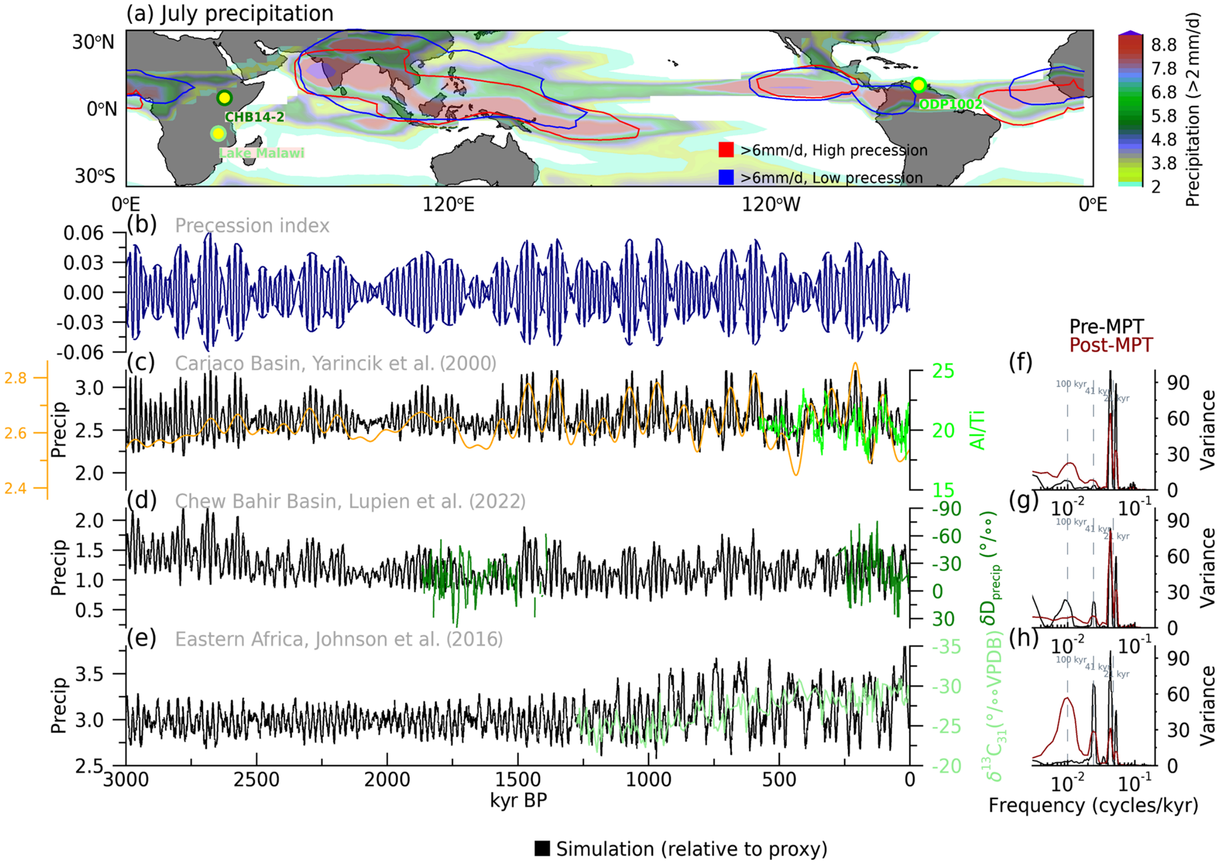

Figure 5. ITCZ changes. **(a)** Simulated July precipitation pattern (unit: $mm\,d^{-1}$) averaged for the 3 Myr period. Each proxy location is displayed in different colors. The tropical precipitation regions greater than 6 $mm\,yr^{-1}$ are displayed for comparison between the phases with high precession (red) and low precession (blue). **(b)** Precession index ($e \cdot \sin\varpi$ where e is the eccentricity and ϖ is the moving longitude of the perihelion). **(c–e)** Precipitation comparison between the proxy and simulation (black): **(c)** Cariaco Basin from ODP 1002 Al/Ti ratio (Yarincik et al., 2000), **(d)** Chew Bahir Basin and Turkana Basin from CHB14-2 and WTKB δD_{precip} (Lupien et al., 2022), and **(e)** Eastern Africa from Lake Malawi $\delta^{13}C_{31}$ (Johnson et al., 2016). The orange line in **(c)** indicates the 80 kyr low-pass filtered Cariaco Basin precipitation in simulation. **(f–h)** Spectral variance of simulated pre-MPT (3–2 Ma; black) and post-MPT (1–0 Ma; brown) precipitations in Cariaco Basin **(f)**, Chew Bahir Basin **(g)**, and Eastern Africa **(h)**. The vertical dashed lines show 21 kyr (precession), 41 kyr (obliquity), and 100 kyr (eccentricity) periods.

3 Ma simulation, where we see an intensification in variability for all monsoon systems, except for Africa. The 100 kyr cyclicity in all monsoon systems, except for Eastern Asia, which is dominated more by obliquity variability in proxies (Clemens et al., 2018) and simulation (Fig. 6c and g), becomes stronger after the MPT (Fig. 6e–h). This intensification in the model is likely brought about by the intensifying amplitudes of ice-sheet and CO_2 forcings and the corresponding impacts on NH hydroclimate.

We next compare the simulated large-scale westerly wind changes with dust and marine productivity reconstructions from ice cores and marine sediment proxies. Figure 7 displays the simulated westerly wind changes in the Pacific and Atlantic Ocean of both the NH and SH. We can see clear precessional and obliquity-scale variability in the simulation, consistent with some wind-sensitive climate and biogeochemical proxies (Lamy et al., 2019; Naafs et al., 2012). For example, the regional characteristics such as strong obliquity response in the North Atlantic (Fig. 7b and f) and a precession signal in the South Pacific (Fig. 7d and h) are captured qualitatively in the model. In our model simulation, there is a pronounced strengthening in the variability of the westerly jet stream after the MPT, which is attributable to the larger glacial cycle amplitudes (Fig. 2a) and CO_2-induced polar amplification (Fig. 4) and resultant stronger differences in the meridional temperature gradient. The 100 kyr cyclicity in the westerlies was also strengthened considerably after the MPT, except for the North Pacific (Fig. 7f–i). Overall, the agreement between model-simulated variability and the proxy record further supports the fidelity of our modeling approach. A more in-depth regional comparison between climate model and proxies, which would account for proxy un-

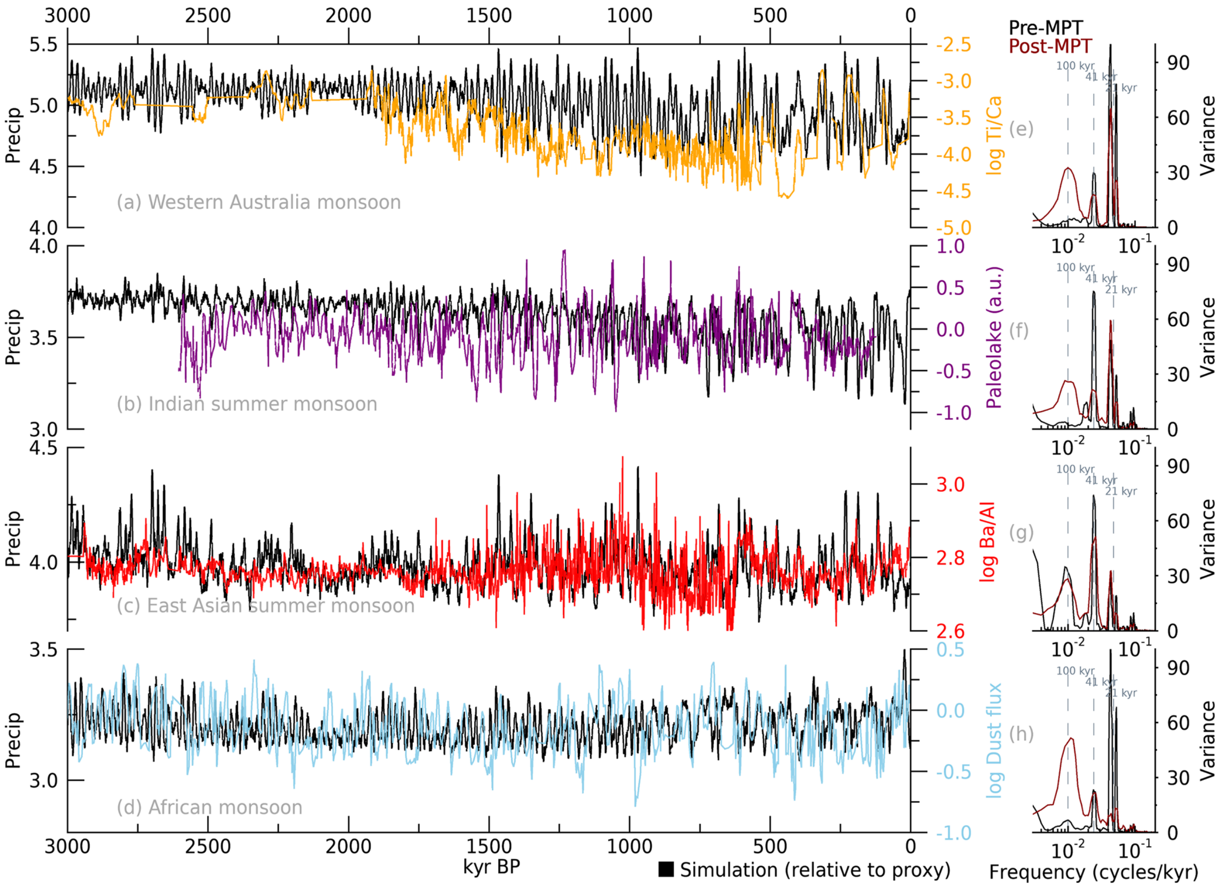

Figure 6. Global hydroclimate changes. Precipitation (unit: mm d^{-1}) comparison between the proxy and simulation: **(a)** western Australia monsoon from simulation averaged over 20–5° S, 110–150° E (black) and from proxies of IODP site U1460 log Ti/Ca (Petrick et al., 2019; orange); **(b)** Indian summer monsoon from simulation averaged over 10–30° N, 70–105° E (black) and from proxies of Lake Heqing (An et al., 2011; purple); **(c)** East Asian summer monsoon from simulation averaged over 20–40° N, 110–130° E (black) and from proxies of ODP 1146 log Ba/Al (Clemens et al., 2008; red); **(d)** western African monsoon from simulation averaged over 25–5° S, 25–50° E (black) and from proxies of ODP 659 log dust flux (Tiedemann et al., 1994; sky blue). The proxy locations and respective monsoon domains are presented in Fig. S2. **(e–h)** Spectral variance of simulated pre-MPT (3–2 Ma; black) and post-MPT (1–0 Ma; brown) precipitations in western Australia monsoon **(e)**, Indian summer monsoon **(f)**, East Asian summer monsoon **(g)**, and western African monsoon **(h)**. The vertical dashed lines show 21 kyr (precession), 41 kyr (obliquity), and 100 kyr (eccentricity) periods.

certainties etc., is beyond the scope of our presentation paper here.

4 Changes in ENSO

In contrast to previous long-term transient modeling studies conducted with EMICs (Timmermann and Friedrich, 2016; Willeit et al., 2019), the CESM1.2 is capable of simulating ENSO variability and associated air–sea coupling process well, even in the coarse resolution adopted here (Liu et al., 2014) – albeit with weaker amplitude as compared to the observations. To take a broad view of the sensitivity of ENSO to external forcings over the past 3 Myr, we first show the entire monthly time series of Niño 3 index, which is defined as 1.5–7-year band-pass filtered (Liu et al., 2014) Niño 3 SST (5° S–5° N, 150–90° W) (see Fig. S4). It includes 7.2 million monthly values. A Morlet wavelet spectrum (Torrence and Compo, 1998) of the Niño 3 SST time series (including annual cycle) (Fig. 8) reveals strong precessional-scale amplitude modulations for the annual time scale variance (i.e., averaged wavelet variance in the 0.5–1.5 year band), in agreement with recent studies (Timmermann et al., 2007; Lu et al., 2019). The annual cycle of Niño 3 SST tends to vary $\sim 90°$ out of phase with the precession index (see Fig. 5b), whereas the interannual (2–8 year) time scale wavelet variance of Niño 3 SST is in phase with the precession index (Karamperidou et al., 2020). This creates an interesting dynamic, in which variance shifts from interannual to annual timescales in response to the precessional cycle.

Furthermore, we characterize, eastern Pacific (EP) and central Pacific (CP) ENSO flavors as the standard deviation of the Niño 3 and Niño 4 (5° S–5° N, 160° E–150° W) SST

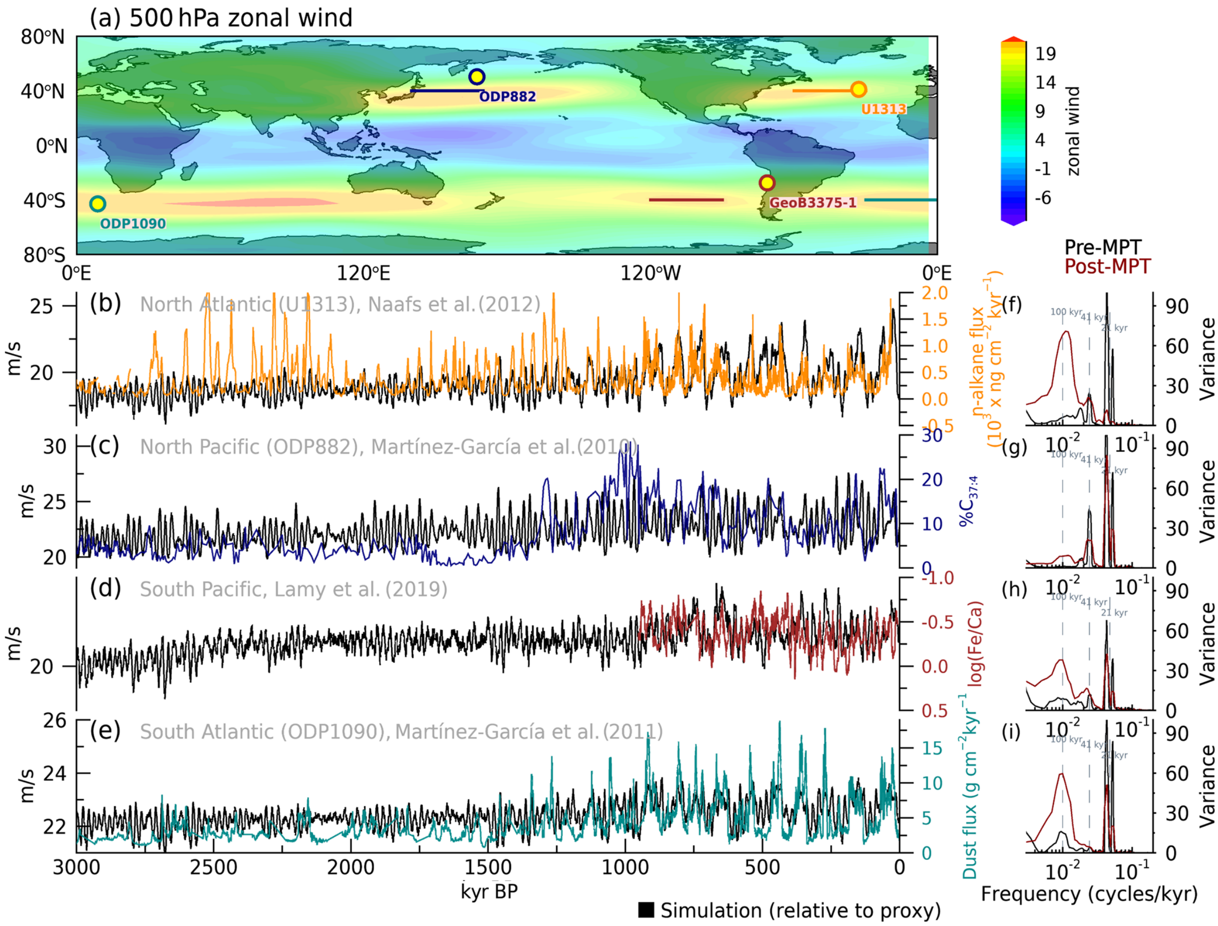

Figure 7. Global westerly wind changes. **(a)** Simulated zonal wind pattern at 500 hPa averaged for the 3 Myr period. Proxy locations and Pacific/Atlantic maximum wind regions at 40° N and 40° S are displayed in different colors. **(b–e)** Westerly comparison between the paleoproxy data and CESM simulation (black): **(b)** North Atlantic wind from U1313 *n*-alkane flux (Naafs et al., 2012) and simulation (averaged over 40° N, 60–33° W). **(c)** North Pacific wind from ODP882 (Martínez-Garcia et al., 2010) and simulation (40° N, 140–170° E), **(d)** South Pacific wind from log Fe/Ca record in fluvial sediment input (Lamy et al., 2019) and simulation (40° S, 120–90° W), and **(e)** South Atlantic wind from ODP1090 dust flux (Martínez-Garcia et al., 2011) and simulation (40° S, 30–0° W). **(f–i)** Spectral variance of simulated pre-MPT (3–2 Ma; black) and post-MPT (1–0 Ma; brown) winds in North Atlantic **(f)**, North Pacific **(g)**, South Pacific **(h)**, and South Atlantic **(i)**. The vertical dashed lines show 21 kyr (precession), 41 kyr (obliquity), and 100 kyr (eccentricity) periods.

indices in a 1000-year window, respectively (Fig. 9a and b). We find that on precessional timescales, EP ENSO variability is in phase with CP ENSO variability and CP ENSO variability on average tends to be larger than EP ENSO variability (i.e., variability ratio shown in Fig. 9c is less than 1.0). The ratio of EP to CP ENSO variability is an indicator for how ENSO flavors change in response to orbital forcing. The ratio exhibits – apart from the precessional cycle – a strong eccentricity component with ~ 100 and ~ 405 kyr periodicities. The timing of the largest ratio (ratio > 2.0 and EP ENSO variability $> 0.6°$) occurs in ~ 1470, ~ 1350, ~ 970, ~ 230, and ~ 130 ka. The timing in the occurrence of ENSO flavors in CESM1.2 relative to the phase of the precessional cycle is similar to that described in recent studies (e.g., Karamperidou et al., 2015). Contrary to the ENSO precessionally dominated variability, the mean state of equatorial EP SST is largely controlled by atmospheric CO_2 variability (Fig. 9d). The different orbital characteristics of both mean state and variability suggest that the ENSO response to Milanković cycles can be attributed to the modulation of the seasonal cycle (Jin et al., 1996) rather than to changing instabilities of air–sea interactions with respect to the background state.

5 Global heat transport

Large-scale insolation and meridional temperature gradients are the main drivers for the global transport of energy. The 3 Ma simulation provides a unique opportunity to study the dominant modes of atmospheric and oceanic energy transport and their responses to orbital-scale forcings. To this end we calculated the meridional heat transport (MHT) at each

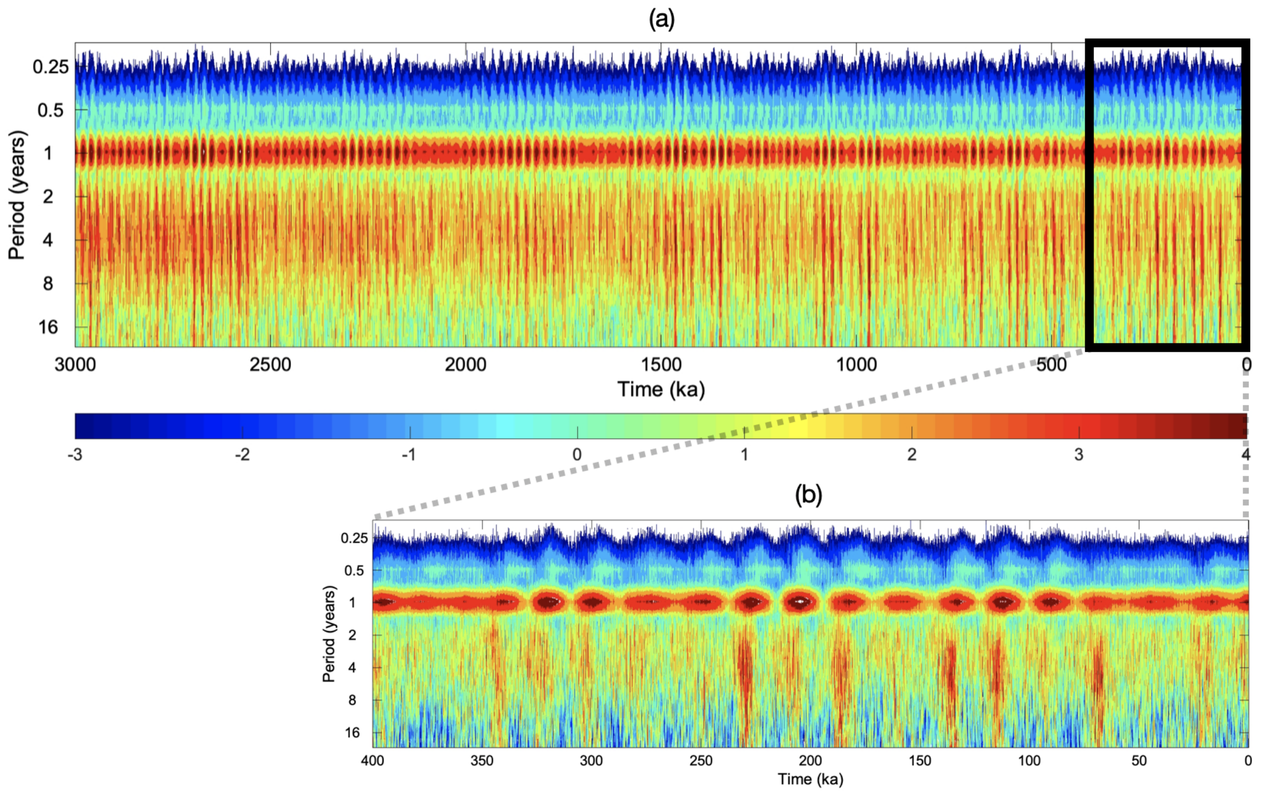

Figure 8. Monthly ENSO spectrum. Wavelet power spectrum (logarithmic variance) of Niño 3 SST (5° S–5° N, 150–90° W) during the period of **(a)** 3 Myr and **(b)** 400 kyr.

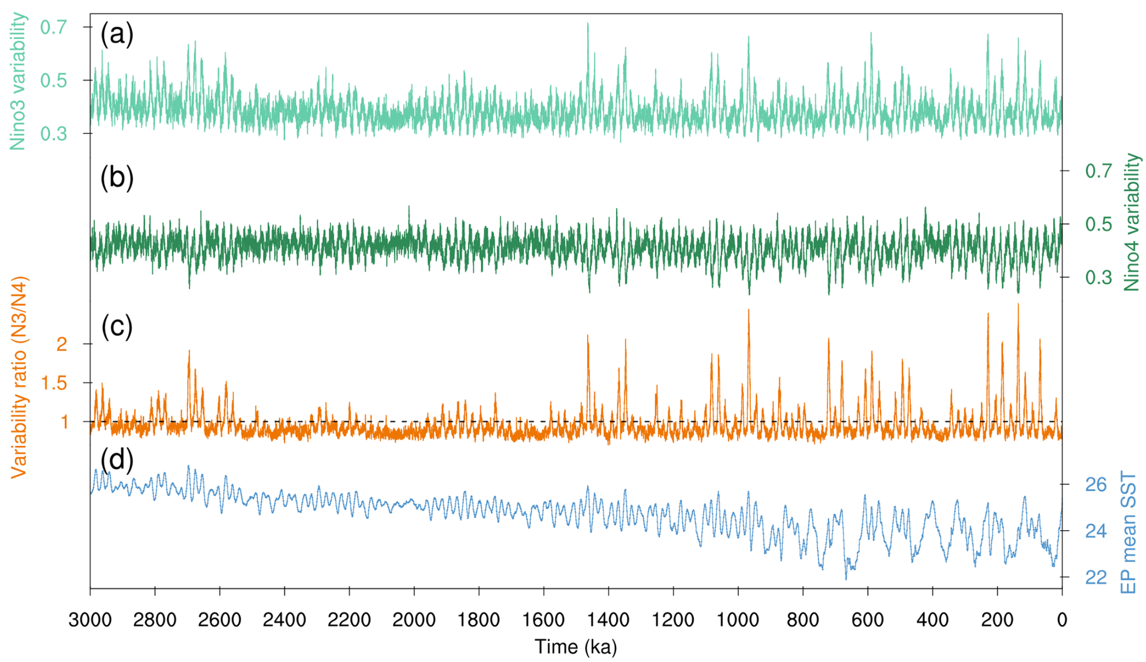

Figure 9. Comparison of monthly Niño 3 and Niño 4 variabilities. Time series of **(a)** Niño 3 SST index variability (°C), **(b)** Niño 4 SST index variability (°C), **(c)** ratio of Niño 3 variability to Niño 4 variability, and **(d)** 1000-year mean Niño 3 SST (°C). The variability in **(a, b)** was calculated as the running standard deviation of SST indices over a sliding 1000-year time window.

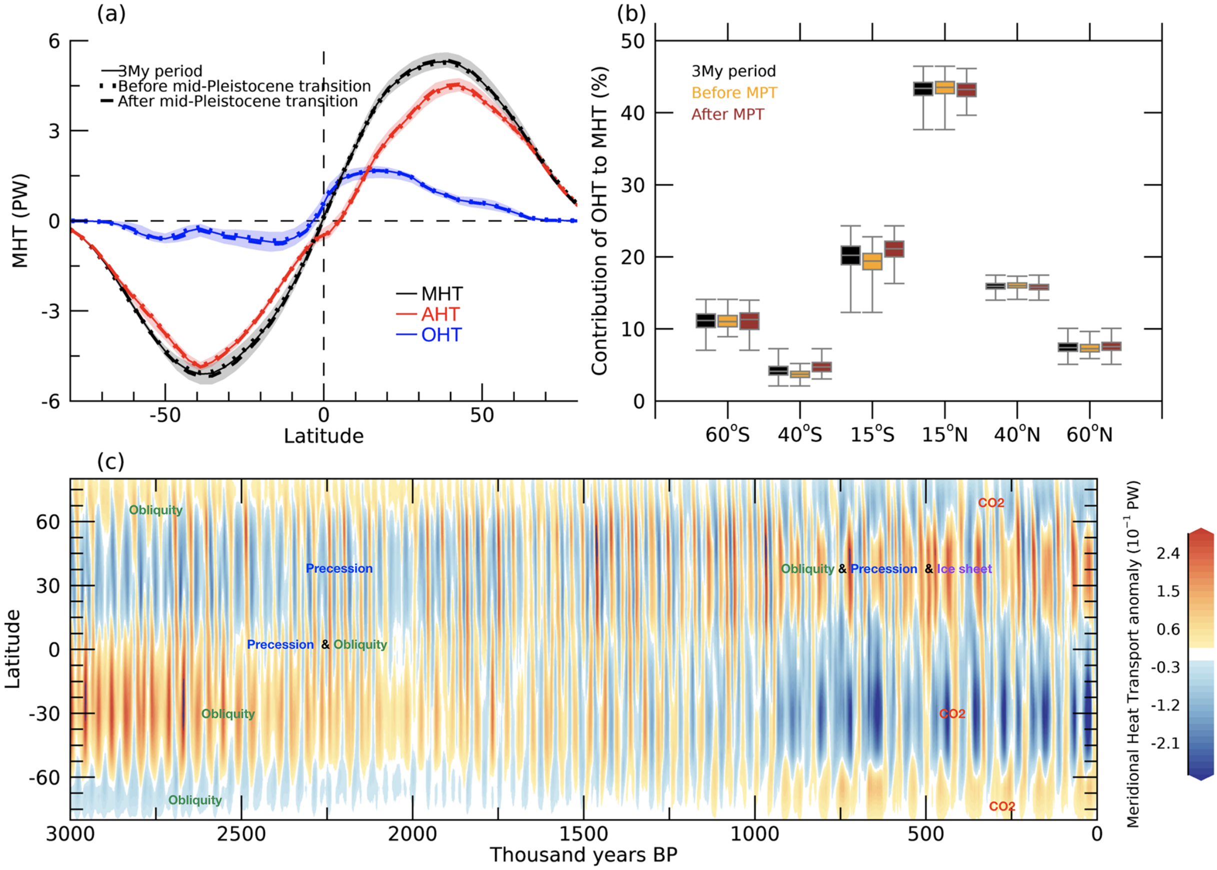

Figure 10. Global heat transport across the 3 Ma simulation. **(a)** The meridional heat transport (MHT; unit: PW; black line), atmospheric MHT (AHT; red line), and oceanic MHT (OHT; blue line) averaged over the entire 3 Myr period (solid), 41 kyr period (i.e., before the Mid-Pleistocene Transition (MPT), about 1 Ma; dotted line), and 100 kyr glacial period (i.e., after the MPT; dashed line). The minimum and maximum range of MHT changes over the 3 Myr period is displayed by corresponding color shading. **(b)** Box-whisker plot (i.e., minimum, 25 %, 50 %, 75 %, maximum range) of contribution of OHT to MHT (unit: %) at the latitude position of 60° S, 40° S, 15° S, 15° N, 40° N, and 60° N during the three different periods: the entire 3 Myr period (black), 41 kyr period (orange), and 100 kyr glacial period (brown). The contribution of AHT to MHT can be estimated by subtracting the contribution of OHT from 100 %. **(c)** The time–latitude plot of MHT anomaly (unit: 10^{-1} PW) relative to the climatological mean. Positive MHT indicates the northward heat transport.

latitude (θ), based on an energetic framework (Donohoe et al., 2020).

$$\mathrm{MHT}(\theta) = -2\pi a^2 \int_{\theta}^{90} \cos(\theta)[\mathrm{ASR}(\theta) - \mathrm{OLR}(\theta)]\mathrm{d}\theta, \qquad (1)$$

where ASR represents the zonal mean absorbed solar radiation and OLR denotes the zonal mean of outgoing long-wave radiation at top-of-atmosphere (TOA). The non-zero global mean values of ASR − OLR were removed from the calculation to attain energy conservation at both poles (Donohoe et al., 2020). The oceanic MHT (OHT) is directly deduced from the advection of the Eulerian mean circulation and mesoscale eddies (i.e., bolus circulation + diffusion) – the latter of which were parameterized but not explicitly resolved. There is also an indirect approach to calculate OHT using surface heat fluxes. A recent study (Yang et al., 2015) documented the consistency between the heat transports obtained from direct and indirect approaches in the CESM. The atmospheric MHT (AHT) is then calculated as the residual of the MHT determined from TOA radiation and the OHT derived from CESM direct output. This residual approach was also applied successfully in previous studies (Donohoe et al., 2020).

Figure 10a displays the patterns of total MHT, AHT, and OHT averaged over the past 3 Myr period (solid lines). In the tropics, the MHT has strong contributions both from the atmosphere and ocean. The main sources are the atmospheric Hadley circulation and the wind-driven oceanic shallow overturning circulation in the Pacific and the deep meridional overturning circulation in the Atlantic (Schneider, 2017; Held, 2001). The poleward transport outside the tropics is mostly caused by the atmospheric eddy activity (i.e., transient eddies and stationary eddies) (e.g., Donohoe et al., 2020). Despite the coarse horizontal resolution, the

CESM1.2 captures the MHT in both atmosphere and ocean realistically (Yang et al., 2015). To further illustrate that our coarse-resolution CESM1.2 version can also capture the present-day partitioning between AHT and OHT, we compare the simulated MHTs with recent observational estimates (see Fig. A1 in Donohoe et al., 2020). The comparison reveals an overall agreement in terms of amplitude and peak latitude; however, the model exhibits a stronger AHT and weaker OHT than the observations, in agreement with previous studies (Donohoe et al., 2020; Yang et al., 2015).

In the following, we further explore the linkage between changes in the MHT (Fig. 10) and external forcings (precession, obliquity, ice sheet, and CO_2). The time–latitude changes of anomalous MHT over the past 3 Myr (Fig. 10c) show a complex spatiotemporal pattern, which documents that all forcings play an important role in controlling the MHT. For example, before the MPT, there are strong signals of both obliquity at most of the latitudes and precession in the tropics and NH mid-latitudes (particularly around 2–1 Ma), whereas after the MPT, we can see an increasing role of CO_2 on the MHTs. High obliquity values weaken the Equator-to-pole temperature gradient (Timmermann et al., 2014b) and thus affect the mid-latitude MHT, in particular prior to the MPT. Precession has a stronger impact in the tropics and NH mid-latitudes, due to the seasonally asymmetric continental responses to the precessional forcing (Merlis et al., 2013; Tigchelaar and Timmermann, 2016). The NH ice sheets alter the surface albedo and topography, thus changing the NH mid-latitude stationary and transient eddy activities (Donohoe and Battisti, 2009), whereas decreasing CO_2 concentrations enhance the southward transport of net surface heat flux toward the high latitudes of Southern Ocean (Kim, 2004).

The combined effect of these forcings leads to complex variations of the MHT by $\sim 10\,\%$ (0.51 PW for maximum – minimum, $1\,\mathrm{PW} = 10^{15}\,\mathrm{W}$) relative to the latitudinal maximum value of ~ 5.3 PW (see Fig. 10a). We can also see that the partitioning of the total MHT into atmospheric and oceanic contributions is time-dependent (Donohoe et al., 2020; Yu and Pritchard, 2019; Newsom et al., 2021; Liu et al., 2017). We find an increasing contribution of the Southern Ocean to the total MHT variability after the MPT (~ 1 Ma) due to the enhanced CO_2 variability (Fig. 10b), which indicates that the MPT caused the shifts in the global energy distribution and corresponding changes in regional climate feedbacks.

To further simplify the complex MHT dynamics shown in Fig. 10c, we perform an empirical orthogonal function (EOF) analysis of the zonally averaged MHT anomalies over the past 3 Myr. The principal component (PC) time series (Fig. 11a and b) of the two dominant MHT modes explain $\sim 92\,\%$ of the total variance. PC1 is characterized by a strong 41 kyr obliquity cycle (correlation coefficient $r \sim 0.7$ with obliquity time series) as well as a negative trend throughout the Pleistocene, whereas PC2 is more related to higher frequency variability associated with the eccentricity-modulated precession cycle (~ 21 kyr cycle; see Fig. S5). The PC1 variability also shows a somewhat stronger 100 kyr cyclicity after the MPT. PC2 changes its overall character after the MPT, when precessional variability with an eccentricity-modulated envelope (early Pleistocene) transitions into variability which has strong eccentricity and CO_2 periodicities in the mean value (middle to late Pleistocene). We can reconfirm these characteristic changes by comparing the simulated PC2 time series with reconstructed variabilities using the precession and CO_2 forcing only (see Fig. S6). The post-MPT shift in PC1 and PC2 can be attributed mostly to the increase in the amplitude of CO_2 radiative forcing and its cyclicity (see Fig. 3c), both of which were generated from the orbitally forced climate-carbon cycle dynamics simulated by the EMIC CLIMBER-2 (Willeit et al., 2019).

The corresponding dominant MHT patterns are obtained by regressing the MHT anomalies against PC1 and PC2 (Fig. 11c and d). The PC1-related net radiation flux anomalies at the TOA and surface (Fig. 11c) show a weakening of the Equator-to-pole insolation gradient (less heat in low latitudes and more heat in high latitudes for positive PC1 values), consistent with high obliquity forcing and the effect of high CO_2 on polar amplification. The PC2-related net radiation flux anomalies (Fig. 11d) show a pronounced interhemispheric radiation gradient (i.e., warmer SH and colder NH for positive PC2). To compensate for the meridional differences of the PC1-related weakening of the Equator-to-pole net radiation gradient (Fig. 11c), an overall weakening of the poleward heat transport (i.e., anomalous northward in the SH and southward in the NH, Fig. 11e) is generated; the PC2-related strengthening of interhemispheric TOA gradient (Fig. 11d) in turn drives an anomalous northward heat transport (Fig. 11f). From these results, we define the two energy transport modes as (i) tropical heat "convergence (or divergence) mode" (PC1) and (ii) (northward or southward) "interhemispheric shift mode" (PC2), respectively. The Pleistocene global energy transport is made up by the different combinations of these two energy transport modes. The underlying processes could be accompanied by characteristic changes in both atmosphere and ocean circulations driven by NH ice-sheet albedo, sea ice albedo, and surface wind changes. The key difference between these two MHT mechanisms is associated with the orbital configuration and the response to the NH ice sheet.

6 Large-scale atmosphere and ocean circulation changes

6.1 Atmosphere

The Northern Annular Mode (NAM) and the Southern Annular Mode (SAM) are fundamental patterns of large-scale atmospheric circulation variability in both the NH and the SH. The positive phase is related to the anomalous low pressure over the polar region and high pressure over the

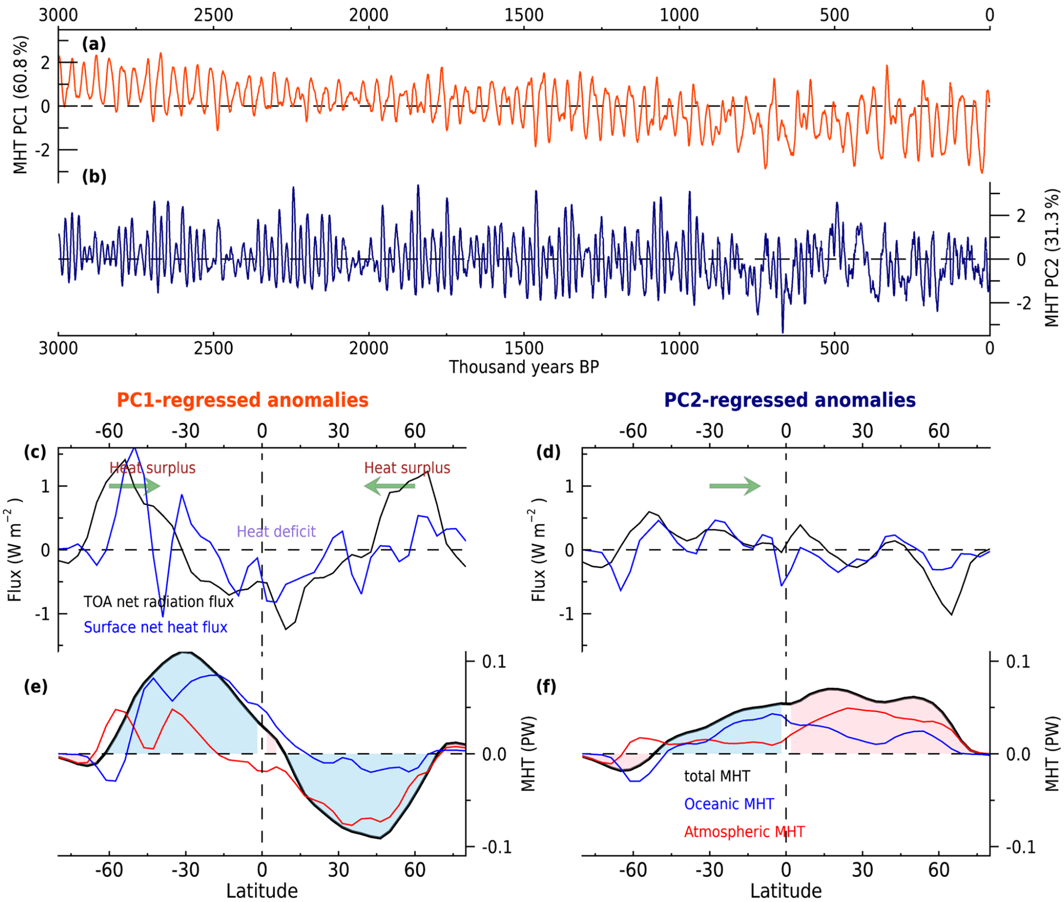

Figure 11. Spatiotemporal modes of global heat transport variability. **(a, b)** The principal component (PC) time series associated with the first two leading modes of MHT anomalies. **(c–f)** The regressed anomalies against the (left) PC1 and (right) PC2 variability: **(c, d)** zonally averaged top-of-atmosphere net radiative flux (downward in positive; unit: W m^{-2}) and surface net heat flux (toward ocean in positive; unit: W m^{-2}), **(e, f)** the total MHT (black), oceanic MHT (OHT; blue), and atmospheric MHT (AHT; red) (unit: PW). Sky-blue and pink shading in **(e, f)** indicates the weakening and strengthening of poleward total MHT, respectively.

mid-latitudes, accompanied by the strengthened (and sometimes poleward-shifted) westerly wind and storm tracks (e.g., Screen et al., 2018). We examine the variations in the NAM and SAM as key indicators for large-scale extratropical circulation changes. Figure 12 shows a strong correlation between the NAM and SAM on orbital and super-orbital timescales (correlation coefficient $r \sim 0.79$ during 3 Myr) (Fig. 12a). Both show a strong amplitude on precessional timescales before the MPT (Fig. 12b and c). However, an important difference between the NAM and SAM appears after the MPT. The post-MPT NAM has a broader spectrum band from precession ($\sim$ 21 kyr), obliquity ($\sim$ 41 kyr), to eccentricity ($\sim$ 100 kyr), which is compared with the precession-only variability of the SAM. This NAM–SAM difference may be due to the existence of NH landmass and post-MPT ice-sheet growth influencing extratropical stationary waves (Yin et al., 2008).

Compared to changes in the SAM, those in the NAM are better correlated with the major two modes of global energy transport shown in Fig. 11 (particularly for PC1-NAM, $r \sim 0.79$ during 3 Myr; $r \sim 0.44$ for PC1-SAM). For positive PC1 and negative PC2 values, the orbitally (high obliquity and low precession) driven increase of incoming insolation in high latitudes would have decreased the NH ice-sheet volume (not interactively simulated here but included implicitly in the tendency of the ice-sheet forcing). The retreat of ice sheets can weaken the large-scale circulations and stationary eddies over the NH mid-latitudes by changes in surface albedo and ice-sheet topography (Yamanouchi and Charlock, 1997). The weakening of stationary eddies leads to the reduced poleward (anomalous southward) AHT, especially in the NH mid-latitudes (see Fig. 11e). This would imply a central role of the NH large-scale circulation in modulating the global energy transport during the Pleistocene.

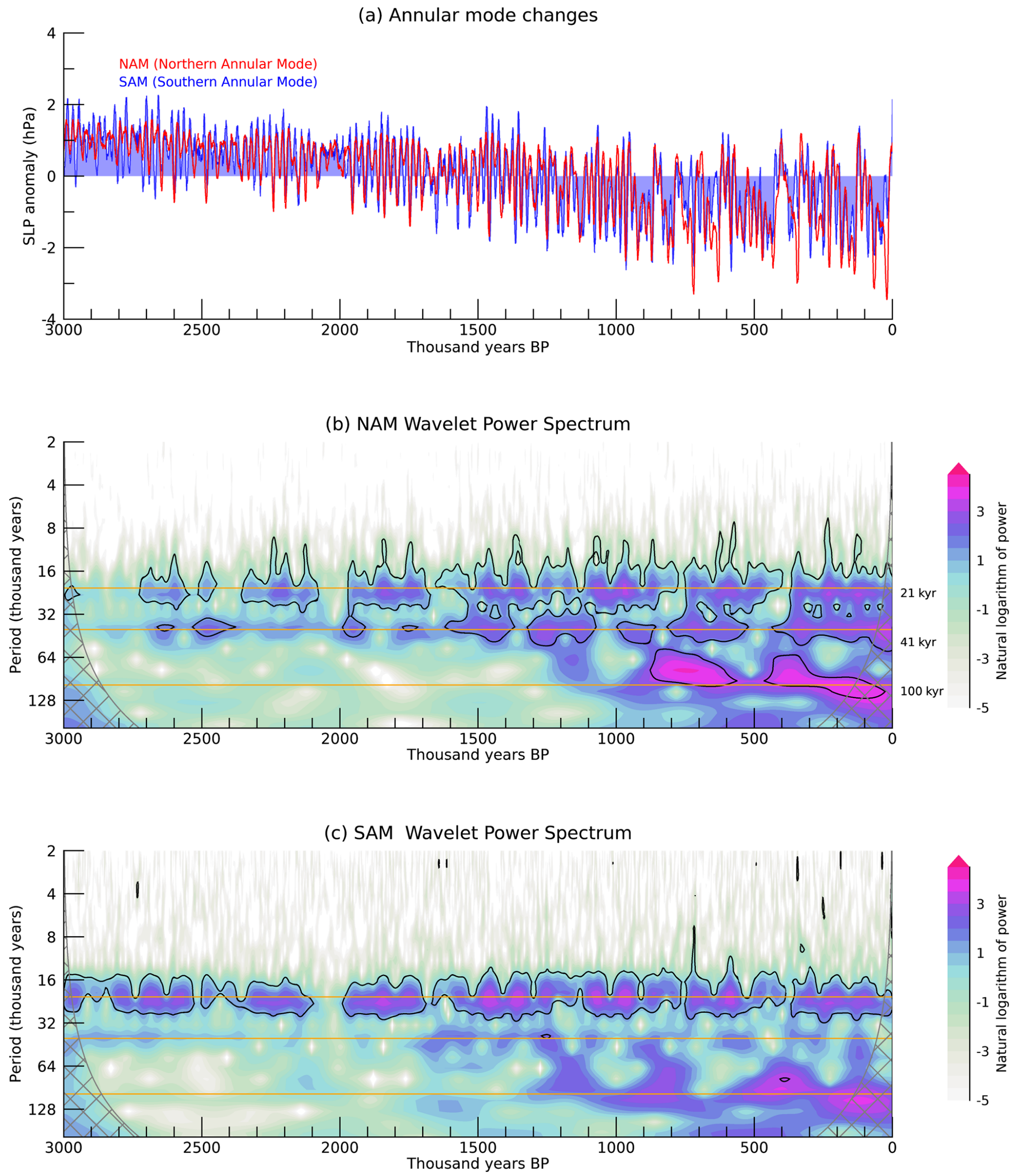

Figure 12. Atmosphere circulation changes. **(a)** The time series of Northern Annular Mode (NAM) and Southern Annular Mode (SAM). Here, the NAM is defined as the difference in zonal mean SLP at 35 and 65° N (Li and Wang, 2003) and the SAM as the difference in zonal mean SLP at 40 and 65° S (Gong and Wang, 1999). **(b, c)** The wavelet power spectrum of **(b)** NAM and **(c)** SAM indices. The black contour indicates the value significant at the 95 % confidence level. The horizonal orange lines show 21 kyr (precession), 41 kyr (obliquity), and 100 kyr (eccentricity) periods.

6.2 Ocean

Previous studies highlighted the importance of the AMOC in global energy transport (Frierson et al., 2013; Yu and Pritchard, 2019). To assess the role of ocean circulation changes in our transient simulation, we investigate the variability of the AMOC (Fig. 13a). The AMOC strength, calculated here as the maximum meridional streamfunction below 500m and north of 28° N, shows increased variability after the MPT on precessional and obliquity timescales (Fig. 13b). Our simulation only shows weak variability on the 80–120 kyr frequency, indicating a relatively minor contribution from CO_2 and ice-sheet forcing on AMOC variability. It should be noted, however, that since our model does not include explicit meltwater forcing or calving from the ice sheets, the simulated AMOC variability on millennial and orbital timescales will be unrealistically small. In

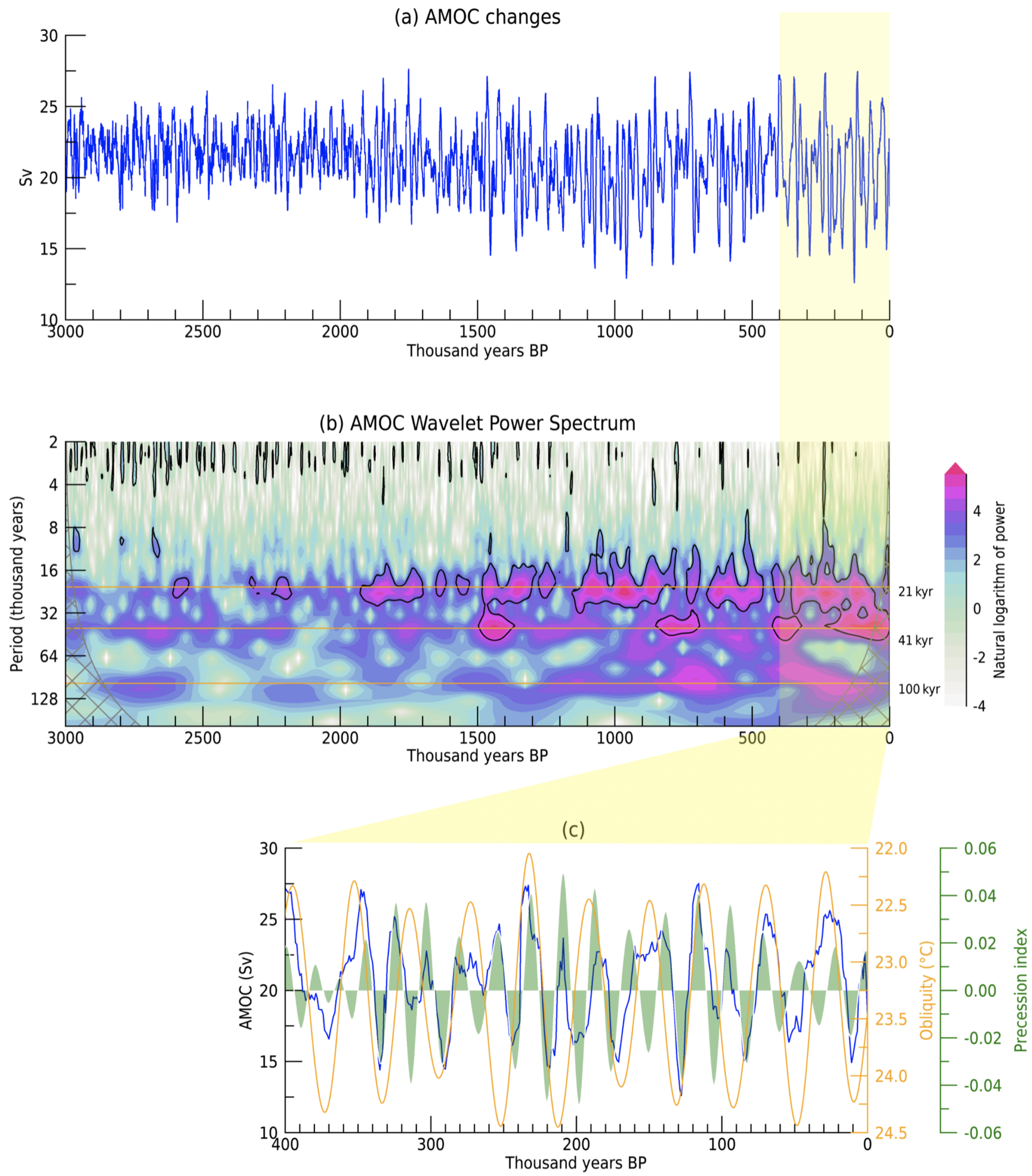

Figure 13. Ocean circulation changes. **(a)** The time series of Atlantic Meridional Overturning Circulation (AMOC). Here, the AMOC amplitude is defined as the maximum meridional stream function below 500 m and north of 28° N. **(b)** The wavelet power spectrum of AMOC amplitude. The black contour indicates the value significant at the 95 % confidence level. **(c)** 400 kyr evolution of AMOC, precession and obliquity variability. The horizonal orange lines show 21 kyr (precession), 41 kyr (obliquity), and 100 kyr (eccentricity) periods.

our simulation the AMOC amplitude varies between a minimum of 12.6 Sv to a maximum of 27.7 Sv. This result illustrates that in the absence of ice-sheet freshwater forcing, orbital forcing can play a more important role in driving an AMOC variability as compared to the GHG forcing alone (Fig. 13c). More specifically, the AMOC strength is strongly controlled by the obliquity and precession cycles associated with the two modes of global energy transport (Fig. 11). As described in Sect. 5, for a positive PC1 we find an orbitally driven weakening of the atmospheric circulation and heat transport (Fig. 11e), which also leads to a reduction in surface winds. In turn this process leads to a weakening in the NH ocean gyre circulation during high obliquity (positive PC1 in Fig. 11a). High precession values corresponding to a positive PC2 (Fig. 11b) are associated with an overall stronger AMOC and poleward heat transport (Fig. 11f). Therefore, the complex interplay between PC1 and PC2 of MHT is characterized by a modulation in the strength of the wind-driven and thermohaline ocean circulation as well as the corresponding changes in MHTs.

CHAPTER 1.9

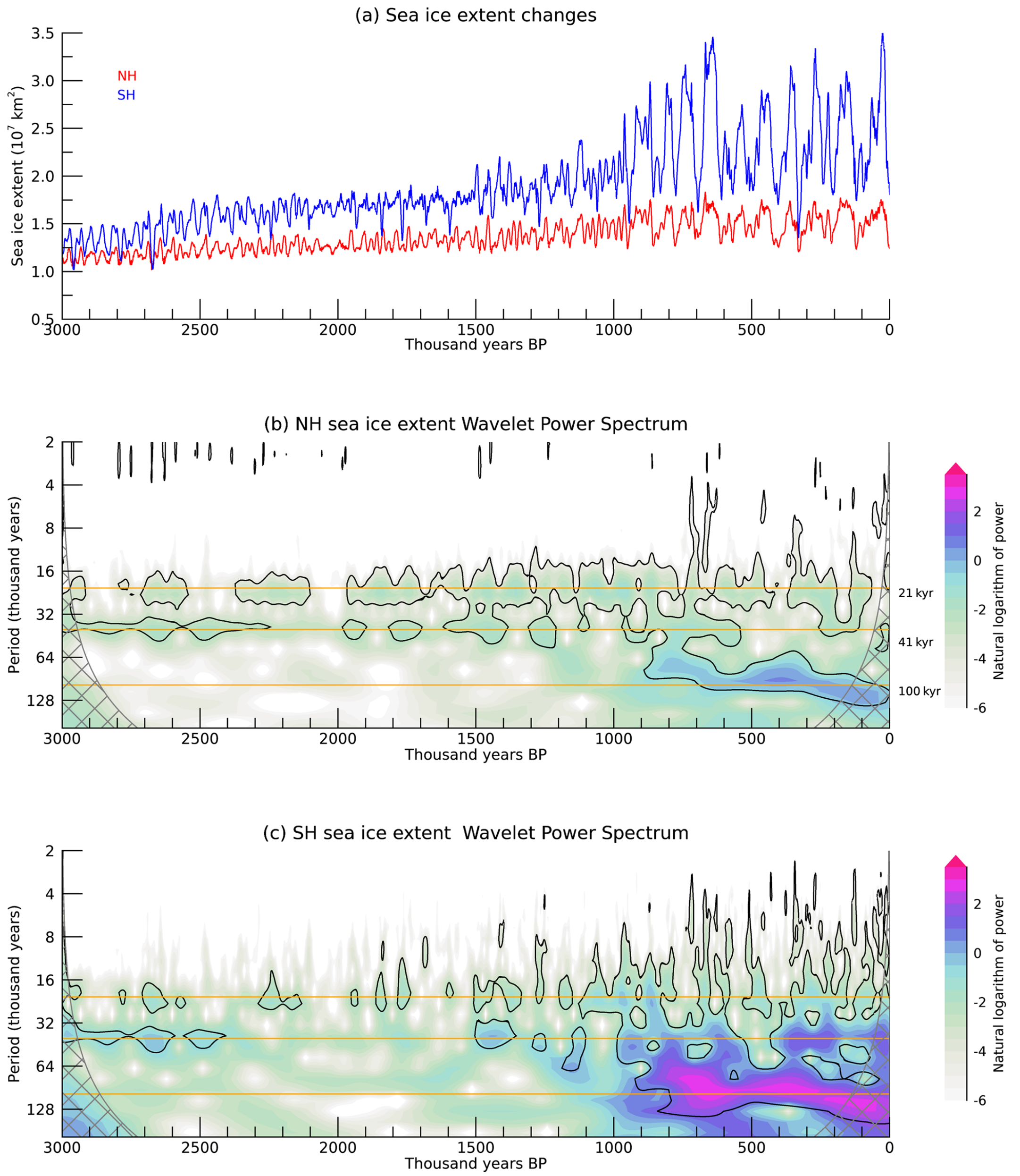

Figure 14. Sea ice changes. **(a)** The time series of sea ice extent over the Northern Hemisphere (NH, red) and Southern Hemisphere (SH, blue). **(b, c)** The wavelet power spectrum of **(b)** NH sea ice and **(c)** SH sea ice. The black contour indicates the value significant at the 95 % confidence level. The horizonal orange lines show 21 kyr (precession), 41 kyr (obliquity), and 100 kyr (eccentricity) periods.

6.3 Sea ice

To further illustrate the impact of external forcings on climate conditions, we focus on sea ice. We find a very high correlation between NH sea ice and SH sea ice ($r \sim 0.9$) (Fig. 14a). But the variance of NH sea ice extent (standard deviation of $\sim 0.16 \times 10^7$ km^2) is considerably smaller than that of SH sea ice (standard deviation of $\sim 0.43 \times 10^7$ km^2). The variability is characterized by increased spectral power on precession ($\sim$ 21 kyr), obliquity ($\sim$ 41 kyr), and CO_2/ice-sheet ($\sim$ 80–120 kyr) frequencies across the 3 Ma (Fig. 14b and c), consistent with the combined effect of GHG and ice-sheet forcing.

Sea ice extents both in the NH and SH exhibit a pronounced post-MPT climate shift. Considering the close relationship between sea ice and mid-latitude westerlies via the modulation of the meridional temperature gradient and the atmosphere's baroclinicity (Timmermann et al., 2014b; Lamy et al., 2019; Menviel et al., 2010), we expect that the post-MPT climate shift would be more robust in the NH than the SH, due to the stronger obliquity-scale frequency of atmospheric circulation in the NH (see Fig. 12b and c). However, the obliquity signal of sea ice extent is more pronounced in the SH. The discrepancy between both hemispheres could be primarily explained by different geographical feature: in the NH, sea ice is mostly limited to the Arctic Ocean, whereas in the SH it is unconstrained. This suggests an interesting feature of interhemispheric asymmetry for global climatic changes. For example, for high obliquity and high atmospheric CO_2 levels (positive PC1 values), the heat is transported equatorward primarily by means of the atmosphere in the NH or the ocean in the SH (see Fig. 11e). In the SH, the increased high-latitude insolation can melt more sea ice and the Southern Ocean then transports more heat through the mean equatorward Ekman transport (Morrison et al., 2016). This would reflect an increasing role of sea ice on Southern Ocean heat transport after the MPT.

7 Discussion, summary, and outlook

We presented results from the first quasi-continuous Pleistocene simulation, conducted with a CGCM, and using time-evolving forcings of the orbital parameters, GHG concentrations, and estimates of NH ice sheets. Our simulation represents well the observed orbital-scale shifts not only in the regional mean temperature changes but also in hydroclimate and large-scale westerly variabilities controlled by the earth's meridional temperature gradients. We identified a rectification mechanism by which eccentricity-modulated precessional cycles in precipitation can introduce mean state variability with periods of 100 and 405 kyr in the tropical climate system. This finding may provide a simple framework for interpreting 405 kyr eccentricity variability in long-term paleoclimatic records (Kocken et al., 2019; Nie, 2018). Simulated ENSO variability is also driven by eccentricity-modulated precessional cycles which cause an anomalous seasonal cycle forcing that interacts with ENSO. Tropical mean state changes, which are in large parts influenced by CO_2 and ice-sheet forcing, show little impact on ENSO variability and flavors.

To provide a larger context for our simulation we focused on the temporal variability of global heat transport. Two dominant modes govern the global energy transport across the 3 Ma Pleistocene: a "tropical convergence mode" related to Equator-to-pole temperature gradient and an "interhemispheric shift mode," which is linked to the interhemispheric temperature difference. These processes are accompanied by characteristic changes in both atmosphere and ocean circulations driven by westerly wind changes, the AMOC, and sea ice albedos. The two MHT modes reveal a robust regime shift for the pre- and post-MPT periods, which is most strongly pronounced for the second MHT mode. During the post-MPT glacial peaks, there is an increasing probability (from 15.3 % to 47 %) of anomalous poleward heat transport (i.e., negative PC1; colder poles than tropics) and southward shifted heat transport (i.e., negative PC2; colder SH than NH), which could contribute to cooling in the NH climate and potentially an intensification of glacial conditions. We emphasize that the regime shift in the major MHT modes plays a pivotal role in reshaping the interhemispheric exchange of energy, thereby contributing to the glacial interhemispheric temperature heterogeneity and interglacial homeostasis during the late Pleistocene.

Our experimental set-up has several unrealistic features, which may impact the results in some regions: (i) we do not consider time-evolving land–sea masks due to sea level changes; (ii) freshwater forcing from the time-evolving ice sheets is not captured; (iii) the model does not include a dynamic vegetation component, nor does it explicitly simulate dust, aerosols, and climate-carbon cycle feedbacks. Using constant LGM land–sea masks throughout the entire simulation can lead to biases in regional temperature and hydroclimate and large-scale atmospheric circulation (e.g., Cao et al., 2019; Di Nezio et al., 2016). In addition, in the absence of ice-sheet-induced millennial to orbital-scale freshwater fluxes, the amplitude of AMOC variability will be underestimated compared to reality. Considering the role of AMOC changes in global energy transport (Frierson et al., 2013; Yu and Pritchard, 2019), the reduced amplitude of AMOC could alter the contribution of OHT to the MHT. The post-MPT increased variance in Southern Ocean sea ice may have further contributed to climate-carbon cycle feedbacks, which are not explicitly resolved in our simulation because we use prescribed CO_2 forcing. In a more realistic setting, which involves an interactive carbon cycle, the two MHT modes and shifts in sea ice may have influenced the outgassing of CO_2 from the ocean to atmosphere on glacial/interglacial timescales (Stein et al., 2020). For example, negative signs of PC1 and PC2 (related to Southern Ocean cooling) would amplify the Southern Ocean CO_2 sequestration, because of the increased sea ice–carbon cycle feedback and increased sinking of carbon-rich deep waters (Stott et al., 2007; Stein et al., 2020) (see Fig. S7). Thus, we hypothesize that the increased occurrence of same-sign PCs anomalies after the MPT may have helped re-enforce the glacial carbon cycle response, whereas prior to the MPT, the opposite signs of PCs may contribute partially to the compensation between CO_2 sequestration and CO_2 outgassing in the SH. Therefore, the global energy redistribution could have served as feedback in triggering glacial carbon cycle response during the late Pleistocene. Despite the limitations mentioned above, our simulation provides paleoclimate support for observational and modeling studies that link changes in atmosphere and ocean circulations to the redistribution of the global energy transport.

In this last paragraph, we will put the simulated global mean surface temperature variability over the past 3 Myr into the context of recent and future anthropogenic climate change. To this end, we ran additional simulations with the CESM1.2 model using the historical forcings (1850–

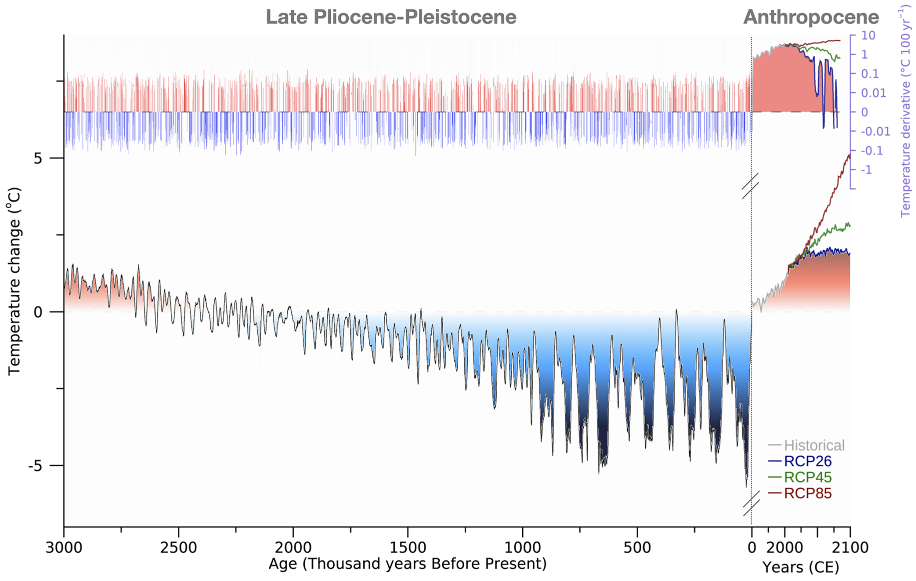

Figure 15. Past-to-future warming context. The simulated global mean surface temperature anomalies relative to 0 ka for 3 Ma and CESM1.2 simulations using historical forcings (1850–2005) and greenhouse warming scenarios following the Representative Concentration Pathway (RCP) 2.6, 4.5, and 8.5 (2006–2100). The upper panel shows the corresponding rate of global mean temperature change (°C 100 yr^{-1}; right axis).

2005) and Representative Concentration Pathway (RCP) 2.6, 4.5 and 8.5 GHG emission scenarios (2006–2100) (Fig. 15). We find that the typical late Pleistocene glacial/interglacial temperature range of 4–6 °C is comparable in amplitude to the RCP8.5 GHG warming projections over the next 7 decades (∼ 5.0 °C) (Fig. 15). In terms of warming rates (°C 100 yr^{-1}), however, the anthropogenic projections exceed the natural variability by almost 2 orders of magnitude. This is likely to push global ecosystems way outside the range of temperature stress that they may have experienced naturally, at least within the last 3 Myr.

Some data from our quasi-continuous CESM1.2 3 Ma simulation have already been used in other studies (Margari et al., 2023; Ruan et al., 2023; Zeller et al., 2023; Timmermann et al., 2022). They have been made available on the OPeNDAP and LAS server https://climatedata.ibs.re.kr (last access: 11 October 2023) and we hope that further analyses of these runs will help in elucidating the mechanisms of past climate shifts and in the interpretation of paleoclimate proxies.

Code and data availability. The transient Pleistocene 3 Ma model data will be made available on the OPeNDAP ICCP climate data server https://climatedata.ibs.re.kr (3Ma-Data, 2023). Codes used in this study are available from the authors upon request. The code and resources for paleoclimate configuration are also available from the CESM1.2 series Paleo-climate toolkit website (https://www.cesm.ucar.edu/models/paleo , CESM1.2 Paleoclimate Toolkit, 2023). Interactive Data Language (IDL) version 8.8 was used to generate all figures.

Supplement. The supplement related to this article is available online at: https://doi.org/10.5194/cp-19-1951-2023-supplement.

Author contributions. AT and KSY designed the study. KSY conducted the CESM1.2 3 Ma simulation and wrote the initial manuscript draft and produced all figures. All authors contributed to the interpretation of the results and to the improvement of the manuscript.

Competing interests. The contact author has declared that none of the authors has any competing interests.

Disclaimer. Publisher's note: Copernicus Publications remains neutral with regard to jurisdictional claims made in the text, published maps, institutional affiliations, or any other geographical representation in this paper. While Copernicus Publications makes every effort to include appropriate place names, the final responsibility lies with the authors.

Acknowledgements. The CESM1.2 simulations were conducted on the IBS supercomputer "Aleph", 1.43 peta flops high-performance Cray XC50-LC Skylake computing system with 18 720 processor cores, 9.59 PB storage, and 43 PB tape archive space. We also acknowledge the support of KREONET.

Financial support. This research has been supported by the Institute for Basic Science (grant no. IBS-R028-D1).

Review statement. This paper was edited by Marisa Montoya and reviewed by two anonymous referees.

References

Abe-Ouchi, A., Saito, F., Kawamura, K., Raymo, M. E., Okuno, J., Takahashi, K., and Blatter, H.: Insolation-driven 100,000-year glacial cycles and hysteresis of ice-sheet volume, Nature, 500, 190–193, https://doi.org/10.1038/nature12374, 2013.

An, Z., Clemens, S. C., Shen, J., Qiang, X., Jin, Z., Sun, Y., Prell, W. L., Luo, J., Wang, S., Xu, H., Cai, Y., Zhou, W., Liu, X., Liu, W., Shi, Z., Yan, L., Xiao, X., Chang, H., Wu, F., Ai, L., and Lu, F.: Glacial-Interglacial Indian Summer Monsoon Dynamics, Science, 333, 719–723, https://doi.org/10.1126/science.1203752, 2011.

An, Z., Guoxiong, W., Jianping, L., Youbin, S., Yimin, L., Weijian, Z., Yanjun, C., Anmin, D., Li, L., Jiangyu, M., Hai, C., Zhengguo, S., Liangcheng, T., Hong, Y., Hong, A., Hong, C., and Juan, F.: Global Monsoon Dynamics and Climate Change, Annu. Rev. Earth Planet. Sci., 43, 29–77, https://doi.org/10.1146/annurev-earth-060313-054623, 2015.

Argus, D. F., Peltier, W. R., Drummond, R., and Moore, A. W.: The Antarctica component of postglacial rebound model ICE-6G_C (VM5a) based on GPS positioning, exposure age dating of ice thicknesses, and relative sea level histories, Geophys. J. Int., 198, 537–563, https://doi.org/10.1093/gji/ggu140, 2014.

Baggenstos, D., Häberli, M., Schmitt, J., Shackleton, S. A., Birner, B., Severinghaus, J. P., Kellerhals, T., and Fischer, H.: Earth's radiative imbalance from the Last Glacial Maximum to the present, P. Natl. Acad. Sci. USA, 116, 14881–14886, https://doi.org/10.1073/pnas.1905447116, 2019.

Barker, S., Knorr, G., Edwards, R. L., Parrenin, F., Putnam, A. E., Skinner, L. C., Wolff, E., and Ziegler, M.: 800,000 Years of Abrupt Climate Variability, Science, 334, 347–351, https://doi.org/10.1126/science.1203580, 2011.

Berger, A.: Long-term variations of caloric insolation resulting from the earth's orbital elements, Quatern. Res., 9, 139–167, https://doi.org/10.1016/0033-5894(78)90064-9, 1978.

Bintanja, R. and van de Wal, R. S. W.: North American ice-sheet dynamics and the onset of 100,000-year glacial cycles, Nature, 454, 869–872, https://doi.org/10.1038/nature07158, 2008.

Bjerknes, J.: Atlantic Air-Sea Interaction, in: Advances in Geophysics, edited by: Landsberg, H. E. and Van Mieghem, J., Elsevier, 1–82, https://doi.org/10.1016/S0065-2687(08)60005-9, 1964.

Cao, J., Wang, B., and Liu, J.: Attribution of the Last Glacial Maximum climate formation, Clim. Dynam., 53, 1661–1679, https://doi.org/10.1007/s00382-019-04711-6, 2019.

Cartagena-Sierra, A., Berke, M. A., Robinson, R. S., Marcks, B., Castañeda, I. S., Starr, A., Hall, I. R., Hemming, S. R., LeVay, L. J., and Party, E. S.: Latitudinal Migrations of the Subtropical Front at the Agulhas Plateau Through the Mid-Pleistocene Transition, Paleoceanogr. Paleoclim., 36, e2020PA004084, https://doi.org/10.1029/2020PA004084, 2021.

CESM1.2 Paleoclimate Toolkit: NCAR CESM1.2 code and resoures for paleoclimate configulation, https://www.cesm.ucar.edu/models/paleo (last access: 11 October 2023), 2023.

Chiang, J. C. H. and Bitz, C. M.: Influence of high latitude ice cover on the marine Intertropical Convergence Zone, Clim. Dynam., 25, 477–496, https://doi.org/10.1007/s00382-005-0040-5, 2005.

Clark, P. U., Archer, D., Pollard, D., Blum, J. D., Rial, J. A., Brovkin, V., Mix, A. C., Pisias, N. G., and Roy, M.: The middle Pleistocene transition: characteristics, mechanisms, and implications for long-term changes in atmospheric $p\mathrm{CO_2}$, Quaternary Sci. Rev., 25, 3150–3184, https://doi.org/10.1016/j.quascirev.2006.07.008, 2006.

Clemens, S. C. and Prell, W. L.: A 350,000 year summer-monsoon multi-proxy stack from the Owen Ridge, Northern Arabian Sea, Mar. Geol., 201, 35–51, https://doi.org/10.1016/S0025-3227(03)00207-X, 2003.

Clemens, S. C., Prell, W. L., Sun, Y., Liu, Z., and Chen, G.: Southern Hemisphere forcing of Pliocene δ^{18}O and the evolution of Indo-Asian monsoons, Paleoceanography, 23, PA4210, https://doi.org/10.1029/2008PA001638, 2008.

Clemens, S. C., Holbourn, A., Kubota, Y., Lee, K. E., Liu, Z., Chen, G., Nelson, A., and Fox-Kemper, B.: Precession-band variance missing from East Asian monsoon runoff, Nat. Commun., 9, 3364, https://doi.org/10.1038/s41467-018-05814-0, 2018.

Clement, A. C., Hall, A., and Broccoli, A. J.: The importance of precessional signals in the tropical climate, Clim. Dynam., 22, 327–341, https://doi.org/10.1007/s00382-003-0375-8, 2004.

Davis, B. A. S. and Brewer, S.: Orbital forcing and role of the latitudinal insolation/temperature gradient, Clim. Dynam. 32, 143–165, https://doi.org/10.1007/s00382-008-0480-9, 2009.

de Garidel-Thoron, T., Rosenthal, Y., Bassinot, F., and Beaufort, L.: Stable sea surface temperatures in the western Pacific warm pool over the past 1.75 million years, Nature, 433, 294–298, https://doi.org/10.1038/nature03189, 2005.

Di Nezio, P. N., Timmermann, A., Tierney, J. E., Jin, F. F., Otto-Bliesner, B., Rosenbloom, N., Mapes, B., Neale, R., Ivanovic, R. F., and Montenegro, A.: The climate response of the Indo-Pacific warm pool to glacial sea level, Paleoceanography, 31, 866–894, https://doi.org/10.1002/2015pa002890, 2016.

Donohoe, A. and Battisti, D. S.: Causes of Reduced North Atlantic Storm Activity in a CAM3 Simulation of the Last Glacial Maximum, J. Climate, 22, 4793–4808, https://doi.org/10.1175/2009jcli2776.1, 2009.

Donohoe, A., Armour, K. C., Roe, G. H., Battisti, D. S., and Hahn, L.: The Partitioning of Meridional Heat Transport from the Last Glacial Maximum to $\mathrm{CO_2}$ Quadrupling in Coupled Climate Models, J. Climate, 33, 4141–4165, https://doi.org/10.1175/jcli-d-19-0797.1, 2020.

Friedrich, T. and Timmermann, A.: Millennial-scale glacial meltwater pulses and their effect on the spatiotemporal benthic δ^{18}O variability, Paleoceanography, 27, PA3215, https://doi.org/10.1029/2012pa002330, 2012.

Friedrich, T., Timmermann, A., Tigchelaar, M., Timm, O. E., and Ganopolski, A.: Nonlinear climate sensitivity and its implications for future greenhouse warming, Sci. Adv., 2, e1501923, https://doi.org/10.1126/sciadv.1501923, 2016.

Frierson, D. M. W., Hwang, Y.-T., Fučkar, N. S., Seager, R., Kang, S. M., Donohoe, A., Maroon, E. A., Liu, X., and Battisti, D. S.: Contribution of ocean overturning circulation to tropical rainfall peak in the Northern Hemisphere, Nat. Geosci., 6, 940–944, https://doi.org/10.1038/ngeo1987, 2013.

Ganopolski, A., Calov, R., and Claussen, M.: Simulation of the last glacial cycle with a coupled climate ice-sheet model of intermediate complexity, Clim. Past, 6, 229–244, https://doi.org/10.5194/cp-6-229-2010, 2010.

Gong, D. and Wang, S.: Definition of Antarctic Oscillation index, Geophys. Res. Lett., 26, 459–462, https://doi.org/10.1029/1999GL900003, 1999.

Goosse, H., Brovkin, V., Fichefet, T., Haarsma, R., Huybrechts, P., Jongma, J., Mouchet, A., Selten, F., Barriat, P. Y., Campin, J. M., Deleersnijder, E., Driesschaert, E., Goelzer, H., Janssens, I., Loutre, M. F., Morales Maqueda, M. A., Opsteegh, T., Mathieu, P. P., Munhoven, G., Pettersson, E. J., Renssen, H., Roche, D. M., Schaeffer, M., Tartinville, B., Timmermann, A., and Weber, S. L.: Description of the Earth system model of intermediate complexity LOVECLIM version 1.2, Geosci. Model Dev., 3, 603–633, https://doi.org/10.5194/gmd-3-603-2010, 2010.

Hahn, L. C., Armour, K. C., Battisti, D. S., Donohoe, A., Pauling, A. G., and Bitz, C. M.: Antarctic Elevation Drives Hemispheric Asymmetry in Polar Lapse Rate Climatology and Feedback, Geophys. Res. Lett., 47, e2020GL088965, https://doi.org/10.1029/2020GL088965, 2020.

Heinemann, M., Timmermann, A., Timm, O. E., Saito, F., and Abe-Ouchi, A.: Deglacial ice sheet meltdown: orbital pacemaking and CO_2 effects, Clim. Past, 10, 1567–1579, https://doi.org/10.5194/cp-10-1567-2014, 2014.

Held, I. M.: The Partitioning of the Poleward Energy Transport between the Tropical Ocean and Atmosphere, J. Atmos. Sci., 58, 943–948, https://doi.org/10.1175/1520-0469(2001)058<0943:Tpotpe>2.0.Co;2, 2001.

Herbert, T. D., Peterson, L. C., Lawrence, K. T., and Liu, Z.: Tropical Ocean Temperatures Over the Past 3.5 Million Years, Science, 328, 1530–1534, https://doi.org/10.1126/science.1185435, 2010.

Hu, A., Meehl, G., Han, W., Timmermann, A., Otto-Bliesner, B., Liu, Z., Washington, W., Large, W., Abe-Ouchi, A., Kimoto, M., Lambeck, K., and Wu, B.: Role of the Bering Strait on the hysteresis of the ocean conveyor belt circulation and glacial climate stability, P. Natl. Acad. Sci. USA, 109, 6417–6422, https://doi.org/10.1073/pnas.1116014109, 2012.

Hurrell, J. W., Holland, M. M., Gent, P. R., Ghan, S., Kay, J. E., Kushner, P. J., Lamarque, J.-F., Large, W. G., Lawrence, D., Lindsay, K., Lipscomb, W. H., Long, M. C., Mahowald, N., Marsh, D. R., Neale, R. B., Rasch, P., Vavrus, S., Vertenstein, M., Bader, D., Collins, W. D., Hack, J. J., Kiehl, J., and Marshall, S.: The Community Earth System Model: A Framework for Collaborative Research, B. Am. Meteorol. Soc., 94, 1339–1360, https://doi.org/10.1175/bams-d-12-00121.1, 2013.

Jin, F. F., Neelin, J. D., and Ghil, M.: El Nino Southern Oscillation and the annual cycle: Subharmonic frequency-locking and aperiodicity, Physica D, 98, 442–465, https://doi.org/10.1016/0167-2789(96)00111-x, 1996.

Johnson, T. C., Werne, J. P., Brown, E. T., Abbott, A., Berke, M., Steinman, B. A., Halbur, J., Contreras, S., Grosshuesch, S., Deino, A., Scholz, C. A., Lyons, R. P., Schouten, S., and Damsté, J. S. S.: A progressively wetter climate in southern East Africa over the past 1.3 million years, Nature, 537, 220–224, https://doi.org/10.1038/nature19065, 2016.

Jouzel, J., Masson-Delmotte, V., Cattani, O., Dreyfus, G., Falourd, S., Hoffmann, G., Minster, B., Nouet, J., Barnola, J. M., Chappellaz, J., Fischer, H., Gallet, J. C., Johnsen, S., Leuenberger, M., Loulergue, L., Luethi, D., Oerter, H., Parrenin, F., Raisbeck, G., Raynaud, D., Schilt, A., Schwander, J., Selmo, E., Souchez, R., Spahni, R., Stauffer, B., Steffensen, J. P., Stenni, B., Stocker, T. F., Tison, J. L., Werner, M., and Wolff, E. W.: Orbital and Millennial Antarctic Climate Variability over the Past 800,000 Years, Science, 317, 793–796, https://doi.org/10.1126/science.1141038, 2007.

Kamae, Y., Yoshida, K., and Ueda, H.: Sensitivity of Pliocene climate simulations in MRI-CGCM2.3 to respective boundary conditions, Clim. Past, 12, 1619–1634, https://doi.org/10.5194/cp-12-1619-2016, 2016.

Kang, S. M., Shin, Y., and Xie, S.-P.: Extratropical forcing and tropical rainfall distribution: energetics framework and ocean Ekman advection, npj Clim. Atmos. Sci., 1, 20172, https://doi.org/10.1038/s41612-017-0004-6, 2018.

Karamperidou, C., Di Nezio, P. N., Timmermann, A., Jin, F. F., and Cobb, K. M.: The response of ENSO flavors to mid-Holocene climate: implications for proxy interpretation, Paleoceanography, 30, 527–547, 2015.

Karamperidou, C., Stuecker, M. F., Timmermann, A., Yun, K.-S., Lee, S.-S., Jin, F. F., Santoso, A., McPhaden, M. J., and Cai, W.: ENSO in a Changing Climate: Challenges, Paleo-Perspectives, and Outlook, in: El Niño Southern Oscillation in a Changing Climate, edited by: McPhaden, M. J., Santoso, A., and Cai, W., John Wiley & Sons, Inc., 471–484, https://doi.org/10.1002/9781119548164.ch21, 2020.

Kaspar, F., Spangehl, T., and Cubasch, U.: Northern hemisphere winter storm tracks of the Eemian interglacial and the last glacial inception, Clim. Past, 3, 181–192, https://doi.org/10.5194/cp-3-181-2007, 2007.

Kim, S. J.: The effect of atmospheric CO_2 and ice sheet topography on LGM climate, Clim. Dynam., 22, 639–651, https://doi.org/10.1007/s00382-004-0412-2, 2004.

Kindler, P., Guillevic, M., Baumgartner, M., Schwander, J., Landais, A., and Leuenberger, M.: Temperature reconstruction from 10 to 120 kyr b2k from the NGRIP ice core, Clim. Past, 10, 887–902, https://doi.org/10.5194/cp-10-887-2014, 2014.

Kocken, I. J., Cramwinckel, M. J., Zeebe, R. E., Middelburg, J. J., and Sluijs, A.: The 405 kyr and 2.4 Myr eccentricity components in Cenozoic carbon isotope records, Clim. Past, 15, 91–104, https://doi.org/10.5194/cp-15-91-2019, 2019.

Kohler, P., Bintanja, R., Fischer, H., Joos, F., Knutti, R., Lohmann, G., and Masson-Delmotte, V.: What caused Earth's temperature variations during the last 800,000 years? Data-based evidence on radiative forcing and constraints on climate sensitivity, Quaternary Sci. Rev., 29, 129–145, https://doi.org/10.1016/j.quascirev.2009.09.026, 2010.

Kutzbach, J. E. and Guetter, P. J.: The Influence of Changing Orbital Parameters and Surface Boundary Conditions on Climate Simulations for the Past 18 000 Years, J. Atmos. Sci., 43, 1726–1759, https://doi.org/10.1175/1520-0469(1986)043<1726:Tiocop>2.0.Co;2, 1986.

Lamy, F., Chiang, J. C. H., Martínez-Méndez, G., Thierens, M., Arz, H. W., Bosmans, J., Hebbeln, D., Lambert, F., Lembke-Jene, L., and Stuut, J.-B.: Precession modulation of the South Pacific westerly wind belt over the past million years, P. Natl. Acad. Sci. USA, 116, 23455–23460, https://doi.org/10.1073/pnas.1905847116, 2019.

Laskar, J., Robutel, P., Joutel, F., Gastineau, M., Correia, A. C. M., and Levrard, B.: A long-term numerical solution for the insolation quantities of the Earth, Astron. Astrophys., 428, 261–285, 2004.

Lawrence, K. T., Herbert, T. D., Brown, C. M., Raymo, M. E., and Haywood, A. M.: High-amplitude variations in North Atlantic sea surface temperature during the early Pliocene warm period, Paleoceanography, 24, PA2218, https://doi.org/10.1029/2008PA001669, 2009.

Li, J. and Wang, J. X. L.: A modified zonal index and its physical sense, Geophys. Res. Lett., 30, 1632, https://doi.org/10.1029/2003GL017441, 2003.

Lilien, D. A., Steinhage, D., Taylor, D., Parrenin, F., Ritz, C., Mulvaney, R., Martin, C., Yan, J. B., O'Neill, C., Frezzotti, M., Miller, H., Gogineni, P., Dahl-Jensen, D., and Eisen, O.: Brief communication: New radar constraints support presence of ice older than 1.5 Myr at Little Dome C, The Cryosphere, 15, 1881–1888, https://doi.org/10.5194/tc-15-1881-2021, 2021.

Lisiecki, L. E. and Raymo, M. E.: A Pliocene-Pleistocene stack of 57 globally distributed benthic δ^{18}O records, Paleoceanography, 20, PA1003, https://doi.org/10.1029/2004PA001071, 2005.

Liu, X., Battisti, D. S., and Donohoe, A.: Tropical Precipitation and Cross-Equatorial Ocean Heat Transport during the Mid-Holocene, J. Climate, 30, 3529–3547, https://doi.org/10.1175/jcli-d-16-0502.1, 2017.

Liu, Y., Lo, L., Shi, Z., Wei, K.-Y., Chou, C.-J., Chen, Y.-C., Chuang, C.-K., Wu, C.-C., Mii, H.-S., Peng, Z., Amakawa, H., Burr, G. S., Lee, S.-Y., DeLong, K. L., Elderfield, H., and Shen, C.-C.: Obliquity pacing of the western Pacific Intertropical Convergence Zone over the past 282,000 years, Nat. Commun., 6, 10018, https://doi.org/10.1038/ncomms10018, 2015.

Liu, Z., Otto-Bliesner, B. L., He, F., Brady, E. C., Tomas, R., Clark, P. U., Carlson, A. E., Lynch-Stieglitz, J., Curry, W., Brook, E., Erickson, D., Jacob, R., Kutzbach, J., and Cheng, J.: Transient Simulation of Last Deglaciation with a New Mechanism for Bølling-Allerød Warming, Science, 325, 310–314, https://doi.org/10.1126/science.1171041, 2009.

Liu, Z., Lu, Z., Wen, X., Otto-Bliesner, B. L., Timmermann, A., and Cobb, K. M.: Evolution and forcing mechanisms of El Niño over the past 21,000 years, Nature, 515, 550–553, 2014.

Lorenz, S. J. and Lohmann, G.: Acceleration technique for Milankovitch type forcing in a coupled atmosphere-ocean circulation model: method and application for the holocene, Clim. Dynam., 23, 727–743, https://doi.org/10.1007/s00382-004-0469-y, 2004.

Lu, Z., Liu, Z., Chen, G., and Guan, J.: Prominent precession band variance in ENSO intensity over the last 300,000 years, Geophys. Res. Lett., 46, 9786–9795, 2019.

Lunt, D. J., Williamson, M. S., Valdes, P. J., Lenton, T. M., and Marsh, R.: Comparing transient, accelerated, and equilibrium simulations of the last 30 000 years with the GENIE-1 model, Clim. Past, 2, 221–235, https://doi.org/10.5194/cp-2-221-2006, 2006.

Lupien, R. L., Russell, J. M., Pearson, E. J., Castañeda, I. S., Asrat, A., Foerster, V., Lamb, H. F., Roberts, H. M., Schäbitz, F., Trauth, M. H., Beck, C. C., Feibel, C. S., and Cohen, A. S.: Orbital controls on eastern African hydroclimate in the Pleistocene, Sci. Rep.-UK, 12, 3170, https://doi.org/10.1038/s41598-022-06826-z, 2022.

Lüthi, D., Le Floch, M., Bereiter, B., Blunier, T., Barnola, J.-M., Siegenthaler, U., Raynaud, D., Jouzel, J., Fischer, H., Kawamura, K., and Stocker, T. F.: High-resolution carbon dioxide concentration record 650,000–800,000 years before present, Nature, 453, 379–382, https://doi.org/10.1038/nature06949, 2008.

Margari, V., Hodell, D. A., Parfitt, S. A., Ashton, N. M., Grimalt, J. O., Kim, H., Yun, K.-S., Gibbard, P. L., Stringer, C. B., Timmermann, A., and Tzedakis, P. C.: Extreme glacial cooling likely led to hominin depopulation of Europe in the Early Pleistocene, Science, 381, 693–699, https://doi.org/10.1126/science.adf4445, 2023.

Martínez-Garcia, A., Rosell-Melé, A., McClymont, E. L., Gersonde, R., and Haug, G. H.: Subpolar Link to the Emergence of the Modern Equatorial Pacific Cold Tongue, Science, 328, 1550–1553, https://doi.org/10.1126/science.1184480, 2010.

Martínez-Garcia, A., Rosell-Melé, A., Jaccard, S. L., Geibert, W., Sigman, D. M., and Haug, G. H.: Southern Ocean dust–climate coupling over the past four million years, Nature, 476, 312–315, https://doi.org/10.1038/nature10310, 2011.

Masson-Delmotte, V., Schulz, M., Abe-Ouchi, A., Beer, J., Ganopolski, A., González Rouco, J. F., Jansen, E., Lambeck, K., Luterbacher, J., Naish, T., Osborn, T., Otto-Bliesner, B., Quinn, T., Ramesh, R., Rojas, M., Shao, X., and Timmermann, A.: Information from paleoclimate archives, in: Climate Change 2013: The Physical Science Basis, Contribution of Working Group I to the Fifth Assessment Report of the Intergovernmental Panel on Climate Change, edited by: Stocker, T. F., Qin, D., Plattner, G.-K., Tignor, M., Allen, S. K., Doschung, J., Nauels, A., Xia, Y., Bex, V., and Midgley, P. M., Cambridge University Press, 383–464, https://doi.org/10.1017/cbo9781107415324.013, 2013.

McClymont, E. L., Sosdian, S. M., Rosell-Melé, A., and Rosenthal, Y.: Pleistocene sea-surface temperature evolution: Early cooling, delayed glacial intensification, and implications for the mid-Pleistocene climate transition, Earth-Sci. Rev., 123, 173–193, https://doi.org/10.1016/j.earscirev.2013.04.006, 2013.

Meehl, G. A., Senior, C. A., Eyring, V., Flato, G., Lamarque, J.-F., Stouffer, R. J., Taylor, K. E., and Schlund, M.: Context for interpreting equilibrium climate sensitivity and transient climate response from the CMIP6 Earth system models, Sci. Adv., 6, eaba1981, https://doi.org/10.1126/sciadv.aba1981, 2020.

Menviel, L., Timmermann, A., Timm, O. E., and Mouchet, A.: Climate and biogeochemical response to a rapid melting of the West Antarctic Ice Sheet during interglacials and implications for future climate, Paleoceanography, 25, PA4231, https://doi.org/10.1029/2009pa001892, 2010.

Menviel, L., Timmermann, A., Timm, O. E., and Mouchet, A.: Deconstructing the Last Glacial termination: the role of millennial and orbital-scale forcings, Quaternary Sci. Rev., 30, 1155–1172, https://doi.org/10.1016/j.quascirev.2011.02.005, 2011.

Menviel, L., Timmermann, A., Friedrich, T., and England, M. H.: Hindcasting the continuum of Dansgaard-Oeschger variability: mechanisms, patterns and timing, Clim. Past, 10, 63–77, https://doi.org/10.5194/cp-10-63-2014, 2014.

Merlis, T. M., Schneider, T., Bordoni, S., and Eisenman, I.: Hadley Circulation Response to Orbital Precession. Part II: Subtropical Continent, J. Climate, 26, 754–771, https://doi.org/10.1175/jcli-d-12-00149.1, 2013.

Morrison, A. K., Griffies, S. M., Winton, M., Anderson, W. G., and Sarmiento, J. L.: Mechanisms of Southern Ocean Heat Uptake and Transport in a Global Eddying Climate Model, J. Climate, 29, 2059–2075, https://doi.org/10.1175/jcli-d-15-0579.1, 2016.

Naafs, B. D. A., Hefter, J., Acton, G., Haug, G. H., Martínez-Garcia, A., Pancost, R., and Stein, R.: Strengthening of North American dust sources during the late Pliocene (2.7 Ma), Earth Planet. Sc. Lett., 317–318, 8–19, https://doi.org/10.1016/j.epsl.2011.11.026, 2012.

Newsom, E. R., Thompson, A. F., Adkins, J. F., and Galbraith, E. D.: A hemispheric asymmetry in poleward ocean heat transport across climates: Implications for overturning and polar warming, Earth Planet. Sc. Lett., 568, 117033, https://doi.org/10.1016/j.epsl.2021.117033, 2021.

Nie, J. S.: The Plio-Pleistocene 405-kyr climate cycles, Palaeogeogr. Palaeocl. Palaeoecol., 510, 26–30, https://doi.org/10.1016/j.palaeo.2017.07.022, 2018.

Petrick, B., Martínez-García, A., Auer, G., Reuning, L., Auderset, A., Deik, H., Takayanagi, H., De Vleeschouwer, D., Iryu, Y., and Haug, G. H.: Glacial Indonesian Throughflow weakening across the Mid-Pleistocene Climatic Transition, Sci. Rep.-UK, 9, 16995, https://doi.org/10.1038/s41598-019-53382-0, 2019.

Ruan, J., Timmermann, A., Raia, P., Yun, K.-S., Zeller, E., Monadanaro, A., Di Febbraro, M., Lemmon, D., Castiglione, S., and Melchionna, M.: Climate shifts orchestrated hominin interbreeding events across Eurasia, Science, 381, 699–704, https://doi.org/10.1126/science.add4459, 2023.

Russon, T., Elliot, M., Sadekov, A., Cabioch, G., Corrège, T., and De Deckker, P.: Inter-hemispheric asymmetry in the early Pleistocene Pacific warm pool, Geophys. Res. Lett., 37, L11601, https://doi.org/10.1029/2010GL043191, 2010.

Schneider, T.: Feedback of Atmosphere-Ocean Coupling on Shifts of the Intertropical Convergence Zone, Geophys. Res. Lett., 44, 11644–11653, https://doi.org/10.1002/2017GL075817, 2017.

Schneider, T., Bischoff, T., and Haug, G. H.: Migrations and dynamics of the intertropical convergence zone, Nature, 513, 45–53, https://doi.org/10.1038/nature13636, 2014.

Schneider von Deimling, T., Ganopolski, A., Held, H., and Rahmstorf, S.: How cold was the Last Glacial Maximum?, Geophys. Res. Lett., 33, L14709, https://doi.org/10.1029/2006GL026484, 2006.

Screen, J. A., Bracegirdle, T. J., and Simmonds, I.: Polar Climate Change as Manifest in Atmospheric Circulation, Curr. Clim. Change Rep., 4, 383–395, https://doi.org/10.1007/s40641-018-0111-4, 2018.

Singarayer, J. S. and Valdes, P. J.: High-latitude climate sensitivity to ice-sheet forcing over the last 120 kyr, Quaternary Sci. Rev., 29, 43–55, https://doi.org/10.1016/j.quascirev.2009.10.011, 2010.

Smith, R. S. and Gregory, J.: The last glacial cycle: transient simulations with an AOGCM, Clim. Dynam., 38, 1545–1559, https://doi.org/10.1007/s00382-011-1283-y, 2012.

Stap, L. B., van de Wal, R. S. W., de Boer, B., Kohler, P., Hoencamp, J. H., Lohmann, G., Tuenter, E., and Lourens, L. J.: Modeled Influence of Land Ice and CO_2 on Polar Amplification and Paleoclimate Sensitivity During the Past 5 Million Years, Paleoceanogr. Paleoclim., 33, 381–394, https://doi.org/10.1002/2017pa003313, 2018.

Stein, K., Timmermann, A., Kwon, E. Y., and Friedrich, T.: Timing and magnitude of Southern Ocean sea ice/carbon cycle feedbacks, P. Natl. Acad. Sci. USA, 117, 4498–4504, https://doi.org/10.1073/pnas.1908670117, 2020.

Stone, P. H.: Constraints on dynamical transports of energy on a spherical planet, Dynam. Atmos. Oceans, 2, 123–139, https://doi.org/10.1016/0377-0265(78)90006-4, 1978.

Stott, L., Timmermann, A., and Thunell, R.: Southern Hemisphere and Deep-Sea Warming Led Deglacial Atmospheric CO_2 Rise and Tropical Warming, Science, 318, 435–438, https://doi.org/10.1126/science.1143791, 2007.

3Ma-Data: Transient 3Ma model simulatation data, https://climatedata.ibs.re.kr. (last access: 11 October 2023), 2023.

Tiedemann, R., Sarnthein, M., and Shackleton, N. J.: Astronomic timescale for the Pliocene Atlantic $\delta^{18}O$ and dust flux records of Ocean Drilling Program Site 659, Paleoceanography, 9, 619–638, https://doi.org/10.1029/94PA00208, 1994.

Tierney, J. E., Zhu, J., King, J., Malevich, S. B., Hakim, G. J., and Poulsen, C. J.: Glacial cooling and climate sensitivity revisited, Nature, 584, 569–573, https://doi.org/10.1038/s41586-020-2617-x, 2020.

Tigchelaar, M. and Timmermann, A.: Mechanisms rectifying the annual mean response of tropical Atlantic rainfall to precessional forcing, Clim. Dynam., 47, 271–293, https://doi.org/10.1007/s00382-015-2835-3, 2016.

Tigchelaar, M., Timmermann, A., Pollard, D., Friedrich, T., and Heinemann, M.: Local insolation changes enhance Antarctic interglacials: Insights from an 800,000-year ice sheet simulation with transient climate forcing, Earth Planet. Sc. Lett., 495, 69–78, https://doi.org/10.1016/j.epsl.2018.05.004, 2018.

Tigchelaar, M., Timmermann, A., Friedrich, T., Heinemann, M., and Pollard, D.: Nonlinear response of the Antarctic Ice Sheet to late Quaternary sea level and climate forcing, The Cryosphere, 13, 2615–2631, https://doi.org/10.5194/tc-13-2615-2019, 2019.

Timm, O. and Timmermann, A.: Simulation of the last 21 000 years using accelerated transient boundary conditions, J. Climate, 20, 4377–4401, https://doi.org/10.1175/jcli4237.1, 2007.

Timm, O., Timmermann, A., Abe-Ouchi, A., Saito, F., and Segawa, T.: On the definition of seasons in paleoclimate simulations with orbital forcing, Paleoceanography, 23, PA2221, https://doi.org/10.1029/2007pa001461, 2008.

Timmermann, A. and Friedrich, T.: Late Pleistocene climate drivers of early human migration, Nature, 538, 92–95, https://doi.org/10.1038/nature19365, 2016.

Timmermann, A., Lorenz, S. J., An, S.-I., Clement, A., and Xie, S.-P.: The Effect of Orbital Forcing on the Mean Climate and Variability of the Tropical Pacific, J. Climate, 20, 4147–4159, https://doi.org/10.1175/jcli4240.1, 2007.

Timmermann, A., Timm, O., Stott, L., and Menviel, L.: The Roles of CO_2 and Orbital Forcing in Driving Southern Hemispheric Temperature Variations during the Last 21 000 Yr, J. Climate, 22, 1626–1640, https://doi.org/10.1175/2008JCLI2161.1, 2009.

Timmermann, A., Knies, J., Timm, O. E., Abe-Ouchi, A., and Friedrich, T.: Promotion of glacial ice sheet buildup 60–115 kyr B.P. by precessionally paced Northern Hemispheric meltwater pulses, Paleoceanography, 25, PA4208, https://doi.org/10.1029/2010pa001933, 2010.

Timmermann, A., Sachs, J., and Timm, O. E.: Assessing divergent SST behavior during the last 21 ka derived from alkenones and G. ruber-Mg/Ca in the equatorial Pacific, Paleoceanography, 29, 680–696, https://doi.org/10.1002/2013pa002598, 2014a.

Timmermann, A., Friedrich, T., Timm, O. E., Chikamoto, M. O., Abe-Ouchi, A., and Ganopolski, A.: Modeling Obliquity and CO_2 Effects on Southern Hemisphere Climate during the Past 408 ka, J. Climate, 27, 1863–1875, https://doi.org/10.1175/jcli-d-13-00311.1, 2014b.

Timmermann, A., Yun, K. S., Raia, P., Ruan, J. Y., Mondanaro, A., Zeller, E., Zollikofer, C., de Leon, M. P., Lemmon, D., Willeit, M., and Ganopolski, A.: Climate effects on archaic human habitats and species successions, Nature, 604, 495–501, https://doi.org/10.1038/s41586-022-04600-9, 2022.

Torrence, C. and Compo, G. P.: A Practical Guide to Wavelet Analysis, B. Am. Meteorol. Soc., 79, 61–78, https://doi.org/10.1175/1520-0477(1998)079<0061:Apgtwa>2.0.Co;2, 1998.

Varma, V., Prange, M., and Schulz, M.: Transient simulations of the present and the last interglacial climate using the Community Climate System Model version 3: effects of orbital acceleration, Geosci. Model Dev., 9, 3859–3873, https://doi.org/10.5194/gmd-9-3859-2016, 2016.

Willeit, M. and Ganopolski, A.: The importance of snow albedo for ice sheet evolution over the last glacial cycle, Clim. Past, 14, 697–707, https://doi.org/10.5194/cp-14-697-2018, 2018.

Willeit, M., Ganopolski, A., Calov, R., and Brovkin, V.: Mid-Pleistocene transition in glacial cycles explained by declining CO_2 and regolith removal, Sci. Adv., 5, eaav733, https://doi.org/10.1126/sciadv.aav7337, 2019.

Yamanouchi, T. and Charlock, T. P.: Effects of clouds, ice sheet, and sea ice on the Earth radiation budget in the Antarctic, J. Geophys. Res.-Atmos., 102, 6953–6970, https://doi.org/10.1029/96JD02866, 1997.

Yang, H., Li, Q., Wang, K., Sun, Y., and Sun, D.: Decomposing the meridional heat transport in the climate system, Clim. Dynam., 44, 2751–2768, https://doi.org/10.1007/s00382-014-2380-5, 2015.

Yarincik, K. M., Murray, R. W., and Peterson, L. C.: Climatically sensitive eolian and hemipelagic deposition in the Cariaco Basin, Venezuela, over the past 578,000 years: Results from Al/Ti and K/Al, Paleoceanography, 15, 210–228, https://doi.org/10.1029/1999PA900048, 2000.

Yin, Q., Berger, A., Driesschaert, E., Goosse, H., Loutre, M. F., and Crucifix, M.: The Eurasian ice sheet reinforces the East Asian summer monsoon during the interglacial 500 000 years ago, Clim. Past, 4, 79–90, https://doi.org/10.5194/cp-4-79-2008, 2008.

Yu, S. and Pritchard, M. S.: A Strong Role for the AMOC in Partitioning Global Energy Transport and Shifting ITCZ Position in Response to Latitudinally Discrete Solar Forcing in CESM1.2, J. Climate, 32, 2207–2226, https://doi.org/10.1175/jcli-d-18-0360.1, 2019.

Zeller, E., Timmermann, A., Yun, K. S., Raia, P., Stein, K., and Ruan, J. Y.: Human adaptation to diverse biomes over the past 3 million years, Science, 380, 604–608, https://doi.org/10.1126/science.abq1288, 2023.

Zhang, S., Yu, Z. F., Gong, X., Wang, Y., Chang, F. M., Lohmman, G., Qi, Y. Q., and Li, T. G.: Precession cycles of the El Nino/Southern oscillation-like system controlled by Pacific upper-ocean stratification, Commun. Earth Environ., 2, 239, https://doi.org/10.1038/s43247-021-00305-5, 2021.

Clim. Past, 20, 151–185, 2024
https://doi.org/10.5194/cp-20-151-2024

Climate of the Past
Open Access

Toward generalized Milankovitch theory (GMT)

Andrey Ganopolski[1]

[1]Potsdam Institute for Climate Impact Research (PIK), Member of the Leibniz Association,
P.O. Box 601203, 14412 Potsdam, Germany

Invited contribution by Andrey Ganopolski, recipient of the EGU Milutin Milankovic Medal 2011.

Correspondence: Andrey Ganopolski (ganopolski@pik-potsdam.de)

Received: 5 July 2023 – Discussion started: 11 July 2023
Revised: 6 November 2023 – Accepted: 16 November 2023 – Published: 18 January 2024

Abstract. In recent decades, numerous paleoclimate records and results of model simulations have provided strong support for the astronomical theory of Quaternary glacial cycles formulated in its modern form by Milutin Milankovitch. At the same time, new findings have revealed that the classical Milankovitch theory is unable to explain a number of important facts, such as the change in the dominant periodicity of glacial cycles from 41 to 100 kyr about 1 million years ago. This transition was also accompanied by an increase in the amplitude and asymmetry of the glacial cycles. Here, based on the results of a hierarchy of models and data analysis, a framework of the extended (generalized) version of the Milankovitch theory is presented. To illustrate the main elements of this theory, a simple conceptual model of glacial cycles was developed using the results of an Earth system model, CLIMBER-2. This conceptual model explicitly assumes the multistability of the climate–cryosphere system and the instability of the "supercritical" ice sheets. Using this model, it is shown that Quaternary glacial cycles can be successfully reproduced as the strongly nonlinear response of the Earth system to the orbital forcing, where 100 kyr cyclicity originates from the phase locking of the precession and obliquity-forced glacial cycles to the corresponding eccentricity cycle. The eccentricity influences glacial cycles solely through its amplitude modulation of the precession component of orbital forcing, while the long timescale of the late Quaternary glacial cycles is determined by the time required for ice sheets to reach their critical size. The postulates used to construct this conceptual model were justified using analysis of relevant physical and biogeochemical processes and feedbacks. In particular, the role of climate–ice sheet–carbon cycle feedback in shaping and globalization of glacial cycles is discussed. The reasons for the instability of the large northern ice sheets and the mechanisms of the Earth system escape from the "glacial trap" via a set of strongly nonlinear processes are presented. It is also shown that the transition from the 41 to the 100 kyr world about 1 million years ago can be explained by a gradual increase in the critical size of ice sheets, which in turn is related to the gradual removal of terrestrial sediments from the northern continents. The implications of this nonlinear paradigm for understanding Quaternary climate dynamics and the remaining knowledge gaps are finally discussed.

1 Introduction

Since the discovery of past glaciations in the mid-19th century, the "ice-age problem" has attracted significant attention and stimulated the first applications of physical science to understand climate dynamics. The idea that changes in Earth's orbital parameters caused glacial ages was proposed soon after the discovery of ice ages (Adhémar, 1842) and has been further developed by a number of prominent scientists (see Berger, 1988, 2012, for the history of the astronomical theory of glacial cycles). Milutin Milankovitch was one of them; he made an important contribution to the development of the astronomical theory of ice ages, published 100 papers on this subject (e.g., Milankovitch, 1920), and presented his result in the most comprehensive form in his 650-page-long *Canon of insolation and the ice-age problem* (Milankovitch, 1941). At present, Milankovitch's version of the astronomical theory of ice ages is usually referred to as the Milankovitch theory. According to this theory, glacial cycles of the Quaternary are forced by variations in boreal summer insolation, which in turn are caused by changes in three Earth astronomical (“orbital”) parameters – obliquity, eccentricity, and precession.

During Milankovitch’s life, this theory was just one of several hypotheses about the origin of past glaciations. Only during the 1970s did spectral analysis of paleoclimate records confirm the presence of periodicities predicted by the Milankovitch theory, which was considered the decisive proof of the astronomical theory. At the same time, analysis of paleoclimate data revealed some facts that the Milankovitch theory cannot explain. Among them are the dominance of 100 kyr cyclicity during the past million years, strong asymmetry of the late Quaternary (hereafter used as a synonym for the 100 kyr world) glacial cycles, and the change in the dominant cyclicity from 41 to 100 kyr around 1 million years ago. These findings stimulated numerous attempts to further develop the original Milankovitch theory or find alternative explanations for the mechanisms of glacial cycles.

The problem of Quaternary glacial cycles has been approached from different perspectives using paleoclimate data analysis, development of simple (conceptual) models, and applying climate and ice sheet models of growing complexity. Despite significant progress in understanding climate dynamics and many publications devoted to modeling glacial cycles, a generally accepted comprehensive theory of glacial cycles has not emerged yet. Among the remaining questions are the mechanism of glacial terminations, the role that different types of ice sheet instability play, and the operation of the climate–carbon cycle feedback during glacial cycles.

The present paper formulates a framework of the extended version of the Milankovitch theory of Quaternary glacial cycles, hereafter called generalized Milankovitch theory (GMT). The paper’s main aim is to summarize the current progress in understanding and modeling Quaternary climate dynamics and facilitate further research in the field. The proposed theory is motivated and partly based on the results of the Earth system model of intermediate complexity CLIMBER-2 (Petoukhov et al., 2000; Ganopolski et al., 2001), which so far is the only physically based model which can simulate glacial cycles during the entire Quaternary using orbital forcing as the only prescribed external forcing (Willeit et al., 2019). However, the theory presented here is not based on a single model and is thus not “model-dependent”. On the contrary, this theory accommodates the results of a large amount of paleoclimate data analysis and numerous modeling studies. It is also important to note that this paper is not a review paper, and only the publications relevant to the theory presented in this paper are cited. The readers can find a wealth of information about other works and alternative theories in review papers such as Berger (2012), Paillard (2001, 2015), and Berends et al. (2021).

The paper is organized as follows. Section 2 describes the classical Milankovitch theory and briefly reviews the work done to test it. Section 3 is devoted to the conceptual models of glacial cycles. Section 4 presents a conceptual model of glacial cycles, which illustrates some essential aspects of the GMT. Section 5 presents a short discussion of the main elements of GMT. In the conclusions, the main advances of GMT and the remaining challenges are discussed.

1.1 Original Milankovitch theory

Milankovitch theory is usually understood as a rather general concept that Quaternary glacial cycles were forced (or “paced”) by changes in boreal summer insolation or, more specifically, that the Northern Hemisphere ice sheets were growing during periods of lower than average and shrinking during periods of higher than average boreal summer insolation. Milankovitch defined summer insolation through the caloric half-year summer insolation and calculated “orbital forcing” for the last 650 000 years for the first time (Milankovitch, 1920, 1941). Later, several other metrics for orbital forcing were proposed, but, irrespective of how “summer insolation” is defined, it contains contributions from obliquity and precession components, and the amplitude of the latter is modulated by the eccentricity (see Appendix A1). This is why, when all these frequencies were found in the late Quaternary paleoclimate records (Hays et al., 1976), this fact was widely considered proof for the Milankovitch theory.

Less is known about the personal contribution of Milutin Milankovitch to the “Milankovitch theory” of ice ages. The most widely known Milankovitch achievement involves meticulous calculations of insolation changes over the past million years. At the same time, the key premise of the Milankovitch theory, namely that glacial cycles are forced by boreal summer insolation changes, was not the original Milankovitch idea – in fact, Joseph John Murphy proposed it half a century before (Murphy, 1876). This idea was further developed in Brückner et al. (1925). Milankovitch adopted this concept following advice from his friend and colleague Wladimir Köppen (Berger, 1988). The real contribution of Milutin Milankovitch to the development of glacial cycle theory was not in proposing a new hypothesis but rather in vigorous testing of the existing hypothesis about the astronomic origin of glacial cycles. To this end, he calculated for the first time variations in insolation for different latitudes and seasons accounting for all three of Earth’s orbital parameters: eccentricity, precession of the equinox, and obliquity. He then tested the astronomical theory by using a simple energy balance model, which also accounted for the effect of positive albedo feedback (Berger, 2021). Milankovitch also considered the influence of other potentially essential processes and the phase relationship between orbital forcing and expected climate response. Finally, he attempted to validate theoretical predictions against available paleoclimate reconstructions and attributed individual ice ages known from geology (Fig. 1).

In Milankovitch’s time, it was not known that the “glacial age” was the dominant mode of operation of the Earth system during the Quaternary. This is why Milankovitch considered ice ages to be the episodes that occurred during pe-

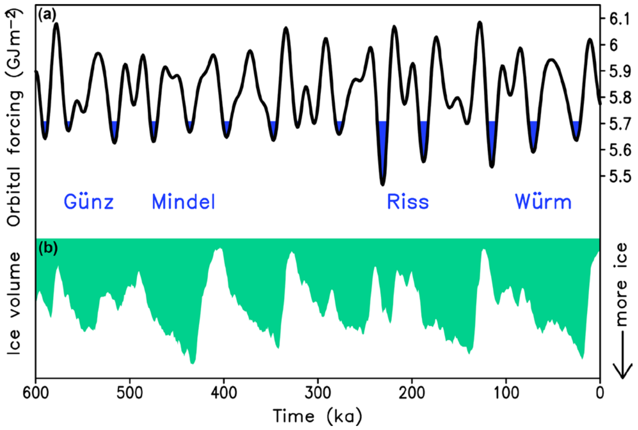

Figure 1. Milankovitch forcing and ice volume variations over the past 600 kyr. **(a)** Caloric summer half-year insolation at 65° N. Blue shading represents insolation below 5.7 GJ m^{-2}, the insolation threshold selected to match best Fig. 57 in Milankovitch (1941). According to the Milankovitch theory, glaciations occurred during periods of low insolation. The names of major glaciations, according to Penck and Brückner (1909), are written below the "Milankovitch curve". **(b)** LR04 (Lisiecki and Raymo, 2005) benthic δ^{18}O stack, a proxy for the global ice volume (inverted for convenience).

riods of low summer insolation. Although Milankovitch did not explicitly formulate his conceptual model of glacial cycles, the text and figures indicate that Milankovitch assumed that ice ages occurred during periods when caloric summer (half-years) insolation was below a certain threshold value (Fig. 1). Using a simple energy balance climate model, Milankovitch estimated that typical changes in summer insolation by 1000 canonical radiation units (1 canonical unit is approximately equal to 0.428 MJ) would cause 5 °C of summer cooling. Such cooling, in turn, is sufficient to lower the snow line by ca. 1 km and cause a widespread glaciation which is further amplified by the snow–albedo feedback. Thus, Milankovitch, for the first time, demonstrated that variations in insolation caused by astronomical factors are capable of driving glacial cycles. According to the Milankovitch conceptual model, three glaciations occurred during the last 120 kyr, which at the time of Milankovitch were known as Würm I, II, and III and now are usually notated as MIS 5d, 4, and 2. Although this was a significant step forward in explaining past glacial cycles, a comparison of the orbital forcing with the Earth system response shown in Fig. 2 reveals problems with the classical Milankovitch theory. It turned out that the Milankovitch conceptual model is more applicable to the 41 kyr world of the early Quaternary rather than the 100 kyr world of the late Quaternary.

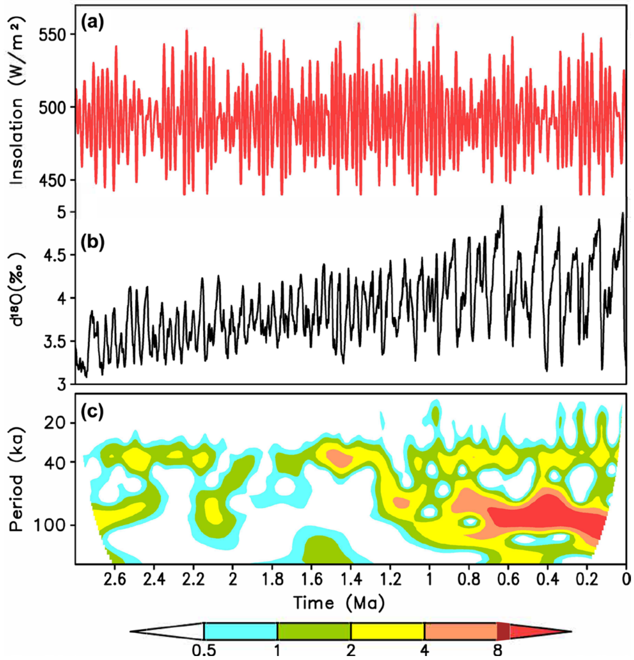

Figure 2. Orbital forcing and the Earth system response during the entire Quaternary period. **(a)** Maximum summer insolation at 65° N computed using Laskar et al. (2004) orbital parameters; **(b)** LR04 (Lisiecki and Raymo, 2005) benthic δ^{18}O stack, a proxy for global ice volume; **(c)** wavelet spectra of LR04 stack (in arbitrary units).

1.2 Testing Milankovitch theory with paleoclimate records

During the life of Milutin Milankovitch, no reliable paleoclimate records of glacial cycles existed to test his theory. Such records based on δ^{18}O in marine sediments became available only during 1960s (Emiliani, 1966), and the first results of their analysis (e.g., Broecker and van Donk, 1970) provided strong support for the Milankovitch theory. Hays et al. (1976) demonstrated that the frequency spectra of planktic δ^{18}O, considered a proxy for the global ice volume, contain both obliquity and precession frequencies, i.e., the frequencies of the Milankovitch insolation curves (Berger, 1976). However, the dominant periodicity of the recent glacial cycles was 100 kyr. This periodicity is absent in the spectrum of insolation but is close to one of the periodicities of eccentricity, which modulates the precession component of orbital forcing. In this landmark paper, the authors also demonstrated a close phase relationship between glacial cycles and eccentricity cycles and proposed that the 100 kyr cyclicity of the late Quaternary glacial cycles originates from a nonlinear climate response to eccentricity.

One of the most comprehensive attempts so far to test and extend Milankovitch theory beyond its original formulation was undertaken in the early 1990s by a large group of scientists (also known as the SPECMAP group after the project acronym) in two papers – Imbrie et al. (1992) and Imbrie et al. (1993). In the first one, it was concluded that 23 kyr (precession) and 41 kyr (obliquity) cycles seen in different paleoclimate records can be explained as a linear response of the climate system to insolation changes in high latitudes of the Northern Hemisphere. In the second paper devoted to the origin of 100 kyr cyclicity in the late Quaternary, the authors discussed several potentially important processes and climate feedbacks but did not arrive at a definite conclusion about the nature of 100 kyr cycles. The SPECMAP group acknowledged that these cycles could originate from the existence in the climate system of internal self-sustained oscillations with a similar periodicity, or, alternatively, 100 kyr cycles represent forced oscillations where the climate system acts as “a nonlinear amplifier which is particularly sensitive to eccentricity driven modulations in the 23 000-year sea level cycle” (Imbrie et al., 1993).

The nature of glacial cycles and Milankovitch theory attracted significant attention in the decades following SPECMAP publications, and numerous ideas of how to test and further develop Milankovitch theory have been proposed. First, the original Milankovitch theory has been turned from the theory of glacial ages into the theory of glacial terminations, and several studies analyzed whether the timing of glacial terminations is consistent with the Milankovitch theory in its new termination version (e.g., Huybers and Wunsch, 2005; Raymo, 1997). Second, instead of caloric half-year summer insolation used by Milankovitch, the June, July, or summer solstice insolation at 65° N became the standard metric for the orbital forcing (e.g., Berger, 1978). Defined this way, the orbital forcing became dominated by precession, while in the original Milankovitch version, the contributions of obliquity and precession were comparable. Third, Antarctic ice core analysis revealed significant variations in CO_2 concentration, which closely followed 100 kyr cycles of global ice volume (Petit et al., 1999). This led to the appreciation of the importance of CO_2 as the driver of glacial cycles and thus to the merging of the Milankovitch and Arrhenius theories, which before were considered to be alternative theories of glacial cycles (e.g., Ruddiman, 2003).

1.3 Testing Milankovitch theory with models

With the development of climate and ice sheet models, efforts to test the validity of the Milankovitch theory also began on the modeling front. The impact of Earth orbital parameter changes was first investigated with atmospheric models (e.g., Kutzbach, 1981). It had been shown that surface air temperature and atmospheric dynamics (e.g., summer monsoons) are strongly affected by orbital parameter changes. Over the past 20 years, several “time slices” (mid-Holocene and the Eemian interglacial) have received special attention in the framework of paleoclimate intercomparison projects (e.g., Braconnot et al., 2007). Results of these studies confirmed the strong influence of orbital forcing on climate even though changes in Earth’s orbital parameters have little effect on global annual mean insolation. It is noteworthy that a typical sensitivity of summer temperature over the Northern Hemisphere land to orbital forcing (about 1 °C per 10 W m^{-2}) found in climate model simulations is rather similar to the original Milankovitch estimate. Thus, the first premise of the Milankovitch theory of ice ages, namely that changes in insolation caused by variations of the Earth’s orbital parameters strongly affect climate, had been confirmed.

The next step in testing the Milankovitch theory was modeling climates favorable for glacial inception. The aim was to verify whether the cooling caused by the lowering of boreal summer insolation is sufficient to trigger large-scale Northern Hemisphere glaciation (“ice age”). Since the last glacial cycles began around 115 ka, the time when boreal summer insolation was about 10 % lower than at present, most such experiments have been performed for this time. Simulations with different climate models show pronounced summer cooling over continents in the Northern Hemisphere. However, as far as the glacial inception (the build-up of ice sheets) was concerned, the results were rather ambiguous: some models simulated the appearance of perennial snow cover at least in several continental grid cells, while others did not (e.g., Royer et al., 1983; Dong and Valdes, 1995; Varvus et al., 2008). This ambiguity is not surprising since the magnitude of climate biases in model simulations is often comparable to models’ responses to orbital forcing. In addition, a rather coarse spatial resolution of climate models used in these studies does not allow resolving topographic details, which may be critical for the appearance of ice sheet nucleation centers (Marshall and Clarke, 1999). In any case, without coupling climate models to ice sheet models, it was impossible to determine whether the simulated climate response to orbital forcing was consistent with the observed ice volume growth rate.

Simulations of glacial cycles with simple ice sheet models began in the 1970s with 1-D models (e.g., Weertman, 1976; Oerlemans, 1980; Pollard, 1983). The latter study produces rather impressive agreement between modeled and reconstructed ice volume. It also demonstrated the importance of the delayed isostatic rebound and what is now called marine ice sheet instability (MISI) for the realistic simulation of glacial cycles. Later, the complexity and spatial resolution of both climate and ice sheet modeling components increased, which allowed simulating the temporal evolution of ice sheets during the past glacial cycles and comparing them with available paleoclimate reconstructions (e.g., Tarasov and Peltier, 1997; Berger et al., 1999; Zweck and Huybrechts, 2003).

More recently, a new class of models, Earth system models of intermediate complexity (EMICs, Claussen et al., 2002), have been used for long transient simulations of the glacial cycles, first with prescribed GHG concentrations (e.g., Charbit et al., 2007; Ganopolski et al., 2010; Heinemann et al., 2014; Choudhury et al., 2020) and finally with the fully interactive carbon cycle (Ganopolski and Brovkin, 2017; Willeit et al., 2019). The latter study also succeeded in simulating the mid-Pleistocene transition from the 41 to 100 kyr world. One of the important results obtained with EMICs was the demonstration of the existence of multiple equilibria states in the phase space of the orbital forcing and that the glacial inception represents a bifurcation transition from one state to another (Calov and Ganopolski, 2005). Only recently have transient simulations with ice sheet models coupled to GCMs become possible, but so far, such simulations have been restricted to modeling only glacial inception (Gregory et al., 2012; Tabor and Poulsen, 2016; Lofverstrom et al., 2022).

2 Conceptual models of glacial cycles

Conceptual models of glacial cycles can be defined as a set of formal rules or mathematical operators that translate a certain metric for orbital forcing (usually boreal summer insolation) into quantitative or qualitative information about the temporal dynamics of glacial cycles. Despite progress with the modeling of glacial cycles using a process-based model, conceptual models remain a popular tool for studying the mechanisms of glacial cycles.

2.1 Qualitative conceptual model of glacial cycles

The term "qualitative" here is applied to models that do not simulate the temporal evolution of climate characteristics but instead provide only qualitative information about glacial cycles. The first model of this sort was proposed by Joseph Adhémar, the author of the first astronomical theory of ice ages. He proposed that ice ages were caused by long winters and occurred with the periodicity of the precession of the equinox, i.e., ca. 23 000 years (Adhémar, 1842). James Croll later changed long to cold winters as the precondition for hemispheric glaciations (Croll, 1864). In turn, Milutin Milankovitch adopted the view that glaciations occurred during "cold summers". In a quantitative form, Milankovitch's theory of glacial ages (see Fig. 1, which is similar to Fig. 48 from Milankovitch, 1941) can be formulated as follows: ice ages occur when summer insolation drops below a certain threshold value.

Among examples of more recent qualitative conceptual models of glacial cycles is the idea that glaciations are triggered by every fourth or fifth precession cycle after "unusually low" summer insolation maxima (Raymo, 1997; Ridgwell et al., 1999). This conceptual model closely relates glacial cycles to the eccentricity cycles since unusually low summer insolation maxima occur during periods of low eccentricity. An alternative conceptual model in which precession plays no role was proposed by Huybers and Wunsch (2005). According to this model, glacial terminations of the late Quaternary were spaced in time with equal probability by two or three obliquity cycles without any relation to other orbital parameters (see also Appendix A3). More recently, Huybers (2011) also accounted for the role of precession in pacing glacial cycles and proposed a conceptual mathematical model where the timing of glacial termination is controlled by a metric of orbital forcing similar to Milankovitch's caloric half-year insolation.

Recently, Tzedakis et al. (2017) proposed a rule which relates the timing of glacial terminations to the original Milankovitch metric for the orbital forcing, namely half-year caloric summer insolation. Tzedakis et al. (2017) found that glacial terminations during the late Quaternary occurred when the "effective energy" (a function of caloric half-year insolation and elapsed time since the previous termination) exceeds a certain value. This conceptual model and its relationship to GMT are discussed in Appendix A3.

2.2 Mathematical conceptual models of glacial cycles

Mathematical conceptual models of glacial cycles are based on one or several equations that describe climate system response to orbital forcing. Usually, the state of the climate system is expressed through the global ice volume (e.g., Imbrie and Imbrie, 1980; Paillard, 1998), but some models also include equations for CO_2 concentration and temperature (e.g., Saltzman and Verbitsky, 1993; Saltzman, 2002; Paillard and Parrenin, 2004; Talento and Ganopolski, 2021) or some dynamical properties of the ice sheets (e.g., Verbitsky et al., 2018). Orbital forcing in such models is represented by a function of Earth's orbital parameters, usually by the maximum summer insolation at 65° N, caloric half-year insolation, or similar characteristics. Conceptual models of glacial cycles can be divided into "inductive" models (like Imbrie and Imbrie, 1980; Paillard, 1998) where governing equations were selected to produce an output close to the paleoclimate records and models where the equations were derived with some assumptions and simplifications from the basic equations describing dynamics of climate and ice sheets (e.g., Tziperman and Gildor, 2003; Verbitsky et al., 2018). The third type of conceptual models, namely models derived using the results of complex Earth system models, is described in the next section.

Calder (1974) and Imbrie and Imbrie (1980) proposed the first models of this type. Both models simulate global ice volume evolution in response to boreal summer insolation variations. While Calder's model simulates glacial cycles, which is dominated by precession and obliquity and has too little energy in the frequency spectra for the 100 kyr periodicity, the Imbrie and Imbrie model (see also Appendix A2) has too much energy in the 400 kyr band, which is another eccentricity periodicity (see also Paillard, 2001). These problems are typical for many conceptual models. An important step in developing conceptual models of glacial cycles was made by Paillard (1998) (P98 hereafter). This model is similar to the Imbrie and Imbrie model, but it additionally postulates the existence of different equilibrium states and different regimes of operation, including a fast regime of deglaciation which occurs after reaching a critical ice volume. The idea of such catastrophic behavior of ice sheets after reaching some critical state was probably first proposed by MacAyeal (1979). This strong nonlinearity enables the model to achieve very good agreement with paleoclimate reconstructions and, in particular, to eliminate the 400 kyr peak in the frequency spectra of ice volume. The P98 model has played a critical role in the development of GMT and will be discussed in more detail in the forthcoming sections.

Admittedly, a number of other conceptual models simulate past glacial cycles with reasonable skill. In many of them, glacial cycles represent self-sustained oscillations with superimposed Milankovitch cycles (see Roe and Allen, 1999, and Crucifix, 2012, for an extensive discussion and comparison of different conceptual models). These studies also revealed that many models produce similarly good agreement with the empirical data despite very different assumptions and formulations. Roe and Allen (1999) concluded the following.

> We find there is no objective evidence in the record in favour of any particular model. The respective merits of the different theories must therefore be judged on physical grounds.

To explain this apparent paradox, a "minimal" model of glacial cycles is described in the next section. The simplicity of the recipes needed to simulate "realistic" glacial cycles explains why different conceptual models produce similar results.

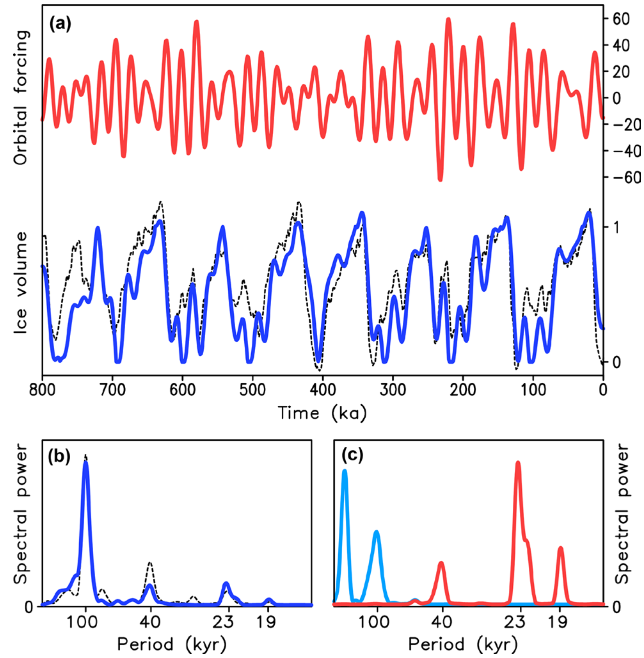

Figure 3. Simulations of late Quaternary glacial cycles with the "minimal" conceptual model MiM. **(a)** Orbital forcing (maximum summer insolation at 65° N) and **(b)** results of MiM versus paleoclimate reconstruction. The solid lines are modeling results, and the dashed line is an arbitrarily scaled LR04 δ^{18}O stack. **(c)** Frequency spectra of MiM in comparison with the frequency spectra of LR04 stack. **(d)** Frequency spectra of orbital forcing (red) and eccentricity (blue).

2.3 "Minimal" conceptual models of glacial cycles

One of the main challenges in modeling the late Quaternary glacial cycles is the dominant 100 kyr periodicity (a single sharp peak in the frequency spectra at the period close to 100 kyr) and the absence of the energy maximum at 400 kyr, which is another eccentricity period. While the linear transformation of orbital forcing would not show any significant energy at eccentricity periods, nonlinear transformations (like Imbrie and Imbrie model, see Appendix A2) contain all eccentricity periodicities. The simplest way to solve this problem is to design a model which possesses self-sustained oscillations with a periodicity close to 100 kyr and where orbital forcing plays a secondary role, namely the role of a pacemaker of long glacial cycles. Such a model with appropriate parameter choices can simulate glacial cycles with the correct frequency spectrum and timing of individual glacial cycles. Furthermore, such a model can be very simple and described by a single equation:

$$\frac{\mathrm{d}v}{\mathrm{d}t} = a_k - bf, \tag{1}$$

where v is the ice volume in arbitrary nondimensional units, time t is in kiloyears, a_k and b are model parameters, and orbital forcing $f = F - F_\mathrm{a}$ where F is the maximum summer insolation at 65° N and F_a is the average value of F over the last million years. The model has two "regimes": $k = 1$ corresponds to the period of ice growth and positive $a_1 = 1/t_1$, while $k = 2$ corresponds to ice decay and therefore negative $a_2 = -1/t_2$. The transitions from the regime $k = 1$ to $k = 2$ occur when $v = 1$ and from $k = 2$ to $k = 1$ when $v = 0$. In the absence of orbital forcing, the solution involves sawtooth-like oscillations with the period $T = t_1 + t_2$. By proper choice of t_1 and t_2, this periodicity can be set to 100 kyr (Table 1). This is the minimal (MiM) model of glacial cycles which is similar to but even simpler than the model described in Leloup and Paillard (2022). This model has only three free parameters. For their optimal values given in Table 1, the model can achieve rather good agreement with the benthic δ^{18}O record (Lisiecki and Raymo, 2005) with a correlation coefficient of 0.81 for the last 800 kyr (Fig. 3). Notably, the model solutions for the last 800 kyr strongly depend on the choice of model parameters but do not depend on the initial condition if the simulations begin from $v = 0$ not later than 1000 kyr before present. The model described by Eq. (1) is the simplest version of the relaxation oscillator, which is phase-locked to orbital forcing. Many other conceptual models have more complex formulations but in terms of dynamics are essentially identical to the model described by Eq. (1).

Table 1. Parameters of conceptual models used in the paper.

Model	Optimal parameters
IIM80	$t_1 = 24$ kyr, $t_2 = 3$ kyr, $c_1 = 0.02\,\mathrm{W^{-1}\,m^2\,kyr^{-1}}$
MiM	$t_1 = 65.6$ kyr, $t_2 = 35.6$ kyr, $c_1 = 0.00126\,\mathrm{W^{-1}\,m^2\,kyr^{-1}}$
Model 2	$a = 0.075\,\mathrm{kyr^{-1}}$, $c = 0.0018\,\mathrm{W^{-1}\,m^2\,kyr^{-1}}$, $g = 0.6$, $\varepsilon = 0.03$, $f_1 = 3.6\,\mathrm{W\,m^{-2}}$, $N = 25$ kyr
Model 3	$t_1 = 30$ kyr, $t_2 = 10$ kyr, $f_1 = -16\,\mathrm{W\,m^{-2}}$, $f_2 = 16\,\mathrm{W\,m^{-2}}$, $v_c = 1.4$

What can be learned from this simple modeling exercise? Obviously, it demonstrates that it is very easy to design a simple model (mathematical transformation) which converts orbital forcing into the benthic δ^{18}O-like curve for the last 800 kyr with sufficiently good accuracy. These recipes are the following. First, the model has to possess two regimes: slow ice growth and fast deglaciation regimes. Second, the transitions between the first and the second regimes should occur after some critical ice volume is reached. Third, the time needed to reach this critical ice volume should be about 100 kyr. What remains to be explained is

1. why the Earth system during the Quaternary behaves like a relaxation oscillator;
2. what the physical meaning of the "critical ice volume" is and why reaching critical volume leads to regime change and deglaciation;
3. why deglaciation is much shorter than the phase of predominant ice sheet growth;
4. whether the Earth system possesses an internal timescale close to 100 kyr or this timescale is directly related to the eccentricity.

These and other questions will be discussed in Sect. 4. In the next section, a new conceptual model will be introduced and used to illustrate a number of essential aspects of GMT.

3 Simple conceptual model of glacial cycles based on CLIMBER-2 results

3.1 Modeling concept

As shown above, even a very simple conceptual model can simulate global ice volume evolution in good agreement with the reconstructed one. The reason why a new conceptual model is presented here is not that it has a better performance than other models of the same class but because it is based on the results of a process-based Earth system model, CLIMBER-2. In turn, it has been shown that CLIMBER-2 can successfully simulate Quaternary glacial cycles using orbital forcing as the only external forcing (Willeit et al., 2019). Thus, this new conceptual model is fundamentally different by design from other conceptual models.

The development of a new conceptual model has been done in two steps. First, based on the analysis of CLIMBER-2 model results (considered hereafter as Model 1), a simple but still physically based reduced-complexity model (Model 2) has been designed. This model is described in Appendix A4. A three-equation version of this model was used in Talento and Ganopolski (2021). Model 2 has then been additionally simplified, and in this way Model 3 was designed. This model is described below.

The key results of CLIMBER-2, which have been obtained in Calov and Ganopolski (2005), Ganopolski and Calov (2011), and Willeit et al. (2019), used to design Models 2 and 3 are the following.

1. The mass balance of ice sheets strongly correlates with the maximum summer insolation at 65° N.
2. The existence of multistability of the climate–cryosphere system in the phase space of orbital forcing with the bifurcation transitions between different states.
3. The typical (relaxation) timescale of the climate–cryosphere is about 20–40 kyr.
4. Robustness of simulated glacial cycles regarding the choice of initial conditions and model parameters.
5. Phase locking of the late Quaternary glacial cycles to the 100 kyr eccentricity cycle.
6. Strong asymmetry between ice sheet growth phase and glacial terminations.

Model 3 does not explicitly account for the role of CO_2 in glacial cycles, which was analyzed in previous studies (e.g., Ganopolski and Calov, 2011; Ganopolski and Brovkin, 2017). For the sake of simplicity, it is assumed here that the role of CO_2 is implicitly represented by ice volume since these two characteristics are highly correlated. The role of CO_2 in shaping glacial cycles will be discussed in the next section.

3.2 Model 3 formulation

The new conceptual model of glacial cycles (Model 3) is based on the existence of multiple equilibrium states found in Calov and Ganopolski (2005) and reproduced by Model 2 (see Appendix A4). The first (interglacial) state is characterized by a warm climate and the absence of continental ice sheets in the Northern Hemisphere. The second one, with the ice sheets covering significant fractions of North America and Eurasia, is the glacial state. In the framework of this concept, the evolution of the Earth system under the influence of orbital forcing is described as the relaxation towards the corresponding equilibrium state. Model 3 contains only one variable – global ice volume v (in nondimensional units), described by the following equation:

$$\frac{\mathrm{d}v}{\mathrm{d}t} = \begin{cases} \frac{V_\mathrm{e}-v}{t_1}, & k=1 \\ -\frac{v_\mathrm{c}}{t_2}, & k=2, \end{cases} \tag{2}$$

with the additional constraint $v \geq 0$. Equation (2) describes two different regimes of ice sheet evolution. The first one ($k=1$), similar to the P98 model, is the glaciation regime when the system relaxes toward the equilibrium glacial state V_e with the timescale t_1. The second regime ($k=2$) is the deglaciation regime when ice volume linearly declines toward zero with the characteristic timescale t_2, with v_c being the model parameter that defines the critical ice volume (see below). The equilibrium state V_e towards which the system is attracted is a function of orbital forcing and, for the bi-stable regime, also depends on ice volume (see Fig. 4a):

$$V_\mathrm{e} = \begin{cases} V_\mathrm{g}, & \text{if } f < f_1, \text{ or } f_1 < f < f_2 \text{ and } v > V_\mathrm{u} \\ V_\mathrm{i}, & \text{if } f > f_2, \text{ or } f_1 < f < f_2 \text{ and } v < V_\mathrm{u} \end{cases}. \tag{3}$$

The glacial equilibrium state is defined as

$$V_\mathrm{g} = 1 + \sqrt{\frac{f_2 - f}{f_2 - f_1}}. \tag{4}$$

The unstable equilibrium which separates the glacial and interglacial attraction domains is defined as

$$V_\mathrm{u} = 1 - \sqrt{\frac{f_2 - f}{f_2 - f_1}}, \tag{5}$$

and the interglacial equilibrium $V_\mathrm{i} = 0$. Here orbital forcing f (in $\mathrm{W\,m^{-2}}$), similar to the minimal conceptual model MiM, is defined as $f = F - F_\mathrm{a}$, where F is the maximum summer insolation at 65° N, F_a is its averaged value over the last million years, and f_1 and f_2 are model parameters. Note that orbital forcing only enters Eq. (2) in a parametric form. Unlike Model 2, from which it was derived, Model 3 does not explicitly include positive and negative feedbacks, but the existence of such feedbacks determines the shape of the stability diagram of Model 3 (Fig. 4), which is the same as for Model 2 (Fig. A4). The only qualitative difference between Models 2 and 3 is that in the latter, the relaxation timescales are fixed, while in the former, they depend on the position in phase space of orbital forcing and ice volume. This explains the very close similarity of the trajectories in this phase space (compare Figs. 4b and A4b).

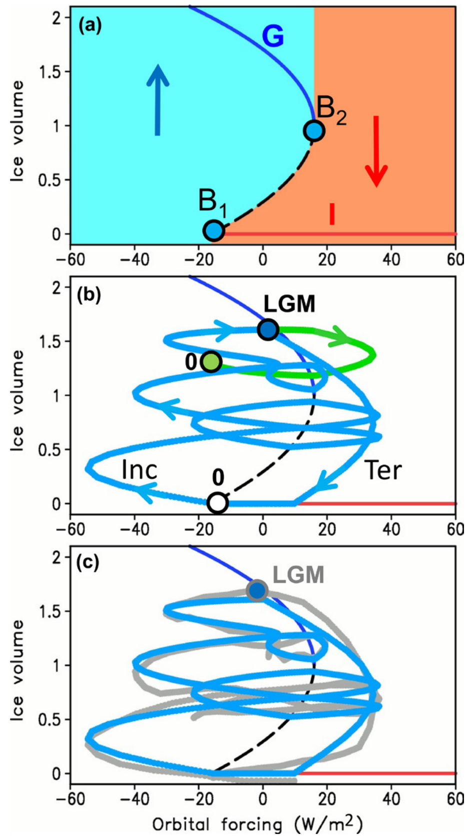

Figure 4. Evolution of the modeled ice volume in the phase space of orbital forcing. **(a)** Two equilibrium solutions: G – glacial, I – interglacial. The blue area is the attraction domain of the glacial state, the red area is the attraction domain of the interglacial state, and the dashed line is an unstable solution separating the two domains. B_1 and B_2 are the bifurcation points, and B_1 corresponds to glacial inception. This diagram corresponds only to the glaciation regime. For the deglaciation regime, there is only one equilibrium state – I. **(b)** Evolution of simulated ice volume (nondimensional) during the past glacial cycle starting at time 120 ka. "Inc" denotes glacial inception, and "Ter" indicates glacial terminations. Note that after the LGM (20 ka) the model without a termination regime (green line) failed to deglaciate. **(c)** Comparison of model simulation with LR04 benthic δ^{18}O stack.

The transition from a glacial ($k=1$) to deglaciation regime ($k=2$) occurs if three conditions are met: $v > v_\mathrm{c}$, $\frac{\mathrm{d}f}{\mathrm{d}t} > 0$, and $f > 0$. The transition from deglaciation to glacial regime occurs if orbital forcing f drops below the glaciation threshold f_1. The interglacial state formally belongs to the deglaciation regime.

The model has five parameters (t_1, t_2, f_1, f_2, v_c), all of which, in principle, can be used to maximize the agreement between simulated and reconstructed ice volume. However, all these parameters have clear physical meaning and can be directly estimated using the results of CLIMBER-2 and paleoclimate data. The value of f_1 (insolation threshold for glacial inception) was rather tightly constrained by the current insolation minimum ($f = -15\,\mathrm{W\,m^{-2}}$) when glaciation did not occur and MIS 19 insolation minimum ($f = -20\,\mathrm{W\,m^{-2}}$) when it did occur (Ganopolski et al., 2016). According to Calov and Ganopolski (2005), the relaxation timescale t_1 is about 30 kyr, and f_2 is positive. It is noteworthy that model results depend on a combination of t_1 and f_2, and essentially identical solutions can be obtained for different combinations of these two parameters. Deglaciation timescale t_2 derived from the model and paleoclimate records is about 10 kyr. The last model parameter, the critical ice volume v_c, controls the dominant periodicity and degree of asymmetry of glacial cycles. As a result, only f_2 and v_c were used as tunable parameters and their values (Table 1) have been chosen to maximize the correlation between simulated ice volume and the benthic δ^{18}O record (LR04) during the past 800 kyr. The δ^{18}O has been used here as the ice volume proxy even though several reconstructions of sea level for the last 800 kyr exist (i.e., Spatt and Lisiecki, 2016). This has been done to enable the comparison of model results with the paleoclimate data for the entire Quaternary. Such a choice is justified by a strong similarity between the LR04 stack and late Quaternary sea level reconstructions. Model 3 is similar to the P98 model by formulation and its results, but it does not contain timescales close to 100 kyr.

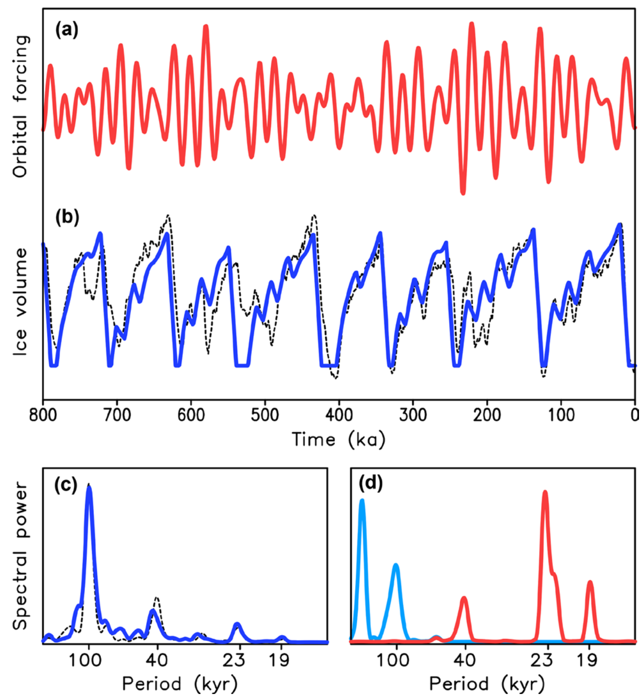

Figure 5. Results of simulations of the last 800 kyr with conceptual Model 3. **(a)** Orbital forcing; **(b)** simulated ice volume in nondimensional units (blue) and scaled LR04 stack (dashed line); **(c)** spectra of simulated ice volume (blue) and LR04 stack (dashed line); **(d)** frequency spectra of the orbital forcing.

3.3 Simulation of the late Quaternary glacial cycles with Model 3

Results of model simulations depicted in Fig. 5 show good agreement with the LR04 stack for the last 800 kyr. The correlation between the model and data is 0.85 for the entire time interval. The agreement is better for the later part (the correlation is 0.9 when only considering the last 400 kyr) than for the earlier part, which can be partly explained by the fact that the model and LR04 are in antiphase around 700 and 490 kyr. Since LR04 has been tuned to the Imbrie and Imbrie model, which has a very strong precession component, the cause of such a large data–model mismatch is unclear. The frequency spectrum of the model results in good agreement with paleodata has a dominant sharp 100 kyr maximum, with little energy in the 400 kyr band and a relatively weak precession component compared to the spectrum of orbital forcing (Fig. 5c). Simulated glacial cycles are rather insensitive to the initial conditions since they converge rapidly to the common solution (Fig. 6c). This agrees with CLIMBER-2 simulations (Willeit et al., 2019) where we concluded that "simulated glacial cycles only weakly depend on initial conditions and therefore represent a quasi-deterministic response of the Earth system to orbital forcing". Modeling results are also robust regarding the choice of model parameters. For example, when keeping other model parameters constant, as in Table 1, essentially the same results are obtained for the range of v_c between 1.32 and 1.49 (Fig. 6b). It is noteworthy that, although Model 3 is based on CLIMBER-2 and aimed to mimic it, Model 3 actually outperforms the CLIMBER-2 model in terms of the agreement with empirical data for the last 800 kyr. In particular, CLIMBER-2 has a problem with simulating the correct timing of Termination V prior to MIS 11 (see Willeit et al., 2019), while Model 3 does not have such a problem.

The existence of two regimes of operation is postulated in Model 3 similarly to P98, and it is absolutely critical for simulating realistic glacial cycles. To demonstrate this, an additional experiment has been performed with Model 3 but without the termination regime. This experiment started from $v = 0$ at 125 ka (Eemian interglacial) and was run to present day. The trajectory of ice volume evolution in the phase space of orbital forcing for this experiment is compared with the standard Model 3 in Fig. 4b. The two model versions are identical before 20 ka when the termination regime is activated in the standard model version. If the termination regime is disabled, the model trajectory in the phase space represents a loop similar to previous precession cycles (green line) and does not result in deglaciation. This result does not depend on the choice of model parameters, and there are no combinations of model parameters that enable the simulation of the realistic glacial cycles without the termination regime.

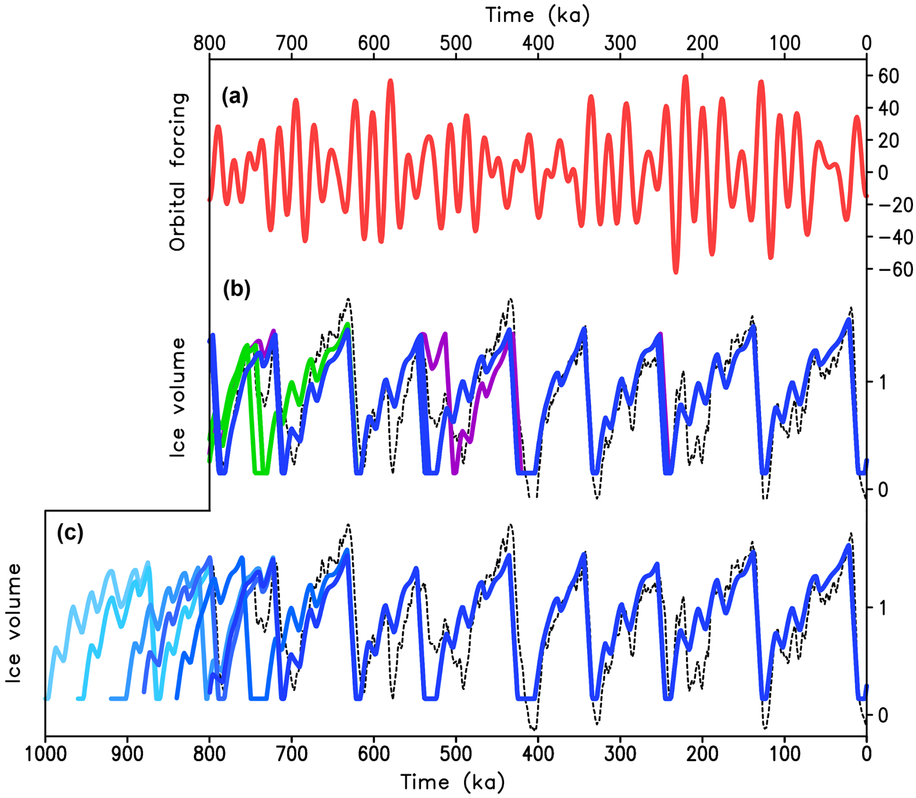

Figure 6. Results of simulations of the last 800 (1000) kyr with conceptual Model 3. **(a)** Orbital forcing; **(b)** simulated ice volume (green lines correspond to the range of v_c 1.32–1.38, blue to the range 1.39–1.48, purple to $v_c = 1.49$). Thus, the timing of most glacial terminations (and all the latest five) coincides for the broad range of v_c from 1.32 to 1.49. **(c)** Simulated ice volume for $v_c = 1.4$ (different colors correspond to different starting times from 1000 to 800 ka with the step 40 ka). All runs converge to the same solution after less than 200 kyr. Note the similarities with Fig. 6b from Ganopolski and Calov (2011). **(b, c)** The LR04 stack is shown by dashed lines.

3.4 Generic orbital forcing and the origin of 100 kyr cyclicity in Model 3

In Ganopolski and Calov (2011) we argued that the "100 kyr peak in the power spectrum of ice volume results from the long glacial cycles being synchronized with the Earth's orbital eccentricity". To understand how this synchronization occurs, Model 3 was forced by a generic orbital forcing instead of the real summer insolation. This generic forcing consists of a periodic precession-like harmonic component with a single periodicity of 23 kyr, with the amplitude modulated by schematic eccentricity-like cycles with a periodicity of 100 kyr:

$$f = A\left(1+\varepsilon \sin\frac{2\pi t}{100}\right)\cos\left(\frac{2\pi t}{23}\right), \tag{6}$$

where A is the magnitude of forcing in $\mathrm{W\,m^{-2}}$ and ε is the nondimensional magnitude of amplitude modulation.

The first experiment is performed with the simplest periodic orbital forcing with $A = 25\,\mathrm{W\,m^{-2}}$ and $\varepsilon = 0$. Figure 7 shows model results for three values of the critical ice volume: $v_c = 1.2$, 1.33, and 1.47. The model simulates periodic glacial cycles with the amplitudes and periods increasing with v_c. Naturally, these periods are multiples of 23 kyr. For $v_c = 1.2$ this period is equal to $3 \times 23 = 69$ kyr, and for $v_c = 1.47$ the period is $6 \times 23 = 140$ kyr; only for $v_c = 1.33$ is the period $4 \times 23 = 92$ kyr relatively close to 100 kyr (Fig. 7c). Note that all these periods are much longer than the relaxation timescale of the model equal to 30 kyr.

Applying amplitude modulation ($\varepsilon = 0.5$) with a periodicity of 100 kyr to this generic forcing leads to quasiperiodic cycles with a sharp peak at 100 kyr in the frequency spectrum and similar timings of glacial terminations for all three values of critical ice volume (Fig. 7b, d and f). This is because, irrespective of the value of v_c, all simulated cycles are phase-locked to the amplitude modulation cycle. This result is very robust with respect to the v_c value and the amplitude and period of precession-like cycles, as well as to the amplitude and periodicity of the amplitude modulation cycle. Similarly, setting the periodicity of precession-like cycles in the range of 10 to 30 kyr has a minimal impact on the results (not shown).

The mechanism of the phase locking of long glacial cycles to the 100 kyr amplitude modulation cycle in the case of the generic orbital forcing is rather straightforward. After ice volume v exceeds a value of about 0.2 v_c, the system

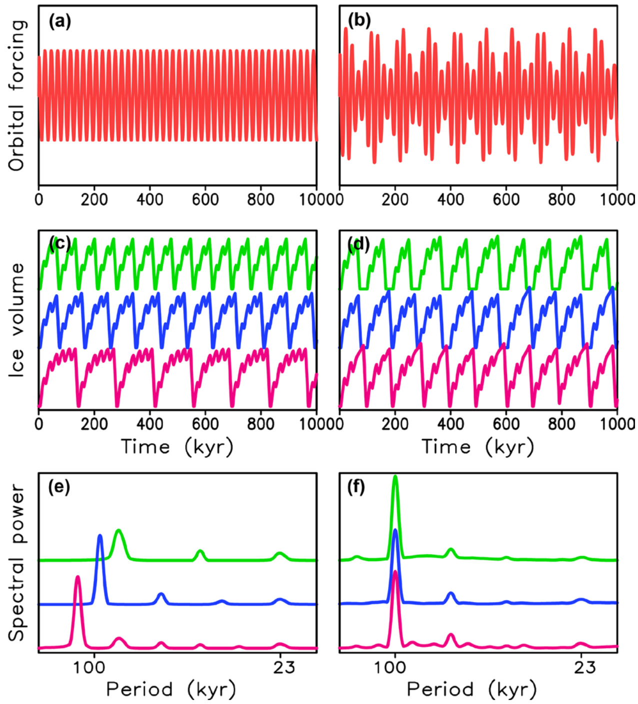

Figure 7. Simulation of glacial cycles with Model 3 for different artificial orbital forcings. **(a, b)** Forcings, **(c, d)** simulated volume in arbitrary units. **(e, f)** Frequency spectra of simulated ice volume. **(a, c, e)** Periodic forcing with $A = 25\,\mathrm{W\,m^{-2}}$, $T = 23$ kyr, and $\varepsilon = 0$ (Eq. 3). **(b, d, f)** Periodic forcing with additional 100 kyr amplitude modulation ($\varepsilon = 0.5$). Green lines correspond to $v_c = 1.2$, blue – $v_c = 1.33$, purple – $v_c = 1.47$.

stays longer in the attraction domain of the glacial state (see Fig. 4). Moreover, the smaller the amplitude of orbital forcing, the longer it stays in the attraction domain of the glacial state when ice is growing. Thus, the likelihood of reaching the critical ice volume v_c is higher during periods of weak orbital forcing, i.e., during periods of low eccentricity. It is also noteworthy that the amplitude of simulated glacial cycles and the height of 100 kyr peaks in the frequency spectrum of ice volume (Fig. 7) are essentially independent of the magnitude of amplitude modulation in a wide range of parameter ε values.

3.5 Is the spectrum of ice volume variability consistent with the phase locking of glacial cycles to eccentricity?

While the formal relationship between eccentricity and late Quaternary glacial cycles has already been established in Hays et al. (1976), some studies (e.g., Muller and MacDonald, 1997; Maslin and Brierley, 2015) argued against the direct link between the 100 kyr cyclicity of glacial cycles and eccentricity. It is known that the direct effect of eccentricity on global insolation is negligibly small (e.g., Paillard, 2001), and this is why the eccentricity can affect climate only through the amplitude modulation of the precession cycle. In principle, the response of any nonlinear system to the forcing, which consists of a quasiperiodic carrier with amplitude modulated by another quasiperiodic signal, should contain periodicities of both carrier and amplitude modulation signal. However, eccentricity also has a strong 400 kyr periodicity which is practically absent in the late Quaternary ice volume reconstructions. In addition, the peak in the eccentricity spectrum near 100 kyr is split into two peaks at 95 and 124 ka, while the spectrum of the reconstructed ice volume contains very little energy at 124 kyr.

Results of the Imbrie and Imbrie model apparently support this critique since the spectrum of their model reveals all problems mentioned above: the low-frequency part of its spectrum is essentially identical to the spectrum of eccentricity (Fig. 8d) and very different from the δ^{18}O spectrum for the last 800 kyr (Fig. 3). However, it is possible to construct a mathematical transformation that converts orbital forcing into realistic ice volume evolution, and Model 3 is an example of such transformation (Fig. 5). To enhance the resolution of the frequency spectrum, the model has been run through the past 3 Myr with the fixed model parameters. Only the last 2.8 were analyzed and are shown in Figs. 8 and 9. Unsurprisingly, the model with parameters tuned to the 100 kyr world cannot reproduce the 41 kyr world, and simulated glacial cycles are realistic only for the last million years. Unlike the Imbrie and Imbrie model, the spectrum of Model 3 does not contain a 400 kyr peak and has a single sharp peak at 95 kyr (Fig. 8d). Such behavior is robust for a wide range of model parameters, for example for v_c in the range between 1.2 and 1.5. The absence of 400 kyr periodicity in the frequency spectra of Model 3 can be explained by the fact that each glacial termination "erases" the system memory, and the amplitude of the next glacial cycle does not depend on the previous one. The main reason why the spectrum of Model 3 is so different from the spectrum of eccentricity is because the eccentricity is not the forcing of glacial cycles, but rather a pacemaker that sets the dominant periodicity and, to some degree, the timing of glacial terminations.

Although the spectrum of simulated glacial cycles is dominated by a sharp peak at around 100 kyr, this does not imply that all glacial cycles have a duration close to 100 kyr. In fact, as Fig. 8e shows, the duration of individual glacial cycles tends to cluster in the intervals of 80–90 and 110–120 kyr, which are both close to the duration of two or three obliquity cycles and four or five precession cycles. On the other hand, most durations are between 80 and 120 kyr, and very few are outside, which would not be the case if glacial cycles simply lasted two or three obliquity cycles. This feature is also seen in the distribution of durations of the last eight real glacial cycles. Also, as in reality, very few simulated glacial cycles have durations between 90 and 110 kyr. This explains the apparent paradox of why none of the glacial cycles of the 100 kyr world have a duration close to 100 kyr.

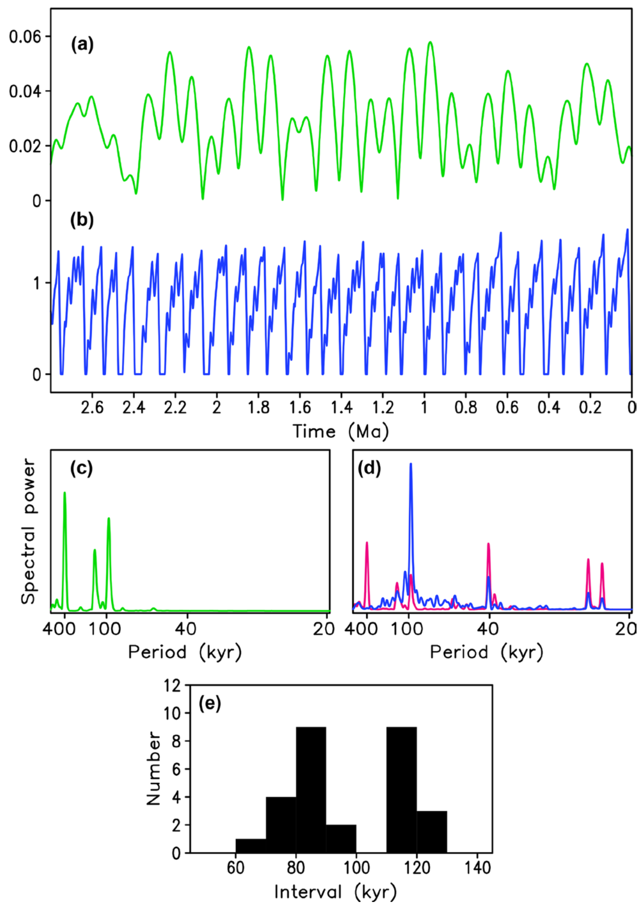

Figure 8. Simulation of the last 2.8 Myr with Model 3 ($v_c = 1.3$). **(a)** Eccentricity, **(b)** simulated ice volume (arbitrary units), **(c)** frequency spectrum of eccentricity, **(d)** spectrum of ice volume simulated with Model 3 (blue) and the Imbrie and Imbrie model (magenta), **(e)** histogram of the durations of individual glacial cycles simulated with Model 3.

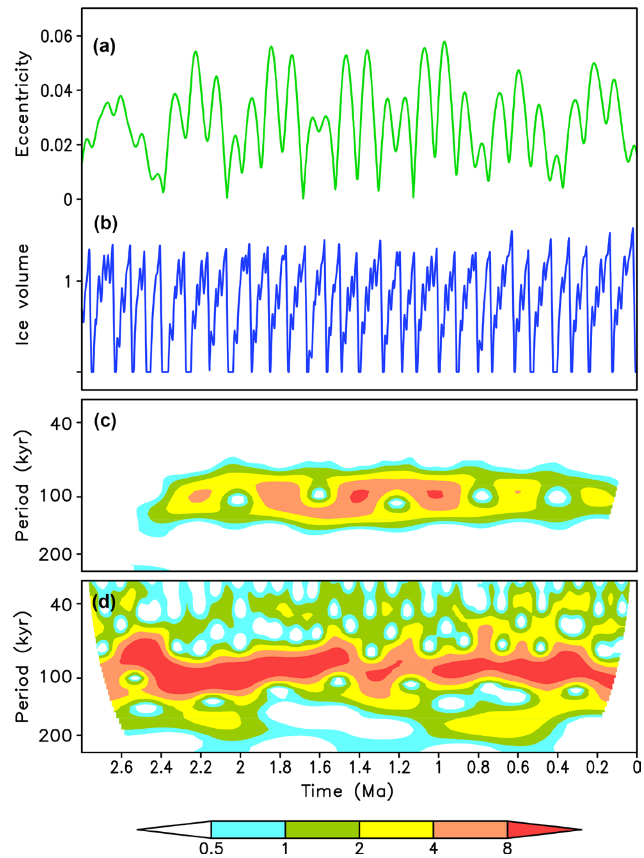

Figure 9. Simulation of the last 2800 kyr with constant critical ice volume parameters ($v_c = 1.3$). **(a)** Eccentricity, **(b)** simulated ice volume (arbitrary units), **(c)** wavelet spectra of eccentricity, and **(d)** wavelet spectra of simulated ice volume.

Another apparent paradox related to the role of eccentricity in glacial cycles is the fact that the energy in the 100 kyr band of the ice volume spectrum was growing over the past million years while the energy in the 100 kyr band of eccentricity was decreasing during the same time (Lisiecki, 2010; see also Fig. 9). Partly, this discrepancy can be explained by the fact that the energy increase in the 100 kyr band of ice volume spectra during the mid-Pleistocene transition (MPT, ca. 1.2–0.8 Ma) was related to changes in the boundary conditions (Willeit et al., 2019). However, even when keeping model parameters constant (Fig. 9), the energy in the 100 kyr band of ice volume spectrum changes in antiphase with the energy in the eccentricity spectrum. This can again be explained by the fact that eccentricity is not the direct forcing of glacial cycles, and the amplitude of glacial cycles is not directly related to the amplitude of the 100 kyr component of eccentricity, which is also clearly seen in the experiments with the generic orbital forcing (Fig. 7).

3.6 Simulation of the mid-Pleistocene transition

When applied to the entire Quaternary, Model 3 with constant parameters tuned to the last million years fails to reproduce the glacial cycles of the early Quaternary (Fig. 9). This is consistent with Willet et al. (2019), where it was shown that orbital forcing alone could not cause the regime change a million years ago. To reproduce the MPT in P98 and Legrain et al. (2023), the critical ice volume was made time-dependent with a smaller value at the beginning of the Quaternary and a larger one toward the present. A similar approach works for Model 3 too. The critical volume v_c is a nonlinear function of time:

$$v_c = 0.5(v_{c1} + v_{c2}) + 0.5(v_{c2} - v_{c1})\tanh((t - t_t)/\tau_t), \qquad (7)$$

where t is time in kiloyears before present (negative), $t_t = -1050$ kyr is the center of the MPT, transition time $\tau_t = 250$ kyr, and the initial and final critical ice volume values are $v_{c1} = 0.65$ and $v_{c2} = 1.38$. Notably, this temporal evolution of v_c closely resembles the temporal evolution of the regolith-free area prescribed in Willeit et al. (2019). Such

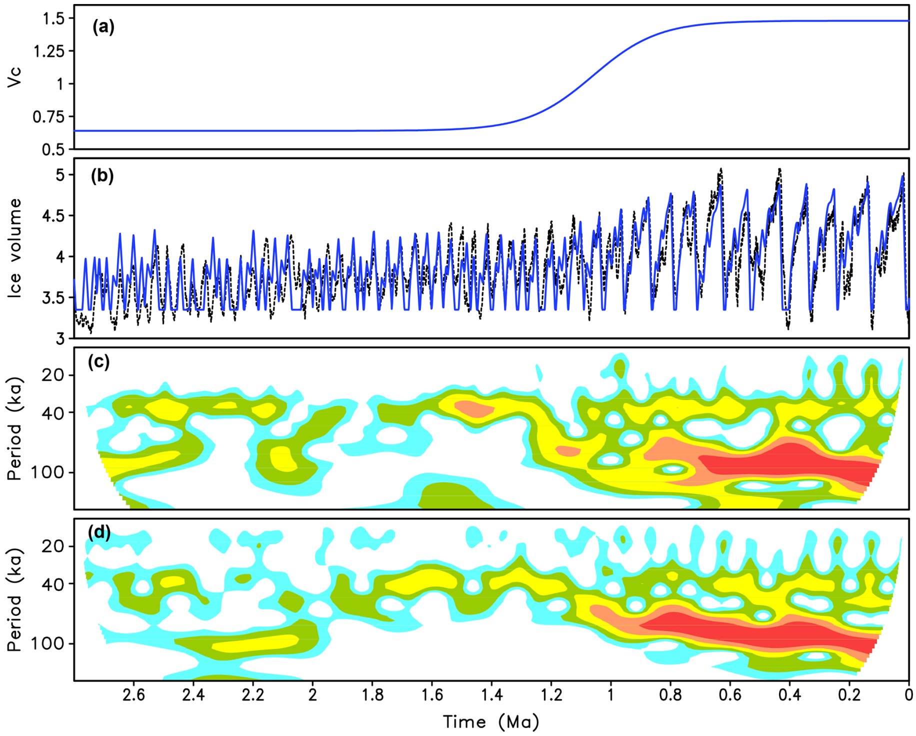

Figure 10. Simulations of MPT with Model 3. **(a)** Temporal dependence of critical ice volume v_c; **(b)** simulated ice volume (blue) versus LR04 (dashed); **(c)** wavelet spectra of LR04 stack; **(d)** wavelet spectra of modeled ice volume.

similarity is in line with the idea that the temporal evolution of the critical size of ice sheets is controlled by sediment removal from northern continents by glacial erosion processes.

With such time-dependent v_c, the model can reproduce a significant increase in the amplitude of glacial cycles and the transition from obliquity dominated 41 to 100 kyr dominated cycles around 1 million years ago. The agreement between model results and LR04 before 2 Ma is rather poor but it improves significantly after 2 Ma (Fig. 10b), and the correlation between modeled ice volume and δ^{18}O over the last 2.7 Myr is 0.75. The wavelet spectrum of ice volume also shows good agreement with the spectrum of the LR04 stack (Fig. 10c and d). Prior to the MPT, the spectrum of modeled ice volume is dominated by obliquity even though the orbital forcing is dominated by precession. Still, the precession component is significantly stronger in model output compared to LR04. This issue will be discussed in the next section and Appendix A6. Similar to LR04 and CLIMBER-2 results (Willeit et al., 2019), the maximum energy in the wavelet spectrum in Model 3 first moves from 40 to 80 kyr (two obliquity cycles) at ca. 1.2 Ma, and only after 0.8 Ma does the 100 kyr periodicity become the dominant one. Also, in agreement with paleodata, the period of energy maximum during the last 0.8 Myr does not remain constant and shows a clear tendency to oscillate around 100 kyr with a 400 kyr periodicity, which is another eccentricity period.

3.7 Glacial cycles in Model 3

Model 3 is an example of a rather simple nonlinear transformation of the traditional orbital forcing into glacial cycles. An important feature of this model is that it is based on simulation results using the Earth system model of intermediate complexity CLIMBER-2. The key element of the model is the existence of two fundamentally different regimes: glacial with the relaxation towards one of two equilibrium states and the deglaciation regimes. The model does not possess self-sustained oscillations and has no intrinsic timescale close to 100 kyr. In fact, this period originates solely from the phase locking of long glacial cycles to the amplitude modulation of precession components of insolation by eccentricity. The model accurately reproduces not only the temporal evolution of the glacial cycles, including the timing of terminations, but also the frequency and wavelet spectra of the late Quaternary. The model helps us to understand how a dominant 100 kyr periodicity originates from the combinations of different eccentricity, obliquity, and precession periods. In the next section, I will discuss how such a mathematical transformation can be explained from the "physical" point of view.

4 Elements of GMT

This section presents the key elements of the GMT; namely, it discusses physical and biogeochemical processes which play a crucial role in Quaternary glacial cycles. It also explains the postulates which make Model 3 so successful. Unlike the simplicity of the conceptual model, the physical basis of the GMT is very complex, and some important processes and mechanisms are still not fully understood. This is why some aspects of the GMT are only preliminary.

4.1 Orbital forcing

When developing his theory, Milankovitch adopted the already proposed idea that changes in boreal summer insolation are critical for understanding ice ages. As the metric for summer insolation, Milankovitch used the integral of insolation during a warm (caloric) half-year. After the revival of interest in the Milankovitch theory in the 1970s, it became more common to use the maximum (or summer solstice), June, or July insolation at 65° N to analyze the relationship between orbital forcing and climate system response. When discussing which single metric best represents orbital forcing, it is important to realize that climate models calculate insolation at each time step and for each grid cell, and therefore climate modelers do not need to decide what definition of “summer insolation” is correct. However, for analysis of paleoclimate records and construction of simple (conceptual) models of glacial cycles, it is required to convert 3-D (latitude – day of the year – the year before or after present) insolation into a single metric. This paper uses maximum summer insolation at 65° N for this purpose, and this choice is discussed in Appendix A1.

Irrespective of the specific choice of the metric for orbital forcing, any summer insolation curve represents a sum of precession and obliquity components. The precession component is a quasiperiodic ($T \approx 23\,000$ years) sine-like function with an amplitude proportional to eccentricity. The obliquity component is a periodic ($T \approx 41\,000$ years) function with the amplitude gradually changing in time. The relative contributions of precession and obliquity components depend on the choice of latitude and definition of “summer”, but, as shown in Appendix A1, it is reasonable to assume that obliquity and precession components are of comparable importance. The only notable exception is the so-called “summer energy” proposed in Huybers (2006), containing very little precession. However, as shown in Appendix A1, “integrated summer energy” is not applicable to the problem of glacial cycles.

4.2 Climate feedbacks

Experiments with climate models which began in the 1970s confirmed the central premise of the Milankovitch theory, namely that variations of Earth’s orbital parameters cause significant (several degrees and more) regional summer temperature changes over the continents. Such temperature changes would result in large vertical displacements of the equilibrium snow line and can, in principle, cause widespread glaciation of some regions. However, it has been found that the direct impact of the orbital forcing on climate in terms of global mean temperature is very small (less than 1 °C). Thus, to understand how orbital forcing during the Quaternary cased global-scale large-amplitude climate oscillations, it is necessary to invoke several climate-related feedbacks.

The first important positive feedback is the albedo feedback, which is already accounted for in Milankovitch calculations (Milankovitch, 1941). Results of modeling studies demonstrated that, even under a constant but sufficiently low CO_2 concentration (lower than the typical interglacial level of 280 ppm), orbital forcing alone could drive glacial cycles with realistic amplitude and periodicities (Berger and Loutre, 2010; Ganopolski and Calov, 2011; Abe-Ouchi et al., 2013). In turn, large continental ice sheets strongly affect global temperature. According to model simulations, ice sheets and associated sea level drop explain about half of the global cooling at the LGM (Hargreaves et al., 2007). However, this effect caused by albedo and elevation changes over large continental ice sheets is rather local and diminishes rapidly with distance from the margins of ice sheets. Moreover, in some regions, due to the modifications of atmospheric circulation, the effect of ice sheets on temperature can even be opposite; i.e., the growth of ice sheets can cause regional warming (Liakka and Lofverstrom, 2018). Another positive feedback is related to the fact that total accumulation over the ice sheet is nearly proportional to the ice sheet area (e.g., Ganopolski et al., 2010). This feedback, although critically important for the growth of ice sheets, lacks a specific name, likely due to its apparent nature. For consistency, it can be named the area–accumulation feedback. At the same time, the expansion of Northern Hemisphere ice sheets into lower latitudes leads to an increase in ablation, and thus this area–ablation feedback is negative.

The main “globalizer” of glacial cycles is CO_2, while methane and N_2O together contribute about 1/3 of CO_2 to the radiative forcing of glacial cycles. Interestingly, the role of CO_2 in glacial cycles was proposed by Svante Arrhenius (Arrhenius, 1896) well before Milankovitch published his first paper. Although Milankovitch was not enthusiastic about Arrhenius’s theory, it is generally accepted now that both the Milankovitch astronomical theory and the Arrhenius CO_2 theory represent two crucial ingredients of the theory of glacial cycles. The role and operation of the global carbon cycle during glacial cycles will be discussed below.

Another potentially important positive feedback (a set of feedbacks) is related to the global dust cycle. Paleoclimate reconstructions and modeling results show that the atmosphere was much dustier (typically by a factor of 2 globally) during the ice ages (Kohfeld and Harrison, 2001; Albani et al., 2018). This fact is attributed to reduced vegetation cover, exposed continental shelf, and dust production due to glacial erosion processes (Mahowald et al., 2006). Radiative forcing of aeolian dust strongly varies regionally, and its globally average magnitude remains uncertain (Bauer and Ganopolski, 2014). Apart from changing optical properties of the atmosphere, dust deposition strongly affects the surface albedo of snow and, therefore, the surface mass balance of ice sheets (Krinner et al., 2006; Ganopolski et al., 2010; Willeit and Ganopolski, 2018). In addition, a significant increase in aeolian dust deposition over the Southern Ocean through the iron fertilization effect led to an increase in net primary production of marine ecosystems and thus contributed to the glacial lowering of the atmospheric CO_2 concentration (Martin, 1990; Watson et al., 2000).

Another regional feedback is climate–vegetation feedback. Modeling results suggest that the biophysical effect of vegetation cover change during glacial times produced about 0.5–1 °C of additional global cooling (Ganopolski, 2003; Crucifix and Hewitt, 2005; O'ishi and Abe-Ouchi, 2013) and that this feedback amplified initial cooling caused by orbital forcing over the northern continents during glacial inceptions (e.g., de Noblet et al., 1996; Calov et al., 2005b; Claussen et al., 2006). At the same time, the effect of terrestrial biosphere changes on the atmospheric CO_2 concentration due to the shrinking of the terrestrial carbon pool during glacial times likely worked in the opposite direction, i.e., produced a negative feedback (see discussion below).

4.3 Timescales of the Earth system response and the nature of 100 kyr cyclicity

As shown in the previous section, the dominant periodicity close to 100 kyr of the glacial cycles during the last million years originates in our models from the phase locking of glacial cycles to the corresponding eccentricity cycle. This mechanism requires the typical duration of glacial cycles forced by obliquity and precession components of orbital forcing to be an order of 100 kyr. However, conceptual models derived from CLIMBER-2 do not have such a long internal timescale. The response time of Northern Hemisphere ice sheets to orbital forcing (30 kyr) used in Model 3 and adopted from Calov and Ganopolski (2005) is much shorter than 100 kyr. However, as shown above (see also Fig. 7), such long glacial cycles can arise if the time needed to reach a critical ice sheet volume is much larger than one precession cycle.

Admittedly, even the existence of a 30 kyr timescale of the cryosphere response to orbital forcing is not trivial. A typical accumulation rate over the Northern Hemisphere ice sheets during glacial conditions is about 0.1–0.3 Sv[1] (Ganopolski et al., 2010), which is consistent with the results of LGM simulations with GCMs. The total Northern Hemisphere surface ablation and the solid ice discharge into the ocean (calving flux) vary strongly in time but are generally around 0.1 Sv each (Ganopolski et al., 2010). Thus, it would be natural to consider 0.1 Sv a typical value for the total ice sheet mass disbalance. Such an estimate corresponds to complete growth and melt of the late Quaternary ice sheet in 10 000 years, which is just one-half of the precession cycle. In reality, such a rate of change is only achieved during glacial terminations, while for the rest of glacial cycles, the typical rate of global ice volume change was several times smaller, which implies that the positive and negative components of the ice sheet mass balance are close to each other by absolute values most of the time. This can be explained by the fact that, apart from the positive albedo and elevation feedbacks, there is strong negative feedback associated with ice sheet southward expansion. Model simulations show that the positive component of mass balance (accumulation) is roughly proportional to the size of ice sheets, whereas ablation increases strongly nonlinearly with the southward expansion of ice sheet margins. This negative feedback prevents North American and Eurasian ice sheets from spreading into low latitudes. As a result, reaching the equilibrium state takes much longer than one would expect from a simple scale analysis. Only under extremely strong orbital forcing (during periods of high eccentricity) can the disbalance between the components of surface mass balance be much larger, and the rate of volume changes increases substantially. This can explain a few "short" glacial cycles at ca. 600 and 220 ka, which Model 3 cannot simulate by design.

As shown in experiments with Model 3, phase locking of glacial cycles to the 100 kyr periodicity of eccentricity originates from the highest likelihood of reaching the critical ice volume during periods of low eccentricity. This is explained by the fact that, while high eccentricity facilitates ice sheet growth during glacial inceptions, the critical ice volume can be reached only if the system stays sufficiently long in the attraction domain of the glacial state, which occurs during periods of low eccentricity. In the case of realistic orbital forcing, the largest probability of reaching the critical ice volume is when a relatively weak maximum of the precession component of insolation coincides with a minimum of obliquity. Thus, according to GMT, the timing and periodicity of glacial cycles of the late Quaternary are set by the shortest (100 kyr) eccentricity cycles. The appearance of the eccentricity period in the spectra of glacial cycles originates from the phase locking rather than the forcing of glacial cycles by eccentricity. This concept eliminates the main criticism of "the eccentricity myth" (Maslin and Brierley, 2015) based on the fact that the direct impact of eccentricity on insolation in terms of the global mean value is too small (about 0.5 $W\,m^{-2}$) to affect glacial cycles. According to GMT, eccentricity affects glacial cycles indirectly through its amplitude modulation of the precession component of insolation, which results in the variations of maximum boreal summer insolation at the top of the atmosphere with an amplitude of more than 50 $W\,m^{-2}$.

[1]Here, the oceanographic unit of volume flux, Sverdrup, is used. $1\,Sv = 10^6\,m^3\,s^{-1}$ is approximately equivalent to 10 m global sea level rise in 1000 years.

Obliquity plays a role in setting the timing of glacial cycles, but as was shown in Ganopolski and Calov (2011), the dominant 100 kyr cyclicity is simulated by CLIMBER-2 even if the obliquity component is artificially eliminated from orbital forcing. The main difference in simulations with and without the obliquity component (see Fig. 3d in Ganopolski and Calov, 2010) is that the elimination of obliquity leads to an increase in energy in the 405 kyr band, which is another eccentricity period. A qualitatively similar effect is seen in Model 3 results (Appendix A5, Fig. A6), but the magnitude of the 405 kyr peak is strongly parameter-dependent. Thus, although obliquity affects the duration of individual glacial cycles, it plays no role in setting the 100 kyr periodicity. In other words, 100 kyr periodicity originates not from the fact that glacial cycles tend to last two or three obliquity cycles with equal probability as proposed by Huybers and Wunsch (2005), but, to the contrary, glacial cycles typically lasted two or three obliquity cycles because $2.5 \cdot 41 \sim 100$ kyr is the periodicity of eccentricity to which long glacial cycles of the late Quaternary are tightly phase-locked.

It is important to stress that, although a sharp peak at 100 kyr in the frequency spectra of the late Quaternary climate variability is successfully reproduced by several physically based models and is robust within a broad range of the parameters of conceptual models, this is a rather peculiar regime of operation of the Earth system. Such a regime is only possible for a "proper" combination of orbital forcing and key boundary conditions: position of continents, regolith distribution, and CO_2 level, among others. This is why this regime was established only about 1 Ma, and it is likely that it will change to another regime in the future due to the natural evolution of the Earth system.

4.4 Multiple equilibrium states of the climate–cryosphere system and escape from the glacial trap

As shown in the previous section, the conceptual model based on multiple equilibrium states successfully simulates Quaternary glacial cycles. The idea that the climate–cryosphere has several equilibrium states has a long history (e.g., Budyko, 1972; Weertman, 1976; Benzi et al., 1982). Multiple equilibrium states of the climate–cryosphere system have also been found in several models that explicitly included ice sheet components (e.g., Pollard and DeConto, 2005; Calov and Ganopolski, 2005; Robinson et al., 2012; Abe-Ouchi et al., 2013). These studies show that different ice sheets have very different stability diagrams in the phase space of orbital forcing, temperature, or CO_2. In the simplest case, the stability diagram of an ice sheet in the phase space of orbital forcing (maximum summer insolation at 65° N) is represented by two branches (glacial and interglacial) as in Model 3 (Fig. 11a). It is also common for illustrating purposes to depict such a bi-stable system in the form of double-well Lyapounov potential (Fig. 11b). Each well represents

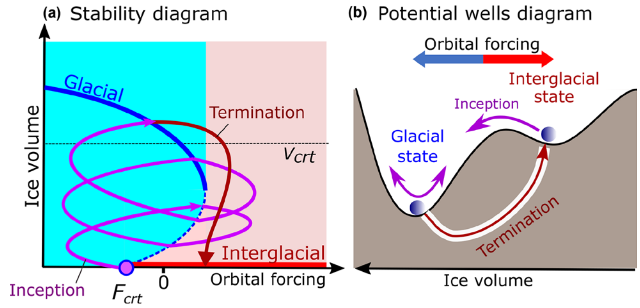

Figure 11. Generalized stability diagram of the climate–cryosphere system. **(a)** Phase portrait in orbital forcing (anomaly of maximum summer insolation at 65° N) space. The notations are the same as in Fig. 4a. **(b)** Two potential wells represent the glacial and interglacial states. The diagram corresponds to the average (zero) orbital forcing, while orbital forcing is considered here to be the external perturbation which moves the system from one equilibrium to another one. Glacial termination is depicted as the tunnel transition under the potential barrier separating two stable states.

one of the equilibrium states, and the depth of the wells represents the stability of each state. Since the shape of such a diagram depends on orbital forcing itself, the diagram in Fig. 11b shows potential for average orbital forcing, i.e., zero forcing anomaly.

If the system is in the interglacial state, it will remain in this state as long as the orbital forcing stays above the critical threshold value F_{crt}. This value depends on CO_2 concentration (Calov and Ganopolski, 2005; Archer and Ganopolski, 2005). In Ganopolski et al. (2016), this dependence on CO_2 has been systematically studied, and a simple logarithmic relationship between the critical value of insolation and CO_2 concentration has been found:

$$F_{crt} = \alpha \ln \frac{CO_2}{280} + \beta, \tag{8}$$

where α and β are constants. In the phase space of orbital forcing, glacial inception represents a bifurcation transition from the glacial to the interglacial state (Calov et al., 2005a). However, this transition is "abrupt" only in the phase space. In reality, because of the very long response time of the climate–cryosphere system to orbital forcing, the system's trajectory differs significantly from the stability diagram shown in Fig. 11a. However, when the system enters the glacial cycle, it tends to stay longer in the domain of the attraction of glacial equilibria even though insolation is below its critical value F_{crt} on average significantly less than 50 % of the time. Figure 11a illustrates this "irreversibility" of glacial inception. While such behavior is entirely consistent with the paleoclimate reconstructions, the principal question arises: if the glacial equilibrium is so stable, why does the Earth system rapidly move into the interglacial state instead of oscillating around the glacial equilibrium state? In other words, how does the Earth system escape its glacial trap? The stability diagram alone shown in Fig. 11a cannot explain such behavior because, as shown above, based on this stability diagram, Model 3 cannot simulate deglaciation without introducing an additional deglaciation regime shown in Fig. 11a by the red line. In Fig. 11b this deglaciation trajectory is shown as the transition through the potential barrier separating two wells. To some extent, this process is analogous to the quantum tunnel effect. This mechanism of escape from the glacial trap represents one of the key elements of the GMT and is discussed below.

4.5 Glacial terminations: the domino effect

The most serious challenge to the classical Milankovitch theory is the strong asymmetry of the glacial cycles during the late Quaternary. The domination of such long glacial cycles requires a relatively small ice sheet to survive periods of rather high summer insolation while larger ice sheets vanish completely even after modest insolation rise as happened, for example, at the onset of MIS 11 ca. 430 ka. The instability of the ice sheets after reaching a "critical size" has been postulated in P98 and is also essential for conceptual models described in this paper. The question is how to explain this instability and what critical size means. The analogy with the mechanical "domino effect" is helpful in answering these questions.

The domino is an example of a mechanical system with different equilibrium states and can respond to an external forcing both linearly and strongly nonlinearly (the domino effect) depending on one parameter value – the distance between the dominos. Let us consider a pendulum hitting the row of dominos, as shown in Fig. 12. If this distance between dominoes is even slightly larger than the height of dominoes, the pendulum will only knock down the dominoes within its reach. In this case, the number of dominoes that fall is proportional to the amplitude of pendulum oscillations. However, if the distance between dominoes is only slightly smaller than their height (this is the situation used in demonstrations of the domino effect), then all dominoes in the row will fall irrespective of the amplitude of pendulum oscillations.

The unstoppable retreat of the Northern Hemisphere ice sheets, which occurs in response to insolation rise and the final result of which (complete deglaciation) does not depend on the magnitude of insolation rise, resembles the domino effect. In this case, the analog for the distance between the dominoes is the critical size of ice sheets. Analysis of CLIMBER-2 model simulations suggests that the concept of critical size applies primarily to the North American ice sheet since the response of the smaller Eurasian ice sheet to orbital forcing is more linear. Other opinions exist; for example, Paillard and Parrenin (2004) attributed critical size to the Antarctic ice sheet.

What causes the domino effect in the case of supercritical ice sheets? It is likely that at least several processes and mechanisms must be considered to explain why a large North American ice sheet is so sensitive to insolation rise and can vanish at a timescale about or even shorter than 10 000 years.

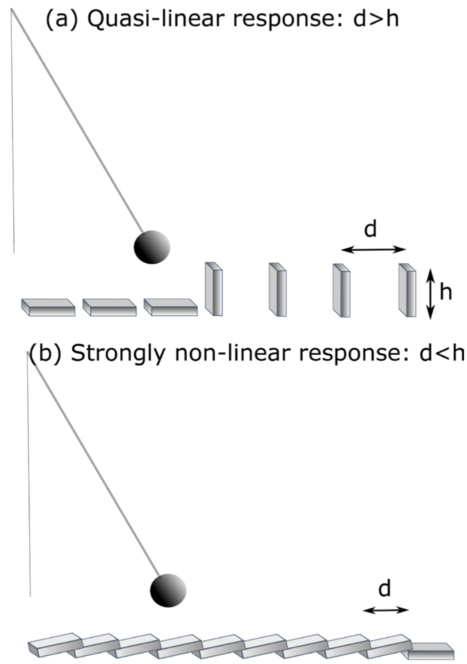

Figure 12. The domino effect.

1. A large North American ice sheet spreads over the vast areas covered by unconsolidated sediments (Great Lakes region, the western prairies of the US and Canada), where the ice sheet is thinner and flatter than over areas with exposed rocks. This is explained by a much larger basal sliding velocity over unconsolidated water-saturated sediments than bare rocks (e.g., Licciardy et al., 1998). This implies that the slope of a large ice sheet near its margins is less steep, and as a result, the ablation area is larger (Fig. 13a), which explains the higher sensitivity of the surface mass balance of such ice sheet to insolation and CO_2 rise.

2. The expansion of ice sheets over the areas covered by a thick terrestrial sediment layer leads to the production of a large amount of glaciogenic dust, which originates from the sediments transported beneath ice sheets across their margins (Mahowald et al., 2006; Ganopolski et al., 2010). A fraction of these sediments become airborne, and while this glaciogenic dust precipitates over the ice sheet, it significantly reduces surface reflectivity as the albedo of snow is very sensitive to even a tiny concentration of impurities. (Warren and Wiscombe, 1980; Dang et al., 2015). This, in turn, has a significant impact on the surface mass balance of ice sheets (Krinner et al., 2006; Willeit and Ganopolski, 2018) and causes the ice sheets to retreat earlier (Fig. 13b).

3. The weight of a mature ice sheet causes significant bedrock depression, roughly equal to 1/3 of the ice sheet thickness, i.e., reaches more than 1 km in the center of continental ice sheets. A typical timescale of the bedrock relaxation towards its unperturbed (approximately modern) state after the removal of the ice sheet is about 5000 years, which is small compared to the timescale of a glacial cycle (100 kyr) but is comparable to the timescale of glacial terminations (10 kyr).

   In the case of rapid retreat of ice sheets, delayed bedrock rebound facilitates surface melt. This is explained by the fact that, for the same thickness of ice sheet, the surface elevation in the ablation zone is lower in the case of delayed relaxation than it would be in the case of instantaneous bedrock adjustment (Fig. 13c). The role of delayed bedrock adjustment in the shaping of glacial cycles has already been demonstrated in Oerlemans (1980) and Pollard (1983). Simulations with a 3-D ice sheet model (Abe-Ouchi et al., 2013) confirmed that delayed bedrock adjustment is important for the complete deglaciations of the Northern Hemisphere at the end of each glacial cycle.

4. Another mechanism which can contribute to fast deglaciation is the so-called “marine ice sheet instability” (Weertman, 1974). This mechanism requires the base of the ice sheet to be located below sea level and the retrograde slope of bedrock (the elevation of bedrock decreases inland). This mechanism can cause a relatively rapid (millennial timescale) disintegration of a significant fraction of the ice sheet without significant surface mass loss. It was proposed that the Barents ice sheet disintegrated through this mechanism around the Bølling warm event (Brendryen et al., 2020).

5. The idea that the formation of proglacial lakes south of the ice sheets during their final retreat plays an important role during glacial terminations (Andrews, 1973) was also first tested in Pollard (1983). Large proglacial lakes are formed in depressions resulting from delayed bedrock relaxation in the process of fast ice sheet retreat. These depression areas are filled by the water from melting ice sheets, and their level can be well above sea level. The formation of the proglacial lakes leads to another mechanism of ice sheet instability which can be considered the freshwater analog of marine ice shelf instability (Quiquet et al., 2021; Hinck et al., 2022). The appearance of proglacial lakes causes a significant increase in the ice flux through the grounding line into the lakes (Fig. 13d). This ice then rapidly melts because it has a low elevation.

6. Rapid CO_2 rise during glacial terminations plays a role in tandem with the insolation rise during glacial terminations. The modeling study suggests that both factors play a comparable role in the ice sheet mass loss (Heinemann et al., 2014; Gregorie et al., 2015). The rapid melting of ice sheets during terminations results in large freshwater flux into the North Atlantic (0.1–0.2 Sv) sufficient to cause a prolonged shutdown of the AMOC, which in turn additionally contributes to the deglacial CO_2 rise and its overshoot at the end of deglaciation (Ganopolski and Brovkin, 2017). At the same time, AMOC shutdown during deglaciation causes anomalous cooling over Europe and slows down deglaciation (negative feedback). Additionally, subsurface warming induced by the AMOC shutdown can destabilize ice shelves in the North Atlantic realm (see below). The net effect of AMOC changes on deglaciation still has to be evaluated with adequate Earth system models.

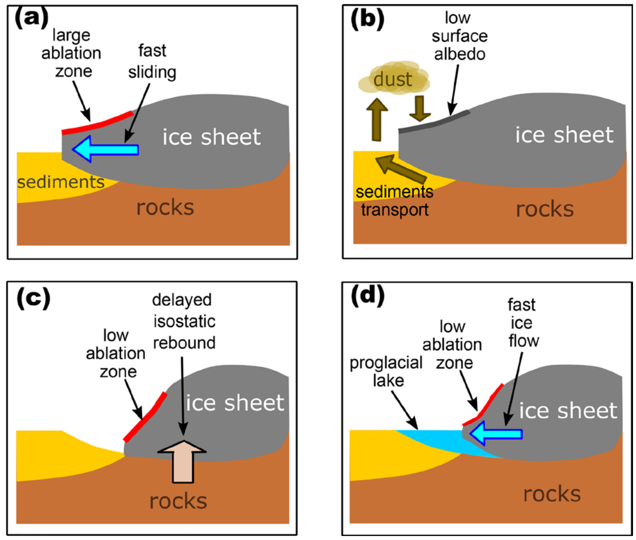

Figure 13. The principal elements of the termination mechanism: **(a)** faster ice sliding and lower elevation over sediment area; **(b)** effect of glaciogenic dust deposition on snow albedo and surface mass balance; **(c)** effect of delayed bedrock relaxation on the altitude of ablation zone; **(d)** effect of proglacial lakes on ice sheet mass loss.

All mechanisms discussed above are likely important for the domino effect. Each of the mechanisms discussed above should not necessarily be “catastrophic”, but when they work together, the combined effect can cause rapid disintegration of large continental ice sheets. It is also important to stress that none of these mechanisms are specific for the 100 kyr world – all of them also operated during the 41 kyr world and MPT. According to GMT, the difference between the 41 kyr world and 100 kyr world is in the critical size of ice sheets after exceedance of which the mechanisms discussed above lead to rapid deglaciation of the Northern Hemisphere.

4.6 The role of climate–carbon cycle feedbacks

It is generally recognized that CO_2 plays a vital role in the dynamics of glacial cycles. It is also important to distinguish between the "effect" of glacial CO_2 on climate variability and the role of carbon cycle feedback during glacial cycles. On geological timescales, the average CO_2 concentration is controlled by the interplay between volcanic outgassing and weathering rate. In turn, this concentration controls the amplitude of glacial cycles (Berger et al., 1999; Ganopolski and Calov, 2011; Abe-Ouchi et al., 2013), and for a sufficiently high CO_2 concentration, glacial cycles are not possible for a realistic range of the Earth's orbital parameters. This is why gradual lowering of the CO_2 concentration below a certain threshold was one of the preconditions for the onset of Quaternary glacial cycles (Willeit et al., 2015). After the CO_2 concentration dropped below this threshold and regular glacial cycles began, climate–carbon cycle feedback amplified glacial cycles, especially their 100 kyr component, and also globalized their impact on climate.

The quest for the mechanisms of glacial–interglacial CO_2 variability discovered thanks to the Antarctic ice cores (Petit et al., 1999; Lüthi et al., 2008) has attracted significant attention during the past 2 decades. However, the mechanisms of this variability are still not fully understood. Results of numerous modeling studies strongly indicate that there is no single mechanism that can explain most of the observed glacial–interglacial CO_2 changes of about 100 ppm, and it has become increasingly clear that at least several processes should be involved (e.g., Archer et al., 2000; Kohfeld and Ridgwell, 2009). Moreover, it is likely that the roles of geochemical (inorganic) and biogeochemical processes in glacial–interglacial CO_2 variability are of comparable importance (Galbraith and de Lavergne, 2019). It is much more certain that glacial CO_2 lowering can only be explained by the ocean carbon uptake since the terrestrial carbon pool was significantly depleted during glacial times due to the shrinking of the vegetation cover (Brovkin et al., 2012; Jeltsch-Thommes et al., 2019). It should be noted that, apart from the redistribution of carbon between atmospheric, land, and ocean pools, the disbalance between volcanic outgassing and weathering rate may also play a role in CO_2 variability at orbital and longer timescales.

It is known that the CO_2 concentration and global ice volume during the late Quaternary are highly correlated – the correlation coefficient between CO_2 and ice volume is above 0.7 for the last 800 kyr. However, the high correlation alone says nothing about causal relationships. Modeling studies suggest that the direct response of the carbon cycle to orbital forcing is weak. This is also supported by the fact that obliquity and precession components are relatively weak in CO_2 records of the late Quaternary. At the same time, modeling results demonstrate that strongly asymmetric glacial cycles with the dominant 100 kyr periodicity can be simulated even with a constant CO_2 concentration if this concentration is sufficiently low (Ganopolski and Calov, 2011; Abe-Ouchi et al., 2013). This is consistent with the concept that 100 kyr cyclicity originates from a nonlinear response of the climate–cryosphere system to orbital forcing and that the climate–carbon cycle feedback amplifies the 100 kyr component of glacial cycles (Ganopolski and Brovkin, 2017). However, while the influence of CO_2 through climate on global ice volume is rather straightforward, the influence of ice sheets on CO_2 concentration is far from trivial. The most direct effect of ice sheet growth on CO_2 is through the decrease in the ocean volume, which leads to the effect opposite to the observed CO_2 changes. Indeed, the decrease of the ocean volume by ca. 3 % at the LGM would cause CO_2 to rise by about 10 ppm. In addition, the growth of ice sheets reduces forest area in the boreal zone, which should also cause a CO_2 rise. The direct effect of ice sheets on the carbon cycle, which can contribute to the glacial CO_2 drawdown, is regional cooling due to higher albedo of ice sheets. This cooling leads to a lowering of ocean temperature, mainly in the vicinity of the ice sheets, and contributes to CO_2 decrease through the solubility effect. However, changes in ice sheet area primarily affect the climate of the Northern Hemisphere, and even the total solubility effect (including lowering of CO_2 and other GHG concentrations) explains not more than 30 ppm of glacial CO_2 decrease (Brovkin et al., 2007; Kohfeld and Ridgwell, 2009).

In addition to global ocean volume change, ice sheets can affect CO_2 through global sea level change. First, this leads to a change in ocean alkalinity through the dissolution or regrowth of shallow-water carbonates, particularly in the form of corrals (Ridgwell et al., 2003). Higher alkalinity, which results from the sea level drop, increases ocean capability to absorb atmospheric CO_2 and thus contributes to glacial CO_2 drawdown. Second, exposed shelves may represent significant additional sources of aeolian dust, and enhanced dust deposition can intensify marine biological productivity in the Southern Ocean, which is iron-limited (Martin, 1990; Watson et al., 2000; Yamamoto et al., 2019). Third, due to the peculiar oceanic hypsometry, even a relatively small initial sea level drop leads to a significant increase in land area. This not only contributes to additional global cooling but also leads to an expansion of vegetation cover and thus serves as the carbon uptake. The latter can work only during the initial phase of glacial cycles because, under full glacial conditions, global decline in terrestrial biomass due to ice sheet expansion and CO_2 lowering overwhelms the effect of land area increase. In this way, there are at least several mechanisms through which ice sheets can cause changes in CO_2 coeval with ice volume changes.

This initial response of atmospheric CO_2 to ice sheet evolution is amplified by several climate–carbon cycle feedbacks: (1) enhanced ocean carbon uptake due to cooling, i.e., solubility effect, in addition to the effect caused by ice sheet growth; (2) the effect on ocean carbon storage caused by changes in the ocean circulation, stratification, and sea ice cover, leading to changes (reduction) in the deep ocean ventilation; and (3) a change in the remineralization depth caused by ocean thermocline temperature lowering, which affects organic carbon flux into the deep ocean. Although the operation of the global carbon cycle during glacial times is still not fully understood, it is likely that the direct effect of ice sheets on CO_2 and the effect of its amplification via climate–carbon cycle feedbacks are of comparable importance.

4.7 Glacial cycles of the early Quaternary (41 kyr world)

Prior to the MPT (ca. 1.2–0.8 Ma), glacial cycles had a smaller magnitude (50 % when compared to the late Quaternary in terms of benthic δ^{18}O), and the dominant periodicity was 41 kyr, which is the periodicity of obliquity with very little energy in the 100 kyr and precession bands (Fig. 2). According to the GMT, a shorter periodicity and smaller magnitude of early Quaternary glacial cycles are explained by the fact that the critical size of ice sheets, which makes the Earth system prone to deglaciation, was smaller before the MPT than after. The most likely explanation for that (see also the next section) is the gradual removal of terrestrial sediments from North America by glacial erosion (Clark and Pollard, 1998). The thick terrestrial sediments make ice sheets more mobile since "temperate" ice (ice at the pressure melting point) moves much faster over sediments than over bare rocks. Thus, the presence of thick sediments allows ice sheets to spread faster and makes them thinner, which also explains the larger sensitivity of ice sheet mass balance to orbital forcing. In addition, the spreading of ice sheets over terrestrial sediment led to the production of a large amount of glaciogenic dust, some of which was then deposited over ice sheets, making them darker and thus increasing surface ablation (Ganopolski and Calov, 2011). As a result, the early Quaternary ice sheets were able to reach their critical size during just one obliquity cycle. Since glacial cycles were much shorter, these cycles look more symmetric than the late Quaternary cycles, but this does not mean that the response of the Earth system to orbital forcing was linear, and it is likely that all elements of the domino effect also operated during glacial terminations of the early Quaternary.

While the dominance of the obliquity component in ice volume variations during the early Quaternary is not surprising and is reproduced in model simulations (Ganopolski and Calov, 2011; Willeit et al., 2019), a strong precession component is also clearly present in the spectra of simulated ice volume. At the same time the precession component is essentially absent during the early Quaternary in many paleoclimate reconstructions, including the canonical LR04 benthic stack. This mismatch is often considered another unsolved problem ("mystery") of the Milankovitch theory (Raymo and Nisancioglu, 2003). A number of explanations for the lack of precession components prior to MPT have been proposed, including the possibility of mutual compensation of precession components originating from the evolution of southern and northern ice sheets (Raymo et al., 2006). However, in recent years, a precession signal during the early Quaternary has started to emerge in paleoclimate records (e.g., Shakun et al., 2016; Liautaud et al., 2020; Barker et al., 2022), and there may be an inherent issue with absolute dating of old paleoclimate records. Appendix A6 illustrates how a simple "orbital tuning" can nearly completely eliminate the precession signal from the ice volume record. However, there is another often overlooked aspect of the 41 kyr mystery: it is generally assumed that the entire Quaternary records are dominated by ice volume variability. While about $2/3$ of benthic δ^{18}O variability (or 80 % in spectral power) is attributed to global ice volume change during the late Quaternary, results of model simulations (Willeit et al., 2019) show that the relative contribution of ice volume to benthic δ^{18}O was only about $1/3$ (or only 20 % in the frequency spectra) before the MPT. This is consistent with Elderfield et al. (2012), which also found that the relative contribution of deep ocean temperature to δ^{18}O prior to MPT was significantly higher than 50 %. This would change the 41 kyr mystery from the challenge of explaining the absence of precession component in global ice volume (which is indeed hard to explain) to the question of why the deep ocean temperature does not contain much precession variability. The latter is a different problem since the deep ocean temperature is controlled by different factors than the ice volume, primarily by CO_2 concentration. Since CO_2 concentration over the past 800 kyr contains very little precession variability (e.g., Petit et al., 1999), it would be natural to assume that this was also the case during the early Quaternary. Thus, the 41 kyr mystery cannot be considered a fundamental problem of the Milankovitch theory.

4.8 Three Quaternary regime changes: PPT, MPT, and MBT

During the past 3 million years, climate variability at orbital timescales revealed three distinct changes in the mode of operation. The first one, referred to as the Pliocene–Pleistocene transition (PPT), is the onset of regular glacial cycles with the dominant 41 kyr periodicity, which happened between 2.8 and 2.7 Ma, i.e., significantly earlier than the "official" stratigraphic Pliocene–Pleistocene border (2.58 Ma). The second transition, the mid-Pleistocene transition (MPT) from the 41 to 100 kyr world, occurred between 1.2 and 0.8 Ma. The third transition, clearly seen only in some paleoclimate records (such as δ^{18}O and CO_2), is referred to as the mid-Brunhes transition[2] and manifests itself in the differences between interglacials before and after MIS 11.

The onset of Quaternary glacial cycles was preconditioned by the general Cenozoic cooling trend (Raymo and Ruddiman, 1992) caused by decreasing CO_2 concentration and

[2] Since no real "event" is associated with this transition, the term MBT seems to be more appropriate than the traditional term "mid-Brunhes event".

the poleward advance of North America during the Cenozoic epoch (Daradich et al., 2017). Several additional proximal causes, including the closing, opening, or deepening of different oceanic gateways and establishing of North Pacific stratification, have been proposed to explain the PPT (e.g., Ruddiman and Raymo, 1988; Cane and Molnar, 2001; Haug and Tiedemann, 1998; Haug et al., 2005) but the role of these events in the onset of Quaternary glacial cycles is not clear. At the same time, it has been shown (Willeit et al., 2015) that even a gradual downward CO_2 trend alone is sufficient to cause the transition from an essentially ice-free Northern Hemisphere to glacial cycles of medium amplitude after the PPT. The critical value of CO_2 concentration of 350–400 ppm, below which regular glaciations in the Northern Hemisphere can begin (Ganopolski et al., 2016), is consistent with the recent CO_2 reconstructions during the PPT (Martínez-Botí et al., 2015).

In the 1.5 million years which followed the PPT, the magnitude of glacial cycles increased gradually, but the dominant periodicity (41 kyr) remained unchanged. However, between 1.2 and 0.8 Ma, climate variability recorded by δ^{18}O changed dramatically from relatively symmetric cycles of the 41 kyr world to strongly asymmetric 100 kyr cycles. The magnitude of glacial cycles expressed in the standard deviation of benthic δ^{18}O doubled across the MPT (Lisiecki and Raymo, 2007).

The MPT has been attributed by Clark and Pollard (1998) to a gradual evolution of terrestrial sediment cover over northern continents (the so-called “regolith hypothesis”). This hypothesis is based on the empirical fact that at present large areas of northern North America and Eurasia are characterized by a thin layer of terrestrial sediments or exposed crystalline rocks, while the rest of these continents are covered by kilometer-thick terrestrial sediments. Since the areas of thin sediments and exposed bedrock coincide with the areas covered by ice sheets most of the time during the Quaternary, it is natural to assume that, prior to the Quaternary, these areas were also covered by a thick sediment layer which was then gradually removed by glacial erosion processes. In turn, the underlying surface type (crystalline rocks or unconsolidated terrestrial sediments) strongly affects ice sheet dynamics as ice can slide much faster over sediments (compared to rocks) when the temperature at the base of ice sheets reaches the pressure melting point. This can explain why ice sheets of the early Quaternary were thinner and thus more susceptible to insolation changes. As a result, ice sheets during the early Quaternary responded to orbital forcing in a more linear manner without any appreciable contribution from the eccentricity cycles. The appearance of large areas of exposed crystalline rocks about 1 million years ago led to the formation of thick and slower-spreading ice sheets with a narrower ablation zone. The latter helped ice sheets to survive several insolation maxima before they spread deep enough into the sediment-covered areas, which made them prone to a rapid collapse during insolation rise. In Ganopolski and Calov (2011) we proposed an additional mechanism that might contribute to the MPT and which is also related to the removal of the regolith layer from the northern continents. This mechanism is based on the fact that, when ice sheets spread over the areas covered by terrestrial sediments, they produce a significant amount of glaciogenic dust, which, in turn, affects surface albedo and ablation (see Sect. 5.5). While this mechanism operated through the entire glacial cycle before the MPT as northern continents were covered by terrestrial sediments, ice sheets spread over the sediment-covered areas only after they approached their critical size after the MPT. Both these mechanisms were incorporated into the CLIMBER-2 model and contributed to the realistic simulation of MPT (Willeit et al., 2019).

It has also been shown by Willeit et al. (2019) that even a gradual expansion of the sediment-free areas from zero to the present one over the past 1500 kyr can explain a relatively rapid transition (over several hundred thousand years) from the 41 to 100 kyr regime. In other words, it has been shown that there is a critical threshold for the exposed rock area, crossing of which leads to the transition from 41 kyr cyclicity to 100 kyr cyclicity. It has to be noted that a gradual reduction of the CO_2 concentration during the Quaternary is considered by some authors (e.g., Berger et al., 1999) to be a possible cause of MPT, but according to Willeit et al. (2019), it is not an alternative mechanism of MPT but rather an important precondition for the onset of long glacial cycles, since for high CO_2 concentrations, only relatively weak and short glacial cycles are possible even for the present-day regolith distribution (Fig. S9 in Willeit et al., 2019). Thus, the onset of the 100 kyr world has been preconditioned both by CO_2 decline and regolith removal. However, the timing of the MPT was likely set by the regolith removal since there is no strong evidence for the decline of the CO_2 level directly prior to the MPT (Hönisch et al., 2009; Chalk et al., 2017; Yamamoto et al., 2022).

Apart from regolith removal and CO_2 lowering, several other mechanisms have been proposed to explain the MPT. For example, it has been speculated that this regime change in glacial climate variability may have been related to changes in the operation of the global carbon cycle and ocean circulation (e.g., Chalk et al., 2017; Farmer et al., 2019; Hasenfratz et al., 2019). However, it is also possible that observed changes in any paleoclimate proxy across the MPT can result from the increase in the magnitude of glacial cycles (i.e., ice volume variations) and not be the cause of this change. It is also likely that the larger magnitude of sea level and temperature fluctuations after the MPT can also explain the expansion of the marine-based Antarctic ice sheet (Ford and Raymo, 2020; Sutter et al., 2019). Only results of Earth system model simulations can confirm or reject a possible contribution of all these mechanisms to the MPT.

The last transition – MBT – is less clearly defined, and the number of long glacial cycles before and after the MBT is too small to obtain robust statistics. The most apparent change across the MBT is seen in $\delta^{18}O$ and CO_2 during interglacials. These differences are consistent with the idea that pre-MBT glacial terminations were “incomplete” and that a certain amount of “glacial” ice (ca. 10–20 m in sea level equivalent) remained in ice sheets and/or ice caps in the Northern Hemisphere outside of Greenland during pre-MBT interglacials. This amount of ice, in combination with a lower interglacial CO_2 concentration, explains the difference in $\delta^{18}O$ of about 0.3 ‰ between Holocene and corresponding values during MIS 15 and MIS 19 interglacials. Interglacials MIS 13 and 17 were even colder, and a significant amount of ice (20 to 40 in meters of sea level equivalent) would be required to explain observed $\delta^{18}O$ differences.

The cause of MBT remains unclear. Although orbital forcing during the intervals 800–400 and 400–0 ka was not identical, there is no obvious reason why pre-MBT terminations were incomplete. One possible explanation for MBT is that glacial cycles of the late Quaternary were affected by glacial erosion not only through gradual regolith removal but also through the curving of straights, fiords, and bays. It is believed that such important features of modern geography as Hudson Bay and Hudson Straight were formed by glacial erosion very recently (on the geological timescale). Pronounced Heinrich-type events were only observed since MIS 12 (Hodell et al., 2008). This type of landscape evolution would lead to the development of fast-moving ice streams over North America, reducing the height of Laurentide ice sheets and facilitating complete deglaciations of the northern continents during post-MBT glacial terminations.

4.9 Forced events versus internal oscillations

As discussed above, formally, there are two different types of conceptual models that can simulate 100 kyr cycles. In the first type, glacial cycles represent self-sustained oscillations with a period close to 100 kyr and which do not require the existence of orbital forcing. In the second type of conceptual model, glacial cycles represent a strongly nonlinear response of the Earth system to orbital forcing. In this case, 100 kyr periodicity is related to eccentricity, and glacial cycles cannot exist without orbital forcing. Note that CLIMBER-2 and our conceptual models (Models 2 and 3) are of the second type. Moreover, so far, none of the Earth system models have been able to simulate 100 kyr long self-sustained internal oscillations.

Deciding which one of these two concepts is correct solely based on the analysis of paleoclimate data is problematic because orbital forcing is always present, and thus it is impossible to conclude whether it is necessary to drive glacial cycles. However, there is one feature of modeled glacial cycles that can be used to distinguish between these two mechanisms. This feature is related to the role of system memory. For self-sustained oscillations, such memory is crucial, and it is not possible for the model’s prognostic variables (e.g., ice volume) to stay constant for a finite time. This is akin to a mechanic clock – it cannot stop for awhile and then resume its work without external influence. On the contrary, in models with forced oscillations (like Model 3), constant (zero) ice volume can stay constant for any duration of time until orbital forcing crosses the glaciation threshold. What do paleoclimate data tell us in this respect? The paleoclimate records suggest that at least during three recent interglacials (Holocene, Eemian, and MIS 11), sea level, CO_2, and other climate characteristics remained nearly constant over a rather long time (ca. 10 kyr during the Holocene and Eemian and probably about 20 kyr during MIS 11). Moreover, under a weak orbital forcing, the Earth system can stay in the interglacial state even longer. According to model simulations (e.g., Loutre and Berger, 2000; Ganopolski et al., 2016) at present, the Earth system is in an unusually long interglacial, which can naturally last (without any anthropogenic influence) for as long as another 50 000 years (i.e., more than two precession cycles). Such a long interglacial never occurred during the previous million years but can happen several times during the next million years (Talento and Ganopolski, 2021). Such long interglacials are inconsistent with the self-oscillatory mechanism of glacial cycles.

4.10 Are glacial cycles “predictable”?

It has been argued (e.g., Crucifix, 2013; Ashwin et al., 2018) that late Quaternary glacial cycles are entirely or at least partly random and therefore “unpredictable”. Since predictability of future glacial cycles cannot be tested in the foreseeable future, the term “predictability” can only be used in an operational sense, i.e., whether an accurate and robust hindcast of past glacial cycles is possible. In practice, this can be formulated as follows: can one expect that a sufficiently “realistic” Earth system model forced solely by orbital variations can reproduce not only the statistical characteristics of past glacial cycles (e.g., amplitude and typical periodicities) but also the correct timing of individual cycles. This would be highly unlikely if glacial cycles are totally unpredictable.

However, the results obtained with the process-based models of different complexity show that not only the statistics but also the timing of the late Quaternary glacial cycles can be accurately reproduced when driving models by orbital forcing alone (Pollard, 1983; Berger et al., 1999; Ganopolski and Calov, 2011; Abe-Ouchi et al., 2013; Willeit et al., 2019). The latter study also demonstrates a weak dependence of the simulated glacial cycles on the initial conditions. These modeling results strongly indicate that glacial cycles are at least quasi-deterministic and thus predictable in principle. This does not contradict the fact that different model solutions can be obtained when using different initial conditions or model parameters. Model simulations show that the timing of some terminations is more robust than others. For example, in Willeit et al. (2019), although the timing of most glacial terminations was robust across the large ensemble of simulations, the last glacial termination occurred earlier than in reality in some model runs.

4.11 Antarctic ice sheet

The previous discussion was mostly restricted by the evolution of the Northern Hemisphere ice sheets. Of course, such a northern-centric approach is only applicable to the direct ice sheet response to the orbital forcing. The carbon cycle–climate feedback which amplifies and globalizes this response is truly global, and, in particular, the Southern Ocean plays an important role in driving glacial–interglacial CO_2 variations. Still, it would be natural to ask about the role of the Antarctic ice sheet (AIS) in glacial cycles, which is by far the largest ice sheet at present.

According to the GMT, the evolution of AIS during glacial cycles represents a passive response to two factors driven from the north: sea level change and GHG concentration variations. Both factors – sea level drop and ocean cooling – led to the turning of the ice shelf into grounding ice. The current estimates of the LGM contribution to the global ice volume are usually within the range of 5–15 meters of sea level equivalent (e.g., Briggs et al., 2014), which is, on average, about 10 % of the "glacial excess" of the global ice volume. This makes AIS a medium amplifier of the glacial cycles forced from the north. The impact of the Antarctic ice sheet expansion on the atmospheric CO_2 through the brine rejection process has been proposed (Bouttes et al., 2012), but this hypothesis should still be tested with realistic ESMs. This is, however, not a trivial task since such models have problems with simulation even of the present-day mode of Antarctic Bottom Water formation.

4.12 Simple rule to determine the timing of glacial terminations

The general concept of GMT allows formulating a very simple rule for the timing of the late Quaternary glacial terminations: glacial terminations occur during periods of rising boreal summer insolation if the previous precession insolation maximum occurred during low eccentricity and was in antiphase with obliquity.

To exclude a few false "positives", an additional constraint is required, namely that glacial termination cannot occur in less than 60 kyr after the previous one. To construct a numerical algorithm for this rule, "low eccentricity" is defined as the interval ±25 kyr around each local eccentricity minimum. "Antiphase with obliquity" means here that the precession maximum occurs any time when obliquity is below its average value. The minimum rate of insolation growth sufficient for triggering deglaciation is set to a small value of $1\,\mathrm{W\,m^{-2}}$ in 1000 years. As Fig. 14 shows, this very simple rule works rather well for the last 900 kyr. Nine of 10 glacial maxima of the late Quaternary are predicted with dating accuracy, i.e., 10 kyr. The only exception is Termination VIII

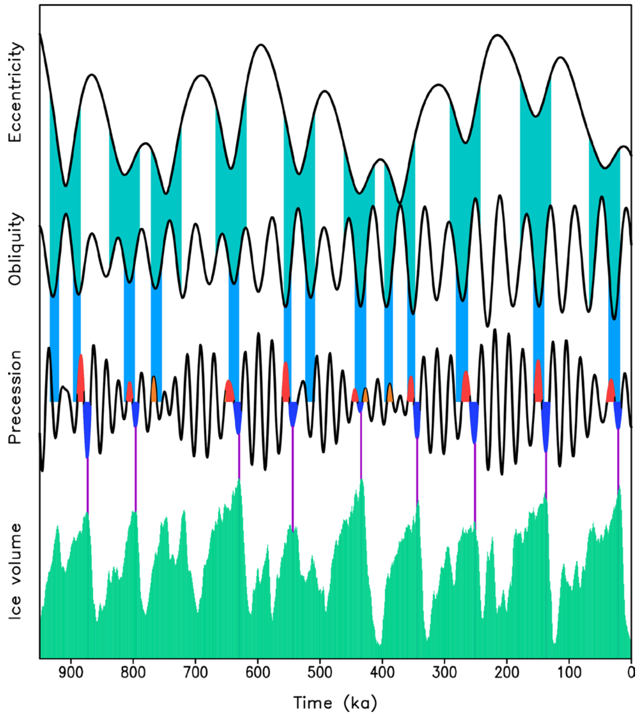

Figure 14. A simple rule to determine the timing of glacial terminations. Grey shaded areas correspond to periods of low eccentricity and light blue to the periods of low obliquity during low eccentricity; red shading on the precession forcing curve highlights positive precession anomalies satisfying GMT criteria, and blue shading corresponds to following precession minima during which critical ice volume was reached (purple vertical line), and deglaciations start soon after these insolation minima. Orange shading on the precession curve corresponds to "false" positives, i.e., the cases when conditions of the termination rule are met, but they occurred earlier than 60 kyr after the previous termination. The lower curve is the LR04 benthic δ^{18}O stack.

at around 720 ka, which this rule does not predict. This termination is unusual as it began at around the obliquity minimum. It is noteworthy that neither CLIMBER-2 nor conceptual models (Model 2 and 3) have problems with simulating the correct timing of Termination VIII.

4.13 Short summary of GMT

According to the GMT, Quaternary glacial cycles represent the direct, strongly nonlinear response of the Earth system to variations of summer insolation in boreal latitudes of the Northern Hemisphere. This nonlinear response to orbital forcing is strongly modified and amplified by several processes and feedbacks. The existence of Quaternary glacial cycles, especially the strongly asymmetric late Quaternary cycles, is a peculiar and possibly absolutely unique feature of the current Earth system "configuration". This explains significant difficulties in modeling and understanding Quaternary climate dynamics.

The onset of Quaternary glacial cycles was preconditioned by changes in the Earth's geography due to continental drift and by a gradual lowering of CO_2 concentration, which eventually brought the Earth system into the state when insolation variations caused regular glaciations of the Northern Hemisphere. Before ca. 1 Ma, medium-amplitude glacial cycles terminated each time positive insolation anomalies due to precession and obliquity components of orbital forcing were in phase, which led to the dominance of obliquity (41 kyr) periodicity. The precession component of orbital forcing also played an essential role in driving early Quaternary glacial cycles, even if this periodicity is not detected in global ice volume reconstructions.

Gradual removal of terrestrial sediments from the northern continents by glacial erosion processes brought the Earth system into a new regime of operation when the dominant periodicity of glacial cycles shifted from 41 to 100 kyr. This regime change is explained by the fact that a large area of exposed rocks in Northern America combined with relatively low CO_2 allowed medium-sized ice sheets to survive periods of high summer insolation and reach a much larger size and volume than the ice sheets of the early Quaternary. However, after reaching some critical state, a combination of several processes and feedbacks which are strongly dependent on the ice sheet size made such ice sheets unstable under boreal summer insolation rise. This led to rapid deglaciations, which explains the strong asymmetry of the late Quaternary glacial cycles. Since the critical ice sheet size can most likely be reached during periods of low eccentricity when one "positive" precession cycle is compensated for by a "negative" obliquity cycle, the glacial termination occurs during or after periods of low eccentricity. As a result, glacial cycles became phase-locked to short (100 kyr) eccentricity cycles, and this explains the sharp 100 kyr peak in the frequency spectra of the late Quaternary glacial cycles.

5 Discussion and conclusions

The central premise of the Milankovitch theory, namely that boreal summer insolation variations are the principal driver of Quaternary glacial cycles, was supported first by analysis of paleoclimate records which reveal the presence of all expected astronomical periodicities and then by modeling results which confirmed that these variations could cause waning and waxing of the continental ice sheets in the Northern Hemisphere. Thus, the Milankovitch theory in its original form has been confirmed, but paleoclimate records also revealed a number of important facts that were not known during Milankovitch's life and which his theory was not able to explain. The first one is that the late Quaternary is dominated by strongly asymmetric glacial cycles with the dominant 100 kyr cyclicity. The explanation for these cycles has attracted significant attention and continues to be regarded by some researchers as a challenge. In fact, the temporal dynamics of the late Quaternary glacial cycles, including the timing of glacial terminations and frequency spectra of climate variability, have already been successfully reproduced with a number of climate–ice models of different complexity ranging from simple 1-D models to a comprehensive Earth system model. In these model simulations, the dominant peak at 100 kyr periodicity in the frequency spectrum of ice volume is explained by the phase locking of long glacial cycles of the late Quaternary to 100 kyr eccentricity cycles. The eccentricity, in this case, serves as a pacemaker for the precession- and obliquity-driven glacial cycles, and the minuscule changes in global annual mean insolation associated with eccentricity cycles play no role here. The real forcing of glacial cycles is large (50–100 $W\,m^{-2}$) changes in boreal summer insolation with precession and obliquity periods.

The idea that 100 kyr cyclicity originates from some strongly nonlinear response of the Earth system to the amplitude modulation of the precessional component of orbital forcing by the eccentricity, of course, is not new. However, it is important to emphasize that the late Quaternary glacial cycles cannot be explained simply by a nonlinear response because an arbitrary nonlinear response to orbital forcing should contain all eccentricity periodicities (95, 124, 400 kyr) as in the case of the Imbrie and Imbrie model, for example. In reality, only a single sharp peak at ca. 100 kyr is observed in the late Quaternary ice volume frequency spectrum. Thus, explaining paleoclimate records requires a very special type of nonlinearity. A number of simple and comprehensive models possess such nonlinearity and are thus able to reproduce the late Quaternary glacial cycles in good agreement with the paleodata. One of the main tasks of the GMT is to explain how such nonlinear responses originate from known processes and feedbacks operating in the Earth system, in particular what determines the critical size of the Northern Hemisphere ice sheets by reaching which they rapidly melt and disintegrate in response to rising boreal summer insolation. Understanding which processes in the Earth system explain such a response is one of the main challenges of contemporary Quaternary climate dynamics. The mechanism of this instability, named a domino effect by analogy with a simple mechanical system, is discussed above and based on the results of CLIMBER-2 and several other studies. Due to the complexity of the processes associated with glacial terminations and the absence of their analogies in present-day climate, a better understanding of the mechanism of glacial terminations requires further studies with comprehensive ESMs.

The processes which convert the seasonal and regional changes in insolation into global climate changes are now reasonably understood, and the Arrhenius idea about the role of CO_2 in ice ages is confirmed. Modeling studies show that the lowering of CO_2 by ca. 100 ppm, reinforced by CH_4 and N_2O drops, explains about half of the maximum glacial cooling, currently estimated at 5–6 °C, while the rest is attributed primarily to ice sheet expansion and sea level drop. It has been shown that CO_2 also plays an important role in amplifying glacial cycles. This aspect of glacial cycles is still lacking a satisfactory explanation. Most studies to date were devoted to simulations of the low CO_2 level at the LGM, and the CO_2 radiative forcing has been prescribed in such studies. While such simulations are useful for testing the capability of modern ESMs to reproduce the carbon cycle response to glacial climate forcings, they do not answer the question of how the ice sheet–climate–carbon cycle feedback loops operated during the late Quaternary. The "stew" of the processes playing a role in glacial–interglacial CO_2 variability has been discussed but still remains tentative and requires further studies with comprehensive Earth system models.

Another widely discussed challenge for the GMT is the nature of the 41 kyr world and the mechanism of the MPT. The difference between the early Quaternary 41 kyr world and the late Quaternary 100 kyr worlds can be solely explained by a gradual increase in the critical size of the ice sheets. As a result, glacial cycles, which are initially locked to obliquity cycles, became locked to the shortest eccentricity cycle. The most straightforward explanation for the increase in critical size is the removal of terrestrial sediments from the northern continents by glacial erosion. This mechanism alone allows reproducing the relatively sharp transition from the 41 to 100 kyr world in the models. The only obvious discrepancy with reality is that in all model simulations, the 41 kyr world contains a clear precession presence, while paleoclimate proxies usually show very little of such presence. The explanations for the lack of precession in the 41 kyr world range from physical mechanisms (antiphase response to the precession of the ice sheets in the Northern and Southern Hemisphere) to interpretation problems (much larger contribution to δ^{18}O temperature signal) or some problems with the processing of paleoclimate data (like orbital tuning). In any case, this is an interesting but not critical issue for understanding how the Earth system responds to orbital forcing.

A comprehensive understanding of the mechanism of Quaternary climate variability still represents a formidable scientific challenge since this is a genuinely multidisciplinary problem. It is additionally complicated by the fact that present-day observational data provide insufficient constraints on the models used for paleoclimate studies, while paleoclimate records usually contain only indirect and incomplete information about past climate changes. Nevertheless, almost a century after the publication of Milankovitch's fundamental work, a framework for the generalized Milankovitch theory has emerged.

Appendix A

A1 Different metrics for orbital forcing

As shown for the first time by Milutin Milankovitch, changes in eccentricity, obliquity, and precession cause the substantial redistribution of insolation between latitudes and seasons. The comprehensive visualization of orbital forcing requires a 3-D plot (latitude – day of the year – time in years before or after present), which is impractical. Instead, different metrics for the orbital forcing were proposed. Milutin Milankovitch used the so-called caloric summer half-year insolation as a metric for orbital forcing, i.e., insolation integrated over the half-year with the highest insolation. In post-Milankovitch times, it became common to use June or July insolation at 65° N (e.g., Berger, 1978), although caloric half-year insolation is also used (e.g., Tzedakis et al., 2017). It is important to realize that using the modern calendar for defining orbital forcing on orbital timescales is problematic because the same calendar month in different years corresponds to different Earth positions relative to the perihelion and aphelion (e.g., Kutzbach and Gallimore, 1988). This is why it is advisable to define the metric for orbital forcing in a way that does not depend on the choice of calendar. Examples for such definitions are maximum summer insolation used in this paper or insolation averaged over a certain period of time, e.g., caloric half-year insolation originally used by Milankovitch. Examples of different insolation curves for 65° N are shown in Fig. A1.

Experiments with the CLIMBER-2 model show that during the late Quaternary, the rate of changes ($\mathrm{d}v/\mathrm{d}t$) in the Northern Hemisphere ice volume, which is primarily related to the surface mass balance of ice sheets, is most correlated with the maximum summer insolation at 65° N. When performing the same analysis but for reconstructed global sea level (Spratt and Lisiecki, 2016), which represents the global ice volume, the best correlation is found for the 65° N insolation average over the 4 months with the highest insolation (i.e., roughly MJJA). However, as Fig. A1 shows, the difference between maximum summer insolation and 4-month insolation is relatively small in obliquity and precession relative contribution. It is thus important to note that neither our model nor data suggest that caloric summer half-year insolation is the best proxy for orbital forcing. This can be explained by the fact that most of the ice melt (both at present and during glacial cycles) occurs only during a few summer months. Both precession and obliquity play essential roles in all computed insolation curves. The quantitative difference is that for the caloric half-year insolation, the contributions of precession and obliquity are comparable most of the time. In contrast, for the maximum summer insolation, the obliquity component is comparable with precession only during periods of a relatively low eccentricity.

However, there is one metric of orbital forcing which contains very little precession variability and is often used for the interpretation of paleoclimate records. This is the so-called "integrated summer insolation" proposed by Huybers (2006) and which is defined as

$$S = \sum_i I_i \text{ for } I_i > I_0, \tag{A1}$$

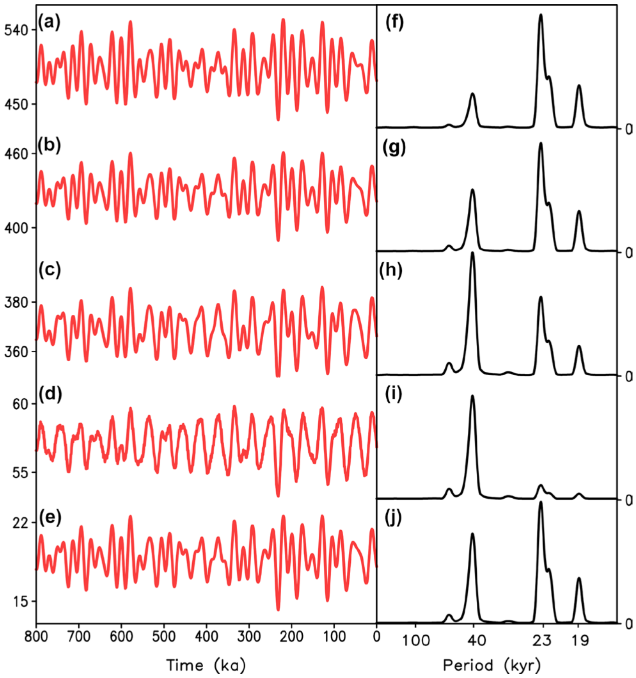

Figure A1. Different proxies for orbital forcing. **(a–e)** Insolation at 65° N during the past 800 kyr and **(f–j)** corresponding frequency spectra. **(a, f)** Maximum summer insolation; **(b, g)** insolation averaged over 4 months with the highest insolation; **(c, h)** insolation averaged over 6 months with the highest insolation (the equivalent of caloric half-year energy but in different units); **(d, i)** "summer energy" computed according to Huybers (2006); (e, j) summer energy computed according to Eq. (A1). Insolation **(a–c)** is in $\mathrm{W\,m^{-2}}$, and summer energy **(d, e)** is in KJ. Frequency spectra are in arbitrary units.

where I_i is the daily insolation at 65° N and I_0 is a constant value set to $275\,\mathrm{W\,m^{-2}}$ in Huybers (2006). This choice of the metric for orbital forcing is justified by the fact that seasonal variations of temperature over land and insolation are rather similar (with about a 1-month lag of temperature behind insolation) and that the melt rate of ice sheets is often parameterized through the so-called positive degree day index defined as $\mathrm{PDD} = \sum_i T_i$ for all daily temperatures $T_i > 0$ (Fig. A2) . However, to correctly translate insolation into PDD index, one should consider the fact that for an arbitrary temperature scale, PDD should be defined as $\mathrm{PDD} = \sum_i (T_i - T_0)$. $T_0 = 0\,°\mathrm{C}$ only for the Celsius temperature scale, and thus T_0 can be omitted in the formula for PDD. However, for example, in the case of the Kelvin temperature scale $T_0 = 273.15\,\mathrm{K}$. Therefore, PDD should be expressed through the insolation as

$$S = \sum_i (I_i - I_0) \text{ for } I_i > I_0. \tag{A2}$$

Obviously, this formulation is significantly different from the original integrated summer insolation (compare Fig. A1d and e), and similarly to other metrics for orbital forcing it contains a strong precession signal. Thus, none of the physically meaningful metrics for orbital forcing are free of a strong precession component, which is important for discussions of the nature of the 41 kyr world.

A2 Imbrie and Imbrie conceptual model

One of the first and most well-known conceptual models of late Quaternary glacial cycles is the Imbrie and Imbrie (1980) model. This model has been applied for the orbital tuning of the widely used LR04 record (Lisiecki and Raymo, 2005). The model is represented by a single equation for global ice volume v (in arbitrary units):

$$\frac{\mathrm{d}v}{\mathrm{d}t} = \frac{V_\mathrm{e} - v}{\tau_k}, \tag{A3}$$

where $V_\mathrm{e} = 1 - c_1 f$ is the equilibrium volume for orbital forcing f, and the c_1 value is constant. The relaxation timescale τ_k depends on the regime: $k = 1$ if $v > V_\mathrm{e}$, and $k = 2$ if $v < V_\mathrm{e}$. If $\tau_1 = \tau_2$, the model is linear and its response to orbital forcing is similar to forcing itself with only obliquity and precession frequencies present. Using τ_2 much larger than τ_1, as in Imbrie and Imbrie (1980), makes the model nonlinear. The model performance is far from perfect (see, e.g., Paillard, 2001), and even for the optimal choice of model parameters, the correlation between modeled v and LR04 stack for the last 800 kyr does not exceed 0.6. Even more important is that the modeled ice volume variability has too much energy in the 400 kyr band and too little energy in the 100 kyr band (Fig. A3).

A3 The rules for the timing of glacial terminations based on two or three obliquity cycles and effective energy

Huybers and Wunsch (2005) analyzed benthic δ^{18}O records and concluded that glacial terminations of the late Quaternary were spaced in time by two or three obliquity cycles, while the link with precession and eccentricity was not found to be statistically significant. Later, Huybers (2009) admitted that precession has a role in glacial cycles, but the concept of "two or three obliquity cycles" remains rather popular. Indeed, there is a clear tendency for glacial terminations to occur during periods of positive obliquity anomalies, although the durations between individual terminations can deviate significantly from two (82) or three (123 kyr) obliquity cycles (see below). When rounding to the nearest integers, the last eight glacial cycles can be expressed in terms of obliquity periods as 2, 2, 2, 3, 2, 2, 3, and 3. The average number of obliquity periods, 2.6, multiplied by obliquity periods gives 97 kyr, which is very close to the observed dominant periodicity of late Quaternary glacial cycles. But it is also clear that the probability of getting the correct sequence of "2" and "3" by random choice is $1/256 = 0.004$, which is a rather low probability, while the models used in this study

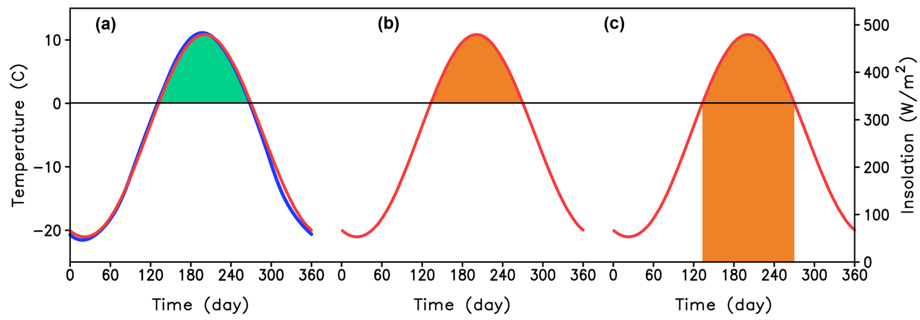

Figure A2. Present temperature and insolation curves at 65° N and different definitions of "summer energy". **(a)** Seasonal surface air temperature variation over land (blue) and insolation shifted by 30 d (red). The green area below the temperature curves represents the positive degree day index. **(b)** The orange area here represents an analogy for the positive degree days. The evolution of this characteristic is shown in Fig. A1e. This is a correct definition of summer energy. **(c)** The definition of summer energy according to Huybers (2006) is shown in Fig. A1d. The horizontal axis is the time of year in days.

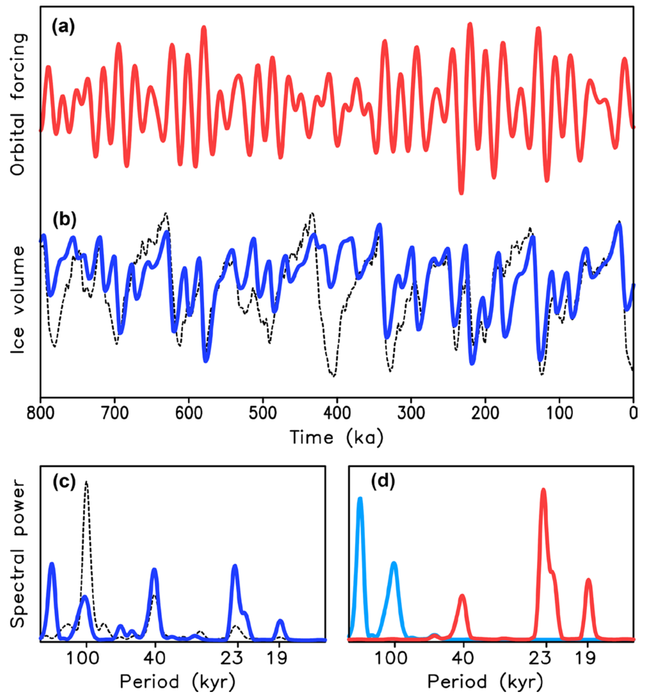

Figure A3. Results of simulations of the last 800 kyr with the Imbrie and Imbrie (1980) model. **(a)** Orbital forcing; **(b)** simulated ice volume (solid) and LR04 stack (dashed); **(c)** frequency spectra of simulated ice volume (blue) and LR04 stack (dashed line); **(d)** frequency spectra of eccentricity (blue) and orbital forcing (red). Vertical scales are arbitrary.

demonstrate that the timing of all glacial terminations of the late Quaternary is relatively robust. Even more problematic for the "two or three" hypothesis is that if this hypothesis is correct, then the duration of individual glacial cycles should cluster around 82 and 123 kyr with equal probabilities of being longer or shorter: 2(3)·41 kyr. In fact, durations of the last eight glacial cycles are rather uniformly distributed between ca. 80 and 120 ka, with five of eight glacial cycles having durations between 90 and 110 kyr, i.e., closer to 100 kyr than to two or three obliquity cycles (e.g., Konijnendijk et al., 2015).

The term effective energy was introduced by Tzedakis et al. (2017). According to this paper, terminations (during the last 600 kyr) occur when the effective energy defined as $I_{\text{peak}} + b(\Delta t)$ exceeds 6.412 GJ m^{-2}. Here I_{peak} is the magnitude of the maximum caloric half-year summer insolation at 65° N, Δt is the time since previous deglaciation, and b is a constant. This rule for glacial terminations implies that the Earth system somehow "knows" in advance whether the effective energy will cross the threshold value, which usually happens well after the beginning of terminations. In some cases (for example, for the penultimate glaciation), glacial terminations have been completed even before the maximum effective energy has been reached. How can this rule and a somewhat similar one described in Huybers (2011) be reconciled with the GMT, which "predicts" terminations not based on the magnitude of insolation maxima but rather by the timing when ice volume exceeds the critical threshold? In fact, it can be shown that, although these rules are based on completely different physical concepts, they indeed give similar timing of glacial terminations. The rule based on "efficient energy" formulated by Tzedakis et al. (2017) implies that glacial terminations occur only during maxima of caloric half-year summer insolation that are above the average value of insolation maxima which occurred close to each obliquity maxima. This can only happen if both precession and obliquity components of summer insolation are positive, and the eccentricity is also above average. Since the period of obliquity (41 kyr) is approximately twice as long as the period of precession and is comparable with half of a 100 kyr eccentricity period, it is highly probable that the previous positive precessional maximum occurred during the obliquity minimum and eccentricity was below average. But this is precisely the condition for reaching the critical ice volume in the GMT. Thus, with the appropriate initial conditions, the

Tzedakis et al. (2017) rule produces the same (or similar) sequence of terminations as the GMT.

A4 Model 2

Model 2 is a one-equation conceptual model aimed at reproducing the principal CLIMBER-2 results. It is derived using several assumptions, among which is that total accumulation (mass gain of ice sheets) G is proportional to the ice sheet area, but since the latter closely followed global ice volume v (e.g., Ganopolski et al., 2010), the total accumulation is parameterized as

$$G = a_1 v. \tag{A4}$$

The total mass loss (including both surface and basal melt, as well as ice calving into the ocean) L is a nonlinear function of ice volume. It also includes an additional term proportional to the rate of ice volume change:

$$L = a_2 v + b v^2 - \delta g v^* \frac{\mathrm{d}v}{\mathrm{d}t}. \tag{A5}$$

The last term is nonzero only for ice sheet decay, i.e., $\delta = 1$ if $\frac{\mathrm{d}v}{\mathrm{d}t} \leq 0$ and $\delta = 0$ if $\frac{\mathrm{d}v}{\mathrm{d}t} > 0$. The value $v^*(t) = \frac{1}{N}\int_{t-N}^{t} v(\tau)\mathrm{d}\tau$ is the memory term defined as the average ice volume over the previous N kiloyears. This term is crucial to simulate glacial terminations through the domino effect. The effect of insolation M (which can be positive and negative) is accounted for through a linear function of orbital forcing f (anomaly of maximum summer insolation at 65° N, see Sect. 4):

$$M = c f', \tag{A6}$$

where $f' = f + f_1$, and f_1 is the model parameter. Of course, orbital forcing can contribute to both "mass loss" and gain and is treated here separately just for convenience.

Temporal evolution of global ice volume (in normalized units) is thus described by the equation

$$\frac{\mathrm{d}v}{\mathrm{d}t} = G - L + M = \left(av - bv^2 - cf'\right) D^{-1}, \tag{A7}$$

where $a = a_1 - a_2$, and $D = 1 - \delta g v^*$.

To prevent the denominator in Eq. (A4) from approaching zero and subsequently becoming negative, it is additionally required that $D \geq \varepsilon$. In these equations, a, b, c, g, ε, and N are model parameters (see Table 1). Mathematically this equation is not much more complex than the governing equation of Model 3, but it has a clearer physical meaning. At the same time, it is easy to show that Model 3 is a simplified version of Model 2. The equilibrium solution of Eq. (A7) for ice volume V_e (see also Fig. A4) is

$$V_\mathrm{e} = \left(a \pm \left(a^2 - 4bcf'\right)^{1/2}\right)(2b)^{-1}. \tag{A8}$$

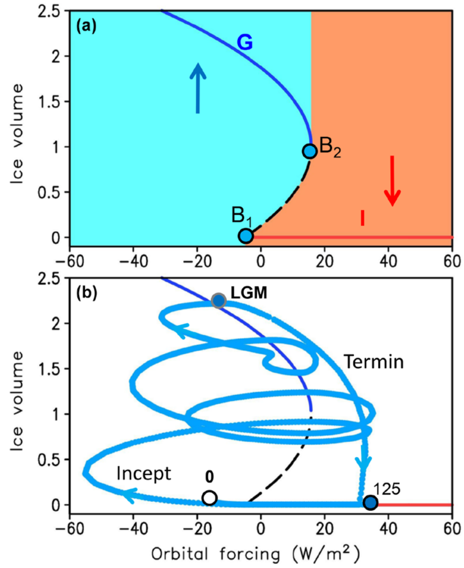

Figure A4. **(a)** Stability diagram for Model 2. Notations are the same as in Fig. 3. **(b)** Trajectory of the system described by Model 2 in the phase space of orbital forcing-ice volume for the last 125 kyr.

This is a rotated counterclockwise parabolic curve, identical to the equilibrium solutions of Model 3 (Fig. 4).

As it follows directly from Eq. (A7), growth of ice volume from zero (glacial inception) can only occur for $f' < 0$, i.e., $f < -f_1$, which means that the value f_1 (bifurcation point B_1) has the same meaning as f_1 in Model 3. The position of the second bifurcation point B_2 in the phase space of orbital forcing (the equivalent of f_2 in Model 3) is defined as $f_2 = \frac{a^2}{4bc} - f_1$. Since the vertical scale of the equilibrium solution is defined by the combination of parameters a and b, the number of parameters can be reduced to six by setting $b = a/2$. This gives the equilibrium solution $V_\mathrm{e}(f_2) = 1$ for ice volume at the bifurcation point B_2, which is the same as in Model 3. While Model 2 has qualitatively the same stability diagram as Model 3, it differs from the latter in that the timescale of relaxation towards the equilibrium solutions in Model 2 is not constant and depends on the position in the insolation-volume phase space. A typical relaxation timescale of Model 2 in the glaciation regime (i.e., when $\mathrm{d}v/\mathrm{d}t > 0$) can be estimated as $2a^{-1}$, which, for the value of a given in Table 1, is ca. 27 kyr, i.e., is similar to the (constant) relaxation timescale of Model 3. In the case of glacial termination, the rate of ice loss increases by the factor D^{-1}, which is an order of 10 when the memory term v^* approaches the critical ice volume equal to g^{-1}.

Figure A5 shows results of simulations of the last 800 kyr in comparison with paleoclimate reconstructions for the optimal set of model parameters (see Table 1). Correlation between the model and LR04 stack is 0.8, which is similar to Model 3. As in the case of Model 3, the "termination" regime described by the term D in Eq. (A7) is absolutely crucial.

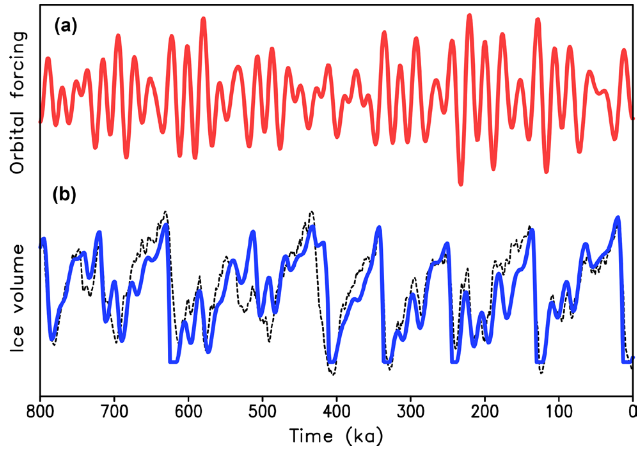

Figure A5. Simulation of late Quaternary glacial cycles with Model 2.

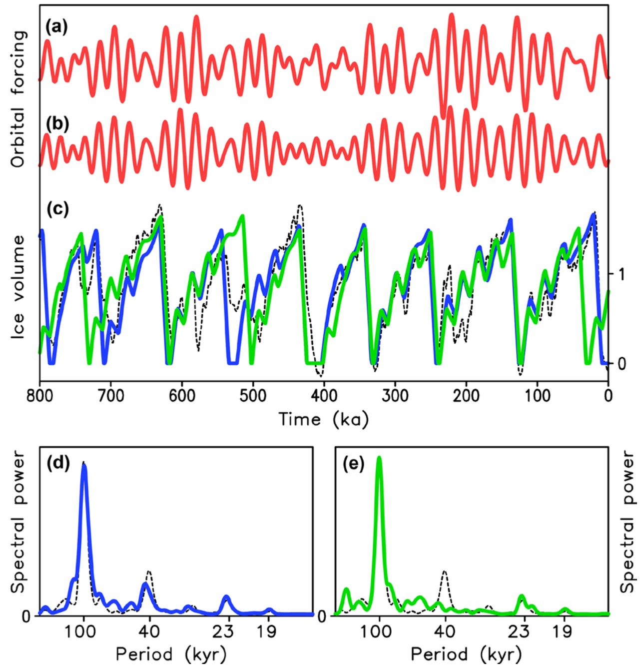

Figure A6. Results of simulations of the last 800 kyr with Model 3 with and without an obliquity component in orbital forcing. **(a)** Full orbital forcing; **(b)** orbital forcing without an obliquity component; **(c)** simulated ice volume with obliquity (blue) and without an obliquity component (green), as well as the LR04 stack (dashed); **(d)** spectra of simulated ice volume with an obliquity component (blue) and LR04 stack (dashed line); **(e)** spectra of simulated ice volume without an obliquity component (green) and LR04 stack (dashed line).

Without this term, Model 2 simulates a weakly nonlinear response with the presence of all Milankovitch frequencies, similar to the one-regime version of Model 3 and the Imbrie and Imbrie model. Compared to Model 3, Model 2 does a better job for the pre-MBT glacial cycles but, similarly to CLIMBER-2 (Willeit et al., 2019), has a problem with simulating long interglacial MIS 11, which Model 3 does not. This is explained by a very weak orbital forcing which triggered Termination V (transition to MIS 11 interglacial). Since in Model 3, the transition to a glaciation regime does not depend on the value of orbital forcing (it should only be growing and positive), it is easier to simulate the correct timing of Termination V with Model 3 than with Model 2, where the magnitude of orbital forcing matters. After MIS 11, Model 2 performs well for a rather broad range of model parameters and the maximum correlation between simulated ice volume and LR04 for this time interval reaches 0.9. Note that the extended version of Model 2, which also includes equations for CO_2 and global temperature, has been developed and applied to future glacial cycle simulations in Talento and Ganopolski (2021).

A5 The role of obliquity in a 100 kyr world

Since obliquity completely dominates δ^{18}O records of the 41 kyr world, it is natural to assume that obliquity also plays an essential role in a 100 kyr world. However, the experiments performed with the CLIMBER-2 model (Ganopolski and Calov, 2011) demonstrate that the dominant 100 kyr periodicity is present even when the obliquity component is completely excluded from the orbital forcing. At the same time, this periodicity cannot be simulated without eccentricity modulation of the precession component. Model 3 demonstrates the same behavior: when forced by the precession component of orbital forcing alone, it simulates a strong maximum in the frequency spectrum at 100 kyr for a broad range of the model parameter v_c. The presence of obliquity affects the timing of some glacial terminations, and therefore the duration of the individual glacial cycles, but not the dominant periodicity (Fig. A6). In the absence of the obliquity component, the durations of individual glacial cycles cluster around four and five precession periods (i.e., ca. 90 and 100 kyr) rather than two and three obliquity periods. Similar to CLIMBER-2 (Ganopolski and Calov, 2011), in Model 3 with obliquity-free orbital forcing, more energy in frequency spectra is seen in the 400 kyr band than in the case of realistic orbital forcing. However, the amount of energy in the 400 kyr band, unlike the 100 kyr, is strongly dependent on the choice of model parameters. In short, model simulations show that, although the obliquity component of orbital forcing plays an important role in climate variability during both the 41 and 100 kyr worlds, it has nothing to do with the dominant 100 kyr periodicity of the glacial cycles of the late Quaternary.

A6 Orbital tuning and the absence of precession in early Quaternary records

One of the potential causes of the absence of precession in the δ^{18}O spectra during the early Quaternary is that these time series are often orbitally tuned using obliquity as the target (e.g., Lisiecki and Raymo 2005). Since obliquity is the dominant frequency in the early Quaternary ice volume variations, such a choice seems to be reasonable. However, in the case of a strongly nonlinear system, tuning the age model to maximize one frequency may lead to the suppression of another one. This is illustrated by Fig. A7, where the results of model simulation described in Sect. 3 and shown in Fig. 10b have been "tuned to obliquity". Simulated ice volume already has a strong obliquity component (Fig. A4c) and the correlation between simulated volume and (negative) obliquity anomaly shifted by 5000 years is about 0.5. However, the spectrum also has pronounced precession maxima. To mimic the potential impact of orbital tuning on the frequency spectrum, the "age" of modeled ice volume has been modified to maximize correlation with obliquity. This time correction satisfies two criteria similar to those used in the actual orbital tuning: (i) the initial (in this case, real) age has not been changed by more than 10 kyr, and (ii) the original timescale was not stretched or squeezed by more than a factor of 2 at any time. Figure A7c shows the change in the original age, which gives the higher correlation between "tuned" volume and the target (obliquity). Now, this correlation reaches 0.65, practically the same value as the correlation between LR04 stack and obliquity (0.66). As Fig. A7 shows, this "tuning" slightly increases spectral energy in the obliquity band but causes a nearly complete disappearance of precession components (Fig. A7e).

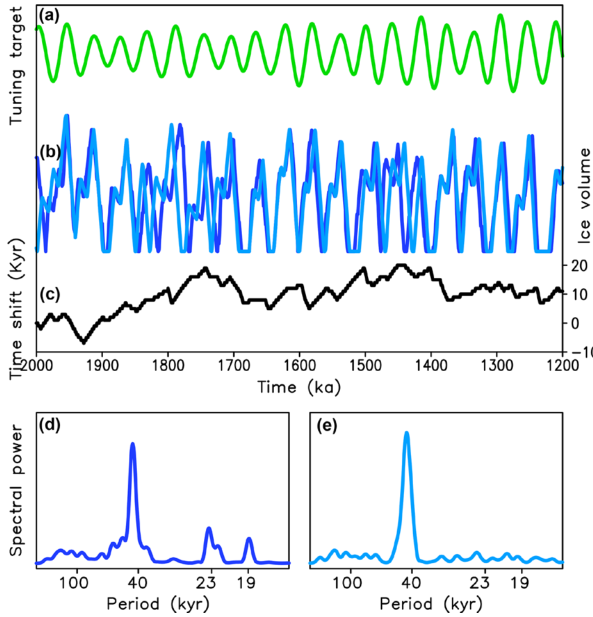

Figure A7. "Minimal orbital tuning". **(a)** Tuning target: negative anomaly of obliquity shifted by 5000 kyr; **(b)** simulated and "tuned" ice volume; **(c)** time shift for the tuned time series; **(d, e)** corresponding frequency spectra. The dark blue line is the original simulation of the 41 kyr world with Model 3 (the same as in Fig. 8), and the light blue line shows optimally tuned Model 3 simulations. The vertical scales in **(d)** and **(e)** are the same.

Code and data availability. The source codes and the output of the model simulations are available on request from the author.

Competing interests. The author has declared that there are no competing interests.

Disclaimer. Publisher's note: Copernicus Publications remains neutral with regard to jurisdictional claims made in the text, published maps, institutional affiliations, or any other geographical representation in this paper. While Copernicus Publications makes every effort to include appropriate place names, the final responsibility lies with the authors.

Special issue statement. This article is part of the special issue "A century of Milankovic's theory of climate changes: achievements and challenges (NPG/CP inter-journal SI)". It is not associated with a conference.

Acknowledgements. The author thanks Michel Crucifix, Martin Claussen, and an anonymous reviewer for valuable comments and suggestions, as well as Mikhail Verbitsky, Matteo Willeit, and Christine Kaufhold for helpful discussions.

Review statement. This paper was edited by Martin Claussen and reviewed by Michel Crucifix and one anonymous referee.

References

Abe-Ouchi, A., Saito, F., Kawamura, K., Raymo, M. E., Okuno, J., Takahashi, K., and Blatter, H.: Insolation-driven 100,000-year glacial cycles and hysteresis of ice-sheet volume, Nature, 500, 190–194, https://doi.org/10.1038/nature12374, 2013.

Adhémar, J. A.: Revolutions de la Mer: Deluges Periodiques, Carilian-Goeury et V. Dalmont, Paris, 1842.

Albani, S., Balkanski, Y., Mahowald, N., Winckler, G., Maggi, V., and Delmonte, B.: Aerosol-climate interactions during the Last Glacial Maximum, Curr. Clim. Change Rep., 4, 99–114, https://doi.org/10.1007/s40641-018-0100-7, 2018.

Andrews, J. T.: The Wisconsin Laurentide ice sheet: dispersal centers, problems of rates of retreat, and climatic implications, Arct. Alp. Res., 5, 185–199, https://doi.org/10.1080/00040851.1973.12003700, 1973.

Archer, D. and Ganopolski, A.: A movable trigger: Fossil fuel CO_2 and the onset of the next glaciation, Geochem. Geophy. Geosy., 6, 1–7, https://doi.org/10.1029/2004gc000891, 2005.

Archer, D., Winguth, A., Lea, D., and Mahowald, N.: What caused the glacial/interglacial atmospheric pCO_2 cycles?, Rev. Geophys., 38, 159–189, https://doi.org/10.1029/1999RG000066, 2000.

Arrhenius, S.: On the influence of carbonic acid in the air upon the temperature of the ground, Philos. Mag., 41, 237–275, 1896.

Ashwin, P., Camp, C. D., and von der Heydt, A. S.: Chaotic and non-chaotic response to quasiperiodic forcing: Limits to predictability of ice ages paced by Milankovitch forcing, Dynam. Stat. Clim. Syst., 3, 1–20, https://doi.org/10.1093/climsys/dzy002, 2018.

Barker, S., Starr, A., van der Lubbe, J., Doughty, A., Knorr, G., Conn, S., Lordsmith, S., Owen, L., Nederbragt, A., Hemming, S., and Hall, I.: Persistent influence of precession on northern ice sheet variability since the early Pleistocene, Science, 376, 961–967, https://doi.org/10.1126/science.abm4033, 2022.

Bauer, E. and Ganopolski, A.: Sensitivity simulations with direct shortwave radiative forcing by aeolian dust during glacial cycles, Clim. Past, 10, 1333–1348, https://doi.org/10.5194/cp-10-1333-2014, 2014.

Benzi, R., Parisi, G., Sutera, A., and Vulpiani, A.: Stochastic resonance in climatic change, Tellus, 34, 10–16, 1982.

Berends, C. J., Köhler, P., Lourens, L. J., and van de Wal, R. S. W.: On the cause of the mid-Pleistocene transition, Rev. Geophys., 59, e2020RG000727, https://doi.org/10.1029/2020RG000727, 2021.

Berger, A.: Obliquity and general precession for the last 5 000 000 years, Astron. Astrophys., 51, 127–135, 1976.

Berger, A.: Long-term variations of daily insolation and quaternary climatic changes, J. Atmos. Sci., 35, 2362–2367, https://doi.org/10.1175/1520-0469(1978)035<2362:Ltvodi>2.0.Co;2, 1978.

Berger, A.: Milankovitch theory and climate, Rev. Geophys., 26, 624–657, https://doi.org/10.1029/RG026i004p00624, 1988.

Berger, A.: A Brief History of the Astronomical Theories of Paleoclimates, in: Climate Change, edited by: Berger, A., Mesinger, F., and Šijački, D., Springer-Verlag, Wien, 107–129, https://doi.org/10.1007/978-3-7091-0973-1, 2012.

Berger, A.: Milankovitch, the father of paleoclimate modeling, Clim. Past, 17, 1727–1733, https://doi.org/10.5194/cp-17-1727-2021, 2021.

Berger, A. and Loutre, M. F.: Modeling the 100-kyr glacial-interglacial cycles, Global Planet. Change, 72, 275–281, https://doi.org/10.1016/j.gloplacha.2010.01.003, 2010.

Berger, A., Li, X. S., and Loutre, M. F.: Modelling northern hemisphere ice volume over the last 3 Ma, Quaternary Sci. Rev., 18, 1–11, https://doi.org/10.1016/s0277-3791(98)00033-x, 1999.

Bouttes, N., Paillard, D., Roche, D. M., Waelbroeck, C., Kageyama, M., Lourantou, A., Michel, E., and Bopp, L.: Impact of oceanic processes on the carbon cycle during the last termination, Clim. Past, 8, 149–170, https://doi.org/10.5194/cp-8-149-2012, 2012.

Braconnot, P., Otto-Bliesner, B., Harrison, S., Joussaume, S., Peterchmitt, J. Y., Abe-Ouchi, A., Crucifix, M., Driesschaert, E., Fichefet, T., Hewitt, C. D., Kageyama, M., Kitoh, A., Laine, A., Loutre, M. F., Marti, O., Merkel, U., Ramstein, G., Valdes, P., Weber, S. L., Yu, Y., and Zhao, Y.: Results of PMIP2 coupled simulations of the Mid-Holocene and Last Glacial Maximum – Part 1: experiments and large-scale features, Clim. Past., 3, 261–277, https://doi.org/10.5194/cp-3-261-2007, 2007.

Brendryen, J., Haflidason, H., Yokoyama, Y., Haaga, K. A., and Hannisdal, B.: Eurasian Ice Sheet collapse was a major source of Meltwater Pulse 1A 14,600 years ago, Nat. Geosci., 13, 363–368, https://doi.org/10.1038/s41561-020-0567-4, 2020.

Briggs, R. D., Pollard, D., and Tarasov, L.: A data-constrained large ensemble analysis of Antarctic evolution since the Eemian, Quaternary Sci. Rev., 103, 91–115, https://doi.org/10.1016/j.quascirev.2014.09.003, 2014.

Broecker, W. S. and Van Donk, J.: Insolation changes, ice volumes, and the O^{18} record in deep-sea cores, Rev. Geophys., 8, 169–198, https://doi.org/10.1029/RG008i001p00169, 1970.

Brovkin, V., Ganopolski, A., Archer, D., and Rahmstorf, S.: Lowering of glacial atmospheric CO_2 in response to changes in oceanic circulation and marine biogeochemistry, Paleoceanography, 22, PA4202, https://doi.org/10.1029/2006pa001380, 2007.

Brovkin, V., Ganopolski, A., Archer, D., and Munhoven, G.: Glacial CO_2 cycle as a succession of key physical and biogeochemical processes, Clim. Past., 8, 251–264, https://doi.org/10.5194/cp-8-251-2012, 2012.

Brückner, E., Köppen, W., and Wegener, A.: Über die Klimate der geologischen Vorzeit, Z. Gletscherkd., 14, 149–169, 1925.

Budyko, M. I.: Future climate, Trans. Am. Geophys. Union, 53, 868–874, https://doi.org/10.1029/EO053i010p00868, 1972.

Calder, N.: Arithmetic of ice ages, Nature, 252, 216–218, https://doi.org/10.1038/252216a0, 1974.

Calov, R. and Ganopolski, A.: Multistability and hysteresis in the climate-cryosphere system under orbital forcing, Geophys. Res. Lett., 32, L21717, https://doi.org/10.1029/2005GL024518, 2005.

Calov, R., Ganopolski, A., Claussen, M., Petoukhov, V., and Greve, R.: Transient simulation of the last glacial inception with an atmosphere-ocean-vegetation-ice sheet. Part I: Glacial inception as a bifurcation of the climate system, Clim. Dynam., 24, 545–561, 2005a.

Calov, R., Ganopolski, A., Petoukhov, V., Claussen, M., Brovkin, V., and Kubatzki, C.: Transient simulation of the last glacial inception. Part II: sensitivity and feedback analysis, Clim. Dynam., 24, 563–576, https://doi.org/10.1007/s00382-005-0008-5, 2005b.

Cane, M. A. and Molnar, P.: Closing of the Indonesian seaway as a precursor to east African aridircation around 3–4 million years ago, Nature, 411, 157–162, https://doi.org/10.1038/35075500, 2001.

Chalk, T. B., Hain, M. P., Foster, G. L., Rohling, E. J., Sexton, P. F., Badger, M. P. S., Cherry, S. G., Hasenfratz, A. P., Haug, G. H., Jaccard, S. L., Martinez-Garcia, A., Palike, H., Pancost, R. D., and Wilson, P. A.: Causes of ice age intensification across the Mid-Pleistocene Transition, P. Natl. Acad. Sci. USA, 114, 13114–13119, https://doi.org/10.1073/pnas.1702143114, 2017.

Charbit, S., Ritz, C., Philippon, G., Peyaud, V., and Kageyama, M.: Numerical reconstructions of the Northern Hemisphere ice sheets through the last glacial-interglacial cycle, Clim. Past., 3, 15–37, https://doi.org/10.5194/cp-3-15-2007, 2007.

Choudhury, D., Timmermann, A., Schloesser, F., Heinemann, M., and Pollard, D.: Simulating Marine Isotope Stage 7 with a coupled climate–ice sheet model, Clim. Past, 16, 2183–2201, https://doi.org/10.5194/cp-16-2183-2020, 2020.

Clark, P. U. and Pollard, D.: Origin of the Middle Pleistocene Transition by ice sheet erosion of regolith, Paleoceanography, 13, 1–9, 1998.

Claussen, M., Mysak, L. A., Weaver, A. J., Crucifix, M., Fichefet, T., Loutre, M. F., Weber, S. L., Alcamo, J., Alexeev, V. A., Berger, A., Calov, R., Ganopolski, A., Goosse, H., Lohmann, G., Lunkeit, F., Mokhov, I., Petoukhov, V., Stone, P., and Wang, Z.: Earth system models of intermediate complexity: closing the gap in the spectrum of climate system models, Clim. Dynam., 18, 579–586, https://doi.org/10.1007/s00382-001-0200-1, 2002.

Claussen, M., Fohlmeister, J., Ganopolski, A., and Brovkin, V.: Vegetation dynamics amplifies precessional forcing, Geophys. Res. Lett., 33, L09709, https://doi.org/10.1029/2006GL026111, 2006.

Croll, J.: On the physical cause of the change of climate during geological epochs, Philos. Mag., 28, 121–137, 1864.

Crucifix, M.: Oscillators and relaxation phenomena in Pleistocene climate theory, Philos. T. Roy. Soc. A, 370, 1140–1165, https://doi.org/10.1098/rsta.2011.0315, 2012.

Crucifix, M.: Why could ice ages be unpredictable?, Clim. Past., 9, 2253–2267, https://doi.org/10.5194/cp-9-2253-2013, 2013.

Crucifix, M. and Hewitt, C. D.: Impact of vegetation changes on the dynamics of the atmosphere at the Last Glacial Maximum, Clim. Dynam., 25, 447–459, https://doi.org/10.1007/s00382-005-0013-8, 2005.

Dang, C., Brandt, R. E., and Warren, S. G.: Parameterizations for narrowband and broadband albedo of pure snow and snow containing mineral dust and black carbon, J. Geophys. Res.-Atmos., 120, 5446–5468, https://doi.org/10.1002/2014JD022646, 2015.

Daradich, A., Huybers, P., Mitrovica, J. X., Chan, N. H., and Austermann, J.: The influence of true polar wander on glacial inception in North America, Earth Planet. Sc. Lett., 461, 96–104, https://doi.org/10.1016/j.epsl.2016.12.036, 2017.

de Noblet, N. I., Prentice, I. C., Joussaume, S., Texier, D., Botta, A., and Haxeltine, A.: Possible role of atmosphere–biosphere interaction in triggering the last glaciation, Geophys. Res. Lett., 23, 3191–3194, 1996.

Dong, B. W. and Valdes, P. J.: Sensitivity studies of northern-hemisphere glaciation using an atmospheric general-circulation model, J. Climate, 8, 2471–2496, https://doi.org/10.1175/1520-0442(1995)008<2471:SSONHG>2.0.CO;2, 1995.

Elderfield, H., Ferretti, P., Greaves, M., Crowhurst, S., McCave, I. N., Hodell, D., and Piotrowski, A. M.: Evolution of Ocean Temperature and Ice Volume Through the Mid-Pleistocene Climate Transition, Science, 337, 704–709, https://doi.org/10.1126/science.1221294, 2012.

Emiliani, C.: Paleotemperature analysis of Caribbean cores P6304-8 and P6304-9 and a generalized temperature curve for the past 425,000 years, J. Geol., 74, 109–124, 1966.

Farmer, J. R., Honisch, B., Haynes, L. L., Kroon, D., Jung, S., Ford, H. L., Raymo, M. E., Jaume-Segui, M., Bell, D. B., Goldstein, S. L., Pena, L. D., Yehudai, M., and Kim, J.: Deep Atlantic Ocean carbon storage and the rise of 100,000-year glacial cycles, Nat. Geosci., 12, 355–360, https://doi.org/10.1038/s41561-019-0334-6, 2019.

Ford, H. L. and Raymo, M. E.: Regional and global signals in seawater $\delta^{18}O$ records across the mid-Pleistocene transition, Geology, 48, 113–117, https://doi.org/10.1130/g46546.1, 2020.

Galbraith, E. and de Lavergne, C.: Response of a comprehensive climate model to a broad range of external forcings: relevance for deep ocean ventilation and the development of late Cenozoic ice ages, Clim. Dynam., 52, 653–679, 2019.

Ganopolski, A.: Glacial integrative modelling, Philos. T. Roy. Soc. Lond. A, 361, 1871–1883, https://doi.org/10.1098/rsta.2003.1246, 2003.

Ganopolski, A. and Brovkin, V.: Simulation of climate, ice sheets and CO_2 evolution during the last four glacial cycles with an Earth system model of intermediate complexity, Clim. Past., 13, 1695–1716, https://doi.org/10.5194/cp-13-1695-2017, 2017.

Ganopolski, A. and Calov, R.: The role of orbital forcing, carbon dioxide and regolith in 100 kyr glacial cycles, Clim. Past., 7, 1415–1425, https://doi.org/10.5194/cp-7-1415-2011, 2011.

Ganopolski, A., Petoukhov, V., Rahmstorf, S., Brovkin, V., Claussen, M., Eliseev, A., and Kubatzki C.: CLIMBER-2: a climate system model of intermediate complexity. Part II: Model sensitivity, Clim. Dynam., 17, 735–751, 2001.

Ganopolski, A., Calov, R., and Claussen, M.: Simulation of the last glacial cycle with a coupled climate ice-sheet model of intermediate complexity, Clim. Past, 6, 229–244, https://doi.org/10.5194/cp-6-229-2010, 2010.

Ganopolski, A., Winkelmann, R., and Schellnhuber, H. J.: Critical insolation-CO_2 relation for diagnosing past and future glacial inception, Nature, 529, 200–204, https://doi.org/10.1038/nature16494, 2016.

Gregoire, L. J., Valdes, P. J., and Payne, A. J.: The relative contribution of orbital forcing and greenhouse gases to the North American deglaciation, Geophys. Res. Lett., 42, 9970–9979, https://doi.org/10.1002/2015GL066005, 2015.

Gregory, J. M., Browne, O. J. H., Payne, A. J., Ridley, J. K., and Rutt, I. C.: Modelling large-scale ice-sheet-climate interactions following glacial inception, Clim. Past., 8, 1565–1580, https://doi.org/10.5194/cp-8-1565-2012, 2012.

Hargreaves, J. C., Abe-Ouchi, A., and Annan, J. D.: Linking glacial and future climates through an ensemble of GCM simulations, Clim. Past, 3, 77–87, https://doi.org/10.5194/cp-3-77-2007, 2007.

Hasenfratz, A. P., Jaccard, S. L., Martinez-Garcia, A., Sigman, D. M., Hodell, D. A., Vance, D., Bernasconi, S. M., Kleiven, H. F., Haumann, F. A., and Haug, G. H.: The residence time of Southern Ocean surface waters and the 100,000-year ice age cycle, Science, 363, 1080–1084, https://doi.org/10.1126/science.aat7067, 2019.

Haug, G. H. and Tiedemann, R.: Effect of the formation of the Isthmus of Panama on Atlantic Ocean thermohaline circulation, Nature, 393, 673–676, https://doi.org/10.1038/31447, 1998.

Haug, G. H., Ganopolski, A., Sigman, D. M., Rosell-Mele, A., Swann, G. E. A., Tiedemann, R., Jaccard, S. L., Bollmann, J., Maslin, M. A., Leng, M. J., and Eglinton, G.: North Pacific seasonality and the glaciation of North America 2.7 million years ago, Nature, 433, 821–825, 2005.

Hays, J., Imbrie, J., and Shackleton, N.: Variations in the earth's orbit: Pacemaker of the ice ages, Science, 194, 1121–1132, https://doi.org/10.1126/science.194.4270.1121, 1976.

Heinemann, M., Timmermann, A., Timm, O. E., Saito, F., and Abe-Ouchi, A.: Deglacial ice sheet meltdown: orbital pacemaking and CO_2 effects, Clim. Past., 10, 1567–1579, https://doi.org/10.5194/cp-10-1567-2014, 2014.

Hinck, S., Gowan, E. J., Zhang, X., and Lohmann, G.: PISM-LakeCC: Implementing an adaptive proglacial lake boundary in an ice sheet model, The Cryosphere, 16, 941–965, https://doi.org/10.5194/tc-16-941-2022, 2022.

Hodell, D. A., Channell, J. E. T., Curtis, J. H., Romero, O. E., and Rohl, U.: Onset of "Hudson Strait" Heinrich events in the eastern North Atlantic at the end of the middle Pleistocene transition (similar to 640 ka)?, Paleoceanography, 23, 16 PA4218, https://doi.org/10.1029/2008pa001591, 2008.

Hönisch, B., Hemming, N. G., Archer, D., Siddall, M., and McManus, J. F.: Atmospheric Carbon Dioxide Concentration Across the Mid-Pleistocene Transition, Science, 324, 1551–1554, https://doi.org/10.1126/science.1171477, 2009.

Huybers, P.: Early Pleistocene glacial cycles and the integrated summer insolation forcing, Science, 313, 508–511, https://doi.org/10.1126/science.1125249, 2006.

Huybers, P.: Pleistocene glacial variability as a chaotic response to obliquity forcing, Clim. Past., 5, 481–488, https://doi.org/10.5194/cp-5-481-2009, 2009.

Huybers, P.: Combined obliquity and precession pacing of late Pleistocene deglaciations, Nature, 480, 229–232, https://doi.org/10.1038/nature10626, 2011.

Huybers, P. and Wunsch, C.: Obliquity pacing of the late Pleistocene glacial terminations, Nature, 434, 491–494, https://doi.org/10.1038/nature03401, 2005.

Imbrie, J. and Imbrie, J.: Modeling the climatic response to orbital variations, Science, 207, 943–953, https://doi.org/10.1126/science.207.4434.943, 1980.

Imbrie, J., Boyle, E. A., Clemens, S. C., Duffy, A., Howard, W. R., Kukla, G., Kutzbach, J., Martinson, D. G., McIntyre, A., Mix, A. C., Molfino, B., Morley, J. J., Peterson, L. C., Pisias, N. G., Prell, W. L., Raymo, M. E., Shackleton, N. J., and Toggweiler, J. R.: On the structure and origin of major glaciation cycles 1. linear responses to milankovitch forcing, Paleoceanography, 7, 701–738, https://doi.org/10.1029/92pa02253, 1992.

Imbrie, J., Berger, A., Boyle, E. A., Clemens, S. C., Duffy, A., Howard, W. R., Kukla, G., Kutzbach, J., Martinson, D. G., McIntyre, A., Mix, A. C., Molfino, B., Morley, J. J., Peterson, L. C., Pisias, N. G., Prell, W. L., Raymo, M. E., Shackleton, N. J., and Toggweiler, J. R.: On the structure and origin of major glaciation cycles. 2. the 100,000-year cycle, Paleoceanography, 8, 699–735, https://doi.org/10.1029/93pa02751, 1993.

Jeltsch-Thommes, A., Battaglia, G., Cartapanis, O., Jaccard, S. L., and Joos, F.: Low terrestrial carbon storage at the Last Glacial Maximum: constraints from multi-proxy data, Clim. Past., 15, 849–879, https://doi.org/10.5194/cp-15-849-2019, 2019.

Kohfeld, K. E. and Harrison S. P.: DIRTMAP: The geological record of dust, Earth Sci. Rev., 54, 81–114, https://doi.org/10.1016/S0012-8252(01)00042-3, 2001.

Kohfeld, K. E., and Ridgwell, A.: Glacial-interglacial variability in atmospheric CO_2, in: Surface ocean-lower atmosphere processes, edited by: Le Quéré, C. and Saltzman, E. S., American Geophysical Union, Washington, DC, https://doi.org/10.1029/2008GM000845, 2009.

Konijnendijk, T. Y. M., Ziegler, M., and Lourens, L. J.: On the timing and forcing mechanisms of late Pleistocene glacial terminations: Insights from a new high-resolution benthic stable oxygen isotope record of the eastern Mediterranean, Quaternary Sci. Rev., 129, 308–320, https://doi.org/10.1016/j.quascirev.2015.10.005, 2015.

Krinner, G., Boucher, O., and Balkanski, Y.: Ice-free glacial northern Asia due to dust deposition on snow, Clim. Dynam., 27, 613–625, https://doi.org/10.1007/s00382-006-0159-z, 2006.

Kutzbach, J. E.: Monsoon climate of the early holocene – climate experiment with the earths orbital parameters for 9000 years ago, Science, 214, 59–61, https://doi.org/10.1126/science.214.4516.59, 1981.

Kutzbach, J. E. and Gallimore, R. G.: Sensitivity of a coupled atmosphere/mixed layer ocean model to changes in orbital forcing at 9000 years B.P., J. Geophys. Res.-Atmos., 93, 803–821, https://doi.org/10.1029/JD093iD01p00803, 1988.

Laskar, J., Robutel, P., Joutel, F., Gastineau, M., Correia, A. C. M., and Levrard, B.: A long-term numerical solution for the insolation quantities of the Earth, Astron. Astrophys., 428, 261–285, https://doi.org/10.1051/0004-6361:20041335, 2004.

Legrain, E., Parrenin, F., and Capron, E.: A gradual change is more likely to have caused the Mid-Pleistocene Transition than an abrupt event, Commun. Earth Environ., 4, 90, https://doi.org/10.1038/s43247-023-00754-0, 2023.

Leloup, G. and Paillard, D.: Influence of the choice of insolation forcing on the results of a conceptual glacial cycle model, Clim. Past, 18, 547–558, https://doi.org/10.5194/cp-18-547-2022, 2022.

Liakka, J. and Lofverstrom, M.: Arctic warming induced by the Laurentide Ice Sheet topography, Clim. Past., 14, 887–900, https://doi.org/10.5194/cp-14-887-2018, 2018.

Liautaud, P. R., Hodell, D. A., and Huybers, P. J.: Detection of significant climatic precession variability in early Pleistocene glacial cycles, Earth Planet. Sc. Lett., 536, 116137, https://doi.org/10.1016/j.epsl.2020.116137, 2020.

Licciardi, J. M., Clark, P. U., Jenson, J. W., and Macayeal, D. R.: Deglaciation of a soft-bedded Laurentide Ice Sheet, Quaternary Sci. Rev., 17, 427–448, https://doi.org/10.1016/s0277-3791(97)00044-9, 1998.

Lisiecki, L. E.: Links between eccentricity forcing and the 100,000-year glacial cycle, Nat. Geosci., 3, 349–352, https://doi.org/10.1038/ngeo828, 2010.

Lisiecki, L. E. and Raymo, M. E.: A Pliocene-Pleistocene stack of 57 globally distributed benthic $\delta^{18}O$ records, Paleoceanography, 20, PA1003, https://doi.org/10.1029/2004pa001071, 2005.

Lisiecki, L. E. and Raymo, M. E.: Plio-Pleistocene climate evolution: trends and transitions in glacial cycle dynamics, Quaternary Sci. Rev., 26, 56–69, https://doi.org/10.1016/j.quascirev.2006.09.005, 2007.

Lofverstrom, M., Thompson, D. M., Otto-Bliesner, B. L., and Brady, E. C.: The importance of Canadian Arctic Archipelago gateways for glacial expansion in Scandinavia, Nat. Geosci., 15, 482–488, https://doi.org/10.1038/s41561-022-00956-9, 2022.

Loutre, M. F. and Berger, A.: Future climatic changes: Are we entering an exceptionally long interglacial?, Climatic Change, 46, 61–90, https://doi.org/10.1023/A:1005559827189, 2000.

Lüthi, D., Le Floch, M., Bereiter, B., Blunier, T., Barnola, J. M., Siegenthaler, U., Raynaud, D., Jouzel, J., Fischer, H., Kawamura, K., and Stocker, T. F.: High-resolution carbon dioxide concentration record 650,000–800,000 years before present, Nature, 453, 379–382, https://doi.org/10.1038/nature06949, 2008.

MacAyeal, D. R.: A catastrophe model of the paleoclimate, J. Glaciol., 24, 245–257, https://doi.org/10.3189/S0022143000014775, 1979.

Mahowald, N. M., Muhs, D. R., Levis, S., Rasch, P. J., Yoshioka, M., Zender, C. S., and Luo, C.: Change in atmospheric mineral aerosols in response to climate: Last glacial period, preindustrial, modern, and doubled carbon dioxide climates, J. Geophys. Res.-Atmos., 111, D10202, https://doi.org/10.1029/2005jd006653, 2006.

Marshall, S. J. and Clarke, G. K. C.: Ice sheet inception: subgrid hypsometric parameterization of mass balance in an ice sheet model, Clim. Dynam., 15, 533–550, https://doi.org/10.1007/s003820050298, 1999.

Martin, J. H.: Glacial-interglacial CO_2 change: the iron hypothesis, Paleoceanography, 5, 1–13, https://doi.org/10.1029/PA005i001p00001, 1990.

Martínez-Botí, M. A., Foster, G. L., Chalk, T. B., Rohling, E. J., Sexton, P. F., Lunt, D. J., Pancost, R. D., Badger, M. P. S., and Schmidt, D. N.: Plio-Pleistocene climate sensitivity evaluated using high-resolution CO_2 records, Nature, 518, 49–54, https://doi.org/10.1038/nature14145, 2015.

Maslin, M. A. and Brierley, C. M.: The role of orbital forcing in the Early Middle Pleistocene Transition, Quatern. Int., 389, 47–55, https://doi.org/10.1016/j.quaint.2015.01.047, 2015.

Milankovitch, M.: Theorie Mathematique des Phenomenes Thermiques Produits par la Radiation Solaire. Academie Yougoslave des Sciences et des Arts de Zagreb, Gauthier Villars, Paris, 1920.

Milankovitch, M.: Kanon der Erdbestrahlung und Seine Andwendung auf das Eiszeitenproblem, in: vol. 33, Spec. Publ. 132, R. Serbian Acad., Belgrade, 633 pp., 1941.

Muller, R. A. and MacDonald, G. J.: Spectrum of 100-kyr glacial cycle: Orbital inclination, not eccentricity, P. Natl. Acad. Sci. USA, 94, 8329–8334, https://doi.org/10.1073/pnas.94.16.8329, 1997.

Murphy, J. J.: The glacial climate and the polar ice-cap, Q. J. Geol. Soc., 32, 400–406, 1876.

Oerlemans, J.: Model experiments on the 100,000-yr glacial cycle, Nature, 287, 430–432, https://doi.org/10.1038/287430a0, 1980.

O'ishi, R. and Abe-Ouchi, A.: Influence of dynamic vegetation on climate change and terrestrial carbon storage in the Last Glacial Maximum, Clim. Past, 9, 1571–1587, https://doi.org/10.5194/cp-9-1571-2013, 2013.

Paillard, D.: The timing of Pleistocene glaciations from a simple multiple-state climate model, Nature, 391, 378–381, https://doi.org/10.1038/34891, 1998.

Paillard, D.: Glacial cycles: Toward a new paradigm, Rev. Geophys., 39, 325–346, https://doi.org/10.1029/2000RG000091, 2001.

Paillard, D.: Quaternary glaciations: from observations to theories, Quaternary Sci. Rev., 107, 11–24, https://doi.org/10.1016/j.quascirev.2014.10.002, 2015.

Paillard, D. and Parrenin, F.: The Antarctic ice sheet and the triggering of deglaciations, Earth Planet. Sc. Lett., 227, 263–271, https://doi.org/10.1016/j.epsl.2004.08.023, 2004.

Penck, A. and Brückner, E.: Die Alpen im Eiszeitalter, CH Tauchnitz, 1909.

Petit, J. R., Jouzel, J., Raynaud, D., Barkov, N. I., Barnola, J. M., Basile, I., Bender, M., Chappellaz, J., Davis, M., Delaygue, G., Delmotte, M., Kotlyakov, V. M., Legrand, M., Lipenkov, V. Y., Lorius, C., Pepin, L., Ritz, C., Saltzman, E., and Stievenard, M.: Climate and atmospheric history of the past 420,000 years from the Vostok ice core, Antarctica, Nature, 399, 429–436, https://doi.org/10.1038/20859, 1999.

Petoukhov, V., Ganopolski, A., Brovkin, V., Claussen, M., Eliseev, A., Kubatzki, C., and Rahmstorf, S.: CLIMBER-2: a climate system model of intermediate complexity. Part I: model description and performance for present climate, Clim. Dynam., 16, 1–17, https://doi.org/10.1007/pl00007919, 2000.

Pollard, D.: A coupled climate-ice sheet model applied to the quaternary ice ages, J. Geophys. Res.-Oceans, 88, 7705–7718, https://doi.org/10.1029/JC088iC12p07705, 1983.

Pollard, D. and DeConto, R .M.: Hysteresis in Cenozoic Antarctic Ice-Sheet variations, Global Planet. Change, 45, 9–21, https://doi.org/10.1016/j.gloplacha.2004.09.011, 2005.

Quiquet, A., Dumas, C., Paillard, D., Ramstein, G., Ritz, C., and Roche, D. M.: Deglacial Ice Sheet Instabilities Induced by Proglacial Lakes, Geophys. Res. Lett., 48, e2020GL092141, https://doi.org/10.1029/2020GL092141, 2021.

Raymo, M. E.: The timing of major climate terminations, Paleoceanography, 12, 577–585, https://doi.org/10.1029/97PA01169, 1997.

Raymo, M. E, and Nisancioglu, K.: The 41 kyr world: Milankovitch's other unsolved mystery, Paleoceanography, 18, 1011, https://doi.org/10.1029/2002PA000791, 2003.

Raymo, M. E. and Ruddiman, W. F.: Tectonic forcing of late cenozoic climate, Nature, 359, 117–122, https://doi.org/10.1038/359117a0, 1992.

Raymo, M. E., Lisiecki, L. E., and Nisancioglu, K. H.: Plio-pleistocene ice volume, Antarctic climate, and the global $\delta^{18}O$ record, Science, 313, 492–495, https://doi.org/10.1126/science.1123296, 2006.

Ridgwell, A. J., Watson, A. J., and Raymo, M. E.: Is the spectral signature of the 100 kyr glacial cycle consistent with a Milankovitch origin?, Paleoceanography, 14, 437–440, https://doi.org/10.1029/1999PA900018, 1999.

Ridgwell, A. J., Watson, A. J., Maslin, M. A., and Kaplan, J. O.: Implications of coral reef buildup for the controls on atmospheric CO_2 since the Last Glacial Maximum, Paleoceanography, 18, 1083, https://doi.org/10.1029/2003PA000893, 2003.

Robinson, A., Calov, R., and Ganopolski, A.: Multistability and critical thresholds of the Greenland ice sheet, Nat. Clim. Change, 2, 429–432, https://doi.org/10.1038/nclimate1449, 2012.

Roe, G. and Allen, M.: A comparison of competing explanations for the 100,000-yr ice age cycle, Geophys. Res. Lett., 26, 2259–2262, https://doi.org/10.1029/1999GL900509, 1999.

Royer, J. F., Deque, M., and Pestiaux, P.: Orbital forcing of the inception of the laurentide ice-sheet, Nature, 304, 43–46, https://doi.org/10.1038/304043a0, 1983.

Ruddiman, W. F.: Oribital insolation, ice volume, and greenhouse gases, Quaternary Sci. Rev., 22, 1597–1629, https://doi.org/10.1016/S0277-3791(03)00087-8, 2003.

Ruddiman, W. F. and Raymo, M. E.: Northern hemisphere climate regimes during the past 3-ma – possible tectonic connections, Philos. T. Roy. Soc. Lond. B, 318, 411–430, https://doi.org/10.1098/rstb.1988.0017, 1988.

Saltzman, B.: Dynamical paleoclimatology: generalized theory of global climate change, in: Vol. 80, Academic Press, ISBN 0-12-617331-1, 2002.

Saltzman, B. and Verbitsky, M. Y.: Multiple instabilities and modes of glacial rhythmicity in the plio-Pleistocene: a general theory of late Cenozoic climatic change, Clim. Dynam., 9, 1–15, https://doi.org/10.1007/BF00208010, 1993.

Shakun, J. D., Raymo, M. E., and Lea, D. W.: An early Pleistocene Mg/Ca-δ^{18}O record from the Gulf of Mexico: Evaluating ice sheet size and pacing in the 41-kyr world, Paleoceanography, 31, 1011–1027, https://doi.org/10.1002/2016pa002956, 2016.

Spratt, R. M. and Lisiecki, L. E.: A Late Pleistocene sea level stack, Clim. Past., 12, 1079–1092, https://doi.org/10.5194/cp-12-1079-2016, 2016.

Sutter, J., Fischer, H., Grosfeld, K., Karlsson, N. B., Kleiner, T., Van Liefferinge, B., and Eisen, O.: Modelling the Antarctic Ice Sheet across the mid-Pleistocene transition – implications for Oldest Ice, The Cryosphere, 13, 2023–2041, https://doi.org/10.5194/tc-13-2023-2019, 2019.

Tabor, C. R. and Poulsen, C. J.: Simulating the mid-Pleistocene transition through regolith removal, Earth Planet. Sc. Let., 434, 231–240, https://doi.org/10.1016/j.epsl.2015.11.034, 2016.

Talento, S. and Ganopolski, A.: Reduced-complexity model for the impact of anthropogenic CO_2 emissions on future glacial cycles, Earth Syst. Dynam., 12, 1275–1293, https://doi.org/10.5194/esd-12-1275-2021, 2021.

Tarasov, L. and Peltier, W. R.: Terminating the 100 kyr ice age cycle, J. Geophys. Res.-Atmos., 102, 21665–21693, https://doi.org/10.1029/97jd01766, 1997.

Tzedakis, P. C., Crucifix, M., Mitsui, T., and Wolff, E. W.: A simple rule to determine which insolation cycles lead to interglacials, Nature, 542, 427–432, https://doi.org/10.1038/nature21364, 2017.

Tziperman, E. and Gildor, H.: On the mid-Pleistocene transition to 100-kyr glacial cycles and the asymmetry between glaciation and deglaciation times, Paleoceanography, 18, 1001, https://doi.org/10.1029/2001PA000627, 2003.

Vavrus, S., Ruddiman, W. F., and Kutzbach, J. E.: Climate model tests of the anthropogenic influence on greenhouse-induced climate change: the role of early human agriculture, industrialization, and vegetation feedbacks, Quaternary Sci. Rev., 27, 1410–1425, https://doi.org/10.1016/j.quascirev.2008.04.011, 2008.

Verbitsky, M. Y., Crucifix, M., and Volobuev, D. M.: A theory of Pleistocene glacial rhythmicity, Earth Syst. Dynam., 9, 1025–1043, https://doi.org/10.5194/esd-9-1025-2018, 2018.

Warren, S. G. and Wiscombe, W. J.: A Model for the Spectral Albedo of Snow. II: Snow Containing Atmospheric Aerosols, J. Atmos. Sci., 37, 2734–2745, https://doi.org/10.1175/1520-0469(1980)037<2734:AMFTSA>2.0.CO;2, 1980.

Watson, A. J., Bakker, D. C. E., Ridgwell, A. J., Boyd, P. W., and Law, C. S.: Effect of iron supply on Southern Ocean CO_2 uptake and implications for glacial atmospheric CO_2, Nature, 407, 730–733, https://doi.org/10.1038/35037561, 2000.

Weertman, J.: Stability of the Junction of an Ice Sheet and an Ice Shelf, J. Glaciol., 13, 3–11, https://doi.org/10.3189/S0022143000023327, 1974.

Weertman, J.: Milankovitch solar radiation variations and ice age ice sheet sizes, Nature, 261, 17–20, https://doi.org/10.1038/261017a0, 1976.

Willeit, M. and Ganopolski, A.: The importance of snow albedo for ice sheet evolution over the last glacial cycle, Clim. Past., 14, 697–707, https://doi.org/10.5194/cp-14-697-2018, 2018.

Willeit, M., Ganopolski, A., Calov, R., Robinson, A., and Maslin, M.: The role of CO_2 decline for the onset of Northern Hemisphere glaciation, Quaternary Sci. Rev., 119, 22–34, https://doi.org/10.1016/j.quascirev.2015.04.015, 2015.

Willeit, M., Ganopolski, A., Calov, R., and Brovkin, V.: Mid-Pleistocene transition in glacial cycles explained by declining CO_2 and regolith removal, Sci. Adv., 5, eaav7337, https://doi.org/10.1126/sciadv.aav7337, 2019.

Yamamoto, A., Abe-Ouchi, A., Ohgaito, R., Ito, A., and Oka, A.: Glacial CO_2 decrease and deep-water deoxygenation by iron fertilization from glaciogenic dust, Clim. Past, 15, 981–996, https://doi.org/10.5194/cp-15-981-2019, 2019.

Yamamoto, M., Clemens, S. C., Seki, O., Tsuchiya, Y., Huang, Y., O'ishi, R., and Abe-Ouchi, A.: Increased interglacial atmospheric CO_2 levels followed the mid-Pleistocene Transition, Nat. Geosci., 15, 307–313, https://doi.org/10.1038/s41561-022-00918-1 2022.

Zweck, C. and Huybrechts, P.: Modeling the marine extent of Northern Hemisphere ice sheets during the last glacial cycle, Ann. Glaciol., 37, 173–180, 2003.

Clim. Past, 5, 259–267, 2009
www.clim-past.net/5/259/2009/

Climate of the Past

The influence of the circulation on surface temperature and precipitation patterns over Europe

P. D. Jones* **and D. H. Lister**

Climatic Research Unit, School of Environmental Sciences, University of East Anglia, Norwich, NR4 7TJ, UK

**Invited contribution by P. D. Jones, recipient of the Hans Oeschger Medal 2002.*

Received: 14 January 2009 – Published in Clim. Past Discuss.: 24 February 2009
Revised: 15 June 2009 – Accepted: 19 June 2009 – Published: 25 June 2009

Abstract. The atmospheric circulation clearly has an important influence on variations in surface temperature and precipitation. In this study we illustrate the spatial patterns of variation that occur for the principal circulation patterns across Europe in the standard four seasons. We use an existing classification scheme of surface pressure patterns, with the aim of considering whether the patterns of influence of specific weather types have changed over the course of the 20th century. We consider whether the long-term warming across Europe is associated with more favourable weather types or related to warming within some of the weather types. The results indicate that the latter is occurring, but not all circulation types show warming. The study also illustrates that certain circulation types can lead to marked differences in temperature and/or precipitation for relatively closely positioned sites when the sites are located in areas of high relief or near coasts.

1 Introduction

The influence of the circulation on surface climate has been known by humans since the beginning of time. Since the advent of climatology these relationships have developed into circulation or weather types developed initially subjectively (e.g. Lamb, 1972 for the British Isles and Hess and Brezowsky, 1977 for Europe – the well know "Grosswetterlagen") but now objectively with a wide range of approaches and techniques (see reviews by Yarnal, 1993 and Huth et al., 2008). The derived weather types have been used in a wide range of applications (see Yarnal, 1993 and Huth et al., 2008) in the field which is now called synoptic climatology.

With growing interest in climate change, many of the objective schemes are being used to study whether the climate is warming because of a greater frequency of 'warm' or less "cold" types or is the overall frequency of basic types relatively unchanged and most types are slightly warmer than they used to be. Two examples of this type of work are the studies undertaken by Osborn and Jones (2000) and van Oldenburgh and van Ulden (2003). In the first, the percentage of the season-to season variability of rainfall and temperature over Britain (using the England and Wales precipitation record, Alexander and Jones, 2001 and the Central England temperature record, Parker et al., 1992) that could be explained by three variables (flow direction and strength and vorticity, which together form the very simplest of objective weather typing) was estimated. The result was that the "weather" explained much of the high-frequency variability, but little in the way of longer (decadal and above) timescale variability. The second study looked at temperatures at De Bilt in the Netherlands and assessed whether 20th century temperature increases were specific to certain wind directions. The result was that temperatures increased for all wind directions except for those from the northeast during winter. Both results emphasize the warming, but highlight different aspects. Beck et al. (2007) also consider similar aspects, but only use monthly resolution data.

Here we extend these studies to the European scale and use continental-scale circulation typing approaches. Philipp et al. (2007) have developed a set of daily North Atlantic/European Circulation Types (CTs) covering the region 70° to 25° N by 70° W to 50° E using a technique involving simulated annealing (a clustering algorithm). The analysis was based on the reconstructed daily mean sea-level pressure

Correspondence to: P. D. Jones
(p.jones@uea.ac.uk)

Published by Copernicus Publications on behalf of the European Geosciences Union.

Table 1. Number of Circulation Types (CTs) for each of the four seasonal analyses.

Season	Number of CTs
DJF	9
MAM	11
JJA	6
SON	8

(MSLP) maps from Ansell et al. (2006) and used the full period of available data from 1850–2003. Different CTs were developed for each of the four standard seasons and also for the twelve sets of two-month seasons (JF, FM etc.).

At larger scales, it is certain that the circulation will explain less than it does on the scales of Britain or the Netherlands. This is because large-scale circulation typing is more complex than the simple objective typing (using flow direction and strength and vorticity) described above. Simpler typing is specific to relatively local scales as in the above two examples. Large-scale CTs consider the dominant atmospheric circulation patterns across the whole of Europe, hence are less influential at the local scale. A simple example of this is the influence of the North Atlantic Oscillation (NAO) on European temperature and precipitation patterns (e.g. Hurrell, 1995). The NAO (based for example on the normalized pressure difference between Gibraltar and Reykjavik) explains up to 40% of the variance of winter season (December to February) temperature variability in southern Scandinavia (Jones et al., 2003), yet if a more local pressure gradient were developed (for this location using, for example, pressure data from Berlin and Stockholm) the explained variance would be considerably higher. The explanatory variable is still essentially the same (the NAO), but in the more local case we are looking at the westerly wind strength specific to the region being considered (southern Scandinavia). The issue of local- versus regional-scale pressure gradients has been commented upon earlier (see Jacobeit et al., 2001 comparing the temperature variance explained by the NAO with a more local zonal index over Central Europe). The results have potential implications for statistical downscaling techniques that use CT-based schemes. Model biases in RCM-based scenarios (dynamic downscaling) are generally used as one of the reasons for developing statistical downscaling techniques, but the use of the simpler objective typing schemes will produce scenarios which are not spatially consistent between neighbouring regions. The use of large-scale CTs is one potential way of deriving spatially consistent scenarios across a much larger region.

Here, we will use the Philipp et al. (2007) CTs for the four standard seasons to look at their surface temperature and precipitation response. We wish to assess whether the long-term change in temperature over Europe (towards warming) and precipitation (drying in Southern Europe and increases in wetness in Northern Europe, see e.g. Fig. 3.14 of Trenberth et al., 2007) is a result of a change in the mix of CTs or is a result of within-type changes in the CTs. The daily surface network of temperature and precipitation data is discussed in Section 2. In Section 3, we briefly introduce the Philipp et al. (2007) method of deriving circulation types and illustrate how the surface temperature data are transformed into anomalies for the time of year. Section 4 discusses a selection of the results and Sect. 5 concludes.

2 Data

The EMULATE project developed a daily temperature (maximum and minimum) and precipitation database encompassing many of the available long-term records for the European continent (see extensive discussion of sources and quality control in Moberg et al., 2006). The quality control of the station database undertaken by Moberg et al. (2006) was extensive, with an emphasis on the extremes in each of the series, but there wasn't a thorough assessment of the long-term homogeneity of the records. The EMULATE series were bolstered by the addition of series developed for the European Climate Analysis and Dataset (ECA&D, see Klok and Klein Tank, 2009). Here we chose those series that were as complete as possible for the period from 1911 to 2000. We use series from Iceland and Portugal in the West to the Ural mountains in the East, so extending about 20° further east than do the CTs from Philipp et al. (2007). The sites used show differences between the three variables and also for the periods of analysis. The locations of the available data used for the illustrated influences of each CT on surface climate will be evident in the subsequent figures.

3 Methods

Table 1 (from Philipp et al., 2007) gives the number of CTs for each of the four 3-month seasons. Figure 1 shows the percent of days in each season classified into each of the CTs for three periods (1911–1940, 1941–1970 and 1971–2000). The number of types in each season was determined by several objective criteria (see Philipp et al., 2007 for details). The ordering of the CTs was determined by the period 1850–2003, so there are differences between the three periods, slightly more so for winter and summer than for the transition seasons. Also in all seasons except spring, the 1971–2000 period differs more from the two earlier periods. All days are classified into one of the types, and readers should be mindful of this when assessing the results. Obviously for a given CT, there will be some days that would be very close to the basic type (referred to by Phillipp et al., 2007 as the centroid pattern), while for others the CT to which they are assigned is the closest of all the possible CTs. In these latter

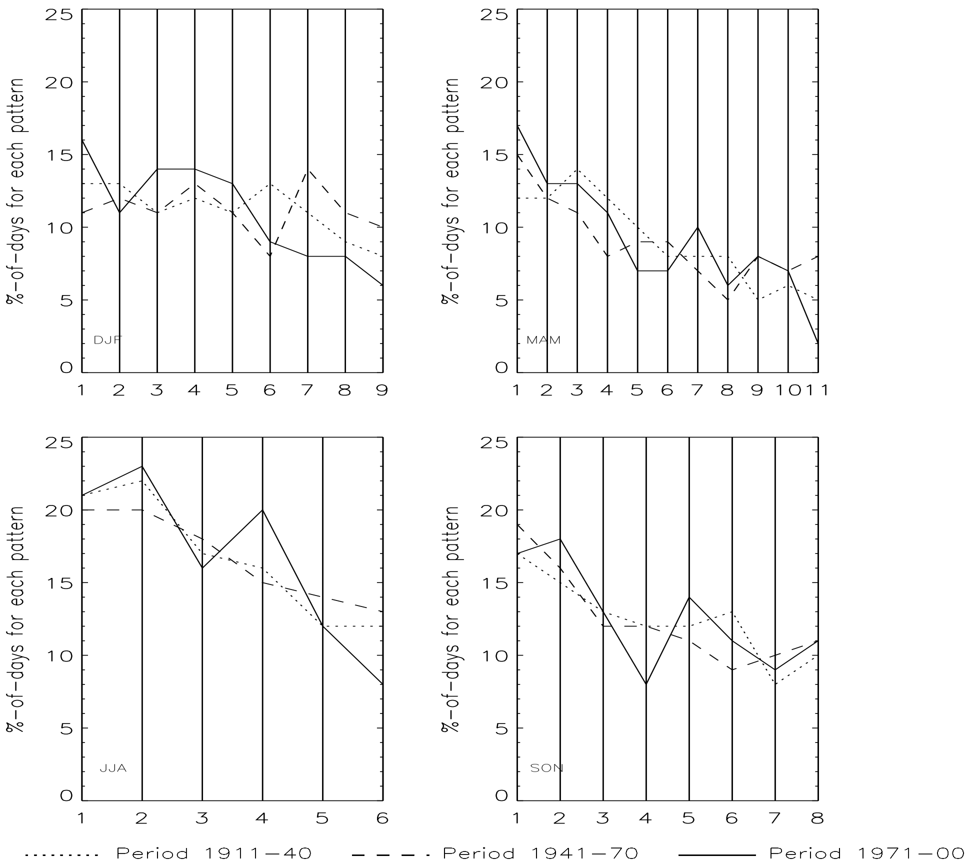

Fig. 1. The percentage of days of each CT within each season. The different line styles show these proportions for each of the three periods (1911–1940, 1941–1970 and 1971–2000). Each day within each season is classified into one of the types for each season, so the sum of the percentages for each period will be 100%.

cases, the surface climate response may be somewhat different from the types which look more like the basic pattern for each CT. Forcing all days into one of the basic types dilutes the patterns compared to the "continuous" nature of typing with the simplified (but necessarily more local) techniques discussed earlier. We use the word "continuous" as in the simpler typing schemes (e.g. Osborn et al., 2000) days are categorised according to three continuous variables (flow strength, wind direction and vorticity). Another possibility would be to weight each day by the correlation of that day's pattern compared with the 'average' pattern for that CT. We do not investigate this or the issue of differences within types further, but instead treat days of one CT type equal, looking at the average spatial response of surface temperature and precipitation to the particular CT. Later, we will consider whether the response to particular CTs changes during the period from 1911 to 2000.

To assess the surface response to each of these CTs, we constructed maps showing the effects on mean temperature, the diurnal temperature range (DTR) and precipitation. As the mean temperature and DTR response will be impacted by the time of year (particularly during the transition seasons), we extracted an annual cycle for each day of the year based on the 1961–1990 period for each station. This was developed separately for maximum and minimum temperature by smoothing the 1961–1990 average (where the raw average was based on the 30 January 1sts, 30 January 2nds, etc). The smoothing used an 11-term binomial filter, which has been recommended by a number of studies (Jones et al., 1999; Horton et al., 2000) as being sufficient to smooth the daily averages from only 30 observations, whilst still leaving a number of important singularities (Lamb, 1950) evident in many regions of Europe. Figure 2 shows an example of the filter for Kiev, a station chosen at random from the almost 200 possibilities. Daily temperature and DTR anomalies were then computed from the smoothed station-specific curves. The same procedure with smoothing was used for precipitation, but this essentially gives each smoothed daily value the 1961–1990 average daily precipitation amount (i.e. the monthly total divided by the number of days in the month).

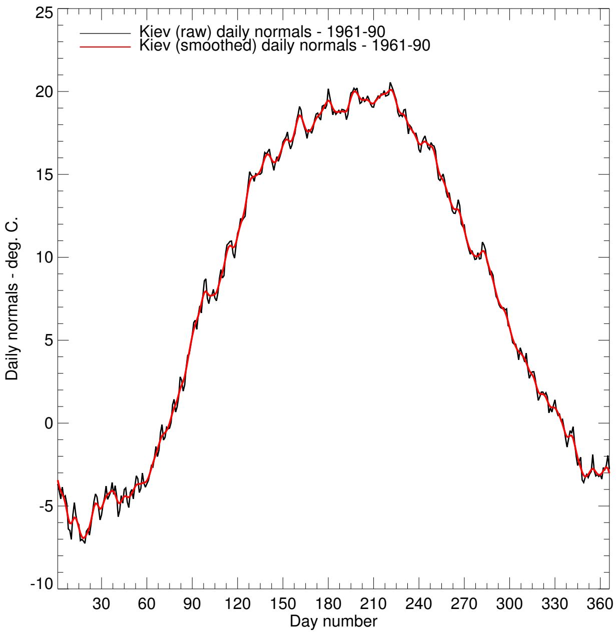

Fig. 2. Example of the daily filter for mean temperature for the station at Kiev.

As the daily station temperature and precipitation data are most complete for the period from the early 20th century, three 30-year periods (1911–1940, 1941–1970 and 1971–2000) were chosen for the analysis. Availability of data still means that there are more series that can be used for the later two 30-year periods compared to the first. For mean temperature, there are 150, 185 and 210 stations for each of the three 30-year periods respectively. Counts are slightly different for precipitation and DTR.

To assess the significance of the departures for temperature, DTR and precipitation, a Monte Carlo procedure was used. In this analysis a distribution for each station was calculated by randomly sampling all days in each season 10 000 times and then compared with the actual value based on the N days of each CT, enabling the statistical significance for each station to be assigned for each CT pattern. In the latter figures, the 95% statistical significance level was used.

4 Results

Thirty four different sets of figures were produced for each of the three 30-year periods. These include maps for each of the types in Table 1. Here we can show only a very small selection, but summarise the results in a single figure for each of the four seasons. We emphasize the results from the extreme seasons, as they are less affected by the changes in the influence of the circulation that occur during the transition seasons. The use of anomalies from the average 1961–1990 annual cycle (particularly for mean temperature) does ameliorate the issue to some extent, but simple examples for some of the patterns shows that some consistently bring warm extremes in May, but cooler than normal temperatures during March. This doesn't happen during the extreme seasons, but is also prevalent in the autumn. It would be ameliorated still further using the two-season CTs from Philipp et al. (2007), but would still be noticeable for some adjacent months (e.g. October and November). It might be possible to undertake the analyses on individual months, but this doesn't overcome the issue of some CTs in some seasons being more dominant during the early or latter months within the season. We don't investigate this further, but it would be important to do so for smaller sub-regions of Europe.

We now show three examples of the CTs, one each for the summer, autumn and spring season. We discuss each in turn and then make some overall comments about the maps, including the 31 that haven't been shown. The full set of 34 circulation patterns and surface responses is included in the Supplementary Information (http://www.cru.uea.ac.uk/projects/emulate-ct/). These comments relate to issues of relatively close stations sometimes giving opposite responses, particularly for DTR.

Figure 3 shows CT1 for the summer season and the response of mean surface temperature, DTR and precipitation amount for the period 1911–1940. In the figure we distinguish between the locations where the anomalies of the three variables are positive and negative and where the deviations are statistically significant at the 95% level using the Monte Carlo procedure detailed earlier. This CT is the classic pattern of an "Azores" high extending NE towards Europe. As expected this gives less precipitation over much of western Europe together with warmer than average temperatures and an enhanced DTR. Over most of the site locations in western Europe the response for these types of CT days is significant. Over eastern Europe, the patterns are weaker and less significant. The response patterns vary little for the two later periods (1941–1970 and 1971–2000, not shown, but see Supplementary Information).

Figure 4 shows CT4 for the spring season (for 1971–2000) and the response patterns for the same three variables as in Fig. 3. This CT involves a relatively deep low (for the time of year) over southern Scandinavia, giving anomalous northwesterly flow over western Europe and anomalous southwesterly flow further east. As expected mean temperatures are cooler than normal over all of western Europe with a reduced DTR. Further east temperatures are warmer than normal with enhanced DTRs over southeastern Europe. Precipitation amounts are greater than normal in central and western Europe and reduced around the peripheries of Europe (Iberia, the Balkans, northeastern Europe and northern Scandinavia). This response pattern is similar for the two earlier periods of 1911–1940 and 1941–1970 (see Supplementary Information).

Figure 5 incorporates CT3 for autumn (for 1941–1970) and its response patterns as in Fig. 3. This CT shows an

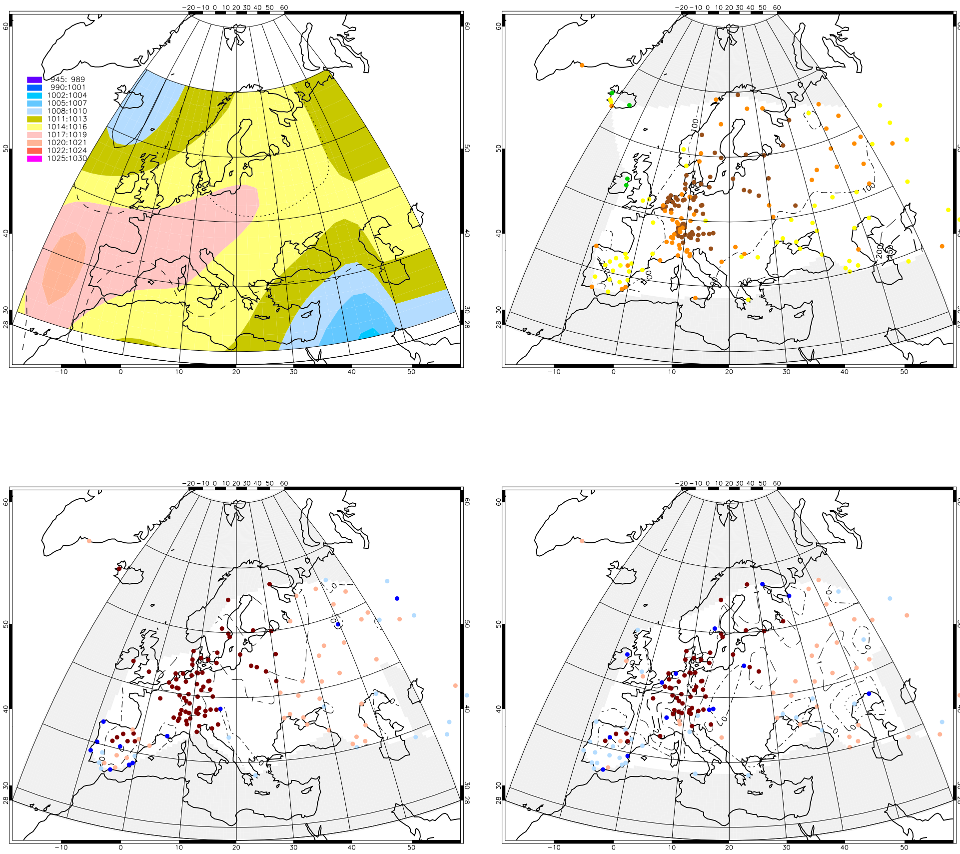

Fig. 3. Response of European surface temperatures, DTR and precipitation to CT1 for Summer (1911–1940). The top left panel shows the absolute MSLP values for the CT (coloured) with the anomaly from 1961-1990 shown by the contour lines. Dotted/solid lines are positive/negative anomalies at 2hPa intervals. The dashed line shows the zero anomaly. The top right panel shows the precipitation response to days of the CT. Yellow/orange dots indicate above/below normal precipitation, while green/brown indicate statistically significant (95% level) above/below normal precipitation. The bottom two panels are for mean temperature (left) and DTR (right). Here above/below normal temperatures and DTR are indicated by pink/light blue dots, while statistically significant departures are given in red/dark blue. Contour intervals for mean temperature and DTR are dashed lines (positive) and dotted lines (negative) and the zero line is dash/dot. For precipitation, above normal values (200%) are dashed while below normal values (50%) are dotted, with normal (100%) dash/dot. Grey shaded areas are outside the range of the stations.

anomalous and deep low centred over the Gulf of Finland together with higher than normal pressures over the Atlantic Ocean west of Ireland. This pattern would bring enhanced northerlies over western Europe and enhanced southerlies over the Ukraine and western Russia. As expected then, mean temperatures are reduced in western Europe from Scandinavia to the northwestern Mediterranean, while they are enhanced from the Black Sea northwards and eastwards. The response patterns are a little different for DTR and precipitation. For this CT the response patterns are similar but inverse for these two variables, showing the relationship that is linked to more clouds (so higher precipitation) and vice versa. DTR is reduced over central Europe encompassing the Low Countries, Germany, Poland and the Baltic States. Precipitation is increased over this same region, but the area with significantly increased precipitation extends further east into western Russia. DTR is enhanced around the Mediterranean, Black and Caspian Sea regions. Precipitation is reduced over the British Isles, western France, Iberia and much of the region around the Mediterranean, Black and Caspian Seas. This pattern is similar in the other two periods (1911–1940 and 1941–1970, not shown, but see Supplementary Information).

Figures 3–5 are just a small percentage of the plots produced in this study (see full set in the Supplementary Information). They show that for the three CTs illustrated, very similar patterns of mean temperature, DTR and precipitation occurred in all three periods. Next we discuss a number of the small-scale features evident on many of the maps. In the figures shown there are a number of instances where closely located sites respond differently in the mean temperature, DTR or precipitation maps. More closely-located

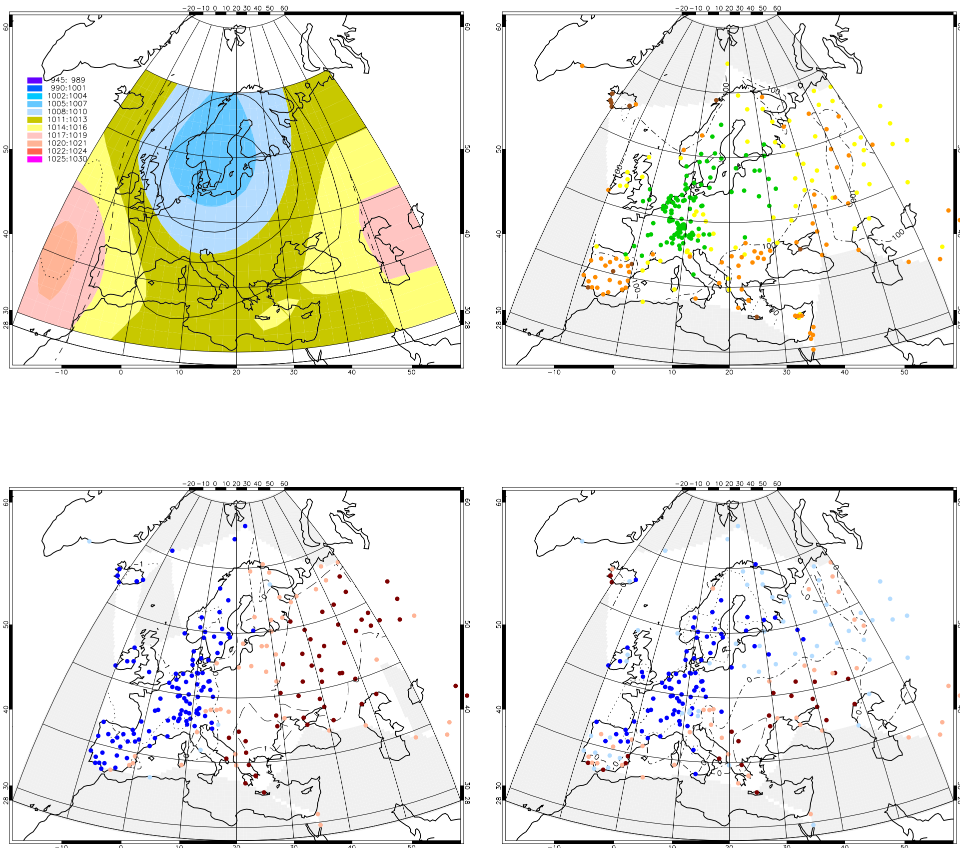

Fig. 4. As Fig. 3 but for Spring CT4 for 1971–2000.

sites respond differently in the DTR maps compared to those for mean temperature and precipitation. This is initially suggestive of homogeneity issues at some sites. It is extremely difficult to ensure good homogeneity of daily maximum and minimum temperature records, and hence DTR. Most aspects that cause discontinuities in temperature records will affect maximum and minimum temperature differently, so will cancel when mean temperature is considered, but the effect will be amplified in DTR. Although homogeneity for DTR may be an issue in some cases, there are numerous examples where the closely-located sites respond differently in all three 30-year periods. The sites are often located, (1) on the coast with the neighbouring site more inland; (2) markedly different elevations within mountain regions and; (3) being located on different sides of major mountain ranges (particularly the Alps). Depending on the wind directions associated with the CTs there can be marked differences either side of mountains (see Fig. 5 for precipitation and DTR), which clearly relate to windward and leeward sides and rain shadows. Away from major highland areas (e.g. the North European Plain) the responses of the sites tend to have hardly any closely-located sites responding differently.

We now return to the two questions posed in the introductory sections. These were (1) do the response patterns to the various CTs change between the three periods 1911–1940, 1941–1970 and 1971–2000 and (2) do the CTs explain any of the longer timescale variance of average temperature change across the large region studied? We address the first question by counting the number of positive and negative and then significantly positive/negative responses at the sites across Europe. We express these counts as percentages as the number of available sites across Europe differs (see earlier) for the three periods and is also different between variables.

Figure 6 shows summary diagrams for the four seasons. We show these plots for the three variables (precipitation, mean temperature and DTR). These plots present a lot of information. The top panels (for precipitation) for each season show which patterns generally bring wetter and which drier conditions to the greater European region. The middle and lower panels (for mean temperature and DTR respectively) show similar information for warmth or coldness across the large region. We begin by discussing the precipitation panels first, beginning with winter. Averaged over Europe, we can see which CTs give significantly above normal precipitation (CTs 4 and 5) at more than half the sites (in at least one of the

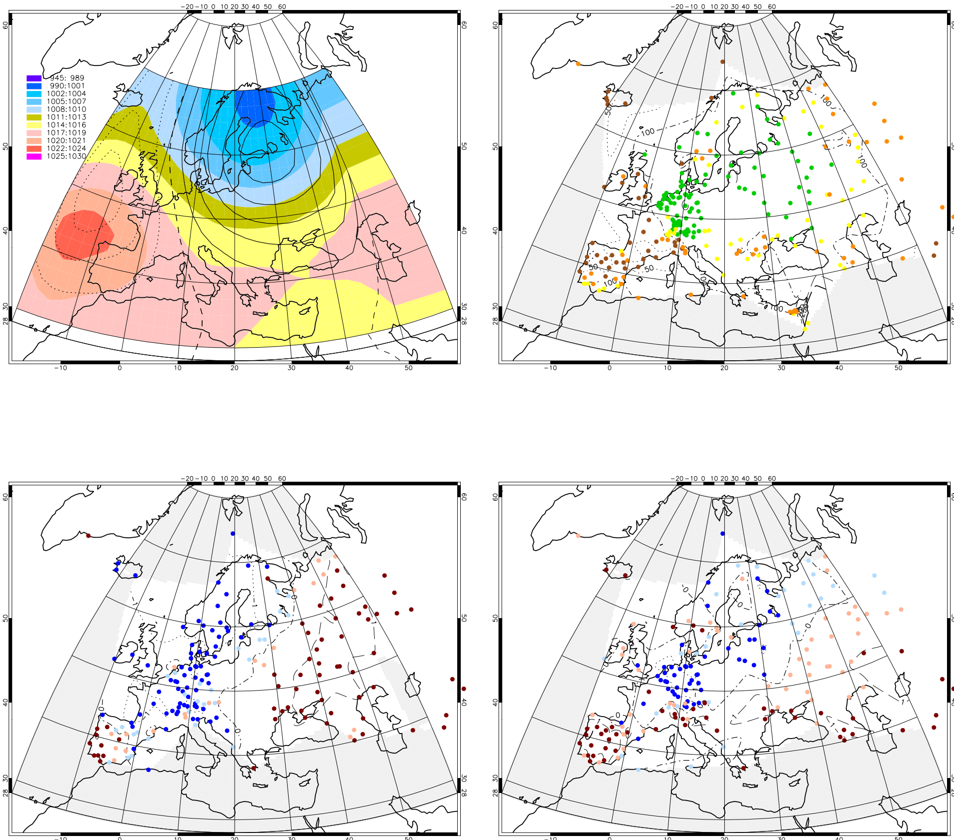

Fig. 5. As Fig. 3 but for Autumn CT3 for 1941–1970.

periods) and which give significantly below normal (CTs 2, 3, and 6). For the three periods, however, there is little difference in the percentage of significantly positive/negative sites between the three periods. For spring, the dominant wet pattern is CT 4, with CT 6 dominantly dry. For summer, there are no dominant wet or dry patterns. For autumn, the dominant wet pattern is CT 6, with the dominant dry pattern being CT 4. For all three seasons as with winter, there is little difference between the three periods.

For the mean temperature panel, for all four seasons, there are more patterns (as expected) which are dominantly cool or warm than evident for precipitation (so affecting at least half the sites, in one of the periods, across the large European region). For winter, there are four dominant warm patterns (CTs 1, 4, 5 and 9) and three which are dominantly cool (CTs 2, 7 and 8). For spring, there are two dominant warm patterns (CTs 7 and 10) with two dominant cool patterns (CTs 1 and 4). For summer, CT1 is a dominant warm pattern and CT2 cool. For autumn, CTs 5 and 6 are dominantly warm and CTs 4 and 7 cool. Unlike precipitation though, the solid lines (for the 1971–2000 period) tend to be slightly above those (indicating warming) for the other periods for many of the CTs in all seasons except autumn. This is clearer for the black lines, whereby we distinguish positive from negative departures. For DTR, there are no dominant patterns with the closest to our significance criterion (more than half the stations significant with the same sign of departure) being CT1 in summer.

For the precipitation and DTR panels in comparison to the mean temperature panels, there is a greater spread of the red, black and blue lines. This implies that there are a large number of stations (25–50% depending on the CT) where there is either more or less precipitation/DTR, but the amount isn't significant. For the mean temperature panel in winter the spread is smaller with only 10–20% of stations for all CTs not having statistically significant anomalies for each CT. This spread is wider for the other seasons for mean temperature, slightly larger for summer compared to spring and autumn. This shows that patterns of mean temperature departures are more organized than for precipitation and DTR, especially so in winter compared to summer. This is evident from the number of patterns which are dominated by one sign of the temperature or precipitation anomaly.

The second question has already been partly addressed for mean temperature by Philipp et al. (2007) in their Fig. 9. In this they compare observed changes in temperature for all four seasons over the central part of our domain (Central Europe, 45–55° N by 5–20° E) with estimates of changes from

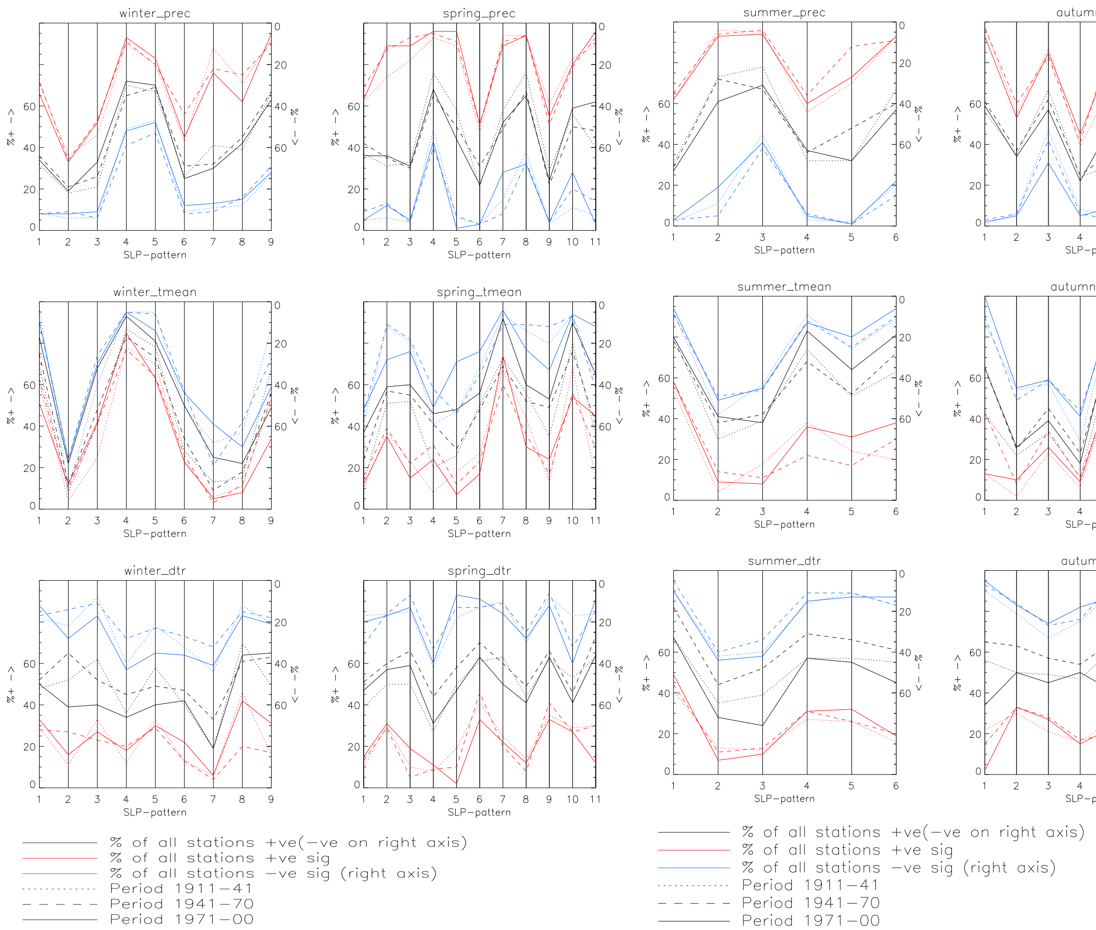

Fig. 6. Summary plots of the overall response of precipitation, surface temperature and DTR for each of the three periods (1911–1940, 1941–1970 and 1971–2000). Winter and Spring are on the left side, with Summer and Autumn on the right. The plots show the percent of stations with positive (warm/greater for mean temperature/DTR, left axis) and negative (cold/lesser for mean temperature/DTR, right axis) anomalies for the three periods (shown by different line styles). For precipitation the red/blue is reversed, so red indicates drier than normal and blue wetter than normal. The red/blue lines indicate the percentage of stations with statistically significant departures in the same three line styles.

regression against the counts of the various CTs in each of the seasons. In all seasons, though, the circulation explains much of the high-frequency temperature variance, implying that the underlying warming would be more statistically significant if the circulation component were extracted. Only in spring (95%) and autumn (90%) did the trend of the circulation component of temperature increase over their study period (1851/2000–2003). Circulation-related temperature trends in spring and summer are slightly negative. This finding is in agreement with Osborn and Jones (2000) and van Oldenburgh and van Ulden (2003), so we don't pursue this any further.

5 Conclusions

The aims of this paper have been to look at the possible changing influence of the atmospheric circulation on surface temperature, precipitation and DTR across Greater Europe. We use the recently developed classification scheme from Philipp et al. (2007) which reduces daily surface pressure maps into 6 to 11 patterns depending on the season. For surface temperature and precipitation data we use long daily series (extending from 1911–2000) developed during the EMULATE and ECA&D projects. We reduce all station series to anomalies from a specifically developed annual cycle for each station. For each of the 34 CTs (grouping all four seasons together) we plot anomaly maps of mean temperature, DTR and precipitation for all days of each CT within the three periods, 1911–40, 1941–70 and 1971–2000. We assess the significance of the average maps using Monte Carlo procedures.

The results reveal that across Greater Europe there are dominant warm and cold patterns for temperature, where more than half the station locations show significantly positive or negative departures. Fewer CTs could be described as dominantly wet or dry when it came to precipitation and even fewer with dominantly high or low DTR. Finally, we addressed the question of whether the circulation influence of these CTs has changed during the three periods. For mean temperature, particularly for winter and to a lesser extent spring and summer, there was evidence of more of the CTs indicating warmer temperatures during the most recent period. For precipitation and DTR, and also mean temperatures in autumn, there was less evidence of changes occurring between the three periods.

Acknowledgements. This work has been supported by the U.S. Department of Energy (grant DE-FG02-98ER62601). The authors also acknowledge support from the EU-EMULATE project (EVK2-CT-2002-00161) which developed the circulation typing scheme and the daily station dataset of temperature and precipitation data. Jucundus Jacobeit and one anonymous reviewer significantly improved the manuscript during the review process.

Edited by: V. Masson-Delmotte
Reviewed by: H. Wanner, J. Jacobeit, and P. Yiou

References

Alexander, L. V. and Jones, P. D.: Updated precipitation series for the United Kingdom, Atmos. Sci. Lett., 1, 142–150, 2001.

Ansell, T. J., Jones, P. D., Allan, R. J., Lister, D., Parker, D. E., Brunet, M., Moberg, A., Jacobeit, J., Brohan, P., Rayner, N. A., Aguilar, E., Alexandersson, H., Barriendos, M., Brandsma, T., Cox, N. J., Della-Marta, P. M., Drebs, A., Founda, D., Gerstengarbe, F., Hickey, K., Jonsson, T., Luterbacher, J., Nordli, A., Oesterle, H., Petrakis, M., Philipp, A., Rodwell, M. J., Saladie, O., Sigro, J., Slonosky, V., Srnec, L., Swail, V., Garcia-Suarez, A. M., Tuomenvirta, H., Wang, X., Wanner, H., Werner, P., Wheeler, D., and Xoplaki, E.: Daily mean sea level pressure reconstructions for the European – North Atlantic region for the period 1850–2003, J. Climate, 19, 2717–2742, 2006.

Beck, C., Jacobeit, J., and Jones, P. D.: Frequency and within-type variations of large-scale circulation types and their effects on low-frequency climate variability in Central Europe since 1780, Int. J. Climatol., 27, 473–491, 2007.

Hess, P. and Brezowsky, H.: Katalog der Grossweterlagen Europas 1881-1976. 3e verbesserte und ergänzie Auflage, Berichte des Deutschen Wetterdienstes 113, Offenbach, Germany, 70 pp., 1977.

Hurrell, J. W.: Decadal trends in the North Atlantic Oscillation: regional temperatures and precipitation, Science, 269, 676–679, 1995.

Huth, R., Beck, C., Phillipp, A., Demuzere, M., Ustrnul,Z., Cahynová, M., Kyselý, J., and Tveito, O.-E.: Classifications of atmospheric circulation patterns: recent advances and applications, Annals of the New York Academy of Sciences, 1146, 105–152, 2008.

Jacobeit, J., Jönsson, P., Bärring, L., Beck, C., and Ekström, M.: Zonal indices for Europe 1780-1995 and running correlations with temperature, Clim. Change, 48, 219–241, 2001.

Jones, P. D., Horton, E. B., Folland, C. K., Hulme, M., and Parker, D. E.: The use of indices to identify changes in climatic extremes, Clim. Change, 42, 131–149, 1999.

Jones, P. D., Osborn, T. J., and Briffa, K. R.: Pressure-based measures of the NAO: A comparison and an assessment of changes in the strength of the NAO and in its influence on surface climate parameters, in: North Atlantic Oscillation, edited by: Hurrell, J. W., Kushnir, Y., Ottersen, G., and Visbeck, M., American Geophysical Union, Washington DC, 51–62, 2003.

Klok, L. and Klein Tank, A. M. G.: Updated and extended European dataset of daily climate observations, Int. J. Climatol., 29, 1182–1191, 2009.

Lamb, H. H.: Types and spells of weather around the year in the British Isles, Quart. J. Roy. Meteor. Soc., 76, 393–438, 1950.

Lamb, H. H.: British Isles weather types and a register of the daily sequence of circulation patterns, 1861-1971. Geophysical Memoir, 116, HMSO, London, 85 pp., 1972.

Moberg, A., Jones, P. D., Lister, D. H., Walther, A., Brunet, M., Jacobeit, J., Alexander, L. V., Della-Marta, P. M., Luterbacher, J., Yiou, P., Chen, D., Klein-Tank, A. M. G., Saladié, O., Sigró, J., Aguilar, E., Alexandersson, H., Almarza, C., Auer, I., Barriendos, M., Begert, M., Bergström, H., Böhm, R., Butler, C.J., Caesar, J., Drebs, A., Founda, D., Gerstengarbe, F.-W., Micela, G., Maugeri, M., Öesterle, H., Pandzic, K., Petrakis, M., Srnec, L., Tolasz, R., Tuomenvirta, H., Werner, P. C., Linderholm, H., Philipp, A., Wanner, H., and Xoplaki, E.: Indices for daily temperature and precipitation extremes in Europe analyzed for the period 1901–2000, J. Geophys. Res., 111, D22106, doi:10.1029/2006/JD007103, 2006.

Osborn, T. J. and Jones, P. D.: Air flow influences on local climate: observed United Kingdom climate variations, Atmos. Sci. Lett., 1, 62–74, 2000.

Parker, D. E., Legg, T. P., and Folland, C. K.: A new daily Central England temperature series, 1772–1991, Int. J. Climatol., 12, 317–342, 1992.

Philipp, A., Della-Marta, P. M., Jacobeit, J., Fereday, D. R., Jones, P. D., Moberg, A., and Wanner, H.: Long-term variability of daily North Atlantic-European pressure patterns since 1850 classified by simulated annealing clustering, J. Climate, 20, 4065–4095, 2007.

Trenberth, K. E., Jones, P. D., Ambenje, P., Bojariu, R., Easterling, D., Klein Tank, A., Parker, D., Rahimzadeh, F., Renwick, J. A., Rusticucci, M., Soden, B., and Zhai, P.: Observations: Surface and Atmospheric Climate Change, in: Climate Change 2007: The Physical Science Basis, Contribution of Working Group 1 to the Fourth Assessment Report of the Intergovernmental Panel on Climate Change, edited by: Solomon, S., Qin, D., Manning, M., Chen, Z., Marquis, M., Averyt, K. B., Tignor M., and Miller, H. L., 235–336, Cambridge University Press, Cambridge, United Kingdom and New York, NY, USA, 2007.

van Oldenborgh, G. J. and van Ulden, A.: On the relationship between global warming, local warming in the Netherlands and changes in the circulation in the 20th century, Int J. Climatol., 23, 1711–1724, 2003.

Yarnal, B.: Synoptic climatology in environmental analysis, Belhaven Press: London, 1993.

Clim. Past, 7, 1261–1284, 2011
www.clim-past.net/7/1261/2011/
doi:10.5194/cp-7-1261-2011

Climate of the Past

Hydrological variability in the Northern Levant: a 250 ka multi-proxy record from the Yammoûneh (Lebanon) sedimentary sequence

F. Gasse[1,], L. Vidal[1], A.-L. Develle[1,*], and E. Van Campo[2,3]**

[1]CEREGE, UMR6635, Marseille Université-CNRS-IRD-Collège de France, BP 80, 13545 Aix-en-Provence cedex 04, France
[2]Université de Toulouse, UPS, INPT, Ecolab, 29 rue Jeanne Marvig, 31055 Toulouse, France
[3]CNRS, Ecolab (Laboratoire d'écologie fonctionnelle), 31055 Toulouse, France
[*]now at: Laboratoire Chrono-Environnement, UMR6249, Université de Franche-Comté, 16 Route de Gray, 25030, Besançon cedex, France

[**]*Invited contribution by F. Gasse, recipient of the EGU Hans Oeschger Medal 2010*

Received: 13 April 2011 – Published in Clim. Past Discuss.: 10 May 2011
Revised: 13 September 2011 – Accepted: 5 October 2011 – Published: 24 November 2011

Abstract. The Levant is a key region in terms of both long-term hydroclimate dynamics and human cultural evolution. Our understanding of the regional response to glacial-interglacial boundary conditions is limited by uncertainties in proxy-data interpretation and the lack of long-term records from different geographical settings.

The present paper provides a 250 ka paleoenvironmental reconstruction based on a multi-proxy approach from northern Levant, derived from a 36 m lacustrine-palustrine sequence cored in the small intra-mountainous karstic Yammoûneh basin from northern Lebanon. We combined time series of sediment properties, paleovegetation, and carbonate oxygen isotopes (δ_c), to yield a comprehensive view of paleohydrologic-paleoclimatic fluctuations in the basin over the two last glacial-interglacial cycles. Integration of all available proxies shows that Interglacial maxima (early-mid MIS 7, MIS 5.5 and early MIS 1) experienced relatively high effective moisture, evidenced by the dominance of forested landscapes (although with different forest types) associated with authigenic carbonate sedimentation in a productive waterbody. Synchronous and steep δ_c increases can be reconciled with enhanced mean annual moisture when changes in seasonality are taken into account. During Glacials periods (MIS 2 and MIS 6), open vegetation tends to replace the forests, favouring local erosion and detrital sedimentation. However, all proxy data reveal an overall wetting during MIS 6, while a drying trend took place during MIS4-2, leading to extremely harsh LGM conditions possibly linked to water storage as ice in the surrounding highlands. Over the past 250 ka, the Yammoûneh record shows an overall decrease in local effective water, coincident with a weakening of seasonal insolation contrasts linked to the decreasing amplitude of the eccentricity cycle.

The Yammoûneh record is roughly consistent with long-term climatic fluctuations in the northeastern Mediterranean region (except during MIS 6). It suggests that the role of seasonality on effective moisture, already highlighted for MIS 1, also explains older interglacial climate. The Yammoûneh record shares some features with speleothem isotope records of western Israel, while the Dead Sea basin generally evolved in opposite directions. Changes in atmospheric circulation, regional topographic patterns and site-specific hydrological factors are invoked as potential causes of spatial heterogeneities.

Further work is needed to refine the Yammoûneh chronology, better understand its functioning through hydrological and climate modelling, and acquire other long records from northern Levant to disentangle the relative effects of local versus regional factors.

Correspondence to: F. Gasse
(gasse@cerege.fr)

Published by Copernicus Publications on behalf of the European Geosciences Union.

1 Introduction

The Levant (Fig. 1), which stretches along the East Mediterranean seashore from Southeast Turkey to northern Egypt and Arabia, straddles the boundary between a typical temperate-warm Mediterranean domain and the subtropical desertic belt. Moisture primarily comes from the eastern Mediterranean Sea (EMS). Rainfall decreases sharply from north to south with latitude and more sharply from west to east due to the orographic effect of mountain ranges running parallel to the coastline. Just eastward, a chain of deep depressions, including the Dead Sea basin, forms a narrow corridor. Altitudes range from more than 3000 m a.s.l. (above sea level) in Lebanon to 425 m b.s.l. (below sea level) along the Dead Sea shore. This complex physiogeographic pattern results in a large diversity of terrestrial environmental conditions which vary dramatically over short distances with latitude, altitude and continentality.

Numerous terrestrial and marine archives have revealed huge Late Quaternary climatic-hydrological fluctuations in the EMS domain. The northeastern Mediterranean region experienced wet-warm interglacials with intense rainfall from the North Atlantic and cold-dry glacial environments when ice sheets over northern Europe reached their maximal extension (e.g., Tzedakis, 2007), as showed, for example, by pollen-inferred reconstructions of climatic parameters (e.g., Guiot et al., 1999). Monsoonal rainfall penetrated the subtropical desertic belt during boreal summer insolation maximums (peak of Interglacials periods) while glacial stages were hyperarid, as revealed by speleothem, lake and groundwater archives (e.g., Gasse, 2000; Hoelzmann et al., 2004; Fleitmann and Matter, 2009).

Between these two domains, changes in water availability in the Levant, which might have influenced the migration of early modern humans out of Africa and the Pleistocene-Holocene cultural dynamics of Eurasia (Bar-Yosef, 1998; Vaks et al., 2007; Shea, 2008; Carto et al., 2009; Frumkin et al., 2011), have been the focus of outstanding climatic-hydrological studies (see the reviews of Robinson et al., 2006; Enzel et al., 2008; Waldmann et al., 2010; Frumkin et al., 2011, and references therein). The best records come from U/Th-dated stable isotope profiles of Israeli speleothems and reconstructed lake-level fluctuations in the Dead-Sea basin (DSB). Long terrestrial pollen records are scarce and poorly dated (e.g., Bottema and Van Zeist, 1981; Weinstein-Evron, 1983; Weinstein-Evron et al., 2001; Meadows, 2005). In southern Levant, sporadic events of speleothems and travertine growth indicate episodes of enhanced effective precipitation in phase with periods of intensified monsoon (Waldmann et al., 2010; Vaks et al., 2010). Just northward, the DSB experienced generally high lake water levels indicating locally high effective moisture during glacial periods and dry conditions during Interglacials attributed to changes in rainfall amount by Enzel et al. (2008). Conversely, speleothems δ^{18}O profiles from western Israel

Fig. 1. The Levant in the eastern Mediterranean region. Location of the Yammoûneh basin and of sites cited in the text. For terrestrial records, 1: Jeita Cave; 2: Aammish marsh; 3: Peqi'in Cave; 4: Soreq Cave; 5: Lake Ohrid; 6: Tenaghi Philippon; 7: Lake Gölhisar; 8: Lake Konya; 9: Lake Urmia; 10: Lake Zeribar; 11: Lake Mirabad.

have suggested dry-cool glacial and wet-warm interglacial conditions (Bar-Matthews et al., 2003). This clearly highlights contrasted or controversial pictures of the hydrological evolution of the Levantine region. Furthermore, the complex regional physiographic pattern, the scarcity of records extending beyond the Last Glacial Maximum (LGM) in northern Levant and the differences in data interpretation might explain part of the heterogeneity of the climate signals. It is also noteworthy to underline that most of the available records are based on a single type of proxy knowing that none of the before cited proxy/archive are univocal when interpreted as a unique climate parameter. Crucial questions remain on the relative contributions of temperature, precipitation, evaporation and seasonal changes to the response of environmental indicators and of hydro-, eco-systems to climate changes. Multi-proxy analyses of sedimentary profiles may help disentangle the impacts of these climatic variables.

This present paper focuses on the interpretation of a multi-approach study, integrating sedimentological, paleobotanical and isotopic data, of a long sedimentary sequence (250 ka). This sub-continuous lacustrine/palustrine sequence comes from a small, intra-mountainous karstic basin lying in the poorly known northern Levant (Yammoûneh, Lebanon). Results already published on the sedimentary profile are briefly summarized (chronology and sedimentary processes for the past 250 ka; carbonate oxygen isotopes for the past 21 ka;

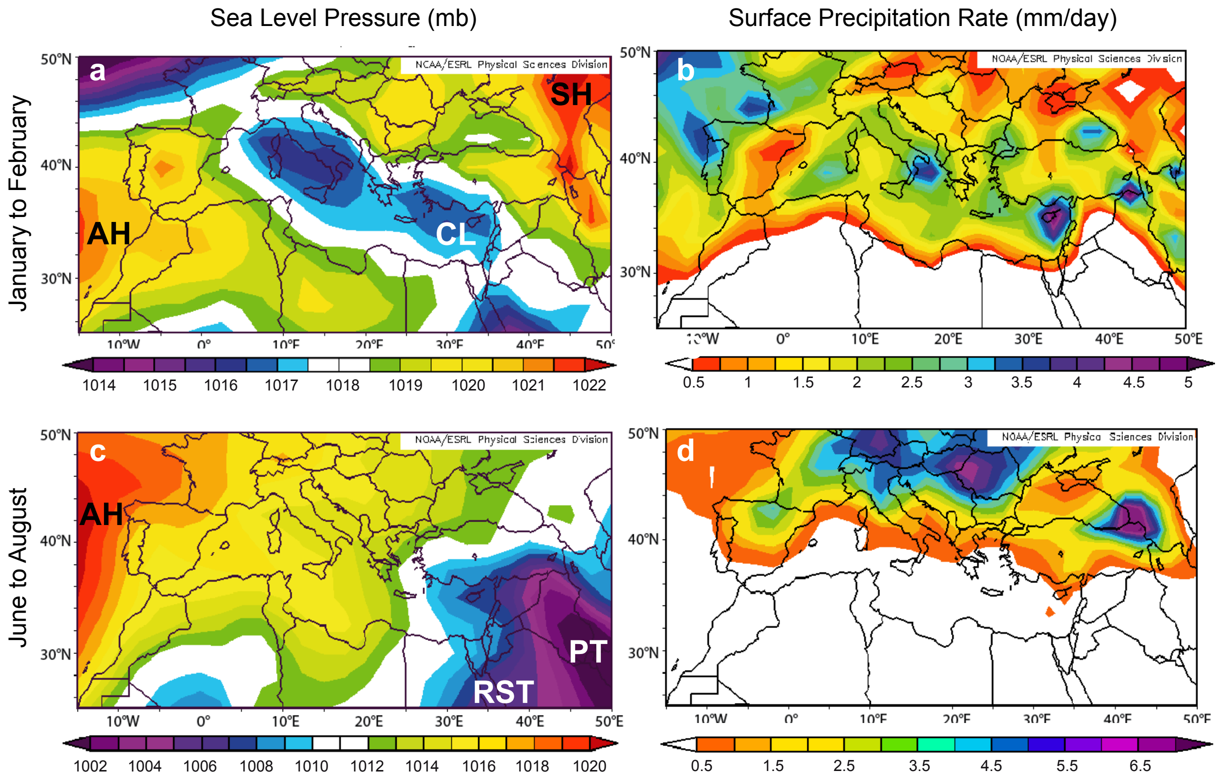

Fig. 2. Sea level pressure and surface precipitation rate in the Mediterranean region in winter – January–February: **(a)**, **(b)** – and summer – June–August: **(c)**, **(d)** – averaged from 1968 to 1996. Source: NCEP/NCAR Reanalysis. NCAA/ESLP Physical Sciences Division (http://www.cdc.noaa.gov/Composites/Day/). AH: Azores High; SH: Siberian High; CL: Cyprus Low; RST: Red Sea Trough; PT: Persian Trough.

Develle et al., 2010, 2011). Attention is paid here to new data: pollen-inferred paleovegetation and biogenic carbonate $\delta^{18}O$ data of the whole sequence. Our main aim is to yield a comprehensive view of the long-term environmental fluctuations in the Yammoûneh basin over the two last glacial-interglacial cycles by integrating the different proxies. Our record is then replaced in its regional context. The paper is underlaid by the following questions:

1. What are the relationships between individual proxies?
2. What are the main environmental characteristics of the Yammoûneh basin during full glacial and interglacial peaks?
3. How does this record from northern Lebanon compare with other long-term records from central and southern Levant and from northeastern Mediterranean?

2 Modern setting

2.1 Main physiogeographic and climate features of the Levant region

The steep topography of the Levant is related to the active Levant Fault System (Le Pichon and Gaulier, 1988) that runs from the NW tip of the Red Sea to SE Turkey through the Arava Valley, the Dead Sea-Jordan Valley-Lake Tiberias-Hula basins to the Ghab basin in Syria (Fig. 1). East of narrow coastal plains, the SSW-NNE mountain ranges culminate at 3083 m a.s.l. in Mount Lebanon at only 20–25 km from the sea shore, while the Dead Sea basin represents the lowest spot of the Earth. Orography and distance from the seashore strongly modulate the local rainfall patterns.

The Levant experiences a Mediterranean climate with wet cool winter and warm dry summer, primarily controlled by the Mediterranean cyclonic system intimately tied to the North Alantic system. Winter precipitation is generated by the cyclonic activity over the Sea (Sharon and Kutiel, 1986), when the Siberian anticyclone is reinforced over SW Asia and the Azores High extends over North Africa and Spain (Fig. 2a and b). The Mediterranean cyclogenesis is influenced by the surrounding regions and possibly by long distance teleconnections, e.g., the North Atlantic Oscillation (NAO) (Ziv et al., 2006, 2010; Dayan et al., 2008; Raible et al., 2010). Cyclones, either generated in the Mediterranean basin or penetrating from the North Atlantic, are steered by the mid-latitude westerlies and tend to propagate eastward along the northern coast of the Mediterranean until reaching the Levant region. When propagating over the relatively warm seawater, air masses become saturated by moisture. In the EMS, polar intrusions create a deep upper-level trough accompanied by low-level cyclogenesis. The strength and position of cyclones formed or reactivated in the EMS (the Cyprus Lows, Fig. 2a) largely control the winter rainfall temporal and spatial variability in the Levant (Enzel et al., 2003; Ziv et al., 2006). In summer (Fig. 2c and d), when the Siberian anticyclone is attenuated and the Azores anticyclone and the mid-latitude westerly belt are shifted northward, the Levantine region is warm and dry. The summer low-pressure systems developed southward and eastward (the Red Sea Trough and the Persian Trough) are generally hot and dry (Kahana et al., 2002).

Several mechanisms indirectly link the Levant to subtropical and tropical climates. Very dry summer conditions over the eastern Mediterranean region and northeastern Sahara are partly due to the subsidence of easterly airflows linked to the Indian monsoon activity (Rodwell and Hopkins, 1996; Ziv et al., 2004). Most of the occasional rainfall events occurring in the Negev desert during spring and autumn are in conjunction with an active Red Sea Trough (Kahana et al., 2002). Heavy dust storms of North African origin are frequent from December to April. Saharan dust influx to the region has often been attributed to the thermal lows of the Sharav cyclones formed over Libya and Egypt (Alpert and Ziv, 1989) and the Red Sea Trough, but the cold Cyprus Lows also play a major role in attracting Saharan dust plumes (Dayan et al., 2008). The Nile River discharge, which depends on tropical rainfall in East Africa, affects the EMS hydrothermal dynamics (Rossignol-Strick and Paterne, 1999) and, thus, sea-land interactions.

2.2 The Yammoûneh basin in Lebanon

The Yammoûneh basin (34.06° N–34.09° N, 36.0° E–36.03° E, 1360 m a.s.l.), 6 km long, 2 km wide, lies at approximately 37 km from the seashore on the eastern flank of Mount Lebanon (Fig. 3). It was occupied in its southern part by a seasonal lake from at least Roman times to the 1930s when it was drained for irrigation of the Bakka plain. It is today entirely cultivated. No paleo-shoreline was observed, suggesting that the paleolake never reached high levels during a period long enough to leave geomorphic evidence. The basin is a SSW-NNE depression of tectonic origin along the Yammoûneh Fault, a segment of the Levant Fault System. It was downfaulted through thick sub-tabular sequence of intensively karstified Cenomanian dolomitic limestones (Dubertret, 1975; Hakim, 1985). The strike-slip

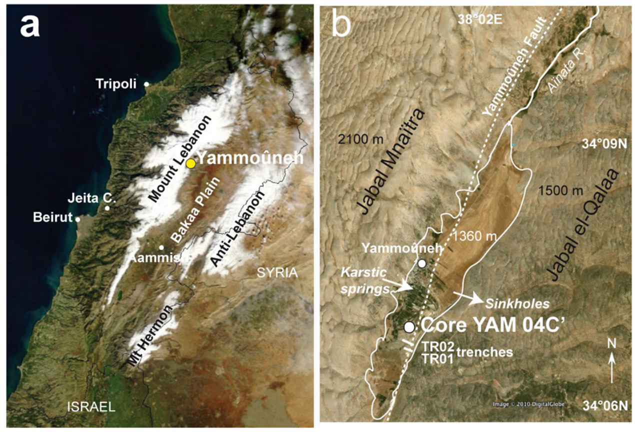

Fig. 3. The Yammoûneh basin in Lebanon. **(a)** Satellite view of Lebanon in winter (January 2003), main morphological structures. **(b)** The Yammoûneh basin with location of the sedimentary profiles. Dashed line: surface trace of the Yammoûneh Fault. Arrows schematize the groundwater circulation, from the Mnaïtra Plateau which provides the main water inflow to the basin via karstic springs emerging along the western edge of the basin, and infiltration along the eastern edge.

Yammoûneh Fault is active (slip rate: 3.8–6.4 mm yr^{-1}), but vertical movements likely remained negligible during the Late Quaternary (Daëron et al., 2004, 2007; A. R. Elias, personal communication, 2009). The Yammoûneh basin is limited by the high Mnaïtra plateau (2100 m a.s.l.) that abruptly rises westward, and by the gently sloping hills (Jabal el-Qalaa, 1500 m a.s.l.) which separates the basin and the large Bakka plain syncline to the East.

In Lebanon (Service Météorologique du Liban, 1977), Mean Annual Precipitation (MAP) ranges from 700–1000 mm along the coast, >1400 mm in Mount Lebanon, to 400 mm in the Bakka plain and <200 mm in the NE. Above 2000 m a.s.l., precipitation is essentially niveous. At Yammoûneh, MAP reaches 900–1000 mm, as snow falls over about 30 days yr^{-1}. The wet-cold season (November–March) culminates in January, while precipitation is almost nil from June to August. Continentality is marked by large diurnal and seasonal variations in temperature and air humidity. Mean Annual Temperature (MAT) is about 15 °C but freezing occurs over 3 months yr^{-1} and temperature maximum largely exceeds 30 °C during the warmest month (July).

The strong rainfall and temperature gradients in Lebanon result in vegetation zones ranging from forest and woodland to open steppe (Abi-Saleh and Safi, 1988). The climatic characteristics and typical plant taxa of vegetation zones are summarized in Table 1. The western slopes of Mount Lebanon present a transition, with increasing elevation, from successive Mediterranean belts with very warm to more temperate climate, a mountain and a subalpine belts characterised by trees of cool-wet conifer forests up to the treeline. Due to the gradual change to continental Mediterranean

CHAPTER 2.2

Table 1. Distribution of the modern vegetation belts in the Yammoûneh area as a function of location, altitude, mean annual precipitation (MAP) and mean annual temperature (MAT). After Abi-Saleh and Safi (1988).

	Altitude (m a.s.l.)	MAP (mm yr^{-1})	MAT (T °C)	Characteristic plant taxa	
Western flank of Mt Lebanon					
Lower Mediterranean belt	0–500	>600	20	*Ceratonia silica, Pistacia lentiscus*, *Myrtus communis*	*Pinus* spp.
Middle Mediterranean belt	500–1000	800–1000	16–18	Evergreen oak *Quercus calliprinos*, *Pinus brutia, P. pinea*	
Upper Mediterranean belt	1000–1500	>900–1000	15–16	Lower part: *Q. calliprinos* Upwards: deciduous oaks: *Q. infectoria, Q. cerris*	
Mountain belt	1500–2000	>1000	5–15	*Cedrus libani, Abies cilicica*	
Subalpine belt	>2000	>1200	0–5	*Juniperus excelsa up to the tree line*	
Eastern flank of Mt Lebanon					
	900–1800	600–800	16–18	*Q. calliprinos, Q. infectoria*	
	>1800	>800	<16	*Juniperus excelsa*	
Bakka plain					
	900–1100	200–600	15	Abundant steppe elements *Hammada eigii Artemisia herba alba Salsola villosa* *Noaea mucronata*	

and sub-desertic conditions, the eastern slopes receive less rainfall than corresponding altitudes in west Lebanon. Only Mediterranean oaks, and junipers at high elevation, are present. The much drier Bakka plain is open to influx of steppe elements from the adjacent Irano-Turanian territory. Human impact has considerably deteriorated and modified the natural ecosystems since millenia.

Hydrologically, the Yammoûneh basin primarily depends on precipitation over the western highlands. Direct precipitation on the paleolake surface ($<1.2 \times 10^6$ m^3 yr^{-1}) and on the small surface watershed ($\sim$105 km^2; Develle et al., 2011) is negligible compared to the important water inflow brought by permanent karstic springs (35–70 $\times 10^6$ m^3 yr^{-1}; Besançon, 1968; Hakim, 1985). Beneath the Mnaïtra plateau, subterranean karstic networks collect snowmelt water feeding a dozen springs along the western edge of the basin. The cool karstic spring water exhibits an isotopic composition (mean: δ^{18}O = ~ -8.9 ‰, δD = ~ -50.8 ‰) very close to that of winter rainfall ($\sim$90 % of MAP) in the watershed (Develle et al., 2010), without significant impact of evaporation or sublimation before infiltration (Aouad et al., 2004). Studies of nearby karstic aquifer systems show that groundwater residence time is negligible on the geological time-scale (from 1 season to 2–3 years; Aouad et al., 2005; El Hakim, 2005). In the basin floor, sinuous channels drain spring and runoff water from the west into karstic sinkholes along the eastern border. The karstified, intensively fissured and faulted substrate, is highly permeable. Hence, the basin is hydrologically open with rapid throughflow. Water residence time and relative evaporation losses may have, however, increased when a permanent lake occupied the basin.

3 Stratigraphy, chronology and sedimentary processes

Descriptions of stratigraphical units, analytical methods applied for chronology and sedimentology, and discussions on result interpretations are detailed in Develle (2010) and Develle et al. (2010, 2011). Main results are summarized below.

3.1 Stratigraphy

The upper 36 m of the sediment core (YAM-04C', 73 m) collected in 2004 from the central part of the Yammoûneh paleolake (Fig. 3) has revealed a sub-continuous accumulation of lacustrine-palustrine sediments. A very simplified stratigraphic log and pictures of some core sections illustrate the variety of lithofacies (Fig. 4). As the uppermost Unit I is truncated in the core, some data were derived from nearby trenches (TR01, TR02, Fig. 3) which contain the whole Holocene period.

The profile shows two main types of sediments, although transitions between stratigraphic units are often gradual:

1. Pale intervals, a few metres thick, dominated by carbonates. They consist of whitish powdery silt or very fine sand (Units I, VI and IX; Fig. 4e) rich in calcified remains of aquatic organisms (gastropods, ostracods,

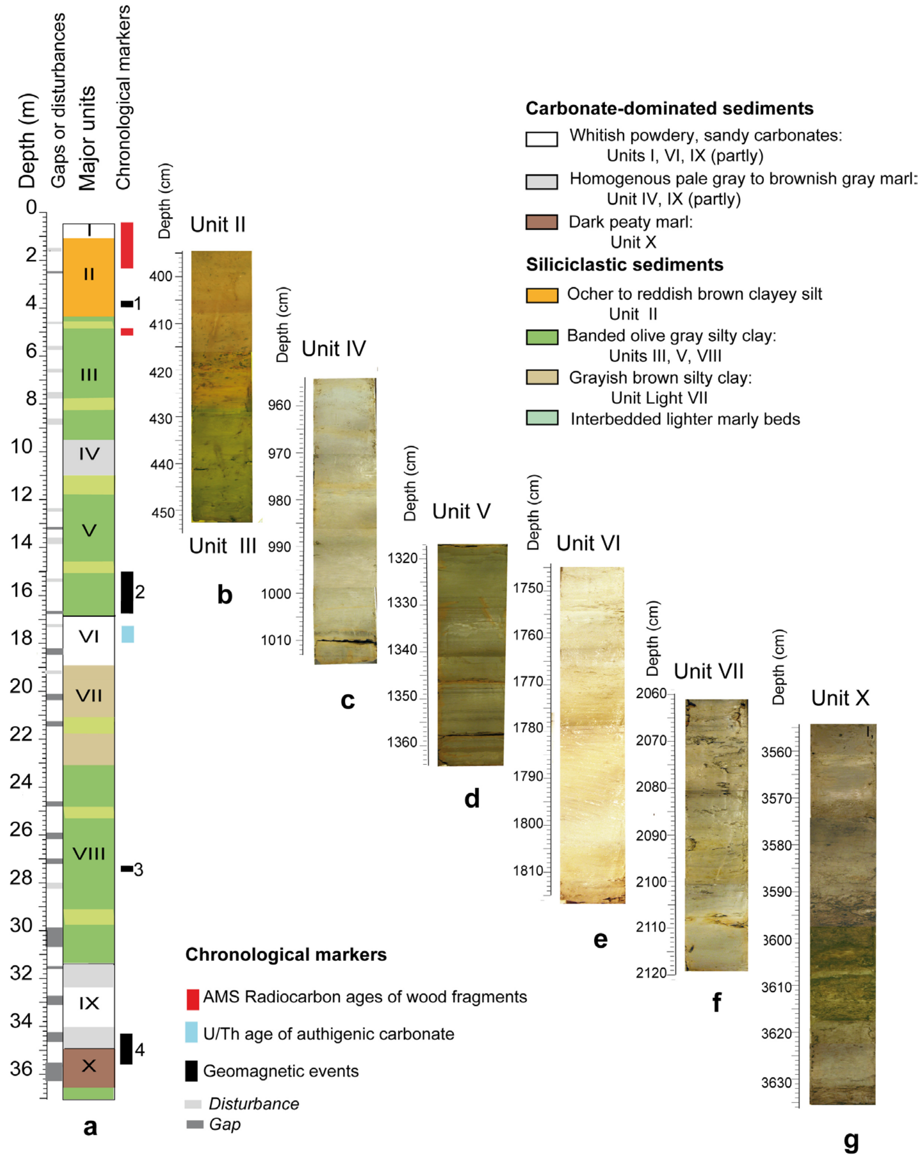

Fig. 4. Stratigraphy and lithofacies of the upper 36 m of core Yam 04 C'. **(a)** Simplified stratigraphic log. Position of gaps in core recovery and of sediment disturbances on the left; position of chronological markers on the right. **(b)** to **(g)** Pictures of some core sections illustrating the facies diversity. **(b)** Transition from reddish, oxidized silt of Unit II to olive gray silty clay of Unit III. **(c)** Pale greenish marl. **(d)** Typical banded greenish marl. **(e)** Typical interglacial calcitic powdery deposits. **(f)** Brownish, coarsely banded silty clay. **(g)** Peaty marl of Unit X.

charophytes, fish otoliths ...), or of light gray to light brown marl (Unit IV and part of Unit IX; Fig. 4c).

2. Thick accumulations of intensively coloured silty clay. This siliciclastic material is almost devoid of shells (besides ostracods). The ocher to reddish brown Unit II (Fig. 4b) shows numerous strongly oxidized, indurated layers and beds of coarse limestone gravels and concretions. Units III, V, VII and VIII consist of plastic olive gray (Fig. 4d) or grayish brown silty clay (Fig. 4f) often organised in bands 2–20 cm thick. Several layers, 3–8 cm thick, suggest paleosoils; a few centimetric intervals are laminated; lighter marly intervals are interbedded in these units.

The lowest carbonate-rich Unit X (Fig. 4g) differs from others by its very dark brownish to black colour and its peaty feature, rich in aquatic plant fragments, beds of fish otoliths and well-preserved mollusc shells. Below 3650 cm, it overlays greenish clays resembling Units III or VIII.

All encountered remains of aquatic organisms are typical of fresh, shallow or even ephemeral waterbodies.

Analyses performed on the core for environmental reconstruction are listed in Table 2.

Table 2. Performed analyses on the upper 36 m of core YAM04-C'. Variables included in the PCA_{PM} analysis (Fig. 8) are numbered in column 2.

Observations and Analyses	Variables included in PCA	Variable		Nb of analysed samples	
Main lithofacies types	1	Whitish powdery, sandy carbonate	1	continous	
		Pale gray to pale brown marl	2	continous	
		Yellowish brown to reddish brown silt	3	continous	
		Olive gray silty clay	4	continous	
		Brownish gray silty clay	5	continous	
		Dark brown, peaty or paleosoil-like levels	6	continous	
Sediment composition	2	XRD mineralgy (% weight dry sediment)	Calcite (+ Aragonite: 0–3 %)	160	Same samples
	3		Quartz	160	
	4		K-Feldspaths + Plagioclases	160	
	5		Dolomite	160	
	6		Clay minerals	160	
	7	TOM (% weight dry sediment)		160	
	8	Total magnetic susceptibility (10^{-5} SI)		2417	
	9	XRF Element relative content	Ca	2109	
	10		Si	2109	
	11		Al	2109	
	12		Fe	2109	
	13		Ti	2109	
	14		K	2109	
Pollen analysis	15	Steppic-desertic landscape	*Artemisia* + *Chenopodiacea* + *Cichoroideae*	225	
	16	Middle Mediterranean zone	*Pinus* + *evergreen Quercus*	225	
	17	Upper Mediterranean zone	Deciduous Quercus	225	
	18	Montane belt	*Cedrus* + *Abies*	225	
	19	Subalpine zone	*Juniperus*	225	
	20	Aquatic + Hydrophilous (% total pollen)	*Myrioplyllus, Potamogeton, Typha, Cyperaceae, Ranunculus*	225	
Carbonate oxygen isotope	21	δ_c derived from ostracod $\delta^{18}O$ values		190	
Microscopic observations		Smear slides		250	
		Scanning electron microscope		52	Same samples
Grain size analysis				52	

3.2 Chronological framework

The age model of core YAM-04C' was based on the combination of radiometric dating and magnetic chronostratigraphy. The position of dated levels along the profile is showed in Fig. 4a.

The top of the sequence was ^{14}C-dated by Accelerator Mass Spectrometry (AMS) on partly carbonized wood fragments (11 levels from 0–21 ka; 0–250 cm). A ^{14}C age at 535 cm (47 ± 4 ka) should be regarded with caution as it reaches the limit of the ^{14}C method applicability. The ^{14}C ages were calibrated using IntCal 09 (Reimer et al., 2009). One level of almost pure authigenic calcite has provided a reliable U/Th age of 124 ± 17 ka at 1770 cm. Four geomagnetic events (1 to 4; Fig. 4a) were identified, based on changes in inclination and relative paleointensity of the Earth magnetic field. The very well identified Event 2 (1590–1660 cm) is the Blake event (∼114–120 ka). Events 1 and 3 likely represent the Laschamp (41 ± 2 ka, 340–370 cm, peaking at 361 cm) and the Iceland Basin event (∼190–194 ka; 2735 cm), respectively. Event 4 (3420–3490 cm) coincides either with the Pringle Falls event (∼211 ka) or the Mamaku event (230 ± 12 ka). An approximate age of 230 (+12/−20) ka was assigned at 3460 cm.

The age-depth relationships were estimated by linear interpolation between the above-mentioned age control points, and Units were tentatively related to the stacked and orbitally-tuned Marine Isotope Stages (MIS; Martinson et al., 1987). We are aware that our age model only provides an approximate time scale, due to the low number of dated points and their age uncertainty, changes in sedimentation rate and possible sedimentation hiatuses. Nevertheless, ^{14}C ages clearly show that Unit I is of Holocene age (MIS 1). According to the U/Th date and the depth position of the geomagnetic Blake event, Unit VI is assigned with confidence to the last Interglacial peak (MIS 5.5). If the age of geomagnetic event 4 is correct, Unit IX represents MIS 7, a hypothesis supported by its lithofacies analogies with Units I and VI (Fig. 4a).

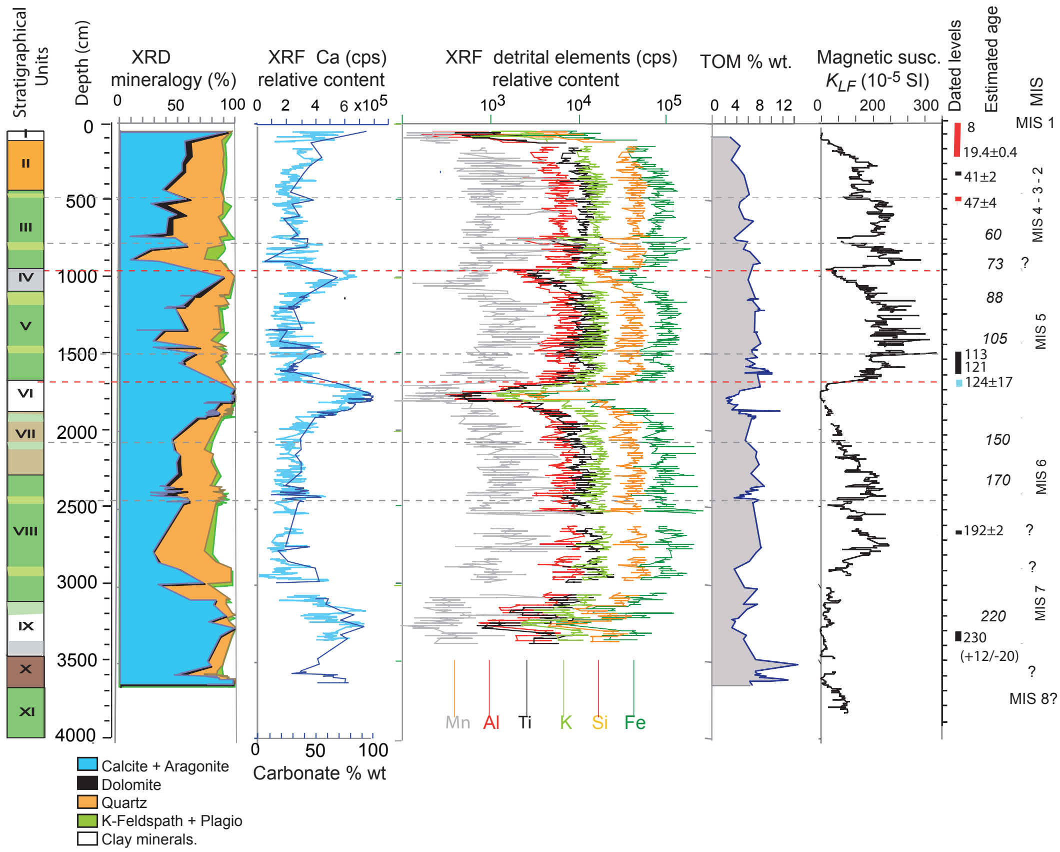

Fig. 5. Sedimentological data. Main proxies versus depth along the stratigraphical profile, after Develle et al. (2011). On the right, chronological information: position and measured ages of the chronological markers, estimated ages of major sedimentation changes (in italic, interpolated ages), and hypothesized relationships with Marine oxygen Isotope Stages (MISs; Martinson et al., 1987). Horizontal dashed lines: major (red) and second order (grey) sedimentation changes.

3.3 Sedimentary processes

Major sedimentary results are illustrated in Fig. 5.

Sedimentation has been primarily controlled by: (i) in situ lacustrine carbonate production, (ii) erosion of the surface watershed, and (iii) eolian inputs.

The whitish Units I, VI and IX coincide with interglacial periods (MIS 7, MIS 5.5, MIS 1). They consist mainly of calcite precipitated into the waterbody (authigenic rhomboedric crystals and biogenic fragments). Lacustrine calcite production was enhanced by high temperature and evaporation, strong biological activity in the lake, and high Ca^{2+} inputs suggesting heavy karstic spring discharge and active circulation in the Mnaïtra karstic system. Low magnetic susceptibility values and relatively low contents of Fe, Ti and K and Total Organic Matter (TOM) were attributed to reduced local erosion and dilution of detrital particles by authigenic carbonates. The quasi-absence of runoff-derived material and high carbonate content may suggest very low rainfall. However, the synchrony of carbonate peaks with the abundance of lacustrine organisms and with the development of arboreal vegetation (see Sect. 4.1) reducing erosion processes rather reflects high water availability in both the karstic recharge zone and the paleolake surroundings.

Coloured clayey silts (Units III, V, VII, VIII) are mainly composed of eolian and local terrigenous material. Lithofacies which include paleosoils and the scarcity of aquatic organisms (mainly ostracod taxa surviving ephemeral conditions) reflect shallow, unstable palustral environments. Quartz, K-feldspars and plagioclases, almost absent in the local bedrock, are obviously allochtonous and windblown from remote sources. Quartz (up to 60 %) largely dominate the non-carbonated fraction, reflecting a high contribution of eolian dust to sedimentation, either from direct falls or reworked from the basin slopes. Calcite, present throughout, generally occurs in aggregates resembling those found in watershed soils or as limestone gravels, indicating its detrital origin. Dolomite is also probably eroded from the bedrock. Clay minerals (smectite mainly, kaolinite, traces of illite) are attributed to weathering and runoff in the basin, implying at least occasional heavy floods. Elements other than Ca prevail and are supported by minerals of detrital origin responsible for high magnetic susceptibility values.

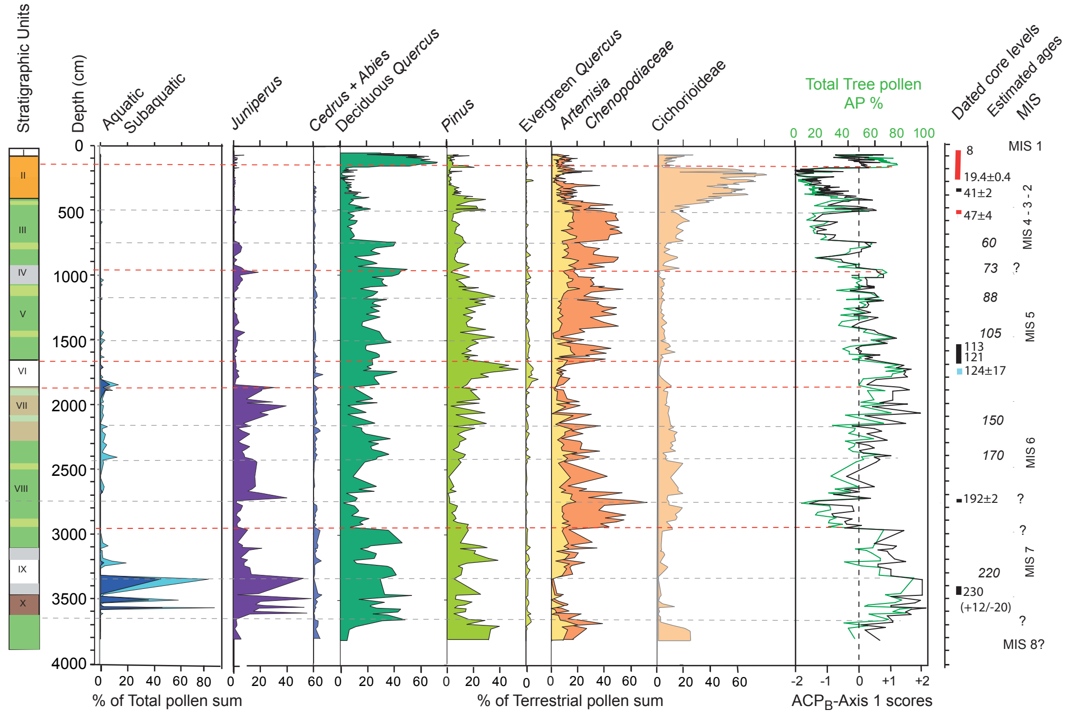

Fig. 6. Palynological data. Relative frequencies of selected pollen taxa versus depth along the stratigraphical profile, total tree pollen percentages (AP %) and ACP_B-Axis 1 scores showing the alternance of forested and steppic landscapes. Chronological information as for Fig. 5. Horizontal dashed lines: major (red) and second order (grey) vegetation changes.

Marls (Unit IV and IX) and pale marly layers interbedded in silty clay are intermediate between these two typical sediment types. The peaty marl of Unit X, rich in TOM and biogenic rests, indicates the occurrence of a productive lake at the core site.

4 New data from the Yammoûneh sequence

4.1 The pollen record

Most of the Yammoûneh sequence contains pollen grains, although its top (<8.3 ka) is sterile possibly due to oxidation after the lake drainage. Vegetation patterns inferred from the pollen record were based on 225 samples prepared for pollen analysis using standard palynological procedures. An average of 465 pollen grains was counted in each sample. A total of 69 pollen taxa were identified, using reference collections and Reille's (1992) pollen atlas.

Pollen results are given as a percentage diagram of selected taxa (Fig. 6). Aquatic (*Myriophyllum* mainly) and marsh (Cyperaceae dominant) plant pollen, indicative of permanent lacustrine conditions or swamps around the core site, respectively, are expressed in percents of the total pollen sum. Both reach their highest percentages in the lower half of the core and then tend to disappear, suggesting drier local conditions above 1800 cm.

Terrestrial pollen taxa are expressed in percents of a basic sum excluding pollen from aquatic and marsh plant pollen. See Table 1 for the modern distribution of major taxa. Main tree pollen include: (1) *Juniperus* and *Cedrus-Abies* representative of cool conifer forests from the subalpine and mountain belts, respectively. Note that *Cedrus* and *Abies*, which require high water availability, do not extend today east of Mount Lebanon; (2) deciduous *Quercus*, common in the temperate and warm-mixed forests of the upper Mediterranean belt;(3) *Pinus*, a rather ubiquitous taxa growing in all Mediterranean vegetation belts; (4) evergreen *Quercus*, a xerophytic Mediterranean tree which spreads in the lower Mediterranean belt and at moderate elevation east of Mount Lebanon; (5) *Artemisia* and Chenopodiaceae, the most significant herbaceous taxa which reflect the development of steppic landscapes; (6) Cichorioideae pollen, which can account for more than 50 % of the terrestrial pollen above 400 cm. Strong representation of this pollen type may result from taphonomic processes and poor preservation conditions (Bottema, 1975), i.e., large water table fluctuations and frequent emersions, as suggested by strongly oxidized and indurated layers in the sedimentary Unit II, indicating unstable but generally dry conditions. This pollen type is present is various amounts throughout the sequence and was not excluded from the pollen calculations.

CHAPTER 2.2

The total percentage of tree pollen (AP %) provides a broad view of the alternance between forested and steppic landscapes, mainly reflecting changes from moist to drier conditions although very cold climate might have limited the tree growth. The few available regional modern pollen spectra prevent any application of a pollen-based transfer function to quantify changes in rainfall amount or in temperature. Terrestrial pollen data were converted into Plant Functional Types (PFTs) and a pollen-derived biomization of the PFTs was elaborated using the appropriate methods for Mediterranean regions (Tarasov et al., 1998). Five pollen-derived biomes (PdBs; scores not shown) were inferred from the Yammoûneh dataset: (1) cool conifer forest; (2) temperate deciduous forest; (3) warm mixed forest; (4) xerophytic woods/shrubs; (5) steppe. Hot and cool steppe biomes were not separated, because of the low representation of discriminating pollen taxa in the spectra. When affinity score differences between biomes are low, the use of the highest-scoring PdB alone may obscure significant vegetation changes. Therefore, a down-core ordination of samples taking into account major changes in all the PdB-scores was obtained by a principal component analysis (PCA_B). The general pattern of the PCA_B scores is not affected when excluding Asteraceae subfam. Cichorioideae from the basic sum. PCA_B-Axis 1 (77.98 % of total inertia) is positively loaded by all forested biomes (PdBs 1 to 4; pollen taxa groups 1 to 4), and negatively by steppe (PdB-5, pollen taxa group 5). Intervals of highest PCA_B-Axis 1 correspond to periods of best development of arboreal vegetation, whereas its lowest values indicate the dominance of open vegetation types. PCA_B-Axis 1 closely resembles the AP % curve, but highlights the development of tree elements below 1800 cm.

Below 3670 cm (>240 ka?), the dominance of steppe (PdB 5) punctuated by stands of pines may represent the MIS 8–MIS 7 transition. The interval 3670–3320 cm (∼240–220 ka?, early-mid MIS 7) has the highest PCA_B-Axis 1. PdB-1 dominated over the basin slopes, as showed by the highest *Juniperus* frequencies associated with *Cedrus*. Highest aquatic pollen frequencies indicate permanent lacustrine conditions, allowing the development of riparian deciduous oak groves (deciduous *Quercus*). This indicates high Precipitation (P) and low Evaporation (E) favoured by cool temperatures. From 3320 to 2970 cm (late MIS 7?) the increase in temperate Mediterranean trees and steppic taxa, responsible for intermediate PCA_B-Axis 1 values, reflects lower effective moisture partly explained by higher temperature as suggested by the falling representation of *Juniperus*.

The interval 2970–1870 cm, assigned to MIS 6 (although its base is ∼10 ka too old in our age model), is first characterised by a strong dominance of steppe (PdB 5), and the almost disappearance of aquatic and palustral pollen. This suggests very dry conditions, although the opening of the landscape may partly result from the lowering of the upper tree line under glacial cooling. Above 2550 cm (180 ka?), a step-wise increase in PCA_B-Axis 1 depicts a progressive development of arboreal vegetation. High affinities to the PdB-1 loaded by *Juniperus*, *Cedrus* and *Abies* point to cool and wet conditions, as confirmed by small peaks of aquatic pollen.

MIS 5.5 (∼1850–1680 cm; ∼130–120 ka) begins with a warming-induced abrupt fall of *Juniperus* and rise of both *Quercus* types. Then, temperate *Quercus* are rapidly replaced by a typical Mediterranean vegetation. PCA_B-Axis 1 become very high when *Pinus* and evergreen *Quercus* reached their maximum percentages, and aquatic/palustral plant pollen disappeared. This vegetation does not lend support to aridity in the Yammoûneh basin, but for high seasonal contrasts. The largest population of evergreen *Quercus* suggests very dry summers, which increase the competitive advantage of Mediterranean sclerophyllous trees (Di Castri, 1981). After this last interglacial optimum, between 1680 and 960 cm, a sharp increase in steppic elements is interrupted by two positive shifts in temperate/Mediterranean tree pollen frequencies, concomitant with small peaks of palustral plant pollen. These shifts, registered at 1520–1480 cm (∼105 ka) and 1015–960 cm (∼80–73 ka), are assigned to MIS 5.3 and MIS 5.1, respectively.

From 960 to 220 cm (∼73–16 ka; MIS 4-3-2), the steppe development clearly depicts an overall drying trend from the beginning of MIS 4. This trend is interrupted by short, humid episodes revealed by positive shifts of PCA_B-Axis 1 at 820–750 cm and 500–410 cm (∼65–60 and 45–40 ka, respectively, in our time scale). The lowest PCA_B-Axis 1 values of the whole record are reached at 240–220 cm (∼21–16 ka). This demonstrates that temperature and/or moisture conditions in the Yammouneh basin, together with very low CO_2 atmospheric concentration, were not compatible with the development of an arboreal vegetation at the end of the LGM.

The last forested stage is recorded by a sharp increase of deciduous *Quercus* (PdB2) starting at 170 cm (13 ka), and culminated from 11 to 9 ka. It indicates the re-establishment of warmer/wetter conditions during the early Holocene.

Major points arising from the pollen study are the following:

- Arboreal vegetation dominates during interglacial optimums (early-mid MIS 7, MIS 5.5 and early MIS 1), reflecting relatively high effective moisture. Vegetation dynamics suggest very wet and cool conditions during MIS 7, strong thermal and hydrological seasonal contrasts during MIS 5.5, and wet temperate conditions during the early Holocene.

- The driest intervals appear at the end of the LGM and during early MIS 6.

- From 240 ka onwards, each successive interglacial PCA_B-Axis 1 peak shows a decreasing amplitude. The same pattern holds true for glacial stages, showing a lower local moisture during the last glacial period than during MIS 6. The overall variation in the pollen record, including aquatic pollen, suggests a progressive decline in effective moisture as a result of the combined effect of temperature, precipitation and $p\mathrm{CO}_2$ fluctuations in the Yammoûneh basin.

4.2 The carbonate oxygen isotope record

The oxygen isotope composition of continental carbonates reflects complex interactions between several climatic variables and site-specific factors. In addition, in the case of biogenic carbonates, species-dependent factors (the so-called "vital effect" and auto-ecology) should be considered. We refer to Develle et al. (2010) and reference therein for analytical procedures, theoretical backgrounds and for the interpretation of the past 21 ka isotope record. Authigenic carbonate δ^{18}O values (δ_c) are primarily controlled by water temperature and isotopic composition of the ambient water, here lake water (δ_L). The δ_L values are governed by the isotopic composition of the water inflow (δ_{in}) and of other terms of the lake water balance (inflow − [Evaporation + outflow]). The term δ_{in} depends on the precipitation δ^{18}O values (δ_P) and the P-E balance in the lake catchment. The δ_P values are in turn controlled by the isotopic composition of the moisture source, here the EMS surface water (δ_{sw}), storm-track trajectories and the negative/positive relationships with local rainfall amount/ground-temperature. In central Levant, Frumkin et al. (1999), Bar-Matthews et al. (2003) and Kolodny et al. (2005) have showed that long-term δ^{18}O fluctuations in inland carbonates are primarily driven by the glacial/interglacial variations in the isotopic composition of the EMS surface water. The rainfall amount probably represents the second order factor (Frumkin et al., 2011). Bar-Matthews et al. (2003) and Bar-Matthews and Ayalon (2004) took the temperature and rainfall amount into account to interpret low interglacial speleothem δ^{18}O values.

The carbonate δ^{18}O record from Yammoûneh was obtained from ostracod valves present and well preserved in most samples. Analyses were performed on the 4 most abundant taxa (*Ilyocypris inermis, I. gibba, Candona neglecta* in Unit I only, and *Fabaeformiscandona balatonica* only present below 1800 cm; none of them occurs in sufficient number in all samples for analyses). Interspecific δ^{18}O differences were determined, all values were normalized to the most widespread taxon (*I. inermis*) and corrected for the vital effect (∼2.4 ‰) estimated for this species (Develle et al., 2010). This correction provides values coeval with that of authigenic calcite (δ_c) which would have precipitated at equilibrium in the same ambient water. Along the entire profile, δ_c values fluctuate by 5.1 ‰, between −12.6 and −7.5 ‰ (Fig. 7a). The profile is characterised by δ_c values generally lower before MIS 5.5, a reverse δ_c trend between the penultimate and the last glacial periods, and very sharp δ_c rises during interglacial peaks.

For the past ∼21 ka (Develle et al., 2010), δ_L was first estimated by correcting δ_c for lake water temperature (assuming that the water temperature of the shallow Yammoûneh waterbody was in equilibrium with air/ground temperature), using the few available data on regional paleotemperatures. Second, isotopic composition of the moisture source (δ_{sw}) was derived from planktonic foraminifera (*G. ruber*) δ^{18}O records (δ_{foram}) in a Levantine core (MD84-632, Fig. 1; Essalami et al., 2007), corrected for surface water temperature using alkenone-based SST ($\mathrm{SST_{alk}}$) records from the same core. Thirdly, the difference $\Delta^{18}\mathrm{O} = \delta_L - \delta_{sw}$ was calculated in order to discuss the impact of the "source effect" on the Yammoûneh isotopic signal, adopting an approach close to that of Almogi-Labin et al. (2009). Develle et al. (2010) concluded that both the "source effect", amplified by increase inland rainfall during the early Holocene, and the large glacial-interglacial temperature changes have been important drivers on δ^{18}O fluctuations. Changes in storm-track trajectories may have also contributed to the signal.

The same approach is attempted here to interpret major glacial/interglacial δ_c changes over the past 250 ka, but should be regarded with great caution because of large uncertainties on the timing and marine data (Fig. 7b–d) used to reconstruct δ_{sw} and δ_L.

4.2.1 Temperature effects

In the Levant, inland quantitative paleotemperature estimates prior to the LGM are limited to punctual data inferred from isotope geochemistry of Soreq Cave speleothems between 140 ka and present (McGarry al., 2004, Fig. 7b; Affeq et al., 2008). EMS $\mathrm{SST_{alk}}$ can serve as a first-order approximation of land paleotemperatures for Levantine inland temperature (Bar-Matthews et al., 2003), at least at Soreq. $\mathrm{SST_{alk}}$ records from the eastern EMS either do not extent over the last 250 ka (Essalami et al., 2007; Castañeda et al., 2010) or are discontinuous (core ODP 967; Emeis et al., 2003). We used the $\mathrm{SST_{alk}}$ record of core MD40-71 (Figs. 1 and 7b) from the northwestern boundary of the Levantine basin (Emeis et al., 2003) as a rough regional indicator of temperature deviations relative to modern, ΔT, at sea level ($\Delta T_{\mathrm{sea\ level}}$). These $\Delta T_{\mathrm{sea\ level}}$ data were used to infer ΔT at Yammoûneh (ΔT_{Yam}) and to correct δ_c for lake water temperature, applying the paleotemperature equation of Craig (1965) to calculate δ_L (Fig. 7e). During Interglacials, we assume that the mean annual temperature difference between sea level and Yammoûneh was the same as today. During glacial periods, the thermal atmospheric lapse rate was steepened by at least 2 °C km^{-1} during the LGM in the Mediterranean domain (Kuhlemann et al., 2008). An additional cooling of 2.5 °C at Yammoûneh and ≥4 °C in the aquifer recharge zone (>2000 m a.s.l.) would have induced an additional decrease of δ_L of ∼0.7 ‰ (water temperature effect), but a larger decrease of δ_P values of ∼ −1.4 to at least −2.3 ‰ due to the "ground-temperature effect" (estimated at ∼0.58 ‰ °C^{-1} in northern mid-latitudes; Rozanski et al., 1993) reducing the $\delta_L - \delta_P$ difference (Fig. 7e). Because most of the

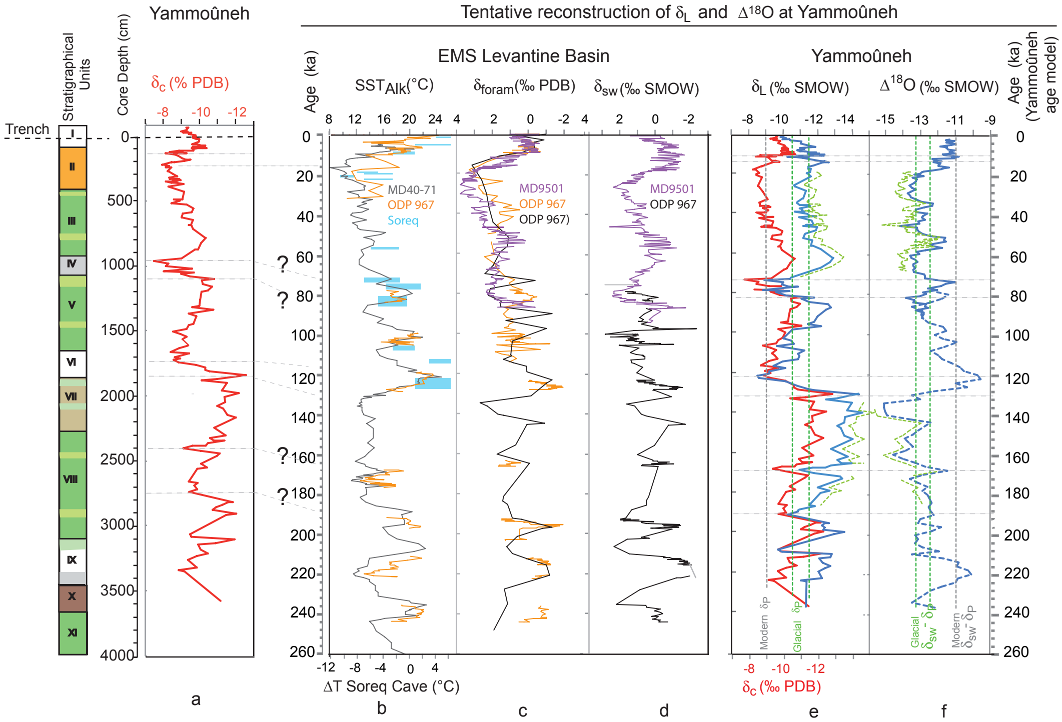

Fig. 7. Carbonate oxygen isotope record. Tentative reconstruction of δ_L and $\Delta\delta^{18}O = \delta_{sw} - \delta_L$ using EMS marine data. **(a)** The Yammoûneh δ_c profile versus depth (values above 0 cm of core depth come from trench TR02 which includes the entire Holocene period). **(b)** SST_{alk} records from cores M40-71 and ODP 967 (Emeis et al., 2003), and inland temperature inferred from Soreq Cave speleothems (McGarry et al., 2004). **(c)** $\delta^{18}O$ records of planktonic foraminifera (δ_{foram}) from cores MD9501 (Almogi-Labin et al., 2009) and ODP 967 (Kroon et al., 1998: black; Emeis et al., 2003: orange). **(d)** Isotopic composition of sea surface water (δ_{sw}) in the Levantine basin calculated from SSTs in core MD40-71 and δ_{foram} from cores MD9501 (0–86 ka) and ODP 967 (78–250 ka, combined Kroon et al., 1998 and Emeis et al., 2003, data). **(e)** The Yammoûneh δ_c profile and reconstructed δ_L versus time (according to our age model). The blue δ_L curve is based on inferred $\Delta T_{sealevel}$ on the modern mean annual temperature difference between sea level and Yammoûneh, the green one accounts for an additional altitudinal cooling during glacial periods. Vertical dashed lines: modern and inferred glacial δ_P values. **(f)** Calculated $\Delta\delta^{18}O$. Colours as for **(e)**. Dashed and full blue curves are based on δ_{sw} derived from cores ODP 967 and MD9501, respectively. Vertical dashed lines: $\delta_{sw} - \delta_P$ values inferred for modern and glacial times. See text for explanation.

precipitation was likely niveous (more depleted than liquid rainfall, Rozanski, 2005), δ_P may have decreased even more.

In order to infer δ_{sw}, we used the high resolution time series of δ_{foram} from core MD-9501 (86 ka; Almogi-Labin et al., 2009) and the poorly-resolved record of ODP 967 from Kroon et al. (1998) complemented by detailed measurements around sapropel events (Emeis et al., 2003) (Figs. 1 and 7c). Although not recorded in SPECMAP (Imbrie et al., 1984), δ_{foram} fluctuations between ~170 and ~150 ka of the same amplitude as in ODP 967 were observed in cores MD84-648 and -637 (Fig. 1) closer to the Nile delta (Ducassou et al., 2007). By combining the $\Delta T_{sealevel}$ and the δ_{foram} values, we applied the same paleotemperature equation as for δ_L to obtain an approximate record of δ_{sw} for the northern Levantine basin (Fig. 7d).

4.2.2 Source effect

The "source effect" was extracted by calculating $\Delta\delta^{18}O = \delta_L - \delta_{sw}$ (Fig. 8f). Large $\Delta\delta^{18}O$ variations indicate that other factors than the "source effect" have acted on δ_L and δ_c. During Interglacials, high $\Delta\delta^{18}O$ values compared to the modern $\delta_P - \delta_{sw}$ difference (~ -11 ‰) suggest enhanced inland rainfall around 220 and 125–120 ka and less clearly around 105, 85–75 ka and 11–9 ka (Fig. 7f). These $\Delta\delta^{18}O$ increases are associated with remarkable rises of δ_c and δ_L, particularly clear at ~126–120 or ~85–75 ka, which classically could suggest deficits in the lake water balance. Several hypotheses can be invoked to explain these apparent discrepancies. First, amplified seasonal thermal contrasts, as expected from orbital forcing, would have induced evaporative ^{18}O-enrichment of δ_{in} and δ_L during the warmer dry seasons. A longer water residence time in the paleolake could have also enhanced the evaporation effects when the waterbody was permanent. Second,

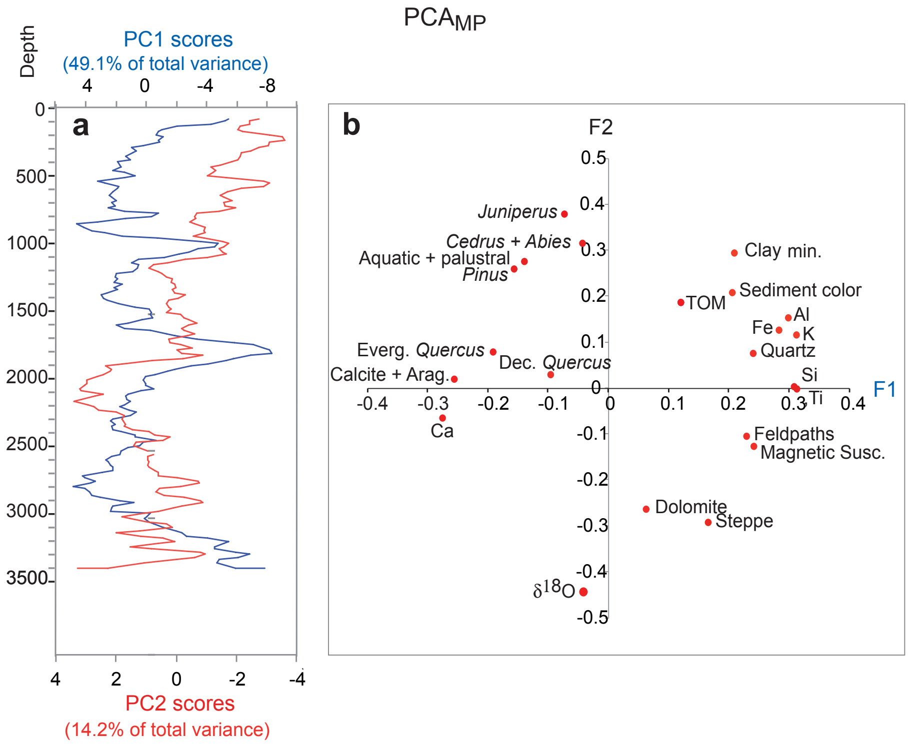

Fig. 8. Principal Component Analysis performed on 22 environmental variables (Tabl 2) in 166 core levels from core YAM04 C' (ACP$_{MP}$). **(a)** Scores of the 2 first components (PC1 and PC2) versus depth. **(b)** Projection of environmental variables in the factorial plan F1–F2.

changes in rainfall seasonality might have affected δ_P and, thus, δ_L and $\Delta\delta^{18}$O. At Yammoûneh, modern winter ^{18}O-precipitation values are lower than spring and autumn values by ~2.5 ‰ (Develle et al., 2010). The transition to higher δ_L and higher $\Delta\delta^{18}$O values could reflect a longer rainy season, increasing the relative contribution of spring and fall precipitation on the mean annual δ_P values. Third, changes in air mass trajectories might have modified δ_P. Presently, at the rainfall event scale, the less ^{18}O-depleted rains close to Beirut (δ_P: −2 to −4 ‰) are associated with air masses from the North (Aouad et al., 2004, 2005). Felis et al. (2004) have suggested increased advection over the near East of cold continental air from the North linked to a high NAO index in winter during MIS 5.5. Enhanced northerly winds might have increased δ_P. However, based on modern data, Vaks et al. (2010) suggested that a negative NAO index is linked to lower winter temperatures in Israel and leads to increased winter precipitation (and, thus, reduced winter δ_P).

During Glacials, $\Delta\delta^{18}$O was generally low, although sharp positive peaks around ~170 ka (in phase with a δ_L increase), ~145 ka and during short MIS 4–3 intervals may reflect short wet pulses. Low δ_c, δ_L and δ_P values (Fig. 7e) suggest the dominance of ^{18}O-depleted winter rains, low water and atmosphere temperatures and low evaporation rates. Freezing over most of the year have likely inhibited evaporative ^{18}O concentration. Changes in storm tracking may have contributed to the isotopic signal. Today, the most ^{18}O-depleted rains reaching Lebanon (δ_P: −6 to −11 ‰) come directly from the west and have a long path over the sea (Aouad et al., 2004, 2005). Major storm-tracks funneled along the southern EMS coast due to ice extent in northern high latitudes, as proposed by Enzel et al. (2008), may have enhanced the δ_P and $\Delta\delta^{18}$O decreases.

4.2.3 To sum-up

Our approach suggests that the isotope balance of the Yammoûneh hydrosystem was initially controlled by the "source effect" (δ_{sw}), but this effect was deeply modulated and modified by other factors associated with glacial/interglacial atmospheric patterns and the site-specific water balance. These factors include annual and seasonal changes in temperature and related evaporation rate, rainfall amount and rainfall isotopic composition.

5 The multi-proxy Yammoûneh record

5.1 Relationships between individual proxies

Information derived from individual indicators from a given sedimentary profile should be considered together and reconciled to gain a comprehensive picture of environmental conditions at a given time/core depth.

Table 3. Significant simple linear correlation coefficients ($p < 0.001$) between environmental variables from Yammoûneh.

	Ca (rel. cont)	Calcite (+ aragonite)	Quartz	Kaolinite + smectite + chlorite	K-Fedspaths + Plagio.	Magnetic Susceptinility	TOM	Al (rel. cont)	Si (rel. cont)	K (rel. cont)	Ti (rel. cont)	Fe (rel. cont)	Deciduous *Quercus* (%)
Calcite (+ aragonite) (%)	0.791												
Quartz (%)	−0.756	−0.970											
Kaolinite + smectite + chlorite (%)	−0.620	−0.674	0.509										
K-Fedspaths + Plagio. (%)	−0.551	−0.807	0.570	0.460									
Magnetic Susceptibility (SI)	−0.607	−0.640	0.663		0.678								
TOM (% wt)	−0.484	−0.411	0.330	0.625		0.526							
Al (rel. cont)	−0.760	−0.728	0.687	0.641	0.602	0.624	0.411						
Si (rel. cont)	−0.754	−0.794	0.787	0.520	0.545	0.661	0.456	0.426					
K (rel. cont)	−0.806	−0.784	0.744	0.640	0.602	0.624	0.592	0.976	0.961				
Ti (rel. cont)	−0.836	−0.812	0.882	0.509	0.587	0.657	0.584	0.927	0.955	0.943			
Fe (rel. cont)	−0.786	−0.732	0.689	0.866	0.528	0.697	0.628	0.868	0.794	0.851	0.828		
Juniperus (%)													
Abies + *Cedrus* (%)													
Deciduous *Quercus* (%)	0.361	0.361	−0.338					−0.342	−0.406	−0.407	−0.392	−0.316	
Everg. *Quercus* + *Pinus* (%)	0.335	0.428	−0.496		−0.410								
Steppic (%)	−0.495	−0.572	0.616		−0.708	0.648		0.387	0.553	0.470	0.578	0.408	−0.674
Aquatic + subaquatic (%)													
δ^{18}O carbonate (PDB ‰)													
AP %	0.51					−0.49							

Environmental variables were initially reconstructed with different depth resolution and along different core length. Thus, data were re-sampled with a common depth-scale (20 cm) between 64 and 3364 cm. This procedure shortens the high resolution and the longest records, but the resulting matrix, based on 166 core levels, is well-suited for numerical analyses. Environmental variables were translated into standard deviation units (s.d.u.). Significant simple linear correlation coefficients between individual variables are plotted in Table 3. Data integration was performed using the Analyseries 2.0 software (Paillard et al., 1996).

We first performed a PCA on the multiproxy matrix (ACP_{MP}) of 22 variables listed in Table 2. Scores of two first principal components PC1 and PC2 (63.3 % of total variane) and the projection of the variables in factorial plans 1–2 are plotted in Fig. 8a and b. PC1 scores confirm the 2 poles (end-members) of sediment fraction, carbonate (Ca, calcite + aragonite) v. all other sediment components (detrital), already highlighted by Develle et al. (2011). Note that carbonate-dominated units are mainly composed of authigenic calcite. Axis 1 shows close linkages between carbonate and arboreal vegetation lying on the negative side, Mediterranean evergreen *Quercus* having the strongest contribution among tree taxa. The positive loading of steppe and siliciclastic (and dolomite) components shows that high contribution of eolian and local detrital influxes to sedimentation prevailed during periods of open vegetation. PC2 differentiates the lower (> 1870 cm) and upper halves of the sequence. This asymmetry is largely due to the strong positive loading on Axis 2 of pollen from cool conifer forests (*Juniperus, Cedrus, Abies*) and aquatic-palustral plants which are poorly represented above 1870 cm. The δ_c values steer Axis 2 on the negative side. The positive correlation between TOM and detrital elements and the distance between aquatic-palustral plant pollen and TOM in factorial plans 1–2 suggests that, in most samples, TOM is derived from the catchment soil erosion rather than from organic production in the local waterbody. The low contribution of δ_c and tree pollen from cool wet forests, *Pinus* and deciduous *Quercus* to Axis 1 suggest that δ_c fluctuations and these tree types are partly independent of the sediment components.

We then computed a PCA_{Sed} based on all sedimentological proxies. Figure 9a shows PCA_{Sed}-Axis 1 (67.8 % of total variance) and resampled PCA_B-Axis 1 based on pollen-derived biomes (see Sect. 4.1). Aquatic/palustral assemblage and δ^{18}O are excluded from this comparison. Visual observation reveals a close link between the highest PCA_B-Axis 1 and the lowest PCA_{Sed}-Axis 1 values, except between ∼500 and ∼200 cm when detrital carbonates became abundant. Drastic decreases in PCA_B-Axis 1 may be partly explained by the lowering of the upper tree line during the coldest periods, but lithofacies above 500 cm indicate that these shifts primarily reflect a local drying. A cross-correlation between the PCA_B-Axis 1 and PCA_{Sed}-Axis 1 scores (Fig. 9b) confirms the negative correlation between the two depth/time-series by a narrow peak centred on depth-lag 0 (−48.6 ‰), reflecting the co-evolution of both signals during the whole sequence.

Relationships between isotope (δ_c) and vegetation dynamics (Fig. 9c and d) are more complex. PCA_B-Axis 1 and δ_c run roughly parallel during the coloured detrital-rich intervals. Overall decrease/increase in δ_c when PCA_B-Axis 1 increased/decreased can be classically interpreted as reflecting wetting/drying trends, respectively (e.g., in the intervals ∼2750–1840 and 780–200 cm). Conversely, clear antiphasing occurred during periods of sharp increases in PCA_B-Axis (development of arboreal vegetation implying relatively high water availability), associated with steep and large δ_c enrichments. Such discrepancies have already been pointed out in several post-glacial records from eastern Mediterranean

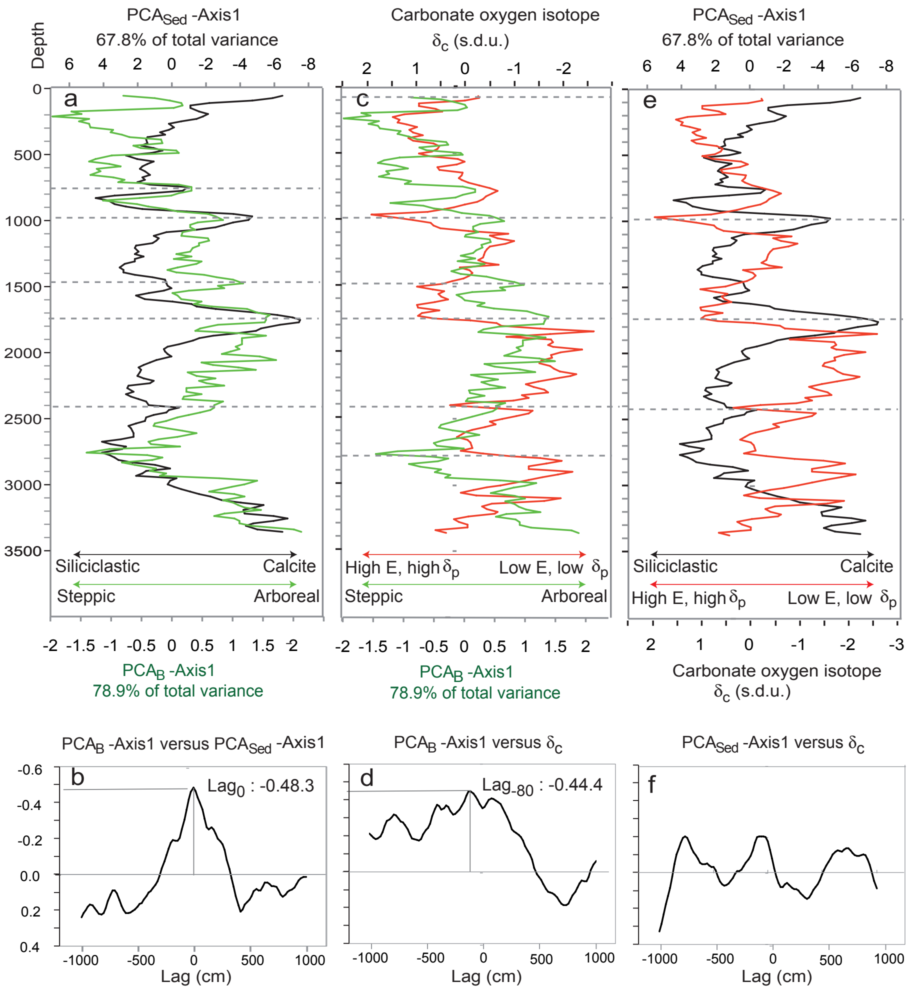

Fig. 9. Relationships between pollen, sediment properties and isotope data. **(a)** PCA_B-Axis 1 and PCA_{Sed}-Axis 1 scores versus depth. **(b)** Cross correlation between these two depth series. **(c)** Carbonate oxygen isotope, δ_c (in standard deviation units, s.d.u.) and PCA_B-Axis 1 versus depth. **(d)** Cross correlation between these two depth series. **(e)** PCA_{Sed}-Axis 1 and δ_c (in standard deviation units, s.d.u.). **(f)** Cross correlation between these two depth series.

lakes. They have been attributed either to a disequilibrium between climate and vegetation (e.g., at Lake Golhisar, Turkey, Fig. 1; Eastwood et al., 2007), or changes in precipitation seasonality (at Lakes Zeribar and Mirabad, NW Iran, Fig. 1; Stevens et al., 2001, 2006). As discussed above from both pollen and isotope data, we favour the hypothesis of seasonal increased hydrological and thermal contrasts with wet cool winters, possibly a longer rainy season, and very dry warm summers generating strong evaporative effects in both the drainage area and the waterbody. Due to reversed relationships between these two proxy depth-series through time, the cross-correlation for the whole record does not show narrow peak, but an overall correlation (maximum negative correlation: −44.4, with a small depth lag of 80 cm). Links between PCA_{Sed}-Axis 1 and δ_c also vary with depth (Fig. 9e and f). These two series are clearly in antiphase during carbonate-rich intervals, but intervening periods do not show clear patterns.

5.2 Major environmental changes through time

The major environmental changes observed at Yammoûneh, as constrained by all analysed indicators (Figs. 5–7), are now discussed versus time (Fig. 10a–g), according to our age model. Figure 10 also displays (with independent time scales) orbital forcing expressed by eccentricity and summer/winter insolation at 34° N (Fig. 10h; Berger, 1978) and MISs reflecting global ice volume (Fig. 10i; Martinson et al., 1987).

The lowest part of the Yammoûneh profile is poorly resolved, partly because several gaps in core recovery (Fig. 4a). The carbonate-rich interval 3670–2970 cm is assigned to MIS 7 (240–190 ka). Its base (3670–3300 cm; ∼240–220 ka?) is characterised by the maximum development of arboreal vegetation dominated by cool conifer forests and temperate deciduous trees indicating cool and wet conditions. A permanent waterbody with high biogenic and in

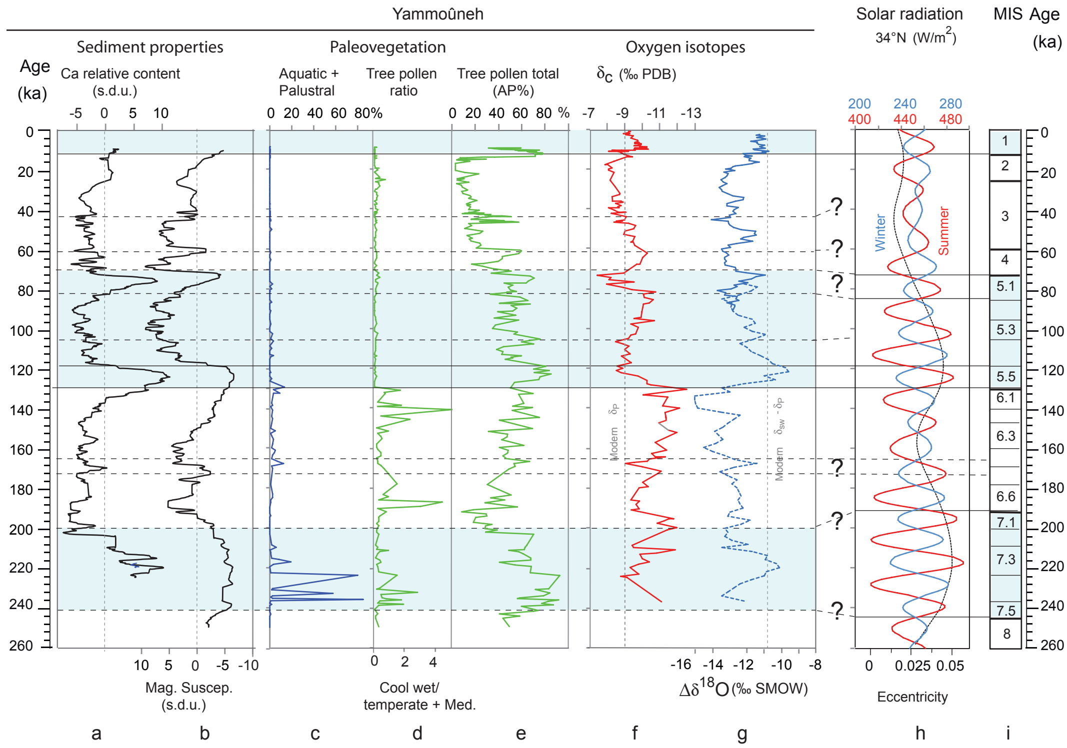

Fig. 10. Major proxies from Yammoûneh versus time according to our age model, and external paleoclimate data (on independent time scale). **(a)** Ca relative content. **(b)** Magnetic susceptibility. For clarity, these two proxies are plotted as the first component factor of a Singular Spectrum Analysis (performed using the Paillard et al., 1996, software) and representing 84 and 92.3 % of the total variance, respectively (s.d.u.: standard deviation units). **(c)** Aquatic + palustral plant pollen (percentage of total pollen grains). **(d)** Ratio of the pollen percentages (percentage of terrestrial pollen) of cool conifer forests/temperate to Mediterranean forests. **(e)** Total tree pollen percentages. **(f)** δ_C. **(g)** $\Delta\delta^{18}O$ (as in Fig. 7f). **(h)** Orbital eccentricity and summer/winter insolation at 34° N (Berger, 1978); **(i)** MISs (Martinson et al., 1987). Questions marks between **(g)** and **(h)** suggest links between major environmental changes at Yammoûneh and global climate changes.

situ carbonate production implies a substantial rise of the local shallow water table. High $\Delta\delta^{18}O$ values around 3250 cm (220 ka?) suggest heavy rainfall. Periods with high δ_c values may result from the ^{18}O enrichment of inflowing water due to a relatively long water residence time in the permanent waterbody, and/or high summer evaporation rate. We interpret this period as reflecting the highest P-E balance of the whole record. Above 3300 cm, a negative shift of aquatic-palustral plant pollen, and the opening of the vegetal cover inducing enhanced erosion and detrital input, record a slight decrease in effective moisture which remained, however, high enough to allow mountain and mixed temperate forest elements to grow. This generally wet interval apparently coincides with period of maximum insolation seasonal contrasts. Its termination is not clearly identified in our record.

The period assigned to MIS 6 (~190–130 ka) is represented from ~2950 to 1850 cm by silty clays interrupted by a marly layer around 2450 cm (~170 ka?) and progressively enriched in carbonate above 2150 cm (~150 ka?). At the base, eolian material prevailed in detrital sediment when the landscape was predominantly steppic. After ~180 ka, cool conifer and/or temperate deciduous forests developed, aquatic vegetation reappeared, and δ_c shifted to reach the lowest values of the profile toward the end of this interval. This suggests an overall increase in local efficient moisture, although $\Delta\delta^{18}O$ decreased possibly due to low temperature (and, thus, low δ_P). This general trend is punctuated by two events. At ~2450 cm (~170 ka?), a narrow peak of carbonate, an increase in marsh plant pollen, and a juniper decline in favour of deciduous oaks suggest a rise of the water table and a moderate warming. This event also shows sharp δ_c and $\Delta\delta^{18}O$ positive shifts, which may reflect an interval of amplified seasonal thermal and hydrological contrasts possibly coincident with high solar radiation seasonality. Above 2150 cm (~150 ka?), junipers became dominant again under the cold conditions of late MIS 6. Even if mean annual precipitation was low, the local available moisture was sufficient to sustain arboreal vegetation, wetlands around the core site and depleted δ_c values when low glacial temperature minimized evaporation and evapotranspiration.

The last interglacial maximum, MIS 5.5 (~1850–1680 cm; ~130–120 ka), is the period of optimal conditions for authigenic carbonate production culminating at ~124 ka. At ~129 ka, an abrupt decline of junipers replaced by deciduous oaks first indicates a warming. Then, a rapid expansion of mesic Mediterranean forests fingerprints the establishment of a typical Mediterranean climate. Aquatic and hydrophilous plant pollen disappeared and a dramatic increase in δ_c values occurred, which, at a first glance, could evoke a drying. Such an interpretation disagrees with very high tree pollen percentages and a synchronous large and positive shift of $\Delta\delta^{18}$O. We interpret this period as reflecting strong orbital-induced seasonal hydrological and thermal contrasts, with cool, strongly rainy winters and possibly a longer rainy season, but very warm, dry summers inducing relatively low mean annual effective moisture inhibiting the growth of mountain and temperate trees. MIS 5.5 coincides with a major change in Yammoûneh environments: after 130 ka, the cool-wet conditions of MIS 7 and late MIS 6 never appeared again.

From ∼120 to ∼80–75 ka, finely banded olive gray silty clay prevailed. Grain-size and colour gradients in each band evoke episodic runoff events followed by quiet decantation periods. The detrital accumulation is interrupted by an interval enriched in carbonate around 1500 cm (∼105 ka) and passes progressively to a light gray marl above 1200 cm (∼85 ka). Open vegetation tends to replace forested landscapes, but this trend is not linear. Peaks of mixed arboreal pollen coincide with carbonate-enriched phases, and reflect wetter conditions than during intervening steppe intervals. These peaks are synchronous with sharp δ_c enrichments and $\Delta\delta^{18}$O increases. The last one resembles MIS 5.5 in its mineral composition and isotope pattern. These two peaks are attributed to MIS 5.3 and MIS 5.1, respectively, although the later is slightly too young in our time scale.

During the last glacial period, MIS 4, 3 and early MIS 2 (∼970–225 cm, ∼75–16 ka), olive gray clay first dominates and the maximum contribution of eolian dust to sedimentation appears around 900 cm (∼70–65 ka). At ∼425 cm (∼40 ka?), the greenish clay passes abruptly to strongly oxidized ocher, reddish clayey silt which contains limestone gravels and carbonate concretions suggesting frequent desiccations at the core site. An increase in carbonate content, mainly detrital, is attributed to physical erosion of the watershed limestones in an environment almost devoid of vegetation. Pollen data clearly show a shift toward steppic-desertic environments consistent with the δ_c increase, interrupted by two moderate humid pulses (around 730 and 500 cm; ∼60 and 45 ka?). The local water availability reached the minimum of the whole record between ∼21 to 16 ka (LGM and Termination 1; MIS 2). Karstic groundwater circulation was considerably reduced. This does not necessarily mean extremely low regional precipitation, but may reflect water storage in Mt Lebanon glaciers and permafrost in the Mnaïtra plateau when temperature was at least 10 °C lower than today. Indeed, permanent glaciers, evidenced by moraines above 2000 m a.s.l. on the western flank of Mt Lebanon, occurred during the LGM (L. Benedetti, personal communication, 2011). The last glacial stage clearly differs from MIS 6 in its trend towards local arid conditions.

After ∼16 ka, the post glacial warming is associated with the rapid re-establishment of humid conditions in the Yammoûneh basin, in response to ice melting and enhanced precipitation. This wetting is evidenced by, successively, a step-wise decrease in δ_c from 16 to 8.5 ka (Develle et al., 2010), the abrupt development of deciduous oaks around 13 ka, and the deposition of a white lacustrine marl rich in rests of aquatic organisms after 11.5 ka. The wetting optimum is reached from ∼11 to 8.5 ka, in phase with S1. In the core, the Holocene is truncated at ∼7.5 ka, but a trend toward aridity starting at ∼7 ka is registered by the isotope record in trench TR02 (Develle et al., 2010). This early Holocene wetting was shown at other sites from Lebanon (see site location in Fig. 1) by changes in growth rate, δ^{18}O and δ^{13}C in a 12 ka speleothem from Jeita Cave (Verheyden et al., 2008), and by the ∼15 ka-pollen records from the Aammish marsh in the Bakka Plain (Hajar et al., 2008, 2010). Pollen data from the Ghab Valley, Syria (Yasuda et al., 2000) show similar trends.

6 Discussion and conclusions

The Yammoûneh record represents the first long multi-proxy paleoenvironmental-paleoclimatic reconstruction based on a single sedimentary sequence and on both biotic and hydrological indicators in the Levant. The combination of pollen, sediment properties and isotope data allowed us to cross-check the information derived from independent proxies and to strengthen the overall interpretation of paleoenvironmental changes. This record covers three Interglacials and two full glacial stages. It fills a geographical gap in data coverage as no other long record is available in northern Levant. Main environmental characteristics of the Yammoûneh basin during interglacial peaks and glacial periods can be drawn as follows.

6.1 Main characteristics of interglacial and glacial stages at Yammoûneh

Interglacial maxima (early-mid MIS 7, MIS 5.5 and early MIS 1) experienced relatively high effective moisture in both the surface and groundwater drainage areas. This is clearly evidenced by sharp increases and dominance of forested landscapes, leading to reduced erosion in the basin slopes. Forested stages are closely correlated with periods of authigenic carbonate sedimentation in the local waterbody which sustained a rich and diversified biocenose. Synchronous and steep δ_c increases can be reconciled with enhanced mean annual moisture when changes in seasonality are taken into account. By analogy with the relatively well-dated early Holocene and MIS 5.5 periods, we suggest (Fig. 10) that other interglacial wet pulses (MIS 5.3–MIS 5.1) and short-lived warmer/wetter events punctuating glacial periods (e.g., ∼170 ka) also match phases of high seasonal insolation contrasts. Despite these common features, the three interglacial maximums differ significantly: very wet and cool conditions prevailed during the MIS 7 peaks; MIS 5.5 is characterised by typical Mediterranean environments with very wet winter and warm evaporative summer conditions, whereas a more temperate wet climate established during early MIS 1.

Glacial periods, characterised by the dominance of coloured silty clay in the sediments, exhibit the highest weight percentages of wind-blown particles, indicating a strong contribution of eolian dust to sedimentation. Forest vegetation cover was generally reduced compared to interglacial stages, favouring local erosion. Environmental conditions evolved, however, in opposite directions during the penultimate and the Last Glacial period. All proxy data reveal an overall wetting during MIS 6 culminating toward the end of this stage, while a drying trend took place during MIS4-2, leading to extremely harsh LGM conditions. We suggest that, under the very cold LGM climate, water was stored by ice in frozen soils in the Yammoûneh depression and in glaciers in the aquifer recharge zone, resulting in extremely low local liquid water availability. As for successive Interglacials, the glacial stages were not identical.

Our record shows an overall decrease in local available water: episodes of maximum moisture occurred during early-mid MIS 7; MIS 6 was wetter than the late glacial stage; the amplitude of wet pulses decreased from MIS 5.5 to the early Holocene. The basin infilling by lake sediments might explain the almost total disappearance of permanent waterbodies after 130 ka and frequent desiccation periods during MIS 2, but not changes in terrestrial vegetation. The long-term aridity trend coincides with a weakening of the seasonal insolation contrasts linked to the decreasing amplitude of the eccentricity cycle. It is as though the Yammoûneh water balance was partly controlled by the amplitude of the seasonal insolation contrast and the relative intensity of winter cooling.

6.2 Comparison with other EMS records

Placed in its regional context, the Yammoûneh record suggests similarities and differences with other records from the EMS region and raises a series of questions on the underlying mechanisms. Some key regional records are illustrated in Fig. 11, which also displays two proxy curves from Yammoûneh for comparison. Sites cited below are located in Fig. 1.

The Yammoûneh evolution generally agrees with data from northeastern Mediterranean and NW Iran, except during MIS 6. This is exemplified (Fig. 11a–c) by pollen records from Albania (L. Ohrid, Lézine et al., 2010), Greece (Tenaghi Philippon, Tzedakis et al., 2006) to NW Iran (L. Urmia, Djamali et al., 2008). During glacial periods, steppe landscapes took place under cool, dry conditions. Nevertheless, several east Mediterranean lakes (e.g., Konya in Turkey, L. Urmia) have experienced relatively high level stands attributed to substantial temperature lowering reducing evaporation loss and enhanced runoff when an open vegetation cover prevailed (Roberts et al., 1999; Djamali et al., 2008). During interglacial peaks, maximum tree pollen percentages reflect warm conditions and higher precipitation from the mid-latitude westerly system. Changes in seasonality were proposed by several authors to explain Holocene climate in the region (Stevens et al., 2001, 2006; Magny, 2007; Tzedakis, 2007; Peyron et al., 2010; Djamali et al., 2010). At Yammoûneh, sharp δ_c increases in phase with arboreal pollen peaks, attributed to enhanced seasonal thermal and hydrological contrasts, suggest that the hypothesis of seasonal changes is valid for older interglacial stages (e.g., MIS 5.5 and MIS 5.1). The specific case of Lake Ohrid, a mountainous karstic lake, is interesting to compare with Yammoûneh: authigenic calcite precipitated during warm phases, when the karstic system was active and forests developed in the catchment area, while detrital siliciclastic particles accumulated and forests are replaced by steppic landscapes during the last glacial period due to strong deficits in available water stored as ice in the mountains (Lézine et al., 2010).

Our record also shares some features with stable isotope spelothem records from western Israel (Peqi'in and Soreq Caves, Fig. 11f) as interpreted by Bar-Matthews et al. (2003). These authors thought that the records integrate the effects of the moisture source (the EMS surface water), rainfall amount and temperature: low/high δ^{18}O reflect wet/dry conditions during interglacial/glacial periods (Bar-Matthews et al., 2003). Paleoprecipitation reconstructions at Soreq (based on present-day relationships between rainwater δ^{18}O and rainfall amount) suggest very high rainfall around 125 ka (MIS 5.5) and a precipitation amount close to modern during early MIS 5.1 (Bar-Matthews et al., 2003; Bar-Matthews and Ayalon, 2004), as proposed from our $\Delta\delta^{18}$O calculations (Figs. 10g and 11e). Sharp negative δ^{18}O shifts fit EMS sapropel events linked to increased Nile River discharge and, thus, to enhanced monsoon strength (Bar-Matthews et al., 2000). These interpretations are in line with marine pollen records from the southern Levantine basin (core MD84-642, Cheddadi and Rossignol-Strick, 1995; core MD-9509; Langgut, 2011). Another striking point arising from both the Soreq and Yammoûneh records is the difference between the penultimate and the last glacial period. At Soreq, the δ^{18}O and δ^{13}C isotopic records from Soreq Cave suggest that, during the entire MIS 6, although the climate was as cold as much of the last glacial, the conditions were never as dry (Ayalon et al., 2002). This Soreq record also shows two major negative shifts in the δ^{18}O–δ^{13}C values (~178 and ~152 ka) interpreted as dramatic increases in rainfall amount, related to the EMS sapropel S6 (the only sapropel event occurring during a glacial phase) and to another EMS event not large enough to form sapropel Bar-Matthews et al., 2003), both associated with increased African monsoon (Fig. 11f, k, l). The wetting events observed at Yammoûneh at ~170 and ~150 ka in our time scale (2450 and 2150 cm) could

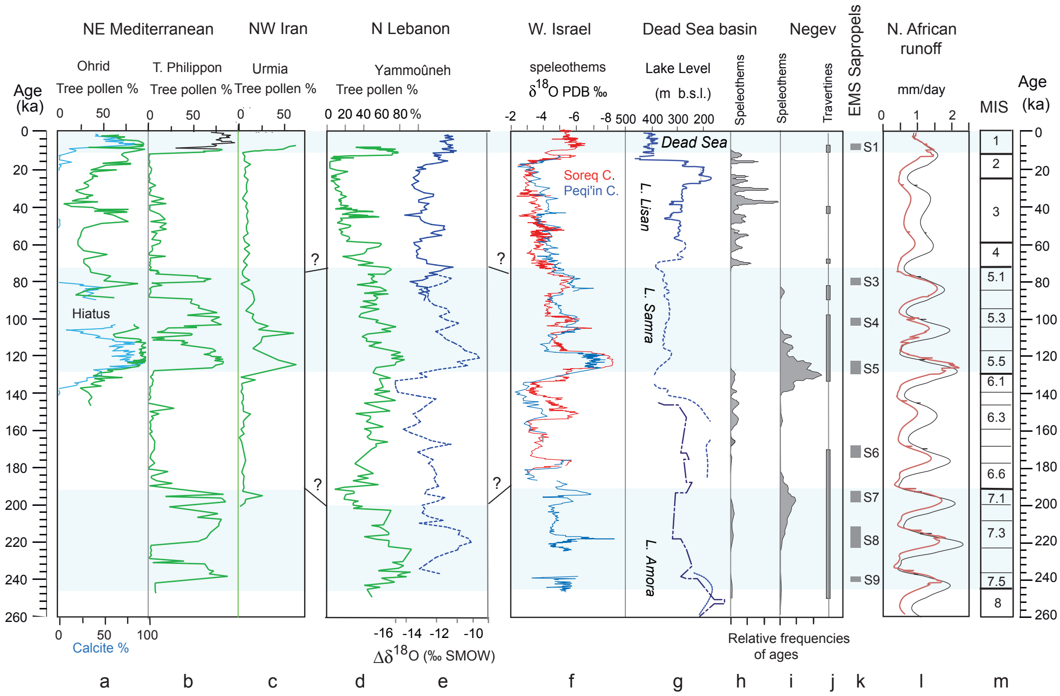

Fig. 11. Environmental changes in the eastern Mediterranean region. **(a)–(c)** Tree pollen percentages in sediments from **a)**: Lake Ohrid, Albania (Lézine et al., 2010); **(b)** Tenaghi Philippon, Macedonia (Tzedakis et al., 2006); **(c)** Lake Urmia, NW Iran (Djamali et al., 2008). **(d)–(e)** Yammoûneh proxy data. **(d)** Tree pollen percentages (as Fig. 10e); **(e)** $\Delta\delta^{18}$O: (as Fig. 10g). **(f)** δ^{18}O record from Soreq and Peqi'in Caves speleothems, western Israel (Bar-Matthews et al., 2003). **(g)** Lake level fluctuations of the Dead Sea and its predecessors (Waldmann et al., 2010). **(h)** Relative frequency of ages of speleothem deposition in the Dead Sea basin (Lisker et al., 2010). **(i)** Relative frequency of ages of speleothem deposition in the Negev (Vaks et al., 2010). **(j)** Periods of travertine deposition deposition in the Arava valley (Waldmann et al., 2010). **(k)** EMS sapropel events (Ziegler et al., 2010). **(l)** Simulated North African runoff to the eastern Mediterranean basin as an indicator of African monsoon (Ziegler et al., 2010). Results from the CLIMBER-2 model using orbital forcing only (black curve), orbital forcing + varying NH ice sheets and greenhouse gas concentrations (red curve). **(m)** MISs (Martinson et al., 1987).

correspond to these Soreq-EMS climatic changes. Keeping in mind that the tropical influence of the Nile River extent as north as Cyprus in the Levantine basin during MIS 3 and MIS 1 (Almogi-Labin et al., 2009), an indirect tropical influence superimposed to the dominant role of the North Atlantic-Mediterranean system might have reached the western Levant by times. A potential impact on this region of the remote Eurasian ice sheet, much larger at 160–130 ka than during the LGM, and of the resulting huge proglacial lakes over central Europe (Svenden et al., 2004; Mangerud et al., 2004) might also be considered.

At the northern limits of the Saharan-Arabian desert, in Negev and the Arava Valley, sporadic events of deposition of speleothems (Vaks et al., 2010; Fig. 11i) and travertine (Waldmann et al., 2010: Fig. 11j) indicate episodes of enhanced effective precipitation in phases with periods of intensified monsoon, schematized by simulated changes in North African river discharge to the EMS and related EMS sapropel events (Fig. 11k and l; Ziegler et al., 2010). These short wet pulses have suggested intrusions of humidity from southern sources during interglacial periods (Waldmann et al., 2010), or simultaneous intensification of monsoon and Atlantic-Mediterranean cyclones (Vaks et al., 2010).

Thus, evidence emerging from the regions evoked above and the Yammoûneh record appears to be in agreement in suggesting dry-cool glacial periods (except MIS 6) and wetter-warm interglacial conditions. In contrast, in the rain shadow of the Judean mountains, the deep, warm Dead Sea basin (DSB), behaved in opposite directions, as indicated by cave stromatolites and periods of speleothem growth/non-deposition (Vaks et al., 2003, 2006, 2010; Fig. 11h; Lisker et al., 2008, 2010) and lake level fluctuations (Fig. 11g; Waldmann et al., 2010) of the Dead Sea (Enzel et al., 2003; Migowski et al., 2006) and its predecessors (Lake Lisan: Bartov et al., 2003; Hazan et al., 2005; Bookmann et al., 2006; Lake Samra: Waldmann et al., 2009; Lake Amora: Torfstein et al., 2009). The only period when the high altitude, small, groundwater-fed Yammoûneh basin roughly evolved in parallel with the DBS is MIS 6. In the DSB, local winds predominate on the large-scale wind components, and local temperature and related evaporation rates are crucial factors controlling the Dead Sea water balance

(Alpert et al., 1997). According to Enzel et al. (2008), increased water availability in the DSB during glacial phases reflect increased rainfall due to the southward deflection of moist westerlies southwards by the presence of ice sheets, as showed by coupled ocean-atmosphere circulation models for the LGM (e.g., Li and and Battisti, 2008; Lainé et al., 2009). An alternative explanation was proposed by Vaks et al. (2003) who suggested reduced evaporation rates during the cold glacial phases leading to a higher P-E balance, and vice-versa during interglacials. This second hypothesis appears consistent with the recent Dead Sea water level lowering, induced by the current warming which results in lower local air humidity and higher evaporation (Shafir and Alpert, 2010).

To sum-up, all records from the eastern Mediterranean region, from southeastern Europe to the northern Sahara-Arabian desert, are in phase with long-term orbitally-induced temperature fluctuations, ice sheet waxing/waning in the Northern Hemisphere, and climatic changes in the North Atlantic system. These linkages reflect, however, different climatic mechanisms, different moisture sources, that resulted in different responses to global changes of individual proxies and individual hydrosystems.

6.3 Perspectives

Further work is required to obtain additional age control points, constrain changes in sedimentation rates and to improve the chronology of environmental changes observed at Yammoûneh.

The impact of seasonal changes in precipitation and temperature on individual proxies should be investigated using modern reference data from the region. Although modern analogues for the glacial periods are missing in the region, quantification of paleoclimatic variables should be attempted.

Hydrological modelling, associated with further investigation of the Mt Lebanon glacier evolution, should help better understand the functioning of the Yammoûneh system.

Our record is based on a single site and its specific climatic and hydrological setting. Other long records from northern Levant and climate modelling are needed to disentangle the effects of local, regional and global climatic-hydrological factors on the basin evolution. Solid scenarios could then be proposed to explain the potential spatial heterogeneity in available moisture in the Levant region.

Acknowledgements. We are grateful to P. Tapponnier, Singapur University and A. Sursock, CNRG-CNRS-Lebanon, who initiated the investigation of the Yammoûneh basin. We thank colleagues from the IPG-P, from the CNRG, and A. Elias, American University in Beyrouth, for their help during fieldwork and fruitful discussions. Thanks are due to M. Decobert and the SETEL team (CEREGE, CNRS) for coring, to D. Kaniewski for his help in the biomization procedure, and to C. Sonzogni (CEREGE), T. Otto and J.-J. Dedoubat (ECOLAB) for technical assistance. L. Lisker (Hebrew University of Jerusalem) and M. Ziegler (Lamont-Doherty Earth Observatory) kindly transmit us their data files on DSB-basin speleothems and simulated African river runoff. We thank the editor M. Fuchs, an anonymous reviewer who took time to comment our initial version and warmly acknowledge N. Roberts for his constructive criticisms on our manuscript. Financial support came from the CNRS-France, the CNRS-Lebanon, the IPG-P, the French Embassy in Lebanon, the CEDRE French-Lebanese programme and the French project INSU-LEFE-EVE-PALEOLIBAN.

Edited by: M. Fuchs

References

Abi-Saleh, B. and Safi, S.: Carte de la végétation du Liban, Ecologia Mediterranea, 14, 123–141, 1988.

Affek, H. P., Bar-Matthews, M., Ayalon, A., Matthews, A., and Eiler, J. M.: Glacial/interglacial temperature variations in Soreq cave speleothems as recorded by "clumped isotope" thermometry, Geochim. Cosmochim. Acta, 72, 5351–5360, 2008.

Almogi-Labin, A., Bar-Matthews, M., Shriki, D., Kolosovsky, E., Paterne, M., Schilman, B., Ayalon, A., Aiznshtat, Z., and Matthews, A.: Climatic variability during the last 90 ka on the southern and northern Levantine basin as evident from marine records and speleothems, Quaternary Sci. Rev., 28, 2882–2896, 2009.

Alpert, P. and Ziv, B.: The Sharav cyclone: observations and some theoretical considerations, J. Geophys. Res., 94, 18495–18514, 1989.

Alpert, P., Shafir, H., and Issahary, D.: Recent changes in the climate of the Dead Sea Valley, Climatic Change, 7, 1–25, 1997.

Aouad, A., Travi, Y., Blavoux, B., Job, J. O., and Najem, W.: Etude isotopique de la pluie et de la neige sur le Mont Liban: premiers résultats, Hydrol. Sci., 49, 429–441, 2004.

Aouad, A., Job, J. O., Khalil, S., Touma, T., Bitar, C., Bocquillon, C., and Najem, W.: Snow in Lebanon: a preliminary study of snow cover over Mount Lebanon and a simple snowmelt model, Hydrol. Sci., 50, 555–569, 2005.

Ayalon, A., Bar-Matthews, M., and Kaufman, A.: Climatic conditions during marine oxygen isotope 6 in the eastern Mediterranean region from the isotopic composition of speleeothems of Soreq Cave, Israel, Geology, 30, 303–306, doi:10.1130/0091-7613(2002)030¡0303:CCDMOI¿2.0.CO;2, 2002.

Bar-Matthews, M. and Ayalon, A.: Speleothems as paleoclimate indicators, a case study from Soreq Cave located in the eastern Mediterranean region, Israel, in: Past Climate through Europe and Africa, edited by: Battarbee, R. W., Gasse, F., and Stickley, C. S., Springer, Dordrecht, 363–391, 2004.

Bar-Matthews, M., Ayalon, A., and Kaufman, A.: Timing and hydrological conditions of sapropel events in the Eastern Mediterranean, as evident from speleothems, Soreq Cave, Israel, Chem. Geol., 169, 145–156, 2000.

Bar-Matthews, M., Ayalon, A., Gilmour, M., Matthews, A., and Hawkesworth, C. J.: Sea-land oxygen isotopic relationship from planktonic foraminifera and speleothems in the Eastern Mediterranean region and their implication for paleorainfall during interglacial intervals, Geochim. Cosmochim. Acta, 67, 3181–3199, 2003.

Bar-Yosef, O.: The Natufian Culture in the Levant, Threshold to the origins of agriculture, Evol. Anthropol., 6, 169–177, 1998.

Bartov, Y., Goldstein, S. L., Stein, M., and Enzel, Y.: Catastrophic arid episodes in the Eastern Mediterranean linked with the North Atlantic Heinrich events, Geology, 31, 439–442, 2003.

Berger, A. L.: Long-term variations of daily insolation and Quaternary climatic changes, J. Atmos. Sci., 35, 2362–2367, 1978.

Besançon, J.: Le poljé de Yammoûné, Revue Libanaise de Géographie, 3, 3–62, 1968.

Bookman, R., Bartov, Y., Enzel, Y., and Stein, M.: The levels of the late Quaternary lakes in the Dead Sea basin: two centuries of research, in: New Frontiers in Dead Sea, Paleoenvironmental Research, edited by: Enzel, Y., Agnon, A., and Stein, M., Geological Society of America Special Paper, 401, 155-17, 2006.

Bottema, S.: The interpretation of pollen spectra from prehistoric settlements (with special attention to Liguliflorae), Palaeohistoria, 17, 17–35, 1975.

Bottema, S. and Van Zeist, W.: Palynological evidence for the climatic history of the Near East, 50,000–6,000 BP, in: Préhistoire du Levant, edited by: Cauvin, J. and Sanlaville, P., Paris-CNRS, 111–132, 1981.

Carto, S., Weaver, A. J., Hetherington, R., Lam, Y., and Wiebe, E. C.: Out of Africa and into an ice age: on the role of global climate change in the late Pleistocene migration of early modern humans out of Africa, J. Human Evol., 56, 139–151, 2009.

Castañeda, I., Shefuss, E., Pätzold, J., Sinninghe Damsté, J. S., Weldeab, S., and Schouten, S.: Millenial-scale sea surface temperature changes in the eastern Mediterranean (Nile River Delta region) over the last 27,000 years, Paleoceanography, 25, PA1208, doi:10.1029/2009PA001740, 2010.

Cheddadi, R. and Rossignol-Strick, M.: Easterm Mediterranean quaternary paloeclimates from pollen and isotope records of marine cores in the Nile cone area, Paleoceanography, 10, 291–300, 1995.

Craig, H.: The measurement of oxygen isotope paleotemperatures, in: Stable Isotopes in Oceanographic Studies and Paleotemperatures, edited by: Tongiorgi, E., Consiglio Nazionale delle Ricerche Laboratorio di Geologia Nucleare, Pisa, 166–182, 1965.

Daëron, M., Benedetti, L., Tapponnier, P., Sursock, A., and Finkel, R. C.: Constraints on the post-25-ka slip rate of the Yammoûneh fault (Lebanon) using in situ cosmogenic ^{36}Cl dating of offset limestone-clast fans, Earth Planet. Sc. Lett., 227, 105–119, 2004.

Daëron, M., Klinger, Y., Tapponnier, P., Elias, A., Jacques, E., and Sursock, A.: 12,000-year-long record of 10 to 13 paleoearthquakes on the Yammoûneh fault, Levant fault system, Lebanon, Bull. Seismol. Soc. Am., 97, 749–771, 2007.

Dayan, U., Ziv, B., Shoob, T., and Enzel, Y.: Suspended dust over southeastern Mediterranean and relation to atmospheric circulations, International J. Climatol., 28, 915–924, doi:10.1002/joc.1587, 2008.

Develle, A.-L.: Changement de l'environnement et du climat continental au cours des derniers cycles glaciaires/interglaciaires, Approche sédimentologique, géochimique et magnétique de la séquence lacustre du bassin de Yammoûneh (Liban), Unpublished PhD thesis, University of Aix-Marseille III, 2010.

Develle, A.-L., Herreros, J., Vidal, L., Sursock, A., and Gasse, F.: Controlling factors on a paleo-lake oxygen isotope record (Yammoûneh, Lebanon) since the Last Glacial Maximum, Quaternary Sci. Rev., 29, 865–886, doi:10.1016/j.quascirev.2009.12.005, 2010.

Develle, A. L., Gasse, F., Vidal, L., Williamson, D., Demory, F., Van Campo, E., Ghaleb, N., and Thouveny, N.: A 250 ka sedimentay record from a small karstic lake in the northern Levant (Yammoûneh, Lebanon), Paleogeogr. Paleocl., 4–5, 10–27, doi:10.1016/j.palaeo.2011.02.008, 2011.

Di Castri F.: Mediterranean-type shrublands of the world, in: Mediterranean-Type Shrublands, edited by: di Castri, F., Goodall, D. W., and Specht, R. L., Elsevier, Amsterdam, 1–52, 1981.

Djamali, M., de Beaulieu, J.-L., Shah-hosseini, M., Anrieu-Ponel, V., Ponel, P., Amini, A., Alkani, H., Leroy, S. A. G., Stevens, L., Lahijani, H., and Brewer, S.: A late Pleistocene long pollen record from Lake Urmia, NW Iran, Quaternary Res., 69, 413–420, 2008.

Djamali, M., Akhani, H., Andrieu-Ponel, V., Braconnot, P., Brewer, S., de Beaulieu, J.-L., Fleitmann, D., Fleury, J., Gasse, F., Guibal, F., Jackson, S. T., Lézine, A.-M., Médail, F., Ponel, P., Roberts, N., and Stevens, L.: Indian Summer Monsoon variations could have affected the early-Holocene woodland expansion in the Near East, Holocene, 20, 813–820, doi:10.1177/0959683610362813, 2010.

Dubertret, L.: Introduction à la carte géologique au 1/50 000 du Liban, Notes et Mémoires du Moyen-Orient, 13, 345–403, 1975.

Ducassou, E., Capotondi, L., Murat, A., Bernasconi, S. M., Mulder, T., Gonthier, E., Migeon, S., Duprat, J., Giraudeau, J., and Mascle, J.: Multiproxy Late Quaternary stratigraphy of the Nile deep-sea turbidite system, Towards a chronology of deep-sea terrigeneous systems, Sediment. Geol., 200, 1–13, 2007.

Eastwood, W. J., Leng, M., Roberts, N., and Davis, B.: Holocene climate change in the eastern Mediterranean region: a comparison of stable isotope and pollen data from Lake Gölhisar, southwest Turkey, J. Quatern. Sci., 22, 327–341, 2007.

El Hakim, M.: Les aquifères karstiques de l'Anti-Liban et du nord de la plaine de la Bekaa: caractéristiques, fonctionnement, évolution et modélisation, d'après l'exemple du système karstique Anjar-Chamsine (Liban), Unpublished PhD thesis, University of Montpellier II, 2005.

Emeis, K. C., Schulz, H., Struck, U., Rossignol-Strick, M., Erlenkeuser, H., Howell, M. W., Kroon, D., Mackensen, A., Ishizuka, S., Oba, T., Sakamoto, T., and Koizumi, I.: Eastern Mediterranean surface water temperatures and δ^{18}O during deposition of sapropels in the late Quaternary, Paleoceanography, 18, 1005, doi:10.1029/2000PA000617, 2003.

Enzel, Y., Bookman, R., Sharon, D., Gvirtzman, H., Dayan, U., Baruch, Z., and Stein, M.: Late Holocene climates of the Near East deduced from Dead Sea level variations and modern regional winter rainfall, Quaternary Res., 60, 263–373, 2003.

Enzel, Y., Amit, R., Dayan, U., Crouvi, O., Kahana, R., Baruch, Z., and Sharon, D.: The climatic and physiographic controls of the eastern Mediterranean over the late Pleistocene climates in the southern Levant and its neighboring deserts, Global Planet. Change, 60, 165–192, 2008.

Essallami, L., Sicre, M. A., Kallel, N., Labeyrie, L., and Siani, G.: Hydrological changes in the Mediterranean Sea over the last 30,000 years, Geochem. Geophy. Geosy., 8, Q07002, doi:10.1029/2007GC001587, 2007.

Felis, T., Lohmann, G., Kuhnert, H., Lorenz, S. J., Sholz, D., Pätzold, J., Al-Rousan, S. A., and Al-Moghrabi, S. M.: Increased seasonality in Middle East temperatures during the last interglacial period, Nature, 429, 164–168, 2004.

Fleitmann, D. and Matter, A.: The speleothem record of climate variability in Southern Arabia, C. R. Geosci., 341, 634–642, 2009.

Frumkin, A., Ford, D. C., and Schwarcz, H. P.: Continental oxygen isotopic record of the last 170,000 years in Jerusalem, Quaternary Res., 51, 317–327, 1999.

Frumkin, A., Bar-Yosef, O., and Schwartz, H. P.: Possible paleohydrological and paleoclimatic effects on hominin migration to and occupation of the Levant between MIS 6 and MIS 4, J. Human Evol., 60, 437–451, 2011.

Gasse, F.: Hydrological changes in the African tropics since the last glacial maximum, Quaternary Sci. Rev., 19, 189–211, 2000.

Guiot, J., Torre, F., Cheddadi, R., Peyron, O., Tarasov, P., Jolly, D., and Kaplan, J. O.: The climate of the Mediterranean Basin and of Eurasia of the Last Glacial Maximum as reconstructed by inverse vegetation modelling and pollen data, Ecologia Mediterranea, 25, 193–204, 1999.

Hajar, L., Khater, C., and Cheddadi, R.: Vegetation changes during the late Pleistocene and Holocene in Lebanon: a pollen record from the Bekaa Valley, Holocene, 18, 1089–1099, 2008.

Hajar, L., Haïdar-Boustani, M., Khater, C., and Cheddadi, R.: Environmental changes in Lebanon during the Holocene: Man vs. climate impacts, J. Arid Environ., 74, 746–755, 2010.

Hakim, B.: Recherches hydrologiques et hydrochimiques sur quelques karsts méditerranéens, Liban, Syrie et Maroc, Université Libanaise, Section des Etudes Géographiques II, Beyrouth, 1985.

Hazan, N., Stein, M., Agnon, A., Marco, S., Nadel, D., Negendank, J. F. W., Schwab, M. J., and Neev, D.: The late Quaternary limnological history of Lake Kinneret (Sea of Galilee), Israel, Quaternary Res., 63, 60–77, 2005.

Hoelzmann, P., Gasse, F., Dupont, L. M., Salzmann, U., Staubwasser, M., Leuchner, D. C., and Sirocko, F.: Palaeoenvironmental changes in the arid and subarid belt (Sahara-Sahel-Arabian Peninsula) from 150 ka to present, in: Past Climate through Europe and Africa, edited by: Battarbee, R. W., Gasse, F., and Stickley, C. S., Springer, Dordrecht, 219–256, 2004.

Imbrie, J., Hays, J. D., Martinson, D. G., Mcintyre, A., Mix, A. C., Morley, J. J., Pisias, N. G., Prell, W. L., and Shackleton, N. J.: The orbital theory of Pleistocene climate: support from revised chronology of the marine $\delta^{18}O$ record, Reidel, Dordrecht, 1984.

Kahana, R., Ziv, B., Enzel, Y., and Dayan, U.: Synoptic climatology of major floods in the Negev desert, Israel, Int. J. Climatol., 22, 867–882, 2002.

Kolodny, Y., Stein, M., and Machlus, M.: Sea-rain-lake relation in the Last Glacial East Mediterranean revealed by $\delta^{18}O$-$\delta^{13}C$ in Lake Lisan aragonites, Geochim. Cosmochim. Acta, 69, 4045–4060, 2005.

Kroon, D., Alexandser, I., Little, M., Lourens, L. J., Mattthewson, A., Robertson, A. H. F., and Sakamoto, T.: Oxygen isotope and sapropel stratigraphy in the Eastern Mediterranean during the last 3.2 millions years, Ocean Drilling Program Scientific Results, 160, College Station, Texas, 181–190, 1998.

Kuhlemann, J., Rohling, E. J., Krumrei, I., Kubik, P., Ivy-Ochs, S., and Kucera, M.: Regional synthesis of Mediterranean atmospheric circulation during the Last Glacial Maximum, Science, 231, 1338–1340, 2008.

Laîné, A., Kageyama, M., Salas-Mélia, D., Voldoire, A., Rivière, G., Ramstein, G., Planton, S., Tyteca, S., and Peterschmitt, J. Y.: Northern hemisphere storm tracks during the last glacial maximum in the PMIP2 ocean-atmosphere coupled models: energetic study, seasonal cycle, precipitation, Clim. Dynam., 32, 593–614, doi:10.1007/s00382-008-0391-9, 2009.

Langgut, D., Almogi-Labin, A., Bar-Matthews, M., and Weinstein-Evron, M.: Vegetation and Climate changes in the Eastern Mediterranean during the last glacial-interglacial cycle: new marine pollen core evidence for the last 86 ka, accepted for publication in Quaternary Sci. Rev., 2011.

Le Pichon, X. and Gaulier, J. M.: The rotation of Arabia and the Levant fault system, Tectonophysics, 153, 271–294, 1988.

Lézine, A.-M., von Grafenstein, U., Andersen, N., Belchemeri, S., Bordon, A., Caron, B., Cazet, J.-P., Erlenkeuser, H., Fouache, E., Grenier, C., Huntsman-Mapila, P., Huzeau-Mazaudier, D., Manelli, D., Mazaud, A., Robert, C., Sulpizio, R., Tiercelin, J.-J., Zanchetta, G., and Zeqolari, Z.: Lake Ohrid, Albania, provides an exceptional multi-proxy record of environmental changes during the last glacial-interglacial cycle, Palaeogeogr. Palaeocl., 287, 116–127, 2010.

Li, C. and Battisti, D. S.: Reduced Atlantic storminess during the Last Galcial Maximum: evidence from a coupled climate model, J. Climate, 21, 3561–3579, 2008.

Lisker, S., Vaks, A., Bar-Matthews, M., Porat, R., and Frumkin, A.: Stromatolites in caves of the Dead Sea Fault Escarpment: implications to latest Pleistocene lake levels and tectonic subsidence, Quaternary Sci. Rev., 28, 80–92, doi:10.1016/j.quascirev.2008.10.015, 2008.

Lisker, S., Vaks, A., and Bar-Matthews, M.: Late Pleistocene palaeoclimatic and palaeoenvironmental reconstruction of the Dead Sea area (Israel), based on speleothems and cave stromatolites, Quaternary Sci. Rev., 29, 1201–1211, doi:10.1016/j.quascirev.2010.01.018, 2010.

Magny, M.: Lake level studies: West-Central-Europe, Encyclopedia of Quaternary Science, 2. Amsterdam, Elsevier, 1389–1399, 2007.

Mangerud, Y., Jakobsson, M., Alexanderson, H., Astakhov, V. I., Clarke, K. C., Henriksen, M., Hjort, C., Krinner, G., Lunkka, J., Möller, P., Murray, A., Nikolskaya, O., Saarnisto, M., and Svenden, J. A.: Ice-damned lakes and rerouting of ice drainage of northern Eurasia during the Last Glaciation, Quaternary Sci. Rev., 23, 1313–1332, doi:10.1016/j.quascirev.2003.12.009, 2004.

Martinson, D. G., Pisias, N. G., Hays, J. D., Imbrie, J., Moore Jr., T. C., and Shackleton, N. J.: Age dating and the orbital theory of the Ice Ages: development of a high-resolution 0 to 300,000-year chronostratigraphy, Quaternary Res., 27, 1–29, 1987.

McGarry, S., Bar-Matthews, M., Matthews, A., Vaks, A., Schilman, B., and Ayalon, A.: Constraints on hydrological and paleotemperature variations in the Eastern Mediterranean region in the last 140 ka given by the D values of speleothems fluid inclusions, Quaternary Sci. Rev., 23, 919–934, doi:10.1016/j.quascirev.2003.06.020, 2004.

Meadows, J.: The Younger Dryas episode and the radiocarbon chronologies of the Lake Huleh and Ghab Valley pollen diagrams, Israel and Syria, Holocene, 15, 631–636, doi:10.1191/0959683605hl838fa, 2005.

Migowski, C., Stein, M., Prasad, S., Negendank, J. F. W., and Agnon, A.: Holocene climate variability and cultural evolution in the Near East from the Dead Sea sedimentary record, Quaternary Res., 66, 421–431, 2006.

Paillard, D., Labeyrie, L., and Yiou, P.: Macintosh program performs term-series analysis, Eos Trans. AGU, 77, 379, 1996.

Peyron, O., Goring, S., Dormoy, I., Kotthoff, U., Pross, J., de Beaulieu, J.-L., Drescher-Schneider, R., Vannière, B., and Magny, M.: Holocene seasonality changes in the central Mediterranean region reconstructed from the pollen sequences of Lake Accesa (Italy) and Tenaghi Philippon (Greece), Holocene, 21, 131–146, doi:10.1177/0959683610384162, 2011.

Raible, C. C., Ziv, B., Saaroni, H., and Wild, M.: Winter synoptic-scale variability over the Mediterranean Basin under future climate conditions as simulated by the ECHAM5, Clim. Dynam., 35, 473–488, doi:10.1007/s00382-009-0678-5, 2010.

Reille, M.: Pollen et spores d'Europe et d'Afrique du Nord, Laboratoire de botanique historique et de palynologie, Marseille, 1992.

Reimer, P. J., Baillie, M. G. L., Bard, E., Bayliss, A., Beck, J. W., Blackwell, P. G., Ramsey, C. B., Buck, C. E., Burr, G. S., Edwards, R. L, Friedrich, M., Grootes, P. M., Guilderson, T. P., Hajdas, I., Heaton, T. J., Hogg, A. G., Hughen, K. A., Kaiser, K. F., Kromer, B., McCormac, F. G., Mannong, S. W., Reimer, R. W., Richards, D. A., Southon, J. R., Talamo, S., Turney, C. S. M., van der Plicht, J., and Weyhenmeye, C. E.: INTERCAL09 and marine09 radiocarbon age and calibration curves, 0–50,000 years, Radiocarbon, 51, 1111–1150, 2009.

Roberts, N., Black, S., Boyer, P., Eastwood, W. J., Griffiths, H. I., Lamb, H. F., Leng, M. J., Parish, R., Reed, J. M., Twigg, D., and Yigitbasioglu, H.: Chronology and stratigraphy of Late Quaternary sediments in the Konya Basin, Turkey : results from the KOPAL Project, Quaternary Sci. Rev., 18, 611–630, 1999.

Robinson, S. A., Black, S., Sellwood, B. W., and Valdes, P. J.: A review of palaeoclimates and palaeoenvironments in the Levant and Eastern Mediterranean from 25,000 to 5000 years BP: setting the environmental background for the evolution of human civilisation, Quaternary Sci. Rev., 25, 1517–1541, doi:10.1016/j.quascirev.2006.02.006, 2006.

Rodwell, M. J. and Hopkins, B. J.: Monsoons and the dynamics of deserts, Q. J. Roy. Meteorol. Soc., 122, 1385–1404, doi:10.1002/qj.49712253408, 1996.

Rossignol-Strick, M. and Paterne, M.: A synthetic pollen record of the eastern Mediterranean sapropels of the last 1 Ma: implication for the time-sacle and formation of sapropels, Mar. Geol., 153, 221–237, 1999.

Rozanski, K.: Isotopes in atmospheric moisture, in: Isotopes in the Water Cycle: Past, Present and Future, a Developing Science, Springer, Dordrecht, 291–302, 2005.

Rozanski, K., Araguás-Araguás, L., and Gonfiantini, R.: Isotopic patterns in modern global precipitation, Climate Change in Continental Isotopic Records, Geophysical Monograph 78, American Geophysical Union, Washington, DC, 1–36, 1993.

Service Météorologique du Liban: Atlas climatique du Liban, Beirut, Lebanon, 1977.

Shafir, H. and Alpert, P.: Regional and local climatic effects on the Dead-Sea evaporation, Climatic Change, 105, 455–468, doi:10.1007/s10584-010-9892-8, 2010.

Sharon, D. and Kutiel, H.: The distribution of rainfall intensity in Israel, its regional and seasonal variations and its climatological evaluation, J. Climatol., 6, 277–291, 1986.

Shea, J. J.: Transitions or turnovers? Climatically-forced extinctions of *Homo sapiens* and Neanderthals in the east Mediterranean Levant, Quaternary Sci. Rev., 27, 2253–2270, doi:10.1016/j.quascirev.2008.08.015, 2008.

Stevens, L. R., Wright Jr., H. E., and Ito, E.: Proposed changes in seasonality of climate during the Lateglacial and Holocene at Lake Zeribar, Iran, Holocene, 11, 747, doi:10.1191/09596830195762, 2001.

Stevens, L. R., Ito, E., Schwalb, A., Wright Jr., H. E.: Timing of atmospheric precipitation in the Zagros mountains inferred from a multi-proxy record from Lake Mirabad, Iran, Quaternary Res., 66, 494–500, 2006.

Svenden, J. A., Alexanderson, H., Astakhov, V. I., Demidov, I., Dowdeswell, J. A., Funder, S., Gataullin, V., Henriksen, M., Hjort, C., Houmark-Nielsen, M., Hubberten, H. W., Ingolfsson, O., Jakobsson, M., Kjær, K. H., Larsen, E., Lokrantz, H., Pekka Lunkka, J., Astrid Lysi, A., Mangerud, J., Matiouchkov, A., Murray, A., Möller, P., Niessen, P., Nikolskaya, O., Polyak, L., Saarnisto, M., Siegert, C., Siegert, M., Spielhagen, R. F., and Stein, R.: Late Quaternary ice sheet of northern Eurasia, Quaternary Sci. Rev., 13, 1229–1271, doi:10.1016/j.quascirev.2003.12.008, 2004.

Tarasov, P. E., Cheddadi, R., Guiot, J., Bottema, S., Peyron, O., Belmonte, J., Ruiz-Sanchez, V., Saadi, F., and Brewer, S.: A method to determine warm and cool steppe biomes from pollen data; application to the Mediterranean and Kazakhstan regions, J. Quatern. Sci., 13, 335–344, 1998.

Torfstein, A., Haase-Schramm, A., Waldmann, N., Kolodny, Y., and Stein, M.: U-series and oxygen isotope chronology of the mid-Pleistocene Lake Amora (Dead Sea basin), Geochim. Cosmochim. Acta, 73, 2603–2630, doi:10.1016/j.gca.2009.02.010, 2009.

Tzedakis, P. C.: Seven ambiguities in the Mediterranean palaeoenvironmental narrative, Quaternary Sci. Rev., 26, 2042–2066, doi:10.1016/j.quascirev.2007.03.014, 2007.

Tzedakis, P. C., Hooghiemstra, H., and Pälike, H.: The last 1.35 million years at Tenaghi Philippon, revised chronostratigraphy and long-term vegetation trends, Quaternary Sci. Rev., 25, 3416–3430, doi:10.1016/j.quascirev.2006.09.002, 2006.

Vaks, A., Bar-Matthews, M., Ayalon, A., Schilman, B., Gilmour, M., Hawkesworth, C. J., Frumkin, A., Kaufman, A., and Matthews, A.: Paleoclimate reconstruction based on the timing of speleothem growth and oxygen and carbon isotope composition in a cave located in the rainshadow in Israel, Quaternary Res., 59, 182–193, doi:10.1016/S0033-5894(03)00013-9, 2003.

Vaks, A., Bar-Matthews, M., Ayalon, A., Matthews, A., Frumkin, A., Dayan, U., Halicz, L., Almogi-Labin, A., and Schilman, B.: Paleoclimate and location of the border between Mediterranean climate region and the Saharo-Arabian Desert as revealed by speleothems from the northern Negev Desert, Israel, Earth Planet. Sc. Lett., 249, 384–399, doi:10.1016/j.epsl.2006.07.009, 2006.

Vaks, A., Bar-Matthews, M., Ayalon, A., Matthews, A., Halicz, L., and Frumkin, A.: Desert speleothems reveal climatic window for African exodus of early modern humans, Geology, 35, 831–834, 2007.

Vaks, A., Bar-Matthews, M., Matthews, A., Ayalon, A., Matthews, A., and Frumkin, A.: Middle-Late Quaternary paleoclimate of northern margins of the Saharian-Arabian Desert: reconstruction from speleothems of Negev desert, Israel, Quaternary Sci. Rev., 29, 2647–2662, doi:10.1016/j.quascirev.2010.06.014, 2010.

Verheyden, S., Nader, F. H., Cheng, H. J., Edwards, L. R., and Swennen, R.: Paleoclimate reconstruction in the Levant region from the geochemistry of a Holocene stalagmite from the Jeita cave, Lebanon, Quaternary Res., 70, 368–381, 2008.

Waldmann, N., Stein, M., Ariztegui, D., and Starinsky, A.: Stratigraphy, depositional environments and level reconstructon of the last interglacial Lake Samra in the Dead Sea basin, Quaternary Res., 72, 1–15, 2009.

Waldmann, N., Torfstein, A., and Stein, M.: Northward intrusions of low- and mid-latitude storms across the Saharo-Arabian belt during past interglacials, Geology, 38, 567–570, doi:10.1130/G30654.1, 2010.

Weinstein-Evron, M.: The Paleoecology of the Early Wurm in the Hula Basin, Israel, Paléorient, 9, 5–19, 1983.

Weinstein-Evron, M., Vogel, J. C., and Kronfeld, J.: Further attempts at dating the palynological sequence of the Gula L07 core, upper Jordan Valley, Radiocarbon, 43, 561–570, 2001.

Yasuda, Y., Kitagawa, H., and Nakagawa, T.: The earliest record of major anthropogenic deforestation in the Ghab Valley, northwest Syria: a palynological study, Quatern. Int., 73/74, 127–136, 2000.

Ziegler, M., Tuenter, E., and Lourens, L. J.: The precession phase of the boreal summer monsoon as viewed from the eastern Mediterranean (ODP site 968), Quaternary Sci. Rev., 29, 1481–1490, doi:10.1016/j.quascirev.2010.03.011, 2010.

Ziv, B., Saaroni, H., and Alpert, P.: The factors governing the summer regime of the eastern Mediterranean, Int. J. Climatol., 24, 1859–1871, 2004.

Ziv, B., Dayan, U., Kuschnir, Y., Roth, C., and Enzel, Y.: Regional and global atmospheric patterns governing rainfall in the southern Levant, Int. J. Climatol., 26, 55–73, doi:10.1016/j.quascirev.2005.07.008, 2006.

Ziv, B., Saaroni, H., Romem, M., Heifetz, E., Harnik, N., and Baharad, A.: Analysis of conveyor belts in winter Mediterranean cyclones, Theor. Appl. Climatol., 99, 441–455, 2010.

Clim. Past, 13, 1181–1197, 2017
https://doi.org/10.5194/cp-13-1181-2017

Climate of the Past
Open Access
EGU

Eurasian contribution to the last glacial dust cycle: how are loess sequences built?

Denis-Didier Rousseau[1,2,*], **Anders Svensson**[3], **Matthias Bigler**[4], **Adriana Sima**[1], **Jorgen Peder Steffensen**[3], and **Niklas Boers**[1]

[1]Ecole Normale Supérieure, UMR CNRS 8539, Laboratoire de Météorologie Dynamique, and CERES-ERTI, 24 rue Lhomond, 75231 Paris CEDEX 5, France
[2]Lamont-Doherty Earth Observatory of Columbia University, Palisades, NY 10964, USA
[3]Centre for Ice and Climate – Niels Bohr Institute, University of Copenhagen, Juliane Maries Vej 30, 2100 Copenhagen OE, Denmark
[4]Physics Institute, Climate and Environment Physics, University of Bern, Sidlerstrasse 5, 3012 Bern, Switzerland
[*] *Invited contribution by Denis-Didier Rousseau, recipient of the EGU Hans Oeschger Medal 2017.*

Correspondence to: Denis-Didier Rousseau (denis.rousseau@lmd.ens.fr)

Received: 4 May 2017 – Discussion started: 22 May 2017
Revised: 10 August 2017 – Accepted: 12 August 2017 – Published: 19 September 2017

Abstract. The last 130 000 years have been marked by pronounced millennial-scale climate variability, which strongly impacted the terrestrial environments of the Northern Hemisphere, especially at middle latitudes. Identifying the trigger of these variations, which are most likely associated with strong couplings between the ocean and the atmosphere, still remains a key question. Here, we show that the analysis of δ^{18}O and dust in the Greenland ice cores, and a critical study of their source variations, reconciles these records with those observed on the Eurasian continent. We demonstrate the link between European and Chinese loess sequences, dust records in Greenland, and variations in the North Atlantic sea ice extent. The sources of the emitted and transported dust material are variable and relate to different environments corresponding to present desert areas, but also hidden regions related to lower sea level stands, dry rivers, or zones close to the frontal moraines of the main Northern Hemisphere ice sheets. We anticipate our study to be at the origin of more sophisticated and elaborated investigations of millennial and sub-millennial continental climate variability in the Northern Hemisphere.

1 Introduction

During the last glacial interval, abrupt climate changes have been documented worldwide in different types of records, but especially in ice cores (Dansgaard et al., 1969, 1982; Johnsen et al., 1992, 1972, 2001). Their interpretation mostly focused on the more spectacular character corresponding to abrupt warmings (named Dansgaard–Oeschger – DO events; Broecker et al., 1990) of some ten degrees to interstadial conditions in Greenland (Kindler et al., 2014). These warmings were followed by a schematic two-step return to stadial conditions. Modeling experiments are able to reconstruct this abrupt warming and the two-step return to stadial conditions, indicating a periodicity of about 1500 years (Schulz, 2002; Rahmstorf, 2003), which, however, still remains questionable (Ditlevsen et al., 2007; Thomas et al., 2011; Boers et al., 2017). More precisely, the very-high-resolution analysis of the last deglaciation in the North Greenland Ice Core Project (NGRIP) record (NGRIP, 2004) revealed that different parameters show different abruptness of the warming events. For the last two warming events (14.7 and 11.7 ka b2k (years before AD 2000)), deuterium excess increased within 1 to 3 years, alongside more gradually increasing temperatures as represented by δ^{18}O. Dust concentration would require at least 15 years to decrease, preceding the deuterium excess increase by 10 ± 5 years (Steffensen et al., 2008). Carefully considering the DO events it was noticed that during the last climatic cycle in NGRIP, some variability that occurs as the last deglaciation timing of transitions does not seem to be reproduced every time in the older parts of the record (Rousseau et al., 2017). The climate trend, cooling and increase in dustiness, within these particular events is variable as well. High-resolution studies of the temperature signal in older interstadials show the occurrence of sub-millennial-scale elements like precursor events of about centennial duration before the interstadial itself, rebound events exhibiting abrupt cooling towards stadial conditions, and cooling events occurring towards the end of the interstadial (Capron et al., 2010). These sub-millennial events make the understanding of the climate variability during these interstadials even more complicated than a simple warming followed by a two-step cooling. Ice cores nevertheless provide much more information than on temperature and dust concentration only, as they release records of numerous components of the climate system, isotope values of the transported water vapor, mineral aerosols and greenhouse gas concentrations, chemical elements, etc., which show different origins and transport patterns to the high-latitude ice sheets. Such richness in proxies allows comparisons with other records of millennial-scale variability preserved in both marine (Henry et al., 2016) and terrestrial deposits, as well as in other ice cores (Barbante et al., 2006; Buizert et al., 2015). In this paper, after briefly describing the abrupt changes observed in the very-high-resolution δ^{18}O and dust records from NGRIP (NGRIP, 2004), we compare the dust particle sedimentation rates over Europe and China as expressed in key loess sequences (Fig. 1). This is a complementary study of Rousseau et al. (2017), which essentially focused on paleosol development. In the last section we provide an interpretation of the link between Greenland dust records and Eurasian loess sequence development.

2 Analysis

We investigate in this study the 18 Greenland interstadials (GIs), labeled from 17.1 to 2 (Rasmussen et al., 2014), which have been identified during the MIS 3 and 2 (59–14 ka b2k) interval. We performed this comparison by studying in parallel the δ^{18}O (NGRIP, 2004; Gkinis et al., 2014) and the dust (Ruth et al., 2003) records from the NGRIP ice core at the highest resolution. These two indices correspond to different sources, marine and continental but also to different origins, mostly Atlantic (Masson-Delmotte et al., 2006) and East Asian (Biscaye et al., 1997; Svensson et al., 2000; Bory et al., 2002). The two indices are not directly related so that if similarities would appear, this should highlight a more global phenomenon.

The compilation of the 18 GIs in the NGRIP record (Rousseau et al., 2017) shows that DO events can be characterized using a numerical algorithm (see Supplement) by an increase in δ^{18}O occurring on average in 36.4 ± 13.4 (1σ) years, with a mean GI duration of 1048 ± 1163 (1σ) years (Table 1). When determined visually by considering the onset of the abrupt change at the start and the return to the same initial value as the end of the event, the δ^{18}O changes occur, on average, in 55.4 ± 16.1 (1σ) years, with a mean duration of 1053 ± 1068 (1σ) years. The larger errors than the mean values are due to the few long intervals. These two methods have been described in detail in Rousseau et al. (2017). Although both methods allow the identification of the GIs and their parameters (onset, transition, and duration), the numerical approach also allows the identification of statistically significant events that the virtual one could consider as questionable. However, we consider that these two methods are complementary, the reason why we decided to release values obtained by both of them. These compiled characteristics fit with the values generally considered from the literature (Wolff et al., 2010; Rasmussen et al., 2014).

Following the detailed correlations defined between Nussloch and NGRIP stratigraphies (Fig. 2) (Rousseau et al., 2002, 2007b, 2017), we then applied the dates obtained for every start and end of a GI, from both the δ^{18}O and the dust NGRIP timescale, to the loess sequence. This was performed by considering that in western European loess sequences, paleosols developed from the underlying loess deposits after a stop of the eolian sedimentation (Taylor et al., 2014), and that the eolian sedimentation itself restarted on top of the developed paleosols. This makes the time evolution nonlinear and a bit more complex than the classical continuous sedimentation observed in other terrestrial, marine, and ice-core records (Kukla and Koci, 1972; Rousseau et al., 2007a). Therefore, a determined eolian interval, equivalent to the Greenland stadial (GS), includes the loess unit and the overlying paleosol (blue arrow in Fig. 3), while the paleosol development itself fits with the GI duration (red arrow in Fig. 3). Doing so, the Nussloch stratigraphy can be read as expressed in Table 2, allowing then to better estimate the sedimentation and the mass accumulation rates required for comparison with other loess records and model outputs. Conversely, in Chinese loess sequences no such paleosols developed during the last climate cycle. Therefore, own reasoning does not apply to these records.

3 Discussion

The mineral dust record in the NGRIP ice core is obtained from variations in dust concentration, measured in the terms of the number of particles larger than $1\,\mu\mathrm{m}\,\mathrm{mm}^{-1}$ of melt water, which also shows abrupt changes that are quite synchronous with the DO events expressed in the δ^{18}O record (Mayewski et al., 1994; Ruth et al., 2003; NGRIP, 2004; Rasmussen et al., 2014). Abrupt decreases in the dust concentration occur in 60 ± 21.2 (1σ) years on average, with a mean GI duration of 1079 ± 1135 (1σ) years when deter-

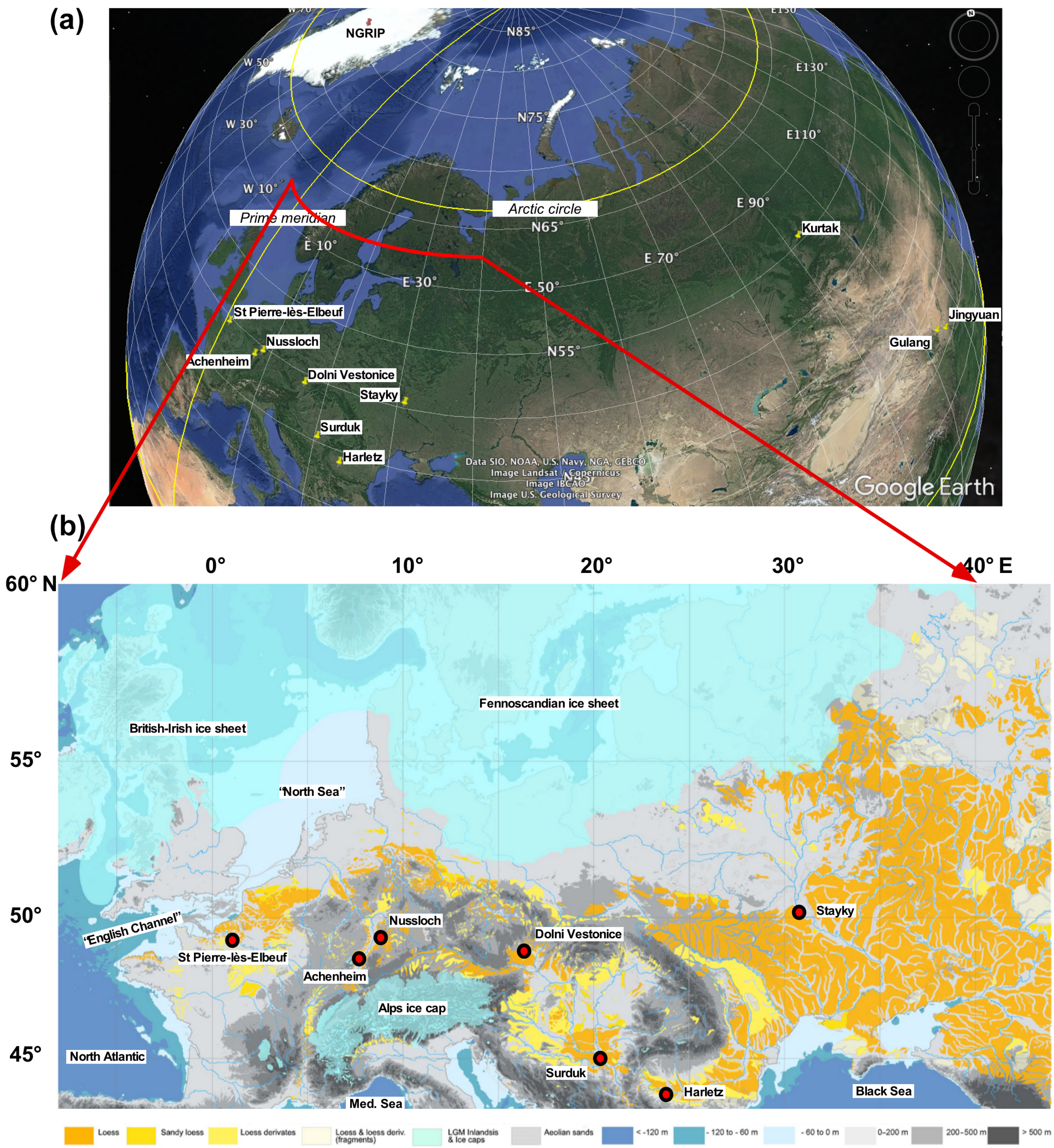

Figure 1. Studied records in this paper. **(a)** Location of the different records over Greenland and Eurasia. **(b)** Map of the European loess. Indication of the depth of the last glacial maximum sea level low stand and of the expansion of the Greenland, Iceland, British, and Fennoscandian ice sheets. Location of European key loess sequences. Map drawn by P. Antoine in Rousseau et al. (2014) modified.

Table 1. NGRIP ice-core record. Estimates of NGRIP GI start, end, and duration and GI abrupt transition start, end, and duration (from Rousseau et al., 2017). Temperature reconstruction for the GI transitions as published by Kindler et al. (2014). Panels **(a)** and **(b)** show NGRIP transition dates determined visually and algorithmically, respectively.

(a) GI	GI visually			Transition			Transition by Kindler	GI
	(a)	(b)	(c)	(d)	(e)	(f)		
No.	δ^{18}O start visual-rounded (yr b2k)	δ^{18}O end visual-rounded (yr b2k)	δ^{18}O duration visual-rounded (yr)	δ^{18}O start transition visual (yr b2k)	δ^{18}O end transition visual-(yr b2k)	δ^{18}O duration visual (yr)	Tp difference (°C) Fig. 3	No.
2	23 370	23 180	200	23 373	23 320	53	−8.5	2
3	27 800	27 470	330	27 795	27 758	37	−14.5	3
4	28 910	28 510	400	28 907	28 873	34	−12.5	4
5	32 520	32 030	500	32 517	32 458	59	−12.5	5
6	33 750	33 370	380	33 748	33 671	77	−9.5	6
7	35 490	34 640	850	35 491	35 431	60	−15.5	7
8	38 230	36 600	1640	38 234	38 189	45	−10	8
9	40 180	39 870	320	40 184	40 125	59	−6.5	9
10	41 480	40 780	700	41 480	41 424	56	−13.5	10
11	43360	42280	1090	43361	43312	49	−16.5	11
12	46 890	44 280	2610	46 893	46 802	91	−12.5	12
13	49 300	48 470	840	49 300	49 246	54	−8.5	13
14	54 230	50 030	4200	54 229	54 175	54	−12.5	14
15.1					0			15.1
15.2	55 830	55 400	430	55 827	55 747	80	−10	15.2
16.1					0			16.1
16.2	58 280	56 450	1830	58 277	58 235	42	−10	16.2
17.1	59 080	58 550	530	59 078	59 042	36	−12.5	17.1
Mean			1053.13			55.38	−11.59	Mean
SD			1068.43			16.12	2.74	SD
Max			4200.00			91.00	−6.50	Max
Min			200.00			34,00	−16.50	Min
	(aa)	(bb)	(cc)	(dd)	(ee)	(ffl)		
No.	Dust start visual-rounded (yr b2k)	Dust end visual-rounded (yr b2k)	Dust duration visual-rounded (yr)	Dust start transition visual (yr b2k)	Dust end transition visual-(yr b2k)	Dust duration visual (yr)	Tp difference (°C) Fig. 3	No.
2	23 370	23 190	180	23 366	23 308	58	−8.5	2
3	27 800	27 510	280	27 795	27 755	40	−14.5	3
4	28 910	28 530	390	28 911	28 881	30	−12.5	4
5	32 500	31 860	640	32 504	32 445	59	−12.5	5
6	33 750	33 310	430	33 746	33 677	69	−9.5	6
7	35 490	34 620	870	35 485	35 415	70	−15.5	7
8	38 220	36 540	1680	38 221	38 182	39	−10	8
9	40 180	39 900	290	40 184	40 075	109	−6.5	9
10	41 490	40 780	710	41 487	41 432	55	−13.5	10
11	43 360	42 200	1160	43 361	43 323	38	−16.5	11
12	46 870	44 190	2680	46 866	46 799	67	−12.5	12
13	49 300	48 420	880	49 300	49 243	57	−8.5	13
14	54 210	50 010	4200	54 214	54 160	54	−12.5	14
15.1								15.1
15.2	55 810	55 380	430	55 811	55 732	79	−10	15.2
16.1								16.1
16.2	58 290	56 380	1910	58 292	58 250	42	−10	16.2
17.1	59 070	58 540	530	59 068	59 026	42	−12.5	17.1
Mean			1078.75			56.75	−11.59	Mean
SD			1078.95			19.61	2.74	SD
Max			4200.00			109.00	−6.50	Max
Min			180.00			30.00	−16.50	Min

Table 1. Continued.

(b) GI	GI algorithmically			Transition			Transition by Kindler	GI
	(a)	(b)	(c)	(d)	(e)	(f)		
No.	$\delta^{18}O$ start algorithm-rounded (yr b2k)	$\delta^{18}O$ end algorithm-rounded (yr b2k)	$\delta^{18}O$ duration algorithm-rounded (yr)	$\delta^{18}O$ start transition algorithm- (yr b2k)	$\delta^{18}O$ end transition algorithm- (yr b2k)	GI $\delta^{18}O$ duration algorithm (yr)	Tp difference (°C) Fig. 3	No.
2	23 380	23 110	270	23 375	23 345	30	−8.5	2
3	27 790	27 460	330	27 790	27 765	25	−14.5	3
4	28 910	28 510	400	28 910	28 875	35	−12.5	4
5	32 520	32 030	500	32 520	32 490	30	−12.5	5
6	33 740	33 390	350	33 735	33 700	35	−9.5	6
7	35 510	34 730	780	35 505	35 440	65	−15.5	7
8	38 240	36 590	1650	38 235	38 200	35	−10	8
9	40 170	39 940	230	40 165	40 155	10	−6.5	9
10	41 480	40 790	690	41 480	41 440	40	−13.5	10
11	43 370	42 100	1270	43 365	43 315	50	−16.5	11
12	46 860	44 290	2580	46 860	46 830	30	−12.5	12
13	49 320	49 110	210	49 315	49 260	55	−8.5	13
14	54 240	49 410	4830	54 235	54 185	50	−12.5	14
15.1	55 010	54 750	260	55 005	54 975	30		15.1
15.2	55 820	55 300	520	55 815	55 765	50	−10	15.2
16.1	58 050	56 470	1590	58 050	58 020	30		16.1
16.2	58 280	56 440	1840	58 280	58 245	35	−10	16.2
17.1	59 080	58 520	570	59 080	59 060	20	−12.5	17.1
Mean			1048.33			36.39	−11.59	Mean
SD			1163.44			13.37	2.74	SD
Max			4830.00			65.00	−6.50	Max
Min			210.00			10.00	−16.50	Min
	(aa)	(bb)	(cc)	(dd)	(ee)	(ff)		
No.	Dust start algorithm-rounded (yr b2k)	Dust end algorithm-rounded (yr b2k)	Dust duration algorithm-rounded (yr)	Dust start transition algorithm- (yr b2k)	Dust end transition algorithm- (yr b2k)	GI Dust duration algorithm (yr)	Tp difference (°C) Fig. 3	No.
2	23 430	22 820	540	23 430	23 350	80	−8.5	2
3	27 800	27 520	250	27 795	27 770	25	−14.5	3
4	28 940	28 510	370	28 935	28 870	65	−12.5	4
5	32 570	31 780	680	32 565	32 450	115	−12.5	5
6	33 750	33 320	390	33 750	33 710	40	−9.5	6
7	35 500	34 620	830	35 500	35 445	55	−15.5	7
8	38 260	36 560	1640	38 255	38 195	60	−10	8
9	40 190	39 940	170	40 185	40 105	80	−6.5	9
10	41 490	40 800	640	41 490	41 440	50	−13.5	10
11	43 370	42 190	1120	43 365	43 310	55	−16.5	11
12	46 910	44 110	2720	46 910	46 825	85	−12.5	12
13	49 310	48 420	830	49 305	49 250	55	−8.5	13
14	54 240	49 480	4710	54 240	54 185	55	−12.5	14
15.1	55 050	54 770	220	55 045	54 985	60		15.1
15.2	55 790	55 390	370	55 790	55 755	35	−10	15.2
16.1	58 050	56 470	1550	58 050	58 015	35		16.1
16.2	58 310	56 360	1890	58 310	58 250	60	−10	16.2
17.1	59 110	58 530	510	59 110	59 040	70	−12.5	17.1
Mean			1079.44			60.00	−11.59	Mean
SD			1134.87			21.21	2.74	SD
Max			4710.00			115.00	−6.50	Max
Min			170.00			25.00	−16.50	Min

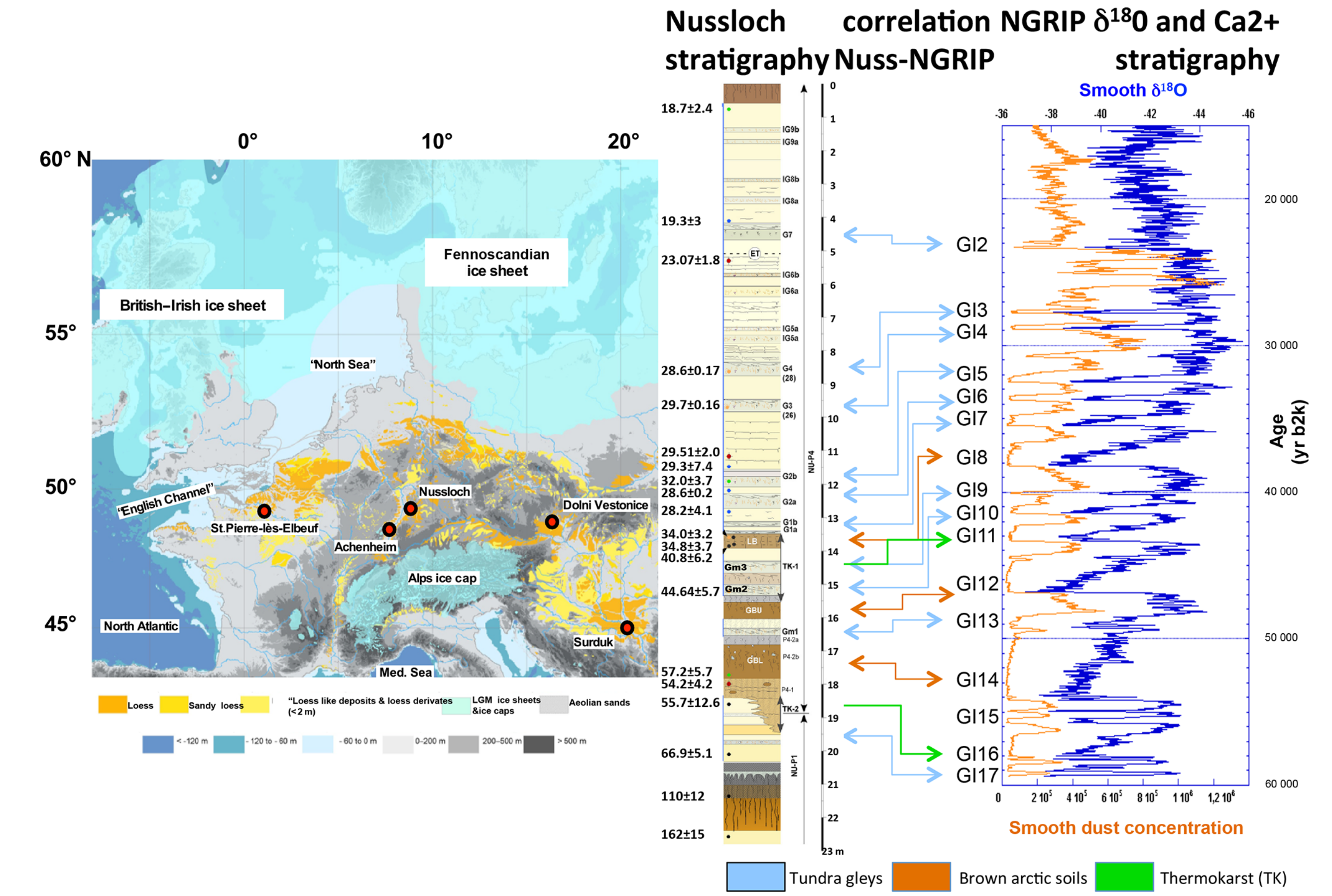

Figure 2. Stratigraphic correlations between Nussloch paleosols and NGRIP interstadials (GIs) (modified from Rousseau et al., 2017). Map as in Fig. 1. δ^{18}O (‰, in blue) and the dust concentration (part/µL, in brown) records in the NGRIP ice core over the interval between 60 ka and 15 ka b2k. Nussloch stratigraphic column from Antoine et al. (2016) modified.

mined with the same algorithm as for δ^{18}O; when determined visually, the dust decrease occurs in 56.8 ± 19.6 (1σ) years on average, with a mean duration of 1079 ± 1079 (1) years (Table 1). Interestingly, the dust change reaches its minimum value on average about 6 years after the δ^{18}O. These abrupt changes also correspond to abrupt temperature differences of on average 11.6 ± 2.7 (1σ) °C for the GIs 17.1 to 2 (Kindler et al., 2014; Table 1 in this paper). The amplitude of the change in the dust concentration corresponds on average to a factor of 6 in about 57 years. These values are different from previous investigations of the NGRIP dust record, which were showing much more rapid changes in a few years, but they seem more realistic than extremely abrupt shifts that would be particularly difficult to interpret from a dynamical point of view.

Isotope studies of the dust recorded in the Greenland ice cores demonstrated an Asian origin for both summer and winter seasons (Biscaye et al., 1997; Svensson et al., 2000), while the analysis of modern dust preserved in modern firn indicates a different origin for summer (essentially Taklimakan Desert) and winter (Taklimakan Desert and northern Chinese and Mongolian deserts) (Bory et al., 2002). The transport of the modern chemical aerosols towards Greenland also partly supports an Asian origin and therefore allows interpretation of the dust record in the ice cores (Goto-Azuma and Koerner, 2001). Indeed, the major dust event recorded in China on 6 April 2001, the largest ever recorded dust storm worldwide, provides relevant information about the Asian dust transport, past and present, towards Northern Hemisphere ice sheets. The identification of the dust particles related to this event on top of Mount Logan, Alaska, indicates that the assumption of Asian dust origin in the past is also particularly adequate (Zdanowicz et al., 2006). The presence of the large Laurentide ice sheet over North America at least at the last glacial maximum caused a split of the polar jet stream, inducing two main pathways for the Asian fine dust transport eastwards (Fig. 4). A comparison of the different GI dust records indicates that the dust concentration falls by a factor of 8 in about 60 years from the beginning of the warming during DO events. These values are similar to the variations of a factor of 5 to 7 during 4 decades observed during the 15.5–11.5 ka b2k interval (Steffensen et al., 2008).

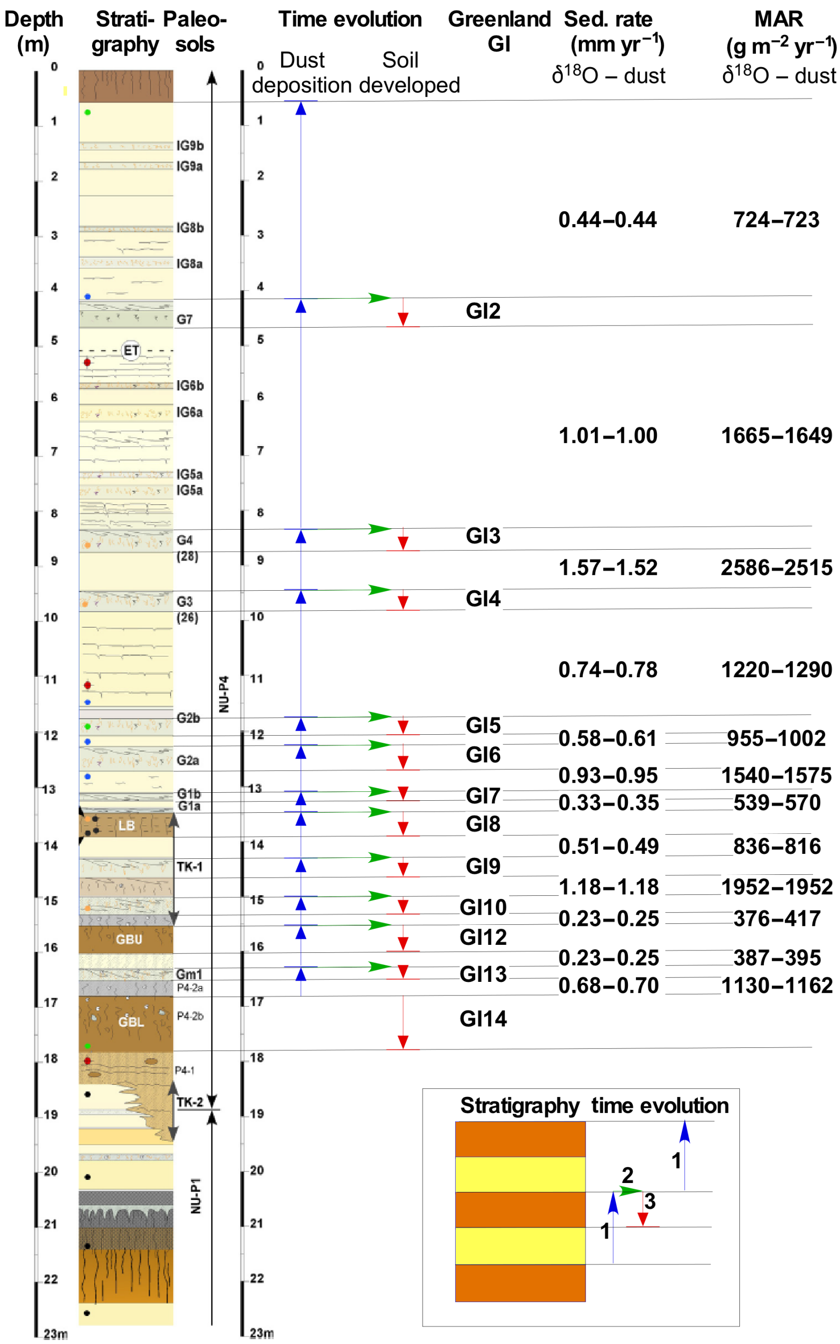

Figure 3. Nussloch stratigraphy with the identification of the loess and paleosol units as discussed in the text. Arrows indicate the direction of the evolution of the time during the dust depositions (in blue) and paleosol developments (in red). Sedimentation and mass accumulation (MAR) rates as estimated from NGRIP $\delta^{18}O$ and dust chronologies. The insert at the bottom of the figure explains how time should be read when considering European loess sequences. Nussloch stratigraphic column from Antoine et al. (2016) modified.

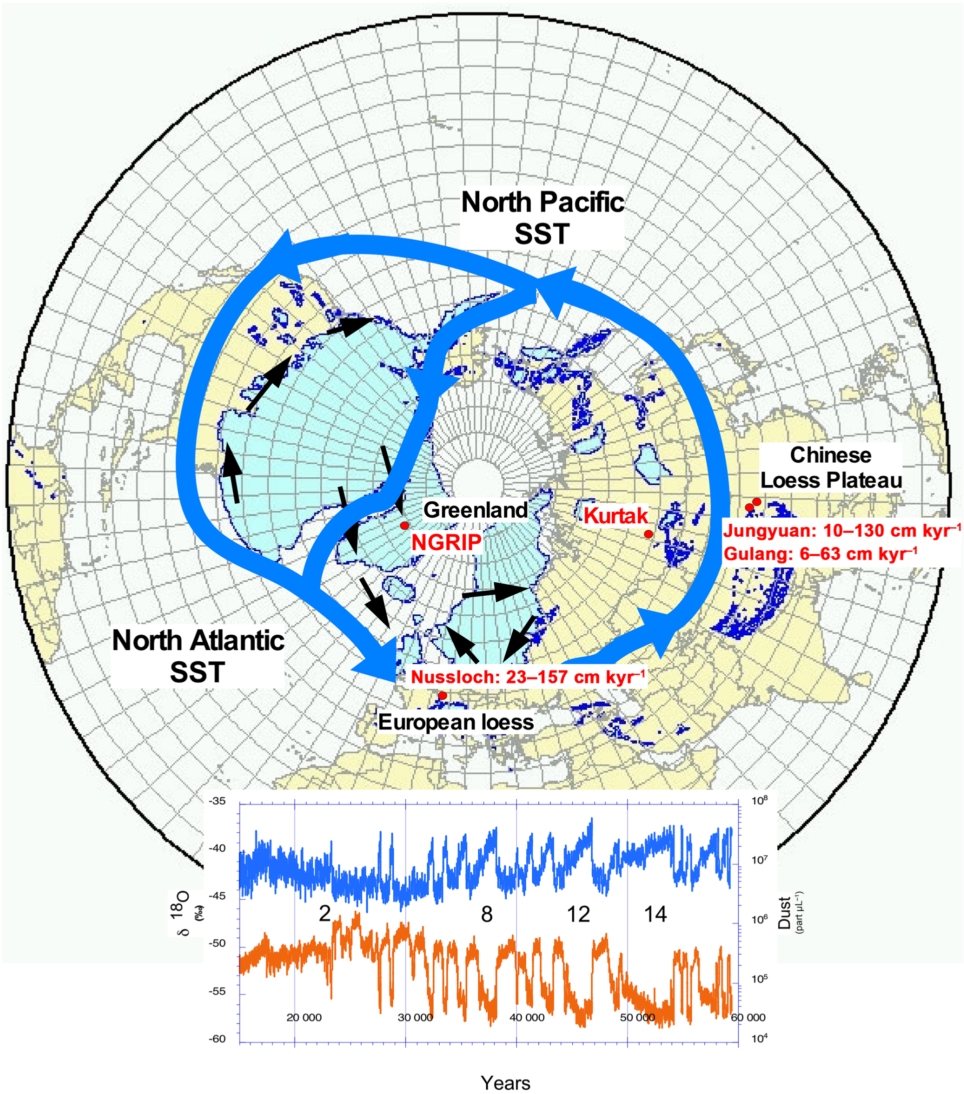

Figure 4. Map of the maximum extension of the last climate cycle ice sheets in northern Europe. Schematic location of the polar jet stream with location of regions or areas (in black) and of sites (in red) discussed in the text. $\delta^{18}O$ (‰, in blue) and the dust concentration (part/µL, in brown) records in the NGRIP ice core over the interval between 60 ka and 15 ka b2k. Dust concentrations are shown on a logarithmic scale. Map was compiled by Jürgen Ehlers available at http://www.qpg.geog.cam.ac.uk/lgmextent.html.

Reducing so drastically the dust concentration in the ice core implies a similar drastic reduction of the dust concentration in the atmosphere, relying on changes in the sources, in the transport, and/or in the deposition of the particles (Fischer et al., 2007).

Concerning the changes in the sources, several points can be taken into consideration. At present the amount of dust emitted from different Chinese deserts into the atmosphere occurs mostly in April, about 43.4 % of the 1451 Mt of dust emitted from 1996 to 2001 (Laurent et al., 2006). However, these sources do not behave similarly. While the average quantity of dust annually emitted is similar in the Gobi and Taklimakan deserts, the frequency of the dust storms is different, being more numerous in the Taklimakan than in the Gobi (Laurent et al., 2005). A reduction in the size of these sources does not seem to be a reliable cause, as these deserts did not vary much in the relevant past (Rittner et al., 2016). Therefore, a reduction in the availability of dust material should be sought by considering atmospheric circulation changes. Studying the electron spin resonance (ESR) intensity signal from marine core MD01-2407 from the Japan Sea, Nagashima et al. (2011) have shown that the Mongolian Gobi source was dominant during the GSs, while the Taklimakan Desert source was dominant during the GIs, with some variation between the interstadials. The analysis of Chinese speleothems from caves located southward of the Chinese Loess Plateau (CLP) indicates millennial-scale variations in the stalagmite growth, related to variations in pre-

Table 2. Nussloch loess sequence loess and paleosol units and their chronological equivalents (GSs and GIs) in the NGRIP ice-core record. Panels **(a)** and **(b)** show NGRIP transition dates determined visually and algorithmically, respectively.

(a) Eolian sedimentation (visually)	Paleosols	Thickness depth (m)	Age end ^{18}O (yr)	Age start ^{18}O (yr)	Duration ^{18}O (yr)	Sedimentation rate ^{18}O (mm yr^{-1})	Age end dust (yr)	Age start dust (yr)	Duration dust (yr)	Sedimentation rate (mm yr^{-1})	MAR ^{18}O (g m^{-2} yr^{-1})	MAR dust (g m^{-2} yr^{-1})	Sed rate ^{18}O cm kyr^{-1}	Sed rate dust cm kyr^{-1}
Top seq. – Top G7 (GI2)		3.59	15 000	23 180	8180	0.44	15 000	23 190	8190	0.44	724	723	43.87	43.82
	G7 (GI2)	0.51	23 180	23 370	190		23 190	23 370	180					
Top G7 – Top G4 (GI3)		4.14	23 370	27 470	4100	1.01	23 370	27 510	4140	1.00	1665	1649	100.90	99.93
	G4 (GI3)	0.41	27 470	27 800	330		27 510	27 800	290					
Top G4 – Top G3 (GI4)		1.11	27 800	28 510	710	1.57	27 800	28 530	730	1.52	2586	2515	156.75	152.45
	G3 (GI4)	0.39	28 510	28 910	400		28 530	28 910	380					
Top G3 – Top G2b (GI5)		2.31	28 910	32 030	3120	0.74	28 910	31 860	2950	0.78	1220	1290	73.92	78.18
	G2b (GI5)	0.29	32 030	32 520	490		31 860	32 500	640					
Top G2b – Top G2a (GI6)		0.49	32 520	33 370	850	0.58	32 500	33 310	810	0.61	955	1002	57.87	60.73
	G2a (GI6)	0.44	33 370	33 750	380		33 310	33 750	440					
Top G2a – Top G1b (GI7)		0.83	33 750	34 640	890	0.93	33 750	34 620	870	0.95	1540	1575	93.33	95.48
	G1b (G7)	0.15	34 640	35 490	850		34 620	35 490	870					
Top G1b – Top LB (GI8)		0.36	35 490	36 600	1110	0.33	35 490	36 540	1050	0.35	539	570	32.69	34.56
	LB (GI8)	0.45	36 600	38 230	1630		36 540	38 220	1680					
Top LB – Top Gm3 (GI9)		0.83	38 230	39 870	1640	0.51	38 220	39 900	1680	0.49	836	816	50.65	49.44
	Gm3 (GI9)	0.35	39 870	40 180	310		39 900	40 180	280					
Top Gm3 – Top Gm2 (GI10)		0.71	40 180	40 780	600	1.18	40 180	40 780	600	1.18	1952	1952	118.28	118.28
	Gm2 (GI10)	0.30	40 780	41 480	700		40 780	41 490	710					
?			41 480	42 280	800		41 490	42 200	710					
	TK1 (GI11)		42 280	43 360	1080		42 200	43 360	1160					
UnitX – Top GBU (GI12)		0.21	43 360	44 280	920	0.23	43 360	44 190	830	0.25	376	417	22.79	25.26
	GBU (GI12)	0.51	44 280	46 890	2610		44 190	46 870	2680					
Top GBU – Top Gm1 (GI13)		0.37	46 890	48 470	1580	0.23	46 870	48 420	1550	0.24	387	395	23.48	23.93
	Gm1 (GI13)	0.22	48 470	49 300	830		48 420	49 300	880					
Top Gm1-Top GBL (GI14)		0.50	49 300	50 030	730	0.68	49 300	50 010	710	0.70	1130	1162	68.49	70.42
	GBL (GI14)	1.02	50 030	54 230	4200		50 010	54 210	4200					
Mean					1508.85	0.70			1508.08	0.71	1159	1172	70.25	71.04
SD					1744.06	0.41			1744.54	0.40	674	654	40.86	39.66
Max					8180.00	1.57			8190.00	1.52	2586	2515	156.75	152.45
Min					190.00	0.23			180.00	0.24	376	395	22.79	23.93

Table 2. Continued.

(b) Eolian sedimentation (Algorithmically)	Paleosols	Thickness depth (m)	Age end ^{18}O (yr)	Age start ^{18}O (yr)	Duration ^{18}O (yr)	Sedimentation rate (mm yr^{-1})	Age end dust (yr)	Age start dust (yr)	Duration dust (yr)	Sedimentation rate (mm yr^{-1})	MAR ^{18}O (g m^{-2} yr^{-1})	MAR dust (g m^{-2} yr^{-1})	Sed rate ^{18}O cm kyr^{-1}	Sed rate dust
Top seq. – Top G7 (GI2)		3.59	15 000	23 310	8310	0.43	15 000	22 820	7820	0.46	713	757	43.19	45.89
	G7 (GI2)	0.51	23 310	23 380	70		22 820	23 430	610					
Top G7 – Top G4 (GI3)		4.14	23 380	27 460	4080	1.01	23 430	27 520	4090	1.01	1673	1669	101.40	101.15
	G4 (GI3)	0.41	27 460	27 790	330		27 520	27 800	280					
Top G4 – Top G3 (GI4)		1.11	27 790	28 150	360	3.09	27 800	28 510	710	1.57	5101	2586	309.14	156.75
	G3 (GI4)	0.39	28 150	28 910	760		28 510	28 940	430					
Top G3 – Top G2b (GI5)		2.31	28 910	32 030	3120	0.74	28 940	31 780	2840	0.81	1220	1340	73.92	81.21
	G2b (GI5)	0.29	32 030	32 520	490		31 780	32 570	790					
Top G2b – Top G2a (GI6)		0.49	32 520	33 390	870	0.57	32 570	33 320	750	0.66	933	1082	56.54	65.59
	G2a (GI6)	0.44	33 390	33 740	350		33 320	33 750	430					
Top G2a – Top G1b (GI7)		0.83	33 740	34 730	990	0.84	33 750	34 620	870	0.95	1384	1575	83.90	95.48
	G1b (G7)	0.15	34 730	35 510	780		34 620	35 500	880					
Top G1b – Top LB (GI8)		0.36	35 510	36 590	1080	0.34	35 500	36 560	1060	0.34	554	565	33.60	34.24
	LB (GI8)	0.45	36 590	38 240	1650		36 560	38 260	1700					
Top LB – Top Gm3 (GI9)		0.83	38 240	39 940	1700	0.49	38 260	39 940	1680	0.49	806	816	48.86	49.44
	Gm3 (GI9)	0.35	39 940	40 170	230		39 940	40 190	250					
Top Gm3 – Top Gm2 (GI10)		0.71	40 170	40 790	620	1.14	40 190	40 800	610	1.16	1889	1920	114.46	116.34
	Gm2 (GI10)	0.30	40 790	41 480	690		40 800	41 490	690					
?			41 480	42 100	620		41 490	42 190	700					
	TK1 (GI11)		42 100	43 370	1270		42 190	43 370	1180					
UnitX – Top GBU (GI12)		0.21	43 370	44 290	920	0.23	43 370	44 110	740	0.28	376	468	22.79	28.33
	GBU (GI12)	0.51	44 290	46 860	2570		44 110	46 910	2800					
Top GBU – Top Gm1 (GI13)		0.37	46 860	49 110	2250	0.16	46 910	48 420	1510	0.25	272	405	16.49	24.57
	Gm1 (GI13)	0.22	49 110	49 320	210		48 420	49 310	890					
Top Gm1 – Top GBL (GI14)		0.50	49 320	49 410	90	5.56	49 310	49 480	170	2.94	9167	4853	555.56	294.12
	GBL (GI14)	1.02	49 410	54 240	4830		49 480	54 240	4760					
Mean					1509.23	1.22			1509.23	0.91	2007	1503	121.65	91.09
SD					1847.47	1.57			1726.75	0.75	2594	1243	157.21	75.32
Max					8310.00	5.56			7820.00	2.94	9167	4853	555.56	294.12
Min					70.00	0.16			170.00	0.25	272	405	16.49	24.57

cipitation over the cave area linked to stronger summer monsoon activity, which are synchronous to the GIs (Wang et al., 2001, 2008). From two key Chinese loess sequences, Sun et al. (2012) have described abrupt millennial-scale changes expressed by detailed synchronous mean grain size variations over the 60–10 ka b2k interval in deposited wind blown material, from coarser material during the GSs to thinner particles during the GIs. The sedimentation rate estimated from the key sequences of Jingyuan and Gulang varies between 6 and 63 cm kyr^{-1} for Jingyuan and between 10 and 130 cm kyr^{-1} for Gulang (Fig. 4). Therefore, as meridional circulation prevailed at least in eastern Asia due to the monsoonal system, aridity could have been reduced during the favorable season (around April, with some variation and delay, depending on the GSs or Heinrich stadials (HS) as observed in eastern Europe by Sima et al., 2013) of dust emission of these short intervals (Sun et al., 2012). A recent study of the decline of the snow cover over northeastern Russia, southwestern Asia, northern India, and the Tibetan Plateau reports that the snow cover decline creates favorable dynamical conditions for strong winds over the Arabian Sea and thus favoring a stronger summer monsoon (Goes et al., 2005). Complementarily, a modeling experiment indicates that a strong East Asian monsoon could be related to planetary waves related to the extension of the Northern Hemisphere ice sheets, affecting the precipitation band at the latitude of the CLP (Yin et al., 2008). However, as the main interval for dust emission is April, one can hardly assume that the summer monsoon is the main driver of a reduction in dust emissions. On the contrary, modern East Asian dust storms are related to surges of cold air originating from Siberia, and such conditions should have been reduced during the GI compared to the GSs at least during April, the main dust emission season. Reduced cold outbreaks could have resulted from the reduction of the snow cover due to warming Eurasia and to a negative feedback related to dust deposition on snow as deduced from another modeling experiment (Krinner et al., 2006).

Europe has been strongly impacted by these North Atlantic millennial-scale climate changes, as observed in different types of deposits (Genty et al., 2003; Müller et al., 2003; Rousseau et al., 2002, 2007b) (Fig. 1). The influence of the westerlies and the position of the polar jet stream were constrained by the variation in the extension of the sea ice during the last glacial interval (Sima et al., 2009, 2013). Furthermore, the presence of ice sheets over Great Britain and Scandinavia, and an ice cap over the Alps enhanced the zonal circulation that reflects the location of the thickest loess deposits (Fig. 1b). Extensive investigation of European loess series along a west-to-east transect at 50° N (Fig. 1b) reveals that the millennial-scale climate variations observed in the North Atlantic are preserved in these particular eolian deposits (2009; Antoine et al., 2001; Rousseau et al., 2002, 2007b). They clearly show alternating loess and paleosol units, which are continental equivalents, respectively, of the GS and GIs (Moine et al., 2017; Rousseau et al., 2017) (Figs. 2, 3). The Nussloch loess sequence along the Rhine Valley is the most detailed record for the interval of 50 to 15 ka b2k. The nature of the observed paleosols is related to the duration of the corresponding GIs themselves (Rousseau et al., 2017): GI8, the longest of the last eight GIs, is represented in Nussloch by a brown arctic soil, while the youngest GIs correspond to tundra gleys or embryonic soils (oxidized horizons) for GI3 and GI2, which are particularly short (Antoine et al., 2009; Rousseau et al., 2002, 2007b) (Figs. 2, 3). An estimate of the duration of the continental equivalent of the GIs can be deduced from the Greenland dust record by considering the interval after the abrupt warming, when the dust concentration was at a minimum in the atmosphere and therefore shows low values in the Greenland ice cores. Such succession is observed over an area more than 2000 km wide from western Europe eastward to Ukraine during the last climatic cycle (Rousseau et al., 2011), showing the influence of the zonal circulation, as it is the case in modern time (Fig. 5a, b). In the Nussloch key sequence, the sedimentation rate of dust particles varies between 23 and 157 cm kyr^{-1} for the loess units synchronous to the GSs. These values are similar to those observed at the northern edge of the CLP by Sun et al. (2012) (Table 2, Figs. 1a, 4), supporting an apparently similar eolian characteristic within more global dynamics. Furthermore, modeling experiments show that dust emission mainly occurred in April (Sima et al., 2009) similar to modern deserts, although the European sources are not deserts at all presently. These modeling studies also indicate that the zonal circulation not only prevailed during the GI intervals but also during the GSs as recorded by loess deposits. For the coarsest material these eolian units are composed of material of local and regional (up to about 500 km) origin, mainly from dried river beds (Rousseau et al., 2014). The finest grains originate from longer distances, but still from deflation areas, mostly located in the emerged English Channel, North Sea, or northern European plain, and at the margin of the Fennoscandian frontal moraines (Sima et al., 2009; Rousseau et al., 2014) (Fig. 1b). Since we observe in Kurtak, Siberia (Figs. 1a, 4) synchronous alternations between eolian loess units and paleosols similar to those observed over Europe (Haesaerts et al., 2005), we infer that a zonal circulation similar to the present one (Fig. 5) prevailed over Eurasia during both the GSs and GIs, synchronizing the loess–paleosol sequences between Europe and Asia (Haesaerts et al., 2005). The initial warming over Greenland and the North Atlantic is transported eastward by the prevailing zonal circulation. As explained above, this propagating warming should have reduced the production of cold surges contributing to the strong atmospheric dynamics (Sun et al., 2012) responsible for the dust emission in northern Chinese deserts, which are the main dust suppliers of both the CLP and Greenland ice sheet. The stronger winds during the GSs and weaker winds during the GIs permitted the record of DO-like intervals in Chinese loess sequences through grain size variations with

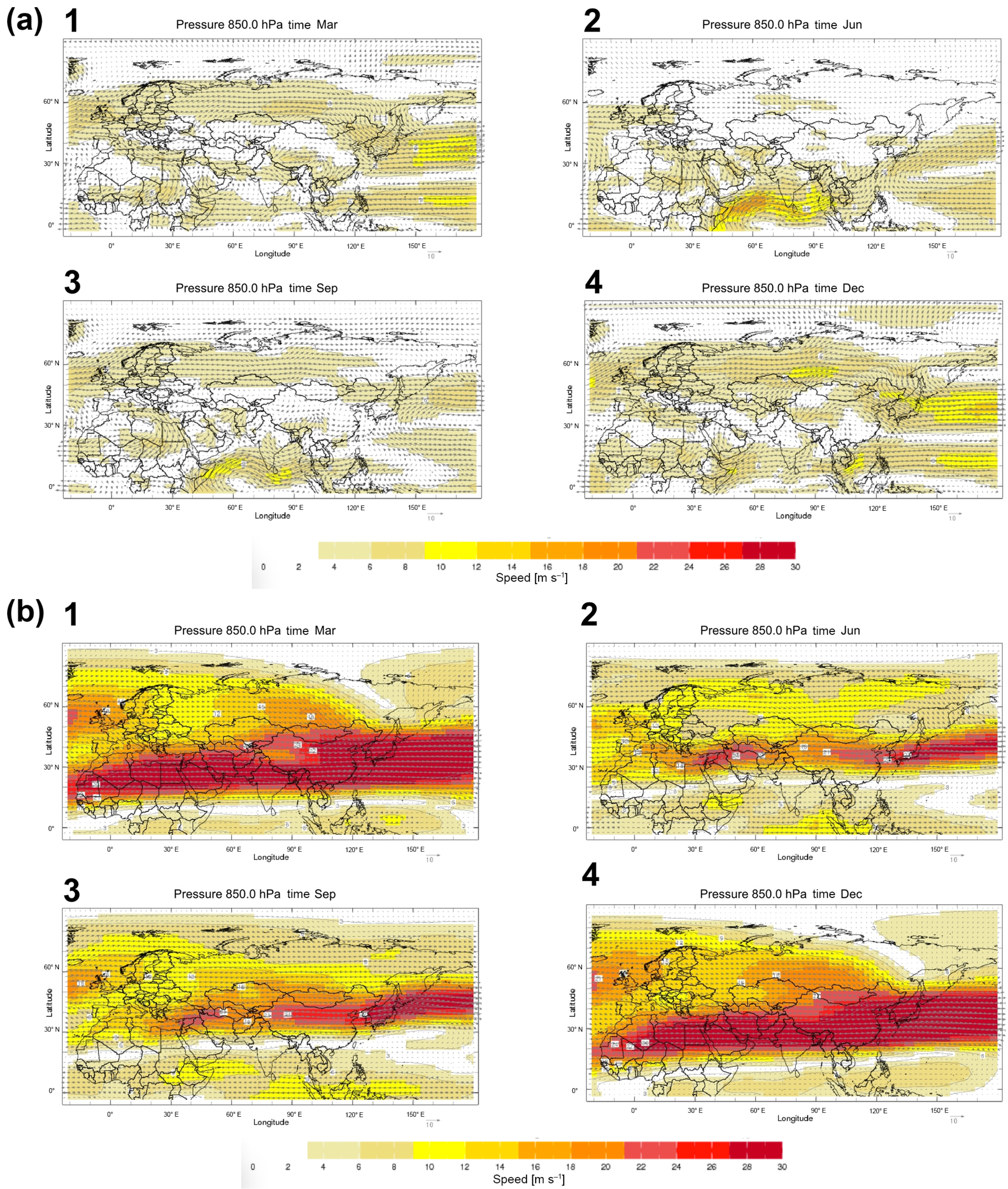

Figure 5. Impact of Atlantic climate conditions over Eurasia. Modern monthly average wind speed ($\mathrm{m\,s^{-1}}$) at 850 hPa **(a)** and at 300 hPa **(b)** pressure levels for March, June, September, December, and April (main dust emission month) over Eurasia. Wind vectors are plotted over shading and contours at $3\,\mathrm{m\,s^{-1}}$ intervals. Data source: NCEP reanalysis monthly wind components on a $2.5° \times 2.5°$ long and lat grid for the interval 1971–2000.

coarser material deposition during the GSs and finer during the GIs (Sun et al., 2012).

All the mechanisms described above involve the Northern Hemisphere and do not address the origin of these abrupt changes. Recent investigations in West Antarctic Ice Sheet Divide (WAIS) ice core (Buizert et al., 2015) have demonstrated the north-to-south-directed transfer of the abrupt changes with Greenland warmings leading Antarctic coolings; the associated heat transfer is argued to be modulated by the Atlantic Meridional Overturning Circulation rather than by the atmosphere (Henry et al., 2016). Although the origin of the DO events is not yet elucidated, the North Atlantic changes still remain the drivers of those observed over Eurasia. Indeed, the modern cyclonic pattern of moisture transport towards the Greenland ice sheet (Masson-Delmotte et al., 2006) depends on the sea surface conditions over the North Atlantic Ocean and clear pathways of this transport have been identified (Chen et al., 1997). During the last climate cycle, this pattern was related to both the sea ice extent and the size and expansion of the Laurentide ice sheet in North America, which impacts the Northern Hemisphere atmospheric circulation (Kutzbach, 1987). The large changes in deuterium excess at the onset of the warming reveal large variations in the moisture source regions. These variations are most likely associated with changes in sea ice extent, which shift the source regions, combined with changes in atmospheric circulation patterns (Masson-Delmotte et al., 2006; Sodemann and Zubler, 2010; Sodemann et al., 2008). Due to the changing albedo, sea ice extent itself directly impacts the atmospheric circulation. Conversely, sea ice is mainly driven by the meridional overturning oscillation, which would have thus induced the observed δ^{18}O and hence temperature changes noticed in the Greenland ice cores (Henry et al., 2016). In turn, this would have also impacted the Northern Hemisphere atmospheric circulation, contributing to the abrupt millennial-scale changes, including the DO events in Eurasian terrestrial records. At middle latitude these changes constrained the emission of local and regional dust particles, their transport, and their deposition in the loess sequences, which can be characterized by similar sedimentation rates over the area corresponding to a general climate dynamics, but nevertheless different mass accumulation rates (MARs) related to the bedrock of the source areas of the deposited material. In a previous study, Kohfeld and Harrison (2003) estimated MARs over CLP varying between 21 and 809 g m^{-2} yr^{-1} for MIS 3 and between 60 and 5238 g m^{-2} yr^{-1} for MIS 2. In Europe, Frechen et al. (2003), applying the same method, indicate MARs varying between 100 and 7000 g m^{-2} yr^{-1}, with particularly high values for Nussloch (1213–6129 g m^{-2} yr^{-1}). These estimates are higher than those determined in our study after reevaluation of the chronology of the key sequence, still following the same calculation, which yields varying MAR values between 376 and 2586 g m^{-2} yr^{-1} (376–1952 g m^{-2} yr^{-1} for MIS3 and 724–2586 g m^{-2} yr^{-1} for MIS2) or between 395 and 2515 g m^{-2} yr^{-1} (395–1952 g m^{-2} yr^{-1} for MIS3 and 723–2515 g m^{-2} yr^{-1} for MIS2) when considering the δ^{18}O- and dust-related NGRIP chronologies, respectively (Table 2). Still, as Nussloch represents an exceptional record of MIS 3 and 2, we consider our results as corresponding to the highest boundary values for this time interval in European deposits.

4 Conclusion

Our study thus shows that a strong emphasis has to be placed on the past dust record, which is still poorly understood and weakly integrated into general circulation models. The important uncertainties associated with mineral aerosols in the recent IPCC report (Solomon et al., 2007) are a clear indication that more must be done on this particular parameter. Because this is a key factor in the climate system, understanding the past dust cycle is an important requirement, especially when estimating the dust load in the past atmospheres, and this should open new fields of investigation for a better constraint of the climate variability in different contexts.

The present study provides new insights into the analysis of the millennial-scale variability and of abrupt climate changes by proposing the links by gathering atmospheric, marine, and continental records. It shows that the complete understanding of the whole climate system requires investigations at high resolution in every domain with the support of modeling experiments. In the present study, we show that both δ^{18}O increase and dust decrease take place over an interval of about 50 years on average from the start of the abrupt change. This corresponds to the 4 decades previously mentioned for the two warmings occurring during the 15.5–11.5 ka b2k interval, which are associated with strong resumptions of the meridional overturning circulation (McManus et al., 2004). This makes the potential change in the atmospheric dynamics more reliable. Our investigation provided an explanation of the record of the abrupt climate changes in the Northern Hemisphere dust records, both in the Greenland ice sheet and over Eurasia. It shows that dust should be considered one of the major players in the past millennial climate variability.

Data availability. The data sets used in this study are available at http://www.icecores.dk.

The Supplement related to this article is available online at https://doi.org/10.5194/cp-13-1181-2017-supplement.

Author contributions. DDR designed the research. DDR, SJJ, AS, MB, AS, and JPS performed the research. SJJ, AS, MB, and JPS performed drilling and analysis of NGRIP ice cores. AS performed the modeling experiment. DDR designed and performed the loess sequences investigation. DDR performed the new Nussloch chronological sequence and calculated the associated sedimentation rates and MARs. NB performed the algorithmic determination of the DO events in both δ^{18}O and dust NGRIP records. DDR, NB, and AS wrote the paper.

Competing interests. The authors declare that they have no conflict of interest.

Acknowledgements. Denis-Didier Rousseau and Anders Svensson are partly supported by ANR Research grant (ACTES: ANR08-BLAN-0227 – CSD 6). Anders Svensson, Matthias Bigler and Jorgen Peder Steffensen are supported by NGRIP. NGRIP is directed and organized by the Ice and Climate research group, Niels Bohr Institute, University of Copenhagen. It is supported by funding agencies in Denmark (FNU), Belgium (FNRS-CFB), France (IPEV and INSU/CNRS), Germany (AWI), Iceland. (RannIs), Japan (MEXT), Sweden (SPRS), Switzerland (SNF) and the USA (NSF, Office of Polar Programs). Niklas Boers acknowledges funding by the Alexander von Humboldt Foundation and the German Federal Ministry for Education and Research. This work started thanks to the support of our dear colleague and friend Sigfus Johnsen to who it is dedicated. Eric Wolff and Jerry McManus are thanked for providing useful comments on drafts of that paper which strongly improved it. CNRS-INSU rejected a support request to DDR for the completion of this study because of the lack of innovation and interest, but hopefully thoughts remain free.

Edited by: Zhengtang Guo
Reviewed by: two anonymous referees

References

Antoine, P., Rousseau, D. D., Zöller, L., Lang, A., Munaut, A. V., Hatté, C., and Fontugne, M.: High-resolution record of the last interglacial-glacial cycle in the loess palaeosol sequences of Nussloch (Rhine Valley-Germany), Quaternary Int., 76/77, 211–229, https://doi.org/10.1016/S1040-6182(00)00104-X, 2001.

Antoine, P., Rousseau, D.D., Moine, O., Kunesch, S., Hatte, C., Lang, A., Tissoux, H., and Zöller, L.: Rapid and cyclic aeolian deposition during the Last Glacial in European loess: a high-resolution record from Nussloch, Germany, Quaternary Sci. Rev. 28, 2955–2973, https://doi.org/10.1016/j.quascirev.2009.08.001, 2009.

Antoine, P., Coutard, S., Guerin, G., Deschodt, L., Goval, E., Locht, J. L., and Paris, C.: Upper Pleistocene loess-palaeosol records from Northern France in the European context: Environmental background and dating of the Middle Palaeolithic, Quaternary Int., 411, 4–24, https://doi.org/10.1016/j.quaint.2015.11.036, 2016.

Barbante, C., Barnola, J. M., Becagli, S., Beer, J., Bigler, M., Boutron, C., Blunier, T., Castellano, E., Cattani, O., Chappellaz, J., Dahl-Jensen, D., Debret, M., Delmonte, B., Dick, D., Falourd, S., Faria, S., Federer, U., Fischer, H., Freitag, J., Frenzel, A., Fritzsche, D., Fundel, F., Gabrielli, P., Gaspari, V., Gersonde, R., Graf, W., Grigoriev, D., Hamann, I., Hansson, M., Hoffmann, G., Hutterli, M. A., Huybrechts, P., Isaksson, E., Johnsen, S., Jouzel, J., Kaczmarska, M., Karlin, T., Kaufmann, P., Kipfstuhl, S., Kohno, M., Lambert, F., Lambrecht, A., Lambrecht, A., Landais, A., Lawer, G., Leuenberger, M., Littot, G., Loulergue, L., Luthi, D., Maggi, V., Marino, F., Masson-Delmotte, V., Meyer, H., Miller, H., Mulvaney, R., Narcisi, B., Oerlemans, J., Oerter, H., Parrenin, F., Petit, J. R., Raisbeck, G., Raynaud, D., Rothlisberger, R., Ruth, U., Rybak, O., Severi, M., Schmitt, J., Schwander, J., Siegenthaler, U., Siggaard-Andersen, M. L., Spahni, R., Steffensen, J. P., Stenni, B., Stocker, T. F., Tison, J. L., Traversi, R., Udisti, R., Valero-Delgado, F., van den Broeke, M. R., van de Wal, R. S. W., Wagenbach, D., Wegner, A., Weiler, K., Wilhelms, F., Winther, J. G., Wolff, E., and Members, E. C.: One-to-one coupling of glacial climate variability in Greenland and Antarctica, Nature, 444, 195–198, https://doi.org/10.1038/nature05301, 2006.

Biscaye, P. E., Grousset, F. E., Revel, M., Van der Gaast, S., Zielinski, G. A., Vaars, A., and Kukla, G.: Asian provenance of glacial dust (Stage 2) in the GISP2 ice core, summit, Greenland, J. Geophys. Res., 102, 26765–26781, https://doi.org/10.1029/97JC01249, 1997.

Boers, N., Chekroun, M. D., Liu, H., Kondrashov, D., Rousseau, D.-D., Svensson, A., Bigler, M., and Ghil, M.: Inverse stochastic-dynamic models for high-resolution Greenland ice-core records, Earth Syst. Dynam. Discuss., https://doi.org/10.5194/esd-2017-8, in review, 2017.

Bory, A. J. M., Biscaye, P. E., Svensson, A., and Grousset, F. E.: Seasonal variability in the origin of recent atmospheric mineral dust at NorthGRIP, Greenland, Earth Planet. Sc. Lett., 196, 123–134, https://doi.org/10.1016/S0012-821X(01)00609-4, 2002.

Broecker, W., Bond, G., and Klas, M.: A salt oscillator in the glacial Atlantic? 1. The concept, Paleoceanography, 5, 469–477, https://doi.org/10.1029/PA005i004p00469, 1990.

Buizert, C., Adrian, B., Ahn, J., Albert, M., Alley, R. B., Baggenstos, D., Bauska, T. K., Bay, R. C., Bencivengo, B. B., Bentley, C. R., Brook, E. J., Chellman, N. J., Clow, G. D., Cole-Dai, J., Conway, H., Cravens, E., Cuffey, K. M., Dunbar, N. W., Edwards, J. S., Fegyveresi, J. M., Ferris, D. G., Fitzpatrick, J. J., Fudge, T. J., Gibson, C. J., Gkinis, V., Goetz, J. J., Gregory, S., Hargreaves, G. M., Iverson, N., Johnson, J. A., Jones, T. R., Kalk, M. L., Kippenhan, M. J., Koffman, B. G., Kreutz, K., Kuhl, T. W., Lebar, D. A., Lee, J. E., Marcott, S. A., Markle, B. R., Maselli, O. J., McConnell, J. R., McGwire, K. C., Mitchell, L. E., Mortensen, N. B., Neff, P. D., Nishiizumi, K., Nunn, R. M., Orsi, A. J., Pasteris, D. R., Pedro, J. B., Pettit, E. C., Price, P. B., Priscu, J. C., Rhodes, R. H., Rosen, J. L., Schauer, A. J., Schoenemann, S. W., Sendelbach, P. J., Severinghaus, J. P., Shturmakov, A. J., Sigl, M., Slawny, K. R., Souney, J. M., Sowers, T. A., Spencer, M. K., Steig, E. J., Taylor, K. C., Twickler, M. S., Vaughn, B. H., Voigt, D. E., Waddington, E. D., Welten, K. C., Wendricks, A. W., White, J. W. C., Winstrup, M., Wong, G. J., Woodruff, T. E., and Members, W. D. P.: Precise interpolar phasing of abrupt climate change during the last ice age, Nature, 520, 661–665, https://doi.org/10.1038/nature14401, 2015.

Capron, E., Landais, A., Chappellaz, J., Schilt, A., Buiron, D., Dahl-Jensen, D., Johnsen, S. J., Jouzel, J., Lemieux-Dudon, B., Loulergue, L., Leuenberger, M., Masson-Delmotte, V., Meyer, H., Oerter, H., and Stenni, B.: Millennial and sub-millennial scale climatic variations recorded in polar ice cores over the last glacial period, Clim. Past, 6, 345–365, https://doi.org/10.5194/cp-6-345-2010, 2010.

Chen, Q. S., Bromwich, D. H., and Bai, L. S.: Precipitation over Greenland retrieved by a dynamic method and its relation to cyclonic activity, J. Climate, 10, 839–870, https://doi.org/10.1175/1520-0442(1997)010<0839:POGRBA>2.0.CO;2, 1997.

Dansgaard, W., Johnsen, S. J., Moller, J., and Langway, C. C.: One thousand centuries of climatic record from Camp Century on the Greenland ice sheet, Science, 166, 377–381, https://doi.org/10.1126/science.166.3903.377, 1969.

Dansgaard, W., Clausen, H. B., Gundestrup, N., Hammer, C. U., Johnsen, S. F., Kristinsdottir, P. M., and Reeh, N.: A new Greenland deep ice core, Science, 218, 1273–1277, https://doi.org/10.1126/science.218.4579.1273, 1982.

Ditlevsen, P. D., Andersen, K. K., and Svensson, A.: The DO-climate events are probably noise induced: statistical investigation of the claimed 1470 years cycle, Clim. Past, 3, 129–134, https://doi.org/10.5194/cp-3-129-2007, 2007.

Fischer, H., Siggaard-Andersen, M.-L., Ruth, U., Rothlisberger, R., and Wolff, E.: Glacial/interglacial changes in mineral dust and sea-salt records in polar ice cores: Sources, transport, and deposition, Rev. Geophys., 45, https://doi.org/10.1029/2005RG000192, 2007.

Frechen, M., Oches, E. A., and Kohfeld, K. E.: Loess in Europe-mass accumulation rates during the Last Glacial Period, Quaternary Sci. Rev., 22, 1835–1857, https://doi.org/10.1016/S0277-3791(03)00183-5, 2003.

Genty, D., Blamart, D., Ouahdi, R., Gilmour, M., Baker, A., Jouzel, J., and Van-Exter, S.: Precise dating of Dansgaard-Oeschger climate oscillations in western Europe from stalagmite data, Nature, 421, 833–837, https://doi.org/10.1038/nature01391, 2003.

Gkinis, V., Simonsen, S. B., Buchardt, S. L., White, J. W. C., and Vinther, B. M.: Water isotope diffusion rates from the NorthGRIP ice core for the last 16,000 years – Glaciological and paleoclimatic implications, Earth Planet. Sc. Lett., 405, 132–141, https://doi.org/10.1016/j.epsl.2014.08.022, 2014.

Goes, J. I., Thoppil, P. G., Gomes, H. D., and Fasullo, J. T.: Warming of the Eurasian landmass is making the Arabian Sea more productive, Science, 308, 545–547, https://doi.org/10.1126/science.1106610, 2005.

Goto-Azuma, K. and Koerner, R. M.: Ice core studies of anthropogenic sulfate and nitrate trends in the Arctic, J. Geophys. Res., 106, 4959–4969, https://doi.org/10.1029/2000JD900635, 2001.

Haesaerts, P., Chekha, V. P., Damblon, F., Drozdov, N. I., Orlova, L. A., and Van der Plicht, J.: The loess-palaeosol succession of Kurtak (Yenisei Basin, Siberia): a reference record for the Karga stage (MIS 3), Quaternaire, 16, 3–24, 2005.

Henry, L. G., McManus, J. F., Curry, W. B., Roberts, N. L., Piotrowski, A. M., and Keigwin, L. D.: North Atlantic ocean circulation and abrupt climate change during the last glaciation, Science, 353, 470–474, https://doi.org/10.1126/science.aaf5529, 2016.

Johnsen, S. J., Dansgaard, W., Clausen, H. B., and Langway, C. C.: Oxygen isotope profiles through the Antartic and Greenland ice sheets, Nature, 235, 429–434, https://doi.org/10.1038/235429a0, 1972.

Johnsen, S. J., Clausen, H. B., Dansgaard, W., Fuhrer, K., Gundestrump, N., Hammer, C. U., Iversen, P., Jouzel, J., Stauffer, B., and Steffensen, J. P.: Irregular glacial interstadials recorded in a new Greenland ice core, Nature, 359, 311–313, https://doi.org/10.1038/359311a0, 1992.

Johnsen, S. J., Dahl-Jensen, D., Gundestrup, N., Steffensen, J. P., Clausen, H. B., Miller, H., Masson-Delmotte, V., Sveinbjörnsdottir, A. E., and White, J.: Oxygen isotope and palaeotemperature records from six Greenland ice-core stations: Camp Century, Dye-3, GRIP, GISP2, Renland and NorthGRIP, J. Quaternary. Sci., 16, 299–307, https://doi.org/10.1002/jqs.622, 2001.

Kindler, P., Guillevic, M., Baumgartner, M., Schwander, J., Landais, A., and Leuenberger, M.: Temperature reconstruction from 10 to 120 kyr b2k from the NGRIP ice core, Clim. Past, 10, 887–902, https://doi.org/10.5194/cp-10-887-2014, 2014.

Kohfeld, K. E. and Harrison, S. P.: Glacial-interglacial changes in dust deposition on the Chinese Loess Plateau, Quaternary Sci. Rev., 22, 1859–1878, https://doi.org/10.1016/S0277-3791(03)00166-5, 2003.

Krinner, G., Boucher, O., and Balkanski, Y.: Ice-free glacial northern Asia due to dust deposition on snow, Clim. Dynam., 27, 613–625, https://doi.org/10.1007/s00382-006-0159-z, 2006.

Kukla, G. J. and Koci, A.: End of the last interglacial in the loess record, Quaternary. Res., 2, 374–383, 1972.

Kutzbach, J. E.: Model simulations of the climatic patterns during the deglaciation of North America, in: North America and Adjacent Oceans during the Last Deglaciation – The Geology of North America, edited by: Ruddiman, W. F. and Wright, H. E., The Geological Society of America, Boulder, 425–446, 1987.

Laurent, B., Marticorena, B., Bergametti, G., Chazette, P., Maignan, F., and Schmechtig, C.: Simulation of the mineral dust emission frequencies from desert areas of China and Mongolia using an aerodynamic roughness length map derived from the POLDER/ADEOS 1 surface products, J. Geophys. Res.-Atmos., 110, D18S04, https://doi.org/10.1029/2004JD005013, 2005.

Laurent, B., Marticorena, B., Bergametti, G., and Mei, F.: Modeling mineral dust emissions from Chinese and Mongolian deserts, Global Planet. Change, 52, 121–141, https://doi.org/10.1016/j.gloplacha.2006.02.012, 2006.

Masson-Delmotte, V., Dreyfus, G., Braconnot, P., Johnsen, S., Jouzel, J., Kageyama, M., Landais, A., Loutre, M.-F., Nouet, J., Parrenin, F., Raynaud, D., Stenni, B., and Tuenter, E.: Past temperature reconstructions from deep ice cores: relevance for future climate change, Clim. Past, 2, 145–165, https://doi.org/10.5194/cp-2-145-2006, 2006.

Mayewski, P. A., Meeker, L. D., Whitlow, S., Twickler, M. S., Morrison, M. C., Bloomfield, P., Bond, G. C., Alley, R. B., Gow, A. J., Grootes, P. M., Meese, D. A., Ram, M., Taylor, K. C., and Wumkes, W.: Changes in atmospheric circulation and ocean ice cover over the North Atlantic during the last 41,000 years, Science, 263, 1747–1751, https://doi.org/10.1126/science.263.5154.1747, 1994.

McManus, J. F., Francois, R., Gherardi, J. M., Keigwin, L. D., and Brown-Leger, S.: Collapse and rapid resumption of Atlantic meridional circulation linked to deglacial climate changes, Nature, 428, 834–837, https://doi.org/10.1038/nature02494, 2004.

Moine, O., Antoine, P., Hatté, C., Landais, A., Mathieu, J., Prud'Homme, C., and Rousseau, D.-D.: The impact of Last Glacial climate variability in west-European

loess revealed by radiocarbon dating of fossil earthworm granules, P. Natl. Acad. Sci. USA, 114, 6209–6214, https://doi.org/10.1073/pnas.1614751114, 2017.
Müller, U. C., Pross, J., and Bibus, E.: Vegetation response to rapid climate change in Central Europe during the past 140,000 yr based on evidence from the Füramoos pollen record, Quaternary Res., 59, 235–245, https://doi.org/10.1016/S0033-5894(03)00005-X, 2003.
Nagashima, K., Tada, R., Tani, A., Sun, Y., Isozaki, Y., Toyoda, S., and Hasegawa, H.: Millennial-scale oscillations of the westerly jet path during the last glacial period, J. Asian Earth Sci., 40, 1214–1220, 2011.
NGRIP (North Greenland Ice Core Project): High-resolution record of Northern Hemisphere climate extending into the last interglacial period, Nature, 431, 147–151, https://doi.org/10.1038/nature02805, 2004.
Rahmstorf, S.: Timing of abrupt climate change: A precise clock, Geophys. Res. Lett., 30, 1510, https://doi.org/10.1029/2003GL017115, 2003.
Rasmussen, S. O., Bigler, M., Blockley, S. P., Blunier, T., Buchardt, S. L., Clausen, H. B., Cvijanovic, I., Dahl-Jensen, D., Johnsen, S. J., Fischer, H., Gkinis, V., Guillevic, M., Hoek, W. Z., Lowe, J. J., Pedro, J. B., Popp, T., Seierstad, I. K., Steffensen, J. P., Svensson, A. M., Vallelonga, P., Vinther, B. M., Walker, M. J. C., Wheatley, J. J., and Winstrup, M.: A stratigraphic framework for abrupt climatic changes during the Last Glacial period based on three synchronized Greenland ice-core records: refining and extending the INTIMATE event stratigraphy, Quaternary Sci. Rev., 106, 14–28, https://doi.org/10.1016/j.quascirev.2014.09.007, 2014.
Rittner, M., Vermeesch, P., Carter, A., Bird, A., Stevens, T., Garzanti, E., Ando, S., Vezzoli, G., Dutt, R., Xu, Z. W., and Lu, H. Y.: The provenance of Taklamakan desert sand, Earth Planet. Sc. Lett., 437, 127–137, https://doi.org/10.1016/j.epsl.2015.12.036, 2016.
Rousseau, D. D., Antoine, P., Hatté, C., Lang, A., Zöller, L., Fontugne, M., Ben Othman, D., Luck, J. M., Moine, O., Labonne, M., Bentaleb, I., and Jolly, D.: Abrupt millennial climatic changes from Nussloch (Germany) Upper Weichselian eolian records during the Last Glaciation, Quaternary Sci. Rev., 21, 1577–1582, 2002.
Rousseau, D. D., Derbyshire, E., Antoine, P., and Hatté, C.: European loess records, in: Encyclopedia of Quaternary Science, edited by: Elias, S., Elsevier, Amsterdam, 1440–1456, 2007a.
Rousseau, D. D., Sima, A., Antoine, P., Hatté, C., Lang, A., Zöller, L.: Link between European and North Atlantic abrupt climate changes over the last glaciation, Geophys. Res. Lett., 34, L22713, https://doi.org/10.1029/2007GL031716, 2007b.
Rousseau, D.-D., Antoine, P., Gerasimenko, N., Sima, A., Fuchs, M., Hatté, C., Moine, O., and Zoeller, L.: North Atlantic abrupt climatic events of the last glacial period recorded in Ukrainian loess deposits, Clim. Past, 7, 221–234, https://doi.org/10.5194/cp-7-221-2011, 2011.
Rousseau, D.-D., Chauvel, C., Sima, A., Hatté, C., Lagroix, F., Antoine, P., Balkanski, Y., Fuchs, M., Mellett, C., Kageyama, M., Ramstein, G., and Lang, A.: European glacial dust deposits: Geochemical constraints on atmospheric dust cycle modeling, Geophys. Res. Lett., 41, 7666–7674, https://doi.org/10.1002/2014GL061382, 2014.
Rousseau, D.-D., Boers, N., Sima, A., Svensson, A., Bigler, M., Lagroix, F., Taylor, S., and Antoine, P.: (MIS3 & 2) millennial oscillations in Greenland dust and Eurasian aeolian records: a paleosol perspective, Quaternary Sci. Rev., 169, 99–113, https://doi.org/10.1016/j.quascirev.2017.05.020, 2017.
Ruth, U., Wagenbach, D., Steffensen, J. P., and Bigler, M.: Continuous record of microparticle concentration and size distribution in the central Greenland NGRIP ice core during the last glacial period, J. Geophys. Res.-Atmos., 108, D34098, https://doi.org/10.1029/2002JD002376, 2003.
Schulz, M.: On the 1470-year pacing of Dansgaard-Oeschger warm events, Paleoceanography, 17, 4.1–4.10, https://doi.org/10.1029/2000PA000571, 2002.
Sima, A., Rousseau, D. D., Kageyama, M., Ramstein, G., Schulz, M., Balkanski, Y., Antoine, P., Dulac, F., and Hatté, C.: Imprint of North-Atlantic abrupt climate changes on western European loess deposits as viewed in a dust emission model, Quaternary Sci. Rev., 28, 2851–2866, https://doi.org/10.1016/j.quascirev.2009.07.016, 2009.
Sima, A., Kageyama, M., Rousseau, D.-D., Ramstein, G., Balkanski, Y., Antoine, P., and Hatté, C.: Modeling dust emission response to North Atlantic millennial-scale climate variations from the perspective of East European MIS 3 loess deposits, Clim. Past, 9, 1385–1402, https://doi.org/10.5194/cp-9-1385-2013, 2013.
Sodemann, H. and Zubler, E.: Seasonal and inter-annual variability of the moisture sources for Alpine precipitation during 1995–2002, Int. J. Climatol., 30, 947–961, https://doi.org/10.1002/joc.1932, 2010.
Sodemann, H., Masson-Delmotte, V., Schwierz, C., Vinther, B. M., and Wernli, H.: Interannual variability of Greenland winter precipitation sources: 2. Effects of North Atlantic Oscillation variability on stable isotopes in precipitation, J. Geophys. Res.-Atmos., 113, D112, https://doi.org/10.1029/2007JD009416, 2008.
Solomon, S., Qin, D., Manning, M., Chen, Z. Y., Marquis, M., Averyt, K. B., Tignor, M., and Miller, H. L. (Eds.): Climate Change 2007: The Physical Basis. Contribution of Working Group I to the Fourth Assessment Report of the Intergovernemental Panel on Climate Change. Cambridge University Press, Cambridge, 2007.
Steffensen, J. P., Andersen, K. K., Bigler, M., Clausen, H. B., Dahl-Jensen, D., Fischer, H., Goto-Azuma, K., Hansson, M., Johnsen, S. J., Jouzel, J., Masson-Delmotte, V., Popp, T., Rasmussen, S. O., Rothlisberger, R., Ruth, U., Stauffer, B., Siggaard-Andersen, M. L., Sveinbjornsdottir, A. E., Svensson, A., and White, J. W. C.: High-resolution Greenland Ice Core data show abrupt climate change happens in few years, Science, 321, 680–684, https://doi.org/10.1126/science.1157707, 2008.
Sun, Y., Clemens, S.C., Morrill, C., Lin, X., Wang, X., and An, Z.: Influence of Atlantic meridional overturning circulation on the East Asian winter monsoon. Nat. Geosci. 5, 46-49, https://doi.org/10.1038/NGEO1326, 2012.
Svensson, A., Biscaye, P. E., and Grousset, F. E.: Characterization of late glacial continental dust in the Greenland Ice Core Project ice core, J. Geophys. Res.-Atmos., 105, 4637–4656, https://doi.org/10.1029/1999JD901093, 2000.
Taylor, S. N., Lagroix, F., Rousseau, D.-D., and Antoine, P.: Mineral magnetic characterization of the Upper Pleniglacial Nuss-

loch loess sequence (Germany): an insight into local environmental processes, Geophys. J. Int., 199, 1463–1480, 2014.

Thomas, A. M., Rupper, S., and Christensen, F.: Characterizing the statistical properties and interhemispheric distribution of Dansgaard-Oeschger events, J. Geophys. Res., 116, D03103, https://doi.org/10.1029/2010JD014834, 2011.

Wang, Y. J., Cheng, H., Edwards, R. L., An, Z. S., Wu, J. Y., Shen, C. C., and Dorale, J. A.: A high-resolution absolute-dated late Pleistocene monsoon record from Hulu Cave, China, Science, 294, 2345–2348, https://doi.org/10.1126/science.1064618, 2001.

Wang, Y. J., Cheng, H., Edwards, R. L., Kong, X., Shao, X., Chen, S., Wu, J., Jiang, X., Wang, X., and An, Z.: Millenial- and orbital-scale changes in the East Asian monsoon over the past 224,000 years, Nature, 451, 1090–1093, https://doi.org/10.1038/nature06692, 2008.

Wolff, E. W., Chappellaz, J., Blunier, T., Rasmussen, S. O., and Svensson, A.: Millennial-scale variability during the last glacial: The ice core record, Quaternary Sci. Rev., 29, 2828–2838, https://doi.org/10.1016/j.quascirev.2009.10.013, 2010.

Yin, Q., Berger, A., Driesschaert, E., Goosse, H., Loutre, M. F., and Crucifix, M.: The Eurasian ice sheet reinforces the East Asian summer monsoon during the interglacial 500 000 years ago, Clim. Past, 4, 79–90, https://doi.org/10.5194/cp-4-79-2008, 2008.

Zdanowicz, C., Hall, G., Vaive, J., Amelin, Y., Percival, J., Girard, I., Biscaye, P., and Bory, A.: Asian dustfall in the St. Elias Mountains, Yukon, Canada, Geochim. Cosmochim. Ac., 70, 3493–3507, https://doi.org/10.1016/j.gca.2006.05.005, 2006.

Clim. Past, 20, 1269–1282, 2024
https://doi.org/10.5194/cp-20-1269-2024

Climate of the Past
Open Access

Local summer temperature changes over the past 440 ka revealed by the total air content in the Antarctic EPICA Dome C ice core

Dominique Raynaud[1,★], Qiuzhen Yin[2,★], Emilie Capron[1,★], Zhipeng Wu[2], Frédéric Parrenin[1], André Berger[2], and Vladimir Lipenkov[3]

[1]Institute of Environmental Geosciences (IGE), Université Grenoble Alpes, CNRS, IRD, INRAE, Grenoble-INP, 38000 Grenoble, France
[2]Earth and Life Institute, Earth and Climate Research Center, Université catholique de Louvain, 1348 Louvain-la-Neuve, Belgium
[3]Climate and Environmental Research Laboratory, Arctic and Antarctic Research Institute, Saint Petersburg, 199397, Russia
[★]These authors contributed equally to this work.

Correspondence: Dominique Raynaud (dominique.raynaud2@univ-grenoble-alpes.fr) and Emilie Capron (emilie.capron@univ-grenoble-alpes.fr)

Received: 15 October 2023 – Discussion started: 17 October 2023
Revised: 14 April 2024 – Accepted: 24 April 2024 – Published: 11 June 2024

Abstract. Seasonal temperature reconstructions from ice cores are missing over glacial–interglacial timescales, preventing a good understanding of the driving factors of Antarctic past climate changes. Here the total air content (TAC) record from the Antarctic EPICA Dome C (EDC) ice core is analyzed over the last 440 ka (thousand years). While the water isotopic record, a tracer for annual mean surface temperature, exhibits a dominant ~ 100 kyr cyclicity, the TAC record is associated with a dominant ~ 40 kyr cyclicity. Our results show that the TAC record is anti-correlated with the mean insolation over the local astronomical summer half-year. They also show for the first time that it is highly anti-correlated with local summer temperature simulated with an Earth system model of intermediate complexity. We propose that (1) the local summer insolation controls the local summer temperature; (2) the latter, through the development of temperature gradients at the near-surface of the ice sheet (< 2 m), is affecting the surface snow structure; and (3) those snow structure changes propagating down to the bottom of the firn through densification are eventually controlling the pore volume at the bubble close-off and consequently the TAC. Hence, our results suggest that the EDC TAC record could be used as a proxy for local summer temperature changes. Also, our new simulations show that the mean insolation over the local astronomical summer half-year is the primary driver of Antarctic summer surface temperature variations, while changes in atmospheric greenhouse gas (GHG) concentrations and Northern Hemisphere (NH) ice sheet configurations play a more important role in Antarctic annual surface temperature changes.

1 Introduction

The analysis of Antarctic ice cores provides paramount information to reconstruct and understand the climate dynamics of the past 800 ka (thousand years). Amongst the key climatic parameters that can be inferred from these deep ice cores are the local mean annual temperature reconstructed from the isotopic composition of ice (e.g., δD Dome Fuji Ice Core Project Members, 2017; Jouzel et al., 2007) and past atmospheric greenhouse gas (GHG) concentrations measured from air trapped in air bubbles (Bereiter et al., 2015; Loulergue et al., 2008; Lüthi et al., 2008). However, the climate during local summer, which is a critical season for polar regions, especially in terms of solar energy received, is seldom discussed, except through the highlighting of local insolation signatures on the O_2 / N_2 ratio of trapped gas (Bender, 2002;

Kawamura et al., 2007; Landais et al., 2012) and the air content in bubbles (Eicher et al., 2016; Epifanio et al., 2023; Lipenkov et al., 2011) in ice core records. In particular, there is no suitable proxy of the local summer temperature. Moreover, a debate remaining in Antarctic climate study is related to whether the Antarctic temperature variations on orbital timescales are controlled by the Northern Hemisphere (NH) insolation or by local insolation (Huybers and Denton, 2008). As the insolation over Antarctica is received mostly during summer, having a proxy of summer temperature would therefore be essential for helping to decipher the role of the NH versus local insolation and the role of other glacial boundary conditions, such as the changes in atmospheric GHG concentrations, in Southern Ocean sea ice extent and in ice sheet configuration.

An imprint of local insolation changes has been evidenced in tracers which are measured in the air trapped in polar ice cores. Indeed, air bubbles close off from the surrounding atmosphere and become trapped in ice, an airtight material resulting from the densification and diagenesis of the snow deposited at the surface. These processes of densification and diagenesis take place in the upper layer at the surface of the ice sheet (typically between 60–120 m deep), which is characterized by an open porosity to the atmosphere and by two successive stages, snow and then firn, associated with different densification regimes (Anderson and Benson, 1963). In the absence of surface melting, which is the case at the EPICA Dome C (EDC) site (75°06′ S, 123°21′ E; 3233 m a.s.l.) on the high plateau of East Antarctica, and, according to the ideal gas law, the amount of air (V) in the bubbles at close-off depends on their physical volume (V_c) and on the pressure (P_c) and temperature (T_c) of the air contained in V_c at the enclosure time (Martinerie et al., 1992). In the first approximation, T_c is equivalent to the mean annual temperature prevailing at the surface of the ice sheet, which is estimated from the isotopic composition of the ice.

Then, V can be defined as the total volume of air in unit mass of ice, measured at standard temperature T_0 and pressure P_0, and V_c is the pore volume per unit mass at close-off:

$$V = V_c P_c / T_c \times T_0 / P_0. \quad (1)$$

Furthermore, the porosity at close-off, V_c, is related to temperature.

During previous works, V (for air content) and TAC (for total air content) have been interchangeably used for designating the same property. In this work we are using TAC, following other recent studies.

Long-term high-resolution studies of TAC records obtained from several deep ice cores in central Antarctica (Lipenkov et al., 2011; Martinerie et al., 1994; Raynaud et al., 2007) revealed a long-term large variability that cannot be explained by changes in T_c or P_c. In particular at EDC, about 85 % of the variance observed in the high-resolution V record covering the last 440 ka can be explained neither by P_c, nor by T_c changes. This led us to consider that other properties, besides the mean annual temperature and barometric pressure at the surface, may also influence TAC. By using continuous wavelet transform (CWT) analysis, Raynaud et al. (2007) found that the EDC TAC record shows significant power in the obliquity and precession bands, with a dominant ~ 40 ka signal, which has been assumed to reflect orbitally driven changes in local summer insolation.

To account for the observed anti-correlation between local summer insolation and TAC, a mechanism has been proposed where the local summer insolation, by controlling the near-surface (< 2 m) snow temperature and temperature gradients during summertime, affects the near-surface snow structure and consequently the porosity of the firn pores at close-off, i.e., the TAC of air bubbles (Lipenkov et al., 2011; Raynaud et al., 2007). Based on such an assumption, TAC was used as an orbital dating tool to constrain ice core chronologies. TAC-based age markers have been used for the latest official chronologies for polar ice cores (AICC2012, Bazin et al., 2013; Veres et al., 2013, and AICC2023, Bouchet et al., 2023). However, the exact physical processes that lead to an imprint of the local summer insolation in the TAC record are unclear. In particular, uncertainties remain regarding the link between TAC and the surface climatic parameters such as local temperature.

In this study, we use the TAC record measured in the EDC ice core covering the last 440 ka (Raynaud et al., 2007). We compare it with a new local insolation index and with transient simulations performed with the model LOVECLIM1.3 to explore the link between insolation, Antarctic summer temperature and TAC, as well as the related mechanisms. Finally, we compare the EDC TAC record with the EDC δD record to understand the major driving factors of the summer and annual mean temperature changes in Antarctica.

2 Method

2.1 TAC measurements

TAC measurements have been performed at the Institute of Environmental Geosciences (Grenoble, France) using an original barometrical method implemented with an experimental setup called STAN (Lipenkov et al., 1995). Results of the numerical data of the measurements versus depth along the EDC ice core can be found in the Appendix in Raynaud et al. (2007). The TAC data shown in Fig. 1 are plotted on the AICC2023 ice age chronology (Bouchet et al., 2023).

2.2 Model and simulations

The model used in this study is LOVECLIM1.3, a three-dimensional Earth system model of intermediate complexity (EMIC), with its atmosphere (ECBilt), ocean and sea ice (CLIO), and terrestrial biosphere (VECODE) components being interactively coupled (Goosse et al., 2010). The

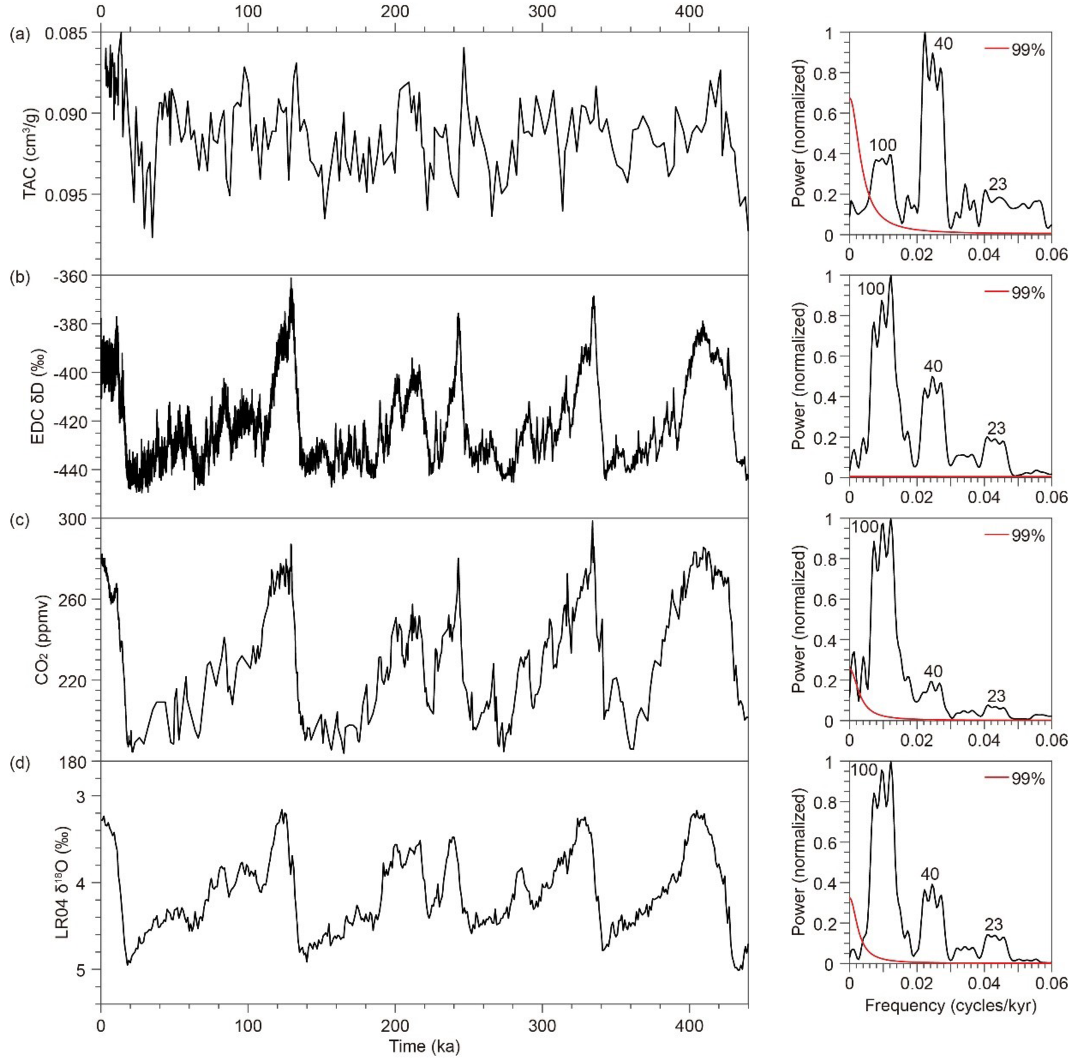

Figure 1. Variations and spectra over the past 440 ka of the **(a)** TAC record (raw data; Raynaud et al., 2007), **(b)** EDC δD record (Jouzel et al., 2007), **(c)** CO_2 concentration (Lüthi et al., 2008) and **(d)** benthic δ^{18}O (Lisiecki and Raymo, 2005). The major periodicities in kyr are indicated. The EDC TAC record, δD record and CO_2 concentrations are plotted on the AICC2023 chronology (Bouchet et al., 2023). The spectra are calculated using the multi-taper method (MTM), the number of tapers is set to 2 and the zero padding is set to 5, and the 99 % confidence limit is shown (red curves).

model setup is the same as the one used in Yin et al. (2021), and a detailed description can be found there. In terms of the Antarctic climate, LOVECLIM1.3 reasonably reproduces the spatial pattern and the magnitude of surface temperature over Antarctica in winter and summer and the annual mean (Fig. 2a). It is slightly cooler in West Antarctica in the model, probably related to its rough resolution. The seasonal temperature cycle at the EDC site (Fig. 2b) and the Antarctic inversion (Fig. 2c) are also well-reproduced by the model.

Although LOVECLIM1.3 is classified as an EMIC model, its complexity is high for this kind of model, and its ocean component is a full general circulation model, so it remains challenging to run full transient simulations with this model. We therefore first performed a transient simulation with 10× acceleration covering the last 800 ka, which allows us to compare the simulated local summer temperature with the TAC record over the entire last 440 ka. In this simulation, the variations in orbital forcing and GHGs were considered, and the global ice sheets were fixed to their pre-industrial condition. Using the same model and the same acceleration technique, it has been shown that 10× acceleration has a significant impact on deep-ocean temperature, but it has no major impact on surface temperature (Yin and Berger, 2015). This is further confirmed in our study where the Antarctic summer and annual mean temperature changes of the 10× acceleration simulation match well with those of the non-accelerated simulations (Fig. S1 in the Supplement).

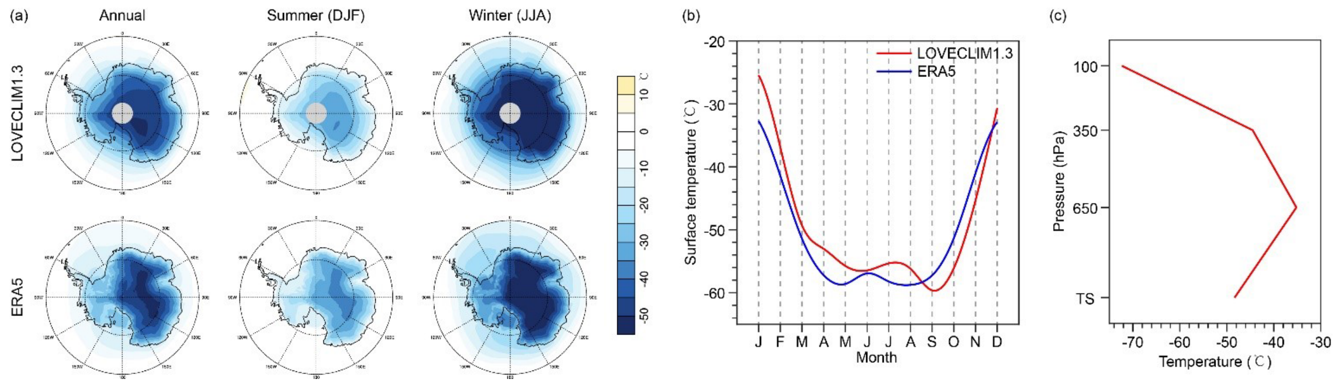

Figure 2. Comparison of the 1971–2000 mean climate in Antarctica simulated by LOVECLIM1.3 and the ERA5 reanalysis (https://cds.climate.copernicus.eu/cdsapp#!/home, last access: 12 February 2024) for mean annual, summer (DJF) and winter (JJA) surface temperature **(a)** and for the seasonal cycle of the surface temperature at the EDC site **(b)**, as well as the simulated vertical mean annual surface temperature profile at the EDC site.

We further performed transient simulations without acceleration for some glacial–interglacial episodes of the last 440 ka to investigate the relative effects of insolation, GHGs and NH ice sheets (see Sect. 5 for simulation periods and results). Each episode includes three simulations. The first two simulations, Orb and OrbGHG, were performed in Yin et al. (2021), and a detailed description of the experiment setup can be found there. Here we only give a brief introduction. In the Orb simulation, only the change in orbital forcing (Berger and Loutre, 1991) was considered, with the GHGs and ice sheets being fixed to their pre-industrial conditions. In the OrbGHG simulation, the change in GHGs (Loulergue et al., 2008; Lüthi et al., 2008; Schilt et al., 2010) was considered in addition to the orbital forcing. In the third simulation, OrbGHGIce, the change in NH ice sheets (Ganopolski and Calov, 2011) was additionally considered, but the Southern Hemisphere (SH) ice sheets remained fixed to the pre-industrial conditions. The initial conditions were provided by a 2000-year equilibrium experiment with the NH ice sheets, GHG concentrations and astronomical parameters at the starting date of the simulated period. In the presence of land ice, albedo, topography, vegetation and surface soil types corresponding to ice-covered conditions were prescribed at corresponding model grids in LOVECLIM1.3. A detailed description of the ice sheet setup can be found in Wu et al. (2023).

3 EDC TAC changes vs. local summer insolation variations over the past 440 ka

The spectral analysis of the TAC record shows that its variations over the last 440 ka are dominated by the 40 kyr cycle (Fig. 1), which corresponds to the main periodicity of obliquity. It also shows the 100 kyr cycle and the 23 and 19 kyr cycles which correspond to the precession cycles (Berger, 1978), but their amplitude in the power spectrum is much weaker. Overall, this spectral characteristic illustrates that the variations in TAC are strongly correlated with the astronomical forcing and could be linked to insolation changes (Lipenkov et al., 2011; Raynaud et al., 2007).

When comparing a proxy record with insolation, it is not necessarily straightforward to decide which insolation index to choose because different insolation metrics exist, and their relationship with climate is not always clear (Berger et al., 1993, 2010). In a previous study presenting the EDC TAC record over the past 440 ka (Raynaud et al., 2007), an integrated summer insolation index (also referred to as ISI) was established and compared with the TAC record in order to find the ISI curve with variations that would most resemble the changes recorded in the TAC record. The ultimate objective of such an exercise was to identify an insolation target to infer dating constraints from TAC based on orbital tuning. The most appropriate orbital tuning target was found by tuning the precession-to-obliquity amplitude ratio of the insolation index on the corresponding spectral signature of the TAC record. It corresponds to the so-called ISI 380 curve that was obtained by summing over the year the daily insolation above a threshold of 380 $W\,m^{-2}$. Hence, this orbital tuning heavily relies on (1) the tuning of the relative amplitudes of the precession and obliquity in the power spectra and (2) as a consequence the selected insolation threshold value. It is also based on the assumption of a time-linear (constant) response of TAC to the selected insolation threshold. To avoid these assumptions, we propose to use a simpler and independent insolation index in the present work: the mean insolation over the astronomical half-year summer at 75° S (the latitude of the EDC site).

The astronomical summer half-year in the SH, which corresponds to the astronomical winter half-year in the NH, is defined as the time interval during which the Earth travels from the fall (September) equinox to the spring (March) equinox on the ecliptic (Berger and Loutre, 1994; Berger and

Yin, 2012; Berger et al., 2024). The advantage of using astronomical seasons is that they allow a change in the length of seasons. The astronomical summer half-year in the SH is the main interval during which the southern polar regions (regions within the Antarctic Circle) receive solar radiation over a year. The length of this half-year summer varies in time and is only a function of precession (Berger and Loutre, 1994; Berger and Yin, 2012; Berger et al., 2024). Over the last 440 ka, it varies between 171.3 and 194.0 d. The total solar radiation received over the half-year astronomical summer is only a function of obliquity (Berger et al., 2010). Therefore, the mean summer insolation at 75° S, which is calculated by dividing the total irradiation received during the half-year summer by its length, is a function of both obliquity and precession, with obliquity being dominant. Compared to the total summer insolation or the integrated insolation above a threshold (ISI), the mean insolation of the astronomical summer half-year (referred to as mean summer insolation hereafter) considers not only the total amount of energy received during the astronomical summer half-year but also the length of the astronomical summer half-year, which could also be important.

Figure 3 shows the comparison between TAC and the mean summer insolation. Since we focus here on the orbital-scale variations, a low-pass filter (> 12 kyr) was applied to the TAC data before the comparison in order to eliminate the high-frequency signals. A good resemblance in terms of temporal structure and amplitude is observed between the two variables, and the two datasets appear well-anti-correlated with an R^2 correlation coefficient of 0.39. This comparison is surprisingly good considering that TAC could also be influenced by other factors.

This new result implies that for dating purposes the mean summer local insolation is more appropriate than the ISI 380 curve (Raynaud et al., 2007) to be used as an orbital dating target. Indeed, it appears preferable to favor the mean summer insolation record as it is fully independent from the TAC record compared to ISI 380, although the degree of anti-correlation with the TAC record is of similar magnitude. While it is beyond the scope of this study to discuss in detail the implications for the definition of TAC-based age markers to constrain the EDC ice core dating (Bouchet et al., 2023), we present in Fig. 4 a comparison of the two insolation indexes over the past 440 ka. We observe a strong resemblance in terms of the relative amplitude and timing of changes in the two records. Following the approach described in Raynaud et al. (2007), we calculate the evolution of the phase delay between the two records filtered in the 15–46 kyr band to provide a quantification of the age differences that could be generated from the use of one curve or the other for orbital dating purposes. On average, the age difference is about 260 years and never above 650 years. These age differences should be regarded as minimal, as they do not account for other sources of age uncertainties when building a TAC-based orbitally tuned chronology. For instance, our ability to define precisely the tie points between the TAC data and the insolation index also depends on the quality of the visual resemblance between TAC and the insolation target. These matters will be fully discussed in a subsequent study.

4 EDC TAC changes vs. local summer temperature changes simulated by the LOVECLIM1.3 model

While it appears that the EDC TAC record is anti-correlated with the local mean summer insolation, its relationship to seasonal surface temperature reconstructions has not been investigated yet. Recently, a quantitative reconstruction of the seasonal temperature changes in West Antarctica has been produced throughout the Holocene (Jones et al., 2023), but to our knowledge no seasonal temperature reconstructions in Antarctic ice cores are available over the longer glacial–interglacial timescale. Hence, we propose to compare the EDC TAC record with the local summer temperature changes obtained from transient simulations performed with LOVECLIM1.3. The comparison of the LOVECLIM1.3-simulated summer temperature in West Antarctica with the one reconstructed by Jones et al. (2023) shows that they compare well in both the trend and the magnitude of temperature change over the Holocene, both showing that the summer temperature in West Antarctica had an increasing trend from the early to mid-Holocene and reached a maximum at ∼ 4 ka BP followed by a decreasing trend (Fig. S2). This validates the LOVECLIM1.3 simulations in reproducing past summer temperature changes in West Antarctica.

Figure 3 shows that the EDC TAC values increase when the modeled local summer temperatures decrease. It also shows that there is a high and positive correlation between the simulated summer temperature and the mean summer insolation. Linear regression analysis shows that TAC and the simulated summer temperature are highly and negatively correlated. The linear coefficient of determination ($R^2 = 0.58$ when a low-pass filter > 12 kyr is applied to the TAC data) indicates that about 58 % of the TAC variability observed in the EDC ice core over the last 440 ka is explained by the half-year summer temperature at the EDC, which suggests that summer temperature variations in the central part of East Antarctica can be regarded as the main driving forcing factor of TAC. The slope of the regression shows an increase of 0.0012 cm^3 in TAC per gram of ice for a cooling of 1 °C of the mean half-year summer local temperature at the EDC. The regression analysis has also been evaluated by using the raw TAC data and a low-pass filter of > 6 kyr. The good anti-correlation between TAC and the summer temperature is not altered, although the regression slope is slightly affected with an increase of about 0.0011 cm^3 in TAC per gram of ice for a cooling of 1 °C. Hence, we propose that the link between summer insolation and TAC variations exists through the summer temperature changes (see also Sect. 6). Indeed, as proposed in previous studies (Lipenkov et al., 2011; Ray-

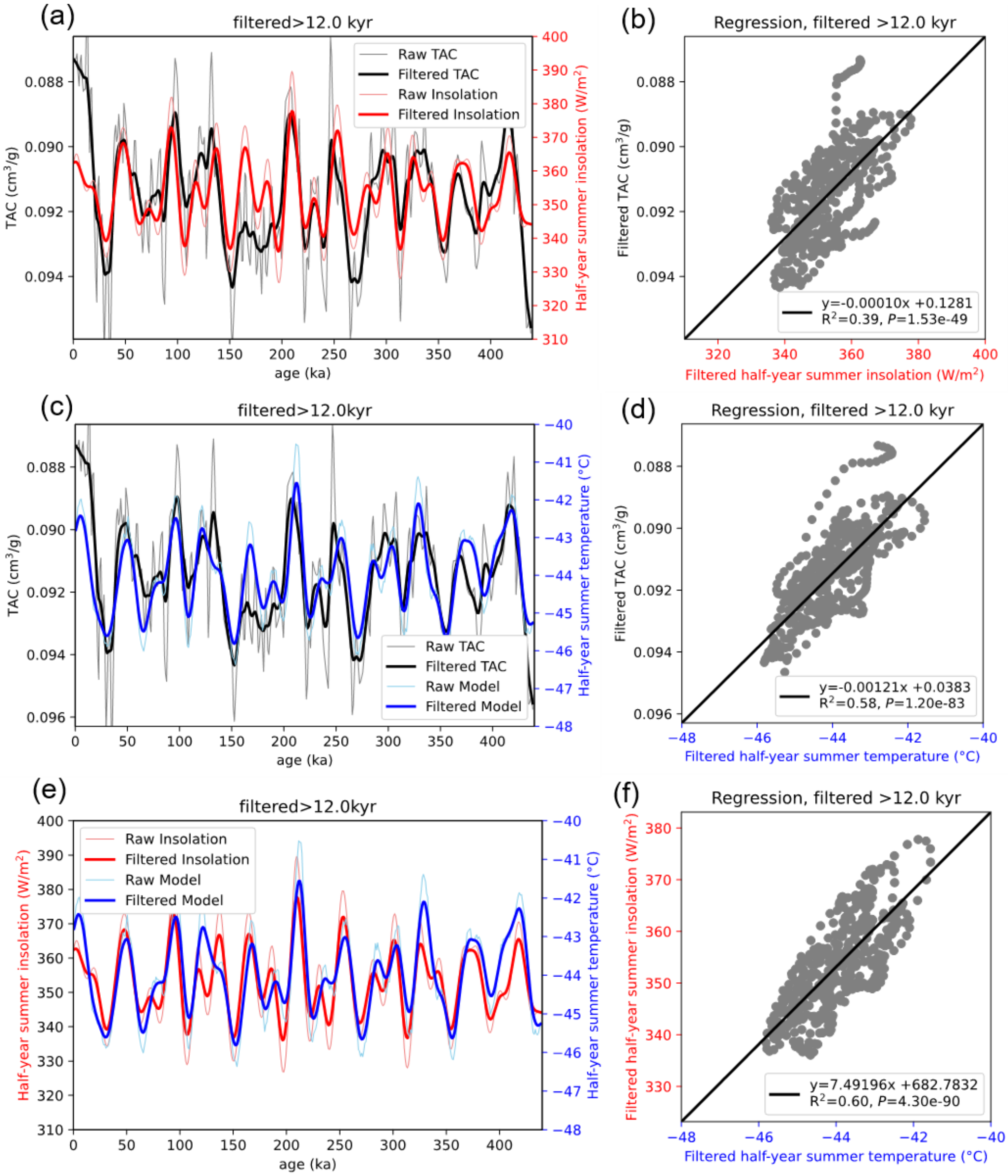

Figure 3. Comparison of the TAC record with **(a)** mean insolation during astronomical half-year summer at 75° S calculated using the solution of Berger and Loutre (1991) and with **(c)** simulated mean half-year summer (October to March) temperature at the EDC site. Their corresponding linear regression analyses are shown in panels **(b)** and **(d)**. **(e)** Comparison of half-year summer insolation with simulated mean half-year summer temperature and corresponding linear regression in panel **(f)**. Low-pass-filtered > 12 kyr is applied to the TAC, insolation and summer temperature raw data before comparison. Note that the y axis for TAC is reversed on the left panels to ease the visual comparison.

naud et al., 2007), the local summer insolation controls the near-surface snow temperature and the vertical temperature gradients in snow. In turn, the latter could affect the near-surface snow structure and consequently the porosity of the firn pores at close-off, i.e., the TAC. The good correlation between the two independent climate variables, TAC measured from ice cores and summer temperature simulated by the LOVECLIM1.3 model, indicates that the EDC TAC record can be used as a proxy for local summer temperature. The relationship between the TAC record from the EDC ice core and local summer temperature should be further investigated in other ice cores from Antarctica and Greenland.

In our study, we did not account for variations in surface elevation. In principle, during glacial periods, the reduced surface accumulation rate leads to lower surface elevation (Raynaud et al., 2007), but there are also dynamical effects

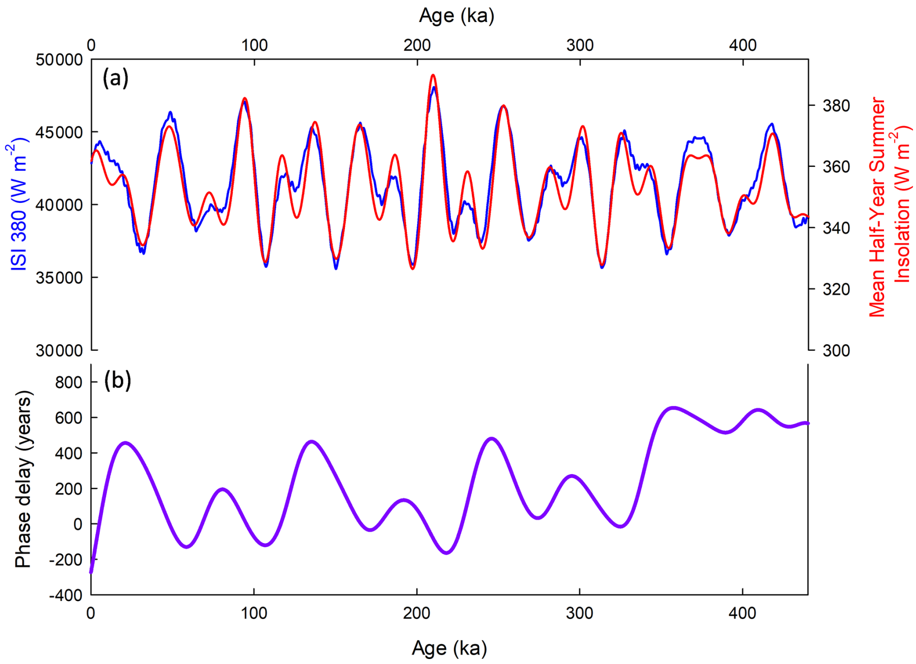

Figure 4. **(a)** Comparison of ISI 380 (blue) with the mean insolation during astronomical half-year summer (red). **(b)** Evolution of the phase delay (purple) between the two insolation curves filtered in the 15–46 kyr band. ISI 380 is represented here as a flux following the definition given in Eicher et al. (2016).

which make these reconstructions of surface elevation uncertain. Surface elevation changes affect our study in two different ways. Firstly, TAC should be corrected for atmospheric pressure changes to get a record of porosity at close-off. Some of these atmospheric pressure changes are due to variations in surface elevation, and another part might be due to the change in atmospheric conditions (like the temperature of the air column). Because the reconstruction of surface elevation changes is uncertain, we have chosen not to correct for this effect. Secondly, surface elevation changes should also be ideally taken into account in our LOVECLIM1.3 simulations of summer or annual temperature changes at the EDC. Unfortunately, in our climate model, the Antarctic ice sheet is fixed, and we did not account for surface elevation changes. We could apply an a posteriori correction for surface elevation changes, but, because the temperature variations (either annual or in summer) are probably underestimated, applying this a posteriori correction would have too strong an influence. Finally, we should note that these two elevation corrections (for TAC and for the climate model) go in the same direction: during glacials, a corrected summer temperature would be warmer, and the corrected TAC of the ice would be smaller, so there is a chance that these two corrections would cancel each other out and that the overall correlation between TAC and the modeled summer temperature would not be much affected.

A wavelet analysis (Fig. 5a and b) shows that the variations in both TAC and the simulated summer temperature are dominated by the ∼ 40 kyr cycle throughout the last 440 ka, indicating the major role of obliquity. They also contain a ∼ 20 kyr cycle, but this cycle is not stable in time, with an amplitude which is relatively strong, for instance, around 100 and 200 ka in both TAC and the simulated summer temperature but weak during other periods. This may be related to the amplitude modulation of eccentricity on precession (Berger and Loutre, 1991). The eccentricity at ∼ 100, 200 and 300 ka was large, leading to large variations in precession and thus stronger effects of precession around these time intervals than during other times. However, the power of obliquity is generally more important than the one of precession when considering the past 440 ka, in particular around 400 ka and during the last 50 ka when eccentricity was small, leading to small variations in precession. The 100 kyr periodicity is also observed in both TAC and the simulated summer temperature but with a weak amplitude. This weak signature of the 100 kyr cycle in both the TAC and the mean half-year summer temperature must not arise from the mean summer insolation because there is no 100 kyr cycle in the mean insolation (Fig. 5c). It must arise from the glacial–interglacial boundary condition changes which are characterized by a major periodicity of 100 kyr (see Sect. 5).

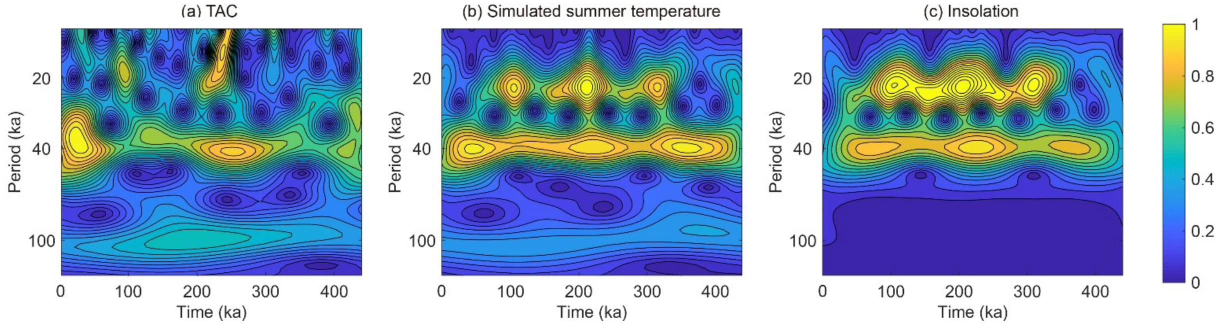

Figure 5. Continuous wavelet transforms of **(a)** the low-pass (> 12 kyr) filtered TAC record, **(b)** the simulated mean half-year summer temperature at the EDC site and **(c)** the mean insolation during astronomical summer half-year at 75° S.

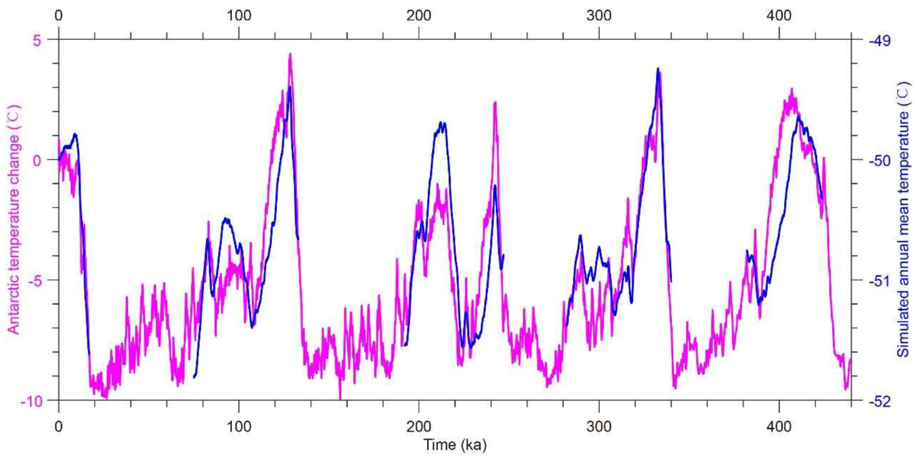

Figure 6. Comparison of the EDC mean annual temperature change record (pink line; Jouzel et al., 2007) with the simulated annual mean temperature of the OrbGHGIce experiments (blue line; this study).

5 Deciphering the driving forcing of past Antarctic summer and annual temperature changes

The δD record from Antarctic ice has been widely used as an important proxy for mean annual precipitation-weighted condensation temperature over Antarctica (Jouzel et al., 2007; Stenni et al., 2010), although it has also been suggested to be biased toward winter temperatures (Laepple et al., 2011). We use it in the present work as a record of the EDC mean annual temperature. Differently from the TAC record, which is dominated by the 40 kyr cycle, the EDC δD record is dominated by the $\sim$ 100 kyr cycle (Fig. 1). The difference in the dominant periodicities between the TAC and δD records suggests that the major driving factors for the summer and annual mean temperatures are different. As shown above, TAC is strongly linked to local summer temperature which is mainly controlled by the local summer insolation. However, the dominant 100 kyr cycle in the δD record suggests that the annual mean temperature is mainly controlled by the glacial–interglacial boundary conditions such as global ice volume and GHGs which are dominated by a strong 100 kyr cycle (Fig. 1).

To investigate the response of Antarctic climate to insolation, GHGs and ice sheets, the three sets of transient simulations (Orb, OrbGHG and OrbGHGIce; see Sect. 2) which cover the last five interglacial–glacial episodes are analyzed here. We first compare the δD-based temperature reconstruction with the simulated annual mean temperature of OrbGHGIce (Fig. 6). We observe that this comparison is quite good over the simulation periods in terms of climate variation pattern, showing the capacity of the model to simulate the orbital-scale climate variations at the EDC site. One may also note that the magnitude of the temperature change between glacial and interglacial is significantly underestimated in the model as compared to the reconstruction. In our simulation, the Antarctic ice sheet and the sea level are kept invariant, which could contribute at least partly to the underestimated amplitude of temperature change in the model. However, a recent study using borehole thermometry and firn properties suggests that the temperature reconstruction using water-stable isotopes calibrated against modern spatial gradients could generate an amplitude of glacial–interglacial temperature change that is too large (Buizert et al., 2021). For example, at the EDC site, the Last Glacial Maximum ($\sim$ 26–

18 ka) temperature relative to the pre-industrial time is about −9 °C according to the δD-based reconstruction (Jouzel et al., 2007), but it is only −4.3±1.5 °C in a more recent reconstruction (Buizert et al., 2021). In our simulation, the EDC annual temperature at 17 ka is −1.7 °C relative to the pre-industrial era, and the largest simulated glacial–interglacial amplitude is ∼ 3 °C, which is within the uncertainty of the recent reconstruction (Buizert et al., 2021). Nevertheless, such small glacial–interglacial difference found in our study seems difficult to explain taking into account the relationship between snow accumulation rate and surface temperature from the saturation–vapor relationship (Cauquoin et al., 2015). However, what is essential for our study is that the model could capture the orbital-scale variability in the reconstructed temperature.

To investigate the relative effect of insolation, GHGs and NH ice sheets on the summer and annual temperatures at the EDC, we take the 133–75 ka period, which includes the last interglacial period and the glacial inception, as an example to compare the Orb, OrbGHG and OrbGHGIce experiments (Fig. 7). As expected, the annual and summer temperatures at the EDC are reduced in response to reduced GHGs and increased NH ice sheets (Fig. 7b and d), with the impact of GHGs being larger than that of the NH ice sheets for both simulated temperatures. As far as the summer temperature is concerned, the variation pattern of OrbGHG and OrbGHGICE is very similar to the one of Orb (Fig. 7b), showing the minor effect of GHGs and NH ice sheets on the temporal variations in summer temperature. Over this period, the largest summer temperature change caused by insolation is 4.4 °C, while it is 1 °C for GHGs and 0.3 °C for ice sheets. However, when the simulated annual temperature is considered (Fig. 7d), its variation pattern is largely altered in response to changes in GHGs and NH ice sheets. Over this period, the largest annual temperature change caused by insolation is 1.2 °C, while it is 1 °C for GHGs and 0.5 °C for ice sheets. These results clearly show that, as compared to insolation, GHGs and NH ice sheets have a relatively weaker effect on the summer temperature, but they have a relatively stronger effect on annual mean temperature. This, at least partly, explains why the TAC and δD records display different dominant periodicities over long timescales.

To better understand the difference between the summer and annual mean temperatures, the simulated winter temperature is also analyzed. The wavelet analysis of the half-year winter temperature shows a very strong ∼ 20 kyr cycle and an obvious ∼ 100 kyr cycle, but the ∼ 40 kyr cycle is very weak (Fig. 8a). The 100 kyr cycle results are most probably from the effect of GHGs. The very strong 20 kyr cycle but very weak 40 kyr cycle is quite intriguing. As far as insolation is concerned, the low-latitude insolation is dominated by the ∼ 20 kyr precession cycle. As the solar energy received in Antarctica is very weak during local winter, the strong 20 kyr cycle in the simulated winter temperature could reflect a strong effect of the low-latitude climate on the Antarctica

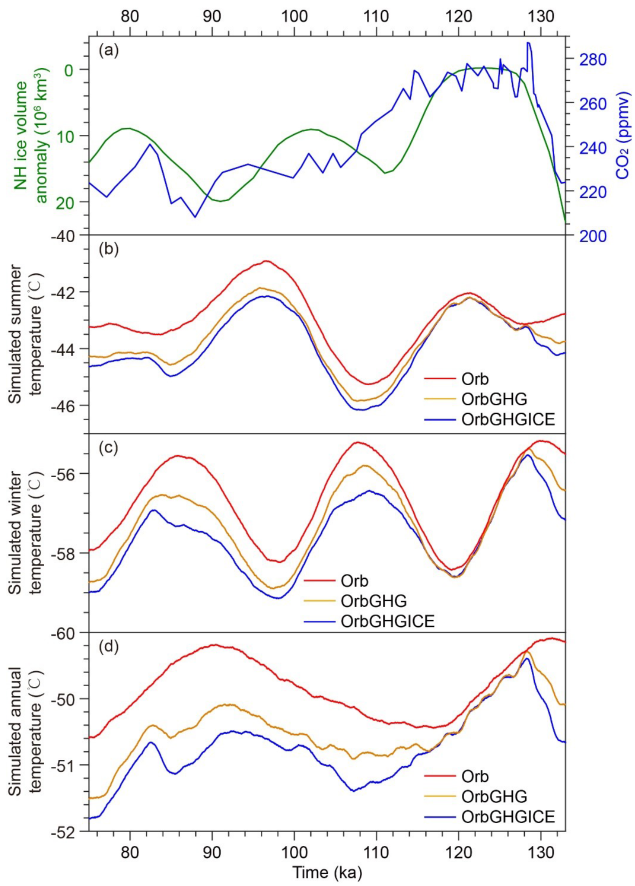

Figure 7. Effect of insolation, GHGs and NH ice sheets on the summer, winter and annual temperatures at the EDC site. **(a)** CO_2 concentration (blue; Lüthi et al., 2008) and NH ice volume anomaly as compared to pre-industry (green; Ganopolski and Calov, 2011). **(b)** Simulated mean half-year summer (October–March) temperature, **(c)** simulated mean half-year winter (April–September) temperature and **(d)** simulated annual mean temperature from the Orb, OrbGHG and OrbGHGICE experiments. The results of the LOVECLIM1.3 transient simulation without acceleration for the period 133–75 ka are used.

temperature during austral winter, possibly via meridional oceanic and atmospheric heat transport. Figure 8b shows a high negative correlation between the simulated EDC winter temperature and precession. This indicates that the EDC winter temperature is strongly affected by boreal summer insolation at low latitudes (small precession parameter leads to high boreal summer insolation and vice versa). It is also shown in Yin and Berger (2012) that during some interglacials such as Marine Isotope Stages 5e, 15 and 17, which are characterized by strong boreal summer insolation, a strong warming could be induced over Antarctica during austral winter, a warming which is even stronger than in many other regions due to polar amplification. Similarly to what happens to the summer temperature, orbital forcing also plays a dominant role in the winter temperature at the EDC (Fig. 7c). As explained above,

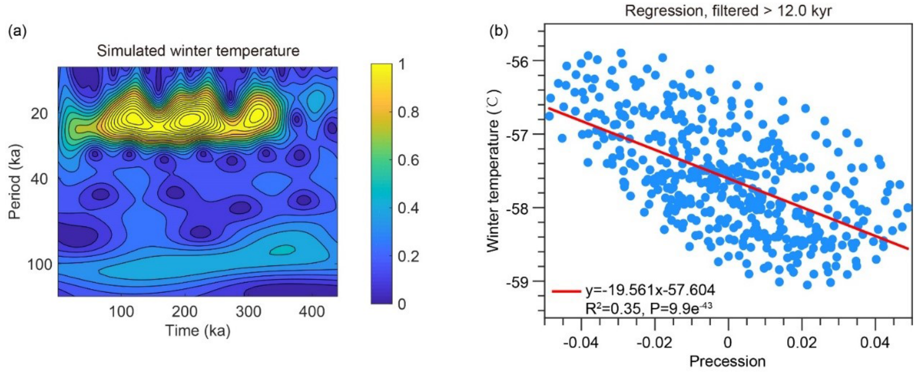

Figure 8. (a) Continuous wavelet transform of the simulated mean half-year winter temperature at the EDC site from the 10× accelerated OrbGHG simulation and **(b)** correlation between this winter temperature and precession. Low-pass-filtered > 12 kyr is applied to the winter temperature raw data.

the winter temperature at the EDC is actually strongly driven by precession and boreal summer insolation, so, on a precession timescale, the orbitally induced temperature variation in winter is in anti-phase with the summer temperature, which is strongly driven by austral summer insolation. This anti-phase relationship leads to a strong weakening of the orbital signal, especially the precession signal, in the mean annual temperature (Fig. 7d), making the effect of GHGs and ice sheets more pronounced and thus leading to strong glacial cycles in the mean annual temperature.

6 Possible mechanisms linking TAC and local summer temperature

The possible mechanism by which summer temperature and near-surface-temperature gradients can affect the pore volume at close-off, V_c, has been proposed assuming a homogenous firn column and neglecting the sealing effect on the total amount of air trapped in ice (Lipenkov et al., 2011; Raynaud et al., 2007). This simplification seems to be reasonable for low-accumulation sites such as the EDC, Vostok and Dome Fuji because at those sites (1) the horizontal extent of snow layers characterized by different physical properties, as a rule, does not exceed a few meters, which suggests a patchy pattern of their spatial distribution on and below the ice sheet surface (Ekaykin et al., 2023; Fujita et al., 2009), and (2) the variability in the density (Hörhold et al., 2011) and microstructural properties (Gregory et al., 2014) of firn is relatively low, as is the stratigraphic-scale variability in the air content of ice (Lipenkov et al., 1997, 2011). In addition, the firn can be affected by layering. Pore closure in denser layers occurs at a shallower depth compared to the pore closure for layers that are less dense. However, in sites with low accumulation it was shown that, regardless of their density (denser or less dense), V_c and hence V are similar in both types of layers (Fourteau et al., 2019).

The snow metamorphism on the cold Antarctic Plateau is essentially a summertime phenomenon. It speeds up when the temperature of the uppermost layers of snow rises well above the mean annual temperature, thus increasing both the equilibrium concentration of water vapor in the snow pores and the temperature gradients in the near-surface snow. Elevated temperatures and strong temperature gradients promote the rapid growth of snow grains and the formation of a coarse-grained snow structure. Small-scale stratigraphic variations in the snow structure, which are typical in the upper few meters of the snow column, progressively disappear with depth (Alley, 1980), while the average grain size remains related to temperature conditions prevailing at the time of snow diagenesis near the ice sheet surface.

According to the model proposed by Arnaud (1997) for the Antarctic ice sheet, the pore volume at close-off, V_c, should increase with the mean annual surface temperature through the competing densification mechanisms: higher temperature leads to an increase in the relative critical density at the transition between snow and firn (at EDC the critical density is reached at a depth of about 25 m below surface), which in turn implies a greater proportion of the ice grain edges occupied by pores at close-off and hence a larger V_c. Our work (Fig. 1) shows a poor correlation and large spectral differences between TAC and mean annual surface temperatures. In contrast we observe a strong anti-correlation between TAC and the simulated mean surface summer temperature. This observation suggests that summer temperature has an inverse effect on V_c compared to the mean annual temperature. Indeed, TAC increases with the ratio of the number of pores to the number of ice crystals at close-off. This latter parameter depends on the critical density of the snow, D_0, which corresponds to the transition between grain boundary sliding (GBS) and power law creep (PLC) as the dominant densification mechanism: the higher the critical density of snow, the greater the number of pores per grain and therefore the larger the TAC value at close-off (Arnaud, 1997). Since GBS decreases for larger grains (Alley, 1987), while PLC does not depend much on the grain size, D_0 should also decrease when the grains are big.

Thus, time periods with a warmer local summer temperature (due to high local insolation) promote a coarser-grained snow structure and hence lower critical density of snow and reduced TAC at pore closure and vice versa. This mechanism is proposed here to explain the strong anti-correlation observed between TAC and the mean summer surface temperature. A numerical model, which takes into account the successive mechanisms involved between the surface snow and the closure of pores, is still required.

7 Conclusions

The lack of seasonal temperature reconstruction on Antarctica hampers a good understanding of the forcing and mechanism of climate changes over this climatically sensitive region. In this study, we revisit the TAC record measured in the EDC ice core covering the last 440 ka. We show that it is dominated by a 40 kyr periodicity and is anti-correlated with the local mean insolation over the astronomical half-year summer. In order to further investigate this link between local summer insolation changes and TAC variations, we look into the correlation between the EDC TAC record and simulated local summer temperature changes by the LOVECLIM1.3 model. We also evidence an anti-correlation between those two independent variables. We explain the anti-correlations between the local summer insolation and the EDC TAC, as well as between the local summer temperature and the EDC TAC, by proposing that (1) the local summer insolation controls the development of strong temperature gradients in the near-surface snow during the summer, (2) those summer temperature gradients are then modifying the surface snow structure and (3) eventually these snow structure changes propagate through the firn during the densification process down to the close-off depth where they impact the pore volume, i.e., the TAC of air bubbles (Lipenkov et al., 2011; Raynaud et al., 2007). These results point towards the fact that the EDC TAC record could be used as a unique proxy for local summer temperature. Future studies should investigate this relationship between TAC variations and local summer temperature changes in other ice core records drilled in Antarctica and Greenland.

The comparison between TAC and δD records indicates that the major driving factors for the summer and annual mean temperatures are different at the EDC. TAC is strongly linked to local summer temperature, while the annual mean temperature is strongly controlled by the glacial–interglacial boundary conditions like the global ice volume and GHGs. We show that the LOVECLIM1.3 model could capture the orbital-scale variability in the δD-based temperature reconstruction. Our transient simulation, which allows us to investigate the relative effect of insolation, atmospheric greenhouse gas concentrations and NH ice sheet volume changes, shows that, as compared to insolation, GHGs and NH ice sheets have a weak effect on the summer temperature but a strong effect on annual mean temperatures. Future modeling studies should also investigate the impact of past Antarctic ice sheet changes on local summer temperatures and consequently on TAC records. Overall, our model results confirm the hypothesis made from the spectral characteristics of the EDC TAC and δD records, explaining why these two records display different orbital periodicities.

Data availability. The data used in this study are available at https://doi.org/10.5281/zenodo.11096723 (Raynaud et al., 2024).

Supplement. The supplement related to this article is available online at: https://doi.org/10.5194/cp-20-1269-2024-supplement.

Author contributions. DR and QY designed the research. QY, ZW and AB performed the research related to the LOVECLIM1.3 simulations. DR, FP, EC and VL performed the research based on the EDC TAC record. QY, EC and DR wrote a draft of the paper with subsequent inputs from all the other authors.

Competing interests. At least one of the (co-)authors is a member of the editorial board of *Climate of the Past*. The peer-review process was guided by an independent editor, and the authors also have no other competing interests to declare.

Special issue statement. This article is part of the special issue "Ice core science at the three poles (CP/TC inter-journal SI)". It is not associated with a conference.

Acknowledgements. The authors would like to warmly thank Jean Jouzel and Paul Duval for insightful discussions. The authors are also grateful to the two anonymous reviewers and Edward Brook for their constructive comments that helped improve this study. This work is a contribution to EPICA, a joint European Science Foundation/European Commission (EU) scientific program, funded by the EU and by national contributions from Belgium, Denmark, France, Germany, Italy, The Netherlands, Norway, Sweden, Switzerland, and the UK. The main logistical support was provided by IPEV and PNRA (at Dome C) and AWI (at Dronning Maud Land). This is EPICA publication no. 322.

Financial support. The modelling part of this work was supported by the Fonds de la Recherche Scientifique-FNRS (F.R.S.-FNRS) under grant nos. T.0246.23 and T.W019.23. Qiuzhen Yin is a research associate at F.R.S.-FNRS. Zhipeng Wu is supported by the F.R.S.-FNRS grant no. T.0246.23. Computational resources have been provided by the supercomputing facilities of the Université catholique de Louvain (CISM/UCL) and the Consortium des Équipements de Calcul Intensif en Fédération Wallonie Bruxelles (CÉCI) funded by the Fond de la Recherche Scientifique de Belgique (F.R.S.-FNRS) under convention 2.5020.11. The research leading to these results has received funding from the French National Research Agency under "Programme d'Investissements d'Avenir" (ANR-19-MPGA-0001) through the Make Our Planet Great Again HOTCLIM project. Emilie Capron also acknowledges financial support from the AXA Research Fund.

Review statement. This paper was edited by Edward Brook and reviewed by two anonymous referees.

References

Alley, R. B.: Densification and Recrystallization of Firn at Dome C, East Antarctica, Institute of Polar Studies, The Ohio State University, Columbus, Ohio, https://kb.osu.edu/items/43b2d2ab-503a-5a53-a962-c433e371c064 (last access: 7 June 2024), 1980.

Alley, R. B.: Firn densification by grain boundary sliding, J. Phys. (Paris), 48, 249–256, 1987.

Anderson, D. L. and Benson, G. S.: The densification and diagenesis of snow: properties, processes and applications, in: Ice and snow: properties, processes, and applications, edited by: Kingery, V. V. D., MIT Press, Cambridge, MA, 391–411, https://authors.library.caltech.edu/records/jm9c7-3d977 (last access: 7 June 2024), 1963.

Arnaud, L.: Modélisation de la transformation de la neige en glace à la surface des calottes polaires, étude du transport des gaz dans ces milieux poreux, PhD thesis, Université Joseph Fourier, Grenoble, https://archivesic.ccsd.cnrs.fr/UNIV-GRENOBLE1/tel-00709566 (last access: 7 June 2024), 1997.

Bazin, L., Landais, A., Lemieux-Dudon, B., Toyé Mahamadou Kele, H., Veres, D., Parrenin, F., Martinerie, P., Ritz, C., Capron, E., Lipenkov, V., Loutre, M.-F., Raynaud, D., Vinther, B., Svensson, A., Rasmussen, S. O., Severi, M., Blunier, T., Leuenberger, M., Fischer, H., Masson-Delmotte, V., Chappellaz, J., and Wolff, E.: An optimized multi-proxy, multi-site Antarctic ice and gas orbital chronology (AICC2012): 120–800 ka, Clim. Past, 9, 1715–1731, https://doi.org/10.5194/cp-9-1715-2013, 2013.

Bender, M. L.: Orbital tuning chronology for the Vostok climate record supported by trapped gas composition, Earth Planet. Sc. Lett., 204, 275–289, 2002.

Bereiter, B., Eggleston, S., Schmitt, J., Nehrbass-Ahles, C., Stocker, T. F., Fischer, H., Kipfstuhl, S., and Chappellaz, J.: Revision of the EPICA Dome C CO_2 record from 800 to 600 yr before present, Geophys. Res. Lett., 42, 542–549, 2015.

Berger, A.: Long-Term Variations of Daily Insolation and Quaternary Climatic Changes, J. Atmos. Sci., 35, 2362–2367, https://doi.org/10.1175/1520-0469(1978)035<2362:LTVODI>2.0.CO;2, 1978.

Berger, A. and Loutre, M. F.: Insolation values for the climate of the last 10 million years, Quaternary Sci. Rev., 10, 297–317, 1991.

Berger, A. and Loutre, M. F.: Long-term variations of the astronomical seasons, in: Topics in Atmospheric and Interstellar Physics and Chemistry. Les Ulis: Les Editions de Physique, edited by: Boutron, C., Les Editions de la physique, 33–61, ISBN 2-86883-241-5, 1994.

Berger, A. and Yin, Q. Z.: Astronomical theory and orbital forcing, in: The Sage handbook of environmental change, edited by: Matthews, J. A., Bartlein, P. J., Briffa, K. R., Dawson, A. G., de Vernal, A., Denham, T., Fritz, S. C., and Oldfield, F., SAGE, London, 405–425, https://doi.org/10.4135/9781446253045.n19, 2012.

Berger, A., Loutre, M. F., and Tricot, C.: Insolation and Earth's orbital periods, J. Geophys. Res.-Atmos., 98, 10341–10362, https://doi.org/10.1029/93JD00222, 1993.

Berger, A., Loutre, M. F., and Yin, Q.: Total irradiation during any time interval of the year using elliptic integrals, Quaternary Sci. Rev., 29, 1968–1982, 2010.

Berger, A., Yin, Q. Z., and Wu, Z. P.: Length of astronomical seasons, total and average insolation over seasons, Quaternary Sci. Rev., 334, 108620, https://doi.org/10.1016/j.quascirev.2024.108620, 2024.

Bouchet, M., Landais, A., Grisart, A., Parrenin, F., Prié, F., Jacob, R., Fourré, E., Capron, E., Raynaud, D., Lipenkov, V. Y., Loutre, M.-F., Extier, T., Svensson, A., Legrain, E., Martinerie, P., Leuenberger, M., Jiang, W., Ritterbusch, F., Lu, Z.-T., and Yang, G.-M.: The AICC2023 chronological framework and associated timescale for the EPICA Dome C ice core, EGUsphere [preprint], https://doi.org/10.5194/egusphere-2023-1081, 2023.

Buizert, C., Fudge, T. J., Roberts, W. H. G., Steig, E. J., Sherriff-Tadano, S., Ritz, C., Lefebvre, E., Edwards, J., Kawamura, K., Oyabu, I., Motoyama, H., Kahle, E. C., Jones, T. R., Abe-Ouchi, A., Obase, T., Martin, C., Corr, H., Severinghaus, J. P., Beaudette, R., Epifanio, J. A., Brook, E. J., Martin, K., Chappellaz, J., Aoki, S., Nakazawa, T., Sowers, T. A., Alley, R. B., Ahn, J., Sigl, M., Severi, M., Dunbar, N. W., Svensson, A., Fegyveresi, J. M., He, C., Liu, Z., Zhu, J., Otto-Bliesner, B. L., Lipenkov, V. Y., Kageyama, M., and Schwander, J.: Antarctic surface temperature and elevation during the Last Glacial Maximum, Science, 372, 1097–1101, 2021.

Cauquoin, A., Landais, A., Raisbeck, G. M., Jouzel, J., Bazin, L., Kageyama, M., Peterschmitt, J.-Y., Werner, M., Bard, E., and Team, A.: Comparing past accumulation rate reconstructions in East Antarctic ice cores using 10Be, water isotopes and CMIP5-PMIP3 models, Clim. Past, 11, 355–367, https://doi.org/10.5194/cp-11-355-2015, 2015.

Dome Fuji Ice Core Project Members: State dependence of climatic instability over the past 720,000 years from Antarctic ice cores and climate modeling, Sci. Adv., 3, e1600446, https://doi.org/10.1126/sciadv.1600446, 2017.

Eicher, O., Baumgartner, M., Schilt, A., Schmitt, J., Schwander, J., Stocker, T. F., and Fischer, H.: Climatic and insolation control on the high-resolution total air content in the NGRIP ice core, Clim. Past, 12, 1979–1993, https://doi.org/10.5194/cp-12-1979-2016, 2016.

Ekaykin, A. A., Lipenkov, V. Y., and Teben'kova, N. A.: Fifty years of instrumental surface mass balance observations in central Antarctica, J. Glaciol., https://doi.org/10.1017/jog.2023.53, in press, 2023.

Epifanio, J. A., Brook, E. J., Buizert, C., Pettit, E. C., Edwards, J. S., Fegyveresi, J. M., Sowers, T. A., Severinghaus, J. P., and Kahle, E. C.: Millennial and orbital-scale variability in a 54 000-year record of total air content from the South Pole ice core, The Cryosphere, 17, 4837–4851, https://doi.org/10.5194/tc-17-4837-2023, 2023.

Fourteau, K., Martinerie, P., Faïn, X., Schaller, C. F., Tuckwell, R. J., Löwe, H., Arnaud, L., Magand, O., Thomas, E. R., Freitag, J., Mulvaney, R., Schneebeli, M., and Lipenkov, V. Ya.: Multi-tracer study of gas trapping in an East Antarctic ice core, The Cryosphere, 13, 3383–3403, https://doi.org/10.5194/tc-13-3383-2019, 2019.

Fujita, S., Okuyama, J., Hori, A., and Hondoh, T.: Metamorphism of stratified firn at Dome Fuji, Antarctica: a mechanism for local insolation modulation of gas transport conditions during bubble close off, J. Geophys. Res., 114, F03023, https://doi.org/10.1029/2008JF001143, 2009.

Ganopolski, A. and Calov, R.: The role of orbital forcing, carbon dioxide and regolith in 100 kyr glacial cycles, Clim. Past, 7, 1415–1425, https://doi.org/10.5194/cp-7-1415-2011, 2011.

Goosse, H., Brovkin, V., Fichefet, T., Haarsma, R., Huybrechts, P., Jongma, J., Mouchet, A., Selten, F., Barriat, P. Y., Campin, J. M., Deleersnijder, E., Driesschaert, E., Goelzer, H., Janssens, I., Loutre, M. F., Morales, Maqueda, M. A., Opsteegh, T., Mathieu, P. P., Munhoven, G., Petterson, J. E., Renssen, H., Roche, D., Schaeffer, M., Tartinville, B., Timmermann, A., and Weber, S. L.: Description of the earth system model of intermediate complexity LOVECLIM version 1.2, Geosci. Model Dev., 3, 603–633, https://doi.org/10.5194/gmd-3-603-2010, 2010.

Gregory, S. A., Albert, M. R., and Baker, I.: Impact of physical properties and accumulation rate on pore close-off in layered firn, The Cryosphere, 8, 91–105, https://doi.org/10.5194/tc-8-91-2014, 2014.

Hörhold, M. W., Kipfstuhl, S., Wilhelms, F., Freitag, J., and Frenzel, A.: The densification of layered polar firn. J. Geophys. Res.-Earth, 116, F01001, https://doi.org/10.1029/2009JF001630, 2011.

Huybers, P. J. and Denton, G. H.: Antarctic temperature at orbital timescales controlled by local summer duration, Nat. Geosci., 1, 787–792, 2008.

Jones, T. R., Cuffey, K. M., Roberts, W. H. G., Markle, B. R., Steig, E. J., Stevens, C. M., Valdes, P. J., Fudge, T. J., Sigl, M., Hughes, A. G., Morris, V., Vaughn, B., Garland, J., Vinther, B. M., Rozmiarek, K. S., Brashear, C. A., and White, J. W. C.: Seasonal temperatures in West Antarctica during the Holocene, Nature, 613, 292–297, 2023.

Jouzel, J., Masson-Delmotte, V., Cattani, O., Dreyfus, G., Falourd, S., Hoffmann, G., Minster, B., Nouet, J., Barnola, J.-M., Fisher, H., Gallet, J.-C., Johnsen, S., Leuenberger, M., Loulergue, L., Luethi, D., Oerter, H., Parrenin, F., Raisbeck, G., Raynaud, D., Schilt, A., Schwander, J., Selmo, J., Souchez, R., Spahni, R., Stauffer, B., Steffensen, J. P., Stenni, B., Stocker, T. F., Tison, J.-L., Werner, M., and Wolff, E. W.: Orbital and millennial Antarctic climate variability over the past 800,000 years, Science, 317, 793–796, 2007.

Kawamura, K., Parrenin, F., Lisiecki, L., Uemura, R., Vimeux, F., Severinghaus, J. P., Hutterli, M. A., Nakazawa, T., Aoki, S., Jouzel, J., Raymo, M. E., Matsumoto, K., Nakata, H., Motoyama, H., Fujita, S., Goto-Azuma, K., Fujii, K.,and Watanabe, O.: Northern hemisphere forcing of climatic cyles over the past 360,000 years implied by accurately dated Antarctic ice cores, Nature, 448, 912–916, 2007.

Laepple, T., Werner, M., and Lohmann, G. S.: Synchronicity of Antarctic temperatures and local solar insolation on orbital timescales, Nature, 471, 91–94, 2011.

Landais, A., Dreyfus, G., Capron, E., Pol, K., Loutre, M. F., Raynaud, D., Lipenkov, V. Y., Arnaud, L., Masson-Delmotte, V., Paillard, D., Jouzel, J., and Leuenberger, M.: Towards orbital dating of the EPICA Dome C ice core using $\delta O_2/N_2$, Clim. Past, 8, 191–203, https://doi.org/10.5194/cp-8-191-2012, 2012.

Lipenkov, V., Candaudap, F., Ravoire, J., Dulac, E., and Raynaud, D.: A new device for air content measurements in polar ice, J. Glaciol., 41, 423–429, https://doi.org/10.3189/S0022143000016294, 1995.

Lipenkov, V. Y., Salamatin, A. N., and Duval, P.: Bubbly-ice densification in ice sheets: II. Applications, J. Glaciol., 43, 397–407, 1997.

Lipenkov, V. Y., Raynaud, D., Loutre, M. F., and Duval, P.: On the potential of coupling air content and O_2/N_2 from trapped air for establishing an ice core chronology tuned on local insolation, Quaternary Sci. Rev., 30, 3280–3289, https://doi.org/10.1016/j.quascirev.2011.07.013, 2011.

Lisiecki, L. E. and Raymo, M. E.: Plio-Pleistocene Stack of 57 Globally Distributed Benthic $\delta^{18}O$ Records, Paleoceanography, 20, PA1003, https://doi.org/10.1029/2004PA001071, 2005.

Loulergue, L., Schilt, A., Spahni, R., Masson-Delmotte, V., Blunier, T., Lemieux, B., Barnola, J. M., Raynaud, D., Stocker, T. F., and Chappellaz, J.: Orbital and millennial-scale features of atmospheric CH_4 over the past 800,000 years, Nature, 453, 383–386, 2008.

Lüthi, D., Le Floch, M., Bereiter, B., Blunier, T., Barnola, J.-M., Siegenthaler, U., Raynaud, D., Jouzel, J., Fischer, H., Kawamura, K., and Stocker, T. F.: High-resolution carbon dioxide concentration record 650,000–800,000 years before present, Nature, 453, 379–382, 2008.

Martinerie, P., Raynaud, D., Etheridge, D. M., Barnola, J.-M., and Mazaudier, D.: Physical and climatic parameters which influence the air content in polar ice, Earth Planet. Sc. Lett., 112, 1–13, https://doi.org/10.1016/0012-821X(92)90002-D, 1992.

Martinerie, P., Lipenkov, V. Y., Raynaud, D., Chappellaz, J., Barkov, N. I., and Lorius, C.: The air content paleo record in the Vostok ice core (Antarctica): a mixed record of climatic and glaciological parameters, J. Geophys. Res., 99, 10565–10576, https://doi.org/10.1029/93JD03223, 1994.

Raynaud, D., Lipenkov, V., Lemieux-Dudon, B., Duval, P., Loutre, M.-F., and Lhomme, N.: The local insolation signature of air content in Antarctic ice. A new step toward an absolute dating of ice records, Earth Planet. Sci. Lett., 261, 337–349, https://doi.org/10.1016/j.epsl.2007.06.025, 2007.

Raynaud, D., Qiuzhen, Y., and Capron, E.: Raynaud et al_Climate_of_the_Past2024_Data [Data set], Zenodo [data set], https://doi.org/10.5281/zenodo.11096723, 2024.

Schilt, A., Baumgartner, M., Schwander, J., Buiron, D., Capron, E., Chappellaz, J., Loulergue, L., Schüpbach, S., Spahni, R., Fischer, H., and Stocker, T. F.: Atmospheric nitrous oxide during the last 140,000 years, Earth Planet. Sc. Lett., 300, 33–43, 2010.

Stenni, B., Selmo, E., Masson-Delmotte, V., Oerter, H., Meyer, H., Röthlisberger, R., Jouzel, J., Cattani, O., Falourd, S., Fischer, H., Hoffmann, G., Lacumin, P., Johnsen, S. J., and Minster, B.: The deuterium excess records of EPICA Dome C and Dronning Maud Land ice cores (East Antarctica), Quaternary Sci. Rev., 29, 146–159, 2010.

Veres, D., Bazin, L., Landais, A., Toyé Mahamadou Kele, H., Lemieux-Dudon, B., Parrenin, F., Martinerie, P., Blayo, E., Blunier, T., Capron, E., Chappellaz, J., Rasmussen, S. O., Severi, M., Svensson, A., Vinther, B., and Wolff, E. W.: The Antarctic ice core chronology (AICC2012): an optimized multi-parameter and multi-site dating approach for the last 120 thousand years, Clim. Past, 9, 1733–1748, https://doi.org/10.5194/cp-9-1733-2013, 2013.

Wu, Z. P., Yin, Q. Z., Ganopolski, A., Berger, A., and Guo, Z. T.: Effect of Hudson Bay closure on global and regional climate under different astronomical configurations, Global Planet. Change, 222, 104040, https://doi.org/10.1016/j.gloplacha.2023.104040, 2023.

Yin, Q. and Berger, A.: Interglacial analogues of the Holocene and its natural near future, Quaternary Sci. Rev., 120, 28–46, 2015.

Yin, Q. Z. and Berger, A.: Individual contribution of insolation and CO_2 to the interglacial climates of the past 800 000 years, Clim. Dynam., 38, 709–724., https://doi.org/10.1007/s00382-011-1013-5, 2012.

Yin, Q. Z., Wu, Z. P., Berger, A., Goosse, H., and Hodell, D.: Insolation triggered abrupt weakening of Atlantic circulation at the end of interglacials, Science, 373, 1035–1040, 2021.

Clim. Past, 17, 1903–1918, 2021
https://doi.org/10.5194/cp-17-1903-2021

Climate of the Past
Open Access

Stalagmite carbon isotopes suggest deglacial increase in soil respiration in western Europe driven by temperature change

Franziska A. Lechleitner[1,2,★], **Christopher C. Day**[1], **Oliver Kost**[3], **Micah Wilhelm**[4], **Negar Haghipour**[3,5], **Gideon M. Henderson**[1], **and Heather M. Stoll**[3]

[1]Department of Earth Sciences, University of Oxford, South Parks Road, OX1 3AN, Oxford, UK
[2]Department of Chemistry, Biochemistry and Pharmaceutical Sciences and Oeschger Centre for Climate Change Research, University of Bern, Freiestrasse 3, 3012 Bern, Switzerland
[3]Department of Earth Sciences, ETH Zurich, Sonneggstrasse 5, 8006 Zurich, Switzerland
[4]Swiss Federal Institute for Forest, Snow and Landscape Research, Zürcherstrasse 111, 8903 Birmensdorf, Switzerland
[5]Laboratory for Ion Beam Physics, ETH Zurich, Otto-Stern-Weg 5, 8093 Zurich, Switzerland
[★]Invited contribution by Franziska A. Lechleitner, recipient of the EGU Climate: Past, Present & Future Division Outstanding Early Career Scientists Award 2021.

Correspondence: Franziska A. Lechleitner (franziska.lechleitner@unibe.ch)

Received: 14 January 2021 – Discussion started: 4 February 2021
Revised: 19 July 2021 – Accepted: 18 August 2021 – Published: 24 September 2021

Abstract. The temperate region of western Europe underwent significant climatic and environmental change during the last deglaciation. Much of what is known about the terrestrial ecosystem response to deglacial warming stems from pollen preserved in sediment sequences, providing information on vegetation composition. Other ecosystem processes, such as soil respiration, remain poorly constrained over past climatic transitions but are critical for understanding the global carbon cycle and its response to ongoing anthropogenic warming. Here we show that speleothem carbon isotope ($\delta^{13}C_{spel}$) records may retain information on soil respiration and allow its reconstruction over time. While this notion has been proposed in the past, our study is the first to rigorously test it, using a combination of multi-proxy geochemical analysis ($\delta^{13}C$, Ca isotopes, and radiocarbon) on three speleothems from the NW Iberian Peninsula and quantitative forward modelling of processes in soil, karst, and cave. Our study is the first to quantify and remove the effects of prior calcite precipitation (PCP, using Ca isotopes) and bedrock dissolution (using the radiocarbon reservoir effect) from the $\delta^{13}C_{spel}$ signal to derive changes in respired $\delta^{13}C$. The coupling of soil gas pCO_2 and $\delta^{13}C$ via a mixing line describing diffusive gas transport between an atmospheric and a respired end-member allows the modelling of changes in soil respiration in response to temperature. Using this coupling and a range of other parameters describing carbonate dissolution and cave atmospheric conditions, we generate large simulation ensembles from which the results most closely matching the measured speleothem data are selected. Our results robustly show that an increase in soil gas pCO_2 (and thus respiration) is needed to explain the observed deglacial trend in $\delta^{13}C_{spel}$. However, the Q_{10} (temperature sensitivity) derived from the model results is higher than current measurements, suggesting that part of the signal may be related to a change in the composition of the soil respired $\delta^{13}C$, likely from changing substrate through increasing contribution from vegetation biomass with the onset of the Holocene.

1 Introduction

The last deglaciation was a period of profound global climate change. Between 22 and 10 ka (thousands of years before 1950), global mean surface air temperatures increased by up to ∼ 6 °C (Tierney et al., 2020), leading to the disintegration of the large Northern Hemisphere ice sheets and a consequent rise in global sea level by ∼ 80–120 m (Bova et al., 2021; Lambeck et al., 2014). On land, shifts in ecosystem types and vegetation productivity accompanied the deglacial climate change, with repercussions for the terrestrial carbon cycle and the release of greenhouse gases to the atmosphere (Clark et al., 2012). The temperate region of western Europe was particularly affected by large and latitudinally diverse environmental changes during the last deglaciation, driven by its proximity to the Scandinavian Ice Sheet and the North Atlantic (Moreno et al., 2014). Over the entire region, terrestrial paleo-climate records indicate a transition from colder to warmer climatic conditions, punctuated by millennial-scale events which closely match the Greenland ice core record (Genty et al., 2006; Moreno et al., 2014). Pollen records from western Europe reveal a general deglacial trend from grassland steppe and tundra ecosystems towards landscapes dominated by temperate forest and provide evidence for a remarkably rapid ecosystem response to temperature changes on millennial scales over the last glacial (Fletcher et al., 2010).

Speleothem carbon isotope ($\delta^{13}C_{spel}$) records from the temperate region of western Europe are often clearly correlated to regional temperature reconstructions during the last glacial (Genty et al., 2003) and the deglaciation (Baldini et al., 2015; Denniston et al., 2018; Genty et al., 2006; Moreno et al., 2010; Rossi et al., 2018; Verheyden et al., 2014) (Fig. 1), pointing towards a regionally coherent mechanism driving the response to the temperature increase. Early on, Genty et al. (2006, 2003) suggested that the temperature sensitivity of $\delta^{13}C_{spel}$ in western Europe was likely related to the response of vegetation and soil respiration to climate warming. Higher concentrations of respired CO_2 in the soil gas lower its $\delta^{13}C$ signature, due to the increase in strongly fractionated organic carbon in the system. Speleothems can capture this change as they are fed by drip water, which equilibrates with soil gas pCO_2 before proceeding to the dissolution of carbonate bedrock. This mechanism could lead to the observed transitions from higher $\delta^{13}C_{spel}$ during colder periods to lower $\delta^{13}C_{spel}$ during warmer periods and may provide a means to quantify past changes in soil respiration, an elusive parameter in the global carbon cycle (Bond-Lamberty and Thomson, 2010). However, formal testing of this mechanism has so far not been attempted, mainly because of the numerous and complex processes that influence $\delta^{13}C_{spel}$ (Fohlmeister et al., 2020).

Speleothem carbon can originate from three sources: atmospheric CO_2, biogenic CO_2 from autotrophic (root and rhizosphere) and heterotrophic (soil microbial) soil respiration (from here onwards jointly referred to as "soil respiration"), and the carbonate bedrock itself (Fig. 2). Recent research has additionally suggested that deep underground reservoirs of carbon ("ground air"; Mattey et al., 2016) or deeply rooted vegetation (Breecker et al., 2012) may play a significant role in the karst carbon cycle. The relative importance of these different sources on $\delta^{13}C_{spel}$ is modulated by hydroclimate and temperature. This can occur as a propagation of a biosphere response to climate change, e.g. changes in vegetation composition (Braun et al., 2019), changes in soil respiration (Genty et al., 2003), and changes in soil turnover rates (Rudzka et al., 2011). Secondly, $\delta^{13}C_{spel}$ can be modulated by changes in karst hydrology, i.e. the carbonate bedrock dissolution regime (Hendy, 1971). Thirdly, compounded changes in hydrology and cave atmospheric pCO_2 can lead to prior calcite precipitation (PCP) during carbonate precipitation (Fohlmeister et al., 2020). Altitudinal transects in caves in the European Alps have shown that changes in soil respiration, vegetation, and temperature have a traceable effect on speleothem fabrics, stable oxygen isotope ratios, and $\delta^{13}C_{spel}$ (Borsato et al., 2015). So far, it has not been possible to disentangle these effects and quantify their relative importance on $\delta^{13}C_{spel}$ records, but this quantification is a crucial step towards evaluating the potential of $\delta^{13}C_{spel}$ as a paleo-soil respiration proxy. Here, we generate a multi-proxy dataset from three stalagmites from the NW Iberian Peninsula and use quantitative forward modelling to show that changes in soil respiration can explain much of the observed deglacial trend in western European $\delta^{13}C_{spel}$. Our approach is the first to leverage differing proxy sensitivities to quantitatively model key environmental parameters, in particular soil gas pCO_2, allowing us to estimate the total temperature sensitivity of soil respiration (Q_{10}), including the effect of changing vegetation communities.

2 Study site and samples

El Pindal and La Vallina caves are located ~30 km apart on the coastal plain in Asturias, NW Iberian Peninsula, at 23 and 70 m a.s.l., respectively (43° 12′ N, 4° 30′ W; Fig. 1). Both caves developed in the non-dolomitic, Carboniferous limestones of the Barcaliente formation, with an overburden of 10–35 m of bedrock for El Pindal Cave and 10–20 m for the gallery in which samples were collected in La Vallina.

Current climate in the NW Iberian Peninsula is characterised by temperate maritime conditions, with clear precipitation seasonality but no summer drought (Peinado Lorca and Martínez-Parras, 1987). The region is strongly affected by North Atlantic climate conditions, in contrast to the rest of the Iberian Peninsula, where North Atlantic and Mediterranean influences persist (Moreno et al., 2010). Both caves are affected by similar climatic conditions, with ~1250 mm/yr annual precipitation (Stoll et al., 2013) and maximum precipitation occurring in November (140 mm/month) (AEMET meteorological stations at Santander and Oviedo, period 1973–2010; AEMET, 2020). Due to the proximity to the coast, temperature exhibits a clear but modest seasonality, with averages of 9 °C for winter months (December–March) and 20 °C for summer months (June–September) (AEMET meteorological station at Santander, period 1987–2000; AEMET, 2020). For the last deglaciation, quantitative estimates of temperature can be derived from marine records from the western and southern Iberian margins. These likely give a reasonable estimate of the deglacial temperature change in caves on the coastal plain, as the re-

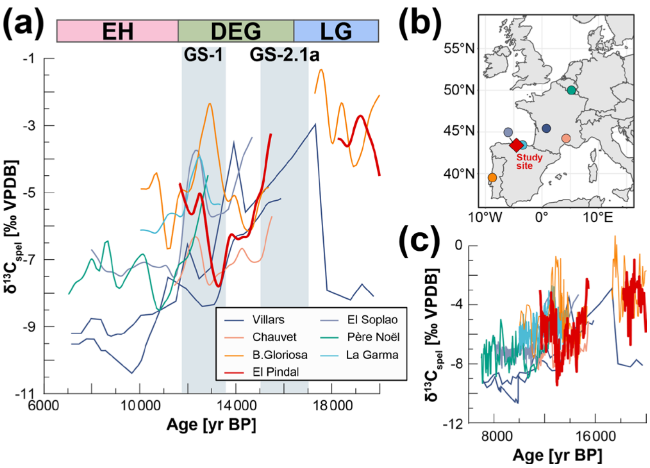

Figure 1. Speleothem $\delta^{13}C$ records covering the last deglaciation in temperate western Europe. **(a)** $\delta^{13}C_{spel}$ vs. age, colour-coded by cave. Villars Cave – stalagmites Vil-stm11 (Genty et al., 2006) and Vil-car-1 (Wainer et al., 2011); Chauvet Cave – stalagmite Chau-stm6 (Genty et al., 2006); El Pindal Cave (studied here)– previously published record from stalagmite Candela (Moreno et al., 2010); La Garma Cave – stalagmite GAR-01 (Baldini et al., 2015); El Soplao Cave – stalagmite SIR-1 (Rossi et al., 2018); Père Noël Cave – stalagmite PN-95-5 (Verheyden et al., 2014); Buraca Gloriosa – stalagmite BG6LR (Denniston et al., 2018). All stalagmite data were extracted from the SISAL database, version 2 (Comas-Bru et al., 2020b, a). Shown here is the millennial-scale trend in the records, calculated using a Gaussian kernel smoother (nest package in R, Rehfeld and Kurths, 2014). Please note that the record from Villars Cave is very low resolution but no hiatus is reported between 18–14 ka. Time slices at the top of the figure are as defined for the modelling in this study. GS: Greenland Stadial, as defined in Rasmussen et al. (2014). **(b)** Cave locations. **(c)** Original (not filtered) records.

gion's modern seasonal cycle displays a similar amplitude to sea surface temperatures (Stoll et al., 2015). Minimum average temperatures are reconstructed for Greenland Stadial 2.1a (GS-2.1a, Heinrich event 1, 18–15 ka; Rasmussen et al., 2014) and are ∼ 8 °C cooler than those of the Early Holocene (∼ 8 ka; Darfeuil et al., 2016).

Previous monitoring data from the two caves reveals seasonal variations in cave air pCO_2 driven by external temperature variations (Moreno et al., 2010; Stoll et al., 2012). Both caves are well ventilated in the cold season with close to atmospheric pCO_2 values but feature elevated CO_2 concentrations during the warm summer season (Stoll et al., 2012). The caves are covered by thin (< 1 m deep) and rocky soils, and modern vegetation is strongly impacted by Late Holocene land use change, including deforestation of native *Quercus ilex* (evergreen oak) for lime kilns above El Pindal Cave, and discontinuous pasture maintained by cycles of burning above both caves. At present, the vegetation above the two caves includes pasture and gorse shrub (*Ulex*), but in some areas above El Pindal Cave, the recent abandonment of pastures has permitted the return of patches of native *Quercus ilex* forest. Above La Vallina Cave, pastures are interspersed with native oak (*Quercus*) and planted groves of *Eucalyptus*, the roots of which penetrate the cave in points directly beneath the tree groves.

Candela is a calcitic stalagmite that grew ∼ 500 m inside El Pindal Cave and was not active at the time of collection (Moreno et al., 2010). Previous investigations revealed that the stalagmite grew between ∼ 25–7 ka and provide high-resolution stable isotope and trace element records (Moreno et al., 2010), as well as radiocarbon (^{14}C) measurements between 15.4–8.8 ka (Rudzka et al., 2011). Growth of Candela is strongly condensed between 18–15.5 and 11–9 ka (Stoll et al., 2013). Stalagmite Laura is from El Pindal Cave, while Galia grew in La Vallina Cave. Both Laura and Galia are also composed of calcite. Previous U–Th dating on Galia revealed intermittent growth between 60 and 4 ka (Stoll et al., 2013), including a short growth phase at 26 ka, which together with the Holocene growth is sampled here. Laura grew between 16.1–14.2 ka, covering the GS-2.1a–Greenland Interstadial 1 (GI-1) interval.

3 Methods

3.1 Geochemical measurements

To minimise sampling bias, samples from all three stalagmites were drilled from the same locations for all geochemical analyses using either a handheld drill or a semi-automated high-precision drill. An aliquot each of the collected powder was used for U–Th dating, $\delta^{13}C$, ^{14}C, and Ca isotopes. In the case of Candela, where a few U–Th dates were available from previous investigations (Moreno et al., 2010), powders for the remaining proxies were drilled from the same sampling holes. Additional paired multi-collector inductively coupled plasma mass spectrometry (MC-ICP-MS) U–Th dates from all three stalagmites are detailed elsewhere (Stoll et al., 2021).

For stable carbon isotopes, an aliquot of powder was analysed on a ThermoFinnigan GasBench II carbonate preparation device at the Geological Institute, ETH Zurich, following the procedure by Breitenbach and Bernasconi (2011). Measurement runs were evaluated using an in-house standard (MS2) that has been linked to NBS19 and the external standard deviation (1σ) for $\delta^{13}C$ is smaller than 0.08 per mil (‰). Isotope values are expressed in per mil and referenced to the Vienna Pee Dee belemnite standard (VPDB).

Radiocarbon measurements were performed at the Laboratory for Ion Beam Physics, ETH Zurich, using a MICADAS (mini radiocarbon dating system) accelerator mass spectrometer (AMS; Synal et al., 2007) coupled to a gas ion source (GIS; Fahrni et al., 2013). Carbonate powders (∼ 1 mg) were dissolved in 85 % H_3PO_4 and the resulting CO_2 gas was directly injected into the GIS. Quality control of the AMS measurements was ensured by measuring oxalic

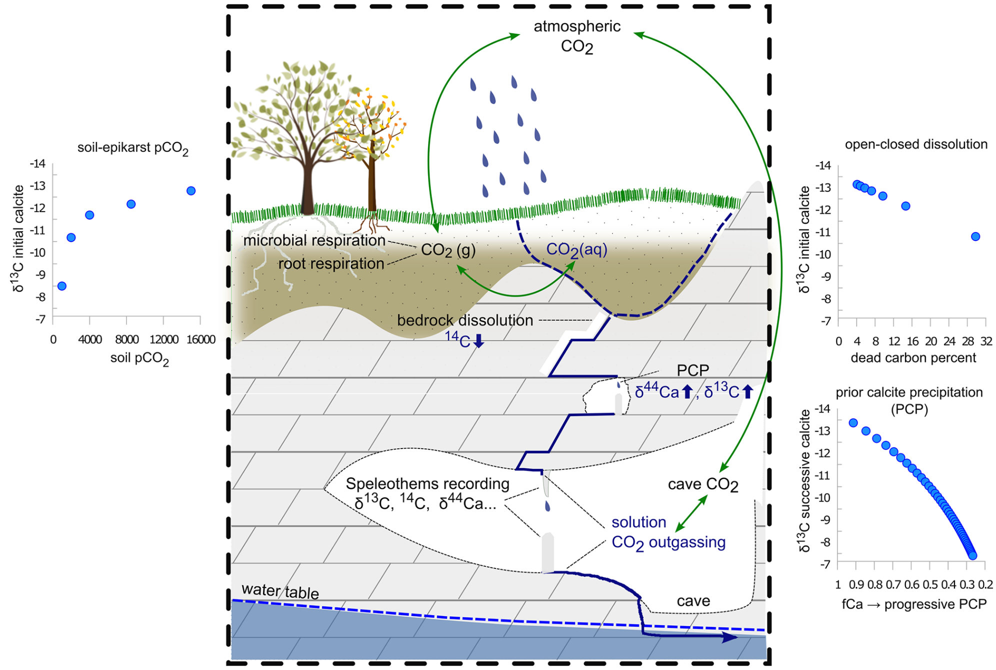

Figure 2. Schematic representation of the main processes modulating $\delta^{13}C$, $\delta^{44/40}Ca$, and ^{14}C in the soil–karst–cave system. The small inserts show the evolution of $\delta^{13}C_{spel}$ in response to changes in soil pCO_2, DCF, and PCP. The dissolution process can be constrained using DCF, while PCP is constrained using $\delta^{44}Ca$. Soil pCO_2 affects all three proxies but can be constrained further using the coupled relationship with $\delta^{13}C$ from the mixing lines. Adapted from Day et al. (2021).

acid II (NIST SRM 4990C), IAEA C-2 as a carbonate standard, and IAEA C-1 as carbonate blank, and measurement precision was better than 10 ‰. We use the ^{14}C reservoir effect ("dead carbon fraction", DCF), which quantifies the amount of fossil carbon incorporated in the speleothems and serves as a tracer for changes in karst hydrology or mean soil carbon age (Genty et al., 2001). The DCF is calculated as the normalised difference between the atmospheric ^{14}C activity ($F^{14}C$; Reimer, 2013) at the time of speleothem deposition (defined through the independent U–Th chronology) and the speleothem ^{14}C activity corrected for decay. Using paired U–Th and ^{14}C ages has the advantage of minimising uncertainty from age modelling interpolation techniques. To account for the uncertainty in matching the speleothem chronology with the atmospheric ^{14}C record (IntCal13 calibration curve; Reimer et al., 2013) the atmospheric record was interpolated to a yearly resolution and matched to 10 000 simulated speleothem ages for each U–Th dating point. The average and standard deviations from these ensembles were then used for the final DCF calculation and uncertainty propagation.

Samples for Ca-isotope analysis were taken from the stalagmites and from three pieces of bedrock overlying both caves. Combined bedrock and stalagmite Ca-isotope analyses allow the reconstruction of the Ca-isotopic composition of the initial growth solution and therefore of the fraction of Ca remaining in solution (f_{Ca}) at the point of stalagmite growth, a quantitative measure for PCP (Owen et al., 2016). Aliquots of $CaCO_3$ (200–650 µg) were dissolved in distilled 2 M HNO_3. The Ca was purified using an automated Ca–Sr separation method (PrepFAST MC, Elemental Scientific, Omaha, NE, USA). This process separates Ca from Sr, Mg, and other matrix elements to avoid isobaric interferences during MC-ICP-MS. Ca-isotope ratios were analysed at the University of Oxford using a Nu Instruments MC-ICP-MS, following the method of Reynard et al. (2011). All solutions were at 10 ± 1 ppm concentration, and the samples were measured with standard-sample bracketing. Each sample was analysed a minimum of 5 times. $\delta^{44/40}Ca$ was calculated using $\delta^{44/40}Ca = \delta^{44/42}Ca \cdot ((43.956 - 39.963)/(43.956 - 41.959))$ (Hippler et al., 2003) and is reported normalised to NIST SRM 915a. Secondary standards HPSnew (in-house standard) and NIST-SRM-915b (purified alongside the samples) were used to determine accuracy and external precision. Measured values for our purified SRM 915b were $\delta^{44/40}Ca = 0.71 \pm 0.06$ ‰ (2se, $n = 12$), which match values obtained by TIMS (thermal ionization mass spectrometry), $\delta^{44/40}Ca = 0.72 \pm 0.04$ ‰ (2se; Heuser and Eisenhauer, 2008). Uncertainty on Ca-isotope data is quoted as the t-distribution-derived 95 % confidence interval on the mean of repeat measurements calculated using either the standard deviation on all repeat measurements on each sample or the standard deviation on all secondary standard analyses, whichever is greater.

3.2 Process modelling and sensitivity analysis

Forward modelling of processes occurring in the soil, karst, and cave allow us to investigate the combination of parameters which would simultaneously simulate $\delta^{13}C_{spel}$, $\delta^{44/40}Ca$, and DCF for each time period sampled. Using $\delta^{44/40}Ca$ and DCF to quantify changes in PCP and bedrock dissolution conditions (open vs. closed system), respectively, we can remove these effects from $\delta^{13}C_{spel}$ and derive soil gas pCO_2 and $\delta^{13}C$ (Fig. 2). We employ the PHREEQC-based, numerical model CaveCalc (Owen et al., 2018), a tool that enables us to evaluate and combine the effects of PCP and bedrock dissolution quantitatively and systematically. We generate large ensembles of simulations from which we then choose the solutions best fitting the measured proxy data. CaveCalc simulates the equilibration between meteoric water and soil CO_2, the subsequent dissolution of the host carbonate rock by this solution, and the degassing of CO_2 from the solution in the cave environment that leads to the formation of speleothem carbonate. Key model inputs (Table 1) are the concentration and isotopic composition of soil CO_2 and the degree to which isotopic exchange during carbonate dissolution occurs under open/closed or intermediate conditions (gas volume relative to solution volume), which set the initial saturation state and isotopic composition of the drip water. Together with the soil gas pCO_2, the pCO_2 of the cave environment is modelled to set the degree of oversaturation the solution will have in the cave, and it determines the amount of carbonate which can precipitate before the solution reaches equilibrium. Constraints on the model parameters are given by $\delta^{13}C_{spel}$, $\delta^{44/40}Ca$, and DCF.

Our primary interest is evaluating constraints on soil respiration, soil gas pCO_2, and its isotopic composition. Soil CO_2 is a mixture of carbon from respired, atmospheric, and bedrock sources, with its concentration depending mainly on temperature, water content, porosity, and soil depth (Amundson et al., 1998; Cerling et al., 1991). Global regressions find growing season soil gas pCO_2 strongly positively correlated with temperature and actual evapotranspiration (Borsato et al., 2015; Brook et al., 1983), and water balance is responsible for a steep gradient in soil pH globally (Slessarev et al., 2016). As soil gas pCO_2 is typically much higher than atmospheric pCO_2, CO_2 diffuses from the soil along concentration gradients, and its concentration and $\delta^{13}C$ value can be approximated using a mixing line between an atmospheric and a soil respired end-member using the Keeling plot approach (Amundson et al., 1998; Cerling et al., 1991; Pataki et al., 2003). Here we use this relationship to test whether changes in soil respiration can realistically explain the observed deglacial $\delta^{13}C_{spel}$ trend. The likely range of values for the soil respired end-member was constrained through monitoring of cave air pCO_2 and $\delta^{13}C_{cave\text{-}air}$ at La Vallina Cave, supplemented by measurements of local atmospheric pCO_2 and $\delta^{13}C$ over 1 year. This is possible because the cave, like the soil, is defined by a two end-member mixing system (soil gas and atmospheric air), driven by seasonal ventilation. Monthly CO_2 measurements reveal a strong correlation between cave air pCO_2 and $\delta^{13}C_{cave\text{-}air}$, in particular during the summer, when soil respiration is highest (Fig. 3a). Our estimation of the modern respired end-member, defined along a mixing line which includes the modern global atmospheric end-member, is -26.9 ± 0.8 ‰. This end-member may be more negative than the preindustrial end-member (which characterised the Early and mid-Holocene growth periods of the stalagmites in this study) because atmospheric $\delta^{13}C$ has decreased by 2 ‰ over the last century due to anthropogenic activities (Suess effect). Assuming modern and decadal age soil carbon pools contributing dominantly to the respired end-member, the preindustrial respired end-member may have been as much as 2 ‰ heavier (~ -25 ‰). If a significant fraction of the respired pool is older, then the preindustrial respired end-member may fall between -27 ‰ and -25 ‰, but this is unlikely since actively growing stalagmites from the cave show rapid post-bomb spike decrease in ^{14}C.

Using this respired end-member, we define mixing lines for relevant periods of the late glacial (LG, before 16.5 ka), deglaciation (DEG, 16.5–11.7 ka), and Early Holocene (EH, after 11.7 ka), using atmospheric CO_2 compositions as published from ice core measurements (Table 1, Fig. 3b). The isotopic composition of the atmospheric CO_2 remains within a few tenths of a per mil of the Holocene value (Schmitt et al., 2012). Therefore, assuming a constant respired end-member, the slope of the mixing line is reduced during periods of lower atmospheric pCO_2 (Fig. 3b). The mixing line may also vary if the respired end-member changes. Although there is variation in the respired end-member both within and among biomes, the mean respired end-member for the potential biomes which may have characterised this site over the last 25 ka – temperate broadleaf, temperate conifer, and boreal – feature mean $\delta^{13}C$ of respired end-members which differ by only 1 ‰ (Fig. 3b; Pataki et al., 2003). This suggests that we cannot predict a systematic change in the $\delta^{13}C$ of the respired end-member with changes in the biome. Moreover, the fact that deglacial trends in $\delta^{13}C_{spel}$ across western Europe are very similar also indicates that highly localised factors that may lead to a strong change in respired $\delta^{13}C$ without a biome change are unlikely. Consequently, we address the potential for variation in the respired end-member by completing a sensitivity analysis of mixing lines which encompass 3 ‰ heavier and lighter respired end-members (Supplement Table S1). For the modelling, we use a maximum soil CO_2 concentration of 8000 ppmv, consistent with predictions based on modern climatology and global regressions of pCO_2 from climatic factors (e.g. Borsato et al., 2015; Brook et al., 1983). Current vegetation density and soil gas pCO_2 may underestimate Holocene conditions that preceded significant land use alteration, but they provide the best available constraints on the end-member. While cave conservation efforts did not permit extensive monitoring of El Pindal Cave, the proximity and similar conditions to La Vallina Cave allow us to use this end-member for both sites.

The sensitivities of the measured speleothem proxies (DCF, $\delta^{44/40}$Ca, and δ^{13}C) to different processes in the soil–karst–cave system allow us to use them to assess the most realistic coupling between measured $\delta^{13}C_{spel}$ and soil gas pCO_2. For each combination of soil gas pCO_2 and δ^{13}C calculated from the mixing lines, changes in mean soil ^{14}C concentration, dissolution conditions (termed "gas volume" and indicating the amount of gas that 1 L of groundwater solution interacts with; Owen et al., 2018), and cave air pCO_2 were allowed to vary within realistic bounds (Table 1). These boundary conditions were set based on the available monitoring data, e.g. cave air pCO_2 was left to vary between atmospheric and the maximum soil gas pCO_2, modelling the effect of cave ventilation dynamics on the proxies. To test whether the system can also be described without invoking changes in soil gas δ^{13}C, we performed a second set of experiments ("sensitivity analysis") where all parameters (soil gas pCO_2, soil ^{14}C, gas volume, cave air pCO_2) were allowed to vary as before but soil gas δ^{13}C was kept constant at −18 ‰ (Table 1).

The model solutions were compared to the measured data from Candela (the stalagmite with the most complete deglacial record) and all solutions matching the measured DCF, $\delta^{44/40}$Ca, and $\delta^{13}C_{spel}$ within a defined interval were extracted. For DCF, the confidence interval of the proxy was chosen, while for $\delta^{13}C_{spel}$ and $\delta^{44/40}$Ca, where measurement uncertainties are much smaller, we defined the threshold at ±1.5 ‰ VPDB and ±0.2 ‰, respectively. Model solutions were filtered sequentially for all three proxies, and each possible permutation of the sequences (e.g. DCF → $\delta^{44/40}$Ca → $\delta^{13}C_{spel}$) was calculated. The median and 25/75 % quantiles of all filtered solution ensembles are used as final model result. To avoid too many solutions without matches to the data, we selected the 5 % simulations closest to the measured proxy value for the sensitivity analysis.

4 Results

4.1 Geochemistry

Both Candela and Galia record a substantial decrease in $\delta^{13}C_{spel}$ between the LG and the EH (Fig. 4). For Candela, $\delta^{13}C_{spel}$ is highest (−2.48 ‰ and −4.43 ‰ VPDB) at 24.9–15.4 ka and then decreases by about 2 ‰ with the onset of GI-1 (14.4–12.9 ka). After a short-lived increase back to values of ∼ −3 ‰ VPDB at 12.3 ka (corresponding to Greenland Stadial 1, GS-1, Younger Dryas), $\delta^{13}C_{spel}$ decreases further to −10 ‰ to −7.7 ‰ VPDB in the EH (8.5–7.9 ka). In Galia, $\delta^{13}C_{spel}$ is −3.88 ‰ VPDB during the LG (26.8 ka) and between −9.78 ‰ and −8.79 ‰ VPDB in the EH (8.7–4.2 ka). Laura covers the time period between 14.3–16.1 ka, where the $\delta^{13}C_{spel}$ decreases from ∼ −1.7 ‰ to −7.8 ‰ VPDB. Importantly, the absolute values and the magnitude

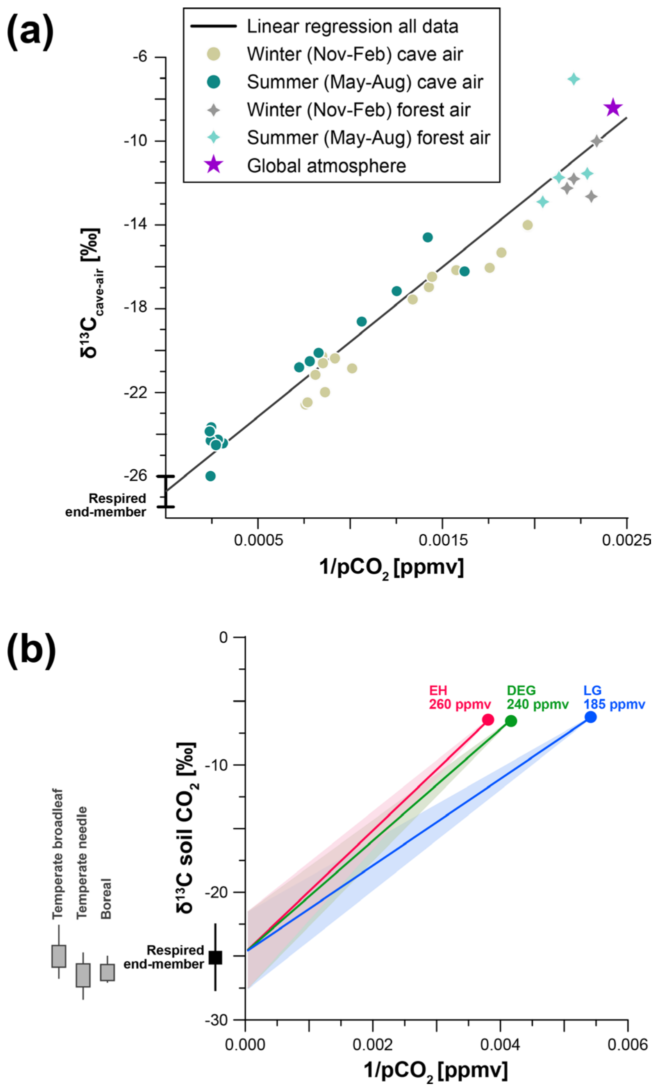

Figure 3. **(a)** Keeling plot of cave and local atmospheric CO_2 used to define the respired end-member of soil gas. The respired end-member is defined through linear regression of the entire dataset. **(b)** Mixing lines defined for the model simulations of past soil gas pCO_2 and δ^{13}C. We define three mixing lines based on the changes in the atmospheric composition (EH, DEG, LG). All three mixing lines use the same respired end-member, with a variability of ±3 ‰ to account for changes in respired substrate. Mean respired δ^{13}C of soil CO_2 across relevant biomes, adapted from Pataki et al. (2003), is shown on the left.

of changes in $\delta^{13}C_{spel}$ in all three stalagmites are comparable over the study period.

The DCF is relatively low in the younger part of the record (∼ 16–4 ka) of all three stalagmites (averages of 6.7 %, 7.2 %, and 13 % for Candela, Galia, and Laura, respectively, Fig. 4). DCF in Candela is slightly higher in the LG portion of the record (∼ 11 %–15 %, 18–20 ka), while values at 24 ka are again comparable with the EH. We disregard the one negative (and physically impossible) DCF value at 24.9 ka, as

Table 1. Model initial parameters used for the mixing line simulations and sensitivity analysis. Model runs were repeated for each time slice (LG, DEG, EH). Details on the mixing line values can be found in Supplement Table S1.

		EH	DEG	LG
Parameters				
T (°C)		12	7	4
Atm. pCO_2 (ppmv)		260	240	185
Soil gas pCO_2 (ppmv)	mixing lines	atm.–8000	atm.–8000	atm.–8000
	sensitivity	280–8000	280–8000	280–8000
Soil gas $\delta^{13}C$ (‰)	mixing lines	atm.–respired	atm.–respired	atm.–respired
	sensitivity	−18	−18	−18
Soil $F^{14}C$		1–0.9	1–0.9	1–0.9
Gas volume (L)		0–500	0–500	0–500
Cave air pCO_2 (ppmv)		atm.–8000	atm.–8000	atm.–8000
Host rock Mg (mmol/mol)		0.6	0.6	0.6
Host rock $\delta^{13}C$ (‰ VPDB)		+3.3	+3.3	+3.3
Host rock $\delta^{44/40}Ca$ (‰)		0.58	0.58	0.58

this is probably an artefact due to issues with U–Th dating in this section (open-system conditions in the basal section of Candela and potentially instrumental issues). For the modelling we use a value of 7 %, which is similar to values obtained for nearby paired U–Th – ^{14}C samples (e.g. 24.2 and 24 ka; Supplement Table S2). The DCF in the LG sample from Galia is much higher (23 %) than any in the three stalagmites, but there is no indication of alteration or other reasons why this sample should not be trusted.

While the absolute $\delta^{44/40}Ca$ values in the individual stalagmites are very different, probably reflecting variations in drip path length and drip interval, leading to different amounts of PCP, their temporal variation is remarkably small. In Candela, a slight tendency towards less negative $\delta^{44/40}Ca$ values can be observed during GS-2.1a, while values are lower during the LG, GS-1, and in the EH (Fig. 4). $\delta^{44/40}Ca$ values in Galia and Laura are within uncertainty of each other. The $\delta^{44/40}Ca$ values of the three bedrock samples are consistent, suggesting a homogeneous source of Ca for the three stalagmites (Fig. 4). This allows us to calculate f_{Ca} and quantitatively estimate the amount of PCP for the stalagmites. By their nature, f_{Ca} values mirror the $\delta^{44/40}Ca$ and suggest that Galia was subject to PCP to a much higher degree than Candela and Laura, where f_{Ca} is comparable. As for the $\delta^{44/40}Ca$, f_{Ca} values in all three stalagmites indicate no major changes over the deglaciation, suggesting minimal changes in PCP.

Comparing the three proxies to temperature reconstructions from the Iberian Margin (Darfeuil et al., 2016), using linear interpolation to roughly match the different records, confirms a negative correlation between $\delta^{13}C_{spel}$ and temperature (−0.63 ‰ °C^{-1} to −0.9 ‰ °C^{-1}, $r^2 = 0.67$–0.96), while the relationship between $\delta^{44/40}Ca$ and DCF to temperature is weak and/or inconsistent (Fig. 5). Since this comparison is meant to simply illustrate the concept, we refrain from using more advanced statistical methods to determine correlations between the records, and also do not consider any chronological and measurement uncertainties associated with either reconstruction.

4.2 Modelling

Each combination of soil gas pCO_2 and $\delta^{13}C$ produced 363 model solutions, resulting in 13 068 solutions for the LG, 11 979 for the DEG, and 10 890 for the EH (the total number of solutions varies due to extrapolation to lower atmospheric pCO_2 during the LG and DEG). However, only a fraction of the simulations resulted in carbonate precipitation (37 % for LG, 40 % for DEG, and 44 % for EH), while for the rest, precipitation was inhibited by the solution not reaching supersaturation with respect to calcium carbonate. Supersaturation was not reached where low soil gas pCO_2 or closed-system conditions reduced the amount of carbonate being dissolved or where the difference between cave air pCO_2 and solution pCO_2 was very small or negative. Thus, there is no need to further prescribe the cave air pCO_2 as a fraction of the soil gas pCO_2, as simulations with unrealistic parameter combinations (i.e. higher cave air pCO_2 than soil gas pCO_2) are automatically discarded.

Simulations from all three mixing lines produce results that match the stalagmite DCF, $\delta^{44/40}Ca$, and $\delta^{13}C_{spel}$ within measurement uncertainty (Fig. 6). Thus, the initial parameter selection was sufficient to constrain the system and the estimate of the soil respired end-member composition is accurate. Test simulations extending the mixing line to pCO_2 higher than 8000 ppmv consistently lead to overestimation of stalagmite $\delta^{44/40}Ca$ values, further validating the initial parameter selection.

The matching solutions from all three mixing lines show an increasing trend in median soil gas pCO_2 values over the deglaciation (Supplement Fig. S1). Soil gas pCO_2 values

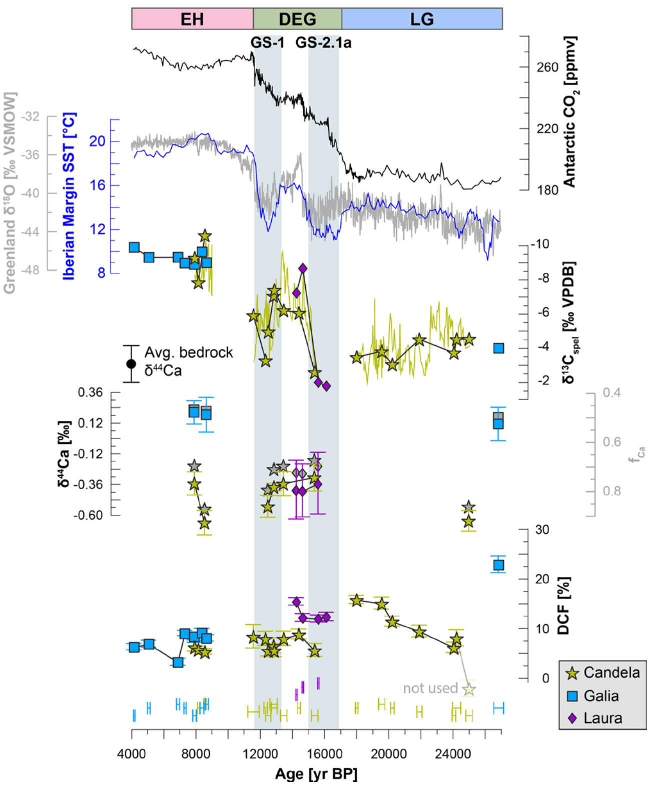

Figure 4. Proxy records from stalagmites Candela, Galia, and Laura over time (see Supplement Table S2), compared to regional temperature reconstructions (TEX_{86}-derived sea surface temperatures from the Iberian Margin; Darfeuil et al., 2016), a Greenland ice core $\delta^{18}O$ record (NGRIP on GICC05 timescale; Wolff et al., 2010), and global CO_2 (ice core composite from Antarctica; Bereiter et al., 2015). The high-resolution $\delta^{13}C_{spel}$ record from Candela (thin green line) is shown for reference and was originally published in Moreno et al. (2010). The DCF values were calculated from ^{14}C measurements paired with U–Th ages. The time periods (LG, DEG, EH) at the top of the figure indicate the intervals used for the modelling to define temperature and atmospheric pCO_2.

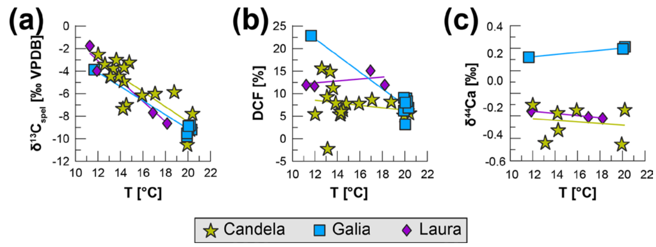

Figure 5. Stalagmite proxies vs. temperature, colour-coded by stalagmite. **(a)** $\delta^{13}C_{spel}$; **(b)** DCF; **(c)** $\delta^{44/40}Ca$. The corresponding paleo-temperatures are linearly interpolated from the Iberian Margin sea surface temperature (SST) record by Darfeuil et al. (2016) without considering chronological and measurement uncertainties in either reconstruction.

are consistently lower during colder time periods (LG, GS-2.1a, and GS-1) and increase during warmer periods (GI-1 and EH), maximising with the onset of the Holocene. This also holds true when considering the results from all mixing lines combined (Fig. 6). Mixing lines 1 and 3 result in few matching solutions for the LG, GS-2.1a, and GS-1, a consequence of the more negative respired end-member $\delta^{13}C$ used (−24.5 ‰ VPDB and −27.5 ‰ VPDB, respectively), compared to mixing line 2 (respired end-member −21.5 ‰ VPDB). Moreover, sensitivity tests using mixing lines with much higher/lower soil gas pCO_2 (10 000 and 4000 ppmv) but keeping the $\delta^{13}C$ as in mixing line 1 again results in increasing soil gas pCO_2 values over the deglaciation.

The model is not very sensitive to the choice of DCF threshold. Tests using a higher DCF confidence interval (±3 %) did not lead to any meaningful change in the results. Changes in $\delta^{44}Ca$, however, are more important, and we had to increase the confidence interval from the uncertainty from the proxy measurement, as lower uncertainty led to the model not finding matching solutions for all three proxies.

The sensitivity analysis allows more degrees of freedom in the model, where soil gas pCO_2, soil gas $F^{14}C$, cave air pCO_2, and gas volume are allowed to freely vary but soil gas $\delta^{13}C$ is kept constant at −18 ‰. While solutions matching DCF and $\delta^{44/40}Ca$ are easily found with this set of parameters, the deglacial trend in $\delta^{13}C_{spel}$ cannot be reproduced (Fig. 6). Only ∼ 2 ‰ of the ∼ 6 ‰ decrease in $\delta^{13}C_{spel}$ (between 24.9 and 8.5 ka) can be explained through processes other than changes in the soil gas $\delta^{13}C$ (Fig. 7). It should be noted that the absolute value of the residual calculated from the measured and modelled $\delta^{13}C_{spel}$ is tied to the initial parameter selection and would vary if we chose differently. The relative differences, however, would remain the same, as long as the initial soil gas $\delta^{13}C$ is not allowed to vary. We have chosen a relatively high initial soil gas $\delta^{13}C$ as more negative values result in very few solutions matching the proxy data. This illustrates how the $\delta^{13}C_{spel}$ trend over the deglaciation requires a change in the initial soil gas $\delta^{13}C$. Holding soil gas pCO_2 constant and letting soil gas $\delta^{13}C$ vary would lead to the entire 6 ‰ change in $\delta^{13}C_{spel}$ being driven by changes in the respired end-member $\delta^{13}C$. This is unrealistic, as biome-level values of respired $\delta^{13}C$ typically show little variation (e.g. Pataki et al., 2003; Fig. 3b), and therefore even a substantial deglacial transition from boreal to forested landscape would likely not lead to such a large shift in $\delta^{13}C$.

5 Discussion

5.1 Estimation of the soil respired end-member from cave air

Combined multi-proxy analysis on three stalagmites and geochemical modelling provide strong evidence that changes in initial soil gas $\delta^{13}C$ are necessary to explain the deglacial trend in $\delta^{13}C_{spel}$ observed in the NW Iberian Peninsula. Here

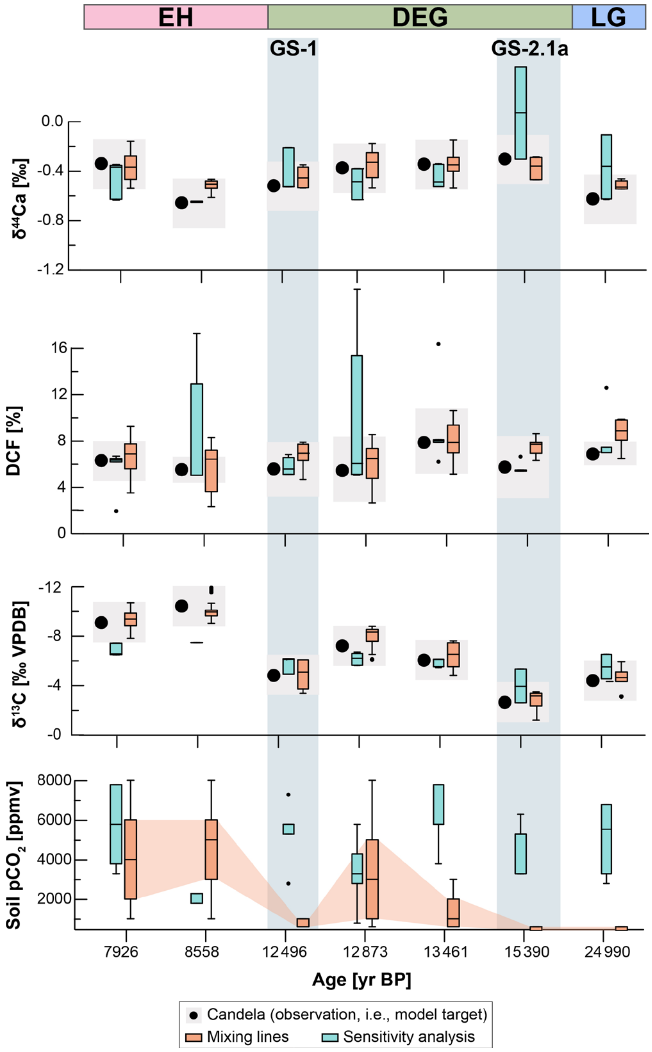

Figure 6. Modelling results compared to measured proxies in stalagmite Candela. Stalagmite measurements ($\delta^{13}C_{spel}$, DCF, $\delta^{44/40}Ca$; black dots) are compared to best-fitting model solutions (colour-coded by simulation type). Simulation results are shown as box plots, with the median and upper and lower quartiles displayed. Outliers are shown as dots. Grey shading indicates intervals of the measured proxy values used to filter the simulations. The soil gas pCO_2 derived from the different model solutions is shown. The time periods (LG, DEG, EH) at the top of the figure indicate the intervals used for the modelling to define temperature and atmospheric pCO_2.

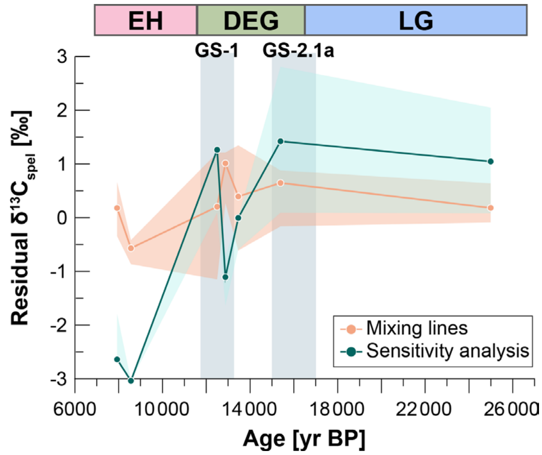

Figure 7. Residual $\delta^{13}C_{spel}$ calculated as the difference between measured and modelled $\delta^{13}C_{spel}$ over time.

we show that this trend is best explained by variations in soil respiration and in the relative proportion of respired vs. atmospheric CO_2 in soil gas. Soil gas CO_2 is a mixture of CO_2 from respiration and atmospheric air (Amundson et al., 1998). Therefore, the pCO_2 and isotopic composition of soil gas over depth can be modelled by a mixing line between the atmospheric and soil respired end-member (Pataki et al., 2003). While more recent research has pointed out that this approach neglects spatio-temporal fluctuations in the isotopic signature of soil CO_2 sources (Goffin et al., 2014), as well as soil storage capacity and the possibility of turbulent transport (Maier et al., 2010), it still provides a valid model with which we can test the overall effects of bulk variations in soil respiration on the drip water solution. In the absence of a full soil monitoring campaign, samples collected from the cave in summer months represent a reasonable approach to estimate the isotopic value of the respired end-member contributing to soil/epikarst gas. This is because the cave, like the soil, is defined by a two end-member mixing system, which is driven by the physical ventilation of the cave. The main fluxes of carbon in a system like El Pindal and La Vallina caves are from soil gas (mainly seeping through the host rock and into the cave) and atmospheric air (through ventilation). Like many mid-latitude and high-latitude cave systems, there is a seasonal reversal in the airflow direction in La Vallina cave (Stoll et al., 2012). In the summer, when cave air is colder than exterior air, cave air flows out the entrance and is replaced by inflow and diffusion of soil/epikarst gas. In this season, the cave air has the highest CO_2 concentrations, with an isotopic composition that falls close to the soil respired end-member on the Keeling plot (Fig. 3a). In the winter, when cave air is warmer than exterior air, exterior air flows in through the cave entrance, bringing the cave closer to the atmospheric end-member. The data from the monitoring of the cave primarily reflects CO_2 from the soil that is drawn through the karst network into the cave. It therefore likely reflects soil column-integrated conditions and the full contribution of respired CO_2 in the soil and epikarst unsaturated zone (below the soil, "ground air"). We do not consider the effect from increasing canopy cover over the deglacial transition, which may affect the soil gas $\delta^{13}C$ through the canopy effect (more depleted CO_2 close to the ground; Buchmann et al., 2002), as well as atmospheric turbulence and advection effects, as these effects lead to small shifts in soil gas $\delta^{13}C$ compared to the recorded signal.

Any contribution of carbon from bedrock dissolution does not significantly affect our estimation of the respired end-member because the intercept defining the respired end-member is most influenced by the summer season cave air pCO_2 data (Fig. 3a). During the summer season drip flow rates are more than an order of magnitude lower than in the winter, and degassing from this drip is suppressed by the high cave air pCO_2. In winter, when drip rates are higher and cave air pCO_2 is lower, degassing may contribute to carbon in cave air, as seen in other systems (Waring et al., 2017). However, winter monitoring data corresponding to ventilated periods are near the global atmospheric composition, suggesting an insignificant impact of degassing of dissolved limestone on our calculated mixing line. Furthermore we do not find evidence for a different Keeling intercept in winter and summer, unlike monitoring studies which infer a strong effect of degassing of a carbon source from limestone dissolution (Waring et al., 2017).

The seasonality of the modern cave air has the advantage of helping to define the modern respired end-member. From our monitoring, we do not find evidence for a different isotopic value of the respired end-member in different seasons. Thus, exploiting the seasonal ventilation of the cave to define the mixing line and respired end-member does not preclude using this respired end-member to interpret records from speleothems in which deposition is dominant in one season. We therefore argue that summer cave air can be used to estimate the isotopic composition of the respired end-member of soil CO_2, when the competing fluxes are minimised.

5.2 Temperature sensitivity of soil respiration as the main driver for $\delta^{13}C_{spel}$

Our modelling results show a consistent pattern of increasing soil gas pCO_2 over the last deglaciation, with absolute values ranging between ∼ 410–600 ppmv during the LG (at 24.9 ka), and ∼ 1000–6000 ppmv during the EH (at 8.6 ka), depending on the mixing line used. An increase in soil respiration rates coinciding with deglacial warming is likely, as higher temperatures promote more rapid soil carbon turnover (Vaughn and Torn, 2019) and the establishment of denser forests (Vargas and Allen, 2008). Climate model simulations confirm that net primary productivity in the NW Iberian Peninsula was lower during the LG than at present (Scheff et al., 2017). Pollen studies from the NW Iberian Peninsula show significant and rapid changes in vegetation type and cover over the Pleistocene–Holocene transition (Moreno et al., 2014). While LG pollen reconstructions suggest a landscape dominated by open grassland (30 %–35 % *Poaceae*) with significant steppe taxa and low arboreal pollen (30 %–50 % primarily *Pinus sylvestris* and *Betula*), the EH pollen assemblage is dominated by arboreal pollen (70 %–90 %; Moreno et al., 2011). It is likely that the rapid response of pollen assemblages to climate warming is due to the region's proximity to documented tree refugia in the Mediterranean region (Fletcher et al., 2010).

Assuming a temperature change of roughly 7 °C between the LG and EH, in line with TEX_{86}-based temperature reconstructions from the Iberian Margin (Darfeuil et al., 2016), the sensitivity of soil respiration to temperature change (Q_{10}, i.e. factor by which soil respiration increases with a 10 °C rise in temperature) derived by our modelling experiments lies between 3.6 and 14.7, depending on the initial conditions of the models. This is higher than the mean global Q_{10} values of 3.0 ± 1.1 found by the soil respiration database (Bond-Lamberty and Thomson, 2010), and may be exaggerated by chronological uncertainty in the marine and speleothem records and by uncertainties in the temperature proxies (> 4 °C, Darfeuil et al., 2016; Tierney and Tingley, 2015). Changes in seasonality between EH and LG could also lead to bias in the temperature reconstruction due to shifts in nutrient availability and marine productivity (Darfeuil et al., 2016). Furthermore, a change in respired substrate over time, leading to a shift in the soil respired end-member $\delta^{13}C$ (Boström et al., 2007), could lead to higher Q_{10} than the global mean. We can exclude changes in vegetation assemblage from C4 to C3 plants, as there is no evidence for the widespread presence of C4 plants during the glacial in the NW Iberian Peninsula (Moreno et al., 2010) or elsewhere at temperate western European sites (Denniston et al., 2018; Genty et al., 2006, 2003). A change in the balance between heterotrophic and autotrophic respiration is another possibility that would influence the soil gas $\delta^{13}C$. Changes in temperature affect root and microbial respiration differently (Wang et al., 2014), as do changes in other environmental variables, e.g. precipitation regimes and nutrient cycling (Li et al., 2018). Microorganisms are typically enriched by 2 ‰–4 ‰ compared to plants (Gleixner et al., 1993), and vertical enrichment by ∼ 2.5 ‰ in soil profiles has been attributed to an increasing contribution of soil microbially derived material with depth to the overall soil carbon turnover (Boström et al., 2007). The release of older and enriched carbon from soils and long-lived plant material through respiration could provide an additional mechanism with which the soil gas $\delta^{13}C$ could be shifted regardless of changes in soil respiration (Fung et al., 1997). Very high Q_{10} values have also been found in winter at a Danish beech forest site, suggesting a stronger temperature (and potentially soil moisture) control during the cold season, potentially resulting in the activation of dormant microbial communities, the alteration of diffusion processes of organic molecules and of cell metabolism (Janssens and Pilegaard, 2003). It is possible that the significant environmental changes occurring over the last deglaciation resulted in similar responses from the soil microbial community, leading to the observed high Q_{10} values. A higher respired $\delta^{13}C$ during the LG is also suggested by the model results, where mixing line 3 with the lowest respired $\delta^{13}C$ (−25.9 ‰) fails to produce solutions matching the speleothem data (Fig. S1). Given the small variation in DCF values in Candela over the deglaciation, we can exclude the possibility that changes in the fraction of bedrock carbon from changing dissolution conditions constitute an important driver of the deglacial signal.

Another intriguing possibility is that the carbon isotopic fractionation of C3 vegetation is controlled by atmospheric pCO_2 (Schubert and Jahren, 2015). A recent global compilation of speleothem records shows that, after correcting for the expected effect of precipitation and temperature on $\delta^{13}C$ of C3 biomass and the temperature-dependent fractionation between CO_2 and calcite, the global average $\delta^{13}C_{spel}$ closely tracks atmospheric pCO_2 over the last 90 ka (Breecker, 2017). The magnitude of the deglacial shift in C3 plant $\delta^{13}C$ has been proposed to lie around 2.1 ‰ (Schubert and Jahren, 2015). The deglacial $\delta^{13}C_{spel}$ record from the NW Iberian Peninsula, however, shows clear millennial-scale variations that coincide with temperature variations, but are not driven by atmospheric CO_2 (Fig. 4). Therefore, while it is possible that a CO_2 fertilisation effect contributed to the overall decrease in $\delta^{13}C_{spel}$ over the deglaciation, this effect is likely not dominant.

Our findings will likely apply more broadly for caves in settings where soil gas pCO_2 is temperature limited. Sites where soil gas pCO_2 is moisture limited, e.g. further south on the Iberian Peninsula, will likely exhibit very different trends in $\delta^{13}C_{spel}$ over glacial–interglacial cycles, as hydroclimate and temperature may have different phasings.

5.3 Other processes affecting $\delta^{13}C_{spel}$

While a change in soil respiration and consequently in the proportion of respired vs. atmospheric CO_2 in the soil gas can explain the deglacial trend in $\delta^{13}C_{spel}$, a number of other, cave-specific processes could also contribute to changes in $\delta^{13}C_{spel}$. The direct effect of the glacial–interglacial temperature change on carbonate equilibria and fractionation factors is small and taken into consideration by running the simulations with EH, DEG, and LG parameters. It is more difficult to assess whether kinetic fractionation effects affected the stalagmite at different times, potentially amplifying the $\delta^{13}C_{spel}$ signal. CaveCalc uses standard kinetic fractionation factors for the CO_2–DIC–carbonate system (Romanek et al., 1992; Zhang et al., 1995), where DIC stands for dissolved inorganic carbon, and therefore such variations are not considered by the model. However, the high degree of coherence between $\delta^{13}C_{spel}$ records from the entire temperate western European region suggests that localised, cave-specific kinetic fractionation effects likely played a minor role in driving the deglacial trend (Fig. 1).

Changes in the amount of PCP the drip water experiences en route to the speleothem can lead to significant variability in $\delta^{13}C_{spel}$ records (Fohlmeister et al., 2020), and they are tightly coupled to changes in cave air pCO_2 and cave ventilation dynamics. Higher cave air pCO_2 and a reduced CO_2 gradient between the supersaturated drip water solution and the cave air result in less PCP and vice versa for lower cave air pCO_2. It is likely that cave air pCO_2 was lower during the last glacial at the study sites, and indeed this is also suggested by our model results (Supplement Fig. S2). Cave air pCO_2 is coupled to soil gas pCO_2, which provides its upper limit, and model results automatically filter out unrealistic scenarios, as no speleothem precipitation occurs when cave air pCO_2 is equal to or higher than soil gas pCO_2. Our multiproxy dataset allows us to evaluate the importance of PCP for $\delta^{13}C_{spel}$ quantitatively, as $\delta^{44/40}Ca$ can provide quantitative PCP reconstructions over time (Owen et al., 2016). Mg/Ca ratios are also often used as a proxy for PCP; however, caution is required in their interpretation in El Pindal Cave because in the Holocene, Mg/Ca is also affected by increasing surf-zone marine aerosol contributions as rising sea level brought the coastline to the foot of the sea cliff in which the cave has its entrance (Supplement Figs. S3 and S4). Over the last deglaciation, $\delta^{44/40}Ca$ and f_{Ca} varied only minimally in both Candela and Galia (Fig. 4), suggesting that changes in PCP were small. This is also reflected in the sensitivity analysis, where changes in $\delta^{13}C_{spel}$ cannot be reproduced while also fitting the $\delta^{44/40}Ca$ curve (Fig. 6). CaveCalc uses cave air pCO_2 to match the degree to which drip water has lost its initial Ca due to calcite precipitation, giving us a measure for PCP. A solution equilibrated with a high soil gas pCO_2 would lose the majority of its carbonate in a simulation where cave air pCO_2 is atmospheric, due to the high degree of oversaturation of the drip water solution compared to cave air. If $\delta^{44/40}Ca$ provides evidence that only a small portion of Ca has been precipitated, then the simulation must match the data by prescribing a higher cave air pCO_2. In reality, the fraction of Ca precipitated from drip waters depends not only on the oversaturation of the solution, but also on the time the water is present as a thin film on the cave ceiling and stalagmite surface before being replaced by a new water parcel (i.e. drip interval; Fohlmeister et al., 2020; Stoll et al., 2012). When the drip interval is short, none of the water parcels will have enough time to fully degas CO_2 and equilibrate with the cave atmosphere, and PCP is lower than what would be possible given the cave air pCO_2. CaveCalc does not model drip interval, and therefore the cave air pCO_2 inferred from the simulations might be overestimated. We test the effect of drip interval length changes on f_{Ca} and PCP using the forward model ISTAL (Stoll et al., 2012), which explicitly models this parameter. Two model scenarios simulate full glacial and Holocene conditions, including changes in temperature, cave air pCO_2, and soil gas pCO_2 for "winter" (i.e. atmospheric) and "summer" (i.e. elevated) cave air pCO_2 (Supplement Fig. S4). The effect of the glacial–interglacial temperature change is only significant for high drip intervals during the cold season, where PCP is slightly higher during interglacial conditions. At high drip intervals, the temperature increase leads to a change in f_{Ca} of ~ -0.1, which translates to a ~ 0.04 ‰ change in $\delta^{44/40}Ca$ and a -0.7 ‰ VPDB change in $\delta^{13}C_{spel}$. This corroborates our expectation from the $\delta^{44/40}Ca$ record and CaveCalc model results, suggesting that only a small part of the shift in Candela $\delta^{13}C_{spel}$ over the last deglaciation was due to changes in PCP.

While it is likely that some or all of these processes affected the deglacial $\delta^{13}C_{spel}$ to some extent, their magnitude is not large enough to explain the measured ∼ 6 ‰ shift, suggesting that changes in soil gas pCO_2 played a significant role.

5.4 Insights into regional hydroclimate over the last deglaciation

Our new multi-proxy record from stalagmites from the NW Iberian Peninsula also offers nuanced insights into local hydroclimate conditions over the last deglaciation. While DCF mainly responds to changes in carbonate dissolution conditions and therefore is sensitive to changes in infiltration, $\delta^{44/40}Ca$ is driven by both infiltration dynamics (determining the initial oversaturation of drip water and the degassing timescale) and cave atmospheric pCO_2 (determining the amount of PCP occurring). The Candela record suggests no substantial shift in infiltration dynamics or PCP occurring between LG and EH (Fig. 6), as both proxies fluctuate around a mean value without long-term trends. This result suggests that the glacial hydroclimate in the NW Iberian Peninsula was not significantly different from the Holocene and stands at odds with previous mainly pollen-based studies that often point towards a drier glacial but with considerable variability over millennial timescales (Fletcher et al., 2010). Recent modelling results have challenged the interpretation of the glacial being cold and dry, suggesting instead that, while precipitation was lower during the LG, topsoil moisture was actually higher than at present (Scheff et al., 2017). Our new stalagmite data support this interpretation, suggesting that temperature, and not hydroclimate conditions, was the main driver of ecosystem productivity over the deglaciation.

6 Conclusions

We have combined multi-proxy ($\delta^{13}C$, $\delta^{44/40}Ca$, and DCF) data from three speleothems and quantitative geochemical modelling to show that the temperature sensitivity of $\delta^{13}C_{spel}$ over the last deglaciation in western Europe is best explained by increasing soil respiration. Generating a large ensemble of forward models of processes in soil, karst, and cave allows the estimation of their likely importance and variability over time. Speleothem geochemical proxies that are sensitive to different components of the soil–karst–cave system can be employed to extract the most likely model solutions from the ensembles, thus quantifying the system's initial conditions, particularly soil gas pCO_2. Our approach involved the coupling of soil gas pCO_2 and $\delta^{13}C$ values, as expected when following a mixing line between a soil respired and an atmospheric end-member, thus allowing us to model changes in soil respiration. While uncertainties remain, in particular with respect to possible changes in the soil respired end-member $\delta^{13}C$ value over time, we find that an increase in soil respiration is necessary to explain the large shifts in $\delta^{13}C_{spel}$ over the last deglaciation in the NW Iberian Peninsula. Given the exceptional regional coherency of $\delta^{13}C_{spel}$ records over temperate western Europe, it is likely that this effect is of broader regional significance. Our study is the first to quantitatively model environmental processes in karst systems using a multi-proxy approach and paves the way towards more nuanced interpretations of $\delta^{13}C_{spel}$ records. Moreover, our multi-proxy records support recent climate model results that reject the long-standing "drier and colder glacial" notion in western Europe, pointing instead toward a dominant forcing of temperature, rather than hydroclimate, on ecosystem productivity.

Code and data availability. The code used for calculation of the stalagmite dead carbon fraction can be found at (https://github.com/flechleitner/DCF_calculator, last access: 16 September 2021, and https://doi.org/10.5281/zenodo.5503025, Lechleitner, 2021). All data used in the study and codes for the modelling can be found at https://github.com/flechleitner/Spain_analysis, last access: 16 September 2021, and https://doi.org/10.5281/zenodo.5503041 (Lechleitner and Wilhelm, 2021) and in the Supplement provided with the article.

Supplement. The supplement related to this article is available online at: https://doi.org/10.5194/cp-17-1903-2021-supplement.

Author contributions. FAL, HS, and GMH designed the study and acquired funding for the project. FAL, NH, and CCD performed the geochemical analysis on speleothem samples. OK collected and measured cave air samples from La Vallina Cave and acquired funding for the monitoring work. FAL and MW performed the modelling experiments in CaveCalc and wrote the R code for the data–model evaluation. FAL wrote the paper and generated the figures. HMS and CCD provided additional input to the text. All authors provided feedback on the paper and approved it before submission.

Competing interests. The authors declare that they have no conflict of interest.

Disclaimer. Publisher's note: Copernicus Publications remains neutral with regard to jurisdictional claims in published maps and institutional affiliations.

Acknowledgements. This study was funded by the Swiss National Science Foundation (SNSF) grant P400P2_180789 awarded to Franziska A. Lechleitner, by ETH core funding to Heather M. Stoll, and by doctoral Fellowship ETH-13 18-1 to Oliver Kost. We thank Yu-Te (Alan) Hsieh for assistance with the $\delta^{44/40}$Ca measurements at the University of Oxford, Madalina Jaggi at ETH Zurich for measurements of δ^{13}C and trace elements, and Saul Gonzalez-Lemos for cave air sampling. We thank two anonymous reviewers and handling editor Marie-France Loutre for their fair and competent assessment of our paper.

Financial support. This research has been supported by the Schweizerischer Nationalfonds zur Förderung der Wissenschaftlichen Forschung (grant no. P400P2_180789), by ETH core, and from ETH doctoral fellowship ETH-13 18-1.

Review statement. This paper was edited by Marie-France Loutre and reviewed by two anonymous referees.

References

AEMET: State Meteorological Agency (AEMET) [WWW Document], available at: http://www.aemet.es/en/portada (last access: 13 September 2021), 2020.

Amundson, R., Stern, L., Baisden, T., and Wang, Y.: The isotopic composition of soil and soil-respired CO_2, Geoderma, 82, 83–114, 1998.

Baldini, L. M., McDermott, F., Baldini, J. U. L., Arias, P., Cueto, M., Fairchild, I. J., Hoffmann, D. L., Mattey, D. P., Müller, W., Constantin, D., Ontañón, R., Garciá-Moncó, C., and Richards, D. A.: Regional temperature, atmospheric circulation, and sea-ice variability within the Younger Dryas Event constrained using a speleothem from northern Iberia, Earth Planet. Sc. Lett. 419, 101–110, https://doi.org/10.1016/j.epsl.2015.03.015, 2015.

Bereiter, B., Eggleston, S., Schmitt, J., Nehrbass-Ahles, C., Stocker, T. F., Fischer, H., Kipfstuhl, S., and Chappellaz, J.: Revision of the EPICA Dome C CO_2 record from 800 to 600 kyr before present, Geophys. Res. Lett., 42, 542–549, https://doi.org/10.1002/2014GL061957, 2015.

Bond-Lamberty, B. and Thomson, A.: A global database of soil respiration data, Biogeosciences, 7, 1915–1926, https://doi.org/10.5194/bg-7-1915-2010, 2010.

Borsato, A., Frisia, S., and Miorandi, R.: Carbon dioxide concentration in temperate climate caves and parent soils over an altitudinal gradient and its influence on speleothem growth and fabrics, Earth Surf. Proc. Land., 40, 1158–1170, https://doi.org/10.1002/esp.3706, 2015.

Boström, B., Comstedt, D., and Ekblad, A.: Isotope fractionation and ^{13}C enrichment in soil profiles during the decomposition of soil organic matter, Oecologia, 153, 89–98, https://doi.org/10.1007/s00442-007-0700-8, 2007.

Bova, S., Rosenthal, Y., Liu, Z., Godad, S. P., and Yan, M.: Seasonal origin of the thermal maxima at the Holocene and the last interglacial, Nature, 589, 548–553, https://doi.org/10.1038/s41586-020-03155-x, 2021.

Braun, K., Bar-Matthews, M., Matthews, A., Ayalon, A., Cowling, R. M., Karkanas, P., Fisher, E. C., Dyez, K., Zilberman, T., and Marean, C. W.: Late Pleistocene records of speleothem stable isotopic compositions from Pinnacle Point on the South African south coast, Quaternary Res., 91, 265–288, https://doi.org/10.1017/qua.2018.61, 2019.

Breecker, D. O.: Atmospheric pCO$_2$ control on speleothem stable carbon isotope compositions, Earth Planet. Sc. Lett., 458, 58–68, https://doi.org/10.1016/j.epsl.2016.10.042, 2017.

Breecker, D. O., Payne, A. E., Quade, J., Banner, J. L., Ball, C. E., Meyer, K. W., and Cowan, B. D.: The sources and sinks of CO_2 in caves under mixed woodland and grassland vegetation, Geochim. Cosmochim. Ac., 96, 230–246, https://doi.org/10.1016/j.gca.2012.08.023, 2012.

Breitenbach, S. F. M. and Bernasconi, S. M.: Carbon and oxygen isotope analysis of small carbonate samples (20 to 100 ug) with a GasBench II preparation device, Rapid Commun. Mass Spectrom., 25, 1910–1914, https://doi.org/10.1002/rcm.5052, 2011.

Brook, G. A., Folkoff, M. E., and Box, E. O.: A World model of soil carbon dioxide, Earth Surf. Proc. Land., 8, 79–88, 1983.

Buchmann, N., Brooks, J. R., and Ehleringer, J. R.: Predicting daytime carbon isotope ratios of atmospheric CO_2 within forest canopies, Funct. Ecol., 16, 49–57, 2002.

Cerling, T. E., Solomon, D. K., Quade, J., and Bowman, J. R.: On the isotopic composition of carbon in soil carbon dioxide, Geochim. Cosmochim. Ac., 55, 3403–3405, https://doi.org/10.1016/0016-7037(91)90498-T, 1991.

Clark, P. U., Shakun, J. D., Baker, P. A., Bartlein, P. J., Brewer, S., Brook, E., Carlson, A. E., Cheng, H., Kaufman, D. S., Liu, Z., Marchitto, T. M., Mix, A. C., Morrill, C., Otto-Bliesner, B. L., Pahnke, K., Russell, J. M., Whitlock, C., Adkins, J. F., Blois, J. L., Clark, J., Colman, S. M., Curry, W. B., Flower, B. P., He, F., Johnson, T. C., Lynch-Stieglitz, J., Markgraf, V., McManus, J., Mitrovica, J. X., Moreno, P. I., and Williams, J. W.: Global climate evolution during the last deglaciation, P. Natl. Acad. Sci. USA, 109, 1134–1142, https://doi.org/10.1073/pnas.1116619109, 2012.

Comas-Bru, L., Atsawawaranunt, K., Harrison, S., and SISAL (Speleothem Isotopes Synthesis and AnaLysis) Working Group Members: SISAL (Speleothem Isotopes Synthesis and AnaLysis Working Group) database version 2.0, University of Reading Research Data Archive [data set], https://doi.org/10.17864/1947.242, 2020a.

Comas-Bru, L., Rehfeld, K., Roesch, C., Amirnezhad-Mozhdehi, S., Harrison, S. P., Atsawawaranunt, K., Ahmad, S. M., Brahim, Y. A., Baker, A., Bosomworth, M., Breitenbach, S. F. M., Burstyn, Y., Columbu, A., Deininger, M., Demény, A., Dixon, B., Fohlmeister, J., Hatvani, I. G., Hu, J., Kaushal, N., Kern, Z., Labuhn, I., Lechleitner, F. A., Lorrey, A., Martrat, B., Novello, V. F., Oster, J., Pérez-Mejías, C., Scholz, D., Scroxton, N., Sinha, N., Ward, B. M., Warken, S., Zhang, H., and SISAL Working Group members: SISALv2: a comprehensive speleothem isotope database with multiple age–depth models, Earth Syst. Sci. Data, 12, 2579–2606, https://doi.org/10.5194/essd-12-2579-2020, 2020b.

Darfeuil, S., Ménot, G., Giraud, X., Rostek, F., Tachikawa, K., Garcia, M., and Bard, É.: Sea surface temperature reconstructions over the last 70 kyr off Portugal: Biomarker data and regional modeling, Paleoceanography, 31, 40–65, https://doi.org/10.1002/2015PA002831, 2016.

Day, C. C., Pogge von Strandmann, P. A. E., and Mason, A. J.: Lithium isotopes and partition coefficients in inorganic carbonates: Proxy calibration for weathering reconstruction, Geochim. Cosmochim. Ac., 305, 243–262, https://doi.org/10.1016/j.gca.2021.02.037, 2021.

Denniston, R. F., Houts, A. N., Asmerom, Y., Wanamaker Jr., A. D., Haws, J. A., Polyak, V. J., Thatcher, D. L., Altan-Ochir, S., Borowske, A. C., Breitenbach, S. F. M., Ummenhofer, C. C., Regala, F. T., Benedetti, M. M., and Bicho, N. F.: A stalagmite test of North Atlantic SST and Iberian hydroclimate linkages over the last two glacial cycles, Clim. Past, 14, 1893–1913, https://doi.org/10.5194/cp-14-1893-2018, 2018.

Fahrni, S. M., Wacker, L., Synal, H.-A., and Szidat, S.: Improving a gas ion source for ^{14}C AMS, Nucl. Instrum. Meth. B, 294, 320–327, https://doi.org/10.1016/j.nimb.2012.03.037, 2013.

Fletcher, W. J., Sanchez Goñi, M. F., Allen, J. R. M., Cheddadi, R., Combourieu-Nebout, N., Huntley, B., Lawson, I., Londeix, L., Magri, D., Margari, V., Müller, U. C., Naughton, F., Novenko, E., Roucoux, K., and Tzedakis, P. C.: Millennial-scale variability during the last glacial in vegetation records from Europe, Quaternary Sci. Rev., 29, 2839–2864, https://doi.org/10.1016/j.quascirev.2009.11.015, 2010.

Fohlmeister, J., Voarintsoa, N. R. G., Lechleitner, F. A., Boyd, M., Brandtstätter, S., Jacobson, M. J., and Oster, J. L.: Main controls on the stable carbon isotope composition of speleothems, Geochim. Cosmochim. Ac., 279, 67–87, https://doi.org/10.1016/j.gca.2020.03.042, 2020.

Fung, I., Field, C. B., Berry, J. A., Thompson, M. V., Randerson, J. T., Malmström, C. M., Vitousek, P. M., James Collatz, G., Sellers, P. J., Randall, D. A., Denning, A. S., Badeck, F., and John, J.: Carbon 13 exchanges between the atmosphere and biosphere, Global Biogeochem. Cy., 11, 507–533, 1997.

Genty, D., Baker, A., Massault, M., Proctor, C., Gilmour, M., Pons-Branchu, E., and Hamelin, B.: Dead carbon in stalagmites: carbonate bedrock paleodissolution vs. ageing of soil organic matter, Implications for ^{13}C variations in speleothems, Geochim. Cosmochim. Ac., 65, 3443–3457, https://doi.org/10.1016/S0016-7037(01)00697-4, 2001.

Genty, D., Blamart, D., Ouahdi, R., Gilmour, M., Baker, A., Jouzel, J., and Van-Exter, S.: Precise dating of Dansgaard-Oeschger climate oscillations in western Europe from stalagmite data, Nature, 421, 833–837, https://doi.org/10.1038/nature01391, 2003.

Genty, D., Blamart, D., Ghaleb, B., Plagnes, V., Causse, C., Bakalowicz, M., Zouari, K., Chkir, N., Hellstrom, J., Wainer, K., and Bourges, F.: Timing and dynamics of the last deglaciation from European and North African δ^{13}C stalagmite profiles – Comparison with Chinese and South Hemisphere stalagmites, Quaternary Sci. Rev., 25, 2118–2142, https://doi.org/10.1016/j.quascirev.2006.01.030, 2006.

Gleixner, G., Danier, H.-J., Werner, R. A., and Schmidt, H.-L.: Correlations between the 13C content of primary and secondary plant products in different cell compartments and that in decomposing basidiomycetes, Plant Physiol., 102, 1287–1290, 1993.

Goffin, S., Aubinet, M., Maier, M., Plain, C., Schack-Kirchner, H., and Longdoz, B.: Characterization of the soil CO_2 production and its carbon isotope composition in forest soil layers using the flux-gradient approach, Agr. Forest Meteorol., 188, 45–57, https://doi.org/10.1016/j.agrformet.2013.11.005, 2014.

Hendy, C. H.: The isotopic geochemistry of speleothems—I. The calculation of the effects of different modes of formation on the isotopic composition of speleothems and their applicability as palaeoclimatic indicators, Geochim. Cosmochim. Ac., 35, 801–824, https://doi.org/10.1016/0016-7037(71)90127-X, 1971.

Heuser, A. and Eisenhauer, A.: The calcium isotope composition ($\delta^{44/40}$Ca) of NIST SRM 915b and NIST SRM 1486, Geostand. Geoanal. Res., 32, 27–32, 2008.

Hippler, D., Schmitt, A.-D., Gussone, N., Heuser, A., Stille, P., Eisenhauer, A., and Nägler, T. F.: Calcium isotopic composition of various reference materials and seawater, Geostand. Newslett., 27, 13–19, 2003.

Janssens, I. A. and Pilegaard, K.: Large seasonal changes in Q_{10} of soil respiration in a beech, Glob. Change Biol., 9, 911–918, 2003.

Lambeck, K., Rouby, H., Purcell, A., Sun, Y., and Sambridge, M.: Sea level and global ice volumes from the Last Glacial Maximum to the Holocene, P. Natl. Acad. Sci. USA, 111, 15296–15303, https://doi.org/10.1073/pnas.1411762111, 2014.

Lechleitner, F: flechleitner/DCF_calculator: (v1.0), Zenodo [code], https://doi.org/10.5281/zenodo.5503025, 2021.

Lechleitner, F. and Wilhelm, M.: flechleitner/Spain_analysis: (v1.0), Zenodo [data set], https://doi.org/10.5281/zenodo.5503041, 2021.

Li, C., Peng, Y., Nie, X., Yang, Y., Yang, L., Li, F., Fang, K., Xiao, Y., and Zhou, G.: Differential responses of heterotrophic and autotrophic respiration to nitrogen addition and precipitation changes in a Tibetan alpine steppe, Sci. Rep., 8, 16546, https://doi.org/10.1038/s41598-018-34969-5, 2018.

Maier, M., Schack-Kirchner, H., Hildebrand, E. E., and Holst, J.: Pore-space CO_2 dynamics in a deep, well-aerated soil, Eur. J. Soil Sci., 61, 877–887, https://doi.org/10.1111/j.1365-2389.2010.01287.x, 2010.

Mattey, D. P., Atkinson, T. C., Barker, J. A., Fisher, R., Latin, J.-P., Durell, R., and Ainsworth, M.: Carbon dioxide, ground air and carbon cycling in Gibraltar karst, Geochim. Cosmochim. Ac., 184, 88–113, https://doi.org/10.1016/j.gca.2016.01.041, 2016.

Moreno, A., Stoll, H., Jiménez-Sánchez, M., Cacho, I., Valero-Garcés, B., Ito, E., and Edwards, R. L.: A speleothem record of glacial (25–11.6 kyr BP) rapid climatic changes from northern Iberian Peninsula, Global Planet. Change, 71, 218–231, https://doi.org/10.1016/j.gloplacha.2009.10.002, 2010.

Moreno, A., Lopez-Merino, L., Leira, M., Marco-Barba, J., Gonzalez-Sampériz, P., Valero-Garcés, B.L., Lopez-Saez, J.A., Santos, L., Mata, P., and Ito, E.: Revealing the last 13,500 years of environmental history from the multiproxy record of a mountain lake (Lago Enol, northern Iberian Peninsula), J. Paleolimnol., 46, 327–349, https://doi.org/10.1007/s10933-009-9387-7, 2011.

Moreno, A., Svensson, A., Brooks, S. J., Connor, S., Engels, S., Fletcher, W., Genty, D., Heiri, O., Labuhn, I., Pers, A., Peyron, O., Sadori, L., Valero-Garcés, B., Wulf, S., Zanchetta, G., and data contributors: A compilation of Western European terrestrial records 60 – 8 ka BP: towards an understanding of latitudinal climatic gradients, Quaternary Sci. Rev., 106, 167–185, https://doi.org/10.1016/j.quascirev.2014.06.030, 2014.

Owen, R. A., Day, C. C., Hu, C., Liu, Y., Pointing, M. D., Blättler, C. L., and Henderson, G. M.: Calcium isotopes in caves as a proxy for aridity: Modern calibration and application to the 8.2 kyr event, Earth Planet. Sc. Lett., 443, 129–138, https://doi.org/10.1016/j.epsl.2016.03.027, 2016.

Owen, R. A., Day, C. C., and Henderson, G. M.: CaveCalc: A new model for speleothem chemistry & isotopes, Comput. Geosci., 119, 115–122, https://doi.org/10.1016/J.CAGEO.2018.06.011, 2018.

Pataki, D. E., Ehleringer, J. R., Flanagan, L. B., Yakir, D., Bowling, D. R., Still, C. J., Buchmann, N., Kaplan, J. O., and Berry, J. A.: The application and interpretation of Keeling plots in terrestrial carbon cycle research, Global Biogeochem. Cy., 17, 1022, https://doi.org/10.1029/2001GB001850, 2003.

Peinado Lorca, M. and Martínez-Parras, J. M.: Castilla-La Mancha, in: La Vegetación de España, Alcala de Henares, Universidad de Alcala de Henares, 163–196, 1987.

Rasmussen, S. O., Bigler, M., Blockley, S. P., Blunier, T., Buchardt, S. L., Clausen, H. B., Cvijanovic, I., Dahl-Jensen, D., Johnsen, S. J., Fischer, H., Gkinis, V., Guillevic, M., Hoek, W. Z., Lowe, J. J., Pedro, J. B., Popp, T., Seierstad, I. K., Steffensen, J. P., Svensson, A. M., Vallelonga, P., Vinther, B. M., Walker, M. J. C., Wheatley, J. J., and Winstrup, M.: A stratigraphic framework for abrupt climatic changes during the Last Glacial period based on three synchronized Greenland ice-core records: Refining and extending the INTIMATE event stratigraphy, Quaternary Sci. Rev., 106, 14–28, https://doi.org/10.1016/j.quascirev.2014.09.007, 2014.

Rehfeld, K. and Kurths, J.: Similarity estimators for irregular and age-uncertain time series, Clim. Past, 10, 107–122, https://doi.org/10.5194/cp-10-107-2014, 2014.

Reimer, P.: Selection and Treatment of Data for Radiocarbon Calibration: An Update to the International Calibration (IntCal) Criteria, Radiocarbon, 55, 1923–1945, https://doi.org/10.2458/azu_js_rc.55.16955, 2013.

Reimer, P., Bard, E., Bayliss, A., Beck, J. W., Blackwell, P. G., Bronk Ramsey, C., Buck, C., Cheng, H., Edwards, R. L., Friedrich, M., Grootes, P. M., Guilderson, T. P., Haflidason, H., Hajdas, I., Hatté, C., Heaton, T. J., Hoffmann, D. L., Hogg, A. G., Hughen, K. A., Kaiser, K. F., Kromer, B., Manning, S. W., Niu, M., Reimer, R. W., Richards, D. A., Scott, E. M., Southon, J. R., Staff, R. A., Turney, C. S. M., and van der Plicht, J.: IntCal13 and Marine13 Radiocarbon Age Calibration Curves 0–50,000 Years cal BP, Radiocarbon, 55, 1869–1887, https://doi.org/10.2458/azu_js_rc.55.16947, 2013.

Reynard, L. M., Day, C. C., and Henderson, G. M.: Large fractionation of calcium isotopes during cave-analogue calcium carbonate growth, Geochim. Cosmochim. Ac., 75, 3726–3740, https://doi.org/10.1016/j.gca.2011.04.010, 2011.

Romanek, C. S., Grossman, E. L., and Morse, J. W.: Carbon isotopic fractionation in synthetic aragonite and calcite: effects of temperature and precipitation rate, Geochim. Cosmochim. Ac., 56, 419–430, 1992.

Rossi, C., Bajo, P., Lozano, R. P., and Hellstrom, J.: Younger Dryas to Early Holocene paleoclimate in Cantabria (N Spain): Constraints from speleothem Mg, annual fluorescence banding and stable isotope records, Quaternary Sci. Rev., 192, 71–85, https://doi.org/10.1016/j.quascirev.2018.05.025, 2018.

Rudzka, D., McDermott, F., Baldini, L. M., Fleitmann, D., Moreno, A., and Stoll, H.: The coupled δ^{13}C-radiocarbon systematics of three Late Glacial/early Holocene speleothems; insights into soil and cave processes at climatic transitions, Geochim. Cosmochim. Ac., 75, 4321–4339, https://doi.org/10.1016/j.gca.2011.05.022, 2011.

Scheff, J., Seager, R., Liu, H., and Coats, S.: Are Glacials Dry? Consequences for Paleoclimatology and for Greenhouse Warming, J. Climate, 30, 6593–6609, https://doi.org/10.1175/JCLI-D-16-0854.1, 2017.

Schmitt, J., Schneider, R., Elsig, J., Leuenberger, D., Lourantou, A., Chappellaz, J., Köhler, P., Joos, F., Stocker, T. F., Leuenberger, M., and Fischer, H.: Carbon isotope constraints on the deglacial CO_2 rise from ice cores, Science, 336, 711–715, 2012.

Schubert, B. A. and Jahren, A. H.: Global increase in plant carbon isotope fractionation following the last glacial maximum caused by increase in atmospheric pCO_2, Geology, 43, 435–438, https://doi.org/10.1130/G36467.1, 2015.

Slessarev, E. W., Lin, Y., Bingham, N. L., Johnson, J. E., Dai, Y., Schimel, J. P., and Chadwick, O. A.: Water balance creates a threshold in soil pH at the global scale, Nature, 540, 567–569, https://doi.org/10.1038/nature20139, 2016.

Stoll, H., Mendez-Vicente, A., Gonzalez-Lemos, S., Moreno, A., Cacho, I., Cheng, H., and Edwards, R. L.: Interpretation of orbital scale variability in mid-latitude speleothem d18O: Significance of growth rate controlled kinetic fractionation effects, Quaternary Sci. Rev., 127, 215–228, https://doi.org/10.1016/j.quascirev.2015.08.025, 2015.

Stoll, H. M., Müller, W., and Prieto, M.: I-STAL, a model for interpretation of Mg/Ca, Sr/Ca and Ba/Ca variations in speleothems and its forward and inverse application on seasonal to millennial scales, Geochem. Geophy. Geosy., 13, 1–27, https://doi.org/10.1029/2012GC004183, 2012.

Stoll, H. M., Moreno, A., Mendez-Vicente, A., Gonzalez-Lemos, S., Jimenez-Sanchez, M., Dominguez-Cuesta, M. J., Edwards, R. L., Cheng, H., and Wang, X.: Paleoclimate and growth rates of speleothems in the northwestern Iberian Peninsula over the last two glacial cycles, Quaternary Res., 80, 284–290, https://doi.org/10.1016/j.yqres.2013.05.002, 2013.

Stoll, H. M., Cacho, I., Gasson, E., Sliwinski, J., Kost, O., Moreno, A., Iglesias, M., Torner, J., Perez, C., Haghipour, N., Cheng, H., Lawrence Edwards, R.: Rapid melting of a large Eurasian Ice Sheet during the penultimate deglaciation, Nat. Geosci., in review, 2021.

Synal, H. A., Stocker, M., and Suter, M.: MICADAS: A new compact radiocarbon AMS system, Nucl. Instrum. Meth. B, 259, 7–13, https://doi.org/10.1016/j.nimb.2007.01.138, 2007.

Tierney, J. E. and Tingley, M. P.: A TEX_{86} surface sediment database and extended Bayesian calibration, Sci. Data, 2, 150029, https://doi.org/10.1038/sdata.2015.29, 2015.

Tierney, J. E., Zhu, J., King, J., Malevich, S. B., Hakim, G. J., and Poulsen, C. J.: Glacial cooling and climate sensitivity revisited, Nature, 584, 569–573, https://doi.org/10.1038/s41586-020-2617-x, 2020.

Vargas, R. and Allen, M. F.: Environmental controls and the influence of vegetation type, fine roots and rhizomorphs on diel and seasonal variation in soil respiration, New Phytol., 179, 460–471, 2008.

Vaughn, L. J. S. and Torn, M. S.: ^{14}C evidence that millennial and fast-cycling soil carbon are equally sensitive to warming, Nat. Clim. Chang., 9, 467–471, https://doi.org/10.1038/s41558-019-0468-y, 2019.

Verheyden, S., Keppens, E., Quinif, Y., Cheng, H., and Edwards, L. R.: Late-glacial and Holocene climate reconstruction as inferred from a stalagmite – Grotte du Pere Noel, Han-sur-Lesse, Belgium, Geol. Belgica, 17, 83–89, 2014.

Wainer, K., Genty, D., Blamart, D., Daëron, M., Bar-Matthews, M., Vonhof, H., Dublyansky, Y., Pons-Branchu, E., Thomas, L., van Calsteren, P., Quinif, Y., and Caillon, N.: Speleothem record of the last 180 ka in Villars cave (SW France): Investigation of a large δ18O shift between MIS6 and MIS5, Quaternary Sci. Rev., 30, 130–146, https://doi.org/10.1016/j.quascirev.2010.07.004, 2011.

Wang, X., Liu, L., Piao, S., Janssens, I. A., Tang, J., Liu, W., Chi, Y., Wang, J., and Xu, S.: Soil respiration under climate warming: differential response of heterotrophic and autotrophic respiration, Glob. Change Biol., 20, 3229–3237, https://doi.org/10.1111/gcb.12620, 2014.

Waring, C. L., Hankin, S. I., Griffith, D. W. T., Kertesz, M. A., Kobylski, V., Wilson, N. L., Coleman, N. V, Kettlewell, G., Zlot, R., Bosse, M., and Bell, G.: Seasonal total methane depletion in limestone caves, Sci. Rep., 7, 8314, https://doi.org/10.1038/s41598-017-07769-6, 2017.

Wolff, E. W., Chappellaz, J., Blunier, T., Rasmussen, S. O., and Svensson, A.: Millennial-scale variability during the last glacial: The ice core record, Quaternary Sci. Rev., 29, 2828–2838, https://doi.org/10.1016/j.quascirev.2009.10.013, 2010.

Zhang, J., Quay, P. D., and Wilbur, D.: Carbon isotope fractionation during gas-water exchange and dissolution of CO_2, Geochim. Cosmochim. Ac., 59, 107–114, 1995.

Clim. Past, 19, 579–606, 2023
https://doi.org/10.5194/cp-19-579-2023

Climate of the Past
Open Access

The new Kr-86 excess ice core proxy for synoptic activity: West Antarctic storminess possibly linked to Intertropical Convergence Zone (ITCZ) movement through the last deglaciation

Christo Buizert[1,*], Sarah Shackleton[2,a], Jeffrey P. Severinghaus[2], William H. G. Roberts[3,4], Alan Seltzer[2,5], Bernhard Bereiter[2,6], Kenji Kawamura[7,8,9], Daniel Baggenstos[6], Anaïs J. Orsi[10,11], Ikumi Oyabu[7], Benjamin Birner[2], Jacob D. Morgan[2], Edward J. Brook[1], David M. Etheridge[12,13], David Thornton[12,13], Nancy Bertler[14,15], Rebecca L. Pyne[14], Robert Mulvaney[16], Ellen Mosley-Thompson[17], Peter D. Neff[18,19], and Vasilii V. Petrenko[19]

[1]College of Earth, Ocean and Atmospheric Sciences, Oregon State University, Corvallis, OR 97331, USA
[2]Scripps Institution of Oceanography, University of California San Diego, La Jolla, CA 92093, USA
[3]Geography and Environmental Sciences, Northumbria University, Newcastle, UK
[4]BRIDGE, School of Geographical Sciences, University of Bristol, Bristol, UK
[5]Marine Chemistry and Geochemistry Department, Woods Hole Oceanographic Institution, Woods Hole, MA 02543, USA
[6]Climate and Environmental Physics, Physics Institute, and Oeschger Centre for Climate Change Research, University of Bern, 3012 Bern, Switzerland
[7]National Institute of Polar Research, 10-3 Midori-cho, Tachikawa, Tokyo 190-8518, Japan
[8]Department of Polar Science, The Graduate University for Advanced Studies, SOKENDAI, Tokyo 190-8518, Japan
[9]Japan Agency for Marine Science and Technology, Yokosuka 237-0061, Japan
[10]Laboratoire des Sciences du Climat et de l'Environnement, LSCE/IPSL, CEA-CNRS-UVSQ, Université Paris-Saclay, l'Orme des merisiers, Gif-sur-Yvette, France
[11]Earth, Ocean and Atmospheric Sciences Department, The University of British Columbia, Vancouver, BC V6T 1Z4, Canada
[12]CSIRO Environment, PMB 1, Aspendale, Victoria 3195, Australia
[13]Australian Antarctic Program Partnership, Institute for Marine & Antarctic Studies, University of Tasmania, Hobart, Tasmania 7004, Australia
[14]Antarctic Research Centre, Victoria University of Wellington, Wellington 6012, New Zealand
[15]GNS Science, Lower Hut 5010, New Zealand
[16]British Antarctic Survey, National Environment Research Council, Cambridge CB3 0ET, UK
[17]Byrd Polar and Climate Research Center, The Ohio State University, Columbus, OH 43210, USA
[18]Department of Soil, Water, and Climate, University of Minnesota, Saint Paul, MN 55108, USA
[19]Department of Earth and Environmental Sciences, University of Rochester, Rochester, NY 14627, USA
[a]present address: Department of Geosciences, Princeton University, Princeton, NJ 08544, USA
[*]*Invited contribution by Christo Buizert, recipient of the EGU Climate: Past, Present & Future Outstanding Early Career Scientists Award 2018.*

Correspondence: Christo Buizert (christo.buizert@oregonstate.edu)

Received: 18 August 2022 – Discussion started: 9 September 2022
Revised: 20 January 2023 – Accepted: 27 January 2023 – Published: 15 March 2023

Abstract. Here we present a newly developed ice core gas-phase proxy that directly samples a component of the large-scale atmospheric circulation: synoptic-scale pressure variability. Surface pressure changes weakly disrupt gravitational isotopic settling in the firn layer, which is recorded in krypton-86 excess ($^{86}Kr_{xs}$). The $^{86}Kr_{xs}$ may therefore reflect the time-averaged synoptic pressure variability over several years (site "storminess"), but it likely cannot record individual synoptic events as ice core gas samples typically average over several years. We validate $^{86}Kr_{xs}$ using late Holocene ice samples from 11 Antarctic ice cores and 1 Greenland ice core that collectively represent a wide range of surface pressure variability in the modern climate. We find a strong spatial correlation ($r = -0.94$, $p < 0.01$) between site average $^{86}Kr_{xs}$ and time-averaged synoptic variability from reanalysis data. The main uncertainties in the analysis are the corrections for gas loss and thermal fractionation and the relatively large scatter in the data. Limited scientific understanding of the firn physics and potential biases of $^{86}Kr_{xs}$ require caution in interpreting this proxy at present. We show that Antarctic $^{86}Kr_{xs}$ appears to be linked to the position of the Southern Hemisphere eddy-driven subpolar jet (SPJ), with a southern position enhancing pressure variability.

We present a $^{86}Kr_{xs}$ record covering the last 24 kyr from the West Antarctic Ice Sheet (WAIS) Divide ice core. Based on the empirical spatial correlation of synoptic activity and $^{86}Kr_{xs}$ at various Antarctic sites, we interpret this record to show that West Antarctic synoptic activity is slightly below modern levels during the Last Glacial Maximum (LGM), increases during the Heinrich Stadial 1 and Younger Dryas North Atlantic cold periods, weakens abruptly at the Holocene onset, remains low during the early and mid-Holocene, and gradually increases to its modern value. The WAIS Divide $^{86}Kr_{xs}$ record resembles records of monsoon intensity thought to reflect changes in the meridional position of the Intertropical Convergence Zone (ITCZ) on orbital and millennial timescales such that West Antarctic storminess is weaker when the ITCZ is displaced northward and stronger when it is displaced southward. We interpret variations in synoptic activity as reflecting movement of the South Pacific SPJ in parallel to the ITCZ migrations, which is the expected zonal mean response of the eddy-driven jet in models and proxy data. Past changes to Pacific climate and the El Niño–Southern Oscillation (ENSO) may amplify the signal of the SPJ migration. Our interpretation is broadly consistent with opal flux records from the Pacific Antarctic zone thought to reflect wind-driven upwelling.

We emphasize that $^{86}Kr_{xs}$ is a new proxy, and more work is called for to confirm, replicate, and better understand these results; until such time, our conclusions regarding past atmospheric dynamics remain speculative. Current scientific understanding of firn air transport and trapping is insufficient to explain all the observed variations in $^{86}Kr_{xs}$. A list of suggested future studies is provided.

1 Introduction

1.1 Motivation and objectives

Proxy records from around the globe show strong evidence for past changes in Earth's atmospheric circulation and hydrological cycle that often far exceed those seen in the relatively short instrumental period.

For example, low-latitude records of riverine discharge captured in ocean sediments (Peterson et al., 2000) and isotopic composition of meteoric water captured in dripstone calcite (Cheng et al., 2016) suggest large variations in tropical hydrology and monsoon strength, commonly interpreted as meridional migrations of the Intertropical Convergence Zone or ITCZ (Chiang and Friedman, 2012; Schneider et al., 2014). Such ITCZ movement is seen in response to insolation changes linked to planetary orbit (Cruz et al., 2005) as well as in response to the abrupt millennial-scale Dansgaard–Oeschger (D–O) and Heinrich cycles of the North Atlantic (Kanner et al., 2012; Wang et al., 2001); the organizing principle is that the ITCZ follows the thermal Equator and therefore migrates towards the warmer (or warming) hemisphere (Broccoli et al., 2006; Chiang and Bitz, 2005).

As a second example, the intensity of the El Niño–Southern Oscillation (ENSO), the dominant mode of global interannual climate variability, has changed through time. A variety of proxy data suggest that ENSO activity in the 20th century was much stronger than in preceding centuries (Emile-Geay et al., 2015; Fowler et al., 2012; Gergis and Fowler, 2009; Thompson et al., 2013). The vast majority of data and model studies suggest weakened ENSO strength in the middle and early Holocene, likely in response to stronger orbitally driven NH summer insolation at that time (Braconnot et al., 2012; Cane, 2005; Clement et al., 2000; Driscoll et al., 2014; Koutavas et al., 2006; Liu et al., 2000, 2014; Moy et al., 2002; Rein et al., 2005; Tudhope et al., 2001; Zheng et al., 2008); yet other studies suggest there may not be such a clear trend and simply more variability (Cobb et al., 2013). Intensification of ENSO (or perhaps a more El Niño-like mean state) may have occurred during the North Atlantic cold phases of the abrupt D–O and Heinrich cycles (Braconnot et al., 2012; Merkel et al., 2010; Stott et al., 2002; Timmermann et al., 2007). Overall, understanding past and future ENSO variability remains extremely challenging (Cai et al., 2015).

As a last example, the strength and meridional position of the Southern Hemisphere westerlies (SHWs) are thought to have changed in the past, which, via Southern Ocean wind-driven upwelling, has potential implications for the global overturning circulation (Marshall and Speer, 2012) and for carbon storage in the abyssal ocean (Anderson et al., 2009; Russell et al., 2006; Toggweiler et al., 2006). The SHWs are thought to have been shifted equatorward (Kohfeld et al., 2013) during the Last Glacial Maximum (LGM), a shift on which climate models disagree (Rojas et al., 2009; Sime et al., 2013). During the abrupt D—O and Heinrich cycles, the SHWs move in parallel with the aforementioned migrations of the ITCZ in both data (Buizert et al., 2018; Marino et al., 2013; Markle et al., 2017) and models (Lee et al., 2011; Pedro et al., 2018; Rind et al., 2001).

As these examples clearly illustrate, evidence of past changes to the large-scale atmospheric circulation is widespread. However, proxy evidence of such past changes is typically indirect – for example via isotopes in precipitation, sea surface temperature, ocean frontal positions, windblown dust, or ocean upwelling – complicating their interpretation. Here we present a newly developed noble-gas-based ice core proxy, Kr-86 excess ($^{86}Kr_{xs}$), that directly samples a component of the large-scale atmospheric circulation: synoptic-scale pressure variability. Owing to the firn air residence time of several years (Buizert et al., 2013) and the gradual bubble trapping process, each ice core sample contains a distribution of gas ages rather than a single age. Therefore, $^{86}Kr_{xs}$ does not record the passing of individual weather systems, but rather the time-averaged intensity of synoptic-scale barometric variability.

Here we provide the first complete description of this new proxy. We validate and calibrate $^{86}Kr_{xs}$ using late Holocene ice core samples from locations around Antarctica and Greenland that represent a wide range of pressure variability in the modern climate. We discuss the difficulties in using this proxy (analytical precision, surface melt, corrections for sample gas loss and thermal fractionation). Next, we use reanalysis data to better understand the drivers of surface pressure variability in Antarctica. Last, we present $^{86}Kr_{xs}$ records from the Antarctic WAIS Divide ice core through the last deglaciation.

1.2 Gravitational disequilibrium and Kr-86 excess

The upper 50–100 m of the ice sheet accumulation zone consists of firn, the unconsolidated intermediate stage between snow and ice. An interconnected pore network exists within the firn, in which gas transport is dominated by molecular diffusion (Schwander et al., 1993). Diffusion in this stagnant air column results in gravitational enrichment in heavy gas isotopic ratios such as $\delta^{15/14}N–N_2$, $\delta^{40/36}Ar$, and $\delta^{86/82}Kr$ (Schwander, 1989; Sowers et al., 1992). In gravitational equilibrium, all these gases attain the same degree of isotopic enrichment per unit mass difference:

$$\delta_{grav}(z) = \left[\exp\left(\frac{\Delta mgz}{RT}\right) - 1\right] \times 1000‰, \tag{1}$$

with Δm the isotopic mass difference (1×10^{-3} kg mol^{-1}), g the gravitational acceleration, z the depth, R the gas constant, and T the temperature in Kelvin.

Besides molecular diffusion, firn air is mixed and transported via three other processes: downward advection with the sinking ice matrix, convective mixing (used in the firn air literature as an umbrella term to denote vigorous air exchange with the atmosphere via, e.g., wind pumping and seasonal convection), and dispersive mixing. These last three transport processes are all driven by large-scale air movement that does not distinguish between isotopologues, and we refer to them collectively as macroscopic air movement. Of particular interest for our proxy is dispersive mixing, which is driven by surface pressure variations. When a low-pressure (high-pressure) system moves into the site, firn air at all depth levels is forced upwards (downwards) to reach hydrostatic equilibrium with the atmosphere – a process called barometric pumping. One can think of the firn layer "breathing" in and out in response to a rising and falling barometer, respectively. Because firn has a finite dispersivity (Schwander et al., 1988), this air movement mixes the interstitial firn air. Note that an upward air movement also exists in the firn column relative to the overall downward advection of the ice, which is caused by the slow reduction of porosity with depth (Rommelaere et al., 1997). This upward airflow due to gradual pore closure (around 10^{-9} to 10^{-8} m s^{-1}) is orders of magnitude smaller than the flows driven via barometric pumping (around 10^{-6} m s^{-1}) and therefore neglected here (Buizert and Severinghaus, 2016).

Any type of macroscopic air movement disturbs the gravitational settling, reducing isotopic enrichment below δ_{grav}. Let $\delta^{86}Kr$, $\delta^{40}Ar$, and $\delta^{15}N$ refer to deviations of $^{86}Kr/^{82}Kr$, $^{40}Ar/^{36}Ar$, and $^{29}N_2/^{28}N_2$, respectively, from their ratios in the well-mixed atmosphere. Gases that diffuse faster (such as N_2) will always be closer to gravitational equilibrium than gases that diffuse slower (such as Kr), and in the absence of thermal fractionation $\delta^{86}Kr/4 < \delta^{40}Ar/4, \delta^{15}N < \delta_{grav}$. The isotopic differences $\delta^{86}Kr/4–\delta^{40}Ar/4$ and $\delta^{86}Kr/4–\delta^{15}N$ thus reflect the degree of gravitational disequilibrium. The magnitudes of the isotopic disequilibria scale in a predictable way following the molecular diffusion coefficients (Birner et al., 2018); because the diffusion coefficients of N_2 and Ar are very similar, their disequilibria are comparable in magnitude. We define Kr-86 excess using the Kr and Ar isotopic difference:

$$^{86}Kr_{xs40} = \frac{\delta^{86}Kr_{corr} - \delta^{40}Ar_{corr}}{\delta^{40}Ar_{corr}} \times 1000 \text{ per meg}‰^{-1}, \tag{2}$$

where the "corr" subscript denotes a correction for gas loss (Appendix A1) and thermal fractionation (Appendix A2). The rationale for including a normalization in the denominator is discussed below. An alternative Kr-86 excess definition is possible using $\delta^{15}N$ instead of $\delta^{40}Ar$:

$$^{86}Kr_{xs15} = \frac{\delta^{86}Kr_{corr}/4 - \delta^{15}N_{corr}}{\delta^{15}N_{corr}} \times 1000 \text{ per meg}‰^{-1}. \tag{3}$$

Note that both definitions rely on having measurements of three isotope ratios ($\delta^{86}Kr$, $\delta^{40}Ar$, and $\delta^{15}N$), as the thermal correction requires δ^{40}Ar and δ^{15}N to be known. The ^{86}Kr$_{xs40}$ definition is preferred because per unit mass difference δ^{40}Ar is less sensitive to thermal fractionation than δ^{15}N is (Grachev and Severinghaus, 2003a, b); this makes it more suitable for interpreting time series. Unless explicitly stated otherwise, we use ^{86}Kr$_{xs40}$ as our definition of Kr-86 excess. The ^{86}Kr$_{xs15}$ does provide a way to check the validity of ^{86}Kr$_{xs40}$ time series, and indeed we find good correspondence between both definitions for the WDC deglacial time series (compare, for example, Figs. A3 and A4). Because the disequilibrium signal is small, we express ^{86}Kr$_{xs}$ in units of per meg (parts per million) of gravitational disequilibrium per per mil of gravitational enrichment. This unit (per meg ‰$^{-1}$) is mathematically identical to per mil, but we use it to emphasize the normalization in the denominator.

In the (theoretical) case of full gravitational equilibrium (and no gas loss or thermal fractionation), $\delta^{86}\mathrm{Kr}/4 = \delta^{40}\mathrm{Ar}/4 = \delta^{15}\mathrm{N} = \delta_{grav}$, and therefore $^{86}\mathrm{Kr}_{xs} = 0$. Any type of macroscopic mixing will cause $\delta^{86}\mathrm{Kr}/4 < \delta^{40}\mathrm{Ar}/4 < \delta^{15}\mathrm{N} < \delta_{grav}$, and thus $^{86}\mathrm{Kr}_{xs} < 0$. In this sense ^{86}Kr$_{xs}$ is a quantitative measure for the degree of gravitational disequilibrium in the firn layer (Birner et al., 2018; Buizert and Severinghaus, 2016).

Kawamura et al. (2013) first describe this gravitational disequilibrium (or kinetic) fractionation effect at the Megadunes site (Severinghaus et al., 2010), where deep firn cracking leads to a 23 m thick convective zone. They suggest that the isotopic disequilibrium can be used to estimate past convective zone thickness. We show here that sites with small convective zones can nevertheless have very negative ^{86}Kr$_{xs}$, and instead we suggest that the ice core ^{86}Kr$_{xs}$ is dominated by dispersive mixing driven by barometric pumping from time-averaged synoptic-scale pressure variability.

The principle behind ^{86}Kr$_{xs}$ is illustrated with idealized firn model experiments in Fig. 1. In the absence of dispersive mixing (Fig. 1a, left panel), all isotope ratios approach δ_{grav} and δ^{86}Kr–δ^{40}Ar is close to zero – but not exactly zero owing to downward air advection. Next, we replace a fraction f of the molecular diffusion with dispersive mixing. With dispersive mixing at $f = 0.1$ and $f = 0.2$ of total mixing (middle and right panels, respectively), isotopic enrichment is progressively reduced below δ_{grav} (dashed line), making δ^{86}Kr–δ^{40}Ar (and consequently ^{86}Kr$_{xs}$) increasingly negative.

The ratio of macroscopic over diffusive transport is expressed via the dimensionless Péclet number, given here for advection and dispersion:

$$Pe_X = \frac{w_{air} L + D_{disp}}{D_X}, \tag{4}$$

where Pe_X is the Péclet number for gas X, w_{air} the (downward) advective air velocity, L a characteristic length scale, D_X the diffusion coefficient for gas X, and D_{disp} the dispersion coefficient (Buizert and Severinghaus, 2016). In agreement with earlier studies (Birner et al., 2018; Kawamura et al., 2013), we find that δ^{86}Kr–δ^{40}Ar is maximized when

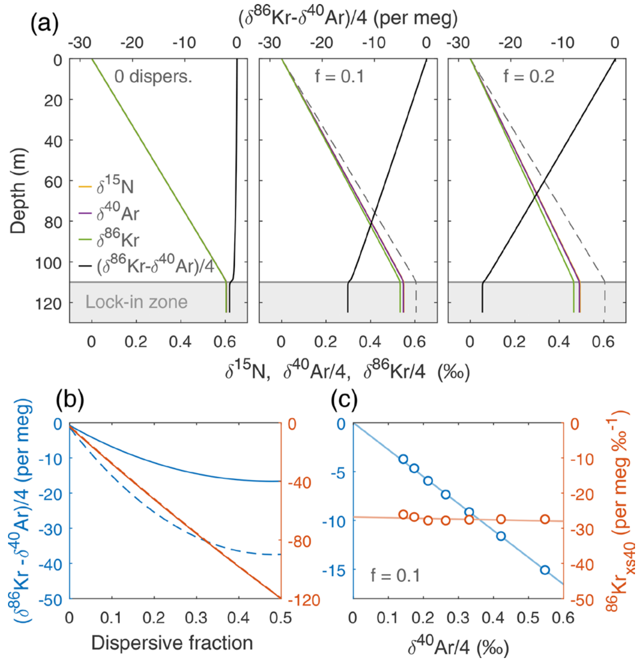

Figure 1. Idealized firn air transport model experiments of ^{86}Kr$_{xs}$. Firn density is calculated using Herron and Langway (1980) and the diffusivity using Schwander (1989). **(a)** Simulations using a fraction of dispersive mixing of $f = 0$ (left panel), $f = 0.1$ (middle panel), and $f = 0.2$ (right panel) for a hypothetical site with an accumulation rate of $A = 2\,\mathrm{cm\,a^{-1}}$ ice equivalent and mean annual temperature $T = -60\,°\mathrm{C}$. At dispersive fraction f, effective molecular diffusivity of all gases is multiplied by (1-f) and dispersive mixing for all gases is set equal to f times the effective molecular diffusivity of CO_2. **(b)** Isotopic disequilibrium as a function of dispersive mixing intensity at two different firn thicknesses of around 100 m (dashed, $A = 2\,\mathrm{cm\,a^{-1}}$ and $T = -60\,°\mathrm{C}$) and 50 m (solid, $A = 2\,\mathrm{cm\,a^{-1}}$ and $T = -43\,°\mathrm{C}$). We compare isotopic disequilibrium without (blue, left axis) and with (orange, right axis) normalization. **(c)** Simulations at 10 % dispersive mixing, with each dot representing different climatic conditions. The accumulation rate is $A = 2\,\mathrm{cm\,a^{-1}}$ ice equivalent, and mean annual temperature is changed from −60 to −30 °C in steps of 5 °C.

molecular mixing and dispersive mixing are equal in magnitude ($f = 0.5$, Fig. 1b), corresponding to $Pe_X \approx 1$. Note that ^{86}Kr$_{xs}$ responds more linearly to f than δ^{86}Kr–δ^{40}Ar does due to δ^{40}Ar in the denominator of Eq. (2).

In a last idealized experiment, we keep the fraction of dispersion fixed at $f = 0.1$ while we reduce the thickness of the firn column by increasing the site temperature (Fig. 1c). We find that δ^{86}Kr–δ^{40}Ar scales linearly with firn thickness, here represented by δ^{40}Ar on the x axis. However, ^{86}Kr$_{xs}$ remains essentially constant due to the normalization by δ^{40}Ar in the denominator of Eq. (2). The normalization step is thus necessary to enable meaningful comparison between different sites and time periods that all have different firn thicknesses. For this reason, the definition of ^{86}Kr$_{xs}$ used here has been updated from the original definition by Buizert and Severinghaus (2016).

Note that these highly idealized experiments assume dispersive mixing to be a fixed fraction of total transport throughout the firn column, equivalent to a constant Péclet number in the diffusive zone (a convective zone is absent in these simulations). In reality, the Péclet number varies greatly on all spatial scales. On the macroscopic scale ($>$ 1 m), Pe reflects the various transport regimes (Sowers et al., 1992), being highest in the convective and lock-in zones. On the microscopic scale ($<$ 1 cm), hydraulic conductance scales as $\propto r^4$ (with r the pore radius), whereas the diffusive conductance scales as $\propto r^2$. This means that the Darcy flow associated with barometric pumping will concentrate in the widest pores and pathways, leading to a range of effective Péclet numbers within a single sample of firn. At intermediate spatial scales of a few centimeters, firn density layering introduces strong heterogeneity in transport properties. It is unclear at present whether the competition between diffusive and non-diffusive transport, which occurs at the microscopic pore level, can be accurately represented in macroscopic firn air models via a linear parameterization as is the current practice.

2 Methods

2.1 Ice core sites

In this study we use ice samples from 11 ice cores drilled in Antarctica and 1 in Greenland. The Antarctic sites are the West Antarctic Ice Sheet (WAIS) Divide core (WDC06A, or WDC), Siple Dome (SDM), James Ross Island (JRI), Bruce Plateau (BRP), Law Dome DE08, Law Dome DE08-OH, Law Dome DSSW20K, Roosevelt Island Climate Evolution (RICE), Dome Fuji (DF), EPICA (European Project for Ice Coring in Antarctica) Dome C (EDC), and South Pole Ice Core (SPC14, or SP). Ice core locations in Antarctica are shown in Fig. 2a. In Greenland, we use samples from the Greenland Ice Sheet Project 2 (GISP2).

We shall refer to late Holocene data from these sites as the calibration dataset, analogous to a core-top dataset in the sediment coring literature. Site characteristics, coordinates, and number of samples included in the calibration dataset are given in Table 1. The DE08-OH site is a recent revisit of the Law Dome DE08 site. The DE08-OH core was measured at sub-annual resolution to understand centimeter-scale $^{86}\mathrm{Kr}_{\mathrm{xs}}$ variations due to, for example, layering in firn density and bubble trapping (Appendix B). In addition to the calibration dataset, we present a record of Kr-86 excess going back to the LGM from WDC.

2.2 Ice sample analysis

We broadly follow analytical procedures described elsewhere (Bereiter et al., 2018a, b; Headly and Severinghaus, 2007; Severinghaus et al., 2003). In short, an 800 g ice sample, its edges trimmed with a band saw to expose fresh surfaces, is placed in a chilled vacuum flask that is then evacuated for 20 min using a turbomolecular pump. Air is extracted from the ice by melting the sample while stirring vigorously with a magnetic stir bar, led through a water trap, and cryogenically trapped in a dip tube immersed in liquid He. Next, the sample is split into two unequal fractions. The smaller fraction (about 2 % of total air) is analyzed for $\delta^{15}\mathrm{N}$–N_2, $\delta^{18}\mathrm{O}$–O_2, $\delta\mathrm{O}_2/\mathrm{N}_2$, and $\delta\mathrm{Ar}/\mathrm{N}_2$ on a 3 kV Thermo Finnigan Delta V plus dual inlet IRMS (isotope ratio mass spectrometer). In the larger fraction, noble gases are isolated via hot gettering to remove reactive gases. The purified noble gases are then analyzed for $\delta^{40/36}\mathrm{Ar}$, $\delta^{40/38}\mathrm{Ar}$, $\delta^{86/82}\mathrm{Kr}$, $\delta^{86/84}\mathrm{Kr}$, $\delta^{86/83}\mathrm{Kr}$, $\delta\mathrm{Kr}/\mathrm{Ar}$, and $\delta\mathrm{Xe}/\mathrm{Ar}$ on a 10 kV Thermo Finnigan MAT253 dual-inlet IRMS. We reject one sample from RICE due to incomplete sample transfer and one sample from WDC due to problems with the water trap. Calibration is done for each measurement campaign by running samples of La Jolla pier air.

All calibration (core-top) data were measured using Method 2 as described by Bereiter et al. (2018a), with a longer equilibration time during the splitting step than used in that study to improve isotopic equilibration between the fractions. The exception is the DE08-OH site, where the ice sample (rather than the extracted gas sample) was split into two fractions – the advantage of this approach is that it does not require a gas splitting step that is time-consuming and may fractionate the isotopes; the downside is that the samples may have slightly different isotopic composition due to the stochastic nature of bubble trapping and the different gas loss histories of the ice pieces.

Measurements of the WDC downcore dataset were performed over five separate measurement campaigns that occurred in February–April 2014, February–April 2015, August 2015, August 2020, and August 2021. The first three campaigns are described by Bereiter et al. (2018b), in which the $^{86}\mathrm{Kr}_{\mathrm{xs}}$ data are a by-product of measuring $\delta\mathrm{Kr}/\mathrm{N}_2$ for reconstructing global mean ocean temperature. Campaigns 1 and 2 are in good agreement, whereas campaign 3 appears offset from the other two by an amount that exceeds the analytical precision (offset around 35 per meg ‰$^{-1}$). To validate the main features in the record, we performed two additional campaigns (4 and 5), in which all the gas extracted from each ice sample was quantitatively gettered and only analyzed for Ar and Kr isotopic composition. The downcore record, as well as the five analytical campaigns, is discussed in detail in Sect. 5.1. Data from the bubble–clathrate transition zone (here 1000 to 1600 m depth, or $\sim$ 4 ka to 7 ka) are excluded owing to the potential for artifacts; the depth range of the bubble–clathrate transition zone is based on observed positive anomalies in $\delta\mathrm{O}_2/\mathrm{N}_2$ in WDC ice.

All samples were analyzed at the Scripps Institution of Oceanography, USA, with the exception of the EDC samples, which were analyzed at University of Bern, Switzerland

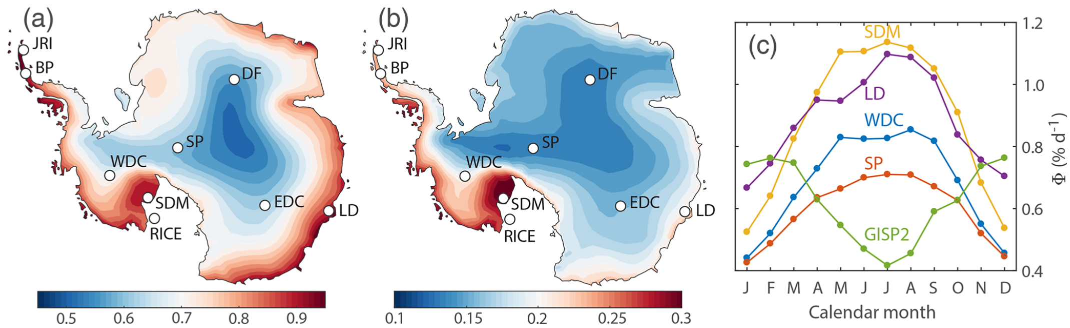

Figure 2. Calibrating Kr-86 excess. **(a)** Annual mean Φ in Antarctica over 1979–2017 in units of percent per day ($\%\,d^{-1}$). **(b)** Interannual variability (1σ standard deviation) of annual mean Φ over 1979–2017 in units of percent per day ($\%\,d^{-1}$). **(c)** Annual cycle in Φ for 1979–2017 for the indicated site.

Table 1. Ice core sites used in this study, with N the number of samples included in the calibration study. See the main text for acronyms.

Site	T (°C)	A (m ice a^{-1})	Φ ($\%\,d^{-1}$)	Latitude	Longitude	N
WDC	−31	0.22	0.68	79.5° S	112.1° W	8[a]
DF	−57	0.028	0.56	77.3° S	39.7° E	3
SP	−51	0.078	0.6	90.0° S	98.2° W	5
SDM	−25	0.13	0.88	81.7° S	149.1° W	3
DSSW20K	−21	0.16	0.89	66.8° S	112.6° E	4
DE08	−19	1.2	0.89	66.7° S	113.2° E	8
DE08-OH	−19	1.2	0.89	66.7° S	113.2° E	8[b]
RICE	−24	0.24	0.79	79.4° S	161.7° W	3[a]
EDC	−55	0.03	0.6	75.1° S	123.4° E	4
JRI	−14	0.68	0.97	64.2° S	57.7° W	5[c]
BRP	−15	2	0.9	66.1° S	64.1° W	2[c]
GISP2	−32	0.23	0.62	72.6° N	38.5° W	4

[a] Not including one sample rejected due to technical problems. [b] Only shallow samples due to strong gas loss in deeper samples attributed to warm storage conditions. [c] Refrozen meltwater present as indicated by elevated Xe/N_2 ratio.

(Baggenstos et al., 2019). Some of the EDC samples analyzed had clear evidence of drill liquid contamination, which acts to artifactually lower $^{86}Kr_{xs}$ via isobaric interference on mass 82; the late Holocene data used here were not flagged for drill liquid contamination (Baggenstos et al., 2019).

The 2σ analytical precision of the $\delta^{15}N$, $\delta^{40}Ar$, and $\delta^{86}Kr$ measurements is around 3, 5, and 26 per meg, respectively, based on the reproducibility of La Jolla air measurements. Via standard error propagation, this results in a ~ 22 per meg $‰^{-1}$ (2σ) analytical uncertainty for both $^{86}Kr_{xs40}$ and $^{86}Kr_{xs15}$ at a site like WDC where $\delta^{40}Ar \approx 1.2\,‰$. We have no true (same-depth) replicates to assess the reproducibility of $^{86}Kr_{xs}$ measurements experimentally. The measured isotope ratios are corrected for gas loss (Δ^{40}_{GL}) and thermal fractionation (Δ^{86}_{TF}, Δ^{40}_{TF}, Δ^{15}_{TF}) before interpretation; details on these corrections are given in Appendix A. For the core-top calibration study, the average magnitude of the gas loss and thermal fractionation corrections is +14 and −15 per meg $‰^{-1}$ in $^{86}Kr_{xs}$, respectively. Note that these two corrections both involve the $\delta^{40}Ar$ isotopic ratio, and therefore they are not independent from each other and not additive – in other words, the total correction is not simply the sum of the two individual corrections.

Our study includes two ice cores from the Antarctic Peninsula: BRP (two ice samples) and JRI (five ice samples). Measured $\delta Xe/N_2$ ratios (and to a lesser extent the $\delta Kr/N_2$ ratios) in all samples from both locations are significantly elevated above the expected gravitational enrichment signal (Fig. A1a), which is clear evidence for the presence of refrozen meltwater in these samples (Orsi et al., 2015). Like xenon, krypton is highly soluble in (melt)water, and therefore $^{86}Kr_{xs}$ cannot be reliably measured in these samples; we reject all samples from the BRP and JRI sites. It is notable that all samples from both sites show evidence of refrozen meltwater, given that the high-accumulation BRP core is nearly entirely free of visible melt layers and that we carefully selected samples without visible melt features at JRI. Visible ice lenses form only when meltwater pools and refreezes on top of low-permeability layers such as wind crusts; our observations suggest meltwater can also refreeze throughout the firn in a way that cannot be detected visually.

3 Calibrating Kr-86 excess

The $^{86}Kr_{xs}$ proxy for synoptic activity was first proposed on theoretical grounds by Buizert and Severinghaus (2016) – here we provide the first experimental validation of this proxy using a core-top calibration of $^{86}Kr_{xs}$ using late Holocene ice core samples from nine locations around Antarctica and one in Greenland that represent a wide range of pressure variability in the modern climate (here: 1979–2017 CE).

3.1 Spatial variation in synoptic-scale pressure variability

Kr-86 excess is sensitive to air movement (both upward and downward), which in turn is controlled by the magnitude of relative air pressure change. Let p_i be a time series of (synoptic-scale) site surface pressure with N data points, time resolution Δt, and mean value $\overline{p}$. The time series can span a month, year, or multi-year period, with $\overline{p}$ potentially different for each month or year. We define the parameter Φ as

$$\Phi = \frac{1}{N\overline{p}} \sum_{i=1}^{N} \left| \frac{p_i - p_{i-1}}{\Delta t} \right|, \tag{5}$$

which we express here in convenient units of percent per day ($\%\,\mathrm{d}^{-1}$). Φ reflects the intensity of barometric pumping in the firn column. Note that Δt should be larger than $\sim 1\,\mathrm{h}$, which is the timescale for the entire firn column to equilibrate with the surface pressure (Buizert and Severinghaus, 2016), and smaller than about a day in order to adequately resolve synoptic-scale pressure events. Here we use ERA-Interim reanalysis data from 1979–2017 with $\Delta t = 6\,\mathrm{h}$ (Dee et al., 2011), from which we calculate monthly and annual Φ values using Eq. (5). A map of annual mean Φ across Antarctica is given in Fig. 2a. At all sites considered, Φ has a strong seasonal cycle with pressure variability and storminess being strongest in the local winter season (Fig. 2c). Interannual differences in Φ are greatest along the Siple coast and coastal West Antarctica (Fig. 2b), mainly reflecting the influence of central Pacific (ENSO, Pacific Decadal Oscillation – PDO) climate variability (Sect. 4).

3.2 Kr-86 excess proxy calibration

Present-day Antarctica has a wide range of Φ (Fig. 2a), which allows us to validate and calibrate $^{86}Kr_{xs}$. In Fig. 3a we plot the site mean $^{86}Kr_{xs40}$ (with $\pm 1\sigma$ error bars) as a function of Φ (averaged over full 1979–2017 period). We find a Pearson correlation coefficient of $r = -0.94$ when using site mean $^{86}Kr_{xs40}$ and $r = -0.83$ when using the $^{86}Kr_{xs40}$ of individual samples ($p < 0.01$). Note that in this particular case the site mean $^{86}Kr_{xs40}$ and $^{86}Kr_{xs15}$ are identical (because by design, after thermal correction $\delta^{15}N = \delta^{40}Ar/4$); the error bars are different, though.

The $^{86}Kr_{xs}$ data have been corrected for gas loss (Appendix A1) and thermal fractionation (Appendix A2), with the gas loss correction being the more uncertain component. Figure 3b shows the correlations of the calibration curve as a function of the gas loss scaling parameter ε_{40}. We find a good correlation over a wide range of ε_{40} values, proving our calibration is not dependent on the choice of ε_{40}. When using uncorrected $^{86}Kr_{xs40}$ data the site mean correlation is $r = -0.71$; when applied individually, both the gas loss and thermal correction each improve the correlation to $r = -0.77$ and $r = -0.79$, respectively (Fig. A3, all $p < 0.05$). Based on these tests we conclude that the observed relationship is not an artifact of the applied corrections. The applied corrections improve the correlation, which increases confidence in the method. The calibration results for $^{86}Kr_{xs15}$ are shown in Fig. A4.

Notably, there is a large spread in $^{86}Kr_{xs}$ across samples from any single site, particularly at the high-Φ sites of SDM and RICE (Fig. 3a, note the $\pm 1\sigma$ error bars). This spread is larger than the measurement uncertainty, and we believe this variance reflects a signal that is truly present in the ice. The Siple coast and Roosevelt Island experience the largest Φ interannual differences in Antarctica (Fig. 2b), and it is therefore likely that our coarse sampling is aliasing the true $^{86}Kr_{xs}$ signal. The variance in $^{86}Kr_{xs}$ may also contain climate information.

Both theoretical considerations and observations thus suggest $^{86}Kr_{xs}$ is a proxy for time-averaged barometric surface pressure variability at the site, and in the remainder of this paper we will interpret it as such.

3.3 Discussion of the Kr-86 excess proxy

Our interpretation of $^{86}Kr_{xs}$ as a proxy for time-averaged pressure variability is somewhat complicated by the possibility of deep convective zones, which have the same $^{86}Kr_{xs}$ signature as barometric pumping. This was discovered at the Megadunes (MD) site, central East Antarctica; at this zero-accumulation site deep cracks form in the firn layer that facilitate a 23 m deep convection zone (Severinghaus et al., 2010). In fact, this observation led earlier work to suggest that noble gas gravitational disequilibrium may be used as a proxy for convective zone thickness (Kawamura et al., 2013) rather than synoptic-scale pressure variability as suggested here. Although megadunes and zero-accumulation zones are ubiquitous and cover 20 % of the Antarctic Plateau (Fahnestock et al., 2000), ice cores are seldom drilled in these areas and it is safe to assume that they never formed at sites like WAIS Divide that had relatively high accumulation rates even during the last glacial period. Performing the corrections for thermal and size-dependent fractionation is challenging at MD, and we suggest that the MD $^{86}Kr_{xs}$ is in the range of -2 to

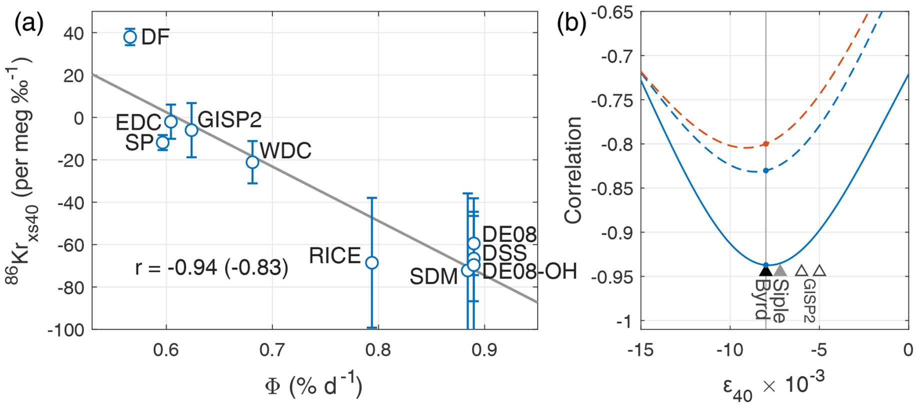

Figure 3. Calibrating Kr-86 excess. **(a)** $^{86}Kr_{xs}$ as a function of Φ for the calibration dataset. Circles give the site mean, and the error bars denote the $\pm 1\sigma$ standard deviation between samples (uncertainty in corrections and measurements not included). The number of samples at each site is given in Table 1. The Pearson correlation coefficient is $r = -0.94$ when considering site data means and $r = -0.83$ when considering all individual samples. Data are corrected for gas loss using $\varepsilon_{40} = -0.008$ (Appendix A1) and corrected for thermal fractionation using site mean ^{15}N excess (Appendix A2). The calibration curve for $^{86}Kr_{xs15}$ is identical in this case, with slightly larger error bars. **(b)** Correlation of the calibration curve as a function of the gas loss correction scaling parameter ε_{40}. The solid line gives the correlation for both site mean $^{86}Kr_{xs15}$ and $^{86}Kr_{xs40}$ (identical); the dashed lines show the correlation using individual samples for $^{86}K_{xs40}$ (blue) and $^{86}Kr_{xs15}$ (orange). Triangles denote the ε_{40} estimate from the Byrd, Siple, and GISP2 ice cores (Fig. A2; Kobashi et al., 2008a; Severinghaus et al., 2003).

-55 per meg ‰$^{-1}$; even at the larger limit, this is still smaller in magnitude than $^{86}Kr_{xs}$ anomalies at several modern-day sites with small convective zones (such as SDM, RICE, and the Law Dome sites), suggesting barometric pumping is capable of producing larger $^{86}Kr_{xs}$ signals than even the most extreme observed case of convective surface mixing. Having $^{86}Kr_{xs}$ measured in MD ice core (rather than firn air) samples would be valuable for a more meaningful comparison to the ice core sample measurements presented here. Windy sites can have substantial convective zones of ~ 14 m (Kawamura et al., 2006), and future studies of $^{86}Kr_{xs}$ at such sites would be valuable.

Currently, 1-D and 2-D firn air transport model simulations underestimate the magnitude of the $^{86}Kr_{xs}$ signal compared to measurements in mature ice samples (Birner et al., 2018), complicating scientific understanding of the proxy. In these models, the effective molecular diffusivity of each gas is scaled linearly to its free air diffusivity. The ratio of krypton to argon free air diffusivity is 0.78. This ratio, which directly sets the magnitude of the simulated $^{86}Kr_{xs}$, may actually be smaller than 0.78 in real firn, as krypton is more readily adsorbed onto firn surfaces, retarding its movement (similar to gases moving through a gas chromatography column). This may be one explanation for why models simulate too little $^{86}Kr_{xs}$.

Another likely explanation for the model–data mismatch is that certain critical sub-grid processes (such as the aforementioned pore size dependence of the Péclet number) are not adequately represented in these models. Barometric pumping may further actively shape the pore network through the movement of water vapor, thereby keeping certain preferred pathways connected and open below the density at which percolation theory would predict their closure (Schaller et al., 2017). The fate of a pore restriction is determined by the balance between the hydrostatic pressure (that acts to close it) and vapor movement away from its convex surfaces (that acts to keep it open); we speculate that barometric Darcy airflow keeps high-flow channels connected longer by eroding convex surfaces. This enhances the complexity (and therefore dispersivity) of the deep firn pore network and possibly creates a nonlinear $^{86}Kr_{xs}$ response to barometric pumping. The hypothesized channel formation in deep firn is driven by a positive feedback on flow volume and somewhat reminiscent of erosion-driven stream network formation in fluvial geomorphology.

Firn models predict that, after correcting for thermal fractionation, the deviation from gravitational equilibrium for the elemental ratios (such as $\delta Kr/Ar$) should be proportional to that deviation in isotopic ratios. However, the observations suggest that the former is usually smaller than would be expected from the latter. As before, adsorption of Kr onto firn grain surfaces may contribute to the observed discrepancy, and laboratory tests of this process are called for. Further, the impacts of gas loss are greater on elemental ratios than on the isotopic ratios, which may also contribute. Including measurements of xenon isotopes and elemental ratios in future measurement campaigns may be able to provide additional constraints to better understand this discrepancy.

Measurements on firn air samples, where available, suggest a smaller $^{86}Kr_{xs}$ anomaly in firn air than found in ice core samples from the same site. We attribute this in part to a seasonal bias that is introduced by the fact that firn air sampling always takes place during the summer months, whereas the synoptic variability that drives the Kr-86 excess anomalies is largest during the winter (Fig. 2c); consequently, firn air observations are biased towards weaker $^{86}Kr_{xs}$. Further, in the deep firn where $^{86}Kr_{xs}$ anomalies are largest, firn air pumping may not yield a representative air sample, but rather be biased towards the well-connected porosity at the expense of poorly connected cul-de-sac-like pore clusters. Since barometric pumping ventilates this well-connected pore space with low-$^{86}Kr_{xs}$ air from shallower depths, the firn air sampling may not capture a representative $^{86}Kr_{xs}$ value of the full firn air content. These explanations are all somewhat speculative, and a definitive understanding of the firn–ice differences is lacking at this stage.

Gas loss and thermal corrections are critical to the interpretation of $^{86}Kr_{xs}$. The thermal correction is applied to account for thermal gradients in the firn (ΔT, defined here as the temperature at the top minus the temperature at the base of the firn), which are chiefly caused by geothermal heat or surface temperature changes at the site. At low-accumulation sites geothermal heating leads to $\Delta T < 0$. We use ^{15}N excess ($\delta^{15}N$–$\delta^{40}Ar/4$) to estimate the thermal gradient in the firn (Appendix A2). Because nitrogen and argon have similar diffusivities but different thermal diffusion coefficients, $\delta^{15}N$–$\delta^{40}Ar$ is relatively insensitive to barometric pumping yet sensitive to thermal fractionation, allowing estimating ΔT.

Besides the actual thermal gradients in the firn, the isotopic composition may also be impacted by seasonal rectifier effects. If the firn air transport properties differ between the seasons (for example due to thermal contraction cracks, convective instabilities, or seasonality in wind pumping), this can result in a thermal fractionation of isotopic ratios in the absence of a thermal gradient ΔT in mean annual temperature (Morgan et al., 2022).

For the WDC, DSS, and GISP2 sites we obtain ΔT values close to zero as expected for these high-accumulation sites; for the SP, SDM, RICE, and DF sites we find ΔT ranging from -0.76 to -1.18 °C, in agreement with the effect of geothermal heat. The high-accumulation DE08 and DE08-OH sites both have an unexpectedly large ΔT of -1.6 °C; the good agreement between the sites suggests that it is likely a real signal, yet we can rule out geothermal heat as the cause. This may suggest that the Law Dome DE08 site is subject to a seasonal rectifier effect or a recent climatic cooling. Last, the EDC site shows an unexpected positive $\Delta T = +1.6 \pm 1.89$ °C. Three possible explanations are the following (1) the aforementioned drill liquid contamination for this core (Baggenstos et al., 2019); (2) a summertime-biased seasonal rectifier; or (3) an overcorrection of $\delta^{40}Ar$ for gas loss, which could occur, for example, if natural gas loss and post-coring fugitive gas loss fractionate $\delta^{40}Ar$ differently and EDC samples were impacted mostly by the former type (our correction is mostly based on measurements of the latter type).

For the Law Dome DE08-OH site we observe large (5-fold) sub-annual variations in $^{86}Kr_{xs}$ (Fig. B1). The magnitude of the $^{86}Kr_{xs}$ layering is truly remarkable. The isotopic enrichment of each gas ($\delta^{15}N$, $\delta^{40}Ar$, $\delta^{86}Kr$) can be converted to an effective diffusive column height (DCH). For the samples with the smallest (greatest) $^{86}Kr_{xs}$ magnitude, this DCH is around 1 m (6 m) shorter for $\delta^{86}Kr$ than it is for $\delta^{15}N$. The firn air transport physics that may explain such phenomena are beyond our current scientific understanding. The sub-annual variations may be related to the seasonal cycle in storminess, though that seems improbable to us at present as the gas age distribution at the depth of bubble closure has a width of several years (Schwander et al., 1993). Another reason may be seasonal layering in firn properties – such as density, grain size, and pore connectivity – that control the degree of disorder and dispersive mixing occurring in the firn and lead to a staggered firn trapping and seasonal variations in Δage (Etheridge et al., 1992; Rhodes et al., 2016). The sample air content estimated from the IRMS inlet pressure is similar for all measurements, making it unlikely that the variations in $^{86}Kr_{xs}$ are caused by remnant open porosity in lower-density layers. In any case it is remarkable that such large variations in gas composition can arise and persist on such small length scales, given the relatively large diffusive, dispersive, and advective transport length scales of the system. More work is needed to establish the origin of the sub-annual variations in ice core $^{86}Kr_{xs}$. At all other sites analyzed here, the sample length exceeds the annual layer thickness; this will remove some, but not all, of the effects of the sub-annual variations.

Another puzzling observation is the positive $^{86}Kr_{xs}$ at the Dome Fuji (DF) site; theoretical considerations suggest it should always be negative. In part this may be due to an overcorrection of $\delta^{40}Ar$ for gas loss, which would act to bias $^{86}Kr_{xs}$ in the positive direction. This correction is largest at DF owing to the very negative $\delta O_2/N_2$ and $\delta Ar/N_2$ (Fig. A1); while we base our correction on published work, it is conceivable that we overestimate the true correction (Appendix A1). In particular, our gas loss correction is based on observations of artifactual post-coring gas loss, which may fractionate $\delta^{40}Ar$ differently than natural fugitive gas loss during bubble close-off. Omitting the gas loss correction indeed makes $^{86}Kr_{xs}$ at DF negative (Fig. A3c and d). Another hypothesis is that the positive $^{86}Kr_{xs}$ signal is an artifact of the seasonal rectifier that Morgan et al. (2022) identify at DF. In this work we assume a linear approach in which the effect of the rectifier can be described by a single ΔT value that is the same for isotopic pairs. In reality, there may be nonlinear interactions between thermal fractionation and firn advection that impact the isotopic values of the various gases in a more complex way than captured in our approach.

The $^{86}Kr_{xs}$ is also correlated with other site characteristics besides Φ. For site elevation we find $r = 0.96$ (0.84) and for mean annual temperature $r = -0.87$ (-0.76); the number in parentheses gives the correlation when using all the individual samples rather than site mean $^{86}Kr_{xs}$. The listed correlations all have $p < 0.01$. For site accumulation we do not find a statistically significant correlation at the 90 % confidence level. The correlations with elevation and temperature are comparable to those we find for Φ; this is no surprise given that elevation, Φ, and T are all strongly correlated with one another, mainly because elevation directly impacts both T (via the lapse rate) and Φ (via its topographic influence on the position of storm tracks). To our knowledge there are no mechanisms through which either elevation or annual mean temperature could drive kinetic isotopic fractionation in the firn layer. Perhaps other unexamined site characteristics (such as the degree of density layering or the magnitude of the annual temperature cycle) could also provide good correlations, suggesting additional hidden controls on $^{86}Kr_{xs}$. The data needed to assess such hidden controls are not available for most sites.

The calibration of the $^{86}Kr_{xs}$ proxy is based on spatial regression. In applying the proxy relationship to temporal records, we make the implicit assumption that proxy behavior in the temporal and spatial dimensions is at least qualitatively similar. This assumption may prove incorrect. In particular, changes in insolation are known to impact firn microstructure and bubble close-off characteristics, which in turn impacts gas records of $\delta O_2/N_2$ and total air content (Bender, 2002; Raynaud et al., 2007). Since $^{86}Kr_{xs}$ is linked to the dispersivity of deep firn, it seems probable that insolation also has a direct impact on $^{86}Kr_{xs}$ via the firn microstructure. We will revisit this issue in our interpretation of the WDC $^{86}Kr_{xs}$ record (Sect. 5). Overall, we anticipate $^{86}Kr_{xs}$ to be a qualitative proxy for synoptic variability yet want to caution against quantitative interpretation based on the spatial regression slope.

The observations presented in this section clearly highlight the fundamental shortcomings of our current understanding of firn air transport, hinting at the existence of complex interactions, presumably at the pore scale, that are not being represented. Percolation theory finds that near the critical point (presumably the lock-in depth) a network becomes fractal in its nature; we suggest that this fractal nature of the pore network likely contributes to nonlinear pore-scale interactions that give rise to the $^{86}Kr_{xs}$ observations in ice. While the observed correlation in Fig. 3a is highly encouraging, further work is critical to understand this proxy. Examples of such future studies are the following: (1) additional high-resolution records that can resolve the true variations that exist in a single ice core, similar to the DE08-OH record; (2) 3-D firn air transport model studies; (3) improvements to the gas loss correction; (4) additional coring sites to extend the spatial calibration and further confirm the validity of the proxy; (5) adding xenon isotopic constraints (^{136}Xe excess) as an additional marker of isotopic disequilibrium; (6) numerical simulations of pore-scale air transport in large-scale firn networks; (7) experimental studies of dispersion and noble gas adsorption in firn samples; (8) percolation theory approaches to study the fractal nature of the pore network of the lock-in zone; and (9) replication of the WDC deglacial $^{86}Kr_{xs}$ record in nearby ice cores such as RICE.

4 Present-day controls on Kr-86 excess in Antarctica

In this section we investigate the large-scale patterns of climate variability in the Southern Hemisphere that could affect Φ and therefore $^{86}Kr_{xs}$ over Antarctica. We begin by investigating the patterns in the wind field that are associated with changes in Φ at ice core sites, before examining how more canonical patterns of Southern Hemisphere climate variability, such as the southern annular mode (SAM), might affect Φ over the whole of Antarctica.

We use ERA-Interim reanalysis data for the 1979–2017 period (Dee et al., 2011) to evaluate the present-day controls on synoptic-scale pressure variability in Antarctica. Kr-86 excess in an ice core sample averages over several years of pressure variability, and therefore we focus on annual mean correlation in our analysis. The annual mean Φ is calculated from the 6-hourly reanalysis data using Eq. (5). Note that we let the year run from April to March to avoid dividing single El Niño and La Niña events across multiple years.

At all Antarctic sites investigated, a similar pattern exists; four representative locations are shown in Fig. 4, where we regress the zonal wind in the lower (850 hPa, color shading) and upper troposphere (200 hPa, contours) onto our surface pressure variability parameter Φ. We find that synoptic pressure variability at these sites is linked to zonal winds along the southern margin of the eddy-driven subpolar jet (SPJ), which extends from the surface to the upper troposphere (Nakamura and Shimpo, 2004; Trenberth, 1991). Sites near the ice sheet margin (Fig. 4a, b and d) are most sensitive to the SPJ edge in their sector of Antarctica, whereas interior sites (Fig. 4c) appear to be sensitive to the overall strength and position of the SPJ. Note that strengthening, broadening, or southward shifting of the SPJ can all in principle enhance site Φ.

Pressure variability at WDC is furthermore correlated with the strength of the Pacific subtropical jet (STJ) aloft (solid contour lines centered around 30° S in the Pacific in Fig. 4a), forming an upper troposphere wind pattern that resembles the wintertime South Pacific split jet (Bals-Elsholz et al., 2001; Nakamura and Shimpo, 2004); this agrees with the finding that a strengthening of the split jet enhances storminess over West Antarctica (Chiang et al., 2014).

Next, we investigate how the well-known patterns of large-scale atmospheric variability, such as SAM and ENSO, impact pressure variability in Antarctica. Figure 5 shows the correlation of Φ with the three leading modes of SH extratropical atmospheric variability; the correlation with various indices and modes for individual ice core locations is given in Table 2. Most teleconnection patterns have a specific season

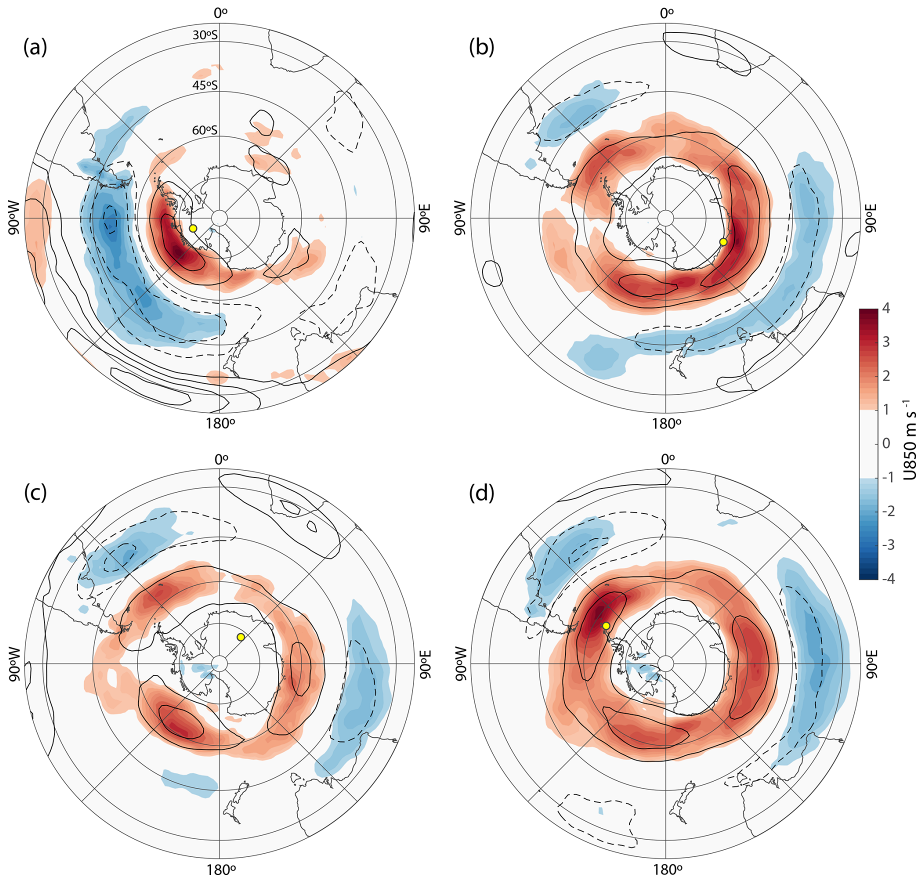

Figure 4. Zonal wind speed at 850 hPa (color shading, see scale bar) and 200 hPa ($2\,\mathrm{m\,s^{-1}}$ contours) regressed onto surface synoptic activity Φ at the Antarctic ice core sites of **(a)** WAIS Divide, **(b)** Law Dome (DE08, DE08-OH, and DSSW20K), **(c)** Dome Fuji, and **(d)** James Ross Island. Yellow dots mark the ice core locations.

during which they are strongest; here we do not differentiate between seasons because $^{86}\mathrm{Kr_{xs}}$ in ice core samples averages over all seasons.

Globally, annual mean Φ is highest over the Southern Ocean (Fig. 5a), a region of enhanced baroclinicity associated with the eddy-driven SPJ (Nakamura and Shimpo, 2004). The green line denotes the latitude of maximum Φ, roughly corresponding to the latitude with the highest storm track density (57.8° S on average).

The dominant mode of atmospheric variability in the SH extratropics is the southern annular mode, representing the vacillation of atmospheric mass between the middle and high latitudes (Thompson and Wallace, 2000). Figure 5b shows 500 hPa geopotential height (Z_{500}) anomalies associated with the SAM as contours, with the color shading giving the correlation between Φ and the SAM index. During the positive SAM phase (negative Z_{500} over Antarctica) we find that the storm tracks and maximum synoptic activity are displaced towards Antarctica (positive Φ correlation poleward of the green line in Fig. 5b). This is associated with a strengthening and poleward displacement of the SH westerly winds that occurs during a positive SAM phase. More locally, Φ on the Antarctic Peninsula is positively correlated with the SAM index (Table 2); Φ at the other sites is not meaningfully impacted. This suggests that the variations associated with the SAM (as commonly defined) do not extend far enough poleward to meaningfully impact Antarctica with the exception of the peninsula. Enhanced synoptic variability on the peninsula during positive SAM phases is consistent with observations of enhanced snowfall at those times (Thomas et al., 2008).

The second mode of SH extratropical variability is the Pacific–South American Mode 1 (PSA1), which reflects a Rossby wave response to sea surface temperature (SST) anomalies over the central and eastern equatorial Pacific (Mo and Paegle, 2001) and is therefore closely linked to ENSO on interannual timescales (we find a correlation of $r = 0.77$ between the annual mean PSA1 and Niño 3.4 indices). Φ in the Amundsen and Ross Sea sectors (WDC, SDM, and RICE) is positively correlated with the PSA1 and Niño 3.4 SST, suggesting larger synoptic activity during El Niño phases and low activity during La Niña phases. The PSA2 pattern, also linked to SST anomalies in the tropical Pacific (Mo and Paegle, 2001), is likewise correlated with Φ in the Amundsen

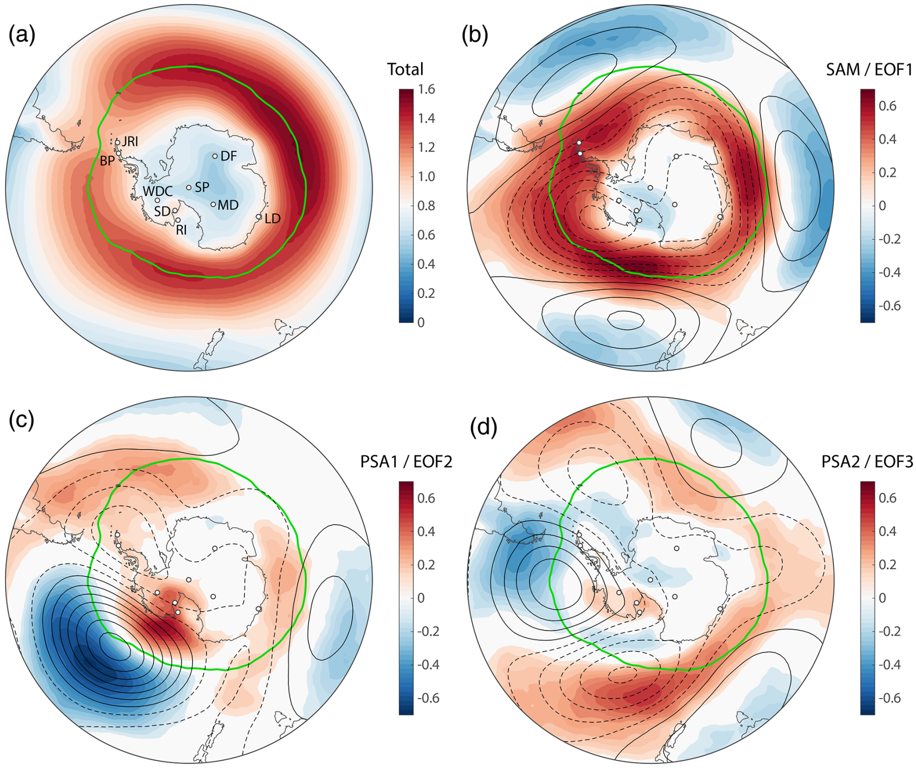

Figure 5. Modes of SH extratropical atmospheric variability and their link to synoptic-scale surface pressure variability in Antarctica. **(a)** Annual mean Φ in units of percent per day (% d^{-1}). **(b)** Colors show correlation between Φ and the southern annular mode (SAM) index, with the 500 hPa geopotential height anomalies superimposed in 10 m contours (positive contours solid, negative contours dashed). **(c)** As panel **(b)**, but for the Pacific–South American Pattern 1 (PSA1). **(d)** As panel **(b)**, but for the Pacific–South American Pattern 2 (PSA2). SAM, PSA1, and PSA2 are defined as the first, second, and third EOFs (empirical orthogonal functions), respectively, of the 500 hPa geopotential height anomalies in 20–90° S monthly values in the 1979–2017 ERA-Interim reanalysis (Dee et al., 2011). In all panels the latitude of maximum Φ is denoted by the green line.

Table 2. Pearson correlation between Φ at the ice coring sites and large-scale atmospheric circulation. Correlations are calculated using annual mean data (all months, April–March). We only list the statistically significant correlations ($p < 0.1$). The Niño 3.4 is calculated over 5° S–5° N, 190–240° E using SST from Huang et al. (2014); the PDO index is from Mantua and Hare (2002).

Site	SAM	PSA1	PSA2	Niño 3.4	PDO	Sea ice Am-Bell	Sea ice Ross
WDC	–	0.31	–	0.31	0.28	–	–
SDM	–	0.47	0.34	0.43	0.45	–	−0.32
RICE	–	0.41	0.34	0.34	0.45	–	−0.30
SP	–	–	−0.32	–	−0.30	–	–
LD	0.45	–	–	–	–	–	–
DF	0.37	–	–	–	–	–	–
EDC	0.30	–	–	–	–	–	–
JRI	0.67	–	–	–	–	0.31	–
BRP	0.68	–	–	–	–	–	–

and Ross Sea sectors (Fig. 5c and Table 2). While all the correlations listed are statistically significant, they explain only a fraction of the total variability.

Next, we consider anomalies in sea ice area and extent (Parkinson and Cavalieri, 2012). We focus on the Ross and Amundsen–Bellingshausen seas where impacts on the WAIS Divide may be expected. At the 90 % confidence level we do not find significant correlations with sea ice area or extent at most core locations (Table 2). Correlations with sea ice extent are (even) weaker than those for sea ice area and consequently not shown. We performed a lead–lag study of the correlations between Φ and sea ice area as well as extent in the various sectors and find that in all cases maximum correlations occur for the sea ice changes lagging 0 to 4 months behind Φ; we interpret this to mean that the sea ice is responding to changes in atmospheric circulation rather than driving them.

Overall, we find that synoptic activity at WAIS Divide, the site of most interest here, is controlled by the position and/or strength of the storm tracks at the southern edge of the SPJ in the Pacific sector of the Southern Ocean (Ross, Amundsen, and Bellingshausen seas), with little sensitivity to the SPJ behavior in the other sectors. Owing to its remote southern location, WDC is only weakly impacted by the commonly defined large-scale modes of atmospheric variability. Most notably, WDC has a modest influence from the tropical Pacific climate, as shown by a correlation around $r \approx 0.3$ with the PSA1, Niño 3.4, and PDO indices (Table 2). We further find statistically significant correlations (up to $r = 0.44$) between WDC Φ and SST in broad regions of the central and eastern tropical Pacific (not shown). We suggest that ENSO weakly impacts storminess at WDC (around 10 % of variance explained) via its impact on the SPJ in the South Pacific.

5 Barometric variability in West Antarctica during the last deglaciation

5.1 The 0–24 ka WAIS Divide Kr-86 excess record

The WAIS Divide downcore $^{86}Kr_{xs}$ dataset we present here was produced during five separate measurement campaigns that occurred in February–April 2014, February–April 2015, August 2015, August 2020, and August 2021. Campaigns 1–3 were reported previously (Bereiter et al., 2018a, b), and campaigns 4 and 5 were meant to resolve conflicts between the $^{86}Kr_{xs}$ datasets from these earlier campaigns. Three slightly different measurement approaches were used. Campaign 1 uses Method 1 from Bereiter et al. (2018a), in which the air sample splitting is done in a water bath for over 12 h to equilibrate the sample. Campaigns 2 and 3 use Method 2 from Bereiter et al. (2018a), in which a bellows is used to split the air samples for over 4 to 6 h. Campaigns 4 and 5 do not involve splitting of the air sample and only analyzed the Kr and Ar isotopic ratios. During campaign 4 a glass bead from the water trap got stuck in the tubing, restricting the flow and likely resulting in incomplete air extraction from the meltwater.

Figure 6 compares $^{86}Kr_{xs40}$ (Fig. 6a) and $^{86}Kr_{xs15}$ (Fig. 6b) from the five campaigns. Campaign 1 is the only campaign that spans the full age range of the record, making it the most valuable of the three campaigns. Campaigns 2 and 3 are mostly restricted to the Pleistocene and Holocene periods, respectively, with little overlap between them. Campaigns 4 and 5 aimed to reproduce some of the most salient features in the earlier three. For ease of visual comparison, a Gaussian smoothing spline to the combined data from the two most extensive campaigns (1 and 2) is added (details below).

Visual inspection suggests that campaigns 1 and 2 agree well for both $^{86}Kr_{xs}$ definitions. Campaign 3 has more scatter and is visibly offset (more negative) for both $^{86}Kr_{xs}$ definitions. Campaign 4 has several data points that agree well with the spline, yet also several fliers with very negative $^{86}Kr_{xs40}$. Campaign 5 appears to be overall more negative in $^{86}Kr_{xs40}$. No true replicate samples were analyzed between the campaigns, in part because the large sample size requirement precludes this. This precludes a direct assessment of campaign offsets. Instead we rely on linear interpolation. First, we linear interpolate the $^{86}Kr_{xs}$ values of campaign 1 onto the sample depths of campaign 2, and vice versa, allowing us to estimate the offsets. In this way, during their period of overlap we estimate offsets of 6 and 13 per meg ‰$^{-1}$ between campaigns 1 and 2 for $^{86}Kr_{xs40}$ and $^{86}Kr_{xs15}$, respectively. This is within the analytical precision (22 per meg), suggesting these two campaigns are in good agreement. Data from campaign 2 appear to have more scatter, possibly reflecting the shorter equilibration time during sample splitting.

We combine data from the first two campaigns and evaluate their offset to data from the other three campaigns again using the linear interpolation method. For campaigns 3, 4, and 5 we find an offset of -32, -22, and -23 per meg ‰$^{-1}$ in $^{86}Kr_{xs40}$, respectively. For campaign 3 the offset is -34 per meg ‰$^{-1}$ in $^{86}Kr_{xs15}$. It is remarkable that all three later campaigns are more negative in $^{86}Kr_{xs}$ than the first two. Campaign 3 shows the greatest offset (greater than analytical precision) and has more scatter in both $^{86}Kr_{xs}$ (Fig. 6) and ^{15}N excess, possibly because for this campaign less care was taken that the IRMS conditions were stable. The offset of campaign 4 may be attributed to the incomplete sample transfer due to the bead stuck in the line; note that for this campaign the offset is caused by two very negative data points. The offset in campaign 5 is hard to explain. The more negative $^{86}Kr_{xs}$ of campaigns 4 and 5 may reflect sample storage effects, as these were measured 5–6 years after campaign 1 and 2. However, this would not explain the negative values of campaign 3. The good $^{86}Kr_{xs}$ agreement between DE08 and DE08-OH, drilled 32 years apart, would also argue against large storage effects. For campaigns 4 and 5 only Ar and Kr isotope ratios were measured, so we lack typical tracers of gas loss ($\delta O_2/N_2$ and $\delta Ar/N_2$) that can be analyzed.

In the remainder of this paper we will interpret the combined data from campaigns 1 and 2, but with the caveat that there is a persistent offset with later campaigns. However, the features we interpret are corroborated by the later campaigns if one takes the offset into account. To aid interpretation of the data, we apply a Gaussian smoothing spline with a smoothing filter width that varies depending on the data density (from 250-year width in the deglaciation itself for which the data density is high to 1750 years in the Holocene and LGM for which data density is low). To estimate the un-

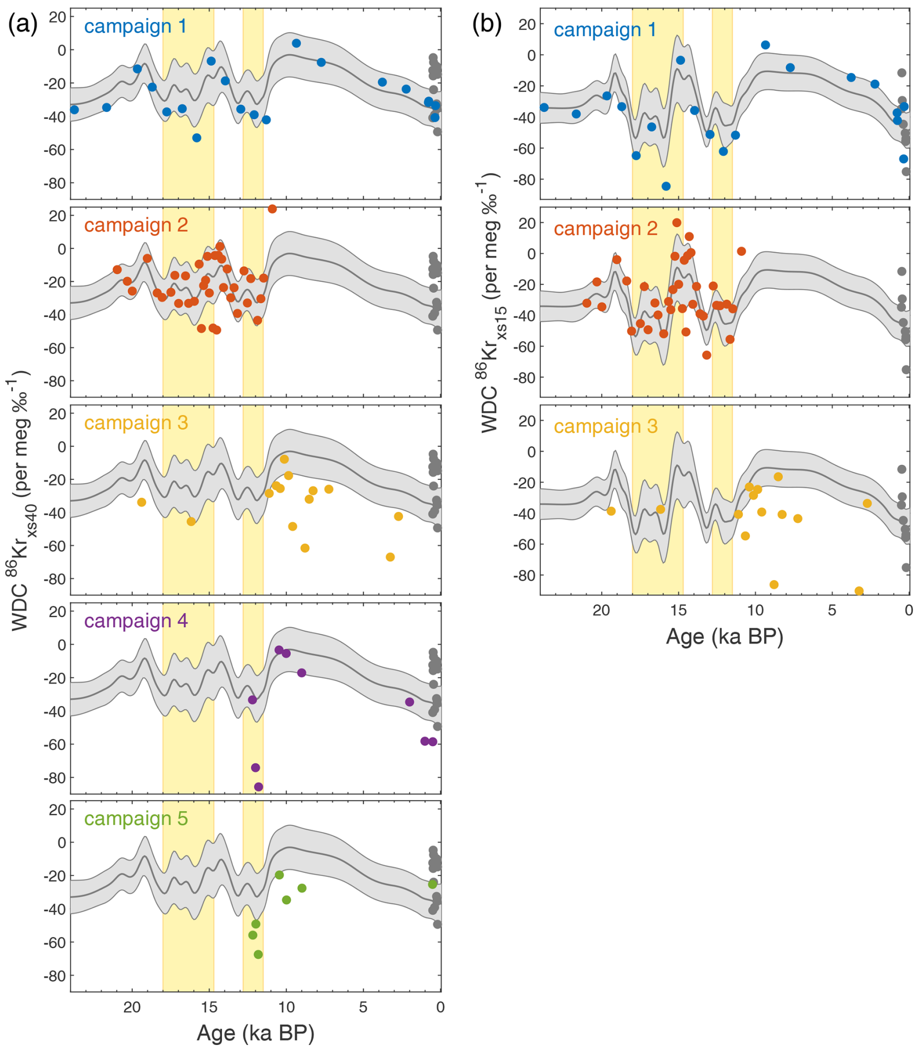

Figure 6. WAIS Divide Kr-86 excess records through the last deglaciation. **(a)** WDC $^{86}Kr_{xs40}$ data from the five measurement campaigns. The gray curve shows a Gaussian smoothing curve to the combined data from the first two campaigns; the light gray shaded area shows the $\pm 1\sigma$ uncertainty envelope based on a 10 000-iteration Monte Carlo sampling of the errors and uncertainties. The WDC calibration data are shown as gray circles for comparison. **(b)** As in panel **(a)**, but for $^{86}Kr_{xs15}$. For campaigns 4 and 5 the sample was not split, and no $\delta^{15}N$ data are available. The Heinrich Stadial 1 and Younger Dryas North Atlantic cold periods are marked in yellow. Thermal corrections in the WDC $^{86}Kr_{xs}$ records are based on firn model simulations; gas loss correction is based on a third-order polynomial fit to the WDC gravity-corrected $\delta O_2/N_2 - -\delta Ar/N_2$ (Fig. A5).

certainty in the smoothing spline we use a Monte Carlo approach that considers uncertainty in following: (1) the gas loss correction by randomly sampling ε_{40} in the range of 0 to -0.016 as well as by randomly adding an offset in the range of -1 ‰ to $+1$ ‰ to the gas loss indicator ($\delta O_2/N_2$–$\delta Ar/N_2$), (2) the thermal correction by randomly scaling the thermal scenario (Fig. A5) by a factor ranging from 0 to 2, and (3) analytical errors by adding random errors to individual data points drawn from a normal distribution with a 2σ width of 22 per meg. The $\pm 1\sigma$ uncertainty range and mean value are shown as the gray envelope and center line in Fig. 6. We believe the following observations to be robust.

– The Holocene shows a trend towards increasingly negative $^{86}Kr_{xs}$, suggesting a gradual increase in synoptic activity toward the present. Minimum synoptic activity in West Antarctica occurs during the early Holocene around 10 ka; the Monte Carlo study suggests $^{86}Kr_{xs40}$ in the early Holocene (8 ka–10 ka) is 30.5 ± 18 per meg ‰$^{-1}$ ($\pm 2\sigma$) below the late Holocene value (last 2 ka). Using the slope of our core-top calibration (Fig. 3), we estimate that early Holocene WDC synoptic activity Φ is ~ 17 % weaker than it is today. This change is comparable to the 2σ magnitude of interannual variations in annual mean Φ at the site today (or about half the peak-to-peak variations thereof). This

Holocene trend is seen in the data from campaigns 1, 3, and 4. Campaign 5 does not suggest a trend but has only one late Holocene data point, making it less robust. The trend in campaign 3 is less robust due to the greater scatter in the data.

- The most pronounced change occurs at the Younger Dryas (YD)–Holocene transition, where $^{86}\mathrm{Kr}_{\mathrm{xs}}$ becomes more positive (by 30.1 ± 16 per meg ‰$^{-1}$, comparing YD and early Holocene), implying a decrease in synoptic activity. This transition is observed in campaigns 1, 2, 4, and 5 that cover this time period (the third campaign does not cover it) and represents a $\sim 17\,\%$ drop in synoptic activity (Φ).
- During the Last Glacial Maximum (LGM), WDC synoptic activity was perhaps slightly weaker than at present, but not significantly so ($^{86}\mathrm{Kr}_{\mathrm{xs40}}$ more positive by 11 ± 13 per meg ‰$^{-1}$). The West Antarctic Ice Sheet elevation was likely higher during the LGM, and a 300 m elevation increase would by itself increase $^{86}\mathrm{Kr}_{\mathrm{xs40}}$ by 10 per meg ‰$^{-1}$, all else being equal (Appendix A3); this is within the analytical error of our observations. This feature is seen in campaign 1 and not covered by the other campaigns.
- The deglaciation itself has enhanced synoptic activity, in particular during the two North Atlantic cold stages Heinrich Stadial 1 (HS1) and the YD as highlighted with yellow bars in Figs. 6 and 7. Synoptic activity during these periods is enhanced relative to the adjacent LGM and early Holocene yet comparable to today. This feature is seen in campaigns 1 and 2 as well as in 4 and 5 for the transition into the Holocene.

Below we will interpret the deglacial WDC $^{86}\mathrm{Kr}_{\mathrm{xs}}$ record in terms of time-averaged barometric variability. Before doing so we want to emphasize that firn processes may have also been imprinted onto the record, in particular on orbital timescales on which firn microstructure responds to local (summer) insolation intensity (Bender, 2002). High summer insolation results in more depleted $\delta O_2/N_2$ and reduced air content, likely via stronger layering and a delayed pore close-off process (Fujita et al., 2009).

Local summer solstice insolation in Antarctica increases through the Holocene, with the highest values in the late Holocene. This may impact $^{86}\mathrm{Kr}_{\mathrm{xs}}$, although it is not a priori clear what the sign of this relationship would be. The sense of the Holocene temporal trends is that a more negative $^{86}\mathrm{Kr}_{\mathrm{xs}}$ coincides with more negative $\delta O_2/N_2$. Note that this is opposite to the trends seen in the spatial calibration, for which sites with the most negative $\delta O_2/N_2$ (DF, SP, EDC) have the most positive $^{86}\mathrm{Kr}_{\mathrm{xs}}$. For now, the impact of local insolation on $^{86}\mathrm{Kr}_{\mathrm{xs}}$ via firn microstructure remains unknown, which is an important caveat in interpreting the orbital-scale changes in WDC $^{86}\mathrm{Kr}_{\mathrm{xs}}$. The abrupt $^{86}\mathrm{Kr}_{\mathrm{xs}}$ increase at the Holocene

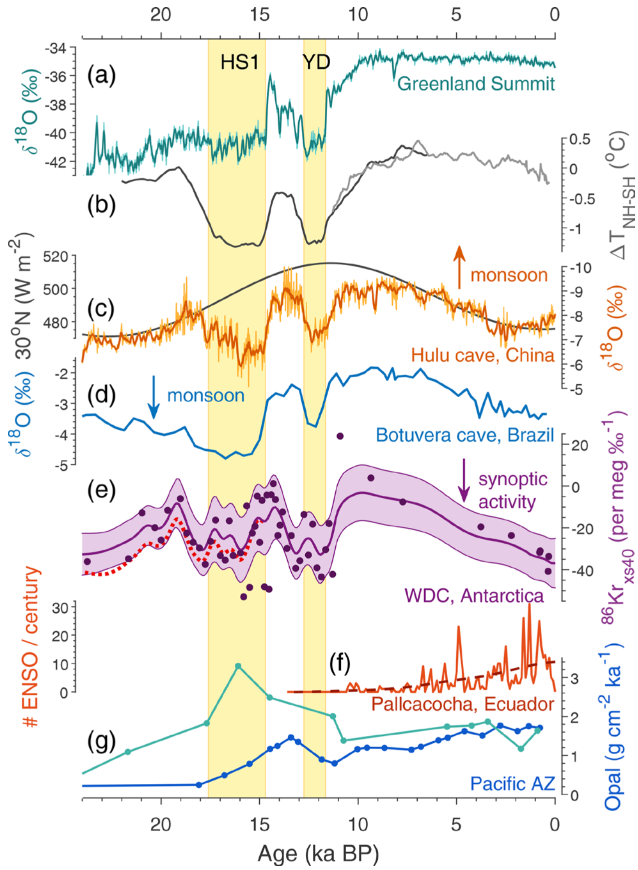

Figure 7. Climate records through the last deglaciation with the Heinrich Stadial 1 (HS1) and Younger Dryas (YD) North Atlantic cold periods marked in yellow. **(a)** Greenland Summit ice core stable water isotope ratio $\delta^{18}O$, here the average of the GISP2 and GRIP ice cores (Grootes et al., 1993). **(b)** Hemispheric temperature difference (McGee et al., 2014) based on global proxy compilations for the Holocene (Marcott et al., 2013) and last deglaciation (Shakun et al., 2012). **(c)** Speleothem calcite $\delta^{18}O$ from Hulu and Dongge caves, China, as a proxy for East Asian summer monsoon strength (Dykoski et al., 2005; Wang et al., 2001). Superimposed is summer solstice (21 June) insolation at 30° N. **(d)** Speleothem calcite $\delta^{18}O$ from Botuvera cave, southern Brazil, as a proxy for South American summer monsoon strength (Cruz et al., 2005; Wang et al., 2007). **(e)** Kr-86 excess record from WAIS Divide (this study), corrected for gas loss and thermal fractionation (Appendix A). The center line and shaded envelope show the mean and $\pm 1\sigma$ uncertainty interval of a 10 000-iteration Monte Carlo smoothing exercise (see text). The dotted red line equals the center line with a correction for elevation change applied (Appendix A) using a simulated elevation history (Golledge et al., 2014). **(f)** Number of El Niño events per century from laminations in sediments from Laguna Pallcacocha, Ecuador (Moy et al., 2002). **(g)** Th-normalized opal flux in the Pacific Antarctic zone (south of the polar front) from cores NBP9802-6PC1 (turquoise; 169.98° W, 61.88° S) and PS75/072-4 (blue; 151.22° W, 57.56° S), reflecting local productivity and (wind-driven) upwelling (Chase et al., 2003; Studer et al., 2015). All water isotope data in this figure are on the Vienna Standard Mean Ocean Water (V-SMOW) scale. Arrows show the direction of increased monsoon strength and synoptic activity.

onset is too abrupt to be caused by insolation changes, and thus we can interpret that change with more confidence.

The scatter in the late Holocene WDC $^{86}Kr_{xs}$ data exceeds the stated analytical precision. Potential explanations include (1) an underestimation of the true analytical precision, (2) interannual to decadal variations in storminess at WDC, and (3) aliasing of centimeter-scale variations in ice core $^{86}Kr_{xs}$ linked to layering in firn microstructural properties. Understanding the cause of this relatively high scatter in the $^{86}Kr_{xs}$ records will require more work, in particular measurements of several high-resolution $^{86}Kr_{xs}$ records in various sectors of Antarctica.

5.2 Barometric variability at WAIS Divide during the last deglaciation

In the present day, synoptic-scale pressure variability at WAIS Divide is correlated with zonal wind strength along the southern margin of the SPJ (Sect. 4). In our interpretation, a more negative $^{86}Kr_{xs}$ reflects a strengthening or southward shift of the SPJ in the Pacific sector. Here we provide a climatic interpretation of the deglacial WDC $^{86}Kr_{xs}$ record and suggest that variations in synoptic variability at WDC are linked to meridional movement of the ITCZ on millennial and orbital timescales.

The main features of the deglacial WDC $^{86}Kr_{xs}$ record listed in Sect. 5.1 resemble similar features seen in records of (sub)tropical hydrology and monsoon strength, such as the speleothem calcite $\delta^{18}O$ records from Hulu Cave, China (Fig. 7c), and from Botuvera cave, southern Brazil (Fig. 7d), which are thought to reflect the intensity of the East Asian and South American summer monsoons, respectively (Cruz et al., 2005; Wang et al., 2001, 2007). These two monsoon records are anticorrelated, showing opposing rainfall trends between the NH and SH on both orbital and millennial timescales. This pattern is commonly attributed to displacement of the mean meridional position of the ITCZ (Chiang and Friedman, 2012; McGee et al., 2014; Schneider et al., 2014), driven by hemispheric temperature differences (Fig. 7b). On orbital timescales such ITCZ migration has a strong precessional component, moving towards the hemisphere with more intense summer peak insolation; on millennial timescales the ITCZ responds to abrupt North Atlantic climate change associated with the D–O and Heinrich cycles (Broccoli et al., 2006; Chiang and Bitz, 2005; Wang et al., 2001), which are in turn linked to changes in meridional heat transport by the Atlantic meridional overturning circulation, or AMOC (Lynch-Stieglitz, 2017; Rahmstorf, 2002).

Changes in mean ITCZ position have a strong influence on the structure and strength of the SH jets. During periods when the NH is relatively cold (such as D–O stadials or periods with negative orbital precession index) the ITCZ is displaced southward and the SH Hadley cell is weakened, thereby also weakening the SH upper-tropospheric subtropical jet (Ceppi et al., 2013; Chiang et al., 2014). The reverse is also true, with the ITCZ shifted northward during NH warmth, associated with a strengthening of the SH Hadley cell and STJ. In a range of model simulations (Ceppi et al., 2013; Lee and Kim, 2003; Lee et al., 2011; Pedro et al., 2018) the weakening of the SH STJ (as during NH cold) is furthermore accompanied by a strengthening and/or southward shift of the SPJ as well as the eddy-driven jet and SH westerly winds. Recently, ice core observations have confirmed that in-phase shifts in the position of the SHWs occur during the D–O cycle in parallel to those of the ITCZ (Buizert et al., 2018; Markle et al., 2017). Marine records of fluvial sediment runoff off the Chilean coast suggest precession-phased movement of the South Pacific SPJ, again in parallel to the ITCZ movement (Lamy et al., 2019).

The SAM index reflects the meridional position of the SHWs and eddy-driven jet. During positive SAM phases the SHWs are displaced poleward and during negative phases equatorward. Present-day month-to-month changes in the SAM index represent a mode of internal variability, with anomalies persisting for only weeks to months – the timescale is longest in late spring and early summer, reflecting a stronger planetary wave–mean flow interaction (Simpson et al., 2011; Thompson and Wallace, 2000). By contrast, shifts in the ITCZ and SH jet structure on millennial and orbital timescales have a much longer lifetime and different dynamics, being driven from the tropics via hemispherically asymmetric changes in Hadley cell and STJ strength. Therefore, present-day SAM internal variability is not expected to be a good analog for past changes in SHW position. We find that the present-day SAM month-to-month internal variability mainly impacts synoptic variability over the Southern Ocean and does not have a statistically significant impact at WDC (Table 2). Such variability is likely to have also occurred during other climatic regimes, possibly just centered around a mean SHW position that is displaced meridionally relative to today. At first glance it may appear contradictory to state, as we do, that synoptic activity at WDC is not sensitive to the SAM while also suggesting that during the last deglaciation synoptic activity at WDC is linked to changes in the position of the SH eddy-driven jet and westerlies. Based on the considerations above, both claims may be true without contradiction.

Besides secular changes to the SPJ position and strength linked to meridional ITCZ movement, WDC $^{86}Kr_{xs}$ may also have imprints from ENSO and tropical Pacific climate. Our analysis suggests a weak but statistically significant link to common ENSO indicators (Table 2). Increased synoptic activity at WDC is linked to enhanced convection in the central and eastern tropical Pacific, which may be due to enhanced frequency or intensity of El Niño events or a mean climate state that is more El Niño-like; it seems likely that the Pacific mean state and ENSO variability are strongly linked (Salau et al., 2012), and the distinction may be irrelevant.

The key features of the WDC $^{86}Kr_{xs}$ record are compatible with paleo-ENSO changes commonly described in the literature. A majority of Holocene ENSO reconstructions (Conroy et al., 2008; Driscoll et al., 2014; Koutavas et al., 2006; Moy et al., 2002; Riedinger et al., 2002; Sadekov et al., 2013) and a wide range of climate model simulations (Braconnot et al., 2012; Cane, 2005; Clement et al., 2000; Liu et al., 2000, 2014; Zheng et al., 2008) all suggest weakened ENSO activity during the early and mid-Holocene, a time with reduced WDC synoptic activity. For example, Fig. 7f shows the number of El Niño events per century (with trend line) reconstructed from inorganic clastic laminae in sediments from Laguna Pallcacocha, Ecuador, a region strongly affected by ENSO (Moy et al., 2002). Likewise, it has been suggested that the SST gradient between the western Pacific warm pool and eastern Pacific cold tongue was enhanced during the mid-Holocene, perhaps indicating a more La Niña-like mean climate state (Koutavas et al., 2002; Sadekov et al., 2013).

Going from the early Holocene to the Younger Dryas (YD), we observe a large increase in WDC synoptic activity. Enhanced ENSO activity during Heinrich stadials is generally supported by climate model simulations (Braconnot et al., 2012; Merkel et al., 2010; Timmermann et al., 2007) and by limited proxy evidence for stadial periods more broadly (Stott et al., 2002). Enhanced ENSO variability during the deglaciation is also found by Sadekov et al. (2013), although their record lacks the temporal resolution to resolve the individual stages. The zonal SST gradient in the equatorial Pacific further reaches a minimum during HS1, also consistent with higher El Niño intensity (Sadekov et al., 2013).

The observed variations in $^{86}\mathrm{Kr}_{\mathrm{xs}}$ and implied changes in WDC synoptic activity may thus have two contributions: (1) ITCZ-driven changes to the South Pacific SPJ position and (2) changes to ENSO activity. Based on previous work, we argue these two amplify one another in driving WDC storminess, yet we expect the former to make the larger contribution. To disentangle zonally uniform changes to the SPJ from changes specific to the Pacific sector (such as ENSO and the split jet), $^{86}\mathrm{Kr}_{\mathrm{xs}}$ records from different sectors of Antarctica are needed. Replication of the deglacial and Holocene WDC $^{86}\mathrm{Kr}_{\mathrm{xs}}$ record presented here is also a high priority at both the WDC itself and the nearby SDM and RICE cores to validate that the signals we describe and interpret here are indeed real and regional in scale.

The position of the SHWs during the LGM has been a topic of much scientific inquiry. Proxy data have been interpreted to show a northward LGM shift of the SHWs – with other scenarios, including no change at all, not excluded by the data (Kohfeld et al., 2013). Such a shift is not supported by most climate models (Rojas et al., 2009; Sime et al., 2013). Our $^{86}\mathrm{Kr}_{\mathrm{xs}}$ record suggests LGM synoptic activity in West Antarctica to be comparable to today after accounting for site elevation effects (the elevation effect on $^{86}\mathrm{Kr}_{\mathrm{xs}}$ is within the analytical error). This would be consistent with a Pacific SPJ position similar to today. Note that our site is mostly sensitive to the position of the southern edge of the SPJ and cannot meaningfully constrain changes to the seasonality, width, and/or northern edge of the storm tracks. Therefore, it is not a priori clear whether our observations can be extrapolated to more general statements about SHW position and strength during the LGM. Our data suggest that SPJ movement follows insolation and the ITCZ position, and hence the LGM period may not be a good target for studying SHW movement in the first place given that it has a precession index similar to the present day.

Changes to the SPJ and its associated westerly surface winds have implications for ocean circulation and marine productivity in the Southern Ocean via wind-driven upwelling. Opal flux records from the Antarctic zone (Fig. 7g), reflecting diatom productivity, are commonly interpreted as a proxy for such upwelling – with enhanced upwelling during southward displacement of the SHWs (Anderson et al., 2009). Here we only show records from the Pacific sector, given that we find WDC $^{86}\mathrm{Kr}_{\mathrm{xs}}$ to reflect purely local SPJ dynamics (Fig. 4a). Both published records suggest enhanced upwelling during the deglaciation (Fig. 7g), consistent with a southward-shifted Pacific SPJ and enhanced storminess at WDC. The record from core PS75/072-4 (blue curve) further indicates an increasing productivity trend through the Holocene (Studer et al., 2018), which is accompanied by a rise in surface nitrogen availability (reconstructed from diatom-bound nitrogen isotopic composition, not shown); this Holocene trend matches our finding of increasing WDC storminess and, by inference, an increasingly southern position of the Pacific SPJ and SHWs. We thus conclude that our interpretation of WDC $^{86}\mathrm{Kr}_{\mathrm{xs}}$ reflecting SPJ movement in parallel with the ITCZ is broadly consistent with indicators of wind-driven upwelling in the Pacific Antarctic zone.

6 Conclusions

Here we present a new gas-phase ice core climate proxy, Kr-86 excess, that reflects time-averaged surface pressure variability at the site driven by synoptic activity. Surface pressure variability weakly disturbs the gravitational settling and enrichment of the noble gas isotope ratios $\delta^{86}\mathrm{Kr}$ and $\delta^{40}\mathrm{Ar}$ via barometric pumping. Owing to its higher diffusion coefficient, argon is less affected by this process than krypton is, and therefore the difference $\delta^{86}\mathrm{Kr}$–$\delta^{40}\mathrm{Ar}$ is a measure of synoptic activity.

This interpretation is supported by a calibration study in which we measure $^{86}\mathrm{Kr}_{\mathrm{xs}}$ in late Holocene ice core samples from 11 Antarctic ice cores and 1 Greenland ice core that represent a wide range of synoptic activity in the modern climate. Two of the Antarctic cores were rejected due to clear evidence of refrozen meltwater. We find a strong correlation ($r = -0.94$ when using site mean data and $r = -0.83$ when using individual samples, $p < 0.01$) between ice core $^{86}\mathrm{Kr}_{\mathrm{xs}}$ and barometric variability at the site.

Current limitations of the new $^{86}\mathrm{Kr}_{\mathrm{xs}}$ proxy are the following: (1) it requires relatively large and nontrivial corrections for gas loss and thermal fractionation; (2) it is moderately sensitive to changes in convective zone thickness; (3) firn air transport models cannot simulate the magnitude of $^{86}Kr_{xs}$ anomalies measured in ice samples; (4) firn air samples show smaller $^{86}Kr_{xs}$ anomalies than ice samples from the same site do; (5) it may be sensitive to the degree of density layering at the site, as a comparison of the nearby Law Dome DE08 and DSSW20K cores suggests; (6) it does not work for warm sites that experience frequent melt; (7) the measurement is challenging (with offsets observed between measurement campaigns), time-consuming, and needs large ice samples; and (8) long-term sample storage may impose data offsets. Due to these limitations, we caution that any interpretation of temporal $^{86}Kr_{xs}$ changes remains speculative at present.

Using atmospheric reanalysis data, we show that synoptic-scale barometric variability in Antarctica is primarily linked to the position and/or strength of the southern edge of the eddy-driven subpolar jet (SPJ, also called the polar front jet) with a southward SPJ displacement enhancing synoptic-scale surface pressure variability in Antarctica. The commonly defined modes of large-scale atmospheric variability, such as the southern annular mode and the Pacific–South American Pattern, impact Antarctic only weakly as they are weighted towards the midlatitudes; the exception is the Antarctic Peninsula, where synoptic activity is well-correlated with the southern annular mode ($r = 0.68$). Sites in the Amundsen and Ross Sea sectors are weakly linked to tropical Pacific climate and ENSO ($r = 0.31$ to $r = 0.43$).

We present a new record of $^{86}Kr_{xs}$ from the WAIS Divide ice core in West Antarctica that covers the last 24 kyr including the LGM, deglaciation, and Holocene. West Antarctic synoptic activity is slightly below modern levels during the Last Glacial Maximum (LGM), increases during the Heinrich Stadial 1 and Younger Dryas North Atlantic cold period, weakens abruptly at the Holocene onset, remains low during the early and mid-Holocene (up to $\sim 17\,\%$ below modern), and gradually increases to its modern value. The WDC $^{86}Kr_{xs}$ record resembles records of tropical hydrology and monsoon intensity that are commonly thought to reflect the meridional position of the ITCZ; the sense of the correlation is that WDC synoptic activity is weak when the ITCZ is in its northward position, and vice versa. We interpret the record to reflect migrations of the eddy-driven SPJ in parallel with those of the ITCZ (Ceppi et al., 2013). Secondary influences may come from tropical Pacific climate and ENSO activity. Our $^{86}Kr_{xs}$ record is consistent with weakened ENSO activity (or a more La Niña-like mean state) during the middle and early Holocene and enhanced ENSO activity during NH stadial periods – both these features have been described in the paleo-ENSO literature. The inferred changes to the SPJ are broadly consistent with proxies that indicate enhanced wind-driven upwelling in the Pacific Antarctic zone during NH cold stadial periods.

Kr-86 excess is a new and potentially useful ice core proxy with the ability to enhance our understanding of past atmospheric circulation. More work to better understand this proxy is warranted, and presently the conclusions of this paper should be considered tentative. In particular, replication of the deglacial Kr-86 excess record presented here in nearby cores is needed before these results can be interpreted with confidence. A full list of suggested follow-up studies is given in Sect. 3.3. Despite the many challenges of Kr-86 excess, its further development is worthwhile owing to the dearth of available proxies for reconstructing SH extratropical atmospheric circulation.

Appendix A: Data corrections

A1 Gas loss correction

Gas loss processes artificially enrich the δ^{40}Ar isotopic ratio used to calculate $^{86}Kr_{xs}$ (Kobashi et al., 2008b; Severinghaus et al., 2003, 2009). Figure A1b shows the relationships between the two most common gas loss proxies, $\delta O_2/N_2$ and $\delta Ar/N_2$, for all samples in the calibration dataset. We find a slope close to the 2 : 1 slope commonly reported in the literature (Bender et al., 1995); the exception is the DE08-OH site where the data fall on a 1 : 1 slope. Depletion in fugitive gases (such as O_2 and Ar) represents the sum of losses during bubble closure in the firn (Bender, 2002; Huber et al., 2006; Severinghaus and Battle, 2006) and those during drilling, handling, storage, and analysis of the samples (Ikeda-Fukazawa et al., 2005). The patterns are inconsistent with storage conditions alone – for example, the DF and EDC cores were stored very cold and SP drilled very recently; yet all three have strong $\delta O_2/N_2$ and $\delta Ar/N_2$ depletion. Natural gas loss from the firn and artifactual loss during drilling likely dominate the signal. The DE08-OH samples were dry-drilled and suffered from poor ice quality for the most depleted samples, which may explain the alternate 1 : 1 slope at the site (Appendix B); note though that a recent work suggests a $\sim 5:1$ slope for post-coring gas loss (Oyabu et al., 2021). The DE08-OH samples were also analyzed differently from those at other sites, with $\delta O_2/N_2$ and $\delta Ar/N_2$ measurements performed on a separate smaller ice piece (see Sect. 2.2); the greater surface-to-volume ratio of such small samples may result in greater gas fractionation while evacuating the sample flasks in the laboratory.

Severinghaus et al. (2009) hypothesize that the apparent 2 : 1 slope of $\delta O_2/N_2$ to $\delta Ar/N_2$ depletion is a combination of two mechanisms: size-dependent fractionation during diffusion through the ice lattice and mass-dependent fractionation (such as molecular or Knudsen diffusion) within ice fractures. In this interpretation, the exact slope would depend on the relative contribution of each process to the total gas loss. It is improbable that both processes would occur in the same ratio at such a wide variety of sites; the 2 : 1 slope is thus more likely an attribute of the gas diffusion rate of

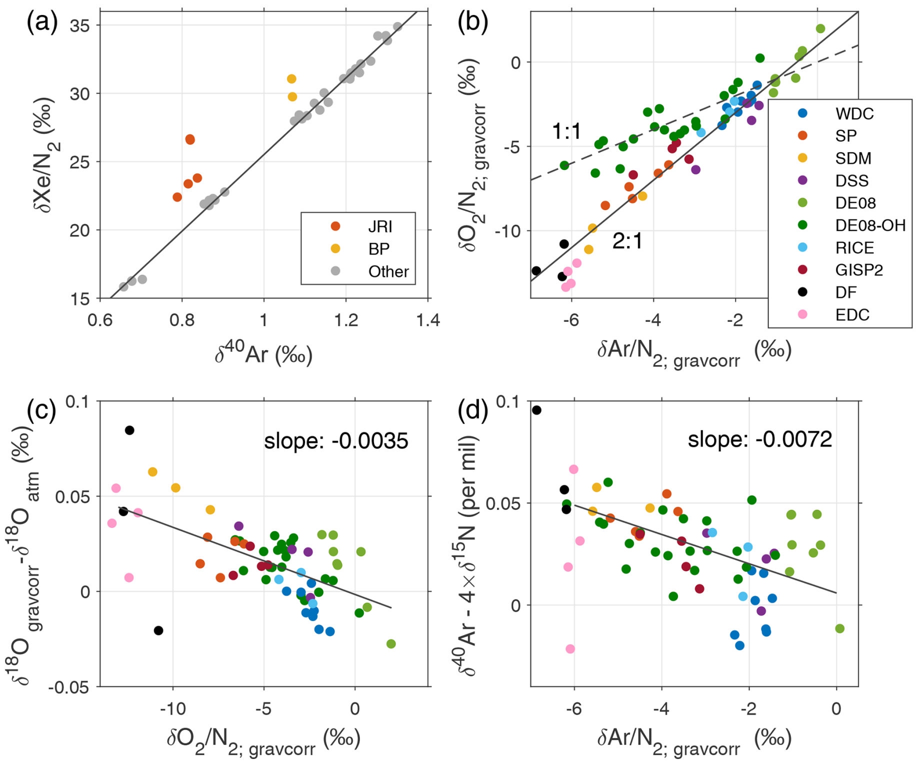

Figure A1. Elemental ratios in the 11-site calibration study of late Holocene samples. **(a)** $\delta Xe/N_2$ vs. $\delta^{40}Ar$ in all ice core samples. $\delta^{40}Ar$ is used solely to illustrate gravitational enrichment, and a similar picture arises when plotted against any isotopic pair. Refrozen meltwater (elevated $\delta Xe/N_2$) was seen in all samples from the Antarctic Peninsula (James Ross Island and Bruce Plateau sites), despite selecting samples free of visible melt features. **(b)** The relationship between the commonly used gas loss proxies $\delta O_2/N_2$ and $\delta Ar/N_2$ corrected for gravity. **(c)** Enrichment in $\delta^{18}O$ (corrected for gravity and atmospheric $\delta^{18}O_{atm}$) plotted against gravity-corrected $\delta O_2/N_2$. **(d)** $\delta^{40}Ar$ enrichment plotted against gravity-corrected $\delta Ar/N_2$. In all panels gravitational correction is applied by subtracting $\delta^{15}N$ times the atomic mass unit difference.

gases through ice itself, which is strongly size-dependent and weakly mass-dependent (Battle et al., 2011).

Gas loss is well-known to enrich ice samples in $\delta^{18}O$–O_2, and following Severinghaus et al. (2009) we plot $\delta^{18}O$ (corrected for gravity and small atmospheric $\delta^{18}O_{atm}$ variations) against gravitationally corrected $\delta O_2/N_2$ in Fig. A1c. We find a slope of 3.5 per meg enrichment in $\delta^{18}O$ per ‰ of $\delta O_2/N_2$ gas loss. This is less than values reported elsewhere (Severinghaus et al., 2009) but provides further evidence for mass-dependent fractionation during gas loss. Our core-top dataset further suggests a correlation between $\delta^{40}Ar - 4 \times \delta^{15}N$ (a measure of $\delta^{40}Ar$ enrichment impacted by both thermal fractionation and gas loss) and gravitationally corrected $\delta Ar/N_2$ (Fig. A1d), suggesting Ar loss leads to enrichment of the remaining $\delta^{40}Ar$.

Following Severinghaus et al. (2009), we assume that the $\delta^{40}Ar$ correction scales with gas loss indicator ($\delta O_2/N_2$–$\delta Ar/N_2$):

$$\Delta^{40}_{GL} = \varepsilon_{40} \times (\delta O_2/N_2 - \delta Ar/N_2)|_{gravcorr}, \tag{A1}$$

with Δ^{40}_{GL} the isotopic gas loss correction on $\delta^{40}Ar$ and ε_{40} a scaling parameter. Note that gravitationally corrected $\delta O_2/N_2$ and $\delta Ar/N_2$ data are used. Here we rely on data from the Antarctic Byrd ice core for a best estimate of ε_{40} (Fig. A2); some samples from this core suffered extreme gas loss with ($\delta O_2/N_2$–$\delta Ar/N_2$) as low as -100 ‰. This dataset suggests $\varepsilon_{40} = -0.008$, or 8 per meg $\delta^{40}Ar$ enrichment per ‰ of ($\delta O_2/N_2$–$\delta Ar/N_2$) gas loss. Because of the 2 : 1 slope between $\delta O_2/N_2$ and $\delta Ar/N_2$, we find that ($\delta O_2/N_2$–$\delta Ar/N_2$) $\approx \delta Ar/N_2$ and therefore the coefficient ε_{40} would have a similar slope when regressed against $\delta Ar/N_2$ instead of ($\delta O_2/N_2$–$\delta Ar/N_2$).

The value of $\varepsilon_{40} = -0.008$ agrees reasonably well with other studies. Kobashi et al. (2008b) compare replicate sample pairs to back-out gas loss and find (statistically significant) correlations between $\delta^{40}Ar$ enrichment and $\delta Ar/N_2$ (again, which is similar to $\delta O_2/N_2$–$\delta Ar/N_2$). Kobashi et al. (2008b) find ε_{40} values of -0.006, -0.005, and $+0.007$, depending on the depth range and analytical campaign evaluated. The positive value is surprising given that most observations, as well as theory, suggest ε_{40} should be negative – we consider this a spurious result given the weak $\delta^{40}Ar$–$\delta Ar/N_2$ correlation in that particular dataset. The other two values of ε_{40} are in reasonable agreement with the Byrd value. For

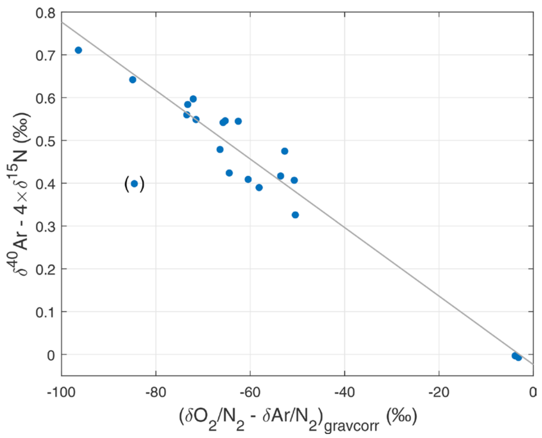

Figure A2. Argon isotopic enrichment due to gas loss in the Byrd core used to determine the δ^{40}Ar gas loss correction (Appendix A1). The enrichment in δ^{40}Ar plotted as a function of gravitationally corrected ($\delta O_2/N_2$–$\delta Ar/N_2$) measured in the deep Antarctic Byrd ice core, which suffered heavy gas loss. Ice samples were analyzed in the Bender Lab at the University of Rhode Island by Jeff Severinghaus in 1997. The slope of the least-square fit is $\varepsilon_{40} = -0.008$. The data point in parentheses is treated as an outlier and excluded from the fitting.

the Siple Dome ice core (Severinghaus et al., 2003), regressing δ^{40}Ar against δKr/Ar gives a slope of +0.007; this implies $\varepsilon_{40} = -0.007$, in good agreement with our findings. Last, our core-top data suggest δ^{40}Ar enrichment with an ε_{40} value of −0.0072 (Fig. A1d), also in good agreement with Byrd.

Given the uncertainty in the gas loss parameter, we verify that our results are valid for a wide range of ε_{40} values (Fig. 3b).

The downcore WDC $^{86}Kr_{xs}$ was measured over five separate measurement campaigns, with $\delta O_2/N_2$ and $\delta Ar/N_2$ data available only for the first three campaigns.

In order to provide a consistent gas loss correction to the five measurement campaigns, including campaigns 4 and 5 for which no $\delta O_2/N_2$ or $\delta Ar/N_2$ data are available, we fit a third-order polynomial to all available gravitationally corrected WDC $\delta O_2/N_2$–$\delta Ar/N_2$ data (Fig. A5a). We can then calculate the expected WDC $\delta O_2/N_2$–$\delta Ar/N_2$ at any given age, also in the absence of $\delta O_2/N_2$ and $\delta Ar/N_2$ data. For consistency, we use this correction method for all data seen in Fig. 6. Note that the WDC $\delta O_2/N_2$–$\delta Ar/N_2$ values are small for all ages and that the gas loss correction is therefore small for this site.

A2 Thermal correction

In the presence of a temperature gradient, thermal diffusion causes isotopic enrichment towards the colder location. The thermal diffusion sensitivity Ω in units of ‰ K^{-1} for the various gases is given as (Grachev and Severinghaus, 2003a, b; Kawamura et al., 2013) follows.

$$\Omega^{15} = \frac{8.656}{T} - \frac{1232}{T^2}$$
$$\Omega^{40} = \frac{26.08}{T} - \frac{3952}{T^2} \qquad \Omega^{86} = \frac{5.05}{T} - \frac{580}{T^2}$$

We estimate the thermal gradient ΔT in the firn using N-15 excess (Severinghaus et al., 1998):

$$\Delta T = \frac{^{15}N_{xs}}{\Omega^{15} - \Omega^{40}/4} = \frac{\delta^{15}N - \left(\delta^{40}Ar + \Delta^{40}_{GL}\right)/4}{\Omega^{15} - \Omega^{40}/4}, \qquad \text{(A2)}$$

with Δ^{40}_{GL} the δ^{40}Ar gas loss correction from Eq. (A1). Positive values of ΔT indicate that the surface is warmer than the firn–ice transition. The ΔT then in turn allows us to estimate the thermal corrections.

$$\Delta^{15}_{TF} = -\Omega^{15}\Delta T$$
$$\Delta^{40}_{TF} = -\Omega^{40}\Delta T$$
$$\Delta^{86}_{TF} = -\Omega^{86}\Delta T \qquad \text{(A3)}$$

The samples from the calibration dataset are from the climatically stable late Holocene period and typically close together in depth; the uncertainty in the ΔT estimation for individual samples therefore exceeds the temporal variability in ΔT. To reduce the uncertainty in the thermal correction we estimate ΔT for individual samples using Eq. (A2) and for each site average the available data to get a site average firn temperature gradient $\overline{\Delta T}$. The thermal correction is then given by the following.

$$\Delta^{15}_{TF} = -\Omega^{15}\overline{\Delta T}$$
$$\Delta^{40}_{TF} = -\Omega^{40}\overline{\Delta T}$$
$$\Delta^{86}_{TF} = -\Omega^{86}\overline{\Delta T} \qquad \text{(A4)}$$

The two methods are compared in Figs. A3c (individual sample ΔT) and Fig. A3d (site mean $\overline{\Delta T}$); it is clear that the $\overline{\Delta T}$ approach reduces the spread in $^{86}Kr_{xs}$ (error bars), but not its mean (white dots). The ΔT estimates in individual samples are subject to errors in the isotopic measurements; some of these errors will cancel out in the $\overline{\Delta T}$.

For the downcore WDC record through the deglaciation we can no longer assume a stationary ΔT; we instead rely on dynamic firn densification model simulations of ΔT (Buizert et al., 2015). A comparison of the simulated and data-based ΔT is shown in Fig. A5 for WDC. The data clearly show a lot more scatter and variability than the simulations do. We interpret this mainly as analytical noise in the δ^{15}N

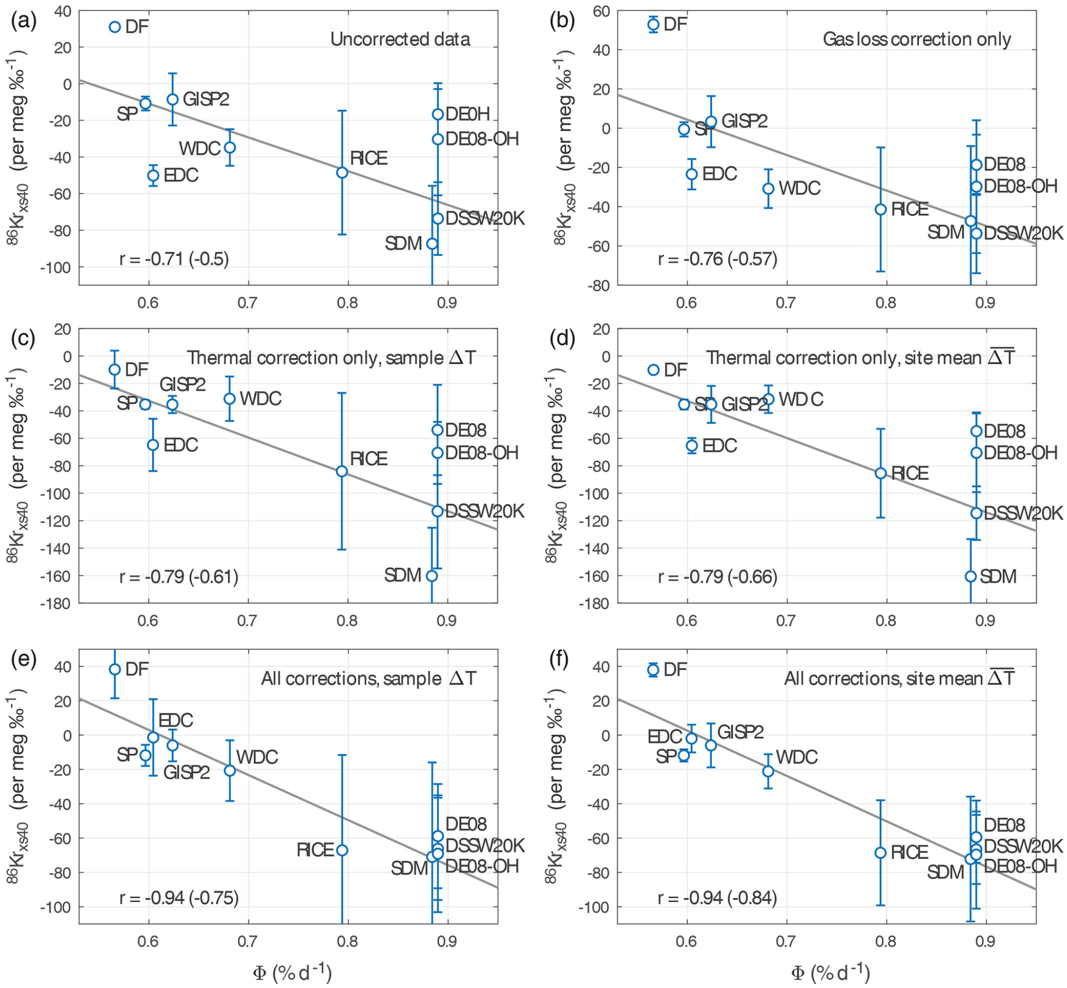

Figure A3. Influence of gas loss and thermal correction on the $^{86}Kr_{xs40}$ calibration. We plot $^{86}Kr_{xs40}$ as a function of Φ **(a)** without any data corrections applied, **(b)** with only the gas loss correction applied ($\varepsilon_{40} = -0.008$), **(c)** with only the thermal correction applied using individual sample ΔT, **(d)** with only the thermal correction applied using individual site mean $\overline{\Delta T}$, **(e)** with both gas loss and thermal corrections applied using individual sample ΔT, and **(f)** with both gas loss and thermal corrections applied using site mean $\overline{\Delta T}$. In each panel the correlations with Φ are listed for the site average and individual sample with the latter in parentheses. For all correlations $p < 0.05$.

and $\delta^{40}Ar$ measurements; however, the gas loss correction (Appendix A1) also impacts the ΔT estimation in individual samples. The comparison suggests that the scatter in the ΔT estimates actually exceeds the magnitude of the simulated thermal signals. Using ΔT of the individual samples would thus introduce a high amount of scatter in the (thermally corrected) $^{86}Kr_{xs}$ records, and we choose to use the modeled ΔT instead.

A3 Elevation correction

To correct the deglacial WAIS Divide record for elevation changes, here we estimate the $^{86}Kr_{xs}$ dependence on site elevation using the calibration dataset. Note that elevation and synoptic activity are strongly correlated for the investigated sites ($r = -0.86$), with synoptic activity decreasing with elevation because the cyclonic systems do not penetrate deeply into the Antarctic interior. Figure A6 shows the result of this exercise. We find a slope of 34 per meg ‰$^{-1}$ of $^{86}Kr_{xs}$ per 1000 m of elevation change, with a correlation of $r = 0.96$ when considering site mean $^{86}Kr_{xs}$ and $r = 0.86$ when considering individual samples. Note that the GISP2 site is not included in the analysis because it is in Greenland where the elevation–$^{86}Kr_{xs}$ relationship may be different from Antarctica – it does, however, fit the Antarctic trend rather well. We further use the simulated WAIS Divide elevation history (Golledge et al., 2014), which simulates an LGM elevation of around 300 m higher than at present at WAIS Divide.

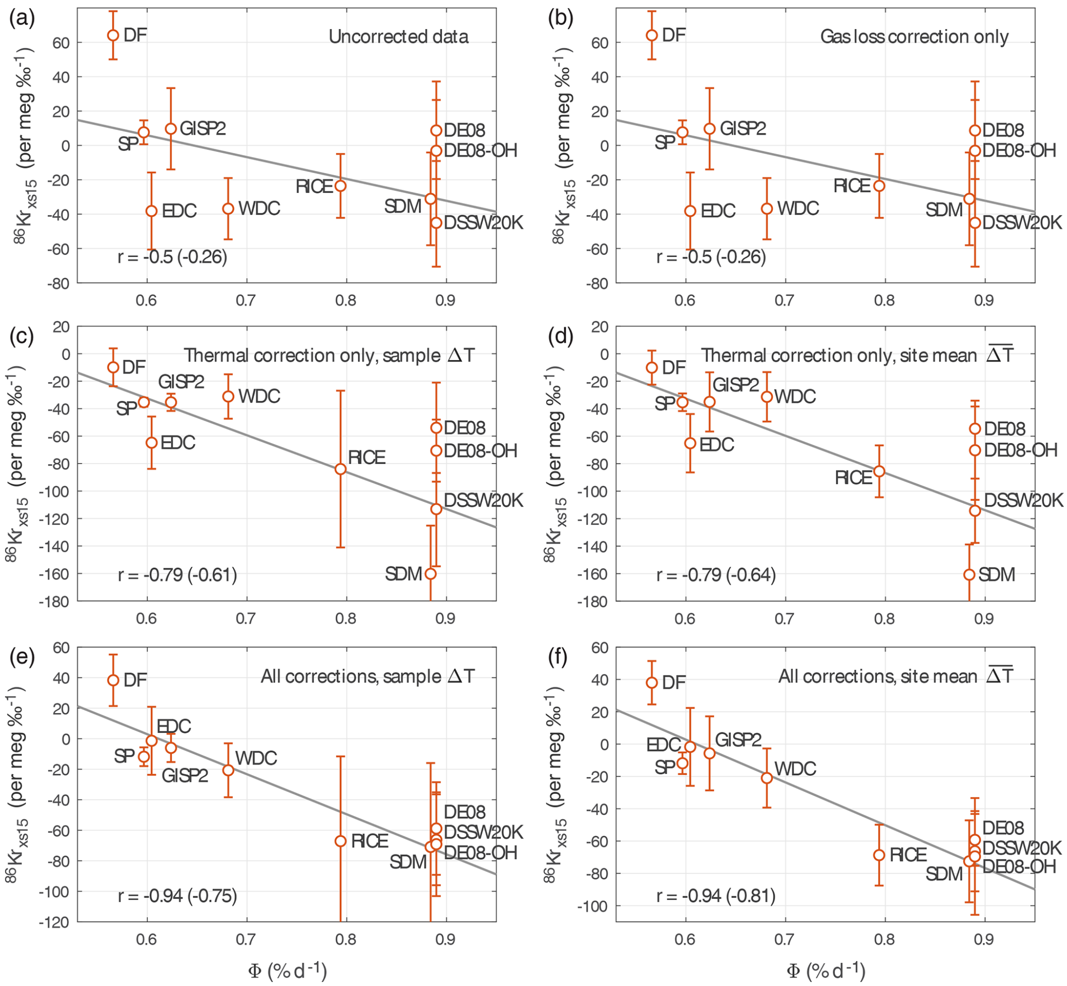

Figure A4. Same as Fig. A3, but for $^{86}Kr_{xs15}$. Note that the gas loss correction **(b)** does not impact $^{86}Kr_{xs15}$. For all correlations $p < 0.05$, except for panels **(a)** and **(b)** for which $p = 0.16$ for the site average correlation.

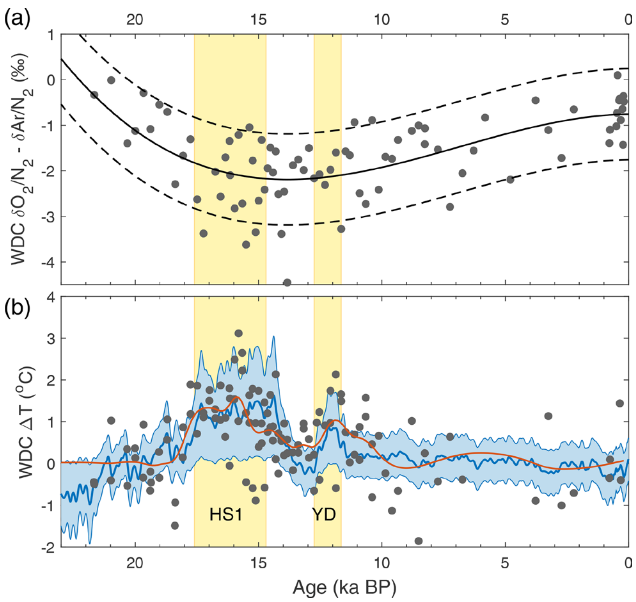

Figure A5. Gas loss and thermal corrections for the WDC time series. **(a)** WDC gravity-corrected $\delta O_2/N_2$–$\delta Ar/N_2$ as a measure of gas loss. The solid line is a third-order polynomial fit to the data; the dashed lines give a ±1 ‰ range around the fit, which captures the majority of the data. **(b)** The ΔT correction applied to the downcore records. The blue envelope shows the $\pm 2\sigma$ range of thermal correction scenarios in the Monte Carlo sampling, together with the mean (blue line). Gray dots show WDC ΔT estimates from available ^{15}N excess data, with the red curve being a Gaussian smoothing function to the data.

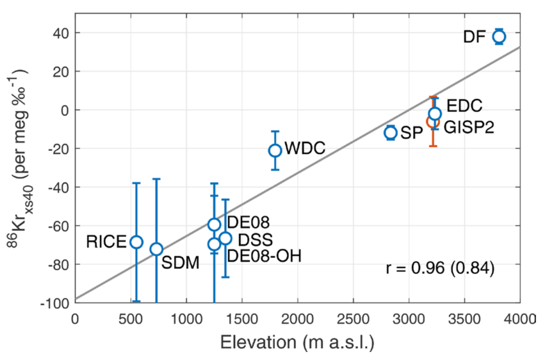

Figure A6. Kr-86 excess dependence on site elevation. The vertical axis is the $^{86}Kr_{xs}$. The linear fit has a slope of 34 per meg ‰$^{-1}$ per 1000 m elevation.

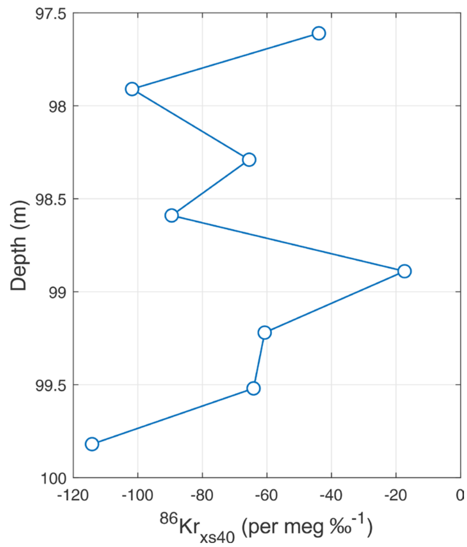

Figure B1. High-resolution sub-annual sampling of $^{86}Kr_{xs40}$ at the DE08-OH site. The annual layer thickness at this depth is around 1.3 m.

Appendix B: Sub-annual $^{86}Kr_{xs}$ variations at DE08-OH

The Law Dome DE08-OH site is a revisit of the DE08 site, drilled in the 2018–2019 austral summer Antarctic field season. We have samples from two separate cores: (1) 13 24 cm long samples from a 10 cm diameter core going from 97 to 193 m depth at ∼ 8 m sample spacing and (2) 8 6 cm long samples from a 24 cm diameter core going from 97.6 to 99.8 m depth at 30 cm sample spacing. The purpose of the first set was to determine possible long-term variations in $^{86}Kr_{xs}$; the purpose of the second set was to assess whether there are sub-annual variations in $^{86}Kr_{xs}$ due to the seasonality in firn properties and bubble trapping.

Both cores were dry-drilled (i.e., no drill liquid was used). The 10 cm diameter core used was drilled at the beginning of the field season and the 24 cm diameter core at the end of the field season. Prior to shipment off the continent, both cores were stored in a chest freezer at Casey Station; due to a miscommunication this freezer was set to −20 °C rather than −26 °C, yet the ice is believed to have stayed below −18 °C.

Both DE08-OH cores experienced more gas loss than the original DE08 core that we also sampled (Fig. A1b). In particular, the samples from the 10 cm diameter core were strongly depleted in $\delta Ar/N_2$, with the most extreme gas loss seen for the deepest samples for which the ice quality was poorest.

Figure B1 shows the high-resolution sub-annual DE08-OH sampling. The data were corrected for gas loss and thermal fractionation using a site mean temperature gradient of $\overline{\Delta T} = -1.6$ °C, possibly related to a rectifier effect (Morgan et al., 2022). We find strong (5-fold) variations in $^{86}Kr_{xs}$ on sub-annual timescales. With an expected annual layer thickness of around 1.3 m at this depth, it appears as though there may be an annual-scale variation in $^{86}Kr_{xs}$; the dataset has insufficient length to establish this firmly.

We refrain from interpreting the long-term variations in $^{86}Kr_{xs}$ in the 10 cm diameter core for two reasons. First, given the strong sub-annual variations seen in the high-resolution sampling, it is unavoidable that we are aliasing the underlying signal in the core. Second, the 10 cm diameter core suffers from strong gas loss (depleted $\delta Ar/N_2$). We attribute this primarily to the dry drilling and imperfect sample storage conditions. Perhaps the greater stresses during drilling a 10 cm core (compared to the 24 cm diameter core) result in more microfractures and gas loss.

Data availability. Data are available at https://www.usap-dc.org/view/project/p0010037 (USAP-DC, 2023).

Author contributions. CB, JS, AJO, and EJB designed research; SS, AS, BB, KK, DB, AJO, JDM, and IO contributed measurements; KK, DME, NB, RLP, RM, EMT, PDN, DT, and VVP contributed ice core samples; CB and WHGR analyzed reanalysis data; CB, AJO, and BB performed firn modeling; CB drafted the paper with input from all authors.

Competing interests. The contact author has declared that none of the authors has any competing interests.

Disclaimer. Publisher's note: Copernicus Publications remains neutral with regard to jurisdictional claims in published maps and institutional affiliations.

Special issue statement. This article is part of the special issue "Ice core science at the three poles (CP/TC inter-journal SI)". It is not associated with a conference.

Acknowledgements. The idea for the Kr-86 excess proxy came out of discussions at the 2014 WAIS Divide Ice Core Science Meeting held at the Scripps Institution of Oceanography in La Jolla, CA. The authors want to thank John Chiang, Justin Wettstein, Zanna Chase, Bob Anderson, Tyler Jones, and Eric Steig for useful discussions, data sharing, and paper feedback, the NSF ice core facility (NSF-ICF, formerly the National Ice Core Laboratory) for curating and distributing ice core samples, the European Centre for Medium-Range Weather Forecasts (ECMWF) for making ERA-Interim reanalysis datasets publicly available, and the US ice drilling program for coordinating ice core drilling in Antarctica. Ice drilling and field support at Law Dome and sample handling in Hobart were provided by the Australian Antarctic Science Program, the Australian Antarctic Division, and (at DE08-OH) the US National Science Foundation.

Financial support. This research has been supported by the National Science Foundation (grant nos. ANT-0944343, ANT-1543267, ANT-1543229, ANT-1643716, and ANT-1643669), the New Zealand Ministry of Business, Innovation and Employment (grant nos. RDF-VUW-1103, 15-VUW-131, and 540GCT32), and the Japan Society for the Promotion of Science KAKENHI grants (grant nos. 17H06320 and 15KK0027).

Review statement. This paper was edited by Hubertus Fischer and reviewed by two anonymous referees.

References

Anderson, R. F., Ali, S., Bradtmiller, L. I., Nielsen, S. H. H., Fleisher, M. Q., Anderson, B. E., and Burckle, L. H.: Wind-Driven Upwelling in the Southern Ocean and the Deglacial Rise in Atmospheric CO_2, Science, 323, 1443–1448, 2009.

Baggenstos, D., Häberli, M., Schmitt, J., Shackleton, S. A., Birner, B., Severinghaus, J. P., Kellerhals, T., and Fischer, H.: Earth's radiative imbalance from the Last Glacial Maximum to the present, P. Natl. Acad. Sci. USA, 116, 14881–14886, https://doi.org/10.1073/pnas.1905447116, 2019.

Bals-Elsholz, T. M., Atallah, E. H., Bosart, L. F., Wasula, T. A., Cempa, M. J., and Lupo, A. R.: The Wintertime Southern Hemisphere Split Jet: Structure, Variability, and Evolution, J. Climate, 14, 4191–4215, 2001.

Battle, M. O., Severinghaus, J. P., Sofen, E. D., Plotkin, D., Orsi, A. J., Aydin, M., Montzka, S. A., Sowers, T., and Tans, P. P.: Controls on the movement and composition of firn air at the West Antarctic Ice Sheet Divide, Atmos. Chem. Phys., 11, 11007–11021, https://doi.org/10.5194/acp-11-11007-2011, 2011.

Bender, M., Sowers, T., and Lipenkov, V.: On the concentrations of O_2, N_2, and Ar in trapped gases from ice cores, J. Geophys. Res., 100, 18651–18660, 1995.

Bender, M. L.: Orbital tuning chronology for the Vostok climate record supported by trapped gas compositionc, Earth Planet. Sc. Lett., 204, 275–289, 2002.

Bereiter, B., Kawamura, K., and Severinghaus, J. P.: New methods for measuring atmospheric heavy noble gas isotope and elemental ratios in ice core samples, Rapid Commun. Mass Spectrom., 32, 801–814, 2018a.

Bereiter, B., Shackleton, S., Baggenstos, D., Kawamura, K., and Severinghaus, J.: Mean global ocean temperatures during the last glacial transition, Nature, 553, 39–44, https://doi.org/10.1038/nature25152, 2018b.

Birner, B., Buizert, C., Wagner, T. J. W., and Severinghaus, J. P.: The influence of layering and barometric pumping on firn air transport in a 2-D model, The Cryosphere, 12, 2021–2037, https://doi.org/10.5194/tc-12-2021-2018, 2018.

Braconnot, P., Luan, Y., Brewer, S., and Zheng, W.: Impact of Earth's orbit and freshwater fluxes on Holocene climate mean seasonal cycle and ENSO characteristics, Clim. Dynam., 38, 1081–1092, 2012.

Broccoli, A. J., Dahl, K. A., and Stouffer, R. J.: Response of the ITCZ to Northern Hemisphere cooling, Geophys. Res. Lett., 33, L01702, https://doi.org/10.1029/2005gl024546, 2006.

Buizert, C. and Severinghaus, J. P.: Dispersion in deep polar firn driven by synoptic-scale surface pressure variability, The Cryosphere, 10, 2099–2111, https://doi.org/10.5194/tc-10-2099-2016, 2016.
Buizert, C., Sowers, T., and Blunier, T.: Assessment of diffusive isotopic fractionation in polar firn, and application to ice core trace gas records, Earth Planet. Sc. Lett., 361, 110–119, 2013.
Buizert, C., Cuffey, K. M., Severinghaus, J. P., Baggenstos, D., Fudge, T. J., Steig, E. J., Markle, B. R., Winstrup, M., Rhodes, R. H., Brook, E. J., Sowers, T. A., Clow, G. D., Cheng, H., Edwards, R. L., Sigl, M., McConnell, J. R., and Taylor, K. C.: The WAIS Divide deep ice core WD2014 chronology – Part 1: Methane synchronization (68–31 ka BP) and the gas age–ice age difference, Clim. Past, 11, 153–173, https://doi.org/10.5194/cp-11-153-2015, 2015.
Buizert, C., Sigl, M., Severi, M., Markle, B. R., Wettstein, J. J., McConnell, J. R., Pedro, J. B., Sodemann, H., Goto-Azuma, K., Kawamura, K., Fujita, S., Motoyama, H., Hirabayashi, M., Uemura, R., Stenni, B., Parrenin, F., He, F., Fudge, T. J., and Steig, E. J.: Abrupt ice-age shifts in southern westerly winds and Antarctic climate forced from the north, Nature, 563, 681–685, 2018.
Cai, W., Santoso, A., Wang, G., Yeh, S.-W., An, S.-I., Cobb, K. M., Collins, M., Guilyardi, E., Jin, F.-F., Kug, J.-S., Lengaigne, M., McPhaden, M. J., Takahashi, K., Timmermann, A., Vecchi, G., Watanabe, M., and Wu, L.: ENSO and greenhouse warming, Nat. Clim. Change, 5, 849–859, 2015.
Cane, M. A.: The evolution of El Niño, past and future, Earth Planet. Sc. Lett., 230, 227–240, 2005.
Ceppi, P., Hwang, Y.-T., Liu, X., Frierson, D. M. W., and Hartmann, D. L.: The relationship between the ITCZ and the Southern Hemispheric eddy-driven jet, J. Geophys. Res., 118, 5136–5146, 2013.
Chase, Z., Anderson, R. F., Fleisher, M. Q., and Kubik, P. W.: Accumulation of biogenic and lithogenic material in the Pacific sector of the Southern Ocean during the past 40,000 years, Deep-Sea Res. Pt. II, 50, 799–832, 2003.
Cheng, H., Edwards, R. L., Sinha, A., Spötl, C., Yi, L., Chen, S., Kelly, M., Kathayat, G., Wang, X., Li, X., Kong, X., Wang, Y., Ning, Y., and Zhang, H.: The Asian monsoon over the past 640,000 years and ice age terminations, Nature, 534, 640–646, 2016.
Chiang, J. C. and Friedman, A. R.: Extratropical cooling, interhemispheric thermal gradients, and tropical climate change, Annu. Rev. Earth Planet. Sci., 40, 383–412, 2012.
Chiang, J. C. H. and Bitz, C. M.: Influence of high latitude ice cover on the marine Intertropical Convergence Zone, Clim. Dynam., 25, 477–496, 2005.
Chiang, J. C. H., Lee, S.-Y., Putnam, A. E., and Wang, X.: South Pacific Split Jet, ITCZ shifts, and atmospheric North–South linkages during abrupt climate changes of the last glacial period, Earth Planet. Sc. Lett., 406, 233–246, 2014.
Clement, A. C., Seager, R., and Cane, M. A.: Suppression of El Niño during the Mid-Holocene by changes in the Earth's orbit, Paleoceanography, 15, 731–737, 2000.
Cobb, K. M., Westphal, N., Sayani, H. R., Watson, J. T., Di Lorenzo, E., Cheng, H., Edwards, R. L., and Charles, C. D.: Highly Variable El Niño–Southern Oscillation Throughout the Holocene, Science, 339, 67–70, 2013.
Conroy, J. L., Overpeck, J. T., Cole, J. E., Shanahan, T. M., and Steinitz-Kannan, M.: Holocene changes in eastern tropical Pacific climate inferred from a Galápagos lake sediment record, Quaternary Sci. Rev., 27, 1166–1180, 2008.
Cruz, F. W., Burns, S. J., Karmann, I., Sharp, W. D., Vuille, M., Cardoso, A. O., Ferrari, J. A., Dias, P. L. S., and Viana, O.: Insolation-driven changes in atmospheric circulation over the past 116,000 years in subtropical Brazil, Nature, 434, 63–66, 2005.
Dee, D. P., Uppala, S. M., Simmons, A. J., Berrisford, P., Poli, P., Kobayashi, S., Andrae, U., Balmaseda, M. A., Balsamo, G., Bauer, P., Bechtold, P., Beljaars, A. C. M., van de Berg, L., Bidlot, J., Bormann, N., Delsol, C., Dragani, R., Fuentes, M., Geer, A. J., Haimberger, L., Healy, S. B., Hersbach, H., Hólm, E. V., Isaksen, L., Kållberg, P., Köhler, M., Matricardi, M., McNally, A. P., Monge-Sanz, B. M., Morcrette, J. J., Park, B. K., Peubey, C., de Rosnay, P., Tavolato, C., Thépaut, J. N., and Vitart, F.: The ERA-Interim reanalysis: configuration and performance of the data assimilation system, Q. J. Roy. Meteorol. Soc., 137, 553–597, 2011.
Driscoll, R., Elliot, M., Russon, T., Welsh, K., Yokoyama, Y., and Tudhope, A.: ENSO reconstructions over the past 60 ka using giant clams (Tridacna sp.) from Papua New Guinea, Geophys. Res. Lett., 41, 6819–6825, 2014.
Dykoski, C. A., Edwards, R. L., Cheng, H., Yuan, D. X., Cai, Y. J., Zhang, M. L., Lin, Y. S., Qing, J. M., An, Z. S., and Revenaugh, J.: A high-resolution, absolute-dated Holocene and deglacial Asian monsoon record from Dongge Cave, China, Earth Planet. Sc. Lett., 233, 71–86, 2005.
Emile-Geay, J., Cobb, K. M., Carré, M., Braconnot, P., Leloup, J., Zhou, Y., Harrison, S. P., Corrège, T., McGregor, H. V., Collins, M., Driscoll, R., Elliot, M., Schneider, B., and Tudhope, A.: Links between tropical Pacific seasonal, interannual and orbital variability during the Holocene, Nat. Geosci., 9, 168–173, https://doi.org/10.1038/ngeo2608, 2015.
Etheridge, D. M., Pearman, G. I., and Fraser, P. J.: Changes in tropospheric methane between 1841 and 1978 from a high accumulation-rate Antarctic ice core, Tellus, 44, 282–294, 1992.
Fahnestock, M. A., Scambos, T. A., Shuman, C. A., Arthern, R. J., Winebrenner, D. P., and Kwok, R.: Snow megadune fields on the East Antarctic Plateau: Extreme atmosphere-ice interaction, Geophys. Res. Lett., 27, 3719–3722, 2000.
Fowler, A. M., Boswijk, G., Lorrey, A. M., Gergis, J., Pirie, M., McCloskey, S. P. J., Palmer, J. G., and Wunder, J.: Multi-centennial tree-ring record of ENSO-related activity in New Zealand, Nat. Clim. Change, 2, 172–176, https://doi.org/10.1038/nclimate1374, 2012.
Fujita, S., Okuyama, J., Hori, A., and Hondoh, T.: Metamorphism of stratified firn at Dome Fuji, Antarctica: A mechanism for local insolation modulation of gas transport conditions during bubble close off, J. Geophys. Res., 114, F03023, https://doi.org/10.1029/2008jf001143, 2009.
Gergis, J. L. and Fowler, A. M.: A history of ENSO events since A.D. 1525: implications for future climate change, Climatic Change, 92, 343–387, 2009.
Golledge, N. R., Menviel, L., Carter, L., Fogwill, C. J., England, M. H., Cortese, G., and Levy, R. H.: Antarctic contribution to meltwater pulse 1A from reduced Southern Ocean overturning, Nat. Commun., 5, 5107, https://doi.org/10.1038/ncomms6107, 2014.

Grachev, A. M. and Severinghaus, J. P.: Determining the thermal diffusion factor for $^{40}Ar/^{36}Ar$ in air to aid paleoreconstruction of abrupt climate change, J. Phys. Chem. A, 107, 4636–4642, 2003a.

Grachev, A. M. and Severinghaus, J. P.: Laboratory determination of thermal diffusion constants for N-29(2)/N-28(2) in air at temperatures from −60 to 0 degrees C for reconstruction of magnitudes of abrupt climate changes using the ice core fossil-air paleothermometer, Geochim. Cosmochim. Ac., 67, 345–360, 2003b.

Grootes, P. M., Stuiver, M., White, J. W. C., Johnsen, S., and Jouzel, J.: Comparison of oxygen isotope records from the GISP2 and GRIP Greenland ice cores, Nature, 366, 552–554, 1993.

Headly, M. A. and Severinghaus, J. P.: A method to measure Kr/N_2 ratios in air bubbles trapped in ice cores and its application in reconstructing past mean ocean temperature, J. Geophys. Res., 112, D19105, https://doi.org/10.1029/2006jd008317, 2007.

Herron, M .M. and Langway, C. C.: Firn densification: An empirical model, J. Glaciol., 25, 373–385, 1980.

Huang, B., Banzon, V. F., Freeman, E., Lawrimore, J., Liu, W., Peterson, T. C., Smith, T. M., Thorne, P. W., Woodruff, S. D., and Zhang, H.-M.: Extended Reconstructed Sea Surface Temperature Version 4 (ERSST.v4). Part I: Upgrades and Intercomparisons, J. Climate, 28, 911–930, 2014.

Huber, C., Beyerle, U., Leuenberger, M., Schwander, J., Kipfer, R., Spahni, R., Severinghaus, J. P., and Weiler, K.: Evidence for molecular size dependent gas fractionation in firn air derived from noble gases, oxygen, and nitrogen measurements, Earth Planet. Sc. Lett., 243, 61–73, 2006.

Ikeda-Fukazawa, T., Fukumizu, K., Kawamura, K., Aoki, S., Nakazawa, T., and Hondoh, T.: Effects of molecular diffusion on trapped gas composition in polar ice cores, Earth Planet. Sc. Lett., 229, 183–192, 2005.

Kanner, L. C., Burns, S. J., Cheng, H., and Edwards, R. L.: High-Latitude Forcing of the South American Summer Monsoon During the Last Glacial, Science, 335, 570–573, 2012.

Kawamura, K., Severinghaus, J. P., Ishidoya, S., Sugawara, S., Hashida, G., Motoyama, H., Fujii, Y., Aoki, S., and Nakazawa, T.: Convective mixing of air in firn at four polar sites, Earth Planet. Sc. Lett., 244, 672–682, 2006.

Kawamura, K., Severinghaus, J. P., Albert, M. R., Courville, Z. R., Fahnestock, M. A., Scambos, T., Shields, E., and Shuman, C. A.: Kinetic fractionation of gases by deep air convection in polar firn, Atmos. Chem. Phys., 13, 11141–11155, https://doi.org/10.5194/acp-13-11141-2013, 2013.

Kobashi, T., Severinghaus, J. P., and Barnola, J. M.: 4 ± 1.5 degrees C abrupt warming 11,270 yr ago identified from trapped air in Greenland ice, Earth Planet. Sc. Lett., 268, 397–407, 2008a.

Kobashi, T., Severinghaus, J. P., and Kawamura, K.: Argon and nitrogen isotopes of trapped air in the GISP2 ice core during the Holocene epoch (0–11,500 B.P.): Methodology and implications for gas loss processes, Geochim. Cosmochim. Ac., 72, 4675–4686, 2008b.

Kohfeld, K. E., Graham, R. M., de Boer, A. M., Sime, L. C., Wolff, E. W., Le Quéré, C., and Bopp, L.: Southern Hemisphere westerly wind changes during the Last Glacial Maximum: paleo-data synthesis, Quaternary Sci. Rev., 68, 76–95, 2013.

Koutavas, A., Lynch-Stieglitz, J., Marchitto, T. M., and Sachs, J.P.: El Niño-Like Pattern in Ice Age Tropical Pacific Sea Surface Temperature, Science, 297, 226–230, 2002.

Koutavas, A., deMenocal, P. B., Olive, G. C., and Lynch-Stieglitz, J.: Mid-Holocene El Niño–Southern Oscillation (ENSO) attenuation revealed by individual foraminifera in eastern tropical Pacific sediments, Geology, 34, 993–996, 2006.

Lamy, F., Chiang, J. C. H., Martínez-Méndez, G., Thierens, M., Arz, H. W., Bosmans, J., Hebbeln, D., Lambert, F., Lembke-Jene, L., and Stuut, J.-B.: Precession modulation of the South Pacific westerly wind belt over the past million years, P. Natl. Acad. Sci. USA, 116, 23455–23460, https://doi.org/10.1073/pnas.1905847116, 2019.

Lee, S. and Kim, H.-K.: The Dynamical Relationship between Subtropical and Eddy-Driven Jets, J. Atmos. Sci., 60, 1490–1503, 2003.

Lee, S. Y., Chiang, J. C., Matsumoto, K., and Tokos, K. S.: Southern Ocean wind response to North Atlantic cooling and the rise in atmospheric CO_2: Modeling perspective and paleoceanographic implications, Paleoceanography, 26, PA1214, https://doi.org/10.1029/2010PA002004, 2011.

Liu, Z., Kutzbach, J., and Wu, L.: Modeling climate shift of El Nino variability in the Holocene, Geophys. Res. Lett., 27, 2265–2268, 2000.

Liu, Z., Lu, Z., Wen, X., Otto-Bliesner, B. L., Timmermann, A., and Cobb, K. M.: Evolution and forcing mechanisms of El Nino over the past 21,000 years, Nature, 515, 550–553, 2014.

Lynch-Stieglitz, J.: The Atlantic Meridional Overturning Circulation and Abrupt Climate Change, Annu. Rev. Mar. Sci., 9, 83–104, 2017.

Mantua, N. J. and Hare, S. R.: The Pacific Decadal Oscillation, J. Oceanogr., 58, 35–44, 2002.

Marcott, S. A., Shakun, J. D., Clark, P. U., and Mix, A. C.: A Reconstruction of Regional and Global Temperature for the Past 11,300 Years, Science, 339, 1198–1201, 2013.

Marino, G., Zahn, R., Ziegler, M., Purcell, C., Knorr, G., Hall, I. R., Ziveri, P., and Elderfield, H.: Agulhas salt-leakage oscillations during abrupt climate changes of the Late Pleistocene, Paleoceanography, 28, 599–606, 2013.

Markle, B. R., Steig, E. J., Buizert, C., Schoenemann, S. W., Bitz, C. M., Fudge, T. J., Pedro, J. B., Ding, Q., Jones, T. R., White, J. W. C., and Sowers, T.: Global atmospheric teleconnections during Dansgaard-Oeschger events, Nat. Geosci., 10, 36–40, 2017.

Marshall, J. and Speer, K.: Closure of the meridional overturning circulation through Southern Ocean upwelling, Nat. Geosci., 5, 171–180, 2012.

McGee, D., Donohoe, A., Marshall, J., and Ferreira, D.: Changes in ITCZ location and cross-equatorial heat transport at the Last Glacial Maximum, Heinrich Stadial 1, and the mid-Holocene, Earth Planet. Sc. Lett., 390, 69–79, 2014.

Merkel, U., Prange, M., and Schulz, M.: ENSO variability and teleconnections during glacial climates, Quaternary Sci. Rev., 29, 86–100, 2010.

Mo, K. C. and Paegle, J. N.: The Pacific–South American modes and their downstream effects, Int. J. Climatol., 21, 1211–1229, 2001.

Morgan, J. D., Buizert, C., Fudge, T. J., Kawamura, K., Severinghaus, J. P., and Trudinger, C. M.: Gas isotope thermometry in the South Pole and Dome Fuji ice cores provides evidence for seasonal rectification of ice core gas records, The Cryosphere, 16, 2947–2966, https://doi.org/10.5194/tc-16-2947-2022, 2022.

Moy, C. M., Seltzer, G. O., Rodbell, D. T., and Anderson, D. M.: Variability of El Niño/Southern Oscillation activity at millennial timescales during the Holocene epoch, Nature, 420, 162–165, https://doi.org/10.1038/nature01194, 2002.

Nakamura, H. and Shimpo, A.: Seasonal Variations in the Southern Hemisphere Storm Tracks and Jet Streams as Revealed in a Reanalysis Dataset, J. Climate, 17, 1828–1844, 2004.

Orsi, A. J., Kawamura, K., Fegyveresi, J. M., Headly, M. A., Alley, R. B., and Severinghaus, J. P.: Differentiating bubble-free layers from melt layers in ice cores using noble gases, J. Glaciol., 61, 585–594, 2015.

Oyabu, I., Kawamura, K., Uchida, T., Fujita, S., Kitamura, K., Hirabayashi, M., Aoki, S., Morimoto, S., Nakazawa, T., Severinghaus, J. P., and Morgan, J. D.: Fractionation of O_2/N_2 and Ar/N2 in the Antarctic ice sheet during bubble formation and bubble–clathrate hydrate transition from precise gas measurements of the Dome Fuji ice core, The Cryosphere, 15, 5529–5555, https://doi.org/10.5194/tc-15-5529-2021, 2021.

Parkinson, C. L. and Cavalieri, D. J.: Antarctic sea ice variability and trends, 1979–2010, The Cryosphere, 6, 871–880, https://doi.org/10.5194/tc-6-871-2012, 2012.

Pedro, J. B., Jochum, M., Buizert, C., He, F., Barker, S., and Rasmussen, S. O.: Beyond the bipolar seesaw: Toward a process understanding of interhemispheric coupling, Quaternary Sci. Rev., 192, 27–46, 2018.

Peterson, L. C., Haug, G. H., Hughen, K. A., and Röhl, U.: Rapid Changes in the Hydrologic Cycle of the Tropical Atlantic During the Last Glacial, Science, 290, 1947–1951, 2000.

Rahmstorf, S.: Ocean circulation and climate during the past 120,000 years, Nature, 419, 207–214, 2002.

Raynaud, D., Lipenkov, V., Lemieux-Dudon, B., Duval, P., Loutre, M. F., and Lhomme, N.: The local insolation signature of air content in Antarctic ice. A new step toward an absolute dating of ice records, Earth Planet. Sc. Lett., 261, 337–349, 2007.

Rein, B., Lückge, A., Reinhardt, L., Sirocko, F., Wolf, A., and Dullo, W.-C.: El Niño variability off Peru during the last 20,000 years, Paleoceanography, 20, PA4003, https://doi.org/10.1029/2004PA001099, 2005.

Rhodes, R. H., Faïn, X., Brook, E. J., McConnell, J. R., Maselli, O. J., Sigl, M., Edwards, J., Buizert, C., Blunier, T., Chappellaz, J., and Freitag, J.: Local artifacts in ice core methane records caused by layered bubble trapping and in situ production: a multi-site investigation, Clim. Past, 12, 1061–1077, https://doi.org/10.5194/cp-12-1061-2016, 2016.

Riedinger, M. A., Steinitz-Kannan, M., Last, W. M., and Brenner, M.: A ~ 6100 ^{14}C yr record of El Niño activity from the Galápagos Islands, J. Paleolimnol., 27, 1–7, 2002.

Rind, D., Russell, G., Schmidt, G., Sheth, S., Collins, D., Demenocal, P., and Teller, J.: Effects of glacial meltwater in the GISS coupled atmosphere-ocean model: 2. A bipolar seesaw in Atlantic Deep Water production, J. Geophys. Res.-Atmos., 106, 27355–27365, 2001.

Rojas, M., Moreno, P., Kageyama, M., Crucifix, M., Hewitt, C., Abe-Ouchi, A., Ohgaito, R., Brady, E. C., and Hope, P.: The Southern Westerlies during the last glacial maximum in PMIP2 simulations, Clim. Dynam., 32, 525–548, 2009.

Rommelaere, V., Arnaud, L., and Barnola, J. M.: Reconstructing recent atmospheric trace gas concentrations from polar firn and bubbly ice data by inverse methods, J. Geophys. Res., 102, 30069–30083, 1997.

Russell, J. L., Dixon, K. W., Gnanadesikan, A., Stouffer, R. J., and Toggweiler, J. R.: The Southern Hemisphere Westerlies in a Warming World: Propping Open the Door to the Deep Ocean, J. Climate, 19, 6382–6390, 2006.

Sadekov, A. Y., Ganeshram, R., Pichevin, L., Berdin, R., McClymont, E., Elderfield, H., and Tudhope, A. W.: Palaeoclimate reconstructions reveal a strong link between El Niño-Southern Oscillation and Tropical Pacific mean state, Nat. Commun., 4, 2692, https://doi.org/10.1038/ncomms3692, 2013.

Salau, O., Schneider, B., Park, W., Khon, V., and Latif, M.: Modeling the ENSO impact of orbitally induced mean state climate changes, J. Geophys. Res., 117, C05043, https://doi.org/10.1029/2011JC007742, 2012.

Schaller, C. F., Freitag, J., and Eisen, O.: Critical porosity of gas enclosure in polar firn independent of climate, Clim. Past, 13, 1685–1693, https://doi.org/10.5194/cp-13-1685-2017, 2017.

Schneider, T., Bischoff, T., and Haug, G. H.: Migrations and dynamics of the intertropical convergence zone, Nature, 513, 45–53, 2014.

Schwander, J.: The transformation of snow to ice and the occlusion of gases in: The Environmental record in glaciers and ice sheets, edited by: Oescher, H. and Langway, C. C., John Wiley, New York, 53–67, ISBN 0471921858, 1989.

Schwander, J., Stauffer, B., and Sigg, A.: Air mixing in firn and the age of the air at pore close-off, Ann. Glaciol., 10, 141–145, https://doi.org/10.3189/S0260305500004328, 1988.

Schwander, J., Barnola, J. M., Andrie, C., Leuenberger, M., Ludin, A., Raynaud, D., and Stauffer, B.: The age of the air in hte firn and the ice at Summit, Greenland, J. Geophys. Res., 98, 2831–2838, 1993.

Severinghaus, J. P. and Battle, M. O.: Fractionation of gases in polar ice during bubble close-off: New constraints from firn air Ne, Kr and Xe observations, Earth Planet. Sc. Lett., 244, 474–500, 2006.

Severinghaus, J. P., Sowers, T., Brook, E. J., Alley, R. B., and Bender, M. L.: Timing of abrupt climate change at the end of the Younger Dryas interval from thermally fractionated gases in polar ice, Nature, 391, 141–146, 1998.

Severinghaus, J. P., Grachev, A., Luz, B., and Caillon, N.: A method for precise measurement of argon 40/36 and krypton / argon ratios in trapped air in polar ice with applications to past firn thickness and abrupt climate change in Greenland and at Siple Dome, Antarctica, Geochim. Cosmochim. Ac., 67, 325–343, 2003.

Severinghaus, J. P., Beaudette, R., Headly, M. A., Taylor, K., and Brook, E. J.: Oxygen-18 of O_2 Records the Impact of Abrupt Climate Change on the Terrestrial Biosphere, Science, 324, 1431–1434, 2009.

Severinghaus, J. P., Albert, M. R., Courville, Z. R., Fahnestock, M. A., Kawamura, K., Montzka, S. A., Muhle, J., Scambos, T. A., Shields, E., Shuman, C. A., Suwa, M., Tans, P., and Weiss, R. F.: Deep air convection in the firn at a zero-accumulation site, central Antarctica, Earth Planet. Sc. Lett., 293, 359–367, 2010.

Shakun, J. D., Clark, P. U., He, F., Marcott, S. A., Mix, A. C., Liu, Z., Otto-Bliesner, B., Schmittner, A., and Bard, E.: Global warming preceded by increasing carbon dioxide concentrations during the last deglaciation, Nature, 484, 49–54, 2012.

Sime, L. C., Kohfeld, K. E., Le Quéré, C., Wolff, E. W., de Boer, A. M., Graham, R. M., and Bopp, L.: Southern Hemisphere westerly wind changes during the Last Glacial Maximum: model-data comparison, Quaternary Sci. Rev., 64, 104–120, 2013.

Simpson, I. R., Hitchcock, P., Shepherd, T. G., and Scinocca, J. F.: Stratospheric variability and tropospheric annular-mode timescales, Geophys. Res. Lett., 38, L20806, https://doi.org/10.1029/2011GL049304, 2011.

Sowers, T., Bender, M., Raynaud, D., and Korotkevich, Y. S.: δ^{15}N of N_2 in air trapped in polar ice: A tracer of gas transport in the firn and a possible constraint on ice age-gas age differences, J. Geophys. Res., 97, 15683–15697, 1992.

Stott, L., Poulsen, C., Lund, S., and Thunell, R.: Super ENSO and Global Climate Oscillations at Millennial Time Scales, Science, 297, 222–226, 2002.

Studer, A. S., Sigman, D. M., Martínez-García, A., Benz, V., Winckler, G., Kuhn, G., Esper, O., Lamy, F., Jaccard, S. L., Wacker, L., Oleynik, S., Gersonde, R., and Haug, G. H.: Antarctic Zone nutrient conditions during the last two glacial cycles, Paleoceanography, 30, 845–862, 2015.

Studer, A. S., Sigman, D. M., Martínez-García, A., Thöle, L. M., Michel, E., Jaccard, S. L., Lippold, J. A., Mazaud, A., Wang, X. T., Robinson, L. F., Adkins, J. F., and Haug, G. H.: Increased nutrient supply to the Southern Ocean during the Holocene and its implications for the pre-industrial atmospheric CO_2 rise, Nat. Geosci., 11, 756–760, 2018.

Thomas, E. R., Marshall, G. J., and McConnell, J. R.: A doubling in snow accumulation in the western Antarctic Peninsula since 1850, Geophys. Res. Lett., 35, L01706, https://doi.org/10.1029/2007GL032529, 2008.

Thompson, D. W. J. and Wallace, J. M.: Annular Modes in the Extratropical Circulation. Part I: Month-to-Month Variability, J. Climate, 13, 1000–1016, 2000.

Thompson, L. G., Mosley-Thompson, E., Davis, M. E., Zagorodnov, V. S., Howat, I. M., Mikhalenko, V. N., and Lin, P.-N.: Annually Resolved Ice Core Records of Tropical Climate Variability over the Past ∼ 1800 Years, Science, 340, 945–950, 2013.

Timmermann, A., Okumura, Y., An, S. I., Clement, A., Dong, B., Guilyardi, E., Hu, A., Jungclaus, J. H., Renold, M., Stocker, T. F., Stouffer, R. J., Sutton, R., Xie, S. P., and Yin, J.: The Influence of a Weakening of the Atlantic Meridional Overturning Circulation on ENSO, J. Climate, 20, 4899–4919, 2007.

Toggweiler, J. R., Russell, J. L., and Carson, S. R.: Mid-latitude westerlies, atmospheric CO_2, and climate change during the ice ages, Paleoceanography, 21, PA2005, https://doi.org/10.1029/2005PA001154, 2006.

Trenberth, K. E.: Storm Tracks in the Southern Hemisphere, J. Atmos. Sci., 48, 2159–2178, 1991.

Tudhope, A. W., Chilcott, C. P., McCulloch, M. T., Cook, E. R., Chappell, J., Ellam, R. M., Lea, D. W., Lough, J. M., and Shimmield, G. B.: Variability in the El Niño-Southern Oscillation through a glacial-interglacial cycle, Science, 291, 1511–1517, 2001.

USAP-DC – US Antarctic Program Data Center: Collaborative research: Kr-86 as a proxy for barometric pressure variability and movement of the SH westerlies during the last deglaciation, USAP-DC [data set], https://www.usap-dc.org/view/project/p0010037, last access: 7 March 2023.

Wang, X., Auler, A. S., Edwards, R. L., Cheng, H., Ito, E., Wang, Y., Kong, X., and Solheid, M.: Millennial-scale precipitation changes in southern Brazil over the past 90,000 years, Geophys. Res. Lett., 34, L23701, https://doi.org/10.1029/2007GL031149, 2007.

Wang, Y. J., Cheng, H., Edwards, R. L., An, Z. S., Wu, J. Y., Shen, C. C., and Dorale, J. A.: A High-Resolution Absolute-Dated Late Pleistocene Monsoon Record from Hulu Cave, China, Science, 294, 2345–2348, 2001.

Zheng, W., Braconnot, P., Guilyardi, E., Merkel, U., and Yu, Y.: ENSO at 6 ka and 21 ka from ocean–atmosphere coupled model simulations, Clim. Dynam., 30, 745–762, 2008.

Clim. Past, 20, 1415–1435, 2024
https://doi.org/10.5194/cp-20-1415-2024

Climate of the Past
Open Access

Continuous synchronization of the Greenland ice-core and U–Th timescales using probabilistic inversion

Francesco Muschitiello[1,2] **and Marco Antonio Aquino-Lopez**[1]

[1]Department of Geography, University of Cambridge, Cambridge CB2 3EN, UK
[2]Centre for Climate Repair, DAMTP, Centre for Mathematical Sciences, Wilberforce Road, Cambridge, CB3 0WA, UK

Correspondence: Francesco Muschitiello (fm476@cam.ac.uk)

Received: 11 August 2023 – Discussion started: 16 August 2023
Revised: 25 April 2024 – Accepted: 14 May 2024 – Published: 28 June 2024

Abstract. This study presents the first continuously measured transfer functions that quantify the age difference between the Greenland ice-core chronology 2005 (GICC05) and the U–Th timescale during the last glacial period. The transfer functions were estimated using an automated algorithm for Bayesian inversion that allows inferring a continuous and objective synchronization between Greenland ice-core and East Asian summer monsoon speleothem data, and a total of three transfer functions were inferred using independent ice-core records. The algorithm is based on an alignment model that considers prior knowledge of the GICC05 counting error but also samples synchronization scenarios that exceed the differential dating uncertainty of the annual-layer count in ice cores, which are currently hard to detect using conventional alignment techniques. The transfer functions are on average 48 % more precise than previous estimates and significantly reduce the absolute dating uncertainty of the GICC05 back to 48 kyr ago. The results reveal that GICCC05 is, on average, systematically younger than the U–Th timescale by 0.86 %. However, they also highlight that the annual-layer counting error is not strictly correlated over extended periods of time and that within the coldest Greenland Stadials the differential dating uncertainty is likely underestimated by up to $\sim 13\,\%$. Importantly, the analysis implies for the first time that during the Last Glacial Maximum GICC05 may overcount ice layers by $\sim 10\,\%$ – a bias possibly attributable to a higher frequency of sub-annual layers due to changes in the seasonal cycle of precipitation and mode of dust deposition to the Greenland Ice Sheet. The new timescale transfer functions provide important constraints on the uncertainty surrounding the stratigraphic dating of the Greenland age scale and enable an improved chronological integration of ice cores as well as U–Th-dated and radiocarbon-dated paleoclimate records on a common timeline. The transfer functions are available as a Supplement to this study.

1 Introduction

The Greenland ice-core chronology 2005 (GICC05; Rasmussen et al., 2006; Svensson et al., 2008) and the U–Th timescale (e.g., Cheng et al., 2016) are among the most widely used independently dated chronological frameworks of the last glacial period. The timescales not only provide the backbone of some of the most unique and detailed records of global climate change, but their robustness makes them exceptionally suited for resolving the temporal structure of Dansgaard–Oeschger (DO) events and other abrupt climate shifts.

The GICC05 is based on annual-layer counting back to 60 kyr before 2000 CE (b2k) and due to the incremental nature of the counting uncertainty, it provides high internal consistency that enables accurate relative age estimates of climate events. The Greenland ice-core timescale underpins a number of high-resolution ice-core records of North Atlantic climate and atmospheric composition. These records have become established Northern Hemisphere templates for the last glacial period and have shaped our understanding of the physical mechanisms driving rapid climate shifts (Andersen et al., 2004; Dahl-Jensen et al., 1998; Legrand and Mayewski, 1997; Schüpbach et al., 2018) and their rates of change (Jansen et al., 2020). By contrast, the U–Th timescale is constructed using high-precision U–Th dating,

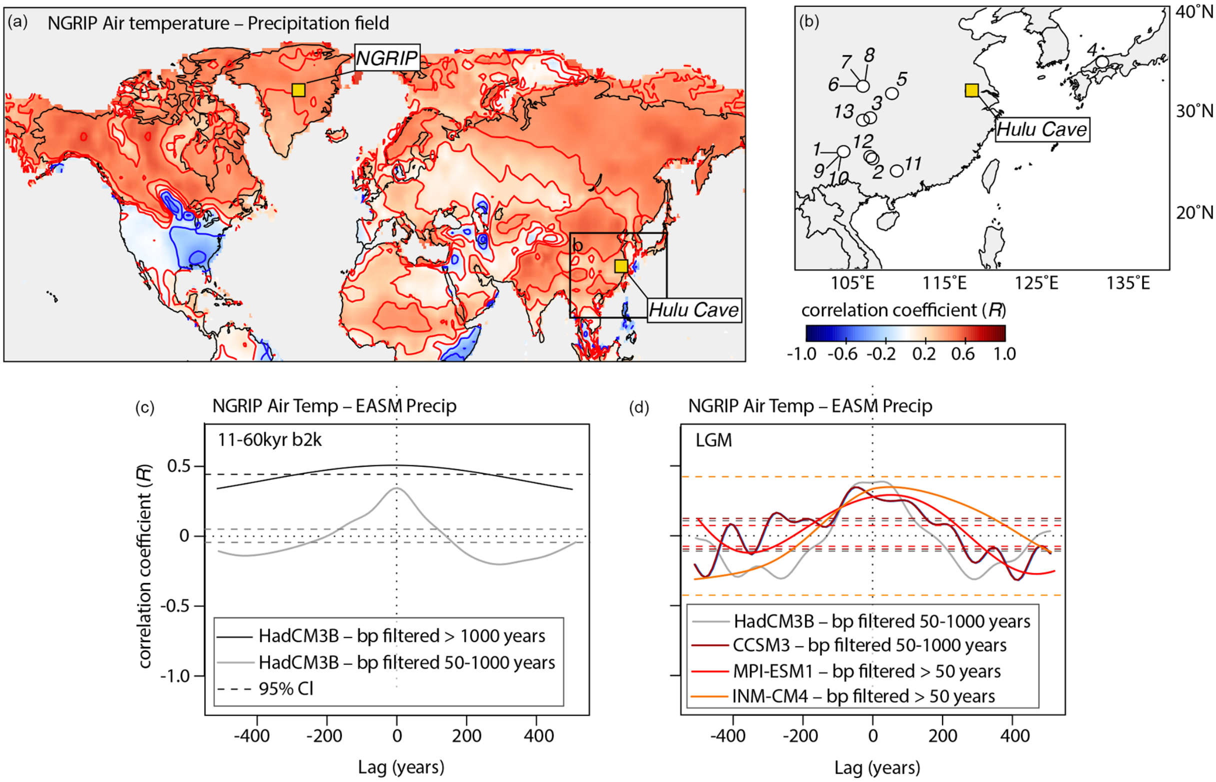

Figure 1. **(a)** Instantaneous (lag 0) spatial correlation between mean decadal surface air temperature at the NGRIP site and mean decadal land surface temperatures during the last glacial period (11–60 kyr b2k) as simulated with the HadCM3B-M2.1 coupled general circulation model (Armstrong et al., 2019). The simulation incorporates Dansgaard–Oeschger cycles, Heinrich events, and shorter-term variability, with a spatial climate fingerprint derived from a Last Glacial Maximum (LGM) freshwater hosing experiment applied over the North Atlantic Ocean. The locations of NGRIP, the East Asian summer monsoon (EASM) region, and Hulu Cave are also shown. **(b)** EASM domain showing the location of speleothem records compiled by Corrick et al. (2020) and used in this study. 1. Dashibao; 2. Dongge; 3. Furong; 4. Maboroshi; 5. Sanbao; 6. Shizi; 7. Songjia1; 8. Songjia3; 9. Wulu3; 10. Wulu32; 11. Xiaobailong; 12. Yamen; 13. Yangkou. Reference to the cave site is provided in Corrick et al. (2020). **(c)** Cross-correlation between simulated NGRIP air temperature and EASM precipitation between 11 and 60 kyr ago. The EASM region is defined here as the average of 10–40° N and 95–125° E. The time series were bandpass-filtered to quantify leads and lags at millennial and shorter timescales, respectively. **(d)** Same as **(c)** but for the LGM using transient climate model simulations (Armstrong et al., 2019; Liu et al., 2009) and equilibrium experiments from CMIP6 (Kageyama et al., 2021). Results from HadCM3B and CCSM3 span the interval ∼ 17.5–21 kyr b2k, whereas for CMIP6 only simulations longer than 200 years were considered for the cross-correlation analysis. Dashed lines reflect the 95 % significance level against first-order autoregressive (AR1) noise.

which yields much smaller uncertainty in the absolute ages than GICC05 during the last glacial. The U–Th timescale provides a temporal framework for speleothem δ^{18}O data, which are largely dominated by records falling into the East Asian summer monsoon (EASM) domain (Corrick et al., 2020) (Fig. 1); altogether, records from this region constitute a key blueprint of low-latitude hydroclimate variability, integrating intensity changes in East Asian monsoon and meridional shifts of the Intertropical Convergence Zone (ITCZ; Wang et al., 2001, 2006).

Both the GICC05 and U–Th timescales serve to test, improve, and constrain chronologies for a wide range of paleoclimate archives and proxy records. These age scales have been used to validate and benchmark Antarctic ice-core chronologies (e.g., Buizert et al., 2015; Sigl et al., 2016), which ultimately enable resolving the interhemispheric phasing of DO events (Buizert et al., 2018) and the rate of greenhouse gas emissions during the last glacial period (Bauska et al., 2021). They are also widely used to constrain paleoceanographic records with poor independent age control (Bard et al., 2013; Hughen and Heaton, 2020; Waelbroeck et al., 2019). To build a chronology for deep-sea sediment cores, proxy signals are commonly correlated with abrupt cooling and warming events observed in ice-core proxies or speleothem δ^{18}O under the assumption of direct synchrony of climate changes. These climatically tuned chronologies, despite limiting our ability to test leads and lags between oceanic and atmospheric processes (Henry et al., 2016; Hughen and Heaton, 2020), still lay the foundations for deriving “best-guess” temporal constraints on a variety of fundamental boundary conditions of glacial ocean circulation and its coupling with the atmosphere system.

Because the Greenland ice-core and U–Th chronologies are constructed independently, the occurrence of systematic timescale offsets and dating biases of the order of hundreds of years complicates the comparisons of events integrated in the proxy records that hinge on these timescales. Perhaps more importantly, the chronology that forms the older portion of the new IntCal20 radiocarbon calibration curve is dominantly reliant on the Hulu Cave speleothem U–Th timescale (Cheng et al., 2016, 2018; Reimer et al., 2020; Southon et al., 2012). During the period spanning ∼ 14–54 kyr b2k, a wealth of ^{14}C datasets have been placed on the Hulu Cave U–Th timescale either indirectly via stratigraphic tuning of paleoclimate data to the high-resolution Hulu δ^{18}O record (Bard et al., 2013; Darfeuil et al., 2016; Hughen and Heaton, 2020) or more directly by means of ^{14}C wiggle matching (e.g., Bronk Ramsey et al., 2020; Turney et al., 2010, 2016). As a result, potential differences between the timescales – if not quantified and corrected for – can hinder a proper assessment of ^{14}C-dated environmental and archeological records within the ice-core climatic framework.

Furthermore, knowledge of the existing timescale offsets is important for high-resolution studies of marine ^{14}C (e.g., Muschitiello et al., 2019). This is crucial for reconstructions whose chronologies are more conveniently anchored to ice-core records rather than the Hulu Cave speleothems, as is often the case for North Atlantic sediment cores that integrate common regional climatic changes (Skinner et al., 2019; Thornalley et al., 2015; Waelbroeck et al., 2019) or sites where isochronous tephra deposits can be traced between ice cores and marine records (e.g., Ezat et al., 2017; Sadatzki et al., 2019). In these instances, potential discrepancies between the GICC05 and U–Th timescales can lead to an imprecise assessment of ocean Δ^{14}C relative to those of the atmosphere inferred from the IntCal datasets, thus affecting the estimation of ocean radiocarbon inventories.

In turn, resolving the differences between the GICC05 and U–Th timescales can help to reduce and characterize their absolute dating uncertainty and facilitate the comparison of ice cores and radiocarbon-dated records on a common timeline. Altogether, this is pivotal to advancing our understanding of the physical mechanisms behind abrupt climate change and to harmonizing climate, environmental, and archeological records of the last glacial cycle.

There are two main types of synchronization to integrate the GICC05 and U–Th timescales: (i) synchronization of climate records and (ii) synchronization of cosmogenic radionuclide data. The first is based on correlation of climatic signals integrated in Greenland ice-core records and speleothem δ^{18}O that are assumed to be synchronous. The second is based on the correlation of externally forced and essentially climate-independent variations in ice-core ^{10}Be and Hulu Cave ^{14}C records.

Despite the circularity that climate synchronization entails, such as precluding testing the synchronicity of teleconnections between Greenland and the East Asian monsoon system, the concerns about a potentially large climate phasing between polar ice-core and EASM speleothem records during the last glacial period have been put to rest. Unlike other regions where there are potentially complex site-specific responses to large-scale change (Adolphi et al., 2018), currently there is ample evidence that the North Atlantic and Asian monsoon climates are coupled on short atmospheric timescales (e.g., Adolphi et al., 2018; Corrick et al., 2020; Cvijanovic et al., 2013) – i.e., likely shorter than the mean resolution of the proxy records used for climate synchronization. The teleconnection mechanism, which is likely modulated by variations in the Atlantic Meridional Overturning Circulation, is well documented and involves coherent meridional shifts of the midlatitude storm tracks, the ITCZ, and the related monsoon systems (e.g., Ceppi et al., 2013; Kageyama et al., 2013; Zhang and Delworth, 2005). This is further supported by climate model simulations, which demonstrate that this atmospheric coupling synchronizes the North Atlantic and EASM region down to multidecadal timescales – a teleconnection that is robust under different glacial boundary conditions (Fig. 1c and d).

Since the construction of the GICC05 chronology, climate synchronizations between Greenland and EASM speleothem records (e.g., Hulu Cave) have been derived by identification of tie points marking sharp transitions in both the ice-core and speleothem stratigraphies (e.g., DO events). The synchronization approach has been performed either by manual, qualitative comparison of the climate records (Corrick et al., 2020; Svensson et al., 2006, 2008; Weninger and Jöris, 2008) or using reproducible, quantitative methods for detecting change points (Adolphi et al., 2018; Buizert et al., 2015). While tie points associated with sharp climate transitions are suitable for proxy synchronization as they typically have a high signal-to-noise ratio, at present, the main methodological drawback of this approach is that it relies on only a discrete set of stratigraphic markers, which prevents quantifying the alignment uncertainties in a continuous fashion.

The approach for synchronizing cosmogenic radionuclide records involve sliding window techniques, such as cross-lagged regression (Muscheler et al., 2014) or more commonly Bayesian wiggle matching (BWM; Adolphi and Muscheler, 2016). The techniques aim at matching relative changes in ^{10}Be and ^{14}C concentrations over a series of time windows and focusing on centennial to multi-centennial variations that are typically dominated by solar-induced – and largely periodic – changes in production rates (Vonmoos et al., 2006). Synchronization using BWM offers high precision and has proved effective during the Holocene when the offsets between the ice-core and ^{14}C timescales are mostly systematic (Adolphi and Muscheler, 2016; Sigl et al., 2016). However, these matching techniques depend heavily on the predefined window length (e.g., Schoenherr et al., 2019) and can lead to biased conclusions about synchrony if the timescale offsets change faster than the time window used for matching. Specifically, BWM only produces a single point of match for each window analysis, which generally spans 1000 to 5000 years, thus averaging out any short-term, nuanced fluctuations in the timescale difference (Adolphi et al., 2018; Adolphi and Muscheler, 2016). As the method leans on analyzing overlapping windows, on one hand it can lead to neighboring offset estimates of the BWM being positively correlated, which results in smoothing out the timescale transfer function. On the other hand, it may lead BWM to identify wrong correlation, thus yielding sudden – and potentially spurious – jumps in the timescale offsets (Muscheler et al., 2014; Muschitiello et al., 2019).

With climate synchronizations standing on a limited number of stratigraphic tie points and the latest alignment of cosmogenic radionuclides on only five BWM estimates (Muscheler et al., 2020), a new continuous synchronization between the GICC05 and U–Th timescales for the last glacial period is urgently required. In particular, the recent revision of the high-resolution Hulu Cave δ^{18}O record (H. Cheng et al., 2016, 2021) with an updated U–Th chronology (H. Cheng et al., 2018, 2021) provides further motivation for re-assessing the synchronization between the Greenland ice-core and U–Th timescales. Lastly, there is a need for improved constraints during the Last Glacial Maximum (LGM), i.e., when the timescales reach their largest offset according to cosmogenic radionuclides (Adolphi et al., 2018; Sinnl et al., 2023), and assess possible fast changes in the timescale difference that are currently challenging to detect.

In this study, some of these limitations are addressed by applying an automated probabilistic synchronization method to produce the first continuous transfer functions that quantify the offset between the GICC05 and U–Th timescales. The method minimizes the misfit between ice-core and speleothem proxy records while accounting for prior knowledge of the uncertainty in annual-layer identification in ice cores using a Bayesian inversion of the GICC05 maximum counting error (MCE) (Rasmussen et al., 2006; Svensson et al., 2008). To minimize noise due to site-specific environmental factors and U–Th dating uncertainties, the speleothem records are integrated using a Monte Carlo principal component analysis procedure that isolates the common EASM hydroclimatic pattern and estimates uncertainties. The new timescale transfer functions considerably improve the precision of earlier estimates and reduce the absolute dating uncertainty of GICC05 in the interval ∼ 11–48 kyr b2k. The results also indicate large and fast fluctuations in the timescale difference during the LGM and other cold stadial periods, suggesting previously unrecognized biases in the ice-core annual-layer counting. The implications of these findings are discussed.

2 Data and methods

2.1 Proxy data and Monte Carlo principal component analysis

The offsets between the GICC05 and U–Th timescales were estimated by performing three synchronizations based on independent Greenland ice-core climate proxy records (CLIM). The proxy data used in this study are presented in Fig. 2. The CLIM synchronizations were established over the period ∼ 11–48 kyr b2k using high-resolution Ca^{2+} concentrations of mineral dust from NGRIP (CLIM1) (Erhardt et al., 2019), δ^{18}O data from NGRIP (CLIM2) (Andersen et al., 2004) and GRIP (CLIM3) (Johnsen et al., 1997), respectively (all on the GICC05 timescale), and revised δ^{18}O data from EASM speleothems on their independent U–Th chronologies (Corrick et al., 2020). As discussed above, the focus on speleothem records from the EASM domain is motivated by (i) the well-established in-phase climate coupling between the North Atlantic and the EASM system, (ii) the overwhelmingly large number of records from this region, and (iii) the key importance of the Hulu Cave U–Th chronology in the calibration of the radiocarbon timescale.

Mineral dust aerosol in Greenland ice cores reflects both source strength and transport conditions from terrestrial sources and primarily originates from Asian deserts (Svensson et al., 2000). Its emissions are strongly dependent on Asian hydroclimate via concerted shifts in the latitudinal position of the ITCZ and the EASM system (Nagashima et al., 2011; Schiemann et al., 2009). Because NGRIP Ca^{2+} indirectly registers lower-latitude hydroclimate changes mediated by latitudinal migrations of the ITCZ, it is suitable for direct comparison to EASM δ^{18}O data, which integrate ITCZ-related shifts in monsoon rainfall over East Asia (Wang et al., 2001, 2006) with comparable durations (Fig. 3). In addition, we performed independent alignments using NGRIP and GRIP δ^{18}O data – an established proxy for Greenland climate – to assess the sensitivity of our synchronization approach and the coherence across different Greenland ice-core proxy records.

As for EASM speleothems, the proxy data are based on a compilation of 14 δ^{18}O records including the U–Th age determinations underlying each speleothem chronology (Corrick et al., 2020) (Figs. 1a, b and 2b, c). The original compilation included 17 records and we removed 3 low-resolution and scarcely dated records, i.e., whose median age resolution was less than 50 years and had on average less than one U–Th age determination per thousand years. The dataset from Hulu Cave was updated here to incorporate recently published higher-temporal-resolution δ^{18}O measurements and additional U–Th dates (H. Cheng et al., 2016, 2021). To integrate all the δ^{18}O data into a single record representative of the EASM region, a Monte Carlo principal component analysis (MCPCA) was used (Fig. 2d). The method follows Anchukaitis and Tierney (2013) and is presented and

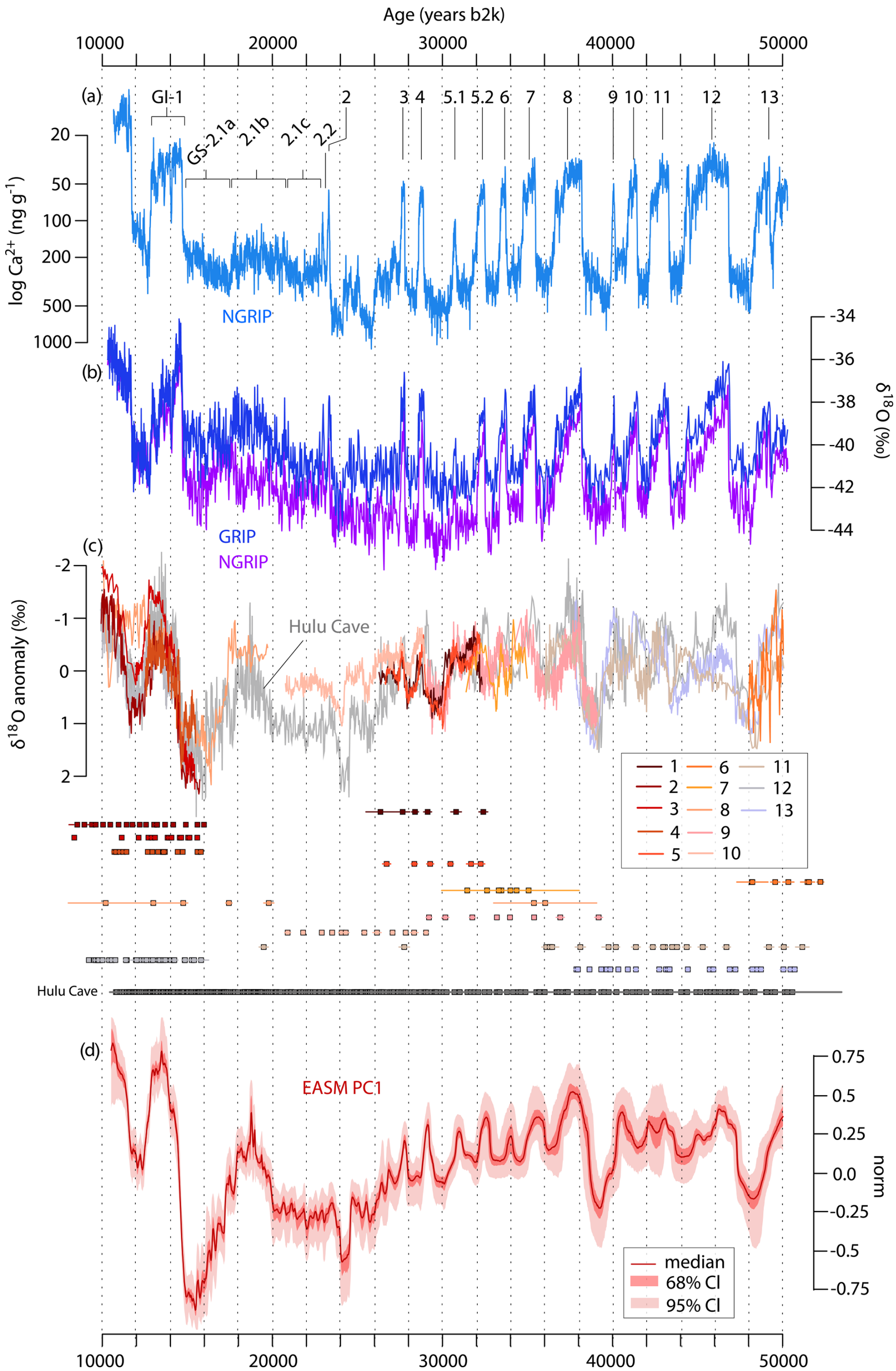

Figure 2. Proxy climate data used for the synchronizations presented in this study and shown on their original timescale. **(a)** Mineral-dust-derived Ca^{2+} ion concentration record from NGRIP (Erhardt et al., 2019) on the GICC05 timescale (Rasmussen et al., 2006; Svensson et al., 2008). Partitioning of Greenland Interstadials (GIs) and Greenland Stadial (GS) 2 is indicated. **(b)** NGRIP and GRIP $\delta^{18}O$ record (Andersen et al., 2004; Johnsen et al., 1997) also on the GICC05 timescale. **(c)** Speleothem $\delta^{18}O$ records from the East Asian summer monsoon (EASM) region presented in Corrick et al. (2020) and used in this study. The high-resolution Hulu Cave $\delta^{18}O$ record (H. Cheng et al., 2016, 2021) on its revised U–Th timescale (H. Cheng et al., 2018, 2021) is shown in gray. $\delta^{18}O$ values are expressed as anomalies from the record mean. Individual U–Th measurements associated with each record are also presented with their $\pm 2\sigma$ uncertainty. Numbering refers to the location of cave sites shown in Fig. 1b. **(d)** First principal component (PC1) of the 14 EASM speleothem records presented in **(c)** from the MCPCA procedure used in this study (see Sect. 2.1 for details). The solid line indicates the median from the 10 000-member ensemble, while shading reflects the empirical 68 % and 95 % confidence intervals from the ensemble.

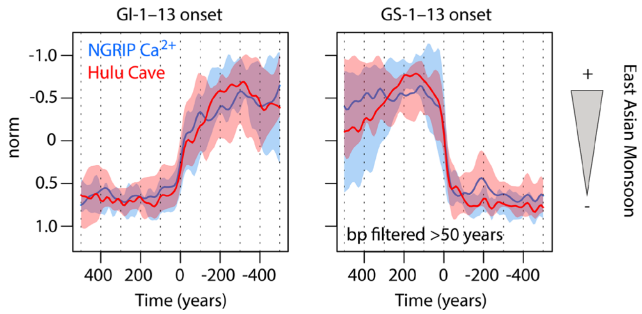

Figure 3. Stack of NGRIP Ca^{2+} and Hulu Cave δ^{18} records using a technique in which 13 individual events are centered at the midpoint of their abrupt transition, i.e., either DO warming (onset of GIs) or DO cooling (onset of GSs). The events were normalized and averaged to highlight the shared climatic signal at multidecadal and centennial timescales (> 50-year low-pass-filtered) and compare the duration of the abrupt DO transitions between Greenland ice cores and Hulu Cave speleothems. Shading reflects the variability across the events used for stacking. The midpoints of the abrupt transitions were identified using a Bayesian change-point analysis method (Erdman and Emerson, 2007).

tested in detail therein. In brief, the procedure allows isolating the common large-scale pattern of hydroclimate variability while accounting for age modeling uncertainties. The MCPCA method uses iterative age modeling of the available U–Th ages and eigen-decomposition of the $\delta^{18}O$ records to produce a reduced set of orthogonal modes that reflect common patterns of $\delta^{18}O$ variability and estimate uncertainties.

In order to perform MCPCA, the different $\delta^{18}O$ records were linearly interpolated to a common time step of 25 years. For this study 10 000 iterations of the MCPCA procedure were generated. In line with Anchukaitis and Tierney (2013), each Monte Carlo iteration consists of the following steps: (1) the U–Th dates of each speleothem record are randomly resampled within their probability distribution imposing that depositional ages increase monotonically with depth; (2) for each record an age–depth model is fit to the resampled U–Th ages using a monotonic piecewise cubic hermite spline; (3) the leading PCA mode (PC1) of the 14 $\delta^{18}O$ proxy records is calculated using probabilistic PCA (Tipping and Bishop, 1999) and ensuring that the sign of the eigenvector is consistent across iterations. The resulting 10 000 ensemble members of the PC1 were used to estimate median and confidence levels, which were ultimately employed as a target record for the synchronization method described below (hereafter referred to as EASM PC1).

2.1.1 Probabilistic algorithm for proxy data synchronization

As discussed in Sect. 1, tie-point and wiggle-matching synchronizations have inherent problems that limit estimating the alignment of proxy time series in a continuous fashion. Although tie-point synchronization is an established and conservative approach, its alignment uncertainty is poorly characterized, tie points can be difficult to reproduce, and even when they are defined statistically the synchronization still does not account for potential shared signal structures in between consecutive ties.

Probabilistic alignment methods have a unique and underexploited potential to correlate proxy time series and move away from pointwise and wiggle-matching synchronization techniques. They are especially well suited for establishing continuous alignments and can help match previously untapped common structures in the signal of climate and cosmogenic radionuclide records. These methods are fully automated and have the advantage of ensuring reproducibility, deriving credible bands associated with the alignment process, and inferring the probability of synchronization solutions based on prior constraints on accumulation rates (e.g., Lin et al., 2014; Muschitiello et al., 2020; Parrenin et al., 2015).

In this study, a continuous synchronization of the GICC05 to the U–Th timescale is established using an appositely developed automated algorithm for probabilistic inversion. The inverse problem is formulated using a Bayesian framework in order to sample the full range of possible GICC05–U–Th synchronization scenarios and explicitly builds in prior ice-core chronological constraints. Assuming that the U–Th timescale is absolute, our inverse scheme simulates the age offset history between GICC05 and the EASM PC1 (i.e., see Sect. 2.1) in response to changes in compaction versus expansion of the Greenland ice-core timescale. The link requires a likelihood function, which quantifies how probable the alignment between ice-core and speleothem records is given a particular simulated ice-layer miscount history.

The numerical approach builds upon previous work using a hidden Markov model for automated synchronization of paleoclimate records (Cutmore et al., 2021; Muschitiello et al., 2019, 2020; Sessford et al., 2019; West et al., 2019, 2021). The model employed here uses constraints imposed by the MCE, i.e., the accumulated absolute annual-layer counting error of the Greenland ice-core chronology, to deform the entirety of an input time series (on the GICC05 timescale) onto a target (on the U–Th timescale). The method minimizes the misfit between the input and the target and finds a sample of alignments between Greenland ice cores and the EASM PC1 record that are physically coherent with the absolute dating uncertainty of GICC05 and some of its counting error properties. However, it should be borne in mind that the model used in this study does not provide a fully comprehensive representation of the complexity that characterizes the ice-core layer counting procedure and its uncertainty (Rasmussen et al., 2006; Svensson et al., 2006). Rather, our approach aims at approximating the counting structure of GICC05 in order to infer estimates of the synchronization uncertainty. The method is also adaptable to a variety of formulations of the inverse problem and to using multiple input and target records simultaneously when determining the alignment.

2.1.2 Inverse modeling approach

In order to establish a continuous alignment between the GICC05 and U–Th timescale, we need to define an alignment function, which relates the GICC05 age of the given input ice-core record (i.e., NGRIP Ca^{2+}, NGRIP $\delta^{18}O$, or GRIP $\delta^{18}O$) to unknown U–Th ages associated with the target EASM PC1 record. The function is defined here by a mathematical representation of the GICC05–U–Th age relationship that effectively allows linearly stretching and compressing the ice-core chronology relative to the U–Th timescale. To estimate this alignment function, we propose a piecewise linear function ($\tau(\cdot)$) with K equally spaced sections within the domain, where the slopes at each section are $m_i > 0$ (note that the slopes, unlike other parameters in the model which are expressed in years, are dimensionless). This ensures no time reversals by guaranteeing that the function is monotonically increasing. The function is also influenced by the initial shift of the alignment. If $\tau(\cdot)$ represents the alignment function, this initial shift can be defined a $\tau_0 = \tau(t_0)$. Hence, the parameters of $\tau(\cdot)$ are defined as $(\tau_0, \boldsymbol{m})$, where $\boldsymbol{m}$ is a K-dimensional vector containing the slopes of each evenly spaced section. The model can then be expressed as

$$\tau(t) = \tau_0 + \sum_{i=1}^{j} \left(m_j \Delta c\right) + m_{i+1}\left(t - c_i\right), \qquad (1)$$

where $c_i \leq t < c_{i+1}, \leq i < K$, and $c_0 < c_1 < \cdots < c_K$ represent evenly spaced time intervals along the GICC05 timeline with length Δc. The slopes $m = (m_1, m_2, \ldots, m_K)$ correspond to the linear sections within each interval. This function is analogous to the one employed to construct age–depth models (Blaauw and Christen, 2011), i.e., a piecewise linear function with positive slopes, which prevents time reversals but preserves the shifts $(m_j \Delta c)$ from younger to older sections. It is important to note that the piecewise linear technique adopted here provides a key advantage compared to a simple global linear function in its ability to accommodate local variations, i.e., approximating the nonlinear nature of the alignment. While a linear model imposes a single linear trend across the entire dataset, the piecewise linear model allows for different shorter linear behaviors within each segment, thereby providing a more nuanced and accurate representation of the alignment. The parameter space created by the piecewise linear model is of size $K+2$. This structure facilitates effective posterior exploration and global optimization as it offers control over the model's parameterization and allows users to adjust its flexibility. This balance enables a thorough yet efficient examination of the parameter space, ensuring the optimal selection of the number of parameters without the computational complexity and overfitting risks associated with a larger number of sections.

However, it should be noted that our proposed method for calculating the alignment function, $\tau(t)$, significantly differs from the one presented by Blaauw and Christen (2011), which employs an autoregressive gamma process for simulating sedimentation rates with downcore dependence. Unlike their method, ours restricts such information exchange, thereby preserving the independence of each section. This feature is suitable given our data context, which underlie very different proxy measurements. It is important to note that since the input and target records are provided on their own independent chronologies, we do not need to model the autocorrelation associated with each timescale. Therefore, our approach, which maintains the independence of each section, is better suited for these datasets.

Our goal is to deploy a method for inferring the alignment function $\tau(t)$, which minimizes the misfit between the ice-core data on the GICC05 timescale $\boldsymbol{t}'$ and the EASM PC1 on the U–Th timescale $\boldsymbol{t}$. Let us define the ith data point in the input ice-core record associated with time t_i' on the GICC05 timescale as g_i. Therefore, the vector $\boldsymbol{g}$ denotes the input signal, containing the NGRIP Ca^{2+}, NGRIP $\delta^{18}O$, or GRIP $\delta^{18}O$ measurements on the GICC05 timescale. Analogously, for the EASM PC1 record, each data point, defined as u_j, represents the target signal at time t_j on the U–Th timescale. The vector $\boldsymbol{u}$ houses this target signal and contains the data from the EASM PC1 record on the U–Th timescale.

With this notation, we regard each datum in $\boldsymbol{u}$ and $\boldsymbol{g}$ as an observation of the proxy at a specific point in time (t_i), following a normal distribution where the mean corresponds to the "true" value of the proxy at time t_i ($\boldsymbol{U}$ and $\boldsymbol{G}$). In this case, the input record is reported without errors, so it can be assumed that $\boldsymbol{G} = \boldsymbol{g}$. On the other hand, the target record is accompanied by uncertainty ($\sigma_{u_i}^2$), so we assume $u_i \sim N(U_i, \sigma_{u_i}^2)$, where $\sigma_{u_i}^2$ denotes the variance of each data point u_i. It should be noted that u_j is associated with a time t_i, and thus the appropriate notation is $u_j(t_i)$. Assuming that both the input and target are adequately synchronized by the alignment function $\tau(t)$, $\forall\, u(t_i) \approx g(\tau(t_i)), t_i \in \boldsymbol{t}$ holds true. It should be borne in mind that this assumption does not imply a perfect fit between $\boldsymbol{u}$ and $\boldsymbol{g}$, but rather the existence of a $\tau(t)$ that maximizes the similarity across the whole records. To evaluate the goodness of the fit between $\boldsymbol{u}$ and $\boldsymbol{g}$, and given that the uncertainty associated with $\boldsymbol{u}$ can be considered a random variable, here we use the approach devised by Christen and Pérez (2009). Accordingly, we define u_i as follows:

$$u_i | \tau_0, m, t_i, \boldsymbol{G}, \sigma_{u_i}^2 \sim t\left(G\left(\tau\left(t_i\right)\right), \sigma_{u_i}^2, a, b\right), \qquad (2)$$

where a and b are the parameters of the t distribution (Christen and Pérez, 2009). It is important to stress that G is set only at discrete times, $\boldsymbol{t}'$, which may not necessarily match an observed U–Th age on the target EASM PC1 record ($\boldsymbol{t}$). To obtain values for $G(\tau(t_i))$ at any specific time, we employ linear interpolation using the observations from GICC05. This method enables us to compute $G(t)$ for any given $t \in (t'_0, t'_m)$, where (t'_0, t'_m) is the time window of the input ice-core record on the GICC05 timescale, whereby $t'_0 = 10.75$ kyr b2k and $t'_m = 48$ kyr b2k. Finally, it is also important to note that before synchronization, the input and target records are scaled between -1 and 1. Despite the potential for scaling to introduce alignment biases when dealing with outliers or extreme maxima and/or minima, our synchronization method employs a continuous function with constraints on the stretching and compression of the input (see Sect. 2.2.3). This approach addresses potential mismatches by considering the overall structure of the data and the assumption of continuity. Moreover, our methodology quantifies the alignment uncertainty by evaluating the quality across the entire record, accounting for the inherent uncertainty in aligning all of the data, ensuring reliable synchronization. Finally, the uncertainty of the target is assigned an overly conservative value of 0.2, and bearing in mind that we allow for a heavy tailed t-distribution error, this effectively ensures covering 60 % of the observable window in the data. By overestimating the variance of the input, we thus augment the model's ability to identify similarities between the target and input, especially over intervals with a clear offset between the two datasets.

2.1.3 Model's likelihood, parameters, and priors

Since the synchronization process is fundamentally uncertain, we apply a Bayesian approach to infer the optimal alignment between $\boldsymbol{u}$ and $\boldsymbol{g}$ that accounts for glaciological information on unobserved changes in the annual-layer miscount of Greenland ice cores. For the correct implementation of this approach we require a likelihood function. This likelihood function evaluates the previously mentioned assumption ($U(t_i) \approx G(\tau(t_i))$) of the aligned ice-core record and the target speleothem data given a particular set of parameter values $\Phi = (\tau_0, m, \boldsymbol{G}, \sigma^2_{u_i})$. The model is defined by Eq. (3), which allow us to calculate the log-likelihood of the data as

$$l \propto \sum_{i=0}^{n} \left[-\log\left(\sigma_{u_i}\right) - \frac{a}{2} \log\left(b + \frac{(G\tau(t_i) - u_i)^2}{2\sigma^2_{u_i}} \right) \right]. \quad (3)$$

In the synchronization problem posed here, the likelihood function determines the goodness of the fit by minimizing the mismatch between the input and the target at every data point on the U–Th timescale, i.e., by optimizing the function $\tau(\cdot)$. τ_0 and m are model parameters, whereas $\boldsymbol{G}$, $\sigma^2_{u_i}$, and t_i are related to the data. $\boldsymbol{G}$ refers to the input data on the GICC05 timescale, and $\sigma^2_{u_i}$ refers to the reported variance of the target record on the U–Th timescale. To provide a more conservative measure of the uncertainty surrounding $\boldsymbol{G}$, we use the t distribution (Christen and Pérez, 2009). Lastly, t_i represents the time of the ith target signal on the U–Th timescale.

The model estimates the probability of a given alignment that relates GICC05 and U–Th ages by evaluating the log-likelihood function described in Eq. (3) together with prior distributions for τ_0 and m. To avoid sampling outside a physically reasonable range and to identify a sample of optimal synchronizations, this probability is based on prior knowledge that the alignment between the input and target is largely limited by the constraints imposed by the absolute counting error of GICC05. Given that the parameters τ_0 and m are largely unknown and must be inferred from the model, we assign uninformative priors to ensure that the posterior alignment is mainly influenced by the data. For τ_0, which defines the initial timescale offset at time t_0, we apply a prior distribution of $\tau_0 \sim 1_{(-\mathrm{MCE}<m_i<\mathrm{MCE})} N(t_0, \sigma_0)$, where $\sigma_0 = \frac{\mathrm{MCE}}{2}$, and MCE is the maximum counting error of GICC05 at t_0.

Since one of the objectives of this study is to infer changes in the GICC05–U–Th timescale difference (hereafter expressed as $\Delta T = t' - t$), we invert the relative counting error (RCE) of GICC05, which is defined as the rate of change of the MCE. The decision to use RCE is justified because it reflects the speed at which the counting error changes, thus making it a suitable metric for constraining the slopes of the function τ. To account for changes in ΔT brought about by possible unaccounted biases in the ice-core annual-layer counting, the prior knowledge should allow sampling an RCE greater than the nominal values imposed by the GICC05, which during the last glacial period range ~ 5 %–10 % (Svensson et al., 2006, 2008). In our model, each slope within the vector m is independent and strictly positive. The slopes reflect the rate at which the age relationship between the GICC05 and U–Th timescales changes over two adjacent sections, whereby $m_i > 1$ implies a linear stretching of GICC05, and $0 > m_i > 1$ implies a compression. With this understanding, we assigned m_i a truncated normal distribution $m_i \sim 1_{(0<m_i<5\mathrm{RCE})} N(0, \sigma^2_m)$, which ensures that m_i remains positive. This effectively allows the model to explore RCE values up to 5 times greater than nominal and consider GICC05–U–Th synchronizations that exceed the range allowed by the MCE, as well as accommodating propagation of the age errors associated with the U–Th timescale. To ensure that m_i follows the GICC05 counting error, σ^2_m is fixed to be half the RCE at a given time t. In our implementation, we have set the value of K to 200, which implies that the time span of $U(t_i)$ is divided into 200 sections (i.e., ~ 180 years per section). This division provides a reasonable compromise between computational performance and alignment resolution, ensuring that each section contains enough data for meaningful results.

In order to calculate a posterior sample of the parameters and optimize the function $\tau(\cdot)$, a Markov chain Monte Carlo methodology is used (see Sect. 2.2.4). This approach not only aims to find the best parameter values but also generates samples of the posterior distributions for each parameter. These samples are valuable for inferring credible intervals related to the alignment and can even be utilized to propagate the latter into the aligned proxies.

2.1.4 MCMC: determining the posterior distribution

Because of the nonlinear nature of the synchronization problem and the fact that there are far too many alignments to calculate all their probabilities, a stochastic Monte Carlo method is required to explore the posterior distribution in a computationally efficient way. Calculation of the posterior probability proceeds by sampling an initial value for each unknown model parameter from the associated prior distributions using Markov chain Monte Carlo (MCMC). MCMC techniques play a key role in statistical analysis, providing a systematic method for sampling from complex, multidimensional posterior distributions. The principles of MCMC algorithms are based on the concept of a Markov chain, where the future state solely depends on the current state, not on the series of previous states. Beginning from an arbitrary point, the MCMC algorithm initiates a sequence of steps or "leaps" across the parameter space. The direction and magnitude of each leap are governed by a set of predefined rules specific to each MCMC method. Over time, this sequence of leaps effectively samples the target distribution. Regardless of where it starts, the algorithm ensures that it will converge to and accurately sample from the target distribution, provided it completes enough iterations (Brooks et al., 2011). The time or number of iterations required for the algorithm to stabilize and accurately reflect the posterior distribution is commonly referred to as the "burn-in" period. This convergence is what allows us to obtain accurate samples from the posterior distribution, enabling us to infer the model's parameters.

In this study, MCMC is driven by a differential evolution Markov chain (DE-MCz) sampler (Ter Braak and Vrugt, 2008), which is particularly effective in dealing with multi-modal posterior probability distributions. The DE-MCZ method is designed to update various segments of the Markov chain simultaneously, which significantly speeds up the processing time for large multidimensional datasets. Additionally, DE-MCz's inherent adaptability makes it an excellent choice for tackling complex problems and an ideal MCMC for our implementation.

The sampler was run for 1.5×10^6 MCMC iterations after disregarding a burn-in time of 0.5×10^6 steps and only retaining every 10th iteration to mitigate the statistical dependence of the model parameters. This was deemed to be a sufficiently long MCMC run for the simulation to reach convergence, as monitored by a multivariate potential scale reduction factor less than 1.1 (Brooks and Gelman, 1998). The sample from the remaining iterations was used to estimate the posterior distribution of each random variable in the model (τ_0 and m). By leveraging samples from these parameters, we computed a posterior sample of alignment functions $\tau(\cdot)$. This posterior sample of functions then allows us to evaluate metrics such as the median and credibility intervals. However, note that this is a simplification of the process behind it: because the resulting output is a sample of random variables, the most appropriate way to report these results is the ensemble of samples from $\tau(\cdot)$. Nevertheless, in order to simplify the output and follow common practice, we reported the median and 95 % credible intervals.

3 Results and discussion

3.1 Synchronization and timescale transfer functions

The leading mode of the MCPCA procedure – i.e., the EASM PC1 – provides the target record for the CLIM synchronizations and is presented in Fig. 2d. The PC1 is dominated by the characteristic EASM hydroclimate signal, and even though the Monte Carlo approach results in some temporal smoothing, the millennial-scale trends and shorter events that punctuated the last glacial period in this region are reasonably well captured. The Hulu Cave record has the largest loading on PC1 as it is the dataset with the highest temporal resolution and the only one stretching over the whole synchronization interval. It loads highly especially between ∼ 16 and 28 kyr b2k where there are fewer speleothem records.

The inverted CLIM synchronizations and related GICC05–U–Th timescale transfer functions are presented in Figs. 4–6. Before we interpret the timescale transfer functions, a consideration should be made. As outlined in Sect. 2.2, the entirety of the input and the target are scaled between −1 and 1 before synchronization. This scaling may introduce a systematic alignment bias when either the input or target features extreme maxima or minima, as these will affect the structure of the records by introducing artificial trends. To test for the sensitivity to scaling, we conducted additional synchronization experiments on NGRIP δ^{18}O by performing localized alignments against the EASM PC1 using shorter intervals of ∼ 10 kyr and after scaling the input and target segments (Fig. S1 in the Supplement). These sensitivity tests reveal that the localized and global alignments are largely coherent throughout the interval ∼ 11–48 kyr b2k and thus support the robustness of our approach. More importantly, they highlight the advantage of estimating a global alignment, whereby the synchronization uncertainty is estimated by jointly considering all the linear sections of the input and target and their respective errors.

Assuming that our methodological approach is adequate, that the U–Th timescale is accurate and considering the age uncertainties associated with EASM PC1, it can be observed that throughout the last glacial period the timescale difference ΔT is well within the MCE limits of GICC05. Notably, GICC05 is systematically younger than the U–Th timescale and the age difference increases with time, indicating, on average, a stretch of 0.97 % for CLIM1, 0.75 % for CLIM2, and 0.86 % for CLIM3 (mean = 0.86 %) during the construction of GICC05, which is comparable to the 0.99 % linear scaling bias estimated by Buizert et al. (2015) after correcting for the new U–Th chronology presented in Cheng et al. (2018) (Fig. S2).

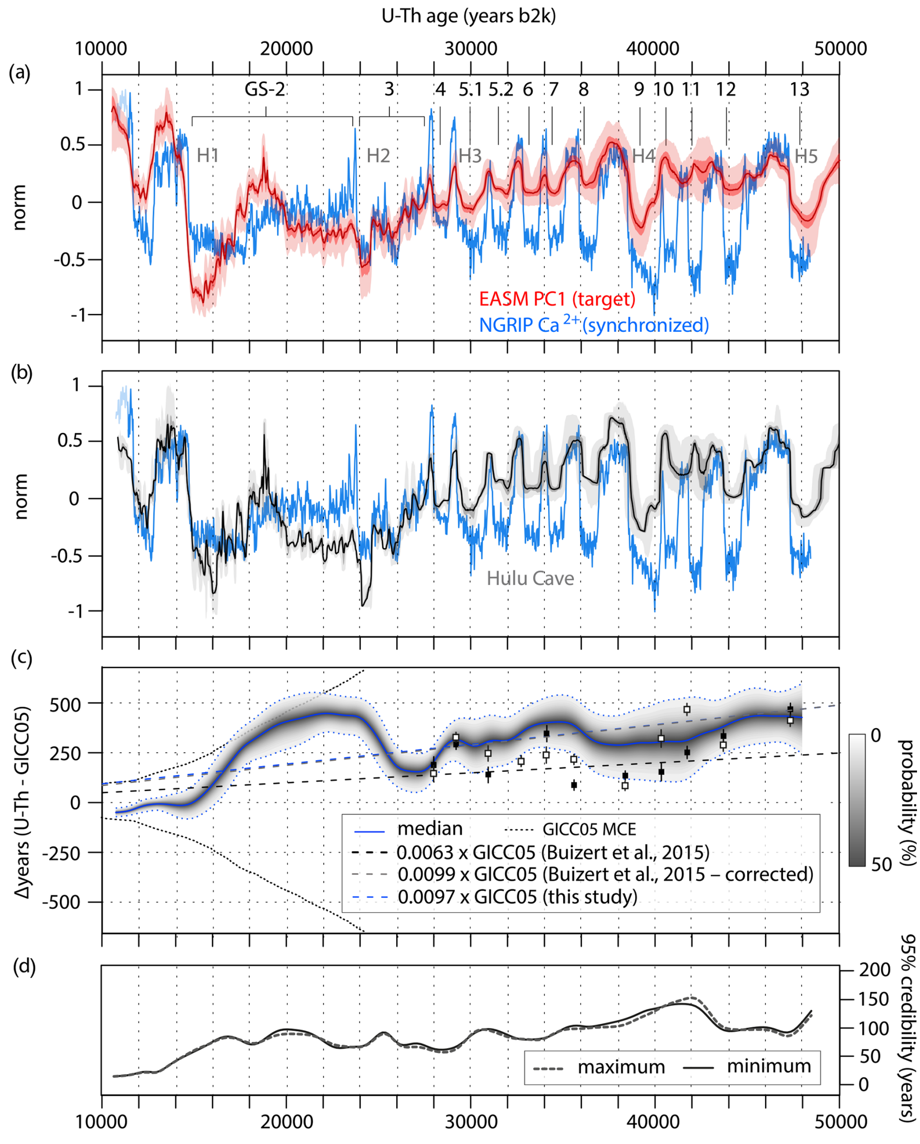

Figure 4. CLIM1 synchronization of GICC05 to the U–Th timescale and resulting timescale transfer function. **(a)** Synchronized NGRIP Ca^{2+} data on the U–Th timescale using the posterior median estimate of the MCMC synchronization. The synchronization was derived from stratigraphic alignment of the NGRIP Ca^{2+} data to the East Asian summer monsoon (EASM) PC1 (see Sect. 2.1 for details). Shading reflects the empirical 68 % and 95 % confidence intervals from the 10 000-member ensemble. Greenland Stadials (GSs) and the timing of Heinrich events (H) are indicated at the top. **(b)** Comparison between the synchronized ice-core data and the Hulu Cave $\delta^{18}O$ record with its associated age uncertainty (gray shading: light, 68 %; dark, 95 %). All proxy records are shown in normalized units. **(c)** Posterior median (blue continuous line) and pointwise 95 % credible intervals (shading and blue dashed lines) of the difference ΔT between the GICC05 and U–Th timescales. The black squares are the Hulu–NGRIP age offsets presented in Buizert et al (2015), and the white squares reflect the same offsets corrected using the updated U–Th chronology presented in Cheng et al. (2018). The corrected offsets were estimated using a cross-correlation analysis of the Hulu Cave $\delta^{18}O$ data on the previous and the latest timescale, respectively (Fig. S2). The linear fit through these data and that estimated from our ΔT values are also shown. Note that the linear models are forced to intersect the origin. **(d)** Posterior credible intervals of the transfer function shown in **(c)**. Gray dashed and black lines reflect the maximum and minimum bound of the credible intervals, respectively.

The CLIM synchronizations are broadly coherent, and superimposed upon this upward trend there are a number of consistent shorter-term ΔT fluctuations. The CLIM results indicate that at the onset of the Holocene, GICC05 is slightly older than the U–Th timescale, yielding a consistent ΔT of -45^{-25}_{-65} years (95 % credible range) for CLIM1 (Fig. 4c), -45^{-30}_{-55} years for CLIM2 (Fig. 5c), and -45^{-30}_{-55} years for CLIM3 (Fig. 6c), which is remarkably similar to previous independent estimates based on corre-

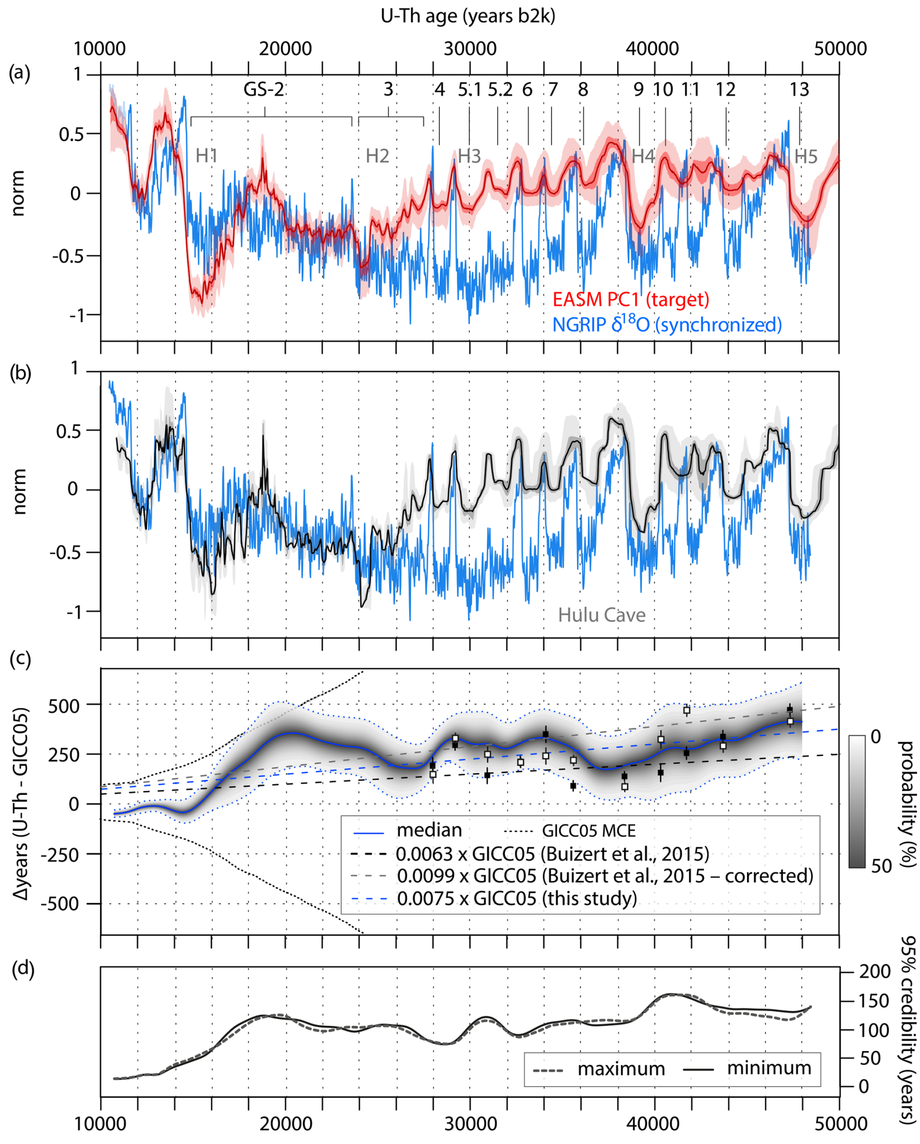

Figure 5. Same as Fig. 4 but for CLIM2, i.e., using NGRIP δ^{18}O data.

lation of ^{14}C and ^{10}Be records (i.e., -65 years; Muscheler et al., 2008). In the interval ~ 15–24 kyr b2k, corresponding to the early stage of GS-2, GICC05 is steadily stretched faster than allowed by the annual counting error, reaching a maximum ΔT between ~ 20 and 22 kyr b2k of $+450^{+550}_{+355}$ years for CLIM1, $+360^{+465}_{+245}$ years for CLIM2, and $+355^{+465}_{+230}$ years for CLIM3 (mean $= \sim 390$ years), which is as large as or a little larger than the MCE permits. Again, this is in good agreement with recent estimates based on BWM of cosmogenic radionuclides (i.e., 375 years; Sinnl et al., 2023) and climate synchronization (i.e., 320 years; Dong et al., 2022), respectively. From ~ 24 to 27 kyr b2k, which corresponds to GS-3 and is approximately in phase with the global LGM ice-volume peak (Hughes and Gibbard, 2015), again the GICC05 annual-layer count changes faster than the counting error allows, highlighting a possible compression of the timescale with ΔT values dropping to $+160^{+250}_{+55}$ years for CLIM1, $+180^{+270}_{+90}$ years for CLIM2, and $+160^{+270}_{+70}$ years for CLIM3 (mean $= \sim 165$ years). Between ~ 28 and 29.5 kyr b2k, another short-term stretch of GICC05 is observed, when ΔT values raise to $+320^{+420}_{+210}$ years for CLIM1, $+330^{+415}_{+245}$ years for CLIM2, and $+315^{+285}_{+235}$ years for CLIM3 (mean $= \sim 320$ years). Thereafter, ΔT values exhibit – within the uncertainty bounds – stable and gradually increasing values until 48 kyr b2k, reaching a maximum of $+430^{+600}_{+250}$ years for CLIM1, $+415^{+555}_{+280}$ years for CLIM2, $+410^{+535}_{+280}$ years for CLIM3 (mean $= \sim 420$ years).

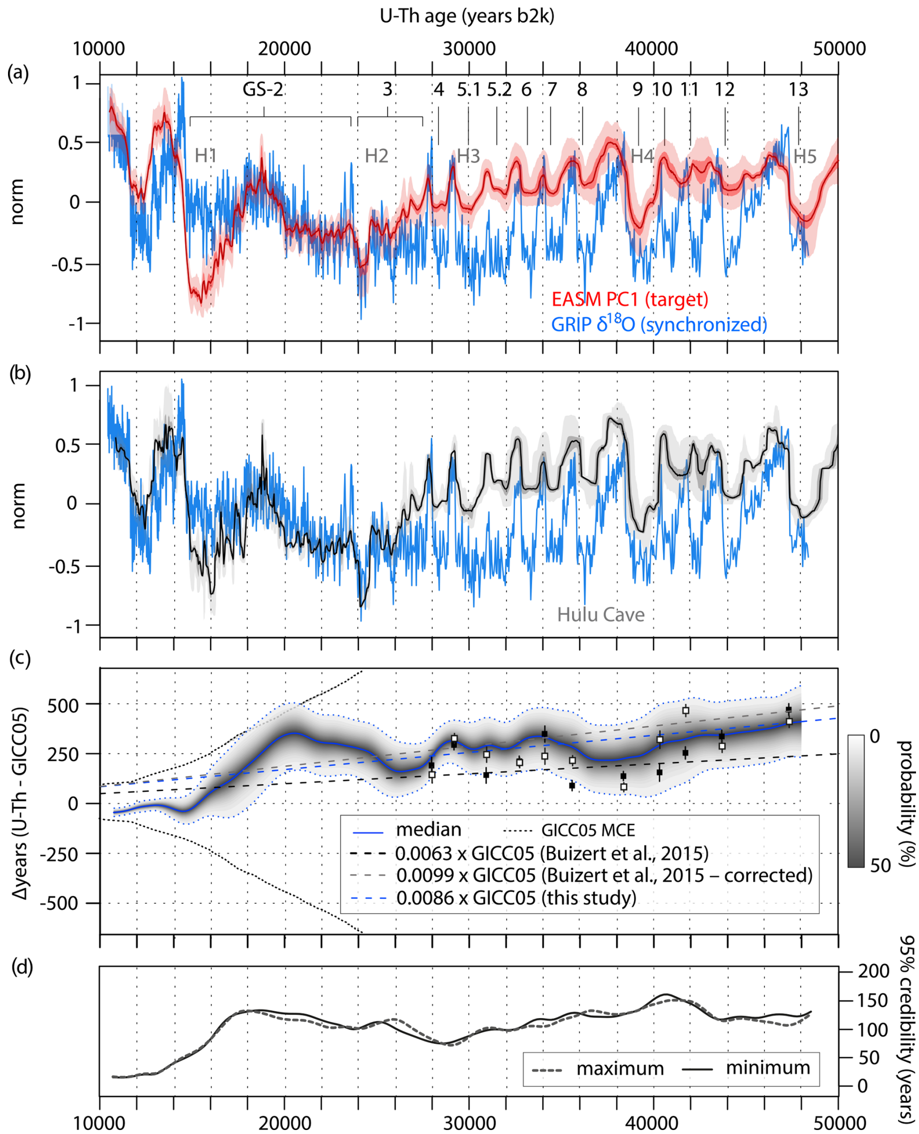

Figure 6. Same as Fig. 4 but for CLIM3, i.e., using GRIP δ^{18}O data.

The largest ΔT excursions between $\sim$ 15 and 28 kyr b2k are primarily controlled by the millennial-scale and shorter-term variability recorded in the Greenland ice-core data and EASM PC1 (Figs. 4a, 5a, and 6a). The overall match is driven by the alignment between the GS-3 dust peaks and coolings in the Greenland ice cores (Rasmussen et al., 2008) and the well-defined declines in monsoon strength observed in EASM PC1, as well as by a few marked proxy excursions during GS-2 (Figs. 4a, 5a, and 6a). However, the transfer function errors are relatively large during GS-2 (Figs. 4d, 5d, and 6d). This is mainly due to the relatively lower signal-to-noise ratio in the climate records across the late glacial and LGM, where the alignment is less robust. In the case of the LGM, further work and independent age constraints would therefore be desirable to improve the match between the GICC05 and U–Th timescales. Before $\sim$ 28 kyr b2k, the ΔT results are largely constrained by the match between stadial–interstadial transitions in Greenland ice cores and the corresponding monsoon events integrated in the EASM PC1 (Figs. 4a, 5a, and 6a), with the exception of the interval surrounding GS-10 and GI-10 at $\sim$ 42 kyr b2k when the speleothem δ^{18}O data underpinning the EASM PC1 exhibit some temporal inconsistencies, thus resulting in a larger synchronization error (Figs. 4d, 5d, and 6d).

A comparison of the CLIM timescale transfer functions alongside published ΔT estimates is presented in Fig. 7. The inferred timescale offset history is in good agreement with independent ΔT estimates based on BWM of cosmogenic radionuclide records and match points between GICC05 and the ^{14}C timescale. The uncertainty bounds are overall $\sim$ 52 % narrower than previous estimates based on BWM (Adolphi et al., 2018; Muscheler et al., 2020) for CLIM1, $\sim$ 47 % for

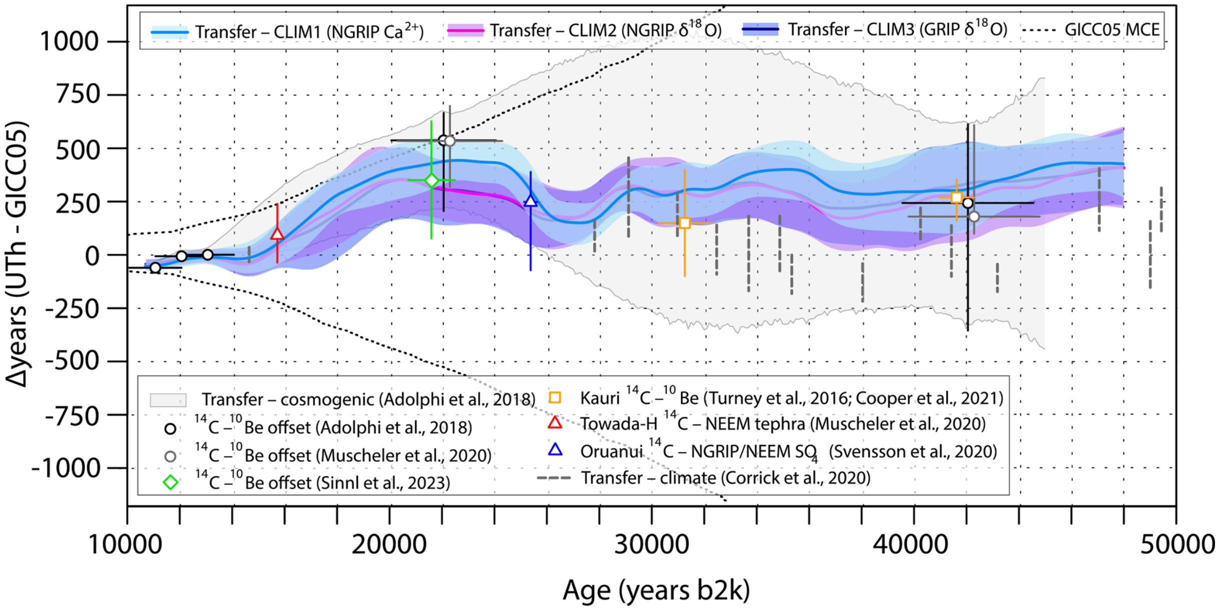

Figure 7. Posterior timescale transfer function based on the CLIM MCMC synchronizations presented in this study. Positive values indicate that the U–Th timescale is older than GICC05. The transfer function is presented with its median (thick lines) and pointwise 95 % credible intervals (shading). The results are compared to the transfer function presented in Adolphi et al. (2018) (gray shading), which is based on a compilation of U–Th-dated ^{14}C records, including the low-resolution and less precisely dated Hulu Cave data (Southon et al., 2012). The markers with error bars ($\pm 2\sigma$) show discrete match points inferred from comparison of ice-core ^{10}Be records and absolutely dated ^{14}C data (Adolphi et al., 2018; Cooper et al., 2021; Muscheler et al., 2020; Sinnl et al., 2023; Turney et al., 2016), ^{14}C-dated volcanic eruptions identified in Greenland ice cores (Muscheler et al., 2020; Svensson et al., 2020), and climate tie points (Corrick et al., 2020). The dashed lines highlight the maximum counting uncertainty of GICC05.

CLIM2, and ∼ 45 % for CLIM3 (mean = 48 %). Uncertainties are on average ∼ 30 % smaller during deglaciation and LGM (i.e., after 28 kyr b2k) for CLIM1, ∼ 24 % for CLIM2, and ∼ 19 % for CLIM3 (mean = 24 %), whereas the precision is improved by up to ∼ 73 % during Marine Isotope Stage 3 (i.e., prior to 28 kyr b2k) for CLIM1, ∼ 70 % for CLIM2, and ∼ 70 % for CLIM3 (mean = 71 %).

It is interesting to note that, during the interval 32–40 kyr b2k, we did not find a compelling match with the ΔT estimates based on climate tie points presented in Corrick et al. (2020). These tie points are also systematically different from the cosmogenic radionuclide ΔT values and the scaling bias estimated by Buizert et al. (2015). Corrick et al. (2020) suggested that such mismatch may stem from their methodological approach, including the application of a revised detrital thorium correction to U–Th dates and/or their depth–age modeling procedure. Additionally, and more fundamentally, Corrick et al. relied on visual identification of the abrupt climate transitions in speleothem δ^{18}O that involved different degrees of subjectivity. This is in contrast with our methodology as well as the statistical approaches adopted for BWM of cosmogenic radionuclides and identification of the match points presented in Buizert et al. (2015), respectively. We hope that these considerations will stimulate further work to reconsider and reconcile these age discrepancies.

In conclusion, not only are the new timescale transfer functions considerably more precise, but the continuous synchronization also brings to light a more complex GICC05–U–Th age difference history than previously assumed. Moreover, our synchronization model allowed identifying a number of potential fast changes in the timescale difference – i.e., features that would have gone undetected had the model been more tightly constrained by the nominal RCE of GICC05.

3.2 Differential dating uncertainty of GICC05

It should be noted that a major assumption of our methodology is that the U–Th timescale is reliable. While this is certainly reasonable, the timescale may be problematic in certain intervals such as between ∼ 40 and 44 kyr b2k (Fig. 2c and d), and results over this period should therefore be treated with caution. Assuming that the U–Th timescale is absolute outside this brief interval, a new picture emerges showing that the identification of uncertain annual layers in the GICC05 is potentially less accurate than previously thought (Figs. 7 and 8). The GICC05 timescale appears to be either missing or gaining time beyond its RCE during some of the longest and coldest stadials (Fig. 8). Most notably, too few annual layers have been identified within H1/GS-2 and GS-4, whereas too many layers have been counted over H2/GS-3,

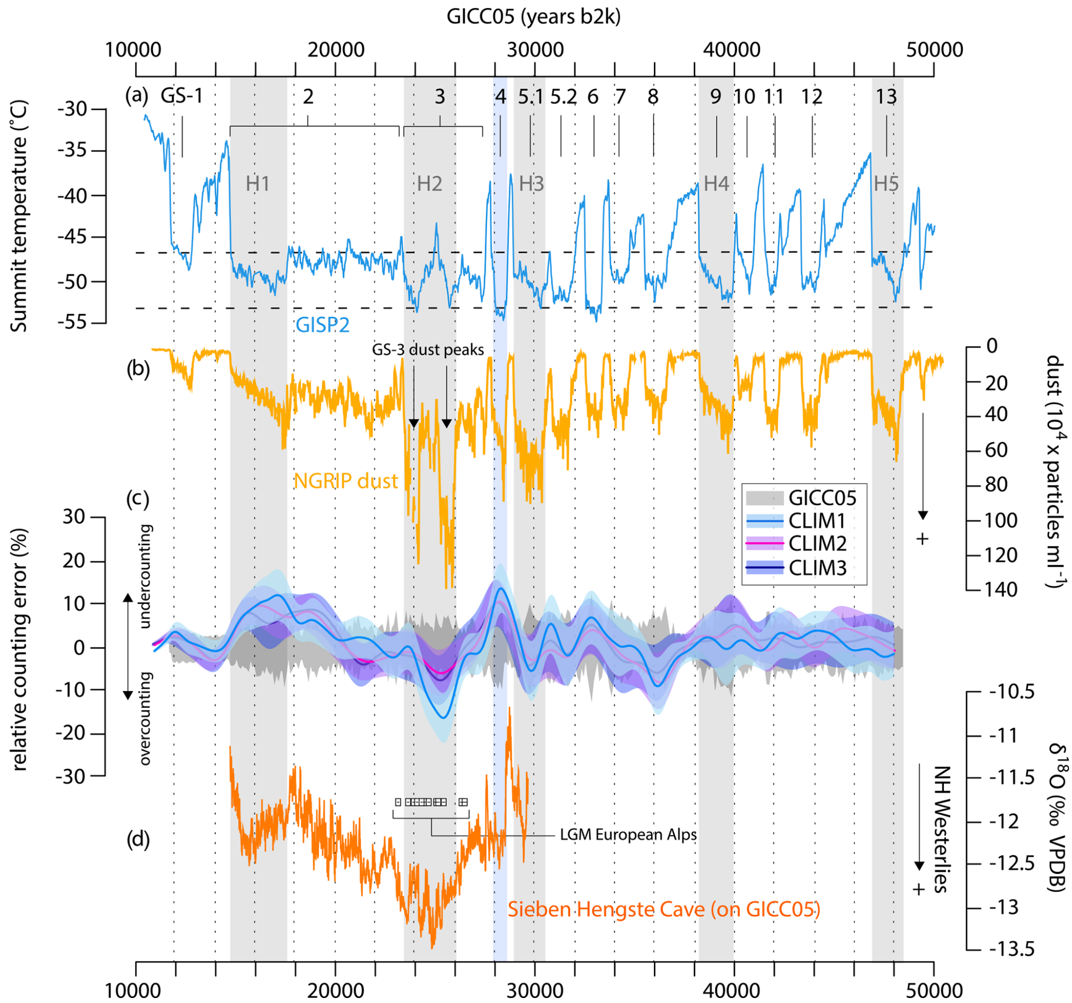

Figure 8. Inferred estimates of the relative annual-layer counting error for the GICC05 chronology based on MCMC synchronization to the U–Th timescale. **(a)** GISP2 temperature reconstruction (Martin et al., 2023) presented with partitioning of Greenland Stadials (GSs) and the timing of Heinrich events (H; gray vertical bars). Underlying dashed levels show the $\pm 2\sigma$ temperature range of stadials GS-1 to GS-13. Interstadial–stadial transitions were identified using a Bayesian change-point procedure (Erdman and Emerson, 2007). The blue vertical bar denotes GS-4, i.e., the coldest stadial (~ 3.3 °C colder than the average). **(b)** NGRIP insoluble dust concentration record (Ruth et al., 2003) (note the reverse scale). **(c)** Comparison between the maximum relative counting error of the GICC05 (gray shading) and the differential dating uncertainties inferred from the CLIM synchronizations presented in this study, respectively, shown with their posterior median (thick lines) and pointwise 68 % credible intervals (shading). Positive (negative) values indicate an undercount (overcount) of ice layers in Greenland ice cores. To emphasize the longer-timescale variance, the data are smoothed to remove variability shorter than 2000 years. **(d)** U–Th dated climate records of the Last Glacial Maximum (LGM) in the European Alps after synchronization to the GICC05 timescale by applying the CLIM1 transfer function presented in this study. U–Th ages of cryogenic cave carbonates (Spötl et al., 2021) with their $\pm 2\sigma$ uncertainty (white squares) indicating the timing of the maximum mountain glacier extent over the European Alps and δ^{18}O values of precipitation from the Sieben Hengste stalagmite record (Luetscher et al., 2015) (orange). The Sieben Hengste record reveals a maximum strengthening and southerly displacement of the westerly winds during GS-3. All records are presented on the GICC05 timescale.

i.e., the LGM. In principle, these results – which are largely consistent across the three CLIM synchronizations – challenge the layer counting method and uncertainty estimates and imply that the bias in the GICC05 layer counting does not systematically depend on accumulation rates.

The observation that GICC05 likely undercounts ice layers during H1/GS-2 is quantitatively comparable to previous results based on BWM of cosmogenic radionuclides (Adolphi et al., 2018; Sinnl et al., 2023) (Fig. 7) and recent estimates based on climate synchronization (Dong et al., 2022). Specifically, the synchronizations highlight that GICC05 counts on average ~ 12 % too few annual layers in the interval ~ 15–18 kyr b2k for CLIM1, ~ 10 % for CLIM2, and ~ 9 % for CLIM3 (mean $= \sim 10$ %). Similarly, during GS-4, which represents the coldest period recorded in Greenland ice cores (Fig. 8a), we observe an undercount of ~ 14 % centered at

~ 28 kyr b2k for CLIM1, ~ 12 % for CLIM2, and ~ 12 % for CLIM3 (mean = ~ 13 %).

Perhaps a more interesting result is that throughout most of LGM/GS-3 there is an increasing tendency to count too many years in the GICC05 stratigraphy, which is particularly evident in CLIM1. The overcount starts at ~ 24 kyr b2k and reaches a maximum rate of change at ~ 26 kyr b2k, when the GICC05 timescale counts on average ~ 16 % too many layers (Fig. 8c). This is less pronounced in CLIM2 and CLIM3 but still evident, indicating an overcount of ~ 6 % and ~ 9 %, respectively (mean = ~ 10 %). The LGM/GS-3 interval is one of the coldest sections of the last glacial period (Fig. 8a and b) and an overcount of annual layers is seemingly at odds with the general assumption that fewer years have been detected during stadials, i.e., when low accumulation rates and thinner ice layers make the identification of annual layers more difficult (Rasmussen et al., 2006; Svensson et al., 2006, 2008). However, a bias towards counting too many ice years during LGM/GS-3 is not unexpected as there are some weak indications that additional annual layers have been counted in other cold sections of the GICC05 stratigraphy (Andersen et al., 2006; Rasmussen et al., 2006; Svensson et al., 2006).

This finding requires further consideration. During LGM/GS-3, the RCE inferred from CLIM maps onto the dust concentration profile in Greenland ice cores (Fig. 8b and c). This interval features the two most distinct and pronounced dust peaks of the last glacial period, in which dust levels increase by a factor of 3 in NGRIP ice cores (Ruth et al., 2003). Since high dust content in the ice is notoriously liable to complicate the annual-layer counting in a number of ways, this correspondence suggests a possible impact of dust deposition on the identification of the annual layers.

The layer counting in the coldest climatic events of the GICC05 stratigraphy relies mostly on the visual identification of annual variations in two parameters over the NGRIP ice cores. Since the chemical records do not resolve the thin stadial layers, counting is constrained using the high-resolution visual stratigraphy (VS) grayscale refraction profile (Svensson et al., 2005) and the electrical conductivity measurement (ECM) on the solid ice (Dahl-Jensen et al., 2002; Hammer, 1980). The VS profile represents the depositional history at NGRIP. Inspections of the VS data throughout the glacial period highlights a strong correlation between the frequency of visible layers and dust concentration, suggesting that the intensity (i.e., the gray value) of each layer is related to its impurity content representing an individual dust depositional event (Svensson et al., 2005). This may result in the VS record containing multiple visible large layers per year, which can complicate the counting and lead to a misinterpretation of the actual annual signal. On the other hand, the ECM is strongly dominated by variations in dust (e.g., Taylor et al., 1997). The ECM profile is attenuated in sections with high concentrations of dust due to the increased alkalinity, thus subduing the annual cycle in the ECM signal and making the resolution of this parameter marginal for the identification of annual layers (Andersen et al., 2006; Rasmussen et al., 2008). For these reasons, greater dust deposition rates may limit the use of the VS and ECM data for direct counting of annual layers.

Moreover, accurate counting over the cold sections that feature multiple depositional events depends on the untested assumption that clusters of peaks in the VS and ECM profiles reflect seasonal variations in dust deposition resembling those observed in the shallower parts of the NGRIP ice core. Modern dust emissions from Asian deserts peak in the Northern Hemisphere spring. This peak is generally associated with enhanced flux of dust to the ice (Beer et al., 1991; Bory et al., 2002; Whitlow et al., 1992) – a signature consistent with that of the warmest sections of the GICC05 stratigraphy and coinciding with layers of high refraction in the VS record (Ram and Koenig, 1997; Rasmussen et al., 2006; Svensson et al., 2008). However, an altered atmospheric circulation and precipitation pattern during the LGM may have caused fundamental changes in the seasonality, magnitude, frequency, and mode of deposition of dust impurities to the Greenland Ice Sheet.

Model simulations of the dust cycle under glacial climate conditions show a prolongation of the dust emission season with a twofold to threefold increase in atmospheric emissions and deposition rates in the high northern latitudes during the LGM compared to modern times (Werner et al., 2002). The dominant factor driving the higher dust emission fluxes at the LGM appears to be increased strength and variability of glacial winds over the dust source regions. Evidence from general circulation models (Kageyama and Valdes, 2000; Li and Battisti, 2008; Löfverström et al., 2016; Ullman et al., 2014) and proxy reconstructions (L. Cheng et al., 2021; Kageyama et al., 2006; Luetscher et al., 2015; Spötl et al., 2021) consistently points towards stronger northern westerlies at the LGM. In particular, GS-3 stands out in the context of the last glacial period as the phase when this altered flow pattern was most extreme (Fig. 8d), i.e., in conjunction with the maximum extent of the Laurentide Ice Sheet, which caused a strengthening and southward deflection of the westerlies (e.g., Löfverström and Lora, 2017).

Increased emissions and transport to Greenland provide an explanation for the high dust concentrations in the ice observed during LGM/GS-3. However, to justify the fact that GICC05 contains ~ 10 % too many annual layers during GS-3, additional factors have to be invoked. For example, changes in the seasonality and mode of precipitation can play a key role in increasing the number of dust depositional events that ultimately control the frequency of sub-annual layers observed in the VS profile. Model simulations suggest that at the LGM Greenland experienced a marked reduction in winter and spring precipitation and a shift to a precipitation regime with a pronounced summer maximum – in contrast to the characteristic modern springtime peak (Krinner et al., 1997; Merz et al., 2013; Werner et al., 2002). It has been shown that lower precipitation rates and a shift in seasonality of precipitation inhibit wet deposition of dust during glacial winter and spring. This leads to a substantial increase in the contribution of dry deposition processes at Summit, which produces dust spikes in ice cores that are less evenly distributed over depth than modern ones (Werner et al., 2002). Dry deposition commonly occurs through gravitational settling and turbulent redistribution of snow to the surface and is thus more conducive to increasing the frequency of annual dust depositional events registered in ice-core records. Hence, the increased seasonality of LGM precipitation and enhanced dry deposition over Greenland may explain the higher frequency of sub-annual layers in the VS signal and the resulting overcount of annual layers in GICC05 during GS-3. A complete understanding of the physical processes that led to the overcount during GS-3 is, however, beyond the scope of this work and requires more detailed investigations using climate model experiments of dust transport and deposition.

4 Conclusions

The first continuous climate synchronizations between the Greenland ice-core chronology 2005 (GICC05) and the U–Th timescale are presented. Three synchronizations were established using an automated alignment algorithm for Bayesian inversion of the annual-layer counting uncertainty of GICC05. The algorithm quantifies the probability of alignments between Greenland ice-core and East Asian summer monsoon speleothem signals and infers the age difference between the underlying timescales. The synchronization method evaluates possible shifts in the timescale difference that exceed the differential dating uncertainty of GICC05, which are not easily quantifiable using traditional tie-point correlation or wiggle-matching techniques.

The new synchronizations, which are internally coherent, are consistent with independent reconstructions and improve the average precision of the GICC05–U–Th timescale transfer function by 48 % relative to previous estimates. Based on the assumed accuracy of the U–Th timescale, the results significantly reduce the absolute dating uncertainty of the Greenland timescale back to 48 kyr b2k and indicate that the MCE is generally a conservative uncertainty measurement.

Yet, our analysis shows that the relationship between the GICC05 and the U–Th timescale is potentially more variable than previously assumed and that the annual-layer counting error of the ice-core chronology is not necessarily correlated over long periods of time. It is found that within the coldest stadials, GICC05 is either missing or gaining time faster than allowed by its nominal differential dating uncertainty. The annual-layer count identifies on average $\sim 10\,\%$ and $\sim 13\,\%$ too few ice years within H1/GS-2 and GS-4, respectively. In contrast $\sim 10\,\%$ too many ice years may have been counted within GS-3, i.e., in conjunction with the LGM.

The results imply a major shift in the differential counting within the interval $\sim$ 24–27 kyr b2k, when the difference between the GICC05 and the U–Th timescale drifts from +390 to +165 years. The reason for this marked overcount is attributed to a misinterpretation of the annual-layer record over GS-3. This is likely due to an increased occurrence of multiple-layer years resulting from a higher frequency of dust depositional events at the LGM in response to changes in seasonality of precipitation and a greater contribution of dry deposition processes. This is an important point, as a large counting bias within GS-3 may explain why it has been difficult to identify a robust bipolar volcanic match between Greenland and Antarctic ice cores during the LGM (Svensson et al., 2020).

This study illustrates the utility of probabilistic inversion methods to infer continuous and objective synchronizations of paleoclimate records. The new timescale transfer functions presented here set important constraints on the biases that accompany the stratigraphic dating of GICC05 and will facilitate the comparison of ice cores as well as U–Th-dated and radiocarbon-dated records on a common timeline.

Code availability. All R code used for synchronization analysis is available from the corresponding author upon request.

Data availability. The stack of speleothem $\delta^{18}O$ records (EASM PC1) presented in Fig. 2 and the CLIM transfer functions presented in Figs. 4–6 are available as a Supplement to this paper.

Supplement. The supplement related to this article is available online at: https://doi.org/10.5194/cp-20-1415-2024-supplement.

Competing interests. The contact author has declared that neither of the authors has any competing interests.

Acknowledgements. This study is a contribution to the INTIMATE (INTegration of Ice-core, Marine, and Terrestrial records) project.

Financial support. This research has been supported by the Isaac Newton Trust (grant no. LCAG/444.G101121) and a Natural Environment Research Council (NERC) Discovery Science Grant (NE/W006243/1) awarded to Francesco Muschitiello.

Review statement. This paper was edited by Denis-Didier Rousseau and reviewed by Florian Adolphi and Anders Svensson.

References

Adolphi, F. and Muscheler, R.: Synchronizing the Greenland ice core and radiocarbon timescales over the Holocene-Bayesian wiggle-matching of cosmogenic radionuclide records, Clim. Past, 12, 15–30, https://doi.org/10.5194/cp-12-15-2016, 2016.

Adolphi, F., Bronk Ramsey, C., Erhardt, T., Edwards, R. L., Cheng, H., Turney, C. S. M., Cooper, A., Svensson, A., Rasmussen, S. O., Fischer, H., and Muscheler, R.: Connecting the Greenland ice-core and U/Th timescales via cosmogenic radionuclides: testing the synchroneity of Dansgaard–Oeschger events, Clim. Past, 14, 1755–1781, https://doi.org/10.5194/cp-14-1755-2018, 2018.

Anchukaitis, K. J. and Tierney, J. E.: Identifying coherent spatiotemporal modes in time-uncertain proxy paleoclimate records, Clim. Dynam., 41, 1291–1306, 2013.

Andersen, K. K., Azuma, N., Barnola, J. M., Bigler, M., Biscaye, P., Caillon, N., Chappellaz, J., Clausen, H. B., Dahl-Jensen, D., Fischer, H., Flückiger, J., Fritzsche, D., Fujii, Y., Goto-Azuma, K., Grønvold, K., Gundestrup, N. S., Hansson, M., Huber, C., Hvidberg, C. S., Johnsen, S. J., Jonsell, U., Jouzel, J., Kipfstuhl, S., Landais, A., Leuenberger, M., Lorrain, R., Masson-Delmotte, V., Miller, H., Motoyama, H., Narita, H., Popp, T., Rasmussen, S. O., Raynaud, D., Rothlisberger, R., Ruth, U., Samyn, D., Schwander, J., Shoji, H., Siggard-Andersen, M. L., Steffensen, J. P., Stocker, T., Sveinbjörnsdóttir, A. E., Svensson, A., Takata, M., Tison, J. L., Thorsteinsson, T., Watanabe, O., Wilhelms, F., and White, J. W. C.: High-resolution record of Northern Hemisphere climate extending into the last interglacial period, Nature, 431, 147–151, https://doi.org/10.1038/nature02805, 2004.

Andersen, K. K., Svensson, A., Johnsen, S. J., Rasmussen, S. O., Bigler, M., Röthlisberger, R., Ruth, U., Siggaard-Andersen, M.-L., Steffensen, J. P., and Dahl-Jensen, D.: The Greenland ice core chronology 2005, 15–42 ka. Part 1: constructing the time scale, Quaternary Sci. Rev., 25, 3246–3257, 2006.

Armstrong, E., Hopcroft, P. O., and Valdes, P. J.: A simulated Northern Hemisphere terrestrial climate dataset for the past 60,000 years, Sci. Data, 6, 265, https://doi.org/10.1038/s41597-019-0277-1, 2019.

Bard, E., Ménot, G., Rostek, F., Licari, L., Böning, P., Edwards, R. L., Cheng, H., Wang, Y., and Heaton, T. J.: Radiocarbon Calibration/Comparison Records Based on Marine Sediments from the Pakistan and Iberian Margins, Radiocarbon, 55, 1999–2019, https://doi.org/10.2458/azu_js_rc.55.17114, 2013.

Bauska, T. K., Marcott, S. A., and Brook, E. J.: Abrupt changes in the global carbon cycle during the last glacial period, Nat. Geosci., 14, 91–96, 2021.

Beer, J., Finkel, R. C., Bonani, G., Gäggeler, H., Görlach, U., Jacob, P., Klockow, D., Langway Jr., C. C., Neftel, A., and Oeschger, H.: Seasonal variations in the concentration of ^{10}Be, Cl^-, NO_3^-, SO_4^{2-}, H_2O_2, ^{210}Pb, ^{3}H, mineral dust, and σ^{18}O in greenland snow, Atmos. Environ. A, 25, 899–904, 1991.

Blaauw, M. and Christen, J. A.: Flexible paleoclimate age-depth models using an autoregressive gamma process, Bayesian Anal., 6, 457–474, https://doi.org/10.1214/11-BA618, 2011.

Bory, A.-M., Biscaye, P. E., Svensson, A., and Grousset, F. E.: Seasonal variability in the origin of recent atmospheric mineral dust at NorthGRIP, Greenland, Earth Planet. Sc. Lett., 196, 123–134, 2002.

Bronk Ramsey, C., Heaton, T. J., Schlolaut, G., Staff, R. A., Bryant, C. L., Brauer, A., Lamb, H. F., Marshall, M. H., and Nakagawa, T.: Reanalysis of the Atmospheric Radiocarbon Calibration Record from Lake Suigetsu, Japan, Radiocarbon, 62, 989–999, https://doi.org/10.1017/RDC.2020.18, 2020.

Brooks, S., Gelman, A., Jones, G., and Meng, X.-L.: Handbook of Markov Chain Monte Carlo, edited by: Brooks, S., Gelman, A., Jones, G., and Meng, X.-L., Chapman & Hall/CRC, ISBN 978-1420079418, 2011.

Brooks, S. P. and Gelman, A.: General methods for monitoring convergence of iterative simulations, J. Comput. Graph. Stat., 7, 434–455, 1998.

Buizert, C., Cuffey, K. M., Severinghaus, J. P., Baggenstos, D., Fudge, T. J., Steig, E. J., Markle, B. R., Winstrup, M., Rhodes, R. H., Brook, E. J., Sowers, T. A., Clow, G. D., Cheng, H., Edwards, R. L., Sigl, M., McConnell, J. R., and Taylor, K. C.: The WAIS Divide deep ice core WD2014 chronology – Part 1: Methane synchronization (68–31 ka BP) and the gas age–ice age difference, Clim. Past, 11, 153–173, https://doi.org/10.5194/cp-11-153-2015, 2015.

Buizert, C., Sigl, M., Severi, M., Markle, B. R., Wettstein, J. J., McConnell, J. R., Pedro, J. B., Sodemann, H., Goto-Azuma, K., Kawamura, K., Fujita, S., Motoyama, H., Hirabayashi, M., Uemura, R., Stenni, B., Parrenin, F., He, F., Fudge, T. J., and Steig, E. J.: Abrupt ice-age shifts in southern westerly winds and Antarctic climate forced from the north, Nature, 563, 681–685, https://doi.org/10.1038/s41586-018-0727-5, 2018.

Ceppi, P., Hwang, Y., Liu, X., Frierson, D. M. W., and Hartmann, D. L.: The relationship between the ITCZ and the Southern Hemispheric eddy-driven jet, J. Geophys. Res.-Atmos., 118, 5136–5146, 2013.

Cheng, H., Edwards, R. L., Sinha, A., Spötl, C., Yi, L., Chen, S., Kelly, M., Kathayat, G., Wang, X., and Li, X.: The Asian monsoon over the past 640,000 years and ice age terminations, Nature, 534, 640–646, 2016.

Cheng, H., Lawrence Edwards, R., Southon, J., Matsumoto, K., Feinberg, J. M., Sinha, A., Zhou, W., Li, H., Li, X., Xu, Y., Chen, S., Tan, M., Wang, Q., Wang, Y., and Ning, Y.: Atmospheric ^{14}C/^{12}C changes during the last glacial period from hulu cave, Science, 362, 1293–1297, https://doi.org/10.1126/science.aau0747, 2018.

Cheng, H., Xu, Y., Dong, X., Zhao, J., Li, H., Baker, J., Sinha, A., Spötl, C., Zhang, H., and Du, W.: Onset and termination of Heinrich Stadial 4 and the underlying climate dynamics, Commun. Earth Environ., 2, 1–11, 2021.

Cheng, L., Song, Y., Wu, Y., Liu, Y., Liu, H., Chang, H., Zong, X., and Kang, S.: Drivers for asynchronous patterns of dust accumulation in central and eastern Asia and in Greenland during the Last Glacial Maximum, Geophys. Res. Lett., 48, e2020GL091194, https://doi.org/10.1029/2020GL091194, 2021.

Christen, J. A. and Pérez, S.: A new robust statistical model for radiocarbon data, Radiocarbon, 51, 1047–1059, 2009.

Cooper, A., Turney, C. S., Palmer, J., Hogg, A., McGlone, M., Wilmshurst, J., Lorrey, A. M., Heaton, T. J., Russell, J. M., McCracken, K., and Anet, J. G.: A global environmental crisis 42,000 years ago, Science, 371, 811–818, 2021.

Corrick, E. C., Drysdale, R. N., Hellstrom, J. C., Capron, E., Rasmussen, S. O., Zhang, X., Fleitmann, D., Couchoud, I., and Wolff, E.: Synchronous timing of abrupt climate changes during the last glacial period, Science, 369, 963–969, https://doi.org/10.1126/science.aay5538, 2020.

Cutmore, A., Ausín, B., Maslin, M., Eglinton, T., Hodell, D., Muschitiello, F., Menviel, L., Haghipour, N., Martrat, B., and Margari, V.: Abrupt intrinsic and extrinsic responses of southwestern Iberian vegetation to millennial-scale variability over the past 28 ka, J. Quaternary Sci., 37, 420–440, https://doi.org/10.1002/jqs.3392, 2021.

Cvijanovic, I., Langen, P. L., Kaas, E., and Ditlevsen, P. D.: Southward intertropical convergence zone shifts and implications for an atmospheric bipolar seesaw, J. Climate, 26, 4121–4137, 2013.

Dahl-Jensen, D., Mosegaard, K., Gundestrup, N., Clow, G. D., Johnsen, S. J., Hansen, A. W., and Balling, N.: Past temperatures directly from the Greenland Ice Sheet, Science, 282, 268–271, https://doi.org/10.1126/science.282.5387.268, 1998.

Dahl-Jensen, D., Gundestrup, N. S., Miller, H., Watanabe, O., Johnsen, S. J., Steffensen, J. P., Clausen, H. B., Svensson, A., and Larsen, L. B.: The NorthGRIP deep drilling programme, Ann. Glaciol., 35, 1–4, 2002.

Darfeuil, S., Ménot, G., Giraud, X., Rostek, F., Tachikawa, K., Garcia, M., and Bard, É.: Sea surface temperature reconstructions over the last 70 kyr off Portugal: Biomarker data and regional modeling, Paleoceanography, 31, 40–65, https://doi.org/10.1002/2015PA002831, 2016.

Dong, X., Kathayat, G., Rasmussen, S. O., Svensson, A., Severinghaus, J. P., Li, H., Sinha, A., Xu, Y., Zhang, H., Shi, Z., and Cai, Y.: Coupled atmosphere-ice-ocean dynamics during Heinrich Stadial 2, Nat. Commun., 13, 5867, https://doi.org/10.1038/s41467-022-33583-4, 2022.

Erdman, C. and Emerson, J. W.: bcp: an R package for performing a Bayesian analysis of change point problems, J. Stat. Softw., 23, 1–13, 2007.

Erhardt, T., Capron, E., Rasmussen, S. O., Schüpbach, S., Bigler, M., Adolphi, F., and Fischer, H.: Decadal-scale progression of the onset of Dansgaard–Oeschger warming events, Clim. Past, 15, 811–825, https://doi.org/10.5194/cp-15-811-2019, 2019.

Ezat, M. M., Rasmussen, T. L., Thornalley, D. J. R., Olsen, J., Skinner, L. C., Hönisch, B., and Groeneveld, J.: Ventilation history of Nordic Seas overflows during the last (de)glacial period revealed by species-specific benthic foraminiferal ^{14}C dates, Paleoceanography, 32, 172–181, https://doi.org/10.1002/2016PA003053, 2017.

Hammer, C. U.: Acidity of polar ice cores in relation to absolute dating, past volcanism, and radio–echoes, J. Glaciol., 25, 359–372, 1980.

Henry, L. G., McManus, J. F., Curry, W. B., Roberts, N. L., Piotrowski, A. M., and Keigwin, L. D.: North Atlantic ocean circulation and abrupt climate change during the last glaciation, Science, 353, 470–474, https://doi.org/10.1126/science.aaf5529, 2016.

Hughen, K. A. and Heaton, T. J.: Updated Cariaco Basin C Calibration Dataset from 0–60 cal kyr BP, Radiocarbon, 62, 1001–1043, https://doi.org/10.1017/RDC.2020.53, 2020.

Hughes, P. D. and Gibbard, P. L.: A stratigraphical basis for the Last Glacial Maximum (LGM), Quatern. Int., 383, 174–185, 2015.

Jansen, E., Christensen, J. H., Dokken, T., Nisancioglu, K. H., Vinther, B. M., Capron, E., Guo, C., Jensen, M. F., Langen, P. L., Pedersen, R. A., Yang, S., Bentsen, M., Kjær, H. A., Sadatzki, H., Sessford, E., and Stendel, M.: Past perspectives on the present era of abrupt Arctic climate change. Nat. Clim. Change, 10, 714–721, https://doi.org/10.1038/s41558-020-0860-7, 2020.

Johnsen, S., Clausen, H. B., Dansgaard, W., Gundestrup, N. S., Hammer, C. U., Andersen, U., Andersen, K., Hvidberg, C., Dahl-Jensen, D., Steffensen, J., Shoji, H., Sveinbjörnsdóttir, Á., White, J., Jouzel, J., Fisher, D., and Johnsen, S. J.: The δ^{18}O record along the Greenland Ice Core Project deep ice core and the problem of possible Eemian climatic instability, J. Geophys. Res.-Oceans, 102, 26397–26410, 1997.

Kageyama, M. and Valdes, P. J.: Impact of the North American ice-sheet orography on the Last Glacial Maximum eddies and snowfall, Geophys. Res. Lett., 27, 1515–1518, 2000.

Kageyama, M., Laîné, A., Abe-Ouchi, A., Braconnot, P., Cortijo, E., Crucifix, M., De Vernal, A., Guiot, J., Hewitt, C. D., and Kitoh, A.: Last Glacial Maximum temperatures over the North Atlantic, Europe and western Siberia: a comparison between PMIP models, MARGO sea–surface temperatures and pollen-based reconstructions, Quaternary Sci. Rev., 25, 2082–2102, 2006.

Kageyama, M., Merkel, U., Otto-Bliesner, B., Prange, M., Abe-Ouchi, A., Lohmann, G., Ohgaito, R., Roche, D. M., Singarayer, J., Swingedouw, D., and Zhang, X.: Climatic impacts of fresh water hosing under Last Glacial Maximum conditions: a multi-model study, Clim. Past, 9, 935–953, https://doi.org/10.5194/cp-9-935-2013, 2013.

Kageyama, M., Harrison, S. P., Kapsch, M.-L., Lofverstrom, M., Lora, J. M., Mikolajewicz, U., Sherriff-Tadano, S., Vadsaria, T., Abe-Ouchi, A., Bouttes, N., Chandan, D., Gregoire, L. J., Ivanovic, R. F., Izumi, K., LeGrande, A. N., Lhardy, F., Lohmann, G., Morozova, P. A., Ohgaito, R., Paul, A., Peltier, W. R., Poulsen, C. J., Quiquet, A., Roche, D. M., Shi, X., Tierney, J. E., Valdes, P. J., Volodin, E., and Zhu, J.: The PMIP4 Last Glacial Maximum experiments: preliminary results and comparison with the PMIP3 simulations, Clim. Past, 17, 1065–1089, https://doi.org/10.5194/cp-17-1065-2021, 2021.

Krinner, G., Genthon, C., and Jouzel, J.: GCM analysis of local influences on ice core δ signals, Geophys. Res. Lett., 24, 2825–2828, 1997.

Legrand, M. and Mayewski, P.: Glaciochemistry of polar ice cores: A review, Rev. Geophys., 35, 219–243, https://doi.org/10.1029/96RG03527, 1997.

Li, C. and Battisti, D. S.: Reduced Atlantic storminess during Last Glacial Maximum: Evidence from a coupled climate model, J. Climate, 21, 3561–3579, 2008.

Lin, L., Khider, D., Lisiecki, L. E., and Lawrence, C. E.: Probabilistic sequence alignment of stratigraphic records, Paleoceanography, 29, 976–989, https://doi.org/10.1002/2014PA002713, 2014.

Liu, Z., Otto-Bliesner, B. L., He, F., Brady, E.C., Tomas, R., Clark, P. U., Carlson, A. E., Lynch-Stieglitz, J., Curry, W., and Brook, E.: Transient simulation of last deglaciation with a new mechanism for Bølling-Allerød warming, Science, 325, 310–314, 2009.

Löfverström, M. and Lora, J. M.: Abrupt regime shifts in the North Atlantic atmospheric circulation over the last deglaciation, Geophys. Res. Lett., 44, 8047–8055, 2017.

Löfverström, M., Caballero, R., Nilsson, J., and Messori, G.: Stationary wave reflection as a mechanism for zonalizing the Atlantic winter jet at the LGM, J. Atmos. Sci., 73, 3329–3342, 2016.

Luetscher, M., Boch, R., Sodemann, H., Spötl, C., Cheng, H., Edwards, R. L., Frisia, S., Hof, F., and Müller, W.: North Atlantic storm track changes during the Last Glacial Maximum recorded by Alpine speleothems, Nat. Commun., 6, 1–6, 2015.

Martin, K. C., Buizert, C., Edwards, J. S., Kalk, M. L., Riddell-Young, B., Brook, E. J., Beaudette, R., Severinghaus, J. P., and Sowers, T. A.: Bipolar impact and phasing of Heinrich-type climate variability, Nature, 617, 100–104, 2023.

Merz, N., Raible, C. C., Fischer, H., Varma, V., Prange, M., and Stocker, T. F.: Greenland accumulation and its connection to the large-scale atmospheric circulation in ERA-Interim and paleoclimate simulations, Clim. Past, 9, 2433–2450, https://doi.org/10.5194/cp-9-2433-2013, 2013.

Muscheler, R., Kromer, B., Björck, S., Svensson, a., Friedrich, M., Kaiser, K. F., and Southon, J.: Tree rings and ice cores reveal ^{14}C calibration uncertainties during the Younger Dryas, Nat. Geosci., 1, 263–267, https://doi.org/10.1038/ngeo128, 2008.

Muscheler, R., Adolphi, F., and Knudsen, M. F.: Assessing the differences between the IntCal and Greenland ice-core time scales for the last 14,000 years via the common cosmogenic radionuclide variations, Quaternary Sci. Rev., 106, 81–87, https://doi.org/10.1016/j.quascirev.2014.08.017, 2014.

Muscheler, R., Adolphi, F., Heaton, T., Bronk Ramsey, C., Svensson, A., van der Plicht, J., and Reimer, P.: Testing and improving the IntCal20 calibration curve with independent records, Radiocarbon, 62, 1079–1094, https://doi.org/10.1017/RDC.2020.54, 2020.

Muschitiello, F., D'Andrea, W. J., Schmittner, A., Heaton, T. J., Balascio, N. L., deRoberts, N., Caffee, M. W., Woodruff, T. E., Welten, K. C., Skinner, L. C., Simon, M. H., and Dokken, T. M.: Deep-water circulation changes lead North Atlantic climate during deglaciation, Nat. Commun., 10, 1272, https://doi.org/10.1038/s41467-019-09237-3, 2019.

Muschitiello, F., O'Regan, M., Martens, J., West, G., Gustafsson, Ö., and Jakobsson, M.: A new 30,000 year chronology for rapidly deposited sediments on the Lomonosov Ridge using bulk radiocarbon dating and probabilistic stratigraphic alignment, Geochronology, 2, 81–91, https://doi.org/10.5194/gchron-2-81-2020, 2020.

Nagashima, K., Tada, R., Tani, A., Sun, Y., Isozaki, Y., Toyoda, S., and Hasegawa, H.: Millennial-scale oscillations of the westerly jet path during the last glacial period, J. Asian Earth Sci., 40, 1214–1220, https://doi.org/10.1016/j.jseaes.2010.08.010, 2011.

Parrenin, F., Bazin, L., Capron, E., Landais, A., Lemieux-Dudon, B., and Masson-Delmotte, V.: IceChrono1: a probabilistic model to compute a common and optimal chronology for several ice cores, Geosci. Model Dev., 8, 1473–1492, https://doi.org/10.5194/gmd-8-1473-2015, 2015.

Ram, M. and Koenig, G.: Continuous dust concentration profile of pre-Holocene ice from the Greenland Ice Sheet Project 2 ice core: Dust stadials, interstadials, and the Eemian, J. Geophys. Res.-Oceans, 102, 26641–26648, 1997.

Rasmussen, S. O., Andersen, K. K., Svensson, A. M., Steffensen, J. P., Vinther, B. M., Clausen, H. B., Siggaard-Andersen, M. L., Johnsen, S. J., Larsen, L. B., Dahl-Jensen, D., Bigler, M., Röthlisberger, R., Fischer, H., Goto-Azuma, K., Hansson, M. E., and Ruth, U.: A new Greenland ice core chronology for the last glacial termination, J. Geophys. Res.-Atmos., 111, D06102, https://doi.org/10.1029/2005JD006079, 2006.

Rasmussen, S. O., Seierstad, I. K., Andersen, K. K., Bigler, M., Dahl-Jensen, D., and Johnsen, S. J.: Synchronization of the NGRIP, GRIP, and GISP2 ice cores across MIS 2 and palaeoclimatic implications, Quaternary Sci. Rev., 27, 18–28, 2008.

Reimer, P. J., Austin, W. E. N., Bard, E., Bayliss, A., Blackwell, P. G., Bronk Ramsey, C., Butzin, M., Cheng, H., Edwards, R. L., Friedrich, M., Grootes, P. M., Guilderson, T. P., Hajdas, I., Heaton, T. J., Hogg, A. G., Hughen, K. A., Kromer, B., Manning, S. W., Muscheler, R., Palmer, J. G., Pearson, C., Van Der Plicht, J., Reimer, R. W., Richards, D. A., Scott, E. M., Southon, J. R., Turney, C. S. M., Wacker, L., Adolphi, F., Büntgen, U., Capano, M., Fahrni, S. M., Fogtmann-Schulz, A., Friedrich, R., Köhler, P., Kudsk, S., Miyake, F., Olsen, J., Reinig, F., Sakamoto, M., Sookdeo, A., and Talamo, S.: The IntCal20 Northern Hemisphere Radiocarbon Age Calibration Curve (0–55 cal kBP), Radiocarbon, 62, 725–757, https://doi.org/10.1017/RDC.2020.41, 2020.

Ruth, U., Wagenbach, D., Steffensen, J. P., and Bigler, M.: Continuous record of microparticle concentration and size distribution in the central Greenland NGRIP ice core during the last glacial period, J. Geophys. Res.-Atmos., 108, 4098, https://doi.org/10.1029/2002JD002376, 2003.

Sadatzki, H., Dokken, T. M., Berben, S. M. P., Muschitiello, F., Stein, R., Fahl, K., Menviel, L., Timmermann, A., and Jansen, E.: Sea ice variability in the southern norwegian sea during glacial dansgaard-oeschger climate cycles, Sci. Adv., 5, eaau6174, https://doi.org/10.1126/sciadv.aau6174, 2019.

Schiemann, R., Lüthi, D., and Schär, C.: Seasonality and interannual variability of the westerley jet in the Tibetan Plateau region, J. Climate, 22, 2940–2957, https://doi.org/10.1175/2008JCLI2625.1, 2009.

Schoenherr, D., Paulick, J., Strauss, B. M., Deisenhofer, A. K., Schwartz, B., Rubel, J. A., Lutz, W., Stangier, U., and Altmann, U.: Identification of movement synchrony: Validation of windowed cross-lagged correlation and -regression with peak-picking algorithm, PLoS One, 14, e0211494, https://doi.org/10.1371/journal.pone.0211494, 2019.

Schüpbach, S., Fischer, H., Bigler, M., Erhardt, T., Gfeller, G., Leuenberger, D., Mini, O., Mulvaney, R., Abram, N. J., Fleet, L., Frey, M. M., Thomas, E., Svensson, A., Dahl-Jensen, D., Kettner, E., Kjaer, H., Seierstad, I., Steffensen, J. P., Rasmussen, S. O., Vallelonga, P., Winstrup, M., Wegner, A., Twarloh, B., Wolff, K., Schmidt, K., Goto-Azuma, K., Kuramoto, T., Hirabayashi, M., Uetake, J., Zheng, J., Bourgeois, J., Fisher, D., Zhiheng, D., Xiao, C., Legrand, M., Spolaor, A., Gabrieli, J., Barbante, C., Kang, J. H., Hur, S. D., Hong, S. B., Hwang, H. J., Hong, S., Hansson, M., Iizuka, Y., Oyabu, I., Muscheler, R., Adolphi, F., Maselli, O., McConnell, J., and Wolff, E. W.: Greenland records of aerosol source and atmospheric lifetime changes from the Eemian to the Holocene, Nat. Commun., 9, 1476, https://doi.org/10.1038/s41467-018-03924-3, 2018.

Sessford, E. G., Jensen, M. F., Tisserand, A. A., Muschitiello, F., Dokken, T., Nisancioglu, K. H., and Jansen, E.: Consistent fluctuations in intermediate water temperature off the coast of Greenland and Norway during Dansgaard-Oeschger events, Quaternary Sci. Rev., 223, 105887, https://doi.org/10.1016/j.quascirev.2019.105887, 2019.

Sigl, M., Fudge, T. J., Winstrup, M., Cole-Dai, J., Ferris, D., McConnell, J. R., Taylor, K. C., Welten, K. C., Woodruff, T. E., Adolphi, F., Bisiaux, M., Brook, E. J., Buizert, C., Caffee, M. W., Dunbar, N. W., Edwards, R., Geng, L., Iverson, N., Koffman, B., Layman, L., Maselli, O. J., McGwire, K., Muscheler, R., Nishiizumi, K., Pasteris, D. R., Rhodes, R. H., and Sowers, T. A.: The WAIS Divide deep ice core WD2014 chronology – Part 2: Annual-layer counting (0–31 ka BP), Clim. Past, 12, 769–786, https://doi.org/10.5194/cp-12-769-2016, 2016.

Sinnl, G., Adolphi, F., Christl, M., Welten, K. C., Woodruff, T., Caffee, M., Svensson, A., Muscheler, R., and Rasmussen, S. O.: Synchronizing ice-core and U/Th timescales in the Last Glacial Maximum using Hulu Cave ^{14}C and new ^{10}Be measurements from Greenland and Antarctica, Clim. Past, 19, 1153–1175, https://doi.org/10.5194/cp-19-1153-2023, 2023.

Skinner, L. C., Muschitiello, F., and Scrivner, A. E.: Marine reservoir age variability over the last deglaciation: implications for marine carboncycling and prospects for regional radiocarbon calibrations, Paleoceanogr. Paleoclimatol., 34, 1807–1815, 2019.

Southon, J., Noronha, A. L., Cheng, H., Edwards, R. L., and Wang, Y.: A high-resolution record of atmospheric ^{14}C based on Hulu Cave speleothem H82, Quaternary Sci. Rev., 33, 32–41, https://doi.org/10.1016/j.quascirev.2011.11.022, 2012.

Spötl, C., Koltai, G., Jarosch, A. H., and Cheng, H.: Increased autumn and winter precipitation during the Last Glacial Maximum in the European Alps, Nat. Commun., 12, 1–9, 2021.

Svensson, A., Biscaye, P. E., and Grousset, F. E.: Characterization of late glacial continental dust in the Greenland Ice Core Project ice core, J. Geophys. Res.-Atmos., 105, 4637–4656, https://doi.org/10.1029/1999JD901093, 2000.

Svensson, A., Nielsen, S. W., Kipfstuhl, S., Johnsen, S. J., Steffensen, J. P., Bigler, M., Ruth, U., and Röthlisberger, R.: Visual stratigraphy of the North Greenland Ice Core Project (NorthGRIP) ice core during the last glacial period, J. Geophys. Res.-Atmos., 110, D02108, https://doi.org/10.1029/2004JD005134, 2005.

Svensson, A., Andersen, K. K., Bigler, M., Clausen, H. B., Dahl-Jensen, D., Davies, S. M., Johnsen, S. J., Muscheler, R., Rasmussen, S. O., and Röthlisberger, R.: The Greenland ice core chronology 2005, 15–42 ka. Part 2: comparison to other records, Quaternary Sci. Rev., 25, 3258–3267, 2006.

Svensson, A., Andersen, K. K., Bigler, M., Clausen, H. B., Dahl-Jensen, D., Davies, S. M., Johnsen, S. J., Muscheler, R., Parrenin, F., Rasmussen, S. O., Röthlisberger, R., Seierstad, I., Steffensen, J. P., and Vinther, B. M.: A 60 000 year Greenland stratigraphic ice core chronology, Clim. Past, 4, 47–57, https://doi.org/10.5194/cp-4-47-2008, 2008.

Svensson, A., Dahl-Jensen, D., Steffensen, J. P., Blunier, T., Rasmussen, S. O., Vinther, B. M., Vallelonga, P., Capron, E., Gkinis, V., Cook, E., Kjær, H. A., Muscheler, R., Kipfstuhl, S., Wilhelms, F., Stocker, T. F., Fischer, H., Adolphi, F., Erhardt, T., Sigl, M., Landais, A., Parrenin, F., Buizert, C., McConnell, J. R., Severi, M., Mulvaney, R., and Bigler, M.: Bipolar volcanic synchronization of abrupt climate change in Greenland and Antarctic ice cores during the last glacial period, Clim. Past, 16, 1565–1580, https://doi.org/10.5194/cp-16-1565-2020, 2020.

Taylor, K. C., Alley, R. B., Lamorey, G. W., and Mayewski, P.: Electrical measurements on the Greenland ice Sheet project 2 core, J. Geophys. Res.-Oceans, 102, 26511–26517, 1997.

Ter Braak, C. J. F. and Vrugt, J. A.: Differential evolution Markov chain with snooker updater and fewer chains, Stat. Comput., 18, 435–446, 2008.

Thornalley, D. J. R., Bauch, H. A., Gebbie, G., Guo, W., Ziegler, M., Bernasconi, S. M., Barker, S., Skinner, L. C., and Yu, J.: A warm and poorly ventilated deep Arctic Mediterranean during the last glacial period, Science, 349, 706–710, 2015.

Tipping, M. E. and Bishop, C. M.: Probabilistic principal component analysis, J. Roy. Stat. Soc. Ser. B, 61, 611–622, 1999.

Turney, C. S. M., Fifield, L. K., Hogg, A. G., Palmer, J. G., Hughen, K., Baillie, M. G. L., Galbraith, R., Ogden, J., Lorrey, A., Tims, S. G., and Jones, R. T.: The potential of New Zealand kauri (Agathis australis) for testing the synchronicity of abrupt climate change during the Last Glacial Interval (60,000–11,700 years ago), Quaternary Sci. Rev., 29, 3677–3682, https://doi.org/10.1016/j.quascirev.2010.08.017, 2010.

Turney, C. S. M., Palmer, J., Bronk Ramsey, C., Adolphi, F., Muscheler, R., Hughen, K. A., Staff, R. A., Jones, R. T., Thomas, Z. A., Fogwill, C. J., and Hogg, A.: High-precision dating and correlation of ice, marine and terrestrial sequences spanning Heinrich Event 3: Testing mechanisms of interhemispheric change using New Zealand ancient kauri (Agathis australis), Quaternary Sci. Rev., 137, 126–134, https://doi.org/10.1016/j.quascirev.2016.02.005, 2016.

Ullman, D. J., LeGrande, A. N., Carlson, A. E., Anslow, F. S., and Licciardi, J. M.: Assessing the impact of Laurentide Ice Sheet topography on glacial climate, Clim. Past, 10, 487–507, https://doi.org/10.5194/cp-10-487-2014, 2014.

Vonmoos, M., Beer, J., and Muscheler, R.: Large variations in Holocene solar activity: Constraints from ^{10}Be in the Greenland Ice Core Project ice core, J. Geophys. Res.-Space, 111, A10105, https://doi.org/10.1029/2005JA011500, 2006.

Waelbroeck, C., Lougheed, B. C., Riveiros, N. V., Missiaen, L., Pedro, J., Dokken, T., Hajdas, I., Wacker, L., Abbott, P., and Dumoulin, J.-P.: Consistently dated Atlantic sediment cores over the last 40 thousand years, Sci. Data, 6, 1–12, 2019.

Wang, X., Auler, A. S., Edwards, R. L., Cheng, H., Ito, E., and Solheid, M.: Interhemispheric anti-phasing of rainfall during the last glacial period, Quaternary Sci. Rev., 25, 3391–3403, https://doi.org/10.1016/j.quascirev.2006.02.009, 2006.

Wang, Y.-J., Cheng, H., Edwards, R. L., An, Z. S., Wu, J. Y., Shen, C.-C., and Dorale, J. A.: A high-resolution absolute-dated late Pleistocene monsoon record from Hulu Cave, China, Science, 294, 2345–2348, 2001.

Weninger, B. and Jöris, O.: A ^{14}C age calibration curve for the last 60 ka: the Greenland-Hulu U/Th timescale and its impact on understanding the Middle to Upper Paleolithic transition in Western Eurasia, J. Hum. Evol., 55, 772–781, 2008.

Werner, M., Tegen, I., Harrison, S. P., Kohfeld, K. E., Prentice, I. C., Balkanski, Y., Rodhe, H., and Roelandt, C.: Seasonal and interannual variability of the mineral dust cycle under present and glacial climate conditions, J. Geophys. Res.-Atmos., 107, AAC 2-1–AAC 2-19, https://doi.org/10.1029/2002JD002365, 2002.

West, G., Kaufman, D. S., Muschitiello, F., Forwick, M., Matthiessen, J., Wollenburg, J., and O'Regan, M.: Amino acid racemization in Quaternary foraminifera from the Yermak Plateau, Arctic Ocean, Geochronology, 1, 53–67, https://doi.org/10.5194/gchron-1-53-2019, 2019.

West, G., Nilsson, A., Geels, A., Jakobsson, M., Moros, M., Muschitiello, F., Pearce, C., Snowball, I., and O'Regan, M.: Late Holocene paleomagnetic secular variation in the Chukchi Sea, Arctic Ocean, Geochem. Geophy. Geosy., 23, e2021GC010187, https://doi.org/10.1029/2021GC010187, 2021.

Whitlow, S., Mayewski, P. A., and Dibb, J. E.: A comparison of major chemical species seasonal concentration and accumulation at the South Pole and Summit, Greenland, Atmos. Environ. A, 26, 2045–2054, 1992.

Zhang, R. and Delworth, T. L.: Simulated tropical response to a substantial weakening of the Atlantic thermohaline circulation, J. Climate, 18, 1853–1860, 2005.

Clim. Past, 2, 99–113, 2006
www.clim-past.net/2/99/2006/

Climate of the Past

The origin of the European "Medieval Warm Period"*

H. Goosse[1], O. Arzel[1], J. Luterbacher[2], M. E. Mann[3], H. Renssen[4], N. Riedwyl[2], A. Timmermann[5], E. Xoplaki[2], and H. Wanner[2]

[1]Institut d'Astronomie et de Géophysique G. Lemaître, Université catholique de Louvain, 2 Chemin du Cyclotron, 1348 Louvain-la-Neuve, Belgium
[2]Institute of Geography, Climatology and Meteorology and NCCR Climate, University of Bern, Hallerstrasse 12, 3012 Bern, Switzerland
[3]Department of Meteorology and Earth and Environmental Systems Institute (EESI), Pennsylvania State University, University Park, PA16 802-5013, USA
[4]Faculty of Earth and Life Sciences, Vrije Universiteit Amsterdam, De Boelelaan 1085, 1081 HV Amsterdam, The Netherlands
[5]IPRC, SOEST, University of Hawaii, 2525 Correa Road, Honolulu, HI 96 822, USA

*Invited contribution by H. Goosse, one of the EGU Outstanding Young Scientist Award winners 2005

Received: 24 April 2006 – Published in Clim. Past Discuss.: 21 June 2006
Revised: 12 September 2006 – Accepted: 18 September 2006 – Published: 19 September 2006

Abstract. Proxy records and results of a three dimensional climate model show that European summer temperatures roughly a millennium ago were comparable to those of the last 25 years of the 20th century, supporting the existence of a summer "Medieval Warm Period" in Europe. Those two relatively mild periods were separated by a rather cold era, often referred to as the "Little Ice Age". Our modelling results suggest that the warm summer conditions during the early second millennium compared to the climate background state of the 13th–18th century are due to a large extent to the long term cooling induced by changes in land-use in Europe. During the last 200 years, the effect of increasing greenhouse gas concentrations, which was partly levelled off by that of sulphate aerosols, has dominated the climate history over Europe in summer. This induces a clear warming during the last 200 years, allowing summer temperature during the last 25 years to reach back the values simulated for the early second millennium. Volcanic and solar forcing plays a weaker role in this comparison between the last 25 years of the 20th century and the early second millennium. Our hypothesis appears consistent with proxy records but modelling results have to be weighted against the existing uncertainties in the external forcing factors, in particular related to land-use changes, and against the uncertainty of the regional climate sensitivity. Evidence for winter is more equivocal than for summer. The forced response in the model displays a clear temperature maximum at the end of the 20th century. However, the uncertainties are too large to state that this period is the warmest of the past millennium in Europe during winter.

Correspondence to: H. Goosse
(hgs@astr.ucl.ac.be)

1 Introduction

The analysis of climate variations during the past millennium can help to establish whether or not late 20th century warmth is unusual in a long-term context. Such an analysis can, in turn, help inform any determination of the relative roles of human activities and natural processes to the recent observed warming (e.g., Stott et al., 2000; Hegerl et al., 2003). At the Northern Hemisphere scale, the available annual mean temperature reconstructions reveal that the last decade of the 20th century has been likely the warmest period of the past thousand years (Jones and Mann, 2004; Moberg et al., 2005; Osborn and Briffa, 2006). The increase of atmospheric greenhouse gas concentrations over the past two centuries appears to have played an essential role in this recent warming (Tett et al. 1999; Stott et al., 2000; Hegerl et al., 2003).

Roughly one thousand years ago, some regions such as Europe, may also have exhibited relatively mild conditions, although the geographical extent of the warm conditions during this period was smaller than during the 20th century (Lamb, 1965; Hughes and Diaz, 1994; Pfister et al., 1998;

Bradley et al., 2003; Osborn and Briffa, 2006). This has led to the introduction of the term "Medieval Warm Period" or "Medieval Warm Epoch", which originated from the examination of primarily western European documentary proxy evidence (Lamb, 1965). The underlying cause for this apparent warm period in Europe has remained unclear. Furthermore, as it preceded the modern rise in anthropogenic greenhouse gas concentrations, the existence of such a past period of warmth provides a classical counterargument against anthropogenic impacts on modern climate change. In this context, the goal of the present study is to describe a plausible explanation of the causes of those particular conditions that likely occurred in Europe at the beginning of the second millennium.

In a larger framework, it is also important to analyze past temperature variations at the regional scale (e.g., European region) because many human activities, human health, phenological aspects and climate extremes are not influenced by hemispheric-scale, annual mean temperature but by the regional variations during the various seasons (Berger and McMichael, 1999; Luterbacher et al., 2004; Thomas et al., 2004; Xoplaki et al., 2005; Casty et al., 2005). Analyses at regional scales are often hampered by the paucity of available data, and by a high degree of spatial and temporal variability which tends to obscure any underlying climate change signal. However, recent continental-scale seasonal multi-proxy-based climate reconstructions spanning the past centuries have been performed (Luterbacher et al., 2004; Xoplaki et al., 2005; Guiot et al., 2005; Pauling et al., 2006). Moreover, simulations of European-scale temperature change can now be obtained using climate models driven by estimated past radiative forcing changes. Those simulations still have clear limitations because of the relatively coarse resolution used and of the uncertainties on past changes in external forcing as well as in the internal climate sensitivity. Nevertheless, the analysis of those simulations provides a very useful possibility to examine the causes of past seasonal temperature changes in Europe, including the enigmatic European "Medieval Warm Period" of roughly one thousand years ago.

While climate reconstructions are required for an estimation of the level of past climate variability, they can not be used directly to assess the physical causes of the recorded temperature variations. For this purpose, climate model simulations that are forced by estimates of past natural and anthropogenic radiative perturbations may be used. Therefore, we apply here the ECBILT-CLIO-VECODE global climate model of intermediate complexity to identify the causes of European climate change over the past millennium. A brief description of the model and forcing is provided in Sect. 2. In addition to the classical model-data comparison, we also use the technique recently proposed by Goosse et al. (2006) to obtain an estimate of the state of the climate system that is compatible with the real observed changes as well as with model physics and forcing in Sect. 3. Section 4 is devoted to a description of the climate of the past millennium over Europe while Sect. 5 investigates the causes of the simulated changes. In Sect. 6, the regional distribution of the signal is analysed, before the conclusions.

2 Model and forcing description

The version of the model ECBILT-CLIO-VECODE used here is identical to the one used in some recent studies (Goosse et al., 2005a, b, 2006; Renssen et al., 2005), but a brief description is given here for the reader's convenience. The atmospheric component is ECBILT2 (Opsteegh et al., 1998), a quasi-geostrophic model with a resolution of 5.6 degree in latitude, 5.6 degree in longitude and 3 level in the vertical. To close the momentum budget near the equator, a parameterization of the ageostophic terms is included. The oceanic component is CLIO3 (Goosse and Fichefet, 1999) that is made up of an ocean general circulation model coupled to a comprehensive thermodynamic-dynamic sea ice model. ECBILT-CLIO is coupled to VECODE, a dynamic global vegetation model that simulates dynamics of two main terrestrial plant functional types, trees and grasses, as well as desert (Brovkin et al., 2002). More information about the model and a complete list of references is available at http://www.knmi.nl/onderzk/CKO/ecbilt-papers.html.

We have performed a total of 125 simulations with the model driven by both natural and anthropogenic forcings (Fig. 1 and Table 1). An existing ensemble of 115 simulations (Goosse et al., 2005b, 2006), covering at least the period 1001 AD-2000AD, is first presented (35 simulations starting in 1 AD, 30 starting in 851 AD and 50 starting in 1001 AD). The forcing due to long-term changes in orbital parameters follows Berger (1978) and the observed evolution of greenhouse gases is imposed over the whole simulated period. Furthermore, the influence of sulphate aerosols due to anthropogenic activity is taken into account during the period 1850–2000 AD through a modification of surface albedo (Charlson et al., 1991). In ECBILT-CLIO-VECODE, we only take into account the direct effect of aerosols. This forcing is thus probably underestimated, but given the uncertainty in the indirect aerosol forcing it is difficult to quantify the magnitude of this underestimation. In addition, the forcing due to changes in land-use is applied here through modifications in the surface albedo, which is the primary effect of land cover change (Matthews et al., 2004). Furthermore, the evolution of solar irradiance and the effect of volcanism are prescribed using different combinations of the available reconstructions, in order to include the uncertainties associated with those forcings (Table 1). The ensemble members differ only in their initial conditions which were extracted from previous experiments covering the past millennia. The different initial conditions represent climate states separated by 150 years. Due to the fact that each of the ensemble members generates an independent realization of internal climate variability, computing the ensemble mean filters out internal

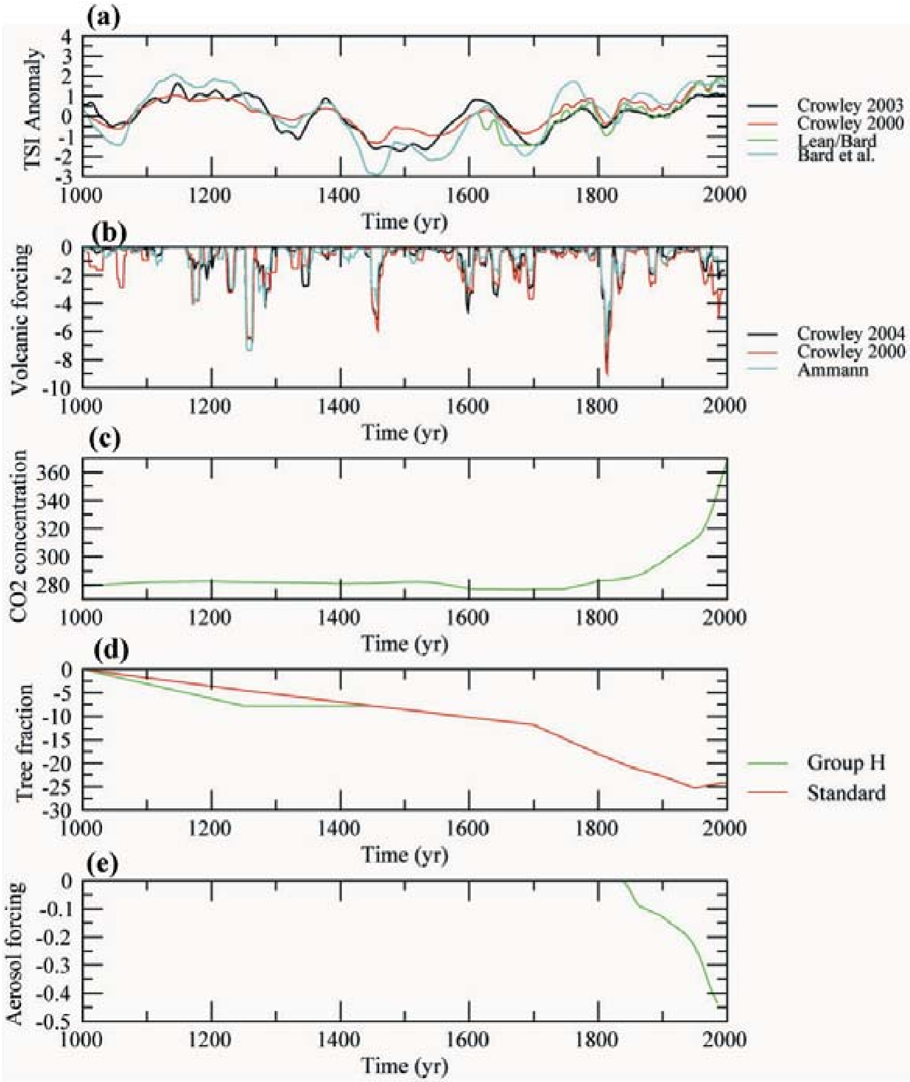

Fig. 1. **(a)** Time variations of solar irradiance (W/m2) at the top of the atmosphere following the reconstructions of Lean et al. (1995) (green), Bard et al. (2000), (turquoise), Crowley (2003) (black) and Crowley (2000) (red). **(b)** Time variations of volcanic forcing (W/m2) scaled as an effective change in solar irradiance for comparison with (a), following the reconstructions of Crowley (2000) (red), Crowley(2003) (black) and Ammann (as described in Jones and Mann (2004), turquoise). **(c)** Time variations CO2 concentration (in ppmv) imposed in our simulation. The time variations of the other greenhouse gases used in the model are not shown here. **(d)** Decrease in the fraction of the surface occupied by forest (in %) averaged over Europe imposed in the simulations as a result of land-use change. The red line corresponds to the scenario used in all the experiments except those of group H (green line). **(e)** Annual mean forcing at the top of the atmosphere (W/m2) caused by the increase in aerosol load. A 10-year running mean has been applied to the time series in order to highlight low frequency variations.

variability and leaves the joint response to the external forcing. (See Goosse et al., 2005b, for more details as well as for a discussion of the impact of the choice of the reconstruction of the solar and volcanic forcing on global surface temperature).

The past evolution of land use is not precisely known and, to our knowledge, comprehensive reconstructions of crop area are only available back to 1700 AD for Europe (Ramankutty and Foley, 1999; Goldewijk, 2001). In the 115 simulations described above, we follow for the earlier period the scenario used in a recent intercomparison exercise (Brovkin et al., 2006) that is based on Ramankutty and Foley (1999) and assumes a linear increase of crop area from zero in 1000 AD to the value reconstructed for 1700 AD. This is of course a strong simplification. In particular, it is well known that, in a large number of regions of France, Belgium, Netherlands, Germany, which are among the European countries where the largest changes occurred in Eu-

Table 1. Description of the experiments (updated from Goosse et al., 2005b).

Number of experiments	Symbol of the group	Starting date	Forcing Solar	Volcanic
25	K	1000 AD	Lean et al. (1995)/Bard et al. (2000)[1]	Crowley (2000)
25	C	1000 AD	Crowley (2000)	Crowley (2000)
35	D	1 AD	Crowley at al. (2003)	Crowley at al. (2003)
15	B	850 AD	Lean et al. (1995)/Bard et al. (2000)[1]	Crowley at al. (2003)
15	M	850 AD	Bard et al. (2000)[1]	Amman (cited in Jones and Mann, 2004)
10	H[2]	1 AD	Crowley at al. (2003)	Crowley at al. (2003)

[1] We are using the reconstruction of Bard et al. (2000) scaled to match the Maunder Minimum irradiance reduction derived by Lean et al. (1995).
[2] This new set of experiments uses the same solar and volcanic forcing as the one of group D but a different scenario for land-use changes that implies a faster deforestation rate during the period 1000–1250 AD.

rope in pre-industrial times, deforestation was particularly intense between 1000 and 1250 AD and weaker during the two following centuries (Goudie, 1993; Simmons, 1996; Steurs, 2004; Guyotjeannin, 2005). In order to estimate the impact of those uncertainties in the timing of land-cover changes, we have tested here another simple scenario in a new ensemble of 10 experiments. The crop fraction increases first linearly during the period 1000–1250 AD, reaching in 1250 AD the value imposed in 1450 AD in the standard scenario (i.e., representing enhanced deforestation during the period 1000–1250 AD). It remains constant during the period 1250–1450 AD and then follows the standard scenario. In those experiments (hereafter referenced as group H, Table 1), the same solar and volcanic forcing are used as in experiments of group D. The comparison of the two ensembles provides thus a direct estimate of the impact of the uncertainties in past land-cover changes. As expected, in the new set of experiments, the ensemble mean temperature tends to be lower during the period 1000–1450 AD. The maximum of the difference occurs in summer, around 1300 AD and reaches 0.1°C (Fig. 2).

Furthermore, in the framework of this study, additional ensembles of experiments covering the period 1001–2000 AD are performed with ECBILT-CLIO-VECODE driven by only one forcing at a time in order to analyze the role of the various forcing components. For each forcing, an ensemble of 10 experiments has been launched, corresponding thus to 60 new experiments. Here, the land use change forcing includes the so-called biogeophysical aspects, i.e. the one related to the changes in the physical characteristics of the surface. The biochemical part of the forcing, i.e. the changes in greenhouse gas concentration due to changes in land use, are taken into account in the run with greenhouse gas forcing since, as we do not have a carbon cycle model, it is not possible to disentangle the contribution of deforestation from the other ones.

ECBILT-CLIO-VECODE has a relatively weak climate sensitivity, with a 1.8°C increase in global mean temperature in response to a doubling of atmospheric CO_2 concentration. The global-mean response of the model to the forcing applied is thus generally in the lower range of the response that would be obtained by atmosphere-ocean general circulation models (AOGCMs) if they were forced by a similar forcing (Goosse et al., 2005b). This is to a large extent due to the very weak changes simulated in the tropical area while at mid-latitude the response ECBILT-CLIO-VECODE is close to the mean of AOGCMs (Selten, 2002; Petoukhov et al., 2005). Furthermore,the comparison of the results of ECBILT-CLIO-VECODE over the past millennium with various proxy records has shown that the model is able to reproduce the main characteristics of the reconstructed changes in the extra-tropics. Interestingly, the simulated variance over the last 500 years in Europe is very close to the one of the reconstruction of (Luterbacher et al., 2004) for summer, winter as well as for annual mean (Goosse et al., 2005a).

3 Selection of the best pseudo simulation and estimation of related uncertainty

For the analyses of temperature changes over Europe and for model data comparison we use here two continental-scale reconstructions (Luterbacher et al., 2004; Guiot et al., 2005) as well as summer temperature reconstructions for the Low Countries (i.e. Belgium and Netherlands) (Van Engelen et al., 2001; Shabalova and Van Engelen, 2003), the Czech Lands (Brázdil, 1996), Western Russia (Klimenko et al., 2001), Fennoscandia (Briffa et al., 1992), Swiss alpine regions (Büntgen et al., 2005) and Burgundy (Chuine et al.,

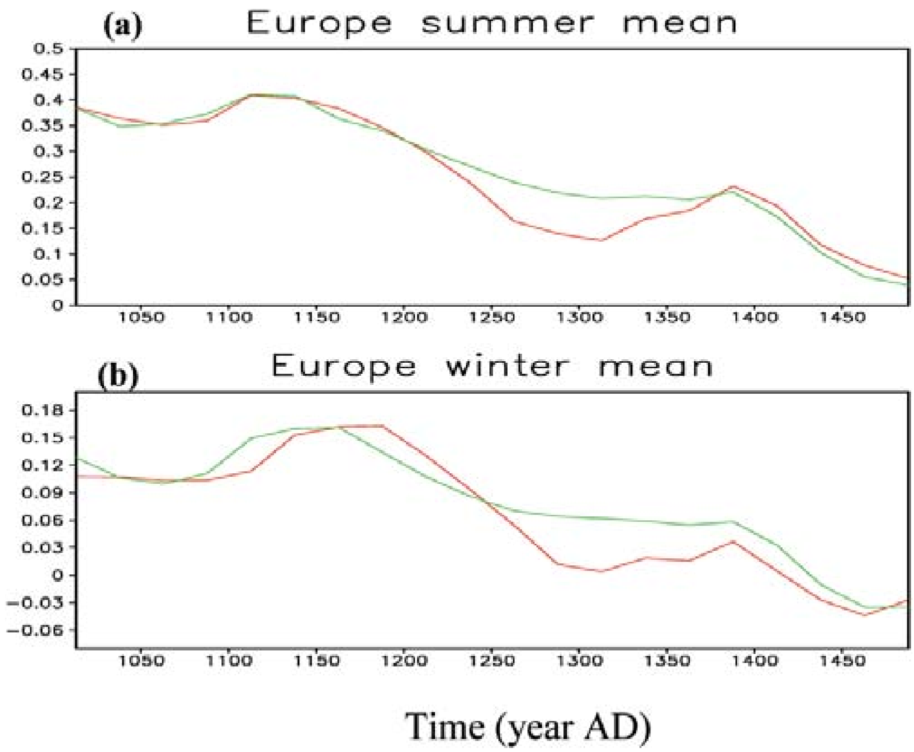

Fig. 2. Anomaly (in Kelvin) of the ensemble mean of **(a)** summer (JJA) and **(b)** winter (DJF) European temperatures averaged over the simulations of group H (in red) and group D (in green). Those two groups of simulation only differ in the scenario used for land-use changes. The times series plotted are averages over 25 seasons.

2004) and winter temperature in the Low Countries (Van Engelen et al., 2001; Shabalova and Van Engelen, 2003), the Czech Lands (Bràzdil, 1996), and Western Russia (Klimenko et al., 2001).

The difference between those reconstructions and an individual member of the ensemble of simulations could be due to a non-climatic signal recorded in the proxy as well as to uncertainties in the forcing or in the model formulation and to different realizations of the internal variability of the system in the model and in the real world. The latter source of discrepancy can be evaluated by plotting the range covered by all the simulations included in the ensemble (Goosse et al., 2005ab). If the reconstruction is out of this range during some periods, it means that no member of the ensemble is able to reproduce the reconstructed temperature anomaly. As a consequence, we must consider that the model and the reconstruction disagree on the temperature anomalies for those periods. If the empirical reconstruction is in this range, this does not necessarily imply that the model results are valid since the agreement could occur for incorrect reasons, but it implies that at least some simulations are compatible with the reconstruction.

Moreover, it is possible to go a step forward as described by Goosse et al. (2006), who propose to select among the ensemble of simulations the one that is the closest to the available reconstructions for a particular period (typically between 1 and 50 years). This is achieved by choosing the simulation that minimizes a cost function evaluated by computing the weighted sum of the squares of the difference between the value provided by the reconstruction and the simulated value in the model grid box(es) that contains the location of the proxy-record. The cost function measures thus the misfit between model results and proxy records. If the cost function is sufficiently low, the selected simulation is compatible with the reconstruction, with model physics and with the forcing used for the particular period. For plotting purposes, it is then possible to group the various states selected for all the periods of interest in order to obtain the best "pseudo simulation". Although the physical interpretation of some low frequency changes could be difficult with this technique, it has been shown that it can be efficiently used to provide temperature changes averaged over regions where a sufficiently large number of proxy-record is available (Goosse et al., 2006). It thus complementary to large-scale reconstructions obtained using statistical methods.

The applicability of this method has been assessed in Goosse et al. (2006) for test cases. Here, we apply it to European temperatures, using all the available information. In particular, this technique is used here to show first that it is possible to find one member of the ensemble that is

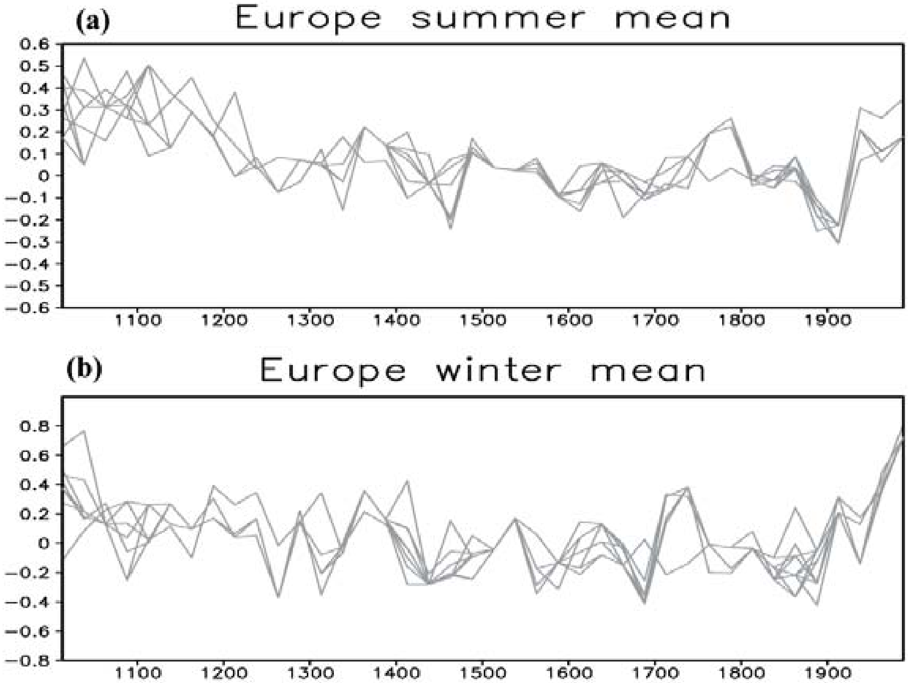

Fig. 3. Anomaly (in Kelvin) of **(a)** summer and **(b)** winter European temperatures in the 13 best "pseudo simulations" obtained by constraining the model results with all the 12 proxy records or using all the subsets containing 11 proxy records. The times series plotted are averages over 25 seasons.

consistent with the proxy records for any period, second to reconstruct the temperature evolution averaged over Europe during the past millennium and third to provide an estimate of the contribution of internal variability in the observed changes.

In the present framework, the cost function will be evaluated using the reconstructions listed above. All the individual reconstructions have the same weight in the evaluation of the cost function while reconstructions at the European scale have a weight 5 times stronger to take into account that they are derived from a compilation of a larger data set. As discussed in Goosse et al. (2006), the results are not sensitive to the selection of those weights.

The selected proxy records provide a sufficiently dense network to give useful information at the European scale. This could be illustrated by performing a test in which only local and regional proxy records are used to constrain model results but not the large-scale reconstructions. In this case, the best pseudo-simulation, using 25-year averages, has a correlation with the reconstruction of Luterbacher et al. (2004) of 0.43 and 0.66 over the period 1500–2000 for summer and winter mean, respectively. Those values are similar or higher than the correlation of the individual proxies with local temperature during the last 150 years. They are also much higher than the correlation between Luterbacher et al. (2004) and individual members of the ensemble that have values of 0.15 and 0.41 for summer and winter mean, respectively. This indicates that the technique is useful to get a better agreement between model results and the observed evolution at European scale. Of course, when all the proxy records and reconstructions are used to evaluate the cost function, the correlation between the best pseudo-simulation and the reconstruction of Luterbacher et al. (2004) is even higher, with values of 0.88, and 0.92 over the period 1500–2000 for summer and winter mean, respectively, using 25-year averages. We would like to emphasise that the reconstruction of Luterbacher et al. (2004) is not completely independent of the regional/local proxy used here as data from the Low Countries and partly from the Czech lands (only the non-continuous data from the 16th century and the winter of 1739/1740 have been used) were included in the large set of records used in Luterbacher et al. (2004). Nevertheless, additional sensitivity experiments have shown that if those records are not included in the analyses perform here, our conclusions concerning the validity of the method are not modified.

In order to estimate the uncertainties associated with the evaluation of the best simulation, we have repeated the procedure used to obtain the best pseudo-simulation removing one proxy at a time in the computation of the cost function (Fig. 3). This provides a total set of 13 alternative best pseudo-simulations. The standard deviation of these 13 time series reaches 0.11°C in summer and 0.16°C in winter at the beginning of the second millennium when the uncertainties in the proxies are large (i.e. 82% and 64% of the standard deviation of the whole ensemble), while the value of this standard deviation is at least a factor three smaller at the end of the simulations because of the better quality of the data. These values will be used when discussing the uncertainties associated to the best pseudo-simulation. The finite size of our ensemble of simulations could also lead to uncertainties in the selection of the best model state (Goosse et al., 2006). Nevertheless, the magnitude of this term is smaller than the one related to the choice of proxies illustrated above and will thus not be included in our discussions.

4 Climate of the past millennium averaged over Europe

European surface air temperatures have risen sharply during the second half of the 20th century, with a larger response in winter than in summer (Fig. 4) (Jones et al., 2003; Luterbacher et al., 2004). This induces a weakening of the seasonal range (defined as the difference between summer and winter temperatures) both in the model and in a land-area (25° W to 40° E and 35° N to 70° N) temperature reconstruction (Luterbacher et al., 2004) covering the last 500 years. For the mean of the ensemble of 125 simulations, this decrease reaches 0.5°C in Europe between 1800 and 2000 (Fig. 4c).

The ensemble mean summer and winter temperatures also display a long-term cooling trend from the beginning of the second millennium into the 19th century. Between 1000 and 1800 AD, the simulated cooling amounts to 0.3°C in winter and 0.4°C in summer. A recent reconstruction for European summer (April–September mean) climate (Guiot et al., 2005), representing the area of 10° W–20° E, 35° N–55° N for the period from 1100 AD to present day, is in the range of changes simulated within the ensemble of simulations. However, in contrast to model results, this reconstruction reveals a relatively stable summer climate without any indications for anomalous medieval summer warmth (Fig. 4a). On the other hand, available independent European regional proxy data (Fig. 5) exhibit a clearer trend towards warmer summer and winter temperatures during the period 1000–1300 than during the period 1500–1850. As a consequence, the mean over all those long proxy records documents warm climate conditions in Europe around 1000 AD that were similar to those of the last decades of the 20th century.

When using all the continental scale and local/regional scale reconstructions to select the model states, the best pseudo-simulation is, as expected, very close to Luterbacher et al. (2004) for the last 500 years (Fig. 4) and agrees well at local/regional scale with the proxy records for the whole second millennium (Fig. 6). These proxy records and the best pseudo-simulation indicate thus relatively mild conditions in Europe during the beginning of the second millennium. However, for the period 1000–1300, the best pseudo-simulation provides an average over Europe that is larger than the one provided by Guiot et al. (2005). It should however be noted that the uncertainty of the reconstructions is particularly large during the early stages of the reconstructions. In particular, the amount of documentary proxy information (e.g. Pfister et al., 1998; Brázdil et al., 2005) decreases back in time with larger associated uncertainties. Hence, an interpretation of these early records has to consider the relative uncertainty in terms of phase and amplitude.

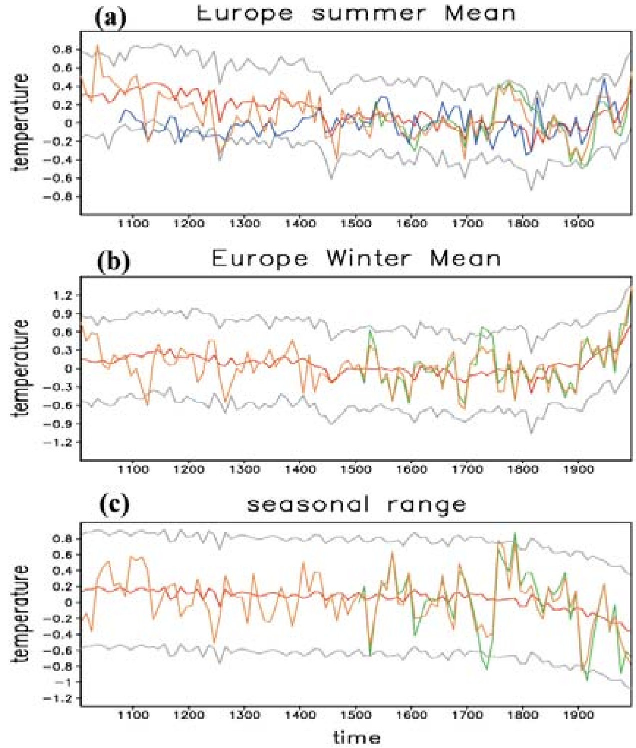

Fig. 4. Proxy-based reconstructions of European temperature anomaly (in Kelvin) during the period 1001–2000 AD compared with model results in **(a)** summer, **(b)** winter, and **(c)** the seasonal temperature range (summer minus winter). The time series plotted are averages over 10 seasons or years. The red line corresponds to the mean over the 125 simulations while the grey lines are the ensemble mean plus and minus two standard deviations of the ensemble at decadal scale. The reconstructions are in green (Luterbacher et al., 2004) and blue (Guiot et al., 2005). The best pseudo simulation is represented by the orange line. The reference period is 1500–1980, i.e. the longest period common to all the reconstructions.

5 Role of the forcings and internal variability

Additional experiments performed with ECBILT-CLIO-VECODE driven by only one forcing at a time are used to compare the simulated temperatures during three 25-year periods: the late 20th century (the years 1976–2000), the beginning of the 19th century (the years 1801–1925), which is one of the coldest periods for the ensemble mean in Europe, and the beginning of the 11th century (the years 1026–1050),

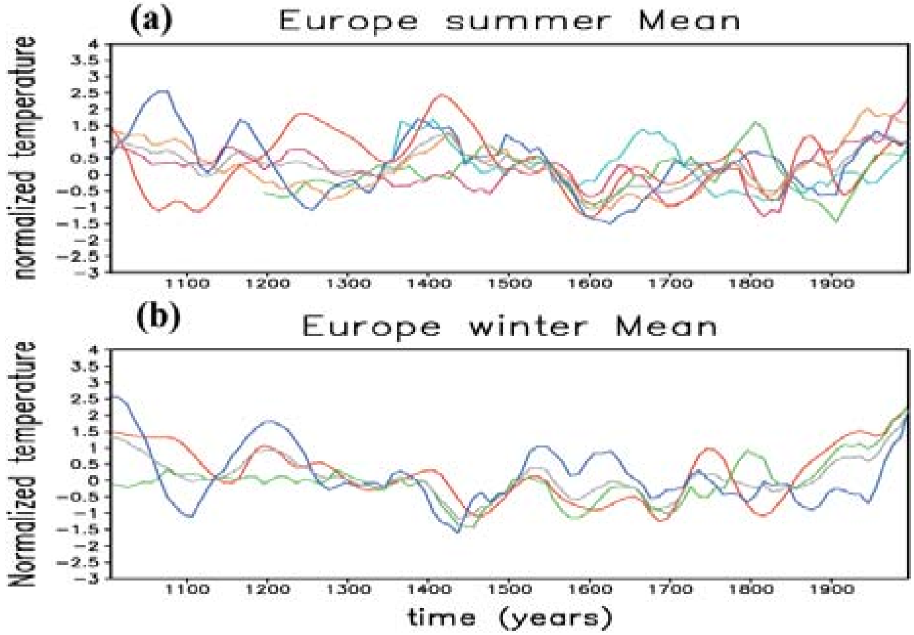

Fig. 5. Local and regional long proxy records of European seasonal temperatures **(a)** in summer and **(b)** in winter. The reference period is 1500–1980. Each proxy has been divided by its standard deviation. The time series plotted are averages over 10 seasons and, in addition, a five-point running mean is applied. In (a), the red, green, dark blue, light blue, pink and orange curves are related to temperature variations in the Low Countries (Belgium and Netherlands), Czech Lands, Western Russia, Burgundy, Swiss alpine area and Fennoscandia, respectively. In (b) the red, green and dark blue curves are related to temperature variation in the Low Countries (Belgium and Netherlands), Czech Lands and Western Russia respectively. The grey lines represent a mean over the records that go back to 1000 AD.

which is a relatively warm period (Fig. 7). This comparison reveals that, in ECBILT-CLIO-VECODE, the recent warming is mainly due to the increase of atmospheric greenhouse gas concentrations, while sulphate aerosol forcing reduces the warming significantly, in good agreement with previous modelling studies (Mitchell and Johns, 1997; Tett et al., 1999; Stott et al., 2000; Andreae et al., 2005). This cooling effect of the aerosols is larger in summer, as it mainly influences the net solar flux at the surface (Mitchell and Johns, 1997). The late 20th century reduction of the annual cycle amplitude is thus mostly due to the reduced summer warming effect of the aerosols and the increased winter warming triggered by greenhouse gases and amplified by positive climate feedbacks, such as the snow-albedo feedback (e.g., Manabe et al., 1992).

When comparing the periods 1026–1050 and 1976–2000 (Fig. 7b) a third anthropogenic radiative forcing – land use change – plays a dominant role in our simulations. Indeed, because of the large-scale changes in land use that occurred in Europe, the simulated European temperature has decreased during the past millennium by 0.5°C in summer and 0.4°C in winter between the periods 1026–1050 and 1976–2000. As a consequence, the total effect of all anthropogenic forcings is slightly negative in summer (though not significant at the 90% level) while it reached 0.3°C in winter in our simulations.

Solar and volcanic forcings have likely played a role in both global and regional changes observed during parts of the millennium (Robock, 2000; Shindell et al., 2001; Luterbacher et al., 2004; Xoplaki et al., 2005; Wagner and Zorita, 2005; Raible et al., 2006). However, using the forcing selected here, they could not have caused the simulated temperature differences between 1976–2000 and 1026–1050, in particular because both periods display a relatively high solar irradiance. On the other hand, the period 1801–1825 is characterised by strong volcanic activity and a negative solar irradiance anomaly compared to 1976–2000 (Fig. 1). As a consequence, those two forcings have contributed to the lower temperature during the period 1801–1825 compared to 1976–2000. However, the magnitude of the response to those forcings is still much smaller than the one to the greenhouse forcing over the same period. Temperature anomalies caused by the solar and volcanic forcings also contribute, in addition to the effect of land use change, to the lower temperature in the model during the period 1801–1825 than during the period 1026–1050. Finally, on these timescales, the role of orbital forcing is weak for Europe in our simulations, although its effect could be significant at large scales for specific months (Bauer and Claussen, 2006).

Except for the response associated with greenhouse gas forcing, the model's internal variability (measured by the standard deviation of the ensemble around the ensemble

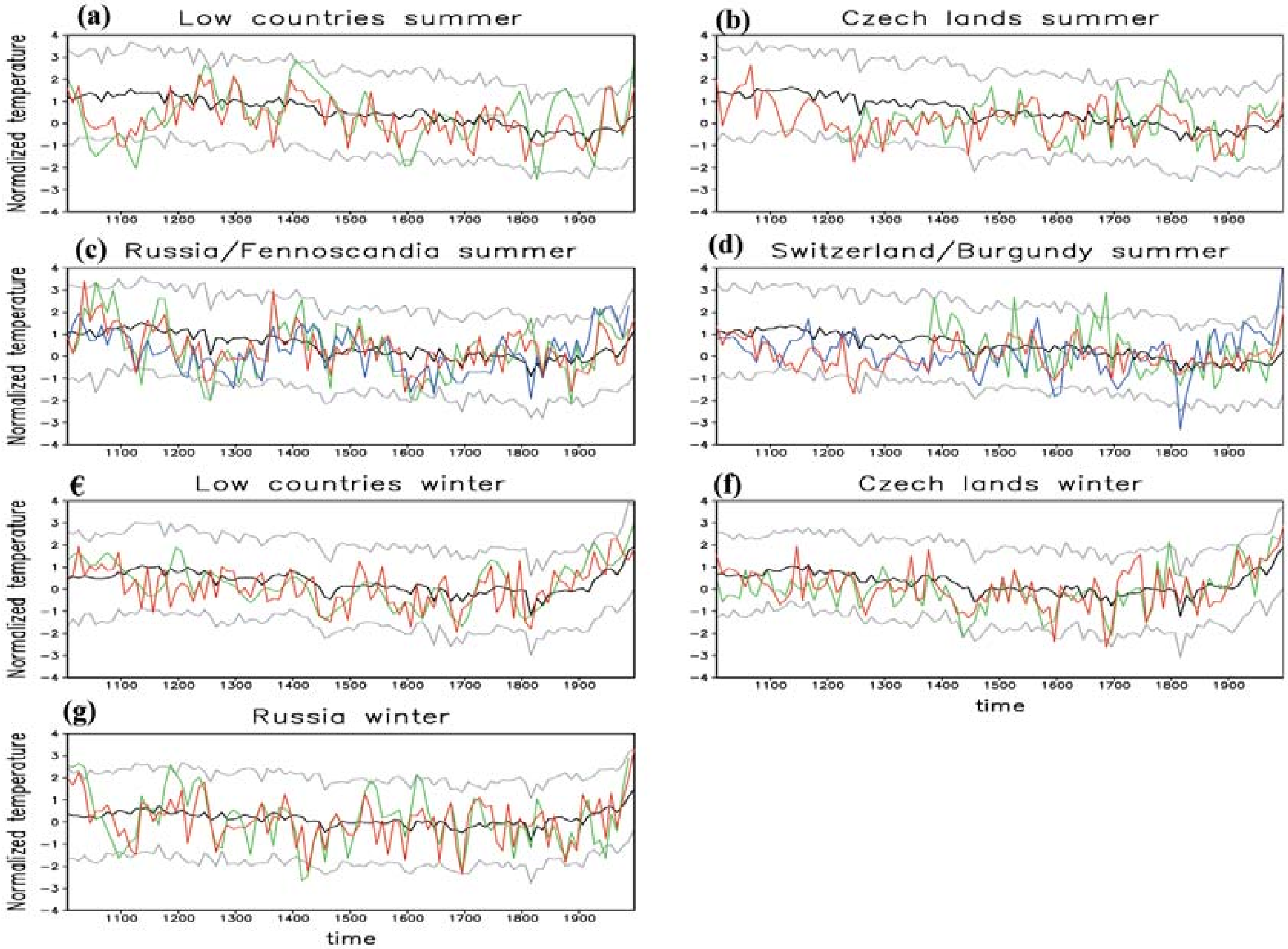

Fig. 6. Comparison of model results and proxy records in Europe during the period 1001–2000 AD. The times series plotted are averages over 10 seasons. The reference period is 1500–1980 AD. Model results and proxy have been divided by their standard deviations. The black line corresponds to the mean over the 125 simulations while the grey lines are the ensemble mean plus and minus two standard deviations of the ensemble at decadal scale. Proxy records are in green and blue. Shown is the compilation of temperature in summer **(a)** for the Low Countries (Belgium and Netherlands), **(b)** the Czech Lands, **(c)** Western Russia in green and Fennoscandia in blue, **(d)** Swiss alpine regions in blue and Burgundy in green and in winter in **(e)**, the Low Countries (Belgium and Netherlands), **(f)** the Czech Lands, and **(g)** Western Russia. The model states that are the closest to all the available proxies are represented by the red lines (i.e., the best pseudo simulation). Regions that are very close to each other like Western Russia/Fennoscandia and Swiss alpine Region/Burgundy are shown on the same panel.

mean) is of the same order of magnitude or larger than the response to individual forcing (Fig. 7). As a consequence, internal variability could be responsible to a large extent to the anomaly observed during some periods (e.g. Goosse et al,. 2005a; Hunt, 2006). Nevertheless, it is not the case in our simulations when comparing the summer temperatures of the years 1976–2000 and 1026–1050. These two periods must thus be considered as having similar simulated anomalies mainly because they exhibit nearly the same net radiative forcing.

In winter, the difference in the forced response between the periods 1976–2000 and 1026–1050 is larger than in summer as it amounts to 1.0 standard deviation of the internal ensemble variability. When using the available proxy records to derive the best pseudo-simulation, the estimated range is reduced by 36%. The difference between those two periods reaches then 1.3 times the standard deviation of the best pseudo-simulation. This indicates that, in winter, due to the large warming during the 20th century, the simulated forced response of the system reached a clear maximum at the end of the second millennium. Nevertheless, based on our results, the uncertainty is still too large to reject at the 90% confidence level the null-hypothesis that European winter temperatures during the late 20th century were similar from those of the early second millennium. In other words, it is possible to obtain warmer simulated temperatures for the

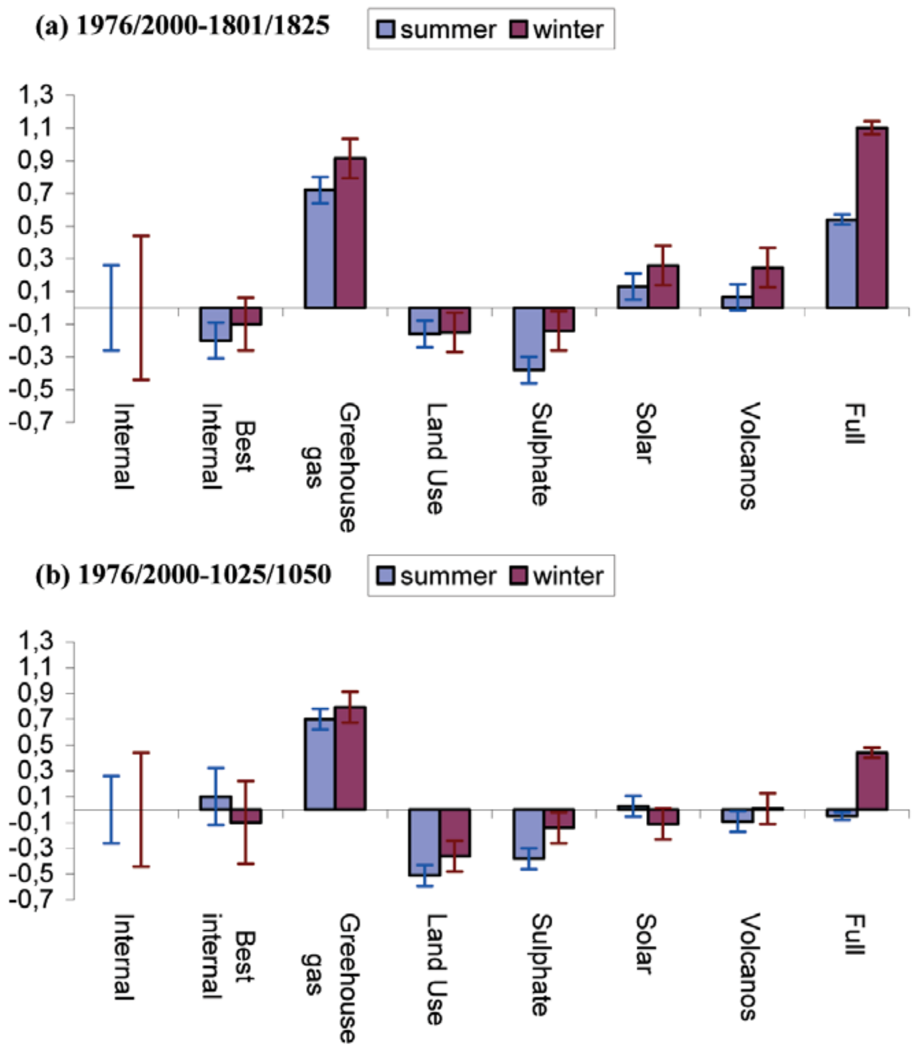

Fig. 7. Identification of the various contributions to the difference between simulated temperatures (in Kelvin) for the period 1976–2000 and **(a)** the period 1801–1825 and **(b)** the period 1025–1050. The range associated with the contribution of internal variability is given by two standard deviations of the ensemble of simulations around the ensemble mean. The best estimate of the internal variability is evaluated as the difference between the best pseudo-simulation and the ensemble mean, using the uncertainty on this best pseudo-simulation. The contributions of the individual forcings are obtained by performing an ensemble of 10 experiments with only one of the 6 forcing studied. The error bar for those forcings is evaluated by computing two standard deviations of the difference between two 25-year periods in a long experiment without any change in external forcing, using an ensemble of 10 simulations. The ensemble mean, using the whole set of forcings, is presented at the right (Full). The response to orbital forcing is not displayed on this figure as we found no significant difference between the periods considered here in our simulations using only this forcing.

period 1026–1050 than in 1976–2000 while being in reasonable agreement with the proxy data used to constrain model results. We thus cannot reasonably state that, in Europe during winter, the period 1976–2000 is warmer than 1026–1050.

On the other hand, compared to the early second millennium, the difference in forced signal between the early 19th century and the late 20th century is more pronounced, because several forcings (i.e., greenhouse gas, volcanic and solar forcings) tend to induce a perturbation of the same sign and the land-use changes were smaller between the 19th and 20th centuries. For the 25-year mean, the difference in the ensemble mean is much larger than the internal variability of the model, reaching 2.1 and 2.5 standard deviations of the ensemble for summer and winter, respectively. This is in good agreement with recent studies that were able to detect the warming effect of increasing greenhouse gas concentrations during the twentieth century in Europe (Zwiers and Zhang, 2003; Stott, 2003).

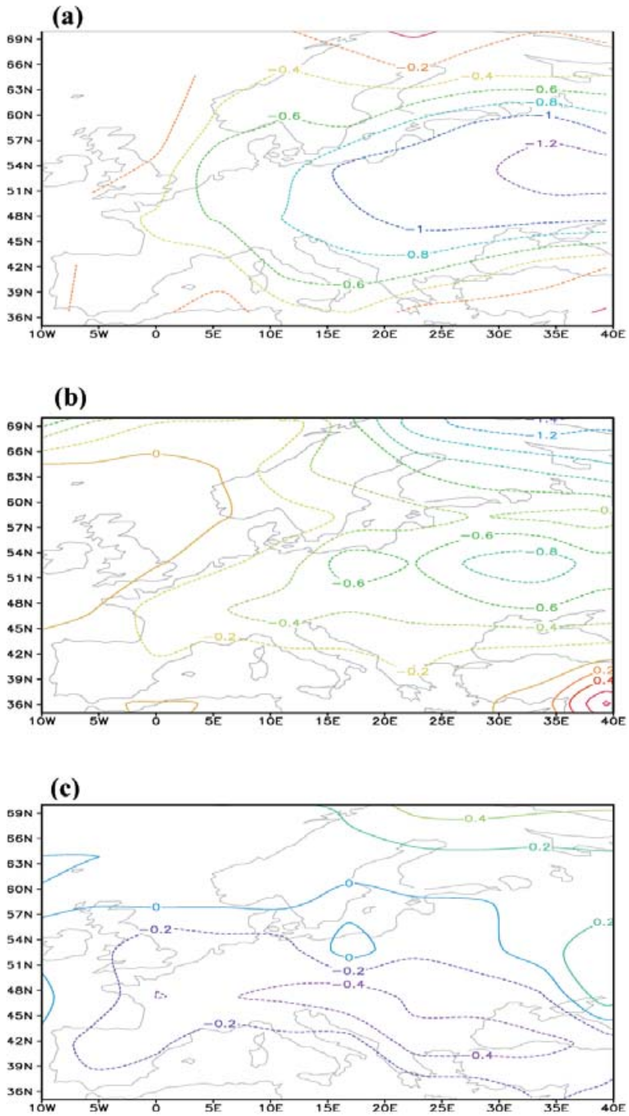

Fig. 8. Geographical distribution of the changes in seasonal range (summer minus winter) between different periods. Shown is **(a)** the difference between the period 1950–2000 and 1500–1900 in the reconstruction of Luterbacher et al. (2004) and **(b)** in ECBILT-CLIO-VECODE for the same periods and **(c)** in ECBILT-CLIO-VECODE for the difference between the period 1801–1825 compared to 1025–1050.

6 Regional distribution of the temperature response

The geographical distribution of the response to an external forcing is largely influenced by internal dynamics (e.g., Manabe et al., 1992). On the one hand, because of the feedback related to snow and ice, the response to a forcing tends to be larger at high latitudes in winter than at low latitudes. On the other hand, processes mainly related to the freshwater cycle, in particular to changes in soil moisture, tend to amplify the summer response in Southern Europe. Consequently, the reduction in the seasonal contrast during the last centuries is

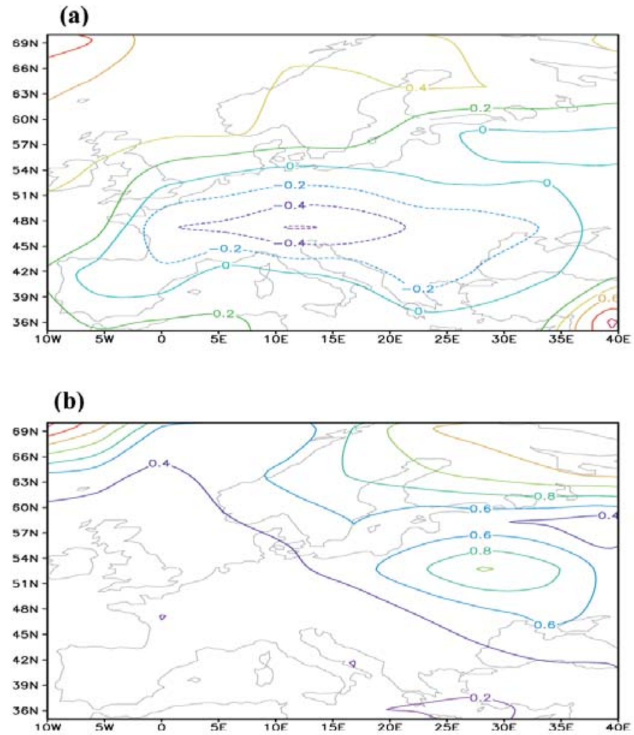

Fig. 9. Difference between ensemble mean temperatures in 1976–2000 compared to 1025–1050 in **(a)** summer and **(b)** winter.

large at high latitudes while in Southern Europe the decrease in the amplitude of the annual cycle is smaller (Fig. 8). The model displays a pattern similar to the one found by Luterbacher et al. (2004) but the amplitude is larger for the latter. However, we must take into account that we are comparing an ensemble mean for the model and a particular realisation of the climate evolution in the reconstruction. We have used in this model-data comparison relatively long periods, in order to limit the amplitude of internal variability compared to the forced one, but this still precludes a detailed quantitative comparison. Nevertheless, the changes in the observed seasonal contrast shown in Fig. 8a are larger than two standard deviations of the seasonal contrast for 50-year averages in all the land areas between 5°–40° E and 40°–60° N. The observed reduction is thus also a robust feature of the reconstruction.

In addition to the role of internal dynamics, the various forcings also have an impact on the geographical distribution of the response. In particular, the forcing due to land-use changes is strong in mid-latitudes, particularly in France and Germany. This results in a larger cooling in those regions during the pre-industrial period. As the response to this forcing tends to be stronger in summer, this is also implies a reduction of the seasonal contrast during this period in those regions (Fig. 8c). The aerosol forcing has also a clear spatial pattern with a larger cooling at mid-latitudes, downstream of the main industrial areas in Europe (Mitchell and Johns, 1997).

As a consequence, an analysis of the difference in the ensemble mean response in ECBILT-CLIO-VECODE for different regions between the late 20th century and the beginning of the millennium (Fig. 9) shows a general warming in winter with a maximum is Eastern Europe. In contrast, for summer, a weak warming is found only at high latitudes while the late 20th century is colder than the early second millennium in mid latitudes.

7 Conclusions

The model used here has a coarse resolution and includes some simplifications in order to be able to make a large number of long simulations. The local features should thus not be considered as robust features and even at continental scale our results should be considered with caution. Ideally, regional models should be used to confirm our conclusions but this is not yet technically possible. The magnitude of the response is also influenced by the model sensitivity and by the uncertainties in the forcing applied. This is especially valid for the scenario of land uses change that must be set up using very crude approximations. Nevertheless, as discussed above, the model results at European scale, both for summer and winter, appear consistent with empirical reconstructions as well as with our present knowledge of forcing time series and of the response to those forcings. We could thus provide a reasonable hypothesis about the evolution of the warm and cold season temperatures at European scale during the past millennium as well as the possible causes of those changes. This hypothesis could then be tested when new information will be available.

In agreement with previous studies, our results show a clear increase in European temperature during the last 150 years. This is mainly caused by the warming effect of the increase in greenhouse gas concentrations, which is only partly compensated by the cooling effect associated with the increase in sulphate aerosol load. Nevertheless, in contrast to hemispheric-scale annual temperatures, there is no compelling evidence from either empirical proxy evidence or model simulation results that the European summer temperature during the last 25 years of the 20th century were the highest of the past millennium. This is largely due to the local negative radiative forcing caused by land-cover changes. The impact of this forcing at hemispheric scale has been underlined in recent studies. However, because of the large deforestation in Europe, land-use changes imply a larger negative temperature anomaly over Europe than on a global scale (e.g., Bertrand et al., 2003; Bauer et al., 2003; Matthews et al., 2004; Feddema et al., 2005; Brovkin et al., 2006). The term "Medieval Warm Period", of limited meaning at hemispheric scale (Jones and Mann, 2004; Bradley et al., 2003; Goosse et al., 2005a; Osborn and Briffa, 2006), nonetheless thus appears reasonable as applied specifically to summer European temperatures, the region the term was originally applied to. In winter, our results are less definitive, and firm conclusions are not possible. Indeed, because of the large warming during the 20th century, the simulated forced response of the system reached a clear maximum at the end of the second millennium. Nevertheless, the uncertainties are still too large to argue with a reasonable confidence that the highest winter temperatures of the past millennium were observed during this period.

The contribution of orbital forcing has been relatively small for the last 1000 years, leading to temperature changes averaged over Europe smaller than 0.15°C for all seasons. For the last 6000 years, however, a reduction of northern hemispheric summer insolation leads to a summer cooling for Europe of more than 1.5°C as documented by a transient Holocene simulation performed with ECBILT-CLIO-VECODE (Renssen et al., 2005). The winter temperatures are more stable in the model. Therefore, on long time-scales as well, the summer temperatures and seasonal contrast of European temperatures has been decreasing. This simulated summer temperature decrease is in good agreement with previous modelling studies (e.g., Masson et al., 1999) and with available proxy records over the European continent which generally exhibit a decrease of summer temperature over the last 6000 years, except for the areas close to the Mediterranean regions (e.g., Davies et al., 2003; Kim et al., 2004).

However, in the decades to come, the evolution of the European temperatures could be quite different since the forcings during the twenty-first century will be different from the ones experienced in the past. First, at the century time scale, the orbital forcing is very weak and can be neglected. Secondly, in Europe, a small reduction of crop area and an increase in forest cover is expected, in contrast to the changes that occurred during the second millennium (e.g., Sitch et al., 2005). Finally, the concentration of greenhouse gases in the atmosphere will almost certainly continue to increase while the aerosol load will likely level off and even decrease (Andreae et al., 2005). As a consequence, the summer and winter European temperatures for the late 21st century are anticipated to greatly exceed the warmth of the past century (Räisänen et al., 2005; Déqué et al., 2006), and thus any period of the past millennium.

Acknowledgements. The authors would like to thank the scientists that made available all their datasets. H. Goosse is Research Associate with the Fonds National de la Recherche Scientifique (Belgium) and is supported by the Belgian Federal Science Policy Office. H. Renssen is sponsored by the Netherlands Organization for Scientific Research (N.W.O). A. Timmermann is supported by the Japan Agency for Marine-Earth Science and Technology (JAMSTEC) through its sponsorship of the International Pacific Research Center. J. Luterbacher, E. Xoplaki and N. Riedwyl are supported by the Swiss National Science Foundation (NCCR Climate). E. Xoplaki and J. Luterbacher were also financially supported he EU project SOAP. M. E. Mann was supported by the U.S. NSF- and NOAA-sponsored Earth System History program.

Edited by: V. Masson-Delmotte

References

Andreae, M. O., Jones, C. D., and Cox, P. M.: Strong present-day aerosol cooling implies a hot future, Nature, 435, 1187–1190, 2005.

Bard, E., Raisbeck, G., You, F., and Jouzel, J.: Solar irradiance during the last 1200 years based on cosmogenic nuclides, Tellus, 52B, 985–992, 2000.

Bauer E., Claussen, M., Brovkin, V., and Huenerbein, A.: Assessing climate forcings of the Earth system for the past millennium, Geophys. Res. Lett., 30, 1276, doi:10.1029/2002GL016639, 2003.

Bauer, E. and Claussen, M.: Analyzing seasonal temperature trends in forced climate simulations of the past millennium, Geophys. Res. Lett., 33, L02702, doi:10.1029/2005GL024593, 2006.

Berger, A. L.: Long-term variations of daily insolation and Quaternary climatic changes, J. Atmos. Sci., 35, 2363–2367, 1978.

Berger, A. and McMichael, A. J.: Climate change and health: evidence and prospect, European Review, 7, 395–412, 1999.

Bertrand, C., Loutre, M.-F., Crucifix, M., and Berger, A.: Climate of the last millennium: a sensitivity study, Tellus, 54A, 221–244, 2002.

Bradley, R. S., Hughes, M. K., and Diaz, H. F.: Climate in Medieval time, Science, 302, 404–405, 2003.

Brázdil, R.: Reconstructions of past climate from historical sources in the Czech Lands, in: Climatic Variations and Forcing Mechanisms of the Last 2000 Years, edited by: Jones, P. D., Bradley, R. S., and Jouzel, J., NATO ASI Series, Springer, Berlin, Heidelberg, New York, 1996.

Bràzdil, R., Pfister, C., Wanner, H., von Storch, H., and Luterbacher, J.: Historical climatology in Europe – The State of the Art, Clim. Change, 70, 363–430, 2005.

Briffa, K. R., Jones, P. D., Bartholin, T. S., Eckstein, D., Schweingruber, F. H., Karlén, W., Zetterberg , P., and Eronen, M.: Fennoscandian summers from AD 500: temperature changes on short and long timescales, Clim. Dyn., 7, 111–119, 1992.

Brovkin, V., Bendtsen, J., Claussen, M., Ganopolski, A., Kubatzki, C., Petoukhov, V., and Andreev, A.: Carbon cycle, vegetation and climate dynamics in the Holocene: experiments with the CLIMBER-2 model, Global Biogeochem. Cycles, 16(4), 1139, doi:10.1029/2001GB001662, 2002.

Brovkin, V., Claussen, M., Driesschaert, E., Fichefet, T., Kicklighter, T., Loutre, M.-F., Matthews, H. D., Ramankutty, N., Schaeffer, M., and Sokolov, A.: Biogeophysical effects of historical land cover changes simulated by six Earth system models of intermediate complexity, Clim. Dyn., 26, 587–600, 2006.

Büntgen, U., Esper, J., Frank, D. C., Nicolussi, K., and Schmidhalter, M.: A 1052-year tree-ring proxy for Alpine summer temperatures, Clim. Dyn., 25, 141–153, 2005.

Casty, C., Wanner, H., Luterbacher, J., Esper, J., and Bohm, R.: Temperature and precipitation variability in the European Alps since 1500, Int. J. Climatol., 25, 1855–1880, 2005.

Charlson, R. J., Langner, J., Rodhe, H., Leovy, C. B., and Warren, S. G.: Perturbation of the Northern Hemisphere radiative balance by backscattering from anthropogenic sulfate aerosols, Tellus, 43AB, 152–163, 1991.

Chuine, I., You, P., Viovy, N., Seguin, B., Daux, V., and Le Roy Ladurie, E.: Grape ripening as a past climate indicator, Nature, 432, 289–290, 2004.

Crowley, T. J.: Causes of climate change over the past 1000 years, Science, 289, 270–277, 2000.

Crowley, T. J., Baum, S. K., Kim, K. Y., Hegerl, G. C., and Hyde, W. T.: Modeling ocean heat content changes during the last millennium, Geophys. Res. Lett., 30, 1932, doi:10.1029/2003GL017801, 2003.

Davis, B. A. S., Brewer, S., Stevenson, A. C., Guiot, J., and Data Contributors.: The temperature of Europe during the Holocene reconstructed from pollen data, Quat. Sci. Rev., 22, 1701–1716, 2003.

Déqué, M., Jones, R. G., Wild, M., et al.: Global high resolution versus Limited Area Model climate change projections over Europe: quantifying confidence level from Prudence results, Clim. Dyn., doi:10.1007/s00382-005-0052-1, 2006.

Esper, J., Cook, E. R., and Schweingruber, F. H.: Low-frequency signals in long tree-ring chronologies for reconstructing past temperature variability, Science, 295, 2250–2253, 2002.

Feddema, J., Olseson, K. Bonan, G., Mearns, L., Washington, W., Meehl, G., and Nychka, D. A.: Comparison of a GCM response to historical anthropogenic land cover change and model sensitivity to uncertainty in present-day land cover representation, Clim. Dyn., 25, 581–609, 2005.

Goldewijk, K. K.: Estimating global land use change over the past 300 years: The HYDE database, Global Biogeochem. Cycles, 15, 417–433, 2001.

Goosse, H. and Fichefet, T.: Importance of ice-ocean interactions for the global ocean circulation: a model study, J. Geophys. Res., 104, 23 337–23 355, 1999.

Goosse, H., Renssen, H., Timmermann, A., and Bradley, R. S.: Internal and forced climate variability during the last millennium: a model-data comparison using ensemble simulations, Quat. Sci. Rev., 24, 1345–1360, 2005a.

Goosse, H., Crowley, T., Zorita, E., Ammann, C., Renssen, H., and Driesschaert, E.: Modelling the climate of the last millennium: What causes the differences between simulations?, Geophys. Res. Lett., 32, L06710, doi:10.1029/2005GL22368, 2005b.

Goosse, H., Renssen, H., Timmermann, A., Bradley, R. S., and Mann, M. E.: Using paleoclimate proxy-data to select optimal realisations in an ensemble of simulations of the climate of the past millennium, Clim. Dyn., 27, 165–184, 2006.

Goudie, A.: The human impact on the natural environment, Blackwell Publishers, Oxford, UK, forth edition, 454 p., 1993.

Guiot, J., Nicault, A., Rathgeber, C., Edouard, J. L., Guibal, F., Pichard, G., and Till, C.: Last-millennium summer-temperature variations in Western Europe based on proxy-data, The Holocene, 15(4), 489–500, 2005.

Guyotjeannin, O.: Atlas de l'histoire de France, IX^e–XV^e siècle, la France médiévale, Editions Autrement, 2005.

Hegerl, G. C., Crowley, T. J., Baum, S. K. Kim, K.-Y., and Hyde, W. T.: Detection of volcanic, solar and greenhouse gas signals in paleo-reconstructions of Northern Hemispheric temperature, Geophys. Res. Lett., 30, 1242, doi:10.1029/2002GL016635, 2003.

Hughes, M. K. and Diaz, H. F.: Was there a "Medieval Warm Period", and if so, where and when?, Clim. Change, 26, 109–142, 1994.

Hunt, B. G.: The Medieval Warm Period, the Little Ice Age and simulated climatic variability, Clim. Dyn., doi:10.1007/s00382-002-0299-8, 2006.

Jones, P. D. and Mann, M. E.: Climate over past millennia, Rev. Geophys., 42(2), RG2002, doi:10.1029/2003RG000143, 2004.

Jones, P. D, Briffa, K. R., and Osborn, T. J.: Changes in the Northern Hemisphere annual cycle: implications for paleoclimatology, J. Geophys. Res., 108(D18), 4588, doi:10.1029/2003JD003695, 2003.

Kim, J. H., Rimbu, N., Lorenz, S. J., Lohmann, G., Nam, S. I., Schouten, S., Rühlemann, C., and Schneider, R. R.: North Pacific and North Atlantic sea-surface temperature variability during the Holocene, Quat. Sci. Rev., 23, 2141–2154, 2004.

Klimenko, V. V., Klimanov, V. A., Sirin, A. A., and Sleptsov, A. M.: Climate changes in Western European Russia in the late Holocene, Doklady Earth Sciences, 377(2), 190–194, 2001.

Lamb, H. H.: The early Medieval warm epoch and its sequel, Palaeogeography, Palaeoclimatology, Palaeoecology, 1, 13–37, 1965.

Lean, J., Beer, J., and Bradley, R.: Reconstruction of solar irradiance since 1610: implications for climate change, Geophys. Res. Lett., 22, 1591–1594, 1995.

Luterbacher, J., Dietrich, D., Xoplaki, E., Grosjean, M., and Wanner, H.: European seasonal and annual temperature variability, trends, and extremes since 1500, Science, 303, 1499–1503, 2004.

Manabe, S., Spelman, M. J., and Stouffer, R. J.: Transient responses of a coupled atmosphere-ocean model to gradual changes of atmospheric CO2, II. Seasonal response, J. Climate, 4, 105–126, 1992.

Mann, M. E., Bradley, R. S., and Hughes, M. K.: Northern Hemisphere temperatures during the past millennium: inferences, uncertainties, and limitations, Geophys. Res. Lett., 26, 759–762, 1999.

Mann, M. E. and Jones, P. D.: Global surface temperatures over the past two millennia, Geophys. Res. Lett., 30, 1820, doi:10.1029/2003GL017814, 2003.

Masson, V., Cheddadi, R., Braconnot, P., Joussaume, S., Texier, D., and PMIP participants: Mid-Holocene climate in Europe: what can we infer from PMIP model-data comparisons?, Clim. Dyn., 15, 163–182, 1999.

Matthews, H. D., Weaver, A. J., Meissner, K. J., Gillet, N. P., and Eby, M.: Natural and anthropogenic climate change: incorporating historical land cover change, vegetation dynamics and the global carbon cycle., Clim. Dyn., 22, 461–479, 2004.

Mitchell, J. F. B. and Johns, T. C.: On modification of global warming by sulphate aerosols, J. Climate, 10, 245–267, 1997.

Moberg, A., Sonechkin, D. M., Holmgren, K., Datsenko, N. M., and Karlén, W.: Highly variable northern hemisphere temperatures reconstructed from low- and high-resolution proxy data, Nature, 433, 613–617, 2005.

Opsteegh, J. D., Haarsma, R. J., Selten, F. M., and Kattenberg, A.: ECBILT: A dynamic alternative to mixed boundary conditions in ocean models, Tellus, 50A, 348–367, 1998.

Osborn, T. J. and Briffa, K. R.: The spatial extent of 20th-century warmth in the context of the past 1200 years, Science, 311, 841–844, 2006.

Osborn, T. J. and Briffa, K. R.: The spatial extent of 20th-century warmth in the context of the past 1200 years, Science, 311, 841–844, 2006.

Pauling, A., Luterbacher, J., Casty, C., and Wanner, H.: 500 years of gridded high-resolution precipitation reconstructions over Europe and the connection to large-scale circulation, Clim. Dyn., 26, 387–405, 2006

Petoukhov, V., Claussen, M., Berger, A., Crucifix, M., Eby, M., Eliseev, A., Fichefet, T., Ganopolski, A., Goosse, H., Kamenkovich, I., Mokhov, I., Montoya, M., Mysak, L. A., Sokolov, A., Stone, P., Wang, Z., and Weaver, A. J.: EMIC Inter-comparison Project (EMIP-CO2): Comparative analysis of EMIC simulations of climate, and of equilibrium and transient responses to atmospheric CO2 doubling, Clim. Dyn., 25, 363–385, 2005.

Pfister, C., Luterbacher, J., Schwarz-Zanetti, G., and Wegmann, M.: Winter air temperature variations in western Europe during the Early and High Middle Ages (AD 750–1300), The Holocene, 8, 535–552, 1998.

Raible, C. C., Casty, C., Luterbacher, J., Pauling, A., Esper, J., Frank, D. C., Büntgen, U., Roesch, A. C., Tschuck, P., Wild, M., Vidale, P.-L., Schär, C., and Wanner, H.: Climate Variability – Observations, Reconstructions, and Model Simulations for the Atlantic-European and Alpine region from 1500–2100 AD, Climatic Change, in press, 2006.

Räisänen, J., Hansson, U., Ullerstig, A., et al.: European climate in the late twenty-first century: regional simulations with two driving global models and two forcing scenarios, Clim. Dyn., 22, 13–31, 2005.

Ramankutty, N. and Foley, J. A.: Estimating historical changes in global land cover: croplands from 1700 to 1992, Global Biogeochem. Cycles, 13(4), 997–1027, 1999.

Renssen, H., Goosse, H., Fichefet, T., Brovkin, V., Driesschaert, E., and Wolk, F.: Simulating the Holocene climate evolution at northern high latitudes using a coupled atmosphere-sea ice-ocean-vegetation model, Clim. Dyn., 24, 23–43, 2005.

Robock, A.: Volcanic eruptions and climate, Rev. Geophys., 38, 191–219, 2000.

Shabalova, M. V. and Van Engelen, F. V.: Evaluation of a reconstruction of winter and summer temperatures in the low countries, AD 764–1998, Climatic Change, 58, 219–242, 2003.

Selten, F.M.: On the response of ECBilt-CLIO to increasing GHG concentrations, available at http://www.knmi.nl/onderzk/CKO/ecbilt.html, 2002.

Shindell, D. T., Schmidt, G. A., Mann, M. E., Rind, D., and Waple, A.: Solar forcing of regional climate change during the Maunder Minimum, Science, 294, 2149–2152, 2001.

Simmons, I. G.: Changing the face of the Earth: Culture, Enviroment, History, Blackwell Publishers, Oxford, UK, Second Edition, 464 p., 1996.

Sitch, S., Brovkin, V., von Bloh, W. van Vuuren, D., Eickhout, B., and Ganopolski, A.: Impacts of future land cover changes on atmospheric CO2 and Climate, Global Biogeochem. Cycles, 19, GB2013, doi:10.1029/2004GB002311, 2005.

Steurs, W.: Evolution dans les campagnes, in: Histoire du Brabant du Duché à nos jours, edited by: van Uyten, R., Bruneel, C., Koldeweij, A. M., van de Sande, A. W. F. M., and van Oudheusden, J. A. F. M., Waadeurs Uitgevers- Fondation de la ville brabançonne, 73–77, 2004.

Stott, P. A., Tett, S. F. B., Jones, G. S., Allen, M. R., Mitchell, J. F. B., and Jenkins, G. J.: External control of 20th century temperature by natural and anthropogenic forcing, Science, 290, 2133–

2137, 2000.

Stott, P. A.: Attribution of regional-scale temperature changes to anthropogenic and natural causes, Geophys. Res. Lett., 30(14), 1728, doi:10.1029/2003GL017324, 2003.

Tett, S. F. B., Stott, P. A., Allen, M. R., Ingram, W. J., and Mitchell, J. F. B.: Causes of twentieth-century temperature change near the Earth's surface, Nature, 399, 569–572, 1999.

Thomas, C. D., Cameron, A., Green, R. E., Bakkenes, M., Beaumont, L. J., Collingham, Y. C., Erasmus, B. F. N., de Siqueira, M. F., Grainger, A., Hannah, L., Hughes, L., Huntley, B., van Jaarsveld, A. S., Midgley, G. F., Miles, L., Ortega-Huerta, M. A., Peterson, A. T., Phillips, O. L., and Williams, S. E.: Extinction risk from climate change, Nature, 427, 145–148, 2004.

van Engelen, A. F. V, Buisman, J., and Ijbnsen, F. A.: millennium of weather, winds and water in the low countries, in: History and climate: memories of the future?, edited by: Jones, P. D., Ogilvie, E. J., Davies, T. D, and Briffa, K. R., Kluwer Acad., Dordrecht, The Netherlands, 101–124, 2001.

Wagner, S. and Zorita, E: The influence of volcanic, solar and CO_2 forcing on the temperatures in the Dalton Minimum (1790–1830): a model study, Clim. Dyn., 25, 205–218, 2005.

Xoplaki, E., Luterbacher, J., Paeth, H., Dietrich, D., Steiner, N., Grosjean, M., and Wanner, H.: European spring and autumn temperature variability and change of extremes over the last half millennium, Geophys. Res. Lett., 32, L15713, doi:10.1029/2005GL023424, 2005.

Zwiers, F. W. and Zhang, X.: Towards regional-scale climate change detection, J. Clim., 16, 793–797, 2003.

Clim. Past, 4, 295–302, 2008
www.clim-past.net/4/295/2008/

Revisiting the absolute calibration of the Greenland ice-core age-scales*

L. C. Skinner

Godwin Laboratory for Palaeoclimate Research, Department of Earth Sciences, University of Cambridge, Downing Street, Cambridge, CB2 3EQ, UK

*Invited contribution by L. Skinner, one of the EGU Outstanding Young Scientist Award winners 2006.

Received: 21 May 2008 – Published in Clim. Past Discuss.: 25 June 2008
Revised: 10 September 2008 – Accepted: 17 October 2008 – Published: 24 November 2008

Abstract. Recently, an absolute "calibration" was proposed for the GRIP and GISP2 Greenland ice-core time scales (Shackleton et al., 2004). This calibration attempted to reconcile the stratigraphic integration of ice-core, marine and speleothem archives with the absolute age constraints that marine and speleothem records incorporate. Here we revisit this calibration in light of the new layer-counted chronology of the NGRIP ice-core (GICC05). The GICC05 age-scale differs from the proposed absolute calibration by up to 1200 years late in the last glaciation, with implications both for radiocarbon cycling and the inferred timing of North Atlantic climate events relative to radiometrically dated archives (e.g. relative sea-level). By aligning the stratigraphy of Iberian Margin marine cores with that of the Greenland ice-cores, it can be shown that either: 1) the radiocarbon content of mid-latitude Atlantic surface-waters was extremely depleted (resulting in average surface reservoir ages up to 1700 years prior to ∼22 ka BP); or 2) the GICC05 age-scale includes too few years (is up to 1200 years too young). It is shown here that both of these possibilities are probably correct to some degree. Based on the assumed accuracy of coral and speleothem U-Th ages, Northeast Atlantic surface reservoir ages should be revised upward by ∼350 years, while the NGRIP age-scale appears to be "missing" time. These findings illustrate the utility of integrated stratigraphy as a test for our chronologies, which are rarely truly "absolute". This is an important point, since probably the worst error that we can make is to entrench and generalise a precise stratigraphical relationship on the basis of erroneous absolute age assignations.

Correspondence to: L. C. Skinner
(luke00@esc.cam.ac.uk)

1 Introduction

All palaeoenvironmental inference hinges on chronostratigraphy. Without a way to accurately link and order our observations spatially and temporally, they remain at best of ambiguous, and at worst of dubious, significance. Nevertheless, a given chronostratigraphy is best viewed as an hypothesis. Much like any proxy, a chronostratigraphy must be employed in a manner that explicitly allows it to be tested. The Greenland and Antarctic ice-core stratigraphies, together with North Atlantic marine archives, low-latitude speleothem and coral records, and the radiometric dates that these latter archives contain, comprise an integrated chronostratigraphic system that is eminently amenable to consistency testing. The integration of these "chronostratigraphic elements" results in a system that remains underdetermined, in that it's chronology cannot be resolved unequivocally. However, this is only true to the extent that proposed stratigraphic links and absolute ages can be questioned, and that radiometric ages are subject to uncertain "calibrations" (i.e. we cannot account for the movement of all radio-isotopes in the system). Nevertheless, this integrated chronostratigraphic system remains explicit, in the sense that any proposed uncertainties or difficulties in the correlations or chronologies carry clear implications that can be explicitly evaluated. Thus if the Greenland, Cariaco, Iberian Margin, Hulu, Dongge and Boutavera records all contain the same "event stratigraphy", then their chronologies must be consistent; both with each other, and with existing radiometric calibrations (such as paired radiocarbon-uranium-series dated corals). Should this not be the case, one can (and must) draw clear conclusions: either regarding absolute age-determinations, radiometric calibrations and/or reservoir effects, or regarding the initial stratigraphic correlations.

Published by Copernicus Publications on behalf of the European Geosciences Union.

Absolute calibration of Greenland revisited

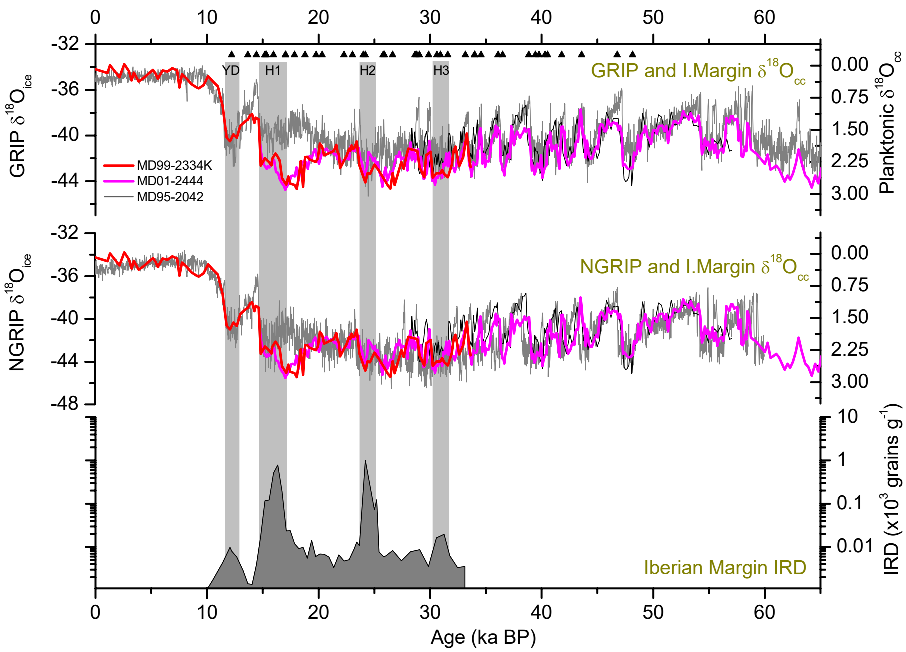

Fig. 1. Correlation between Greenland and planktonic δ^{18}O from three Iberian Margin sediment cores. Black filled triangles indicate a selection of published radiocarbon dates performed on Iberian Margin planktonic foraminifera (Bard et al., 2004b; Shackleton et al., 2004; Skinner and Shackleton, 2004). Upper plot shows the GRIP ice-core and planktonic δ^{18}O, both on the SFCP04 age-scale. Middle plot shows the NGRIP ice-core on the GICC05 age-scale compared to planktonic δ^{18}O on the SFCP04 age-scale. This illustrates the chronostratigraphic discrepancies between the age-scales. Lower plot shows spikes in ice-rafted debris abundance recorded in MD99-2334K from ~33 ka BP, also on the SFCP04 age-scale, indicating Heinrich-layer deposition (Skinner et al., 2003).

It is worth noting that much hinges on the fine-scale accuracy of the Greenland ice-core chronology. Importantly, this includes a determination of the precise timing of sea-level change relative to abrupt North Atlantic and Antarctic climate change (Chappell, 2002). On its own, this phase relationship sets important constraints on the mechanisms responsible for past abrupt climate change (Knutti et al., 2004). At present, the precise phasing of sea-level and abrupt climate change remains highly uncertain (Siddall et al., 2003; Skinner et al., 2007), partly because of a current paucity of sub-millennial resolution sea-level reconstructions, and partly because of the difficulty of obtaining a perfectly accurate ice-core chronology and "Δ-age" (ice-age versus gas-age) estimation technique.

With the aim of helping to set firm constraints on the timing of millennial events recorded in the Greenland ice-core, we revisit the "absolute calibration" of the GRIP age-scale recently proposed by Shackleton et al. (2004). This is carried out in the light of the new layer-counted GICC05 age-scale for the NGRIP ice-core (Svensson et al., 2008), and based on new radiometric dating of marine and speleothem archives (Hughen et al., 2006; Wang et al., 2006). The aim of this exercise is not to propose a "final" age-scale for the Greenland ice-cores (which would best be derived from glaciological constraints), but rather to illustrate the first order importance and utility of stratigraphy in assessing the accuracy of a given North Atlantic event chronology. After investigating the consistency of Greenland, North Atlantic, low-latitude speleothem and coral archives, it is concluded that biases (as opposed to random errors) may exist in both the marine radiocarbon dataset and the Greenland glaciological age-scale. This is despite the very great merits of the most recent developments of the Greenland ice-core chronology.

2 Methods

In a seminal paper, Shackleton et al. (2000) demonstrated a remarkably close coupling between surface-water temperature changes recorded on the Iberian Margin and stadial – interstadial temperature changes recorded in the Greenland ice-cores (Fig. 1). More recent studies have successfully replicated and confirmed this close stratigraphical link, which has allowed a variety of marine archives from the Iberian Margin to be securely tied to the Greenland chronostratigraphy (Vautravers and Shackleton, 2006; Martrat et al., 2007). For the most part, the correlation illustrated in Fig. 1 relies on near identical surface temperature signals; however Heinrich layers (ice-rafted debris) deposited on the Iberian Margin also provide robust markers for major Greenland stadial – interstadial transitions. This is particularly important during Marine Isotope Stage (MIS) 2, where the similarity between Iberian Margin and Greenland temperature-proxy signals degrades (Skinner et al., 2003). Thus one constraint on stratigraphic correlation is that the Iberian Margin record cannot "slip" relative to Greenland in a way that significantly alters the inferred timing of Heinrich events with respect to Greenland stadial – interstadial transitions. In this respect, the placement of Heinrich events 2 and 3 just prior to Greenland Interstadials (GIS) 2 and 4 appears to be a robust set of tie-points. An alternative correlation that would for example place Heinrich 3 well before or just after GIS 4 (see middle panel of Fig. 1) would represent a marked departure from the pattern indicated by other Heinrich events/stadials, which generally occur just before major Greenland stadial – interstadial transitions. Support for this canonical view is provided by assessments of the relative timing of the most pronounced Antarctic millennial warm (AIM) events (EPICA community members, 2006), as well as the phasing of major precipitation anomalies recorded in low-latitude speleothem deposits (Wang et al., 2001, 2004, 2006).

One opportunity that arises from the alignment of Iberian Margin and Greenland records, which has long been recognised and exploited by Edouard Bard and colleagues, is that of being able to place marine radiocarbon dates from Iberian Margin sediment cores onto an independent glaciological age-scale. Seen from one angle, this may provide a useful radiocarbon calibration tool (Bard et al., 2004a). Seen from another angle, it may simply provide a crosscheck for a given Greenland/Iberian Margin stratigraphical alignment (Skinner and Shackleton, 2004). Going further still, it may be used to transfer radiometric dates from marine cores (or indeed speleothems) to the Greenland stratigraphy, thus effectively "calibrating" the Greenland age-scale. This approach was used by Shackleton et al. (2004) to propose the "absolutely calibrated" SFCP04-GRIP age-scale for Greenland (hereafter referred to as SFCP04). Perhaps most significantly, this calibration attempt served as a reminder that glaciological age-scales may not necessarily represent absolute calendar age-scales.

More recently, a new age-scale has been devised for the NGRIP Greenland ice-core based on careful layer counting and associated uncertainty estimates (Andersen et al., 2006; Svensson et al., 2008). This new age-scale (hereafter referred to as GICC05) has in effect superseded previous Greenland age-scales, and one of its great advantages is that it possesses clearly defined uncertainty estimates. However, the GICC05 age-scale differs from the apparently well-conceived SFCP04 age-scale by up to 1200 years. We are therefore in the possession of no fewer than 5 different Greenland age-scales, none of which are in complete agreement. If the GICC05 age-scale can be said to represent the current best estimate for the timing of the North Atlantic event stratigraphy, a clear explanation of its differences with regard to the "absolutely calibrated" SFCP04 age-scale seems necessary.

Figure 2 shows a compilation of planktonic radiocarbon dates performed in four Iberian Margin cores (Bard et al., 2004b; Shackleton et al., 2004; Skinner and Shackleton, 2004), expressed as deviations from modern atmospheric $\Delta^{14}C$. This way of presenting the radiocarbon dates accentuates the dynamic range of their deviations from stratigraphically assigned (ice-core) calendar ages. Two ice-core age-scales are adopted in Fig. 2: SFCP04 and GICC05. What this figure shows is that, when placed on the SFCP04 age-scale, Iberian Margin radiocarbon dates are in apparent agreement with available radiocarbon calibration datasets back to ~35 ka BP, including the coral datasets of both Bard et al. (1998) and Fairbanks et al. (2005), and the Cariaco Basin dataset of Hughen et al. (2006). The Cariaco dataset shown in Fig. 2 adopts the Hulu speleothem uranium-series age-scale, and is hereafter referred to as "Huliaco". It is noteworthy that the Huliaco chronostratigraphy reproduces a very similar history of atmospheric $\Delta^{14}C$ change as predicted independently by paired U-Th/^{14}C dates performed on tropical corals. It is also noteworthy that the Iberian Margin reproduces a similar history of atmospheric $\Delta^{14}C$ change when placed on the SFCP04 Greenland age-scale (most importantly between ~20 and 32 ka BP). If ascribed younger calendar ages, the Iberian Margin and Cariaco $\Delta^{14}C$ records would fall below the coral data (which are assumed here to be correct and representative of atmospheric $\Delta^{14}C$), unless the reservoir ages in both settings were increased by a commensurate amount. Hence a ^{14}C date that is assigned a revised calendar age 1200 years younger will maintain its $\Delta^{14}C$ at appropriate levels if it is also assigned a revised reservoir age 1200 higher. Under the proviso that reservoir ages have remained close to ~420 years in the Cariaco Basin (Hughen et al., 2006), and ~500 years on the Iberian Margin (Shackleton et al., 2004), Fig. 2 would therefore suggest close agreement between the SFCP04 Greenland age-scale and radiometric dating of tropical corals, Hulu, Cariaco Basin and the Iberian Margin.

At first sight, the same is not true of the GICC05 age-scale. As shown in Fig. 2, Iberian Margin radiocarbon dates placed on the GICC05 Greenland age-scale (and corrected for a 500 year reservoir age) do not agree with Huliaco or tropical coral dates. The immediate implication that arises from Fig. 2 is that either the GICC05 age-scale is right and Iberian Margin reservoir ages should be more than doubled (to as much as 1700 years); or the GICC05 age-scale is "missing time", in particular between Greenland interstadials (GIS) 2 and 8. Below we discuss each of these possibilities in turn.

Absolute calibration of Greenland revisited

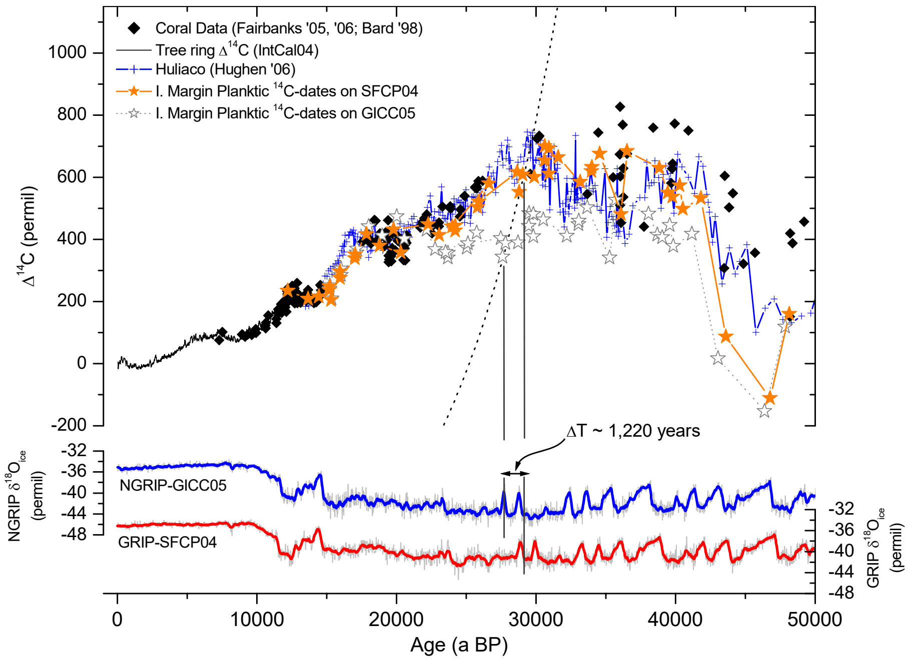

Fig. 2. Past atmospheric Δ^{14}C variability as inferred from: the INTCAL tree-ring dataset (solid black line); paired radiocarbon and uranium-series dating of tropical corals (Bard et al., 1998; Fairbanks et al., 2005) (filled diamonds); Cariaco planktonic radiocarbon dates placed on the Hulu chronology (Hughen et al., 2006) (crosses); Iberian Margin planktonic radiocarbon dates placed on the SFCP04 age-scale (filled stars); and Iberian Margin planktonic radiocarbon dates placed on the GICC05 age-scale (open stars). Lower panels show NGRIP on the GICC05 age-scale compared with GRIP on the SFCP04 age-scale (Svensson et al., 2008); vertical lines indicate the difference between SFCP04 and GICC05 for Greenland Interstadial (GIS) 3. The dotted curve is a decay line showing how altering the calendar age of GIS 3 affects Δ^{14}C inferred from Iberian Margin radiocarbon dates.

3 Discussion

One way to assess Iberian Margin reservoir ages, relative to Cariaco basin reservoir ages, is to compare radiocarbon dates performed on correlative stratigraphical events from each region. This is illustrated in Fig. 3, where Cariaco Basin grey-scale is shown correlated to Iberian Margin planktonic δ^{18}O; and offsets between the GICC05 and SFCP04 age-scales are compared with differences between correlative Iberian Margin and Cariaco radiocarbon dates. For this comparison, radiocarbon dates have been interpolated from the much higher resolution radiocarbon dataset. The reason for interpolating Cariaco dates in this way is to permit, as far as possible, a comparison of radiocarbon dates from precisely the same stratigraphic interval. A comparison of dates from a given "event", yet from different times within that event would not be sufficient. What emerges from Fig. 3 is that Iberian Margin reservoir ages are indeed likely to explain much of the discrepancy between the GICC05 and SFCP04 age-scales, as surmised by Svensson et al. (2008). Furthermore, Iberian Margin reservoir ages are likely to be larger than Cariaco Basin reservoir ages by ~430 years on average, prior to ~22 ka BP. Revising the Iberian Margin reservoir ages upward to ~850 years (420+430 years) prior to 22 ka BP goes some way in reconciling the GICC05 chronology with Huliaco, coral and speleothem dates. However, it does not go quite far enough: between ~24 and 38 ka BP the discrepancy between GICC05 and SFCP04 is significantly larger than the difference between Iberian Margin and Cariaco radicarbon dates. This statement must be true unless the grey line in the bottom panel of Fig. 3 can be said to be representative of the distribution of black crosses in the same figure. Increased Iberian Margin reservoir ages alone cannot therefore resolve the SFCP04/GICC05 age-scale discrepancy between ~24 and 38 ka BP.

If instead Cariaco and Iberian Margin reservoir ages are both increased further, for example to 800 and 1230 years respectively (in order to completely reconcile Iberian Margin radiocarbon dates with both the GICC05 age-scale and tropical coral dates), then agreement between the Huliaco and coral datasets is destroyed. Therefore, if we accept the Hulu age-scale for Cariaco and the coral dates, then we cannot increase Cariaco and Iberian Margin reservoir ages much higher than ~420 and 850 years respectively. This would also suggest that GICC05 ages tend to be "too young", at least between GIS 2 and 8.

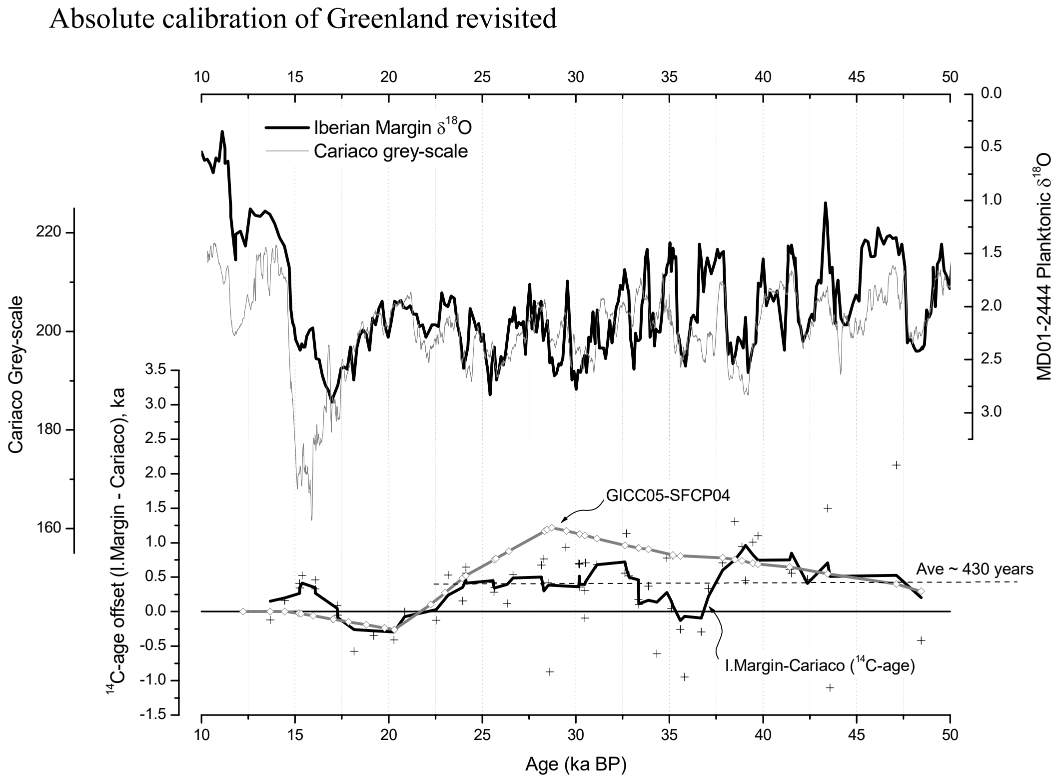

Fig. 3. Assessment of radiocarbon surface-water reservoir ages on the Iberian Margin, relative to the Cariaco Basin. Upper plot shows Cariaco grey-scale correlated with Iberian Margin planktonic δ^{18}O from core MD01-2444 (Vautravers and Shackleton, 2006). Lower plot shows the offset between Iberian Margin radiocarbon dates and their Cariaco correlates (black crosses and 5-point running mean), and the offset between the GICC05 and SFCP04 ages-scales (grey line and open diamonds). Dashed horizontal line indicates the overall average radiocarbon age-offset prior to GIS 2 (~430 years). For Cariaco Basin reservoir ages ~420 years (Hughen et al., 2006), Iberian Margin reservoir ages should therefore approach ~850 years on average prior to GIS 2.

In order to assess the "absolute" accuracy of GICC05 and SFCP04 further, a comparison can be made with ages drawn from uranium-series dated speleothem records. The comparison of speleothem records shown in Fig. 4 is used as an illustration of the reproducibility (and hence uncertainty) of the event stratigraphy and chronology in these archives. It is noteworthy that despite the greater accuracy of "absolute" dating in the speleothem records, they do not all exhibit the exact same stratigraphic signal, nor are they in complete agreement on the precise timing of individual event boundaries. Differences between speleothem event ages (i.e. their true uncertainty) can be as large as ~1100 years. This serves as a reminder that stratigraphic reproducibility ultimately constrains the true uncertainty limits of our records.

The correlations shown in Fig. 4 also allow the Iberian Margin radiocarbon compilation to be placed on an age-scale that is consistent with average Hulu and Boutavera uranium-series ages inferred for Greenland event boundaries. Because Huliaco is broadly consistent with this age-scale no attempt has been made to alter it, with the exception of one small modification that has been made to bring it into better agreement with the high resolution Boutavera Cave record at ~28 ka BP. This results in slightly younger calendar ages than provided by Hughen et al. (2006) near 28 ka BP.

Figure 5 now shows the Iberian Margin radiocarbon compilation placed on: 1) the GICC05 age-scale; and 2) the "speleothem age-scale" illustrated in Fig. 4. If our marine reservoir age estimates are accurate, and the GICC05 age-scale is consistent with speleothem ages, all of the Δ^{14}C time-series should overlap. While there is good agreement in Fig. 5 between the coral data, Huliaco and the Iberian Margin on a "speleothem age-scale" (thus tentatively confirming the reservoir age corrections proposed above), there remain significant discrepancies when the Iberian Margin is placed on the GICC05 age-scale. The GICC05 age-scale thus still appears to be slightly too young relative to speleothem ages (as observed relative to SFCP04 ages) between GIS 2 and GIS 6 in particular, even when higher reservoir ages are applied. The age offsets are not extremely large (~800 years at most), and notably are within the maximum counting error ascribed to the GICC05 age-scale (Svensson et al., 2008). Nevertheless, they are consistently positive rather than randomly

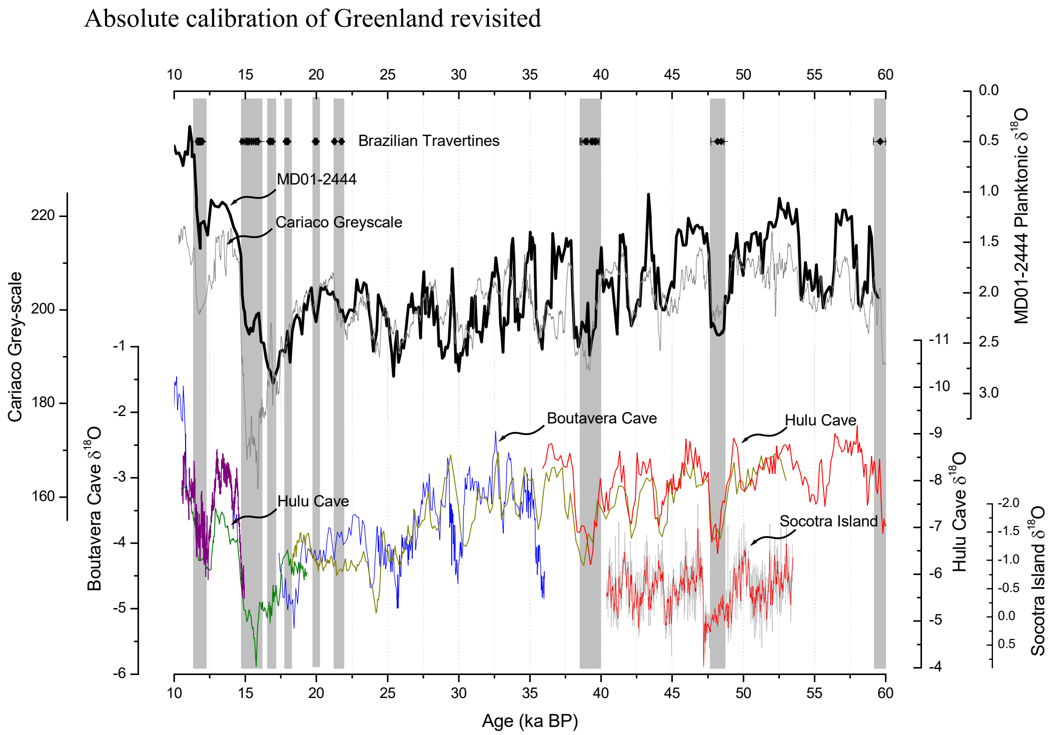

Fig. 4. Correlation of Iberian Margin planktonic $\delta^{18}O$ from core MD01-2444 (Vautravers and Shackleton, 2006) with both the Hulu Cave and Boutavera Cave speleothem records (Wang et al., 2001, 2006). These records are shown compared with absolutely dated Brazilian travertine deposits (indicative of wet-periods coincident with North Atlantic stadials) (Wang et al., 2004), the Socotra Island speleothem record (Burns et al., 2003, 2004), and Cariaco grey-scale on the Hulu chronology (Hughen et al., 2006). The Cariaco age-scale has been slightly modified from (Hughen et al., 2006) near ~28 ka BP to bring it into closer agreement with Boutavera, but is otherwise unchanged.

distributed about zero, which would tend to suggest a bias in the GICC05 age-scale towards younger ages. The non-random bias in age-offsets between GICC05 and speleothem records (with speleothem ages tending to be older) is also apparent in Fig. 4 and 6 of (Svensson et al., 2008). We might therefore conclude that while much of the original discrepancy between GICC05 and SFCP04 can indeed be attributed to larger than expected glacial reservoir ages on the Iberian Margin, some may still be attributable to missing years in the GICC05 age-scale. Arguably, this type of bias might be expected, especially during the height of the last glacial period, when accumulation rates over Greenland were low and annual layers are therefore difficult to discern (Andersen et al., 2006).

It is important to note that the method of chronostratigraphic integration outlined here has been used to suggest a slight bias in both marine radiocarbon ages on the Iberian Margin and in the GICC05 age-scale (in both cases between approximately 400 and 800 years). This specific conclusion is premised primarily on the accuracy of combined radiocarbon and uranium-series coral dating and of the speleothem chronostratigraphy, especially in the interval between GIS 1 and GIS 4, and especially in the Hulu Cave record (which tends to yield older ages for GIS 2–4). It also hinges on the proposed correlations between the Iberian Margin, Cariaco, Hulu and Greenland. Therefore, as the speleothem chronostratigraphy improves in future and as our correlations are reassessed, it may be possible (and necessary) to revise the explanation of the discrepancy between the GICC05 and SFCP04 age-scales proposed here. The method outlined in this paper indicates one way that this can be done. One obvious and important improvement in future will be the development of an adequate quantitative statistical analysis of the correlations and age discrepancies discussed here, in order to constrain more precisely the magnitude of possible (reservoir or ice-core) age biases.

4 Conclusions

The primary purpose of this investigation has been to illustrate a viable method of testing for chronostratigraphic convergence on an accurate Greenland calendar age-scale. In doing so, it has been suggested that a distinction can still be made between even the best glaciological ages and "absolute" ages. Thus, for example, it appears that the GICC05 age-scale cannot be made consistent with *both*

Absolute calibration of Greenland revisited

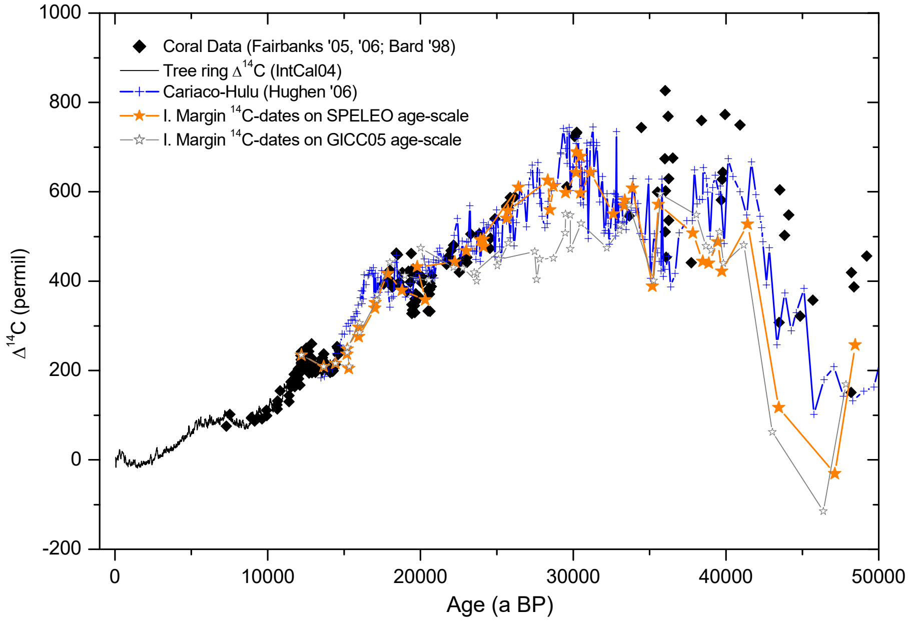

Fig. 5. Past atmospheric $\Delta^{14}C$ variability as inferred from: the INTCAL tree-ring dataset (solid black line); paired radiocarbon and uranium-series dating of tropical corals (Bard et al., 1998; Fairbanks et al., 2005) (filled diamonds); Cariaco planktonic radiocarbon dates placed on the slightly modified Hulu chronology shown in Fig. 4 (crosses); Iberian Margin planktonic radiocarbon dates placed on a speleothem age-scale (filled stars); and Iberian Margin planktonic radiocarbon dates placed on the GICC05 age-scale (open stars). Iberian Margin radiocarbon dates are corrected for a 500-year reservoir age after GIS 2, and for an 850-year reservoir age before GIS 2, as per Fig. 3.

Huliaco and paired ^{14}C-U/Th coral dates, even if increased marine reservoir ages are applied to the Cariaco radiocarbon dates. Iberian Margin radiocarbon dates tend to support this suggestion, which essentially hinges on an apparent bias in GICC05 ages (younger) relative to speleothem ages (older). If this specific conclusion proves to be incorrect, then it will be due to either: 1) biases in uranium-series ages for either Hulu or the corals (too old); or 2) biases in coral radiocarbon ages (too young). In both cases there are implications for inferred surface reservoir ages and changes in carbon cycling during the last glacial period. It is hoped that this type of analysis will in future contribute to the further improvement of the North Atlantic event chronostratigraphy (including glaciological age-scales), in particular as this bears on the timing of millennial climate events with respect to "absolutely-dated" sea level, palaeoceanographic or archaeological archives. The determination of the phasing of millennial sea-level fluctuations relative to North Atlantic climate events and Atlantic overturning circulation perturbations represents a case in point. The methodology presented here would suggest that paired radiocarbon and uranium-series dating performed on corals amenable to sea-level reconstructions could eventually allow coral-based sea-level estimates, ice-cores and ocean circulation proxies to be successfully integrated.

Edited by: F. Peeters

References

Andersen, K. K., Svensson, A., Johnsen, S. J., Rasmussen, S. O., Bigler, M., Rothlisberger, R., Ruth, U., Siggaard-Andersen, M.-L., Steffensen, J. P., Dahl-Jensen, D., Vinther, B. M., and Clausen, H. B.: The Greenland Ice Core Chronology 2005, 15–42 ka. Part 1: constructing the time scale, Quaternary Sci. Rev., 25, 3246–3257, 2006.

Bard, E., Arnold, M., Hamelin, B., Tisnerat-Laborde, N., and Cabioche, G.: Radiocarbon calibration by means of mass spectrometric 230Th/234U and 14C ages of corals: An updated database including samples from Barbados, Mururoa and Tahiti, Radiocarbon, 40, 1085–1092, 1998.

Bard, E., Menot-Combes, G., and Rostek, F.: Present status of radiocarbon calibration and comparison records based on Polynesian corals and Iberian Margin sediments, Radiocarbon 46, 1189–1202, 2004a.

Bard, E., Rostek, F., and Menot-Combes, G.: Radiocarbon calibration beyond 20 000 14C yr B.P. by means of planktonic foraminifera of the Iberian Margin, Quaternary Res., 61, 204–214, 2004b.

Burns, S. J., Fleitmann, D., Matter, A., Kramers, J., and Al-Subbary, A. A.: Indian Ocean climate and absolute chronology over Dansgaard/eschger events 9 to 13, Science, 301, 1365–1368, 2003.

Burns, S. J., Fleitmann, D., Matter, A., Kramers, J., and Al-Subbary, A. A.: Corrections and Clarifications - Indian ocean climate and an absolute chronology over Dansgaard-Oeschger events 9 to 13, Science, 305, 1567, 2004.

Chappell, J.: Sea level changes forced ice breakouts in the Last Glacial cycle: new results from coral terraces, Quaternary Sci. Rev., 21, 1229–1240, 2002.

EPICA community members: One-to-one coupling of glacial variability in Greenland and Antarctica, Nature, 444, 195–198, 2006.

Fairbanks, R. G., Mortlock, R. A., Chiu, T.-C., Cao, L., Kaplan, A., Guilderson, T., Fairbanks, T. W., Bloom, A. L., Grootes, P. M., and Nadeau, M.-J.: Radiocarbon calibration curve spanning 0-50 000 years BP based on paired 230Th/234U/238U and 14C dates on pristine corals, Quaternary Sci. Rev., 24, 1781–1796, 2005.

Hughen, K., Southon, J., Lehman, S., Bertrand, C., and Turnbull, J.: Cariaco Basin 14C calibration and activity record over the past 50 000 years updated from the Cariaco Basin, Quaternary Sci. Rev., 25, 3216–3227, 2006.

Knutti, R., Fluckiger, J., Stocker, T. F., and Timmerman, A.: Strong interhemispheric coupling of glacial climate through freshwater discharge and ocean circulation, Nature, 430, 851–856, 2004.

Martrat, B., Grimalt, J. O., Shackleton, N. J., de Abreu, L., Hutterli, M. A., and Stocker, T. F.: Four climatic cycles of recurring deep and surface water destabilizations on the Iberian Margin, Science, 317, 502–507, 2007.

Shackleton, N. J., Fairbanks, R. G., Chiu, T.-C., and Parrenin, F.: Absolute calibration of the Greenland time scale: implications for Antarctic time scales and for D14C, Quaternary Sci. Rev., 23, 1513–1522, 2004.

Shackleton, N. J., Hall, M. A., and Vincent, E.: Phase relationships between millennial-scale events 64 000–24 000 years ago, Paleoceanography, 15, 565–569, 2000.

Siddall, M., Rohling, E., Almogi-Labin, A., Hemleben, C., Meischner, D., Schmelzer, I., and Smeed, D. A.: Sea-level fluctuations during the last glacial cycle, Nature, 423, 853–858, 2003.

Skinner, L. C., Elderfield, H., and Hall, M.: Phasing of millennial events and Northeast Atlantic deep-water temperature change since ∼50 ka BP, in: "Past and Future Changes of the Ocean's Meridional Overturning Circulation: Mechanisms and Impacts", edited by: Schmittner, A., Chiang, J., and Hemming, S. R., AGU Monograph, 197–208, 2007.

Skinner, L. C. and Shackleton, N. J.: Rapid transient changes in Northeast Atlantic deep-water ventilation-age across Termination I., Paleoceanography, 19, 1–11, doi:10.1029/2003PA000983, 2004.

Skinner, L. C., Shackleton, N. J., and Elderfield, H.: Millennial-scale variability of deep-water temperature and d18Odw indicating deep-water source variations in the Northeast Atlantic, 0–34 cal. ka BP, Geochem. Geophy. Geosy., 4, 1–17, doi:10.1029/2003GC000585, 2003.

Svensson, A., Andersen, K. K., Bigler, M., Clausen, H. B., Dahl-Jensen, D., Davies, S. M., Johnsen, S. J., Muscheler, R., Parrenin, F., Rasmussen, S. O., Röthlisberger, R., Seierstad, I., Steffensen, J. P., and Vinther, B. M.: A 60 000 year Greenland stratigraphic ice core chronology, Clim. Past, 4, 47–57, 2008, http://www.clim-past.net/4/47/2008/.

Vautravers, M. and Shackleton, N. J.: Centennial scale surface hydrology off Portugal during Marine Isotope Stage 3: Insights from planktonic foraminiferal fauna variability, Paleoceanography, 21, 1–13, doi:10.1029/2005PA001144, 2006.

Wang, X., Auler, A. S., Edwards, R. L., Cheng, H., Cristalli, P. S., Smart, P. L., Richards, D. A., and Shen, C.-C.: Wet periods in northeastern Brazil over the past 210 kyr linked to distant climate anomalies, Nature, 432, 740–743, 2004.

Wang, X., Auler, A. S., Edwards, R. L., Cheng, H., Ito, E., and Solheid, M.: Interhemispheric anti-phasing of rainfall during the last glacial period, Quaternary Sci. Rev., 25, 3391–3403, 2006.

Wang, Y. J., Cheng, H., Edwards, R. L., An, Z. S., Wu, J. Y., Shen, C.-C., and Dorale, J. A.: A high-resolution absolute-dated late Pleistocene monsoon record from Hulu Cave, China, Science, 294, 2345–2348, 2001.

Clim. Past, 14, 1015–1033, 2018
https://doi.org/10.5194/cp-14-1015-2018

Climate of the Past
Open Access
EGU

Paleoceanography and ice sheet variability offshore Wilkes Land, Antarctica – Part 2: Insights from Oligocene–Miocene dinoflagellate cyst assemblages

Peter K. Bijl[1,*], Alexander J. P. Houben[2], Julian D. Hartman[1], Jörg Pross[3], Ariadna Salabarnada[4], Carlota Escutia[4], and Francesca Sangiorgi[1]

[1]Marine Palynology and Paleoceanography, Laboratory of Palaeobotany and Palynology, Department of Earth Sciences, Faculty of Geosciences, Utrecht University. P.O. Box 80.115, 3508 TC Utrecht, the Netherlands
[2]Geological Survey of the Netherlands, Netherlands Organisation for Applied Scientific Research (TNO), Princetonlaan 6, 3584 CB, Utrecht, the Netherlands
[3]Paleoenvironmental Dynamics Group, Institute of Earth Sciences, Heidelberg University, Im Neuenheimer Feld 234, 69120 Heidelberg, Germany
[4]Instituto Andaluz de Ciencias de la Tierra, CSIC-UGR, 18100 Armilla, Spain
[*]Invited contribution by Peter K. Bijl, recipient of the EGU Arne Richter Award for Outstanding Early Career Scientists 2014.

Correspondence: Peter K. Bijl (p.k.bijl@uu.nl)

Received: 13 November 2017 – Discussion started: 5 December 2017
Revised: 9 May 2018 – Accepted: 21 June 2018 – Published: 11 July 2018

Abstract. Next to atmospheric CO_2 concentrations, ice-proximal oceanographic conditions are a critical factor for the stability of Antarctic marine-terminating ice sheets. The Oligocene and Miocene epochs (∼34–5 Myr ago) were time intervals with atmospheric CO_2 concentrations between those of present-day and those expected for the near future. As such, these past analogues may provide insights into ice-sheet volume stability under warmer-than-present-day climates. We present organic-walled dinoflagellate cyst (dinocyst) assemblages from chronostratigraphically well-constrained Oligocene to mid-Miocene sediments from Integrated Ocean Drilling Program (IODP) Site U1356. Situated offshore the Wilkes Land continental margin, East Antarctica, the sediments from Site U1356 have archived the dynamics of an ice sheet that is today mostly grounded below sea level. We interpret dinocyst assemblages in terms of paleoceanographic change on different timescales, i.e. with regard to both glacial–interglacial and long-term variability. Our record shows that a sea-ice-related dinocyst species, *Selenopemphix antarctica*, occurs only for the first 1.5 Myr of the early Oligocene, following the onset of full continental glaciation on Antarctica, and after the Mid-Miocene Climatic Optimum. Dinocysts suggest a weaker-than-modern sea-ice season for the remainder of the Oligocene and Miocene. The assemblages generally bear strong similarity to present-day open-ocean, high-nutrient settings north of the sea-ice edge, with episodic dominance of temperate species similar to those found in the present-day subtropical front. Oligotrophic and temperate surface waters prevailed over the site notably during interglacial times, suggesting that the positions of the (subpolar) oceanic frontal systems have varied in concordance with Oligocene–Miocene glacial–interglacial climate variability.

1 Introduction

The proportion of the East Antarctic ice sheet that is presently grounded below sea level is much larger than originally interpreted (Fretwell et al., 2013). This implies that a larger part of the continental ice sheet is sensitive to basal melting by warm waters than previously thought (Shepherd et al., 2012; Rignot et al., 2013; Wouters et al., 2015), and that a higher amplitude and faster rate of sea-level rise is to be expected under future climate warming than previously acknowledged (IPCC, 2013). Studying the amount of and variability in Antarctic ice volume in periods with high atmospheric CO_2 concentrations (pCO_2) provides addi-

Published by Copernicus Publications on behalf of the European Geosciences Union.

tional insight into ice–ocean feedback processes. Foster and Rohling (2013) compared sea-level and atmospheric pCO_2 concentrations on geological timescales. Their study suggests that global ice sheets were rather insensitive to climate change when atmospheric pCO_2 ranged between 400 and 650 parts per million in volume (ppmv). During the Oligocene and Miocene, atmospheric pCO_2 ranged between 400 and 650 ppmv (Foster et al., 2012; Badger et al., 2013; Greenop et al., 2014). Crucially, similar pCO_2 levels are expected for the near future given unabated carbon emissions (IPCC, 2013), implying that global ice volume may not change much under these pCO_2 scenarios.

In contrast to the invariant global ice volume inferred by Foster and Rohling (2013), a strong (up to 1 per mille, ‰) variability is preserved in deep-sea benthic foraminiferal oxygen isotope (hereafter benthic $\delta^{18}O$) data (e.g. Pälike et al., 2006b; Beddow et al., 2016; Holbourn et al., 2007; Liebrand et al., 2011, 2017; De Vleeschouwer et al., 2017). These benthic $\delta^{18}O$ data reflect changes in continental ice volume (primarily on Antarctica) and deep-sea temperature. The latter is strongly coupled to polar surface water temperature, as deep-water formation was predominantly at high latitudes at that time (Herold et al., 2011). High-amplitude variations in benthic $\delta^{18}O$ thus suggest either (i) strong climate dynamics in the high latitudes with relatively minor ice volume change (which would be in accordance with numerical modelling experiments (Barker et al., 1999) and the interpretation of Foster and Rohling, 2013), or (ii) strong fluctuations in Antarctic ice volume, with relatively subdued temperature variability (which would be in accordance with indications for unstable Antarctic ice sheets under warmer-than-present climates (Cook et al., 2013; Greenop et al., 2014; Rovere et al., 2014; Sangiorgi et al., 2018). If one assumes a present-day $\delta^{18}O$ composition (−42 ‰ versus standard mean ocean water) for Oligocene–Miocene Antarctic ice sheets and modern deep-water temperature (2.5 °C), the benthic $\delta^{18}O$ fluctuations during the Oligocene–Miocene suggest long-term ice-sheet variability to have fluctuated considerably (Liebrand et al., 2017). Similarly strong fluctuations were observed in sedimentary records from the Gippsland Basin, southeast Australia (Gallagher et al., 2013). Meanwhile, deep-sea temperatures have fluctuated considerably as well during the Oligocene and Miocene (Lear et al., 2004), which is further evident from ice-free geologic episodes (Zachos et al., 2008). Therefore, a combination of deep-sea temperature and ice volume changes is likely represented in these records. Further ice-proximal reconstructions of climate, ice-sheet and oceanographic conditions are required to provide an independent assessment of the stability of ice sheets under these higher-than-present-day pCO_2 concentrations.

While Oligocene–Miocene climates may bear analogy to our future in terms of pCO_2 concentrations, the uncertainties and differences in Antarctic paleotopography must be considered in any such comparison, as this factor critically determines the proportion of marine-based versus land-based ice. An Antarctic continent with low topography would result in more ice sheets being potentially sensitive to basal melt and as such a higher sensitivity of these ice sheets to climate change. Moreover, the fundamentally different paleogeographic configuration of the Southern Ocean during that time compared to today should also be considered (Fig. 1). The development and strength of the Antarctic Circumpolar Current (ACC) connecting the Atlantic, Indian and Pacific ocean basins (Barker and Thomas, 2004; Olbers et al., 2004) depend on the basin configuration (i.e. the width and depth of the gateways as well as the position of the land masses). The exact timing when the ACC reached its modern-day strength is still uncertain, ranging from the middle Eocene (41 Ma) to as young as Miocene (23 Ma; Scher and Martin, 2004; Hill et al., 2013; Scher et al., 2015). Whether and, if so, how the development of the ACC has influenced latitudinal heat transport, ice–ocean interactions and the stability of Antarctic continental ice has remained poorly understood.

To directly assess the role of ice-proximal oceanography on ice-sheet stability during the Oligocene–Miocene, ice-proximal proxy records are required. Several ocean drilling expeditions have been undertaken in the past to provide insight into the history of the Antarctic ice sheets (Barrett, 1989; Wise and Schlich, 1992; Barker et al., 1998; Robert et al., 1998; Wilson et al., 2000; Cooper and O'Brien, 2004; Exon et al., 2004; Harwood et al., 2006; Escutia and Brinkhuis, 2014). For some of the retrieved sedimentary archives, age control was particularly challenging due to the paucity of useful means to calibrate them to the international timescale. As a consequence, the full use of these archives for the generation of paleoceanographic proxy records and ice-sheet reconstructions has remained limited.

In 2010, Integrated Ocean Drilling Program (IODP) Expedition 318 drilled an inshore-to-offshore transect off Wilkes Land (Fig. 1a), a sector of East Antarctica that is interpreted to be highly sensitive to continental ice-sheet melt (Escutia et al., 2011). The sediments recovered from IODP Site U1356 are from the continental rise of this margin (Escutia et al., 2011) and hence contain a mixture of shelf-derived material and pelagic sedimentation. Dinocyst events in this record have been recently tied to the international timescale through integration with calcareous nannofossil, diatom and magnetostratigraphic data (Bijl et al., 2018a). By Southern Ocean standards, the resulting stratigraphic age frame for the Oligocene–Miocene record of Site U1356 (Fig. 2; Table 1) is of high resolution. In this paper, we investigate the dinocyst assemblages from this succession by utilising the strong relationships between dinocyst assemblage composition and surface water conditions of today's Southern Ocean (Prebble et al., 2013). We reconstruct the oceanographic regimes during the Oligocene and mid-Miocene and evaluate their implications. We further compare the palynological data with lithological observations and their interpretations from Salabarnada et al. (2018). Pairing the sedimentological interpretations and biomarker-derived absolute sea-surface tem-

Table 1. Age constraints for the Oligocene–Miocene of Hole U1356A.

Type	FO/LO	Genus, chron	Age (Gradstein et al., 2012)	Top core	Top interval	Bottom core	Bottom interval	Depth average	Error
CONOP			10.76					98.66	
CONOP			10.92					133.80	
CONOP			13.41					133.81	
PM	(o)	C5ACn	14.07	22R-2,	75	22R-2,	90	203.23	0.07
PM	(y)	C5Bn.2n	15.03	30R-2,	50	30R-2,	75	279.63	0.13
PM	(o)	C5Cn.1n	16.27	39R-1,	35	39R-1,	65	364.10	0.15
PM	(o)	C5Cn.3n	16.72	42R-2,	59	43R-1,	25	398.28	3.98
			17.50	44R-CC		45R-CC		416.90	
			23.00	44R-CC		45R-CC		416.91	
PM	(o)	C6Cn.2n	23.03	45R-CC	40	46R-1	65	426.78	5.00
PM	(o)	C6Cn.3n	23.30	50R-1,	0			469.00	9.00
PM	(y)	C7An	24.76	63R-3,	85	63R-3,	120	597.12	0.17
PM	(o)	C7An	24.98	64R-1,	130	64R-1,	135	604.33	0.02
PM	(o)	C8n.1n	25.26	68R-2,	20	68R-2,	75	643.38	0.27
PM	(y)	C8n.2n	25.30	69R-2,	20	69R-2,	25	652.58	0.02
PM	(o)	C8n.2n	25.99	71R-6,	115	72R-1,	10	678.98	0.92
PM	(y)	C9n	26.42	73R-4,	90	75R-1,	15	701.66	7.09
PM	(o)	C9n	27.44	76R-6,	35	76R-6,	40	725.09	0.02
PM	(o)	C11n.2n	29.97	82R-6,	35	82R-6,	40	782.68	0.03
PM	(y)	C13n	33.16	93R-1,117		93R-2,	28	878.00	0.23

perature (SST) reconstructions from Site U1356 (Hartman et al., 2017) with our dinocyst assemblage data, we reconstruct the paleoceanographic conditions off Wilkes Land and assess their variability on both glacial–interglacial and longer-term timescales.

2 Material

2.1 Site description for IODP Hole U1356A

Samples were taken from IODP Hole U1356A, the only hole from Site U1356, cored on the continental rise of the Wilkes Land margin, East Antarctica (Fig. 1a; present coordinates 63°18.6′ S, 135°59.9′ E; Escutia et al., 2011). The paleolatitude calculator of van Hinsbergen et al. (2015) was used to reconstruct the paleolatitudinal history of the site (Fig. 1, between -59.8 ± 4.8 and $-61.5 \pm 3.3°$ S between 34 and 13 Ma, respectively). Hole U1356A reaches a depth of 1006.4 m into the seabed (Escutia et al., 2011). Oligocene to upper Miocene sediments were recovered between 890 and 3 m b.s.f. (metres below sea floor, Fig. 2; Tauxe et al., 2012; revised according to Bijl et al., 2018a). The uppermost 95 m of the hole was poorly recovered; sediments consisted of unconsolidated mud strongly disturbed by rotary drilling (Escutia et al., 2011). Hence, we focused our investigation on the interval between Cores 11R and 95R Section 3 (95.4–894 m b.s.f.; 10.8–33.6 Ma; Fig. 2).

2.2 Lithology in IODP Hole U1356A

In the interval between 95.4 and 894 m b.s.f., nine lithologic units have been recognised during shipboard analysis (Fig. 2; Escutia et al., 2011). Salabarnada et al. (2018) present a detailed lithologic column of the Oligocene and Miocene sediments. The lithologic facies described in Salabarnada et al. (2018) will help us compare paleoceanographic differences among climatic extremes. Salabarnada et al. (2018) distinguished various lithologies along with interpretations of their depositional settings which can be summarised as (1) laminated silty clay sediments (interpreted as glacial deposits; hereafter Fg), (2) bioturbated siltstones and claystones that in some intervals are carbonate cemented (interpreted as interglacial deposits, hereafter Fi), and (3) perturbed mass transport deposits (MTDs): slumps and debris flows. We refer to Salabarnada et al. (2018; Fig. S2 in their Supplement) for a detailed description of these facies, and to the supplementary datasets on PANGAEA (Bijl et al., 2018b) for more detailed separation of our palynological results per facies type.

2.3 Bio-magnetostratigraphic age model for IODP Hole U1356A

Stratigraphic constraints for the Oligocene–Miocene succession from IODP Hole U1356A are provided through calcareous nanoplankton, radiolarian, diatom and sparse palynological biostratigraphy, complemented by magnetostratigraphy (Tauxe et al., 2012). Bijl et al. (2018a) and Cramp-

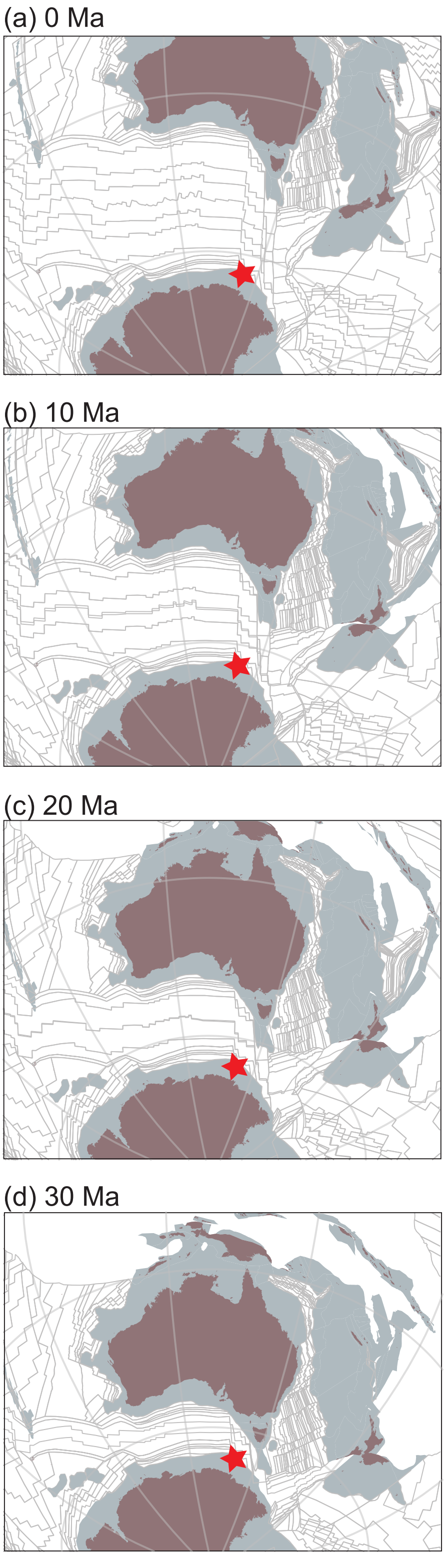

Figure 1. Paleogeography of the southwestern Pacific Ocean and position of IODP Site U1356 (red star) at **(a)** 0 Ma, **(b)** 10 Ma, **(c)** 20 Ma and **(d)** 30 Ma. Figures are modified after Bijl et al. (2018a). Reconstructions were adapted from G plates, with the plate circuit from Seton et al. (2012) and absolute plate positions of Torsvik et al. (2012).

ton et al. (2016) have updated the existing age model for Site U1356 for the Oligocene and Miocene parts of the succession, respectively. In their efforts, they recalibrated the tie points to the international timescale of Gradstein et al. (2012). We here follow their revision of the age model (Table 1). We infer ages by linear interpolation among tie points (Fig. 2; Table 1).

2.4 Depositional setting at IODP Site U1356

The depositional setting at Site U1356 changed from a shallow mid-continental shelf in the early Eocene (Bijl et al., 2013a) to a deep continental rise environment by the Oligocene (Houben et al., 2013) due to subsidence of the Wilkes Land margin (e.g. Close et al., 2009). Regional correlation of the facies at Hole U1356A via seismic profiles suggests a mix of distal-submarine fan and hemipelagic sedimentation during the early Oligocene, grading into channel–levee deposits in the later Oligocene (Escutia et al., 2011). The boundary between these two different depositional settings is at ~ 650 m b.s.f.; there, sedimentation rates increase, and the documentation of mass-transport deposits from this depth upwards suggests shelf-derived erosion events on the Wilkes Land continental slope (Escutia et al., 2011).

3 Methods

3.1 Palynological sample processing

The sample processing and analytical protocols as followed in this study are in accordance with standard procedures and have been previously described by Bijl et al. (2013b, 2018a). The 25 species of dinocysts new to science, which are formally (two species) and informally (23 species) described in Bijl et al. (2018a), fit into known and extant genera, and therefore could be confidently included in the ecological groups as described below. We refer to Bijl et al. (2018a) for an extensive overview (including plates) of the dinocyst species encountered.

3.2 Ecological grouping of dinocyst taxa

Bijl et al. (2018a) provided additional statistical evidence to distinguish in situ dinocysts from those that are reworked from older strata. In this paper, we follow the interpretations of Bijl et al. (2018a) and divide the dinocyst species into a reworked and an in situ group (Table 2). To use the in situ dinocyst assemblages for oceanographic reconstructions, we rely on the observation that many taxa in the fossil assemblages have morphologically closely related modern counterparts. This approach takes advantage of studies on the present-day relationship between Southern Ocean microplankton in general and dinoflagellate cysts in particular and their surface water characteristics (e.g. Eynaud et al., 1999; Esper and Zonneveld, 2002, 2007; Prebble et

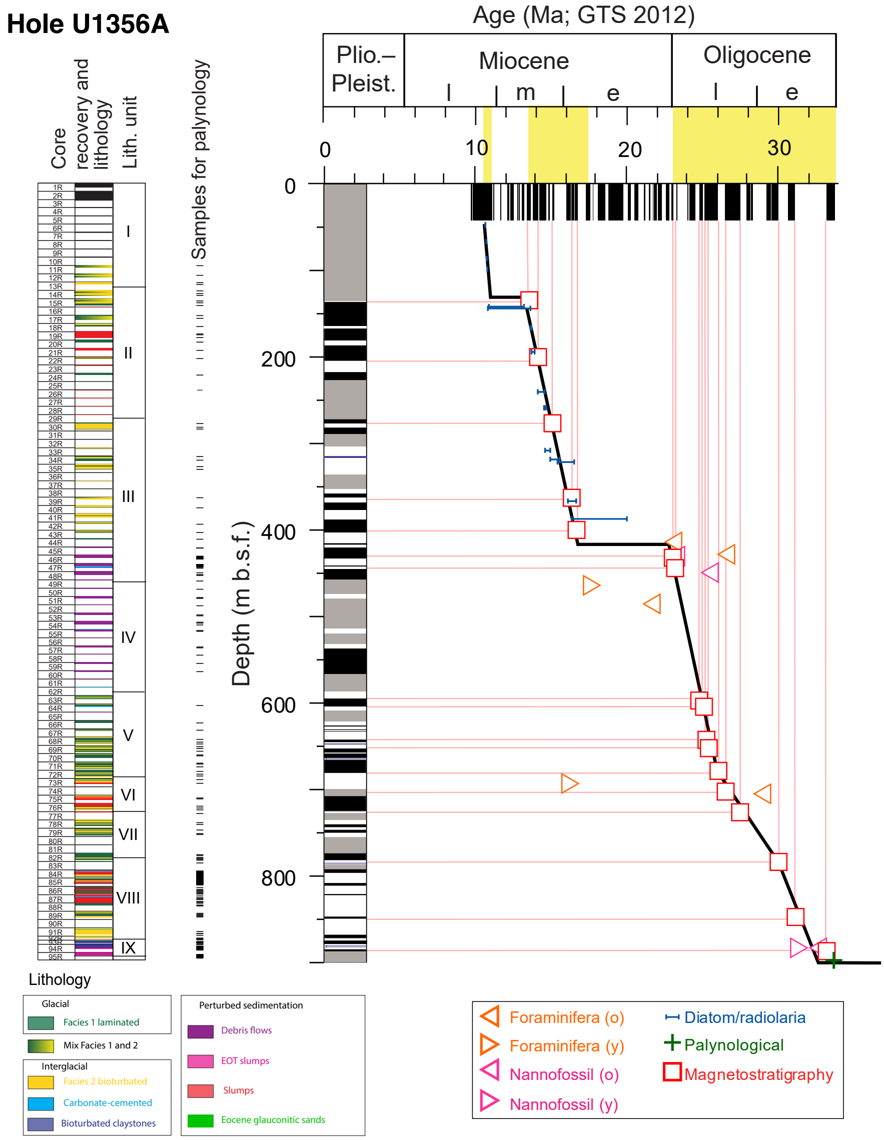

Figure 2. Age model for the Oligocene–Miocene interval of Hole U1356A. Core recovery, lithostratigraphic facies after Salabarnada et al. (2018; see also Sangiorgi et al., 2018) and lithostratigraphic units (Escutia et al., 2011). Samples taken for palynology and age–depth plot (tie points were derived from Tauxe et al., 2012, which has been recalibrated to the GTS2012 timescale of Gradstein et al., 2012, and modified based on Crampton et al., 2016). Grey intervals in paleomagnetic data reflect unknown paleomagnetic orientation, either due to absence of core recovery or poor signal. (o): old end; (y): young end. Figure modified from Bijl et al. (2018a).

al., 2013). We assign Oligocene–Miocene dinocyst taxa to present-day eco-groups interpreted from the clusters identified by Prebble et al. (2013), which appear to be closely related to the oceanic frontal systems in the Southern Ocean (Fig. 3). Supporting evidence for the ecologic affinities of the dinocyst groups comes from empirical data, such as correlation of abundances with other sediment properties or proxies (Sluijs et al., 2005; Egger et al., 2018), for instance with regard to the affinities of *Nematosphaeropsis labyrinthus*, *Operculodinium* spp., *Pyxidinopsis* cpx. (this includes *Corrudinium* spp. and *Cerebrocysta* spp.) and *Impagidinium* spp. There is further abundant evidence, both empirically (e.g. Sluijs et al., 2003; Houben et al., 2013) and from modern observations (Zonneveld et al., 2013; Prebble et al., 2013; Eynaud et al., 1999), that links the abundance of protoperidinioid dinocysts to high surface water productivity. The arguably most important inference from the surface-sediment sample study of Prebble et al. (2013) is that *Selenopemphix antarctica* is common to dominant (10–90 %) south of the Antarctic polar front (AAPF). In particular, the Antarctic continental shelf exhibits a consistently high relative abundance of *Selenopemphix antarctica*. In addition to the sur-

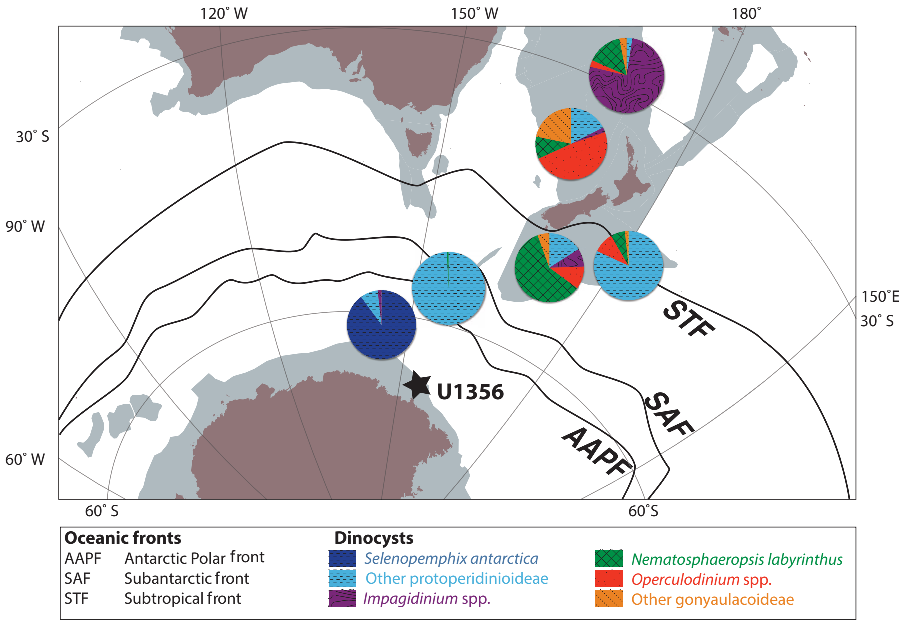

Figure 3. Generic representation of present-day distributions of dinocysts in surface sediments in the Southern Ocean. The dinocyst pie charts represent average dinocyst assemblage compositions for surface sediments underneath oceanic frontal zones in the Southern Ocean. Figure modified from Sangiorgi et al. (2018); data replotted from Prebble et al. (2013).

face samples of Prebble et al. (2013), this is also evident at the Wilkes Land margin proper (IODP Site U1357; Julian D. Hartman, Peter K. Bijl, and Francesca Sangiorgi, personal observation), at Prydz Bay (Storkey, 2006), in the Weddell (Harland and Pudsey, 1999) and Ross seas (Julian D. Hartman, Peter K. Bijl, and Francesca Sangiorgi, personal observation), and in the southern Indian Ocean (Marret and De Vernal, 1997): samples all contain very abundant to dominant (> 50 to 90 %) *S. antarctica*. The dominance of this species becomes even stronger when considering that assemblages in these surface samples often include cysts that are not easily preserved in older sediments such as that of *Polarella glacialis*. Leaving these dinocysts out of the dinocyst sum increases the relative abundance of *Selenopemphix antarctica* in surface samples. Notably, surface-sediment samples outside of the AAPF never have dominant (∼ 90 %) *Selenopemphix antarctica* (Prebble et al., 2013). Another important observation is that the surface-sediment samples south of the AAPF are generally devoid of gonyaulacean dinocysts, with the exception of two species of *Impagidinium* (i.e. *I. pallidum* and *I. sphaericum*) that may occur, although neither abundantly (Prebble et al., 2013) nor exclusively (e.g. Zevenboom, 1995; Zonneveld et al., 2013), in ice-proximal locations. Abundant *Nematosphaeropsis labyrinthus* occurs exclusively in regions outside of the subantarctic front, and particularly near the subtropical front. Thus, we conclude from the available literature a dominance of *S. antarctica* south of the AAPF, a dominance of other protoperidinioid dinocysts at and north of the AAPF, mixed protoperidinioid and gonyaulacoid dinocysts (with a notable occurrence of *Nematosphaeropsis labyrinthus* at the subantarctic front, and mixed gonyaulacoid dinocysts at and outside of the subtropical front. These trends represent a north–south transition from sea-ice-influenced conditions to cold-upwelling, high-nutrient conditions to warm-temperate, lower-nutrient conditions. We use these affinities to reconstruct past oceanographic conditions at the Wilkes Land continental margin.

4 Results

4.1 Palynological groups

In our palynological analysis we separated palynomorph groups into four categories: reworked dinocysts (following Bijl et al., 2018a; Table 2), in situ dinocysts, acritarchs and terrestrial palynomorphs. Our palynological slides further contain a varying amount of pyritised diatoms and a minor component of amorphous organic matter, which is not further considered in this study. The relative and absolute abundances of the four palynomorph groups vary considerably throughout the studied interval (Fig. 4). Reworked dinocysts are ubiquitous throughout the record, and are particularly abundant in the lowermost 40 m of the Oligocene and in the upper Oligocene. In situ dinocysts dominate mid-Oligocene and mid-Miocene palynomorph assemblages. Chorate, sphaeromorph and *Cymatiosphaera*-like acritarchs (which are not further taxonomically subdivided) dominate the assemblage in the upper Oligocene and into the mid-Miocene, while terrestrial palynomorphs (which are consid-

Table 2. List of assumed in situ and reworked dinoflagellate cyst taxa encountered in this study. See Bijl et al. (2018a) for informal species descriptions and discussion about which species are considered reworked and in situ.

In situ taxa	Reworked taxa
Adnatosphaeridium? sp.	*Achilleodinium biformoides*
Ataxodinium choane	*Achomosphaera alcicornu*
Batiacasphaera compta	*Aiora fenestrata*
Batiacasphaera spp. (pars.)	*Aireiana verrucosa*
Batiacasphaera hirsuta	*Adnatosphaeridium* spp.
Batiacasphaera micropapillata	*Alisocysta circumtabulata*
Batiacasphaera minuta	*Alterbidinium distinctum*
Batiacasphaera sphaerica	*Apectodinium* spp.
Batiacasphaera sp. A	*Arachnodinium antarcticum*
Batiacasphaera sp. B	*Areoligera* spp. (pars)
Batiacasphaera sp. C	*Areoligera semicirculata*
Batiacasphaera sp. D	*Cerebrocysta bartonensis*
Brigantedinium simplex	*Charlesdowniea clathrata*
Brigantedinium pynei	*Charlesdowniea edwardsii*
Brigantedinium sp. A	*Cooksonidinium capricornum*
Brigantedinium sp. B	*Cordosphaeridium fibrospinosum*
Brigantedinium sp. C	*Cordosphaeridium furniculatum*
Brigantedinium sp. D	*Corrudinium incompositum*
Cerebrocysta WR small	*Corrudinium regulare*
Cerebrocysta delicata	*Cribroperidinium* spp.
Cerebrocysta sp. A	*Damassadinium crassimuratum*
Cleistosphaeridium sp. B	*Dapsilidinium* spp.
Cleistosphaeridium sp. A	*Deflandrea* sp. A sensu Brinkhuis et al. (2003a, b)
Cordosphaeridium minutum	*Deflandrea antarctica*
Corrudinium labradori	*Deflandrea cygniformis*
Corrudinium sp. A	*Diphyes colligerum*
Cryodinium? sp.	*Deflandrea* spp. indet
Distatodinium spp.	*Eisenackia circumtabulata*
Edwardsiella sexispinosa	*Enneadocysta diktyostila*
Elytrocysta sp. A	*Enneadocysta multicornuta*
Elytrocysta brevis	*Eocladopyxis tessellata*
Gelatia inflata	*Fibrocysta axialis*
Habibacysta? spp.	*Glaphyrocysta intricata*
Homotryblium spp.	*Glaphyrocysta pastielsii*
Hystrichokolpoma bullatum	*Heteraulacacysta leptalea*
Huystrichosphaeropsis obscura	*Histiocysta palla*
Impagidinium spp. (pars)	*Hystrichokolpoma pusilla*
Impagidinium aculeatum	*Hystrichokolpoma rigaudiae*
Impagidinium cantabrigiense	*Hystrichokolpoma truncatum*
Impagidinium elegans	*Hystrichosphaeridium truswelliae*
Impagidinium elongatum	*Hystrichosphaeridium tubiferum*
Impagidinium pacificum	*Impagidinium maculatum*
Impagidinium pallidum	*Impagidinium waipawense*
Impagidinium paradoxum	*Kenleyia* spp.
Impagidinium patulum	*Manumiella druggii*
Impagidinium plicatum	*Melitasphaeridium pseudorecurvatum*
Impagidinium velorum	*Membranophoridium perforatum*
Impagidinium victorianum	*Octodinium askiniae*
Impagidinium sp. A	*Odontochitina* spp.
Impagidinium sphaericum	*Operculodinium* spp.
Invertocysta tabulata	*Phthanoperidinium antarcticum*
Islandinium spp.	*Phthanoperidinium stockmansii*
Lejeunecysta attenuata	*Polysphaeridium* spp.
Lejeunecysta adeliense	*Rhombodinium* sp.
Lejeunecysta fallax	*Schematophora speciosa*

Table 2. Continued.

In situ taxa	Reworked taxa
Lejeunecysta cowei	*Schematophora obscura*
Lejeunecysta acuminata	*Senegalinium* spp.
Lejeunecysta rotunda	*Spinidinium luciae*
Lejeunecysta katatonos	*Spinidinium macmurdoense*
Malvinia escutiana	*Spinidinium schellenbergii*
Nematosphaeropsis labyrinthus	*Spiniferites ramosus* cpx
Oligokolpoma galeotti	*Thalassiphora pelagica*
Operculodinium tiara	*Turbiosphaera filosa*
Operculodinium sp. A	*Turbiosphaera sagena*
Operculodinium piaseckii	*Vozzhennikovia apertura*/*S. schellenbergii* group
Operculodinium janduchenei	*Vozzhennikovia netrona*
Operculodinium cf. *eirikianum*	*?Vozzhenikovia* large
Operculodinium eirikianum	*Wetzeliella articulata*
Paleocystodinium golzowense	
Paucisphaeridium spp.	
Phthanoperidinium amoenum	
Pyxidinopsis spp. (pars)	
Pyxidinopsis sp. A	
Pyxidinopsis sp. B	
Pyxidinopsis sp. C	
Pyxidinopsis sp. D	
Pyxidinopsis vesciculata	
Pyxidinopsis tuberculata	
Pyxidinopsis reticulata	
Pyxidinopsis fairhavensis	
Reticulatosphaera actinocoronata	
Selenopemphix antarctica	
Selenopemphix nephroides	
Selenopemphix dioneacysta	
Selenopemphix sp. A	
Selenopemphix undulata	
Selenopemphix brinkhuisi	
Spiniferites sp. B	
Spiniferites sp. A	
Spiniferites sp. C	
Stoveracysta ornata	
Stoveracysta kakanuiensis	
?Svalbardella spp.	
Tectatodinium spp.	
Unipontedinium aquaeductus	
Protoperidinioid indet	
Protoperidinium sp. B	
Protoperidinium sp. A	
Protoperidinium sp. C	
Protoperidinium sp. D	

ered in situ and not reworked from older strata; Strother et al., 2017) are a constant minor (a few percent of the total palynomorph assemblage) component of the total palynomorph assemblage (Fig. 4). The terrestrial palynomorphs and the paleoclimatic and paleoecological interpretations derived from them will be presented in another study.

4.2 In situ dinocyst assemblages

Throughout the Oligocene, in situ dinocyst assemblages are dominated by protoperidinioid dinocysts, notably *Brigantedinium* spp., *Lejeunecysta* spp., *Malvinia escutiana* and *Selenopemphix* spp. (Fig. 4), all of which are cysts of heterotrophic dinoflagellates (e.g. Esper and Zonneveld, 2007). Among these protoperidinioid cysts, *S. antarctica* is fre-

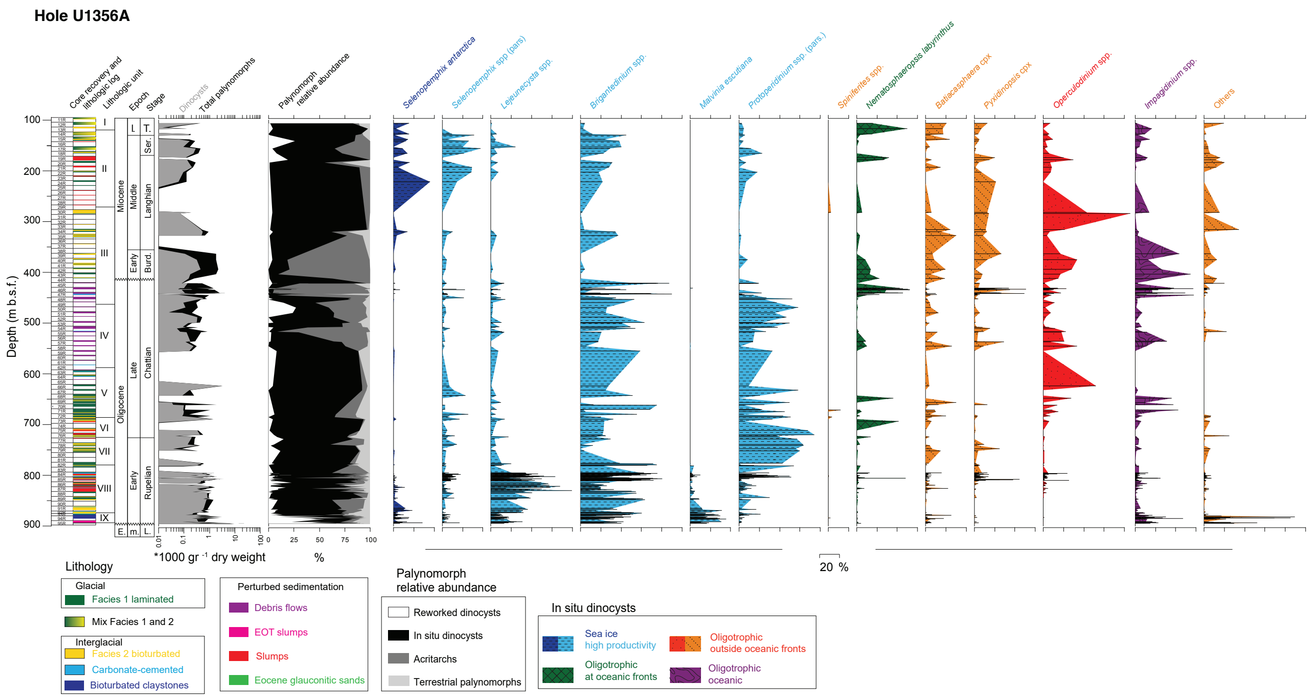

Figure 4. Core recovery, lithostratigraphic facies (after Salabarnada et al., 2018, and Sangiorgi et al., 2018), lithologic units (Escutia et al., 2011), chronostratigraphic epochs (E: Eocene) and stages (L: Lutetian; Burd.: Burdigalian; Ser.: Serravallian; T.: Tortonian), absolute palynomorph (grey) and in situ dinocyst (black) concentrations (number per gram of dry sediment, presented on a logarithmic scale), palynomorph content (reworked dinocysts, in situ dinocysts, acritarchs, terrestrial palynomorphs (given in percentages of total palynomorphs), and relative abundance of in situ dinocyst eco-groups (in percent of in situ dinocysts) for the Oligocene–Miocene of Hole U1356A.

quently present (up to 39 % of the in situ assemblage), but only between 33.6 and 32.1 Ma (earliest Oligocene) and after 14.2 Ma (i.e. during and after the mid-Miocene climatic transition, MMCT; Fig. 5). The remainder of the record is almost entirely devoid of *S. antarctica*. This is much in contrast to the dinocyst assemblages near Site U1356 today, which are dominated by this taxon (Prebble et al., 2013). Instead of *S. antarctica*, during the Oligocene and Miocene other protoperidinioid dinocysts such as *Brigantedinium* spp., several *Lejeunecysta* species and *Selenopemphix nephroides*, which have close affinities to high-nutrient conditions in general (e.g. Harland and Pudsey, 1999; Zonneveld et al., 2013) but are not specifically restricted to sea-ice proximity or the Southern Ocean, dominate. Today, these three genera dominate dinocyst assemblages in high-nutrient settings at or outside of the AAPF (Prebble et al., 2013). A varying abundance of protoperidinioid dinocysts could not be placed with confidence into established protoperidinioid dinocyst genera. These are grouped under "protoperidinium spp. (pars.)" (Fig. 4; Bijl et al., 2018a) and are here assumed to exhibit the same heterotrophic lifestyle as the other protoperidinioid dinocyst genera.

Next to protoperidinioid dinocysts, gonyaulacoid dinocysts also occur in relatively high abundances throughout the record from Site U1356. They comprise both known and previously unknown (Bijl et al., 2018a) species of *Batiacashaera*, *Pyxidinopsis*, *Corrudinium*, *Cerebrocysta*, *Nematosphaeropsis*, *Impagidinium*, *Operculodinium* and *Spiniferites* (Figs. 4, 5). The "others" group represents exclusively gonyaulacoid species such as *Invertocysta tabulata* and *Gelatia inflata*. Except for the extinct genera *Batiacasphaera* and *Cerebrocysta* and some genera in the "others" group, all the other genera are still extant and represent phototrophic dinoflagellates (Zonneveld et al., 2013). Their abundance is at the expense of the assumed heterotrophic protoperidinioid dinocysts. A marked increase in abundance of gonyaulacoid cysts is associated with the Mid-Miocene Climatic Optimum (MMCO, between ∼ 17 and 15 Ma; Figs. 4, 5; Sangiorgi et al., 2018). Of the gonyaulacoid taxa, *Nematosphaeropsis labyrinthus* is associated with frontal systems of the present-day Southern Ocean (Prebble et al., 2013) and of the North Atlantic Ocean (Boessenkool et al., 2001; Zonneveld et al., 2013).

4.3 Comparison between palynological data and lithological facies

The Oligocene–Miocene sediments from Site U1356 comprise distinctive alternations of lithologic facies throughout the section (Salabarnada et al., 2018; their Fig. S2). Lami-

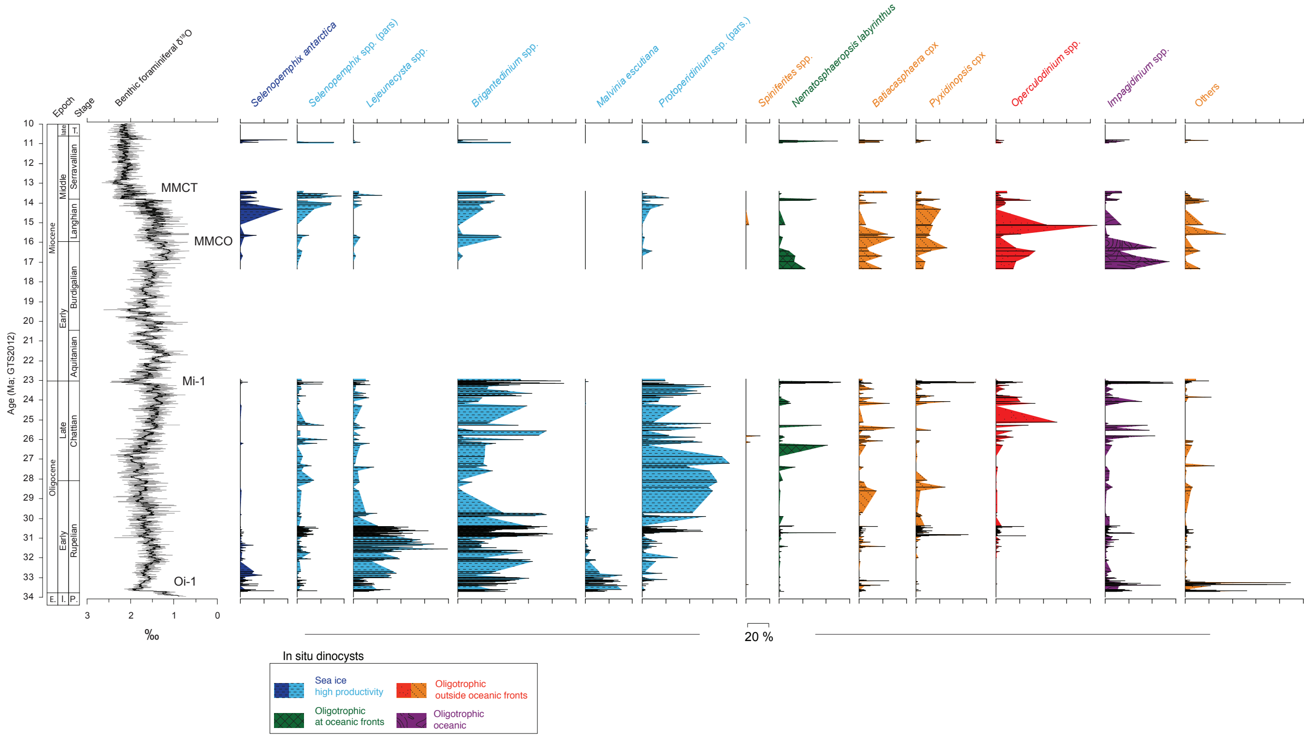

Figure 5. Megasplice of benthic foraminiferal oxygen isotope data (De Vleeschouwer et al., 2017) from Site 1146 (Holbourn et al., 2013), Site 1338, (Holbourn et al., 2014), Site 1337 (Holbourn et al., 2015), Site 1090 (Billups et al., 2004), Site 926 (Pälike et al., 2006a) and Site 1218 (Pälike et al., 2006b), with a 15-point running mean. In situ dinocyst assemblage data from Site U1356. The age–depth model specified in Fig. 2 and Table 1 was used. E.: Eocene; l.: late; P.: Priabonian; T.: Tortonian.

nated (Fg) and bioturbated sediments, which in some intervals are carbonate-rich (Fi), alternate on orbital timescales and this pattern is in some intervals disrupted by slumps and/or debris flows. Here we evaluate and compare the palynological content of each of these facies in terms of both absolute and relative abundance of the main palynomorph groups: reworked dinocysts, in situ dinocysts, acritarchs and terrestrial palynomorphs, and relative abundance of in situ dinocyst eco-groups.

4.3.1 Palynomorph groups and lithology

There are distinct differences in the relative and absolute abundances of the palynomorph groups among the different lithologies (Fig. 6). The highest relative and absolute abundances of reworked dinocysts occur in the slump and Fi facies (Fig. 6), particularly those of early Oligocene age (Eocene–Oligocene transition (EOT) slumps and bioturbated siltstones in Supplement datasets), in line with observations of Houben et al. (2013). Reworking is a minor component of the palynomorph assemblage in the other lithologies for most samples, with a higher absolute abundance in Fi deposits than in glacial deposits. This suggests that submarine erosion of Eocene continental shelf material was particularly prominent during interglacial times, when arguably sea level along the Wilkes Land margin was lower (Stocchi et al., 2013). The relative and absolute abundance of in situ dinocysts is highest in the interglacial and glacial deposits and the slumps (Fig. 6). Acritarchs reach the highest relative and absolute abundances in Fi facies and in the debris flows (Fig. 6). Terrestrial palynomorphs are most abundant in the lower Oligocene slumps and Fi sediments (Supplement tables) but have low relative abundance in all lithologies (Fig. 6).

4.3.2 In situ dinocyst eco-groups and their abundance per facies

The in situ dinocyst eco-groups are also compared with the lithological facies (Fig. 7). The Fg glacial facies contains generally more peridinioid (heterotrophic) dinocysts, while the Fi interglacial facies contains more gonyaulacoid (oligotrophic) dinocysts, but more information is to be seen when focusing on the individual eco-groups. The abundance of *Selenopemphix antarctica* is low throughout the record (0–5 %), with the exception of the interval post-dating the MMCO and the lowermost Oligocene, when the taxon occasionally reaches more than 20 % (Figs. 4, 5). *S. antarctica* reaches the highest abundances in the slump facies and Fg and is less abundant in the other lithologies (Fig. 7). *Selenopemphix* spp. reaches the highest relative abundances

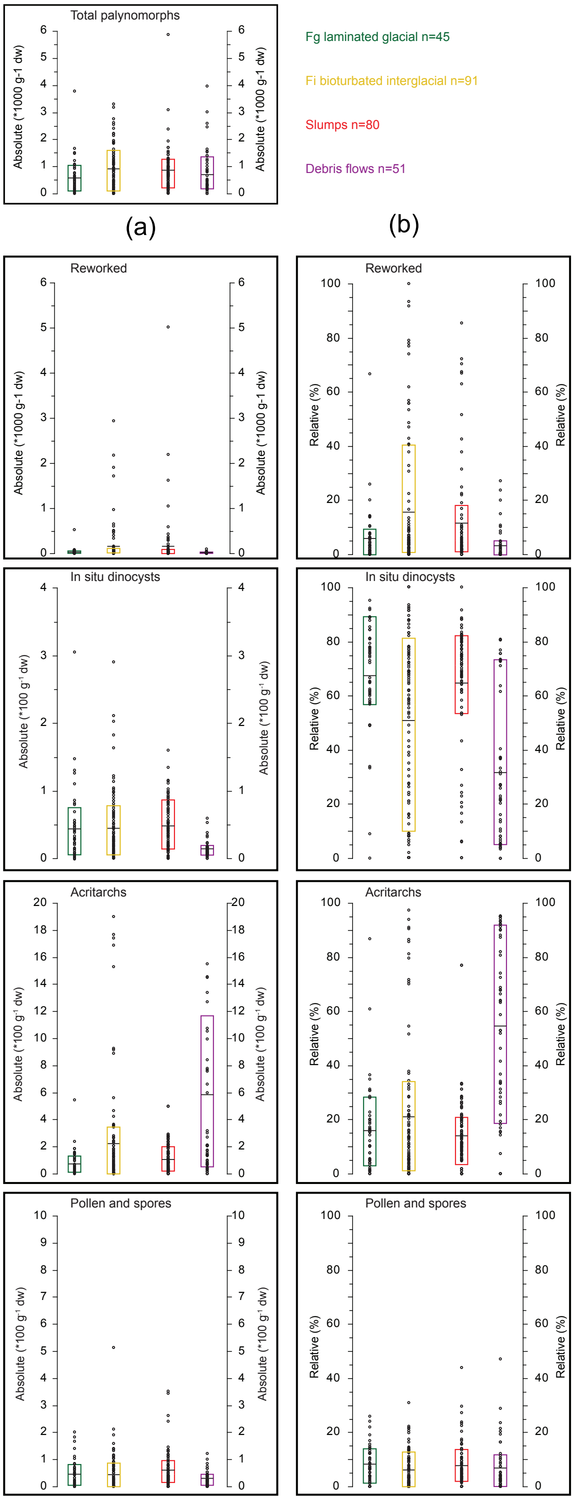

Figure 6. Comparison of absolute (**a**, in number per gram of dry weight) and relative (**b**; in percent of total palynomorphs) abundances of palynomorph groups per lithology for Hole U1356A. Average (black lines) and 17–83 % percentile (coloured bar) of absolute and relative abundances of total palynomorphs, reworked dinocysts, in situ dinocysts, acritarchs and terrestrial palynomorphs grouped for the different facies (Salabarnada et al., 2018).

in the Fg facies. *Lejeunecysta* spp. and *Protoperidinium* spp. pars. show no noticeable variance in relative abundance in any of the lithologies. *Brigantedinium* spp. is clearly more abundant in the Fg facies than in the Fi facies. *Malvinia escutiana* abundances seem to be higher in Fi than in Fg (Fig. 7), although this species has a stratigraphic occurrence that is limited to the early Oligocene (Bijl et al., 2018a). *Nematosphaeropsis labyrinthus*, *Pyxidinopsis* cpx, *Operculodinium* spp. and *Impagidinium* spp. reach higher relative abundances in the Fi than in Fg facies, whereas the abundance of *Batiacasphaera* spp. seems invariant to facies.

5 Discussion

5.1 Paleoceanographic interpretation of the dinocyst assemblages

The composition of the dinoflagellate cyst assemblages in the Wilkes Land record reflect changes in surface-ocean nutrients, sea-surface temperature conditions and paleoceanographic features. We will discuss these implications in the following.

5.1.1 Surface-ocean nutrient conditions

The general dominance of heterotrophic dinocysts in the Oligocene–Miocene assemblages indicates overall high nutrient levels in the surface waters. Given the offshore geographic setting, we therefore infer that surface waters at Site U1356 experienced upwelling associated with the AAPF during most of the Oligocene and Miocene. We can exclude the possibility that nutrients were brought to the site via river run-off given the anticipated small catchment area that experienced liquid precipitation in the Wilkes Land hinterland, the low amounts of terrestrially derived (amorphous) organic matter in the palynological residues and relatively low branched over isoprenoid tetraether (BIT) index values (Hartman et al., 2017) that indicate predominantly marine organic matter. The exception may be the MMCO (Sangiorgi et al., 2018) when considerable soil-derived organic matter reached the site.

The occasionally abundant gonyaulacoid cyst taxa encountered in our record suggest that at times surface waters that were much less nutrient-rich supported the growth of oligotrophic dinoflagellates. Notably, these taxa are typical for outer-shelf to oceanic or outer neritic settings (e.g. Sluijs et al., 2005; Zonneveld et al., 2013; Prebble et al., 2013), which makes it unlikely that they were reworked from the continental shelf. Indeed, they show low relative abundances in the perturbed deposits (Fig. 7). Although the members of these genera have relatively long stratigraphic ranges extending back into the Eocene, most of the species encountered at Site U1356 are not present in Eocene continental shelf sediments in the region (e.g. Wrenn and Hart, 1988; Levy and Harwood, 2000; Brinkhuis et al., 2003a, b; Bijl et al.,

Figure 7. Relative abundance of in situ eco-groups within various lithologies at Hole U1356A. Average (black line) and 17–83 % percentile (coloured bar) of relative abundances of grouped taxa from samples from the different facies (Salabarnada et al., 2018).

2010, 2011, 2013a, b). This makes it unlikely that they are reworked from Eocene strata. In addition, statistical analysis also yields that these species are part of the in situ assemblage (Bijl et al., 2018a). These different lines of evidence lead us to interpret them as part of the in situ pelagic assemblage in our study, which allows us to interpret their paleoceanographic implications based on their modern affinities. The absence of these taxa in modern surface waters south of the AAPF is probably caused by a combination of different factors: it can be connected to low sea-surface temperatures and an isolation by strong eastward currents but also to the abundance and seasonally concentrated availability of nutrients, all of which make the proximal surface waters off Antarctica a highly specialistic niche unfavourable for these species. Apparently, surface water conditions during the Oligocene and Miocene were such that these oligotrophic species could at times proliferate so close to the Antarctic margin.

5.1.2 Sea-surface temperature

The best modern analogues for the dinocyst assemblages in our record are to be sought off the southern margins of New Zealand and Tasmania (as inferred from Prebble et al., 2013; Fig. 2). Today, these regions feature a mix between protoperidinioid dinocysts along with gonyaulacoid dinocyst genera such as *Nematosphaeropsis*, *Operculodinium* and *Impagidinium*. These assemblages prevail in surface waters with mean annual temperatures of 8–17 °C (Prebble et al., 2013) and therefore suggest relatively warm surface water temperatures close to the Wilkes Land margin. In support of this, a Bayesian approach on the TEX_{86} index values at Site U1356 (presented in Sangiorgi et al., 2018; Hartman et al., 2017) also suggests the Southern Ocean mid-latitudes as a modern-analogue region and reconstructs a paleotemperature range of 8–20 °C for the Oligocene–Miocene at Site U1356, with values in excess of 24 °C for the late Oligocene (Hartman et al., 2017). Further, supporting evidence for temperate Oligocene–Miocene surface waters comes from the abundance of nannofossils encountered in the sediments (Escutia et al., 2011; Salabarnada et al., 2018). Today, carbonate-producing plankton is rare in high-latitude surface waters south of the AAPF (Eynaud et al., 1999). Moreover, the remains of the few pelagic carbonate-producing organisms living at high latitudes rarely reach the ocean floor because of strong upwelling of relatively CO_2-rich, corrosive waters (e.g. Olbers et al., 2004). Hence, the presence of carbonate-rich intervals during the Oligocene–Miocene at Site U1356 along with the encountered oligotrophic, temperate dinocysts suggests fundamentally warmer surface water conditions than today.

5.1.3 Surface paleoceanography

The strong similarity of Oligocene–Miocene dinocyst assemblages at Site U1356 with those today occurring much further north (i.e. around Tasmania and southern New Zealand (Prebble et al., 2013) suggests a fundamentally different modus operandi of Southern Ocean surface oceanography. The strict latitudinal separation of dinocyst assemblages in the Southern Ocean today (Prebble et al., 2013) is likely due to different surface water masses present across the oceanic fronts where strong wind-driven divergence around 60° S (known as the Antarctic Divergence; e.g. Olbers et al., 2004), strong sea-ice season and/or the vigorous ACC are in place. The strength and position of the AAPF during the Oligocene–Miocene is not well understood. General circulation model (GCM) experiments under Miocene boundary conditions suggest that west and east wind drifts prevailed south and north of 60° S, respectively (Herold et al., 2011). This wind orientation determined the average position of the Antarctic Divergence at 60° S during the Oligocene and Miocene, similar to today. This suggests that Site U1356 was likely directly overlain by the AAPF. However, the significantly warmer, more oligotrophic dinocyst assemblages off Wilkes Land throughout the Oligocene–Miocene argue against proximity to the AAPF. The position of the AAPF relative to that of Site U1356 strongly determines the likelihood of southward transport of low-latitude waters towards the site. A southward position of the AAPF relative to Site U1356 would greatly enhance the possibility for a southward migration of temperate surface water masses towards the site. A northward position of the AAPF relative to the site would make such a latitudinal migration much more difficult. The presence of carbonate in these deep marine sediments also suggests that upwelling of corrosive waters through the (proto-)Antarctic Divergence was either much reduced or located elsewhere. Therefore, we deduce that the occurrence of the oligotrophic, temperate dinocysts is evidence for a southward position of the AAPF relative to the position of Site U1356. This would allow a higher connectivity between the site and the lower latitudes and promote preservation of carbonate on the sea floor. Also, such an oceanographic setting would be in line with reduced sea ice along the Wilkes Land margin.

The separate averaging of dinocyst assemblages for glacial and interglacial facies from Site U1356 (Fig. 7) allows us to reconstruct glacial–interglacial changes in surface water conditions throughout the Oligocene. First of all, our observations suggest that Oligocene glacial–interglacial cycles were connected to substantial paleoceanographic dynamics off Wilkes Land. In agreement with the 2–3 °C SST variability as documented for this site during glacial–interglacial cycles (Hartman et al., 2017), dinocyst assemblages contain more oligotrophic, temperate dinocysts during interglacial times compared to glacial times when more eutrophic, colder dinocysts proliferated (Fig. 7). This could be the result of a slight latitudinal movement of oceanic frontal systems (notably the AAPF) as it has been reconstructed for the Southern Ocean fronts during the most recent glacial-to-interglacial transition (e.g. Bard and Rickaby, 2009; Kohfeld et al., 2013; Xiao et al., 2016). In such a scenario, the AAPF would reach a southern position during interglacials, allowing for temperate oligotrophic surface waters to reach the site, while it would migrate northward over Site U1356 during glacials, thereby causing cold, high-nutrient surface water conditions and obstructing low-latitude influence.

5.2 Implications for Oligocene–Miocene ocean circulation

At Site U1356, dinocyst assemblages bear similarities to present-day proximal-Antarctic assemblages (Prebble et al., 2013) only in the lowermost Oligocene and in strata deposited after the MMCO (after 14.2 Ma); in particular, they are characterized by high abundances (up to 39 %) of *Selenopemphix antarctica*. Even in those intervals, however, the relative abundances of *S. antarctica* do not reach present-day values at the same site (Prebble et al., 2013). The absence of a strong shift towards modern-day-like assemblages in our record can be interpreted to reflect a weaker-than-present ACC. This interpretation is in line with numerical models (Herold et al., 2012; Hill et al., 2013). The ACC itself represents an important barrier for latitudinal surface water transport towards the Antarctic margin, in addition to the Antarctic Divergence (Olbers et al., 2004). Our data suggest an increase in the influence of oligotrophic dinocysts at the Antarctic margin during the late Oligocene and during the MMCO, which argues against the installation of a vigorous ACC at 30 Ma as recently inferred by Scher et al. (2015): No particular change in sea-surface conditions emerges from our dinoflagellate cyst data around 30 Ma, and there is no major change in the benthic $\delta^{18}O$ data either (Fig. 5). Instead, if the Tasmanian Gateway had opened to an extent that allowed ACC development (Scher et al., 2015), the ACC must have been much weaker throughout the Oligocene and Miocene than at present, which has also emerged from modelling experiments (Hill et al., 2013). The strongly different dinocyst assemblages compared to present-day dinocyst assemblages near Site U1356 throughout our record imply that a strong coherent ACC was not installed until after the MMCT (11 Ma). This is consistent with inferences from the lithology at the same site (Salabarnada et al., 2018), suggesting a proto-ACC much weaker than at present and, likewise, weaker Southern Ocean frontal systems. An alternative explanation is that the ACC increased in strength during the Oligocene–Miocene, but that this strengthening had no influence on the dinocyst assemblages at Site U1356. However, the vigorous nature of the ACC influencing surface as well as bottom waters and governing eddy water circulation in the Southern Ocean (Olbers et al., 2004) in combination with the high sensitivity of dinoflagellates to changes in surface water conditions (e.g. Zonneveld et al., 2013; Prebble et al., 2013) makes such a scenario very unlikely. Nevertheless, to firmly clarify whether the ACC reached its present-day strength only after the MMCT (as suggested by our data), ocean-circulation modelling of time slices younger than the Oligocene (Hill et al., 2013) will be required.

Our results also seem difficult to reconcile with indications of bottom-water formation at the Wilkes Land margin, as seen from neodymium isotope analyses on the same sediments (Huck et al., 2017). It could be that bottom-water formation took place only when surface waters cooled down in wintertime, and the organic proxies are more representative of spring–summer conditions. Salabarnada et al. (2018) interpret bottom-current activity in the Oligocene at Site U1356 and suggest it may be spilling over from the Ross Sea, like today. Our dinocyst results and the SST reconstructions by Hartman et al. (2017) suggest that surface waters at the Wilkes Land margin were too warm to allow local bottom-water formation; therefore our data also support the suggestion that bottom water along the Wilkes Land margin was sourced from the Ross Sea.

5.3 Implications for ice-sheet and sea-ice variability

The relative abundances of the sea-ice-related *Selenopemphix antarctica* are consistently lower in our record than in present-day dinocyst assemblages near Site U1356 (Prebble et al., 2013; Fig. 3). This suggests that sea-ice conditions were never similar to today during the studied time interval. More specifically, our dinocysts suggest the occurrence of sea ice near the site only during two time intervals: the first 1.5 million years following the Oi-1 glaciation (33.6–32.1 Ma; Fig. 5), and during and after the MMCT (after 14.2 Ma; Fig. 5). Numerical ice-sheet and sea-ice modelling (DeConto et al., 2007) has suggested sea ice to develop only if the continental ice sheets reach the coastline. Our lack of sea-ice indicators during most of the Oligocene and Miocene could thus point towards a much-reduced Antarctic continental ice sheet during that time. The finding of a weaker sea-ice season throughout most of the Oligocene–Miocene at Site U1356 is important because it suggests a decrease in the potential formation of Antarctic bottom waters at this site.

The relative abundance of oligotrophic dinocyst taxa broadly follows long-term Oligocene–Miocene benthic $\delta^{18}O$ trends (see Fig. 5): during times of low $\delta^{18}O$ values in deep-sea benthic foraminifera (and thus high deep-sea temperatures and/or less ice volume, e.g. at 32, 24 and 15 Ma; Fig. 5), the abundance of oligotrophic temperate dinocysts was high (Fig. 5). At times of higher $\delta^{18}O$ values, lower deep-sea temperatures and higher ice volume (e.g. at 33.5, 27, 23, and 13 Ma; Fig. 5), temperate dinocysts were reduced in abundance and high-nutrient, sea-ice indicators (re)appeared. Altogether, on long timescales this pattern suggests that there was a stronger influence of warm surface waters at the Wilkes Land margin at times when ice sheets were smaller and climate was warmer and less influence of warm surface waters during times of larger ice sheets. Hence a connection existed between ice-sheet expansion–retreat and paleoceanography.

Oxygen-isotope mass-balance calculations suggest that a modern-day-sized Antarctic ice sheet formed at the Eocene–Oligocene boundary (DeConto et al., 2008). Benthic $\delta^{18}O$ records suggest that ice sheets must have fluctuated considerably in size during the subsequent Oligocene and Miocene (Liebrand et al., 2017), although this inference lacks an independent assessment of the deep-sea temperature effect in these $\delta^{18}O$ values. The same conclusion was reached based on detailed microfossil, geochemical and facies analyses on sediments from the Gippsland Basin, southeast Australia (Gallagher et al., 2013). This study suggests that ice volume during the early Oligocene varied by as much as 140–40 % of its present-day size, of which the maximum ice volume estimates far exceed those implied by our data. However, there is consistency in the observation of considerable glacial–interglacial and long-term dynamics in the ice–ocean system. This is in contrast to the heavy $\delta^{18}O$ values for Oligocene benthic foraminifera from Maud Rise (ODP Site 690), which suggest Antarctic ice sheets were near present-day size throughout the Oligocene (Hauptvogel et al., 2017). It remains to be seen whether the variability in paleoceanography as indicated by our data can be extrapolated to larger parts of the Antarctic margin, including regions of deep-water formation. Given the high temperatures and only weak sea-ice influence, the Wilkes Land margin was likely not the primary sector of deep-water formation (see, e.g. Herold et al., 2012), although there is ample evidence for bottom-current activity at the site (Salabarnada et al., 2018; Huck et al., 2017). Instead, it appears that bottom-water formation during the Oligocene took place along the Wilkes Land coast (Huck et al., 2017). If the oceanographic and climate variability that we reconstruct offshore Wilkes Land also characterises regions of deep-water formation, some (if not all) of the variability on both long and orbital timescales as documented in benthic δ^{18}O records would be due to changes in deep-sea temperature rather than Antarctic ice volume (see also Hartman et al., 2017). Meanwhile, we find little support in our study for the large (and, by implication, marine-terminating) continental ice sheets in this sector of East Antarctica during the Oligocene as implied by Hauptvogel et al. (2017) given the absence of dominance of sea-ice dinocysts and the presence of in situ terrestrial palynomorphs (Strother et al., 2017). As an alternative explanation for the difference in δ^{18}O values between Maud Rise (Site 690) and the equatorial Pacific (Site 1218) during the Oligocene (Hauptvogel et al., 2017), we suggest that these two sedimentary archives have recorded the characteristics of two different deep-water masses, with those at Maud Rise (Site 690) being much colder and more saline than those in the equatorial Pacific (Site 1218).

6 Conclusions

The dinocyst assemblages in the Oligocene–Miocene (33.6–11 Ma) of Site U1356 were interpreted in terms of surface water paleoceanography via comparison with present-day dinocyst distribution patterns. Based on our results, we suggest that the Oligocene–Miocene surface paleoceanography of the Southern Ocean was fundamentally different from that of today. A sea-ice signal (weaker still than at present) emerges for the Wilkes Land margin only for the first 1.5 million years of the Oligocene (33.6–32.1 Ma) and during and after the MMCT (after 14.2 Ma). During the remainder of the Oligocene–Miocene, surface waters off Wilkes Land were warm and relatively oligotrophic; notably, they lack indications of a prominent sea-ice season. Upwelling at the Antarctic Divergence was profoundly weaker during Oligocene and Miocene times than at present, or significantly displaced southward from its present-day position. Furthermore, the continental ice sheets were much reduced at the Wilkes Land subglacial basin for most of the Oligocene–Miocene compared to today. The influence of warm oligotrophic surface waters appears strongly coupled to deep-sea δ^{18}O values, suggesting enhanced low-latitude influence of surface waters during times of light δ^{18}O in the deep sea and vice versa. The absence of (a trend towards a stronger) paleoceanographic isolation of the Wilkes Land margin throughout the Oligocene to mid-Miocene suggests that the ACC may not have attained its full, present-day strength until at least after the mid-Miocene climatic transition. Moreover, we note considerable glacial–interglacial amplitude variability in this oceanographic setting. Stronger influence of oligotrophic, low-latitude-derived surface waters prevailed over Site U1356 during interglacial times and more eutrophic, colder waters during glacial times. This pattern may suggest considerable latitudinal migration of the AAPF over the course of Oligocene and Miocene glacial–interglacial cycles.

Data availability. The datasets to this article are available at PANGAEA (Bijl et al., 2018b) and in the Supplement.

Supplement. The supplement related to this article is available online at: https://doi.org/10.5194/cp-14-1015-2018-supplement.

Author contributions. PKB, FS, CE and JP designed the research. AJPH, FS and PKB carried out dinocyst analyses for the earliest Oligocene, the Miocene and the Oligocene–Miocene boundary interval, respectively. AS and CE provided the lithological data. PKB integrated, cross-validated, and compiled the data and wrote the paper with input from all co-authors.

Competing interests. The authors declare that they have no conflict of interest.

Acknowledgements. This research used data and samples from the Integrated Ocean Drilling Program (IODP). IODP was sponsored by the US National Science Foundation and participating countries under management of Joined Oceanographic Institutions Inc. Peter K. Bijl and Francesca Sangiorgi thank NWO-NNPP grant no. 866.10.110 and NWO-ALW VENI grant no. 863.13.002 for funding and Natasja Welters for technical support. Jörg Pross acknowledges support through the IODP priority program of the German Research Foundation (DFG). Carlota Escutia and Ariadna Salabarnada thank the Spanish Ministerio de Economía y Competitividad for grant CTM2014-60451-C2-1-P. We thank Kasia Śliwińska, Stephen Gallagher and the anonymous reviewer for their constructive comments that considerably improved our paper.

Edited by: David Thornalley
Reviewed by: Stephen Gallagher, Kasia K. Śliwińska, and one anonymous referee

References

Badger, M. P. S., Lear, C. H., Pancost, R. D., Foster, G. L., Bailey, T. R., Leng, M. J., and Abels, H. A.: CO_2 drawdown following the middle Miocene expansion of the Antarctic Ice Sheet, Paleoceanography, 28, 42–53, 2013.

Bard, E. and Rickaby, R. E. M.: Migration of the subtropical front as a modulator of glacial climate, Nature, 460, 380–383, 2009.

Barker, P., Camerlenghi, A., Acton, G., Brachfeld, S., Cowan, E., Daniels, J., Domack, E., Escutia, C., Evans, A., Eyles, N., Guyodo, Y., Iorio, M., Iwai, M., Kyte, F., Lauer, C., Maldonado, A., Moerz, T., Osterman, L., Pudsey, C., Schuffert, J., Sjunneskog, C., Vigar, K., Weinheimer, A., Williams, T., Winter, D., and Wolf-Welling, T.: Antarctic glacial history and sea-level change – Leg 178 samples Antarctic Peninsula margin sediments, JOIDES Journal, 24, 7–10, 1998.

Barker, P. F. and Thomas, E.: Origin, signature and paleoclimatic influence of the Antarctic Circumpolar Current, Earth-Sci. Rev., 66, 143–162, 2004.

Barker, P. F., Barrett, P. J., Cooper, A. K., and Huybrechts, P.: Antarctic glacial history from numerical models and continental margin sediments, Palaeogeogr. Palaeocl., 150, 247–267, 1999.

Barrett, P. J.: Antarctic Cenozoic history from the CIROS-1 drillhole, McMurdo Sound, Science Information Publishing Centre DSIR Bulletin, 245, Wellington, 1989.

Beddow, H. M., Liebrand, D., Sluijs, A., Wade, B. S., and Lourens, L. J.: Global change across the Oligocene-Miocene transition: High-resolution stable isotope records from IODP Site U1334 (equatorial Pacific Ocean), Paleoceanography, 31, 81–97, 2016.

Bijl, P. K., Houben, A. J. P., Schouten, S., Bohaty, S. M., Sluijs, A., Reichart, G. J., Sinninghe Damsté, J. S., and Brinkhuis, H.: Transient Middle Eocene Atmospheric Carbon Dioxide and Temperature Variations, Science, 330, 819–821, 2010.

Bijl, P. K., Pross, J., Warnaar, J., Stickley, C. E., Huber, M., Guerstein, R., Houben, A. J. P., Sluijs, A., Visscher, H., and Brinkhuis, H.: Environmental forcings of Paleogene Southern Ocean dinoflagellate biogeography, Paleoceanography, 26, PA1202, https://doi.org/10.1029/2009PA001905, 2011.

Bijl, P. K., Bendle, A. P. J., Bohaty, S. M., Pross, J., Schouten, S., Tauxe, L., Stickley, C. E., McKay, R. M., Röhl, U., Olney, M., Sluijs, A., Escutia, C., Brinkhuis, H., and Expedition 318 scientists: Eocene cooling linked to early flow across the Tasmanian Gateway, P. Natl. Acad. Sci. USA, 110, 9645–9650, 2013a.

Bijl, P. K., Sluijs, A., and Brinkhuis, H.: A magneto-chemo-stratigraphically calibrated dinoflagellate cyst zonation of the early Paleogene South Pacific Ocean, Earth-Sci. Rev., 124, 1–31, 2013b.

Bijl, P. K., Houben, A. J. P., Bruls, A., Pross, J., and Sangiorgi, F.: Stratigraphic calibration of Oligocene–Miocene organic-walled dinoflagellate cysts from offshore Wilkes Land, East Antarctica, and a zonation proposal, J. Micropalaeontol., 37, 105–138, https://doi.org/10.5194/jm-37-105-2018, 2018a.

Bijl, P. K., Houben, A. J. P., Hartmann, J. D., Pross, J., Salabarnada, A., Escutia, C., and Sangiorgi, F.: Palynological counts from the Oligocene-Miocene of IODP Site 318-U1356, Wilkes Land Margin, Antarctica, PANGAEA, https://doi.org/10.1594/PANGAEA.890160, 2018b.

Billups, K., Pälike, H., Channell, J. E. T., Zachos, J. C., and Shackleton, N. J.: Astronomic calibration of the late Oligocene through early Miocene geomagnetic polarity time scale, Earth Planet. Sc. Lett., 224, 33–44, 2004.

Boessenkool, K. P., Van Gelder, M., Brinkhuis, H., and Troelstra, S. R.: Distribution of organic-walled dinoflagellate cysts in surface sediments from transects across the Polar Front offshore southeast Greenland, J. Quaternary Sci., 16, 661–666, 2001.

Brinkhuis, H., Munsterman, D. M., Sengers, S., Sluijs, A., Warnaar, J., and Williams, G. L.: Late Eocene to Quaternary dinoflagellate cysts from ODP Site 1168, off western Tasmania, in: Proceedings of the Ocean Drilling Program, Scientific Results, edited by: Exon, N. and Kennett, J. P., 189, U.S. Government Printing Office, College Station, Texas, 2003a.

Brinkhuis, H., Sengers, S., Sluijs, A., Warnaar, J., and Williams, G. L.: Latest Cretaceous to earliest Oligocene, and Quaternary dinoflagellates from ODP Site 1172, East Tasman Plateau, in: Proceedings of the Ocean Drilling Program, Scientific Results, edited by: Exon, N. and Kennett, J. P., 189, U.S. Government Printing Office, College Station, Texas, 2003b.

Close, D. I., Watts, A. B., and Stagg, H. M. J.: A marine geophysical study of the Wilkes Land rifted continental margin, Antarctica, Geophys. J. Int., 177, 430–450, 2009.

Cook, C. P., Van De Flierdt, T., Williams, T., Hemming, S. R., Iwai, M., Kobayashi, M., Jimenez-Espejo, F. J., Escutia, C., González, J. J., Khim, B., McKay, R. M., Passchier, S., Bohaty, S. M., Riesselman, C. R., Tauxe, L., Sugisaki, S., Galindo, A. L., Patterson, M. O., Sangiorgi, F., Pierce, E. L., Brinkhuis, H., Klaus, A., Fehr, A., Bendle, J. A. P., Bijl, P. K., Carr, S. A., Dunbar, R. B., Flores, J. A., Hayden, T. G., Katsuki, K., Kong, G. S., Nakai, M., Olney, M. P., Pekar, S. F., Pross, J., Röhl, U., Sakai, T., Shrivastava, P. K., Stickley, C. E., Tuo, S., Welsh, K., and Yamane, M.: Dynamic behaviour of the East Antarctic ice sheet during Pliocene warmth, Nat. Geosci., 6, 765–769, 2013.

Cooper, A. K. and O'Brien, P. E.: Leg 188 synthesis: Transitions in the glacial history of the Prydz Bay region, East Antarctica, from ODP drilling, Proceedings of the Ocean Drilling Program: Scientific Results, 188, 1–42, 2004.

Crampton, J. S., Cody, R. D., Levy, R., Harwood, D., McKay, R., and Naish, T. R.: Southern Ocean phytoplankton turnover in response to stepwise Antarctic cooling over the past 15 million years, P. Natl. Acad. Sci. USA, 113, 6868–6873, 2016.

DeConto, R. M., Pollard, D., and Harwood, D.: Sea-ice feedback and Cenozoic evolution of Antarctic climate and ice sheets, Paleoceanography, 22, PA3214, https://doi.org/10.1029/2006PA001350, 2007.

DeConto, R. M., Pollard, D., Wilson, P. A., Pälike, H., Lear, C. H., and Pagani, M.: Thresholds for Cenozoic bipolar glaciation, Nature, 455, 652–657, 2008.

De Vleeschouwer, D., Vahlenkamp, M., Crucifix, M., and Pälike, H.: Alternating Southern and Northern Hemisphere climate response to astronomical forcing during the past 35 m.y., Geology, 45, 375–378, 2017.

Egger, L. M., Bahr, A., Friedrich, O., Wilson, P. A., Norris, R. D., van Peer, T. E., Lippert, P. C., Liebrand, D., and Pross, J.: Sea-level and surface-water change in the western North Atlantic across the Oligocene–Miocene Transition: a palynological perspective from IODP Site U1406 (Newfoundland margin), Mar. Micropaleontol., 139, 57–71, 2018.

Escutia, C. and Brinkhuis, H.: From Greenhouse to Icehouse at the Wilkes Land Antarctic Margin: IODP Expedition 318 Synthesis of Results, Dev. Mar. Geol., 7, 295–328, 2014.

Escutia, C., Brinkhuis, H., Klaus, A., and Expedition 318 Scientists: Proceedings of the Integrated Ocean Drilling Program, Initial Results, 318, Integrated Ocean Drilling Program Management International, Inc., Tokyo, 2011.

Esper, O. and Zonneveld, K. A. F.: Distribution of organic-walled dinoflagellate cysts in surface sediments of the Southern Ocean (eastern Atlantic sector) between the Subtropical Front and the Weddell Gyre, Mar. Micropaleotol., 46, 177–208, 2002.

Esper, O. and Zonneveld, K. A. F.: The potential of organic-walled dinoflagellate cysts for the reconstruction of past sea-surface conditions in the Southern Ocean, Mar. Micropaleontol., 65, 185–212, 2007.

Exon, N. F., Kennet, J. P., and Malone, M.: Leg 189 Synthesis: Cretaceous-Holocene history of the Tasmanian Gateway, in: Proceedings of the Ocean Drilling Program, Scientific Results, edited by: Exon, N. F., Kennett, J. P., and Malone, M. J., 189, Ocean Drilling Program, College Station, TX, USA, 2004.

Eynaud, F., Giraudeau, J., Pichon, J., and Pudsey, C. J.: Sea-surface distribution of coccolithophores, diatoms, silicoflagellates and dinoflagellates in the South Atlantic Ocean during the late austral summer 1995, Deep-Sea Res. Pt. I, 46, 451–482, 1999.

Foster, G. L. and Rohling, E. J.: Relationship between sea level and climate forcing by CO_2 on geological timescales, P. Natl. Acad. Sci. USA, 110, 1209–1214, 2013.

Foster, G. L., Lear, C. H., and Rae, J. W. B.: The evolution of $p\mathrm{CO}_2$, ice volume and climate during the middle Miocene, Earth Planet. Sc. Lett., 341–344, 243–254, 2012.

Fretwell, P., Pritchard, H. D., Vaughan, D. G., Bamber, J. L., Barrand, N. E., Bell, R., Bianchi, C., Bingham, R. G., Blankenship, D. D., Casassa, G., Catania, G., Callens, D., Conway, H., Cook, A. J., Corr, H. F. J., Damaske, D., Damm, V., Ferraccioli, F., Forsberg, R., Fujita, S., Gim, Y., Gogineni, P., Griggs, J. A., Hindmarsh, R. C. A., Holmlund, P., Holt, J. W., Jacobel, R. W., Jenkins, A., Jokat, W., Jordan, T., King, E. C., Kohler, J., Krabill, W., Riger-Kusk, M., Langley, K. A., Leitchenkov, G., Leuschen, C., Luyendyk, B. P., Matsuoka, K., Mouginot, J., Nitsche, F. O., Nogi, Y., Nost, O. A., Popov, S. V., Rignot, E., Rippin, D. M., Rivera, A., Roberts, J., Ross, N., Siegert, M. J., Smith, A. M., Steinhage, D., Studinger, M., Sun, B., Tinto, B. K., Welch, B. C., Wilson, D., Young, D. A., Xiangbin, C., and Zirizzotti, A.: Bedmap2: improved ice bed, surface and thickness datasets for Antarctica, The Cryosphere, 7, 375–393, https://doi.org/10.5194/tc-7-375-2013, 2013.

Gallagher, S. J., Villa, G., Drysdale, R. N., Wade, B. S., Scher, H., Li, Q., Wallace, M. W., and Holdgate, G. R.: A near-field sea level record of east Antarctic ice sheet instability from 32 to 27 Myr, Paleoceanography, 28, 1–13, 2013.

Gradstein, F. M., Ogg, J. G., Schmitz, M. D., and Ogg, G. M.: The Geologic Time Scale 2012, Elsevier, Amsterdam, the Netherlands, 1–2, 1–1144, 2012.

Greenop, R., Foster, G. L., Wilson, P. A., and Lear, C. H.: Middle Miocene climate instability associated with high-amplitude CO_2 variability, Paleoceanography, 29, 845–853, 2014.

Harland, R. and Pudsey, C. J.: Dinoflagellate cysts from sediment traps deployed in the Bellingshausen, Weddell and Scotia seas, Antarctica, Mar. Micropaleontol., 37, 77–99, 1999.

Hartman, J. D., Sangiorgi, F., Salabarnada, A., Peterse, F., Houben, A. J. P., Schouten, S., Escutia, C., and Bijl, P. K.: Oligocene TEX_{86}-derived seawater temperatures from offshore Wilkes Land (East Antarctica), Clim. Past Discuss., https://doi.org/10.5194/cp-2017-153, in review, 2017.

Harwood, D., Levy, R., Cowie, J., Florindo, F., Naish, T., Powell, R., and Pyne, A.: Deep Drilling with the ANDRILL Program in Antarctica, Sci. Dril., 3, 43–45, https://doi.org/10.2204/iodp.sd.3.09.2006, 2006.

Hauptvogel, D. W., Pekar, S. F., and Pincay, V.: Evidence for a heavily glaciated Antarctica during the late Oligocene “warming” (27.8–24.5): stable isotope records from ODP Site 690, Paleoceanography, 32, 384–396, 2017.

Herold, N., Huber, M., and Müller, R. D.: Modeling the Miocene Climatic Optimum. Part I: Land and atmosphere, J. Climate, 24, 6353–6373, 2011.

Herold, N., Huber, M., Müller, R. D., and Seton, M.: Modeling the Miocene Climatic Optimum: Ocean circulation, Paleoceanography, 27, PA1209, https://doi.org/10.1029/2010PA002041, 2012.

Hill, D. J., Haywood, A. M., Valdes, P. J., Francis, J. E., Lunt, D. J., Wade, B. S., and Bowman, V. C.: Paleogeographic controls on the onset of the Antarctic circumpolar current, Geophys. Res. Lett., 40, 5199–5204, 2013.

Holbourn, A., Kuhnt, W., Schulz, M., Flores, J., and Andersen, N.: Orbitally-paced climate evolution during the middle Miocene “Monterey” carbon-isotope excursion, Earth Planet. Sc. Lett., 261, 534–550, 2007.

Holbourn, A., Kuhnt, W., Clemens, S., Prell, W., and Andersen, N.: Middle to late Miocene stepwise climate cooling: Evidence from a high-resolution deep water isotope curve spanning 8 million years, Paleoceanography, 28, 688–699, 2013.

Holbourn, A., Kuhnt, W., Lyle, M., Schneider, L., Romero, O., and Andersen, N.: Middle Miocene climate cooling linked to intensification of eastern equatorial Pacific upwelling, Geology, 42, 19–22, 2014.

Holbourn, A., Kuhnt, W., Kochhann, K. G. D., Andersen, N., and Meier, K. J.: Global perturbation of the carbon cycle at the onset of the Miocene Climatic Optimum, Geology, 43, 123–126, 2015.

Houben, A. J. P., Bijl, P. K., Pross, J., Bohaty, S. M., Passchier, S., Stickley, C. E., Röhl, U., Sugisaki, S., Tauxe, L., Van De Flierdt, T., Olney, M., Sangiorgi, F., Sluijs, A., Escutia, C., and Brinkhuis, H.: Reorganization of Southern Ocean plankton ecosystem at the onset of Antarctic glaciation, Science, 340, 341–344, 2013.

Huck, C. E., van de Flierdt, T., Bohaty, S. M., and Hammond, S. J.: Antarctic climate, Southern Ocean circulation patterns, and deep water formation during the Eocene, Paleoceanography, 32, 674–691, 2017.

IPCC: Climate Change 2013: The Physical Science Basis, Contribution of Working Group I to the Fifth Assessment Report of the Intergovernmental Panel on Climate Change, Cambridge University Press, Cambridge, United Kingdom and New York, NY, USA, 2013.

Kohfeld, K. E., Graham, R. M., de Boer, A. M., Sime, L. C., Wolff, E. W., Le Quéré, C., and Bopp, L.: Southern Hemisphere westerly wind changes during the Last Glacial Maximum: paleo-data synthesis, Quaternary Sci. Rev., 68, 76–95, 2013.

Lear, C. H., Rosenthal, Y. Coxall, H. K., and Wilson, P. A.: Late Eocene to early Miocene ice sheet dynamics and the global carbon cycle, Paleoceanography, 19, PA4015, https://doi.org/10.1029/2004PA001039, 2004.

Levy, R. H. and Harwood, D. M.: Tertiary marine palynomorphs from the McMurdo Sound erratics, Antarctica, in: Paleobiology and Paleoenvironments of Eocene rocks, McMurdo Sound, East Antarctica, edited by: Stilwell, J. D. and Feldmann, R. M., AGU Antarctic Research Series, 183–242, 2000.

Liebrand, D., Lourens, L. J., Hodell, D. A., de Boer, B., van de Wal, R. S. W., and Pälike, H.: Antarctic ice sheet and oceanographic response to eccentricity forcing during the early Miocene, Clim. Past, 7, 869–880, https://doi.org/10.5194/cp-7-869-2011, 2011.

Liebrand, D., de Bakker, A. T. M., Beddow, H. M., Wilson, P. A., Bohaty, S. M., Ruessink, G., Pälike, H., Batenburg, S. J., Hilgen, F. J., Hodell, D. A., Huck, C. E., Kroon, D., Raffi, I., Saes, M. J. M., van Dijk, A. E., and Lourens, L. J.: Evolution of the early Antarctic ice ages, P. Natl. Acad. Sci. USA, 110, 3867–3872, 2017.

Marret, F. and De Vernal, A.: Dinoflagellate cyst distribution in surface sediments of the southern Indian Ocean, Mar. Micropaleontol., 29, 367–392, 1997.

Olbers, D., Borowski, D., Völker, C., and Wölff, J.: The dynamical balance, transport and circulation of the Antarctic Circumpolar Current, Antarct. Sci., 16, 439–470, 2004.

Pälike, H., Frazier, J., and Zachos, J. C.: Extended orbitally forced palaeoclimatic records from the equatorial Atlantic Ceara Rise, Quaternary Sci. Rev., 25, 3138–3149, 2006a.

Pälike, H., Norris, R. D., Herrle, J. O., Wilson, P. A., Coxall, H. K., Lear, C. H., Shackleton, N. J., Tripati, A. K., and Wade, B. S.: The Heartbeat of the Oligocene Climate System, Science, 314, 1894–1898, 2006b.

Prebble, J. G., Crouch, E. M., Carter, L., Cortese, G., Bostock, H., and Neil, H.: An expanded modern dinoflagellate cyst dataset for the Southwest Pacific and Southern Hemisphere with environmental associations, Mar. Micropaleontol., 101, 33–48, 2013.

Rignot, E., Jacobs, S., Mouginot, J., and Scheuchl, B.: Ice-shelf melting around Antarctica, Science, 341, 266–270, 2013.

Robert, C., Anderson, J., Armienti, P., Atkins, C., Barrett, P., Bohaty, S., Bryce, S., Claps, M., Curran, M., Davey, F. J., De Santis, L., Ehrmann, W., Florindo, F., Fielding, C., Hambrey, M., Hannah, M., Harwood, D. M., Henrys, S., Hoelscher, F., Howe, J. A., Jarrard, R., Kettler, R., Kooyman, S., Kopsch, C., Krissek, L., Lavelle, M., Levac, E., Niessen, F., Passchier, S., Paulsen, T., Powell, R., Pyne, A., Rafat, G., Raine, I. J., Roberts, A. P., Sagnotti, L., Sandroni, S., Scholz, E., Simes, J., Smellie, J., Strong, P., Tabecki, M., Talarico, F. M., Taviani, M., Verosub, K. L., Villa, G., Webb, P. N., Wilson, G. S., Wilson, T., Wise, S. W., Wonik, T., Woolfe, K., and Wrenn, J. H.: Summary of Results from CRP-1, Cape Roberts Project, Antarctica, Terra Antarctica, 5, 125–137, 1998.

Rovere, A., Raymo, M. E., Mitrovica, J. X., Hearty, P. J., O'Leary, M. J., and Inglis, J. D.: The Mid-Pliocene sea-level conundrum: Glacial isostasy, eustasy and dynamic topography, Earth Planet. Sc. Lett., 387, 27–33, 2014.

Salabarnada, A., Escutia, C., Röhl, U., Nelson, C. H., McKay, R., Jiménez-Espejo, F. J., Bijl, P. K., Hartman, J. D., Strother, S. L., Salzmann, U., Evangelinos, D., López-Quirós, A., Flores, J. A., Sangiorgi, F., Ikehara, M., and Brinkhuis, H.: Paleoceanography and ice sheet variability offshore Wilkes Land, Antarctica – Part 1: Insights from late Oligocene astronomically paced contourite sedimentation, Clim. Past, 14, 991–1014, https://doi.org/10.5194/cp-14-991-2018, 2018.

Sangiorgi, F., Bijl, P.K., Passchier, S., Salzmann, U., Schouten, S., McKay, R., Cody, R. D., Pross, J., Van De Flierdt, T., Bohaty, S. M., Levy, R., Williams, T., Escutia, C., and Brinkhuis, H.: Southern Ocean warming and Wilkes Land ice sheet retreat during the mid-Miocene, Nat. Commun., 9, 317, https://doi.org/10.1038/s41467-017-02609-7, 2018.

Scher, H. D. and Martin, E. M.: Circulation in the Southern Ocean during the Paleogene inferred from neodymium isotopes, Earth Planet. Sc. Lett., 228, 391–405, 2004.

Scher, H. D., Whittaker, J. M., Williams, S. E., Latimer, J. C., Kordesch, W. E. C., and Delaney, M. L.: Onset of Antarctic Circumpolar Current 30 million years ago as Tasmanian Gateway aligned with westerlies, Nature, 523, 580–583, 2015.

Seton, M., Müller, R. D., Zahirovic, S., Gaina, C., Torsvik, T., Shephard, G., Talsma, A., Gurnis, M., Turner, M., Maus, S., and Chandler, M.: Global continental and ocean basin reconstructions since 200 Ma, Earth-Sci. Rev., 113, 212–270, 2012.

Shepherd, A., Ivins, E. R., Geruo, A., Barletta, V. R., Bentley, M. J., Bettadpur, S., Briggs, K. H., Bromwich, D. H., Forsberg, R., Galin, N., Horwath, M., Jacobs, S., Joughin, I., King, M. A., Lenaerts, J. T. M., Li, J., Ligtenberg, S. R. M., Luckman, A., Luthcke, S.B., McMillan, M., Meister, R., Milne, G., Mouginot, J., Muir, A., Nicolas, J. P., Paden, J., Payne, A. J., Pritchard, H., Rignot, E., Rott, H., Sørensen, L. S., Scambos, T. A., Scheuchl, B., Schrama, E. J. O., Smith, B., Sundal, A. V., Van Angelen, J. H., Van De Berg, W. J., Van Den Broeke, M. R., Vaughan, D. G., Velicogna, I., Wahr, J., Whitehouse, P. L., Wingham, D. J., Yi, D., Young, D., and Zwally, H. J.: A reconciled estimate of ice-sheet mass balance, Science, 338, 1183–1189, 2012.

Sluijs, A., Brinkhuis, H., Stickley, C. E., Warnaar, J., Williams, G. L., and Fuller, M.: Dinoflagellate cysts from the Eocene – Oligocene transition in the Southern Ocean: Results from ODP Leg 189, in: Proceedings of the Ocean Drilling Program, Scientific Results, edited by: Exon, N. and Kennett, J. P., U.S. Government Printing Office, College Station, Texas, USA, 189, 2003.

Sluijs, A., Pross, J., and Brinkhuis, H.: From greenhouse to icehouse; organic walled dinoflagellate cysts as paleoenvironmental indicators in the Paleogene, Earth-Sci. Rev., 68, 281–315, 2005.

Stocchi, P., Escutia, C., Houben, A. J. P., Vermeersen, B. L. A., Bijl, P. K., Brinkhuis, H., DeConto, R. M., Galeotti, S., Passchier, S., Pollard, D., Klaus, A., Fehr, A., Williams, T., Bendle, J. A. P., Bohaty, S. M., Carr, S. A., Dunbar, R. B., Flores, J. A., Gonzàlez, J. J., Hayden, T. G., Iwai, M., Jimenez-Espejo, F. J., Katsuki, K., Kong, G. S., McKay, R. M., Nakai, M., Olney, M. P., Pekar, S. F., Pross, J., Riesselman, C., Röhl, U., Sakai, T., Shrivastava, P. K., Stickley, C. E., Sugisaki, S., Tauxe, L., Tuo, S., Van De Flierdt, T., Welsh, K., and Yamane, M.: Relative sea-level rise around East Antarctica during Oligocene glaciation, Nat. Geosci., 6, 380–384, https://doi.org/10.1038/ngeo1783, 2013.

Storkey, C. A.: Distribution of marine palynomorphs in surface sediments, Prydz Bay, Antarctica, MSc thesis Victoria University of Wellington, New Zealand, available at: http://hdl.handle.net/10063/21 (last access: July 2018), 2006.

Strother, S. L., Salzmann, U., Sangiorgi, F., Bijl, P. K., Pross, J., Escutia, C., Salabarnada, A., Pound, M. J., Voss, J., and Woodward, J.: A new quantitative approach to identify reworking in Eocene to Miocene pollen records from offshore Antarctica using red fluorescence and digital imaging, Biogeosciences, 14, 2089–2100, https://doi.org/10.5194/bg-14-2089-2017, 2017.

Tauxe, L., Stickley, C. E., Sugisaki, S., Bijl, P. K., Bohaty, S., Brinkhuis, H., Escutia, C., Flores, J. A., Iwai, M., Jimenez-Espejo, F., McKay, R., Passchier, S., Pross, J., Riesselman, C., Röhl, U., Sangiorgi, F., Welsh, K., Klaus, A., Bendle, J. A. P., Dunbar, R., Gonzalez, J., Olney, M. P., Pekar, S. F., and van de Flierdt, T.: Chronostratigraphic framework for the IODP Expedition 318 cores from the Wilkes Land Margin: constraints for paleoceanographic reconstruction, Paleoceanography, 27, PA2214, https://doi.org/10.1029/2012PA002308, 2012.

Torsvik, T. H., Van der Voo, R., Preeden, U., Niocaill, C. M., Steinberger, B., Doubrovine, P. V., van Hinsbergen, D. J. J., Domeier, M., Gaina, C., Tohver, E., Meert, J. G., McCausland, P. J., and Cocks, L. R. M.: Phanerozoic polar wander, palaeogeography and dynamics, Earth-Sci. Rev., 114, 325–368, 2012.

Van Hinsbergen, D. J. J., De Groot, L. V., Van Schaik, S. J., Spakman, W., Bijl, P. K., Sluijs, A., Langereis, C. G., and Brinkhuis, H.: A paleolatitude calculator for paleoclimate studies, PLoS ONE, 10, e0126946, https://doi.org/10.1371/journal.pone.0126946, 2015.

Wilson, G. S., Bohaty, S. M., Fielding, C. R., Florindo, F., Hannah, M. J., Hardwood, D. M., Mcintosh, W. C., Naish, T. R., Roberts, A. P., Sagnotti, L., Scherer, R. P., Strong, C. P., Verosub, K. L., Villa, G., Webb, P., and Woolfe, K. J.: Chronostratigraphy of CRP-2/2A, Victoria Land Basin, Antarctica, Terra Antarctica, 7, 647–654, 2000.

Wise, S. W. and Schlich, R.: Proceedings of the Ocean Drilling Program, Scientific Results, U.S. Government Printing Office, College Station, Texas, 120, 1992.

Wouters, B., Martin-Español, A., Helm, V., Flament, T., van Wessem, J. M., Ligtenberg, S. R. M., van den Broeke, M. R., and Bamber, J. L.: Dynamic thinning of glaciers on the Southern Antarctic Peninsula, Science, 348, 899–903, 2015.

Wrenn, J. H. and Hart, G. F.: Paleogene dinoflagellate cyst biostratigraphy of Seymour Island, Antarctica, Geological Society of America Memoires, 169, 321–447, 1988.

Xiao, W., Esper, O., and Gersonde, R.: Last Glacial-Holocene climate variability in the Atlantic sector of the Southern Ocean, Quaternary Sci. Rev., 135, 115–137, 2016.

Zachos, J. C., Dickens, G. R., and Zeebe, R. E.: An early Cenozoic perspective on greenhouse warming and carbon-cycle dynamics, Nature, 451, 279–283, 2008.

Zevenboom, D.: Dinoflagellate cysts from the Mediterranean late Oligocene and Miocene, PhD thesis Utrecht University, Utrecht, the Netherlands, 1995.

Zonneveld, K. A. F., Marret, F., Versteegh, G. J. M., Bogus, K., Bonnet, S., Bouimetarhan, I., Crouch, E., de Vernal, A., Elshanawany, R., Edwards, L., Esper, O., Forke, S., Grøsfjeld, K., Henry, M., Holzwarth, U., Kielt, J., Kim, S., Ladouceur, S., Ledu, D., Chen, L., Limoges, A., Londeix, L., Lu, S., Mahmoud, M. S., Marino, G., Matsouka, K., Matthiessen, J., Mildenhall, D. C., Mudie, P., Neil, H.L., Pospelova, V., Qi, Y., Radi, T., Richerol, T., Rochon, A., Sangiorgi, F., Solignac, S., Turon, J., Verleye, T., Wang, Y., Wang, Z., and Young, M.: Atlas of modern dinoflagellate cyst distribution based on 2405 data points, Rev. Palaeobot. Palyno., 191, 1–197, 2013.

Clim. Past, 9, 525–546, 2013
www.clim-past.net/9/525/2013/
doi:10.5194/cp-9-525-2013

Climate of the Past
Open Access

Modulation of Late Cretaceous and Cenozoic climate by variable drawdown of atmospheric pCO_2 from weathering of basaltic provinces on continents drifting through the equatorial humid belt

D. V. Kent[*1,2] **and G. Muttoni**[3,4]

[1]Department of Earth and Planetary Sciences, Rutgers University, Piscataway, NJ 08854, USA
[2]Lamont–Doherty Earth Observatory of Columbia University, Palisades, NY 10964, USA
[3]Department of Earth Sciences, University of Milan, via Mangiagalli 34, 20133 Milan, Italy
[4]ALP – Alpine Laboratory of Paleomagnetism, via Madonna dei Boschi 76, 12016 Peveragno (CN), Italy
[*]*Invited contribution by D. V. Kent, one of the EGU Petrus Peregrinus Medal winners 2006.*

Correspondence to: D. V. Kent (dvk@rutgers.edu)

Received: 23 August 2012 – Published in Clim. Past Discuss.: 13 September 2012
Revised: 5 January 2013 – Accepted: 22 January 2013 – Published: 4 March 2013

Abstract. The small reservoir of carbon dioxide in the atmosphere (pCO_2) that modulates climate through the greenhouse effect reflects a delicate balance between large fluxes of sources and sinks. The major long-term source of CO_2 is global outgassing from sea-floor spreading, subduction, hotspot activity, and metamorphism; the ultimate sink is through weathering of continental silicates and deposition of carbonates. Most carbon cycle models are driven by changes in the source flux scaled to variable rates of ocean floor production, but ocean floor production may not be distinguishable from being steady since 180 Ma. We evaluate potential changes in sources and sinks of CO_2 for the past 120 Ma in a paleogeographic context. Our new calculations show that decarbonation of pelagic sediments by Tethyan subduction contributed only modestly to generally high pCO_2 levels from the Late Cretaceous until the early Eocene, and thus shutdown of this CO_2 source with the collision of India and Asia at the early Eocene climate optimum at around 50 Ma was inadequate to account for the large and prolonged decrease in pCO_2 that eventually allowed the growth of significant Antarctic ice sheets by around 34 Ma. Instead, variation in area of continental basalt terranes in the equatorial humid belt (5° S–5° N) seems to be a dominant factor controlling how much CO_2 is retained in the atmosphere via the silicate weathering feedback. The arrival of the highly weatherable Deccan Traps in the equatorial humid belt at around 50 Ma was decisive in initiating the long-term slide to lower atmospheric pCO_2, which was pushed further down by the emplacement of the 30 Ma Ethiopian Traps near the equator and the southerly tectonic extrusion of SE Asia, an arc terrane that presently is estimated to account for 1/4 of CO_2 consumption from all basaltic provinces that account for $\sim 1/3$ of the total CO_2 consumption by continental silicate weathering (Dessert et al., 2003). A negative climate-feedback mechanism that (usually) inhibits the complete collapse of atmospheric pCO_2 is the accelerating formation of thick cation-deficient soils that retard chemical weathering of the underlying bedrock. Nevertheless, equatorial climate seems to be relatively insensitive to pCO_2 greenhouse forcing and thus with availability of some rejuvenating relief as in arc terranes or thick basaltic provinces, silicate weathering in this venue is not subject to a strong negative feedback, providing an avenue for ice ages. The safety valve that prevents excessive atmospheric pCO_2 levels is the triggering of silicate weathering of continental areas and basaltic provinces in the temperate humid belt. Excess organic carbon burial seems to have played a negligible role in atmospheric pCO_2 over the Late Cretaceous and Cenozoic.

1 Introduction

Deep water temperatures determined from the continuous benthic oxygen isotope record (Cramer et al., 2009, 2011; Miller et al., 2005b; Zachos et al., 2001) (Fig. 1a) document

Published by Copernicus Publications on behalf of the European Geosciences Union.

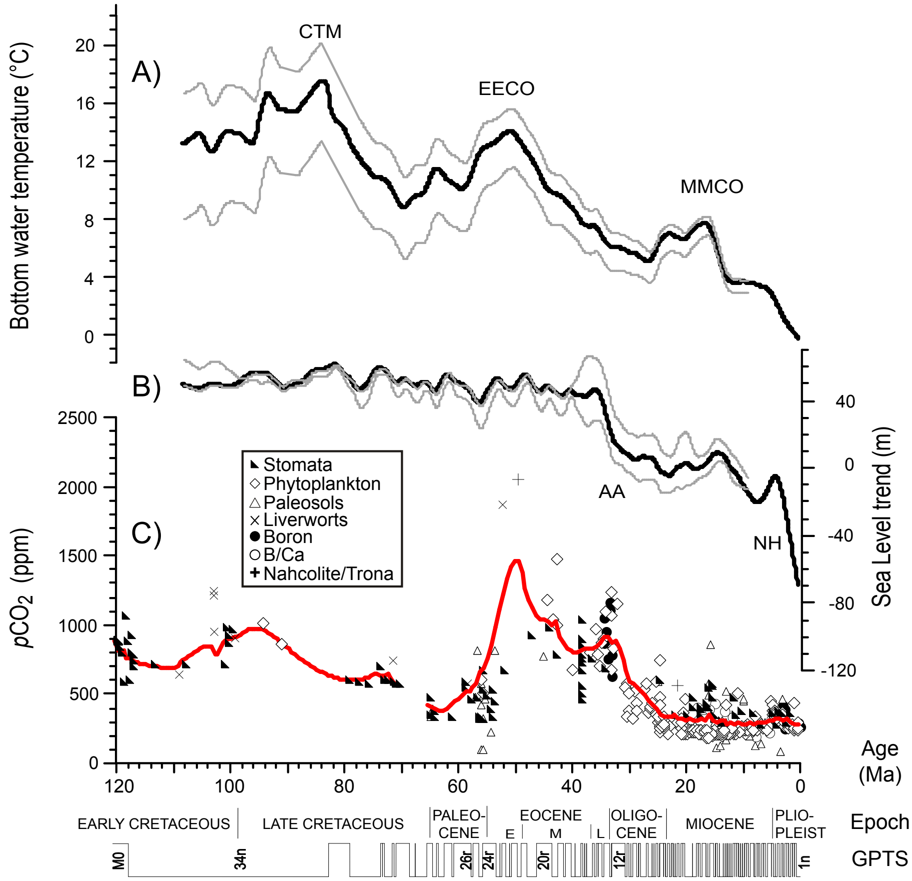

Fig. 1. Bottom water temperatures **(A)** and reconstructed sea levels **(B)** since the Early Cretaceous (Cramer et al., 2011) smoothed to emphasize variations on > 5 Myr timescales. CTM is Cretaceous thermal maximum, EECO is early Eocene climatic optimum, and MMCO is middle Miocene climatic optimum; AA is sea-level drop at the inception of Antarctic ice sheets, and NH is sea-level drop at the inception of Northern Hemisphere ice sheets. **(C)** Atmospheric pCO_2 estimates from various proxies from compilation of Royer (2010) for pre-70 Ma interval (except paleosol estimates, which are highly scattered and have not been plotted) and of Beerling and Royer (2011) for post-70 Ma interval. Simple smoothing functions have been fit (heavy curved line) through the mean pCO_2 estimates provided in the compilations. Ages and epochs registered to GPTS (geomagnetic polarity time scale) of Cande and Kent (1995).

that global climate over the past 120 Myr experienced extremes ranging from equable polar climates with bottom water temperatures over 15 °C during the Cretaceous Thermal Maximum (CTM $\sim$ 90 Ma; Wilson et al., 2002) and the early Eocene climatic optimum (EECO, $\sim$ 50 Ma) to a cooling trend during the Middle and Late Eocene with a major sea level fall (Fig. 1b) at around the Eocene–Oligocene boundary ($\sim$ 34 Ma), marking the inception of major polar (Antarctic) ice sheets.

The equable conditions at the CTM and especially the EECO are associated with warmer global (polar and tropical) sea surface temperatures (Pearson et al., 2001, 2007) that most likely resulted from an enhanced greenhouse effect due to higher atmospheric pCO_2 concentrations as inferred from various proxies (Fig. 1c; see review with references in Beerling and Royer, 2011; Royer, 2010). These high pCO_2 levels have been conventionally attributed to higher rates of ocean crust production and associated increased CO_2 outgassing (Berner et al., 1983), for example, a presumed pulse of increased global sea-floor spreading and the emplacement of the North Atlantic igneous province at the EECO (Miller et al., 2005a; Rea et al., 1990; Thomas and Bralower, 2005; Zachos et al., 2001). Decreasing pCO_2 levels (Pagani et al., 2005, 2011) and the coincident cooling trend that followed the EECO could then be due to reduced outgassing flux from lower global ocean floor production rates that eventually led to a major buildup of Antarctic ice sheets at around the Eocene–Oligocene boundary (DeConto and Pollard, 2003), whose precise timing may have been influenced by openings of Southern Ocean gateways (Kennett, 1977; Livermore et al., 2007; Stickley et al., 2004).

A spreading rate-dependent CO_2 outgassing factor (Berner, 1994; Berner et al., 1983; Engebretson et al., 1992) is intuitively appealing and usually regarded as the most important parameter driving variations in pCO_2 in the current generation of carbon cycling models (Berner, 2004) but there are conflicting estimates of global ocean floor production rates. For example, Muller et al. (2008) and Seton et al. (2009) postulate high production in the Late Cretaceous and decreasing production in the Cenozoic, whereas Cogné and Humler (2004, 2006) show high production earlier in the Cretaceous, reduced production in the Late Cretaceous, and increasing production over the Cenozoic. Provocatively, Rowley (2002) showed that the observed area-age versus age distribution of oceanic crust does not require substantial production rate changes since the breakup of Pangea at 180 Ma; the fact that more than 50 % of oceanic lithosphere younger than 55.7 Ma (70 % younger than ∼ 89 Ma, 85 % younger than ∼ 120 Ma) has already been removed by subduction means that reconstructions of oceanic lithosphere history are invariably based on substantial and often poorly constrained extrapolations (Rowley, 2008). Moreover, carbon uptake by oceanic crust may tend to cancel any residual spreading rate-dependent variations in CO_2 outgassing (Berner, 1990a,b; Brady and Gislason, 1997; Staudigel et al., 1989, 1990a,b). Increased CO_2 flux from mantle plumes most likely occurred during the relatively short emplacement times of individual LIPs but the time-integrated effect may not be very important on the million year time scale (Marty and Tolstikhin, 1998), an assessment supported by new proxy measurements of $p\mathrm{CO}_2$ that support models (e.g. Caldeira and Rampino, 1990; Dessert et al., 2001) showing that increases associated with a major LIP emplacement decay away on less than a million year time scale (Schaller et al., 2011).

The generally high $p\mathrm{CO}_2$ levels and warm polar climates that characterized the mid-Cretaceous to early Eocene may have had a substantial contribution from the protracted subduction of Tethyan pelagic carbonates deposited on the Indian plate during northward drift from ∼ 120 Ma until the collision of Greater India with Asia (Lhasa block) at ∼ 50 Ma (Edmond and Huh, 2003; Hansen et al., 2008; Kent and Muttoni, 2008; Schrag, 2002). The ensuing long-term trend of decreasing $p\mathrm{CO}_2$ levels and temperatures from 50 Ma to the onset of Antarctic glaciation at 34 Ma may thus have resulted from re-equilibration to the reduced CO_2 flux with the shutdown of the Tethyan decarbonation factory. Concomitantly, intense weathering of the Deccan Traps as they drifted into the equatorial humid belt may have increased the consumption of CO_2 (Dessert et al., 2003; Kent and Muttoni, 2008).

In this paper, we elaborate on the tectonic forcing of $p\mathrm{CO}_2$ variations using plate tectonic reconstructions in a paleolatitudinal reference frame and attempt to quantify (a) the decarbonation potential of Tethyan subduction since ∼ 120 Ma as a potential additional source of CO_2, and (b) the silicate weathering potential for higher consumption of CO_2 of continental areas and especially highly weatherable basaltic provinces as they drifted through the equatorial humid belt, the most potent venue for continental silicate weathering (Dessert et al., 2003). We evaluate the relative contributions of these modes of steering atmospheric $p\mathrm{CO}_2$ as well as other alternative mechanisms, including proposed changes in organic carbon burial inferred from trends in δ^{13}C carbonate records (Katz et al., 2005) and the Himalayan uplift-weathering hypothesis (Raymo and Ruddiman, 1992; Raymo et al., 1988). The degree of sensitivity of global climate to changes in atmospheric $p\mathrm{CO}_2$ is difficult to gauge but we mainly seek to explain the pattern of generally high $p\mathrm{CO}_2$ levels from the CTM to EECO (∼ 90 to 50 Ma) and the decrease to generally low $p\mathrm{CO}_2$ levels that characterize the Oligocene to present (from ∼ 34 Ma). Modeling studies point to threshold decreases in atmospheric $p\mathrm{CO}_2$ as the most likely causes for widespread Antarctic glaciation at around the Eocene–Oligocene boundary (Oi-1, ∼ 34 Ma; DeConto and Pollard, 2003; DeConto et al., 2008) and the onset of permanent Northern Hemisphere glaciations in the late Pliocene (∼ 3 Ma; Lunt et al., 2008).

The main outcome of our calculations is that they point to the viability and primacy of variations in carbon sinks rather than sources, especially changes in silicate weathering consumption as continents in general and those land masses with basaltic provinces in particular drifted through climate belts, on controlling atmospheric $p\mathrm{CO}_2$ over at least the past 120 Ma.

"... there is a special need, in both carbon cycle and climate modeling, to consider only those land areas that have sufficient rain and are sufficiently warm to exhibit appreciable chemical weathering." (R. A. Berner and Z. Kothalava, 2001)

2 Paleogeographic reconstructions from 120 Ma to present

In the absence of compelling evidence for long-term secular changes in global ocean floor production rates, we assume that the background CO_2 outgassing rate held steady and was comparable to the present-day global volcanic CO_2 emission rate from spreading centers, mantle plumes and arc volcanoes with a preferred estimate of ∼ 260 Mt CO_2 yr^{-1} or 5.91×10^{12} mol CO_2 yr^{-1}, with a range of plausible estimates of 180 to 440 Mt CO_2 yr^{-1} (Gerlach, 2011; Marty and Tolstikhin, 1998). To estimate contributions of CO_2 outgassing from the subduction of carbonate-rich sediments and consumption of CO_2 from silicate weathering of continental areas as they drifted through different climate zones, we generated paleogeographic reconstructions of the main continents using a composite apparent polar wander path (APWP) (Fig. 2; Table 1) and the finite rotation poles used by Besse and Courtillot (2002) from Muller and Roest (1992), Muller et al. (1993) and Srivastava and Tapscott (1986). The composite APWP uses paleopoles from all the main continents rotated to common coordinates (in this case, North America) and averaged in a sliding 20 Myr window every 10 Myr. The mean paleopole for 60 to 120 Ma is an average of global igneous data from Kent and Irving (2010) for a standstill in APW in North American coordinates; we averaged their 60,

Table 1. APW paths used for paleogeographic reconstructions.

				NAM		SAM		AFR		EUR		IND		AUS		ANT	
A1 (Ma)	A2 (Ma)	N	A95 (°)	Lat (° N)	Lon (° E)	Lat (° N)	Lon (° E)	Lat (° N)	Lon (° E)	Lat (° N)	Lon (° E)	Lat (° N)	Lon (° E)	Lat (° N)	Lon (° E)	Lat (° N)	Lon (° E)
10	8.3	54	2.0	85.0	168.1	85.9	151.0	85.3	173.5	85.4	162.5	86.2	216.4	87.0	254.3	86.0	160.8
20	18.9	38	2.7	83.3	164.2	84.7	133.8	83.9	175.9	84.0	154.8	84.0	246.8	82.8	287.8	85.4	151.9
30	29.5	23	3.8	81.5	169.2	83.7	132.6	81.8	190.7	82.8	158.1	79.1	266.1	76.6	291.0	85.1	162.2
40	40.0	24	3.2	79.5	174.4	82.6	139.2	79.0	201.1	81.3	162.4	73.1	272.4	71.7	289.8	84.3	172.4
50	52.2	31	3.4	77.9	179.3	82.1	141.8	76.9	210.3	80.9	164.4	63.3	276.4	68.2	293.0	84.7	174.7
60*	*	4	1.7	75.9	192.8	82.4	162.8	74.4	221.9	80.7	184.0	52.5	277.1	65.1	292.9	84.6	203.5
70*	*	4	1.7	75.9	192.8	83.2	157.7	74.2	224.4	81.0	182.5	39.1	280.0	64.4	298.5	86.6	209.5
80*	*	4	1.7	75.9	192.8	83.3	163.5	71.7	231.3	81.0	180.9	31.6	282.1	62.5	302.0	87.6	243.4
90*	*	4	1.7	75.9	192.8	84.8	161.1	68.2	239.5	80.8	179.7	24.2	288.2	61.3	309.3	88.5	341.6
100*	*	4	1.7	75.9	192.8	86.0	178.1	63.5	247.4	80.8	178.5	16.3	293.6	59.3	316.1	85.5	11.7
110*	*	4	1.7	75.9	192.8	87.9	217.6	59.8	254.9	80.6	178.9	11.3	294.9	57.2	325.2	80.5	22.0
120*	*	4	1.7	75.9	192.8	86.9	284.3	56.3	262.0	80.4	180.5	6.2	298.4	54.3	335.0	74.5	26.8

Paleopoles from different continents (NAM, North America; SAM, South America; AFR, Africa; EUR, Eurasia; IND, India; AUS, Australia; ANT, East Antarctica) had been transferred to common (NAM) coordinates using rotation parameters from Besse and Courtillot (2002) and averaged in 20 Myr windows stepped every 10 Myr. The mean paleopoles of the composite APW path were then transferred from NAM coordinates to the different continents. Mean paleopoles for 10 to 50 Ma are from Besse and Courtillot (2003); mean paleopole for 60–120 Ma is the standstill superpole in NAM coordinates from Kent and Irving (2010). A1 is age of center of 20 Myr averaging window, A2 is mean age of poles in the 20 Myr window, N = number of paleomagnetic pole entries, Lat is latitude and Lon is longitude of mean paleomagnetic pole and A95 is its radius of circle of 95 % confidence. * Based on average of mean poles listed in Kent and Irving (2010; Table 6) for 60, 80, 100 and 120 Ma windows in NAM coordinates and propagated to other continents via interpolated Euler poles from Besse and Courtillot (2002).

80, 100 and 120 Ma mean poles, which are independent but not significantly different, to derive a 60–120 Ma superpole. Mean paleopoles for 10 to 50 Ma, which are dominated by global igneous data and thus also less prone to be biased by sedimentary inclination error, are from Besse and Courtillot (2002, 2003). The composite APWP should record the geocentric axial dipole field, hence the different APWP for the various continents shown in Fig. 2 simply reflect their relative motions according to the finite rotation model. Uncertainty in latitudinal positions of the continents should be on the order of the radii of circles of 95 % confidence around the mean paleopoles (∼ 3°; Table 1).

The main elements of the plate tectonic scenario are the convergence of Greater India with the Lhasa block, which was accreted to Asia before the Late Jurassic (Allègre et al., 1984; Chang and Cheng, 1973), and the convergence of Arabia with the Iran block, which was accreted to Asia during the Late Triassic–Early Jurassic Cimmerian orogeny (e.g. Muttoni et al., 2009; Zanchi et al., 2009) and was only moderately disrupted by oblique subduction of the Tethyan Ocean in the Cretaceous (Moghadam et al., 2009). A related tectonic feature is the extrusion of the SE Asian blocks during the indentation of India into Asia (Molnar and Tapponnier, 1975). There is a vast literature on various aspects of the tectonics of the Himalaya and adjacent Tibetan Plateau (e.g. more than 330 cited references in a review paper by Yin and Harrison, 2000 and more than 500 cited references in one by Hatzfeld and Molnar, 2010), but what is critical to our analysis is to locate within these reconstructions the position of the Asian margin (Lhasa, Iran) and of the SE Asian blocks, which was done as follows.

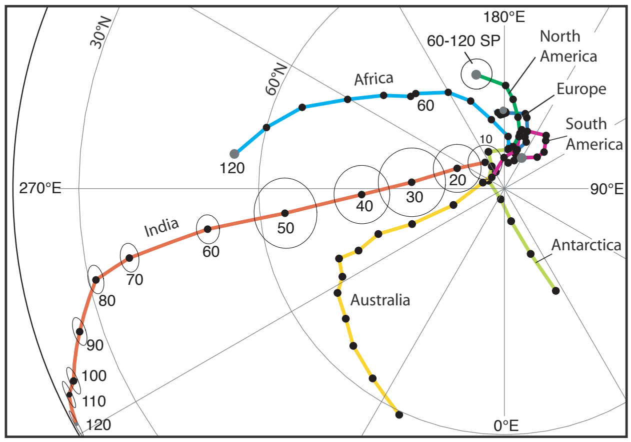

Fig. 2. Apparent polar wander paths for Africa, Antarctica, Australia, Eurasia, India, North America and South America based on a composite APWP using paleopoles from all the main continents that were brought to common coordinates using finite rotation poles used by Besse and Courtillot (2002), averaged with a sliding 20 Myr window every 10 Myr, and the mean poles transferred back to the different continents; hence the differences in APWP for the various continents reflect relative motions according to the finite rotation poles used for the plate reconstructions. Mean paleopoles for 10 to 50 Ma are from Besse and Courtillot (2002, 2003); mean paleopole for 60 to 120 Ma is an average of global igneous data (superpole labeled 60–120 Ma SP with 95 % confidence circle and based on 60, 80, 100 and 120 Ma mean poles from Kent and Irving, 2010) for a standstill in apparent polar wander in North American coordinates (Table 1). Circles of 95 % confidence that are shown on the India APWP are in common for the APWP projected to other continents.

Table 2. Total rotation poles for the SE Asian blocks.

Age	W. Sumatra			N. Indochina			S. Indochina–E. Sumatra–Java			C. Indochina–Borneo		
Ma	Lat	Lon	Ω	Lat	Lon	Ω	Lat	Lon	Ω	Lat	Lon	Ω
0	0.0	0.0	0.0	0.0	0.0	0.0	0.0	0.0	0.0	0.0	0.0	0.0
5	13.7	94.5	5.2	11.5	90.7	5.3	11.5	90.7	5.3	11.5	90.7	5.3
10	11.4	96.2	9.2	9.4	92.0	9.2	9.4	92.0	9.2	9.4	92.0	9.2
15	14.1	102.2	9.7	7.5	91.5	9.7	7.5	91.5	9.7	7.5	91.5	9.7
30	10.6	90.8	21.9	7.2	86.6	22.2	7.2	86.6	22.2	7.2	86.6	22.2
40	4.6	93.3	28.8	5.9	88.6	28.5	1.9	90.2	29.1	4.1	90.4	33.1
50	4.5	93.6	29.3	5.8	89.0	29.0	1.8	90.6	29.6	4.0	90.7	33.6
60	3.4	99.3	30.2	4.6	95.0	29.6	0.7	96.4	30.2	2.8	95.8	34.3
70	3.5	99.0	29.9	4.7	94.5	29.3	0.8	96.0	30.0	2.9	95.4	34.0
80	3.6	98.5	29.8	4.8	94.1	29.3	0.9	95.5	30.0	3.0	95.0	34.0
90	3.6	98.1	30.0	4.9	93.7	29.5	1.0	95.1	30.2	3.1	94.7	34.2
100	3.7	97.7	30.0	4.9	93.3	29.5	1.0	94.7	30.1	3.1	94.3	34.2
110	3.7	97.8	30.2	4.9	93.4	29.7	1.0	94.8	30.4	3.1	94.4	34.3
120	3.6	98.2	30.4	4.8	93.8	29.9	0.9	95.3	30.6	3.0	94.8	34.6

Rotation poles (Lat = latitude ° N, Lon = longitude ° E, Ω = rotation angle, positive counterclockwise) obtained by multiplying the paleomagnetic Euler poles of Eurasia (derived from Table 1) with the step-by-step Euler poles of the SE Asian blocks relative to Siberia (Eurasia) accumulated in the 0–40 Ma time window (derived from Replumaz and Tapponnier, 2003). For the previous 50–120 Ma interval, the SE Asia blocks are considered tectonically coherent and moved with Siberia (Eurasia). N = North, S = South, E = East, W = West, C = Central.

1. The southern (collisional) margin of the Lhasa block was drawn assuming that it coincided with the northern margin of Greater India (which is much easier to place using the APWP described above) at full India–Lhasa collision at 50 Ma; for pre-50 Ma times, the Lhasa margin was kept coherent and therefore rotated with Asia. The ∼ 50 Ma collision age, instrumental to locating the position of the margin, is based on several lines of geological evidence (Garzanti, 2008; Garzanti et al., 1987; Zhu et al., 2005; and references therein), and is supported by the marked decrease in convergence rate between India and Eurasia observed in the Indian Ocean between magnetic Anomaly 22 (∼ 49.5 Ma) and Anomaly 21 (∼ 48.5 Ma) (Copley et al., 2010; Patriat and Achache, 1984; see also Cande and Stegman, 2011; Molnar and Stock, 2009). An age of ∼ 50 Ma for the India–Lhasa collision is preferred to the much younger age of ∼ 35 Ma envisaged by Aitchison et al. (2007) and Ali and Aitchison (2008) essentially for the arguments made by Garzanti (2008). Our reconstructions are in substantial agreement with the available albeit sparse paleomagnetic data indicating that the margin had a paleolatitude comprised between ∼ 10° N and ∼ 20° N in the Cretaceous–early Cenozoic (Achache et al., 1984; Chen et al., 1993, 2012). Other results and compilations of paleomagnetic data that try to take into account sedimentary flattening of paleomagnetic directions suggest that collision of northern India with the Lhasa block occurred at 46 ± 8 Ma (Dupont-Nivet et al., 2010) and that the southern margin of the Lhasa block extended as far south as 20° N during the Eocene (Lippert et al., 2011), which we regard as in substantial agreement with our reconstructed tectonic framework given the uncertainties in reference paleopoles.

2. Following similar reasoning, the southern (collisional) margin of the Iran block was drawn assuming that it coincided with the northern margin of Arabia at full collision at ∼ 20 Ma. The Arabia–Iran collision may have started at ∼ 35 Ma based on geologic evidence (Agard et al., 2005; Allen and Armstrong, 2008); however, complete western Tethys closure seems not to have occurred until ∼ 20 Ma based on recent apatite fission-track data indicating that the last oceanic lithosphere between Arabia and Eurasia was not consumed until the early Miocene (Okay et al., 2010).

3. The position of the SE Asian blocks (north, central, and south Indochina, west and east Sumatra, Borneo, and Java) have been reconstructed in the 0–40 Ma interval using the (cumulative) rotation poles of Replumaz and Tapponnier (2003) relative to Siberia (Eurasia) (Table 2). For the previous 50–120 Ma interval, the SE Asian blocks are considered tectonically coherent and moved with Siberia (Eurasia). Accordingly, our Cretaceous reconstructions are similar to those of Chen et al. (1993) with Indochina placed using Cretaceous paleomagnetic data from Yang and Besse (1993) across paleolatitudes spanning from ∼ 10° N to 30° N close to Siberia. Moreover, our 65 Ma reconstruction predicts a paleolatitude for western Yunnan (North Indochina

block) that is consistent, within paleomagnetic resolution, with a paleolatitude of $17° \pm 9°$ N calculated for the area from (sparse) paleomagnetic data from the Paleocene (Yang et al., 2001). Southward extrusion of the SE Asian blocks basically stopped at about 15 Ma with cessation of seafloor spreading in the South China Sea (Briais et al., 1993) even though overall southerly movement continued as Eurasia rotated clockwise according to its APWP. Our reconstructions are similar to the classic India–SE Asia indentor-extrusion model (Molnar and Tapponnier, 1975; Replumaz and Tapponnier, 2003; Royden et al., 2008) and differ from alternative reconstructions that question evidence for extrusion and locate the SE Asian blocks since before the onset of India–Asia collision at essentially the latitudes they are found today (Aitchison et al., 2007; Hall et al., 2008; see also exchange between Garzanti, 2008 and Aitchison et al., 2008). Hall et al. (2008) support their fixist reconstructions citing paleomagnetic data from Borneo and surrounding regions (Fuller et al., 1999; Schmidtke et al., 1990) that (a) do not seem to indicate a clear pattern of clockwise rotations, and (b) show no consistent southward displacement of blocks over the Cenozoic, both expected from the extrusion model. As acknowledged by Fuller et al. (1999), however, the quality of the paleomagnetic data from Borneo is problematical given that many results come from igneous intrusions with no control on paleo-horizontal and "the intimate mixing throughout Borneo of rotated and unrotated results is easier to explain in terms of remagnetization than by a special distribution of local shears". The details of the paleolatitudinal evolution of Borneo can hardly be resolved by these data. However, results from the Late Cretaceous and early Cenozoic Segamat basalts and supporting data from the Kuantan dike swarm all from the Malaysia Peninsula indicate paleolatitudes at time of emplacement of 20° N (compared to a present-day latitude of $\sim 2.5°$ N) (Richter et al., 1999) and provide in our opinion robust (e.g. not influenced by sedimentary inclination flattening) paleomagnetic data in support of the SE Asia southward extrusion model and Eurasia clockwise rotation.

To summarize in a broader paleogeographic context, Greater India resided for much of the Mesozoic in the southern hemisphere as part of the classical Gondwana supercontinental assembly (Smith and Hallam, 1970), which began to disperse in the Late Jurassic with the opening of the Somali basin (Rabinowitz et al., 1983) and the separation of East Gondwana (which included India, Madagascar, Antarctica, and Australia) from West Gondwana (Africa and South America). Greater India commenced its ~ 6000 km northward drift toward Lhasa (Asia) when it separated (with Madagascar) from Antarctica at around 120 Ma (Fig. 3a) and continued its journey after separation from Madagascar at around 84 Ma, approached the equatorial belt (5° S–5° N) at 65 Ma (Fig. 3b) and began to collide with Lhasa (Asia) at around 50 Ma (Fig. 3c). The extrusion of the SE Asian blocks with the indentation of India into Asia was such that at ~ 30 Ma Borneo was approaching the equatorial humid belt (Fig. 3d). Convergence between Arabia–Iran caused final collision at ~ 20 Ma, whereas the southward extrusion of SE Asia largely ceased by ~ 15 Ma (Fig. 3e). Continued clockwise rotation of Eurasia gradually brought SE Asia to its present position during which time New Guinea, on the northern margin of the Australia plate, impinged on the equatorial humid belt from the south (Fig. 3f).

3 Did the Tethyan CO_2 factory produce Cretaceous–Eocene greenhouse climate?

The northward drift of India involved the subduction under Asia of oceanic crust that must have transited through the equatorial belt (Fig. 3a–c). This is because the paleomagnetic (i.e. latitudinal) constraints indicate that the Lhasa (Asia) southern margin remained in the northern hemisphere (10° N–20° N) from practically the time India separated from Antarctica at ~ 120 Ma until incipient collision at ~ 50 Ma. In modern oceans, equatorial regions are generally associated with upwelling and high organic productivity, giving rise to enhanced deposition of biogenic sediments (Berger and Winterer, 1974) that sequester CO_2 from the atmosphere. This has been especially true since the diversification of planktonic marine protists by the mid-Mesozoic, when open oceans became important loci of carbonate deposition, progressively replacing shallow water carbonates (Wilkinson and Walker, 1989). Calcareous nannoplankton became the most efficient sediment-forming group in Cretaceous oceans, sometimes forming thick chalk deposits, whereas planktonic foraminifers became relevant sediment-producers only since the Late Cretaceous (Erba, 2004). Biogenic sediments deposited on oceanic crust are more readily subducted than shallow water carbonates on buoyant continental crust, hence pelagic sediments are more prone to metamorphic decarbonation, potentially augmenting the global flux of CO_2 to the atmosphere (Caldeira, 1992; Volk, 1989). The subduction of Tethyan sea floor from 120 to 50 Ma may thus have constituted a productive source of additional CO_2, which according to some scenarios may have been responsible for the generally equable climates in the Cretaceous to Eocene (Edmond and Huh, 2003; Hansen et al., 2008; Kent and Muttoni, 2008; Schrag, 2002). Alternatively, much of the subducted carbon may have remained buried in a deep-seated mantle reservoir (Selverstone and Gutzler, 1993). Here we attempt to estimate the maximum amount of subducted carbon as a source of CO_2 to the atmosphere by invoking high biogenic productivity on oceanic crust and assuming that an appreciable fraction of the subducted carbon is returned to the atmosphere.

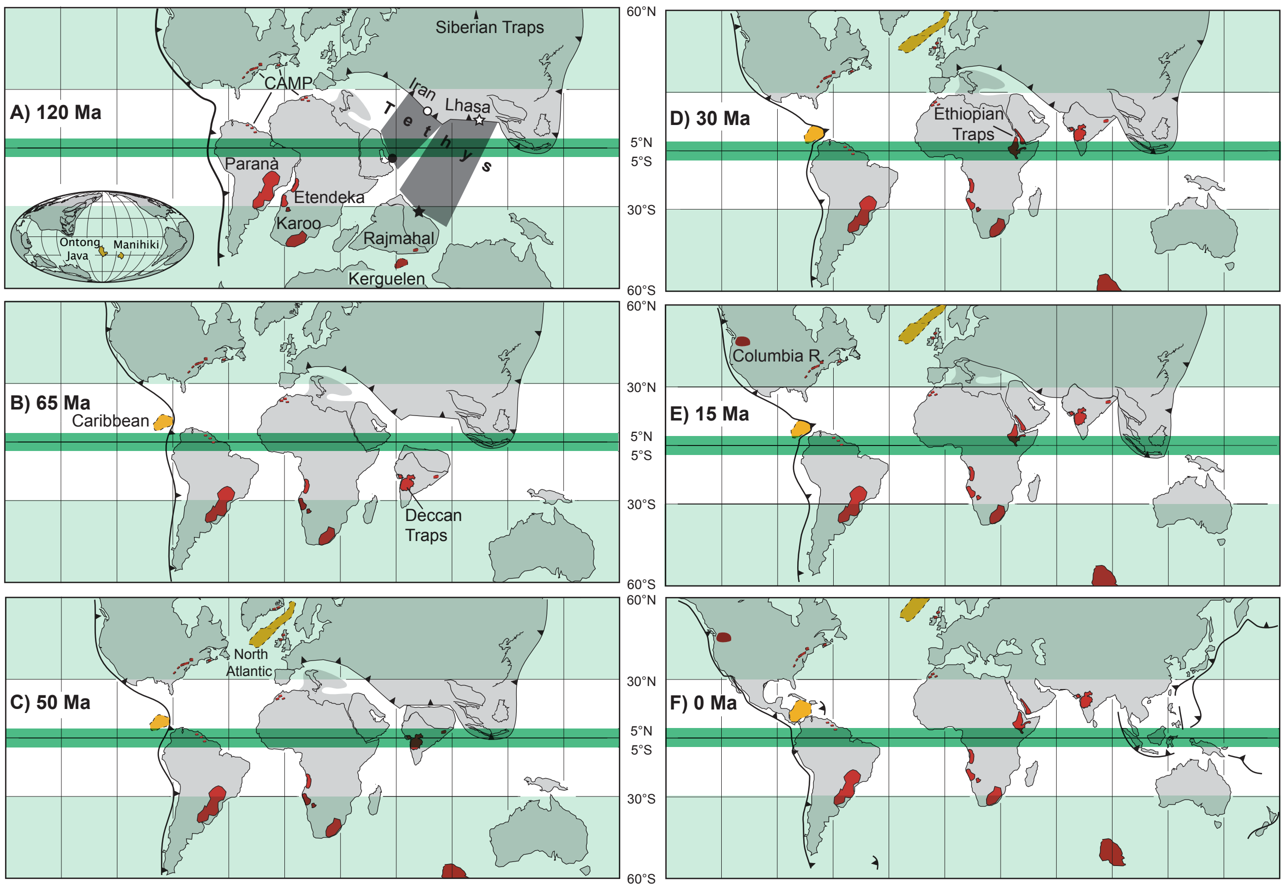

Fig. 3. Paleogeographic reconstructions based on a composite APWP (Table 1, Fig. 2), the finite rotation poles given by Besse and Courtillot (2002) from Muller and Roest (1992), Muller et al. (1993), and Srivastava and Tapscott (1986) for the major continents and the rotation poles of Replumaz and Tapponnier (2003) for SE Asian blocks, as discussed in text. **(A)** 120 Ma at about Magnetic Anomaly M0; **(B)** 65 Ma at about Anomaly 29; **(C)** 50 Ma at about Anomaly 21; **(D)** 30 Ma at about Anomaly 11; **(E)** 15 Ma at about Anomaly 5B; **(F)** present-day geography. The equatorial humid belt ($P > E$: precipitation > evaporation) between 5° S and 5° N is represented by darker green shading, the temperate humid belts ($P > E$) from 30° to beyond the latitudinal limits (60°) of our paleogeographic reconstructions are represented by lighter green shading, with the intervening arid belts ($P < E$) unshaded, all based on general circulation climate model with idealized geography by Manabe and Bryan (1985). Large continental basaltic provinces are shown in red, large submarine provinces in orange. Paleogeographic maps were made with PaleoMac software (Cogné, 2003).

We estimated the productivity of the Tethyan CO_2 factory over the Cretaceous–Cenozoic by reconstructing the latitudinal component of motion for a point on the northern margin of the Indian plate (filled star in Fig. 3a) compared with the latitudinal evolution of a point on the Lhasa southern margin (unfilled star in Fig. 3a). The paleolatitude curves (Fig. 4a) were used to predict the timing of subduction of oceanic crust attached to Greater India that was loaded with equatorial (5° S–5° N) bulge sediments. In a simple 2-plate model, the onset of northward motion of Greater India at ~ 120 Ma presaged the onset of subduction of the equatorial bulge underneath the Lhasa margin at around 97 Ma and until the bulge that formed under the equatorial belt at around 72 Ma was subducted at ~ 55 Ma and the last sediments were consumed in the trench at 50 Ma. In other words, a full equatorial load of sediment was probably continuously subducted in southern Asia trenches from at least ~ 97 Ma to collision at 50 Ma.

The amount of equatorial bulge sediments subducted with time can be estimated from the loading time, loading area, and mass accumulation rate, as follows:

1. The time spent by the Tethyan crust under the presumed 5° S–5° N upwelling belt (loading time) was calculated acknowledging that the Tethyan crust was loading sediments under the 5° S–5° N belt since well before the onset of India–Asia convergence; we therefore assumed an initial, nominal loading duration of 20 Myr to which we added the loading times directly derived from the plate's latitudinal velocity (Fig. 4b). For example, oceanic crust entering the Lhasa trench at ~ 80 Ma (Fig. 4a) was already sediment-loaded for 20 Myr when

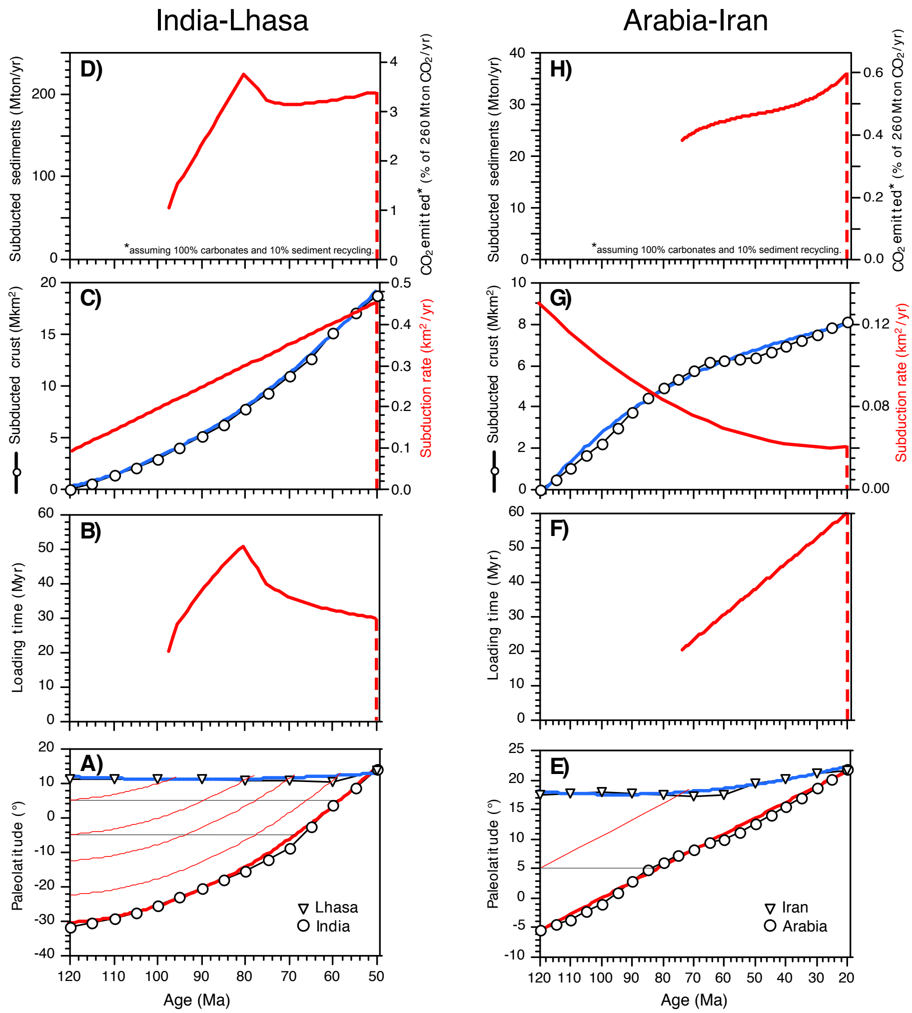

Fig. 4. Estimates of decarbonation in Tethyan subduction factory. Panels **(A)–(D)** refer to the subduction of Tethyan crust between Greater India and Lhasa (Asia). **(A)** Paleolatitude curves for northern Greater India (filled star in Fig. 3a) and southern Lhasa block (unfilled star in Fig. 3a) with 2nd order polynomial fits used to calculate the subduction time and the loading time of oceanic crust during passage through hypothesized equatorial upwelling belt (5° S–5° N). **(B)** Sediment loading time for passage through equatorial upwelling belt (5° S–5° N) of oceanic crust subducted under Asia. Curve starts at 97 Ma with a nominal 20 Myr loading time because the oceanic crust was sitting in the equatorial belt since appearance of pelagic carbonates and well before onset of subduction. **(C)** Amount of Tethyan crust as function of time between northern Greater India and southern Lhasa block that was eventually subducted under Asia plotted with a 2nd order polynomial fit resampled every 1 Myr (blue line) and red curve showing subduction rate (scale on right) as 1st derivative of the polynomial subduction curve. **(D)** Amount of equatorial bulge sediments on Tethyan crust subducted under Asia per unit time as a function of geologic age. The axis on the right is the CO_2 emitted by these sediments expressed as percentage of the present-day global volcanic CO_2 emission rate of 260 Mt yr^{-1}, assuming the sediments were 100 % carbonates and 10 % recycled. Panels **(E)–(H)** refer to the subduction of Tethyan crust between Arabia and Iran (Asia) following the same procedure illustrated for India–Lhasa in panels **(A)–(D)**, with the only notable differences that the time scale extends to 20 Ma and the paleolatitude curves – in **(E)** – are for the southeastern margin of Arabia (filled circle in Fig. 3a) and the western margin of the Iran block (unfilled circle in Fig. 3a).

it started moving from 5° S at 120 Ma across the equatorial belt to 5° N at 89 Ma thus accumulating additional ∼ 31 Myr of loading (total of ∼ 51 Myr at subduction; Fig. 4b). As another example, oceanic crust entering the Lhasa trench at ∼ 70 Ma (Fig. 4a) was already sediment-laden for 20 Myr when it crossed the equatorial belt from ∼ 93 Ma to ∼ 78 Ma accumulating an additional ∼ 16 Myr of loading (total of ∼ 36 Myr at subduction; Fig. 4b).

2. The surface area of Indian oceanic crust displaced northward at any given time and eventually consumed at the trench (subduction rate) was calculated from the paleogeographic reconstructions (Fig. 3 and additional ones) and found to steadily increase

from $\sim 0.09\,km^2\,yr^{-1}$ to $\sim 0.45\,km^2\,yr^{-1}$ for a total subducted crust of $\sim 19.0\,Mkm^2$ (Fig. 4c). Most of this crust ($\sim 14.7\,Mkm^2$) resided on or crossed the equatorial upwelling belt before being subducted, whereas the remainder ($\sim 4.3\,Mkm^2$) was located between 5° N and the Lhasa margin and presumably never got loaded with equatorial sediments (see Fig. 3a).

3. A nominal mass accumulation rate (MAR) of $1.5\,g\,cm^{-2}\,kyr^{-1}$ ($15\,t\,km^{-2}\,yr^{-1}$) for the Tethyan equatorial belt 5° S–5° N was derived from estimates for the Cretaceous equatorial Pacific Ocean (Ogg et al., 1992), which is within the range of values found for the Cenozoic equatorial Pacific (Mitchell and Lyle, 2005; Mitchell et al., 2003).

Summarizing and clarifying the above, oceanic crust transiting under the equatorial upwelling belt gets a full biogenic (calcareous and biosiliceous) sediment load that is estimated by multiplying the loading time (1) by the loading area (2) by the MAR value (3). This subducted load is found to vary between $\sim 60\,Mt\,yr^{-1}$ at ~ 120 Ma up to $\sim 220\,Mt\,yr^{-1}$ at ~ 80 Ma and dropping to virtually zero at 50 Ma (Fig. 4d). Even allowing the subducted sediment to be entirely carbonate, a recycling rate of 10 % (although generally less) based on ^{10}Be data in arc volcanics (Tera et al., 1986) would imply that the amount of CO_2 that was potentially generated by the decarbonation of Tethyan pelagic biogenic sediments was maximally $\sim 9.7\,Mt\,CO_2\,yr^{-1}$ at around 80 Ma, corresponding to only ~ 4 % of the present-day global volcanic CO_2 emission rate of $\sim 260\,Mt\,CO_2\,yr^{-1}$ (Fig. 4d).

A similar scenario of convergence and equatorial bulge subduction can be traced between Arabia and Iran in the western Tethys (Fig. 4e–h). Using the procedure outlined above for India, the mean latitudinal velocity of a point on the northeastern margin of Arabia (filled circle in Fig. 3a) is used in conjunction with the paleolatitude evolution of a point on the southwestern Iran margin (unfilled circle in Fig. 3a) to predict that the oceanic crust loaded with equatorial bulge sediments started subducting at around 74 Ma and ended at ~ 20 Ma with the terminal Arabia–Iran collision (Fig. 4e). The loading time of this subducted oceanic crust was estimated to steadily increase from an initial value of ~ 20 Myr (for similar reasons previously illustrated for India) to a maximum of ~ 60 Myr (Fig. 4f). The subduction rate was found to decrease from $\sim 0.18\,km^2\,yr^{-1}$ to $\sim 0.04\,km^2\,yr^{-1}$ for a total subducted crust of $\sim 8.1\,Mkm^2$ (Fig. 4g). Of this crust, only $\sim 2.1\,Mkm^2$ resided on or crossed the equatorial upwelling belt before being subducted, whereas the remainder presumably never got loaded with equatorial sediments (see Fig. 3a). These numbers lead us to calculate a subducted sediment load that varies between $\sim 23\,Mt\,yr^{-1}$ at 70 Ma and $\sim 35\,Mt\,yr^{-1}$ at 20 Ma (Fig. 4h); assuming again that the subducted sediments were entirely carbonates and a recycling rate of ~ 10 %, the maximum amount of CO_2 that was potentially generated by the decarbonation of these biogenic sediments was $\sim 1.6\,Mt\,CO_2\,yr^{-1}$ at around 20 Ma, corresponding to only ~ 0.6 % of the present-day global volcanic CO_2 emission rate of $\sim 260\,Mt\,CO_2\,yr^{-1}$ (Fig. 4h).

It appears that subduction decarbonation of Tethyan pelagic sediments may have reached $\sim 10\,MtCO_2\,yr^{-1}$ from 80 to 50 Ma, which is only ~ 4 % of the present-day global volcanic CO_2 emission rate of $260\,Mt\,CO_2\,yr^{-1}$.

We can also approach this from the long-term mean ocean production rate of $3.4\,km^2\,yr^{-1}$ from Rowley (2002), which would imply that $340\,Mkm^2$ of oceanic crust was subducted globally in the 100 Myr from 120 Ma (about when pelagic carbonates and chalks become important) to 20 Ma (end of major Tethyan subduction after which there has been only minor overall subduction of pelagic carbonates elsewhere, mainly Central America), or nearly 13-fold what was calculated for subduction just of Tethyan crust ($\sim 27\,Mkm^2$ for India plus Arabia). However, a substantial fraction of the oceanic crust that was subducted must have been in the Pacific which did not systematically transit through the equatorial upwelling belt and consequently probably had a much lower MAR, perhaps by an order of magnitude ($\sim 1.5\,t\,km^{-2}\,yr^{-1}$) than for equatorial bulge pelagic sedimentation (Mitchell and Lyle, 2005). Even if additional subduction decarbonation doubled the rate estimated just for Tethyan pelagic sediments, to perhaps $20\,Mt\,CO_2\,yr^{-1}$, this would nevertheless still be a small fraction (less than 10 %) of the present-day global volcanic CO_2 emission rate. This leads us to conclude that unless its efficiency was much higher (Johnston et al., 2011) the decarbonation subduction factory was a rather modest contributing factor in producing higher pCO_2 and presumably related warm climate in the Cretaceous–Eocene. We also note that the total deep (mantle) carbon storage of about 1000 Tt CO_2 for the past 125 Myr suggested by Selverstone and Gutzler (1993) to be in response to the Alpine–Himalaya collision amounts to about the same magnitude flux ($8\,Mt\,CO_2\,yr^{-1}$) as the decarbonation flux albeit of opposite sign and would thus further reduce its relative importance as a net long-term source of CO_2. More generally, subduction decarbonation would seem to be precluded as a major source of CO_2 prior to when open oceans became important loci of carbonate deposition with the abundant appearance of calcareous plankton at ~ 120 Ma. Edmond and Huh (2003) reached similar conclusions about the general efficacy of subduction decarbonation as a source of CO_2.

Mantle CO_2 that emanated from the emplacement of submarine LIPs (e.g. Ontong Java Plateau, Caribbean Plateau) probably significantly increased global pCO_2 levels that may have triggered environmental responses like oceanic anoxic events (e.g. Jenkyns, 2003; Tejada et al., 2009) but for not over much longer durations than each of their relatively short emplacement times (Self et al., 2005). This is because model calculations (Dupré et al., 2003; Misumi et al., 2009) and available supporting proxy measurements (Schaller et al.,

2011) indicate that the excess CO_2 would be adsorbed by negative feedback mechanisms on less than a million year time scale. In fact, continental LIPs are likely to be net CO_2 sinks due to enhanced consumption from their weathering (Dessert et al., 2003; Schaller et al., 2012).

4 Variable weathering sinks of CO_2

If the long-term source flux of CO_2 stayed basically constant and experienced only transient changes, persistent variations in CO_2 sink fluxes must have been in the driver's seat in controlling the concentration of atmospheric pCO_2. The most important CO_2 sink is weathering of continental silicates (Walker et al., 1981), a negative feedback mechanism dependent on surface temperature and runoff as a function of the CO_2 greenhouse effect and incorporated in most quantitative carbon-cycling models (e.g. Berner, 1991, 1994, 2006; Berner and Kothalava, 2001; Berner et al., 1983; Goddéris and Joachimski, 2004; Goddéris et al., 2008).

Recent evaluations have emphasized the importance of continental basalt weathering as a major sink for atmospheric CO_2, representing anywhere from one-third to nearly one-half of the CO_2 consumption flux from weathering of all continental silicates even though subaerial basalt provinces today constitute less than 5 % of world land area (Table 2 in Dessert et al., 2003). The compilation of Dessert et al. (2003) also shows that for a given gross basin lithology (granitic or basaltic), chemical weathering and CO_2 consumption rates are strongly dependent on runoff and temperature, which are markedly potent in the equatorial humid belt. It is noteworthy that SE Asia in the equatorial humid belt with a mean annual temperature of 25 °C and nearly 140 cm yr^{-1} runoff has by far the highest CO_2 consumption flux (1.033×10^{12} mol yr^{-1} = 45.5 Mt CO_2 yr^{-1}), which constitutes about 25 % of the total CO_2 consumption flux estimated for all basaltic provinces and small volcanic islands (4.08×10^{12} mol yr^{-1} = 180 Mt CO_2 yr^{-1} for total land area of 7.249 Mkm^2; Dessert et al., 2003), even though SE Asia represents less than 8 % of their combined surface area. In contrast, basalt provinces in cold or dry regions are not weathering rapidly and are thus consuming far less CO_2. For example, the Siberian Traps, a LIP that was emplaced in the latest Permian and presently straddles the Arctic Circle with a mean annual temperature of −10 °C and 40 cm yr^{-1} runoff, contributes a paltry 1.3 % (2.3 Mt CO_2 yr^{-1}) to the overall basalt CO_2 consumption flux even though it represents about 11 % of the surface area of all continental basalt provinces and small volcanic islands today (Dessert et al., 2003). The Ethiopian Traps, with a comparable surface area to the Siberian Traps, are just within the tropical arid belt with a much higher mean annual temperature of 21 °C but only 13 cm yr^{-1} runoff and hence end up contributing ∼ 3 % (5.3 Mt CO_2 yr^{-1}) to the overall basalt total CO_2 consumption flux (Dessert et al., 2003). Mg and Ca-poor granitic terranes have total CO_2 consumption fluxes that are 2 to 10 times lower than basaltic provinces in comparable climate conditions (Dessert et al., 2001; Gaillardet et al., 1999).

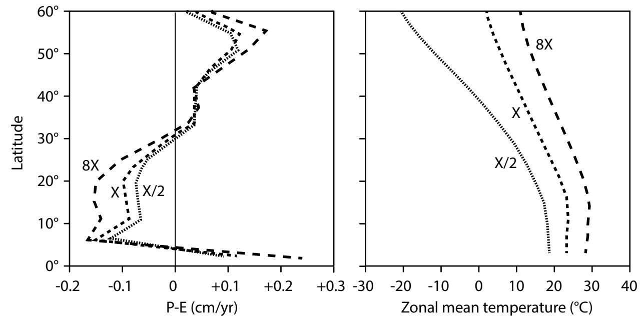

Fig. 5. Latitudinal distributions of (left panel) zonal average precipitation minus evaporation ($P-E$) and (right panel) zonal mean surface air temperature based on a general circulation model with an annual mean insolation and idealized geography obtained for various multiples of atmospheric pCO_2 (pre-industrial) values, shown here ranging from one-half ($X/2$) to eight fold ($8X$) (extracted from Figs. 4 and 19 in Manabe and Bryan, 1985).

To gauge the latitudinal position of climate belts in the past, we use values for zonal mean annual surface air temperature and the difference between precipitation and evaporation ($P-E$) based on a general circulation model from Manabe and Bryan (1985) with idealized geography, an annual mean insolation, and atmospheric pCO_2 concentrations that vary from one-half to 8-times the modern (pre-industrial: 280 ppm) value (Fig. 5). Compared with studies of silicate weathering rate using more comprehensive global climate numerical models (e.g. Donnadieu et al., 2006; Godderis et al., 2008) that include a variety of feedbacks as well as monsoons and other phenomena related to details of geography, the idealized zonal model employed here has the advantage, at this stage, of allowing us to keep the latitudinal dependency of climate more or less fixed while the distribution of land masses varies with plate tectonics. Indeed, their idealized zonal climate model "... completely bypasses the interaction of climate and the carbon cycle itself" (Manabe and Bryan, 1985, p. 11705).

Although the amplitude or climate severity of $P-E$ increases with increasing pCO_2, the latitudinal positions of the crossovers ($P-E=0$) stay relatively fixed (Manabe and Bryan, 1985) (Fig. 5, left panel). Accordingly, we set the equatorial humid belt ($P > E$) as occurring between 5° S and 5° N and the hemispheric limits of the tropical arid belts ($P < E$) as extending from 5° to 30° latitude and that of the temperate humid belts from 30° to the latitudinal limits (60°) of our paleogeographic maps (Fig. 3). Zonal mean temperatures generally increase with higher pCO_2 but for any given pCO_2 level they are uniformly high in the tropics (nominally 23° S to 23° N) before decreasing to about two-thirds of equatorial values by the lower latitude regions of the temperate humid belts (30° N or S) and to around freezing (0 °C) by 60° N or S for today's pCO_2 level (Fig. 5, right panel). The most potent and persistent combination of high temperature and high moisture for silicate weathering clearly resides in the equatorial humid belt (5° S–5° N, constituting 44 Mkm^2 or 8.7 % of Earth's total surface area) at any pCO_2 level and that is where we focus attention in estimating CO_2 consumption rates.

5 Quantification of CO_2 silicate weathering sinks

Total continental area in the equatorial humid belt was relatively steady at $\sim 12\,Mkm^2$, which is a little more than one-quarter (27 %) of the available surface area in this zone and about 8 % of present total continental land area ($\sim 150\,Mkm^2$), from at least 120 Ma to around 65 Ma (Fig. 6a; see also paleogeography in Fig. 3a and b). Over this time interval, South America had a decreasing areal contribution that was essentially balanced by Africa plus Arabia's increasing areal contribution in the equatorial humid belt. Other land areas had almost negligible contributions until the arrival of Greater India, whose northward passage through the equatorial humid belt provides the distinctive humped signature of the total area curve (Fig. 6a). From the peak of 15 Mkm^2 at ~ 55 Ma, total land area within the equatorial humid belt decreased with the northward indentation of India into Asia and leveled out at around 11 Mkm^2 by 25 Ma when the southerly motion of SE Asia (plus the widening equatorial expanse of South America and the northerly motion of New Guinea attached to Australia) balanced the decreasing contributions from the narrowing equatorial expanse of Africa.

The only large land-based basalt province straddling the equatorial humid belt during the entire Mesozoic was the 201 Ma (earliest Jurassic) Central Atlantic magmatic province (CAMP; Marzoli et al., 1999), whereas the 250 Ma Siberian Traps remained in high (> 60° N) latitudes, the 130 Ma Parana and Entendeka provinces of South America and Africa were in the austral tropical arid belt, and the ~ 120 Ma Rajmajal Traps formed poleward of 50° S in the austral temperate humid belt (Fig. 3). CAMP basalts were apparently thin (100–200 m-thick) but emplaced over a large area across tropical Pangea (5–10 Mkm^2; Marzoli et al., 1999; McHone 2003), and only minor exposures of lavas in isolated rift basins and widely scattered presumed feeder dikes now remain (McHone, 2003). The bulk of the CAMP lavas were probably weathered, eroded or buried soon after their emplacement, very likely within a few hundred thousand years of volcanic activity as suggested by estimates of atmospheric pCO_2 from paleosols interbedded and overlying CAMP lavas in eastern North America (Schaller et al., 2012) and tantalizing indications of rapid global cooling (Schoene et al., 2010). In any case, we suppose that any remaining exposed CAMP fragments were probably too small or had already drifted out of the equatorial humid belt to be important factors in weathering CO_2 consumption by Cretaceous times. The more or less constant area (0.9 Mkm^2) of basaltic rocks from 120 to 50 Ma is mostly in the Andes with some contribution from the Sumatra–Java arc (Fig. 6b).

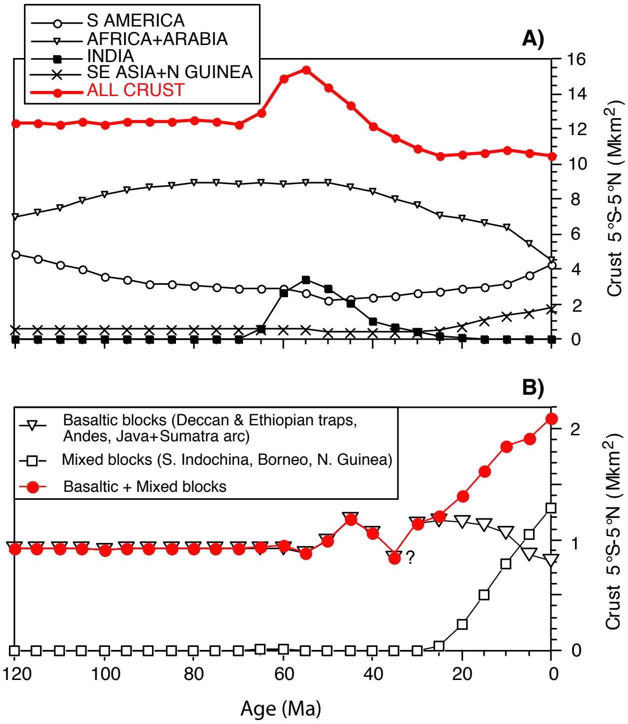

Fig. 6. (A) Estimates of land area within equatorial humid belt (5° S–5° N) as a function of time since 120 Ma obtained by applying the composite APWP (Table 1; Fig. 2) and finite rotation poles of Besse and Courtillot (2002) for major continental blocks and the rotation poles of Replumaz and Tapponnier (2003) for SE Asian blocks as discussed in text. **(B)** Estimates of key (most weatherable in the most favorable environment) land areas comprised of volcanic arc provinces (Java, Sumatra, Andes), large basaltic provinces (Deccan Traps, Ethiopian Traps), and mixed igneous-metamorphic provinces (South Indochina, Borneo, New Guinea) in the equatorial humid belt (5° S–5° N) as a function of time from 120 Ma to present. The rest of the world's continental regions in the equatorial humid belt are generally characterized by low elevation (Amazon and Congo basins), hence weathering tends to be low and transport-limited.

The Deccan Traps (current surface area of 0.5 Mkm^2; original volume of $\sim 2\,Mkm^3$; Courtillot and Renne, 2003) were emplaced at ~ 65 Ma in the austral arid belt (Fig. 3b) and in our view became a major consumer in the long-term CO_2 budget only when the Indian plate with the Deccan drifted into the equatorial humid belt at 50 Ma (Fig. 3c), just about when Greater India began to collide with Asia. At 30 Ma, the Ethiopian Traps (current surface area of 0.4 $Mkm^2 = 1/2$ of original extent; Rochette et al., 1998) erupted virtually on the equator just as the Deccan Traps drifted out of the equatorial humid belt where Java and Sumatra already began to impinge (Fig. 3d). Tectonic extrusion of SE Asia may have effectively ceased by 15 Ma but a gradual southerly drift due to Eurasia clockwise rotation brought Borneo into the equatorial humid belt (Fig. 3e) where it was eventually joined by New Guinea (attached to Australia) coming from the south (Fig. 3f). Today, there are more than 2 Mkm^2 of highly weatherable basaltic and mixed arc and related rocks in the equatorial humid belt (Fig. 6b).

To estimate the total CO_2 consumption rate of the varying land areas within the equatorial humid belt as a function of time, we use the following rates for the dominant lithologies. The rate for basaltic-rich provinces (Deccan and Ethiopian Traps, Andes, Java and Sumatra arc) was set to a nominal value of $100\,t\,CO_2\,yr^{-1}$ per km^2; this value represents a rounded estimate falling in the lower (conservative) side of a present-day total CO_2 consumption span ranging from $84.5\,t\,CO_2\,yr^{-1}$ per km^2 ($1.92 \times 10^6\,mol\,CO_2\,yr^{-1}\,km^{-2}$) for SE Asia in toto to $282\,t\,CO_2\,yr^{-1}$ per km^2 ($6.41 \times 10^6\,mol\,CO_2\,yr^{-1}\,km^{-2}$) for the island of Java alone (Dessert et al., 2003). A nominal 1/2 of the basalt weathering rate ($50\,t\,yr^{-1}$ per km^2) was applied to mixed (basaltic-granitic-gneissic) land areas (South Indochina, Borneo, New Guinea) following Dessert et al. (2001); for example, the basaltic island of Réunion (21° S; $\sim 240\,cm\,yr^{-1}$ runoff, 19 °C mean annual temperature) has an annual total CO_2 consumption rate that is roughly twice that of the climatically similar, mixed basaltic-granitic island of Puerto Rico (18° N, $\sim 360\,cm\,yr^{-1}$ runoff, 22 °C mean annual temperature; Fig. 2 in Dessert et al., 2001). Total CO_2 consumption rates for continental cratonic regions are expected to be much lower due to much less weatherable granitic lithologies and generally low topographic relief (i.e. transport-limited regimes; see Sect. 7 below). With all due caveats, we use $5\,t\,yr^{-1}$ per km^2 for continental cratonic areas, a rate that is an order of magnitude less than for mixed lithology land areas like New Guinea and compatible with the relative sense of total CO_2 consumption rates deduced from the chemistry of large rivers in such areas (Gaillardet et al., 1999).

In applying these weathering rates to the past, we would note that paleotemperature estimates from planktonic foraminiferal oxygen isotope records point to tropical climate throughout the Eocene only a few degrees warmer than modern sea-surface temperatures (Pearson et al., 2007). Extrapolation to the past of modern total CO_2 consumption rates for the tropics should therefore provide reasonably compatible estimates as far as the temperature component is concerned although the ancient weathering rates are likely to be underestimated due to more vigorous hydrological cycles when atmospheric pCO_2 levels were higher (Manabe and Bryan, 1985; Held and Soden, 2006), as they almost invariably were over the past 120 Myr and longer.

Total CO_2 consumption values corresponding to these rates were calculated for areas of subaerial basalts and mixed crust and for the remaining continental cratonic areas in the equatorial humid belt in 5 Myr intervals (Fig. 7). Under these assumptions, areas of subaerial basalts and mixed crust contribute about 50 % more than the remaining much vaster continental cratonic areas (all in the equatorial humid belt) from 120 to 50 Ma, after which the contribution of subaerial basalts and mixed crust eventually increases to nearly 3.5 times that of the remaining continental cratonic areas. The combined CO_2 consumption profile for all subaerial crust in the equatorial humid belt (top curve in Fig. 7) has much of the character of the potent subaerial basalts and mixed crust component, for example, the downward blip at ~ 35 Ma is essentially due to an apparent gap of highly weatherable basalts in the equatorial humid belt between the northward drift of the Deccan Traps out of the belt before the eruption of the Ethiopian Traps at 30 Ma (Fig. 6b). We

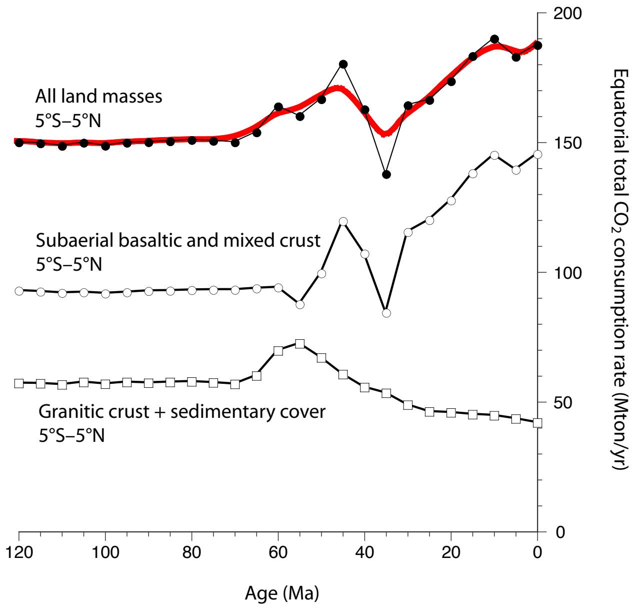

Fig. 7. Total CO_2 consumption rates from silicate weathering since 120 Ma of land areas in equatorial humid belt (5° S–5° N) obtained by multiplying a nominal CO_2 consumption rate of $100\,t\,CO_2\,yr^{-1}\,km^{-2}$ for basaltic provinces and $50\,t\,yr^{-1}\,km^{-2}$ for mixed basaltic-metamorphic provinces (Dessert et al., 2003) and an order of magnitude less ($5\,t\,yr^{-1}\,km^{-2}$) for the remaining continental land areas (Gaillardet et al., 1999) to the corresponding cumulative distribution curves in Fig. 6. Note that these total consumption rates should be divided by 2 for net CO_2 consumption rates because half of the CO_2 consumed by silicate weathering is returned to the atmosphere–ocean during carbonate precipitation. For example, total CO_2 consumption of $190\,Mt\,CO_2\,yr^{-1}$ would correspond to a net CO_2 consumption of $190/2 = 95\,Mt\,CO_2\,yr^{-1}$, or ~ 35 % of present-day global volcanic CO_2 outgassing of $260\,Mt\,CO_2\,yr^{-1}$. For reference, the consumption of $1\,Mt\,CO_2\,yr^{-1}$ can be sustained by introducing into the equatorial humid belt or rejuvenating roughly 10 000 km^2 (or $\sim 20\,000$ km^2 for net) of the SE Asia arc terrane every million years.

cannot exclude that this short-term variation might in part be an artifact associated with uncertainties of a few degrees in continent paleolatitudes combined with the tight and fixed latitudinal bounds of the equatorial humid belt in the simple zonal climate model we used. Hence the smoothed curve in Fig. 7 may provide at this juncture a more substantiated representation of the secular change in total equatorial consumption of CO_2. Even allowing that the total consumption flux of CO_2 should be halved to account for the CO_2 returned to the atmosphere–ocean during carbonate precipitation, it is remarkable that the net CO_2 consumption rate of up to $190/2 = 95\,\mathrm{Mt\,CO_2\,yr^{-1}}$ from silicate weathering of only a small fraction of total land with basaltic and mixed crust provinces currently residing in the equatorial humid belt may balance a substantial fraction ($\sim 35\,\%$) of the present-day global volcanic emission rate of $260\,\mathrm{Mt\,CO_2\,yr^{-1}}$.

6 Himalayan uplift-erosion hypothesis

According to the uplift-erosion hypothesis (Raymo and Ruddiman, 1992), uplift of the Himalayas and Tibetan Plateau as a consequence of the India–Asia collision resulted in enhanced silicate weathering rates and higher associated consumption of CO_2, causing Earth's climate to cool with the eventual formation of Antarctic ice sheets by ~ 34 Ma. This was largely based on the supposition that the progressive increase in $^{87}Sr/^{86}Sr$ values of marine carbonates since ~ 40 Ma (Hess et al., 1986; Richter et al., 1992) was due to enhanced delivery of radiogenic Sr from increased global chemical weathering rates from mountain building, especially the uplift of the Himalayas (Raymo et al., 1988). It is not clear in this model what would have been responsible for initiating decreasing atmospheric $p\mathrm{CO_2}$ over the prior 10 Myr since the $^{87}Sr/^{86}Sr$ seawater curve is essentially flat from at least 50 Ma (when cooling starts according to $\delta^{18}O$ data, see Fig. 1a) to 40 Ma. More importantly, others have argued rather persuasively that most of the overall increase in $^{87}Sr/^{86}Sr$ resulted from the unroofing and chemical erosion of particularly radiogenic Himalayan rocks, such as leucogranites (Edmond, 1992) and metasediments (Harris, 1995) including metamorphosed limestones (Quade et al., 1997), in which case the $^{87}Sr/^{86}Sr$ seawater curve would not serve as a simple proxy for *global* weathering rates of continental silicates.

The general principle of the uplift-erosion hypothesis is nevertheless difficult to dismiss and the drift-weathering idea proposed here bears a general resemblance to it: both call upon tectonic mechanisms (uplift, plate motion) to initiate and sustain higher CO_2 consumption via silicate weathering. Compared to a carbon cycling model driven on the supply-side, a sink-side model like the uplift-erosion hypothesis may have to contend with the absence of an effective feedback mechanism that is well-coupled to the climate system to stabilize atmospheric $p\mathrm{CO_2}$ levels even over relatively short geologic time scales (e.g. Berner and Caldiera, 1997; Broecker and Sanyal, 1998). Kump and Arthur (1997) modified the Himalayan uplift-erosion concept by invoking compensatory factors to high local (Himalayan) chemical erosion and associated CO_2 drawdown: according to their model, global chemical erosion rates did not increase over the Cenozoic because higher erosion rates in the Himalayan region were more or less balanced by decreased erosion rates elsewhere as climate cooled. What caused CO_2 to decline, according to them, was that the continents somehow became more susceptible to chemical erosion, or more weatherable, since the Miocene (20 Ma), even though their calculated weatherability factor was flat or even decreased from 50 to 20 Ma over which time global cooling started, atmospheric $p\mathrm{CO_2}$ levels declined and there was even a major glacioeustatic fall at 34 Ma (Fig. 1).

But what if tectonic uplift occurred closer to the equator: global climate would cool with the drawdown of CO_2 but the resulting decreased silicate weathering and reduced CO_2 consumption elsewhere might not be able to compensate for the continued drawdown of CO_2 due to the presence of more weatherable landmasses in the relatively warm and wet conditions of the equatorial humid belt. This is effectively the drift-weathering scenario and may be the ongoing case today with the high landmasses of the SE Asian islands like Java, Sumatra, Borneo (world's 3rd largest island at $0.75\,\mathrm{Mkm^2}$ with mountain peaks rising to over 4000 m), as well as New Guinea (2nd largest island after Greenland at $0.79\,\mathrm{Mkm^2}$ with peaks rising to nearly 5000 m) impinging upon the equatorial humid belt and shedding prodigious amounts of sediment intensely weathering in the heat and humidity of the lowland aprons, even though atmospheric $p\mathrm{CO_2}$ levels are very low (probably as a result). This is also reflected by the global annual fluvial sediment flux from the world's main drainage basins to the oceans that shows a disproportionately high contribution to the global sediment yield by the SE Asian islands straddling the modern equator (Milliman, 1990).

Although the weathering flux per unit area on the Ganges floodplain may be appreciable (West et al., 2002), it seems to us that the specific Himalayan uplift-erosion hypothesis does not actually do enough early enough and for long enough in terms of CO_2 drawdown from silicate weathering to account for the cooling over the Cenozoic that led to the formation of major polar ice sheets. Besides, there are mountains in many parts of the world that at any given time are being actively eroded. The action really needs to happen in the equatorial humid belt where whenever significant weatherable lithologies are inserted via horizontal plate motion and/or vertical uplift – as is presently happening – negative feedbacks may not be efficient enough to inhibit net CO_2 drawdown and an eventual ice age.

7 Transport-limited negative feedback

The relatively small surficial carbon reservoir compared to the large carbon fluxes implies that there is close parity on million year time scales between inputs (volcanic outgassing and metamorphism) and outputs (silicate weathering followed by deposition of carbonate minerals and burial of organic carbon) to maintain a stable level of CO_2 in the atmosphere (Berner and Caldeira, 1997). This fine balance requires a negative feedback that depends strongly on the level of atmospheric CO_2. A powerful concept for policing the CO_2 content of the atmosphere is the CO_2-silicate weathering feedback mechanism of Walker et al. (1981) that underlies the BLAG model (Berner et al., 1983) and the GEOCARB lineage of supply-side carbon cycling models (Berner, 2004): increases or decreases in CO_2 outgassing induce an opposing response from higher or lower chemical weathering rates via associated greenhouse effects. A stabilizing negative feedback is more difficult to identify in a sink-side model, for example, an uplift-weathering mechanism (i.e. model of Raymo and Ruddiman, 1992) left uncoupled to the CO_2 content of the atmosphere would eventually produce a crash in atmospheric $p\text{CO}_2$ (Kump and Arthur, 1997). After evaluating alternative mechanisms, such as a possible albeit tenuous link between erosion and organic carbon burial (Raymo, 1994), Broecker and Sanyal (1998) concluded that the $p\text{CO}_2$ level of the atmosphere almost certainly has to act as the controller of a silicate weathering feedback.

So what is to keep atmospheric $p\text{CO}_2$ from plunging or wildly oscillating in our drift-weathering, sink-side model? We suggest that as a continental silicate province drifts into the equatorial humid belt and is subject to relatively intense chemical weathering, there may eventually be a transition from weathering-limited to transport-limited regimes with thickening of cation-deficient soils that will tend to retard further chemical weathering of the bedrock; this is likely to characterize cratonic areas with low relief (Kump et al., 2000; West et al., 2005). In the case of continental basaltic provinces entering the equatorial humid belt, they are provided with initial relief from plume head uplift and the stacking of lava flows that would prolong the weathering-limited phase; nevertheless, they may eventually be either consumed by intense weathering or drift out of the intense weathering regime, resulting in a reduction to their contribution to CO_2 drawdown. The Deccan and Ethiopian Traps soon enough drifted out of the equatorial humid belt and escaped this fate of complete consumption by weathering and erosion, whereas most of the once widespread CAMP lavas were evidently largely consumed probably not long after their emplacement at around 201 Ma (Schaller et al., 2012), leaving only a few remnants amongst the now-dispersed Atlantic-bordering continents.

An interesting exception is SE Asia, a major CO_2 sink (Dessert et al., 2003) that has been straddling the equatorial humid belt since at least 25 Ma and which, as a set of island arc terranes, has been continuously rejuvenated by uplift and magmatism and therefore subjected to persistent intense weathering. There would be rather weak negative feedbacks in this case, making SE Asia (along with New Guinea) a prime candidate responsible for very weakly regulated consumption of enough CO_2 to plunge Earth's climate system into a glacial mode and keep it there in the later part of the Cenozoic. Higher east–west sea-surface temperature gradients and more vigorous Walker circulation in the equatorial Pacific, much like normal conditions today, apparently resulted from the end of continual El Nino due to global shoaling of the oceanic thermocline at around 3 Ma (Fedorov et al., 2006; Ravelo, 2006); we are tempted to speculate that increased rainfall over the SE Asia–New Guinea equatorial archipelago may have caused sufficiently higher CO_2 consumption from runoff-enhanced silicate weathering to trigger Northern Hemisphere glaciations.

8 Temperate-latitude safety valves

Although significant variations in potential sources of CO_2 such as oceanic crust production rates and hydrothermal activity cannot be precluded even though they are notoriously difficult to calibrate, the drift-weathering model of varying CO_2 sinks arising from the changing latitudinal distribution of land masses, and especially basaltic provinces and island arc terranes, provides a measurable and hence testable mechanism to account for long-term variations in atmospheric $p\text{CO}_2$ levels over the Late Cretaceous and Cenozoic, and further back in Earth's history.

The key is the sporadic presence of highly weatherable continental basalt provinces in the equatorial humid belt, the engine of Earth's climate system that is characterized by warm temperatures and high rainfall at widely varying atmospheric $p\text{CO}_2$ levels. With no highly weatherable basaltic provinces in the equatorial humid belt from at least 120 to 50 Ma, atmospheric $p\text{CO}_2$ levels tended to be elevated giving rise to warm climates such as the intervals centered on the CTM and the EECO. These super-greenhouse conditions would have activated enhanced weathering of continents and especially basaltic provinces in a warmer and wetter temperate humid belt. For example, many of the lavas of the British Tertiary igneous province, a subprovince of the North Atlantic igneous province LIP of late Paleocene to early Eocene age that was emplaced and remained at mid-paleolatitudes of $\sim 45°$ N (Ganerød et al., 2010), were erupted subaerially (Saunders et al., 1997) and are often closely associated with well-developed laterites, such as the 30 m-thick unit belonging to the Interbasaltic Formation in Antrim, Northern Ireland (Hill et al., 2000) and the red boles on the Isles of Mull and Skye in Scotland (Emeleus et al., 1996). Elsewhere in ostensibly temperate Europe, bauxite was named from Les Baux-de-Provence in France ($\sim 44°$ N) for a lateritic aluminum ore that mainly formed on carbonate rocks

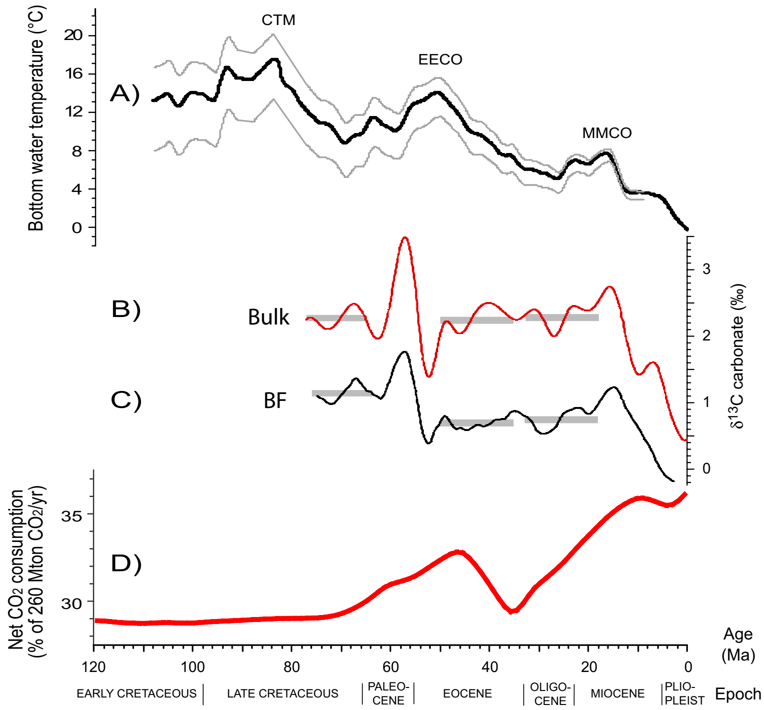

Fig. 8. (A) Bottom water temperatures (Cramer et al., 2011; see caption to Fig. 1 for explanation); **(B)** $\delta^{13}C$ carbonate data from whole sediment (Bulk) (smoothed SSA curve from Katz et al., 2005) and **(C)** $\delta^{13}C$ carbonate data from benthic foraminifera (BF) from the Pacific (smoothed trend from Cramer et al., 2009), with mean values over selected intervals (77–65, 50–35, 33–18 Ma) shown by gray bars in both curves; **(D)** Secular change in net (one-half of total) CO_2 consumption rate from silicate weathering of all land masses in equatorial humid belt (5° S–5° N) (smoothed curve from Fig. 7) expressed as percentage of the present-day global volcanic CO_2 emission rate of 260 Mt CO_2 yr^{-1} (Gerlach, 2011; Marty and Tolstikhin, 1998).

of Jurassic and Cretaceous age (Retallack, 2010). In western North America, some of the highest calculated denudation rates for crystalline bedrock for non-glacial times were documented in the Green River Basin (42° N) and ascribed to enhanced silicate dissolution rates associated with elevated atmospheric pCO_2 levels that occurred during the EECO (Smith et al., 2008).

These and other examples support the concept that basaltic provinces outside the equatorial humid belt effectively act as safety valves that limit extreme accumulations of CO_2 in the atmosphere. Equable climates are the norm or default mode; ice ages are the exception, due to fortuitous latitudinal distributions of potent silicate weathering sinks of CO_2 with only weak negative feedbacks. In other words, the silicate-weathering thermostat, so effective at the high temperature end, sometimes cannot sufficiently decrease weathering rates of highly weatherable (i.e. basaltic) continental provinces in the equatorial humid belt that is only loosely coupled to atmospheric pCO_2 levels, thus paving the way to an ice age as in the late Cenozoic (or at the extreme, a Snowball Earth: Hoffman and Schrag, 2002; Godderis et al., 2003).

9 Role of organic carbon burial

Excess burial of organic carbon has been suggested as contributing to the progression from greenhouse climate of the Mesozoic to icehouse conditions that prevailed by the late Cenozoic (Katz et al., 2005) and is briefly considered here. The relative fractions of carbonate and organic carbon buried in sediments are reflected in carbon isotopes of carbonate produced in surface waters (Broecker and Woodruff, 1992; Kump, 1991) as revealed, for example, by the bulk sediment record compiled by Katz et al. (2005) that mainly reflects calcareous plankton. A comparison between this ($\delta^{13}C_{carb}$) dataset and the benthic foraminifera $\delta^{13}C_{BF}$ record compiled by Cramer et al. (2009), which is reasonably continuous from ∼ 77 Ma to present (Fig. 8), also provides insight into the evolving role of the biological pump that transfers carbon from the shallow to deep water reservoirs (Volk and Hoffert, 1985).

The organic fraction (f_{org}) of the total carbon burial flux at steady state can be estimated according to Kump and Arthur (1999):

$$f_{org} = \left(\delta'_w - \delta_{carb}\right)/\Delta_B$$

where δ'_w is the average carbon isotopic composition of the riverine flux (assumed to be −5 ‰), δ_{carb} is the isotopic composition of carbonate sediments that reflect the oceanic carbon reservoir, and Δ_B represents the isotopic difference between organic matter and carbonate deposited from the ocean. If Δ_B is assumed to be constant (say −29 ‰) from 77 to 15 Ma, the mean δ_{carb} of 2.3 ‰ would imply a typical average f_{org} of 0.25; a dependence of Δ_B on ambient pCO_2 (Kump and Arthur, 1999) would tend to slightly increase the average organic burial fraction with declining atmospheric pCO_2 levels since ∼ 35 Ma, for example, f_{org} would be 0.27 for pCO_2 of ∼ 350 ppm. The large (up to ∼ 2.5 ‰) decrease in the bulk sediment (and benthic) records from 15 Ma to present (Fig. 8b and c) was interpreted by Shackleton (1987) as due to a decreasing fraction of organic carbon burial although its origin has remained enigmatic (Broecker and Woodruff, 1992). Katz et al. (2005) suggested that about 1.1 ‰ of the decrease could be accounted for by the rise of C4 photosynthetic pathways with the remaining ∼ 1.4 ‰ decrease due to weathering (i.e. unburial) of organic-rich shales. Although France–Lanord and Derry (1997) suggested that net burial of organic carbon during Himalayan sedimentation consumed several times more CO_2 than weathering of Himalayan silicates in the Neogene, there seems to be little evidence for increasing net organic carbon burial on global scale to account for cooling climate from the middle Miocene climate optimum (MMCO) (Flower and Kennett, 1994; Miller et al., 1987; Wright et al., 1992; You et al., 2009).

The other prominent feature in the bulk (and benthic) sediment carbon isotope record is the 1.5 ‰ increase starting at around 62.5 Ma that peaks at 57 Ma and followed by a 2 ‰ decrease to a prominent trough at 52 Ma (Fig. 8b). The run-up to the peak at 57 Ma implies an increasing fraction of organic carbon burial (f_{org} up to 0.3), which may be related to burial of organic-rich sediments, whereas the subsequent large decrease in carbon isotope values (implying f_{org} decreased to ∼ 0.22) starting at around 57 Ma may mark the exhumation and oxidation of organic carbon-rich Tethyan marine sediments during the early stages of the India–Asia collision according to Beck et al. (1995), who suggested that this may have increased atmospheric pCO_2 sufficiently to have contributed to global warming in the early Cenozoic (albeit somewhat prior to peak warmth at the EECO).

A comparison between the bulk sediment and benthic carbonate $\delta^{13}C$ records (Fig. 8b and c) shows that the average value for benthic data between 77 Ma to just before the Cretaceous–Paleogene boundary perturbation at 65 Ma (D'Hondt et al., 1998) is 1.2 ‰, about 1.1 ‰ higher than the bulk sediment $\delta^{13}C$ mean of 2.3 ‰. From 50 Ma, just after the Paleocene–Eocene boundary perturbation (Hilting et al., 2008), to 35 Ma, just before Oi-1 at around the Eocene–Oligocene boundary, as well as from 33 Ma, just after Oi-1, to 18 Ma, just before the MMCO, the benthic means are 0.7 ‰ or about 1.6 ‰ lighter compared to the corresponding bulk sediment means of 2.3 ‰. It would thus appear that the biological pump spun-up soon after EECO (∼ 50 Ma), well before the inception of large Antarctic ice sheets and the strengthening of ocean circulation at Oi-1 at around 34 Ma (e.g. Cramer et al., 2009; Kennett, 1977), and stayed relatively constant from 35–50 to 18–33 Ma. A sustained higher input of nutrients, notably phosphates (Schrag et al., 2002), may have resulted from enhanced weathering of continental silicates starting with the arrival of the Deccan in the equatorial humid belt at ∼ 50 Ma (marked also by the formation of abundant cherts in the world's oceans; Muttoni and Kent, 2007). This may have spurred biological productivity even though the fraction of organic carbon burial hardly varied in concert.

10 Conclusions

1. Contrary to what has sometimes been assumed including in our earlier work (Kent and Muttoni, 2008), the degree to which decarbonation of pelagic sediments contributes to atmospheric pCO_2 is calculated to be rather modest compared to present-day global volcanic outgassing, suggesting that subduction decarbonation was not a decisive factor in the higher atmospheric pCO_2 levels associated with warm climates of the Late Cretaceous and early Cenozoic let alone earlier, before proliferation of pelagic carbonate deposition in the deep sea.

2. The small estimated contribution of decarbonation along with the null hypothesis of a constant rate of ocean crust production (Rowley, 2002) suggest that changes in the long-term budget of atmospheric pCO_2 are more likely governed by the carbon sinks rather than in response to variations in the carbon supply as typically invoked in many carbon cycling models for at least the late Mesozoic and Cenozoic.

3. To explain long-term changes in atmospheric pCO_2, we consider a time-varying CO_2 sink model largely driven by the amount of land area, and highly weatherable subaerial basaltic terranes in particular, brought by tectonic plate motions into the equatorial humid belt, the most potent venue for continental silicate weathering and associated consumption of CO_2.

4. According to the drift-weathering hypothesis, the long-term decrease in atmospheric pCO_2 levels since the EECO was initiated by the arrival of Greater India carrying the highly weatherable Deccan Traps into the equatorial humid belt at around 50 Ma, and was sustained by the emplacement of the 30 Ma Ethiopian Traps near the equator, the southerly tectonic extrusion of SE Asia, an arc terrane that presently is estimated to account for ∼ 1/4 of the total CO_2 consumption by continental basalt weathering and volcanic islands that in

turn represents ~ 1/3 of total continental silicate weathering (Dessert et al., 2003), joined by the incursion of New Guinea into the equatorial belt from the south.

5. The equatorial humid belt is likely to maintain potent (warm and wet) conditions for weathering over a broad range of atmospheric pCO_2 levels with only weak negative feedbacks to limit weathering rates, which would therefore tend to dwell on the high side. Low atmospheric pCO_2 levels leading to global cooling and glaciation depend on enhanced and sustained presence of weatherable rocks, especially subaerial basalts, near the equator.

6. Paleosols and other evidence of more intense chemical weathering in temperate latitudes tend to be associated with times of very high atmospheric pCO_2 levels and warm global climates, for example, *terra rossa* between subaerial lavas of the North Atlantic igneous province of late Paleocene to early Eocene age, which evidently acted as safety valves providing the strong negative feedback that acts to squelch a runaway greenhouse when there are insufficient weatherable terranes in the equatorial humid belt to adequately balance CO_2 outgassing.

7. The drift-weathering hypothesis bears some resemblance to the Himalayan uplift-erosion hypothesis of Raymo and Ruddiman (1992) to the extent that it does not seem to make much difference whether more weatherable lithologies are introduced by horizontal plate motion – as we suggest – or as vertical uplift in mountain building processes, as long as it happens close to the warm and humid equatorial belt.

8. Basalt terranes are highly weatherable and thus very effective in CO_2 consumption within the equatorial humid belt but large changes in area of more typical continental lithologies are also capable of affecting the atmospheric pCO_2 balance (Godderis et al., 2003, 2008).

9. Comparison of bulk (mainly planktic) carbonate and benthic carbon isotope records indicates that the biological pump (surface to deep ocean isotopic gradient) increased just after the EECO (~ 50 Ma) and continued at more or less the same high level through most of the rest of the Cenozoic, a pattern that could reflect higher productivity associated with increased availability of nutrients from the same silicate weathering in the equatorial humid belt that was drawing down atmospheric pCO_2.

10. The drift-weathering hypothesis provides motivation for obtaining accurate estimates of the latitudinal distribution of landmasses and especially basaltic provinces over time, independent of inferences about sea-floor production rates, and incorporating climate models that take into account factors like relief, lithology and vegetation and include the necessary feedbacks and adequate spatiotemporal resolution for a more comprehensive understanding of the carbon cycle and climate change.

Appendix A

Acronyms and abbreviations.

APWP	apparent polar wander path
CAMP	Central Atlantic Magmatic Province
CTM	Cretaceous Thermal Maximum
EECO	Early Eocene climatic optimum
kyr	10^3 yr
Ma	10^6 yr ago
MAR	mass accumulation rate
Mkm^2	10^6 square-kilometers
MMCO	Middle Miocene climatic optimum
Mt	megaton, 10^9 kilograms
Myr	10^6 yr
$P-E$	precipitation minus evaporation
Tton	teraton, 10^{15} kg
SE Asia	Southeast Asia

Acknowledgements. We acknowledge constructive comments and informative discussions after presentations of evolving versions of this work that challenged us to look deeper and more broadly at the problem of carbon sinks sparked by a passing remark by Claude Allègre to the senior author about the high weathering potential of basaltic islands. In particular, we are grateful to Ben Cramer, Bob Kopp, Peter Molnar and Morgan Schaller for detailed written comments, Wally Broecker, Mimi Katz and Ken Miller for valuable critical exchanges on earlier versions of the manuscript, and the CP reviewers (David Kidder and two anonymous referees) for perceptive and highly constructive critiques that allowed us to improve the paper. Ben Cramer and Mimi Katz generously provided digital files of compiled carbon isotope data. Lamont–Doherty Earth Observatory contribution #7665.

Edited by: Y. Godderis

References

Achache, J., Courtillot, V., and Zhou, Y. X.: Paleogeographic and tectonic evolution of southern Tibet since middle Cretaceous time: New paleomagnetic data and synthesis, J. Geophys. Res.,89, 10311–10339, 1984.

Agard, P., Omrani, J., Jolivet, L., and Mouthereau, G.: Convergence history across Zagros (Iran): Constraints from collisional and earlier deformation, Int. J. Earth Sci., 94, 401–419, 2005.

Aitchison, J. C., Ali, J. R., and Davis, A. M.: When and where did India and Asia collide?, J. Geophys. Res., 112, B05423, doi:10.1029/2006JB004706, 2007.

Aitchison, J. C., Ali, J. R., and Davis, A. M.: Reply to comment by Eduardo Garzanti on "When and where did India and Asia collide?", J. Geophys. Res., 113, B04412, doi:10.1029/2007JB005431, 2008.

Ali, J. R. and Aitchison, J. C.: Gondwana to Asia: Plate tectonics, paleogeography and the biological connectivity of the Indian sub-continent from the Middle Jurassic through latest Eocene (166–35 Ma), Earth-Sci. Rev., 88, 145–166, 2008.

Allègre, C. J., Courtillot, V., Tapponnier, P., Hirn, A., Mattauer, M., Coulon, C., Jaeger, J. J., Achache, J., Scharer, U., Marcoux, J., Burg, J. P., Girardeau, J., Armijo, R., Gariepy, C., Gopel, C., Tindong, L., Xuchang, X., Chenfa, C., Guangqin, L., Baoyu, L., Jiwen, T., Naiwen, W., Guoming, C., Tonglin, H., Xibin, W., Wanming, D., Huaibin, S., Yougong, C., Ji, Z., Hongrong, Q., Peisheng, B., Songchan, W., Bixiang, W., Yaoxiu, Z., and Xu, R.: Structure and evolution of the Himalaya-Tibet orogenic belt, Nature, 307, 17–22, 1984.

Allen, M. B. and Armstrong, H. A.: Arabia-Eurasia collision and the forcing of mid-Cenozoic global cooling, Palaeogeogr. Palaeocl., 265, 52–58, 2008.

Beck, R. A., Burbank, D. W., Sercombe, W. J., Olson, T. L., and Khan, A. M.: Organic carbon exhumation and global warming during the early Himalayan collision, Geology, 23, 387–390, 1995.

Beerling, D. J. and Royer, D. L.: Convergent Cenozoic CO_2 history, Nat. Geosci., 4, 418–420, 2011.

Berger, W. H. and Winterer, E. L.: Plate stratigraphy and the fluctuating carbonate line, in: Pelagic Sediments: On Land and Under the Sea, Special Publications of the International Association of Sedimentologists, No. 1, edited by: Hsu, K. J. and Jenkins, H. C., Blackwell Scientific Publications, Oxford, 11–48, 1974.

Berner, R. A.: Global CO_2 degassing and the carbon cycle: Comment on "Cretaceous ocean crust at DSDP sites 417 and 418: Carbon uptake from weathering vs. loss by magmatic outgassing", Geochim. Cosmochim. Acta, 54, 2889–2890, 1990a.

Berner, R. A.: Response to criticism of the BLAG model, Geochim. Cosmochim. Acta, 54, 2892–2893, 1990b.

Berner, R. A.: A model for atmospheric CO_2 over Phanerozoic time, Am. J. Sci., 291, 339–376, 1991.

Berner, R. A.: GEOCARB II: A revised model of atmospheric CO_2 over Phanerozoic time, Am. J. Sci., 294, 56–91, 1994.

Berner, R. A.: The Phanerozoic Carbon Cycle, Oxford University Press, Oxford, p. 150, 2004.

Berner, R. A.: GEOCARBSULF: A combined model for Phanerozoic atmospheric O_2 and CO_2, Geochim. Cosmochim. Acta, 70, 5653–5664, 2006.

Berner, R. A. and Caldeira, K.: The need for mass balance and feedback in the geochemical carbon cycle, Geology, 25, 955–956, 1997.

Berner, R. A. and Kothalava, Z.: GEOCARB III: A revised model of atmospheric CO_2 over Phanerozoic time, Am. J. Sci., 301, 182–204, 2001.

Berner, R. A., Lasaga, A. C., and Garrels, R. M.: The carbonate-silicate geochemical cycle and its effect on atmospheric carbon dioxide over the past 100 million years, Am. J. Sci., 283, 641–683, 1983.

Besse, J. and Courtillot, V.: Apparent and true polar wander and the geometry of the geomagnetic field over the last 200 Myr, J. Geophys. Res., 107, 2300, doi:10.1029/2000JB000050, 2002.

Besse, J. and Courtillot, V.:, Correction to "Apparent and true polar wander and the geometry of the geomagnetic field over the last 200 Myr": J. Geophys. Res., 108, 2469, doi:10.1029/2003JB002684, 2003.

Brady, P. V. and Gislason, S. R.: Seafloor weathering controls on atmospheric CO_2 and global climate, Geochim. Cosmochim. Acta, 61, 965–973, 1997.

Briais, A., Patriat, P., and Tapponnier, P.: Updated interpretation of magnetic anomalies and seafloor spreading stages in the South China Sea: Implications for the Tertiary tectonics of southeast Asia, J. Geophys. Res., 98, 6299–6328, 1993.

Broecker, W. S. and Sanyal, A.: Does atmospheric CO_2 police the rate of chemical weathering?, Global Biogeochem. Cy., 12, 403–408, 1998.

Broecker, W. S. and Woodruff, F.: Discrepancies in the oceanic carbon isotope record for the last fifteen million years?, Geochim. Cosmochim. Acta, 56, 3259–3264, 1992.

Caldeira, K.: Enhanced Cenozoic chemical weathering and the subduction of pelagic carbonate, Nature, 357, 578–581, 1992.

Caldeira, K. and Rampino, M. R.: Carbon dioxide emissions from Deccan volcanism and a K/T boundary greenhouse effect, Geophys. Res. Lett., 17, 1299–1302, 1990.

Cande, S. C. and Kent, D. V.: Revised calibration of the geomagnetic polarity time scale for the Late Cretaceous and Cenozoic, J. Geophys. Res., 100, 6093–6095, 1995.

Cande, S. C. and Stegman, D. R.: Indian and African plate motions driven by the push force of the Reunion plume head, Nature, 475, 47–52, 2011.

Chang, C.-F. and Cheng, H.-L.: Some tectonic features of the Mt. Jolmo Lungma area, southern Tibet, China, Scientia Sin., 16, 257–265, 1973.

Chen, W., Yang, T., Zhang, S., Yang, Z., Li, H., Wu, H., Zhang, J., Ma, Y., and Cai, F.: Paleomagnetic results from the Early Cretaceous Zenong Group volcanic rocks, Cuoqin, Tibet, and their paleogeographic implications, Gondwana Res., 22, 461–469, 2012.

Chen, Y., Courtillot, V., Cogne, J.-P., Besse, J., Yang, Z., and Enkin, R. J.: The configuration of Asia prior to the collision of India: Cretaceous paleomagnetic constraints, J. Geophys. Res., 98, 21927–21941, 1993.

Cogné, J.-P. and Humler, E.: Temporal variation of oceanic spreading and crustal production rates during the last 180 My, Earth Planet. Sc. Lett., 227, 427–439, 2004.

Cogné, J. P.: PaleoMac: A Macintosh™ application for treating paleomagnetic data and making plate reconstructions: Geochemistry, Geophysics, Geosystems, 4, 1007, doi:10.1029/2001GC000227, 2003.

Cogné, J. P. and Humler, E.: Trends and rhythms in global seafloor generation rate, Geochem. Geophy. Geosy., 7, Q03011, doi:10.1029/2005GC001148, 2006.

Copley, A., Avouac, J.-P., and Royer, J.-Y.: India-Asia collision and the Cenozoic slowdown of the Indian plate: Implications for the forces driving plate motions, J. Geophys. Res., 15, B03410, doi:10.1029/2009JB006634, 2010.

Courtillot, V. E. and Renne, P. R.: On the ages of flood basalt events, Comptes Rendus Geoscience, 335, 113–140, 2003.

Cramer, B. S., Toggweiler, J. R., Wright, J. D., Katz, M. E., and Miller, K. G.: Ocean overturning since the Late Cretaceous: Inferences from a new benthic foraminiferal isotope compilation, Paleoceanography, 24, PA4216, doi:10.1029/2008PA001683,

2009.
Cramer, B. S., Miller, K. G., Toggweiler, J. R., Barrett, P. J., and Wright, J. D.: Late Cretaceous-Neogene trends in deep ocean temperature and continental ice volume: reconciling records of benthic foraminiferal geochemistry (δ^{18}O and Mg/Ca) with sea level history, J. Geophys. Res.-Oceans, 116, C12023, 2011.
D'Hondt, S., Donaghay, P., Zachos, J. C., Luttenberg, D., and Lindinger, M.: Organic carbon fluxes and ecological recovery from the Cretaceous-Tertiary mass extinction, Science, 282, 276–279, 1998.
DeConto, R. M. and Pollard, D.: Rapid Cenozoic glaciation of Antarctica induced by declining atmospheric CO_2, Nature, 421, 245–249, 2003.
DeConto, R. M., Pollard, D., Wilson, P. A., Palike, H., Lear, C. H., and Pagani, M.: Thresholds for Cenozoic bipolar glaciation, Nature, 455, 652–656, 2008.
Dessert, C., Dupré, B., Francois, L. M., Schott, J. J., Gaillardet, J., Chakrapani, G., and Bajpai, S.: Erosion of Deccan Traps determined by river geochemistry: impact on the global climate and the ^{87}Sr/^{86}Sr ratio of seawater, Earth Planet. Sc. Lett., 188, 459–474, 2001.
Dessert, C., Dupré, B., Gaillardet, J., Francois, L., and Allègre, C.: Basalt weathering laws and the impact of basalt weathering on the global carbon cycle, Chem. Geol., 202, 257–273, 2003.
Donnadieu, Y., Goddéris, Y., Pierrehumbert, R., Dromart, G., Fluteau, F., and Jacob, R.: A GEOCLIM simulation of climatic and biogeochemical consequences of Pangea breakup, Geochem. Geophy. Geosy., 7, Q11019, doi:10.1029/2006GC001278, 2006.
Dupont-Nivet, G., Lippert, P. C., Van Hinsbergen, D. J. J., Meijers, M. J. M., and Kapp, P.: Palaeolatitude and age of the Indo–Asia collision: palaeomagnetic constraints, Geophys. J. Int., 182, 1189–1198, 2010.
Dupré, B., Dessert, C., Oliva, P., Goddeìris, Y., Viers, J., François, L., Millot, R., and Gaillardet, J.: Rivers, chemical weathering and Earth's climate, Comptes Rendus Geoscience, 335, 1141–1160, 2003.
Edmond, J. M.: Himalayan tectonics, weathering processes, and the strontium isotope record in marine limestones, Science, 258, 1594–1597, 1992.
Edmond, J. M. and Huh, Y.: Non-steady state carbonate recycling and implications for the evolution of atmospheric pCO$_2$, Earth Planet. Sc. Lett., 216, 125–139, 2003.
Emeleus, C. H., Allwright, E. A., Kerr, A. C., and Williamson, I. T.: Red tuffs in the Palaeocene lava successions of the Inner Hebrides, Scottish J. Geol., 32, 83–89, 1996.
Engebretson, D. C., Kelley, K. P., Cashman, H. J., and Richards, M. A.: 180 million years of subduction, GSA Today, 2, 93–95, 1992.
Erba, E.: Calcareous nannofossils and Mesozoic Oceanic Anoxic Events, Mar. Micropaleontol., 52, 85–106, 2004.
Fedorov, A. V., Dekens, P. S., McCarthy, M., Ravelo, A. C., deMenocal, P. B., Barreiro, M., Pacanowski, R. C., and Philander, S. G.: The Pliocene paradox (Mechanisms for a permanent El Nino), Science, 312, 1485–1499, 2006.
Flower, B. P. and Kennett, J. P.: The middle Miocene climatic transition: East Antarctic ice sheet development, deep ocean circulation and global carbon cycling, Palaeogeogr. Palaeocl., 108, 537–555, 1994.
France-Lanord, C. and Derry, L. A.: Organic carbon burial forcing of the carbon cycle from Himalayan erosion, Nature, 390, 65–67, 1997.
Fuller, M., Ali, J. R., Moss, S. J., Frost, G. M., Richter, B., and Mahfi, A.: Paleomagnetism of Borneo, J. Asian Earth Sci., 17, 3–24, 1999.
Gaillardet, J., Dupré, B., Louvat, P., and Allègre, C. J.: Global silicate weathering and CO_2 consumption rates deduced from the chemistry of large rivers, Chem. Geol., 159, 3–30, 1999.
Ganerød, M., Smethurst, M. A., Torsvik, T. H., Prestvik, T., Rousse, S., McKenna, C., v. Hinsbergen, J. J., and Hendriks, B. W. H.: The North Atlantic Igneous Province reconstructed and its relation to the Plume Generation Zone: the Antrim Lava Group revisited, Geophys. J. Int., 182, 183–202, 2010.
Garzanti, E.: Comment on "When and where did India and Asia collide?" by Jonathan C. Aitchison, Jason R. Ali, and Aileen M. Davis, J. Geophys. Res., 113, B004411, doi:10.1029/2007JB005276, 2008.
Garzanti, E., Baud, A., and Mascle, G.: Sedimentary record of the northward flight of India and its collision with Eurasia (Ladakh Himalaya, India), Geodinam. Acta, 1, 297–312, 1987.
Gerlach, T.: Volcanic versus anthropogenic carbon dioxide, EOS Trans. Am. Geophys. Union, 92, 201–202, 2011.
Goddéris, Y. and Joachimski, M. M.: Global change in the late Devonian: modeling the Frasnian-Famennian short-term carbon isotope isotope excursions, Paleogeogr. Paleocl., 202, 309–329, 2004.
Godderis, Y., Donnadieu, Y., Nedelec, A., Dupré, B., Dessert, C., Grard, A., Ramstein, G., and Francois, L. M.: The Sturtian "snowball" glaciation: fire and ice, Earth Planet. Sc. Lett., 211, 1–12, 2003.
Godderis, Y., Donnadieu, Y., de Vargas, C., Pierrehumbert, R. T., Dromart, G., and van de Schootbrugge, B.: Causal or casual link between the rise of nannoplankton calcification and a tectonically-driven massive decrease in Late Triassic atmospheric CO_2?, Earth Planet. Sc. Lett., 267, 247–255, 2008.
Hall, R., vanHattum, M. W. A., and Spakman, W.: Impact of India–Asia collision on SE Asia: The record in Borneo, Tectonophysics, 451, 366–389, 2008.
Hansen, J., Sato, M., Kharecha, P., Beerling, D., Berner, R., Masson-Delmotte, V., Pagani, M., Raymo, M., Royer, D. L., and Zachos, J. C.: Target atmospheric CO_2: Where should humanity aim?, Open Atmos. Sci. J., 2, 217–231, 2008.
Harris, N.: Significance of weathering Himalayan metasedimentary rocks and leucogranites for the Sr isotope evolution of seawater during the early Miocene, Geology, 23, 795–798, 1995.
Hatzfeld, D. and Molnar, P.: Comparisons of the kinematics and deep structures of the Zagros and Himalaya and of the Iranian and Tibetan plateaus and geodynamic implications, Rev. Geophys., 48, RG2005, doi:10.1029/2009RG000304, 2010.
Held, I. M. and Soden, B. J.: Robust responses of the hydrological cycle to global warming, J. Climate, 19, 5686–5699, 2006.
Hess, J., Bender, M. L., and Schilling, J.-G.: Evolution of the ratio of strontium-87 to strontium-86 in seawater from Cretaceous to Present, Science, 231, 979–984, 1986.
Hill, I. G., Worden, R. H., and Meighan, I. G.: Geochemical evolution of a palaeolaterite: the Interbasaltic Formation, Northern Ireland, Chem. Geol., 166, 65–84, 2000.

Hilting, A. K., Kump, L. R., and Bralower, T. J.: Variations in the oceanic vertical carbon isotope gradient and their implications for the Paleocene–Eocene biological pump, Paleoceaeanography, 23, PA3222, doi:10.1029/2007PA001458, 2008.

Hoffman, P. F. and Schrag, D. P.: The snowball Earth hypothesis: testing the limits of global change, Terra Nova, 14, 129–155, 2002.

Jenkyns, H. C.: Evidence for rapid climate change in the Mesozoic–Palaeogene greenhouse world, Philos. T. Roy. Soc. Lond. A, 361, 1885–1916, 2003.

Johnston, F. K. B., Turchyn, A. V., and Edmonds, M.: Decarbonation efficiency in subduction zones: Implications for warm Cretaceous climates, Earth Planet. Sc. Lett., 303, 143–152, 2011.

Katz, M. E., Wright, J. D., Miller, K. G., Cramer, B. S., Fennel, K., and Falkowski, P. G.: Biological overprint of the geological carbon cycle, Mar. Geol., 217, 323–338, 2005.

Kennett, J. P.: Cenozoic evolution of Antarctic glaciation, the circum-antarctic ocean and their impact on global paleoceanography, J. Geophys. Res., 82, 3843–3860, 1977.

Kent, D. V. and Irving, E.: Influence of inclination error in sedimentary rocks on the Triassic and Jurassic apparent polar wander path for North America and implications for Cordilleran tectonics, J. Geophys. Res., 115, B10103, doi:10.1029/2009JB007205, 2010.

Kent, D. V. and Muttoni, G.: Equatorial convergence of India and early Cenozoic climate trends, P. Natl. Acad. Sci., 105, 16065–16070, 2008.

Kump, L. R.: Interpreting carbon-isotope excursions: Strangelove oceans, Geology, 19, 299–302, 1991.

Kump, L. R. and Arthur, M. A.: Global chemical erosion during the Cenozoic: Weatherability balances the budgets, in: Tectonic Uplift and Climate Change, edited by: Ruddiman, W. F., Plenum Press, New York, 399–426, 1997.

Kump, L. R. and Arthur, M. A.: Interpreting carbon-isotope excursions: carbonates and organic matter, Chem. Geol., 161, 181–198, 1999.

Kump, L. R., Brantley, S. L., and Arthur, M. A.: Chemical weathering, atmospheric CO_2, and climate, Annu. Rev. Earth Planet. Sc., 28, 611–667, 2000.

Lippert, P. C., Zhao, X., Coe, R. S., and Lo, C.-H.: Palaeomagnetism and $^{40}Ar/^{39}Ar$ geochronology of upper Palaeogene volcanic rocks from Central Tibet: implications for the Central Asia inclination anomaly, the palaeolatitude of Tibet and post-50 Ma shortening within Asia, Geophys. J. Int., 184, 131–161, 2011.

Livermore, R., Hillenbrand, C. D., Meredith, M., and Eagles, G.: Drake Passage and Cenozoic climate: An open and shut case?, Geochem. Geophy. Geosy., 8, Q01005, doi:10.1029/2005GC001224, 2007.

Lunt, D. J., Foster, G. L., Haywood, A. M., and Stone, E. J.: Late Pliocene Greenland glaciation controlled by a decline in atmospheric CO_2 levels, Nature, 454, 1102–1105, 2008.

Manabe, S. and Bryan, K.: CO_2-induced change in a coupled ocean-atmosphere model and its paleoclimatic implications, J. Geophys. Res., 90, 11689–11707, 1985.

Marty, B. and Tolstikhin, I. N.: CO_2 fluxes from mid-ocean ridges, arcs and plumes, Chem. Geol., 145, 233–248, 1998.

Marzoli, A., Renne, P. R., Piccirillo, E. M., Ernesto, M., Gellieni, G., and De Min, A.: Extensive 200-million-year-old continental flood basalts of the Central Atlantic Magmatic Province, Science, 284, 616–618, 1999.

McHone, J. G.: Volatile emissions from Central Atlantic Magmatic Province basalts: Mass assumptions and environmental consequences, in: The Central Atlantic Magnatic Province: Insights from Fragments of Pangea, Geophysical Monograph 136, edited by: Hames, W. E., McHone, J. G., Renne, P. R., and Ruppel, C., American Geophysical Union, Washington, DC, 241–254, 2003.

Miller, K. G., Fairbanks, R. G., and Mountain, G. S.: Tertiary oxygen isotope synthesis, sea level history, and continental margin erosion, Paleoceanography, 2, 1–19, 1987.

Miller, K. G., Kominz, M. A., Browning, J. V., Wright, J. D., Mountain, G. S., Katz, M. E., Sugarman, P. J., Cramer, B. S., Christie-Blick, N., and Pekar, S. F.: The Phanerozoic record of global sea-level change, Science, 310, 1293–1298, 2005a.

Miller, K. G., Wright, J. D., and Browning, J. V.: Visions of ice sheets in a greenhouse world, Mar. Geol., 217, 215–231, 2005b.

Milliman, J. D.: Fluvial sediment in coastal seas: flux and fate, Nat. Resour., 26, 12–22, 1990.

Misumi, K., Yamanaka, Y., and Tajika, E.: Numerical simulation of atmospheric and oceanic biogeochemical cycles to an episodic CO_2 release event: Implications for the cause of mid-Cretaceous Ocean Anoxic Event-1a, Earth Planet. Sc. Lett., 286, 316–323, 2009.

Mitchell, N. C. and Lyle, M. W.: Patchy deposits of Cenozoic pelagic sediments in the central Pacific, Geology, 33, 49–52, 2005.

Mitchell, N. C., Lyle, M. W., Knappenberger, M. B., and Liberty, L. M.: Lower Miocene to Present stratigraphy of the equatorial Pacific sediment bulge and carbonate dissolution anomalies, Paleoceanography, 18, 1038, doi:10.1029/2002PA000828, 2003.

Moghadam, H. S., Whitechurch, H., Rahgoshay, M., and Monsef, I.: Significance of Nain-Baft ophiolitic belt (Iran): Short-lived, transtensional Cretaceous back-arc oceanic basins over the Tethyan subduction zone, C. R. Geoscience, 341, 1016–1028, 2009.

Molnar, P. and Stock, J. M.: Slowing of India's convergence with Eurasia since 20 Ma and its implications for Tibetan mantle dynamics, Tectonics, 28, TC3001, doi:10.1029/2008TC002271, 2009.

Molnar, P. and Tapponnier, P.: Cenozoic tectonics of Asia: effects of a continental collision, Science, 189, 419–426, 1975.

Muller, R. D. and Roest, W. R.: Fracture zones in the North Atlantic from combined Geosat and Seasat data, J. Geophys. Res., 97, 3337–3350, 1992.

Muller, R. D., Royer, J. Y., and Lawver, L. A.: Revised plate motions relative to the hotspots from combined Atlantic and Indian Ocean hotspot tracks, Geology, 21, 275–278, 1993.

Muller, R. D., Sdrolias, M., Gaina, C., Steinberger, B., and Heine, C.: Long-term sea-level fluctuations driven by ocean basin dynamics, Science, 319, 1357–1362, 2008.

Muttoni, G. and Kent, D. V.: Widespread formation of cherts during the early Eocene climate optimum, Palaeogeogr. Palaeocl., 253, 348–362, 2007.

Muttoni, G., Mattei, M., Balini, M., Zanchi, A., Gaetani, M., and Berra, F.: The drift history of Iran from the Ordovician to the Triassic, Special Publications, Geol. Soc. London, 312, 7–29, 2009.

Ogg, J. G., Karl, S. M., and Behl, R. J.: Jurassic through Early Cretaceous sedimentation history of the Central Equatorial Pacific and of Sites 800 and 801, Proc. Ocean Drill. Prog., 129, 571–613, 1992.

Okay, A. I., Zattin, M., and Cavazza, W.: Apatite fission-track data for the Miocene Arabia–Eurasia collision, Geology, 38, 35–38, 2010.

Pagani, M., Zachos, J. C., Freeman, K. H., Tipple, B., and Bohaty, S.: Marked decline in atmospheric carbon dioxide concentrations during the Paleogene, Science, 309, 600–603, 2005.

Pagani, M., Huber, M., Liu, Z., Bohaty, S. M., Henderiks, J., Sijp, W., Krishnan, S., and DeConto, R. M.: The role of carbon dioxide during the onset of Antarctic glaciation, Science, 334, 1261–1264, 2011.

Patriat, P. and Achache, J.: India-Eurasia collision chronology has implications for crustal shortening and driving mechanism of plates, Nature, 311, 615–621, 1984.

Pearson, P. N., Ditchfield, P. W., Singano, J., Harcourt-Brown, K. G., Nicholas, C. J., Olsson, R. K., Shackleton, N. J., and Hall, M. A.: Warm tropical sea surface temperatures in the Late Cretaceous and Eocene epochs, Nature, 413, 481–488, 2001.

Pearson, P. N., vanDongen, B. E., Nicholas, C. J., Pancost, R. D., Schouten, S., Singano, J. M., and Wade, B. S.: Stable warm tropical climate through the Eocene Epoch, Geology, 35, 211–214, 2007.

Quade, J., Roe, L., DeCelles, P. G., and Ojha, T. P.: The Late Neogene $^{87}Sr/^{86}Sr$ record of lowland Himalayan rivers, Science, 276, 1828–1831, 1997.

Rabinowitz, P. D., Coffin, M. F., and Falvey, D.: The separation of Madagascar and Africa, Science, 220, 67–69, 1983.

Ravelo, A. C.: Walker circulation and global warming: Lessons from the geologic past, Oceanography, 19, 114–122, 2006.

Raymo, M. E.: The Himalayas, organic carbon burial, and climate in the Miocene, Paleoceanography, 9, 399–404, 1994.

Raymo, M. E. and Ruddiman, W. F.: Tectonic forcing of late Cenozoic climate, Nature, 359, 117–122, 1992.

Raymo, M. E., Ruddiman, W. F., and Froelich, P. N.: Influence of late Cenozoic mountain building on ocean geochemical cycles, Geology, 16, 649–653, 1988.

Rea, D. K., Zachos, J. C., Owen, R. M., and Gingerich, P. D.: Global change at the Paleocene-Eocene boundary: climatic and evolutionary consequences of tectonic events, Palaeogeogr. Palaeocl., 79, 117–128, 1990.

Replumaz, A. and Tapponnier, P.: Reconstruction of the deformed collision zone between India and Asia by backward motion of lithospheric blocks, J. Geophys. Res., 108, 2285, doi:10.1029/2001JB000661, 2003.

Retallack, G. J.: Lateritization and bauxitization events, Econom. Geol., 105, 655–667, 2010.

Richter, B., Schmidtke, E., Fuller, M., Harbury, N., and Samsudin, P. D.: Paleomagnetism of Peninsular Malaysia, J. Asian Earth Sci., 17, 477–519, 1999.

Richter, F. M., Rowley, D. B., and DePaolo, D. J.: Sr isotope evolution of seawater: the role of tectonics, Earth Planet. Sc. Lett., 109, 11–23, 1992.

Rochette, P., Tamrat, E., Feraud, G., Pik, R., Courtillot, V., Ketefo, E., Coulon, C., Hoffmann, C., Vandamme, D., and Yirgu, G.: Magnetostratigraphy and timing of the Oligocene Ethiopian traps, Earth Planet. Res. Lett., 164, 497–510, 1998.

Rowley, D. B.: Rate of plate creation and destruction: 180 Ma to present, Geol. Soc. Am. Bull., 114, 927–933, 2002.

Rowley, D. B.: Extrapolating Oceanic Age Distributions: Lessons from the Pacific Region, J. Geol., 116, 587–598, 2008.

Royden, L. H., Burchfiel, B. C., and van der Hilst, R. D.: The geological evolution of the Tibetan Plateau, Science, 321, 1054–1058, 2008.

Royer, D. L.:, Fossil soils constrain ancient climate sensitivity, P. Natl. Acad. Sci., 107, 517–518, 2010.

Saunders, A. D., Fitton, J. G., Kerr, A. C., Norry, M. J., and Kent, R. W.: The North Atlantic Igneous Province, in: Large Igneous Provinces: Continental, Oceanic, and Planetary Flood Volcanism, Geophysical Monograph 100, edited by: Mahoney, J. J. and Coffin, M. F., American Geophysical Union, Washington, D.C., 45–93, 1997.

Schaller, M. F., Wright, J. D., and Kent, D. V.: Atmospheric $p\mathrm{CO_2}$ perturbations associated with the Central Atlantic Magmatic Province, Science, 331, 1404–1409, 2011.

Schaller, M. F., Wright, J. D., Kent, D. V., and Olsen, P. E.: Rapid emplacement of the Central Atlantic Magmatic Province as a net sink for CO_2, Earth Planet. Sc. Lett., 323–324, 27–39, 2012.

Schmidtke, E., Fuller, M., and Haston, R.: Paleomagnetic data from Sarawak, Malaysian Borneo and the Late Mesozoic and Cenozoic tectonics of Sundaland, Tectonics, 9, 123–140, 1990.

Schoene, B., Guex, J., Bartolini, A., Schaltegger, U., and Blackburn, T. J.: Correlating the end-Triassic mass extinction and flood basalt volcanism at the 100,000-year level, Geology, 38, 387–390, 2010.

Schrag, D. P.: Control of atmospheric CO_2 and climate through Earth history, Geochim. Cosmochim. Acta, 66, p. A688, 2002.

Schrag, D. P., Berner, R. A., Hoffman, P. F., and Halverson, G. P.: On the initiation of a snowball Earth, Geochem. Geophy. Geosy., 3, doi:10.1029/2001GC000219, 2002.

Self, S., Thordarson, T., and Widdowson, M.: Gas fluxes from flood basalt eruptions, Elements, 1, 283–287, 2005.

Selverstone, J. and Gutzler, D. S.: Post-125 Ma carbon storage associated with continent-continent collision, Geology, 21, 885–888, 1993.

Seton, M., Gaina, C., Muller, R. D., and Heine, C.: Mid-Cretaceous seafloor spreading pulse: Fact or fiction?, Geology, 37, 687–690, 2009.

Shackleton, N. J.: The carbon isotope record of the Cenozoic: history of organic carbon burial and of oxygen in the ocean and atmosphere, Special Publications, Geol. Soc. London, 26, 423–434, 1987.

Smith, A. G. and Hallam, A.: The fit of the southern continents, Nature, 225, 139–144, 1970.

Smith, M. E., Carroll, A. R., and Mueller, E. R.: Elevated weathering rates in the Rocky Mountains during the Early Eocene Climatic Optimum, Nat. Geosci., 1, 370–374, 2008.

Srivastava, S. P. and Tapscott, C. R.: Plate kinematics of the North Atlantic, in: The Geology of North America, The Western North Atlantic Region, edited by: Tucholke, B. E. and Vogt, P. R., Geological Society of America, Boulder, 379–404, 1986.

Staudigel, H., Hart, S. R., Schmincke, H.-U., and Smith, B. M.: Cretaceous ocean crust at DSDP Sites 417 and 418: Carbon uptake from weathering versus loss by magmatic outgassing, Geochim. Cosmochim. Acta, 53, 3091–3094, 1989.

Staudigel, H., Hart, S. R., Schmincke, H.-U., and Smith, B. M.: Reply to “Global CO_2 degassing and the carbon cycle”: A Comment by R. A. Berner, Geochim. Cosmochim. Acta, 54, 2891, 1990a.

Staudigel, H., Hart, S. R., Schmincke, H.-U., and Smith, B. M.: Reply to R. A. Berner's response, Geochim. Cosmochim. Acta, 54, 2893, 1990b.

Stickley, C. E., Brinkhuis, H., Shellenberg, S. A., Sluijs, A., Rohl, U., Fuller, M., Grauert, M., Huber, M., Warnaar, J., and Williams, G. L.: Timing and nature of the deepening of the Tasmanian Gateway, Paleoceanography, 19, PA4027, doi:4010.1029/2004PA001022, 2004.

Tejada, M. L. G., Suzuki, K., Kuroda, J., Coccioni, R., Mahoney, J. J., Ohkouchi, N., Sakamoto, T., and Tatsumi, Y.: Ontong Java Plateau eruption as a trigger for the early Aptian oceanic anoxic event, Geology, 37, 855–858, 2009.

Tera, F., Brown, L., Morris, J., Sacks, I. S., Klein, J., and Middleton, R.: Sediment incorporation in island-arc magmas: Inferences from ^{10}Be, Geochim. Cosmochim. Acta, 50, 535–550, 1986.

Thomas, D. J. and Bralower, T. J.: Sedimentary trace element constraints on the role of North Atlantic Igneous Province volcanism in late Paleocene-early Eocene environmental change, Mar. Geol., 217, 233–254, 2005.

Volk, T.: Sensitivity of climate and atmospheric CO_2 to deep-ocean and shallow-ocean carbonate burial, Nature, 337, 637–640, 1989.

Volk, T. and Hoffert, M. I.: Ocean carbon pumps: Analysis of relative strengths and efficiencies in ocean-driven atmospheric $C0_2$ changes, Am. Geophys. Union Monogr., 32, 99–110, 1985.

Walker, J. C. G., Hays, P. B., and Kasting, J. F.: A negative feedback mechanism for the long-term stabilization of Earth's surface-temperature, J. Geophys. Res.-Atmos., 86, 9776–9782, 1981.

West, A. J., Bickle, M. J., Collins, R., and Brasington, J.: Small-catchment perspective on Himalayan weathering fluxes, Geology, 30, 355–358, 2002.

West, A. J., Galy, A., and Bickle, M.: Tectonic and climatic controls on silicate weathering, Earth Planet. Sc. Lett., 235, 211–228, 2005.

Wilkinson, B. H. and Walker, J. C. G.: Phanerozoic cycling of sedimentary carbonate, Am. J. Sci., 289, 525–548, 1989.

Wilson, P. A., Norris, R. D., and Cooper, M. J.: Testing the Cretaceous greenhouse hypothesis using glassy foraminiferal calcite from the core of the Turonian tropics on Demerara Rise, Geology, 30, 607–610, 2002.

Wright, J. D., Miller, K. G., and Fairbanks, R. G.: Early and Middle Miocene stable isotopes: Implications for deepwater circulation and climate, Paleoceanography, 7, 357–389, 1992.

Yang, Z. and Besse, J.: Paleomagnetic study of Permian and Mesozoic sedimentary rocks from Northern Thailand supports the extrusion model for Indochina, Earth Planet. Sc. Lett., 117, 525–552, 1993.

Yang, Z., Yin, J., Sun, Z., Otofuji, Y.-I., and Sato, K.: Discrepant Cretaceous paleomagnetic poles between Eastern China and Indochina: a consequence of the extrusion of Indochina, Tectonophysics, 334, 101–113, 2001.

Yin, A. and Harrison, T. M.: Geologic evolution of the Himalayan–Tibetan Orogen, Annu. Rev. Earth Planet. Sci., 28, 211–280, 2000.

You, Y., Huber, M., Muller, R. D., Poulsen, C. J., and Ribbe, J.: Simulation of the Middle Miocene Climate Optimum, Geophys. Res. Lett., 36, L04702, doi:10.1029/2008GL036571, 2009.

Zachos, J., Pagani, M. N., Sloan, L., Thomas, E., and Billups, K.: Trends, rhythms, and aberrations in global climate 65 Ma to Present, Science, 292, 686–693, 2001.

Zanchi, A., Zanchetta, S., Garzanti, E., Balini, M., Berra, F., Mattei, M., and Muttoni, G.: The Cimmerian evolution of the Nakhlak–Anarak area, Central Iran, and its bearing for the reconstruction of the history of the Eurasian margin, Special Publications, Geol. Soc. London, 312, 261–286, 2009.

Zhu, B., Kidd, W. S. F., Rowley, D. B., Currie, B. S., and Shafique, N.: Age of initiation of the India–Asia collision in the east-central Himalaya, J. Geol., 113, 265–285, 2005.

Clim. Past, 18, 2117–2142, 2022
https://doi.org/10.5194/cp-18-2117-2022

Climate of the Past
Open Access
EGU

Shallow marine carbonates as recorders of orbitally induced past climate changes – example from the Oxfordian of the Swiss Jura Mountains

André Strasser[1]

[1]Department of Geosciences, University of Fribourg, Fribourg, 1700, Switzerland
Invited contribution by André Strasser, recipient of the EGU Jean Baptiste Lamarck Medal 2021.

Correspondence: André Strasser (andreas.strasser@unifr.ch)

Received: 18 March 2022 – Discussion started: 25 March 2022
Revised: 4 August 2022 – Accepted: 9 August 2022 – Published: 14 September 2022

Abstract. Today and in the geologic past, climate changes greatly affect and have affected Earth surface processes. While the climatic parameters today can be measured with high precision, they have to be interpreted from the sedimentary record for ancient times. This review is based on the detailed analysis of stratigraphic sections of Oxfordian (Late Jurassic) age, with the aim to reconstruct and discuss the climate changes that controlled the sedimentation on the shallow marine carbonate platform that today is represented in the Swiss Jura Mountains. The sediments formed under subtropical conditions in which carbonate-producing organisms proliferated, and ooids and oncoids were common. The sections are composed of hierarchically stacked elementary, small-scale, and medium-scale depositional sequences wherein facies changes imply deepening–shallowing trends. The major sequence boundaries Ox 6, Ox 7, and Ox 8 can be correlated with those of other European basins and place the studied sections in a broader framework. The chronostratigraphic tie points imply that the medium- and small-scale sequences formed in tune with the orbital eccentricity cycles of 405 and 100 kyr, respectively, and the elementary sequences with the precession cycle of 20 kyr. Orbitally controlled insolation changes at the top of the atmosphere translated into climate changes: low insolation generally resulted in low amplitudes of sea level fluctuations at the 20 kyr frequency and in a cool and humid climate at the palaeolatitude of the Jura platform. Terrigenous material was eroded from the hinterland and distributed over the platform. High insolation led to sea level rise, as well as to warm and semiarid to arid conditions in which coral reefs could grow. However, nutrient input favoured growth of microbialites that encrusted the corals. The reconstruction of high-frequency sea level fluctuations based on facies analysis compares well with the curve of insolation changes calculated for the past 550 kyr. It is therefore assumed that the sea level fluctuations were mainly due to thermal expansion and retraction of ocean surface water. Two models are presented that explain the formation of elementary sequences: one for low and one for high insolation. Despite the important lateral facies variations typical of a shallow marine platform, and despite the uncertainties in the reconstruction of sea level changes, this study demonstrates the potential of carbonate ecosystems to record past climate changes at a time resolution of 20 000 years. Relatively short time windows can thus be opened in the deep geologic past, and processes and products there can be compared with those of the Holocene and the Anthropocene. For example, it appears that today's anthropogenically induced sea level rise is more than 10 times faster than the fastest rise reconstructed for the Oxfordian.

1 Introduction

In today's world of global climate change and its impact on *Homo sapiens*, research into past climate variability as recorded in sediments is becoming particularly interesting. Rapid and profound climate-induced changes in palaeoecosystems can thus be documented and may serve as examples of changes we may experience in the near future.

Orbital cycles (Milankovitch cycles) are an important factor steering global climate as they control the amount of so-

Published by Copernicus Publications on behalf of the European Geosciences Union.

lar energy received by the Earth. The quasi-periodicities of these cycles (precession, obliquity, short and long eccentricity) have been calculated from today back to the Precambrian (e.g. Berger et al., 1992; Laskar et al., 2011; Hinnov, 2018). They are used to calibrate geological timescales (e.g. Gradstein et al., 2020) and to reconstruct past climate changes with a high time resolution. At the Equator, the daily insolation fluctuates around 400 $W m^{-2}$, with the precession cycle modulated by the eccentricity cycles. At higher latitudes the insolation values are higher, with higher amplitudes, and the obliquity signal is better expressed (Fig. 1). Today, the frequency peaks of precession are at 21 and 23 kyr, the obliquity at 41 kyr, the short eccentricity at 100 kyr, and the long eccentricity at 405 kyr. While the eccentricity cycles stay constant through time, precession and obliquity were shorter in the geological past (Berger et al., 1992; Hinnov, 2018). In the Oxfordian (Late Jurassic) considered here, the precession cycle had a value of about 20 kyr.

In deep-water sedimentary records, the effects of the orbital cycles on sedimentation have been well documented for many geological periods. For example, Amies et al. (2019) explained how sapropel formation in the Mediterranean basin reflects a northward migration of the monsoon rain belt over North Africa during the last interglacial, and this migration was controlled by the precession cycle (Lourens et al., 1996). Another example comes from the Valanginian and Hauterivian in the Vocontian basin analysed by Martinez (2018), where precession, obliquity, and the two eccentricity cycles are held responsible for the formation of repetitive, hemipelagic limestone–marl alternations and which help refining the duration of these two stages. In the Kimmeridge Clay Formation of the UK, Armstrong et al. (2016) documented the short and long eccentricity cycles that periodically induced extremely humid conditions leading to high burial of organic matter. In the Paleogene–Neogene Ebro Basin, Valero et al. (2014) described a 20 Myr lacustrine sedimentary record that formed in tune with the orbital eccentricity cycles.

In deep marine or deep lacustrine basins, there is a good chance that sedimentation was relatively continuous and interrupted only by tectonic pulses or gravitational flows. Sea level falls have an indirect influence by forcing progradation and thus an increase in turbidity currents and debris flows. On shallow platforms and ramps, however, minor sea level drops can lead to subaerial exposure and thus to hiatuses in the sedimentary record (e.g. Sadler, 1994; Strasser, 2015). Also, the depositional environment is much less homogenous than in deep-water settings: facies changes may occur over short (100 m scale) distances, creating facies mosaics (e.g. Rankey and Reeder, 2010). Nevertheless, shallow marine carbonates also have potential to record climate changes at a (geologically speaking) high time resolution.

Carbonate-producing marine organisms such as corals, calcareous algae, bivalves, gastropods, echinoderms, foraminifera, or serpulids are sensitive to water depth, water temperature, water energy, water chemistry, turbidity, nutrients, and substrate, which are all factors that are directly or indirectly controlled by climate. Carbonate particles such as ooids or oncoids commonly form under the influence of microbes, and calcifying microbes can build up stromatolites or thrombolites. The microbial communities again are dependent on multiple ecological factors and thus on climate.

Orbital cycles induce insolation changes at the top of the atmosphere, dependent on the latitude (Fig. 1). The translation of insolation changes into climate changes that ultimately influence the shallow marine carbonate platform or ramp is complex and passes through atmospheric and oceanic circulation (Fig. 2), which are themselves dependent on latitude, orography, and land–ocean distribution, as well as on the shape and position of the oceanic basins (e.g. Feng and Poulsen, 2014). Multiple feedback processes occur with different frequencies and amplitudes. For example, vegetation or ice cover will modify the albedo, or sea level change, ocean dynamics, and nutrient cycling may impact atmospheric CO_2 levels and water chemistry (e.g. Wallmann et al., 2016). This will finally result in the regional climate that influences the carbonate platform under investigation (air and water temperature, rainfall, wind, and seasonality). However, it also has to be considered that if the seasonal insolation change is below a certain threshold it may not induce a significant climate change and will not be recorded in the sedimentary system (Hinnov, 2018). In this paper, only subtropical carbonate systems are considered, and the following case study deals with such sediments. In fact, carbonates are produced in different "factories", from tropical to cool water and from shallow to deep (Flügel, 2004; Reijmer, 2021).

Sea level is an important factor that controls water depth. Water depth influences the growth of calcareous algae that use photosynthesis and of carbonate-producing organisms that contain light-dependent symbionts such as corals. Wave action in shallow water reworks the sediment and winnows out the mud fraction, while in deeper water carbonate mud can accumulate. The formation of ooid shoals is most efficient in a regime of tidal currents, which are strongest in shallow channels (e.g. Flügel, 2004; Reijmer, 2021). Sea level also controls accommodation, i.e. the potential to accumulate the sediment. Eustatic sea level changes were highly asymmetrical in icehouse worlds through slow buildup of polar ice caps and mountain glaciers, followed by rapid melting. The amplitudes were of the order of tens of metres (120 m during the last glacial–interglacial cycle; Shackleton, 1987). In greenhouse worlds such as the Late Jurassic (e.g. Sellwood and Valdes, 2008), the sea level changes were metre-scale only, caused by changes in ice volume of small polar ice caps and glaciers, thermally controlled volume changes in the ocean surface waters, density-controlled volume changes in deep ocean waters, and/or changes in the volume of fresh water sequestered on the continents (Schulz and Schäfer-

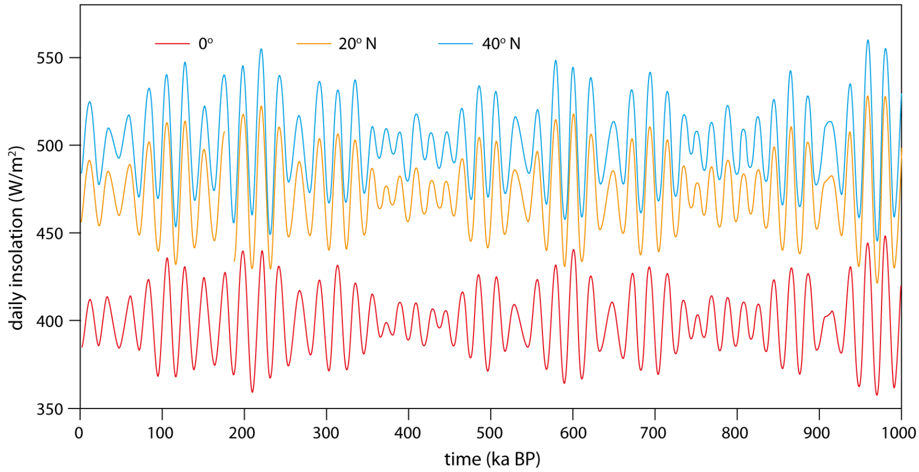

Figure 1. Mean daily insolation values for 21 June (northern summer solstice) at different latitudes, calculated for the last million years (modified from Hinnov, 2018).

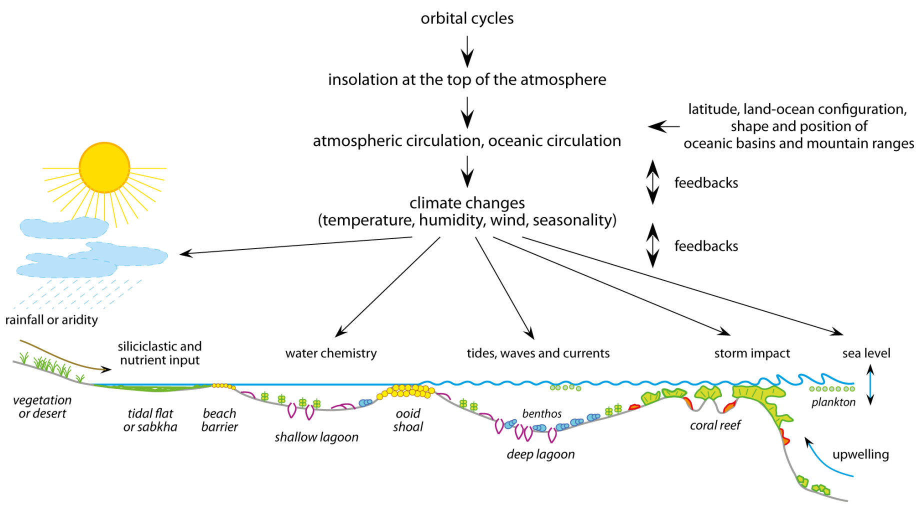

Figure 2. Chain of factors that influence a hypothetical, subtropical, shallow marine carbonate platform, including feedback processes. Amplitudes and frequencies of these factors may vary through time. The idealized cross section includes typical carbonate-producing environments (modified from Strasser, 2018).

Neth, 1997; Church and Clark, 2013; Sames et al., 2016; Ray et al., 2019).

If it can be shown that the physical and ecological parameters reigning over a sedimentary system were controlled by climate, and assuming that climate was at least partly controlled by orbital cycles, then a time resolution of the order of the shortest such cycles, which is the precession cycle of about 20 kyr, becomes possible. This is still far from the day-to-day monitoring of Anthropocene climate changes or of the yearly to centennial time resolution obtained for the Holocene, but it is better than the million-year scales that are proposed in many Mesozoic palaeoclimate models (e.g. Sellwood et al., 2000). In the following, the potential of shallow marine carbonates as recorders of orbitally controlled climate changes will be illustrated with an example from the Oxfordian of the Swiss Jura Mountains.

2 Oxfordian case study

2.1 Stratigraphy and palaeogeography

The Oxfordian sedimentary rocks in the Swiss Jura Mountains have been well studied by Gygi (1995, 2000). He established a lithostratigraphic scheme and dated it biostratigraphically by numerous ammonites (Fig. 3). In addition, Gygi et al. (1998) defined sequence boundaries that are correlated with the boundaries found in the chart of Hardenbol et al. (1998) that summarizes the sequence stratigraphy of

European basins. In the present study, the focus is on the interval between sequence boundaries Ox 6 and Ox 8 (Fig. 3).

The numerical ages of sequences and ammonite zones used in the chart of Hardenbol et al. (1998) are taken from the work of Berggren et al. (1995). The base of the Oxfordian there is dated at 159.4 ± 3.6 Ma and its top at 154.1 ± 3.2 Ma, implying a duration of about 5.3 Myr, albeit with wide error margins (Fig. 4). The ages of ammonite zones and sequence boundaries are interpolations between these values. Strasser et al. (2000) and Strasser (2007) performed a cyclostratigraphic analysis of Oxfordian platform sections and noticed that the sequences identified by Hardenbol et al. (1998) in many European basins actually correspond to sequences that formed in tune with the 405 kyr long eccentricity cycle or multiples thereof (Fig. 4). In the Geologic Time Scale (GTS) of 2012, Ogg et al. (2012) revised the duration of the Oxfordian, making it last 6.2 Myr. In the GTS of 2020, Hesselbo et al. (2020) attributed a still longer time interval of 6.75 Myr to the Oxfordian. Based on the analysis of several deep-water sections and aligned with the biostratigraphy and chronostratigraphy of Ogg et al. (2016), Huang (2018) counted three 405 kyr cycles in the interval between sequence boundaries (SB) Ox 6 and Ox 8. The discrepancies in radiometric dating are quite large and preclude a precise attribution of ages to the interval studied here. Furthermore, in the GTS 2020 the sequences boundaries are not dated, and there are differences in the position of sequence boundaries with respect to ammonite zones between the charts of Hardenbol et al. (1998) and Ogg et al. (2012). Also, the upper boundary of the Oxfordian has been shifted from the top of the Planula zone (Hardenbol et al., 1998) to the middle of the Bimammatum zone (Ogg et al., 2012) and finally to the base of the Bimammatum zone (Hesselbo et al., 2020; Fig. 4). Because the biostratigraphy and lithostratigraphy of Gygi (1995, 2000) agree with the biostratigraphy of Hardenbol et al. (1998), their scheme is adopted here. According to Ogg et al. (2012), sequence boundary Ox 7 sits in the middle between Ox 6 and Ox 8, but Strasser (2007) proposed a control by the long eccentricity cycle with a duration of 800 kyr between SB Ox 6 and Ox 7 and 400 kyr between SB Ox 7 and Ox 8 (Fig. 4). For the purpose of the present study it is important that the duration of the interval between SB Ox 6 and Ox 8 appears to be relatively stable: Hardenbol et al. (1998) attributed 155.81 Ma to SB Ox 6 and 154.63 to SB Ox 8, implying a duration of 1.18 Myr. Basically, the same value (1.2 Myr) was found by Strasser (2007) and Huang (2018). Ogg et al. (2012) dated SB Ox 6 at 159.4 Ma and SB Ox 8 at 158.2 Ma, also making the interval 1.2 Myr long. Consequently, this duration will be applied in the present study.

In the Oxfordian, the Jura platform was part of the wide passive margin to the north of the Tethys ocean. This margin was a complex array of shallow and deeper marine areas, with several emergent Hercynian massifs that were surrounded by siliciclastic aprons (Carpentier et al., 2006; Fig. 5). The platform was structured by synsedimentary faults (Allenbach, 2001; Strasser et al., 2015). Its palaeolatitude was 26 to 27° N (Dercourt et al., 1993), corresponding to the subtropical climate belt.

The average global climate during Oxfordian times was that of a greenhouse world; i.e. large polar ice caps were absent. Consequently, orbitally induced sea level changes were of low amplitude (see Sect. 1). Late Jurassic climate models have been proposed by e.g. Weissert and Mohr (1996), Rais et al. (2007), and Louis-Schmid et al. (2007), and a general circulation model has been developed by Sellwood and Valdes (2008). These models, however, only indicate million-year trends and do not consider high-frequency climate fluctuations in a restricted palaeogeographic area.

2.2 Definition and correlation of depositional sequences

Depositional sequences are defined here in terms of sequence stratigraphy (e.g. Catuneanu et al., 2009). Their formation is controlled by sea level changes. Sequence boundaries (SBs) form when sea level drops rapidly, which, on a shallow platform, may lead to subaerial exposure. Lowstand deposits are commonly very thin or absent on the platform because there is no room to accommodate the sediment. A transgressive surface (TS) forms when sea level rise leads to flooding of the platform, and the sediments above this surface then display a deepening-up trend (transgressive deposits). The fastest rise of sea level is indicated by the relatively deepest-water fauna and/or condensed deposits if sediment accumulation cannot keep up with sea level rise (MF: maximum flooding interval). Also, clays may accumulate below the wave base that has risen following the sea level rise. If a hardground develops or a rapid facies change occurs, a maximum flooding surface (MFS) can be defined. Slowing sea level rise then allows the sediment to fill the space created during maximum flooding, and a shallowing-up facies evolution is recorded (highstand deposits). A new sea level drop then terminates the sequence. These definitions are independent of the size of the sequences and the time involved in their formation (Mitchum and Van Wagoner, 1991; Strasser et al., 1999). Sea level changes may be local or regional (caused by tectonic uplift or subsidence) or global. The latter eustatic sea level fluctuations may be long-term (million-year scale caused by volume changes in ocean basins as a result of plate tectonics and basalt injections) or short-term (caused by orbital cycles; see Sect. 1).

The detailed analysis of facies evolution in the Oxfordian sections studied in the Swiss Jura Mountains allows defining depositional sequences of three different orders, which can be correlated between the sections. An exhaustive sequence stratigraphic and cyclostratigraphic analysis based on 19 sections covering the middle Oxfordian to late Kimmeridgian interval was carried out by Strasser (2007), but no palaeoclimatic interpretation was offered. For the purpose of the present study, only five sections covering the middle to late Oxfordian interval are presented (Figs. 6, 7). The Pertuis section is found where the road from Dombresson to

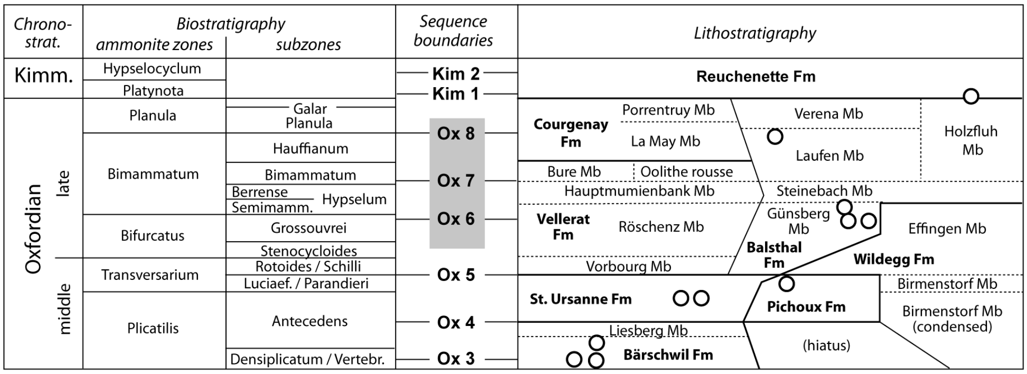

Figure 3. Stratigraphic scheme of the middle to late Oxfordian. Lithostratigraphy and biostratigraphy (white circles marking biostratigraphically significant ammonites) according to Gygi (1995, 2000). Sequence boundaries according to Hardenbol et al. (1998) and Gygi et al. (1998). Fm: formation; Mb: member; Kimm: Kimmeridgian. The focus of this study is indicated in grey.

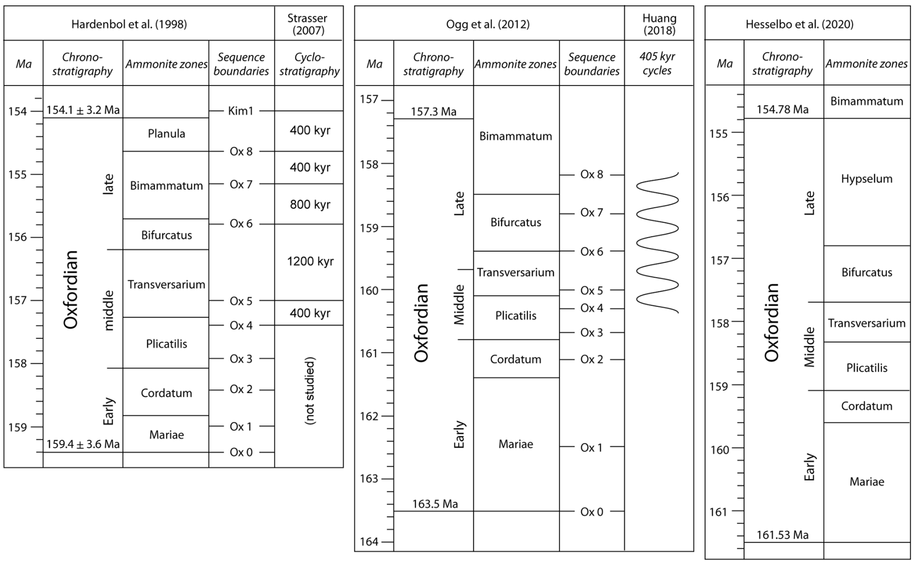

Figure 4. Comparison of three different timescales for the Oxfordian and cyclostratigraphic interpretations of Strasser (2007) and Huang (2018). Note that Strasser (2007) simplified the duration of the long eccentricity cycle to 400 kyr, while Huang (2018) used 405 kyr. For an explanation refer to the text.

St. Imier cuts through the Pertuis anticline (Pittet, 1996; Védrine, 2007). The La Chamalle section was studied by Jordan (1999) along a forest road towards La Chamalle farm to the northeast of the village of Péry-Reuchenette. The Péry-Reuchenette section was logged by Pittet (1996) and Hug (2003) in a quarry south of the village of Péry-Reuchenette at the exit of the canyon cutting through the first Jura anticline north of the city of Biel. The Gorges de Court section, studied by Hug (2003) and Védrine (2007), follows a footpath along the Birs River north of the Village of Court. The Hautes-Roches section was analysed by Dupraz (1999), Védrine (2007), and Stienne (2010). It runs along a forest trail southwest of the village of Hautes-Roches, north of Moutier.

The correlation lines of the depositional sequences in Fig. 7 are based on the interpretation of facies and sedimentary structures as explained above. The biostratigraphy established by Gygi (1995, 2000; see Fig. 3) allows correlating three of the five prominent sequence boundaries shown in Fig. 7 with the boundaries defined in European basins by Hardenbol et al. (1998), i.e. Ox 6, Ox 7, and Ox 8. The prominent transgressive surface at the base of the Hauptmumienbank and Steinebach beds is situated in the Semimammatum subzone (lowermost Bimammatum zone; Fig. 3) and formed shortly after the beginning of a major million-year-scale transgressive trend identified by Hardenbol et al. (1998) at the limit between the Bifurcatus and Bimammatum ammonite zones. Assuming that the time interval between Ox 6 and Ox 8 represents about 1.2 Myr (Fig. 4), it is suggested that each of the four prominent sequences shown in Fig. 7 represents 400 kyr (termed medium-scale sequences;

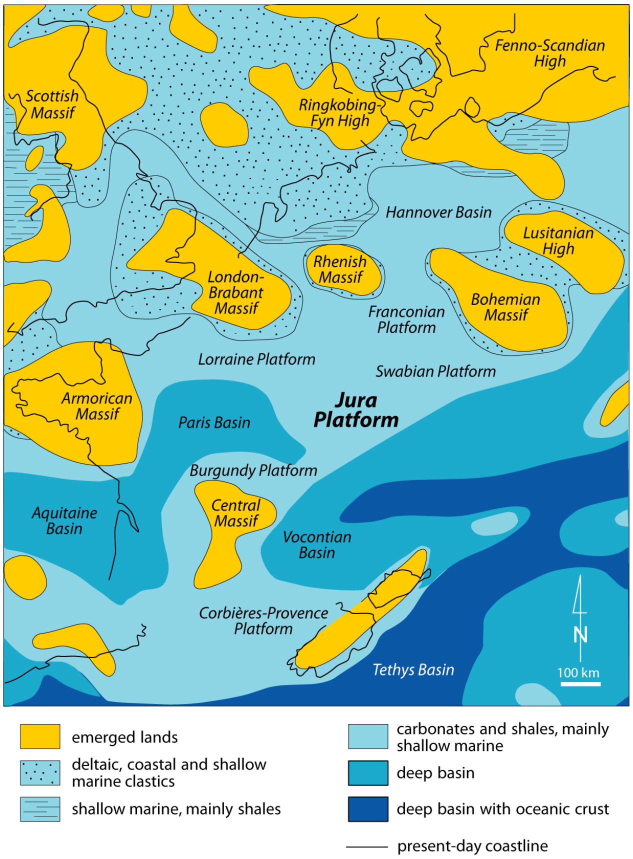

Figure 5. Palaeogeographic setting of the Jura platform during the Oxfordian. Modified from Carpentier et al. (2006).

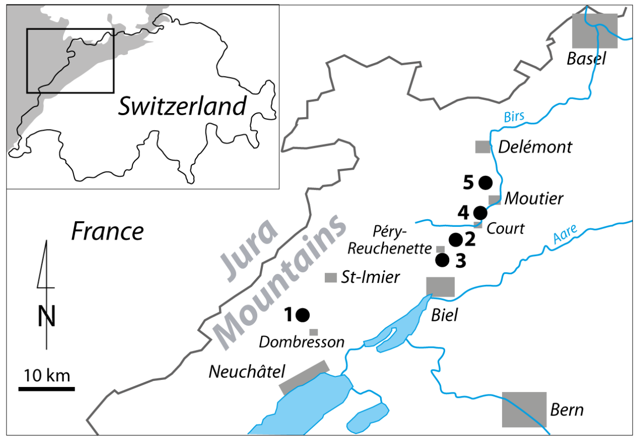

Figure 6. Locations of the sections presented in Fig. 7. 1: Pertuis; 2: La Chamalle; 3: Péry-Reuchenette; 4: Gorges de Court; 5: Hautes-Roches. Grey shade in the inset: Jura Mountains in France and Switzerland.

Strasser, 2007). Each 400 kyr sequence is composed of four small-scale sequences, implying that these lasted 100 kyr. Considering the hierarchical stacking pattern of these sequences and the timing, it is proposed that they formed in tune with orbital cycles: 405 kyr for the long eccentricity cycle and 100 kyr for the short one (note that, for simplification, the value of 400 kyr is used for the medium-scale sequences, although they formed in tune with the 405 kyr long eccentricity cycle). These long eccentricity cycles have also been found to be dominant in the early to middle Oxfordian Terres Noires Formation in southeastern France (Boulila et al., 2010). The medium- and small-scale sequences correlate well across the entire Jura platform (Strasser et al., 2015), implying that the sea level changes at the 405 and 100 kyr scales affected the entire carbonate platform, despite the facies mosaics and the morphological irregularities (Fig. 2).

The small-scale sequences are composed of individual beds, the number of which varies between 2 and 20 per small-scale sequence (Figs. 7, 8). These individual beds are more difficult to attribute to an orbital frequency (obliquity or precession) because, on the shallow platform, local processes such as lateral migration of sediment bodies could also have produced beds, independent of orbitally controlled sea level changes (e.g. Pratt and James, 1986; Strasser, 1991). Also, hiatuses were frequent, hampering a straightforward interpretation of such high-frequency cyclicity (e.g. Sadler, 1994; Strasser, 2015). However, many individual beds show a deepening–shallowing facies evolution that can be interpreted as resulting from a sea level cycle (e.g. Strasser et al., 1999). Many bed limits are underlined by thin marly layers, which reflect a more humid climate and/or a sea level drop that washed clays into the sedimentary system. If, in addition, a small-scale sequence is composed of five such well-defined beds, these can be attributed to the 20 kyr precession cycle and are called elementary sequences. Sub-Milankovitch cycles, i.e. cycles with frequencies shorter than those of the precession cycle, have been described and interpreted for shallow and deep marine successions (e.g. Zühlke, 2004; de Winter et al., 2014), but there is no evidence for such cycles in the studied Oxfordian sections.

Figure 8 shows an example of correlation of elementary sequences between the sections of Fig. 7. The prominent transgressive surface at the base of the Hauptmumienbank and Steinebach members is found all over the Swiss Jura (Gygi, 1995; Védrine and Strasser, 2009). It overlies marly sediments that locally contain fully marine fauna (echinoderms, brachiopods) mixed with freshwater algae (charophytes), suggesting that the sediment deposited during the sea level lowstand terminating the previous sequence was reworked in the early phases of the transgression (Védrine, 2007). The rapid shift to carbonates then implies that the whole platform was flooded and siliciclastic input was stopped. Elementary sequences are defined by prominent bedding surfaces and/or by rapid shifts in facies. The sequence boundary of the small-scale sequence (also shown in Fig. 7) in Gorges de Court is furthermore marked by birdseyes that formed on a tidal flat and by siliciclastics in Pertuis and Hautes-Roches. The abrupt termination of carbon-

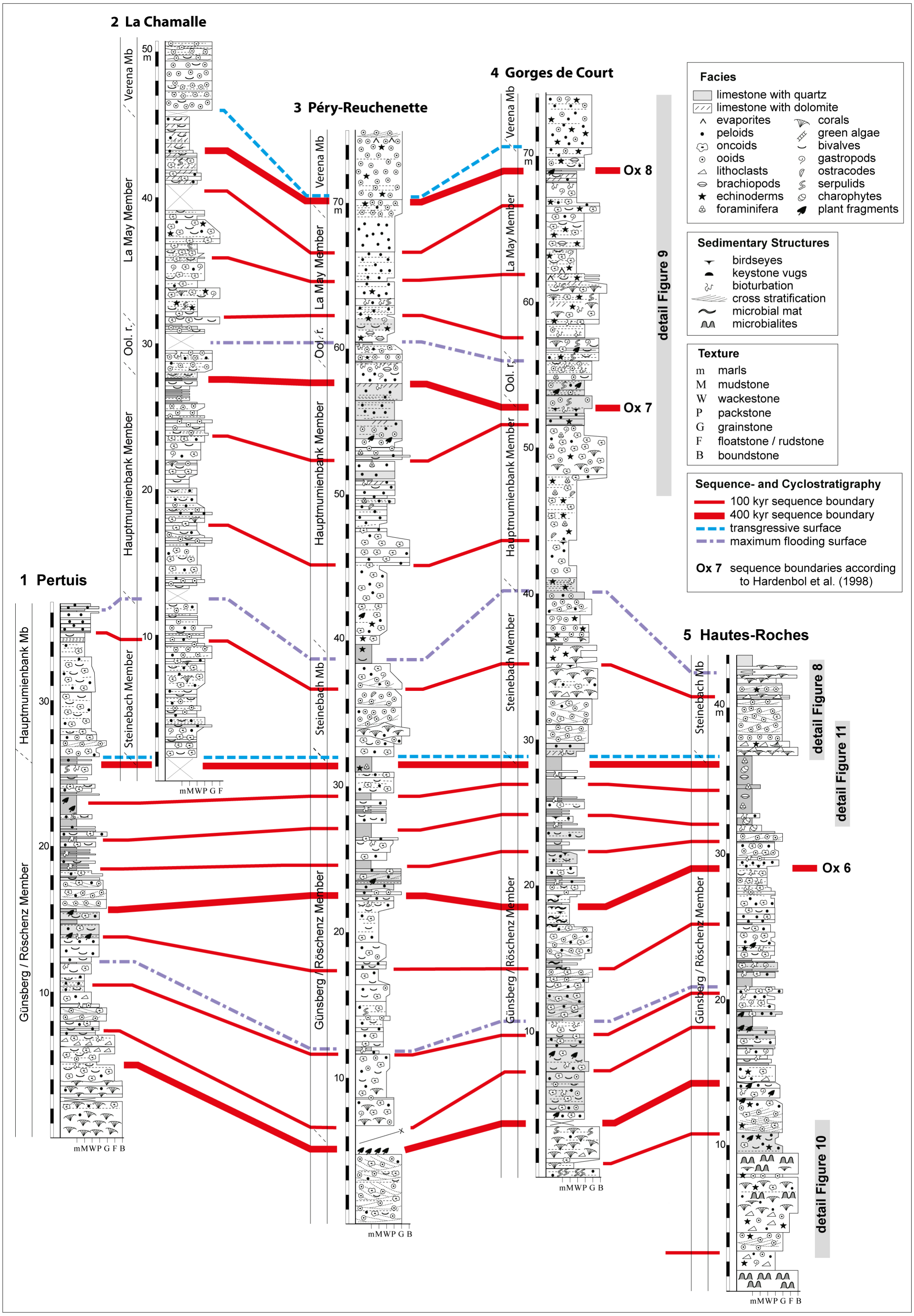

Figure 7. Facies evolution and correlation of five sections logged in the Swiss Jura Mountains (based on Strasser, 2007). Texture terminology according to Dunham (1962) and Embry and Klovan (1971). For explanations refer to the text.

ate sedimentation and the input of clays are interpreted as representing a maximum flooding surface, which is that of the medium-scale, 400 kyr sequence leading up to sequence boundary Ox 7 (Fig. 7). Between the prominent transgressive surface and the small-scale sequence boundary, five elementary sequences are counted in four of the sections. Péry-Reuchenette is dominated by oolites, which formed on constantly shifting shoals and where the formation of clear sequence boundaries was precluded. The sections of Pertuis and La Chamalle are dominated by oncoids that formed in lagoons, while the other three sections display oolites and coral reefs. The reefs did not develop at the same time in these sections, which is explained by the facies mosaics and the shifting depositional environments as illustrated in Fig. 2. One elementary sequence may correspond to several beds visible in the outcrop. This is due to reactivation surfaces in high-energy shoals and to localized shifting of sediment bodies by currents and waves in low-energy lagoons. The differences in thickness of the small-scale sequence are related to the faulted structure of the platform (Strasser et al., 2015): quiet-water lagoons formed behind high-energy ridges where reefs built up and ooid shoals developed, as well as where the preservation potential was less (Fig. 2).

In the following, three examples chosen from the sections in Fig. 7 will be discussed in detail.

2.3 Description and interpretation of characteristic sections

2.3.1 Gorges de Court

This detailed section (Fig. 9) has been chosen because it represents a well-developed stacking pattern reflecting the orbital cycles. It starts with wackestones of a low-energy, protected lagoon, followed by a boundstone composed of corals and oncoids in the Hauptmumienbank (meaning "main mummy bed", referring to the oncoids). Corals indicate warm, oligotrophic conditions, and both corals and echinoderms point to normal marine salinity. Oncoids form in lagoons with high microbial activity. The top of this bed is slightly dolomitized, suggesting shallow water and semiarid conditions. This is where a first sequence boundary can be placed.

The following part of the section is characterized by terrigenous components (up to 5 % quartz, feldspar, and terrestrial organic matter). At the top of the fourth thin bed, birdseyes point to a tidal flat, and a second SB can be placed there. The facies is reddish, and the ooids explain the name of Oolithe rousse Member. This whole interval points to generally low sea level, albeit with high-frequency fluctuations in water depth to explain the passage from tidal flat to ooid bar. The siliciclastics originated from erosion in the hinterland under a humid climate, and low sea level favoured their progradation into the lagoon. The terrigenous organic matter equally suggests a humid climate, allowing for growth of vegetation, in contrast to the dolomite just below.

Above follow facies varying between bioturbated packstones (low water energy) and grainstones (high energy). The main components, ooids, oncoids, bivalves, and serpulids, all imply lagoonal conditions. Corals, commonly encrusted by microbialites, become dominant in the middle part of the section, where the individual beds are also thickest (up to 1.8 m). Nevertheless, several bed tops in this interval show dolomitization, suggesting rapid changes between sea level rise to accommodate the coral patch reefs under fully marine conditions and by sea level drops to allow for penecontemporaneous dolomitization on tidal flats. Between metres 15 and 16, even some pseudomorphs after anhydrite are found, pointing to an arid climate.

The facies above the coral-rich interval are dominated by oncoids, which formed in protected, low-energy lagoons (wackestones, packstones, and floatstones). Tidal flats still occur in the lower part of this interval. Echinoderms and brachiopods point to normal marine salinity. The strongly bioturbated surface at metre 20.6 is interpreted as a maximum flooding surface: no sedimentation for a certain time and several generations of organisms that burrowed through the seafloor. An important change occurs at metre 21.3 of this section: after an intensely dolomitized tidal flat, two 2 to 3 cm thick layers rich in terrigenous organic matter imply the formation of marshes and ponds, in which marginal marine vegetation could grow. The climate must have changed rapidly from arid or semiarid to humid. Sea level was low and allowed the formation of a major sequence boundary. After this important sequence boundary, sea level rose to accommodate a fully marine lagoon with brachiopods and echinoderms and then thick-bedded, high-energy ooid and peloid bars.

According to Gygi (1995), the Oolithe rousse Member belongs to the Bimammatum subzone (Fig. 3) and thus also contains SB Ox 7 of Hardenbol et al. (1998). The organic-rich layers at metre 21.3 occur in the upper part of the La May Member, which corresponds to the limit between the Bimammatum and Planula zones and thus to SB Ox 8 (Fig. 3). According to the sequence- and cyclostratigraphic interpretation of the Jura platform by Strasser (2007), the interval between SB Ox 7 and Ox 8 corresponds to about 400 kyr (Fig. 4). This is close to the value of the long eccentricity cycle (405 kyr), and it can thus be postulated that this major sequence observed at Gorges de Court formed in tune with this orbital cycle.

While SB Ox 8 is represented by two thin layers rich in terrestrial organic material testifying to a sea level drop, SB Ox 7 is less well defined. It has been interpreted at the top of the bed with birdseyes (indicating a tidal flat) at metre 6.2, but the entire siliciclastic-rich interval implies low sea level. This is why a sequence boundary zone is indicated in Fig. 9, corresponding to a time interval that favoured the formation of surfaces that qualify as sequence boundaries (Montañez

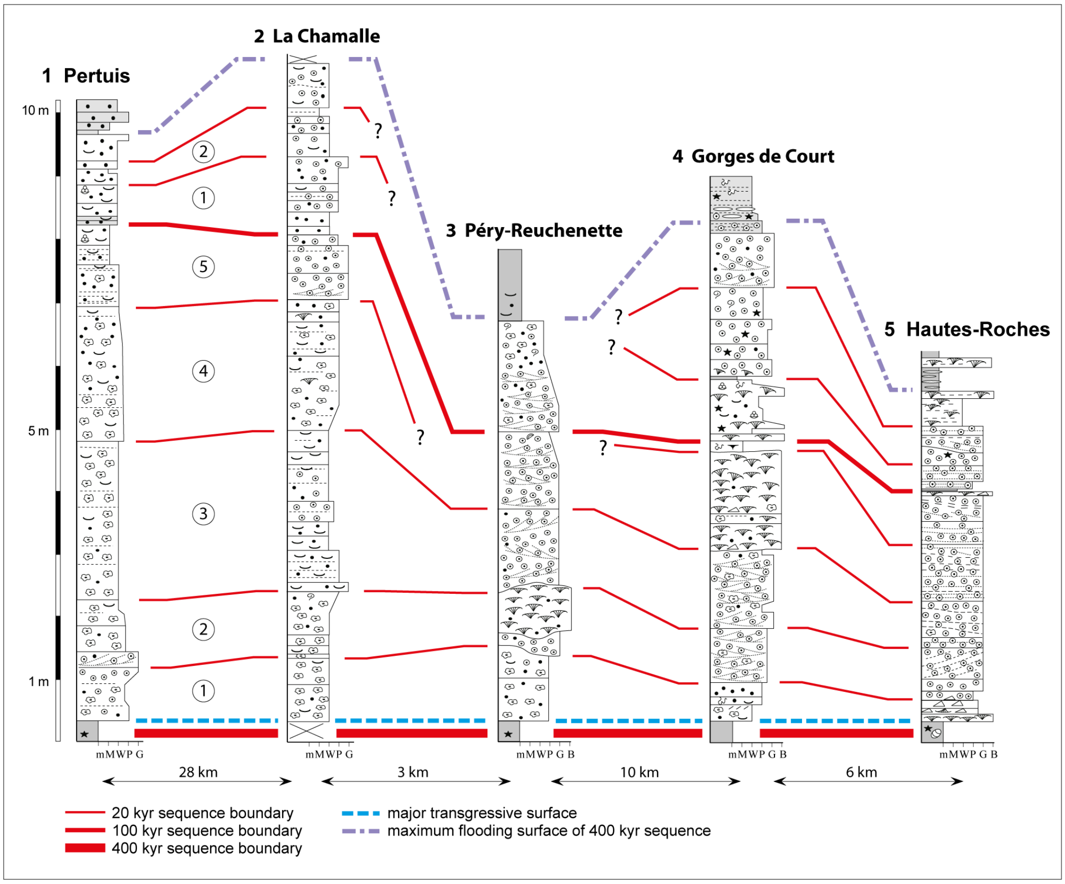

Figure 8. Correlation of elementary sequences between the prominent transgressive surface forming the base of the Hauptmumienbank and Steinbach members as well as the maximum flooding surface of the corresponding medium-scale sequence (based on Védrine, 2007). For discussion refer to the text.

and Osleger, 1993; Strasser et al., 1999). The same holds for the maximum flooding zone in Fig. 9: the thickest beds and most open marine facies define an interval where sea level rose rapidly to create accommodation and fully marine conditions. SB Ox 7 and Ox 8 as well as the maximum flooding zone correlate well with other sections on the Swiss Jura platform (Strasser, 2007; Fig. 7).

Between SB Ox 7 and Ox 8, 22 beds are counted (Fig. 9). These beds are separated by thin layers of marls, the clays having been washed into the system during high-frequency sea level drops and/or during phases of more rainfall in the hinterland. Thus, they qualify as elementary sequences, even if their facies do not always display deepening then shallowing-up trends (Strasser et al., 1999). 405 kyr divided by 22 results in 18.4 kyr, which is close to the 20 kyr duration of the orbital precession cycle in the Oxfordian (Berger et al., 1992). Considering the complexity of the translation of orbitally induced insolation cycles into the sedimentary system (Fig. 2) and considering the possibility of local processes potentially creating beds, it is not astonishing that the fit is not perfect.

The identification of the small-scale sequences reflecting the short eccentricity cycle of 100 kyr in this outcrop is not easy. Their boundaries are not well developed and are mainly inferred from correlation with other sections (Fig. 7; Strasser, 2007). In Fig. 9, they correspond to rapid changes from high-energy grainstone or floatstone facies (implying shallower water with waves and currents) to low-energy wackestone or packstone facies formed below wave base (thus implying an increase in water depth). Following these criteria, four such sequences are counted within the 400 kyr sequence. The small-scale sequences are composed of four to six individual beds. Again, the perfect fit would have been five beds per sequence, but the sedimentary system was complex and did not always translate the orbital cyclicity one-to-one.

2.3.2 Hautes-Roches A

In the Hautes-Roches section, two coral-rich intervals are encountered (Fig. 7; Dupraz, 1999). The lower one (Fig. 10) corresponds to a small-scale sequence that formed in tune with the 100 kyr eccentricity cycle. In this outcrop, the boundaries of the sequence are defined by sharp transgressive

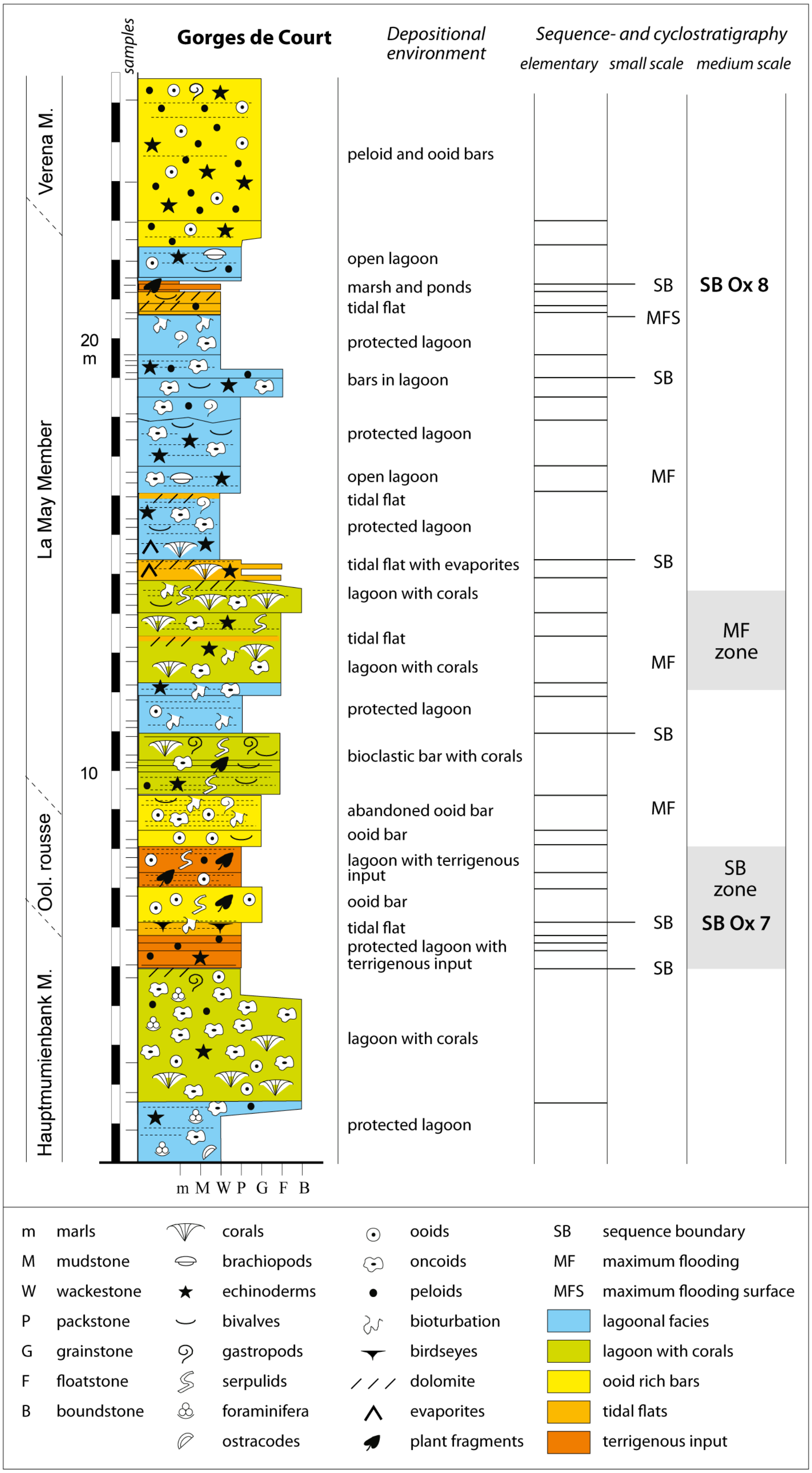

Figure 9. Detail of the Gorges de Court section. Log and facies are according to Hug (2003), and the sequence stratigraphic and cyclostratigraphic interpretation is based on Strasser et al. (2000). Ool. rousse: Oolithe rousse Member. For discussion refer to the text.

surfaces (TSs), which superpose cross-stratified ooid grainstones over lagoonal sediments (the sequence boundaries are hidden in the sediments just below the TSs or amalgamated to them; Strasser et al., 1999). This suggests that, at the beginning of a sea level rise, ooid shoals migrated over lagoons. The bed above the first ooid shoal still contains ooids but also coral debris, suggesting that a nearby coral reef was being dismantled by storms. Healthy corals then grew on top of the rubble, implying increasing water depth. Later, the corals adopted a flat shape, possibly because they had to increase their surface to catch enough light for the photosynthetic zooxanthellae, which again points to increasing water depth. Coral diversity was high (mainly *Microsolena, Heliocoenia, Stylina, Isastraea*, and *Calamophylliopsis*; Dupraz, 1999). The corals gradually became covered by microbialites, which implies increased nutrient input and eutrophication of the system (Hallock and Schlager, 1986; Dupraz and Strasser, 2002). A sharp surface terminates this bed. Above, coral growth sets in again, but the corals are covered by microbialites, and oncoids are present. The Microsolenids in particular are associated with microbialites, suggesting that this family supported some degree of eutrophication. A washover deposit rich in echinoderms interrupted the growth of this reef, implying that a major storm passed over it. Above a last large coral head (probably not in situ but toppled) and flat corals, only microbialites are present; they have a thrombolite texture and include some sponges. This sequence, from ooid shoal through coral reef to thrombolite, suggests that water energy decreased through time, that the water became deeper and more turbid to hamper the photosynthesis of the coral symbionts, and that nutrient excess favoured microbial growth that eventually suffocated the corals.

This evolution ends with a bioturbated, nodular layer capped by a bored hardground, indicating that the seafloor was exposed over some time to become cemented and perforated by lithophaga bivalves. The hardground also marks the end of a deepening-up trend and is thus considered a maximum flooding surface (MFS). Above the hardground, brachiopods indicate normal marine salinity. Quartz sand and (in the upper part of the bed) plant debris testify to terrigenous input and progradation of lagoonal sediments. These is interpreted as shallowing-up highstand deposits. A thin bed with echinoderms (possibly a tempestite) and a new ooid shoal then represent the beginning of a new sequence.

The sequence is composed of seven beds. One, however, is an event deposit (the washover), and one belongs to the composite hardground covering the thrombolite. Considering the architecture of depositional sequences observed on the Jura platform where the transgressive parts of small-scale sequences are commonly composed of limestones while the regressive highstand parts are in many cases marly (Strasser et al., 2015), it is suggested that the sequence shown here corresponds to the 100 kyr short eccentricity cycle and that the formation of each bed was controlled by the orbital precession cycle of 20 kyr. The bed limits are transgressive surfaces or maximum flooding surfaces; the sequence boundaries are not developed (Strasser et al., 1999). The washover deposit that served as a substratum for renewed coral growth is attributed to elementary sequence 4, but the storm event may also have occurred at the end of sequence 3. During the first four precession cycles, conditions were those of a gradual transgression, which ended in the hardground. The highstand deposits took only 20 kyr to form, making the record of this 100 kyr cycle highly asymmetrical.

2.3.3 Hautes-Roches B

The second interval at Hautes-Roches shown here is dominated by lagoonal marls. The section illustrated in Fig. 11 starts with a firmground that covers lacustrine mudstones to wackestones with charophytes. Above, a first thin bed still has lacustrine facies. The following thin bed contains charophytes as well as marine fossils, implying a marine, transgressive pulse that reworked lacustrine elements. A second transgressive surface then leads to a strongly bioturbated lagoon. The next 2 m contain echinoderms and brachiopods, implying normal marine salinity. Three nodular beds are found in this interval. They are thickening up, and quartz content increases upwards to up to 20 % (Stienne, 2010). This evolution is typical of a shallowing-upwards highstand deposit. In this case, the maximum flooding interval can be placed at the strongly bioturbated bed, while a sequence boundary is identified at the base of the third nodular bed (Fig. 11). Five elementary sequences are identified, leading to the hypothesis that they correspond to the 20 kyr precession cycle and the small-scale sequence they make up to the 100 kyr short eccentricity cycle. This small-scale sequence is also found in the other sections shown in Fig. 7. Each of the elementary sequences has a lower carbonate-rich part interpreted as transgressive deposits and a siliciclastic-rich upper part that represents the highstand deposits.

The following 1.2 m are composed of lagoonal marls with a fully marine fauna. They are covered by a sharp transgressive surface, above which grew a reef composed of small corals. This same transgressive surface is illustrated in Fig. 8. It marks the base of the coral- and ooid-rich Steinebach Member and of the oncoid-bearing Hauptmumienbank Member, respectively (Fig. 3). The corresponding sequence boundary is hidden in the marls below the TS, as suggested by the presence of freshwater charophytes mixed with marine fauna (Védrine, 2007). Elementary sequences cannot be recognized.

Reef development in this section was short-lived. Above the thin reefal boundstone with low coral diversity (mainly *Isastraea* and *Microsolena*; Dupraz, 1999), only reworked coral clasts appear that, however, suggest that reef growth continued in the neighbourhood. The phase of reef development was then interrupted by ooid shoals, one of which displays sigmoidal cross-beds formed by tidal currents.

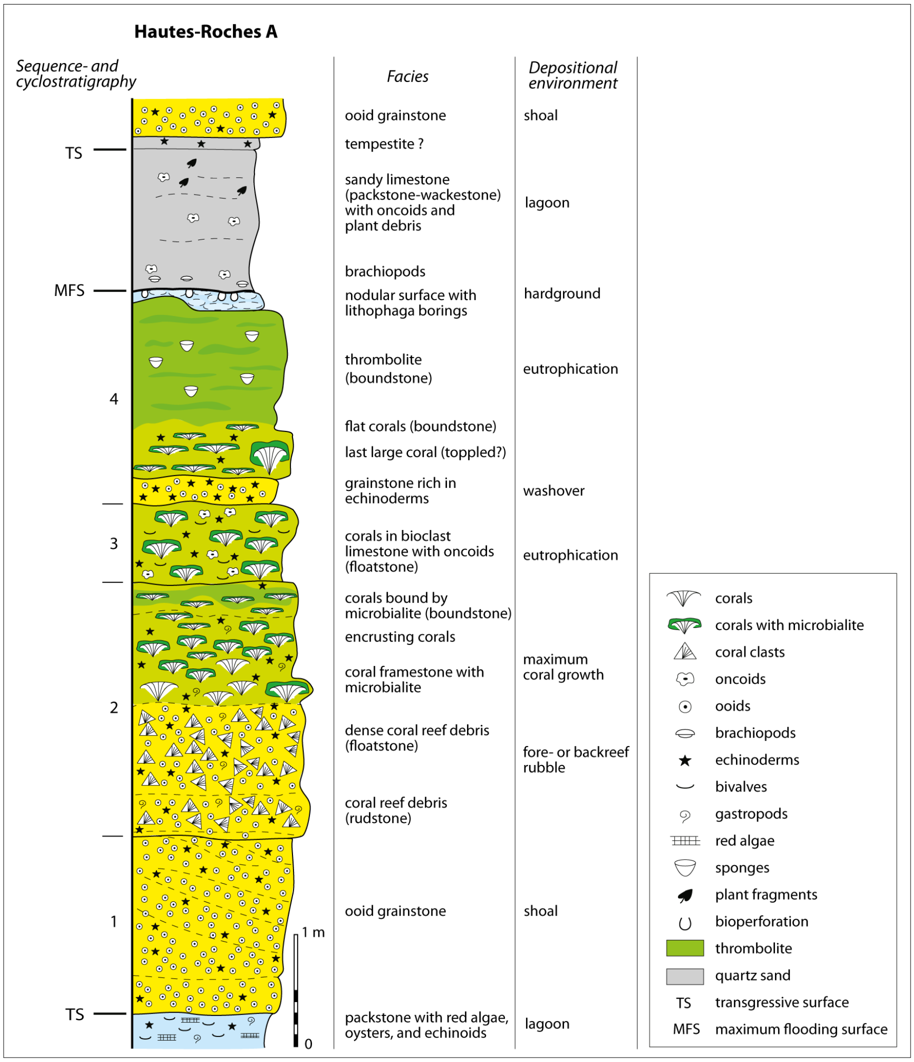

Figure 10. Detail of the Hautes-Roches section A. Log and facies based on Dupraz (1999). For discussion refer to the text.

3 Discussion

Although the climate factors influencing a shallow marine carbonate platform are intimately linked (Fig. 2), they will be discussed here separately.

3.1 Water temperature

In ancient carbonates, oxygen isotope ratios are often used as a proxy for the temperature of the water in which they formed. This, however, requires that the original mineralogy be preserved in the fossil record. In shallow marine carbonates, this is rarely the case: early freshwater diagenesis dissolves the aragonite of corals, gastropods, and green algae, and the high-Mg calcite of echinoderms is transformed into low-Mg calcite. An exception are brachiopod shells, which have a relatively stable low-Mg calcite composition and are found in the studied sections. However, the δ^{18}O values that are recorded also depend on the geochemistry of the platform waters, which may vary considerably across a complexly structured platform such as the one in the Jura Mountains (e.g. Immenhauser et al., 2003; Colombié et al., 2011).

Among the tropical and subtropical carbonate-producing organisms, corals are the most sensitive to temperature changes. Today, reef-building zooxanthellate corals do not support water temperatures below 18 °C and above 34 °C (Wood, 1999). For short periods, however, they tolerate fluctuating and even higher temperatures (e.g. Schoepf et al., 2015). Aragonite saturation in seawater, which is important for efficient coral skeleton formation, closely follows water temperature (Wood, 1999). If it is assumed that Oxfordian corals had the same requirements regarding temperature as the recent ones, a high-diversity reef would be a proxy for water temperatures ranging from about 23 to 29 °C. In the middle and late Oxfordian, coral reefs were widely distributed between the palaeolatitudes of 40° N in Japan to

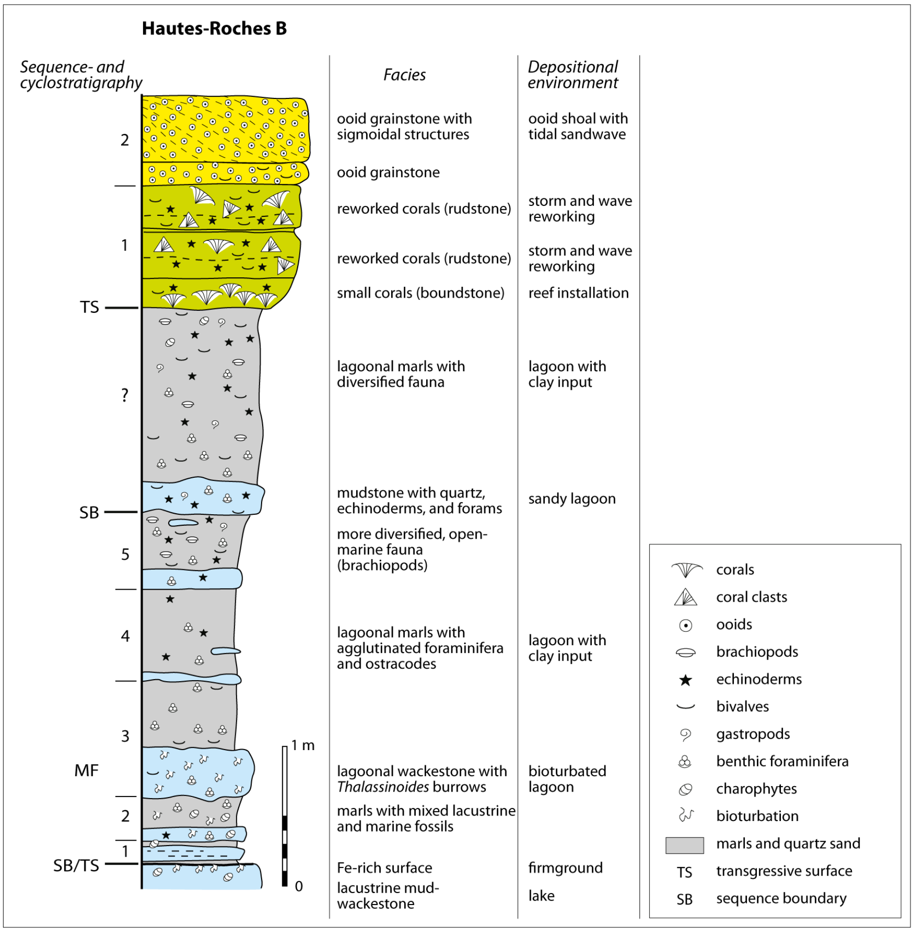

Figure 11. Detail of the Hautes-Roches section B. Log and facies based on Dupraz (1999) and Stienne (2010). For discussion refer to the text.

45° S in the Neuquén Basin (Leinfelder et al., 2002) where these water temperatures were common. The reef in the Hautes-Roches section (Fig. 10) with a relatively high coral diversity may thus indicate water temperatures between 23 and 29 °C. Low diversity, however, may not only be an effect of temperature but also of other unfavourable conditions such as water that is too shallow or too deep, high sediment input that makes the water turbid and thus hinders photosynthesis of the symbionts, nutrient excess that favours microbialites and fleshy algae that compete with the corals, or water acidification that impacts skeletal growth.

Based on a mean value of −3.50 ‰ $\delta^{18}O$ in micritic whole rock (which averages the isotopic signal of the different components) from middle Oxfordian sections in the Swiss Jura, Plunkett (1997) calculated ambient water temperatures of 26 to 27 °C (following Anderson and Arthur, 1983). This compares well with Frakes et al. (1992), who indicate up to 27 °C for late Oxfordian ocean surface temperatures according to oxygen isotope ratios measured on planktonic foraminifera and belemnites. Martin-Garin et al. (2010) measured oxygen isotope ratios on brachiopods and oysters from outcrops in the Swiss Jura. They calculated water temperatures of below 20 °C for the low-diversity coral reefs (15 genera) in the Liesberg Member (Fig. 3), about 25 °C for the high-diversity reefs (37 genera) in the St. Ursanne Formation, and about 20 °C in the Günsberg Member where coral diversity declined (13 genera). The reef complex shown in Fig. 10 is situated in this latter member.

For the carbonate platform in the French Jura, Olivier et al. (2015) interpreted a climate evolution going from warm and humid to warm and arid in the course of the Bimammatum zone. This corresponds to the time interval between sequence boundaries Ox 6 and Ox 8 discussed here (Fig. 3). In the Paris Basin, Brigaud et al. (2014) cite sea surface temperatures of 20 to 29 °C for the Late Jurassic, with an optimum during the middle Oxfordian. At the onset of the late Oxfordian, water temperatures dropped by 6 to 7 °C, and rainfall increased. Carpentier et al. (2010) state that, in the eastern Paris Basin, after a warm and arid interval favouring carbonate production in the Transversarium zone, the climate became cooler and more humid in the Rotoides and Stenocyloides subzones. In the southern North Sea, Abbink et al. (2001) analysed sporomorphs as palaeoclimate proxies and showed that there was a temperature drop between the boreal Serratum and Regulare ammonite zones. This corresponds to the Semimammatum subzone in the Tethyan realm (Fig. 3), in which the major transgressive surface is situated and in which coral reefs began growing (Figs. 7, 8). It thus appears that, while the water temperature in the Tethys ocean increased, the North Sea was cool.

3.2 Sea level

Sea level changes in the Milankovitch frequency band are an important proxy as they reflect changes in global air and water temperature. During the Quaternary, glaciation cycles controlled by the 100 kyr short eccentricity cycle led to important asymmetrical sea level fluctuations due to slow buildup of ice caps followed by rapid melting (Shackleton, 1987; Fig. 13). In greenhouse worlds, i.e. when major ice caps were absent, the translation of orbitally controlled insolation changes into eustatic sea level changes was more direct. Thermal expansion and retraction of ocean surface water were important factors controlling sea level fluctuations, in tune with the eccentricity cycles of 100 and 405 kyr (Sames et al., 2016). Schulz and Schäfer-Neth (1997) proposed that thermally induced volume changes in deep-water circulation resulted in sea level changes. Water storage and release on the continents (aquifer eustasy; Jacobs and Sahagian, 1993; Sames et al., 2014; Wendler and Wendler, 2016) depend on the climate over the land areas: sea level rise is linked to a drier climate with less precipitation, when aquifers empty more rapidly than they fill up. Consequently, aquifer eustasy is dependent on the latitudes at which the land areas occur and on the atmospheric circulation cells; i.e. it is also controlled by the obliquity and precession cycles. Obliquity is dominant at high latitudes and cannot be identified in the studied sections. The 20 kyr precession cycles, on the other hand, are potentially recorded in the elementary sequences.

For Cretaceous high-frequency sea level cycles, Davies et al. (2020) proposed the combined effects of thermal expansion, glacioeustasy, and aquifer eustasy to produce the 65, 30, and 50 m amplitudes observed in the Valanginian, Turonian, and Maastrichtian, respectively. Aquifer eustasy taken alone would be responsible for amplitudes of less than 5 m, which is in the range of the reconstructed Oxfordian amplitudes (see below). Wendler et al. (2016) suggested that aquifer eustasy could drive sea level changes even of the order of 30 to 40 m at the frequency of the long eccentricity cycle that shifted the Hadley circulation and the width of the equatorial humid belt.

For the part of the Gorges de Court section shown in Fig. 9, Strasser (2018) reconstructed a sea level curve that explains the observed stacking pattern of beds. For this, the section was first decompacted according to facies (Goldhammer, 1997; Strasser and Samankassou, 2003). The following decompaction factors are applied: 1.2 for grainstones, 1.5 for packstones, 2 for wackestones, 2.5 for mudstones, and 3 for marls. Boundstones have resisted compaction, and a factor of 1.2 is used. Floatstones with their micritic matrix are treated like packstones. Estimation of water depth for the different facies of course is not easy: the facies depend not only on water depth but also on water energy, and the same facies may be present over a wide depth range. For this exercise, the following values have been assumed: tidal flats form within the tidal range and are set at 0 m. These are the tie points on the reconstructed curve (Fig. 12). Grainstones often result from winnowing by waves and currents, and a water depth of 1 m is attributed. Packstones and floatstones with abundant fauna are set at a minimum of 2 m. Coral patch reefs can potentially grow up to sea level but are assumed to have needed at least 2 m water depth to develop. When an open marine fauna (e.g. brachiopods) is present, a minimum water depth of 3 m is assumed. By this, only trends in the evolution of water depth are reconstructed, and no error bars are applied. To accumulate the sediment pile between Ox 7 and Ox 8 (15.3 m today, 26 m when decompacted; Strasser, 2018), a gain in accommodation of 26 m is needed (Fig. 12). This is created by subsidence and long-term sea level rise. This long-term trend can be subdivided into four portions according to the space needed to accumulate the individual small-scale, 100 kyr sequences. Deducing these trends from the reconstructed sea level curve, the deviation of sea level change from the average accommodation gain can be visualized for each 100 kyr sequence. It is interesting to note that, for the medium-scale sequence, two candidates for a maximum flooding zone can be proposed, both situated in the interval of high accommodation gain (Fig. 12). However, when comparing with other sections in the Swiss Jura, it is rather the lower one that is recognized all over the platform (Strasser, 2007; Fig. 7).

Small-scale sequences 3 and 4 are well defined, and each contains five elementary 20 kyr sequences. Sequence boundary Ox 7, which defines the limit between small-scale sequences 0 and 1, is placed at the tidal flat. This results in only four elementary sequences for small-scale sequence 0 and six for small-scale sequence 1 (Fig. 12). This misfit may be explained by a wrong definition of the elementary sequences or by factors other than sea level that created a topographic high to install the tidal flat (differential subsidence, lateral migration of sediment bodies). The top of the second small-scale sequence (elementary sequence 14 in Fig. 12) shows corals, microbialites, and lithophaga borings but also evaporites, pointing to rapid changes in water depth. It is possible that the fifth elementary sequence was not recorded due to lack of accommodation.

The next step is to reconstruct the amplitudes of the highest-frequency sea level fluctuations corresponding to the 20 kyr precession cycle by subtracting the 100 kyr trends (Fig. 13). When compared to the envelope curve based on the calculated insolation changes at the Equator and for the last 550 kyr, a partial correspondence becomes visible: stronger insolation due to the 100 and 405 kyr cyclicity generally translates into higher sea level amplitudes for the 20 kyr cycles. Even considering the complex facies distribution on a shallow marine platform and accommodation changes due to differential subsidence, and even considering the uncertainties in estimating decompaction factors and water depth, it can be concluded that, in the Oxfordian case discussed here, orbitally controlled insolation changes translated into sea level changes. The similarity of the symmetrical changes in amplitude at the 100 and 405 kyr scales between the reconstructed sea level fluctuations and the calculated insolation changes (Fig. 13) suggests that the translation from insolation to sea level was mainly via thermal expansion and retraction of the ocean surface water, which is a process that depends on air temperature. Aquifer eustasy and low-amplitude glacioeustasy were certainly present but are difficult to quantify in the present study.

It has to be kept in mind that the precession cycle today has a 21 and 23 kyr periodicity, while in the Oxfordian the periodicity was at about 20 kyr (Berger et al., 1992; Hinnov, 2018). The number of high-frequency cycles in Fig. 13 is therefore not the same for the Quaternary and Gorges de Court. On the other hand, the 100 and 405 kyr cycles are stable through time and can be directly compared. A synthesis of 12 Oxfordian sections in the Swiss Jura showed that many small-scale sequences controlled by the 100 kyr short eccentricity cycle are composed of a lower transgressive part dominated by high-energy, carbonate-dominated facies (e.g. ooid or bioclastic shoals, coral reefs), while the upper regressive part displays low-energy carbonate facies (e.g. tidal flats) or marls (Strasser et al., 2015). The conclusion is that during a warming climate sea level rise pushed back the terrigenous delivery, and clear, oligotrophic, warm, and deepening waters allowed for carbonate production and accumulation. During a cooler climate, sea level dropped, siliciclastics prograded, water depth diminished, and carbonate production was reduced. A cooler climate coincided with more rainfall (see below), thus reinforcing erosion on the land areas.

Pittet and Gorin (1997) analysed the palynofacies in the Vellerat Formation (Fig. 3). They found that the ratio between land-derived particulate organic matter (plant debris, pollen and spores) and marine particles (phytoplankton, foraminifer linings) reflects proximal to distal trends, which depended on the land–ocean configuration but also on sea level changes. The analysis of associations of benthic foraminifera at the Oxfordian–Kimmeridgian boundary in the Paris Basin by Lefort et al. (2011) revealed a correlation with sea level changes: a highly diversified association composed of small agglutinated and calcitic forms characterizes high sea level stands, while an association richer in large agglutinated foraminifera is abundant when sea level was low. Unfortunately, there is no indication of the duration of the sea level cycles.

1 °C of global warming today leads to 20 to 60 cm of sea level rise through thermal expansion of the ocean water (Church and Clark, 2013). If the same values are assumed for Oxfordian times, and if thermal expansion is considered the main factor, a sea level rise of 2 m (Fig. 13) would suggest an atmospheric warming of 3 to 10 °C. Insolation by itself would not have allowed for this warming, but its input was enhanced by feedbacks due to greenhouse gases. For example, Ikeda et al. (2020) suggested that ca. 10 Myr orbital variations controlled summer monsoon dynamics, which changed terrestrial weatherability, affected atmospheric $p\mathrm{CO}_2$, and eventually led to variations in sea surface temperatures of the order of 3 to 7 °C. At the scale of obliquity cycles, Laurin et al. (2015) explained the $\delta^{13}\mathrm{C}_{\mathrm{carb}}$ signature in the Late Cretaceous English Chalk by recycling of carbon through formation and decay of reservoirs of organic matter and/or methane on land, in lakes, and in euxinic marine settings.

It is interesting to compare rates of sea level rise between the Oxfordian and today. Taking two examples from Fig. 12, it can be estimated that, to accommodate elementary sequence 5, sea level must have risen by about 2 m within 10 000 years (half a precession cycle) and by about 3 m for elementary sequence 9. This amounts to values of 0.2 mm per year for the first case and 0.3 mm yr^{-1} for the second one (under the condition that sea level change was mainly controlled by thermal expansion of the ocean water and thus followed a symmetrical curve). Based on the detailed analysis of one elementary sequence in the Röschenz Member, Strasser et al. (2012) estimated a rise of 0.3 mm yr^{-1} during maximum flooding, i.e. during the fastest rise of the sea level cycle. Today, due to anthropogenically induced global warming, global mean sea level rose by 3.7 mm yr^{-1} between 2006 and 2018 (Masson-Delmotte et al., 2022), i.e. more than 10 times faster than in the Oxfordian.

3.3 Rainfall

Terrigenous material (clays, quartz, feldspar, terrestrial organic matter) appears at regular intervals in the studied sections. Thin, only millimetre- or centimetre-thick marl layers commonly from the limits between individual beds, and several metre-thick intervals around sequence boundaries Ox 6 and Ox 7 are dominated by siliciclastics and contain plant fragments. The maximum flooding zone at metre 40 in the Péry-Reuchenette and Gorges de Court sections also contains clays and 1 % quartz (Fig. 7; Hug, 2003). According to the sequence stratigraphic interpretation, these intervals commonly correspond to low sea level stands, with the exception of the maximum flooding at metre 40. Falling sea level increases erosion of the hinterland, i.e. of the Hercynian massifs (Fig. 5). Deltas prograde, and terrigenous material is delivered into the lagoons. A second factor of course is rainfall in the hinterland, which activates the rivers that transport the siliciclastics and plant fragments towards the ocean. Input of aeolian quartz under an arid climate cannot be excluded, but transport by rivers is considered to have been the main

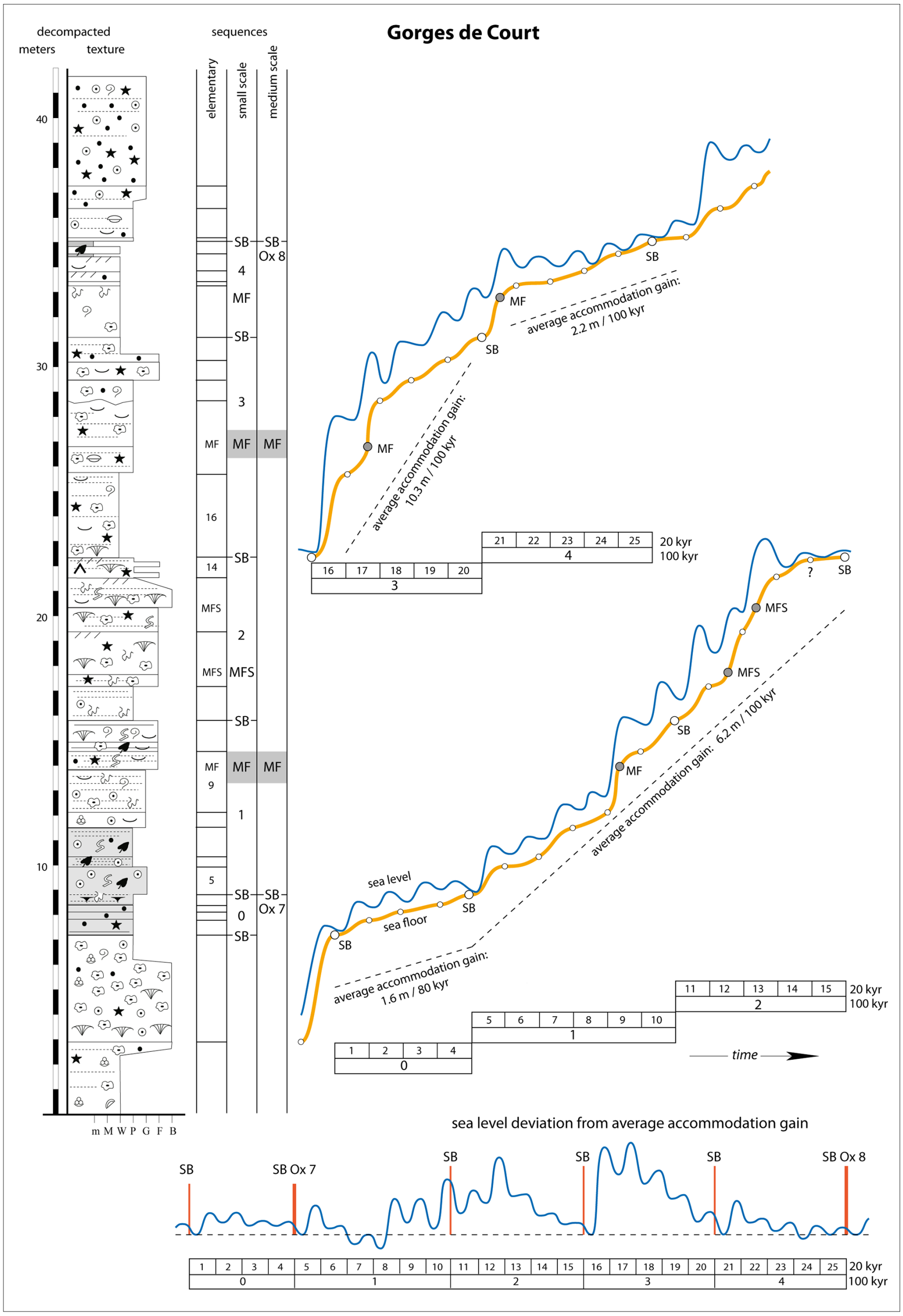

Figure 12. Reconstruction of high-frequency sea level changes for the Gorges de Court section (modified from Strasser, 2018). The section (Fig. 9) is first decompacted according to facies, and for each facies a water depth is attributed. Elementary sequences are assumed to correspond to the 20 kyr precession cycle and small-scale sequences to the 100 kyr one. Average accommodation gain needed to record the small-scale sequences varies through time. By deducing these trends, a sea level curve is reconstructed that serves as input to Fig. 13. Symbols and abbreviations are as in Fig. 7.

process in the case study presented here (Gygi and Persoz, 1986; Hug, 2003).

From Fig. 7 it is clear that the terrigenous material is not recorded equally in the studied sections. This can be explained by the variable platform morphology including highs where the siliciclastics bypassed and lows where they were ponded (e.g. Strasser, 2018). Furthermore, currents picked up the clays and redistributed them over the platform.

At a palaeolatitude of 26 to 27° N (Dercourt et al., 1993), the studied platform was situated in the subtropical zone, which is confirmed by the diversity and type of carbonate-producing organisms typical of such platforms (Reijmer,

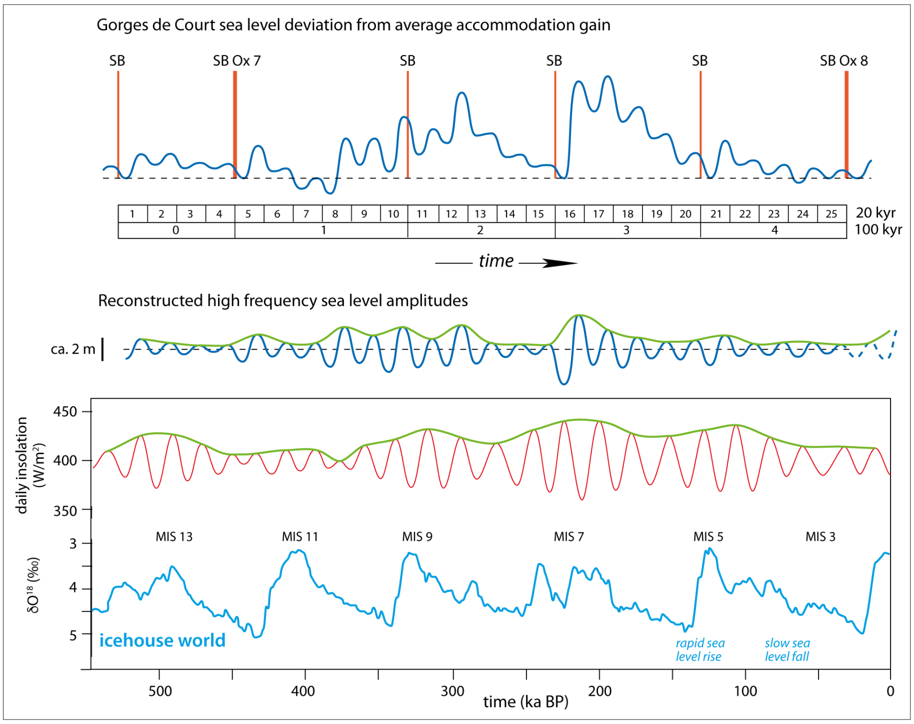

Figure 13. Comparison between the high-frequency, metre-scale sea level changes reconstructed for the Gorges de Court section and the insolation curve calculated for the Equator for the last 550 kyr (Hinnov, 2018). The envelopes of the two curves (green lines) reflect the 100 and 405 kyr eccentricity cycles, suggesting that the sedimentary record at Gorges de Court was at least partly controlled by insolation cycles. During icehouse times, the sea level changes had a much higher amplitude (tens of metres; Shackleton, 1987) and were highly asymmetrical (δ^{18}O values serving as a proxy for sea level changes; simplified from Railsback et al., 2015; MIS: marine isotope stage). For discussion refer to the text.

2021). At this latitude and at the insolation maximum, atmospheric circulation was controlled by the Hadley cell, while at the insolation minimum, the Ferrel cell was active (e.g. Matthews and Perlmutter, 1994). Orbital cyclicity thus caused latitudinal shifts of atmospheric cells and shifts between high-pressure and low-pressure zones. For example, Khon et al. (2012) showed how insolation changes at the 100 kyr scale between the last interglacial (Eemian; MIS 5e) and the early Holocene controlled feedback loops between sea surface temperatures, easterly winds, water evaporation, shifting of the Intertropical Convergence Zone, and circulation patterns of the Hadley and Walker cells. These insolation changes thus indirectly controlled rainfall at a given latitude. Cecca et al. (2005) documented latitudinal shifts of climate belts based on the distribution of coral reefs and ammonites during the Oxfordian. Following the general circulation model developed by Sellwood et al. (2000), they concluded that the late Oxfordian was characterized by low rainfall in the Tethyan Mediterranean area (0.5 to 2 mm per day) and slightly higher rainfall (2 to 4 mm per day) in central and northern Europe.

Orographic effects modifying the atmospheric circulation were probably minor as there was no high mountain range near the Jura platform but only widely dispersed, low-relief massifs (Fig. 5). Insolation minima corresponded to low sea levels (Fig. 13), and this explains why many sequence boundaries in the studied sections contain terrigenous material that was eroded from the hinterland under humid conditions.

More arid conditions prevailed during transgression and maximum flooding, when climate was warmer and sea level rose, allowing for the growth of coral reefs under oligotrophic conditions. However, nutrients were washed into the system, which stimulated microbial growth that eventually smothered the corals, as illustrated in Fig. 10. While corals could still grow at the beginning of the second 20 kyr sequence, they were suffocated by microbialites at the end of this elementary sequence when eutrophication increased. Towards the end of the transgressive part of the small-scale, 100 kyr sequence, eutrophication was such that corals could not grow anymore (Fig. 10). This evolution suggests that nutrients were washed in from the hinterland and affected the reef during transgression and maximum flooding, before the siliciclastics arrived and covered the coral–microbial buildup. The demise of Oxfordian coral reefs in the Swiss Jura due to nutrient and siliciclastic input was documented by Dupraz (1999) and Dupraz and Strasser (2002). Eutrophication can also be caused by increased upwelling bringing nutrients from deep to shallow waters. However, considering the position of the Jura platform far from the open Tethys ocean (Fig. 5), this scenario is less likely.

Védrine et al. (2007) showed that the morphology of oncoids in the Hauptmumienbank Member varied according to water depth, water energy, and terrigenous nutrient influx; all of these are related to climate changes induced by the 100 and 20 kyr orbital cycles. Analysing coral–microbialite relationships such as those illustrated in Fig. 10, Dupraz (1999) and Dupraz and Strasser (2002) came to the same conclusion. On a ramp at the southern margin of the French Jura platform, Olivier et al. (2011) described abundant microbial carbonates (oncoids and coral–microbialite reefs) that formed during the Bimammatum zone, i.e. during the interval shown in Fig. 7. This they explained by a humid and relatively cool climate, terrigenous nutrient input, and mesotrophic conditions.

On the Aalenian to Oxfordian platform in western France, Andrieu et al. (2016) found that high carbonate productivity correlated with high eccentricity intervals, which promoted a dry climate and oligotrophic conditions for the carbonate-producing organisms. However, they referred to the ca. 9 Myr eccentricity cycle evidenced by Martinez and Dera (2015) in Jurassic to Early Cretaceous Tethyan sections.

A rapid shift from a cool and humid climate to warmer and more arid conditions is recorded in the North Sea at the end of the early Oxfordian (Densiplicatum subzone) and may have been of global extent, related to hydrothermalism at the onset of rifting in the North and South Atlantic (Abbink et al., 2001). From the middle Oxfordian to the Kimmeridgian, the general evolution was towards warmer and more arid conditions (Olivier et al., 2015; Carpentier et al., 2010). However, at the beginning of the late Oxfordian, rainfall increased in the Paris Basin (Brigaud et al., 2014). In the Swiss Jura, this corresponds to the interval around sequence boundary Ox 6 where siliciclastics and terrigenous organic matter are present (Fig. 7). Superimposed on these general trends, rainfall patterns were controlled by the orbital cycles. Above sequence boundary Ox 6, siliciclastics predominate. A well-developed medium-scale sequence controlled by the 405 kyr long eccentricity cycle then leads to sequence boundary zone Ox 7, which again is rich in siliciclastics. Arid conditions are indicated by evaporites in the middle of the next medium-scale sequence (Figs. 7, 9). SB Ox 8 contains only a thin interval of terrigenous material, thus confirming the general trend towards arid conditions in the early Kimmeridgian (Abbink et al., 2001). An interesting issue is the presence of siliciclastics at the maximum flooding of the medium-scale sequences (e.g. at the top of the Steinebach Member at metre 40; Fig. 7). Either there was a pulse of rainfall related to the northward expansion of the Intertropical Convergence Zone (e.g. Khon et al., 2012) or sea level was high enough to reach deep into the land areas and mobilize terrigenous material there.

In the Hautes-Roches and Gorges de Court sections, siliciclastics and plant material are present below sequence boundary Ox 6 (Fig. 7). Marls become important above Ox 6 in all sections shown in the figure, up to the major transgressive surface marking the base of the Steinebach and Hauptmumienbank members. This implies rainfall over the emerged land areas. The same interval also corresponds to the end of the large-scale regressive trend documented in European basins by Hardenbol et al. (1998), meaning that sea level was generally low, that more land was exposed to erosion, and that terrigenous material was forced to prograde into the ocean. More exposed land areas also led to more continental weathering, potentially drawing down atmospheric CO_2 levels. This has been modelled for million-year timescales by e.g. Goddéris et al. (2012), and the feedbacks between weathering and atmospheric CO_2 have also been discussed for future climate change (e.g. Beaulieu et al., 2012). In hemipelagic carbonates in the Jura Mountains and the Vocontian basin, Padden et al. (2002) found negative $\delta^{13}C$ excursions in the Transversarium and Bifurcatus ammonite zones (i.e. below SB Ox 6; Fig. 3), which are explained by the release of methane, introducing light ^{12}C into the marine carbon reservoir. If methane was also released into the atmosphere, it may have contributed to greenhouse effects that led to warming and increased precipitation over the land areas and thus to more siliciclastic input. The general cooling trend due to CO_2 drawdown may thus have been punctuated by short warming periods, but humidity was maintained.

Clay minerals also hold palaeoclimatic information, and the ratio between kaolinite and illite is commonly used to define humid versus arid conditions during soil formation: a high K/I ratio generally indicates a warmer and more humid climate (Curtis, 1990; Thiry, 2000). On the Jura platform, kaolinite becomes dominant over illite above sequence boundary Ox 6 (Gygi and Persoz, 1986). However, rates of soil formation are slow, and the time resolution of the clays deposited in the ocean therefore is considered to be low (1 to 2 Myr; Thiry, 2000). Furthermore, clays may be stored in deltas, ponded in lagoons, and distributed across the platform at different times. Thus, the climate information they contain may not correspond to the time at which they were finally recorded at a given position on the platform. Nevertheless, Védrine (2007) and Strasser et al. (2012) found that in the Hauptmumienbank Member the K/I ratio increases slightly around sequence boundaries and maximum flooding intervals of the small-scale, 100 kyr sequences. At the sequence boundaries, kaolinite is associated with quartz. This implies that the climate was humid during low sea level, and quartz and clays were eroded from the hinterland. At maximum flooding, with the ocean encroaching on the land areas, only clays were mobilized and transported across the platform. As discussed above, there might have also been a humid phase during maximum flooding related to the northward expansion of the Intertropical Convergence Zone.

The importance of the palaeolatitude in the distribution of rainfall patterns is illustrated by the comparison of Oxfordian sequences in the Swiss Jura and in the Soria region of Spain (Pittet and Strasser, 1998). In the small-scale, 100 kyr sequences in the Swiss Jura, siliciclastics are commonly concentrated around the sequence boundaries, while in Spain they occur preferentially in the maximum flooding intervals. The sections studied in Spain were at a palaeolatitude of 23 to 24° N (Dercourt et al., 1993), i.e. 3 to 4° farther south than the Jura sections. This latitudinal difference may explain why the humid periods during a 100 kyr cycle did not occur at the same time.

3.4 Wind and storms

During the Oxfordian, the Jura platform was situated in the subtropical zone and under the influence of trade winds. These would have forced currents into a westerly direction, but the presence of several emergent landmasses certainly deviated these currents. Nevertheless, considering the palaeogeography shown in Fig. 5, it is probable that the siliciclastics found on the Jura platform stemmed mainly from the Bohemian Massif. This massif lies on a more northern palaeolatitude, which implies that rainfall could have increased weathering and erosion there, while on the Jura platform more arid conditions prevailed. This may explain the direct superposition of marly layers on a dolomitized carbonate facies (Fig. 9). Nutrients in a dissolved state travelled faster across the platform and nourished the microbialites before the siliciclastics arrived (Fig. 10).

The cross-bedded ooid and bioclastic shoals encountered in the studied outcrops were mainly controlled by tidal currents, the direction of which varied according to the platform morphology.

Storms episodically affected the platform. Being far away from the open ocean, fetch was reduced. Nevertheless, the presence of reef rubble and washovers (Fig. 10) testifies to currents and waves strong enough to dismantle a reef and throw sediment over topographic highs. As is the case today with global warming, storm frequency and intensity were likely to increase when water temperature increased (Masson-Delmotte et al., 2022). Pittet and Gorin (1997) noted an increase in tempestites and washovers in the marly interval above sequence boundary Ox 6, which corresponds to the highstand of the corresponding 400 kyr sequence (Fig. 7). The abundance of siliciclastics in the interval, however, implies humid conditions and generally low sea level with a cooler climate. Possibly, a preservational bias has to be considered: in very shallow water or in the intertidal zone, only thin layers of sediment are deposited during a storm (for example, on the tidal flats of the Bahamas; Rankey et al., 2004). In deeper water, however, there is room to accommodate the reworked sediment. In the Kimmeridgian of Aquitaine (France), limestone–marl alternations are regularly interrupted by thin tempestite layers (Colombié et al., 2018). It has been shown that tempestite occurrence (and thus storm frequency) was highest during maximum flooding intervals of the sequences controlled by the 405 kyr long eccentricity cycle. Maximum flooding relates to rapid sea level rise forced by a warming of the climate.

3.5 Combined climatic effects at orbital scale

From the discussion above it becomes clear that the sedimentary record of shallow marine carbonate systems is controlled by several interdependent climatic processes. For the Oxfordian in the Swiss Jura, two models are proposed to explain the interactions of climate drivers and the resulting sedimentary record. The shortest decipherable timescale is chosen, i.e. a sea level cycle related to the 20 kyr orbital precession cycle. This approaches the time frame in which Holocene processes took place during the last 10 kyr, and comparisons are thus facilitated. For example, Parkinson (1989) describes a Holocene sedimentary sequence in southwestern Florida where transgression over the Pleistocene substrate started at about 10 ka BP. A first deposit of peat was followed by transgressive coastal marine sediments. As sea level rise decelerated, the turn-around to regressive highstand deposits occurred at 3.5 to 3.2 ka BP, leading to intertidal oyster accumulations and mangrove islands. From 1900 to 2021, however, sea level in southern Florida rose at an average of 2.52 mm yr^{-1}, and from 2000 to 2021 this average was 6.47 mm yr^{-1} (Parkinson and Wdowinski, 2021). Sediment accumulation cannot keep up with this rate, and a transgression occurs. For comparison, the reconstructed Oxfordian rates of the fastest sea level rise are 0.2 to 0.3 mm yr^{-1} (see Sect. 3.2). This recent transgression is due to anthropogenically induced global warming that overrides the orbitally controlled insolation, which has diminished since its peak about 9000 years ago (Fig. 1; Crucifix et al., 2002).

To simplify, the sea level cycle in the models is assumed to have been symmetrical, but asymmetries due to processes mentioned above were certainly present. Accommodation gain is the sum of subsidence and long-term sea level rise. Subsidence in the Late Jurassic of the Jura platform was about 3 m per 100 kyr (Wildi et al., 1989). Long-term sea level rise is taken from the example in Fig. 12: 405 kyr to accumulate 26 m of decompacted sediment up to the tidal flat at sequence boundary Ox 8 (Fig. 9) results in 6.4 m per 100 kyr of total accommodation gain. This value minus the subsidence gives 3.4 m per 100 kyr long-term sea level rise. This is consistent with the major transgressive evolution in European basins from the Oxfordian to the Kimmeridgian, which started in the Semimammatum subzone with the major transgressive surface above sequence boundary Ox 6 (Hardenbol et al., 1998).

Two hypothetical models for the formation of depositional sequences are presented in Fig. 14. Model (a) (inspired from the middle part of the detailed Gorges de Court section; Fig. 9) describes the formation of an elementary sequence controlled by the 20 kyr precession cycle. This cycle is situated in the middle of a 100 kyr and/or 405 kyr cycle when insolation was high (Fig. 1). It is thus expected that sea level amplitudes on the 20 kyr scale were relatively high: of the order of a few metres (Figs. 12, 13). For the model, an amplitude of 3 m is chosen, and it is assumed that the base and top of the elementary sequence are at zero sea level. At the beginning of the cycle, the climate at the given subtropical latitude is humid, sea level is low, and siliciclastics are eroded from the emergent massifs, transported across the platform, and accumulated at the base of the sequence. Accommodation is low, and only a thin sediment layer can be recorded. With increasing insolation, the climate becomes progressively dry, the water becomes warmer and expands to rise sea level, coastlines retreat, rivers are less active, and siliciclastic input is reduced. At still low sea level, a tidal flat forms and can keep up for a while with rising sea level before it is drowned. With increasing water depth, conditions become ideal for carbonate production, and high accommodation gives room for the accumulation of ooid shoals and the growth of coral reefs. Of course, depending on the position on the platform, lateral facies variations are considerable: while at one point reef growth can keep up with rising sea level, at another point a deep lagoon develops (Fig. 2). The demise of the hypothetical coral reef could be due to eutrophication like in the example of Fig. 10 or to smothering by sediment that progrades because sea level rise slows down. Still under a warm and arid climate, sea level rise slows down and allows the sediment to fill in the available space. If sea level then drops below the sediment surface and the climate becomes humid again, a karst develops. If the sediment surface stays in the intertidal or supratidal zone as in Fig. 14a, evaporites form in a sabkha under an arid climate. When insolation decreases in the second part of the 20 kyr cycle, climate at this given latitude becomes cooler and more humid, and the cycle starts over again. It is clear from Fig. 14a that the time interval of vigorous sedimentation covers only a short part of the 20 000 years and that much time is represented by the sequence boundaries (e.g. Strasser, 2015).

Model (b) (inspired from the Ox 7 sequence boundary zone at Gorges de Court; Fig. 9) illustrates the situation during generally low insolation at the 100 kyr and/or 405 kyr scale (Fig. 1). Sea level amplitudes at the 20 kyr scale are low (Fig. 13), and an amplitude of 1 m is chosen for the model. The climate is rather cool and humid. Consequently, more land areas are exposed, rainfall favours their erosion, rivers are active, and deltas prograde. Consequently, the elementary sequence will be dominated by siliciclastics. A relatively short time interval of less humid conditions and warmer temperatures allows for some carbonate production, but siliciclastics are still present. Again, much time of this cycle is spent in intertidal to supratidal conditions.

From the graphs in Fig. 14 (representing decompacted sediment) sedimentation rates can be deduced. At the fastest accumulation on the seafloor during about 2000 years (corresponding to the fastest rise of sea level) about 1 m of coral reef is built in model (a). This results in a sedimentation rate of $0.5\,\mathrm{mm\,yr^{-1}}$. In model (b), representing a siliciclastic-dominated scenario, only 30 cm of lagoonal facies accumulate in 2000 years, giving a sedimentation rate of $0.15\,\mathrm{mm\,yr^{-1}}$. Holocene rates for these environments reach $14\,\mathrm{mm\,yr^{-1}}$ for a healthy reef and between 1 and $2\,\mathrm{mm\,yr^{-1}}$ for a tidal flat (Enos, 1991; Strasser and Samankassou, 2003). This discrepancy does not necessarily imply that sedimentation rates in the Oxfordian were generally lower than in the Holocene but rather that the time of non-deposition, reworking, and/or condensation is underestimated in the models (Sadler, 1994; Strasser, 2015).

These two models must undergo many modifications depending on the position on the platform, the currents distributing nutrients and siliciclastics, and the ecology of the carbonate-producing organisms. Also, they are idealized cases in which facies evolution exhibits deepening–shallowing trends within an elementary sequence. In the studied sections, this is not always the case, and facies may stay the same throughout the sequence (with the exception of the marly layers at the sequence boundaries). This may be due to bioturbation that homogenized the sediment in a lagoon or to constant reworking by waves and currents in the case of an ooid shoal. Nevertheless, the models illustrate the potential of shallow marine carbonates to record climate changes at a relatively high time resolution.

4 Conclusions

Orbital cycles controlling the energy received by the Earth from the sun are important drivers of environmental changes that occur on land and in the ocean. In the case study presented here, it is shown that, during the Oxfordian (Late Jurassic), the shallow marine carbonate systems on the platform of the Swiss Jura Mountains reacted to these changes at the frequencies of the long and short eccentricity cycles (405 and 100 kyr, respectively) as well as the precession cycle (20 kyr in the Oxfordian). The main controlling factors were metre-scale sea level changes and climate changes between humid and arid. Insolation changes translated more or less directly into eustatic sea level changes through thermal expansion and retraction of the ocean surface waters. In addition, glacioeustasy and aquifer eustasy certainly occurred but are difficult to quantify. At all frequencies, humid and cool periods corresponded to low insolation and low sea level, while arid and warm periods prevailed during intervals of high insolation and high sea level. At a subtropical latitude on the shallow marine platform, many carbonate-producing organisms (e.g. algae, foraminifera, gastropods, bivalves, serpulids) were present, and coral reefs were especially sensitive to environmental changes. Ooids, oncoids, and microbialites also contributed to the sediment.

An interval of 1.2 Myr is discussed, calibrated by biostratigraphy, chronostratigraphy, and sequence stratigraphy. Three detailed sections are chosen to illustrate the evo-

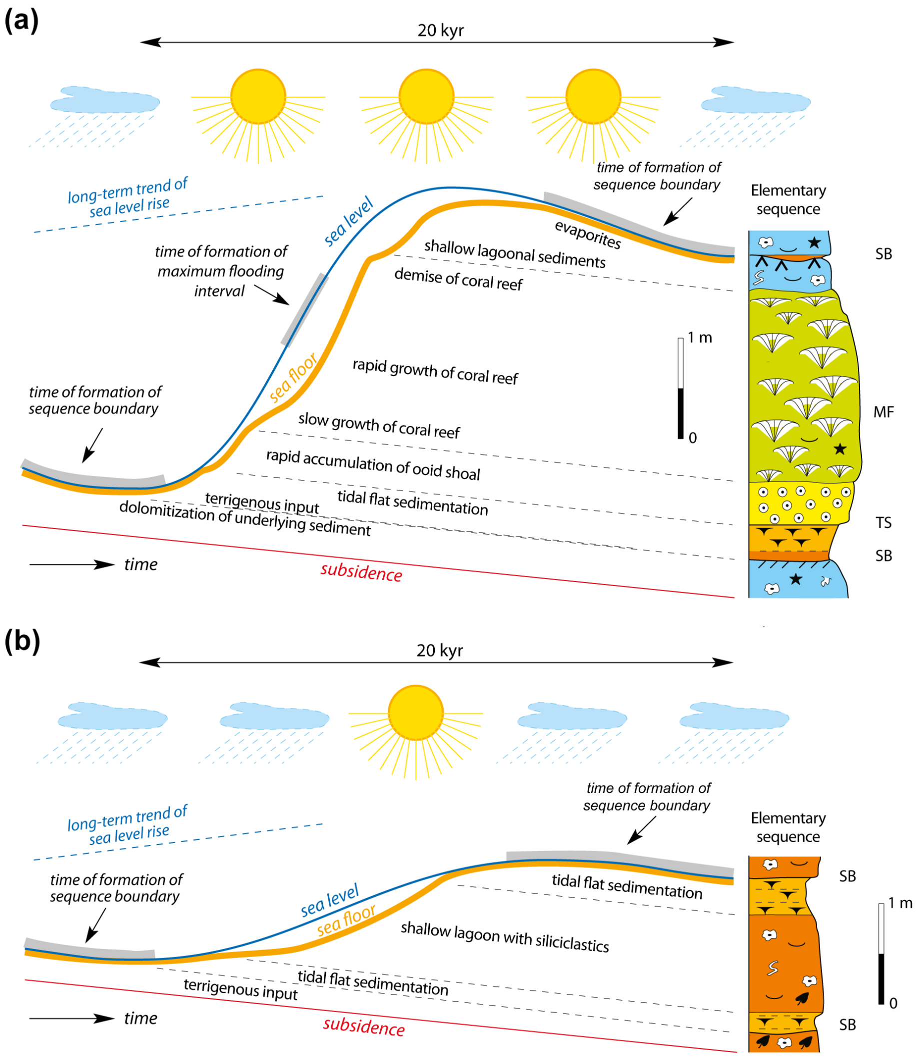

Figure 14. Conceptual models that explain the formation of elementary sequences as a function of climate changes in tune with the orbital precession cycle. **(a)**: high insolation within a 100 and/or 405 kyr eccentricity cycle; **(b)**: low insolation. For discussion refer to the text. Symbols and abbreviations are as in Fig. 7.

lution of the facies and stacking pattern of the depositional sequences within this interval. During high insolation in the middle of a 405 kyr cycle, high amplitudes of sea level fluctuations and arid conditions allowed for the development of ooid shoals and coral reefs. However, the corals were regularly encrusted by microbialites, suggesting nutrient input even under an arid climate. At low insolation, low sea level amplitudes, and more humid and cooler conditions, siliciclastics were washed into the system and hampered the organic carbonate production.

The orbital frequencies are reflected in the hierarchical stacking of sequences: medium- and small-scale sequences formed in tune with the 405 and 100 kyr eccentricity cycles, respectively, while the 20 kyr precession cycles controlled the formation of elementary sequences. The obliquity cycle was not detected in the studied outcrops. After decompaction of the sections and estimation of the water depths in which the different facies evolved, a composite sea level curve has been reconstructed. It compares well with the curve of insolation changes over the last 550 kyr.

Based on the studied sections and the facies encountered, two models are presented. Model (a) describes the growth and demise of a coral reef in warm waters and a high-amplitude sea level rise to accommodate the reef. Arid conditions are exemplified by evaporites. Model (b) simulates a low-amplitude sea level cycle and rainfall in the hinterland that washed siliciclastics and plant matter onto the platform. The sedimentation rates deduced from the models are below those of Holocene sedimentary environments, implying that the time of non-deposition in the models is probably underestimated.

Despite the high lateral and vertical facies variability on the Oxfordian carbonate platform, despite the uncertainties in attributing water depth and compaction factors to the different facies, and despite the multiple feedback loops between insolation at the top of the atmosphere and the depositional environment, this study demonstrates the potential of shallow marine carbonates to record climate changes at the frequencies of orbital cycles. The time resolution of 20 000 years (the precession cycle) offers the opportunity to estimate rates of sea level change, ecological processes, and sediment accumulation in the geologic past. The interpretation of the evolution of ancient sedimentary systems can thus be refined and better compared to today's changes in ecosystems. Concerning the rate of climate change, this study implies that anthropogenically induced global warming and subsequent sea level rise today are occurring more than 10 times faster than the fastest rise reconstructed for the Oxfordian.

Data availability. All data are published in the cited papers and theses.

Competing interests. The author has declared that there are no competing interests.

Disclaimer. Publisher's note: Copernicus Publications remains neutral with regard to jurisdictional claims in published maps and institutional affiliations.

Acknowledgements. I thank the editor Denis-Didier Rousseau for having invited me to write this contribution. It is based on fieldwork and research carried out by many MSc and PhD students at the University of Fribourg and was financed mainly by the Swiss National Science Foundation. Their intellectual, institutional, and financial support is gratefully acknowledged. I also thank the reviewers Simon Andrieu and Marc Aurell, whose constructive comments greatly improved the paper.

Financial support. I acknowledge the funding by the Swiss National Science Foundation (grant nos. 20-41888, 20-43150, 20-46625, 20-56491, 20-67736, 20-109214).

Review statement. This paper was edited by Denis-Didier Rousseau and reviewed by Marc Aurell and Simon Andrieu.

References

Abbink, O., Targarona, J., Brinkhuis, H., and Visscher, H.: Late Jurassic to earliest Cretaceous palaeoclimatic evolution of the southern North Sea, Global Planet. Change, 30, 231–256, https://doi.org/10.1016/S0921-8181(01)00101-1, 2001.

Allenbach, R. P.: Synsedimentary tectonics in an epicontinental sea: a new interpretation of the Oxfordian basins of northern Switzerland, Eclogae Geol. Helv., 94, 265–287, 2001.

Andrieu, S., Brigaud, B., Barbarand, J., Lasseur, E., and Saucède, T.: Disentangling the control of tectonics, eustasy, trophic conditions and climate on shallow-marine carbonate production during the Aalenian–Oxfordian interval: From the western France platform to the western Tethyan domain, Sed. Geol., 345, 54–84, https://doi.org/10.1016/j.sedgeo.2016.09.005, 2016.

Amies, J. D., Rohling, E. J., Grant, K. M., Rodriguez-Sanz, L., and Marino, G.: Quantification of African monsoon runoff during last interglacial sapropel S5, Paleoceanogr. Paleoclim., 34, 1487–1516, https://doi.org/10.1029/2019PA003652, 2019.

Anderson, T. F. and Arthur, M. A.: Stable isotopes of oxygen and carbon and their application to sedimentology and paleoenvironmental problems, SEPM Short Course, 10, 151 p., 1983.

Armstrong, H. A., Wagner, T., Herrinshaw, L. G., Farnsworth, A. J., Lunt, D. J., Harland, M., Imber, J., Loptson, C., and Atar, E. F. L.: Hadley circulation and precipitation changes controlling black shale deposition in the Late Jurassic Boreal Seaway, Paleoceanography, 31, 1041–1053, https://doi.org/10.1002/2015PA002911, 2016.

Beaulieu, E., Goddéris, Y., Donnadieu, Y., Labat, D., and Roelandt, C.: High sensitivity of the continental-weathering carbon dioxide sink to future climate change, Nat. Clim. Change, 2, 346–349, https://doi.org/10.1038/NCLIMATE1419, 2012.

Berger, A., Loutre, M.-F., and Laskar, J.: Stability of the astronomical frequencies over the Earth's history for paleoclimatic studies, Science, 255, 560–566, https://doi.org/10.1126/science.255.5044.560, 1992.

Berggren, W. A., Kent, D. V., Aubry, M. P., and Hardenbol, J. (Eds.): Geochronology, Time Scales and Global Stratigraphic Correlation, SEPM Spec. Publ., 54, 386 pp., 1995.

Boulila, S., Galbrun, B., Hinnov, L. A., Collin, P.-Y., Ogg, J. G., Fortwengler, D., and Marchand, D.: Milankovitch and sub-Milankovitch forcing of the Oxfordian (Late Jurassic) Terres Noires Formation (SE France) and global implications, Basin Res., 22, 717–732, https://doi.org/10.1111/j.1365-2117.2009.00429.x, 2010.

Brigaud, B., Vincent, B., Carpentier, C., Robin, C., Guillocheau, F., Yven, B., and Huret, E.: Growth and demise of the Jurassic carbonate platform in the intracratonic Paris Basin (France): Interplay of climate change, eustasy and tectonics, Marine Petrol. Geol., 53, 3–29, https://doi.org/10.1016/j.marpetgeo.2013.09.008, 2014.

Carpentier, C., Lathuilière, B., and Ferry, S.: Sequential and climatic framework of the growth and demise of a carbonate platform: implications for the peritidal cycles (Late Jurassic, north-eastern France), Sedimentology, 57, 985–1020, https://doi.org/10.1111/j.1365-3091.2009.01128.x, 2010.

Carpentier, C., Martin-Garin, B., Lathuilière, B., and Ferry, S.: Correlation of reefal Oxfordian episodes and climatic implications in the eastern Paris Basin (France), Terra Nova, 18, 191–201, https://doi.org/10.1111/j.1365-3121.2006.00679.x, 2006.

Catuneanu, O., Abreu, V., Bhattacharya J. P., Blum, M. D, Dalrymple, R. W., Eriksson, P. G., Fielding, C. R., Fisher, W. L., Galloway, W. E., Gibling, M. R., Giles, K. A., Holbrook, J. M., Jordan, R., Kendall, C. G. St. C., Macurda, B., Martinsen, O. J., Miall, A. D., Neal, J. E., Nummedal, D., Pomar L., Posamentier H. W., Pratt, B. R., Sarg, J. F., Shanley, K. W., Steel, R. J., Strasser, A., Tucker, M. E., and Winker, C.: Towards the standardization of sequence stratigraphy, Earth-Sci. Rev., 92, 1–33, https://doi.org/10.1016/j.earscirev.2008.10.003, 2009.

Cecca, F., Martin-Garin, B., Marchand, D., Lathuilière, B., and Bartolini, A.: Paleoclimatic control of biogeographic and sedimentary events in Tethyan and peri-Tethyan areas during the Oxfordian (Late Jurassic), Palaeogeo., Palaeoclim., Palaeoecol., 222, 10–32, https://doi.org/10.1016/j.palaeo.2005.03.009, 2005.

Church, J. A. and Clark, P. U. (coordinating lead authors): Sea Level Change, in: Climate Change 2013: The Physical Science Basis. Contribution of Working Group I to the Fifth Assessment Report of the Intergovernmental Panel on Climate Change, Cambridge Univ. Press, 1137–1216, 2013.

Colombié, C., Carcel, D., Lécuyer, C., Ruffel, A., and Schnyder, J.: Temperature and cyclone frequency in Kimmeridgian Greenhouse period (late Jurassic), Global Planet. Change, 170, 126–145, https://doi.org/10.1016/j.gloplacha.2018.08.005, 2018.

Colombié, C., Lécuyer, C., and Strasser, A.: Carbon- and oxygen-isotope records of palaeoenvironmental and carbonate production changes in shallow-marine carbonates (Kimmeridgian, Swiss Jura), Geol. Mag., 148, 133–153, https://doi.org/10.1017/S0016756810000518, 2011.

Crucifix, M., Loutre, M.-F., Tulkens, P., Fichefet, T., and Berger, A. : Climate evolution during the Holocene: a study with an Earth system model of intermediate complexity, Clim. Dynam., 19, 43–60, https://doi.org/10.1007/s00382-001-0208-6, 2002.

Curtis, C. D.: Aspects of climate influence on the clay mineralogy and geochemistry of soils, paleosols and clastic sedimentary rocks, J. Geol. Soc. London, 147, 351–357, https://doi.org/10.1144/gsjgs.147.2.0351, 1990.

Davies, A., Gréselle, B., Hunter, S. J., Baines, G., Robson, C., Haywood, A., David C. Ray, D. C., Simmons, M. D., and van Buchem, F. S. P.: Assessing the impact of aquifer-eustasy on short-term Cretaceous sea-level, Cretaceous Res., 112, 104445, https://doi.org/10.1016/j.cretres.2020.104445, 2020.

Dercourt, J., Ricou, L. E., and Vrielynck, B. (Eds): Atlas: Tethys Palaeoenvironmental Maps, Gauthier-Villars, Paris, 1993.

de Winter, N. J., Zeeden, C., and Hilgen, F. J.: Low-latitude climate variability in the Heinrich frequency band of the Late Cretaceous greenhouse world, Clim. Past, 10, 1001–1015, https://doi.org/10.5194/cp-10-1001-2014, 2014.

Dunham, R. J.: Classification of carbonate rocks according to depositional texture, AAPG Mem., 1, 108–121, 1962.

Dupraz, C.: Paléontologie, paléoecologie et évolution des faciès récifaux de l'Oxfordien moyen-supérieur (Jura suisse et français), Ph.D. thesis, GeoFocus, 2, Fribourg, Switzerland, 247 pp., 1999.

Dupraz, C. and Strasser, A.: Nutritional modes in coral-microbialite reefs (Jurassic, Oxfordian, Switzerland): evolution of trophic structure as a response to environmental change, Palaios, 17, 449–471, https://doi.org/10.1669/0883-1351(2002)017<0449:NMICMR>2.0.CO;2, 2002.

Embry, A. F. and Klovan, J. E.: A late Devonian reef tract on northeastern Banks Island, N.W.T., Bull. Canadian Petrol. Geol., 19, 730–781, 1971.

Enos, P.: Sedimentary parameters for computer modeling, Kansas Geol. Survey Bull., 233, 63–99, 1991.

Feng, R. and Poulsen, C. J.: Andean elevation control on tropical Pacific climate and ENSO, Paleoceanography, 29, 795–809, https://doi.org/10.1002/2014PA002640, 2014.

Flügel, E.: Microfacies of Carbonate Rocks, Springer, Berlin, Germany, 976 pp., ISBN 354022016X, 2004.

Frakes, L. A., Francis, J. E., and Syktus, J. I.: Climate Modes of the Phanerozoic, Cambridge Univ. Press, 274 pp., 1992.

Goddéris, Y., Donnadieu, Y., Lefebvre, V., Le Hir, G., and Nardin, E..: Tectonic control of continental weathering, atmospheric CO_2, and climate over Phanerozoic times, C. R. Geoscience, 344, 652–662, https://doi.org/10.1016/j.crte.2012.08.009, 2012.

Goldhammer, R. K.: Compaction and decompaction algorithms for sedimentary carbonates, J. Sed. Res., 67, 26–35, https://doi.org/10.1306/D42684E1-2B26-11D7-8648000102C1865D, 1997.

Gradstein, F. M., Ogg, J. G., Schmitz, M. D., and Ogg, G. (Eds.): Geologic Time Scale 2020, Vol. 1, Elsevier, Amsterdam, The Netherlands, 1357 pp., 2020.

Gygi, R. A.: Datierung von Seichtwassersedimenten des Späten Jura in der Nordwestschweiz mit Ammoniten, Eclogae Geol. Helv., 88, 1–58, 1995.

Gygi, R. A.: Integrated stratigraphy of the Oxfordian and Kimmeridgian (Late Jurassic) in northern Switzerland and adjacent southern Germany, Mem. Swiss Acad. Sci., 104, 152 pp., 2000.

Gygi, R. A. and Persoz, F.: Mineralostratigraphy, litho- and biostratigraphy combined in correlation of the Oxfordian (Late Jurassic) formations of the Swiss Jura range, Eclogae Geol. Helv., 79, 385–454, 1986.

Gygi, R. A., Coe, A. L., and Vail, P. R.: Sequence stratigraphy of the Oxfordian and Kimmeridgian stages (Late Jurassic) in northern Switzerland, SEPM Spec. Publ., 60, 527–544, 1998.

Hallock, P. and Schlager, W.: Nutrient excess and the demise of coral reefs and carbonate platforms, Palaios, 1, 389–398, 1986.

Hardenbol, J., Thierry, J., Farley, M. B., Jacquin, T., de Graciansky, P.-C., and Vail, P. R.: Jurassic sequence chronostratigraphy, in: Mesozoic and Cenozoic Sequence Stratigraphy of European Basins, edited by: de Graciansky, P.-C., Hardenbol, J., Jacquin, T., and Vail, P. R, SEPM Spec. Publ., 60, 1998.

Hesselbo, S. P., Ogg, J. G., and Ruhl, M.: The Jurassic Period, in: Geologic Time Scale 2020, vol. 1, edited by: Gradstein, F. M., Ogg, J. G., Schmitz, M. D., and Ogg, G., Elsevier, Amsterdam, The Netherlands, 955–1021, 2020.

Hinnov, L. A.: Cyclostratigraphy and astrochronology in 2018, in: Stratigraphy and Timescales, vol. 3, edited by: Montenari, M., Elsevier, Amsterdam, The Netherlands, 1–80, https://doi.org/10.1016/bs.sats.2018.08.004, 2018.

Huang, C.: Astronomical time scale for the Mesozoic, in: Stratigraphy and Timescales, vol. 3, edited by: Montenari, M., Elsevier, Amsterdam, The Netherlands, 81–150, https://doi.org/10.1016/bs.sats.2018.08.005, 2018.

Hug, W.: Sequenzielle Faziesentwicklung der Karbonatplattform des Schweizer Jura im späten Oxford und frühesten Kimmeridge, Ph.D. thesis, GeoFocus 7, Univ. Fribourg, Switzerland, 156 pp., 2003.

Ikeda, M., Ozaki, K., and Legrand, J.: Impact of 10-Myr scale monsoon dynamics on Mesozoic climate and ecosystems, Nat. Sci. Rep., 10, 11984, https://doi.org/10.1038/s41598-020-68542-w, 2020.

Immenhauser, A., Della Porta, G., Kenter, J. A. M., and Bahamonde, J. R.: An alternative model for positive shifts in shallow-marine carbonate $\delta^{13}C$ and $\delta^{18}O$, Sedimentology, 50, 953–959, https://doi.org/10.1046/j.1365-3091.2003.00590.x, 2003.

Jacobs, D. K. and Sahagian, D. L.: Climate-induced fluctuations in sea level during non-glacial times, Nature, 361, 710–712, https://doi.org/10.1038/361710a0, 1993.

Jordan, P.: Géologie de la région de Montoz (Jura bernois) avec analyse séquentielle de deux profiles de l'Oxfordien moyen et supérieur. Unpubl. diploma thesis, Univ. Fribourg, Switzerland, 104 pp., 1999.

Khon, V. C., Park, W., Latif, M., Mokhov, I. I., and Schneider, B.: Tropical circulation and hydrological cycle response to orbital forcing, Geophys. Res. Lett., 39, L15708, https://doi.org/10.1029/2012GL052482, 2012.

Laskar, J., Fienga, A., Gastineau, M., and Manche, H.: La2010: a new orbital solution for the long term motion of the Earth, Astron. Astrophys., 532, A89, https://doi.org/10.1051/0004-6361/201116836, 2011.

Laurin, J., Meyers, S. R., Uličnyì, D., Jarvis, I., and Sageman, B. B.: Axial obliquity control on the greenhouse carbon budget through middle- to high-latitude reservoirs, Paleoceanography, 30, 133–149, https://doi.org/10.1002/2014PA002736, 2015.

Lefort, A., Lathuilière, B., Carpentier, C., and Huault, V.: Microfossil assemblages and relative sea-level fluctuations in a lagoon at the Oxfordian/Kimmeridgian boundary (Upper Jurassic) in the eastern part of the Paris Basin, Facies, 57, 649–662, https://doi.org/10.1007/s10347-010-0259-4, 2011.

Leinfelder, R. R., Schmid, D. U., Nose, M., and Werner, W.: Jurassic reef patterns – the expression of a changing globe, SEPM Spec. Publ., 72, 465–520, 2002.

Louis-Schmid, B., Rais, P., Schaeffer, P., Bernasconi, S. M., and Weissert, H.: Plate tectonic trigger of changes in pCO_2 and climate in the Oxfordian (Late Jurassic): Carbon isotope and modeling evidence, Earth Planet. Sci. Lett., 258, 44–60, https://doi.org/10.1016/j.epsl.2007.03.014, 2007.

Lourens, L. J., Hilgen, F. J., Raffi, I., and Vergnaud-Grazzini, C.: Early Pleistocene chronology of the Vrica Section (Calabria, Italy), Paleoceanography, 11, 797–812, https://doi.org/10.1029/96PA02691, 1996.

Martin-Garin, B., Lathuilière, B., Geister, J., and Ramseyer, K.: Oxygen isotopes and climatic control of Oxfordian coral reefs (Jurassic, Tethys), Palaios, 25, 721–729, https://doi.org/10.2110/palo.2010.p10-027r, 2010.

Martinez, M.: Mechanisms of preservation of the eccentricity and longer-term Milankovitch cycles in detrital supply and carbonate production in hemipelagic marl-limestone alternations, in: Stratigraphy and Timescales, vol. 3, edited by: Montenari, M., Elsevier, Amsterdam, The Netherlands, 189–218, https://doi.org/10.1016/bs.sats.2018.08.002, 2018.

Martinez, M. and Dera, G.: Orbital pacing of carbon fluxes by a $\sim$9-My eccentricity cycle during the Mesozoic, P. Natl. Acad. Sci. USA, 112, 12604–12609, https://doi.org/10.1073/pnas.1419946112, 2015.

Masson-Delmotte, V., Zhai, P., Pirani, A., Connors, S. L., Péan, C., Berger, S., Caud, N., Chen, Y., Goldfarb, L., Gomis, M. I., Huang, M., Leitzell, K., Lonnoy, E., Matthews, J. B. R., Maycock, T. K., Waterfield, T., Yelekçi, O., Yu, R., and B. Zhou, B. (Eds.): Climate Change 2021: The Physical Science Basis. Contribution of Working Group I to the Sixth Assessment Report of the Intergovernmental Panel on Climate Change, Cambridge Univ. Press, 2022.

Matthews, M. D. and Perlmutter, M. A.: Global cyclostratigraphy: an application to the Eocene Green River basin, in: Orbital Forcing and Cyclic Sequences, edited by: de Boer, P. and Smith, D. G., IAS Spec. Publ., 19, 459–481, 1994.

Mitchum Jr., R. M. and Van Wagoner, J. C.: High-frequency sequences and their stacking patterns: sequence-stratigraphic evidence of high-frequency eustatic cycles, Sed. Geol., 70, 131–160, https://doi.org/10.1016/0037-0738(91)90139-5, 1991.

Montañez, I. A. and Osleger, D. A.: Parasequence stacking patterns, third-order accommodation events, and sequence stratigraphy of Middle to Upper Cambrian platform carbonates, Bonanza King Formation, southern Great Basin, AAPG Mem., 57, 305–326, 1993.

Ogg, J. G., Hinnov, L. A., and Huang, C.: Jurassic, in: The Geologic Time Scale 2012, edited by: Gradstein, F. M., Ogg, J. G., Schmitz, M. D., and Ogg, G., Elsevier, Amsterdam, The Netherlands, 731–791, 2012.

Ogg, J. G., Ogg, G., and Gradstein, F.: A Concise Geologic Time Scale 2016, Elsevier, Amsterdam, The Netherlands, 234 pp., ISBN 978-0-444-63771-0, 2016.

Olivier, N., Cariou, E., and Hantzpergue, P.: Evolution of a late Oxfordian – early Kimmeridgian carbonate platform, French Jura Mountains, Swiss J. Geosci., 108, 273–288, https://doi.org/10.1007/s00015-015-0189-9, 2015.

Olivier, N., Colombié, C., Pittet, B., and Lathuilière, B.: Microbial carbonates and corals on the marginal French Jura platform (Late Oxfordian, Molinges section), Facies, 57, 469–492, https://doi.org/10.1007/s10347-010-0246-9, 2011.

Padden, M., Weissert, H., Funk, H., Schneider, S., and Gansner, C.: Late Jurassic lithological evolution and carbon-isotope stratigraphy of the western Tethys, Eclogae geol. Helv., 95, 333–346, 2002.

Parkinson, R. W.: Decelerating Holocene sea-level rise and its influence on Southwest Florida coastal evolution: a transgressive/regressive stratigraphy, J. Sed. Petrol., 59, 960–972, 1989.

Parkinson, R. W. and Wdowinski, S.: Accelerating sea level rise and the fate of South Florida coastal wetlands, SSRN, https://doi.org/10.2139/ssrn.3967429, 2021.

Pittet, B.: Contrôles climatiques, eustatiques et tectoniques sur des systèmes mixtes carbonates-siliciclastiques de plate-forme: exemples de l'Oxfordien (Jura suisse, Normandie, Espagne), Ph.D. thesis, Univ. Fribourg, Switzerland, 258 pp., 1996.

Pittet, B. and Gorin, G. E.: Distribution of sedimentary organic matter in a carbonate-siliciclastic platform environment: Oxfordian in the Swiss Jura Mountains, Sedimentology, 44, 915–937, https://doi.org/10.1046/j.1365-3091.1997.d01-58.x, 1997.

Pittet, B. and Strasser, A.: Long-distance correlations by sequence stratigraphy and cyclostratigraphy: examples and implications (Oxfordian from the Swiss Jura, Spain, and Normandy), Geol. Rundsch., 86, 852–874, https://doi.org/10.1007/s005310050181, 1998.

Plunkett, J. M.: Early Diagenesis of shallow platform carbonates in the Oxfordian of the Swiss Jura Mountains, PhD thesis, Univ. Fribourg, Switzerland, 155 pp., 1997.

Pratt, B. R. and James, N. P.: The St George Group (Lower Ordovician) of western Newfoundland: tidal flat island model for carbonate sedimentation in shallow epeiric seas, Sedimentology, 33, 313–343, https://doi.org/10.1111/j.1365-3091.1986.tb00540.x, 1986.

Railsback, L. B., Gibbard, P. L., Head, M. J., Voarintsoa, N. R. G., and Toucanne, S.: An optimized scheme of lettered marine isotope substages for the last 1.0 million years, and the climatostratigraphic nature of isotope stages and substages, Quaternary Sci. Rev., 111, 94–106, https://doi.org/10.1016/j.quascirev.2015.01.012, 2015.

Rais, P., Louis-Schmid, B., Bernasconi, S. M., and Weissert, H.: Palaeoceanographic and palaeoclimatic reorganization around the Middle-Late Jurassic transition, Palaeogeo., Palaeoclim., Palaeoeco., 251, 527–546, https://doi.org/10.1016/j.palaeo.2007.05.008, 2007.

Rankey, E. C. and Reeder, S. L .: Controls on platform-scale patterns of surface sediments, shallow Holocene platforms. Bahamas, Sedimentology, 57, 1545–1565, https://doi.org/10.1111/j.1365-3091.2010.01155.x, 2010.

Rankey, E. C., Enos, P., Steffen, K., and Druke, D.: Lack of impact of Hurricane Michelle on tidal flats, Andros Island, Bahamas: Integrated remote sensing and field observations, J. Sed. Res., 74, 654–661, https://doi.org/10.1306/021704740654, 2004.

Ray, D. C., van Buchem, F. S. P., Baines, G., Davies, A., Gréselle, B., Simmons, M. D., and Robson, C.: The magnitude and cause of short-term eustatic Cretaceous sea-level change: a synthesis, Earth-Sci. Rev., 197, 102901, https://doi.org/10.1016/j.earscirev.2019.102901, 2019.

Reijmer, J. J. G.: Marine carbonate factories: review and update, Sedimentology, 68, 1729–1796, https://doi.org/10.1111/sed.12878, 2021.

Sadler, P. M.: The expected duration of upward-shallowing peritidal carbonate cycles and their terminal hiatuses, Bull. Geol. Soc. Am., 106, 791–802, https://doi.org/10.1130/0016-7606(1994)106<0791:TEDOUS>2.3.CO;2, 1994.

Sames, B., Wagreich, M., Wendler, J. E., Haq, B. U., Conrad, C. P., Melinte-Dobrinescu, M. C., Hu, X., Wendler, I., Wolfgring, E., Yilmaz, I., and Zorina, S. O.: Review: Short-term sea-level changes in a greenhouse world – a view from the Cretaceous, Palaeogeo. Palaeoclim., Palaeoeco., 441, 393–411, https://doi.org/10.1016/j.palaeo.2015.10.045, 2016.

Schoepf, V., Falter, J. L., and McCulloch, M. T.: Limits to the thermal tolerance of corals adapted to a highly fluctuating, naturally extreme temperature environment, Sci. Rep., 5, 17639, https://doi.org/10.1038/srep17639, 2015.

Schulz, M. and Schäfer-Neth, C.: Translating Milankovitch climate forcing into eustatic fluctuations via thermal deep water expansion: a conceptual link, Terra Nova, 9, 228–231, https://doi.org/10.1111/j.1365-3121.1997.tb00018.x, 1997.

Shackleton, N. J.: Oxygen isotopes, ice volume and sea level, Quaternary Sci. Rev., 6, 183–190, https://doi.org/10.1016/0277-3791(87)90003-5, 1987.

Sellwood, B. W. and Valdes, P. J.: Jurassic climates, Proc. Geol. Assoc., 119, 5–17, https://doi.org/10.1016/S0016-7878(59)80068-7, 2008.

Sellwood, B. W., Valdes, P. J., and Price, G. D.: Geological evaluation of multiple general circulation model simulations of Late Jurassic palaeoclimate, Palaeogeo. Palaeoclim. Palaeoeco., 156, 147–160, https://doi.org/10.1016/S0031-0182(99)00138-8, 2000.

Stienne, N.: Paléoécologie et taphonomie comparative en milieux carbonatés peu profonds (Oxfordien du Jura suisse et Holocène du Belize), Ph.D. thesis, GeoFocus, 22, Univ. Fribourg, Switzerland, 248 pp., 2010.

Strasser, A.: Lagoonal-peritidal sequences in carbonate environments: autocyclic and allocyclic processes, in: Cycles and Events in Stratigraphy, edited by: Einsele, G., Ricken, W., and Seilacher, A., Springer, Heidelberg, Germany, 709–721, 1991.

Strasser, A.: Astronomical time scale for the Middle Oxfordian to Late Kimmeridgian in the Swiss and French Jura Mountains, Swiss J. Geosci., 100, 407–429, https://doi.org/10.1007/s00015-007-1230-4, 2007.

Strasser, A.: Hiatuses and condensation: an estimation of time lost on a shallow carbonate platform, Depositional Record, 1, 91–117, https://doi.org/10.1002/dep2.9, 2015.

Strasser, A.: Cyclostratigraphy of shallow-marine carbonates – limitations and opportunities, in: Stratigraphy and Timescales, vol. 3, edited by: Montenari, M., Elsevier, Amsterdam, The Netherlands, 151–187, https://doi.org/10.1016/bs.sats.2018.07.001, 2018.

Strasser, A. and Samankassou, E.: Carbonate sedimentation rates today and in the past: Holocene of Florida Bay, Bahamas, and Bermuda vs. Upper Jurassic and Lower Cretaceous of the Jura Mountains (Switzerland and France), Geol. Croatica, 56, 1–18, 2003.

Strasser, A., Pittet, B., Hillgärtner, H., Pasquier, J.-B.: Depositional sequences in shallow carbonate dominated sedimentary systems: concepts for a high-resolution analysis, Sed. Geol., 128, 201–221, https://doi.org/10.1016/S0037-0738(99)00070-6, 1999.

Strasser, A., Hillgärtner, H., Hug, W., and Pittet, B.: Third-order depositional sequences reflecting Milankovitch cyclicity, Terra Nova, 12, 303–311, https://doi.org/10.1046/j.1365-3121.2000.00315.x, 2000.

Strasser, A., Védrine, S., and Stienne, N.: Rate and synchronicity of environmental changes on a shallow carbonate platform (Late Oxfordian, Swiss Jura Mountains), Sedimentology, 59, 185–211, https://doi.org/10.1111/j.1365-3091.2011.01236.x, 2012.

Strasser, A., Pittet, B., and Hug, W.: Palaeogeography of a shallow carbonate platform: The case of the Middle to Late Oxfordian in the Swiss Jura Mountains, J. Palaeogeo., 4, 251–268, https://doi.org/10.1016/j.jop.2015.08.005, 2015.

Thiry, M.: Palaeoclimatic interpretation of clay minerals in marine deposits: an outlook from the continental origin, Earth-Sci. Rev., 49, 201–221, https://doi.org/10.1016/S0012-8252(99)00054-9, 2000.

Valero, L., Garcés, M., Cabrera, L., Costa, E., and Sáez, A.: 20 Myr of eccentricity paced lacustrine cycles in the Cenozoic Ebro Basin, Earth Planet. Sci. Lett., 408, 183–193, https://doi.org/10.1016/j.epsl.2014.10.007, 2014.

Védrine, S.: High-frequency palaeoenvironmental changes in mixed carbonate–siliciclastic sedimentary systems (Late Oxfordian, Switzerland, France, and southern Germany), Ph.D. thesis, GeoFocus, 19, Univ. Fribourg, Switzerland, 216 pp., 2007.

Védrine, S. and Strasser, A.: High-frequency palaeoenvironmental changes on a shallow carbonate platform during a marine transgression (Late Oxfordian, Swiss Jura Mountains), Swiss J. Geosci., 102, 247–270, https://doi.org/10.1007/s00015-009-1326-0, 2009.

Védrine, S., Strasser, A., and Hug, W.: Oncoid growth and distribution controlled by sea-level fluctuations and climate (Late Oxfordian, Swiss Jura Mountains), Facies, 53, 535–552, https://doi.org/10.1007/s10347-007-0114-4, 2007.

Wallmann, K., Schneider, B., and Sarnthein, M.: Effects of eustatic sea-level change, ocean dynamics, and nutrient utilization on atmospheric $p\mathrm{CO}_2$ and seawater composition over the last 130000 years: a model study, Clim. Past, 12, 339–375, https://doi.org/10.5194/cp-12-339-2016, 2016.

Weissert, H. and Mohr, H.: Late Jurassic climate and its impact on carbon cycling, Palaeogeo. Palaeoclim., Palaeoecol., 122, 27–43, https://doi.org/10.1016/0031-0182(95)00088-7, 1996.

Wendler, J. E. and Wendler, I.: What drove sea-level fluctuations during the mid-Cretaceous greenhouse climate? Palaeogeo. Palaeoclim., Palaeoeco., 441, 412–419, https://doi.org/10.1016/j.palaeo.2015.08.029, 2016.

Wendler, J. E., Wendler, I., Vogt, C., and Kuss, J.: Link between cyclic eustatic sea-level change and continental weathering: evidence for aquifer-eustasy in the Cretaceous, Palaeogeo. Palaeoclim., Palaeoeco., 441, 430–437, https://doi.org/10.1016/j.palaeo.2015.08.014, 2016.

Wildi, W., Funk, H., Loup, B., Amato, E., and Huggenberger, P.: Mesozoic subsidence history of the European marginal shelves of the Alpine Tethys (Helvetic realm, Swiss Plateau and Jura), Eclogae Geol. Helv., 82, 817–840, 1989.

Wood, R.: Reef Evolution, Oxford Univ. Press, 432 pp., ISBN 9780198577843, 1999.

Zühlke, R.: Integrated cyclostratigraphy of a model Mesozoic carbonate platform – the Latemar (Middle Triassic, Italy), SEPM Spec. Publ., 81, 183–211, 2004.

Clim. Past, 20, 1039–1065, 2024
https://doi.org/10.5194/cp-20-1039-2024

Climate of the Past
Open Access

Stable isotope evidence for long-term stability of large-scale hydroclimate in the Neogene North American Great Plains

Livia Manser[1,★], **Tyler Kukla**[2], **and Jeremy K. C. Rugenstein**[2]

[1]Department of Earth Sciences, ETH Zürich, Zürich, Switzerland
[2]Department of Geosciences, Colorado State University, Fort Collins, CO, USA
[★]*Invited contribution by Livia Manser, recipient of the EGU Climate: Past, Present & Future Outstanding Student Poster and PICO Award 2019.*

Correspondence: Livia Manser (livia.manser@alumni.ethz.ch) and Jeremy K. C. Rugenstein (jeremy.rugenstein@colostate.edu)

Received: 10 September 2023 – Discussion started: 28 September 2023
Revised: 1 February 2024 – Accepted: 14 March 2024 – Published: 29 April 2024

Abstract. The Great Plains of North America host a stark climatic gradient, separating the humid and well-watered eastern US from the semi-arid and arid western US, and this gradient shapes the region's water availability, its ecosystems, and its economies. This climatic boundary is largely set by the influence of two competing atmospheric circulation systems that meet over the Great Plains – the wintertime westerlies bring dominantly dry air that gives way to moist, southerly air transported by the Great Plains low-level jet in the warmer months. Climate model simulations suggest that, as CO_2 rises, this low-level jet will strengthen, leading to greater precipitation in the spring but less in the summer and, thus, no change in mean annual precipitation. Combined with rising temperatures that will increase potential evapotranspiration, semi-arid conditions will shift eastward, with potentially large consequences for the ecosystems and inhabitants of the Great Plains. We examine how hydroclimate in the Great Plains varied in the past in response to warmer global climate by studying the paleoclimate record within the Ogallala Formation, which underlies nearly the entire Great Plains and provides a spatially resolved record of hydroclimate during the globally warmer late Miocene. We use the stable isotopes of oxygen ($\delta^{18}O$) as preserved in authigenic carbonates hosted within the abundant paleosol and fluvial successions that comprise the Ogallala Formation as a record of past hydroclimate. Today, and coincident with the modern aridity gradient, there is a sharp meteoric water $\delta^{18}O$ gradient with high (-6 ‰ to 0 ‰) $\delta^{18}O$ in the southern Great Plains and low (-12 ‰ to -18 ‰) $\delta^{18}O$ in the northern plains. We find that the spatial pattern of reconstructed late Miocene precipitation $\delta^{18}O$ is indistinguishable from the spatial pattern of modern meteoric water $\delta^{18}O$. We use a recently developed vapor transport model to demonstrate that this $\delta^{18}O$ spatial pattern requires air mass mixing over the Great Plains between dry westerly and moist southerly air masses in the late Miocene – consistent with today. Our results suggest that the spatial extents of these two atmospheric circulation systems have been largely unchanged since the late Miocene and any strengthening of the Great Plains low-level jet in response to warming has been isotopically masked by proportional increases in westerly moisture delivery. Our results hold implications for the sensitivity of Great Plains climate to changes in global temperature and CO_2 and also for our understanding of the processes that drove Ogallala Formation deposition in the late Miocene.

1 Introduction

The Great Plains of North America rise slowly in elevation from the wooded lowlands near sea level west of the Mississippi River to the greater than 4 km high "purple mountain majesties above the fruited plain" (Bates, 1911) that comprise the North American Cordillera. Though this region contains some of the flattest landscapes in the United States (Fonstad et al., 2007; Dobson and Campbell, 2014), these plains belie a remarkable climatic setting and geologic history which have conspired to shape the modern-day water resources, ecosystems, and economies of the Plains region. Boreal spring heralds the onset of the Great Plains low-level jet (GPLLJ), a primarily nocturnal, southerly jet responsible for transporting more than 30 % of the water vapor that enters the continental US every year (Helfand and Schubert, 1995). Interactions between the GPLLJ and midlatitude storm systems yield some of the largest and most intense convective systems on the planet (Song et al., 2019). These spring and summertime rains nurture the vast grasslands of the Plains, which return this moisture to the atmosphere via transpiration, often seeding additional precipitation on subsequent days and resulting in one of the tightest couplings between land and atmosphere anywhere on Earth (Koster, 2004). On multi-annual timescales, these same interactions – modified by long-term climatic oscillations such as the El Niño–Southern Oscillation or the North Atlantic Oscillation – are the proximal cause for the extensive floods and deep droughts that frequent this region (Byerle, 2003), perhaps best exemplified by the 1930s Dust Bowl (Schubert, 2004), an event which reshaped American governance and society and has been labeled the worst environmental catastrophe in US history (Egan, 2006).

Climatically, the Great Plains are characterized by a sharp aridity gradient with a more humid climate to the east and a more arid climate to the west (Fig. 1). This aridity gradient spans the 100th meridian and marks a dramatic change in the long-term patterns of precipitation, vegetation, and, consequently, agriculture and human development (Powell, 1879, 1890; Webb, 1931; Seager et al., 2018b). A convenient measure of aridity is the aridity index (AI), which is the ratio of precipitation (P) to potential evapotranspiration (PET): conditions are considered arid – or water-limited – if P / PET is less than 1. The Great Plains today straddle the transition between the wet, eastern US (AI > 1) and the water-limited western US (AI < 1) (Seager et al., 2018b). Consequently, regions to the east are more densely populated and farms rely on rainfed agricultural practices; to the west, settlement is more limited and agriculture relies extensively on groundwater withdrawals or irrigation diversions.

This groundwater – sourced from the Ogallala Aquifer (black polygon outlined in Fig. 1) and replenished by spring and summertime rains – is hosted in the Ogallala Formation, a nearly continuous formation that underlies the Plains from southwest Texas and southeast New Mexico into the southern part of South Dakota, making it one of the largest and most laterally continuous sedimentary formations in North America. Comprised of sediments shed off the Rockies, the Ogallala Formation has been interpreted as a series of alluvial or telescoping megafans (Seni, 1980; Willett et al., 2018; Korus and Joeckel, 2023a) that prograded towards the east and completely buried the pre-existing erosional landscape that, in the southern Great Plains, is cut into Triassic and Permian bedrock, and, in the northern Great Plains, lies on the White River or Arikaree Group. In places, the Ogallala Formation is overlain by alluvial and/or eolian deposits, and, particularly in the southern Great Plains, there is frequently a prominent calcium carbonate caprock that separates the Ogallala from overlying sedimentary units (Gustavson and Winkler, 1988). Deposition began in the middle Miocene and ended in the late Miocene or earliest Pliocene. However, precisely why the Great Plains experienced a prolonged period of deposition, followed by a period of incision that continues to the present day, remains uncertain, with most studies attributing this period of deposition to dynamic topography effects associated with the passage of the Farallon Plate beneath the Great Plains (Moucha et al., 2009; Karlstrom et al., 2011; Willett et al., 2018).

During this time, substantial ecological changes occurred, largely yielding the pre-anthropogenic landscape that characterized the Quaternary Great Plains. Though grasslands were likely present before the middle Miocene, they continued expanding throughout the Plains during the cooling following the peak of mid-Miocene warmth (Jacobs et al., 1999; Stromberg, 2005; Strömberg and McInerney, 2011). These predominantly C_3 grasslands were progressively replaced by C_4 grasslands starting in the latest Miocene and continuing through the Pliocene (Fox and Koch, 2003, 2004). Largely coincident with these changes, large mammal diversity gradually declined on the Plains from its peak during the middle Miocene to a relative low in the Quaternary (Janis et al., 2000; Fritz et al., 2016). Since cessation of Ogallala deposition, a combination of base-level fall and uplift along the Front Range led to incision of the major Plains rivers through the Ogallala Formation (McMillan et al., 2002; Duller et al., 2012), leaving the former Ogallala landscape abandoned and perched above the major Plains valleys (Willett et al., 2018). Today, much of the Ogallala Formation is visible as a prominent escarpment protected by the indurated nature of its many calcic-rich sediments; dotting much of the length of this escarpment are wind turbines powered, to no small extent, by the exceptionally predictable and windy Great Plains low-level jet.

This combination of climate and geology has helped to promote development and agriculture on the Plains, with Ogallala Aquifer water supplying any deficit due to insufficient rainfall. However, the aquifer remains critically overdrawn in many places; further, anthropogenically driven increases in atmospheric CO_2 and associated changes in global climate may affect water availability on the Plains. Indeed, this area appears to be exceptionally sensitive to even small changes in climate and land cover due to the tight coupling between land and atmosphere in this region (Koster, 2004; de Noblet-Ducoudre et al., 2012; Laguë et al., 2019). Thus, small changes in precipitation and/or PET may shift the precise location of the "climatological 100th meridian" (i.e., the approximate location of the boundary between arid and wet ecosystems) with important consequences for ecosystems and agricultural systems. Further, global climate model (GCM) simulations tend to predict only a small change in summer precipitation, though a large shift in the seasonal-

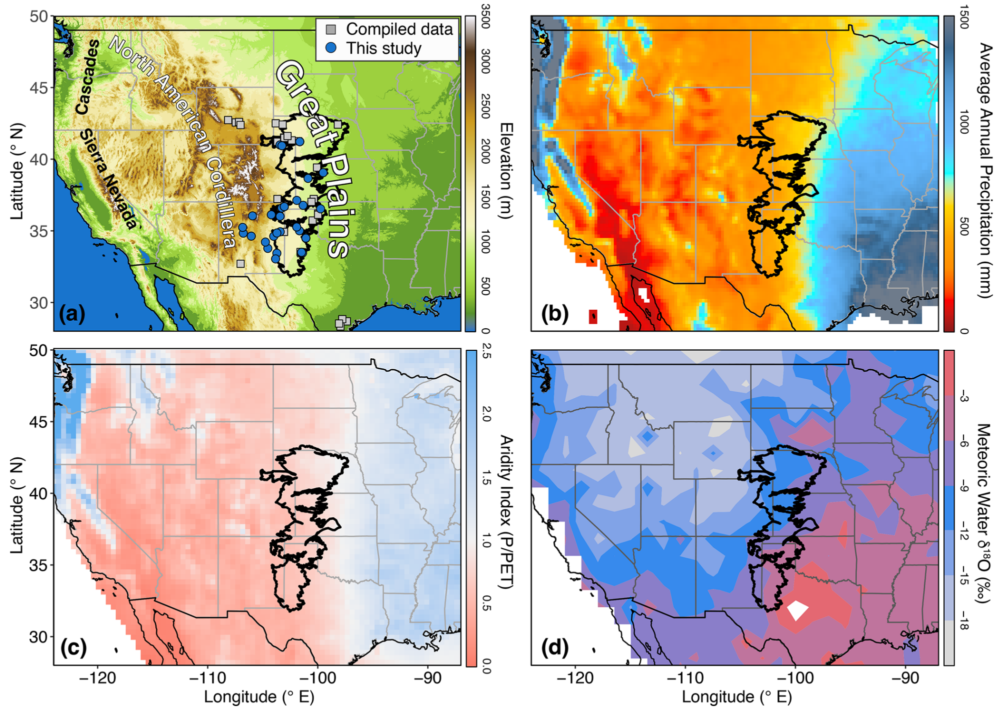

Figure 1. **(a)** Extent of the continuous Ogallala Formation (thick black outline), with new sites presented in this study (squares) and sites compiled from the PATCH Lab (circles) (Kukla et al., 2022a). Shading is elevation (m). **(b)** Map of average annual precipitation (mm) from the Global Precipitation Climatology Project (Meyer-Christoffer et al., 2011). **(c)** Aridity index (AI), which is calculated as P / PET. P as in panel **(b)**; PET is from the Global Land Evaporation Amsterdam Model (GLEAM) (Miralles et al., 2011; Martens et al., 2017). **(d)** Interpolated distribution of $\delta^{18}O$ of modern meteoric waters, derived from rivers and streams, groundwater, tap water, spring water, and precipitation $\delta^{18}O$ measurements and compiled from Waterisotopes.org (Waterisotopes Database, 2019). Thick black outline in all panels is the areal extent of the continuous Ogallala Formation.

ity of that precipitation is driven by dynamical shifts in the westerly jet and the GPLLJ (Cook et al., 2008; Bukovsky et al., 2017; Zhou et al., 2021a). Combined with rising temperatures, this negligible change in summer precipitation implies that the arid conditions characteristic of the western Great Plains may expand eastward with global warming as increases in PET outpace increases in P over the Plains (Seager et al., 2018b; Overpeck and Udall, 2020). However, models still struggle to properly simulate the GPLLJ and its associated precipitation-bearing convective systems. Changes in the interactions between vegetation, soil moisture, and rainfall at higher atmospheric CO_2 remain similarly difficult to model (Bukovsky et al., 2017; Zhou et al., 2021a). Further, paleoclimate data indicate that, in general, warmer periods have actually been wetter and/or greener (Caves et al., 2016; Burls and Fedorov, 2017; Ibarra et al., 2018; Feng et al., 2022), in conflict with many model predictions of drier future conditions (e.g., Scheff, 2018). As a consequence, there is substantial uncertainty regarding how aridity on the Plains – and the interactions between the GPLLJ, precipitation, and vegetation – will change as atmospheric CO_2 rises and global temperature increases.

In this contribution, we take advantage of the remarkable spatial extent of Neogene sediments afforded by the Ogallala Formation to understand how changes in global climate impacted the Plains during periods of higher atmospheric CO_2 and warmer global temperatures. Mid-Miocene global temperatures were 7–8 °C warmer than today and atmospheric CO_2 levels were around 500 ppm or higher (Herbert et al., 2016; Steinthorsdottir et al., 2021; CenCO2PIP Consortium, 2023). Since the mid-Miocene, temperature and atmospheric CO_2 have gradually declined, establishing the bipolar glaciation that characterizes Quaternary climate. The Neogene therefore provides an opportunity to answer the question of how aridity has changed on the Plains and whether the climatological 100th meridian shifted eastward in the past as global climate models suggest for the future. The spatial extent of the Ogallala also permits us to examine the mechanisms by which any shifts in aridity may have occurred due to, for example, shifts in the distribution of precipitation as a result of strengthening or weakening of the GPLLJ in a warmer climate. Further, any shifts in climate may point towards the mechanisms that generated the sediment that formed the Ogallala Formation, permitting distinctions between climatically or tectonically controlled generation of the Ogallala Formation (i.e., Molnar and England, 1990; Zhang et al., 2001).

To answer these questions, we rely on the stable isotopes of authigenic carbonates – a material that is particularly abundant within the fluvial and paleosol facies of the Ogallala Formation and which is thought to record precipitation $\delta^{18}O$. Precipitation oxygen isotopes ($\delta^{18}O_p$) are sensitive to the moisture source and rainout history of air masses that reach a given location. Because of this sensitivity, spatially resolved datasets of carbonate oxygen isotopes ($\delta^{18}O_c$) interpreted to track $\delta^{18}O_p$ have been successfully used to constrain how large-scale hydroclimate has changed in response to atmospheric and orographic forcing through time (Fox and Koch, 2004; Mix et al., 2011; McDermott et al., 2011; Kocsis et al., 2014; Caves et al., 2015; Caves Rugenstein and Chamberlain, 2018). The Plains today host a steep $\delta^{18}O$ gradient oriented NE–SW that roughly tracks, but is somewhat oblique to, the aridity gradient at the 100th meridian (Fig. 1c). Given this concurrence, we hypothesize that the Ogallala authigenic carbonate $\delta^{18}O_c$ record over space and time will reflect changes in the large-scale hydroclimate and aridity over the Great Plains. In the following sections, we explain how $\delta^{18}O$ can be used to track hydroclimate and our approach to sampling and to building a spatially extensive dataset. We then investigate the climatic drivers behind the modern $\delta^{18}O_p$ gradient over the Plains and compare this to reconstructed maps of $\delta^{18}O_p$ during Ogallala deposition. Lastly, we apply a recently developed reactive transport model to quantitatively assess our observations of $\delta^{18}O$ and how these data relate to overall hydroclimate on the Plains. We find that large-scale atmospheric circulation and the position of the climatological 100th meridian have been remarkably stable, despite correspondingly large changes in global climate since the late Miocene.

2 Background

2.1 Modern hydroclimate of the North American Great Plains

Spring and summer precipitation in the Great Plains overwhelmingly originates from the Gulf of Mexico, where the Bermuda High drives southeasterly flow while a high-pressure system over the Great Basin effectively blocks Pacific moisture. The combination of these two high-pressure systems creates the conditions for the Great Plains low-level jet, which carries moisture deep into the interior of the North American continent (Helfand and Schubert, 1995). Though the precise mechanisms that generate the GPLLJ are complex (see Shapiro et al., 2016), critically for our purposes, both the existence of the high topography of the North American Cordillera and the east–west-sloping terrain of the Great Plains appear crucial for generating and maintaining a low-level jet over the Plains. For example, in model simulations where cordillera topography is removed, the GPLLJ is weakened or non-existent (Ting and Wang, 2006; Jiang et al., 2007). During winter, the GPLLJ is inactive and precipitation originates largely from the Pacific Ocean due to storms routed by the midlatitude westerly jet. These wintertime storms traverse the wide expanse of topography that comprises the North American Cordillera – including ranges such as the Sierra Nevada, Cascades, and Wasatch – which removes moisture from these midlatitude cyclones. Consequently, precipitation across the Plains typically occurs during interaction with cold Arctic air masses that can penetrate as far south as the southern Great Plains (Nativ and Riggio, 1990; Brubaker et al., 1994). Thus, the combination of topography with atmospheric circulation generates much of the seasonal precipitation pattern that prevails today over the Great Plains.

The position of the 100th meridian aridity boundary is shaped by the relative strength of these two circulation systems (Seager et al., 2018b), yielding a sharp humidity gradient that approximately coincides with the boundary between southerly maritime Gulf of Mexico air and dry continental air (Hoch and Markowski, 2005). On an interannual basis, this boundary can shift depending upon the strength of the midlatitude westerlies relative to the GPLLJ; with increasing westerly wind strength, for example, the 100th meridian shifts east (Hoch and Markowski, 2005). On longer timescales, winter aridity and weaker westerlies have been linked to grassland expansion and forest dieback in the Great Plains in the early Miocene (Kukla et al., 2022b). Besides these two large-scale atmospheric systems, several other factors determine the location and orientation of the sharp aridity gradient that characterizes the Great Plains today (Seager et al., 2018b). First, evapotranspiration of water from the land surface to the atmosphere is critical in determining precipitation. For example, return of water to the atmosphere from the land surface (largely through transpiration) may supply up to 40 % of the precipitation in the Great Plains during spring and summer (Burde et al., 2006; van der Ent et al., 2010). The importance of the land surface may be further enhanced by the widespread grasslands that populate the Plains landscape. Grasses can much more rapidly modify their stomatal conductance and, hence, total transpiration than can trees and shrubs to take advantage of periodic rainstorms (Ferretti et al., 2003; Hetherington and Woodward, 2003). Such rapid water use leads to higher recycling rates of water from the land surface back to the atmosphere. As a consequence, the spread of grasslands onto the Plains during the Miocene has been hypothesized to have fundamentally increased the recycling of water between the land surface and the atmosphere (Mix et al., 2013; Chamberlain et al., 2014).

Model simulations project distinct changes in precipitation and hydroclimate associated with dynamical and thermodynamic responses to warming. GCMs and regional climate models robustly predict that precipitation seasonality will shift from the summer to the spring (Cook et al., 2008). As global temperatures rise, the westerly jet shifts poleward, permitting a stronger and more northerly GPLLJ, producing more precipitation in the late spring (Bukovsky et al., 2017; Zhou et al., 2021a). In contrast, the continued northward shift of the GPLLJ as summer progresses weakens the jet over the Great Plains, leading to enhanced late summer drying (Zhou et al., 2021a). Despite this shift in the timing of the wet season, mean annual precipitation is not expected to change (Bukovsky et al., 2017). With constant mean annual precipitation, the increase in PET owed to rising temperatures will decrease the AI and shift the climatological 100th meridian eastward (Seager et al., 2018a).

2.2 Precipitation oxygen isotopes reflect this hydroclimatic pattern

This annual mixing between the GPLLJ and the westerlies results in a steep spatial gradient in precipitation δ^{18}O mostly due to the differences in topography traversed by each air mass (Kendall and Coplen, 2001). Mountain ranges tend to increase the net loss of moisture from an air mass, preferentially removing ^{18}O and decreasing $\delta^{18}O_p$ (Rozanski et al., 1993; Poage and Chamberlain, 2001; Winnick et al., 2014; Mix et al., 2019; Kukla et al., 2019). Thus, precipitation derived from the westerlies has low δ^{18}O values by the time it reaches the Great Plains. In contrast, GPLLJ moisture, which has not traversed major topographic barriers and is augmented by a high degree of evapotranspiration that replenishes the GPLLJ, is about 10 ‰ higher than equivalent westerly moisture (Mix et al., 2013; Winnick et al., 2014). The aridity gradient, which depends on the relative contributions of westerly vs GPLLJ moisture, is therefore encoded in the value of $\delta^{18}O_p$ across the Great Plains, which can generally be understood as the precipitation-weighted average of the end-member sources. This precipitation δ^{18}O signal is captured by authigenic carbonates but is further modified by both the temperature of carbonate formation and other potentially spatially variable factors associated with mineral formation, such as differences in precipitation seasonality and evaporation (Breecker et al., 2009; Caves, 2017; Huth et al., 2019; Kelson et al., 2020, 2023).

3 Geological setting and sampling approach

The sediments of the Ogallala Formation originate from the Rocky Mountains, and eroded material from the Miocene Rockies was transported by braided, high-energy, ephemeral streams and eolian processes across the Plains (Joeckel et al., 2014; Smith and Platt, 2023; Korus and Joeckel, 2023b). The result was the Ogallala Formation, which spans from South Dakota to southern Texas (black outline in Fig. 1). Though the headwaters of these rivers and fans have since been eroded away, except in southern Wyoming, discontinuous remnants of the Ogallala have been mapped nearly up to their sources in eastern New Mexico (Frye et al., 1982). Consisting of gravel, sand, silt, and clay deposits, the Ogallala Formation also contains abundant calcic paleosols and calcic-rich sediments distributed throughout the formation and across the entire N–S extent of the formation (Gustavson, 1996; Joeckel et al., 2014; Smith et al., 2016; Smith and Platt, 2023). The Ogallala Formation in the southern Great Plains unconformably overlies Permian through Cretaceous strata (Gustavson and Holliday, 1999). In the northern Great Plains, the Ogallala Formation is underlain by the late Oligocene to early Miocene Arikaree Group and the White River Group, upper Eocene to Oligocene in age. Chronostratigraphy of the Ogallala Formation is based on fossil vertebrate faunas of Barstovian to Hemphillian North American land mammal ages (NALMAs) and scattered volcanic ash beds and basalt flows (Kitts, 1965; Leonard and Frye, 1978; Frye et al., 1978; Thomasson, 1979; Winkler, 1985; Schultz, 1990; Swisher, 1992; Gustavson, 1996; Tedford, 1999; Tedford et al., 2004; Cepeda and Perkins, 2006; Smith et al., 2016, 2018). Due to the nature of the largely fluvial and eolian deposits, the Ogallala exhibits substantial heterogeneity north to south. Consequently, different workers have classified the Ogallala Formation as a group (in the northern Great Plains) (Tedford et al., 2004) or as a formation, primarily in Kansas and to the south (Gustavson, 1996; Ludvigson et al., 2009). Herein, we refer to the Ogallala exclusively as a formation. However, in the northern Great Plains, there are further distinct formations such as the Valentine, Ash Hollow, and Olcott formations (Joeckel et al., 2014; Smith et al., 2017), each with defined age constraints based upon biostratigraphy and ashes (Tedford et al., 2004). In the southern Great Plains, previous workers have proposed elevating the Ogallala Formation to group status based upon subdividing the Ogallala into the Bridwell and Couch formations (Winkler, 1985; Gustavson and Winkler, 1988). However, in the southern Great Plains, we adopt the terminology of Gustavson (1996), who concluded that these formations are difficult to map and contain little dateable material, suggesting that the Ogallala remain with formation status. The thickness of Ogallala sediments generally varies relative to the underlying topography between 250 m, in regions where it fills paleovalleys, and 10–30 m in the interfluves between paleovalleys (Gustavson and Holliday, 1999). In the southern Great Plains, there is frequently an erosion-resistant caliche or caprock calcrete that separates the Ogallala Formation from the predominantly eolian Plio-Pleistocene Blackwater Draw Formation and, locally, the lacustrine Blanco Formation (Gustavson, 1996; Gustavson and Holliday, 1999). These caliche caprocks are thought to have developed during one or multiple periods of extended landscape stability and likely record a multi-genetic history (Brock and Buck, 2009; Henry, 2017). In contrast, in the northern Great Plains, the Ogallala Formation is overlain by several high-energy deposits, including the Crooked Creek Formation in Kansas and the Broadwater Formation in Nebraska (Swinehart and Diffendal, 1987).

To capture spatial changes in precipitation δ^{18}O – and hence shifts in the aridity gradient – we collected samples spanning nearly the entire N–S and E–W extent of the Ogallala Formation from paleosol authigenic carbonate material to reconstruct paleo-precipitation δ^{18}O. We build upon previous work (Fox and Koch, 2003, 2004) that developed a spatially extensive dataset of paleosol carbonate isotopes, collected primarily to understand changes in C_3 and C_4 vegetation during the late Miocene. We build upon these datasets, focusing on filling gaps in the southern and southwestern Great Plains (Texas and New Mexico), while also contributing additional data in the central and northern Great Plains.

Though the Ogallala Formation provides an unparalleled opportunity to collect spatially extensive $\delta^{18}O_c$ data, the precise chronology of Ogallala deposition remains uncertain. In many places, specific formations have been dated using biostratigraphy and radiometrically dated ashes (Tedford et al., 2004); however, in many other places, particularly those Ogallala outcrops to the west and disconnected from the primary exposure of the Ogallala, temporal constraints are provided by lithologic correlations (Frye et al., 1982). Even in the formations which have been dated using biostratigraphy, the age constraints are relatively broad, typically limited by the precision of the North American land mammal ages. Lastly, the relatively thin veneer of Ogallala sedimentation combined with the potentially long time span covered by deposition suggests that there are frequent and temporally extensive unconformities within many sections (Smith and Platt, 2023). As a consequence, it remains difficult to correlate sections across the large expanse of the Great Plains.

For the purposes of our study, we use the published age constraints (Table 1) either from the study that originally analyzed the sampled section in detail or from later publications that provide a more precise age. Because we are only interested in broadly comparing samples spatially, we treat all samples in a given section as having the same age. We bound this age by considering the maximum possible age range for the given formation, which is either the Ogallala Formation or, in the northern Great Plains, one of the formations within the Ogallala Group. For example, in locations where we sample well-defined and dated subdivisions of the Ogallala Group (for example, samples from the Ash Hollow Formation at Lake McConaughy State Recreation Area in Nebraska; Joeckel et al., 2014), we consider our sample ages to be bound by the full age range of the formation. In other cases, we know only that our data lie above or below a certain dated ash (for example, samples from Wildcat Bluff Nature Center in Texas; Cepeda and Perkins, 2006), and therefore one bound on the age is provided by the dated material. In some cases, the sampled unit has only been correlated with the Ogallala Formation and there are no other age constraints to narrow the large possible range of ages. We therefore adopt the full possible range of ages given the identification of the unit as the Ogallala Formation. For example, for many sections in New Mexico, Ogallala outcrops have been identified by lithologic or geomorphic correlation with the contiguous body of the Ogallala Formation to the east, but no dateable material has been recovered (Frye et al., 1982). Despite these broad age constraints, we find that our results are not sensitive to the uncertainty in our correlations or to the precise chronology of Ogallala deposition because $\delta^{18}O_c$ is largely invariant within any given section.

Lastly, we also collected samples from the Miocene-age Tesuque Formation within the Santa Fe Group within the Rio Grande Rift. These samples are the only samples we collected west of the original spatial extent of the Ogallala Formation. Unlike the Ogallala Formation, the Santa Fe Group comprises thick basin fill shed off the Sangre de Cristo Range during ongoing rift extension (Galusha and Blick, 1971; Kuhle and Smith, 2001) and chronological constraints are provided by a combination of magnetostratigraphy (Barghoorn, 1981, 1985), biostratigraphy (Galusha and Blick, 1971; Tedford and Barghoorn, 1993; Aby et al., 2011), and radiometric dates (Mcintosh and Quade, 1996; Izett and Obradovich, 2001; Koning et al., 2013). The Tesuque Formation contains abundant authigenic carbonates, including nodules, root casts, groundwater cements, and laterally extensive Bk horizons (Kuhle and Smith, 2001). To place our samples within an existing stratigraphic framework, we collected samples along the Arroyo de los Martinez section and refer readers to Koning et al. (2013) for a detailed description of this section.

4 Methods

4.1 Stable isotope measurements

We collected carbonates ($n = 344$) from paleosols from 32 distinct sites within the Ogallala Formation or from the Tesuque Formation. In every section, we sampled a wide variety of carbonate types, including rhizoliths, nodules, burrows, carbonate-cemented matrix samples, and caliches in order to test whether these different carbonate types reveal different spatial isotope patterns. Individual sample types for each sample are listed in Table S1 in Manser et al. (2023). During sampling, we first removed the weathered surface layer before selecting samples. Sampling sites are shown in Fig. 1a, sample types are depicted in Fig. 2, and coordinates are reported in Table 1. Samples were powdered for isotopic analysis with a Dremel tool or crushed with a mortar and pestle to obtain a homogeneous powder. Before powdering nodules, caliches, and matrix samples, any outer weathered rind was first discarded. Carbon and oxygen isotope ratios of the carbonate were measured with a ThermoFisher Gas Bench II coupled via a ConFlow IV interface to a Delta V Plus mass spectrometer at ETH Zürich following procedures described in detail in Breitenbach and Bernasconi (2011). Briefly, 140–300 µg of the powdered sample, depending on carbonate content, was reacted with five drops of 104 % phosphoric acid at 70 °C in He-flushed exetainers.

Table 1. Site-averaged data. Values of $\delta^{13}C$ are reported in ‰ relative to VPDB. Values of $\delta^{18}O$ are reported in ‰ relative to VSMOW. n is the number of samples collected from the site. Mean annual temperature data are retrieved from NARR (Mesinger et al., 2006).

Lat (°N)	Long (°E)	ID	$\delta^{13}C$	$\delta^{13}C$ 1σ	$\delta^{18}O_c$	$\delta^{18}O_p$	$\delta^{18}O$ 1σ	$\delta^{18}O$ range	Bottom age (Ma)	Top age (Ma)	MAT (°C)	n	Reference
34.91	−103.45	BV	−4.64	1.86	25.36	−5.15	0.45	1.80	23	5	15.35	18	Gustavson (1996)
40.98	−103.47	CB1	−6.69	0.36	21.86	−9.70	0.67	2.78	31.8	5	10.91	22	Galbreath (1953); Tedford (1999); Tedford et al. (2004)
40.92	−103.29	CB2	−6.27	0.18	22.72	−8.82	0.59	1.23	31.8	5	10.99	5	Galbreath (1953); Tedford (1999); Tedford et al. (2004)
34.45	−101.11	CC	−7.34	0.75	26.29	−3.85	0.31	1.04	11.6	7.6	16.92	17	Lehmann and Schnable (1992)
36.57	−103.30	CLSP	−6.63	0.64	24.98	−6.07	0.11	0.23	23	5	13.08	3	Frye et al. (1978)
33.41	−103.75	CP	−6.18	1.55	25.26	−4.91	1.24	3.53	13.6	10.3	16.83	13	Henry (2017)
38.64	−100.91	DB	−6.01	0.56	23.91	−7.08	0.47	1.90	11.4	7.5	13.28	19	Smith et al. (2011), (2016)
33.75	−104.58	EPB	−5.00	0.71	25.13	−4.91	0.43	1.41	23	5	17.40	8	Frye et al. (1982)
36.02	−105.97	ESP	−5.93	1.05	19.81	−12.10	2.12	7.82	16.2	14	9.50	58	Koning et al. (2013)
34.59	−104.04	GVR	−5.68	0.47	25.03	−5.40	0.33	0.97	8.3	4.7	15.73	8	Gustavson (1996)
41.21	−101.67	MCA	−6.58	0.26	19.56	−11.98	0.70	2.13	13	5	10.99	7	Joeckel et al. (2014)
41.20	−101.67	MCC	−7.00	0.46	19.61	−11.94	0.85	2.74	13	5	10.99	16	Joeckel et al. (2014)
41.21	−101.67	MCE	−6.75	0.48	19.83	−11.72	1.04	3.11	13	5	10.98	6	Joeckel et al. (2014)
36.10	−104.26	MI	−5.55	0.57	25.61	−5.74	0.13	0.23	23	5	11.78	3	Frye et al. (1978)
36.10	−104.26	MI2	−2.27	1.30	26.12	−5.23	0.55	1.16	23	5	11.80	4	Frye et al. (1978)
34.98	−101.69	PD	−6.34	0.59	25.41	−5.02	0.28	0.89	23	5	15.72	9	Lucas et al. (2001)
33.01	−103.87	PO	−6.50	0.80	25.71	−4.36	0.44	2.01	11	4.5	17.29	20	Gustavson (1996); Henry (2017)
37.10	−101.94	PoR	−6.13	0.75	24.51	−6.18	0.44	1.02	23	5	14.58	7	Smith et al. (2015)
35.99	−103.46	REA	−4.01	1.51	25.21	−5.58	0.81	2.52	23	5	14.15	7	Frye et al. (1978)
35.99	−103.46	REA2	−4.82	0.65	25.69	−5.10	0.79	1.60	23	5	14.16	4	Frye et al. (1978)
35.99	−103.46	REA3	−4.71	3.39	25.51	−5.27	0.14	0.31	23	5	14.16	4	Frye et al. (1978)
34.82	−103.75	RG	−5.80	0.55	25.78	−4.71	0.37	1.12	8.3	4.7	15.44	11	Gustavson (1996)
34.19	−104.79	RSE	−5.41	1.20	25.14	−5.24	0.80	1.94	23	5	15.92	9	Frye et al. (1982)
39.04	−99.54	S9A	−7.48	0.67	25.16	−5.88	0.50	1.62	11.6	3.6	13.07	9	Thomasson (1979)
39.04	−99.54	S9A2	−7.04	0.15	25.07	−5.98	0.42	1.01	11.6	3.6	13.07	5	Thomasson (1979)
36.67	−103.07	SNE	−5.47	0.17	24.71	−6.11	0.06	0.12	23	5	14.01	5	Leonard and Frye (1978)
36.67	−103.07	SNE2	−4.41	1.34	25.00	−5.82	0.28	0.48	23	5	14.01	3	Leonard and Frye (1978)
33.43	−101.41	SQ3	−6.90	0.49	26.17	−3.87	0.51	1.46	10.3	4.9	17.40	7	Henry (2017); Fox and Koch (2004); Gustavson (1996)
33.47	−101.51	SQ4	−6.15	1.88	26.76	−3.30	0.32	0.80	13.6	10.3	17.31	4	Henry (2017); Fox and Koch (2004); Gustavson (1996)
35.24	−101.95	WC	−8.57	1.96	23.10	−7.37	4.39	7.69	10	5	15.52	3	Cepeda and Perkins (2006)
34.47	−101.11	WK	−6.78	0.71	26.37	−3.77	0.25	0.99	11	4.5	16.92	19	Gustavson (1996); Gustavson and Holliday (1999)
34.60	−106.08	WW	−3.16	1.00	24.88	−6.43	0.21	0.59	23	5	11.96	9	Frye et al. (1982)

Each batch of 79 samples included 16 replicates of the internal standards MS2 ($\delta^{13}C = +2.13$ ‰, $\delta^{18}O = -1.81$ ‰) and ETH-4 ($\delta^{13}C = -10.19$ ‰, $\delta^{18}O = -18.71$ ‰) interspersed throughout the run. The standards are used for drift corrections and data normalization and are calibrated to the international reference materials NBS 19 ($\delta^{13}C = +1.95$ ‰, $\delta^{18}O = -2.2$ ‰) and NBS 18 ($\delta^{13}C = -5.01$ ‰, $\delta^{18}O = -23.00$ ‰; Bernasconi et al., 2018). Analytical reproducibility of the standards was better than 0.1 ‰ (1σ for both δ^{13}C and δ^{18}O). We convert our $\delta^{18}O_c$ data from VPDB to VSMOW using the equations in Brand et al. (2014), and we report all $\delta^{18}O_c$ data relative to VSMOW.

4.2 HYSPLIT

Because $\delta^{18}O_p$ is heavily influenced by the pathway that moisture takes to reach a certain site, we use NOAA's Hybrid Single-Particle Lagrangian Trajectory Model (HYSPLIT) (Draxler and Hess, 1998; Stein et al., 2015) to analyze the pathways by which moisture reaches the Great Plains. HYSPLIT is commonly used to understand modern precipitation $\delta^{18}O_p$ data (Sjostrom et al., 2006; Bershaw et al., 2012; Li and Garzione, 2017; Zhu et al., 2018; San Jose et al., 2020) and to yield insights into the controls on reconstructed paleo-precipitation δ^{18}O (Oster et al., 2012; Lechler and Galewsky, 2013; Caves et al., 2014, 2015; Wheeler and Galewsky, 2017; Zhu et al., 2018). To track air parcels back in time and space from a given location, we use North American Regional Reanalysis (NARR) data, which have a 32×32 km resolution (Mesinger et al., 2006), as the HYSPLIT climatological model input. To resolve spatial variability in the origins and pathways of storms, we simulate the origin and pathway of the air parcels for four selected sites (32° N and −97° E; 32° N and −105° E; 42° N and −97° E; 42° N and −105° E). At each site, we initialize the air parcel at 1000 m above ground. We choose this height as this level encapsulates much of the bulk moisture transported by the GPLLJ, which has maximum wind speeds between 500–1000 m above ground level (Jiang et al., 2007), and also captures moisture transport by the midlatitude westerlies (Lechler and Galewsky, 2013; Wheeler and Galewsky, 2017). The sites were chosen to encapsulate nearly the full latitudinal and longitudinal range represented by the carbonate stable isotope data. At each site, we generate nearly 53 000 back trajectories (i.e., one trajectory every 6 h from 1980–2016) and filter these trajectories for only those that are estimated to produce precipitation within 6 h of reaching the endpoint (e.g., Lechler and Galewsky, 2013; Caves et al., 2015). This results in approximately 4000 to 11 000 trajectories at each site. We further use HYSPLIT's built-in clustering algorithm to calculate the percentage of trajectories that originate from the Gulf of Mexico. Lastly, we note two critical assumptions regarding this HYSPLIT analysis. First, we assume that, by tracking air parcels using HYSPLIT, we are also tracking moisture; however, HYSPLIT does not account for moisture addition by evaporation or removal by precipitation and does not track diffusion of moisture into and out of an air mass. The assumption of moisture transport by advection is sometimes violated in regions of strong air mass mixing, such as in the Great Plains (Draxler and Hess, 1998); however, comparison of HYSPLIT results with the results of a more rigorous moisture tracking model – the Water Accounting Model (WAM-2layers) – generally shows close agreement (Driscoll et al., 2024). Second, our HYSPLIT results are strictly only applicable to understand the modern climate. Nevertheless, we use these results to develop insights into the controls on past precipitation δ^{18}O.

4.3 Vapor transport model

Given the moisture pathways predicted by HYSPLIT, we use a one-dimensional vapor transport model (Kukla et al., 2019) to predict the isotopic composition of precipitation transported along these pathways. This model links spatial patterns of $\delta^{18}O_p$ to the balance of three moisture fluxes – precipitation (P), evapotranspiration (ET), and transport. It uses energetic and mass balance limits on evapotranspiration to place constraints on the relationship between P and ET, which is a key parameter that controls spatial patterns of $\delta^{18}O_p$ (Salati et al., 1979; Gat and Matsui, 1991; Lee et al., 2007; Winnick et al., 2014; Bailey et al., 2018; Kukla et al., 2019). Together with the dry and moist adiabatic lapse rate (Γ, K m^{-1}) and an assumed environmental lapse rate (γ, K m^{-1}), orographic rainout is incorporated into the model following the work of Smith (1979) and Smith and Barstad (2004). Though there are a variety of topographic parameterizations, for our simulations of westerly-derived moisture we use an idealized topography with a Gaussian-shaped mountain range combined with an orogenic plateau in the lee of the range. In our simulations of GPLLJ $\delta^{18}O_p$, we assume flat terrain. Even though the Plains gently rise by more than 1000 m from the Gulf Coast to the Front Range, the model of orographic precipitation applies to adiabatic ascent over topography – a process that does not occur over the Plains. Equation (1) is used to calculate the column-integrated precipitable water content (w, kg m^{-2}) as a function of advection (u, m s^{-1}; the movement of an air parcel) and eddy diffusion, precipitation (P, kg m^{-2}), and evapotranspiration (ET, kg m^{-2} s^{-1}) (Kukla et al., 2019).

$$\frac{\partial w}{\partial t} = \nabla \cdot (D \nabla \cdot w) - u \nabla \cdot w + \mathrm{ET} - P, \tag{1}$$

where t is time and D is the coefficient for eddy diffusion (m^2 s^{-1}).

Equation (2) is used to calculate the isotopic ratio of precipitable water (r_w) over space (x) in steady state following Eq. (1). The isotope ratio of precipitation (r_P) is derived by assuming equilibrium fractionation during moisture condensation. The isotope ratio of ET (r_{ET}) is derived as a function of the transpired fraction of ET ($T/E+T$) and the balance of equilibrium and kinetic isotope fractionation. For further details, we refer the reader to Kukla et al. (2019).

$$0 = D\left(\frac{d^2 r_w}{dx^2} + 2\frac{1}{w}\frac{dw}{dx}\frac{dr_w}{dx}\right) - u\frac{dr_w}{dx} + \frac{\mathrm{ET}}{w}(r_{ET} - r_w) - \frac{P}{w}(r_P - r_w) \tag{2}$$

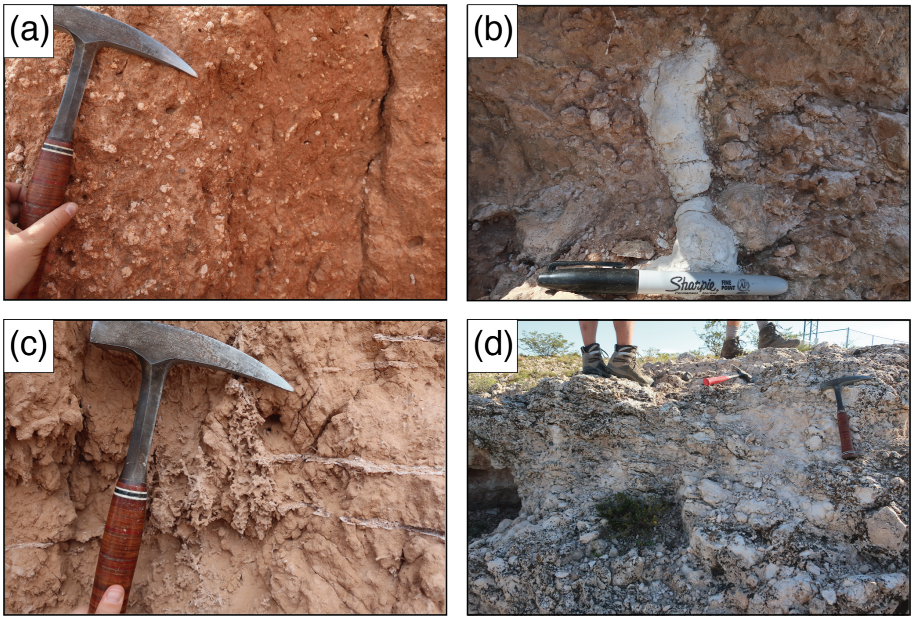

Figure 2. Field photos representing the primary types of authigenic carbonate sampled in this study. **(a)** Carbonate nodules. **(b)** Burrows. **(c)** Root casts. **(d)** Caprock calcrete, as pictured in SE New Mexico.

Here, r refers to the $^{18}O\,/\,^{16}O$ ratio and subscripts ET, P, and w refer to evapotranspiration, precipitation, and precipitable water, respectively.

Equations (1) and (2) ensure mass conservation and permit the reduction of precipitable water and of the ^{18}O of precipitable water by precipitation. Mass conservation relationships between potential evapotranspiration (PET), evapotranspiration (ET), and precipitation (P) are encapsulated within a Budyko hydrologic balance framework that limits moisture recycling based on energy (when PET $\leq P$) or water (when $P \leq$ PET). Equation (3) can be used to calculate a so-called "Budyko curve", which determines a unique hydroclimate solution for each isotope gradient using a given value of ω – a non-dimensional free parameter that captures land surface characteristics (such as vegetation, bedrock lithology, ruggedness) and modulates the partitioning of precipitation into either runoff or evapotranspiration (Budyko, 1974; Fu, 1981; Zhang et al., 2004; Greve et al., 2015; Kukla et al., 2019).

$$\mathrm{ET} = P\left(1 + \frac{\mathrm{PET}}{P} - \left(1 + \left(\frac{\mathrm{PET}}{P}\right)^{\omega}\right)^{\frac{1}{\omega}}\right) \qquad (3)$$

To populate the parameters in this model, we again use North American Regional Reanalysis (NARR) data (long-term monthly mean for years 1979–2000) (Mesinger et al., 2006). We show input values for model parameters in the Appendix (Table A1). For ω, we use the global mean value of 2.6 (Greve et al., 2015). For the transpired fraction of ET ($T/E+T$) we use a value of 0.64 (Good et al., 2015).

We simplify the longitudinal differences in simulated GPLLJ trajectories (see Fig. 3) as a 1-D storm track that transports moisture from the Gulf of Mexico to the Great Plains. To reflect the general curvilinear trajectories of the GPLLJ, partly caused by the influence of the North American Cordillera (Jiang et al., 2007), we implement a bend in our simplified trajectories at 32° N. From this bend, the simulated trajectory runs along the 101° meridian. This trajectory ends at 43° N, the latitude of our northernmost site. This trajectory passes over the middle of the present-day exposure of the Ogallala Formation and, hence, captures a representation of the atmospheric processes that result in $\delta^{18}O_p$ over the Great Plains.

To test for the influence of westerly moisture in the Great Plains (as indicated by the HYSPLIT results), we initialized the vapor transport model with annual mean NARR data interpolated to a simplified 1-D trajectory representing the westerlies (Fig. 8). The trajectory latitude is chosen to lie between the northern and southern boundary of the Ogallala Formation. To account for the known effects of orographic rainout on westerly moisture (Friedman et al., 2002; Lechler and Galewsky, 2013; Mix et al., 2019), we use a simplified topography, based on the modern observed topographic profile, that follows a Gaussian-shaped mountain with a flat plateau in the lee.

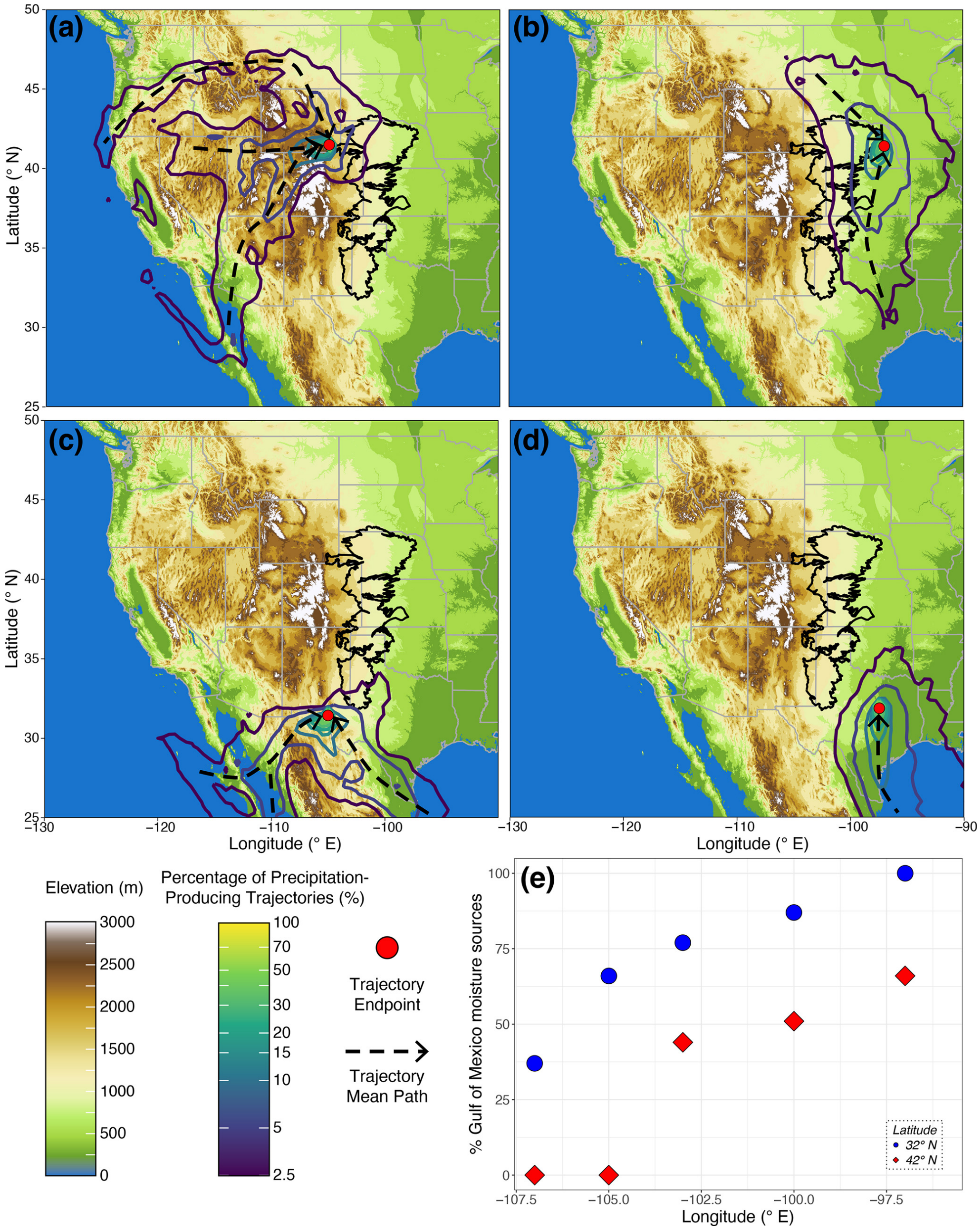

Figure 3. Map showing the percentage of precipitation-producing storm tracks at four localities on the Great Plains that bound the latitudinal and longitudinal extent of our data. HYSPLIT air parcels at all four sites are initialized at 1000 m above ground. **(a)** 42° N, −105° E. **(b)** 42° N, −97° E. **(c)** 32° N, −105° E. **(d)** 32° N, −97° E. The resulting mean storm trajectories are demarcated with dashed black lines with an arrow showing the direction of transport. In panels **(a)–(d)**, the extent of the Ogallala is shown in black. **(e)** An estimate of the percentage of gulf and southeasterly moisture that reaches each location as a function of longitude. Red points represent a transect of HYSPLIT simulations along the 42° N parallel; blue points represent a transect of HYSPLIT simulations along the 32° N parallel.

5 Results

5.1 Moisture sources and precipitation trajectories

Contour plots in Fig. 3a–d show the percentage of trajectories that produce precipitation at 1000 m above ground level for each of the plotted locations over the course of a year. Western sites receive a substantial portion of their moisture from westerly or southwesterly trajectories that traverse the high topography of the North American Cordillera. In particular, the northwesternmost site (Fig. 3a) receives little moisture from the gulf. In contrast, the southeasternmost site (Fig. 3d) receives predominantly gulf moisture. These patterns vary somewhat seasonally, with gulf and southeasterly moisture more dominant in the spring and summer months and westerly moisture more dominant in the winter months. Our results from HYSPLIT's clustering algorithm show that northern locations receive less gulf and southeasterly moisture than southern locations; however, regardless of latitude, the percentage of storms sourced from the gulf increases to the east (Fig. 3e).

5.2 $\delta^{18}O_c$ and $\delta^{13}C$ results

Our new $\delta^{18}O_c$ data range from a minimum of 17.0 ‰ to a maximum of 27.3 ‰ (Table S1 in Manser et al., 2023). When averaged by section, our new $\delta^{18}O_c$ data range from 19.6 ‰ to 26.8 ‰ (Table 1). The compiled data have a much larger range, reflecting their larger latitudinal distribution, with the average section $\delta^{18}O_c$ ranging from 13.6 ‰ to 27.0 ‰ (Appendix Table A2). Within individual sections, there is very little variance: the mean range and standard deviation of $\delta^{18}O$ in individual sections are ±1.8 ‰ and ±0.68 ‰, respectively, indicating that temporal shifts in $\delta^{18}O_c$ in the sampled sections are small (Table 1; Fig. 4b). If we exclude data outside Ogallala Formation, the mean range and standard deviation of $\delta^{18}O_c$ in individual sections are lower at ±1.7 ‰ and ±0.6 ‰, respectively, indicating that carbonates in the Ogallala Formation have very little variance.

Our new Ogallala $\delta^{13}C$ data have a mean value of -6.14 ± 1.4 (1σ) ‰ (Table 1) (excluding data from the Tesuque Formation). In contrast, our compiled Ogallala Formation data have a mean $\delta^{13}C$ value of -6.74 ± 0.8 (1σ) ‰. This discrepancy is due to relatively high $\delta^{13}C$ values in the sections in New Mexico identified via lithologic or geomorphic correlation by Frye et al. (1982) to be Ogallala outcrops. When these Frye et al. (1982) data are excluded, the mean $\delta^{13}C$ value in our new data is -6.69 ± 0.9 (1σ) ‰, which is statistically indistinguishable from the compiled data $\delta^{13}C$ mean.

5.3 Spatial distribution of $\delta^{18}O_p$

For each site, we calculate a mean reconstructed $\delta^{18}O_p$ value and compare these mean values with modern water $\delta^{18}O$ (retrieved from Waterisotopes.org; Waterisotopes Database, 2019). To reconstruct paleo-precipitation $\delta^{18}O$, we use the modern 2 m air temperature from NARR to estimate the formation temperature of soil carbonate along with the fractionation factors of Kim and O'Neil (1997). Means, standard deviations, and full $\delta^{18}O$ ranges for each site with new data are presented in Table 1, and the previously published $\delta^{18}O$ data – converted to paleo-precipitation $\delta^{18}O_p$ – are presented in Appendix Table A2. All of the $\delta^{18}O_c$ data are available as supporting material (Table S1) in Manser et al. (2023). The spatial distribution of the reconstructed $\delta^{18}O_p$ shows a nearly identical spatial distribution to that of modern $\delta^{18}O$ (Fig. 4a). From the Gulf Coast inland, paleo-$\delta^{18}O$ follows the modern $\delta^{18}O$ gradient, with lower values to the west and to the north. The maximum change in both paleo-$\delta^{18}O$ and modern $\delta^{18}O$ occurs along a southeast–northwest trend, running roughly from the Gulf Coast in Texas to northern Colorado.

We further test whether decreasing temperatures northward significantly influences our reconstructed $\delta^{18}O_p$ values. The modern mean annual temperature gradient in the Great Plains (from 28.3 to 43° N) is −1.2 °C per 100 km. In June–July–August (JJA), this gradient is reduced to 0.4 °C per 100 km. We use these two temperature gradients to calculate the effect of changing the spatial pattern of temperature on our reconstructed $\delta^{18}O_p$, as well as testing a hypothetical case with latitudinally constant temperature of 25° C. Using the JJA temperature gradient, the reconstructed $\delta^{18}O_p$ gradient is slightly shallower (red circles in Fig. 5) compared to the modern $\delta^{18}O$ gradient (gray dots) and compared to the reconstructed $\delta^{18}O_p$ gradient (blue circles) using modern yearly mean NARR temperature data (Fig. 5b). The likely maximum difference that a reduced temperature gradient – relative to the modern – can impart on our results is captured in the scenario of spatially uniform temperatures, which represents an extreme end-member scenario where poleward warming in a higher-CO_2 world results in a negligible latitudinal temperature gradient. Even spatially uniform temperatures only result in an increase of 2.9 ‰ in the northernmost sites relative to the assumption of a modern temperature gradient, still within the range of modern $\delta^{18}O$ across the Plains. These results suggest that our reconstructed $\delta^{18}O_p$ values are relatively insensitive to assumptions of carbonate formation temperatures in a warmer world with a potentially reduced meridional temperature gradient (Feng et al., 2016; van Dijk et al., 2020).

There is not only a pronounced N–S $\delta^{18}O$ gradient in the paleo-data, but also substantial W–E variation. Figure 6 shows modern and reconstructed $\delta^{18}O_p$ plotted against longitude using the NARR mean annual temperature to constrain the formation temperature of carbonate. Again, as with the comparison against latitude (Fig. 5), all reconstructed $\delta^{18}O_p$ estimates fall within the same range as the modern $\delta^{18}O$ when projected to longitude. Though again this conclusion is tempered by our assumption of carbonate formation temperatures, we suggest, as above, that this is likely to be a negligible effect, particularly given the relative insensitivity in the ^{18}O fractionation factor to temperature (~ 0.2 ‰ K^{-1}) (Kim and O'Neil, 1997).

5.4 Reactive transport modeling of $\delta^{18}O_p$

The vapor transport model (Kukla et al., 2019) allows us to predict $\delta^{18}O_p$ along a given storm track, reflecting the balance between transport, precipitation, and evapotranspiration. Our model of GPLLJ $\delta^{18}O_p$ simulates higher $\delta^{18}O$ at the end of the trajectory compared to both modern and reconstructed $\delta^{18}O_p$ values (Fig. 7a). Consistent with higher $\delta^{18}O$ values, the model also predicts higher atmospheric moisture content and relative humidity than indicated by NARR, suggesting it is underpredicting rainout from air masses that

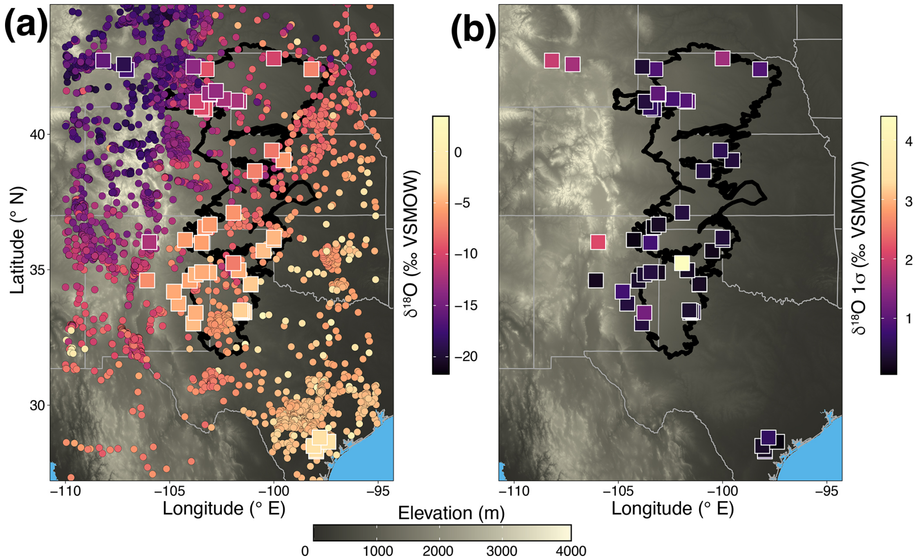

Figure 4. Spatial distribution of $\delta^{18}O$ **(a)** and reconstructed $\delta^{18}O_p$ 1σ **(b)**. **(a)** Comparison of reconstructed $\delta^{18}O_p$ from $\delta^{18}O_c$ (large squares) calculated using the yearly mean of monthly long-term temperature data retrieved from NARR for each site. Modern meteoric water $\delta^{18}O$ (small circles) is derived from modern groundwater, river water, or stream water retrieved from Waterisotopes.org (Waterisotopes Database, 2019). Data points are colored by their $\delta^{18}O$ values. **(b)** The 1σ of the reconstructed $\delta^{18}O_p$ derived from the variability in the $\delta^{18}O_c$ values from each stratigraphic section. In both panels, the black polygon marks the extent of modern-day exposure of the Ogallala Formation.

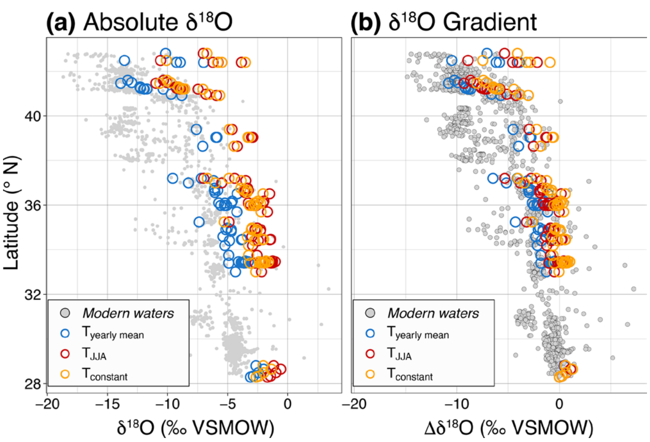

Figure 5. **(a)** Reconstructed $\delta^{18}O_p$ plotted against latitude. Reconstructed $\delta^{18}O_p$ is calculated assuming a spatially uniform temperature of 25 °C (yellow circles), annual mean temperatures (blue circles), or June–July–August (JJA) mean temperatures (red circles). Annual mean and JJA temperatures are taken from monthly long-term mean data retrieved from NARR (Mesinger et al., 2006). Gray circles are modern meteoric water $\delta^{18}O$, including groundwater and river or stream water, retrieved from Waterisotopes.org (Waterisotopes Database, 2019). **(b)** The same as **(a)** but the x axis sets the southernmost data (∼ 28° N) to zero to emphasize the effect on the spatial gradient in $\delta^{18}O$.

reach the northern plains or that the single air mass assumption implicit in this model is not valid in this region (Fig. 7b).

Our model of westerly moisture $\delta^{18}O_p$ suffers from a similar mismatch between simulated $\delta^{18}O_p$ and both modern $\delta^{18}O$ and reconstructed $\delta^{18}O_p$ (Fig. 8a). Though our westerly trajectory uses an idealized topography to simulate the topography of the North American Cordillera, we are able to approximately reproduce the decrease in $\delta^{18}O_p$ that occurs close to the coast of North America. Variations in simulated $\delta^{18}O_p$ after the initial orographic rainout are primarily driven by temperature that varies with elevation in the NARR data. This leads to minor discrepancies where elevation decreases $\delta^{18}O_p$ in modern waters but increases $\delta^{18}O_p$ in the model due to colder temperatures raising $\delta^{18}O_p$. Nevertheless, simulated $\delta^{18}O_p$ approximates meteoric water $\delta^{18}O$ along the westerly trajectory until this trajectory reaches the Great Plains at a distance of around 1550 km. At distances larger than this, the model substantially underestimates meteoric water $\delta^{18}O$ and reconstructed $\delta^{18}O_p$ on the Great Plains. Again examining climatological measures related to $\delta^{18}O_p$, there is a distinct discrepancy in atmospheric moisture content between the modeled output and the NARR data over the Great Plains at a distance of around 1550 km from the starting point of the simulated westerly trajectory (Fig. 8b).

6 Discussion

Our new spatially resolved data provide insight into moisture transport to the Great Plains during the late Neogene. In brief, the overall constancy of $\delta^{18}O$ between the late Miocene and the present suggests that the features of atmospheric cir-

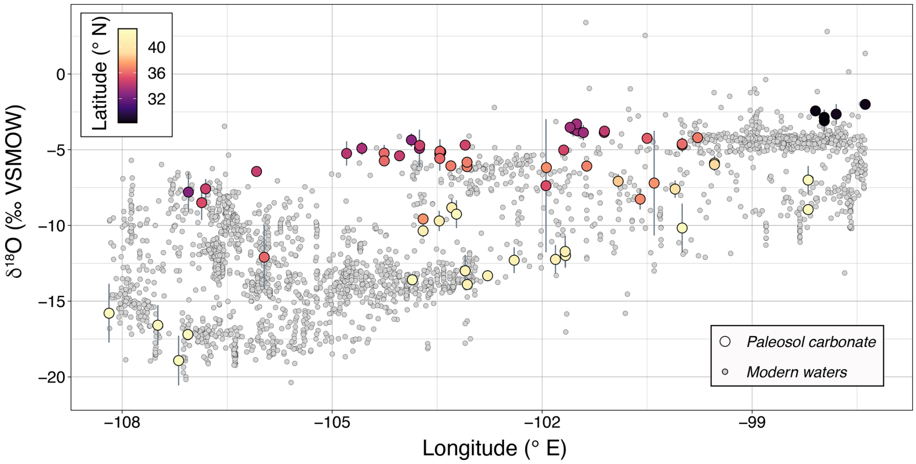

Figure 6. Modern meteoric water δ^{18}O (small, gray circles) and reconstructed $\delta^{18}O_p$ (large, colored circles) versus longitude. Reconstructed $\delta^{18}O_p$ is colored with respect to latitude. Modern meteoric water data include δ^{18}O data from groundwater, river water, and stream water retrieved from Waterisotopes.org (Waterisotopes Database, 2019). Vertical error bars are 1σ of the mean section δ^{18}O data.

culation most responsible for moisture delivery to the Great Plains today – notably the Great Plains low-level jet and the wintertime westerlies – have likely been the dominant features since at least the late Miocene. Further, that the reconstructed $\delta^{18}O_p$ gradient is indistinguishable from today's δ^{18}O gradient indicates that the balance of GPLLJ and westerly moisture has hardly changed since the late Miocene. Either these circulation features have undergone no substantial change in net rainout, or, if one has, its effect was masked by countervailing changes in the other. Overall, these results bolster earlier findings by Fox and Koch (2004), who found a consistent south-to-north gradient in $\delta^{18}O_c$ in the Great Plains that they attributed to a similar latitudinal temperature gradient in the Miocene.

Below, we discuss our findings in more detail, place these data in the context of previous work in the region, and discuss how our new data permit a re-interpretation of the controls on long-term climate in the Great Plains. We also discuss several important caveats in our data that point towards the need for future work to study more nuanced changes in climate than can be resolved with this dataset.

6.1 Constancy of $\delta^{18}O_p$ in relation to climate change

The Miocene was warmer than the present day, particularly during the Miocene Climate Optimum (MCO) (Westerhold et al., 2020; Steinthorsdottir et al., 2021), and was characterized by a long-term cooling trend after the MCO (Herbert et al., 2016). Even after this cooling interval, the lack of extensive Northern Hemisphere ice sheets and likely a smaller Antarctic ice sheet indicate that the late Miocene was warmer than today, with a reduced latitudinal temperature gradient (LaRiviere et al., 2012; Feng et al., 2016). The warmer climate and shallower temperature gradient could impact $\delta^{18}O_p$, yet the decrease in reconstructed $\delta^{18}O_p$ with latitude appears identical to today (Fig. 4). This result is perhaps not surprising, since temperature appears to have only a secondary effect on the latitudinal gradient of $\delta^{18}O_p$ (Fig. 5a). Instead, such constancy in $\delta^{18}O_p$ through time indicates that the mixing of westerly and southerly moisture – the primary control on the latitudinal δ^{18}O gradient – was similar to today.

The results of our vapor transport modeling support the contention that mixing between dry, low-δ^{18}O westerly air masses and moist, high-δ^{18}O southerly air masses is required to explain the long-standing presence of this steep latitudinal gradient in $\delta^{18}O_p$. The vapor transport model adequately predicts $\delta^{18}O_p$ in westerly- or GPLLJ-dominated regions, but it performs poorly where these air masses meet (Figs. 7 and 8). Air mass mixing is neglected in the 1-D vapor transport model, so the model's poor performance in these regions points to mixing as an important control on the latitudinal $\delta^{18}O_p$ gradient. Notably, this region of air mass mixing is closely tied to the east–west aridity gradient because it tracks the trade-off between drier westerly air and the wetter GPLLJ. Thus, the surprisingly static spatial $\delta^{18}O_p$ pattern across the Great Plains since the Miocene could be interpreted to reflect no change in the relative mixing of dry and moist air masses over time, maintaining the spatial pattern of the modern aridity gradient. The presence of the North American Cordillera – likely high since the Eocene (Chamberlain et al., 2012; Mix et al., 2013) – suggests that orographic rainout on the western margin of North America is also a long-standing feature, resulting in low-δ^{18}O moisture that is advected to the Great Plains from the west. What is more surprising is that the strength of the GPLLJ appears to be similar to today even in the warmer Miocene, given that this jet and its moisture transport are likely to be sensitive to global climate change (Cook et al., 2008; Zhou et al., 2021a).

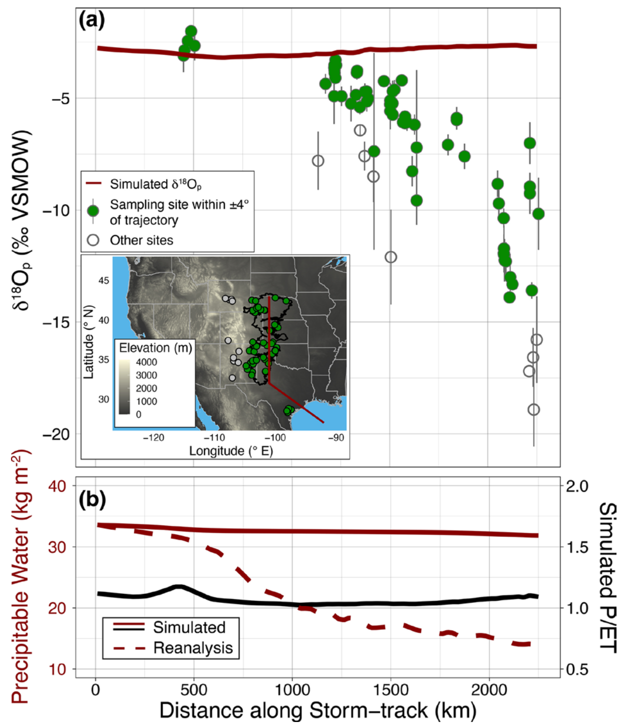

Figure 7. Vapor transport model simulation of $\delta^{18}O_p$ along an idealized Great Plains low-level jet (GPLLJ) trajectory. **(a)** The red line is the modeled $\delta^{18}O_p$ along the simulated storm track (exact location of the storm track is shown as a red line in the inset). Green points are reconstructed $\delta^{18}O_p$ within ±4° longitude of the trajectory. Gray circles are data greater than ±4° longitude from the simulated trajectory. Vertical error bars are 1σ of the mean section reconstructed $\delta^{18}O_p$. **(b)** Simulated precipitable water (solid red) and P / ET (solid black) plotted along the simulated storm track. The dashed line shows the actual annual mean precipitable water along this storm track retrieved from NARR.

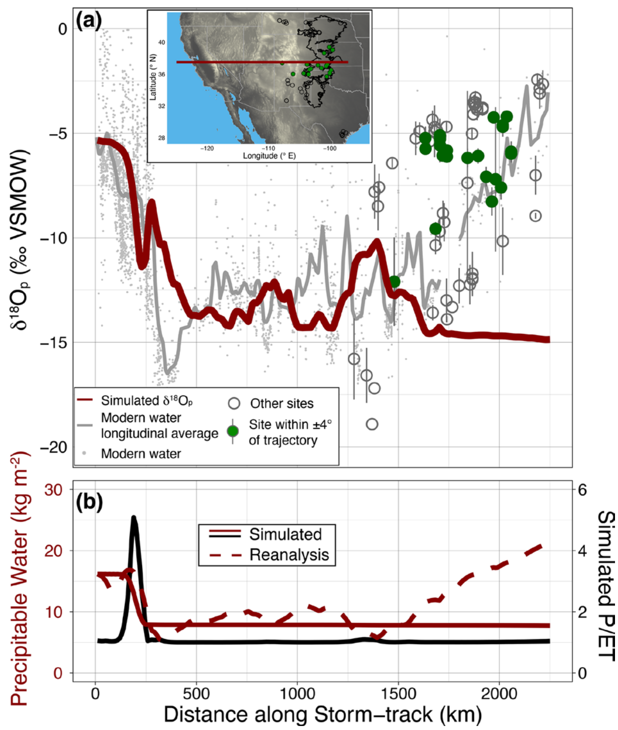

Figure 8. Vapor transport model simulation of $\delta^{18}O_p$ along an idealized westerly trajectory. **(a)** The red line is the modeled $\delta^{18}O_p$ along the simulated storm track (exact location of the storm track is shown as a red line in the inset). Green points are reconstructed $\delta^{18}O_p$ data within ±4° latitude from the storm track. Large, unfilled gray circles are data greater than ±4° latitude from the simulated trajectory. Vertical error bars are 1σ of the mean section reconstructed $\delta^{18}O_p$. Small gray circles are modern meteoric water $\delta^{18}O$, including stream water, river water, and groundwater, retrieved from Waterisotopes.org (Waterisotopes Database, 2019). The gray line is a kernel-smoothed average of the meteoric water $\delta^{18}O$ against distance along the storm track. **(b)** Simulated precipitable water (solid red) and P / ET (solid black) plotted along the simulated storm track. The dashed line shows the actual annual mean precipitable water along this storm track retrieved from NARR.

Overall, our vapor transport modeling indicates that a purely southerly source of moisture would result in $\delta^{18}O_p$ values that are too high in the northern plains (Fig. 7), whereas a purely westerly source brings $\delta^{18}O_p$ values that are too low (Fig. 8). To be clear, a static $\delta^{18}O_p$ gradient does not require static precipitation and evaporation rates over time. In contrast, precipitable water, P, and E likely all increased in the warmer Miocene (Held and Soden, 2006; Siler et al., 2018), but in such a way that net rainout (and thus the $\delta^{18}O_p$ fingerprint of hydrological change) did not vary substantially.

6.2 Additional factors that influence $\delta^{18}O_c$

There are a number of additional factors, both climatic and non-climatic, that may affect the $\delta^{18}O_c$ data, potentially decoupling $\delta^{18}O_c$ values from $\delta^{18}O_p$ and conflicting with our interpretation above. Such factors include changes in soil temperatures and evaporation and also imprecision in the chronologies of the sections we sampled. Below, we discuss these factors and why our interpretations are robust to assumptions regarding these factors.

6.2.1 Effect of temperature and evaporation on $\delta^{18}O_c$

Given that temperature affects the fractionation of ^{18}O between water and calcite (Kim and O'Neil, 1997), spatial changes in temperature may alter our reconstructed $\delta^{18}O_p$ gradient. However, we found that even extreme scenarios for changes in the spatial pattern of temperature over the Great Plains (ranging from the modern annual average latitudinal temperature gradient to a null latitudinal temperature gradient) had only a small effect on the overall latitudinal gradient of reconstructed $\delta^{18}O_p$ (Fig. 5). We therefore conclude that, while temperature change since the Miocene has likely impacted the absolute value of $\delta^{18}O_c$, it does not substantially alter our conclusion that the reconstructed $\delta^{18}O_p$ spatial pattern is similar to today.

While the spatial pattern of temperature change in the Plains does not appear to have had a major influence on our reconstructed $\delta^{18}O_p$ gradient, for any reasonable temperature scenario (annual, JJA, or spatially uniform 25 °C), reconstructed $\delta^{18}O_p$ absolute values are typically higher than modern $\delta^{18}O_p$ by 2 ‰–3 ‰. Fox and Koch (2004) also found that $\delta^{18}O_c$ was typically higher than predicted, particularly in the southern Great Plains, and attributed this observation to both higher temperatures and $\delta^{18}O_p$. We suggest that, while the gradient of $\delta^{18}O_p$ does not appear to have substantially changed since the Miocene, the starting value of marine vapor $\delta^{18}O$ may have been slightly higher in the warmer Miocene due to elevated precipitable water, elevating $\delta^{18}O_p$ across the Great Plains (i.e., van Dijk et al., 2020).

Recent work has indicated that evaporative conditions (i.e., low AI values) may elevate $\delta^{18}O_c$, thereby leading to an overestimate of $\delta^{18}O_p$ (Kelson et al., 2023). We suggest that our overall conclusion of a similar spatial pattern of $\delta^{18}O_p$ in the late Miocene is likely not overly influenced by changes in the spatial pattern of evaporation. Today, the latitudinal gradient in AI is negligible (Seager et al., 2018b); instead, the strongest gradient in AI is west to east (Fig. 1). Consequently, the stark latitudinal gradient in reconstructed $\delta^{18}O_p$ is unlikely to be driven by differential evaporative conditions. While higher marine vapor $\delta^{18}O$ may explain the elevated reconstructed absolute $\delta^{18}O_p$ values (2 ‰–3 ‰ above modern meteoric water $\delta^{18}O$), another explanation may be pervasive evaporative enrichment of pedogenic carbonates across the Great Plains, though this evaporative enrichment does not appear to vary latitudinally.

6.2.2 Changes in precipitation seasonality

Soil carbonates are thought to form mostly seasonally, particularly in the warm season and perhaps as soils dry and plants senesce, causing soil CO_2 to decline and carbonates to form (Breecker et al., 2009; Huth et al., 2019). However, the timing of soil carbonate formation may shift as the timing of precipitation and plant productivity varies due to climate change, and such shifts have been invoked to explain a wide range of soil carbonate records in the western US and elsewhere (Caves, 2017; Kukla et al., 2022b; Rugenstein et al., 2022). GCMs indicate that precipitation seasonality over the Great Plains will change substantially in a warmer world, with precipitation shifting towards the spring and away from the late summer (Cook et al., 2008; Bukovsky et al., 2017; Zhou et al., 2021a). Though it is difficult to assess the timing of even modern soil carbonate formation in the Great Plains, our reconstructed Miocene $\delta^{18}O_p$ data agree most closely with modern water $\delta^{18}O$ when using mean annual temperatures. Though we have no a priori reason to suspect that Miocene carbonates may record mean annual temperatures, this close agreement suggests that Miocene carbonates may have formed in the shoulder seasons (i.e., spring and fall), thereby recording intermediate temperatures and, likely, a mixture of summertime GPLLJ moisture and wintertime westerly moisture.

That Miocene soil carbonates formed in the shoulder seasons would help to reconcile our findings of a largely invariant spatial pattern of $\delta^{18}O_p$ since the Miocene with previously published records that show a large (2 ‰–4 ‰) increase in $\delta^{18}O_c$ during the Pliocene–Quaternary in the Great Plains (Fox et al., 2012; Mix et al., 2013; Chamberlain et al., 2014). We suggest that this discrepancy (i.e., a static late Miocene $\delta^{18}O_p$ spatial pattern but increasing $\delta^{18}O_c$ in the Pliocene–Quaternary) likely arises due to changes in the seasonality of soil carbonate formation between the late Miocene and Quaternary. For example, as the world cooled into the Quaternary, the southward shift of the westerly jet would suppress the springtime GPLLJ, while enhancing GPLLJ precipitation over the Great Plains during the summer – the opposite response than observed in GCMs as CO_2 rises (Cook et al., 2008; Bukovsky et al., 2017; Zhou et al., 2021a). Such a seasonality shift might shift the timing of soil carbonate formation towards the summer, elevating $\delta^{18}O_c$ as it records higher summertime $\delta^{18}O_p$ (Liu et al., 2010) and thereby elevating $\delta^{18}O_c$ relative to the late Miocene.

6.2.3 Imprecision in chronologies and timing of carbonate formation

Our interpretation hinges upon correlating sections across the vast expanse of the Great Plains; however, ages for many Ogallala sections are only poorly constrained, typically via biostratigraphy (Kitts, 1965; Skinner et al., 1977; Thomasson, 1979; Winkler, 1987, 1990; Tedford et al., 2004) or, less frequently, via radiometric dates (Swisher, 1992; Cepeda and Perkins, 2006; Henry, 2017; Smith et al., 2018). Where biostratigraphy has been used, age resolution is typically limited to the scale of the North American land mammal ages. In many places in eastern New Mexico, the Ogallala Formation is recognized by its clay lithology and its topographic position relative to the laterally extensive caprock to the east (Frye et al., 1978, 1982). Further, the character of Ogallala deposition – large alluvial megafans that gradually filled in pre-existing valleys and covered intervening interfluves combined with its relative thinness – suggests that deposition was often sporadic with frequent and cryptic unconformities associated with many of the paleosols distributed throughout the formation. Consequently, correlations across the entirety of the Ogallala Formation are likely to be imprecise and our treatment of the data likely mixes data from the late middle Miocene and the latest Miocene.

Nevertheless, this imprecision in correlation likely does not affect our conclusions. We note that nearly all of our sections have low $\delta^{18}O_c$ variability (Fig. 4b; Table 1), suggesting that, throughout deposition of the Ogallala, there was very little change in $\delta^{18}O_p$. Ludvigson et al. (2016), analyzing two cores drilled through the Ogallala Formation in western Kansas, found similarly very low variability in $\delta^{18}O_c$ across the 50–60 m of sampled core material. This low variability, which contrasts with sections located to the west within the North American Cordillera, indicates that even large discrepancies in correlated sections likely do not affect our overall conclusion that the south-to-north $\delta^{18}O_p$ gradient has remained similar to today since the late Miocene.

Further, previously published Neogene $\delta^{18}O_c$ records show almost no change in $\delta^{18}O_c$ during the Miocene (Fox and Koch, 2004; Mix et al., 2013; Chamberlain et al., 2014), again suggesting that imprecision in our correlations is not likely to impact our conclusions. In contrast, modeling studies that have examined changes in $\delta^{18}O_p$ in the Great Plains in the Miocene have suggested that the south-to-north $\delta^{18}O_p$ gradient should increase by several per mille as a consequence of higher CO_2 and a shallower Equator-to-pole temperature gradient (Feng et al., 2016; Lee, 2019). These studies used boundary conditions thought to approximate the middle Miocene, with atmospheric CO_2 of 560 ppm. Disagreement between our results and these model results may arise for a variety of reasons. One such reason may revolve around uncertainty in dating of the Ogallala Formation. While these modeling studies used middle Miocene boundary conditions and 560 ppm CO_2, our data likely come from the late Miocene, following substantial cooling after the peak of Neogene warmth during the middle Miocene (Herbert et al., 2016). Consequently, the environment in which much of the Ogallala Formation was deposited may differ from that simulated by Feng et al. (2016) and Lee (2019). Alternatively, given the difficulty in simulating the land–atmosphere coupling over the Great Plains in modern-day simulations (Bukovsky et al., 2017; Laguë et al., 2019; Zhou et al., 2021a) and the importance of the land surface in modulating $\delta^{18}O_p$, minor misrepresentations in the land surface parameterizations within these models may yield outsize impacts on the simulated $\delta^{18}O_p$ gradient. While a thorough review comparing our results to simulated Miocene $\delta^{18}O_p$ over the Great Plains is outside the scope of this paper, our new spatially resolved dataset provides an opportunity to test model predictions of late Miocene climate simulation skill over central North America.

We additionally assume that the authigenic carbonates that we sampled formed in the late Miocene. Several studies (Joeckel et al., 2014; Smith and Platt, 2023) have noted that some caliche units in the northern and central Great Plains may reflect post-depositional case hardening rather than syndepositional carbonate formation based upon lateral discontinuities in these units. Given the low variance in our Ogallala samples (typically much less than 1 ‰), we suggest that all of the carbonates in our study formed from the same meteoric water. Further, the $\delta^{13}C$ values of our carbonate samples are relatively low (~ -7 ‰). Given the expansion of C_4 plants during the Plio-Pleistocene, the $\delta^{13}C$ values of authigenic carbonates formed in the Plio-Pleistocene are substantially higher (~ -2 ‰) (Fox and Koch, 2003). Thus, the low $\delta^{13}C$ values of our carbonate samples indicate that they formed during the late Miocene under a dominantly C_3 grassland environment. The only exception to these low $\delta^{13}C$ values in our sections is from carbonates sampled in eastern New Mexico from outcrops identified as Ogallala by Frye et al. (1982). In many of these sections, there are authigenic carbonate samples with $\delta^{13}C$ values > -5 ‰ and frequently the caprock caliche samples have $\delta^{13}C$ values approaching 0 ‰ (Table S1 in Manser et al., 2023). This suggests that these outcrops either may not be correlative with the Ogallala (Henry, 2017) or that authigenic carbonate formation in these sections occurred substantially later than Ogallala deposition. However, we have no independent age constraints with which to better constrain the ages of these units, and we therefore include them in our study. We do note that the reconstructed $\delta^{18}O_p$ from these sections is indistinguishable from modern $\delta^{18}O_p$ in eastern New Mexico, further suggesting that the long-term pattern of $\delta^{18}O_p$ in the Great Plains has remained invariant. Thus, the combination of the low $\delta^{13}C$ values and the low variance in our $\delta^{18}O_c$ data suggests that our assumption of late Miocene carbonate formation is robust.

7 Implications

That atmospheric circulation over the Great Plains has remained relatively constant since the late Miocene provides important context for understanding how Great Plains hydroclimate and environments may respond to higher atmospheric CO_2. Further, our data provide insight into the climatic and tectonic controls that may have driven deposition of the Ogallala Formation. In both cases, our data places critical constraints on our understanding of both past environments and the future evolution of climate in the Great Plains.

7.1 Response of Great Plains hydroclimate to CO_2

Of concern as atmospheric CO_2 rises is whether and how the climatological 100th meridian, which demarcates the semi-arid west from the humid east, will shift. The current position of this climatological 100th meridian is partly set today by the boundary between dry westerly air masses that have lost much of their moisture from passage over the North American Cordillera and moist southerly masses transported by the GPLLJ. If dynamical relative shifts in the strength of these two predominant circulation systems were to occur as CO_2 rises, one might expect the boundary between low $\delta^{18}O_p$ and high $\delta^{18}O_p$ to shift. For example, model simulations indicate that the poleward shift of the westerly jet and North Atlantic Subtropical High with warming should enhance GPLLJ moisture transport in the spring but suppress it in the summer (Zhou et al., 2021a, b). If the overall tendency were a weaker GPLLJ with warming, we might expect less northward moisture transport and thereby a shift of this $\delta^{18}O_p$ boundary southward and eastward. Instead, we find that the spatial pattern of $\delta^{18}O_p$ has remained unchanged since the late Miocene, suggesting that the relative strength of these two circulation systems was not substantially different in a warmer, higher-CO_2 world. Such findings bolster GCM results that, overall, mean wet-season precipitation does not change substantially and that therefore the boundary between the GPLLJ and the westerlies is not overly sensitive to warming.

Though dynamical shifts in circulation may affect hydroclimate over the Great Plains, additional thermodynamic mechanisms have been invoked to explain shifts in the climatological 100th meridian with warming. Because PET will rise faster than P across the Plains, aridity will increase (Seager et al., 2018a, b). However, this will be complicated by how actual ET – and therefore the partitioning of moisture returned to the atmosphere versus to runoff – responds to warming. How ET changes with warming depends on a variety of factors including plant water use efficiency (Swann et al., 2016; Lemordant et al., 2018) and the temporal distribution of precipitation (Scheff et al., 2022). Our results imply that either (1) the effect of increasing PET relative to P had a small effect on net rainout – and hence $\delta^{18}O_p$ – in the Miocene, or (2) decreases in ET efficiency with warming, perhaps driven by more efficient plant water use (Lemordant et al., 2018) and which would reduce ^{18}O return to the atmosphere, counteracted the expected increase in $\delta^{18}O_p$ due to increasing PET relative to P.

Though the late Miocene was likely warmer than today with higher than pre-industrial CO_2 (Herbert et al., 2016; Mejía et al., 2017; Sosdian et al., 2018; CenCO2PIP Consortium, 2023), the precise global climate that our new data reflect is uncertain. This uncertainty arises not only because of the chronological uncertainty associated with the Ogallala Formation, but also due to uncertainty in both global temperature and CO_2 reconstructions. The late Miocene may have seen global temperatures elevated by 5° higher relative to pre-industrial (Westerhold et al., 2020; Ring et al., 2022) and atmospheric CO_2 between 350 and 500 ppm (Tanner et al., 2020; Brown et al., 2022; CenCO2PIP Consortium, 2023). However, these estimates – particularly for CO_2 – remain imprecise, and it is therefore difficult to determine just how insensitive the Great Plains hydroclimate is to warming and higher CO_2. Further, while the land surface plays a critical role in modifying Great Plains hydroclimate, the late Miocene Great Plains were already dominated by grassland ecosystems (Stromberg, 2005). Though C_4 plants have a greater water use efficiency than C_3 plants (Osborne and Sack, 2012), the invariant $\delta^{18}O_p$ spatial pattern suggests that overall ecosystem water use (i.e., transpiration to the atmosphere) was likely similar to today and overall hydroclimate in the late Miocene resembled the hydroclimate today in the Great Plains.

7.2 Implications for understanding the origin of the Ogallala Formation

Why much of the Great Plains shifted from a dominantly erosive landscape to a depositional landscape for several million years, before returning to the dominantly erosive landscape of today, has remained a major outstanding question in North American geology (Heller et al., 2003). As the sediments of the Ogallala Formation are sourced in the Rocky Mountains, this question has been intimately linked to what process drove this major late Cenozoic erosional event, producing the alluvial fans and megafans that blanketed the Great Plains in the late Miocene (Trimble, 1980; Molnar and England, 1990). Paleoaltimetry data have suggested that much of the North American Cordillera has been high since the Eocene (Forest et al., 1995; Mix et al., 2011). If mean elevation has not changed for much of the Cenozoic, then changes in climate – perhaps driven by increasingly variable, orbitally controlled glacial cycles – may have driven the increase in erosion (Molnar and England, 1990; Gregory and Chase, 1994; Zhang et al., 2001). In contrast, multiple studies that have analyzed paleo-slopes of the Ogallala Formation fluvial sediments conclude that the Ogallala Formation must have been tilted post-deposition due to a long-wavelength uplift (McMillan et al., 2002; Heller et al., 2003), perhaps associated with dynamic topography effects driven by continued subduction of the Farallon Plate (Willett et al., 2018).

Our data suggest that hydroclimate was not substantially different in the late Miocene and was therefore unlikely to be the proximal cause of widespread erosion of the Rocky Mountains and deposition of the Ogallala Formation. Instead, we suggest that, because overall hydroclimate – and, in particular, runoff – was similar to today, deposition of the Ogallala Formation must have been driven by long-wavelength tilting of the North American plate that uplifted portions of the Rocky Mountains. Estimates of the uplift necessary to explain post-depositional tilting are less than 1 km (McMillan et al., 2002; Leonard, 2002). Such uplift was likely not substantial enough to either (1) be detectable in paleo-altimetry datasets or (2) substantially modify the strength of the GPLLJ (Jiang et al., 2007). Uplift might be expected to result in lower $\delta^{18}O_p$ in late Cenozoic basins in the Rocky Mountains due to orographic forcing of precipitation. However, in this region, orographic forcing is limited to GPLLJ storms that reach the Front Range, and continued mixing with low-$\delta^{18}O_p$ westerly moisture would make it very difficult to discern such a signal. We thus conclude that hydroclimate was not substantially different in the late Miocene in the Great Plains and that long-wavelength tilting must be a necessary component of the formation of the Ogallala Formation.

8 Conclusion

Our new spatially resolved late Miocene $\delta^{18}O_c$ data from across the Great Plains reveal that the spatial pattern of reconstructed $\delta^{18}O_p$ is indistinguishable from the spatial pattern of modern meteoric water $\delta^{18}O$. Despite changes in global climate, we suggest that this static $\delta^{18}O$ spatial pattern reflects an atmospheric circulation system over the Great Plains that in the late Miocene was largely identical to today: wintertime westerly air masses, dried by transit over the North American Cordillera, delivered low-$\delta^{18}O$ moisture to the northern Great Plains, while southerly moisture, transported by the Great Plains low-level jet, brought high-$\delta^{18}O$ moisture to the southern Great Plains. Thus, on the timescales preserved within the Ogallala Formation, the mixing zone between these two circulation systems was similar to today. Given that these two atmospheric circulation systems are responsible for a nearly 15 ‰ $\delta^{18}O$ gradient north to south along the Great Plains, these results appear to be robust to assumptions regarding temperature, evaporation, and precipitation seasonality changes since the late Miocene and also insensitive to uncertainties in our correlations across the expanse of the Ogallala Formation.

These results suggest that, on geological timescales, large-scale hydroclimate in the Great Plains is relatively insensitive to changes in global temperature and atmospheric CO_2. Model projections tend to indicate that mean annual precipitation will not increase substantially as CO_2 rises (Bukovsky et al., 2017; Zhou et al., 2021a), and our results support this contention, in that a static $\delta^{18}O$ spatial pattern suggests that net rainout in the late Miocene across the Great Plains was likely not substantially different than today. In contrast, our results do not support projections that aridity will increase over the Plains (Seager et al., 2018a). While increases in PET are robust in models (Scheff et al., 2017), our results suggest that countervailing decreases in actual ET efficiency likely offset any change in PET, yielding an approximately constant spatial pattern of P / ET. Further, our results indicate that large-scale changes in climate (Zhang et al., 2001) are likely not the cause of the widespread erosional event responsible for deposition of Ogallala sediments. Instead, the fact that Great Plains hydroclimate in the late Miocene was similar to today supports the notion that long-wavelength uplift (Moucha et al., 2009; Karlstrom et al., 2011; Willett et al., 2018) shifted the Great Plains from a dominantly erosive landscape to an aggradational one.

The Great Plains lie at a unique climatic and geologic intersection, and this confluence has inspired more than a century of work to understand the relationship between climate, geology, and ecosystems over geologic time in the Plains (Powell, 1879, 1890; Seni, 1980; Fox and Koch, 2003; Jiang et al., 2007; Seager et al., 2018b; Willett et al., 2018). However, the sharp geologic and climatic gradients that characterize this landscape complicate efforts to understand past changes. Nevertheless, our results suggest that spatially resolved datasets provide a powerful means to constrain the position and shape of these gradients in the past. Additional work that utilizes newly developed proxy systems and/or pairs well-established proxies with our continental-scale data will provide an even sharper picture of the climatic and geologic forces that have shaped this remarkable landscape.

Appendix A

Table A1. Input parameters for the reactive transport model. All inputs are retrieved from NARR data except ω, which is set to the global average of 2.6 (Greve et al., 2015), and the transpired fraction of ET, which is set to 0.64 (Good et al., 2015).

Parameter	GPLLJ trajectory	Westerly trajectory
Temperature (MAT)	295 K	287 K
Potential ET (PET)	2150 mm yr^{-1}	1960 mm yr^{-1}
Wind speed (U)	2 m s^{-1}	3.2 m s^{-1}
Precipitable water (W)	33.6 kg m^{-2}	16.2 kg m^{-2}
Relative humidity (RH)	80 %	74 %
Dryness index (DI)	2.2	3.4
ω	2.6	2.6
Transpired fraction of ET (T / ET)	0.64	0.64

Table A2. Site averages for previously published data, accessed via the PATCH Lab (Kukla et al., 2022a). Values of $\delta^{13}C$ are reported in ‰ relative to VPDB. Values of $\delta^{18}O$ are reported in ‰ relative to VSMOW. No standard deviation or range is reported for sites that only include one sample. Note that n/a means not applicable.

Lat (°N)	Long (°E)	$\delta^{13}C$	$\delta^{13}C$ 1σ	$\delta^{18}O_c$	$\delta^{18}O_p$	$\delta^{18}O$ 1σ	$\delta^{18}O$ range	Age (Ma)	MAT (°C)	Reference
28.29	−97.97	−7.29	1.29	25.75	−3.09	0.74	2.65	8.50	22.81	Godfrey et al. (2018)
28.34	−97.97	−5.49	0.67	25.99	−2.86	0.26	0.87	8.50	22.82	Godfrey et al. (2018)
28.50	−98.10	−7.27	0.81	26.39	−2.44	0.30	0.70	8.00	22.89	Godfrey et al. (2018)
28.65	−97.38	−9.62	0.10	27.02	−2.01	0.11	0.32	8.50	22.00	Godfrey et al. (2018)
28.80	−97.80	−4.65	1.89	26.34	−2.65	0.66	1.90	8.00	22.14	Godfrey et al. (2018)
33.41	−101.56	−6.51	0.68	26.41	−3.64	0.49	1.70	6.80	17.39	Fox and Koch (2003)
33.50	−101.60	−5.91	0.36	26.58	−3.52	0.34	1.90	13.05	17.14	Fox and Koch (2003)
34.90	−103.10	−7.20	0.33	25.81	−4.69	0.23	0.80	6.40	15.37	Fox and Koch (2003)
35.70	−100.50	−6.92	0.89	26.16	−4.24	0.19	0.60	6.65	15.82	Fox and Koch (2003)
36.10	−100.00	−7.37	0.32	25.83	−4.69	0.47	0.90	9.60	15.29	Fox and Koch (2003)
36.18	−100.00	−7.41	0.91	25.92	−4.62	0.42	1.10	8.75	15.24	Fox and Koch (2003)
39.40	−100.10	−6.99	0.44	23.53	−7.60	0.57	1.60	9.55	12.72	Fox and Koch (2003)
41.20	−103.70	−5.57	0.78	21.31	−10.36	0.43	1.50	7.25	10.47	Fox and Koch (2003)
41.24	−101.81	−7.04	0.24	19.32	−12.24	0.95	2.80	7.25	10.92	Fox and Koch (2003)
41.30	−102.40	−6.63	0.44	19.30	−12.29	0.85	3.70	8.65	10.82	Fox and Koch (2003)
41.47	−103.07	−6.60	0.14	17.73	−13.90	0.15	0.21	7.00	10.65	Fan et al. (2014)
41.50	−103.10	−6.79	0.45	18.64	−12.99	1.05	4.40	9.10	10.63	Fox and Koch (2003)
41.60	−102.78	−7.00	n/a	18.34	−13.32	n/a	0.00	9.00	10.53	Fan et al. (2014)
42.37	−107.06	−6.50	n/a	15.35	−17.20	n/a	0.00	10.50	6.93	Fan et al. (2014)
42.40	−98.20	−7.00	0.28	22.90	−8.95	0.14	0.20	12.69	9.74	Fox and Koch (2003)
42.40	−98.20	−8.36	0.91	24.84	−7.01	0.93	2.60	13.70	9.74	Fox and Koch (2003)
42.40	−103.22	−7.18	0.50	22.56	−9.25	0.92	2.90	17.50	9.89	Fox and Koch (2003)
42.49	−103.85	−7.60	0.14	18.29	−13.59	0.37	0.52	18.50	9.63	Fan et al. (2014)
42.58	−107.19	−6.10	0.17	13.57	−18.92	1.64	2.89	14.17	7.19	Fan et al. (2014)
42.72	−108.19	−3.27	2.41	17.06	−15.79	1.94	5.73	13.02	5.72	Chamberlain et al. (2012)
42.80	−100.00	−6.49	1.16	21.67	−10.16	1.61	3.80	14.30	9.80	Fox and Koch (2003)

Code availability. The R code for the vapor transport model has been published as supporting material to Kukla et al. (2019).

Data availability. The datasets used in this study are listed below.

- Compiled, published $\delta^{18}O$ data (Appendix Table A2, accessed via the PATCH Lab https://geocentroid.shinyapps.io/PATCH-Lab/, Kukla et al., 2022a)
- Modern water isotope data (https://wateriso.utah.edu/waterisotopes/pages/spatial_db/SPATIAL_DB.html, Waterisotopes Database, 2019)
- North American Regional Reanalysis (Mesinger et al., 2006)
- Table S1, available from the data repository Dryad (Manser et al., 2023, https://doi.org/10.5061/dryad.5hqbzkhc5)

Author contributions. JKCR conceived the project idea, acquired funding, and provided overall supervision. LM conducted the investigation, curated the data, conducted the formal analysis, and prepared the original draft of this paper. TK provided resources and supervised the use of the vapor transport model. All authors contributed to the review and editing of the paper.

Competing interests. The contact author has declared that none of the authors has any competing interests.

Disclaimer. Publisher's note: Copernicus Publications remains neutral with regard to jurisdictional claims made in the text, published maps, institutional affiliations, or any other geographical representation in this paper. While Copernicus Publications makes every effort to include appropriate place names, the final responsibility lies with the authors.

Acknowledgements. This study benefited from discussions with Sean Willett regarding the Ogallala Formation and landscape evolution. We thank Sean Willett for first piquing our interest in this unique and still mysterious paleo-landscape. We thank Madalina Jaggi, Ulrich Treffert, Niklaus Loeffler, and Emilija Krsnik for assistance in the laboratory, Katharina Methner for field assistance, and Dan Koning and Frank Pazzaglia for assistance with finding key outcrops in New Mexico. We also benefited from discussions with Vincenzo Picotti, Giuditta Fellin, and Derek Sjostrom regarding Ogallala paleosol and sandstone petrology. We thank Rusty Winn of RE Janes Gravel Co (Lubbock, TX, USA) for facilitating our access and guiding us to remarkable Ogallala outcrops in the southern Great Plains. We also thank Phillip Osborne for permission to sample on his property and the Wildcat Bluff Nature Center for permission to sample within their preserve. Samples from Lake McConaughy State Recreation Area were collected under a permit issued by the Central Nebraska Public Power and Irrigation District, and samples collected at Palo Duro and Caprock Canyons state parks in Texas were collected under permit 2018-R5-08. Lastly, we thank an anonymous review, David L. Fox, and Jon Smith for reviews that substantially improved this paper. This study was funded by an ETH SEED grant, ETH and Alexander von Humboldt postdoctoral fellowships, and NSF grant EAR-2202916 to Rugenstein.

Financial support. This research has been supported by the ETH Zürich Foundation (fellowship grant no. 0-20282-17, career seed grant no. 0-20435-18), the Alexander von Humboldt Foundation, and the NSF Directorate for Geosciences (grant no. EAR-2202916).

Review statement. This paper was edited by Alberto Reyes and reviewed by David L. Fox and one anonymous referee.

References

Aby, S. B., Morgan, G. S., and Koning, D. J.: A paleontological survey of a part of the Tesuque formation near Chimayo, New Mexico, and a summary of the biostratigraphy of the Pojoaque member (Middle Miocene, Late Barstovian), in: New Mexico Geological Society Guidebook, 62nd Field Conference, Geology of the Tusas Mountains – Ojo Caliente, edited by: Koning, D. J., Karlstrom, K. E., Kelley, S. A., Lueth, V. W., and Aby, S. B., 347–358, https://nmgs.nmt.edu/publications/guidebooks/downloads/62/62_p0347_p0358.pdf (last access: 19 April 2024), 2011.

Bailey, A., Posmentier, E., and Feng, X.: Patterns of Evaporation and Precipitation Drive Global Isotopic Changes in Atmospheric Moisture, Geophys. Res. Lett., 45, 7093–7101, https://doi.org/10.1029/2018GL078254, 2018.

Barghoorn, S.: Magnetic-polarity stratigraphy of the Miocene type Tesuque Formation, Santa Fe Group, in: the Espanola Valley, New Mexico., Geol. Soc. Am. Bull., 92, 1027–1041, https://doi.org/10.1130/0016-7606(1981)92<1027:MSOTMT>2.0.CO;2, 1981.

Barghoorn, S. F.: Magnetic polarity stratigraphy of the Tesuque Formation, Santa Fe Group in the Española Valley, New Mexico, with a taxonomic review of the fossil camels, PhD thesis, Columbia University, https://www.proquest.com/openview/3953a8793e030406f417eb7fb4e4253d/1 (last access: 19 April 2024), 1985.

Bates, K. L.: America the Beautiful: And Other Poems, Thomas Y. Crowell Company, New York, NY, 305 pp., 1911.

Bernasconi, S. M., Müller, I. A., Bergmann, K. D., Breitenbach, S. F., Fernandez, A., Hodell, D. A., Jaggi, M., Meckler, A. N., Millan, I., and Ziegler, M.: Reducing Uncertainties in Carbonate Clumped Isotope Analysis Through Consistent Carbonate-Based Standardization, Geochem. Geophy. Geosy., 19, 2895–2914, https://doi.org/10.1029/2017GC007385, 2018.

Bershaw, J., Penny, S. M., and Garzione, C. N.: Stable Isotopes of Modern Water across the Himalaya and Eastern Tibetan Plateau: Implications for Estimates of Paleoelevation and Paleoclimate, J. Geophys. Res.-Atmos., 117, D02110, https://doi.org/10.1029/2011JD016132, 2012.

Brand, W. A., Coplen, T. B., Vogl, J., Rosner, M., and Prohaska, T.: Assessment of international reference materials for isotope-ratio analysis (IUPAC technical report), Pure Appl. Chem., 86, 425–467, https://doi.org/10.1515/pac-2013-1023, 2014.

Breecker, D., Sharp, Z., and McFadden, L.: Seasonal bias in the formation and stable isotopic composition of pedogenic carbonate in modern soils from central New Mexico, USA, Geol. Soc. Am. Bull., 121, 630–640, https://doi.org/10.1130/B26413.1, 2009.

Breitenbach, S. F. M. and Bernasconi, S. M.: Carbon and oxygen isotope analysis of small carbonate samples (20 to 100 µg) with a GasBench II preparation device, Rapid Commun. Mass Sp., 25, 1910–1914, https://doi.org/10.1002/rcm.5052, 2011.

Brock, A. L. and Buck, B. J.: Polygenetic development of the Mormon Mesa, NV petrocalcic horizons: Geomorphic and paleoenvironmental interpretations, CATENA, 77, 65–75, https://doi.org/10.1016/j.catena.2008.12.008, 2009.

Brown, R. M., Chalk, T. B., Crocker, A. J., Wilson, P. A., and Foster, G. L.: Late Miocene cooling coupled to carbon dioxide with Pleistocene-like climate sensitivity, Nat. Geosci., 15, 664–670, https://doi.org/10.1038/s41561-022-00982-7, 2022.

Brubaker, K. L., Entekhabi, D., and Eagleson, P. S.: Atmospheric water vapor transport and continental hydrology over the Americas, J. Hydrol., 155, 407–428, https://doi.org/10.1016/0022-1694(94)90180-5, 1994.

Budyko, M.: Climate and Life, International Geophysical Series, vol. 18, Academic Press, New York, ISBN 0121394506, 1974.

Bukovsky, M. S., McCrary, R. R., Seth, A., and Mearns, L. O.: A mechanistically credible, poleward shift in warm-season precipitation projected for the U.S. Southern Great Plains?, J. Climate, 30, 8275–8298, https://doi.org/10.1175/JCLI-D-16-0316.1, 2017.

Burde, G. I., Gandush, C., and Bayarjargal, Y.: Bulk Recycling Models with Incomplete Vertical Mixing. Part II: Precipitation Recycling in the Amazon Basin, J. Climate, 19, 1473–1489, https://doi.org/10.1175/JCLI3688.1, 2006.

Burls, N. J. and Fedorov, A. V.: Wetter subtropics in a warmer world: Contrasting past and future hydrological cycles, P. Natl. Acad. Sci. USA, 114, 12888–12893, https://doi.org/10.1073/pnas.1703421114, 2017.

Byerle, L. A.: Modulation of the Great Plains low-level jet and moisture transports by orography and large-scale circulations, J. Geophys. Res., 108, 8611, https://doi.org/10.1029/2002JD003005, 2003.

Caves, J. K.: Late Miocene Uplift of the Tian Shan and Altai and Reorganization of Central Asia Climate, GSA Today, 27, 20–26, https://doi.org/10.1130/GSATG305A.1, 2017.

Caves, J. K., Sjostrom, D. J., Mix, H. T., Winnick, M. J., and Chamberlain, C. P.: Aridification of Central Asia and Uplift of the Altai and Hangay Mountains, Mongolia: Stable Isotope Evidence, Am. J. Sci., 314, 1171–1201, https://doi.org/10.2475/08.2014.01, 2014.

Caves, J. K., Winnick, M. J., Graham, S. A., Sjostrom, D. J., Mulch, A., and Chamberlain, C. P.: Role of the westerlies in Central Asia climate over the Cenozoic, Earth Planet. Sc. Lett., 428, 33–43, https://doi.org/10.1016/j.epsl.2015.07.023, 2015.

Caves, J. K., Moragne, D. Y., Ibarra, D. E., Bayshashov, B. U., Gao, Y., Jones, M. M., Zhamangara, A., Arzhannikova, A. V., Arzhannikov, S. G., and Chamberlain, C. P.: The Neogene de-greening of Central Asia, Geology, 44, 887–890, https://doi.org/10.1130/G38267.1, 2016.

Caves Rugenstein, J. K. and Chamberlain, C. P.: The evolution of hydroclimate in Asia over the Cenozoic: A stable-isotope perspective, Earth-Sci. Rev., 185, 1129–1156, https://doi.org/10.1016/j.earscirev.2018.09.003, 2018.

CenCO2PIP Consortium: Toward a Cenozoic history of atmospheric CO_2, Science, 382, eadi5177, https://doi.org/10.1126/science.adi5177, 2023.

Cepeda, J. C. and Perkins, M. E.: A 10 million year old ash deposit in the Ogallala Formation of the Texas Panhandle, Tex. J. Sci., 58, 3–12, 2006.

Chamberlain, C. P., Mix, H. T., Mulch, A., Hren, M. T., Kent-Corson, M. L., Davis, S. J., Horton, T. W., and Graham, S. A.: The Cenozoic climatic and topographic evolution of the western North American Cordillera, Am. J. Sci., 312, 213–262, https://doi.org/10.2475/02.2012.05, 2012.

Chamberlain, C. P., Winnick, M. J., Mix, H. T., Chamberlain, S. D., and Maher, K.: The impact of neogene grassland expansion and aridification on the isotopic composition of continental precipitation, Global Biogeochem. Cy., 28, 992–1004, https://doi.org/10.1002/2014GB004822, 2014.

Cook, K. H., Vizy, E. K., Launer, Z. S., and Patricola, C. M.: Springtime intensification of the great plains low-level jet and midwest precipitation in GCM Simulations of the twenty-first century, J. Climate, 21, 6321–6340, https://doi.org/10.1175/2008JCLI2355.1, 2008.

de Noblet-Ducoudre, N., Boisier, J.-P., Pitman, A., Bonan, G. B., Brovkin, V., Cruz, F., Delire, C., Gayler, V., van den Hurk, B. J. J. M., Lawrence, P. J., van der Molen, M. K., Müller, C., Reick, C. H., Strengers, B. J., and Voldoire, A.: Determining Robust Impacts of Land-Use-Induced Land Cover Changes on Surface Climate over North America and Eurasia: Results from the First Set of LUCID Experiments, J. Climate, 25, 3261–3281, https://doi.org/10.1175/JCLI-D-11-00338.1, 2012.

Dobson, J. E. and Campbell, J. S.: The Flatness of U.S. States, Geogr. Rev., 104, 1–9, https://doi.org/10.1111/j.1931-0846.2014.12001.x, 2014.

Draxler, R. R. and Hess, G.: An Overview of the HYSPLIT_4 Modelling System for Trajectories, Dispersion, and Deposition, Australian Meteorological Magazine, 47, 295–308, 1998.

Driscoll, E., Needham, M. R., Keys, P. W., and Rugenstein, J. K. C.: Cenozoic stable isotope constraints on the Eurasian continental interior hydroclimate response to high CO_2, Earth Planet. Sc. Lett., 630, 118623, https://doi.org/10.1016/j.epsl.2024.118623, 2024.

Duller, R. A., Whittaker, A. C., Swinehart, J. B., Armitage, J. J., Sinclair, H. D., Bair, A., and Allen, P. A.: Abrupt landscape change post-6 Ma on the central Great Plains, USA, Geology, 40, 871–874, https://doi.org/10.1130/G32919.1, 2012.

Egan, T.: The worst hard time: the untold story of those who survived the great American Dust Bowl, Mariner, Boston, Mass., ISBN 9780618773473, 2006.

Galbreath, E. C.: A contribution to the Tertiary Geology and Paleontology of Northeastern Colorado, Vertebrata, 4, 1–120, https://kuscholarworks.ku.edu/bitstream/handle/1808/3788/paleo.article.013op.pdf (last access: 19 April 2024), 1953.

Fan, M., Hough, B. G., and Passey, B. H.: Middle to late Cenozoic cooling and high topography in the central Rocky Mountains: Constraints from clumped isotope geochemistry, Earth Planet. Sc. Lett., 408, 35–47, https://doi.org/10.1016/j.epsl.2014.09.050, 2014.

Feng, R., Poulsen, C. J., and Werner, M.: Tropical circulation intensification and tectonic extension recorded by Neogene terrestrial $\delta^{18}O$ records of the western United States, Geology, 44, 971–974, https://doi.org/10.1130/G38212.1, 2016.

Feng, R., Bhattacharya, T., Otto-Bliesner, B. L., Brady, E. C., Haywood, A. M., Tindall, J. C., Hunter, S. J., Abe-Ouchi, A., Chan, W.-L., Kageyama, M., Contoux, C., Guo, C., Li, X., Lohmann, G., Stepanek, C., Tan, N., Zhang, Q., Zhang, Z., Han, Z., Williams, C. J. R., Lunt, D. J., Dowsett, H. J., Chandan, D., and Peltier, W. R.: Past Terrestrial Hydroclimate Sensitivity Controlled by Earth System Feedbacks, Nat. Commun., 13, 1306, https://doi.org/10.1038/s41467-022-28814-7, 2022.

Ferretti, D. F., Pendall, E., Morgan, J. A., Nelson, J. A., LeCain, D., and Mosier, A. R.: Partitioning evapotranspiration fluxes from a Colorado grassland using stable isotopes: Seasonal variations and ecosystem implications of elevated atmospheric CO_2, Plant Soil, 254, 291–303, https://doi.org/10.1023/A:1025511618571, 2003.

Fonstad, M., Pugatch, W., and Vogt, B.: Kansas Is Flatter Than a Pancake, Annals of Improbable Research, 9, 16–18, https://doi.org/10.3142/107951403782200100, 2007.

Forest, C. E., Molnar, P., and Emanuel, K. A.: Palaeoaltimetry from energy conservation principles, Nature, 374, 347–350, 1995.

Fox, D. L. and Koch, P. L.: Tertiary history of C_4 biomass in the Great plains, USA, Geology, 31, 809–812, 2003.

Fox, D. L. and Koch, P. L.: Carbon and oxygen isotopic variability in Neogene paleosol carbonates: constraints on the evolution of the C_4-grasslands of the Great Plains, USA, Palaeogeogr. Palaeocl., 207, 305–329, https://doi.org/10.1016/j.palaeo.2003.09.030, 2004.

Fox, D. L., Honey, J. G., Martin, R. A., and Peláez-Campomanes, P.: Pedogenic carbonate stable isotope record of environmental change during the Neogene in the southern Great Plains, southwest Kansas, USA: Oxygen isotopes and paleoclimate during the evolution of C_4-dominated grasslands, Bull. Geol. Soc. Am., 124, 431–443, https://doi.org/10.1130/B30402.1, 2012.

Friedman, I., Harris, J., Smith, G., and Johnson, C.: Stable isotope composition of waters in the Great Basin, United States 1. Air-mass trajectories, J. Geophys. Res., 107, 4400, https://doi.org/10.1029/2001JD000565, 2002.

Fritz, S. A., Eronen, J. T., Schnitzler, J., Hof, C., Janis, C. M., Mulch, A., Böhning-Gaese, K., and Graham, C. H.: Twenty-million-year relationship between mammalian diversity and primary productivity, P. Natl. Acad. Sci. USA, 113, 10908–10913, https://doi.org/10.1073/pnas.1602145113, 2016.

Frye, J. C., Leonard, A. B., and Glass, H. D.: Late Cenozoic Sediments, Molluscan Faunas, and Clay Minerals in Northern New Mexico, New Mexico Bureau of Mines & Mineral Resources Circular, 160, 32, https://doi.org/10.58799/C-160, 1978.

Frye, J. C., Leonard, A. B., and Glass, H. D.: Western extent of Ogallala Formation in New Mexico, New Mexico Bureau of Mines & Mineral Resources Circular, 175, 41, https://doi.org/10.58799/C-175, 1982.

Fu, B. P.: On the calculation of the evaporation from land surface, Scientia Atmospherica Sinica, 5, 23–31, 1981.

Galusha, T. and Blick, J. C.: Stratigraphy of the Santa Fe Group, New Mexico, B. Am. Mus. Nat. Hist., 144, 127, http://hdl.handle.net/2246/1633 (last access: 20 April 2024), 1971.

Gat, J. R. and Matsui, E.: Atmospheric water balance in the Amazon basin: An isotopic evapotranspiration model, J. Geophys. Res., 96, 179–13, https://doi.org/10.1029/91JD00054, 1991.

Good, S. P., Noone, D., and Bowen, G.: Hydrologic connectivity constrains partitioning of global terrestrial water fluxes, Science, 349, 175–177, https://doi.org/10.1126/science.aaa5931, 2015.

Gregory, K. M. and Chase, C. G.: Tectonic and climatic significance of a late Eocene low-relief, high- level geomorphic surface, Colorado, J. Geophys. Res., 99, 20141–20160, https://doi.org/10.1029/94jb00132, 1994.

Greve, P., Gudmundsson, L., Orlowsky, B., and Seneviratne, S. I.: Introducing a probabilistic Budyko framework, Geophys. Res. Lett., 42, 2261–2269, https://doi.org/10.1002/2015GL063449, 2015.

Godfrey, C., Fan, M., Jesmok, G., Upadhyay, D., and Tripati, A.: Petrography and stable isotope geochemistry of Oligocene-Miocene continental carbonates in south Texas: Implications for paleoclimate and paleoenvironment near sea-level, Sediment. Geol., 367, 69–83, https://doi.org/10.1016/j.sedgeo.2018.02.006, 2018.

Gustavson, T. C.: Fluvial and Eolian Depositional Systems, Paleosols, and Paleoclimate of the Upper Cenozoic Ogallala and Blackwater Draw Formations, Southern High Plains, Texas and New Mexico, Bureau of Economic Geology, Report of Investigations No. 239, https://doi.org/10.23867/RI0239D, 1996.

Gustavson, T. C. and Holliday, V. T.: Eolian sedimentation and soil development on a semiarid to subhumid grassland, Tertiary Ogallala and Quaternary Blackwater Draw formations, Texas and New Mexico High Plains, J. Sediment. Res., 69, 622–634, https://doi.org/10.2110/jsr.69.622, 1999.

Gustavson, T. C. and Winkler, D. A.: Depositional facies of the Miocene-Pliocene Ogallala Formation, northwestern Texas and eastern New Mexico, Geology, 16, 203, https://doi.org/10.1130/0091-7613(1988)016<0203:DFOTMP>2.3.CO;2, 1988.

Held, I. and Soden, B.: Robust responses of the hydrological cycle to global warming, J. Climate, 19, 5686–5699, 2006.

Helfand, H. M. and Schubert, S. D.: Climatology of the simulated Great Plains low-level jet and its contribution to the continental moisture budget of the United States, J. Climate, 8, 784–806, https://doi.org/10.1175/1520-0442(1995)008<0784:COTSGP>2.0.CO;2, 1995.

Heller, P. L., Dueker, K., and McMillan, M. E.: Post-Paleozoic alluvial gravel transport as evidence of continental tilting in the U.S. Cordillera, Geol. Soc. Am. Bull., 115, 1122–1132, https://doi.org/10.1130/B25219.1, 2003.

Henry, K. D.: ^{40}Ar / ^{39}Ar Detrital Sanidine Dating of the Ogallala Formation, Llano Estacado, Southeastern New Mexico and West Texas, Master Thesis, New Mexico Tech, https://nmt.on.worldcat.org/oclc/1012939850 (last access: 20 April 2024), 2017.

Herbert, T. D., Lawrence, K. T., Tzanova, A., Peterson, L. C., Caballero-Gill, R., and Kelly, C. S.: Late Miocene global cooling and the rise of modern ecosystems, Nat. Geosci., 9, 843–847, https://doi.org/10.1038/ngeo2813, 2016.

Hetherington, A. M. and Woodward, F. I.: The role of stomata in sensing and driving environmental change, Nature, 424, 901–908, 2003.

Hoch, J. and Markowski, P.: A Climatology of Springtime Dryline Position in the U.S. Great Plains Region, J. Climate, 18, 2132–2137, https://doi.org/10.1175/JCLI3392.1, 2005.

Huth, T. E., Cerling, T. E., Marchetti, D. W., Bowling, D. R., Ellwein, A. L., and Passey, B. H.: Seasonal Bias in Soil Carbonate Formation and Its Implications for Interpreting High-Resolution Paleoarchives: Evidence From Southern Utah, J. Geophys. Res.-Biogeo., 124, 616–632, https://doi.org/10.1029/2018JG004496, 2019.

Ibarra, D. E., Oster, J. L., Winnick, M. J., Rugenstein, J. K., Byrne, M. P., and Chamberlain, C. P.: Warm and cold wet states in the western United States during the Pliocene-Pleistocene, Geology, 46, 355–358, https://doi.org/10.1130/G39962.1, 2018.

Izett, G. A. and Obradovich, J. D.: ^{40}Ar / ^{39}Ar ages of Miocene tuffs in basin-fill deposits (Santa Fe group, New Mexico, and troublesome formation, Colorado) of the Rio Grande rift system, Mountain Geologist, 38, 77–86, 2001.

Jacobs, B. F., Kingston, J. D., and Jacobs, L. L.: The Origin of Grass-Dominated Ecosystems, Ann. Mo. Bot. Gard., 86, 590–643, 1999.

Janis, C. M., Damuth, J., and Theodor, J. M.: Miocene ungulates and terrestrial primary productivity: Where have all the browsers gone?, P. Natl. Acad. Sci. USA, 97, 7899–7904, https://doi.org/10.1073/pnas.97.14.7899, 2000.

Jiang, X., Lau, N.-C., Held, I. M., and Ploshay, J. J.: Mechanisms of the Great Plains Low-Level Jet as Simulated in an AGCM, J. Atmos. Sci., 64, 532–547, https://doi.org/10.1175/JAS3847.1, 2007.

Joeckel, R. M., Wooden Jr, S. R., Korus, J. T., and Garbisch, J. O.: Architecture, heterogeneity, and origin of late Miocene fluvial deposits hosting the most important aquifer in the Great Plains, USA, Sediment. Geology, 311, 75–95, 2014.

Karlstrom, K. E., Hansen, S. M., McKeon, R., Ouimet, W., MacCarthy, J., Aslan, A., Kelley, S., Dueker, K., Garcia, R. V., Feldman, J., Kirby, E., Schmandt, B., Coblentz, D., Heizler, M., Aster, R., Darling, A., Donahue, M. S., Stockli, D. F., Karlstrom, K. E., Crow, R., Crossey, L. J., Hoffman, M., Lazear, G., Van Wijk, J., and Stachnik, J.: Mantle-driven dynamic uplift of the Rocky Mountains and Colorado Plateau and its surface response: Toward a unified hypothesis, Lithosphere, 4, 3–22, https://doi.org/10.1130/l150.1, 2011.

Kelson, J. R., Huntington, K. W., Breecker, D. O., Burgener, L. K., Gallagher, T. M., Hoke, G. D., and Petersen, S. V.: A Proxy for All Seasons? A Synthesis of Clumped Isotope Data from Holocene Soil Carbonates, Quaternary Sci. Rev., 234, 106259, https://doi.org/10.1016/j.quascirev.2020.106259, 2020.

Kelson, J. R., Huth, T. E., Passey, B. H., Levin, N. E., Petersen, S. V., Ballato, P., Beverly, E. J., Breecker, D. O., Hoke, G. D., Hudson, A. M., Ji, H., Licht, A., Oerter, E. J., and Quade, J.: Triple oxygen isotope compositions of globally distributed soil carbonates record widespread evaporation of soil waters, Geochim. Cosmochim. Ac., 355, 138–160, https://doi.org/10.1016/j.gca.2023.06.034, 2023.

Kendall, C. and Coplen, T. B.: Distribution of oxygen-18 and deuterium in river waters across the United States, Hydrol. Process., 15, 1363–1393, https://doi.org/10.1002/hyp.217, 2001.

Kim, S. T. and O'Neil, J. R.: Equilibrium and nonequilibrium oxygen isotope effects in synthetic carbonates, Geochim. Cosmochim. Ac., 61, 3461–3475, https://doi.org/10.1016/S0016-7037(97)00169-5, 1997.

Kitts, D. B.: Geology of the Cenozoic Rocks of Ellis County, Oklahoma, Oklahoma Geological Survey Circular 69, http://www.ogs.ou.edu/pubsscanned/Circulars/circular69mm.pdf (last access: 20 April 2024), 1965.

Kocsis, L., Ozsvárt, P., Becker, D., Ziegler, R., Scherler, L., and Codrea, V.: Orogeny forced terrestrial climate variation during the late Eocene-early Oligocene in Europe, Geology, 42, 727–730, https://doi.org/10.1130/G35673.1, 2014.

Koning, D. J., Grauch, V., Connell, S. D., Ferguson, J., McIntosh, W., Slate, J. L., Wan, E., and Baldridge, W. S.: Structure and tectonic evolution of the eastern Española Basin, Rio Grande rift, north-central New Mexico, Geol. S. Am. S., 494, 185–219, https://doi.org/10.1130/2013.2494(08), 2013.

Korus, J. and Joeckel, R.: Telescopic Megafans on the High Plains, USA Were Signal Buffers in a Major Source-To-Sink System, Sedimentary Record, 21, 1–14, https://doi.org/10.2110/001c.89096, 2023a.

Korus, J. T. and Joeckel, R. M.: Exhumed fluvial landforms reveal evolution of late Eocene-Pliocene rivers on the Central and Northern Great Plains, USA, Geosphere, 19, 695–718, https://doi.org/10.1130/GES02587.1, 2023b.

Koster, R. D.: Regions of Strong Coupling Between Soil Moisture and Precipitation, Science, 305, 1138–1140, https://doi.org/10.1126/science.1100217, 2004.

Kuhle, A. J. and Smith, G. A.: Alluvial-slope deposition of the skull ridge member of the Tesuque formation, Española Basin, New Mexico, New Mexico Geology, 23, 30–37, https://doi.org/10.58799/NMG-v23n2.30, 2001.

Kukla, T., Winnick, M. J., Maher, K., Ibarra, D. E., and Chamberlain, C. P.: The sensitivity of terrestrial δ^{18}O gradients to hydroclimate evolution, J. Geophys. Res.-Atmos., 124, 563–582, https://doi.org/10.1029/2018JD029571, 2019.

Kukla, T., Rugenstein, J. K. C., Driscoll, E., Ibarra, D. E., and Chamberlain, C. P.: The PATCH Lab V1.0: A database and workspace for Cenozoic terrestrial paleoclimate and environment reconstruction, Am. J. Sci., 322, 1124–1158, https://doi.org/10.2475/10.2022.02, 2022a (data available at: https://geocentroid.shinyapps.io/PATCH-Lab/, last access: 17 April 2024).

Kukla, T., Rugenstein, J. K. C., Ibarra, D. E., Winnick, M. J., Strömberg, C. A., and Chamberlain, C. P.: Drier winters drove Cenozoic open habitat expansion in North America, AGU Advances, 3, e2021AV000566, https://doi.org/10.1029/2021AV000566, 2022b.

Laguë, M. M., Bonan, G. B., and Swann, A. L. S.: Separating the Impact of Individual Land Surface Properties on the Terrestrial Surface Energy Budget in both the Coupled and Uncoupled Land–Atmosphere System, J. Climate, 32, 5725–5744, https://doi.org/10.1175/jcli-d-18-0812.1, 2019.

LaRiviere, J. P., Ravelo, A. C., Crimmins, A., Dekens, P. S., Ford, H. L., Lyle, M., and Wara, M. W.: Late Miocene decoupling of oceanic warmth and atmospheric carbon dioxide forcing, Nature, 486, 97–100, https://doi.org/10.1038/nature11200, 2012.

Lechler, A. R. and Galewsky, J.: Refining paleoaltimetry reconstructions of the Sierra Nevada, California, using air parcel trajectories, Geology, 41, 259–262, https://doi.org/10.1130/G33553.1, 2013.

Lee, J.: Understanding Neogene Oxygen Isotopes in the Southern Great Plains Using Isotope-Enabled General Circulation Model Simulations, J. Geophys. Res.-Atmos., 124, 2452–2464, https://doi.org/10.1029/2018JD028894, 2019.

Lee, J.-E., Fung, I., DePaolo, D. J., and Henning, C. C.: Analysis of the global distribution of water isotopes using the NCAR atmospheric general circulation model, J. Geophys. Res., 112, D16306, https://doi.org/10.1029/2006JD007657, 2007.

Lehman, T. and Schnable, J.: Geology of the Southern High Plains, Southwestern Association of Student Geological Societies, Lubbock, Texas, 120 pp., https://ttu-ir.tdl.org/bitstreams/42eb7632-ccd1-4f32-9850-bbe6a224876c/download (last access: 19 April 2024), 1992.

Lemordant, L., Gentine, P., Swann, A. S., Cook, B. I., and Scheff, J.: Critical impact of vegetation physiology on the continental hydrologic cycle in response to increasing CO_2, P. Natl. Acad. Sci. USA, 115, 201720712, https://doi.org/10.1073/pnas.1720712115, 2018.

Leonard, A. B. and Frye, J. C.: Paleontology of Ogallala Formation, northeastern New Mexico, New Mexico Bureau of Mines & Mineral Resources Circular, 161, 21, https://doi.org/10.58799/C-161, 1978.

Leonard, E. M.: Geomorphic and tectonic forcing of late Cenozoic warping of the Colorado piedmont, Geology, 30, 595–598, https://doi.org/10.1130/0091-7613(2002)030<0595:GATFOL>2.0.CO;2, 2002.

Li, L. and Garzione, C. N.: Spatial Distribution and Controlling Factors of Stable Isotopes in Meteoric Waters on the Tibetan Plateau: Implications for Paleoelevation Reconstruction, Earth Planet. Sc. Lett., 460, 302–314, https://doi.org/10.1016/j.epsl.2016.11.046, 2017.

Liu, Z., Bowen, G. J., and Welker, J. M.: Atmospheric circulation is reflected in precipitation isotope gradients over the conterminous United States, J. Geophys. Res., 115, D22120, https://doi.org/10.1029/2010JD014175, 2010.

Lucas, S. G., Hunt, A. P., Kues, B. S., Heckert, A. B., and McLemore, V. T.: First-day road log, from Tucumcari to the edge of the Llano Estacado at Gruhlkey, Texas, Palo Duro Canyon, Texas, and San Jon Hill, New Mexico, in: Geology of the Llano Estacado, edited by: Lucas, S. and Ulmer-Scholle, D., New Mexico Geological Society 52nd Annual Fall Field Conference Guidebook, 1–23, https://doi.org/10.56577/ffc-52.1, 2001.

Ludvigson, G. A., Sawin, R. S., Franseen, E. K., Watney, W. L., West, R. R., and Smith, J. J.: A Review of the Stratigraphy of the Ogallala Formation and Revision of Neogene ("Tertiary") Nomenclature in Kansas, Kansas Current Research in Earth Sciences Bulletin, 256, 1–9, 2009.

Ludvigson, G. A., Mandel, R., MacFarlane, A., and Smith, J. J.: Capturing the Record of Neogene Climate Change from Strata of the High Plains Aquifer in Kansas: Research Activities and Findings, Tech. rep., Kansas Geological Survey, https://www.kgs.ku.edu/Publications/OFR/2016/OFR16_31/ (last access: 20 April 2024), 2016.

Manser, L., Kukla, T., and Rugenstein, J. K. C.: Data from: Stable isotope evidence for long-term stability of large-scale hydroclimate in the Neogene North American Great Plains, DRYAD [data set], https://doi.org/10.5061/dryad.5hqbzkhc5, 2023.

Martens, B., Miralles, D. G., Lievens, H., van der Schalie, R., de Jeu, R. A. M., Fernández-Prieto, D., Beck, H. E., Dorigo, W. A., and Verhoest, N. E. C.: GLEAM v3: satellite-based land evaporation and root-zone soil moisture, Geosci. Model Dev., 10, 1903–1925, https://doi.org/10.5194/gmd-10-1903-2017, 2017.

McDermott, F., Atkinson, T. C., Fairchild, I. J., Baldini, L. M., and Mattey, D. P.: A first evaluation of the spatial gradients in $\delta^{18}O$ recorded by European Holocene speleothems, Global Planet. Change, 79, 275–287, https://doi.org/10.1016/j.gloplacha.2011.01.005, 2011.

McIntosh, W. C. and Quade, J.: $^{40}Ar/^{39}Ar$ geochronology of tephra layers in the Santa Fe Group, Espanola Basin, New Mexico, in: Geology of the Santa Fe Region, edited by: Bauer, P. W., Kues, B. S., Dunbar, N. W., Karlstrom, K. E., and Harrison, B., New Mexico Geological Society 46th Annual Fall Field Conference Guidebook, 279–287, https://doi.org/10.56577/FFC-46.279, 1996.

McMillan, M. E., Angevine, C. L., and Heller, P. L.: Postdepositional tilt of the Miocene-Pliocene Ogallala Group on the western Great Plains: Evidence of late Cenozoic uplift of the Rocky Mountains, Geology, 30, 63–66, 2002.

Mejía, L. M., Méndez-Vicente, A., Abrevaya, L., Lawrence, K. T., Ladlow, C., Bolton, C., Cacho, I., and Stoll, H.: A diatom record of CO_2 decline since the late Miocene, Earth Planet. Sc. Lett., 479, 18–33, https://doi.org/10.1016/j.epsl.2017.08.034, 2017.

Mesinger, F., DiMego, G., Kalnay, E., Mitchell, K., Shafran, P. C., Ebisuzaki, W., Jović, D., Woollen, J., Rogers, E., Berbery, E. H., Ek, M. B., Fan, Y., Grumbine, R., Higgins, W., Li, H., Lin, Y., Manikin, G., Parrish, D., and Shi, W.: North American regional reanalysis: A long-term, consistens, high-resolution climate dataset for the North American domian, as a major improvement upon the earlier global reanalysis datasets in both resolution and accuracy, B. Am. Meteorol. Soc., 87, 343–360, https://doi.org/10.1175/BAMS-87-3-343, 2006.

Meyer-Christoffer, A., Becker, A., Finger, P., Rudolf, B., Schneider, U., and Ziese, M.: GPCC Climatology Version 2011 at 0.25°: Monthly Land-Surface Precipitation Climatology for Every Month and the Total Year from Rain-Gauges Built on GTS-Based and Historic Data, in: GPCC: Offenbach, Germany, Global Precipitation Climatology Centre (GPCC), at Deutscher Wetterdienst, Offenbach, https://doi.org/10.5676/DWD_GPCC/CLIM_M_V2015_025, 2011.

Miralles, D. G., Holmes, T. R. H., De Jeu, R. A. M., Gash, J. H., Meesters, A. G. C. A., and Dolman, A. J.: Global land-surface evaporation estimated from satellite-based observations, Hydrol. Earth Syst. Sci., 15, 453–469, https://doi.org/10.5194/hess-15-453-2011, 2011.

Mix, H. T., Mulch, A., Kent-Corson, M. L., and Chamberlain, C. P.: Cenozoic migration of topography in the North American Cordillera, Geology, 39, 87–90, https://doi.org/10.1130/G31450.1, 2011.

Mix, H. T., Winnick, M. J., Mulch, A., and Page Chamberlain, C.: Grassland expansion as an instrument of hydrologic change in Neogene western North America, Earth Planet. Sc. Lett., 377–378, 73–83, https://doi.org/10.1016/j.epsl.2013.07.032, 2013.

Mix, H. T., Caves Rugenstein, J. K., Reilly, S. P., Ritch, A. J., Winnick, M. J., Kukla, T., and Chamberlain, C. P.: Atmospheric flow deflection in the late Cenozoic Sierra Nevada, Earth Planet. Sc. Lett., 518, 76–85, https://doi.org/10.1016/j.epsl.2019.04.050, 2019.

Molnar, P. and England, P.: Late Cenozoic uplift of mountain ranges and global climate change: chicken or egg?, Nature, 346, 29–34, https://doi.org/10.1038/346029a0, 1990.

Moucha, R., Forte, A. M., Rowley, D. B., Mitrovica, J. X., Simmons, N. A., and Grand, S. P.: Deep mantle forces and the uplift of the Colorado Plateau, Geophys. Res. Lett., 36, L19310, https://doi.org/10.1029/2009GL039778, 2009.

Nativ, R. and Riggio, R.: Precipitation in the southern High Plains: Meteorologic and isotopic features, J. Geophys. Res., 95, 22559, https://doi.org/10.1029/JD095iD13p22559, 1990.

Osborne, C. P. and Sack, L.: Evolution of C_4 plants: A new hypothesis for an interaction of CO_2 and water relations mediated by plant hydraulics, Philos. T. R. Soc. B, 367, 583–600, https://doi.org/10.1098/rstb.2011.0261, 2012.

Oster, J. L., Montañez, I. P., and Kelley, N. P.: Response of a modern cave system to large seasonal precipitation variability, Geochim. Cosmochim. Ac., 91, 92–108, https://doi.org/10.1016/j.gca.2012.05.027, 2012.

Overpeck, J. T. and Udall, B.: Climate change and the aridification of North America, P. Natl. Acad. Sci. USA, 117, 11856–11858, https://doi.org/10.1073/pnas.2006323117, 2020.

Poage, M. A. and Chamberlain, C. P.: Empirical relationships between elevation and the stable isotope composition of precipitation and surface waters: Considerations for studies of paleoelevation change, Am. J. Sci., 301, 1–15, https://doi.org/10.2475/ajs.301.1.1, 2001.

Powell, J. W.: Report on the lands of the arid region of the United States, with a more detailed account of the lands of Utah, Government Printing Office, Washington, D.C., https://doi.org/10.3133/70039240, 1879.

Powell, J. W.: The irrigable lands of the arid region, Century Magazine, 39, 766–776, 1890.

Ring, S. J., Mutz, S. G., and Ehlers, T. A.: Cenozoic Proxy Constraints on Earth System Sensitivity to Greenhouse Gases, Paleoceanography and Paleoclimatology, 37, e2021PA004364, https://doi.org/10.1029/2021PA004364, 2022.

Rozanski, K., Araguás-Araguás, L., and Gonfiantini, R.: Isotopic patterns in modern global precipitation, in: Climate Change in Continental Isotopic Records, edited by: Swart, P. K., Lohmann, K. C., McKenzie, J. A., and Savin, S. M., Wiley Online Library, 1–36, https://doi.org/10.1029/GM078p0001, 1993.

Rugenstein, J. K. C., Methner, K., Kukla, T., Mulch, A., Lüdecke, T., Fiebig, J., Wegmann, K. W., Zeitler, P. K., and Chamberlain, C. P.: Clumped isotope constraints on warming and precipitation seasonality in Mongolia following Altai uplift, American J. Sci., 322, 28–54, https://doi.org/10.2475/01.2022.02, 2022.

Salati, E., Dall'Olio, A., Matsui, E., and Gat, J. R.: Recycling of water in the Amazon Basin: An isotopic study, Water Resour. Res., 15, 1250–1258, https://doi.org/10.1029/WR015i005p01250, 1979.

San Jose, M., Caves Rugenstein, J. K., Cosentino, D., Faccenna, C., Fellin, M. G., Ghinassi, M., and Martini, I.: Stable Isotope Evidence for Rapid Uplift of the Central Apennines since the Late Pliocene, Earth Planet. Sc. Lett., 544, 116376, https://doi.org/10.1016/j.epsl.2020.116376, 2020.

Scheff, J.: Drought Indices, Drought Impacts, CO_2, and Warming: a Historical and Geologic Perspective, Current Climate Change Reports, 4, 202–209, https://doi.org/10.1007/s40641-018-0094-1, 2018.

Scheff, J., Seager, R., Liu, H., and Coats, S.: Are Glacials Dry? Consequences for Paleoclimatology and for Greenhouse Warming, J. Climate, 30, 6593–6609, https://doi.org/10.1175/JCLI-D-16-0854.1, 2017.

Scheff, J., Coats, S., and Laguë, M. M.: Why do the Global Warming Responses of Land-Surface Models and Climatic Dryness Metrics Disagree?, Earth's Future, 10, e2022EF002814, https://doi.org/10.1029/2022EF002814, 2022.

Schubert, S. D.: On the Cause of the 1930s Dust Bowl, Science, 303, 1855–1859, https://doi.org/10.1126/science.1095048, 2004.

Schultz, G. E.: Clarendonian and Hemphillian Vertebrate Faunas from the Ogallala Formation (Late Miocene-Early Pliocene) of the Texas Panhandle and Adjacent Oklahoma, in: Geologic framework and regional hydrology: Upper Cenozoic Blackwater Draw and Ogallala Formations, Great Plains, edited by: Gustavson, T. C., Bureau of Economic Geology, The University of Texas, Austin, TX, 56–97, https://store.beg.utexas.edu/symposia/3521-sp0006.html (last access: 20 April 2024), 1990.

Seager, R., Feldman, J., Lis, N., Ting, M., Williams, A. P., Nakamura, J., Liu, H., and Henderson, N.: Whither the 100th Meridian? The Once and Future Physical and Human Geography of America's Arid–Humid Divide. Part II: The Meridian Moves East, Earth Interact., 22, 1–24, https://doi.org/10.1175/EI-D-17-0012.1, 2018a.

Seager, R., Lis, N., Feldman, J., Ting, M., Williams, A. P., Nakamura, J., Liu, H., and Henderson, N.: Whither the 100th Meridian? The Once and Future Physical and Human Geography of America's Arid–Humid Divide. Part I: The Story So Far, Earth Interact., 22, 1–22, https://doi.org/10.1175/EI-D-17-0011.1, 2018b.

Seni, S. J.: Sand-body geometry and depositional systems, Ogallala Formation, Texas, Bureau of Economic Geology, University of Texas, Report of Investigations, 105, 36, https://repositories.lib.utexas.edu/bitstreams/b4fbcaf5-33e6-415e-824e-e7be531c4eb7/download (last access: 24 April 2024), 1980.

Shapiro, A., Fedorovich, E., and Rahimi, S.: A Unified Theory for the Great Plains Nocturnal Low-Level Jet, J. Atmos. Sci., 73, 3037–3057, https://doi.org/10.1175/JAS-D-15-0307.1, 2016.

Siler, N., Roe, G. H., and Armour, K. C.: Insights into the zonal-mean response of the hydrologic cycle to global warming from a diffusive energy balance model, J. Climate, 31, 7481–7493, https://doi.org/10.1175/JCLI-D-18-0081.1, 2018.

Sjostrom, D. J., Hren, M. T., Horton, T. W., Waldbauer, J. R., and Chamberlain, C. P.: Stable isotopic evidence for a pre–late Miocene elevation gradient in the Great Plains–Rocky Mountain region, USA, in: Special Paper 398: Tectonics, Climate, and Landscape Evolution, Geological Society of America, 398, 309–319, https://doi.org/10.1130/2006.2398(19), 2006.

Skinner, M. F., Skinner, S., and Gooris, R.: Stratigraphy and biostratigraphy of late Cenozoic deposits in central Sioux County, western Nebraska, B. Am. Mus. Nat. Hist., 158, 263–370, 1977.

Smith, J. J. and Platt, B. F.: Reconstructing late Miocene depositional environments in the central High Plains, USA: Lithofacies and architectural elements of the Ogallala Formation, Sediment. Geol., 443, 106303, https://doi.org/10.1016/j.sedgeo.2022.106303, 2023.

Smith, J. J., Platt, B. F., Ludvigson, G. A., and Thomasson, J. R.: Ant-nest ichnofossils in honeycomb calcretes, Neogene Ogallala Formation, High Plains region of western Kansas, U.S.A., Palaeogeogr. Palaeocl., 308, 383–394, https://doi.org/10.1016/j.palaeo.2011.05.046, 2011.

Smith, J. J., Platt, B. F., Ludvigson, G. A., Sawin, R. S., Marshall, C. P., and Olcott-Marshall, A.: Enigmatic red beds exposed at point of rocks, Cimarron national Grassland, Morton county, Kansas: Chronostratigraphic constraints from uranium-lead dating of detrital zircons, Current Research in Earth Sciences: Kansas Geological Survey, 261, 1–17, http://www.kgs.ku.edu/Current/2015/Smith/index.html (last access: 19 April 2024), 2015.

Smith, J. J., Layzell, A., Lukens, W., Morgan, M., Keller, S., Martin, R. A., and Fox, D. L.: Getting to the bottom of the High Plains aquifer, in: Unfolding the Geology of the West, vol. 44, Geological Society of America, 93–124, https://doi.org/10.1130/2016.0044(04), 2016.

Smith, J. J., Ludvigson, G. A., Layzell, A., Möller, A., Harlow, R. H., Turner, E., Platt, B., and Petronis, M.: Discovery of Paleogene Deposits of the Central High Plains Aquifer In the Western Great Plains, U.S.A., J. Sediment. Res., 87, 880–896, https://doi.org/10.2110/jsr.2017.48, 2017.

Smith, J. J., Turner, E., Möller, A., Joeckel, R. M., and Otto, R. E.: First U-Pb zircon ages for late Miocene ashfall Konservat-Lagerstätte and Grove Lake ashes from eastern Great Plains, USA, PLoS ONE, 13, 1–19, https://doi.org/10.1371/journal.pone.0207103, 2018.

Smith, R. B.: The Influence of Mountains on the Atmosphere, Adv. Geophys., 21, 87–230, https://doi.org/10.1016/S0065-2687(08)60262-9, 1979.

Smith, R. B. and Barstad, I.: A Linear Theory of Orographic Precipitation, J. Atmos. Sci., 61, 1377–1391, https://doi.org/10.1175/1520-0469(2004)061<1377:ALTOOP>2.0.CO;2, 2004.

Song, F., Feng, Z., Leung, L. R., Houze Jr, R. A., Wang, J., Hardin, J., and Homeyer, C. R.: Contrasting Spring and Summer Large-Scale Environments Associated with Mesoscale Convective Systems over the U.S. Great Plains, J. Climate, 32, 6749–6767, https://doi.org/10.1175/JCLI-D-18-0839.1, 2019.

Sosdian, S. M., Greenop, R., Hain, M. P., Foster, G. L., Pearson, P. N., and Lear, C. H.: Constraining the evolution of Neogene ocean carbonate chemistry using the boron isotope pH proxy, Earth Planet. Sc. Lett., 498, 362–376, https://doi.org/10.1016/j.epsl.2018.06.017, 2018.

Stein, A. F., Draxler, R. R., Rolph, G. D., Stunder, B. J. B., Cohen, M. D., and Ngan, F.: NOAA's HYSPLIT Atmospheric Transport and Dispersion Modeling System, B. Am. Meteorol. Soc., 96, 2059–2077, https://doi.org/10.1175/BAMS-D-14-00110.1, 2015.

Steinthorsdottir, M., Coxall, H. K., de Boer, A. M., Huber, M., Barbolini, N., Bradshaw, C. D., Burls, N. J., Feakins, S. J., Gasson, E., Henderiks, J., Holbourn, A. E., Kiel, S., Kohn, M. J., Knorr, G., Kürschner, W. M., Lear, C. H., Liebrand, D., Lunt, D. J., Mörs, T., Pearson, P. N., Pound, M. J., Stoll, H., and Strömberg, C. A. E.: The Miocene: The Future of the Past, Paleoceanography and Paleoclimatology, 36, e2020PA004037, https://doi.org/10.1029/2020PA004037, 2021.

Stromberg, C. A. E.: Decoupled taxonomic radiation and ecological expansion of open-habitat grasses in the Cenozoic of North America, P. Natl. Acad. Sci. USA, 102, 11980–11984, https://doi.org/10.1073/pnas.0505700102, 2005.

Strömberg, C. A. E. and McInerney, F. A.: The Neogene transition from C_3 to C_4 grasslands in North America: assemblage analysis of fossil phytoliths, Paleobiology, 37, 50–71, https://doi.org/10.1666/09067.1, 2011.

Swann, A. L. S., Hoffman, F. M., Koven, C. D., and Randerson, J. T.: Plant responses to increasing CO_2 reduce estimates of climate impacts on drought severity, P. Natl. Acad. Sci. USA, 113, 10019–10024, https://doi.org/10.1073/pnas.1604581113, 2016.

Swinehart, J. B. and Diffendal Jr., R. F.: Duer Ranch, Merrill County, Nebraska : Contrast between Cenozoic fluvial and eolian deposition, in: Geological Society of America Centennial Field Guide–North-Central Section, edited by: Biggs, D., Geological Society of America, Charlottesville, VA, 23–28, https://doi.org/10.1130/0-8137-5403-8.23, 1987.

Swisher III, C. C.: ^{40}Ar / ^{39}Ar dating and its application to the calibration of the North American land mammal ages, PhD thesis, University of California, Berkeley, http://books.google.com/books?id=fX1LAQAAMAAJ (last accessed: 20 April 2024), 1992.

Tanner, T., Hernández-Almeida, I., Drury, A. J., Guitián, J., and Stoll, H.: Decreasing Atmospheric CO_2 During the Late Miocene Cooling, Paleoceanography and Paleoclimatology, 35, 1–25, https://doi.org/10.1029/2020PA003925, 2020.

Tedford, R. and Barghoorn, S. F.: Neogene stratigraphy and mammalian biochronology of the Española Basin, northern New Mexico, New Mexico Museum of Natural History and Science Bulletin, 2, 159–168, 1993.

Tedford, R. H.: Rocks and faunas, Ogallala Group, Pawnee Buttes area, Weld County, Colorado, in: The Tertiary record of Weld County, Northeastern Colorado, edited by: Evanoff, E., Tedford, R. H., and Graham, R. W., Denver Museum of Natural History, Denver, Colorado, 31–47, https://coloscisoc.org/wp-content/uploads/2018/09/Rocks_and_Faunas_Ogallala_Group_Pawnee_Buttes_Area_CO.pdf (last access: 20 April 2024), 1999.

Tedford, R. H., Albright, L. B., Barnosky, A. D., Ferrusquia-Villafranca, I., Hunt, R. M., Storer, J. E., Swisher, C. C., Voorhies, M. R., Webb, S. D., and Whistler, D. P.: Mammalian Biochronology of the Arikareean Through Hemphillian Interval (Late Oligocene Through Early Pliocene Epochs), in: Late Cretaceous and Cenozoic Mammals of North America, edited by: Woodburne, M. O., Chap. 6, Columbia University Press, New York, NY, USA, 169–231, https://doi.org/10.7312/wood13040-008, 2004.

Thomasson, J. R.: Late Cenozoic Grasses and Other Angiosperms from Kansas, Nebraska, and Colorado: Biostratigraphy and Relationships to Living Taxa, Kansas Geological Survey Bulletin 218, https://www.kgs.ku.edu/Publications/Bulletins/218/index.html (last access: 20 April 2024), 1979.

Ting, M. and Wang, H.: The Role of the North American Topography on the Maintenance of the Great Plains Summer Low-Level Jet, J. Atmos. Sci., 63, 1056–1068, https://doi.org/10.1175/JAS3664.1, 2006.

Trimble, D. E.: Cenozoic tectonic history of the Great Plains contrasted with that of the Southern Rocky Mountains: A synthesis, The Mountain Geologist, 17, 59–69, 1980.

van der Ent, R. J., Savenije, H. H. G., Schaefli, B., and Steele-Dunne, S. C.: Origin and fate of atmospheric moisture over continents, Water Resour. Res., 46, W09525, https://doi.org/10.1029/2010WR009127, 2010.

van Dijk, J., Fernandez, A., Bernasconi, S. M., Caves Rugenstein, J. K., Passey, S. R., and White, T.: Spatial Pattern of Super-Greenhouse Warmth Controlled by Elevated Specific Humidity, Nat. Geosci., 13, 739–744, https://doi.org/10.1038/s41561-020-00648-2, 2020.

Waterisotopes Database: Query: North Latitude =50, South Latitude = 26, East Longitude = −125, West Longitude = −85, Type= Groundwater, River or Stream, https://wateriso.utah.edu/waterisotopes/pages/spatial_db/SPATIAL_DB.html (last access: 20 August 2019), 2019.

Webb, W. P.: The Great Plains, Ginn and Company, Boston, MA, ISBN 0803297025, 1931.

Westerhold, T., Marwan, N., Drury, A. J., Liebrand, D., Agnini, C., Anagnostou, E., Barnet, J. S., Bohaty, S. M., De Vleeschouwer, D., Florindo, F., Frederichs, T., Hodell, D. A., Holbourn, A. E., Kroon, D., Lauretano, V., Littler, K., Lourens, L. J., Lyle, M., Pälike, H., Röhl, U., Tian, J., Wilkens, R. H., Wilson, P. A., and Zachos, J. C.: An astronomically dated record of Earth's climate and its predictability over the last 66 million years, Science, 369, 1383–1388, https://doi.org/10.1126/SCIENCE.ABA6853, 2020.

Wheeler, L. B. and Galewsky, J.: Atmospheric Flow Patterns Around the Southern Alps of New Zealand and Implications for Paleoaltimetry, Geophys. Res. Lett., 44, 11601–11605, https://doi.org/10.1002/2017GL074753, 2017.

Willett, S. D., McCoy, S. W., and Beeson, H. W.: Transience of the North American High Plains landscape and its impact on surface water, Nature, 561, 528–532, https://doi.org/10.1038/s41586-018-0532-1, 2018.

Winkler, D. A.: Stratigraphy, vertebrate paleontology, and deposition history of the Ogallala Group in Blanco and Yellowhouse Canyons, Northwestern Texas, PhD, The University of Texas at Austin, 243 pp., http://hdl.handle.net/2152/34167 (last access: 20 April 2024), 1985.

Winkler, D. A.: Vertebrate-bearing eolian unit from the Ogallala Group (Miocene) in northwestern Texas (USA), Geology, 15, 705–708, https://doi.org/10.1130/0091-7613(1987)15<705:VEUFTO>2.0.CO;2, 1987.

Winkler, D. A.: Sedimentary facies and biochronology of the Upper Tertiary Ogallala Group, Blanco and Yellowhouse canyons, Texas Panhandle, in: Geologic frame work and regional hydrology; Upper Cenozoic Blackwater Draw and Ogallala formations, Great Plains, edited by: Gustavson, T. C., The University of Texas at Austin, Bureau of Economic Geology, Austin, TX, 39–55, https://store.beg.utexas.edu/symposia/3521-sp0006.html (last access: 20 April 2024), 1990.

Winnick, M. J., Chamberlain, C. P., Caves, J. K., and Welker, J. M.: Quantifying the isotopic "continental effect", Earth Planet. Sc. Lett., 406, 123–133, https://doi.org/10.1016/j.epsl.2014.09.005, 2014.

Zhang, L., Hickel, K., Dawes, W. R., Chiew, F. H. S., Western, A. W., and Briggs, P. R.: A rational function approach for estimating mean annual evapotranspiration, Water Resour. Res., 40, 1–14, https://doi.org/10.1029/2003WR002710, 2004.

Zhang, P., Molnar, P., and Downs, W. R.: Increased sedimentation rates and grain sizes 2–4 Myr ago due to the influence of climate change on erosion rates, Nature, 410, 891–897, https://doi.org/10.1038/35073504, 2001.

Zhou, W., Leung, L. R., and Lu, J.: Seasonally dependent future changes in the US Midwest hydroclimate and extremes, J. Climate, 35, 17–27, https://doi.org/10.1175/jcli-d-21-0012.1, 2021a.

Zhou, W., Leung, L. R., Song, F., and Lu, J.: Future Changes in the Great Plains Low-Level Jet Governed by Seasonally Dependent Pattern Changes in the North Atlantic Subtropical High, Geophys. Res. Lett., 48, e2020GL090356, https://doi.org/10.1029/2020GL090356, 2021b.

Zhu, L., Fan, M., Hough, B., and Li, L.: Spatiotemporal distribution of river water stable isotope compositions and variability of lapse rate in the central Rocky Mountains: Controlling factors and implications for paleoelevation reconstruction, Earth Planet. Sc. Let., 496, 215–226, https://doi.org/10.1016/j.epsl.2018.05.047, 2018.